

**ELEVENTH INTERNATIONAL CONFERENCE
ON COMPOSITE MATERIALS**

**Gold Coast, Queensland, Australia
14th - 18th July 1997**

PROCEEDINGS

VOLUME IV

**COMPOSITES PROCESSING
AND MICROSTRUCTURE**

**Editor
Murray L. Scott**

**AUSTRALIAN COMPOSITE STRUCTURES SOCIETY
WOODHEAD PUBLISHING LIMITED**

TABLE OF CONTENTS

Processing

RTM Processing of High Performance Composites	1
<i>Walter Krenkel, Volkmar Dollhopf</i>	
The Role of Voids in Reducing the Interlaminar Shear Strength of RTM Laminates	11
<i>A.A. Goodwin, C.A. Howe, R.J. Paton</i>	
The Permeability of Glass Fiber Mat and its Influence on the Filling Time of RTM Process	20
<i>Yulu Ma, Xiaobin Hu, Dongdi Wu</i>	
Analysis of Resin Transfer Molding Process with Progressive Resin Injection	27
<i>Moon Koo Kang, Woo Il Lee</i>	
Effects of Microwave Resin Preheating on the Quality of RTM Laminates	37
<i>M.S. Johnson, C.D. Rudd, D.J. Hill</i>	
A Comparison Between Voids in RTM and Prepreg Carbon/Epoxy Laminates	46
<i>C.A. Howe, R.J. Paton, A.A. Goodwin</i>	
Resin Transfer Moulding for Missile Shroud Production	55
<i>J. Ludick</i>	
RTM Processing of GRP-Phenolic Composites	64
<i>Nigel A. St John, James R. Brown, Mark W. Taylor, Karen E. Challis</i>	
Resin Transfer Molding of Complex Textile Composite Components	75
<i>V. Sarma Avva, Robert L. Sadler, Kunigal N. Shivakumar, James R. Campbell</i>	
Automated Fabrication of High Performance Composites: an Overview of Research at the Langley Research Center	85
<i>N.J. Johnston, T.W. Towell, J.M. Marchello, R.W. Grenoble</i>	
Design of Experiments Analysis of the On-Line Consolidation Process	92
<i>Po-Jen Shih, Alfred C. Loos</i>	
Design and Manufacturing Study for a Small, Complex Component Required in Large Production Volumes	103
<i>K.D. Potter, A. Towse, M.R. Wisnom</i>	
A New Impregnation Tool for On-Line Manufacturing of Thermoplastic Composites	113
<i>A. Lutz, R. Funck, T. Harmia, K. Friedrich</i>	
Simulation of Temperature and Curing Profiles in Pultruded Composite Rods	123
<i>Basuki R. Suratno, Lin Ye, Yiu-Wing Mai</i>	
The Use of a Small Pultruder for Specimen Preparation	133
<i>John O. Outwater</i>	
Characterisation and Modelling of the High Speed Pultrusion of Commingled Glass Fibre/Polypropylene Composites	139
<i>A. Miller, A.G. Gibson</i>	
Numerical Modelling of Resin Cure Using a General Purpose FE Package	150
<i>S.C. Joshi, Liu Xiao-Lin, Y.C. Lam</i>	
Curing of Composite Prepreg Laminates by Resistance Heating of Internal Carbon Veils	161
<i>Charles E. Bakis, Frank J. Bantell</i>	

Optimized Cure Cycle to Minimize Fiber Stresses in Polymer Matrix Composites	171
<i>Mohamed S. Genidy, Madhu S. Madhukar, John D. Russell</i>	
Bisallyoxyimides- New Co-Reactants for Bismaleimides	181
<i>T.C. Morton, B. Dao</i>	
Curing and Deformation Analysis in SMC Compression Molding	190
<i>Hiroyuki Hamada, Keigo Futamata, Hajime Naito</i>	
Influence of Filler on SMC Roll Forming	200
<i>Tsutao Katayama, Kazumasa Kurokawa, Masahiro Shinohara, Yuuzou Hayakawa, Masahiro Hakotani</i>	
Impregnation of Thermoplastic Composites Manufactured by Double Belt Press Technique	210
<i>Xiaoming Wang, Christoph Mayer, Manfred Neitzel</i>	
Use of Optical Fiber Sensors in Autoclave Molding of GFRP Laminates	217
<i>Jianye Jiang, Katsuhiko Osaka, Takehito Fukuda, Shinya Motogi, Hisashi Tsukatani, Shintaro Kitade</i>	
Permeability of Fiber Reinforcements After Shear Deformation	227
<i>Chyi-Lang Lai, Wen-Bin Young</i>	
Wetting and Consolidation of Nylon 6 Powder Coated Carbon Fiber Tow	237
<i>M. Rammoorthy, J. Muzzy</i>	
Manufacture of Thermoplastic Towpregs by Using the Aqueous Foam Technique	246
<i>Manoj Kashiramka, Youqi Wang</i>	
The Elastic Stress in a Fibre Network Impregnated with Molten Polypropylene	255
<i>Colin Servais, Staffan Toll, Jan-Anders E. Månson</i>	
Blends of Poly (Ethylene Terephthalate) and Epoxy Resin as a Matrix Material for Continuous Fibre-Reinforced Composites	263
<i>A. Saalbrink, M. Mureau, T. Peijs</i>	
Electron Beam Cure of Composites for Aerospace Structures	271
<i>Allan S. Crasto, Ran Y. Kim, Brian P. Rice</i>	
A New Technique for the Preparation of Polyethylene Fibre/Polyethylene Matrix Composites and the Resulting Mechanical Properties	279
<i>F. v. Lacroix, M. Werwer, K. Schulte</i>	
Basic Principles of Filament Winding	288
<i>Leng Xingwu, Wo Dingzhu</i>	
Manufacture and Evaluation of Continuous Fibre-Reinforced Metal Composites	293
<i>V.D. Scott, R.S. Bushby, A.S. Chen</i>	
Determination of Manufacturing Distortion in Laminated Composite Components	302
<i>D.W. Radford, T.S. Rennick</i>	
Compression Moulding of Sandwich Structures of GMTs and Co-Mingled Materials for Optimised Macro and Micro Mechanical Properties	313
<i>M.D. Wakeman, T.A. Cain, C.D. Rudd, R. Brooks, A.C. Long</i>	
Curing Strains Developed During the Manufacture of GRP Tubes	324
<i>J.F. Oosthuizen, W.H. Groenewald</i>	
Material Models for the Process Simulation of Thermoplastic Sandwich Forming	333
<i>Frank Möller, Martin Maier</i>	

Prediction of Damage Width in Laser Drilling of Printed Wiring Board Using FEM	343
<i>Toshiki Hirogaki, Eiichi Aoyama, Hisahiro Inoue, Hiromichi Nobe, Keiji Ogawa, Youji Kitahara, Tsutao Katayama</i>	
Numerical Analysis of Shape Fixability of Continuous Fibre Reinforced Thermoplastics	352
<i>R.J. Dykes, D.P.W. Horrigan, D. Bhattacharyya</i>	
Secondary Structure Effects on the Process-Induced Residual Stress Development of Cylinder Structure	360
<i>Yeong K. Kim, Scott R. White</i>	
Simulation of Mechanical Alloying in a Shaker Ball Mill with Variable Size Particles	370
<i>Dmitri Gavrilov, Oleg Vinogradov, William J.D. Shaw</i>	
The Effect of Thermoforming on the Tensile Strength of Unidirectional Discontinuous Aligned Fiber Composites	379
<i>Jens Schuster</i>	
Electrostatic Powder Spray Manufacture of Long Fiber Composite Materials for Injection Molding	389
<i>Mark S. Duvall, Nana Tzeng, Karthik Ramani</i>	
Squeeze Flow Testing of Polypropylene and Glass Mat Thermoplastics at Compression Moulding Strain Rates	400
<i>J.H. Bland, H.E.N. Bersee, A.G. Gibson</i>	
The Drape Forming of a Rudder Tip Preform	411
<i>Paul Andrews, Rowan Paton, John Wang</i>	
The Effect of Aged Materials on the Autoclave Cure of Thick Composites	422
<i>Evan A. Kempner, H.Thomas Hahn, Hoon Huh</i>	
Issues in Modeling Discontinuous Random Fiber SRIM Composites	431
<i>O. Ochoa, T. Eason</i>	
Key Factors Affecting the Permeability Measurement in Continuous Fiber Reinforcements	441
<i>M.L. Diallo, R. Gauvin, F. Trochu</i>	
Preparation of Short Carbon Fiber Reinforced Polyphenylene Sulfide Composites by Impregnation in Suspension	452
<i>Xiao Wang, Jiarui Xu, Bingyuan Xie, Hanmin Zeng</i>	
The Fabric Cowoven with Peek and Carbon Fibre and their Composite	459
<i>Lou Kuiyang, Zhu Bo, Chen Xiangbao</i>	
Local and Non-local Rheological Equations for Fibre Reinforced Power Law Melts	465
<i>Staffan Toll, A. Geoffrey Gibson</i>	
An Air-Jet Compaction System for Draping and Consolidation in the Automated Manufacture of Composite Components	474
<i>Li Ma, Rodney A. Peck, Israel Herszberg, Sabu John</i>	
Press Forming of Glass Mat Reinforced Thermoplastic Sheet	482
<i>Yasunori Nakamura, Yoshikazu Kontani</i>	
The Development of Fiber-Reinforced Thermoplastic Polystyrene Composites for Pultrusion (I)	491
<i>Chin-Hsing Chen, Wen-Si Wang</i>	
Porosity Calculation of Mixtures of Fibrous Particles	500
<i>R.P. Zou, A.B. Yu, D.L. Xu</i>	

Flow Characterisation of Sheet Moulding Compounds (SMC)	510
<i>G. Kotsikos, A.G. Gibson</i>	
A Quantitative Investigation into the Effect of Processing Conditions and Moulding Thickness on Fibre Orientation in Short Fibre-Reinforced Thermoplastics	519
<i>C.Y. Hsu, R. Brooks</i>	
Cure Simulation Model for Resistance Cured Composites	528
<i>Renata S. Engel, Steven A. Weller</i>	
Surface Modification of Inorganic Ultrafine Particles by the Grafting of Polymers	537
<i>Norio Tsubokawa, Kazue Kawatsura, Yukio Shirai</i>	
Elastoplastic Finite-Element Analysis of Heat-Sealed Area in Laminated Plastic Film Used for Liquid Packaging Bags Under Different Temperatures	547
<i>E. Umezaki, Y. Kubota, A. Shimamoto, K. Futase</i>	
Characterising the Hot Drape Forming Process and the Effect of Fibre Shearing on the Mechanical Properties of Highly Draped Composite Components	559
<i>D. Standley</i>	
Blending Effect of Vinyl Ester Resin on the Epoxy Matrix System	569
<i>Jae-Rock Lee, Soo-Jin Park, Won-Bae Park</i>	

Fibres

Weibull Fibre Strength Parameters Determined by Single Fibre Fragmentation Tests	578
<i>Shiqiang Deng, Lin Ye, Yiu-Wing Mai, Hong-Yuan Liu</i>	
Characterisation of New Generation Small Diameter SiC Fibres at High Temperature	587
<i>N. Hochet, M.H. Berger, A.R. Bunsell</i>	
Modelling of Time-Dependence in Cellulosic Fibres Based on Raman Spectroscopy	598
<i>Wadood Y. Hamad</i>	
The Distribution Model of Whisker Aspect Ratio	608
<i>Xun Zhao, Jixiang Jiang, Bing Jiang, Guang Yang</i>	
Preparation of SiC Coated Carbon Fiber Based on Rayon Using PSI Processes	615
<i>Xiaodong Li, Ping Peng, Ge Wang, Xiuying Liu, Chunxiang Feng, Xiaozhong Huang, Yingchu He</i>	
Influence of Stiffness Increase on a Wavy Single Fiber Composite	623
<i>Piyush K. Dutta, Madhu S. Madhukar</i>	
Dynamic and Transient Characterization of Silicon Carbide Fibers at Elevated Temperatures	633
<i>R.C. Warren, C.D. Weaver, S.S. Sternstein</i>	
Production of Boron Carbide Fibers Using Boric Acid and Cellulose Fibers	643
<i>Y. Bohne, H.-P. Martin, E. Müller</i>	

Interphase and Interface

Characterization of Microphenomena in Composite Materials	652
<i>P.F.M. Meurs, P.J.G. Schreurs, T. Peijs</i>	

Prediction of Residual Stresses in Composites Interface by Finite Element Method	662
<i>Yong-Qui Jiang, Huo-Jun Fu</i>	
Interfacial Aspects of Fiber Reinforced Brittle/Ductile Matrix Composites Using Micromechanics Techniques and Acoustic Emission	671
<i>Joung-Man Park, Sang-H Lee, Dong-Jin Yoon, Dong-Woo Shin</i>	
Influence of the Sizing Interphase on the Static and Dynamic Behavior of Advanced Thermoplastic Composites	681
<i>C. Mayer, M. Neitzel</i>	
Interface Molecular Engineering of Carbon Fibre Composites	691
<i>D. Tripathi, A. Kettle, N. Lopattananon, A. Beck, F.R. Jones</i>	
A Study of the Tensile Failure Mode of Laser Micro-Perforated Carbon Fibre Reinforced Thermoplastics	701
<i>T.J. Matthams, T.W. Clyne</i>	
Effect of Interfacial Shear Debonding on the Tensile Strength and Reliability of Fibrous Composites : Finite Element Simulation	712
<i>Koichi Goda</i>	
Fibre/Matrix Adhesion in Thermoplastic Composites : Is Transcrystallinity a Key?	723
<i>Andrew Beehag, Lin Ye</i>	
Time Dependency of Microcrack Initiation and Evolution in Interlayer of Composite	731
<i>Y.Q. Sun, J. Tian</i>	
Interphase Between Carbon Fibre and Thermotropic Copolyester	741
<i>T. W. Shyr, J.G. Tomka, D.J. Johnson</i>	
Influence of Graphitization Processing Upon the Carbon-Carbon Composite Interfacial Properties	747
<i>Sun Wenxun, Huang Yudong, Zhang Zhiqian, Wang Junshan</i>	
The Modification of Carbon Fiber Surface of 3-D Woven Preform and its Effects on the Interfacial Bond Properties	754
<i>Huang Yudong, Feng Zhihai, Sun Wenxun, Gao Wen</i>	
Influence of Surface Treatment on the Dynamic-Mechanical Properties of Natural Fiber Reinforced Plastics	762
<i>Jochen Gassan, Andrzej K. Bledzki</i>	
Modified Epoxy Resin Matrix with Crosslinking State Unhomogeneity	771
<i>Shen Chao</i>	
Thermal Resistant Blends of Bismaleimide with Polyphenylene Oxide	779
<i>Zhi-yu Xia, Franklin G. Shin, Tze-chung Chan</i>	
A New Class of the Thermotropic Liquid Crystal Polymer: Poly(Aryl Ether Ketone)s	790
<i>Shanju Zhang, Yubin Zheng, Zhongwen Wu, Decai Yang, Ryutoku Yosomiya</i>	
Effect of Surface Treatment on Mode I Interlaminar Fracture Behaviour of Plain Glass Woven Fabric Composites: Report of a Round Robin Test I	798
<i>H. Saidpour, M. Sezen, Y.J. Dong, H.S. Yang, Y.L. Bai, T.X. Mao, C. Bathias, P. Krawczak, R. Bequignat, J. Pabiot, S. Pinter, G. Banhegyi, J.K. Kim, M.L. Sham, I. Verpoest, H. Hamada, Y. Hirai, K. Fujihara, C.Y. Yue, K. Padmanabhan, Y. Suzuki, K. Schulte, J.K. Karger-Kocsis, W.J. Cantwell, R. Zulkifli, L. Ye, A. Lowe, S.V. Hoa, V.V. Smirnov, L.T. Drzal, W.R. Broughton, J.J. Lesko, T. Tanimoto</i>	

Wear and Creep

Thermoplastic Composite Bearings: Tribological Properties as a Function of the Material Structure	808
<i>F. Haupt, K. Friedrich, R. Reinicke</i>	
Tensile Creep Property of Unsymmetrical and Multidirectional GFRP Laminates	816
<i>Ken Kurashiki, Masaharu Iwamoto, Shigetoshi Araki, Toshihiko Maesaka</i>	
Creep Dependence of the Conductivity of Steel Fiber Reinforced Polyphenylene Ether Resin	824
<i>Satoshi Somiya, Shigeki Katayama, Kazuo Igarashi</i>	
A Fibre Optic Acoustic Emission Sensor with Inherent Drift Compensation	833
<i>Anders Henriksson, Simon Sandgren, Pierre-Yves Fonjallas</i>	
Creep Study of FRP Composite Rebars for Concrete	844
<i>Piyush K. Dutta, David Hui</i>	
Study of Sliding Friction and Wear Properties of Bismaleimide and its Composite Against AL	856
<i>Qu Jianjun, Luo Yunxia, Zhang Zhiqian, Qi Yulin, Li Xiaoguang</i>	

RTM PROCESSING OF HIGH PERFORMANCE COMPOSITES

Walter Krenkel, Volkmar Dollhopf

DLR Institute of Structures and Design, Pfaffenwaldring 38-40 70569 Stuttgart, Germany

SUMMARY: Resin transfer moulding (RTM) has a high potential for the cost effective manufacture of net-shaped structures of continuous fibre reinforced polymer composites. The future application in primary structures requires the reliable processing of resins which polycondense during curing, resulting typically in a high release of gaseous products. The basic approach of this paper was directed towards the development of a technique applying a condensation-like polymer and fibre preforms of carbon, ceramic and quartz fibres with high fibre volume contents of 50 to 65 %, resulting in void-free composites which are competitive to autoclave processed parts. A RTM process has been established which allows the infiltration of fabrics of nearly any shape and contour. Processing details as well as mechanical properties which have been evaluated at temperatures up to 300° C are described.

KEYWORDS: resin transfer moulding, viscosity, polycondensation, polystyrylpyridine, 2D-fibre architecture, permeability

INTRODUCTION

The resin transfer moulding process is a well known technique for the injection of a liquid thermosetting resin matrix into a closed mould containing a positioned fibre preform of continuous fibres. Principally, the RTM technique is one of the most promising manufacturing processes for high performance composites with respect to costs, as expensive raw materials like prepregs are not necessary. Additionally, the process can be principally fully automatized e.g. by cutting the preforms with water jet or by stacking the preforms with roboters into the moulds. In the past, many investigations have been conducted concerning numeric modelling and simulations of the RTM process and manufacturing of prototypes. For that, specifically fabrics with low flow resistance and one-part epoxy resin systems, specially adapted to RTM conditions, have been developed [1,2].

Nevertheless, to compete with other composite manufacturing routes and to enter the civil engineering market with composite primary structures, high fibre volume fractions of more than 50 % of commercially available fabrics must be achieved via RTM. Additionally, high temperature matrix systems, often cured via a polycondensation reaction, must be available as resins of low viscosity. Resins, which polycondense during curing, result typically in a high release of gaseous products, which consequently lead to a more or less porous matrix when processing in a closed mould, resulting in poor mechanical properties.

In this study, the resin polystyrylpyridine (PSP) has been chosen to establish a RTM technique which should solve these problems exemplarily and, demonstrate that high performance composites with nearly void-free matrices and high fibre volume contents can be fabricated reproducibly. PSP resin, prepared from the polycondensation reaction of a methylated pyridine and aromatic dialdehyde, was originally developed by the French company SNPE and modified by Dow Chemical [3,4]. This commercially available polymer exhibits excellent thermomechanical properties and very good flame resistance but failed to attract widespread commercial application because it requires a long cure schedule and evolves volatiles during the polycondensation curing. Nevertheless, this one-part polymer is an attractive candidate as a matrix system for structures of aero-engines and aircrafts.

MATERIAL DESCRIPTION AND MOULD DESIGN

Generally, the resin's viscosity should be as low as possible when infiltrating the highly packed array of fibres in the mould. This is desirable since high injection pressures may cause mould deformation or fibre wash-out, i.e. the reinforcement is washed away from its original position. The mould should be heated to a temperature where the resin reaches the desired viscosity. This is not necessarily the lowest possible one, since higher temperatures not only reduce the viscosity but also reduce the time of gelation. The key point for infiltration is therefore to determine a mould temperature providing a viscosity as low as possible without causing premature gelation. During curing, polycondensation-like resins form volatile by-products like vapour which may lead to a high content of voids in the finished composites. As a consequence, the curing pressure must be beyond the vapour pressure, resulting in stiff and tight moulds of steel.

At room temperature, neat PSP resins are solid with a density of 1.14 g/cm^3 . When increasing the temperature, the viscosity of the resin decreases drastically and reaches the lowest value of about 15 mPas at 200°C . The time remaining at this viscosity amounts to 30 minutes which seems to be sufficient for the infiltration of even large and complex shaped reinforcements.

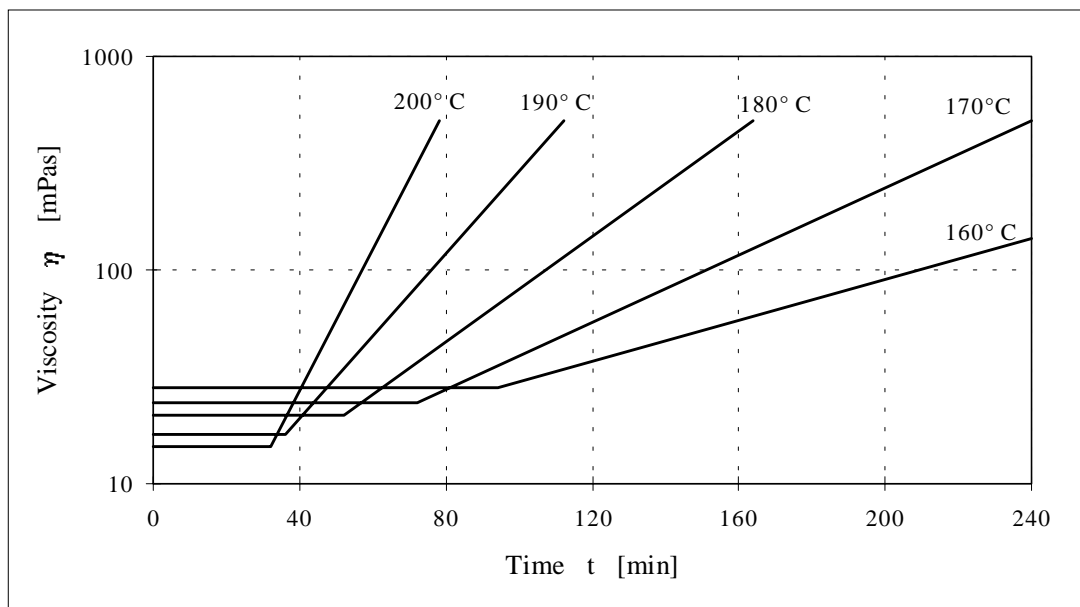


Figure 1: Viscosity of PSP resin at constant temperatures after heating-up with 2 K/min

Nevertheless, lower levels of constant temperatures combined with a higher viscosity increase the time of injection considerably (Fig. 1). As a good compromise between low viscosity and long infiltration time, a infiltration temperature of 170° C was chosen for all studies.

Commercial 2D-fabrics of carbon, ceramic and quartz fibres have been used as reinforcement (Table 1). The carbon fibres were evaluated in all common modifications of high tenacity (HT), intermediate modulus (IM) and high modulus (HM), representing typical reinforcements for structural CFRP components. Ceramic and quartz fabrics were investigated with three different types of fibres as possible reinforcements for composites with more functional properties, i.e. in radome applications. The number of filaments, the fibre radii and the areal weight in terms of gram per m² differ considerably for all materials. As a result, a variable number of fabric layers were necessary to keep the fibre volume contents relatively constant in the mould.

Table 1: Typical data of woven fabrics used as reinforcements

Material	Fibre Type	Weaving Mode	Filament Number	Fibre Radius [µm]	Areal Weight [g/m ²]	Fibre Density [g/cm ³]
Carbon	Akzo HTA	Plain	3000	3.5	245	1.76
	Toray T800	Plain	6000	2.5	270	1.81
	Toray M40	Twill 2/2	3000	3.25	200	1.81
Ceramic	Nicalon NL 207	Plain	500	7	275	2.55
	Ube Tyranno Lox M	Plain	1600	5	260	2.37
Quartz	Ciba Lyvertex 20766	8 H Satin	68	7.5	290	2.32

A composite panel size of 300 x 300 x 3 mm³ was selected to be suitable for principal investigations. An injection mould has been manufactured, designed as a two-chamber mould with an integrated reservoir for heating-up the resin as well as the fibres simultaneously before infiltration. The RTM mould was fabricated out of a steel alloy to ensure durability and to allow high internal pressures without any essential deformations. To protect the steel against acid agents while curing, the mould was coated with chromium as a corrosion-resistant surface coating. The mould was tightened with plates and covered with electric cartridge heat elements and insulation packages of glass felts to ensure a homogeneous temperature distribution within the total mould. A cross-view of the RTM-mould is depicted in Fig. 2, showing the basic elements of this injection tool.

For impregnation, the dry preform of fibre reinforcement was arranged into the fibre chamber, whereas the solid resin was placed into the resin chamber, both connected by a tubular channel. After closing the mould the total arrangement was set up vertically as shown in Fig. 2. Two valves, each on the top of the two chambers, ensured the flow of the resin into the fibre chamber after reaching the infiltration temperature. The valve in the resin chamber was connected with a tank of pressured nitrogen to facilitate the injection as well as to apply the necessary pressure while curing. The ventilation port at the rear side of the fibre chamber was connected with a vacuum pump to evacuate air and volatiles before and during infiltration.

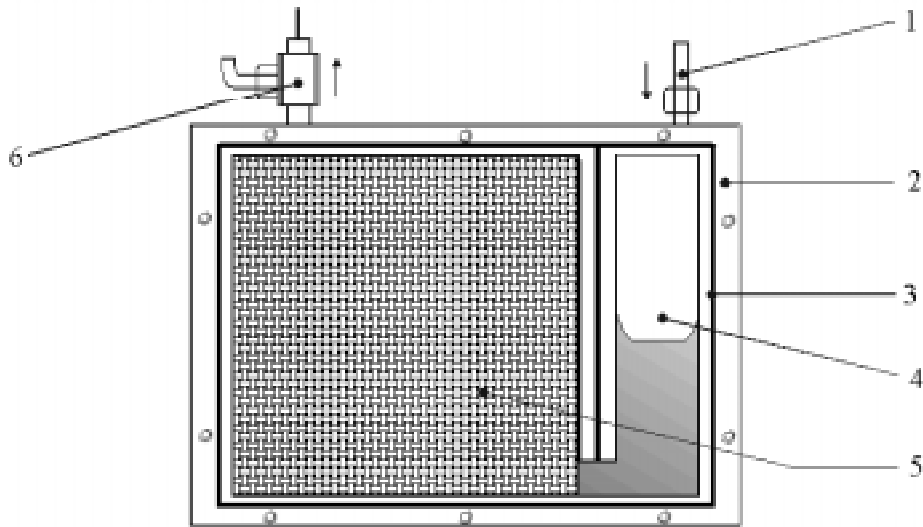


Figure 2: Two-chamber RTM-mould

- | | |
|---------------|--------------------|
| 1 Gas inlet | 4 Resin chamber |
| 2 Steel frame | 5 Fibre chamber |
| 3 Sealing | 6 Ventilation port |

As the resin was embedded before melting and as the mould was hermetically gas tight except the valves, any exposure of workers to chemicals and toxic volatiles could be excluded. This was one essential goal of the mould design ensuring a high process safety and acceptance for a future usage as a medium to high volume production facility.

PROCESSING PARAMETERS

The resin flow through a three dimensional fibrous preform can be described by Darcy's law in vectorial form :

$$\underline{V} = -\frac{1}{\eta} \cdot \underline{K} \cdot \nabla p \quad (1)$$

where η is the viscosity, p the pressure, \underline{V} the infiltration velocity and \underline{K} the tensor of permeability. If one considers the vertical position of the mould and assumes a horizontal resin front, which is constant over the preform's thickness, the infiltration kinetics can be written one-dimensional as

$$V = -\frac{1}{\eta} \cdot \frac{k}{L} \cdot \Delta p \quad (2)$$

where L is the length of the preform and k the permeability in the direction of infiltration. The macroscopic flow in the mould is governed mainly by the geometry of the fibre architecture, i.e. by the fibre volume content Φ and the fibre radius r [5,6]. The permeability k can then be expressed by the formulation of Carman and Kozeny

$$k = \frac{r^2}{4 \cdot K_z} \left(\frac{(1-\phi)^3}{\phi^2} \right) \quad (3)$$

with K_z as the Kozeny constant.

This equation indicates for example that for fibre contents of 100 % or for infinitively small fibres, respectively, the permeability leads theoretically to zero. Vice versa, the infiltration velocity increases with thicker fibres and lower fibre volume contents. Practically this means that fibre preforms made of T800 fibres show half of the infiltration velocity of HTA preforms with the same fibre content, because of their by 30 % thinner fibre radius (see Table 1).

To validate the theory, a number of tests have been conducted. In several pre-tests the permeability constant k has been determined experimentally for carbon fabrics. With HTA plain woven fabrics of 61 % fibre content, k amounts to $1.63 \cdot 10^{-11} \text{ m}^2$, corresponding to a Kozeny constant K_z of

$$K_z = 0.03$$

Assuming, that this is a material constant for this kind of preform and mould, the dependance of k on fibre radius r and fibre volume content ϕ can be determined according to equation (3). Fig. 3 shows this relationship for technical relevant values of r and ϕ in general.

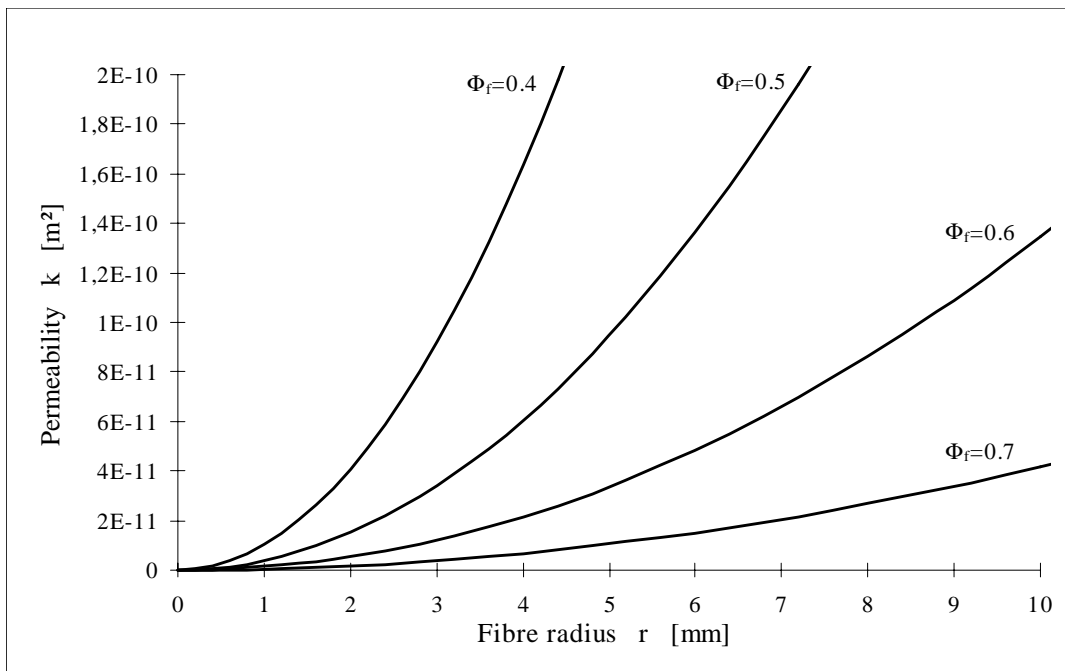


Figure 3: Relationship between permeability and fibre volume content and fibre radius, respectively, for HTA carbon preforms

With these results, an estimation of a suitable RTM cycle in terms of pressure difference Δp and the infiltration time t for a complete preform impregnation can be conducted. By transformation of equation (2) one obtains the equation for the pressure difference between the two ends of the preform

$$\Delta p = \frac{L^2 \cdot \eta}{2 \cdot k \cdot t} \quad (4)$$

Fig. 4 shows graphically for three distinct viscosities, that low pressures below 1 bar can only be achieved with long infiltration times of up to 30 minutes for HTA preforms of the required impregnation length of 300 mm. Considerably faster impregnations within 10 minutes are possible with preforms of fibre contents lower than 60 % and applied pressures up to 10 bar.

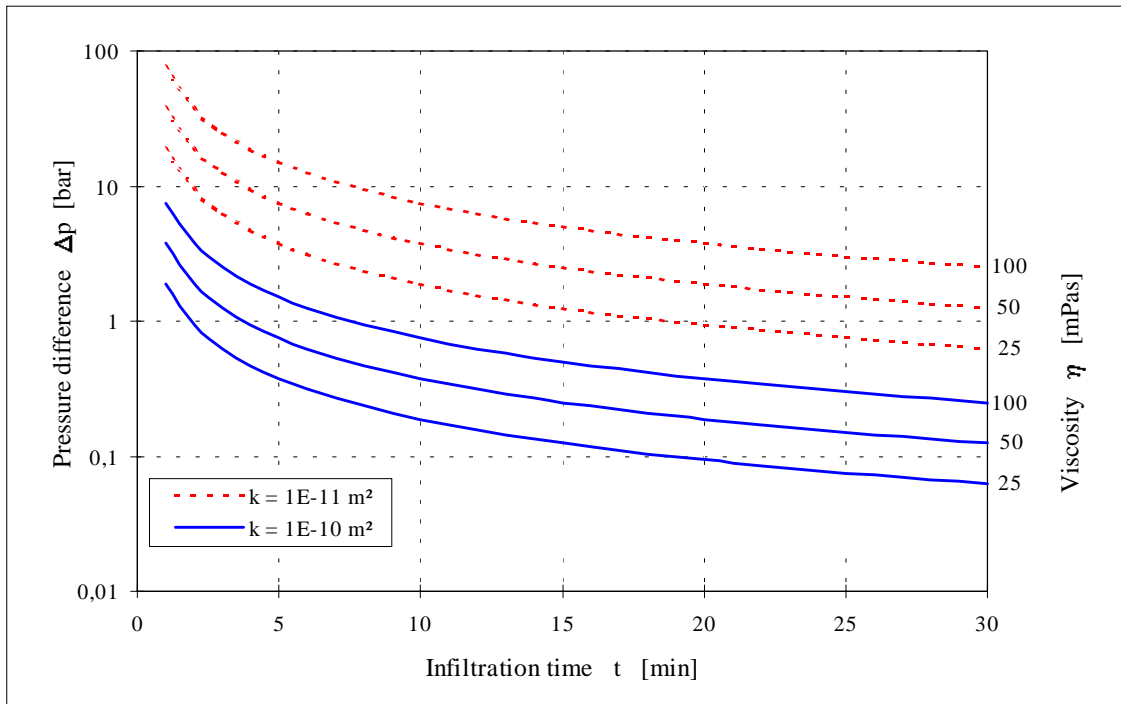


Figure 4: Required pressure difference Δp vs infiltration time t for the impregnation of HTA carbon fibre preform of 300 mm in length

These calculations and the rheological properties of PSP resin lead to a RTM manufacturing cycle which has been standardized for all investigations, i.e. each fabric was infiltrated with the same process parameters. Generally, this process can be divided into four major steps:

- Melting of the resin in the heated mould,
- Infiltration of the preform at 170° C under low pressure,
- Degassing of condensates between 170° C and 208° C,
- Polymerisation under high pressure (21 bar).

Prior to infiltration, woven fabrics were cut to size and reliably stacked into the fibre chamber to obtain controlled fibre volume contents of 50-65 %. Orthotropic as well as quasi-isotropic lay-ups have been examined. After sealing and closing the mould, both chambers were heated up simultaneously with a rate of 2 K/min up to 170° C without any pressure. The duration of infiltration depended on the permeability of the fabric and the applied pressure difference, which was determined from the process simulation parameters. In all cases, the mould temperature increased after 30 minutes with a heating rate of 0.5 K/min up to the curing temperature of 208° C. During this period, the ventilation port of the fibre chamber was open to allow volatiles to escape. Polymerisation was conducted at 21 bar, i.e. beyond the vapour pressure of water at this temperature. The composite panels were cured for 8 hours at 208° C within the mould. After cooling they were removed from the mould and partly post-cured in

an oven at 240° C for 8 hours. Fig. 5 shows the main steps of the selected RTM cycle in combination with the curve of the resin's viscosity.

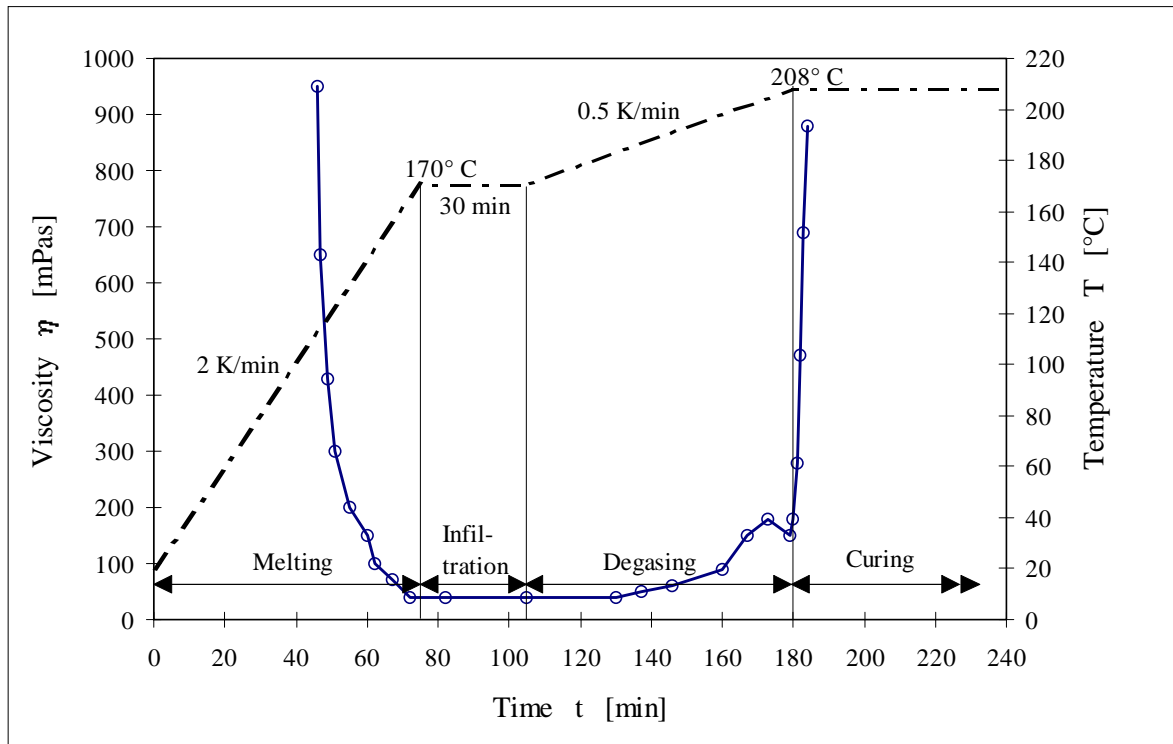


Figure 5: Manufacturing cycle for the resin transfer moulding of PSP resin into woven fabrics

EXPERIMENTAL RESULTS

After curing and post-curing, respectively, the microstructure of the composites has been examined by SEM microscopy. Typically, only cured samples showed a matrix which is nearly free of voids and encloses the fibre filaments with a high degree of regularity (Fig. 6).

The open porosity, measured via water absorption by the Archimedes method, lay in the range of 1 %, corresponding to a density of ca. 1.50 g/cm³ for carbon fibres, 1.65 g/cm³ for the SiO₂-quartz fibre reinforcements and 1.75 g/cm³ for the composites reinforced with ceramic fibres.

After post-curing, a certain amount of transversal cracks occurred in the matrix, due to the mismatch of thermal elongations between fibres and the relatively brittle matrix. As a result, the open porosity was measured to be twice the one of the non-treated samples.

Mechanical tests have been conducted at temperatures up to 300° C to evaluate the thermal stability of the composites. In place of all fibre variations, only carbon fibre reinforced composites will be described in the following. All post-cured samples showed relatively constant levels over the temperature concerning short beam strength with the lowest values for HM fibres (Fig. 7). The post-curing treatment led to a strong and stable bonding between the carbon fibres and the matrix, even at high temperatures.

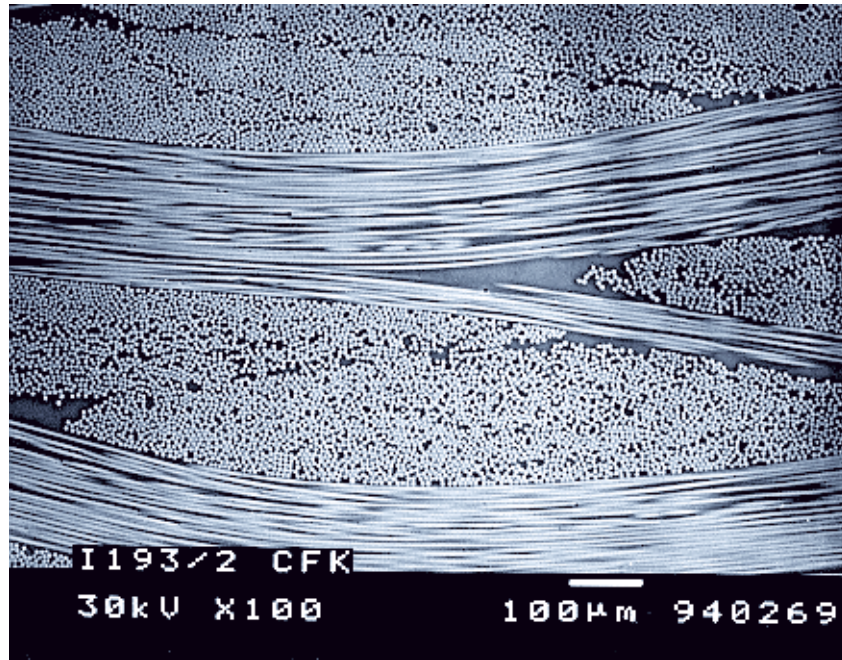


Figure 6: SEM micrograph (100 x) of a CFRP composite with 57 % fibre volume content.

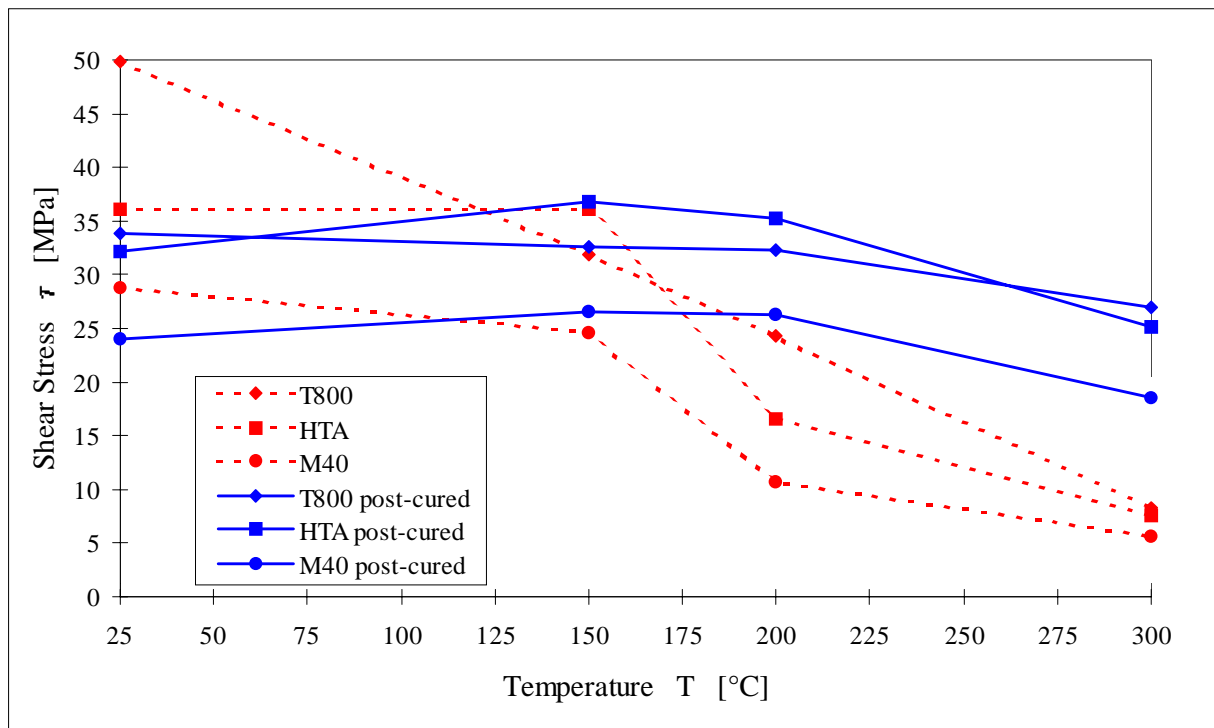


Figure 7: Interlaminar shear strength vs testing temperature of CFRP composites before and after post-curing at 240° C / 8 h

In contrast, only the cured samples showed a high degree of dependence on test temperature and fibre type. Differing widely at room temperature, all ILSS values at 300° C were far below the strength levels of post-cured materials at the same temperature indicating the necessity of the post-cure step after curing to get a composite of high thermal stability.

Additionally, plates with thicknesses of 1 to 30 mm (Fig. 8) as well as thin walled tubes of 300 mm length have been fabricated in similar moulds with the same RTM process. First prototypes with complex geometries like blades and vanes have been realized for demonstration purposes and have shown the feasibility of this RTM technology for the manufacture of high performance components in principal.

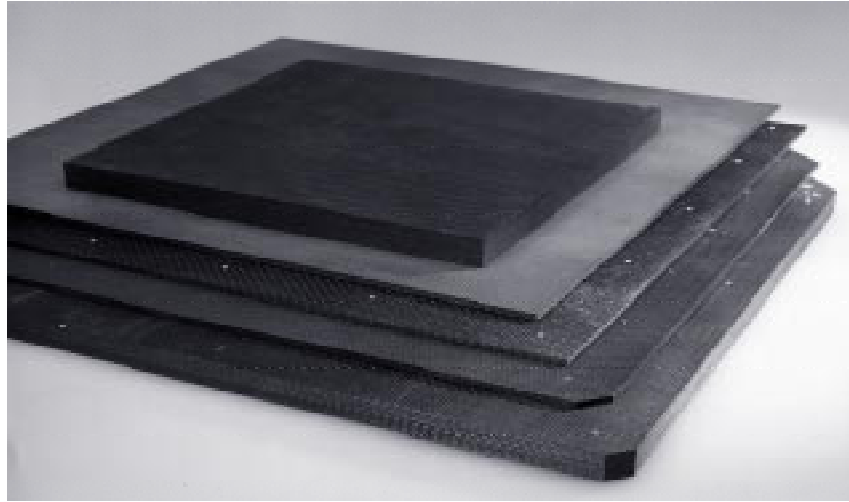


Figure 8: Examples of CFRP plates with various thicknesses, manufactured via RTM

CONCLUSIONS

A process for resin transfer moulding has been established using commercially available 2D-fibre fabrics and polystyrylpyridine resins. Carbon, quartz as well as ceramic fibres have been embedded in a mould of steel and impregnated with a RTM cycle, derived from numeric simulation models based on Darcy's law. A suitable design of the mould as the most critical step to achieve homogeneous and thermal stable matrices via condensation-like resins has been realised. Despite of the relatively long processing times and the still labour intensive manufacture, a RTM equipment is now available which allows the near-net shape fabrication of components with high fibre contents. These investigations demonstrated the suitability of the RTM technology for high performance composites in advanced aerospace and automotive structures.

REFERENCES

1. Thirion, J.-M., Girardy, H. and Waldvogel U., "New Developments for Producing High-Performance Composite Components by the RTM Process", *Composites*, N°3, 1988.
2. Sundsrud, G. J., "Advantages of a One-Part Resin System for Processing Aerospace Parts by Resin Transfer Moulding (RTM)", *European SAMPE*, Birmingham UK, Oct. 1993.
3. SNPE, "Chemistry of Polystyrylpyridine (PSP) Resins", *Datasheet*, 1985.
4. Earls, J. D., La Tulip, R. J., Robinson, J. W., "New High Temperature Styrylpyridine Resins", *17th National SAMPE Techn. Conf.*, Oct. 22-24, 1985.
5. Åström, B.T., "On Flow Through Aligned Fiber Beds and Its Application to Composite Processing", *Journal of Composite Materials*, Vol 26, N°9, 1992.
6. Brusckke, M.V., Advani, S.G., "RTM : Filling Simulation of Complex Three Dimensional Shell-Like Structures", *SAMPE Quarterly*, Oct. 1991.

THE ROLE OF VOIDS IN REDUCING THE INTERLAMINAR SHEAR STRENGTH IN RTM LAMINATES

A. A. Goodwin¹, C. A. Howe¹, R. J. Paton²

¹ *Department of Materials Engineering, Monash University,
Wellington Road, Clayton, Victoria, 3168, Australia*

² *Cooperative Research Centre for Advanced Composite Structures,
506 Lorimer Street, Fishermen's Bend, Victoria, 3207, Australia*

SUMMARY: Void shape, size and content were investigated in laminates containing two different carbon reinforcements, manufactured by resin transfer moulding (RTM). The effect of voids in each laminate system on the interlaminar shear strength was determined and a difference in the void-strength relationship between the two laminates was observed. The difference was correlated to the variation in void morphology, arising from the different pore-space geometries of the reinforcements. The fracture mechanism of the short beam shear test and the effect of voids on crack failure behaviour during this test were investigated. Cracks were observed to initiate from medium to large sized voids with sharp corners, but not from small spherical voids. Voids were also observed to affect the crack propagation path, with cracks terminating at voids.

KEYWORDS: voids, resin transfer moulding, fracture mechanisms, interlaminar shear strength

INTRODUCTION

The basic aim of the resin injection stage in resin transfer molding (RTM) is to completely fill a reinforcement preform with resin without the formation of defects. Defects can cause a reduction in the mechanical properties of polymer composites [1]. Defects common to the RTM laminate are commonly referred to as dry spots, voids or porosity [2]. A dry spot is defined as a region of preform that has not been filled by resin while porosity is primarily caused by the mechanical entrapment of air or volatiles [3-5]. This entrapment arises from the combination of an irregular resin flow front and obstructions within the reinforcement, such as crimps and stitches [5]. Leaks are a problem in vacuum-assisted RTM, allowing air to displace resin from the impregnated preform and thus creating voids.

Lundstrum *et.al.* have shown that voids formed within fibre tows have the shape of cylindrical tubes, while voids formed between tows resemble spherical bubbles [6]. The size and geometry of the free space located between fibre tows is a function of the fabric design and level of compaction within the preform. This free space influences the morphology of bubbles, which are not always spherical in shape. Therefore, RTM laminates with different reinforcements will have different void shapes and sizes. The mechanisms of void formation, the level of bubble transport during mould filling, and void stability during cure will

determine the distribution and content of voids within the laminate. Parameters such as injection pressure, vacuum assistance, resin viscosity and wet-out all influence void formation, stability and transport during the RTM process [3,6].

The effect of voids on the mechanical properties of polymer composites has been reported in a number of papers. Many researchers use the interlaminar shear strength test (ILSS) to investigate the effect of voids on the strength of a laminate. A comparison of published results shows a significant variation in the decrease in strength caused by void content. Ghiorse determined that the differences can be related to the accuracy of the void content measurement technique used [7]. Oliver *et.al.* showed how void size differences within prepreg laminates of identical void content can cause a difference in the extent of strength reduction [8] while Hancox suggested that void locations, shapes and sizes may influence the values of measured strengths [9].

While previous research studies have identified the general morphology of voids in RTM laminates, and other research studies have suggested that void morphology influences the level of strength reduction, there is a lack of research combining these two areas. The objectives of this study were to determine how different fabric types influence the size, shape and distribution of voids within carbon/epoxy RTM laminates, and how the nature of voids formed within the laminate affect the interlaminar shear strength. It is considered important to combine property data on void-strength effects with detailed investigations into the void location, shape and size for specific laminate systems to help determine the mechanism by which voids reduce the ILSS. Post-test optical image analysis studies of defective and non-defective RTM laminate coupons were also carried out to determine the types of failure cracks common to the ILSS test, and how such cracks interact with voids.

EXPERIMENTAL

Specimen Manufacture

Carbon/Epoxy Laminates

Two laminate systems were selected to determine the effect of void shape, size and location on the interlaminar shear strength. The difference between the laminates was the type of weave for the carbon reinforcement selected. Two 3K AS4 carbon fibre fabrics, supplied by Ciba Composites, a plain weave of 200 g/m² and a 5-harness satin weave of 285 g/m² were used. Figure 1 shows the weave geometry of each fabric type. The epoxy was a three part system (Araldite F), containing LY 556 resin, HY 918 hardener and DY 052 catalyst. The mix ratio was 100:90:1 (resin:hardner:catalyst). The fibre volume fraction was calculated as 57% for both laminates.

Laminate Manufacture

The laminates were manufactured by RTM using a pressure pot as the injection source. An aluminium mould base with cavity dimensions of 480 mm x 13 mm x 3.2 mm was used, with a toughened glass plate as the mould top. Resin was injected at one end of the mould, and air was removed from the opposite end. A partial vacuum (-80 kPa) was applied to the mould outlet during injection. The injection pressure was 200 kPa, and the mould temperature was 20°C. After injection the laminates were cured at 80°C for one hour.

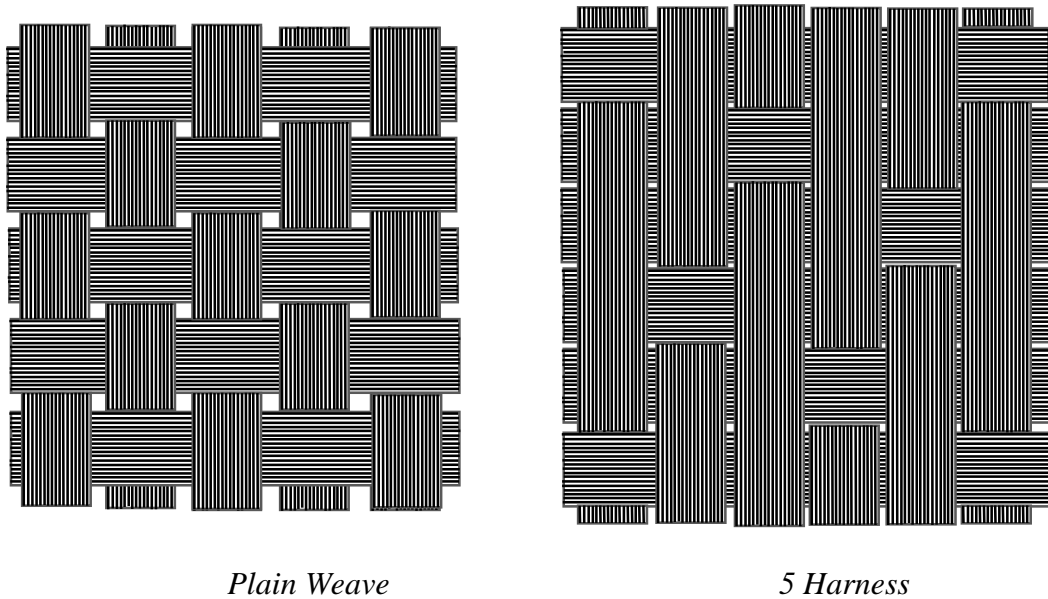


Fig. 1: Schematic diagram identifying reinforcement geometry for a plain weave and 5-harness carbon fabric

Defect (Void) Formation

Defective laminates were produced with varying levels of porosity content. This was achieved by intentionally producing a dry spot within the panel. The level of porosity around the perimeter of a dry spot varied from 0 to 20% void volume fraction (V_v). During the initial stages of injection the resin was allowed to “racetrack” around the perimeter of the preform. The resin reached the outlet before the preform was completely filled, resulting in the formation of an unfilled region. The inlet end of the panel was already completely filled out when the dry spot was originally formed. The porosity content within the inlet region of the panel was between 0 and 2% V_v . The flow front through the preform in this region of the panel was relatively smooth, with the resin flow front between the tows slightly ahead of the flow front within the tows. Any bubbles formed were flushed towards the flow front edge near the dry spot perimeter. When the dry spot was trapped, the flow front around it became slow and irregular, with resin leading within the tows. This led to the entrapment of voids between the tows around the perimeter of the dry spot. During the early stages of cure, the resin continued to move into the dry spot region within the tows, while porosity remained between the tows.

Void Content Determination

The void content, shape, size and location within a section of the laminate was determined by Optical Image Analysis. The image analysis system included a Reichart optical microscope, a Videk camera, a Videk Megaplus frame grabber, and a Macintosh computer with the image analysis software Image 1.58. Non-destructive Ultrasonic C-scan inspection was also used to determine the void content throughout a laminate panel. The equipment used was an Infometrics “Test Pro” system and a Meccasonic laboratory scanning tank. The Test Pro is a PC based ultrasonic testing instrument incorporating scanning frame control. Ultrasonic

signals were provided by a Panametrics receiver (model 5052PR), driving a 15MHz focused probe. The total system gain was 26 dB. The scanning grid was 1mm x 1mm.

In selecting an ILSS test coupon, a laminate section adjacent to it in the panel was used to estimate the void content of the mechanical test specimen. This was done by locating two adjacent samples which contained the same level of surface porosity and the same level of dB loss. The level of surface porosity was determined by OIA. The level of dB loss was determined by C-scan analysis. One of the adjacent sections, which had the same dimensions as the potential test coupon, was then cross-sectioned into three segments. The samples were mounted in polyester resin, and finely polished by an automatic Prepamatic polishing machine. The porosity content was determined at X32 magnification, with 6 random areas chosen from each of the three segments. The average of 18 measurements was calculated and taken to be the volumetric porosity content of the coupon.

Interlaminar Shear Strength Testing

The interlaminar shear strength test was conducted according to the short beam shear test method ASTM D2344. Fifty samples for each laminate system were selected from defective laminates, which contained varying porosity contents, to determine the effect of void content, size, shape and location on the interlaminar shear strength. The ILSS coupons were prepared by cutting with a diamond saw, and the sides polished with 400 wet and dry paper to remove any flaws caused by cutting. The tests were performed using an INSTRON 4505 mechanical testing machine. A 100 kN load cell was used, with the crosshead speed set at 1.3 mm/min. The dimensions of the specimens were 19.2 mm x 6.4 mm x 3.2 mm.

RESULTS AND DISCUSSION

Void Characterisation for Carbon/Epoxy Laminates

Void Shape

A comparison of the voids present in the two carbon fabric composites was made for the laminates containing less than 10% V_v porosity. In the plain weave laminate, the most common void shape observed between the tows was an elliptical bubble, as shown in Fig. 2. At the ply interface, the bubbles were observed to be linked, forming a much larger void, but this void tended to retain a symmetrical shape, with the corners avoiding a low radii of curvature. For the 5-harness weave laminate, the shape of voids located between tows ranged from elliptical to the more common asymmetric shaped void, as shown in Fig. 3. The radii of curvature of the asymmetric voids varied between 5 and 20 μm for the 5-harness fabric, compared with 35 to 110 μm for the elliptical bubbles observed in the plain weave fabric, as shown in Fig. 4. The higher irregularity in void shape for the 5-harness fabric compared to the plain weave fabric can be explained in terms of the fabric design.

The 5-harness fabric is a much tighter knit compared with the plain weave fabric, as shown in Fig. 1. The distance between adjacent fibre tows for the plain weave fabric is typically 0.5 mm, compared with 0.1 mm for the 5-harness fabric. The available space at a fibre tow intersection is larger than that between adjacent tows for both fabrics. A plain weave fabric contains five times more fibre tow intersections per ply than a 5-harness fabric. A plain weave fabric, therefore, would be expected to accommodate larger bubbles with more energetically

favourable shapes at fibre tow intersections. This was confirmed by through-thickness OIA of void-containing laminates.

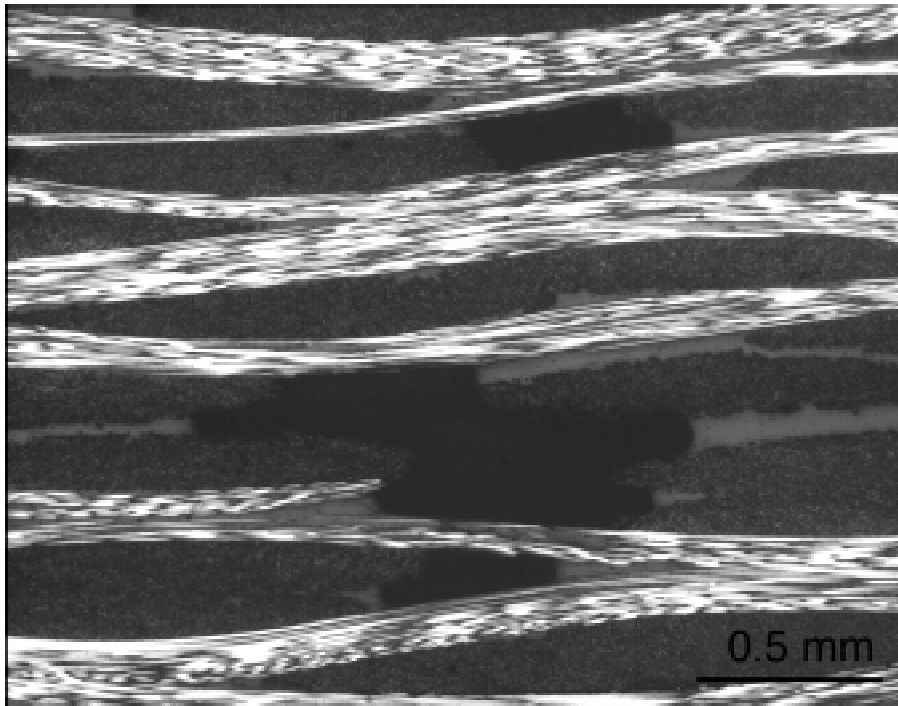


Fig. 2: Micrograph showing void morphology in the plain weave carbon laminate

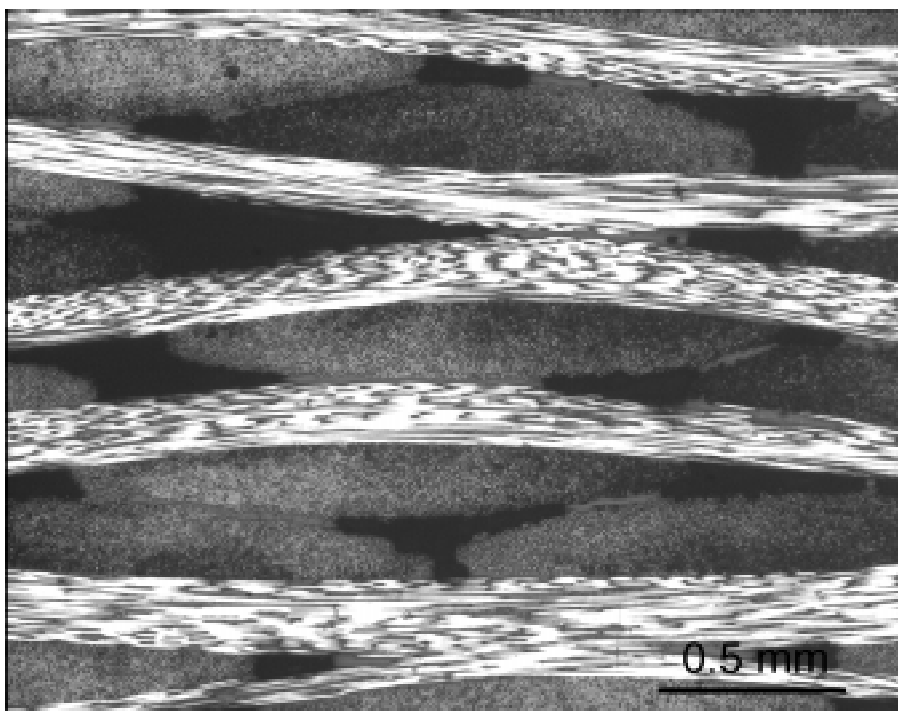


Fig. 3: Micrograph showing void morphology in the 5-harness carbon laminate

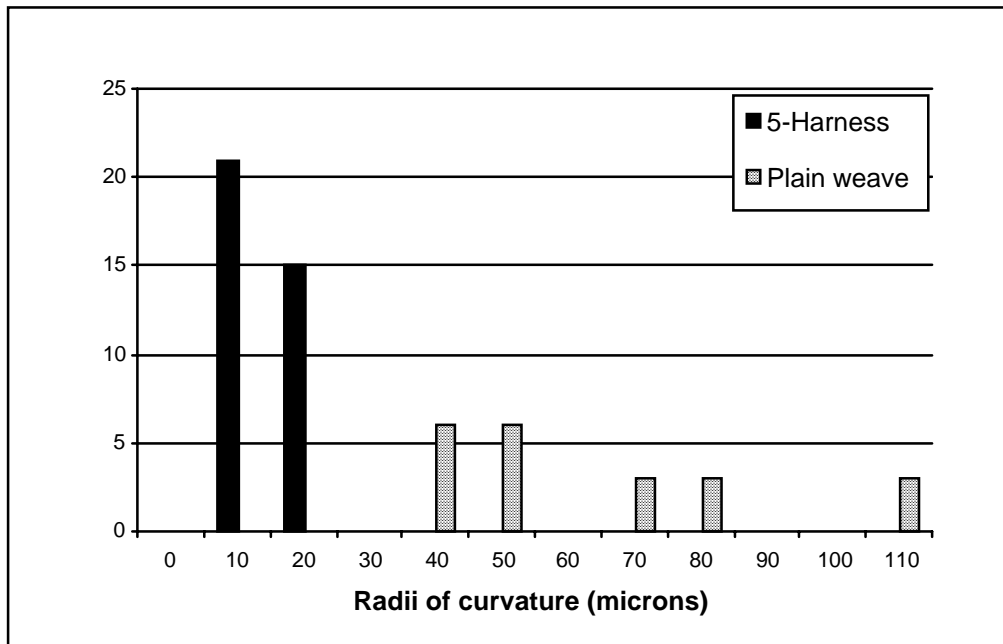


Fig. 4: Distribution of radii of curvature of voids located in the plain weave and 5-harness laminates

Void Size and Distribution

The size of each void was characterised by its cross-sectional area, for a known void content. This showed that the 5-harness composite contained a higher quantity and distribution of small voids (usually asymmetric in shape), than the plain weave laminate, which contained a higher level of medium to large voids, but a relatively low quantity of small voids.

The majority of the large voids within the plain weave laminate did not contain sharp corners. This contrasted with the 5-harness laminate where, within the 5 to 8.6% V_v range, the majority of the available pockets between tows were occupied by a sharp-cornered void.

For the plain weave fabric the size of voids which incorporated no more than two adjacent fibre tow intersections varied from 50 μm to 1.2 mm in length, and 20 to 500 μm in height. For the 5-harness fabric, the size of an equivalently positioned void ranged from 50 μm to 3 mm in length, and 20 to 350 μm in height. With a loose knit design, such as the plain weave fabric, voids had greater through-thickness linkage, while for the 5-harness fabric voids had greater in-plane linkage.

Effect of Porosity on ILSS for Carbon/Epoxy Laminates

Level of ILSS Reduction

Fig. 5 compares the effect of porosity on the interlaminar shear strength for the two different laminate systems. For the 5-harness fabric laminate the trend showed a 7% reduction in ILSS per 1% increase in porosity up to 10% V_v . The plain weave fabric laminate showed a 4% reduction in ILSS per 1% increase in porosity over this range.

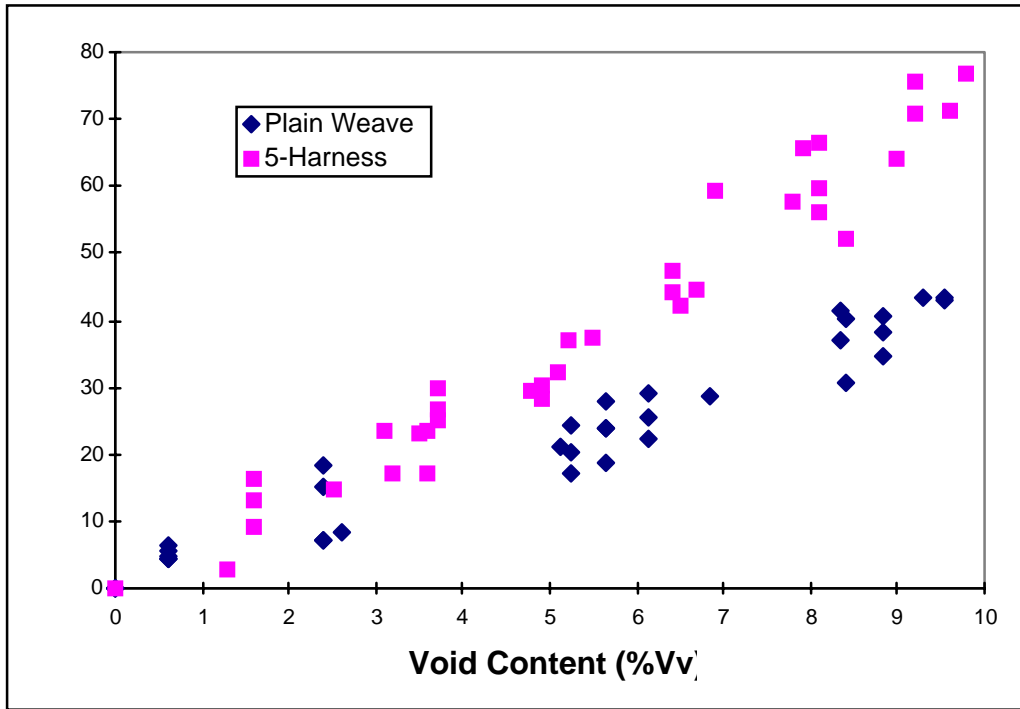


Fig. 5: Effect of porosity on ILSS for Carbon (5H,3K)/Araldite-F RTM laminate and for Carbon (plain weave, 3K)/Araldite-F RTM laminate

The failure of the short beam shear coupons tested in this study were mainly dependent on the formation of a series of inter- and intra-laminar cracks, rather than by one single crack. The effect of voids on reducing the strength of the laminate can be observed by its influence on crack failure. Intralaminar cracks were observed to initiate at voids, as seen in Fig. 6 [11]. These intralaminar cracks propagated to the ply interface, and were transformed into interlaminar cracks.

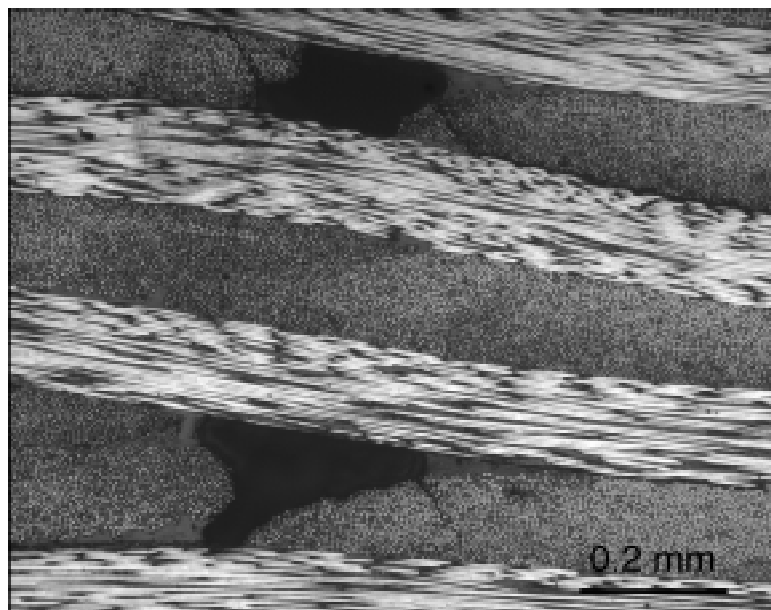


Fig. 6: Micrograph of failed ILSS coupon showing crack failure at voids.

The difference in the effect of porosity on the ILSS for the plain weave and 5-harness laminates, seen in Fig. 5, can be attributed to the void morphology, size, and distribution [8,9]. Firstly, the 5-harness fabric contains a higher level of asymmetric voids with corners of lower radii compared with the more symmetrically shaped elliptical voids within the plain weave composite. Voids of lower radii of curvature lead to higher stress concentrations [10]. Therefore, a crack is more likely to initiate at a sharp void than a smooth-cornered void. In addition, the voids in the 5-harness laminate were of greater length, which results in a higher stress intensification [11]. Furthermore, cracks are likely to be initiated in a 5-harness laminate at a lower applied stress due to the higher population and distribution of voids throughout the laminate.

Post-mortem Study of ILSS Coupons for Carbon/Epoxy Void-Free Laminates

Microcracks

Further analysis of ILSS carbon/epoxy composite beams showed the presence of resin microcracks at the initiation point of intralaminar and interlaminar cracks within the central region of the beam. It appeared that crack initiation occurred at the fibre/matrix interface, with the microcracks being oriented at 45° to the longitudinal fibres, and ultimately coalescing into larger intralaminar and delamination cracks. The form of these cracks were similar to those referred to as 'shear hackles' which are a fracture characteristic observed in mode II studies. They have been identified as a series of parallel platelets of fractured resin formed perpendicular to the maximum resolved tensile stress[12].

CONCLUSIONS

The main findings of this study were:

- The 5-harness laminates contained a greater number of small asymmetric voids than the plain weave laminates, which contained larger, spherical voids. This is attributed to the different reinforcement geometry and resulting 'free' space within the fabric .
- The reduction in ILSS for plain weave laminates was less than that of 5-harness laminates with comparable void content. This resulted from the greater numbers of cracks formed in the 5-harness laminates due to the higher population of sharp-cornered voids.
- Both intra and inter-laminar cracks formed during ILSS testing and resin microcracks were also observed. Voids acted to initiate cracks.

REFERENCES

1. Patel, N., Rohatgi, V., & Lee, L., "Void formation and removal in liquid composite moulding", *49th Annual Conference, Composite Institute, The Society of the Plastics Industry, Inc.* February 7-9, 1994, Session 10-D.
2. Parnas, R.S. & Phelan, "The effect of heterogeneous porous media on mold filling in resin transfer molding", *SAMPE Quarterly*, January (1991), pp. 53-60.

3. Hayward, J. S. & Harris, B., "Effect of process variables on the quality of RTM mouldings", *SAMPE Journal*, Vol. 26, No. 3 (1990), pp. 39-46.
4. Rohatgi, V, Patel, N. & James Lee, L., "Experimental investigation of flow- induced microvoids during impregnation of unidirectional stitched fiberglass mat", *Polymer Composites*, Vol. 17, No. 2 (1996), pp161-170.
5. Patel, N, Rohatgi, V. & James Lee, L., "Micro scale flow behaviour and void formation mechanism during impregnation through a unidirectional stitched fibreglass mat", *Polymer Engineering and Science*, Vol. 35, No. 10 (1995), pp.837-851.
6. Lundstrom, T.S., Gebart, B.R. & Lundemo, "Influence from process parameters on void formation in Resin transfer Molding", *Polymer Composites*, Vol. 15, No. 1 (1994), pp 25-33
7. Ghiorse, S.R., "Effect of void content on the mechanical properties of carbon/epoxy laminates", *SAMPE Quarterly*, January 1993, pp 54-59.
8. Oliver, P., Cottu, J.P., & Ferret, B., "Effects of cure cycle pressure and voids on some mechanical properties of carbon/epoxy laminates", *Composites*, Vol. 26, No. 7 (1995), pp 509-515.
9. Hancox, N. L., "The effects of flaws and voids on the shear properties of CFRP", *J. Mater. Sci.*, Vol 12 (1977), pp 884-92
10. Hull, D., *An introduction to composite materials*, Cambridge University Press, England (1981)
11. Wisnom, M. R., Reynolds, T. & Gwilliam, N., "Reduction in interlaminar shear strength by discrete and distributed voids", *Composites Science and Technology*, Vol 56 (1996), pp 93-101
12. Bascom, W. D. & Gweon, S. Y., "Fractography and Failure Mechanisms of Carbon Fiber-Reinforced Composite Materials", in *Fractography and Failure Mechanisms of Polymers and Composites*, edited by A. C. Roulin-Moloney, (Elsevier Applied Science, London (1989)), pp 351 -385

THE PERMEABILITY OF GLASS FIBER MAT AND ITS INFLUENCE ON THE FILLING TIME OF RTM PROCESS

Yulu Ma, Xiaobin Hu and Dongdi Wu

Research Institute of Process Equipment, East China University of Science and Technology, Shanghai, 200237, P. R. China

SUMMARY: Resin transfer molding (RTM) is an attractive process of fiber reinforced polymer composite manufacturing. The permeability of the preform or flow mobility is an important parameter which indicates all the detailed microscopic interactions between the fluid and the fiber preform architecture. It influences the flow of resin in the mold. This work took random distributed continuous glass fiber mat as an example which is widely used in RTM process, studied the relationship between preform permeability and fiber volume fraction in the mold. The influence of the preform architecture on the permeability and mold filling time as well as resin impregnation was analyzed. The relationship between permeability and mold filling time was investigated.

KEYWORDS: resin transfer molding, preform permeability measurement, polymer processing

INTRODUCTION

Resin transfer molding (RTM) is an attractive process for polymer composites manufacturing. In this process, a fiber preform of reinforcing material is placed in the mold. The mold is then closed, and the precured resin is injected into the mold. The resin impregnates the fiber preform and fills the mold where it cures to create a composite part.

The mold filling pattern for flow of a fluid through the fiber preform depends on a number of parameters. The part geometry, the location of the injection gates, injection pressures or flow rates are perhaps the most obvious ones. Another parameter which will influence the mold filling pattern is the structure of the fiber preform. Fiber preforms with different geometries or fiber arrangements will offer different resistance to the flow[1].

Most liquid composite molding (LCM) such as resin transfer molding (RTM) and structural reaction injection molding (SRIM) mold filling models apply Darcy's law in which the flow characteristic of the fabric reinforcement is represented by the permeability[2]. For one-dimensional flow of Newtonian fluids, the Darcy's law is given by

$$u = -\frac{k}{\mu} \frac{dp}{dx} \quad (1)$$

in which u is the volume averaged velocity in the porous medium, k is the permeability of the porous medium, μ is the viscosity of the fluid and $\frac{dp}{dx}$ is the pressure drop.

Although the permeability of simple fibrous structures such as unidirectional fibers with ideal packing can be predicted[3], most of commercially used fabric reinforcements do not have simple structure and their permeability has to be measured experimentally[4].

The random distributed continuous glass fiber mat is a kind of reinforcement which is widely used in RTM process. The measurement of its permeability will give a great help to the composites industry. In this work, the permeability of different volumes of random distributed continuous glass fiber mat reinforcement in the mold was measured. In order to compare the permeability between random distributed continuous glass fiber mat and other different structure reinforcement, the permeability of certain volumes of bi-directional woven fabric in the mold was measured too. The relationship between the permeability of glass fiber mat and the mold filling time was investigated, and the influence of the preform architecture on the permeability and mold filling time as well as resin impregnation was analyzed.

EXPERIMENTAL

Materials

The measurement liquid is DOP oil (diphenyl-octyl-phthalate). Its viscosity was a function of temperature and ranged from 0.038 to 0.050 Pa · s (38 to 50 cp) at room temperature. A vinyl-ester resin (MFE-2, Hua Chang Polymer Corporation, Shanghai) was used for analyzing the difference of the permeability and the mold filling time between random distributed continuous glass fiber mat and bi-directional woven fabric. The viscosity of the resin was 0.45 to 0.55 Pa · s(25°C, spinning viscosity meter) at room temperature.

The two types of glass fiber mats were random distributed continuous glass fiber mat of 450g/m² surface density (Nanjing Institute of Glass Fibers, Nanjing) and a bi-directional woven fabric of 283g/m² surface density (Yao Hua Glass Fiber factory, Shanghai).

Equipment

In this work, the one-dimensional flow experiments were conducted. A rectangular mold cavity was created by placing a 4 mm thick spacer between two platens of metal. The cavity dimension was 250×110×4 mm. The spacer was drilled at both ends to create an end gate and a vent directly across from the gate. The fiber mats were positioned in the mold cavity 10 mm from the inlet to leave the injection point uncovered. Thus, it eliminates radial flow and create a line source for axial flow. The liquid was forced through the molds from a pressure-pot system. The fluid flow was measured at a mold exit with volumetric measurements. The pressure was measured at the inlet with a pressure transducer.

Permeability Measurement

It is well known that many of the difficulties in the experimental permeability measurement of composite reinforcements lie in the cutting and handling procedures required to place the materials in the experimental molds [5]. Therefore, the fiber reinforcements are prepared and

placed in the mold very carefully in order to minimize the edge effect and achieve constantly reproducible results.

Assuming Darcy's law is valid during the mold filling, then the flow Q and pressure p data collected during the experiments were analyzed to get the permeability values. The surficial velocity u was computed by dividing the flow by the total cross sectional area of the fluid flow path A and the superficial velocity was then plotted as a function of the pressure gradient. According to the Darcy's law, the slop of a linear least squares fit of the data is k/η . The value used for the fiber volume fraction was the total preform weight divided by the approximate density of glass ($\approx 2.5\text{g/cm}^3$).

In the actual permeability measurement, because the flow leakage along the side of the fabric reinforcement, the effective permeability must be larger than the real values. In fact, the edge effect is unavoidable in the one-dimensional flow in the actual production. Therefore, here the effective permeability were measured.

If we want to account for the edge effect, the proposed method estimating the edge flow effect in Ref. 6 can be used. The method in Ref. 6 can be summarized as following. In the unidirectional flow measurement, in addition to the central region with bulk permeability k_c , the regions near the side walls are assumed to be with a different permeability k_e , as shown in Fig.1. Using two fiber samples with different widths, we can derive the following relationship,

$$\frac{Q_1 \mu L}{h p_1} = W_1 k_1 = 2W_e (k_e - k_c) + W_1 k_c \quad (2a)$$

$$\frac{Q_2 \mu L}{h p_2} = W_2 k_2 = 2W_e (k_e - k_c) = W_2 k_c \quad (2b)$$

where the subscripts 1 and 2 represent two different sample widths, and k_1 and k_2 are the effective permeabilities.

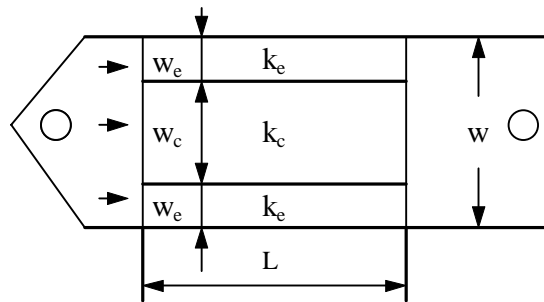


Fig. 1: Schematic of the edge flow effect in unidirectional flow

RESULTS AND DISCUSSIONS

In-plane Permeability of Random Continuous Fiber Mat

For random distributed continuous glass fiber mat, the measured effective permeability and calculated permeability using the empirical model suggested by Raymond Gauvin et al. in Ref.7 are shown in Table 1 and Fig. 2.

Table 1: The measured and calculated permeability data for random distributed continuous glass fiber mat

Layers of fiber mat n	Fiber volume fraction v_f	Measured effective permeability $k / \times 10^{-9} \text{ m}^2$	Calculated permeability $k / \times 10^{-9} \text{ m}^2$
4	0.180	2.83	2.92
5	0.225	1.76	1.88
6	0.270	1.23	1.42
7	0.315	0.97	1.15
8	0.360	0.85	0.96

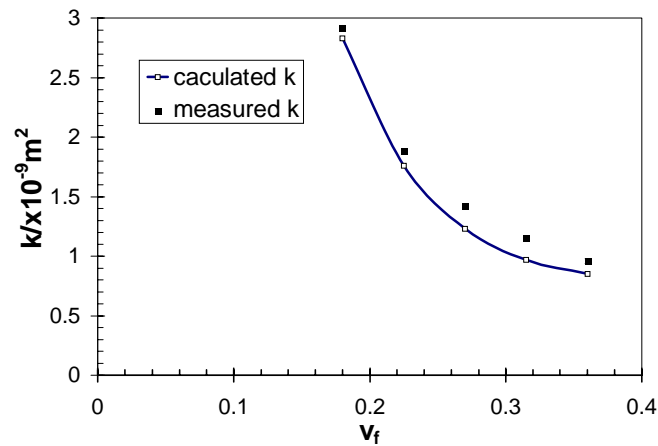


Fig. 2: The relationship between permeability k and fiber volume fraction v_f

From Table 1 and Fig. 2, it can be seen that the fiber volume fraction in the mold has the important effects on the preform effective permeability. For in-plane permeability of random continuous glass fiber mat, the relationship can be roughly expressed as

$$k = Av_f^3 + Bv_f^2 + Cv_f + D \quad (3)$$

here $A \approx -457.25$

$B \approx 437.04$

$C \approx -143.19$

$D \approx 17.196$

$$v_f = \frac{n\xi}{H\rho_g 10^{-3}}$$

where n is the number of layers of fiber mat, ξ the surface density of the reinforcement (g/m^2), H the laminate thickness (m) and ρ_g the glass mass density (kg/m^3).

The experimental data of effective permeability is close to the calculated permeability using the empirical model for the permeability prediction of continuous strand reinforcing mats by Raymond Gauvin et al. in Ref. 7:

$$k = a + b \exp(c\phi) \quad \text{for } 0.65 \leq \phi \leq 0.90 \quad (4)$$

where ϕ is the porosity. Taking a , b , c from the Table 2 of Ref. 7 (U101 from Vetrotex, they are 736.6, 4.46×10^{-3} , 15.95 respectively).

Filling time vs. Effective permeability

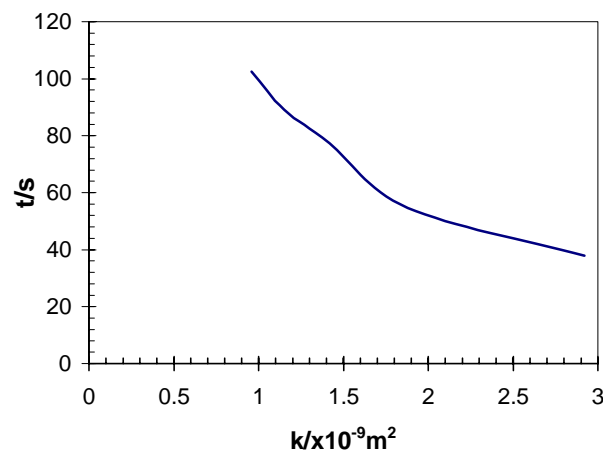


Fig. 3: The relationship between mold filling time t and permeability k

Fig. 3 shows the relationship between mold filling time t and measured effective permeability k . It indicates, at a constant flow rate (here 10ml/s). The higher the permeability, the shorter the mold filling time is needed.

In the experiment, some considerations must be taken into account. The volume of the fiber reinforcement can not be too high and too low. If the volume fraction of the fiber is too high, it is very difficult to close the mold. The excessive clamping forces must be applied, which will cause the deformation of the mold. The higher fiber fraction and lower permeability in the mold need higher mold filling pressure which may cause the deformation of the mold or make the reinforcement deform. It will affect the distribution of the preform in the mold. In molding practice, it decreases the size accuracy of the molded parts and the deformed reinforcement will affect the properties of the designed article.

If the volume fraction of the fiber reinforcement is too low, The preform may slip and form wrinkles or fold locally, when the fluid passes through the fiber preform. A small change in flow rate or filling pressure can be sensed during mold filling.

The effects of the preform architecture

Fig. 4 shows the comparison of the mold filling time for random distributed continuous glass fiber mat with bi-directional woven fabric.

In order to analyze the effect of the architecture of the fabric reinforcement on its permeability, the bi-directional woven fabric was chosen as an example to compare with the

random distributed continuous glass fiber mat. We measured the permeability of bi-directional woven fabric. When the $v_f = 0.36$, its effective permeability is $0.42 \times 10^{-9} \text{ m}^2$. This value is almost half the permeability of random distributed continuous fiber mat.

At the same filling pressure (0.1 MPa), the mold filling time is shown in Fig. 4 (150 seconds for random distributed continuous glass fiber mat, 341 seconds for bi-directional woven fabric). The filling time of bi-directional woven fabric is more than two times than that of random distributed continuous fiber mat.

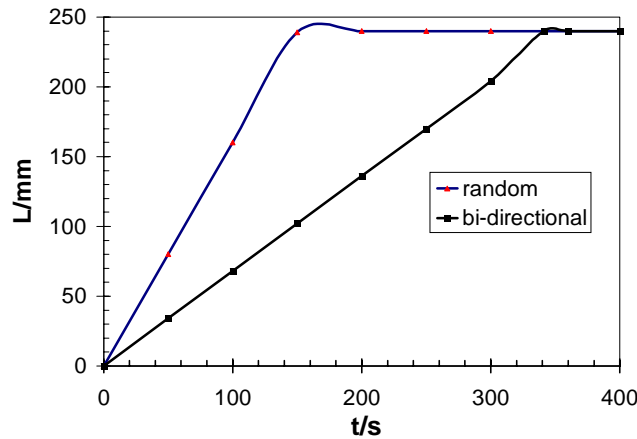


Fig. 4: The comparison of the filling time for random continuous glass fiber mat with bi-directional woven fabric

After the resin cured, we cut some samples from the molded parts to analyze the fiber impregnation. It was found that the impregnation of the random continuous glass fiber mat is much better than that of bi-directional woven fabric. Especially at the filament-filament crossover points of bi-directional woven fabric, the impregnation of the fabric is poor. The reason of poor impregnation was analyzed as following. In bi-directional woven fabrics system, we can treat it as two kinds of regions. The first kind of region is associated with regions bordered by adjacent filaments of each weave direction. The second kind of region is the filament-filament crossover points. At a crossover point, filaments of one weave direction intersect filaments of another. The permeability in these regions is much lower than the first kind of regions. They offer the largest resistance to the forced penetration of a fluid. From the macroflow point of view, the fluid passed through those regions. But from the microflow point of view, the fluid did not penetrate the fiber filament. The poor fiber impregnation will affect the interface bound strength of fiber and resin and the mechanical properties of the molded composites.

CONCLUSIONS

The fiber volume fraction in liquid composites molding (LCM) influences the preform permeability. The relationship between permeability k and fiber volume fraction v_f for random distributed continuous fiber mat can be expressed as a polynomial equation. In one-dimensional flow permeability measurement, the edge effect is inevitable, but it can be minimized by careful sample preparations to get the reproducible results. The architecture of the fiber reinforcement has great influence on the preform permeability. For the preform of same fiber volume fraction, but different architecture, their permeability can be much

different. In the actual LCM production, the permeability measurement and calculation should be carried out for different architecture and different fiber volume fractions. The mold filling time depends on the reinforcement permeability at some extent. The random continuous fiber mat has much higher permeability than bi-directional woven fabric even the fiber volume fraction is the same. The molded composite using random continuous fiber mat as reinforcement has better fiber impregnation than that using bi-directional woven fabrics.

ACKNOWLEDGMENT

The authors would like to acknowledge the financial support of National Science Foundation of China and the Overseas Student Foundation of China.

REFERENCES

1. Advani, S. G., *Flow and Rheology in Polymer Composites Manufacturing*, Elsevier Science BV., 1994, pp. 466-511.
2. Wu, C. H., Wang, T. J. and Lee, L. J., "Permeability measurement and Its Applications in Liquid Composite Molding", *Proceedings of 48th Annual Conference*, Composites Institute, The Society of the Plastic Industry, Inc., Cincinnati, USA, February 1993, Session 8-E.
3. Gebart, B. R., "Permeability of Unidirectional Reinforcements for RTM", *Journal of Composite Materials*, Vol.26, No.1, 1992, pp. 1100-1133.
4. Adams, K. L., Miller, B. and Rebenfeld, L., "Forced In-plane Flow of an Epoxy Resin in Fibrous Networks", *Polymer Engineering and Science*, Vol. 26, No. 20, 1986, pp. 1434-1441.
5. Parnas, R. S., Howard, J. G., Luce, T. L. and Advani, S. G., "Permeability Characterization. Part I: A Proposed Standard Reference Fabric for Permeability", *Polymer Composites*, Vol. 16, No. 6, 1995, pp. 429-445.
6. Wang, T. J., Wu, C. H. and Lee, L. J., "In-Plane Permeability Measurement and Analysis in Liquid Composite Molding", *Polymer Composites*, August 1994, Vol. 15, No. 4, pp. 278-288.
7. Gauvin, R., Kerachni, A. and Fisa, B., "Variation of Mat Surface Density and Its Effect on Permeability Evaluation for RTM Modeling", *Proceedings of 48th Annual Conference*, Composites Institute, the Society of the Plastics Industry, Inc., Cincinnati, USA, February 1993, Session 8-F.

ANALYSIS OF RESIN TRANSFER MOLDING PROCESS WITH PROGRESSIVE RESIN INJECTION

Moon Koo Kang and Woo Il Lee

Department of Mechanical Engineering, Seoul National University, Seoul 151-742, Korea

SUMMARY: In resin transfer molding, the increase of fiber volume fraction decelerates the resin flow. For a fast resin flow without increasing injection pressure, multiple injection ports are used. If all the injection ports are opened simultaneously, the resin front become very complicated and numerous weld lines and air bubbles may form. In this study, injection ports were opened in a sequential manner as the resin front advances. Mold filling process was simulated numerically using Control Volume Finite Element Method (CV-FEM). An optimized schedule for opening each resin injection port was obtained from numerical simulation. Experiments were performed following the proposed schedule. The resin front shapes observed from the experiments were compared with the numerical results. Close agreement was found. The progressive opening of the injection ports reduced the injection pressure as well as the injection time by a big margin.

KEYWORDS: resin transfer molding (RTM), progressive opening of multiple injection ports, mold filling simulation, visualized mold filling experiment

INTRODUCTION

Resin Transfer Molding (RTM) is an effective method for the manufacturing of composite parts, especially for large and complex geometries. RTM is performed at low pressure and low temperature (typically below 5atm. and 100°C). As the process is performed at a low pressure, the mold can be made of light metals, or even of composites. The tooling cost for molds can be remarkably saved and the manufacturing cost may be also broken down by a big margin compared to other composite processes. Therefore, RTM is suitable for manufacturing composite parts with frequent model changes at a low capital investments. RTM is performed by injecting catalyzed thermoset resin through a gate into the mold cavity pre-loaded with porous fibrous reinforcement, which is called a preform. The impregnation of fiber preform with resin is performed by transferring resin through the micro pores within the fibrous texture until the mold is fully charged (see Figure 1). As the fiber carries most of the mechanical load, the increase of the volumetric fraction of fiber is crucial in enhancing the specific strength and modulus, and thus reducing the weight, of the product. In order to achieve the premium properties of RTM products, it is necessary to enhance the fiber volume fraction. As the fiber volume fraction increases, the size of the micro pores within fibrous texture is decreased and the permeability of preform is also decreased. Thus, high fiber volume fraction leads to a deceleration of the resin flow speed during the resin impregnation into the preform, subsequently increasing the manufacturing time. Higher injection pressure enables faster resin flow, but the preform may be deformed or washed out at excessively high injection pressure. As a result, mold filling in RTM gets difficult with increasing fiber volume

fraction, so RTM process becomes impractical to manufacture relatively large parts for fiber volume fraction over 40~50%.

In order to reduce the processing time, one of the widely used practice is to elevate the resin temperature by heating the mold. If the resin is heated, the viscosity decreases and thus the flow speed is enhanced. Due to the heat transfer from the mold to the thermoset, cure reaction take place during the mold filling. Since the cure reaction during mold filling advances the gelation of resin, the time required for the post-curing can be reduced. Hence, the heated mold reduces the total manufacturing time by accelerated curing as well as by reduced resin viscosity. However, if the resin temperature is raised excessively, the gelation of resin may be reached too fast and the resin flow may prematurely stop before completion of mold filling.

A more effective method for enhancing the flow is to use multiple injection gates. Each injection gate in a multi-gate system fills smaller area than was responsible for in a single gate system, and the time required for mold filling can be remarkably reduced. The problem in a multi-gate system is the entrapment of numerous air bubbles where the flow fronts from two or more gates merge together (see Figure 2a). In this study, the opening of the gates is progressively performed along a well-designed sequence, not simultaneously. Each injection gate in the present multi-gate system is automatically controlled to be opened at the exact moment when the flow front has just passed over the gate. Thus the flow front remains simple and the number of ventilation ports can be minimized (see Figure 2b). Another advantage from the progressive opening of multiple injection gates is that the flow front velocity can be regulated within a bounded range. The flow front slows down as it moves away from the injection gate, because the gradient of pressure decreases with increasing distance between the gate and the flow front. The flow front velocity can be restored by opening a new gate at the moment when the flow front passes over the gate as shown in Figure 3.

The mold filling simulation for resin transfer molding has been conducted using different numerical techniques. A number of investigations have been performed using finite difference method (FDM) using boundary fitted coordinate[1] and finite element method with moving grids[2]. In these techniques, the calculation meshes change every time step as the calculation domain changes. Even though the flow front can be traced precisely, regeneration of the meshes at each time step imposes a great amount of extra computational efforts. In order to circumvent the problem with mesh regeneration, control volume finite element method (CVFEM) [4,5] is widely used. In this numerical scheme, computation is relatively fast due to the fixed finite element mesh, while the exact location of the resin front is difficult to determine. Um and Lee [3] applied boundary element method (BEM) for two dimensional flat mold in which the permeability and the resin viscosity are constant.

The progressive opening of multiple injection gates in RTM has been previously practiced in the industrial manufacturing processes. Chan and Morgan[6] investigated the resin flow during mold filling with progressively opened multiple injection gates focused on the microscopic flow within fiber bundles for a simplified one dimensional rectangular flow.

In this study, control volume finite element method (CVFEM) was employed to simulate the flow of resin during mold filling. Especially, the effect of the progressive opening of the injection ports on the fill time was investigated both numerically and experimentally for realistic multidimensional geometries. In the experiment, sensors were developed to detect the arrival of resin front. The sensors were validated by comparing the detection signal with the observation of a visualized flow during mold filling.

MATHEMATICAL MODELING

Consider a mold with a thin cavity loaded with fibrous preform. The permeability of the preform may be anisotropic and nonuniform. The mold cavity is assumed as a three dimensional shell, as the thickness of the cavity is negligibly small compared to other dimensions. Resin is injected at a number of designed points. The mold is heated to facilitate the resin flow and the curing. The problem is to find out the resin front location, pressure, temperature and degree of cure distributions as functions of time.

The flow of the resin inside the mold through the fiber preform can be assumed to follow the Darcy's law given by

$$\vec{V} = -\frac{K}{\mu} \nabla p \quad (1)$$

where \vec{V} is the resin velocity, p is the pressure and μ is the resin viscosity. $[K]$ is the permeability tensor for anisotropic porous media and can be a function of location. The mass conservation requires

$$\nabla \cdot \vec{V} = 0 \quad (2)$$

Substituting Eq.(1) into Eq.(2) yields

$$\nabla \cdot \left(\frac{K}{\mu} \nabla p \right) = 0 \quad (3)$$

The energy conservation equation is given by

$$\rho c \frac{\partial T}{\partial t} + \rho_r c_r \vec{V} \cdot \nabla T = k \nabla^2 T + \phi \dot{G} \quad (4)$$

where ρ , c and k are the density, specific heat and thermal conductivity, respectively. ϕ is the fiber volume fraction and the subscript r denote the resin. \dot{G} is the heat generation due to the curing reaction and is given by

$$\dot{G} = \Delta H \dot{m} \quad (5)$$

where ΔH is the heat of reaction and \dot{m} is the generation of mass of cured resin.

The conservation of the chemical species is given by

$$\frac{\partial \alpha}{\partial t} + \frac{1}{\phi} \vec{V} \cdot \nabla \alpha = \dot{m} \quad (6)$$

where α is the degree of cure. \dot{m} is given by an empirical relation[7]

$$\begin{aligned} \dot{m} &= (k_1 + k_2 \alpha^m)(1 - \alpha)^n \\ k_1 &= A_1 \exp\left(-\frac{E_1}{RT}\right), \quad k_2 = A_2 \exp\left(-\frac{E_2}{RT}\right) \end{aligned} \quad (7)$$

where m , n , A_1 , A_2 , E_1 , E_2 are constants which are determined from experimental data.

The boundary conditions for the above governing equations are given as

Flow Inlet:

$$P=P_0 \text{ or } V=V_0; \quad T=T_0; \quad \alpha=0$$

Solid Boundary:

$$\frac{dp}{dn} = 0 \quad (8)$$

Free Surface: $p = 0; q_{in} = (1 - \phi)\rho_f c_f V_n (T_f - T)$

where T_f represents the temperature of the fiber.

During and after mold filling, the resin undergoes an exothermic cure reaction after which the resin can be solidified.

Dusi et al [8] suggested a modification to the model of Kamal and Sorour[7] to account for that resin curing reaction cannot proceed beyond a certain level if the resin is exposed to a given temperature below a critical value. In this model, the isothermal degree of cure, β is defined similar to the degree of cure in Kamal and Sorour's model.

$$\frac{d\beta}{dt} = (k_1 + k_2\beta^m)(1 - \beta)^n \quad (9)$$

$$k_1 = A_1 \exp\left(-\frac{E_1}{RT}\right), \quad k_2 = A_2 \exp\left(-\frac{E_2}{RT}\right)$$

The actual degree of cure α is related to the isothermal degree of cure β as,

$$\alpha = \frac{H_T}{H_U} \beta \quad (10)$$

where H_T is the heat of reaction which can be liberated under a given temperature, while H_U is the total heat of reaction possibly generated when the temperature is sufficiently raised so that the resin is perfectly cured. The relation between H_T and H_U is again approximated as a piecewise linear function of temperature as,

$$\frac{H_T}{H_U} = C_1 \times T + C_2 \quad T < T_c \quad (11)$$

$$H_T = H_U \quad T \geq T_c$$

where C_1 , C_2 and T_c are the constants which can be experimentally obtained.

The viscosity of the resin can be modeled as follows as a function of temperature and degree of cure [9].

$$\mu = \mu_\infty \exp\left(\frac{\Delta E_\mu}{RT} + \kappa\alpha\right) \quad (12)$$

Here, μ_∞ , ΔE_μ and κ are constants which can be determined experimentally.

In order to optimize the design of the injection gates and opening time, numerical simulation is required for the resin flow during mold filling. The present mold filling problem has a moving boundary, continuously changing the shape at every time step. In order to solve the governing equations along with the boundary conditions, the control volume finite element method (CVFEM) is used in combination with the fixed grid method for the efficiency in solving the present moving boundary problem. By applying the control volume approach to the governing equations, a system of algebraic equations can be obtained. The detailed formulation process can be found elsewhere[10].

EXPERIMENTS

Experimental setup used in this study is shown in Figure 4. Lower mold plate was made of steel while upper plate was made of 30mm thick transparent Plexiglas. Location of the injection port was selected by inspection. The moving resin front was recorded using a video

camera located right above the mold. Oil was supplied from a cylindrical reservoir which was pressurized by compressed nitrogen. Pressure of the oil was measured using a pressure transducer installed right before the injection port. The pressure of the nitrogen gas was regulated to maintain a constant injection pressure. The viscosity of the oil was also measured using a rheometer (RMS). In order to detect the resin front passing over the individual injection gates, flow front sensors are required. Photo-sensors, made by assembling an infrared LED and a photo detector in a single package, were flush mounted near the injection gates to detect the flow front. The mechanism of the detection of the flow front is illustrated in Figure 5. The optical refractive index of resin is very similar to that of glass fiber, while the refractive index of the air is much different to that of fiber. Before the resin front arrives, the dry fiber preform scatter the infrared light emitted by the LED, and much of the emitted light will be refracted back to the sensor, to produce a high output voltage (see Figure 5a). When the resin front reaches the sensor, since the refractive indices of fiber and resin are quite similar, the infrared light emitted by the LED passes through the wet medium of resin-fiber mixture with little refraction, and the output voltage from the sensor by the refracted light is low (see Figure 5b). Figure 5c illustrates the output voltage from the sensor before and after the arrival of the resin front. A clear difference of no less than 2.0V was observed in the output voltage. In order to prevent a premature opening of the injection gates, the sensors were located at some distances downstream to the resin flow. Each injection gate was logically connected to their neighboring sensors except for the first injection gate which must be initially open with the start of mold filling. Three additional sensors were planted in order to verify the numerical prediction of the flow front location at more points. The locations of the injection gates and sensors are shown in Figure 6.

An experiment for the single gate injection has been performed at a constant pressure of 100kPa. The mold assembly was maintained at room temperature of 15°C. Engine oil (SAE 10W-30 from Honam Petroleum, Inc.) was used to imitate the resin in the experiments. The viscosity at the room temperature was 0.1569Pa·s. The fiber preform was made by stacking seven plies of chopped glass strand mats (LG Owens-Corning CM450-723). The fiber volume fraction was found to be 0.393. The permeability of the preform was measured following the procedure described in [12] and found to be $2.40 \times 10^{-10} \text{ m}^2$. The experimental result of the shape of the flow front at different times injected at a single gate is illustrated in Figure 7. Numerical predictions are also compared with the experimental observations. Close agreement was found between the numerical prediction and the experimental results. The contour plots in the numerical simulation is the distribution of pressure at each time step. Progressive injection has been performed in the designed sequence. The process conditions were identical to those in the single gate injection. Figure 8 shows the experimental and numerical results for this case. Close agreement was also found between the two results. The volumetric filled fraction of the mold cavity during mold filling has been compared for the single and multiple gate injections. As was predicted, Figure 9 shows that multiple gates reduce the mold filling time by a big margin of 39% compared to the case of single gate injection. In order to emphasize the effectiveness of the multi-port injection, another numerical result was shown for a comparison. The additional numerical result was obtained for the case of single port injection when the injection pressure is doubled to 200kPa. The comparison shows that the mold filling time for single gate injection may still be longer than multi-gate injection even if the injection pressure is doubled.

FURTHER NUMERICAL EXAMPLES

In this example, the method of progressive opening of multiple injection gates has been applied to a realistic three dimensional geometry. The geometry considered was the front panel of a tourist bus, the dimensions of which have been taken from the actual values of an existing model. The width of the panel is 2844mm, and the height is 670mm at the front face. The depth of the panel was 468mm. The geometry and mesh system are shown in Figure 10a. The striped plot is for the flow front location at an equal time interval of 40s. The result from single gate injection is shown in Figure 10b. The injection has been performed at a point on the center line of the panel. The time interval for each stripe is 40s. The mold filling time was estimated to be 2,390s. With a multi-gate system, the injection has been performed starting at the same point as the single gate injection. Four more injection gates, prepared at some designed points optimized through a number of numerical simulations, were progressively opened as the resin flow advances, and the flow front velocity is restored. Figure 10c illustrates the location of flow fronts at an equal interval time of 40s. The restoration of the flow front velocity at the opening of new gates can be clearly seen from the figure. The processing parameters were identical to the case of single gate injection. The total mold filling time was reduced down to 940s by multi-gate injection, and hence the reduction in filling time was as much as 60%.

CONCLUSION

A numerical code was developed to simulate resin transfer mold filling process with progressive opening of multiple injection ports. The resin flow can be predicted using the developed code considering heat transfer and resin cure reaction. To verify the validity of the numerical code, experiments were performed, showing a close agreement with the numerical prediction. The effectiveness of multi-gate injection was confirmed through numerical and experimental observations. The computer code developed in this study can be applied with reasonable accuracy in predicting the resin flow and related process variables and thus aids in the design of the mold and process conditions.

REFERENCES

1. Coulter, J.P. and Güceri, S.I., "Resin Impregnation during the Manufacturing of Composite Materials," *CCM Report No.88-07*, University of Delaware, 1988
2. Chan, A.W. and Hwang, S.T., "Modeling of the impregnation Process during Resin Transfer Molding," *Polymer Engineering and Science*, 31, 15, 1149-1156, 1991
3. Um, M.K. and Lee, W.I., "A Study on the Mold Filling Process in Resin Transfer Molding," *Polymer Engineering and Science*, 31, 11, 765-771, 1991
4. Bruschke, M.V. and Advani, S.G., "RTM: Filling Simulation of Complex Three Dimensional Shell-Like Structures," *SAMPE QUARTERLY*, October, 2-11, 1991
5. Lin, R., Lee, L.J. and Liou, M., 1991. "Non-isothermal Mold Filling and Curing Simulation in Thin Cavities with Preplaced Fiber Mats," *Intern. Polymer Processing VI*, 56-369, 1991
6. Chan, A.W. and Morgan, R.J., Sequential Multiple Port Injection for Resin Transfer Molding of Polymer Composites, *SAMPE Quarterly*, October, 45-49, 1992
7. Kamal, M.R. and Sorour, S., "Kinetics and Thermal Characterization of Thermoset Resin," *Polymer Engineering and Science*, 13-59, 1973

8. Dusi, M.R., Lee, W.I., Ciriscioli, P.R. and Springer, G.S., "Cure Kinetics and Viscosity of Fiberite 976 resin," *Journal of Composite Materials*, 27, 243-261, 1987
9. Stolin, A.M., Merzhanov, A.G. And Malkin, A.Y., "Non-Isothermal Phenomena in Polymer Engineering and Science: A review, Part II: Non-Isothermal Phenomena in Polymer Deformation," *Polym. Eng. Sci.*, Vol. 19, 1074-1080, 1979
10. Kang, M.K, Lee, W.I., Yoo, J.Y. and Cho, S.M, "Simulation of Mold Filling Process during Resin Transfer Molding", *J. of Materials Processing & Manufacturing Science*, Vol.3, No 3, 297-313, 1995
11. Adams, K.L. and Rebenfeld, L., "Permeability Characteristics of Multilayer Fiber Reinforcements. Part I: Experimental Observations," *Polymer Composites*, Vol.12, No.3, 179-185, 1991

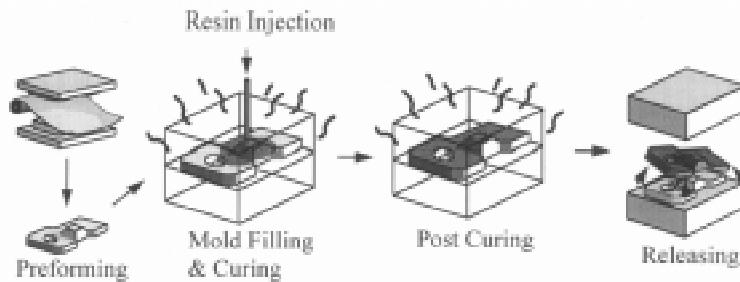


Figure 1. Resin transfer molding (RTM) process

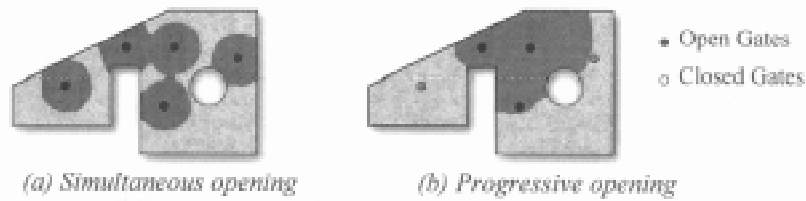


Figure 2. Progressive opening in comparison with simultaneous opening of multiple injection gates

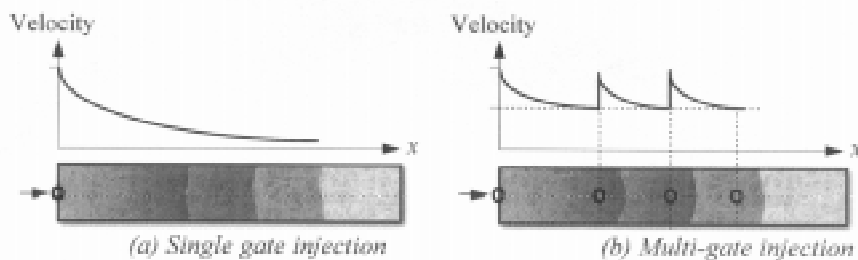


Figure 3. Resin flow velocities in single port injection and multiple ports injection

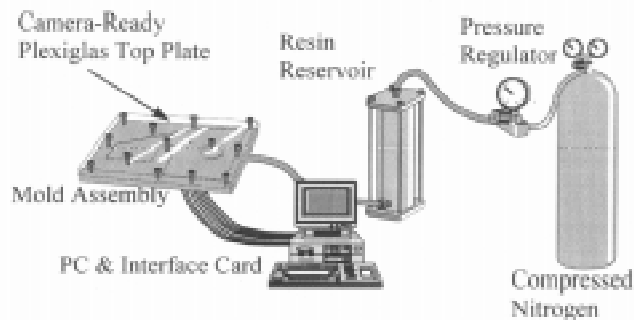


Figure 4. Experimental Apparatus

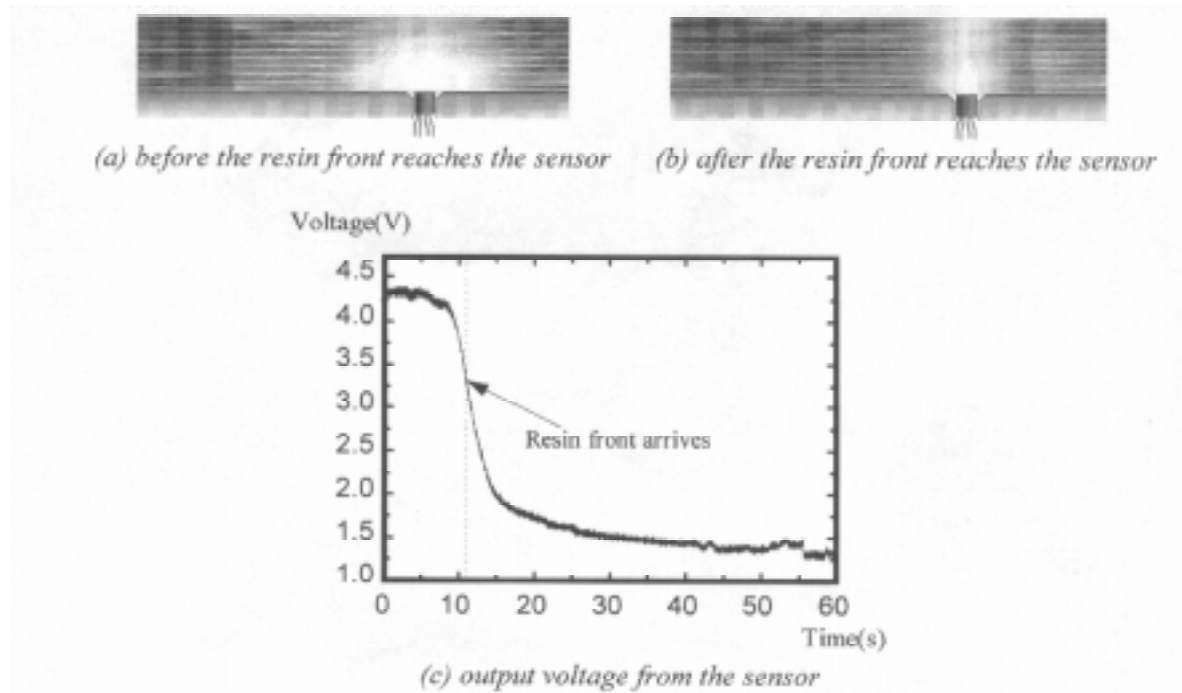


Figure 5. Flow sensor to detect the arrival of the resin front

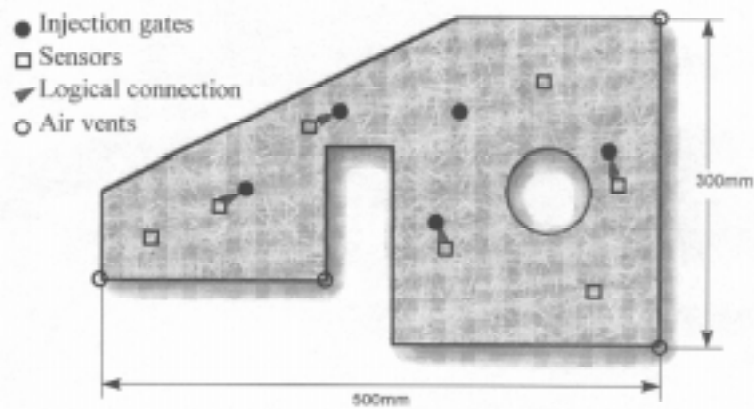
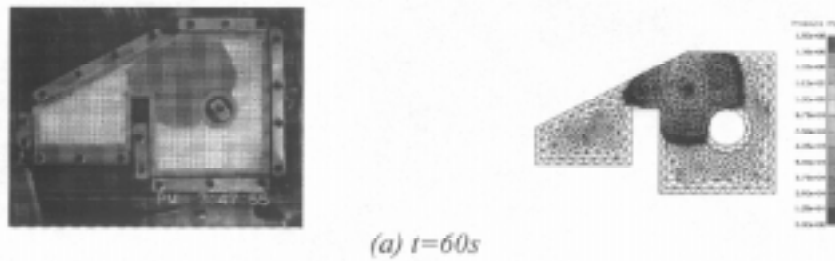


Figure 6. Mold Geometry and Locations of Injection and Ventilation Ports



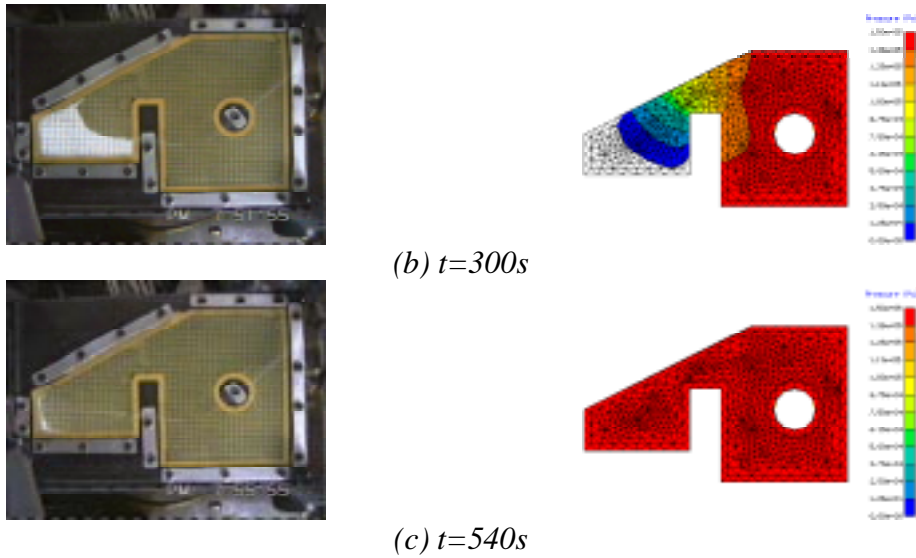


Figure 7. Experimental observation (left) and numerical prediction (right) of resin flow by single point injection

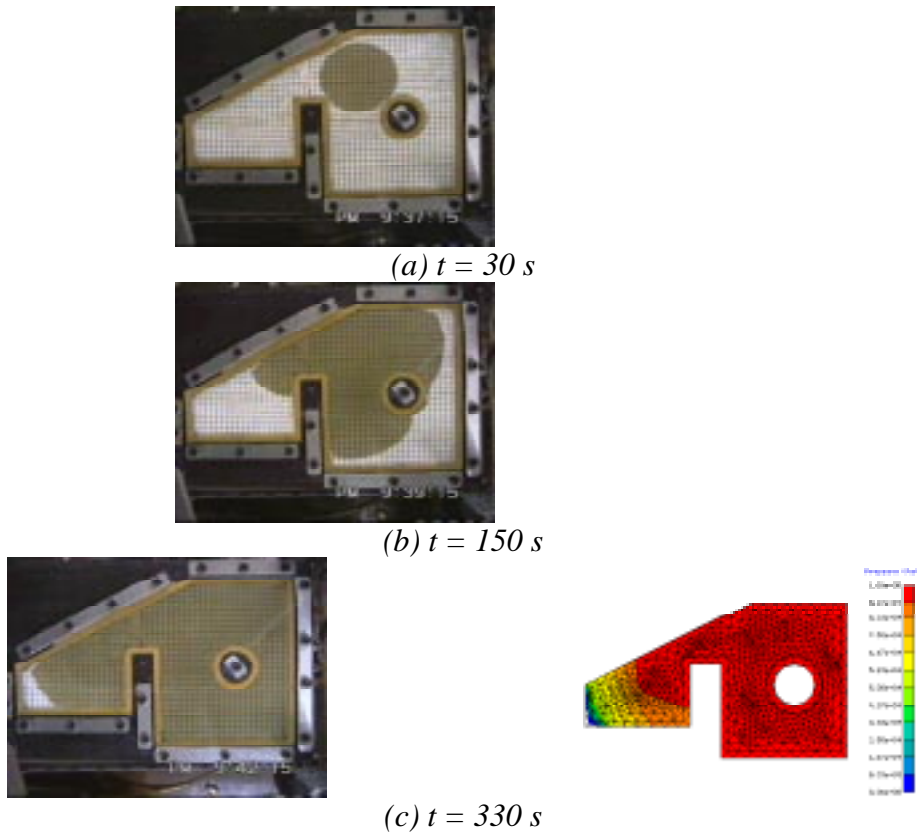


Figure 8. Experimental observation (left) and numerical prediction (right) of resin flow by progressively opened multiple injection gates

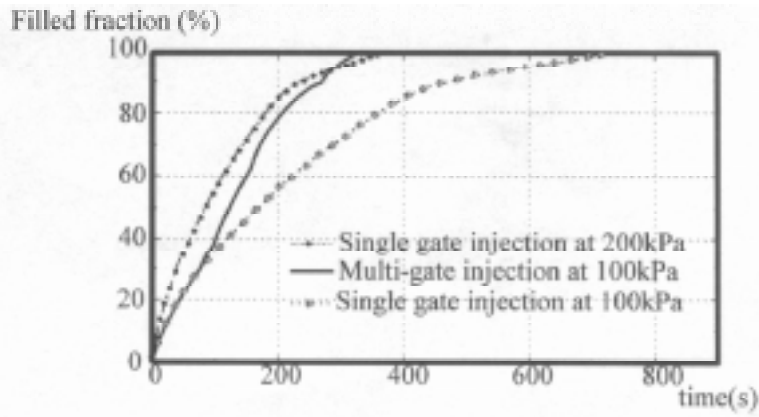


Figure 9. Volumetric filled fractions from different injection strategies as functions of time

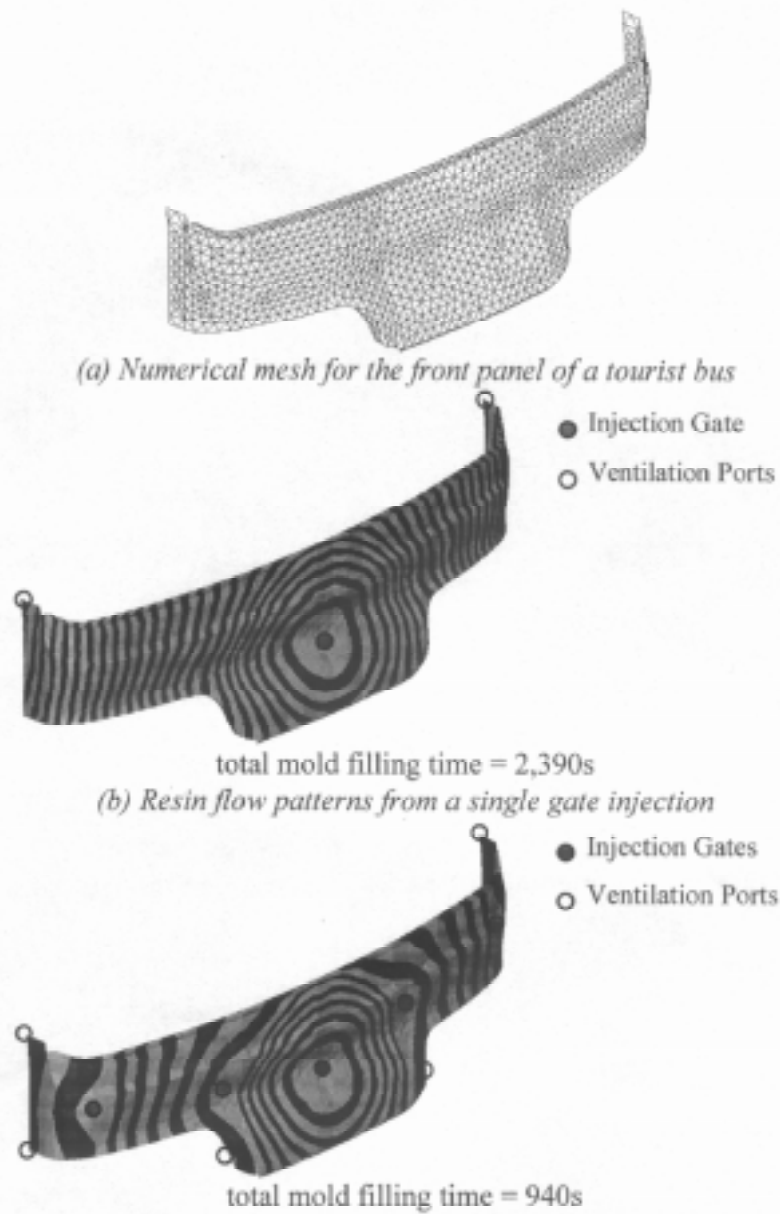


Figure 10. Mold filling simulation of a front panel of a tourist bus with single and multiple injection ports

EFFECTS OF MICROWAVE RESIN PREHEATING ON THE QUALITY OF RTM LAMINATES

M. S. Johnson¹, C. D. Rudd², and D. J. Hill³

¹ *Cooperative Research Centre for Advanced Composite Structures Limited
506 Lorimer Street, Fishermens Bend, Victoria, 3207 Australia.*

² *Department of Mechanical Engineering, The University of Nottingham
University Park, Nottingham, NG7 2RD, UK.*

³ *Ford Motor Company, Material Science Department, Dearborn, Michigan 48121, USA.*

SUMMARY: An in-line microwave resin preheating system has been used to reduce the RTM cycle significantly. Microwave preheating lowers the resin viscosity during injection and modifies the thermal “age” of the resin, potentially influencing the quality of RTM laminates. Tensile properties of RTM laminates were measured with regard to improved fibre wet-out by the lower viscosity resin. Microwave resin preheating had an insignificant effect on the tensile modulus and strength of the laminates. Degree of cure measurements established that microwave resin preheating does not alter resin conversion within the laminate significantly. Localised pressure that develops within the mould during the cure phase can lead to mould deflections. Variations in the laminate thickness associated with these deflections are presented, and the use of microwave resin preheating to reduce these variations is discussed.

KEYWORDS: microwave heating, resin preheating, injection temperature profiling, thermal quench, resin transfer moulding, RTM, cycle time, laminate tensile properties

INTRODUCTION

Widespread acceptance of resin transfer moulding (RTM) within the high volume manufacturing sector has been inhibited by excessive production cycles. RTM comprises a fibre preforming stage, followed by resin injection into the preform with subsequent curing. Methods to accelerate the preforming stage are ongoing [1], with parallel research efforts being directed towards reductions in the moulding cycle time [2]. Thermal quench occurring when ambient temperature resin is injected into a heated mould has been identified as a principal cause of extended cycle times. Additional time is required to heat the mould and laminate to the resin initiation temperature, permitting the curing process to begin. The processing delays caused by thermal quench are compounded by lightweight shell tooling, having rapid thermal response characteristics. Previous work has demonstrated that thermal quench, and consequently, the cycle time can be reduced significantly by preheating the resin prior to injection [3]. An in-line microwave resin preheating system has been developed for this purpose at the University of Nottingham. The effect of microwave resin preheating on RTM laminates is addressed in this paper. Preheating alters the viscosity and thermal “age” of thermosetting resins. A lower resin viscosity was expected to improve fibre wet-out, increasing the mechanical properties of the laminate. Furthermore, altering the thermal age of the resin was anticipated to affect the degree of resin cure. In addition, microwave resin preheating can reduce the pressure that develops near

the injection gate during the cure phase. As a result, mould deflections and laminate thickness variations were expected to be reduced.

IN-LINE MICROWAVE RESIN PREHEATING FOR RTM

A rapid temperature drop (thermal quench) occurs near the injection gate as cool resin contacts the hot mould surface. This region remains quenched until the end of injection at which time heat is recovered gradually and the resin activation temperature is reached. Resin cures last at the injection gate, dictating the cycle time, as a result of thermal quench and a comparatively short residence time within the mould. One means of reducing thermal quench is to preheat the resin prior to injection. More rapid curing occurs since the heat required to initiate cure is decreased, resulting from a decreased temperature differential between the resin and the mould. Furthermore, the resin viscosity is lowered by preheating, facilitating flow through the mould and fibre reinforcement. Consequently, both impregnation and cycle times can be reduced.

Rapid heating of low thermal conductivity polymers (typically 0.3 W/mK [4]) is difficult to accomplish using standard conduction heating methods. A large thermal gradient between the heat transfer surface and the resin core is likely develop, inducing premature cure of reactive thermosetting resin systems. Unlike conduction heating, microwave heating is primarily volumetric, providing an even temperature distribution throughout the material. Rapid heat up rates and fast response times resulting from the low thermal capacity of the resin are possible due to the high power densities achievable using microwaves. The power density (P) within a dielectric material exposed to a microwave field can be expressed as:

$$P = 2\pi f E^2 \epsilon_0 \epsilon'' \quad (1)$$

where f is the microwave frequency (2.45 GHz), and ϵ_0 is the dielectric permittivity of free space. Equation 1 indicates that the power density within the material is a function of the electric field squared (E) and the dielectric loss factor (ϵ'') rather than the thermal properties of the material.

The effects of microwave processing on laminate properties is disputed. Research in this area has been confined to microwave curing, as opposed to microwave preheating. Yue and Boey [5] measured a 50% increase in the tensile modulus of epoxy cured using microwaves as opposed to conduction heating. Marand et al.[6] concluded that microwave processing led to a lower degree of cure and was expected to result in inferior mechanical properties. Lewis and Shaw [7] attempted to reconcile these contradictory findings by suggesting that the cure reaction rate is altered by microwave processing. Resins that contain a great number of microwave absorbing functional groups could produce a highly crosslinked laminate by microwave curing. These same reactive functional groups would not be affected by conventional conduction heating.

THE EXPERIMENTAL RTM FACILITY

Figure 1 is a schematic of the in-line microwave resin preheating system installed within the experimental RTM facility at the University of Nottingham. Prototype automotive undershield components were produced within a lightweight nickel shell mould. The undershield protects the engine and transmission assembly from heavy impact damage under rally conditions. The mould was instrumented with thermocouples and pressure transducers for process control. Hot oil heating was used to maintain a stable mould temperature. A constant pressure injection system consisting of a 30 litre resin storage vessel (maximum pressure of 7 bar) was used. Precatalysed resin was delivered to a centrally located pin gate in the lower mould half via the microwave

preheater. The distance between the microwave outlet and the injection gate was limited to 380 mm to minimise heat losses within the preheated resin before entering the mould. Resin flowed through the mould to two peripheral vents, expelling air in the process.

The microwave resin preheating system was operated within the automatic RTM cycle. A digital to analogue (DAC) board was installed within the personal computer (PC), and was linked, in turn, to a programmable logic controller (PLC). A digital switching facility on the card turned the power ON and OFF at appropriate times during the moulding sequence. Microwave power was adjusted through an analogue channel on the board via a proportional-integral-derivative (PID) controller. A feedback control loop based on the resin temperature at the microwave outlet and incorporating the PID power controller enabled a user defined resin temperature to be maintained during injection. A load cell on the resin storage vessel was used to monitor the amount of resin that entered the mould.

RTM CYCLE EFFECTS DUE TO IN-LINE MICROWAVE RESIN PREHEATING

Use of the in-line microwave system allowed resin to be heated at either a constant temperature during injection or according to a prescribed heating profile. Cycle time reductions of 26% have been demonstrated using constant temperature resin injection, however, this approach does not permit cycle time optimisation. Profiled resin preheating allowed the cure sequence to be controlled, minimising the cycle time, and limiting the in-mould pressure during cure [8].

A series of mouldings was produced by profiling the resin temperature during injection to alter the cure sequence. A benchmark moulding, representing conventional RTM, was made by injecting polyester resin [Synolac 6345 initiated with 2% acetyl acetone peroxide (Trigonox 44B) and 0.5% cobalt accelerator (NL49P)] at ambient temperature (24°C) into a mould heated to 40°C. Four additional mouldings were produced by ramping the resin temperature as follows: 40-45°C, 40-50°C, 40-55°C, and 40-60°C. The preheating sequence was based upon a linear ramping of the resin set point temperature as a function of the total mass of resin injected. The set point temperature was initialised to 40°C at the start of injection (0 kg injected), and increased to the maximum temperature by the end of injection (9 kg injected). Applying a temperature ramp from 40-50°C led to coincident resin cure across the mould surface with a 36% reduction in cycle time compared to the moulding produced by conventional RTM. This situation represented the minimum cycle time possible for the given moulding conditions.

Figure 2 shows that the pressure within the mould cavity during cure increased along the diagonal from the mould periphery to the injection gate for mouldings produced by conventional RTM (resin temperatures of 22°C and 24°C). This high pressure, termed the pre-exotherm pressure, was identified by Kendall [9] as a characteristic of centre gate injection. Resin cured first at the mould periphery creating a rigid seal, entrapping a pool of uncured resin within the mould. The resin temperature increased through mould heating and the exothermic cure reaction. As a result, thermal expansion of the resin occurred, generating a pressure that was transmitted into the liquid pool. Compression within the liquid pool increased as the cure front advanced inward, generating a consecutively higher pre-exotherm pressure. Thus, the intensity of the pre-exotherm pressure was greatest at the injection gate. Kendall [9] recorded pre-exotherm pressures five times greater than the injection pressure, concluding that they were an important consideration in mould design. Constant temperature resin injection had no effect on the cure sequence so that high pre-exotherm pressures were measured at all elevated resin temperatures. Ramping the resin temperature to promote coincident cure reduced this pre-

exotherm pressure to the hydrostatic level as no entrapment of the pool occurred. This suggested that mould deflections were reduced during the cure phase.

THICKNESS VARIATIONS IN RTM LAMINATES

High pre-exotherm pressure could lead to damage in moulds not designed to prevent pressure induced deflections. In addition, these deflections could result in part thickness variations. Kendall [9] produced a series of plaque mouldings with pre-exotherm pressures ranging from 0 bar to 28 bar. The thickness of the laminate increased by an average of 10% at 28 bar leading to the conclusion that high pre-exotherm pressures influenced component quality appreciably.

A study was performed to determine whether high pre-exotherm pressures at the injection gate affected the thickness of the undershield component. Disks (19 mm in diameter) were cut from four laminates near the mould periphery and the injection gate. Two mouldings (Numbers 5454 and 5456) exhibited a typical cure sequence from the periphery to the centre of the mould and had high pre-exotherm pressures at the injection gate (between 17 bar and 25 bar). The other two mouldings (Numbers 5437 and 5435) were produced using a coincident cure sequence and exhibited low pre-exotherm pressures at the injection gate (approximately 1 bar). Variation in thickness of the disks between the mould periphery and injection gate was determined with the results being presented in Tables 1 and 2.

The thickness across the mouldings with a high pre-exotherm pressure (Table 1) increased on average by 8.8% from the mould periphery to the injection gate. The average increase was reduced substantially to 4.1% for mouldings produced with a low pre-exotherm pressure (Table 2). These results confirmed the findings by Kendall, and suggested that component quality is related directly to the pre-exotherm pressure.

Table 1: Variation in Laminate Thickness for Mouldings with a Maximum Pre-Exotherm Pressure of 25 Bar

Reference No.	Moulding Thickness		Thickness Increase(%)
	Periphery	Gate	
5456	7.84	8.51	8.5
5454	7.48	8.16	9.1
Average Values	7.66	8.34	8.8

Table 2: Variation in Laminate Thickness for Mouldings with a Maximum Pre-Exotherm Pressure of 2 Bar

Reference No.	Moulding Thickness		Thickness Increase(%)
	Periphery	Gate	
5437	9.26	9.59	3.6
5435	9.10	9.51	4.5
Average Values	9.18	9.55	4.1

TENSILE PROPERTIES OF RTM LAMINATES

Rudd and Revill [10] demonstrated that the tensile properties of RTM laminates were sensitive to cycle time. Decreasing the cycle time reduced the period available for fibre wet-out, prompting a decrease in the tensile modulus and strength of continuous filament random mat (CFRM) laminates. Reducing the resin viscosity was expected to promote better flow through the

preform and enhance fibre wet-out, for improved tensile properties. Hayward and Harris [11] showed that lowering resin viscosity by increasing the mould temperature produced no difference in the shear strength or modulus of moulded components.

Five laminates were produced by injecting polyester resin [Synolac 6345 initiated with 2% bis t-butyl peroxy dicarbonate (Perkadox 16)] at 22°C, 30°C, 40°C, 45°C and 50°C into a mould heated to 60°C. A CFRM reinforcement was used resulting in a fibre volume fraction of 16%. Seven specimens were cut from each undershield (250 mm × 25 mm × 6 mm) along the weft direction of the glass mat as shown in Figure 3. The tensile modulus (E) and ultimate tensile strength (UTS) of the specimens were measured. The laminates were tested to BS 2782:Part 10:Method 1003 on an Instron Universal Mechanical Tester Model 1195 having a 100 kN load cell. Longitudinal displacements were recorded by an extensometer at a crosshead speed of 5 mm/min.

Figure 4a shows the variation in modulus as a function of the resin preheat temperature. Average modulus values ranged from 5.5 GPa to 7.0 GPa, although no statistically significant difference was measured. Figure 4b shows similar results for the laminate tensile strength as a function of resin preheat temperature. Variation in average strength values were negligible ranging from 112 MPa at 40°C and 126 MPa at 22°C. These results suggested that preheating the resin to a constant temperature during injection did not affect the tensile properties of RTM laminates appreciably.

Analysis of tensile properties provided information on the overall effect of resin preheating on fibre reinforced laminates. However, further investigation was necessary to determine its effect on the resin system.

DEGREE OF CURE MEASUREMENTS BY GAS CHROMATOGRAPHY

Compared to resin injected at ambient temperature, resin injected at a constant elevated temperature experiences a different thermal history. As a result, the properties of the matrix could be altered. Preheated resin would be nearer to its activation temperature at the end of injection, so that the polymerisation reaction may be initiated preferentially, resulting in a more highly crosslinked structure. Tensile tests on the laminates did not confirm this hypothesis. However, the strength of the fibre reinforcement, and the fibre to matrix interface was expected to dominate these results. A measurement of the degree of cure was necessary to understand fully the effect of resin preheating on the matrix.

Experimental Procedure for Degree of Cure Measurements Using Gas Chromatography

A polyester resin consists of an unsaturated resin molecule dissolved in a styrene monomer to form a homogeneous solution. Curing involves copolymerisation of the styrene and unsaturated resin. In principle, copolymerisation will cease automatically when all the styrene has reacted [12]. Based upon the homogeneous nature of the resin, it is convenient to define the fully cured state as having 0% residual styrene and the uncured state as having 100% residual styrene. The amount of residual styrene in the polyester resin can be measured by gas chromatography.

Residual styrene content measurements were made on two laminates produced by constant temperature resin injection at 20°C and 50°C in a mould heated to 60°C. Glass fibre blanks were removed from the preform at eight locations along the mould diagonal before injection to form pure resin samples at those locations. Resin disks (19 mm diameter) were cut from the laminate

directly after demoulding. The samples were prepared for gas chromatography testing according to a modified version of BS 2782:Part 4:Method 453A. A Perkin-Elmer 8500 Gas Chromatograph was used to measure residual styrene content in the samples.

Results of the Degree of Cure Measurements Using Gas Chromatography

The amount of residual styrene at locations along the mould diagonal (positions 2-5) is shown in Figure 5. Insignificant variations in residual styrene levels were measured between the two mouldings. The majority of the laminates (positions 2-4) were cured to approximately 93%. A higher degree of cure (97%) was measured at the injection gate for both laminates. The reason for a higher degree of cure at the injection gate was not clear, however, Huang et al. [13] have suggested that increased pressure could increase the overall degree of cure. This explanation would be compatible with the higher cure pressures occurring near the injection gate as shown in Figure 2 for conventional RTM.

The results shown in Figure 5 demonstrate that resin preheating had no significant effect on the degree of cure for RTM laminates. Figure 6 provides further evidence to support this claim. Preheating the resin to 50°C reduced the amount of thermal quench at the injection gate compared to the moulding produced with resin at 22°C. However, the similarity in shape of the thermal histories above the mould temperature (60°C) suggests that the cure reaction proceeded at the same rate for both mouldings.

CONCLUSIONS

Use of an in-line microwave resin preheating system reduced RTM production cycle times by compensating for thermal quench at the injection gate. Profiling of the resin preheat temperature reduced localised in-mould pressures during the cure phase, and decreased mould deflections. As a result, the variation in the component thickness along the length of the component decreased by more than 50%. Furthermore, this suggested that lighter and more thermally responsive shell moulds could be employed.

Resin preheated to a constant temperature during injection had an insignificant effect on the tensile properties of RTM laminates. Tensile tests on laminates produced at a series of resin temperatures showed an insignificant effect on the modulus and strength. This implied that preheating the resin to lower its viscosity did not improve fibre wet-out. However, since impregnation times were reduced, this suggested that the equivalent fibre wet-out had occurred over a shorter interval. These results indicate that resin preheating could be used to reduce cycle times without lowering the structural integrity of RTM components.

Preheating resin was determined to have no effect on the degree of cure for the laminates. This suggested that while resin preheating altered the thermal history of the resin, it did not change the kinetics of the cure reaction.

ACKNOWLEDGMENTS

The authors would like to acknowledge the support of Mr A. Harrison and Mr S. Scarborough of the Ford Motor Company Ltd. Mr. A. Kingham deserves recognition for his technical support.

REFERENCES

- [1] J. A. Chestney and M Sarhadi. "A Prototype Manufacturing Cell for Automated Assembly of Fibre Reinforced Composite Preforms," pages 439-446. The 4th International Conference on Automated Composites, Nottingham, England, September 1995.
- [2] G. Lebrun, R. Gauvin, and K. N. Kendall. "Experimental Investigation of Resin Temperature and Pressure during Filling and Curing in a Flat Steel RTM Mould." *Composites Part A* 27A pages 347-355, 1996.
- [3] M. S. Johnson, C. D. Rudd, and D. J. Hill. "Cycle Time Reductions in Resin Transfer Moulding Using Microwave Preheating." *Proceedings of the Institution of Mechanical Engineers Journal of Engineering Manufacture* 209 pages 443-453, 1995.
- [4] G. Kaye and T. Laby. "Tables of Physical and Chemical Constants and Some Mathematical Functions." 15th edition, Longman Group Ltd., pages 287-290, 1986.
- [5] C. Y. Yue and F. Y. Boey. "The Effect of Microwave and Thermal Curing on the Interfacial Properties of an Epoxy-Glass Composite," Paper 12 pages 1-8. *Proceedings of the Deformation and Fracture of Composites Conference*, Manchester, England, March 1993.
- [6] E. Marand, K. R. Baker, and J. D. Graybeal. "Comparison of Reaction Mechanisms of Epoxy Resins Undergoing Thermal and Microwave Cure from In Situ Measurements of Microwave Dielectric Properties and Infrared Spectroscopy." *Macromolecules* 25(8) pages 2243-2252, 1992.
- [7] D. A. Lewis and J. M. Shaw. "Recent Developments in the Microwave Processing of Polymers." *MRS Bulletin* pages 37-40, November 1993.
- [8] M. S. Johnson, C. D. Rudd, and D. J. Hill. "Microwave Assisted Resin Transfer Moulding," pages 1-29. The 4th International Conference on Flow Processes in Composite Materials, Aberystwyth, Wales, September 1996.
- [9] K. N. Kendall, C. D. Rudd, M. J. Owen, and V. Middleton. "Characterisation of the Resin Transfer Moulding Process." *Composites Manufacturing* 3(4) pages 235-249, 1992.
- [10] C. D. Rudd and I. D. Reville. "Effects of Wetting Times on the Tensile Properties of Glass Fibre/Polyester Laminates," pages 20-24. *Composites 1990*, University of Patras, Greece, August 1990.
- [11] J. S. Hayward and B. Harris. "Processing Factors Affecting the Quality of Resin Transfer Moulded Composites." *Plastics and Rubber Processing and Applications* 11(4) pages 191-198, 1989.
- [12] L. Roskott and A. A. M. Groenendaal. "Residual Styrene Content-What Does This Mean to the Polyester Processor," Section 5-B pages 1-5. *The Society of Plastics Industry. The 33rd Annual Conference, Reinforced Plastics/Composites Institute*, 1978.
- [13] Yan-Jyi Huang, Tian-Jyh Lu, and Wei Hwu. "Curing of Unsaturated Polyester Resins-Effects of Pressure." *Polymer Engineering and Science* 33(1) pages 1-17, 1993.

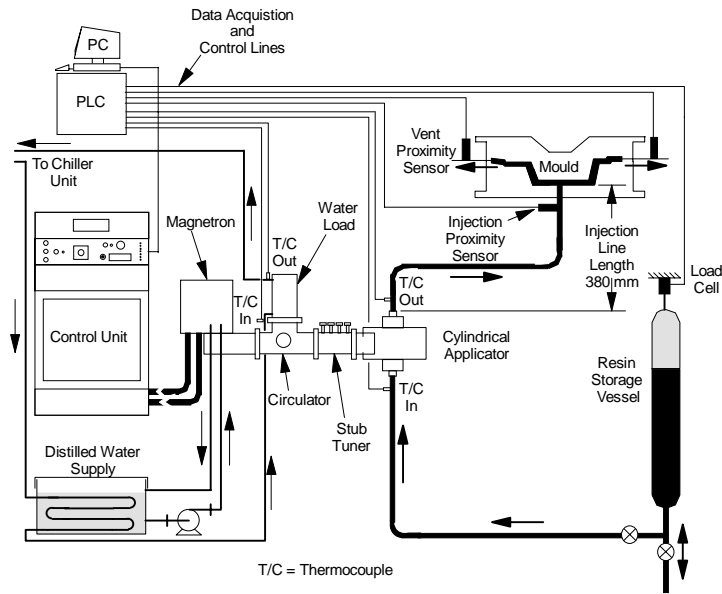


Figure 1: Schematic of the RTM Facility

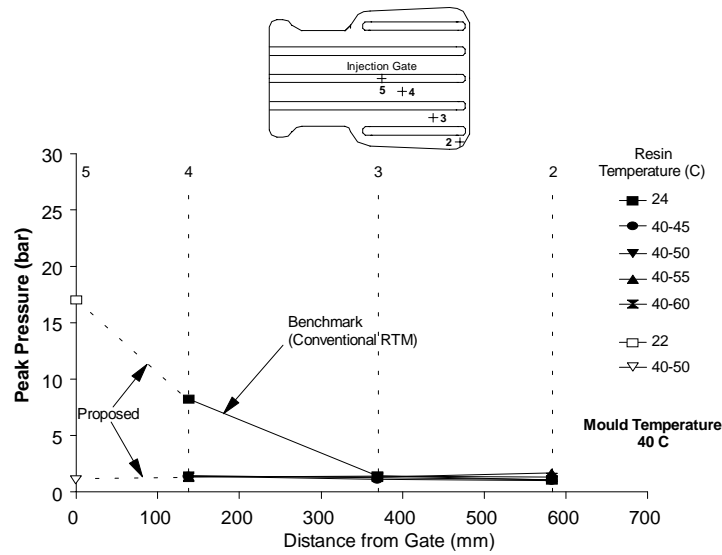


Figure 2: Effect of ramped resin temperature injection on the peak pre-exotherm pressures across the undershield mould

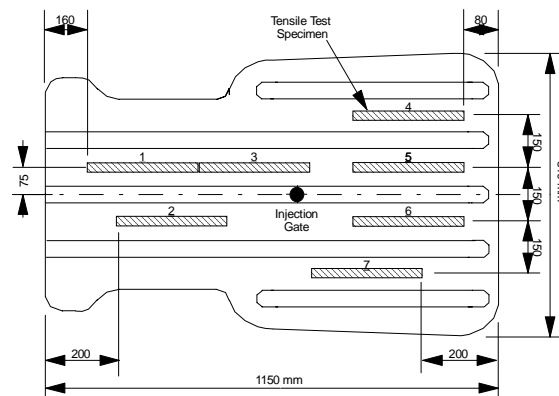


Figure 3: Orientation of tensile test specimens on the undershield component

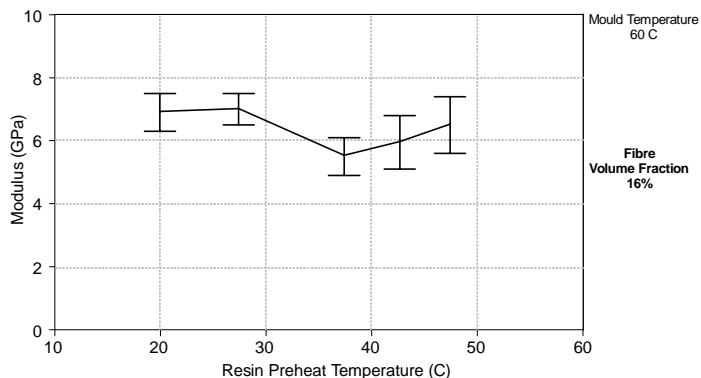


Figure 4a: Average modulus values for RTM laminates

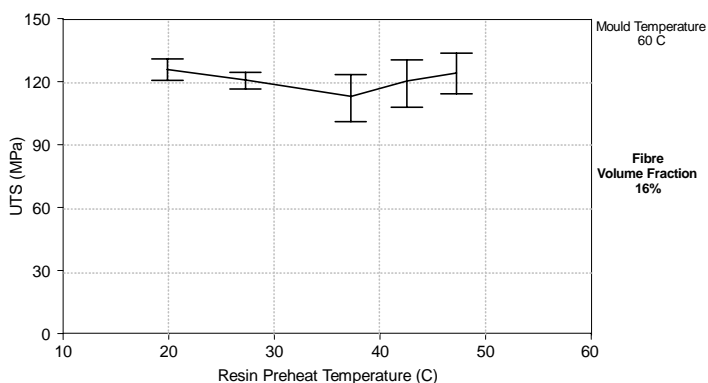


Figure 4b: Average UTS values for RTM laminates

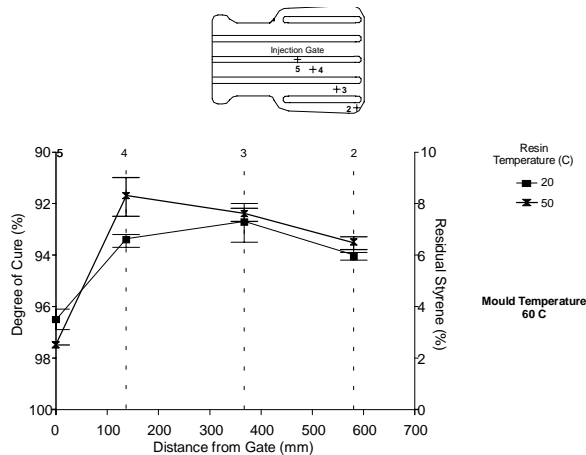


Figure 5: Degree of cure along undershield moulding produced with resin injected at 20C and 50C

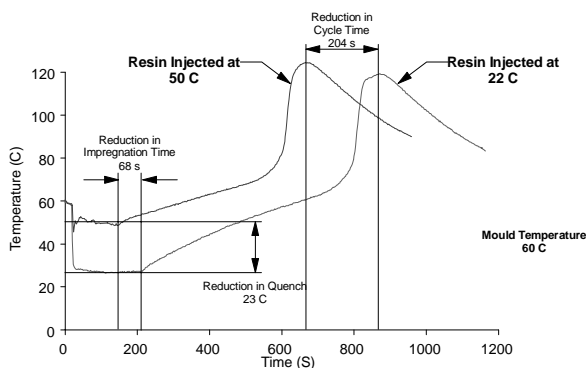


Figure 6: Thermal histories at the injection gate (position 5) demonstrating the similarities in resin cure kinetics between mouldings made with and without resin preheating

A COMPARISON BETWEEN VOIDS IN RTM AND PREPREG CARBON/EPOXY LAMINATES

C.A. Howe¹, R.J. Paton², A.A. Goodwin¹

¹ *Department of Materials Engineering, Monash University,
Wellington Road, Clayton, Victoria 3168, Australia*

² *Cooperative Research Centre for Advanced Composite Structures Limited (CRC-ACS),
506 Lorimer Street, Fishermens Bend, Victoria, 3207, Australia*

SUMMARY: Voids were intentionally produced in carbon/epoxy laminates which were manufactured by two different processes used in the aerospace industry. These processes were Resin Transfer Moulding and the autoclave moulding of prepreg. Voids in the laminates were characterised with respect to location, shape, size and volume fraction, using optical image analysis. This information was used to determine the effect of voids on the interlaminar shear strength of prepreg and RTM laminates. It was shown that the effect of voids on the mechanical properties varied between the two manufacturing techniques, based on the different void morphology and distribution within the test coupon. It was also shown that different void morphologies within the RTM laminate have different degrees of effect on the mechanical properties.

KEYWORDS: voids, carbon/epoxy laminates, resin transfer moulding, prepreg, interlaminar shear strength, morphology

INTRODUCTION

Polymer composites are susceptible to a loss in mechanical properties arising from defects introduced during manufacture [1,2]. Autoclave moulding of prepreg and Resin Transfer Moulding (RTM) are two composite manufacturing operations that inherently form defects, such as voids. Voids are particularly detrimental to the compressive strength of composites [3], and matrix-dominated properties, such as interlaminar shear strength [4]. In order that a composite can be used in demanding applications, the effect of voids on the mechanical properties should be determined.

Prepreg manufacture involves the pre-impregnation of the reinforcement with resin before the lay-up, which allows for easier handling. The reinforcement is usually supplied as a unidirectional tape or woven fabric, which is impregnated with a partially-cured catalysed resin. The composite is made by aligning the plies on a mould, which is covered with a vacuum bag. The entire assembly is placed in an autoclave where the combination of heat, pressure and vacuum consolidates and cures the laminate [5].

There are various sources of porosity in a cured prepreg laminate. The most common form is found positioned between plies. This form of porosity can be the result of absorbed or dissolved water and gases in the prepreg, the entrapment of air between plies during the manufacture process, or residual gases produced from the cure reaction. Porosity within the ply is not as common, but can be caused by the incomplete wetting of the fibre tows [6].

Resin Transfer Moulding essentially involves the injection of a reactive resin into a mould cavity containing a dry fibre preform. The dry preform is aligned in the mould tool. The resin is heated to a temperature where the viscosity is sufficiently low that it will fill the preform under the application of an external pressure. Vacuum is commonly applied to the mould cavity to assist in the resin filling process. Once the mould is filled the resin is cured [7].

Voids are primarily formed due to the mechanical entrapment of air during resin flow [8, 9]. At the flow front, when resin impregnates the dry preform, there are two main avenues that the resin can travel, that is between the fibre tows and within the fibre tows. The applied pressure, fibre preform permeability, fibre volume fraction, and resin properties govern the flow speed within each avenue [10]. An irregular flow front can lead to the trapping of air pockets in the preform [11, 12]. Another form of void is due to gas created by reactions taking place within the resin [13]. Voids can also be introduced into the system in the form of bubbles, when the resin, prior to injection, is insufficiently degassed [10].

The effect of voids in prepreg laminates has been reported [1-4, 14]. However, there is little information on the effect of voids in high performance RTM laminates. Oliver et.al. [14] observed that prepreg laminate properties are dependent on defect size, location and shape. The types of voids observed in RTM laminates are somewhat different to those seen in prepreg laminates. Therefore, it would be unwise to assume that the effect of voids in RTM laminates is similar to their effect in prepreg laminates. A comparison between the two processes may be beneficial to industries contemplating the substitution of RTM parts for prepreg parts.

The objective of this paper is to characterise voids in prepreg and RTM laminates with respect to shape, size and concentration by optical image analysis. This information is then used to determine the effect of voids on the mechanical properties of prepreg and RTM laminates.

EXPERIMENTAL

Specimen Manufacture

A composite material system was chosen, which could be manufactured by both prepreg and RTM processes. A 370 g/m² 5-harness satin weave carbon fabric and Hercules 3501-6 epoxy resin were used.

For Resin Transfer Moulding, a two piece mould was used with cavity dimensions of 480 by 13 by 3.2 mm. The mould was coated with a release agent, Frekote 700. The woven fibre reinforcement was laid up with a unidirectional orientation [0]_g. The fibre volume fraction was 59%. The resin was slowly heated to a pourable viscosity, and then degassed by applying vacuum. The resin was injected into the heated mould at one end of the mould cavity by a pneumatic, heated injection cylinder. Vacuum assistance was used. The panel was cured after injection was complete.

Defective RTM panels were deliberately produced by forming a "dry spot" within the preform. The "dry spot" was produced by allowing for the racetracking of resin around the perimeter of the preform. A network of porosity, with varying concentrations and morphologies was formed around the dry spot region.

Four prepreg laminates were made using the same layup as that used in making the RTM laminates. Two laminates with dimension 450 mm x 200 mm x 3.1 mm were made under normal conditions to produce low-porosity panels, with 61%V_f. The laminae were laid up on an aluminium plate coated with Frekote release agent. The lay-up was debulked at three stages; ie after the addition of three plies. A cork dam, 3.2 mm thick, was placed around the perimeter of the lay-up. Perforated film, bleeder cloth, breather cloth and nylon vacuum bag were placed over the lay-up, in preparation for the autoclave procedure. Two additional laminates with dimension 450 mm x 200 mm x 3.1 mm were made under varied conditions to produce high porosity panels. These variations included eliminating the debulking process,

spraying fine water droplets between plies, and bleeding excess resin from the laminate. Both sets of laminates were cured at 177°C for two hours.

Void Content Determination

The void content, shape, size and location within a section of the laminate was determined by Optical Image Analysis. The image analysis system included a Reichart optical microscope, a Videk camera, a Videk Megaplus frame grabber, and a Macintosh computer with the image analysis software Image 1.58. Non-destructive Ultrasonic C-scan inspection was also used to determine the void content throughout a laminate panel. The equipment used was an Infometrics "Test Pro" system and a Meccasonic laboratory scanning tank. The Test Pro is a PC based ultrasonic testing instrument incorporating scanning frame control. Ultrasonic signals were provided by a Panametrics receiver (model 5052PR), driving a 15MHz focused probe. The total system gain was 26 dB. The scanning grid was 1mm x 1mm.

A combination of C-scan and optical image analysis was used to determine the void content of an interlaminar shear strength test coupon. A laminate section neighbouring the mechanical test coupon in the laminate panel was used to determine the total void content of the test coupon. If the neighbouring coupon contained the same dB loss according to the C-scan image, and the same surface porosity level, as compared with the test coupon, then it was used as the representative. The representative laminate section, which had the same dimensions as the test coupon, was cross-sectioned into three segments. The samples were mounted in vinyl ester resin, and finely polished by a Prepmatic polishing machine. The porosity content was determined at X32 magnification, with 6 random areas chosen from each of the three segments. The average of the 18 measurements were calculated to be the volumetric porosity content of the representative specimen.

To investigate the variation in porosity throughout a defective panel, specimens were selected from certain points, ie near the inlet and outlet ports, the centre of the panel, and the region surrounding a dry spot. The specimens were polished by hand on universal polishing wheels. The total void content of the specimen was measured parallel to the surface, at each ply interface. The surface area of the specimen was ~225 mm².

Mechanical Testing

The effect of void content, and the type of void, on the interlaminar shear strength was determined by testing 70 samples from the prepreg and RTM laminate panels, which contained various forms and levels of porosity. The testing was done according to the short beam shear test method specified in ASTM standard D2344. The surface porosity of the test coupons was first measured using the optical image analysis technique. The coupons were prepared by cutting with a diamond saw, and the sides polished with 400 wet and dry paper to remove any flaws caused by cutting. The tests were performed using INSTRON 4505 equipment. A 100 kN load cell was used, with the cross-head speed set at 1.3 mm/min. The dimensions of the RTM specimen were 19.2 mm x 6.4 mm x 3.2 mm, and 18.6 mm x 6.4 mm x 3.1 mm for the prepreg specimen. The test span was 12.8 mm and 12.4 mm for the RTM and prepreg specimens respectively.

RESULTS AND DISCUSSION

Void Characterisation

The voids formed in the RTM and Prepreg laminate panels were classified by location, shape and size. The comparison between voids in the RTM and prepreg laminates was limited to the 0 to 5% void volume fraction (V_v) range. The reason for this upper limit is that the maximum observed porosity content in the prepreg laminates was 5.2% V_v .

In the prepreg laminates it was generally easy to identify the ply interfaces, due to relatively little intermingling between tows from different plies, and due to the voids all being located between fabric plies. The prepreg fabric appeared to have been passed through rollers, as there was little distinction between adjacent parallel tows in each 5-harness ply—the structure was quite similar to that of a tape prepreg laminate in this regard. No voids were found between tows of the same ply. Voids appeared to be pancake-shaped, as indicated in Fig. 1.

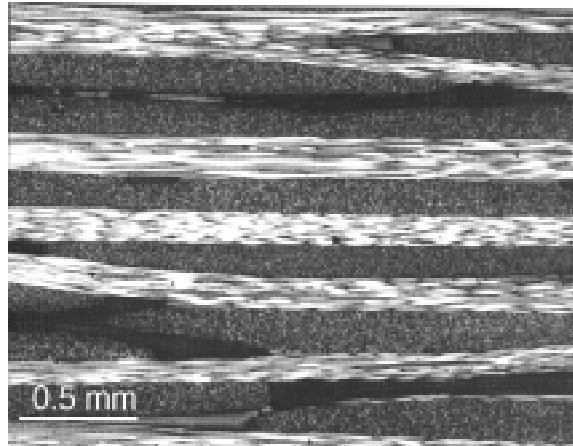


Fig. 1: Voids located between plies in prepreg laminates

The in-plane dimension (length) of these voids ranged from 100 μm to 9 mm, and the through-thickness (height) dimension typically ranged from 25 to 300 μm . Some of these voids were many tows wide, sometimes passing between several pairs of parallel tows. This was not seen in the RTM panels, due to the greater intermingling of tows in the RTM panels. Large bubbles occupying the space at tow intersections were observed, as seen in Fig. 1; however these tended to be longer than those in the RTM panels, due to the lesser degree of intermingling. The voids tended to be geometric-shaped, with arrow-shaped ends, and relatively constant heights. They appeared to be the result of gases trapped between the plies during moulding.

In the RTM laminate, ply intersections were less well defined, with more intermingling of tows in different plies, and little of the intermingling of parallel tows within each ply seen in the prepreg laminate. The cross-sections showed the boundaries of individual tows within a ply more clearly, and the tows have the undulation expected of a woven fabric. Voids were found to be located both between and inside individual fabric plies. Voids located between plies were generally localised at warp tow/weft tow intersections. The shape of these voids varied from spherical to asymmetric—there were no long voids as found in the prepreg laminates at this void content. Small bubbles (see Fig. 2) were typically near-spherical or elliptical, with a diameter between 100 and 200 μm . This type of porosity is referred to as spherical porosity. Larger voids, which were essentially larger bubbles confined to the geometry of the preform, were more irregular in shape, as shown in Fig. 3. These voids are referred to here as asymmetric porosity, with a height between 150 μm and 400 μm , and a length between 250 μm and 4 mm. Most voids, whether large or small, had blunt, rounded edges, apparently because the resin viscosity was sufficiently low to allow the edges of the bubble to take up the lowest surface-energy shape—which is spherical. Above the 5% V_v range it was observed that voids at a fibre intersection can link with neighbouring voids to form a network of porosity, with the length of voids extending up to 30 mm.

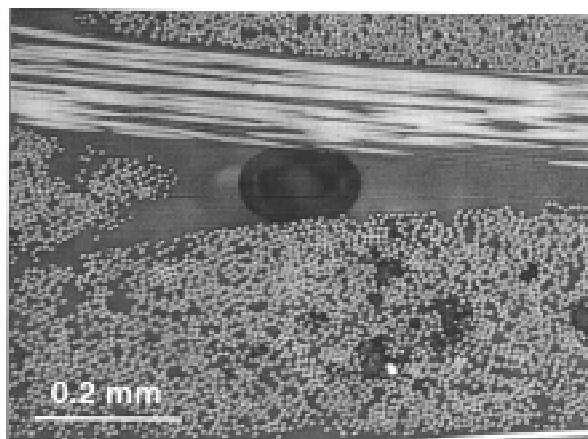


Fig. 2: Micrograph showing spherical bubble between tows in RTM laminate

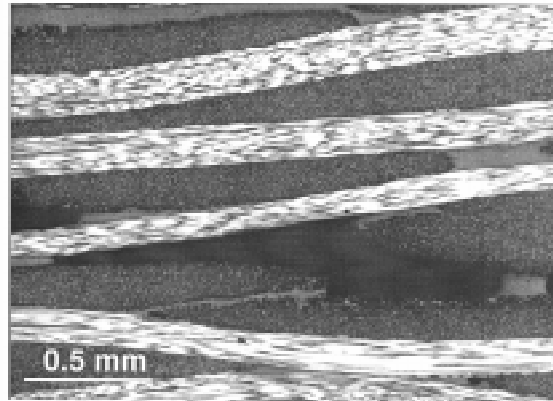


Fig. 3: Micrograph showing asymmetric void in RTM laminate

voids they had a higher aspect ratio than the RTM voids. This can be seen by comparing the large voids in Fig. 1 and Fig. 3.

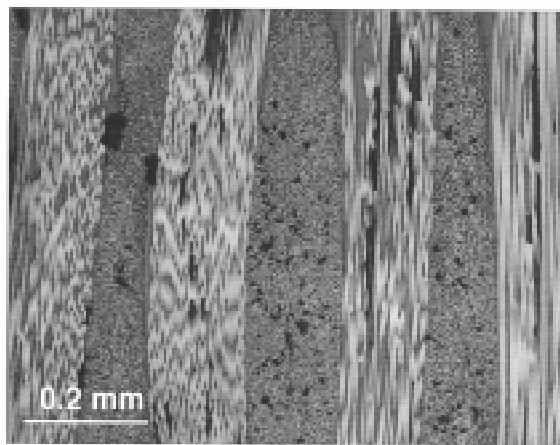


Fig. 4: Cylindrical porosity in RTM laminate

A small quantity of cylindrical shaped bubbles located within tows, with a 5-10 μ m diameter, as shown in Fig. 4, was observed in the RTM laminate. This type of bubble was rarely seen in the prepreg laminate. Above the 5% V_v porosity range, the RTM laminates also had much larger cylindrical air pockets, which were observed engulfing a group of dry fibres, with a void diameter up to 100 μ m. The length of these voids ranged from 50 μ m to 7 mm.

Void Distribution

The distribution of the void types identified above depended on location in the defective RTM and prepreg laminates. A complex network of asymmetrical, spherical and cylindrical porosity was observed in the RTM laminates. This network of porosity extended up to 50 mm from the edge of the completely dry area (the dry spot edge). There was a high population of asymmetric porosity closer to the dry spot edge. Further away from the dry spot edge, the void content and size decreased, with the void shape being more spherical. Outside the perimeter of the porosity associated with the dry spot, there was a general scatter of spherical porosity throughout the laminate, with a void content ranging up to 1.5% V_v . Cylindrical porosity was concentrated at the actual dry spot edge.

Image analysis showed that the level of porosity was several times greater at the surface than internally. This was particularly so for asymmetric porosity and to a lesser extent for spherical and cylindrical porosity. This is thought to be caused by the higher amount of free space (space between the tows) at the mould surface. In the interior of the laminate, the fibre tows are able to intermingle to reduce the available free space that resin or voids can occupy. This form of intermingling cannot occur at the mould surface.

In the prepreg laminates, the main type of porosity formed was associated with trapped gases and exacerbated by excess resin bleed. This is consistent with the higher level of porosity in the laminate close to the outlet ports. As with the RTM laminates, the level of porosity at the surface of the laminate was higher than that internally. Large voids, as seen in Fig. 1, were

commonly observed in prepreg laminate regions with both low and high void contents. However, large voids in RTM laminates were only seen in regions with high void contents.

Interlaminar Shear Strength

The effect of void content on the apparent interlaminar shear strength of RTM laminates is shown in Fig. 5. Each point on the graph represents a single test result. The results are classified according to whether the largest void observed within the ILSS coupon was spherical or asymmetrical.

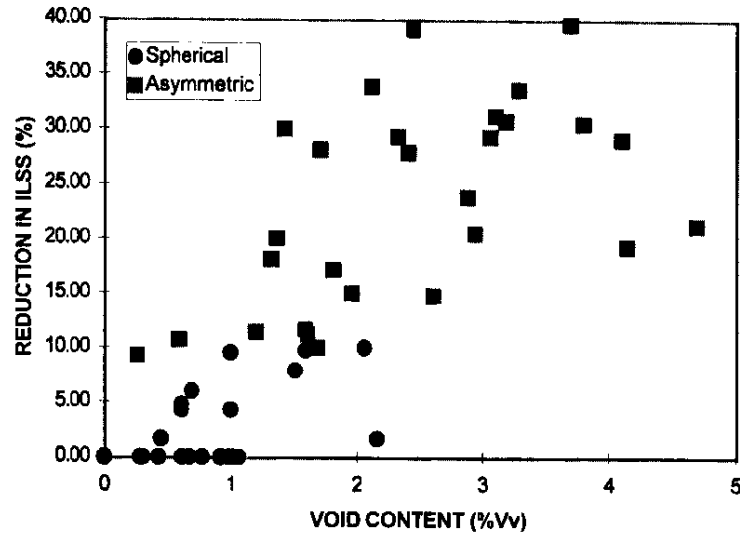


Fig. 5: Graph showing the reduction in ILSS with respect to porosity content and shape for the RTM laminate

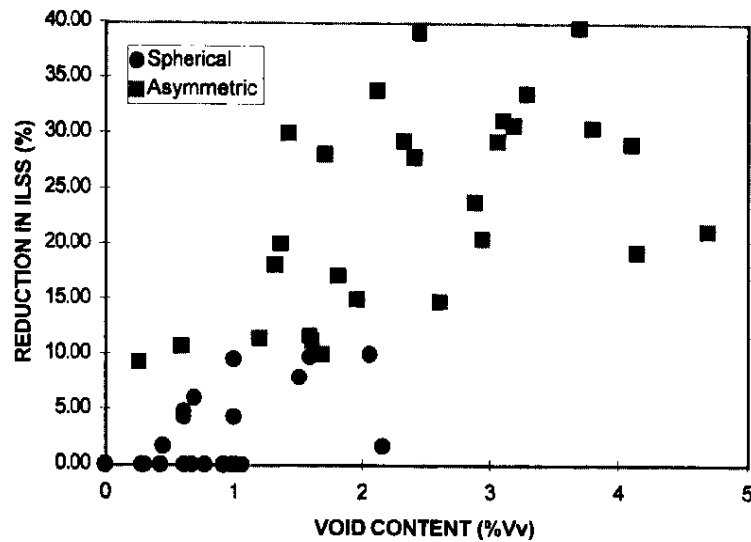


Fig. 5: Graph showing the reduction in ILSS with respect to porosity content and shape for the RTM laminate

Despite the scatter in results, there is a general trend from the plot indicating a 8% decrease in ILSS per 1% increase in porosity. The region between 0 and 2% V_v provides a comparison between the effect of spherical and asymmetric porosity. Even at a void concentration of 2% V_v , there was little effect of bubble porosity on the ILSS. The effect of asymmetric porosity is shown to be greater than that of spherical porosity, at the same void volume fraction. This may be due to the larger flaw size and irregular shape of asymmetric porosity. Defects increase local stress concentrations [15]. A sharper flaw edge, or a longer flaw, leads to a higher stress concentration [16]. Hence a delamination crack is likely to initiate at a lower load at an asymmetric void.

In the 2 to 5% V_v range, the high scatter in results may be related to the location of the voids within the coupon [15]. There is up to a 25% difference in ILSS strength between coupons containing the same void content. Examination of failed ILSS coupons showed that the failure region contained a series of intralaminar and interlaminar cracks located in the midsection of the coupon (beam). The strength of the coupon was associated with the size and content of voids within this critical region. Analysis of a pair of failed coupons with 2.5% V_v , but different ILSS results, showed that the lower-strength coupon had two large asymmetric voids located in the critical region. The higher-strength coupon had asymmetric voids concentrated at one end of the coupon, outside of the critical region. Furthermore, various other test coupons in the 2 to 5% V_v range showed that the size of the largest asymmetric voids in the critical region of the coupons were similar. If the void content in the critical region in the centre of the ILSS coupon could have been measured, it is thought that the scatter in Fig. 5 would have been considerably reduced.

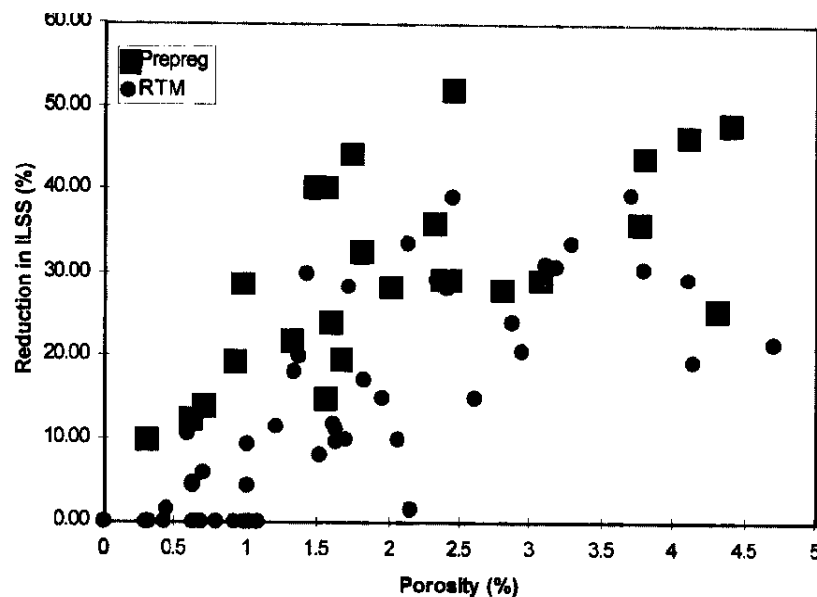


Fig. 6: Graph showing the reduction in ILSS for RTM and Prepreg laminates with respect to void content

A comparison between the effect of porosity on the prepreg and RTM laminates is shown in Fig. 6. Each point on the graph represents a single test result. For the prepreg laminate, the plot suggests a general trend of a 12% reduction in ILSS per 1% increase in porosity content, which is similar to Ghiorse's results [1]. The prepreg results appear to be quite similar to the RTM results for asymmetric voids alone, but with a greater drop in ILSS. The voids in the prepreg laminate coupons were primarily pancake-shaped with sharper edges, ie. with a higher aspect ratio. This would seem to explain the greater level of strength reduction compared to the RTM results.

CONCLUSION

Carbon/epoxy laminates manufactured by RTM and prepreg processes from the same materials, and with similar fibre volume fraction, showed quite different void morphologies. This difference in void morphology led to a difference in the level of reduction in interlaminar shear strength. For the RTM laminate, there was a significant difference in void shapes and sizes, depending on the location near the dry spot. This led to a high scatter in the ILSS results, but it was shown how small spherical bubbles had less effect on the reducing the ILSS than asymmetric voids. Furthermore, the location of asymmetric voids within the coupon affected the level of ILSS reduction.

ACKNOWLEDGMENTS

The authors would like to thank the staff at the CRC-ACS, Aerospace Technologies of Australia (ASTA), and the Aeronautical Marine Research Laboratories (AMRL) for providing their equipment and valuable effort for this research paper. The Australian Research Council (ARC) is thanked for funding this research.

REFERENCES

1. Ghiorse, S.R., "Effect of void content on the mechanical properties of carbon/epoxy laminates", *SAMPE Quarterly*, January 1993, pp 54-59.
2. de Almeida, S. F. M. and Neto, Z. S. N., "Effect of void content on the strength of composite laminates", *Composite Structures*, Vol. 28, 1994, pp. 139-148.
3. Suarez, J. C., Molleda, F., and Guemes, A., "Void content in carbon fibre/epoxy resin composites and its effects on compressive properties", pp 589-596
4. Bowles, k. J. and Frimpong, S., Void effects on the interlaminar shear strength of unidirectional graphite-fiber-reinforced composites, *Journal of Composite Materials*, Vol. 26, No. 10, 1992, pp 1487-1509.
5. Wood, J.R., and Bader, M.G., "Void control for polymer-matrix composites (2): experimental evaluation of a diffusion model for the growth and collapse of gas bubbles", *Composites Manufacturing*, Vol. 5, No. 3, 1994, pp. 149-158.
6. Wood, J.R. and Bader, M.G., "Void control for polymer-matrix composites (1): experimental evaluation of a diffusion model for the growth and collapse of gas bubbles", *Composites Manufacturing*, Vol. 5, No. 3, 1994, pp. 140-148.
7. Parnas, R.S. and Phelan, "The effect of heterogeneous porous media on mold filling in resin transfer molding", *SAMPE Quarterly*, January, 1991, pp. 53-60.
8. Patel, N., Rohatgi, V., and Lee, L., "Void formation and removal in liquid composite molding", *49th Annual Conference, Composite Institute, The Society of the Plastics Industry, Inc.* February 7-9, 1994, Session 10-D.

9. Lundstrom, T.S., Gebart, B.R. and Lundemo, *Proc. of 47th Ann. SPI Compos. Inst. Conf. Session 16-F*, 1992, Session 16-F.
10. Hayward, J. S. and Harris, B., Effect of process variables on the quality of RTM mouldings, *SAMPE Journal*, Vol. 26, No. 3, 1990, pp. 39-46.
11. Rohatgi, V, Patel, N. and Lee, J.L., "Experimental investigation of flow-induced microvoids during impregnation of unidirectional stitched fiberglass mat", *Polymer Composites*, Vol. 17, No. 2, 1996, pp 161-170.
12. Patel, N, Rohatgi, V. and Lee, J.L., "Micro scale flow behaviour and void formation mechanism during impregnation through a unidirectional stitched fiberglass mat", *Polymer Engineering and Science*, Vol. 35, No. 10, 1995, pp. 837-851.
13. Groenendaal N., *Reinforced Plastics*, July 1992, p50.
14. Oliver, P., Cottu, J.P., and Ferret, B., "Effects of cure cycle pressure and voids on some mechanical properties of carbon/epoxy laminates", *Composites*, Vol. 26, No. 7, 1995, pp 509-515.
15. Wisnom, M. R., Reynolds, T. and Gwilliam, N., "Reduction in interlaminar shear strength by discrete and distributed voids", *Composites Science and Technology*, Vol 56, 1996, pp 93-101.
16. Hull, D., *An introduction to composite materials*, Cambridge University Press, Great Britain, 1981

RESIN TRANSFER MOULDING FOR MISSILE SHROUD PRODUCTION

J. Ludick

*Process Engineer, Denel Aviation,
Atlas Road, Kempton Park, 1620, Republic of South Africa*

SUMMARY: The resin transfer moulding(RTM) process is the preferred technique for production of structurally loaded components with complex three dimensional shapes. The resemblance to plastic injection moulding, which is a well understood industrial process, is the main contributing factor towards the popularity of RTM. The industrialization of the process to produce high quality aerospace products with a low reject rate and very few finishing operations requires careful studying of the factors that influence the process and ultimately the product. Many numerical flow models of the RTM process have been developed in attempts to quantify the effects associated with filling a non-homogeneous cavity with a liquid of which the viscosity changes during the process. Naturally many problems exist due to the complexity of the process and many assumptions have to be made regarding the boundary conditions along the perimeter of the cavity.

This study gives physical insight into the RTM process by studying the process visually, in a transparent tooling system. Moulding problems can be spotted immediately and the effect that changes to the tooling and fibre-pack have on the process can be witnessed. Visualizing the filling of the cavity with pigmented resin not only gives the tool designer a magnificent feel for the process but also eliminates many hours spent trying to model the process with little feel for the accuracy of the results.

The use of castable elastomeric tooling with which relatively big tooling changes can easily be accommodated limits development cost to the minimum and provides an excellent alternative to preforming by inserting the layers into the flexible cavity.

KEYWORDS: resin transfer moulding, transparent tooling, mould fill rate, process visualization, fibre density

INTRODUCTION

The RTM process is suited to the production environment probably due to the many similarities with plastic injection moulding. The addition of **oriented continuous** fibres , however, makes the process far more sophisticated and does not merely require the filling of a mould cavity with a homogenous molten thermoplastic under high pressures. The structural requirements and performance of the component places an additional complication onto the process besides the geometric difficulties and in many instances the requirement to have fibres placed in required directions of principal stress and keeping them there during moulding far exceeds the geometric complexity.

The manufacturing of a composite shroud and wings in one integral step was investigated as a feasibility project funded under Kentron internal technology. The shroud would form part of an air launched anti tank missile currently under development as part of the Rooivalk attack helicopter weapon arsenal.

PROJECT OBJECTIVES

The introduction of light weight components at the early development stages of a missile is the ideal situation as the mass distribution and accompanying mass moments of inertia of the weapon are the very first characteristics to be defined and fixed at a systems engineering level. The mass distribution will determine the maximum turn rate and lateral acceleration as well as the required structural mass to obtain specified stiffness values. It is therefore important to have an accurate estimate of the mass of a component and unlike conventional materials, the component mass of a composite structure is very much dependent on the process used to manufacture it as well as many variables within the process.

The objectives of the project were:

- To evaluate the RTM process as a possible production process
- To structurally test the produced prototypes
- To obtain an accurate estimate of the mass of the component
- To obtain a cost estimate of the component

A total of four prototypes were manufactured which are shown in figure 1

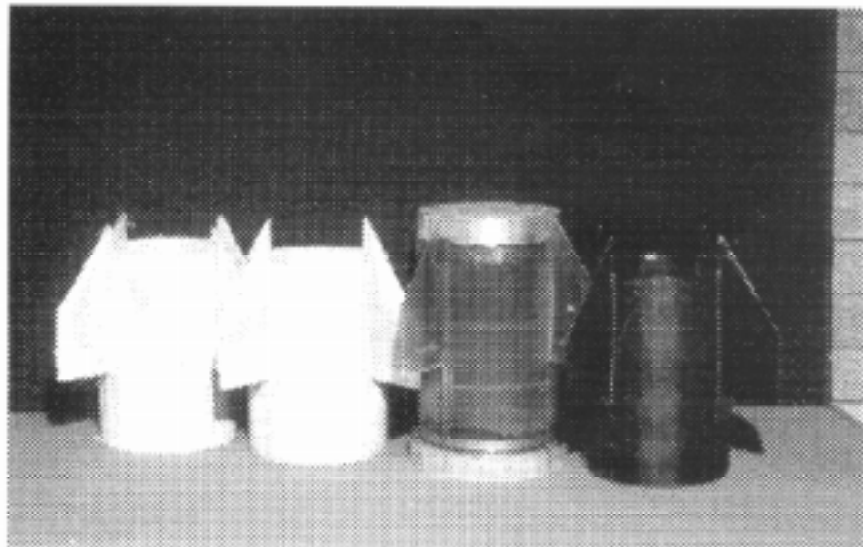


Figure 1: Prototype Shrouds

PROTOTYPE TOOLING SYSTEM

The prototype shrouds were made using the RTM process with vacuum only as definite sealing problems would be encountered when trying to apply positive pressure. The cavity perimeter therefore was not sealed but a “wet” tool philosophy was followed for prototyping. The tooling schematic is shown in figure 2.

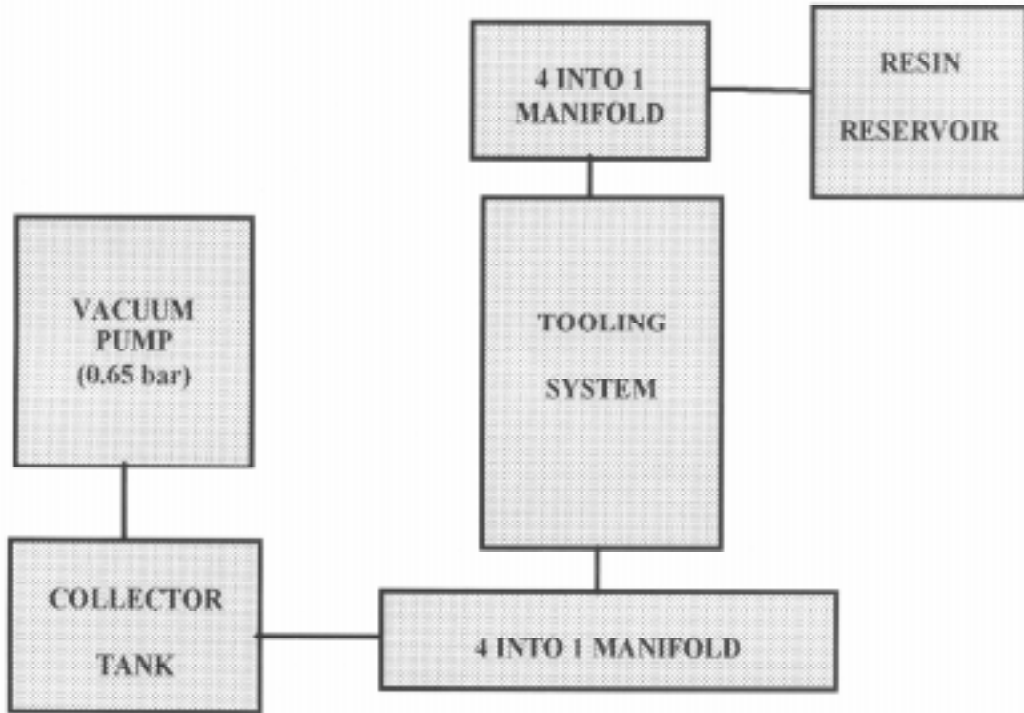


Figure 2: Prototype tooling schematic

PROTOTYPE RESULTS

The prototype quality rapidly improved and by the third attempt it was realized that no further improvement could be possible without changes to the tooling and fibre lay-up.

Although structurally sound shrouds were made, it was realized that the production quality of the shrouds was not in order and that repeatability of the process was far too much dependent on the mould preparation and fibre placing.

The major problems occurring with the process and the component were:

Excessive mould fill time

The mould was assumed to be filled when all four exhaust lines were filled with clear resin free of bubbles and interrupted turbulent flow. Resin reached the exhaust lines after approximately 1 minute at 60°C and 0.6 bar vacuum, but the assumption that the mould was filled proved wrong with the existence of dry spots on all four wings and adjacent shroud segments noticed upon curing and demoulding.

Applying vacuum for at least 10 minutes from connecting the inlet ports resolved this problem, but produced around 600g of unused cured resin in the reservoir at the vacuum pump end of the tool.

Absence of fibres in the wing apex

Figure 3 shows the absence of fibres in the wing apexes which was observed on all four wings of all the shrouds. The integrity of the edges of the wings is of obvious importance and the presence of fibres in these areas is a definite requirement to ensure damage tolerance during handling and assembly processes.

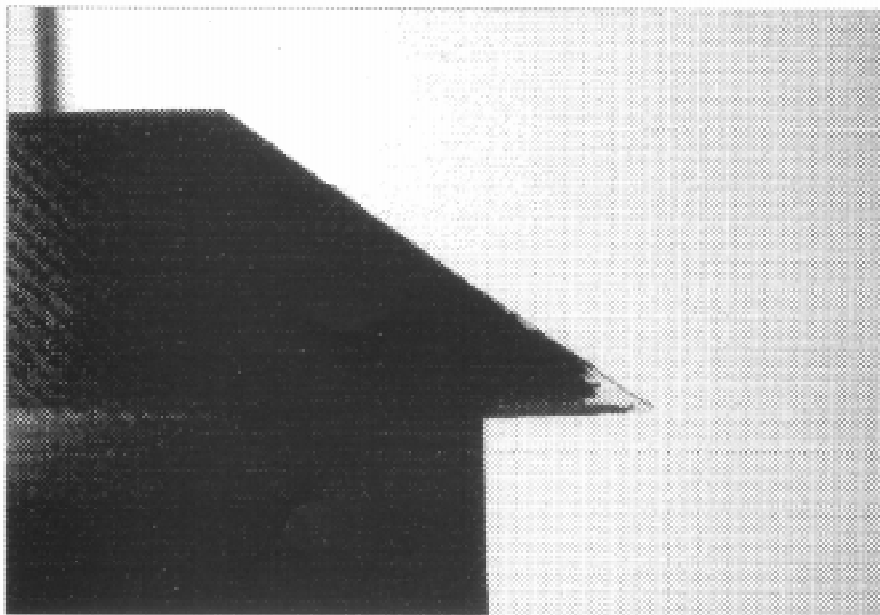


Figure 3: Fibre absence in wing apex

High resin content in wing roots

Figure 4 shows a picture of the wing root taken from the inside of the shroud with a very resin rich area all along the root. The fact that this problem was not observed at all the roots was a reason for concern as far as the repeatability and resulting structural integrity of the wings are concerned.

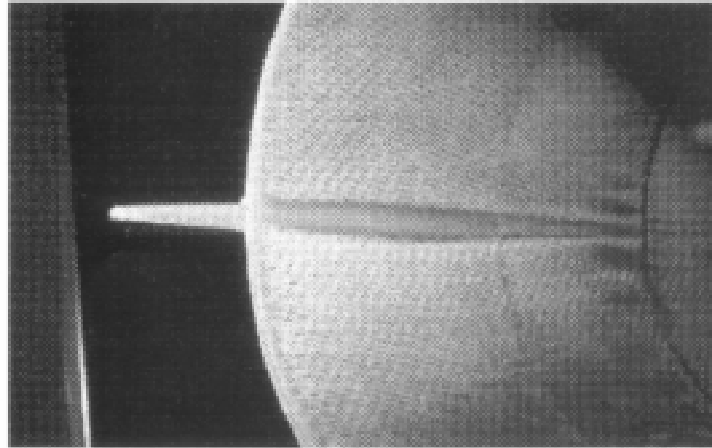


Figure 4: Resin rich root area (viewed from shroud centreline)

On the positive side the following results were obtained:

- The third shroud was structurally loaded to a load representing 112% of the ultimate load with delamination in the root occurring as shown in figure 5.

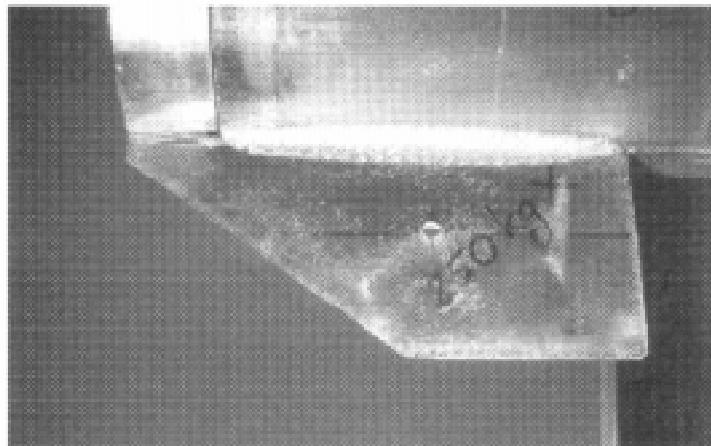


Figure 5: Structural failure in root at 112% ultimate load

- A fibre volume fraction of 56% was achieved with a mass saving over the conventional aluminium shroud of around 40%.
- A total cycle time of 3 hours including curing using only one tool is possible.

MOULD FILL RATE VISUALIZATION

The prototype stage highlighted the fact that the RTM process needed to be fine tuned to enable **production** of complex shaped components and that localized problems like the abovementioned need to be solved without compromising on component quality or tooling simplicity. The need to “know what’s going on inside the tool” during the process encouraged the use of transparent tooling and pigmented resin to witness in real time the filling of the cavity.

A tooling box of Polymethylmethacrylate (PMMA) was made with the cavity cast around the master pattern using a clear silicone rubber. A cross-section of the tooling system representing one quarter of the shroud is shown in figure 6.

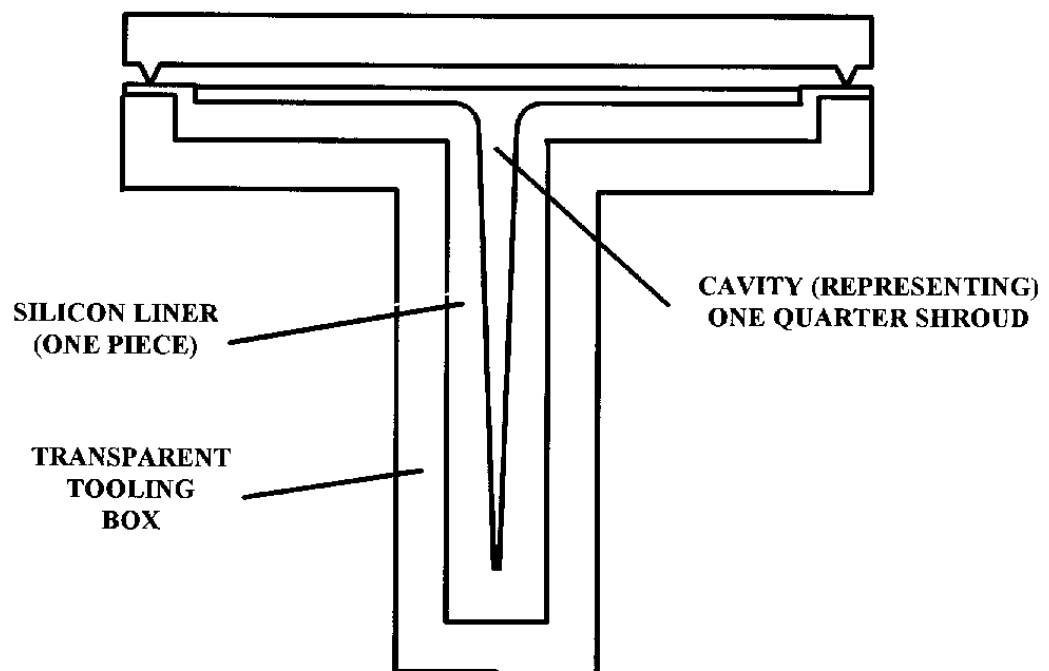


Figure 6: Transparent tooling section

All the experiments were done inside a vacuum chamber to ensure equal pressure inside and outside the tool in order to avoid deflection of the tool due to a pressure differential.

RESULTS

The reason for having an excessive mould fill time as well as the absence of fibres in the wing apexes can be explained by viewing the following snapshot in figure 7 of the fill rate of the original lay-up taken shortly after full vacuum was applied.

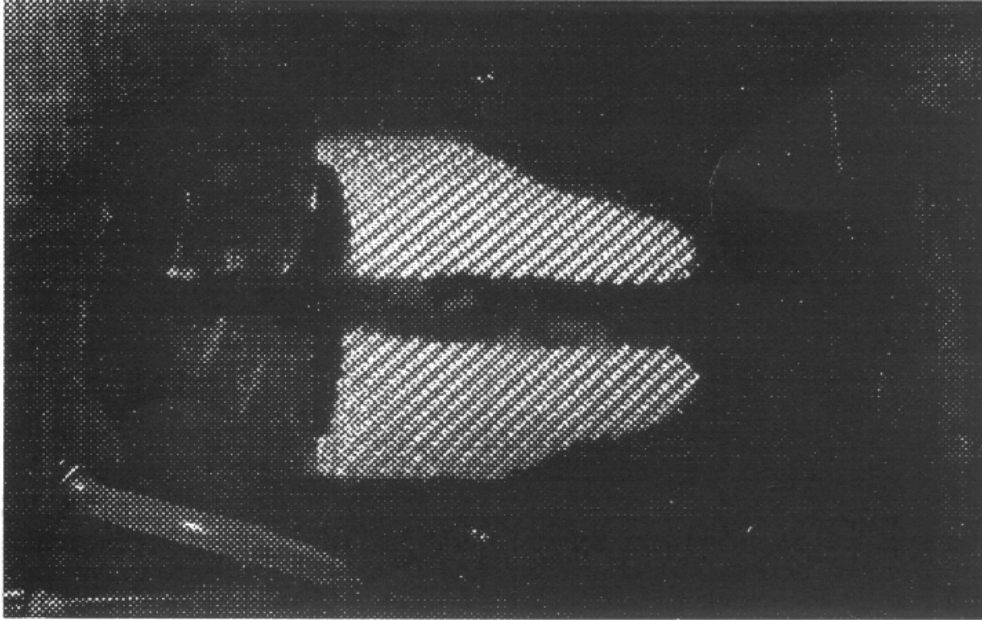


Figure 7: Excessive root fill rate

The rapid filling of the root section is evident by the horizontal band running from the trailing edge(right) to the leading edge(left) of the wing with the shroud section evidently lagging. This explains why resin emerges into the exhaust lines rapidly after vacuum was applied to the tooling system but dry areas still exist if one assumes the mould was filled. Applying vacuum for longer periods solved this problem, as mentioned earlier, and the 600g wasted resin is the collection of resin that flow through the less dense wing roots which is a practical proof of the well known Darcy formula:

$$V = -\frac{K}{\mu} \nabla P$$

Which simply states that the flow velocity (V) is proportional to the product of the pressure gradient (∇P) and the fibre-pack permeability (K) and inversely proportional to the resin viscosity (μ).

The high permeability (low fibre density) in the root area calls for high flow velocities in this area and is an inherent geometric problem due to the existence of dissimilar thicknesses and a fillet radius at the wing /shroud interface.

The presence of short fibres in the wing apexes, mostly transverse to the flow in this area, also explains the fibre washing problem in these areas.

A cross section of the cured wing root (Figure 8) shows that the fibre distribution in the root is unacceptable from a structural point of view and is a sure recipe for inconsistency of strength and stiffness within a production environment.

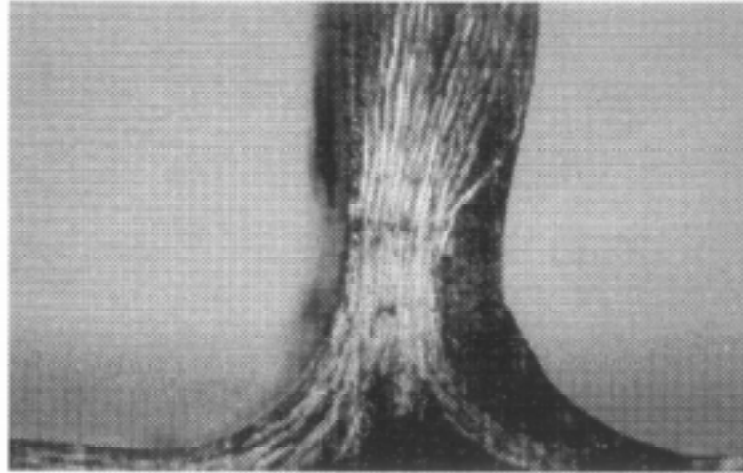


Figure 8: Wing root cross-section

Densifying the root by adding more fibres to the root section is a step towards obtaining a more constant fill rate but is very difficult to control .

The addition of a core to the wing root is the easiest way to obtain a repeatable fibre density in the wing roots and sufficiently densifies the root to ensure a more uniform fill rate. The resulting fibre distribution in the root (Figure 9) is indicative of a sound interface.

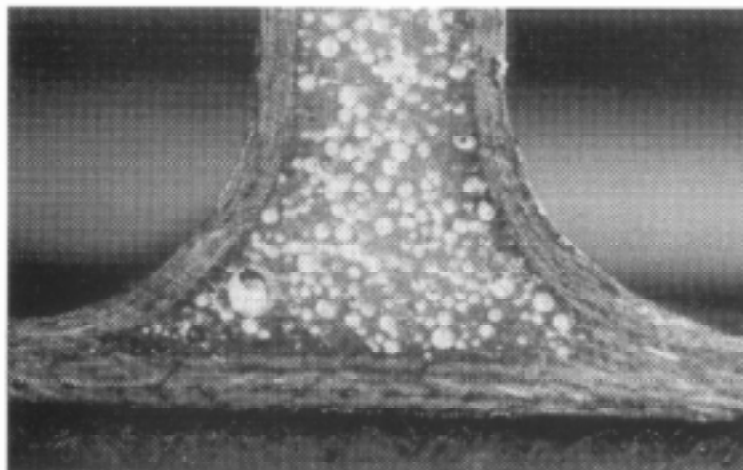


Figure 9: Root fibre distribution with core added

CONCLUSIONS

The visualization of the filling of the cavity during the experiments in this study, provided excellent insight into the problems that can occur with RTM of a complex geometry component such as the shroud. The following conclusions based on witnessing the RTM process from "within" the mould are readily drawn:

- Fill rate visualization is an excellent means of rapidly accessing problems that can occur with your process without employing risky guesswork associated with modeling the process
- The economic production (low resin wastage) of the components requires a uniform fibre pack permeability to avoid some sections filling up long before others.
- Elastomeric tooling can be used as a low cost mould face ,backed by a rough machined tooling box. This system of tooling can easily accommodate relatively large changes in the development phase of a project at low cost.
- The use of an elastomeric liner facilitates easy sealing of complex moulds as split lines on the wings, for instance, are not required due to the fact that the liner is removable and flexible enough to demould the component.
- The wing lay-up can be done by wedging the folded fabric into the flexible cavity from the root end thus preforming into the mould which ensures fibre presence along the wing perimeter.
- The incompressibility of the resin inside a sealed tool combined with the high coefficient of thermal expansion of the liner, if elevated temperature curing is applied, provides a promising solution to traditional low fibre volume fractions with RTM.

REFERENCES

1. Handbook of Composites, George Lubin , Second edition, Addison Wesley, 1992
2. Engineered Materials Handbook, Volume1, Composites, Society of Automotive Engineers, 1991
3. Model for Determining the Vent Locations and the Fill Time for Resin Transfer Moulds, Alexis Boccard, Woo Il Lee and George S. Springer, Department of Aeronautics and Astronautics, Stanford University, *Journal of Composites Materials*, Vol. 29, No. 3/1995
4. The Flexible Resin Transfer Moulding Process, Michael F. Foley, The Charles Stark Draper Lab, Inc., Cambridge, MA. *Sampe Journal*, Vol. 28, No. 6, November/December 1992

RTM PROCESSING OF GRP-PHENOLIC COMPOSITES

Nigel A. St John, James R. Brown, Mark W. Taylor and Karen E. Challis

*DSTO, Aeronautical and Maritime Research Laboratory
P.O. Box 4331, Melbourne, Victoria, 3001, Australia*

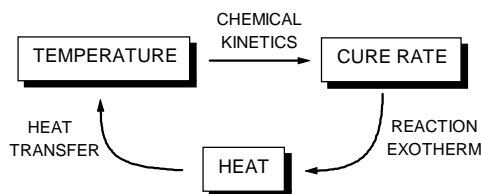
SUMMARY: GRP-phenolic composites are inherently fire retardant and resin transfer moulding (RTM) provides several advantages for their fabrication. To facilitate a better understanding of the issues associated with RTM of acid-catalysed phenolic resole resins, the cure has been studied using isothermal differential scanning calorimetry and viscosity measurements over a range of temperatures. The results are analysed using a series of empirical formulas that describe the changes in extent of reaction, heat flow and viscosity with time and temperature. The total heat of reaction is 347 J.g^{-1} and the consequences for RTM processing are discussed. Also identified is the importance of additional cure above 70°C to achieve satisfactory mechanical properties.

KEYWORDS: phenolic resole resin, GRP-phenolic, DSC, viscosity, RTM, chemorheology

INTRODUCTION

The increasing use of glass reinforced polymer (GRP) composites in the transport, building and maritime industries has required the development of materials with improved performance under fire conditions. Phenolic resins are inherently fire retardant so that on exposure to fire they give longer ignition times, lower heat release rates and a lower amount of smoke compared to polyester, vinyl ester and epoxy resins [1]. The development of low viscosity phenolic resole resins that are curable at low temperatures and pressures using acid catalysts has enabled their application as laminating resins for the production of GRP-phenolic composites [2]. The phenolic laminating resins have several features, including a short pot life, that have limited their use in GRP composites fabricated by conventional methods such as hand lay-up. Resin transfer moulding (RTM), as well as providing general improvements to part quality, including improved fibre wet-out, also offers the advantage of removing the pot-life constraint. RTM processing is thus becoming a preferred method of fabricating GRP-phenolic composites [3].

RTM processing of phenolic resole resins requires special attention to temperature control as there is a temperature ceiling of approximately 90°C imposed by the water that is present in the neat resin and which is generated by the cure reaction [4]. If this temperature is exceeded, the vaporisation of the water can be catastrophic in a closed mould due to the increased internal pressure. The issue becomes more critical because the reaction is exothermic which results in a temperature feedback loop as described by Scheme 1.



Scheme 1

The parameters that control the degree of feedback and thus the temperature stability are the chemical kinetics and the reaction exotherm, which are intrinsic properties of the resin, and the heat transfer properties which are dependent on the design and material properties of the mould, the shape and dimensions of the part being fabricated, the reinforcement and the environment. If either the reaction exotherm is too high or the heat transfer is too slow, the heat flow will be positive and cause the temperature to rise and the reaction rate to increase. If this feedback is too strong the temperature will quickly reach the point where water will vapourise.

Another important parameter in RTM processing is the resin viscosity which is dependent on both the temperature and the extent of reaction (Scheme 2), as well as in some cases the shear rate. The viscosity can be related to the resin flow rate and the mould filling pressure using the permeability of the reinforcement and Darcy's law [5].



Scheme 2

Once the chemical kinetics-reaction exotherm-viscosity relationships (i.e. chemorheology) are determined for a particular resin system, RTM simulation software can be used to model the filling of a resin transfer mould if its physical properties are known [5]. Little information exists in the literature on the chemorheological behaviour of low viscosity acid-catalysed phenolic resole resin systems, so this work has focussed on characterising these properties.

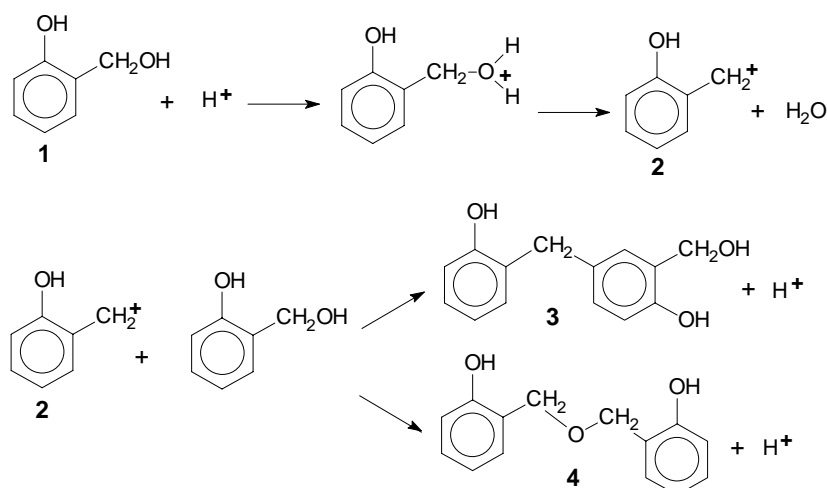
EXPERIMENTAL

The phenolic resole resin Resinox[®] CL1916 and acid catalyst Resinox[®] AH1964F from the Huntsman Chemical Co. Australia Pty Ltd were used in a ratio of 7 parts catalyst to 100 parts resin. Differential scanning calorimetry (DSC) was performed using a Dupont Instruments 910 Differential Scanning Calorimeter with 15-20 mg samples in hermetically sealed pans. Viscosity measurements were made using a Brookfield DV II digital viscometer with controlled isothermal temperature.

RESULTS AND DISCUSSION

Resin Chemistry

Phenolic resole resins are produced from the alkali-catalysed reaction of phenol and formaldehyde which results in varying degrees of methylol group substitution at the *para* and *ortho* positions of the phenol ring [6]. The resin is primarily the mono-substituted species (eg. **1** in Scheme 3) and when catalysed with an acid, reacts via the formation of benzylic carbonium ions (**2** in Scheme 3), with vacant substitution sites on phenol rings to yield methylene links (**3** in Scheme 3) or with other methylol groups to yield ether links (**4** in Scheme 3). The ether links can then thermally decompose with the release of formaldehyde to yield methylene links, though this occurs at temperatures higher than the usual cure temperatures. The resin also contains 20 - 30 % disubstituted phenols which provide the crosslinking necessary to form a rigid material. Thus, for the production of methylene links, one unit of water is produced for every unit of methylol groups reacted. For the full cure of a phenolic resole resin, this results in approximately 11 wt% water being formed. The variety of different species in the resin and their different reactivities [6] mean that there is no simple mechanistic description of the cure kinetics.



Scheme 3: Acid-catalysed cure reactions of phenolic resole resins

Differential Scanning Calorimetry

The cure of the catalysed resin can be followed by DSC which measures the heat flow from a sample under controlled conditions. The amount of heat flow (dq/dt) is proportional to the rate of chemical reaction ($d[A]/dt$) and the heat of reaction (ΔH_A) as shown in Eqn 1 where A and B refer to different reactions. The integration of Eqn 1 with respect to time yields a value for total heat released and thus the heat of reaction. The cumulative integral also gives a measure of the extent of reaction (α) versus time.

$$\frac{dq}{dt} = \Delta H_A \frac{d[A]}{dt} + \Delta H_B \frac{d[B]}{dt} + \dots \quad (1)$$

Fig. 1 shows heat flow data for a catalysed resin sample during a $5^\circ\text{C}\cdot\text{min}^{-1}$ dynamic DSC scan. The curve follows the same trend to that obtained by Focke *et al.* [7] for a similar resin

system with two peaks being evident which is indicative of two separate reactions. The higher temperature peak may result from the thermal decomposition of ether links (2 in Scheme 3) but this has not yet been confirmed by spectroscopic studies. The total heat obtained by integrating the peaks is 346 J.g^{-1} which is significantly higher than the 228 J.g^{-1} obtained by Focke *et al.*, however Gupta *et al.* [8] have shown that the heat of reaction for the cure of phenolic resoles is very sensitive to the pH.

Isothermal DSC measurements can provide accurate kinetic data at the temperatures of interest that closely reflect the conditions used in practice. Fig. 2(a) shows the isothermal heat flow produced by a resin sample cured at 40°C , starting at a maximum and then decreasing rapidly. This is significantly different to what is observed for the cure of polyester and vinyl ester resins which show no significant heat produced until the resin gels. This 'front end' exotherm is significant in relation to RTM processing when Scheme 1 is considered as it means that the major heat effects occur during and just after the filling of a mould.

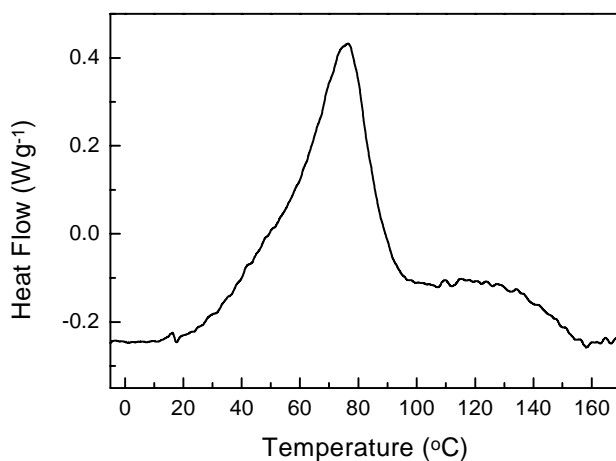


Fig.1: Dynamic DSC scan at 5°C.min^{-1} of catalysed phenolic resole resin

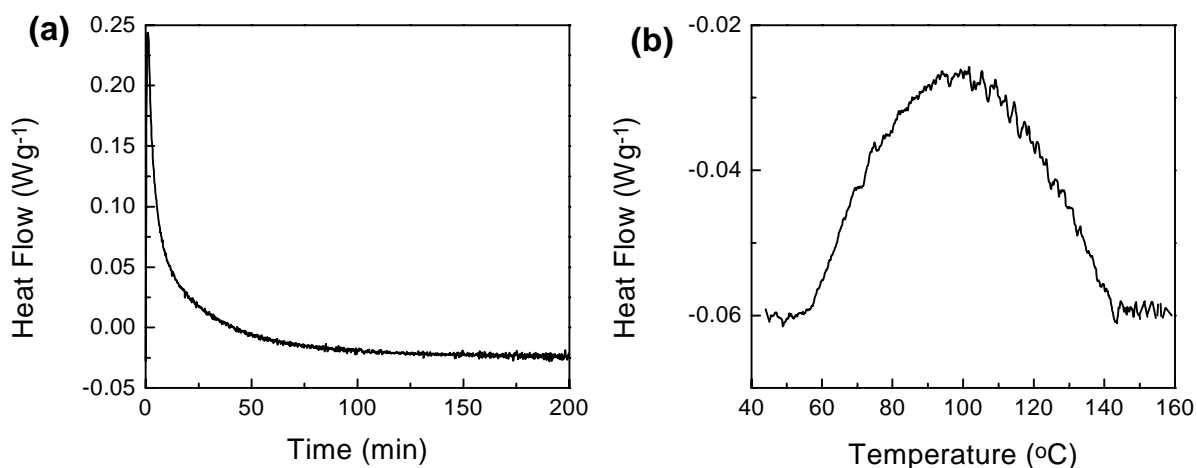


Fig. 2: DSC of catalysed phenolic resole resin (a) isothermal at 40°C and (b) residual heat scan at 1°C.min^{-1}

Table 1: Heats of reaction (ΔH_{iso} , ΔH_{res} , ΔH_{tot}) and isothermal extent of reaction (α_{iso}) for catalysed phenolic resole resin

Temperature (°C)	ΔH_{iso} (J.g ⁻¹)	ΔH_{res} (J.g ⁻¹)	ΔH_{tot} (J.g ⁻¹)	α_{iso}
35	222	125	347	0.641
40	228	119	347	0.657
45	242	110	352	0.687
50	261	98	359	0.728
55	262	87	349	0.751

The total heat produced at various isothermal temperatures, ΔH_{iso} , are summarised in Table 1. After each isothermal run, the sample was subjected to a 1°C.min⁻¹ dynamic DSC scan to measure the residual heat of reaction, ΔH_{res} (Table 1), and the sum of the two measured heats yields a value for the total heat of reaction, ΔH_{tot} (Table 1). Also shown in Table 1 is the extent of reaction at each isothermal temperature (α_{iso}) calculated using the heats of reaction. The extent of reaction ($\alpha = \Delta H_t / \Delta H_{\text{tot}}$) calculated using the cumulative integral of heat flow ΔH_t and ΔH_{tot} are plotted versus time in Fig. 3. The results show that while the maximum extent of reaction increases with cure temperature, the increase is not large and even at 55°C 25 % remains unreacted. The significance of the extra cure at high temperatures to the matrix properties was investigated by measuring the tensile properties of cast resin cured for 5 h at 40°C and then postcured for 5 h at 80°C. The results (Table 2) show a major increase in properties with postcure which is indicative of an increase in crosslink density. The effective degree of functionality of the phenolic resin is about 1.2 which means that at 70 % conversion the resin matrix is probably more akin to a high molecular weight branched polymer than a crosslinked network, which would explain the low strength and modulus after curing at 40°C. The final 30 % conversion is thus essential to achieving a well crosslinked matrix and this can only be obtained by further cure above about 70°C (see Fig. 2(b)).

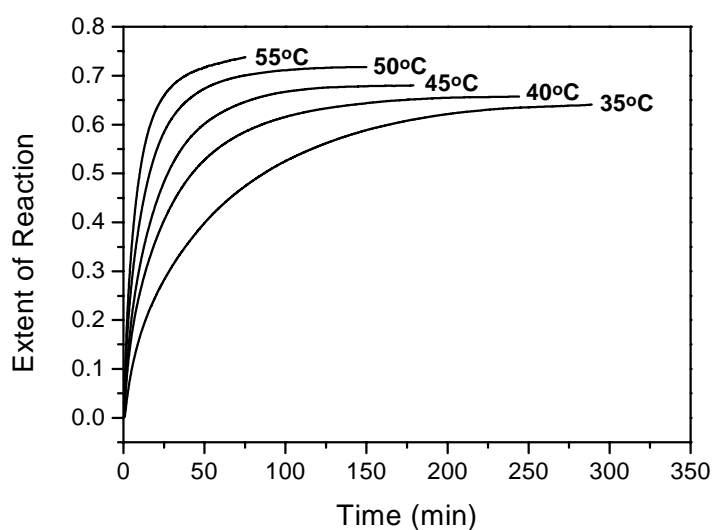


Fig 3: Extent of reaction versus cure time for catalysed phenolic resole resin at different temperatures.

Table 2: Tensile properties of cast resin

Cure	Tensile Strength (MPa)	Tensile Modulus (GPa)	Elongation to Break (%)
5 h at 40°C	10.2	1.37	0.79
5 h at 40°C + 5 h at 80°C	33.4	2.79	1.28

Modelling the filling of a resin transfer mould requires mathematical descriptions of the cure kinetics and their temperature dependence. As discussed earlier, a mechanistic description of the cure kinetics is very complex and thus impractical, so an empirical approach has been adopted. The analysis of the cure profiles revealed that it was necessary to distinguish between a fast reaction that occurs during the initial stage of cure and the remainder of the cure. The early reaction, designated as reaction A which represents 0.08 of the total measured reaction, was found to follow a first order kinetic relationship (Eqn 2) with the rate constant k_A (min^{-1}) described by an Arrhenius relationship (Eqn 3) with temperature, T , in absolute units (K).

$$\frac{d\alpha_A}{dt} = k_A(1 - \alpha_A) \quad (2)$$

$$\ln k_A = -\frac{8199}{T} + 22.56 \quad (3)$$

The remainder of the isothermal cure (i.e. 0.92 of the total), designated as reaction B, can be described by a modified second order kinetic relationship (Eqn 4) in which the rate constant k_B is described by Eqn. 5 and the total isothermal conversion, α_{iso} , calculated using Eqn. 6. There may be a more appropriate form for the kinetic relationship for the cure but Eqns 2 and 4 give very good correlations with the experimental results.

$$\frac{d\alpha_B}{dt} = k_B((1 - \alpha_B)^2 - (1 - \alpha_{iso})^2) \quad \text{for } \alpha_B < \alpha_{iso} \quad (4)$$

$$\ln k_B = -\frac{9990}{T} + 28.26 \quad (5)$$

$$\ln \alpha_{iso} = -\frac{846}{T} + 2.29 \quad \text{for } \alpha_{iso} \leq 1 \quad (6)$$

The kinetic relationships enable the reaction rate to be calculated, and thus the extent of reaction, at a particular temperature. Eqn 7 can then be used to calculate the heat flow (W.g^{-1}) generated by a reacting sample which either goes to raising the temperature or is lost through heat transfer.

$$\frac{dq}{dt} = 0.458 \frac{d\alpha_A}{dt} + 5.325 \frac{d\alpha_B}{dt} \quad (7)$$

It should be noted that the kinetic relationships were derived using isothermal data between 35 and 55°C and so do not cover the higher temperature reaction seen in Fig. 1. However the main focus of this work is to describe the resin behaviour during, and immediately following, the filling of a resin transfer mould. The relationship derived for maximum conversion at a particular temperature (Eqn 6) predicts total conversion at 96°C and above, however this assumes the same reaction occurs through to total conversion which as discussed earlier may not be the case. For this type of resin system, a postcure at 80°C is usually recommended, which according to Eqn 6 will only yield a conversion of 0.9. Further work is being undertaken to determine the most appropriate postcure schedule.

Viscosity

The isothermal shear viscosities of the catalysed resin versus time for temperatures between 25 and 45°C are shown in Fig. 4. The viscosity upper limit of 60 Pa.s imposed by the viscometer used is well beyond the values applicable to the filling of a resin transfer mould, which are usually below 1 Pa.s (1000cps). The viscosity increases during cure from the onset and rises rapidly with increasing cure reflecting the fast reaction rate early in the cure observed in the DSC studies.

A plot of the logarithm of shear viscosity, μ , versus time yields a linear relationship as shown in Fig. 5. After an initial decrease due to temperature equalisation, a fast increase in viscosity is observed for a short period before settling into a slower linear increase for the rest of the measured results. The point of crossover from the faster to the slower rate of increase was assigned as occurring at time X_t minutes. The slopes were measured as C_A and C_B for the early and later regions, respectively. The intercepts were also recorded as pseudo initial viscosity values μ_A^0 and μ_B^0 . All these terms follow an Arrhenius type relationship, with correlation coefficients of 0.999 or better. The equations describing the changes in viscosity up to the maximum measured values are shown as Eqns 7-13.

It is notable that the activation energies derived from the Arrhenius equations for the reaction rate constants (Eqns 3 and 5) and the viscosity rate constants (Eqns 9 and 10) summarised in Table 3 correlate closely for the two cure stages. This supports the analytical approach, with the early reaction clearly reflecting a different reaction to the bulk of the cure. The nature of reaction A is not known though it may be the reaction of the 9 % free phenol present in the resin, which may react faster than the substituted phenols and would have a more pronounced effect on the resin viscosity. The faster cure from reaction A is significant for RTM processing as it generates extra heat and a faster viscosity increase during the mould filling stage.

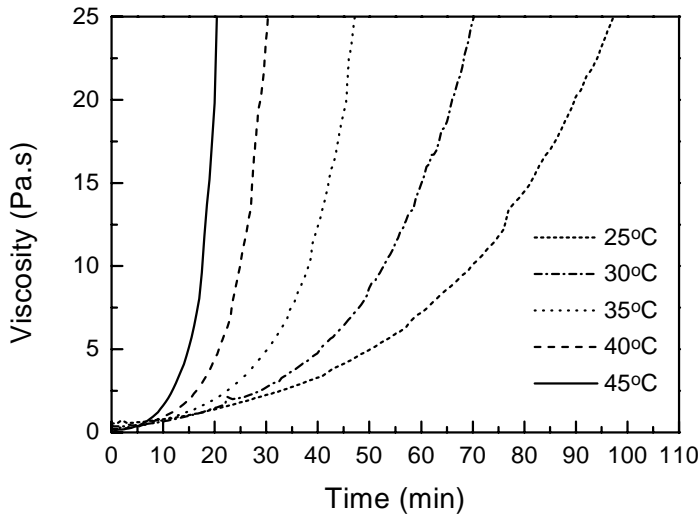
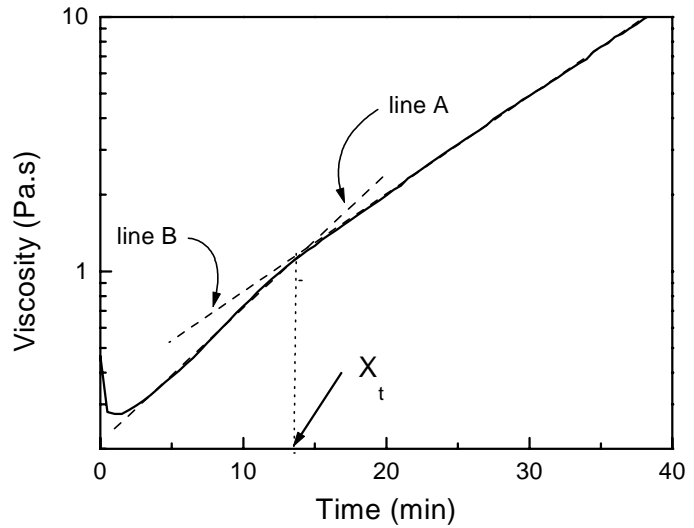


Fig.4: Viscosity versus time for catalysed phenolic resole resin at different isothermal cure temperatures

Fig. 5: Analysis of viscosity data at 35°C.



$$\ln \mu = C_A t + \ln \mu_A^0 \quad \text{for } t < X_t \quad (7)$$

$$\ln \mu = C_B t + \ln \mu_B^0 \quad \text{for } t > X_t \quad (8)$$

$$\ln C_A = -\frac{7579}{T} + 22.49 \quad (9)$$

$$\ln C_B = -\frac{10100}{T} + 30.45 \quad (10)$$

$$\ln \eta_A^0 = \frac{6990}{T} - 17.32 \quad (11)$$

$$\ln \eta_B^0 = \frac{11441}{T} - 31.39 \quad (12)$$

$$\ln X_t = \frac{9971}{T} - 29.75 \quad (13)$$

Table 3: Arrhenius parameters

Term	Activation Energy (kJ.mol ⁻¹)	
	A	B
k (DSC)	68	83
C (viscosity)	63	84

The derived relationships enable the viscosity to be calculated at any time for an isothermal cure. However for use in simulations using a variable temperature, it is necessary to describe a relationship between viscosity and extent of reaction. By interpolating the DSC extent of reaction versus time data to match times with those of the viscosity data, a plot such as Fig. 6(a) for 40°C is obtained. It is important to note however that there is always a degree of uncertainty introduced when combining data collected from different techniques that use different sample masses and environments.

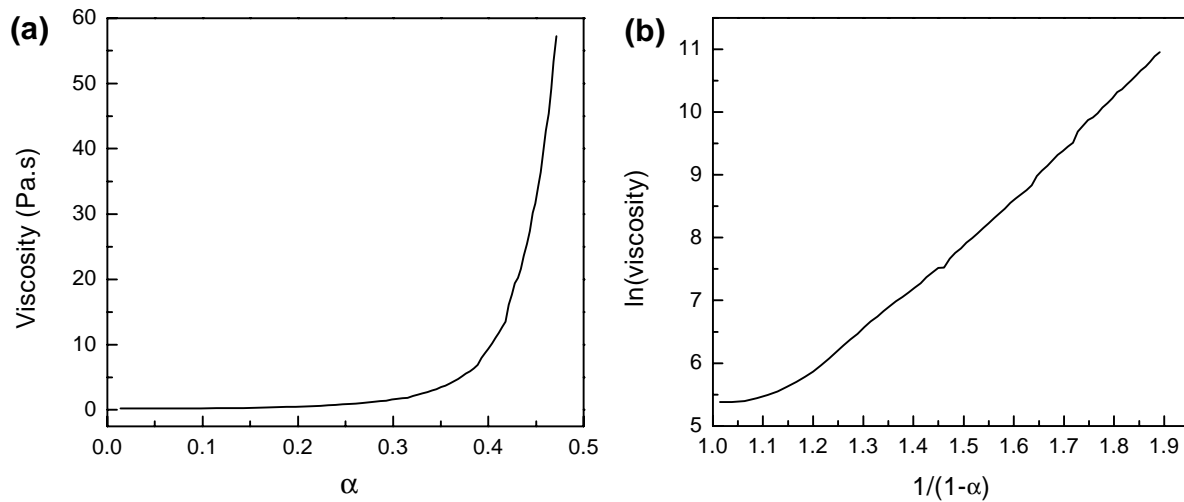


Fig. 6: Plot of (a) viscosity versus extent of reaction (α) and (b) $\ln(\text{viscosity})$ versus $1/(1-\alpha)$ for isothermal cure of catalysed phenolic resole resin at 40°C.

The viscosity of a polymeric fluid is related to its viscosity average molecular weight, M_v , which in turn is related to the number average molecular weight M_n . If it is assumed that up to a conversion of 0.5, the level of crosslinking is small such that the cure can be characterised as a step-growth polymerisation, then M_n can be estimated using the Carothers equation (Eqn 14) where M_0 is the molecular weight of the repeat unit and α is the extent of reaction as described earlier.

$$M_n = \frac{M_0}{(1-\alpha)} \quad (14)$$

A plot of the logarithm of the viscosity versus $1/(1-\alpha)$, as shown for 40°C in Fig. 6(b), gives a linear relationship from which Eqns 15 and 16 were derived. The relationship underestimates the viscosity during the first 10 % conversion which may be due to reaction A, although there may be some errors in the viscosity and DSC data in this region due to warm-up effects. Eqns 15 and 16 are essentially empirical but the term B in Eqn 15 can be viewed as a temperature

shift factor that reflects through Eqn 16 the energy required for molecules to leave their equilibrium position and move across one another. It is quite likely that the relationship breaks down at higher conversions as gelation is approached, but this is irrelevant to RTM processing.

$$\ln \mu = \frac{8.005}{(1 - \alpha)} - B \quad (15)$$

$$B = -\frac{8740}{T} + 31.76 \quad (16)$$

RTM Processing

Despite the inherently complex nature of the acid-catalysed cure of phenolic resole resins, it has been possible to derive empirical relationships to describe the cure kinetics and viscosity changes over the temperatures of practical interest for RTM processing. Only one stoichiometry of a commercial resin has been studied, however the approach developed should be applicable to other similar systems. The utility of the derived empirical relationships lies in their predictive capacity for actual RTM processing applications and this can be realised through simulation models that include the physical properties of the reinforcement and mould, the filling pressure and the applied temperature profile [5].

There are some general observations from the results that can be made in relation to the processing of acid-catalysed phenolic resins. Firstly there is the degree of exothermicity of the cure reaction which for total cure is 347 J.g⁻¹. This is sufficient to raise the temperature of the resin (C_p = 2.1 J.g⁻¹.°C⁻¹) by 165°C, or to raise the temperature from 25 to 100°C and then convert 0.12 g of water to steam for every 1 g of resin. However, in practice under stable conditions, it is only the first 60 % of reaction (Fig. 3) which produces 208 J.g⁻¹ that is important. Of course normally the heat effect is much less, as most of the heat is lost to the surroundings, but when the heat flow profile seen in Fig. 2(a) is considered in conjunction with Scheme 1, it is clear why the acid-catalysed phenolic resole resins have short pot lives (eg. 5 min at 20°C for 1kg). The pot life is not a problem in RTM processing if the resin and catalyst are mixed just prior to injection into the mould as this avoids having to handle any bulk catalysed resin. Once the resin is distributed with the reinforcement there is more heat required to raise the temperature, for example with a 50 wt% glass loading a potential increase with no heat loss of 72°C (60 % conversion) is calculated.

The higher temperature cure reaction highlighted by the DSC work (Fig. 2(b)) is essential to the development of satisfactory mechanical properties. While this final reaction can be completed with a postcure after removal from the mould it is probably judicious that a part experiences above 50°C before demoulding. It is thus necessary to have the capacity to heat a resin transfer mould if it is to be used with these resins. An interesting aspect of the cure modelling is that it potentially allows one to determine a temperature schedule that uses the heat produced by the cure to raise the overall temperature to a desired level without additional external heating. However to achieve this a good knowledge of the heat transfer properties of the mould used is needed.

The relevance to RTM processing of the viscosity changes during cure depends on several features related to the part being made. The fill time and maximum injection pressure are important, as when a large part is being made it is necessary to ensure that the viscosity at the

flow front does not increase to a level where a greater pressure than is available is required to complete the filling of the mould. This can be overcome by filling the mould faster using a higher initial injection pressure or by using a lower initial temperature to reduce the rate of viscosity increase, though this will tend to increase the fill time. It is also important to achieve good wet-out of the reinforcement and if the resin flow is too fast, bubbles can get entrapped behind the flow front. This depends on the type and volume fraction of the reinforcement used. It is thus usually necessary to compromise between the fill time, injection pressure and temperature, and such decisions require a knowledge of viscosity changes during filling of a mould.

CONCLUSIONS

The RTM processing of GRP-phenolic composites requires an understanding of the nature of the cure behaviour of phenolic laminating resins which differs in several ways to that of polyester and vinyl ester resins. To facilitate this, the cure of an acid cured phenolic resole resin has been studied using isothermal DSC and viscosity measurements over a range of temperatures and the results have been described by a series of empirical formulas. These empirical formulas can be used to simulate the changes occurring during RTM processing of a particular part which would identify any risks associated with the high exothermicity of the cure reaction. The need for an additional cure step above 70°C to achieve satisfactory physical properties has also been confirmed.

REFERENCES

1. Gibson, A. G. and Hume, J., "Fire Performance of composite panels for large marine structures", *Plastics Rubber and Composites Processing and Applications*, Vol 23, 1995, pp. 175-183.
2. Hunter, J. and Forsdyke, K. L., "Phenolic GRP and its Recent Applications", *Composite Polymers*, Vol. 2, No. 3, 1989, pp. 169-185.
3. Mekjian, A., "Phenolic RTM - A Boon to Mass Transit", *49th Annual Conference, Composites Institute, The Society of the Plastics Industry Inc.*, February 7-9, 1994, 4-A.
4. Brown, J.R. and St John, N.A., "Fire-retardant Low-temperature-cured Phenolic Resins and Composites", *Trends in Polymer Science*, Vol. 4, No. 12, 1996, pp. 416-420.
5. Trochu, F., Gauvin, R. and Gao, D.M., "Numerical Analysis of the Resin Transfer Molding Process by the Finite Element Method", *Advances in Polymer Technology*, Vol. 12, 1993, pp. 329-342.
6. Knop, A. and Pilato, L.A., *Phenolic Resins: Chemistry, Applications and Performance*, Springer-Verlag, Berlin Heidelberg, 1985.
7. Focke, W.W., Smit, M.S. Tolmay, A.T., Van der Walt, L.S. and Van Wyk, W.L., "Differential Scanning Calorimetry Analysis of Thermoset Cure Kinetics: Phenolic Resole Resin", *Polymer Engineering and Science*, Vol. 31, 1991, pp. 1665-1669.
8. Gupta, M.K., Salee, G. and Hoch, D.W., "Curing Studies of Phenolic Resoles as a Function of pH", *Polymer Preprints*, Vol. 27, No. 1, 1986, pp. 309-310.

RESIN TRANSFER MOLDING OF COMPLEX TEXTILE COMPOSITE COMPONENTS

V. Sarma Avva, Robert L. Sadler, Kunigal N. Shivakumar, and James R. Campbell

*Center for Composite Materials Research
Department of Mechanical Engineering
N. C. A & T State University
Greensboro, NC 27411 USA*

SUMMARY: It has been established that composite parts with considerable geometric complexity and close dimensional tolerances can be fabricated with high fiber volume, low void content and a dependable fiber architecture by using the resin transfer molding (RTM) process. This paper addresses the techniques utilized for obtaining a composite box section with 55-58% fiber volume using eight plies of a 4-harness carbon fabric with a quasi-isotropic stacking sequence. One of the enabling features of the fabrication procedure was using a tackified fabric to shape a preform that fits into the mold cavity. The mold was heated with hot oil. The matrix, 3M's PR-500 Epoxy, was injected into an evacuated mold using a Graco RTM Injector. Test coupons were cut from the composite boxes to determine various mechanical properties. The properties from sides of the box were compared with those from the bottom of the box. The mechanical properties of the corners (through-the-thickness tensile strength) of the box were also determined. The tensile properties from the box compared favorably with the panel data but compression properties did not. The properties of the sides and the bottom of the box compared favorably. The paper contains the details of the composite box fabrication process as well as the determination of its mechanical properties.

KEYWORDS: Resin transfer molding; Composite fabrication and testing; Casket molding techniques; Tackified textile fabrics; Mechanical property evaluation.

INTRODUCTION

The interest in the fabrication of geometrically complex aircraft parts utilizing the resin transfer molding (RTM) processes is increasing. RTM parts are now being used in critical structural components of both commercial and military aircraft. This use is due, in part, to improvements in RTM fabrication methods which allow parts to be produced with greater geometric complexity and closer dimensional tolerances than possible using other (customary) composite manufacturing methods [1]. RTM fabrication also allows parts to be manufactured with fiber volume ratios comparable to those achievable with autoclave processing techniques [2-7]. The objective of the present research was to design, fabricate, analyze and test a high performance RTM composite component. The composite component should incorporate a complex geometric configuration, close dimensional tolerances and a high fiber volume using a high performance matrix and fiber. This paper details the mold design, RTM process and the evaluation of the mechanical properties of an illustrative aircraft part.

TECHNICAL APPROACH

The design of the part was based on an aircraft type spar that might be included in the tail section of an advanced aircraft. The part was sized to be compatible with existing RTM equipment. It contained eight plies of IM7-6k-4HS carbon fiber fabric stacked in quasi-isotropic sequence. It was designed in an open-box configuration about seven inches long and

three inches wide with a uniform wall thickness. The sides were two inches high and were at right angles to the base. The selection of the size was based on an interest in obtaining the tensile-, compression-, and 'L-beam'- test coupons from the same box section. The angle (called here as L-beam) section, subject of an earlier research [8], required two-inch long legs for comparative studies. The eight (fabric) plies were to be consolidated to 0.067 inches of wall thickness to obtain a fiber volume in the range of 55-58%.

The matrix used was 3M company's PR-500 Epoxy Resin. It is an advanced fluorinated epoxy packaged as a one component system especially formulated for RTM [1]. The matrix system is compatible with our Graco Heated RTM Supply Pump. Since the matrix is a thick paste at room temperature, the pumping and plumbing system must be controlled at an elevated temperature. The mold design selected was of the casket- type. This type of mold concept is especially useful for vacuum filling because it only has two matrix ports and one O'ring seal. In addition, the casket components are heated by hot oil which provides for rapid heating and cooling as well as uniform temperature control. The casket design concept is especially useful as it provides an opportunity to reduce the cost of individual composite components by injecting a multi-cavity mold with one injection cycle.

Because of the geometric complexity of the part design, tackified woven fabric was used so that the preform could be fully consolidated into the part configuration before it is placed into the mold cavity. This concept assures the stability of the ply architecture when the sides of the preform are put in shear as the mold closes. The mold was held in a compression press during the RTM process because the liquid matrix was to be held at 150 psi during the fabrication process. The press platens keep the mold closed and minimize the deflection of the mold components at this hydraulic pressure as well as affect a vacuum- and fluid- seal.

MATERIALS

Matrix: The matrix chosen for this project was PR-500 Epoxy Resin produced and marketed by the 3M Company [2]. It is a proprietary one-component fluorinated epoxy resin especially formulated for the fabrication of advanced composites by the RTM process. It is a high strength epoxy with exceptionally good mechanical properties, especially under wet conditions. The Graco Heated RTM Supply Pump [8] was designed for injecting the matrix material into an RTM mold. The matrix contains a powdered catalyst suspended in the thick epoxy matrix paste. The catalyst melts at approximately 280⁰ F. The latent catalyst must be melted before it reaches the fiber preform., otherwise the preform would filter the powdered catalyst out of the matrix before it dissolves in the epoxy. This feature was particularly useful for the RTM process because it allowed the matrix to be pumped through the plumbing before the matrix was activated by dissolving the powdered catalyst. Therefore, the plumbing between the pump and the mold was almost all reusable between injection cycles without cleaning.

Reinforcement: The reinforcement chosen was IM7-6k-4HS provided by Dow-UT. It was a 4-harness fabric woven from 6k-IM7 carbon fibers with a tackifying agent added to one surface. Dow-UT distributes and fuses a powdered version of PR-500, labeled as PT-500, to the fabric as a tackifying agent. The tackifying agent allows for the construction of a preform out of a stack of fabric plies to fit a mold cavity with complex geometry. The tackified material melts during the preform molding and resolidifies upon cooling. The preform not only was shaped but also consolidated to the part thickness to minimize the stress on the preform during mold closing.

FABRICATION PROCESS

Mold: The following illustration, Fig. 1, is useful in describing the primary features of the casket mold design. The casket cavity and casket top plate are designed to contain hot oil channels for heating and cooling the mold. Inside the casket cavity was the cavity insert. This insert contains the mold cavity which forms the outside surface of the composite part. Attached to the casket top plate was the cavity punch. One of the surfaces of the punch

formed the inside surface of the composite part. The cavity insert also contained the matrix manifold. The matrix manifold distributed the matrix along the long edge of the part. The matrix entered the casket cavity along one edge of the part and overflowed on the other edge as it exited the mold cavity. An O-ring seal was used to form the required vacuum seal between the casket top plate and the casket cavity. The carbon fiber preform fits into the mold cavity as shown. The entire assembly was clamped by a compression press. The fit between the casket cavity and the cavity insert was a slip fit. The space shown between the mold components in Fig. 1 is for the purpose of illustration only. The illustration also exaggerates the taper between the cavity insert and the casket cavity. The mold was machined from tool steel to close tolerances and with a good machine finish on important surfaces.

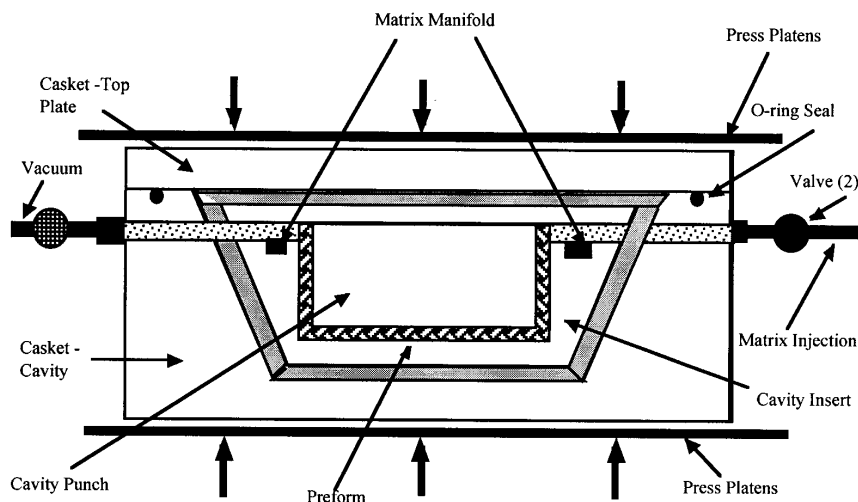


Fig. 1: Casket Mold for RTM

The Graco Heated RTM Supply Pump: The Graco Heated RTM Supply Pump [3] was designed to inject a single component matrix with a high room-temperature viscosity. The machine was designed to utilize the matrix shipping container as the matrix supply vessel. A can opener was used to convert the shipping container to matrix supply vessel by cutting off the friction fastener ledge. The temperature controlled Wiper Plate Assembly was pressed into the top of the can by the two air cylinders and allowed to rest on the top of the matrix surface as shown in Fig. 2. The heat from the Wiper Plate Assembly reduces the viscosity of the matrix so that it may be pumped into the mold. The matrix was pumped with an air powered reciprocating piston pump. Each stroke of the pump delivers 6 ml of matrix. A needle valve in the plumbing system regulates the matrix flow rate. The flow rate selected for this part was 6 ml per minute. It is imperative that the temperature of the plumbing be carefully controlled. If it is too cold, the matrix will not flow, and if it is too hot, the matrix will set-up in the plumbing thereby stopping the flow and damaging the plumbing for future use. For PR-500, the in-let plumbing temperature was set at 150⁰ F. The out-let plumbing temperature was set 200⁰ F. As the matrix is pumped out of the container, the air cylinders keep a constant pressure on the matrix hot plate to maintain its contact with the surface of the matrix in the supply container. In addition, the system only heats the matrix in contact with the heated hot plate. It minimizes the heat history of the matrix not immediately required.

Plumbing System: The plumbing system is illustrated in Fig. 3. The mold was placed in the compression press and the copper tubing was assembled as shown. Copper tubing, 1/4 inch outer diameter with 37 degree flared tube fittings, was used throughout. At the time of assembly a small amount of vacuum grease was applied to each joint to enhance the vacuum seal. All of the plumbing on the matrix entrance side of the mold was wrapped with electrical heating tape and adjusted to 150⁰ F. The plumbing temperature on the matrix exit side of the mold was set at 200⁰ F. The exit side of the mold contained a shut-off valve, a matrix trap,

vacuum gage and a vacuum pump. The entrance side of the mold contained a shut-off valve, a needle valve and the Graco Heated RTM Supply Pump.

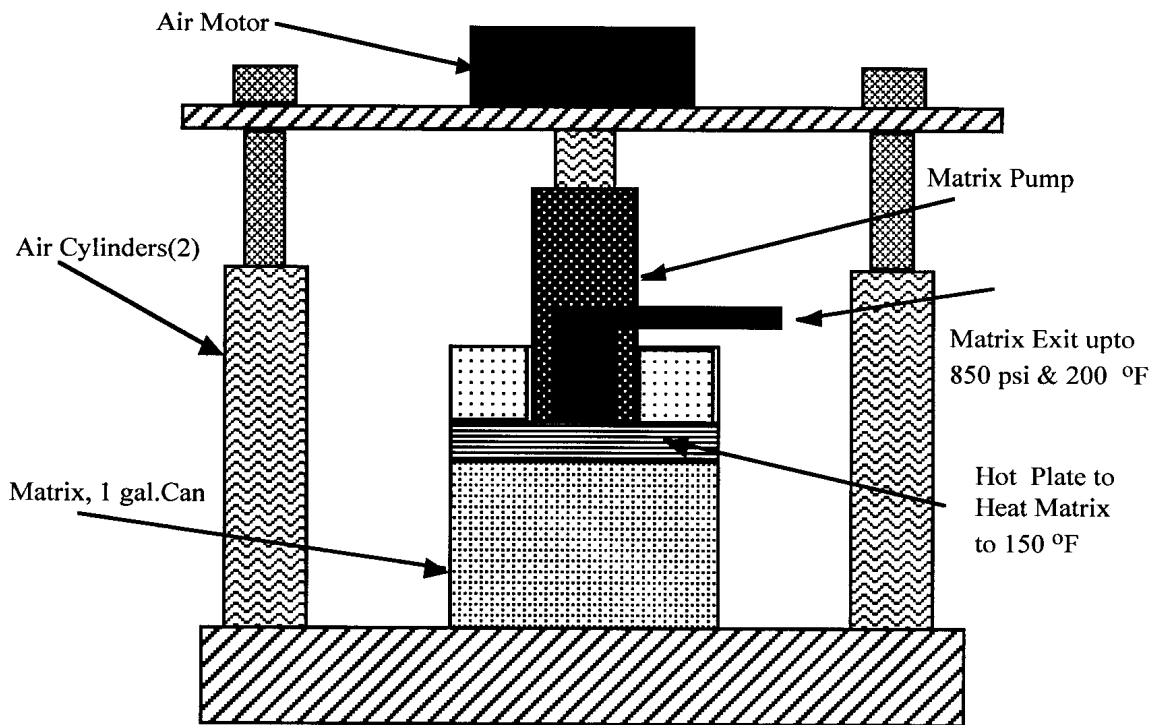


Fig. 2: Graco Heated RTM Supply Pump

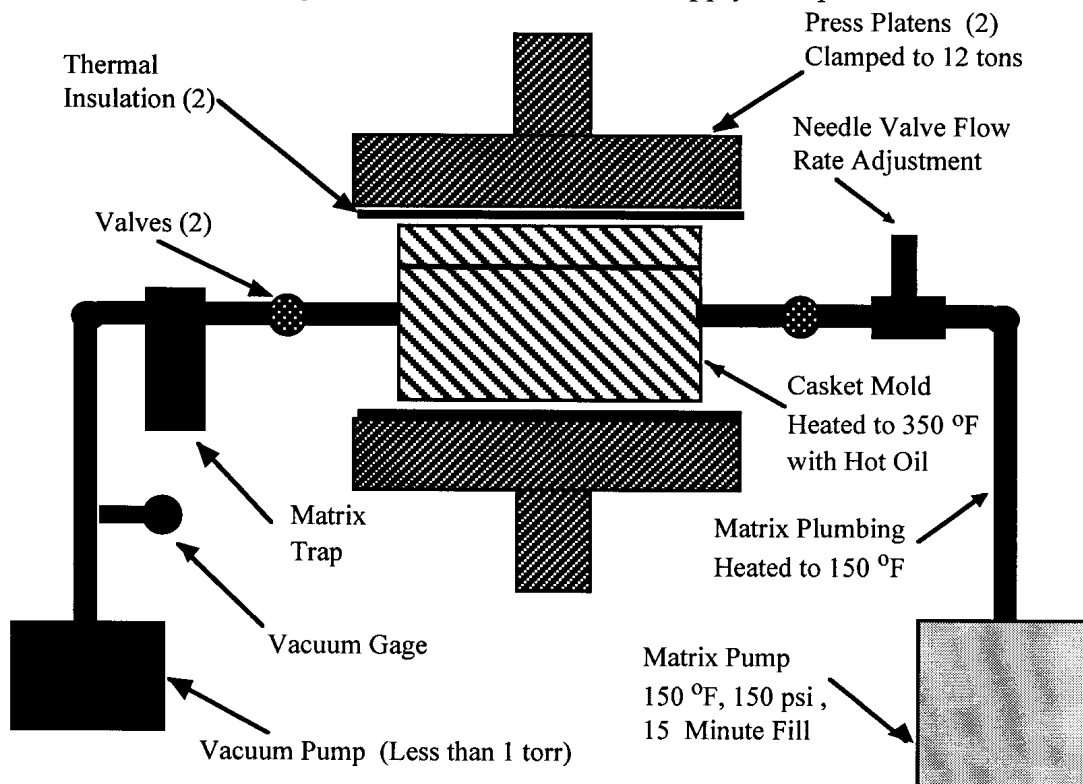


Fig. 3: Injection Set-up Showing Plumbing Arrangement

The plumbing was vacuum tested to determine if the system was vacuum tight. This was accomplished by closing the inlet valve, opening the outlet valve and turning on the vacuum pump. After the vacuum reached about 30 inches of Mercury, the vacuum pump was turned off and the vacuum gage was observed for vacuum leaks. If the gage indicated a leak of over one inch in 15 minutes, all of the plumbing connections were retightened and retested. A vacuum tight plumbing system is required for a successful RTM molding cycle.

Fabrication: The preform was constructed of eight plies of IM7-6k-4HS tackified carbon fiber fabric stacked in a quasi-isotropic sequence. A template was developed which provided a preform that exactly fit the mold cavity. The template was positioned on the fabric in various positions to obtain fiber orientations of +45, -45, 90 and 0 degrees. The plies were then stacked in a sequence of $[+45/0/-45/90]_s$. The stack was placed on the preform molding tool and vacuum bagged as illustrated in Fig. 4.

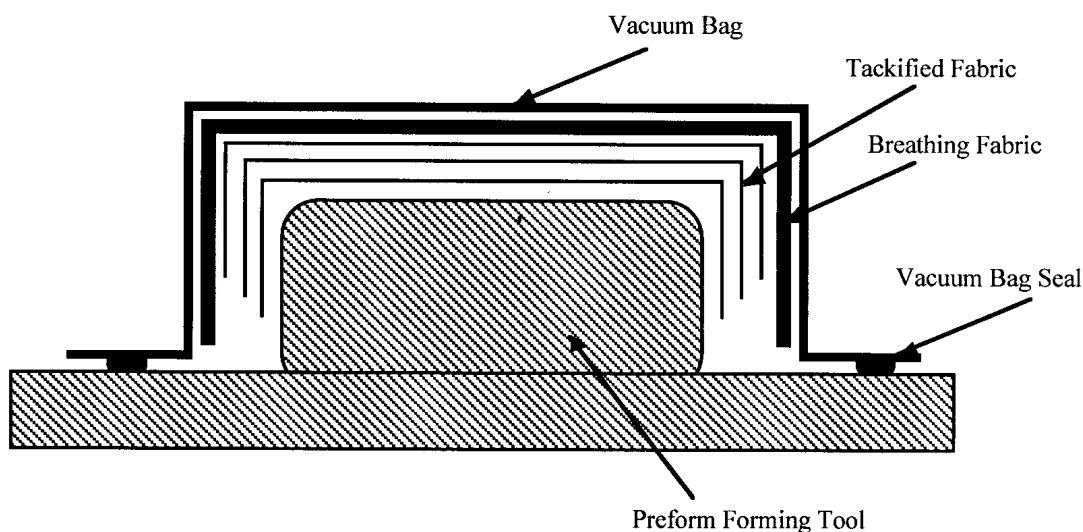


Fig. 4: Tool for Molding Preform

The preform tool was fitted with a thermocouple for temperature measurement. The vacuum bagged preform was placed in an oven preheated to 220⁰ F and the vacuum was then applied to the bag. As the vacuum level increased, the plies of fabric were pulled tight against the preform tool. When the tool reached the oven temperature, it was held for 20 minutes. At this point, the resin had melted. The tool was cooled down to room temperature before the vacuum is released. The result is a molded preform having the shape of the tool and compressed to the approximate consolidation thickness. The preform at this stage can be handled, inspected, and the edges trimmed to precise dimensions. The box design included partially opened corners. The open corners were obtained by trimming the preform about 1/8 inch from each corner. This minimized the problem of trying to mold corners in the box which was unnecessary for the intended box design.

Matrix Injection: The set-up and conditions illustrated in Fig. 3 are used to inject the matrix. A coat of mold release was applied to all surfaces of the mold. The O'ring and O'ring groove were cleaned, lubricated with vacuum grease, and assembled. The preform was placed on the punch and pressed into the mold cavity with the compression press. The equipment arrangement (without the plumbing and the hot oil heating lines) is illustrated in Fig. 5. The vacuum pump, heat to matrix plumbing, heat to Graco wiper plate assembly and heat to the

mold were turned on and allowed to stabilize. Thermocouples were attached to various locations in the matrix plumbing- and mold- equipment. The mold temperature was set at 350⁰ F, the matrix in-let plumbing and Graco wiper plate assembly temperatures were set at 150⁰ F and the matrix out-let plumbing was set at 200⁰ F.

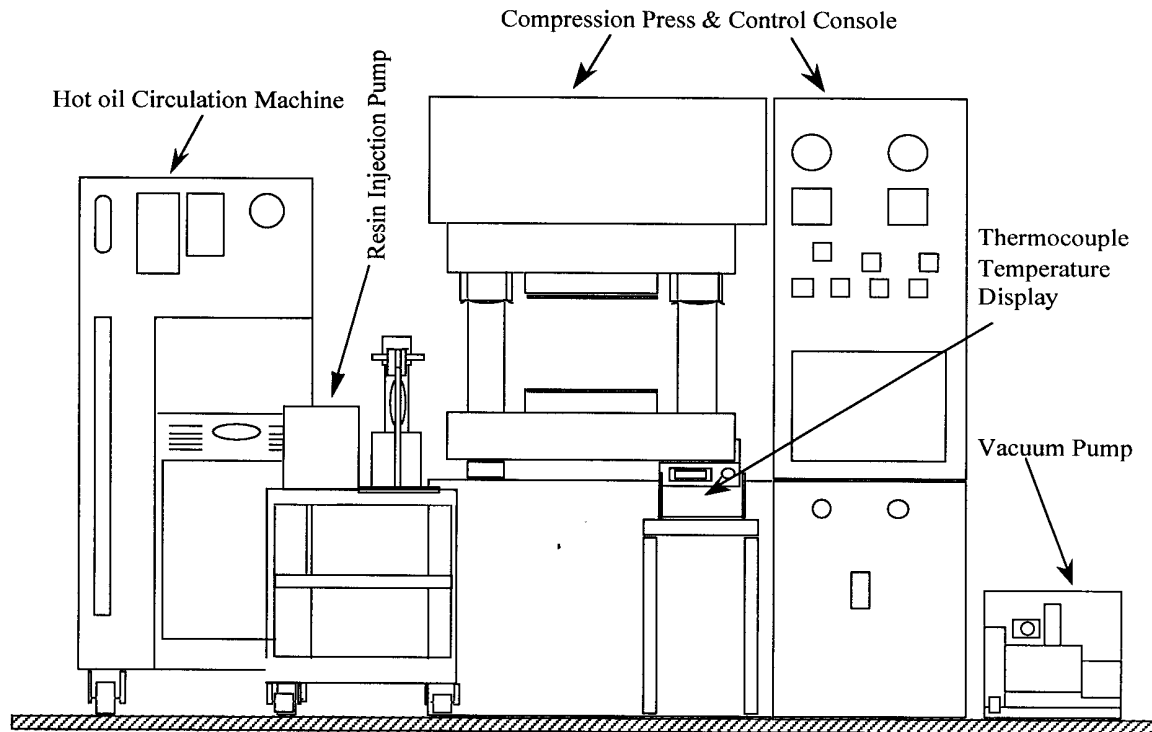


Fig. 5: Equipment Set-up

Before commencing the matrix injection, the vacuum seal was rechecked to determine if the plumbing joints continued to seal at elevated temperature. If a leak was found, it was repaired and rechecked. The compressed air to the Graco was adjusted to 40 psi with the needle valve closed. The air to the air cylinders was set at 10 psi and the air to the matrix pump was set at 22 psi. The vacuum pump was turned off. The needle valve was slowly opened and the frequency of the pump stroke was observed and the needle valve adjusted to provide one stroke per minute. When the matrix was observed to flow into the matrix trap, the matrix exit valve was closed and the matrix pump increased the liquid matrix pressure to 150 psi. The exit valve was opened briefly two times to “burp” a small amount of matrix through the mold. Finally, the matrix was pressurized to 150 psi and held for 30 minutes.. The referenced literature indicated that the matrix would gel in 30 minutes at 350⁰ F. This pressurization reduced the size of any remaining air voids and matrix polymerization shrinkage.

Cure and Part Removal: The mold was held at 350⁰ F for two hours as recommend by the matrix manufacturer to achieve a full cure. The removal of the part from the mold caused some initial difficulty. After a number of attempts, the following part ejection technique was determined. Four undercut slots, 0.25” wide x 2.0” long x 0.030” deep, were added to the cavity punch. These under cuts aided removal of the part from the cavity insert by having the part remain on the punch as the mold halves were separated. The mold halves were separated at the cure temperature of 350⁰ F and the part was removed from the punch after the punch

reached room temperature. This sequence was necessary because the part had a lower thermal coefficient of expansion than the mold steel.

MECHANICAL TESTING

The mechanical properties of the molded box were determined by extracting test coupons from both the bottom and sides of the box. The data determined for the bottom and side coupons were kept separate in order to compare the properties of the composite materials from the two locations. A difference in properties may occur because the sides of the preform are in shear and compression as the mold closes while the bottom is only in compression. The mechanical test selected are: tensile, compression and L-beam. Standard ASTM test procedures were used in testing the specimens. The L-beam test method was described in detail by Avva et. al. [8]. This test method measures the “through-the-thickness” tensile strength which is useful for designing structures subjected to out-of-plane loads.

Test Coupon Dimensions: The procedures for the compression and tensile testing follow the ASTM D 3410 and ASTM D 3039 standards, respectively. The test coupon size was scaled down to fit the size limitations that resulted from the composite box. For example, normally the standard ASTM tension coupons are cut from panels with 0.100-inch thick, but the box in the present case was only 0.067-inch thick. The scaling resulted in coupons that were approximately 67% of the ASTM’s standard size. The L-beam specimen includes material taken from the side, corner and bottom of the box section. The L-beam coupons tested here are also scaled-down versions of geometry and dimensions as shown in [8].

Tensile Data - Box Bottom

<u>Box/Number</u>	<u>Failure Strength</u>	<u>Axial Strain</u>	<u>Modulus</u>	<u>Poisson’s Ratio</u>
5/21	99.8 ksi	1.31 %	7.6 Msi	.32
5/30	102.8	1.40	7.6	.33
6/18	97.4	1.30	7.5	.34
6/25	92.7	1.20	7.6	---
7/30	95.4	1.30	7.3	.30
8/19	107.7	1.27	8.2	.30
8/26	98.0	1.30	7.7	.33
9/30	106.3	1.34	8.0	.38
Average	100.0/689(ksi/MPa)	1.30 %	7.7/53(Msi/GPa)	.33

Tensile Data - Box Side

<u>Box/Number</u>	<u>Failure Strength</u>	<u>Axial Strain</u>	<u>Modulus</u>	<u>Poisson’s Ratio</u>
5/21	95.5 ksi	1.30 %	7.3 Msi	.32
5/30	100.7	1.30	7.8	.33
6/18	102.1	1.38	7.4	.31
6/25	93.6	1.21	7.7	.34
7/30	91.5	1.20	7.6	.31
8/19	100.1	1.32	7.6	.31
8/26	91.3	1.30	7.2	.34
9/30	107.3	1.34	8.1	.39
Average	97.8/674 (ksi/MPa)	1.29 %	7.6/52 (Msi/GPa)	.33

Compression Data - Box Bottom

<u>Box/Number</u>	<u>Failure Strength</u>	<u>Axial Strain</u>	<u>Modulus</u>	<u>Poisson's Ratio</u>
5/21	60.7 ksi	1.20 %	5.5 Msi	.30
5/30	56.6	0.81	6.9	.30
6/18	57.7	1.00	5.6	.31
6/25	70.6	1.06	6.5	.32
8/19	71.5	0.71	7.6	.36
9/30	67.9	0.70	8.4	.40
Average	64.2/443(ksi/MPa)	0.91 %	6.8/46.9 (Msi/GPa)	.33

Compression Data - Box Side

<u>Box/Number</u>	<u>Failure Strength</u>	<u>Axial Strain</u>	<u>Modulus</u>	<u>Poisson's Ratio</u>
5/21	54.9 ksi	0.88 %	6.3 Msi	.36
5/30	62.4	0.98	6.3	.32
6/18	68.6	1.06	6.6	.35
6/25	57.4	0.90	6.5	.31
8/19	69.8	0.80	7.9	.40
9/30	66.2	0.70	8.5	.40
Average	63.2/436(ksi/MPa)	0.89 %	7.0/48.2 (Msi/GPa)	.36

Fiber Volume

<u>Box/Number</u> <u>Gravity</u>	<u>Fiber Volume</u>	<u>Specific</u>
5/21	54.7 %	1.53
5/30	54.7	1.53
6/18	49.4	1.51
6/25	52.6	1.52
7/30	55.2	1.57
8/19	53.7	1.60
8/26	61.8	1.60
9/30	58.1	1.62
Average	55.0 %	1.56

L-Beam Data

<u>Box/Number</u>	<u>Failure Strength, ksi</u>
8/26- 1	1.18
2	1.75
3	1.89
Average	1.61/11.1 (ksi/MPa)

ANALYSIS OF DATA

One concern of the fabrication process was the possibility of observing differences in the mechanical properties obtained in testing coupons extracted from the bottom and sides of the molded composite box. In this case, a significant variation of mechanical property data obtained from the referenced two locations was not indicated. One may therefore conclude that the fiber architecture of the side panels was not disturbed by the shear of the preform as the mold was closed.

The only published data for property comparison located in the literature was in the 3M Company's PR-500 Product Bulletin [2]. The 3M data for tensile properties on IM7-6k-4HS in a quasi-isotropic lay-up were on coupons that were 0.100 inches thick and a 58% fiber volume. For this condition, the data reported for the tensile strength was 110 ksi and the tensile modulus was 8.0 Msi. When the tensile data for the box bottom was normalized to a 58% fiber volume, the tensile strength was 105.5 ksi and the tensile modulus was 8.1 Msi. These results compare favorably.

The compression properties do not compare as well as the tensile properties described above. The 3M data for compression strength was 87 ksi and the compression modulus was 7.7 Msi. When the data for the box bottom compression strength was normalized to a 58% fiber volume, the compression strength was 67.7 ksi and compression modulus was 7.1 Msi. Compression testing is a complex arena. It is felt that the scaling from a coupon thickness of 0.100 inches to a thickness of 0.067 may not be logical and could be a source for obtaining property variation. This issue need to be addressed further at a later time.

The L-beam data also proved to be a problem to verify. Through-the-thickness tensile strength [8] for laminated and 3D braided composites were much higher than the present material. A possible explanation could be the difference between the thickness of the test coupons. The data reported in [8] was 2 to 3 times greater than that determined from the coupons taken from current RTM part. To further explain the lower strength values, it is suggested that additional studies be conducted to assess the effect of 'scaling down or up' of the 'standard' specimen dimensions.

CONCLUSIONS

This research was successful in producing a quality aircraft type composite component by the RTM process using the state-of-the-art materials and processes. Test coupons removed from the molded parts were tested for tensile, compressive and through-the-thickness properties. The tensile properties agreed very well with published data, but, unfortunately, the compressive and through-the-thickness data was below the expectations. Scaling down the dimensions of the test coupons was believed to be a problem, however, additional work would be required to verify this belief.

ACKNOWLEDGMENTS

The authors wish to thank numerous staff members at the Lockheed Martin Aeronautical Systems, Atlanta, GA, USA for financial and technical support in this research through its

US Air Force-sponsored Mentor-Protégé Program. In addition, they also wish to thank Prof. Leon Skeen for the design and procurement of the tooling and fixtures required in the project.

REFERENCES

1. Gerald J. Sundsrud, "Advantages of a One-part Resin System for Processing Aero-space Parts by Resin Transfer Molding (RTM)" was presented at the *Composites in Manufacturing Conference (SME), Pasadena, CA, January 19, 1993*
2. Product Bulletin, 3M PR-500 Epoxy Resin, Issue No. 3, February 1, 1994
3. Instructions-Parts List, Heated RTM Supply Pump, Graco Inc., Revision D, 1991
4. S. Senibi, E. C. Klang, R. L. Sadler and V. S. Avva, "Resin Transfer Molding (RTM): Experiments with Vacuum Assisted Methods", *Presented at Ninth International Conference on Composite Materials, July 12-16, 1993, Madrid, Spain.*
5. R. L. Sadler, V.S. Avva, S.D. Senibi and E. C. Klang, "Experiments Related to the Fabrication of Graphite/Epoxy Tubes by the Resin Transfer Molding (RTM) Process", *Conference on Flow Processes in Composite Materials '94, University of Galway, July 7-9, 1994, Galway, Ireland.*
6. R. L. Sadler, V. S. Avva, S. D. Senibi and E. C. Klang, "Development of a Resin Transfer Molding (RTM) Process for Fabricating a Seamless Composite Tube" was *Presented at the 26th International SAMPE Technical Conference, October 24-27, 1994, Atlanta, GA.*
7. R. L. Sadler, B. D. Morgan, V. S. Avva and D. J. McPherson Sr., "Resin Transfer Molding of 3-D Braided Through-The-Thickness® Pan-Based Carbon Fiber Preforms with a Cyanate Ester" was *presented at the 1995 JANNAF Interagency Propulsion Subcommittee Joint Meetings, December 4-7, 1995, at Tampa, FL.*
8. V. S. Avva, H. G. Allen and K. N. Shivakumar, "Through-the-Thickness Tension Strength of 3-D Braided Composites", *Journal of Composite Materials, Pages 51-68, Vol. 30, No1/1996.*

AUTOMATED FABRICATION OF HIGH PERFORMANCE COMPOSITES: AN OVERVIEW OF RESEARCH AT THE LANGLEY RESEARCH CENTER

N. J. Johnston¹, T. W. Towell¹, J. M. Marchello² and R. W. Grenoble²

¹*NASA Langley Research Center, Hampton, VA 23681 USA*

²*Old Dominion University, Norfolk, VA 23529 USA*

SUMMARY: Automated heated placement of consolidated fiber reinforced polymer ribbon/tape is a rapid, cost effective technique for net shape fabrication of high performance composites. Several research efforts in the United States are developing the heated head robotic hardware and associated software needed to bring this technology into widespread use for building aircraft parts. These efforts emphasize the use of pre-consolidated thermoplastic ribbon or tape which is thermally welded on-the-fly. The approach provides in-situ consolidation and obviates the need for autoclave processing and massive debulking, thereby reducing costs.

Addressed in this paper are some key issues being pursued at NASA Langley related to this technology. These include (a) preparation of high quality intermediate materials forms such as thermoplastic powders, powder-coated towpreg and consolidated ribbon/tape and (b) achievement of precise control of the following: robot head positioning on the tool; material placement; heat delivery to the lay-down zone; and cut/add, start/stop capability. Heated head development has dealt with the use of hot gases alone and in combination with focused infrared radiation as heat sources.

KEYWORDS: automation, powders, ribbon, tape, robot, polyimides

INTRODUCTION

To be economically viable in competition with metals for high performance applications, fiber reinforced polymer composite fabrication must utilize high quality material forms and fully exploit automated processing technology. Automated processes employed in the composites industry include pultrusion, filament winding, automated tow/tape placement (ATP) and the textile processes of weaving and braiding in combination with resin transfer molding or resin infusion molding.

The automated placement of composite tow/tape is one of the most promising fabrication methods for rapid, cost effective, net shape composite part manufacture.¹ To apply this technique in various aerospace research programs, NASA Langley Research Center is emphasizing an approach where preconsolidated high temperature, thermoplastic, graphite fiber reinforced ribbon or tape is thermally welded on-the-fly. This approach provides for in-situ consolidation of the part and eliminates the need for laborous debulking and autoclave post-placement processing. As ATP research and development efforts proceed, important issues that require resolution have been identified. Examples include open section residual

stresses, autohesion requirements, prepreg material quality and post annealing of semi-crystalline polymers.

PRECONSOLIDATED COMPOSITE RIBBON AND TAPE

Most basic of these issues is the requirement for high quality, fully consolidated, thermoplastic ribbon and tape having close dimensional tolerances. The old axiom, 'garbage in, garbage out,' cannot be overemphasized in ATP practice. An important part of the NASA program has dealt with developing ways to fabricate the required product forms. The necessary and important restrictions on the processes were as follows. (a) Utilize no solvents, therefore no solvents would have to be removed in subsequent fabrication steps. (b) Avoid melt impregnation; it is almost an impossible task with the high melt viscosities of high performance polymers such as polyimides and polyarylene ethers. The scheme finally developed at Langley utilized impregnation of finely ground polymer powder onto a spread unsized carbon fiber tow bundle followed by thermoplastic forming of the towpreg into consolidated ribbon and tape.

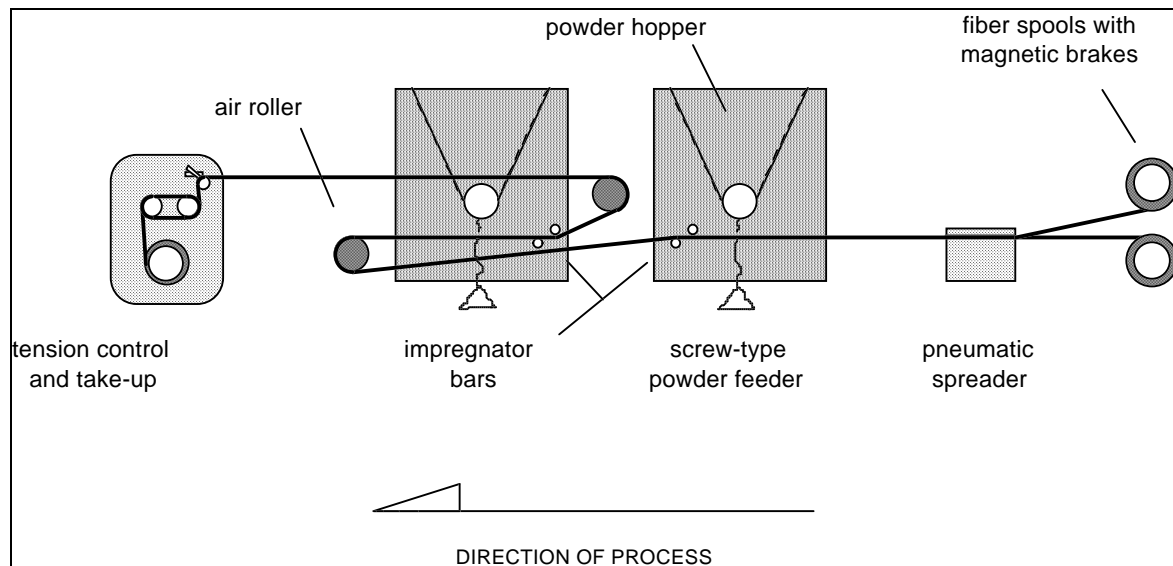


Figure 3. Schematic of the NASA Powder-Coating Line

Powder Impregnation

Processes for making towpreg have been developed from both slurry and dry powder techniques.² An optimized process, called 'powder curtain' was found at Langley to be the most efficient way of distributing solid polymer particles throughout continuous filament tows (see Figure 1). The resulting towpreg yarn was flexible, bulky and abrasive. Composites made with this material by frame-winding followed by press molding gave mechanical properties quite favorable to those made from solution prepregging (Table 1).³

Table 1. Mechanical properties of LARC™ IAX/IM7 polyimide composites made by solution and powder-coated prepreg*

Property	Test Temp., °C	Solution Coated	Powder Coated
SBS Str., ksi	RT	15.8	22.1
	177	7.9	8.9
0°Flex. Str., ksi	RT	213	314
	177	105	213
0°Flex Mod., msi	RT	18.6	19.8
	177	15.1	19.8
0°Compress. Str., ksi	RT	167	202
0°Compress. Mod., msi	RT	23.4	23.7

*Data normalized to 60/40 fiber/resin vol. %; Polyimides were formulated to 4% offset in favor of the diamine and endcapped with phthalic anhydride.

Consolidated Ribbon/Tape

Robotic placement heated heads are generally designed to utilize stiff, preconsolidated ribbons or tapes having consistent cross-section. A number of debulking techniques were studied to convert powder-coated towpreg yarns into fully preconsolidated ribbon and tape.⁴ Issues included towpreg material quality, transverse squeeze-flow, appropriate timing for heating and pressure application and tool contact/release. Several processing methods were designed, built and experimentally evaluated. Four powder-coated towpreg yarns, Aurum™-500/IM-8, PIXA-M™/IM-7, LARC™-IA/IM-7 and APC-2™ (PEEK/AS-4) were used in this evaluation. Reactive plasticizers and solvents were excluded. The work concentrated on the fabrication of 0.63 cm wide ribbon from two 12K IM-7 powder coated tows and 7.6 cm wide tape from twenty-five powder-coated tows.^{4,5}

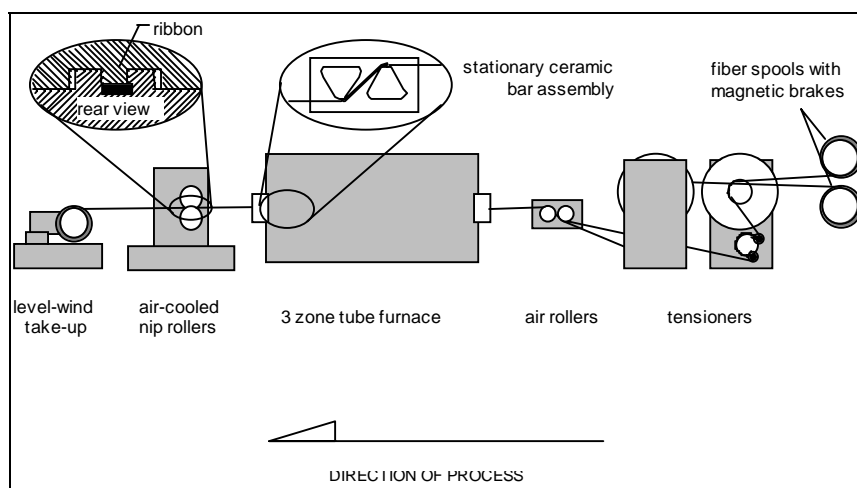


Figure 4: Schematic of NASA Ribbon/Tape Line

By utilizing desirable attributes of several of the designs, a novel processing technique was developed. The equipment was comprised of two primary components (Figure 2). The

ceramic hot bar fixture facilitated transverse melt squeeze flow while the cool nip-roller assembly solidified the ribbon/tape into preconsolidated ribbon/tape with consistent cross-section. The heat transfer and pulling force were modeled from fundamental principles to develop a basic understanding of the process for application to a variety of polymer materials.

AUTOMATED FIBER PLACEMENT

ATP Process

During automated placement, preconsolidated composite ribbon and tape are fed from spools through a delivery system located on the placement head. A band of collimated ribbons or the tape is placed with heat and pressure to laminate it onto the work surface.

Fiber placement differs from filament winding in that it requires the tow placement tool tip to contact the surface of the part rather than floating off the part. This allows for placement in non-natural paths which may be required for complex parts.¹ Contrasted to filament winding which is limited to continuous placement on closed part geometry, ATP with its cut/add capability can place on open as well as closed parts.

Specific work cell configurations for fiber placement depend upon the geometry of the parts to be fabricated. However, the following elements are common to all fiber placement machines:

- Placement Head
- Automated Machine Platform
- Electronic Controls and Software
- Placement Tool

The placement head is a stand alone end effector that feeds, cuts, places and laminates the ribbons or tape.⁶ The platform is usually a commercially available gantry or an articulated arm unit to which additional degrees of freedom may be added.¹

NASA ATP Facility

Acquisition and utilization of an automated thermoplastic fiber placement machine for materials and processing evaluation was an important part of the NASA program.⁷ The machine, shown in Figure 3, was manufactured by Automated Dynamics Corporation (ADC) and is comprised of an Asea Brown Boveri robotic arm with an ADC thermoplastic fiber delivery head (Figure 4) and placement tools. The latter are comprised of both flat and cylindrical steel tooling. The computer control system and software for the work cell were jointly developed by ADC and Composite Machine Company (CMC). ADC performed the total system integration.

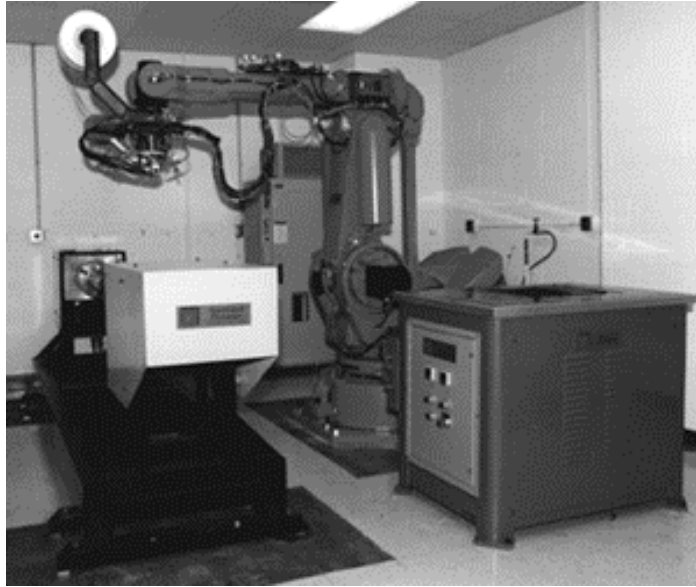


Figure 5. Photograph of NASA Robot, Heated Head and Heated Flat Tool

Machine Development

Materials and processing evaluation activities carried out with the ATP machine at Langley were an integral part of several NASA aerospace research programs involving even larger and more sophisticated proprietary machines being developed at several corporate research laboratories. These NASA/industry research programs continue to address ATP requirements such as precise control of robot head positioning, material placement rates, heat delivery to the lay-down zone and cut/add, start/stop capability. Machine development for thermoplastics has dealt with the use of hot gases, lasers, focused infrared radiation and combinations of these as heat sources. Current work also is directed toward start-on-the part, turning radius limitations, autoadhesion requirements and development of sensors that give on-line part quality information that could be used for on-line placement defect repair. The latter would yield a remarkable cost-savings for fabrication of commercial aerospace composite structure.

Modeling

Consolidation models have been developed to relate ATP machine design, operating parameters and sensor readings to the processing conditions necessary for making good quality composite parts. In-situ bonding models have served to establish a processing window bounded by the upper and lower limiting values of the processing conditions within which acceptable parts can be made. The models attempt to describe the mechanisms involved in the ATP process. These include heat transfer, tow thermal deformation and degradation, intimate contact, bonding and void consolidation.⁸ Finite element analysis, neural networks and fuzzy logic techniques have been used in these computer-based models.⁹

One of the primary purposes for developing models has been to aid on-line control. The computer execution time is therefore critical. Unfortunately, even in their most simplified form, most models take too long for predictive use on-line. As a result, the models are run off-line for various parameters in the processing window and a computer look-up table constructed that can be used as a guide to on-line control.⁹

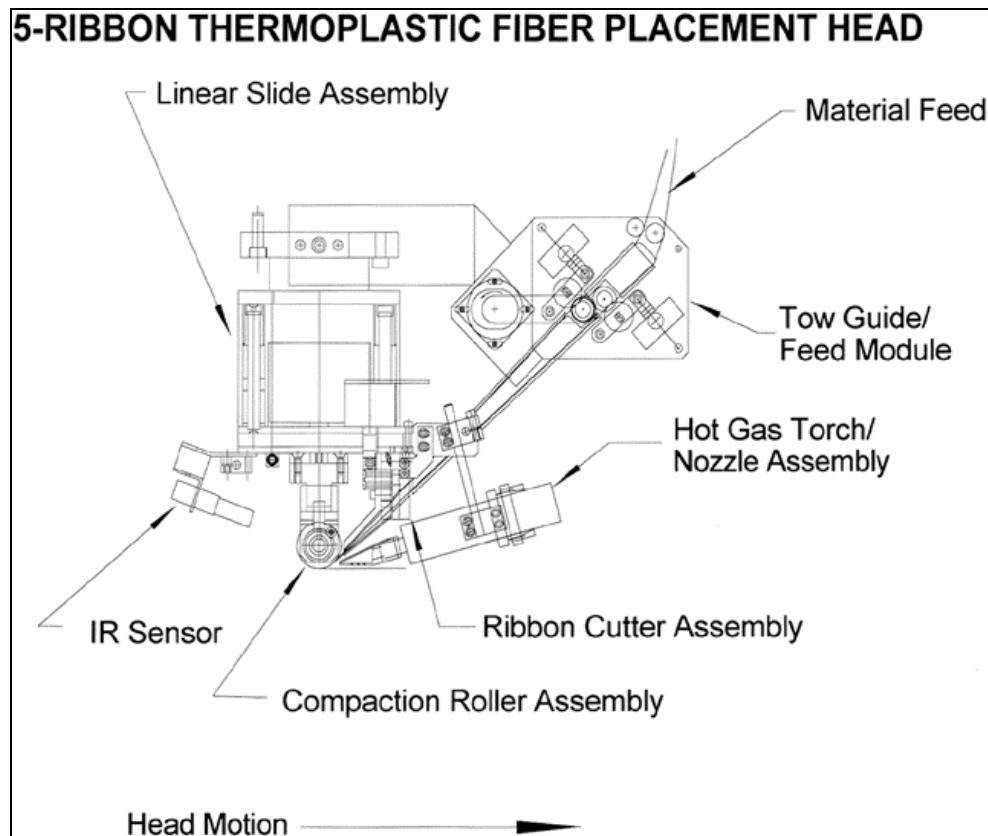


Figure 6. Schematic of the NASA Heated Head

Table 2. Open Hole Compression Strengths of Quasi-isotropic Thermoplastic Composites

Process	APC-2™ (PEEK)/AS4	APC-2™ (PEEK)/IM6	AURUM™ PIXA/ IM7
Hand Lay-up/Autoclave	47 ksi	46 ksi	46 ksi
Adv. Tow Placement	40 ksi	43 ksi	39 ksi
% Retention	85	93	85

Composite Fabrication/Testing

During the past year, in-situ consolidated laminates have been prepared from high temperature polyimides such as AURUM™ PIXA/IM7, AURUM™ PIXA-M/IM7 and LARC™ PETI-5/IM7 and polyarylene ethers and sulfides such as APC-2™ (PEEK)/AS4, APC-2™ (PEEK)/IM6, PEKK/AS4 and PPS/AS4. It should be noted that thermosetting materials such as the LARC™ PETI-5/IM7 require a high temperature postcure to optimize their performance. Some properties of PEEK and PIXA panels made by ATP on large industrial equipment are given in Table 2 and compared with properties obtained from panels made by hand lay-up/autoclave procedures. The ATP panels exhibited from 85 to 93 percent of the properties of composites made by hand lay-up/autoclave. These results indicate that heated head ATP technology can be used to effectively fabricate quality high performance

composite materials. The ATP goal of the period ahead is to achieve 100 percent of hand lay-up/autoclave results.

CONCLUDING REMARKS

Significant progress has been made in developing automated heated head tow/tape placement technology for the fabrication of high performance composites. The key activities included development of methods for making good quality thermoplastic ribbons and tape, determination of machine design and operating requirements for in-situ placement and establishment of a base knowledge of the fundamental mechanisms involved in both ribbon/tape preparation and in-situ consolidation.

Studies during the period ahead will include the development of focused infrared/hot gas heating, on-line sensors and start-on-the part methods. Particularly important will be material qualification studies at NASA and the fabrication of large test specimens and component structures at several industrial laboratories.

REFERENCES

1. Smith, A. and Anthony, D., "Robotic Placement of Complex Thermoplastic Structures", *Internatl. SAMPE Tech. Conf. Series*, Vol. 24, 1992, pp. 101-115.
2. Baucom, R. M. and Marchello, J. M., "Powder Curtain Prepreg Process", *J. Adv. Materials*, Vol. 25, 1994, pp. 31-35.
3. Hou, T. H., Johnston, N. J., Weiser, E. S and Marchello, J. M., "Processing and Properties of IM7 Composites Made From LARC™-IAX Polyimide Powders", *J. Adv. Mtls.*, Vol. 27 (4), 1996, pp. 37-46.
4. Sandusky, D. A., Marchello, J. M. and Johnston, N. J., "Ribbonizing Powder Impregnated Towpreg", *Sci. Adv. Matl. Process Eng. Series*, Vol. 39, 1994, pp. 2612-2625.
5. Belvin, H. L., Cano, R. J., Grenoble, R. W. and Marchello, J. M., "Fabrication of Composite Tape from Thermoplastic Powder-Impregnated Tows", *Internatl. SAMPE Tech. Conf. Series*, Vol. 28, pp. 1996, 1309-1316.
6. Steiner, K. V., Faude, E., Don, R. C. and Gillespie, J. W., "Cut and Refeed Mechanics for Thermoplastic Tape Placement", *Sci. Adv. Matl. Process Eng. Series*, Vol. 39, 1994, pp. 116-125.
7. Towell, T. W., Johnston, N. J., Grenoble, R. W., Marchello, J. M. and Cox, W. R., "Thermoplastic Fiber Placement Machine for Materials and Processing Evaluations", *Sci. Adv. Matl. Process Eng. Series*, Vol. 41, 1996, pp. 1701-1711.
8. Hinkley, J. A. and Marchello, J. M., "Thermoplastic Ribbon-Ply Bonding Model", *NASA Tech. Mem. 110203*, September 1995; Hinkley, J. A., Working, D. C. and Marchello, J. M., "Graphite/Thermoplastic Consolidation Kinetics", *Sci. Adv. Mtls. Process Eng. Series*, Vol. 39, 1994, pp. 2604-2611; Hinkley, J. A., Marchello, J. M. and Messier, B. C., "Characterization of Polyimide Composite Ribbon Weld Bonding", *Sci. Adv. Mtls. Process Eng. Series*, Vol. 41, 1996, pp. 1335-1345.
9. Ranganathan, S., Advani, S. G. and Lamontia, M. A., "A Model for Consolidation and Void Reduction during Thermoplastic Tow Placement", *Internatl. SAMPE Tech. Conf. Series*, Vol. 25, 1993, pp. 620-631.

DESIGN OF EXPERIMENTS ANALYSIS OF THE ON-LINE CONSOLIDATION PROCESS

Po-Jen Shih and Alfred C. Loos

*Department of Engineering Science and Mechanics and
National Science Foundation Science and Technology Center;
High Performance Polymer Adhesives and Composites
Virginia Polytechnic Institute and State University
Blacksburg, Virginia 24061-0219, USA*

SUMMARY: An on-line consolidation system, which includes a computer-controlled filament winding machine and a consolidation head assembly, has been designed and constructed to fabricate composite parts from thermoplastic towpregs. The present study examines the impact of processing conditions on thickness reduction, void content, density, degree of crystallinity, and interlaminar shear strength (ILSS) of the consolidated parts. A central composite experimental design was used to select the processing conditions for manufacturing the composite cylinders and to analyze the effect of processing parameters on quality of resulting composite cylinders. A response surface of ILSS was constructed to reveal the impact of the individual parameters. In general, higher nippoint temperature and lower winding speed tend to yield composite cylinders with higher ILSS and lower void content. APC-2 (PEEK/Carbon fiber) composite cylinders fabricated by the on-line consolidation technique had an ILSS of 58 MPa and less than 1% void content.

KEYWORDS: On-line (In-situ) consolidation, thermoplastic composites, design of experiments, interlaminar shear strength, APC-2 towpreg, void content, degree of crystallinity.

INTRODUCTION

On-line consolidation is a composite manufacturing process where the resin impregnated fiber bundles (“towpreg” or “prepreg”) are continuously oriented, laid down, consolidated, and cured onto the tool surface in a single step. Once the surface of the designed structure has been covered and the thickness has been achieved, the part is finished. Secondary processing steps such as autoclave or hot-press consolidation are eliminated. When integrated with a computer controlled system, the process can be fully automated which leads to further cost saving in fabrication by increasing productivity and reducing labor cost.

In addition to the reduced cost, on-line consolidation also offers benefits for design flexibility and performance. With localized heating, this process is inherently suitable for manufacturing parts with large surfaces and moderate curvatures, such as fuselage structures and deep submersibles [1]. Because the towpreg is fully consolidated and locked in the vicinity of the melting point as it is placed onto the structure, conceptually there is no limitation on producing parts with thick cross-sections and large surface areas [2]. Furthermore, complex, non-geodesic, and even concave winding paths are also achievable, thus allowing design flexibility [3].

In order to realize the potential advantages of on-line consolidation, the significant processing parameters must be identified and the effects of the processing parameters on the quality of the composite must be understood.

Therefore, the objectives of this investigation are to use a design of experiments approach to determine the importance of the processing parameters and their effect on the mechanical and physical properties of the consolidated composite.

EXPERIMENTAL

On-Line Consolidation System

Over the past decade, many investigations have been devoted to development of the on-line consolidation manufacturing technique [4-12]. Almost all existing on-line consolidation systems have similar processing steps that start with unwinding prepreg from the spool. The continuous towpreg passes through a tensioner and guide rollers and then arrives at the nip point, where the towpreg and composite substrate meet. Energy from a highly focused heat source melts the interface while, at the same time, the compacting roller compresses the material and squeezes out excess resin. Finally, the towpreg is solidified and consolidated onto the tool surface.

The on-line consolidation system used in the present investigation is schematically illustrated in Figure 1 and includes a towpreg delivery system, a computer-controlled filament winding machine and a consolidation head assembly. Figure 2 shows a photograph of the on-line consolidation system.

The on-line consolidation system, described above, was used to manufacture composite cylinders from 6.35 mm wide APC-2 towpreg (carbon fiber and PEEK) from Fiberite, Inc. The winding pattern was generated by the computer software, CADWIND®. The winding procedure was performed on a computer controlled two-axis filament winding machine. All cylinders investigated are hoop-wound and have an inner diameter of 146 mm (5.75 in).

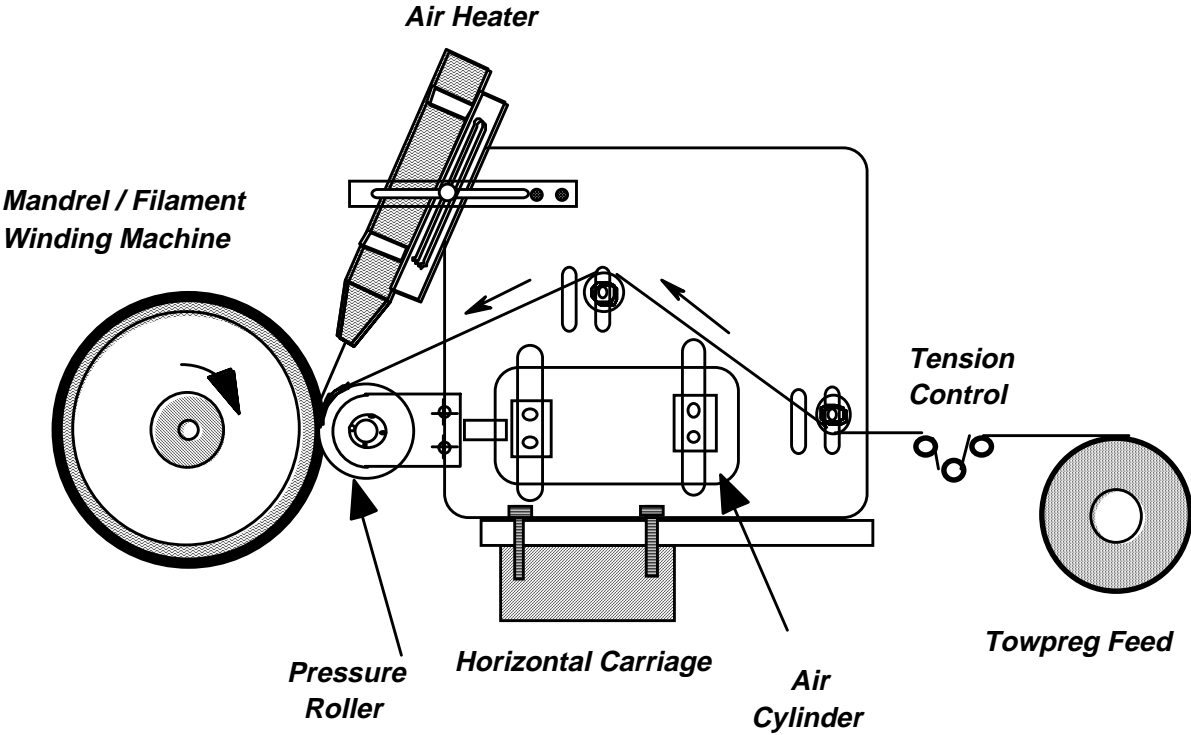


Figure 1 Illustration of the on-line consolidation system.

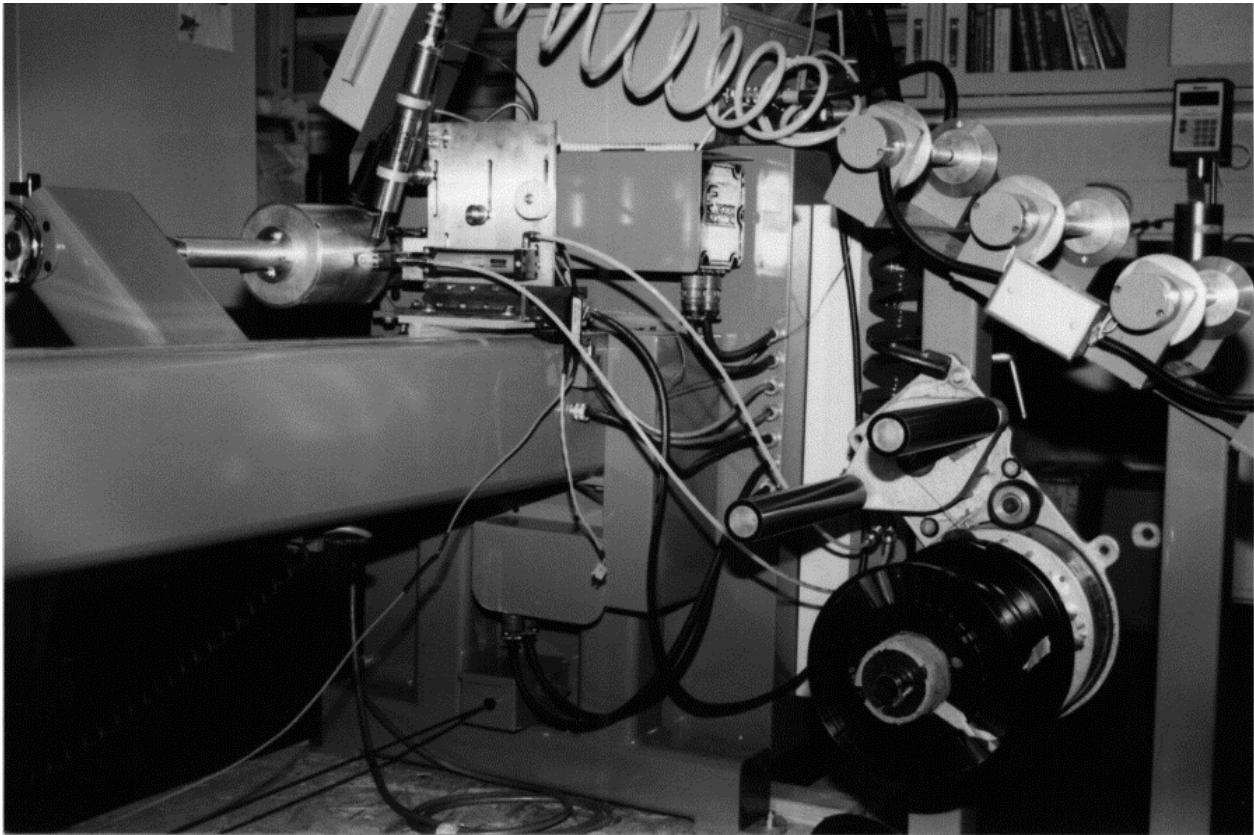


Figure 2 Photograph of the on-line consolidation system.

Mechanical and Physical Tests

Once a composite cylinder was produced, its thickness was measured and recorded at twenty different locations around the circumference. The composite cylinders were then sent to the machine shop for fabricating test coupons. First, a 6.35 mm wide ring was cut out from the center portion of the cylinder. Second, a thin diamond cutter was used to cut open the ring and the opening dimension was then recorded. Different displacements indicate that the process-induced residual stresses have varied due to different processing conditions. Third, fifteen ILSS coupons were machined to conform to the dimensional requirements as described in ASTM standard D2344.

To gage the overall quality, density and void content tests were performed on all composite cylinders. The density measurements were performed in accordance with ASTM standard D792-91 and the void content measurements were performed in accordance with ASTM standard D2734-91. The material densities required by the void content calculation are given in Table 1. The density of APC-2 at 30% crystallinity was determined following the procedures described in Ref. 13.

Table 1 Material Properties for Density Calculation.

Property	AS-4 Fiber	PEEK	
		Amorphous	Crystallinity
Volume Fraction	60%	40%	
Degree of Crystallinity	na	na	30%
Density (kg/m ³)	1780.0	1262.6	1400.6

STATISTICAL INVESTIGATION OF THE PROCESSING WINDOW

The motivation for using a statistical method was to study the impact of individual processing parameters and to establish the processing window for a given material system. In contrast to randomly selected processing conditions or to conducting one-factor-at-a-time studies, a carefully planned experimental design for studying the impact of all variables and their interactions will be more cost-effective.

Processing Parameters

In the present design, there are five separately controllable system parameters namely, winding speed, pressure of compaction roller, nozzle temperature, distance between nozzle and nip point, and air pressure for the heater.

Observations from initial experiments showed that the nip point temperature can be several hundred degrees Celsius lower than the nozzle temperature and is very sensitive to the following three system parameters: nozzle temperature, air flow rate in heater and distance between nip point and nozzle. Meanwhile, we found that using nip point temperature to construct the processing window has two major advantages. First, it is more realistic since nip point temperature is the actual temperature that the towpregs are subjected to. Second, by using nip point temperature to represent three of the system parameters, the number of

parameters was reduced from five down to three, i.e. winding speed, roller pressure, and actual nippoint temperature.

Nippoint Temperature

In order to investigate the individual impact of these three parameters and their interaction on the nippoint temperature, a three-factor, Box-Behnken design was conducted [14]. There are fifteen possible factor-level combinations in this experimental design. The low, midpoint, and high values are listed as the following.

- Distance between nozzle to nippoint: 12.7 mm (0.5 in), 19.1 mm (0.75 in) and 25.4 mm (1.0 in).
- Air pressure: 27.6 kPa (4 psi), 55.2 kPa (8 psi) and 82.7 kPa (12 psi).
- Nozzle temperature of hot air heater : 538°C (1000°F), 593°C (1100°F) and 649°C (1200°F).

The nippoint temperature was measured by a K-type, air-probe thermocouple for each factor-level combination. A second-order linear regression analysis for three independent variables yields,

$$\begin{aligned} \text{Nippoint Temperature} (^{\circ}\text{C}) = & \\ & 138.14 + 26.682D - 1.151P - 0.3427T - 0.209D^2 \\ & - 0.002P^2 + 0.0017T^2 + 0.002DP - 0.0417TD + 0.0016PT \end{aligned} \quad (1)$$

where D is the distance from nozzle to nippoint, P is the heater air pressure, and T is nozzle temperature.

Processing Window For On-Line Consolidation System

The processing window for the on-line consolidation system is determined by adjusting the three system processing parameters, namely roller pressure, winding speed, and nippoint temperature. To simplify the approach a step further, a fixed roller pressure of 380 kPa (55 psi) was chosen for fabricating all cylinders. It should be noted that we are not presuming that there is no significant impact of pressure on the quality of composite cylinders; a fixed roller pressure is simply a system constraint for the present design. For now, the study is focused on the impact of winding speed and nippoint temperature on composite quality.

First, a two-factor central composite design of experiments was used to define the combination of processing parameters. Second, the density and the thickness of the resulting cylinders were measured and then, as described in the previous section, their void content was calculated. Micrographs of the cross sections of each consolidated part are used to qualitatively describe the consolidation for a set of processing conditions. Differential scanning calorimetry (DSC) was used to measure the degree of crystallinity. Finally, the interlaminar shear strength of consolidated parts was measured.

Central Composite Design

A central composite design of experiments was used to systematically study the processing window and to maximize the quality of composite parts. An illustration of the two-factor central composite design is given in Figure 3. The levels for winding speed range from about 4-10 mm/s and the nippoint temperature has a high value of 660°C (1220°F) and a low value of 493°C (920°F). Nine composite cylinders, 26-ply thick and 19 mm (3/4 in) wide were

fabricated under the prescribed processing conditions given by the experimental design. The winding time ranges from 77 to 172 minutes.

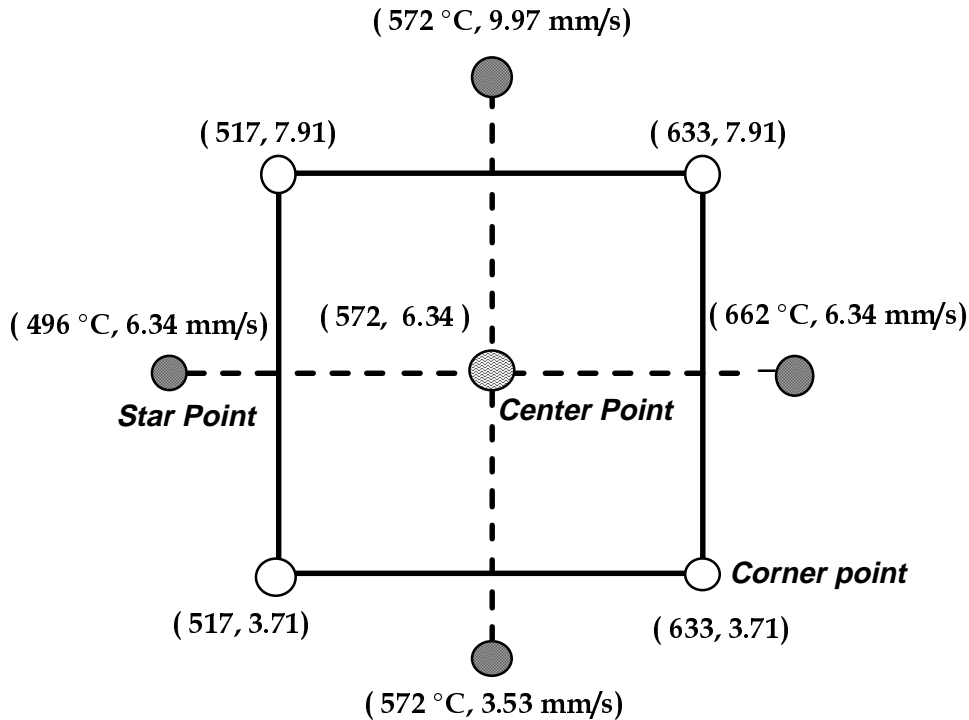


Figure 3 Illustration of a two-factor central composite design.

Micrograph Study on Quality of Consolidated Cylinders

The purpose of the optical micrographs taken at cross sections of each composite cylinder is three-fold. First, we can visually observe the degree of intimate contact between layers since intimate contact is the necessary condition for good bonding. Second, we can examine whether or not the fiber distribution is uniform. Third, we can observe the size and location of voids, for void content reflects composite quality. As a result, the micrographs give a qualitative description of the composite quality.

Specimens were cut from each composite cylinder and mounted in an epoxy potting compound. Each cross section was carefully polished and analyzed under an optical microscope. Figure 4 shows results for cylinders #2 and #8. Cylinder #2 was manufactured under a nippoint temperature of 633°C (1172°F) and a winding speed of 3.71 mm/s (8.76 in/min.), and the micrographs are shown in Figures 4(a)-4(c). Virtually no voids are observed at the interply region (Figure 4(a)) and the fiber distribution is uniform (Figure 4(b)). No significant fiber waviness confirms that on-line consolidation does have an advantage over conventional autoclave consolidation where fiber waviness usually occurs (Figure 4(c)).

As expected, not all cylinders yield the same high quality. In the case of cylinder #8, manufactured under a nippoint temperature of 517°C and a winding speed of 7.91 mm/s, large, resin-rich areas exist at almost every interply region as shown in Figure 4(d). Under external loading, the resin-rich areas are the most vulnerable due to the lack of surrounding reinforcement. This observation suggests that the specimens from cylinder #8 may fail much

more easily than the specimens cut from a well-consolidated cylinder in which the fibers are distributed more uniformly.

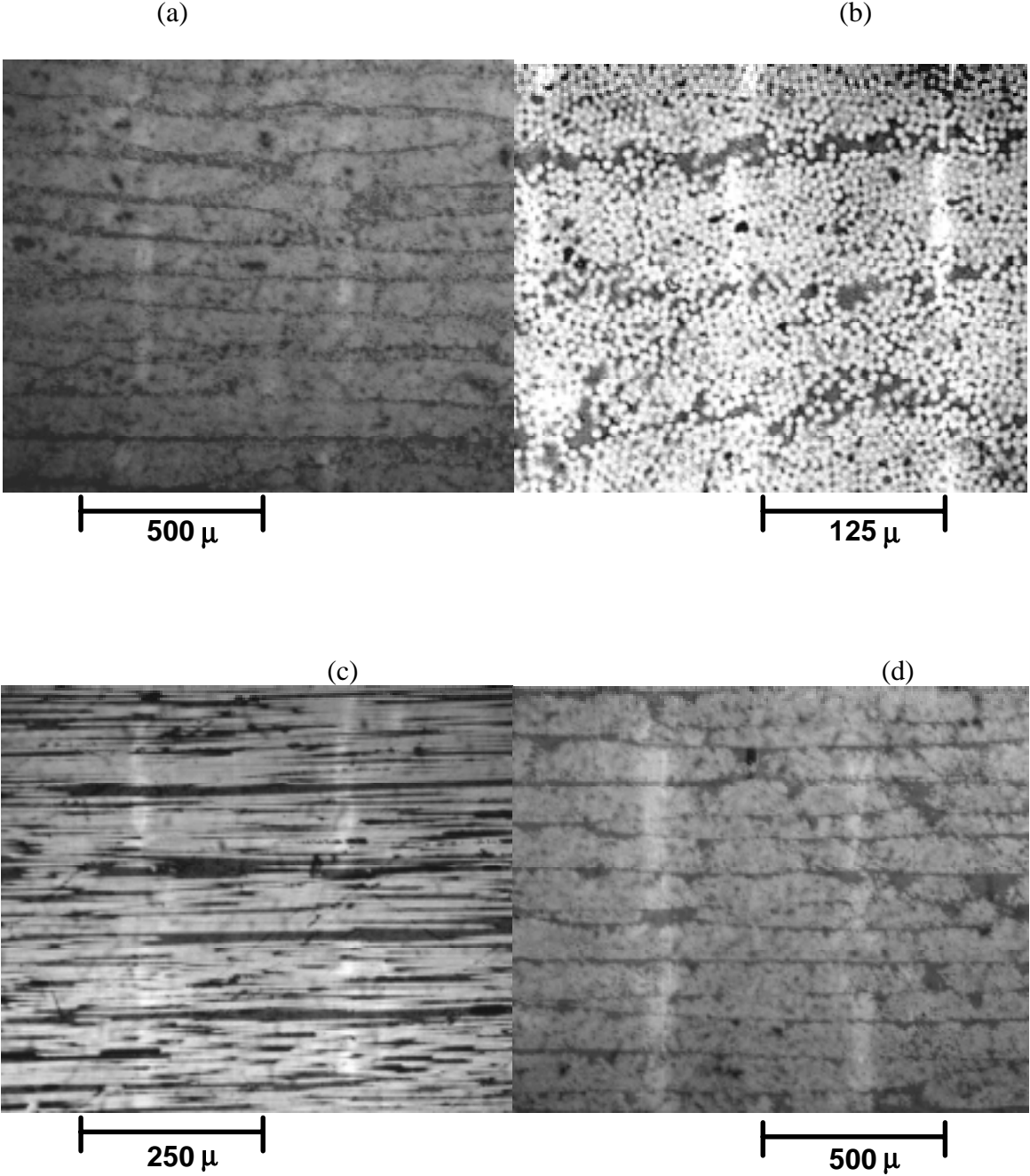


Figure 4 Photo micrographs of cross-section of Cylinders #2 and #8.

Table 2: Properties of towpreg and consolidated APC-2 cylinders.

Cylinder Number	Nippoint Temp. °C	Processing Speed mm/s	Density kg/m ³ (std. dev.)	Void % (std. dev.)	Thickness mm (std. dev.)	ILSS Mpa (std. dev.)	Degree of Crystallinity%
APC-2	na	na	1470.1 (6.0)	7.3 (0.8)	na	na	15.1
1	572	6.34	1543.5 (3.4)	2.9 (0.2)	3.20 (0.03)	45.20 (0.66)	32.8
2	633	3.71	1584.2 (6.3)	0.4 (0.3)	2.91 (0.04)	58.4 (1.49)	29.4
3	572	9.97	1523.3 (2.9)	4.2 (0.2)	3.47 (0.02)	33.44 (1.50)	29.0
4	572	5.53	1563.4 (3.3)	1.7 (0.2)	3.18 (0.07)	52.38 (1.90)	32.7
5	517	3.71	1544.5 (3.0)	2.8 (0.2)	3.25 (0.02)	49.00 (0.82)	33.6
6	662	6.34	1565.6 (3.6)	1.5 (0.2)	3.06 (0.03)	54.67 (1.26)	29.2
7	496	6.34	1514.6 (13.8)	4.7 (0.9)	3.58 (0.02)	30.74 (1.74)	30.4
8	517	7.91	1516.0 (4.0)	4.6 (0.2)	3.60 (0.02)	24.74 (1.20)	26.5
9	633	7.91	1545.6 (3.6)	2.8 (0.2)	3.26 (0.02)	46.26 (0.84)	27.4

Effect of Processing Parameters on Interlaminar Shear Strength

After investigating the impact of processing parameters on the density, void content and degree of crystallinity, the next logical step was to conduct interlaminar shear strength (ILSS) tests that give a quantitative description of the bonding quality of the resulting cylinders. Table 2 shows the density, void content, degree of crystallinity and ILSS for all consolidated cylinders. For an APC-2 composite, an interlaminar shear strength of 72 MPa (10.4 ksi) has been reported by

using the manufacturer's recommended processing conditions, i.e. 380°C for 5 minutes under a hot press loading at 1380 kPa (200 psi) [7]. The average ILSS obtained from cylinder #2 is about 80% of the ILSS of flat compression molded composite laminates. Therefore, we consider the present design of the on-line consolidation system an acceptable one.

In order to study how ILSS varies under various settings of processing conditions, a response surface using a two-factor central composite design was constructed. A second order linear regression model can be written as follows:

$$ILSS = -14.9207 + 0.31192 NT - 19.663 WS \\ - 0.000278 NT^2 + 0.1643 WS^2 + 0.0244 NT \times WS \quad (2)$$

where:

ILSS = interlaminar shear strength, MPa,

NT = nippoint temperature, °C,

WS = winding speed, mm/s.

Figure 5 shows the impact of nippoint temperature and winding speed on the interlaminar shear strength of consolidated composite cylinders. In general, higher nippoint temperature and lower winding speed yield higher ILSS. For convenience, a contour plot of the response surface is given in Figure 6. If the highest strength is desired, we can wind the cylinder at a lower speed and a higher temperature. However, if productivity is a concern, winding the cylinder at a higher speed and at a higher nippoint temperature will not sacrifice too much strength. It should be noted that all observations made here are good only for the range investigated for each variable and cannot be used to explicitly study the ILSS response outside this range.

CONCLUSIONS

A statistical approach was used to determine the significant processing parameters and their effect on the mechanical and physical properties of composite cylinders fabricated by on-line consolidation of thermoplastic towpreg. A central composite experimental design was used to select the processing conditions for manufacturing the composite cylinders. The thickness, density, void content, degree of crystallinity and interlaminar shear strength (ILSS) were measured for each composite cylinder. A second order linear regression analysis was used to construct a response surface relating nippoint temperature and winding speed to interlaminar shear strength (ILSS). Results of the analysis give the proper combinations of nippoint temperature and winding speed that will result in well consolidated composite cylinders. Under optimal processing conditions, an ILSS of 58 MPa and a void content of <1% were achieved with APC-2 towpreg.

ACKNOWLEDGMENTS

This work was supported by the NSF Science and Technology Center; High-Performance Polymeric Adhesives and Composites (NSF grant number DMR-912004). The authors also wish to thank Mr. Steven Garrette of Fiberite, Inc. for supplying the APC-2 towpreg.

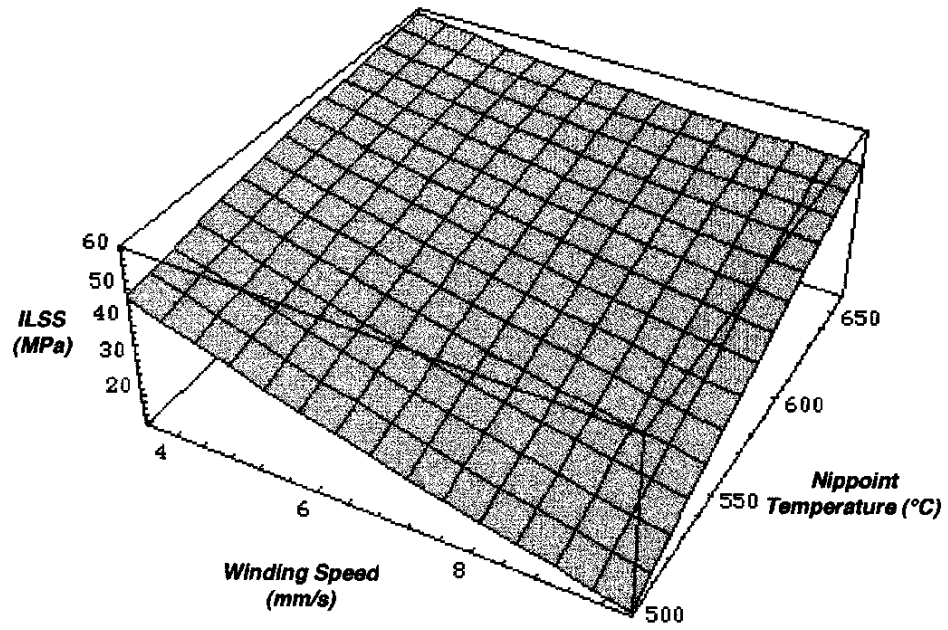


Figure 5 Impact of nippoint temperature and winding speed on the interlaminar shear strength.

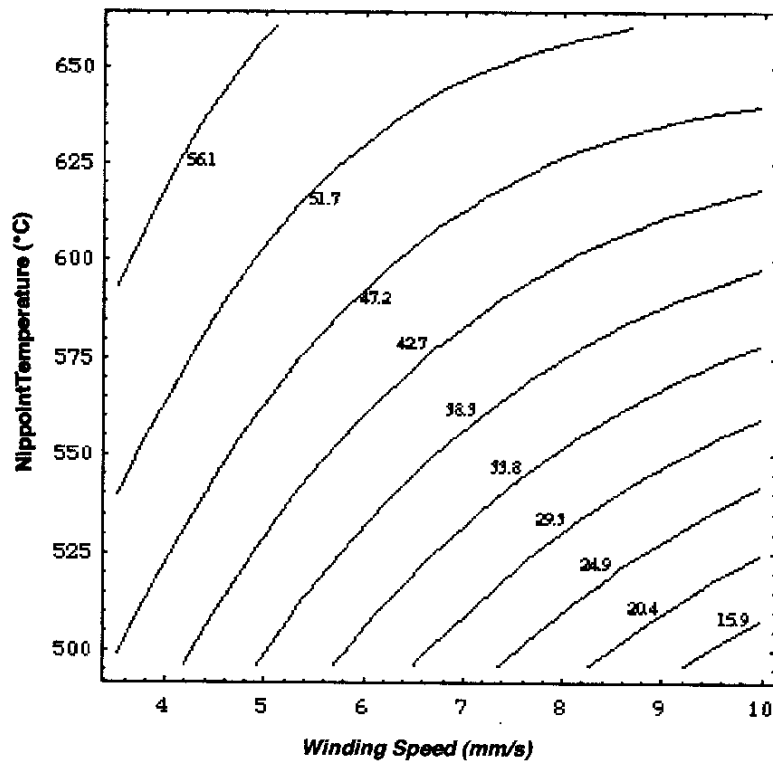


Figure 6 Contours of constant ILSS, in MPa.

REFERENCES

- [1] Coffenberry, B. S., D. E. Hauber and M. Cirino. "Low Cost Alternative: In-Situ Consolidated Thermoplastic Composite Structures" *38th International SAMPE Symposium*, pp.1640-1650 (1993).
- [2] Ghasemi Nejjhad, M. N., R. D. Cope and S. I. Güçeri, "Thermal Analysis of In-situ Thermoplastic Composite Tape Laying" *Journal of Thermoplastic Composite Materials*, 4:20-45 (1991).
- [3] Wells, G. M. and K. F. McAnulty. "Computer Aided Winding Using Non-Geodesic Trajectories," Proceedings, Sixth International Conference on Composite Materials, Second European Conference on Composite Materials, ICCM & ECCM, 1:1.161-1.173 (1987).
- [4] Beyeler, E., W. Phillips and S. I. Güçeri, "Experimental Investigation of Laser-Assisted Thermoplastic Tape Consolidation" *Journal of Thermoplastic Composite Materials*, 1:107-121 (1988).
- [5] Irwin, R. G. and S. I. Güçeri, "Recent Advances in Laser Heated On-line Consolidation of Thermoplastic Composites" *Heat Transfer Effects in Materials Processing ASME HTD-Vol. 233* , 53-60 (1992).
- [6] Carpenter, C. E. and Colton, J. S. "On-line Consolidation Mechanism in Thermoplastic Filament Winding (Tape Laying)" *38th International SAMPE Symposium*, pp. 205-216 (1993).
- [7] Mantell, S. C. and G. S. Springer. "Manufacturing Process Models for Thermoplastic Composites" *Journal of Composite Materials*, 26(16): 2348-2377 (1992).
- [8] Roderic, C. D., S. T. Holmes, K. V. Steiner and J. W. Gillespie, Jr. "Integrated Process Models for Control of Thermoplastic Tow Placement with On-line Consolidation" *25th International SAMPE Technical Conference* pp.713-724 (1993).
- [9] Buijs, J.A.H.M. and P. J. Nederveen. "A Study of Consolidation in Filament Winding with Thermoplastic Prepregs" *Journal of Thermoplastic Composite Materials*, 5:276-286 (1992).
- [10] Mazumdar, S. K. and S. V. Hoa. "Determination of Optimum Processing Conditions by Taguchi Method for On-line Consolidation of PEEK/Carbon Thermoplastic Composites" *39th International SAMPE Symposium*, pp.1546-1553 (1994).
- [11] Lauke, B. and K. Friedrich. "Evaluation of Processing Parameters of Thermoplastic Composites Fabricated by Filament Winding" *Composites Manufacturing*, 4(2): 93-101 (1993).
- [12] Sharp, R., S. Holmes, and C. Woodall, "Material Selection/Fabrication Issues for Thermoplastic Fiber Placement" *Journal of Thermoplastic Composite Materials*, 8:2-14 (1995).
- [13] Shih, P. J., "On-Line Consolidation of Thermoplastic Composites", Ph.D. Dissertation, Department of Engineering Science and Mechanics, VPI&SU, Blacksburg, VA., 1997.
- [14] Mason, R. L., R. F. Gunst and J. L. Hess "Statistical Design and Analysis of Experiments with Applications to Engineering and Science" John Wiley and Sons, Inc. New York (1989).

DESIGN AND MANUFACTURING STUDY FOR A SMALL, COMPLEX COMPONENT REQUIRED IN LARGE PRODUCTION VOLUMES

K. D. Potter, A. Towse & M. R. Wisnom

*Department of Aerospace Engineering, University of Bristol, Queen's Building,
University Walk, Bristol, BS8 1TR, UK.*

SUMMARY: The purpose of this paper is to demonstrate that it is possible to develop an approach to the design of small, complex, composite components that is driven by the requirements of minimum cost manufacture. The approach depends on identifying those geometrical features that are critical in the required component and allowing the rest of the component geometry to be dictated by the deformation characteristics of the chosen reinforcement. To explore the applicability of this concept a study has been made of one specific component required in large numbers at low cost, to form the node elements in a truss structure for a space-plane application. This application has been studied by both practical manufacture and test of components and by FEA. Both practical test and analysis agree that the design approach gives rise to a structurally acceptable solution of very low manufacturing cost.

KEYWORDS: design for manufacture, reinforcement deformation, finite element analysis

INTRODUCTION

Conventional practice in composite component design and manufacture has followed the procedures used with metallic design. That is to say that a design is drawn, analysed and released for manufacture. In view of the constraints that are placed on many designs by the necessity to fit within predetermined geometries this methodology is, in general, the appropriate way to proceed. If rigidly applied this sort of approach can lead to designs that are difficult or costly to manufacture. Additionally, defects can be induced during manufacture if the design does not accurately reflect the capabilities of the reinforcements and processes used and the skill of the labour force used to convert them into components.

Over the years a body of understanding has grown up that defines thicknesses, bend radii, lay-up procedures etc. that serve to minimise the probability of defects in mouldings (ref. 1) and experienced designers will incorporate this understanding into their designs. Utilising these "best practice" approaches to maximise moulding quality does, however, tend to have a negative influence on both the costs of lay-up and the amount of training and support required to be given to shop floor labour. In part offsetting this influence there is increasing stress being laid on design for manufacture and ensuring that the required geometry and properties can be achieved at the minimum costs. One might paraphrase the traditional approach as asking "how can the fibres be persuaded to have the necessary trajectories?". The design for manufacture approach builds on this simply by adding the caveat "at the lowest possible cost" to the above formulation.

This paper describes an alternative approach to the design of composite components and illustrates this by reference to a specific case study. The approach described here is essentially to drive the design process from the manufacturing end, specifically from the geometries that can be formed from the reinforcement with minimal deformation and thus can be manufactured by less skilled labour to high quality standards. Clearly such a methodology cannot be used for the great bulk of components, however where the approach is usable a stable, low cost, high quality result should be obtainable.

Reinforcement Deformability

All reinforcements are capable of some deformation, by a variety of modes and over a wide range of deformations limits (ref. 2). However, when an attempt is made to deform reinforcements it is often found that wrinkling of the reinforcement occurs well before the theoretical deformation limits are reached (ref. 3). The key to successful generation of shapes from hard to form reinforcements lies in minimising the deformation required. Even the limited deformability that is available with unidirectional prepreg can be used to create complex 3D geometries in conjunction with techniques such as curved line folding.

The critical point being made here is not, however, that the complex shapes that we draw on component lay-up diagrams can be made by utilising the deformability of the reinforcements; this is very often simply not the case and substantial tailoring is required with high associated costs. The point is rather that, at least in some cases, an understanding of what the reinforcements would “like” to do can be used to drive the definition of the geometry to be moulded. It should be fairly clear that, if the reinforcement does not have to be extensively tailored, simpler lay-ups should be possible; and that the prospect is held out of lay-up in flat format followed by a simple and rapid forming operation to give the required geometry. The concept of laying up a flat or generically shaped preform followed by a shaping step is not novel (ref. 4), indeed it is central to many applications of RTM processing (ref. 5). However applying the concept of following “natural” deformation paths should greatly reduce the probability of deformation induced defect formation. These deformation induced defects include wrinkles and folds in the preform and are very deleterious to the properties of the cured components. Additionally, if “natural” fibre paths can be generated one would intuitively expect smoother stress distributions, especially in terms of out of plane stresses.

It should be noted that the use of the word “natural” does not imply that no deformations must be imposed, nor that the deformation modes initiated will be those that are required unless some element of control is established. It would be very difficult to determine a rigorous definition of a natural deformation path and for the purposes of this paper we will define it as that deformation path that leads to the minimum deformation to achieve the required geometry. Ideally, one would like to be able to define these “natural” paths analytically so that the application of this concept to part design could form part of the, more or less, normal CAD design approach. Initially, however, it was necessary to test out the concept; to determine whether “natural” paths could be established; to determine the ease of manufacture of components utilising such paths; and to determine the performance of such components.

To meet these aims a demonstrator component was chosen and a mould was manufactured in such a way that the reinforcement could follow a “natural” path. The demonstrator component chosen for this study was a connecting node for a UK based private enterprise one stage to orbit space plane concept, designed by Reaction Engines Limited. The Reaction Engines Skylon vehicle fuselage (refs 6&7) is built up from a trusswork of carbon fibre tubes bonded

together at 10 way nodes. At each node six of the tubes lie essentially in one plane and the other four are out of the plane. In order to ensure that joints can be assembled it is necessary to split the nodes into sections. The main split will be between the six way node element and the four way node element. The six way node element will also have to be split “horizontally” to allow ease of assembly and a relatively simple route to be used for node manufacturing. The necessity for a simple manufacturing route is driven by the fact that around 30,000 nodes are required in one Skylon structure, equating to 60,000 mouldings just for the six way elements. This production volume is far in excess of the volumes normally experienced for high strength composite components. It is generally accepted that no ideal manufacturing routes exist for the mass production of small complex components from high performance composite materials (ref. 8). The work described here was aimed at demonstrating some elements of a suitable manufacturing process. These were; lay-up of a preform in flat format to minimise costs and simplify the development of a suitable automated process, and the conversion of the flat preform into a contoured shape that could function as a node. One critical element in this is that the conversion must not introduce unreliability into the component, the choice of a “natural” fibre path is seen as been critical to this aim of ensuring reliable low cost manufacturing.

DESIGN OF NODE FOR MANUFACTURING STUDY

The basic design chosen is a half shell, split on the mid line of the tubes, with all tubes intersecting on their axis. UD carbon fibre has been chosen as the reinforcement to be used and this is utilised in prepreg form to maximise strength and simplify handling. In keeping with the aim of minimising manufacturing costs through simplicity of design, constant width strips of prepreg are used, the width being set at half the circumference of the relevant tubes. If increased strength is required additional material in the form of woven cloth prepreg could be introduced in the crossover region without disrupting the basic design aim of simplicity. The basic design is as shown in fig 1.

It should be noted that the geometry shown in figure 1 is derived from an attempt to model the geometry produced experimentally using a solid modelling package. The match between experimental and analytical geometry is close but not perfect.

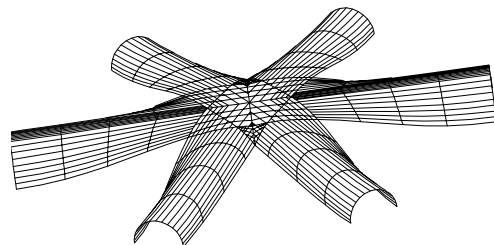


Fig 1. Schematic geometry of the six way node

As can be seen from fig 1, the node may be subject to bending failure when loaded along the arms in tension; due to the out of plane fibre trajectories. To overcome this, several possibilities can be considered. A low density foam can be used to fill the centre part of the node; the two half shells could be held together with a titanium bolt that also serves as the attachment point for the out of plane tube end fittings; a block could be bonded between the two halves during node assembly. This last option was selected for this study.

Definition of Geometry and Mould Tool Manufacture

The basic geometry chosen was 15mm ID for the major tube node connection and 10mm ID for the minor tube node connection. (Dimensions chosen largely for ease of manufacture of a master model) The major and minor tubes intersect on their centre line at an angle of 26.6° ,

see fig 2. A master model to this geometry was acquired and strips of glass fibre/913 epoxy prepreg were then laid up along each arm of the master and taped down to the surface at some distance (~4.5cm) from the intersection point of the node arms. The positions of the tape were adjusted until the fibre trajectories appeared to be smooth without excessive local changes in fibre direction.

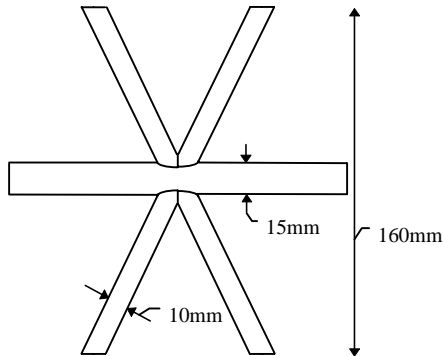


Fig 2. Basic dimensions of master model

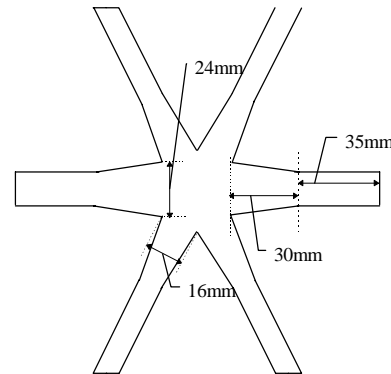


Fig 3. Approximate dimensions of finished tool

This lay-up was cured at 120°C without the application of any pressure. The inside surface of the resulting glass fibre moulding represented the required outside surface of the mould tool. The surface roughness of the GRP was then filled with wax and the GRP shell was used to manufacture a mould tool from Al filled epoxy that could be used at cure temperatures up to 120°C, see fig 3.

Lay-up of Reinforcement

The lay-up was selected as 6 plies of reinforcement along each arm of the node, corresponding to 0.75mm cured thickness in the arms.

The reinforcement used for the manufacture of prototypes was XAS/913 prepreg as this had the correct cure temperature. Zero bleed moulding was used in conjunction with vacuum bag moulding to simplify the moulding process as far as possible.

Two approaches were taken to the lay-up of reinforcement on to the mould tool. The first was to lay up directly onto the tool surface forming each ply as it was laid down. This was done primarily to prove out the tool and demonstrate that the geometry of the tool was correct. It proved very easy to lay up the prepreg such that it followed the tool contour. However, there was a tendency for the prepreg to stretch in the 90° direction as it was laid down producing a slightly over width moulding and great care had to be taken to ensure that the edges of subsequent plies of prepreg coincided.

The second approach was to lay up all six plies on a flat surface (without any debulking stage to minimise costs). A 10mm wide strip of prepreg was laid up at the end of each arm at the mid point of the lay-up with the fibre direction across the arm. This strip was intended to counter the tendency of the prepreg to stretch sideways. It proved to be much quicker to lay up the prepreg in flat format and much easier to keep the edges of subsequent plies coincident. Equally, it proved to be very easy to conform the flat prepreg lay-up to the geometry of the tool, although care was needed to ensure that the lay-up stayed central with respect to the

arms of the node. In a production node tool (based on compression rather than vacuum bag moulding) some feature would have to be provided to ensure perfect orientation. A series of mouldings were made using unskilled labour with no previous experience of handling composites. All mouldings appeared to be of high quality with good fibre alignment. The weight of the mouldings was approximately 11 gr. The cost of the manufacturing route cannot currently be quantified as it is intended that a large measure of automation be applied. Even in the absence of this it should be possible to streamline the manufacturing process to give production costs that are acceptable in view of the proposed application.

ASSEMBLY AND TEST OF NODE

The prototype node mouldings were wet assembled into a six way node structure using aluminium rods to simulate the tubes that would be required in the real structure, the adhesive used was 3M9323 a high strength, 120⁰C cure, two part epoxy.

The assembled node was set up in a model 1341 Instron servohydraulic test machine operating under displacement control.

Failure of the bondline in one node arm occurred at 12.56KN. Failure occurred at the CFRP/adhesive interface. The bondline was seen to be partially voided and the rod was offset in the arm as shown in fig 4.

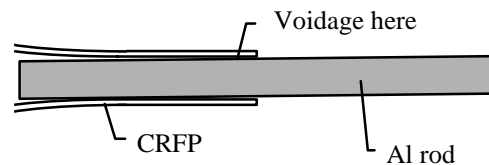


Fig 4. Misalignment of rod with respect to node and position of voidage

Factoring from Reaction Engines data for loads on the Skylon vehicle a load in this arm of 12KN represents the worst case condition. The bond-line failure therefore occurred at 5% above the maximum load. The measured thickness of the node arms was 0.8mm giving a cross sectional area of 27.14mm² at an ID of 10mm. At the failure load of 12.56KN the average stress in the loaded CFRP node arms would be 463MPa and the strain would be 0.35%. The joint strength was 400N/mm of joint width. The test was carried out on one of the pairs of 10mm arms, the deviation of the fibre paths on these arms is greater than for the larger arms so the result for the 10mm arms should also be indicative for the 15mm arms. From previous work on bonded joints (ref. 9) the mode of failure exhibited in this joint is unexpected. The most likely modes of failure are adhesive cracking for joints with large fillets and adhesive cracking/delamination in the CFRP for joints with small or no fillets. The release agent used on the node tool was mould wax, because of the tendency for cast moulds to have slightly rough and porous surfaces. It is possible that a transfer of this release agent occurred and that insufficient material was removed from the CFRP to guarantee a good bonding surface. It should be possible to greatly improve on the bond strength exhibited in this test by improvements in surface preparation and better geometry at the end of the joint.

Visual and microscopic examination (up to x 100) of the tested node showed no damage as a result of the test on the outside surface of the node. It would not be possible to disassemble the bonded node without damage, so the condition of the inside of the node is unknown. The out of plane misalignment of the prepreg in the node in the cross-over regions at the centre of the node will increase from the inside to the outside of the node. As the most likely form of damage would be cracking and delamination at these cross-over regions the absence of damage on the outside is strongly indicative that no damage will be seen on the inside of the

node. The indication is therefore that the node has some strength in reserve in the mode tested. It is not possible to determine what level of strength reserve is available at this time.

Despite the great simplicity of the design from the manufacturing viewpoint it has proven to be much more difficult to model the geometry analytically to permit FEA. The procedure that was arrived at to model the geometry on I-Deas is outlined below.

FINITE ELEMENT MODELLING

The geometry is as depicted in Fig 5. Only one dimension was taken from the final moulding, and this was the dimensions of the (assumed) arc ADB of Fig 5. This arc was used to locate point B in space, the only other line which was known was the straight line AE which extends out along the top of the Dia 15 arm of the node. The surface was built in sections, with the lines BC and EC related to the circumference of the semicircle on the Dia 10 arm and the quarter circle on the Dia 15 arm respectively. Hence, BC was constrained to be $(\pi \cdot 10/2)$, or 15.71mm and EC to be $(\pi \cdot 15/4)/(\cos(26.6^\circ))$ or 13.17mm in length. In this way, the surface has not stretched in the transverse fibre direction and therefore the fibre trajectories as modelled by the software will bear close relation to the practical moulding. The length of the arms was 45mm from the centre to the end of the flared section, as indicated previously.

A quarter model was used, which was meshed using eight-noded quadratic quadrilateral shells wherever possible, and quadratic triangle shell elements where necessary. The fibre trajectories were based on the underlying CAD part, and were seen to bear close resemblance to what would be expected in the actual moulding, although no data is available to support this.

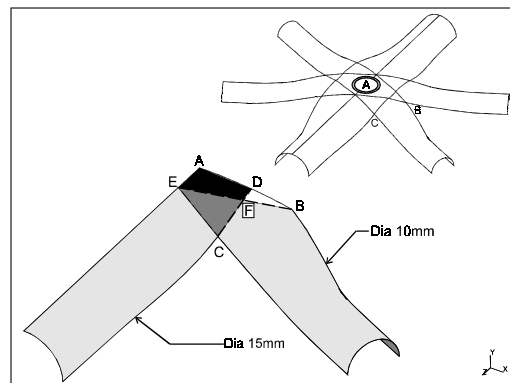


Fig 5. FE quarter model schematic

Element Formulation

As would be expected from the previous discussion on the lay-up, the moulding is neither balanced nor symmetric. Furthermore, although the tooled surface is smooth, the outside surface alters between 6, 12 and 18 ply thickness. Consequently, four lay-ups were used in the model, as depicted in Fig 6. The main arms (light grey) were $[0^\circ]_6$, area CEF was $[0, -63]_6$, area BDF was $[0, +53]_6$ and ADFE was $[0, +53, -63]_6$. All these lay-ups are relative to the local directions which were defined in I-Deas, as shown in Fig 7, and are referred to as lay-ups A, B, C and D respectively.

It can be seen from Fig 6 that between 6 and 12 'null' plies have been included to ensure the correct offset between areas of differing lay-up in the model.

The lay-up for each area was input into the I-Deas FE program, which calculated the A, B and D matrices from Classical Laminate Theory. The properties of each individual lamina in the lay-up were based on unidirectional T800-924 from Hexcel, as this material would be used in production. The null material was taken to be 1% of the elastic moduli of the T800.

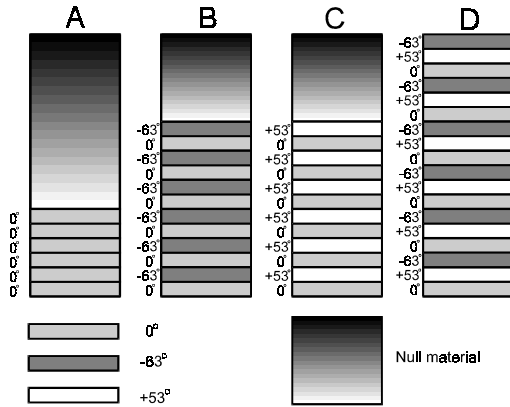


Fig 6. Model lay-ups

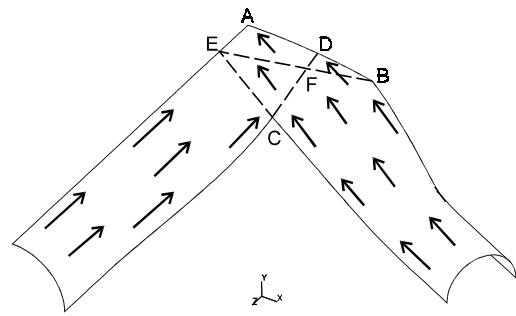


Fig 7. Local element 'x' direction

Analysis and Results

A linear elastic analysis was carried out with mechanical loadcases of 8kN on the dia 15 arm, and 4kN on the dia 10 arm (equivalent to 32kN and 8kN tension/tension for the full node). Symmetric boundary conditions were applied along the cut edges, and a rigid tube was modelled at the centre of the node as shown in Fig 5 as mentioned earlier.

The greatest cause for concern in terms of the stresses in the node was seen to be the transverse tensile stresses on ply 1, the inside surface of the main diameter 15 arm. As the tensile load is applied, the node will attempt to straighten out, resulting in a bending moment on the main arm. This will place ply 1 into transverse tension, and ply 6 into transverse compression. It was seen from the results that the loading in the transverse direction on the dia 15 arm was not pure bending, but approximately 59MPa of transverse tensile membrane stress was also present. The stresses from the mechanical load on the main arm are shown in Fig 8.

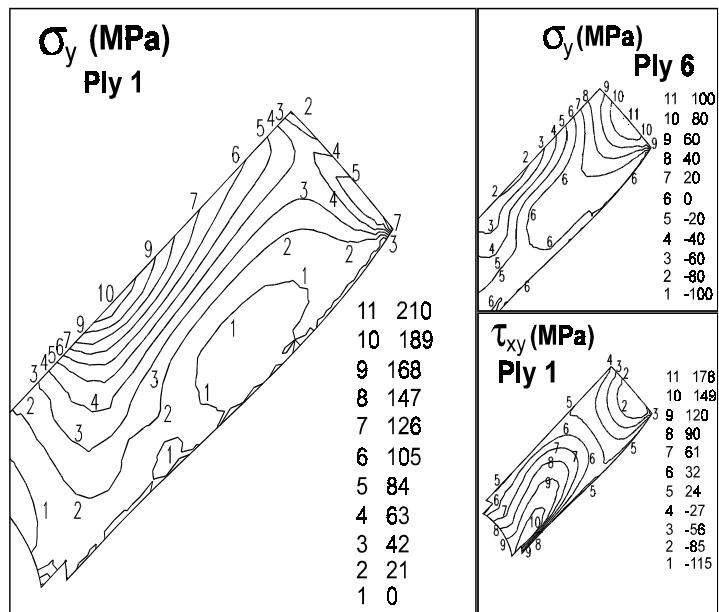


Fig 8. Transverse tensile and intralaminar shear for main arm under tensile loading (MPa)

It can be seen from Fig 8 that a peak transverse tensile stress of 205MPa acts on the unidirectional main arm. This stress is driven directly from the geometry of the flare of the node. It is highly likely that a transverse crack would appear in the arm at relatively low loads, which, as the lay-up is UD, would rapidly crack the remaining plies until the main arm would split into two pieces. The consequences of such a crack on the structural integrity of the node (especially under compressive loading) would be severe.

It can also be seen that a high in-plane (intralaminar) shear stress is present at the end of the node, due to the differing axial stiffness of the main arm centreline and edge. This results in a

non-uniform stress distribution, with the top (initially straight) edge carrying most of the load, with the free (curved) edge carrying essentially no load. A large deflection, non-linear analysis would be needed to see this curved edge begin to pick up load. This has not been carried out to date.

It was also seen that the 'B' lay-up $[0,-63]_6$ also suffered from high transverse tensile stresses on ply 1, due to bending of the section caused by the offset in neutral axes between lay-ups A and B.

Suggested Modified Lay-Up

In light of the high transverse tensile stresses seen in the model, the logical solution was to stiffen the unidirectional arms to both membrane stresses and against bending. The easiest way to achieve this would be by placing a single 90° ply as far away from the neutral axis as possible.

To minimise deformation of this extra ply between areas of differing lay-up, it was decided to place the 90° material on the tool edge side of the neutral axis. Ideally (from a bending stiffness viewpoint) this would mean ply 1, although that would mean bonding directly to a 90° ply, which was believed to be disadvantageous. The compromise was to include an extra 90° layer to the lay-up at ply 3, meaning the lay-ups were now (from the tooled surface):

$$\begin{array}{ll} A': [0]_2[90][0]_4[\text{null}]_{14} & B': [0,-63]_2[90,+26.6][0,-63]_4[\text{null}]_7 \\ C': [0,53]_2[90,-37][0,53]_4[\text{null}]_7 & D': [0,53,-63]_2[90,-37,+26.6][0,53,-63]_4 \end{array}$$

The analysis was repeated with these new lay-ups, and it was seen that the peak transverse tension in the main arm was reduced from 205MPa to 131MPa (a reduction of 36%). The stress distribution was now almost pure bending, with ply 3 (the 90° layer) picking up the membrane stresses. The level of the transverse tension is, therefore, reduced, but is still at a level at which ply cracking can be expected from the tooled surface under tensile loading. However, the consequences of this First Ply Failure (FPF) would now not be as severe as the 90° ply is likely to arrest transverse cracks from jumping from ply 2 to ply 4. The B' lay-up peak transverse tension was also reduced, from 169MPa to 120MPa (a reduction of 29%), although it is still well above that required to crack the ply. Again, the lay-up here is sufficiently multidirectional to ensure that this FPF would probably not lead to global failure.

The main thrust of this paper has been the fact that the geometry has been driven by what is practically quick and easy to achieve, and by what the fibres 'naturally' wish to deform into. To demonstrate the difference compared with a node designed without considering the manufacture of the node, a second FE model was built based simply on interconnecting tubes filleted together, as shown in Fig 10. A diam 15 tube was intersected by two diameter 10 tubes, which were then filleted with 8mm and 6mm fillet radii. It was assumed that a similar method to that used before would be used to manufacture the node, i.e. laying down strips of material for each arm, and to that end the surfaces were trimmed to ensure the reinforcement widths did not alter. This resulted in the same lay-ups A,B,C and D as before, but with different shapes as shown in Fig 10 (e.g. EFC is again the $[0,-63]_6$ lay-up).

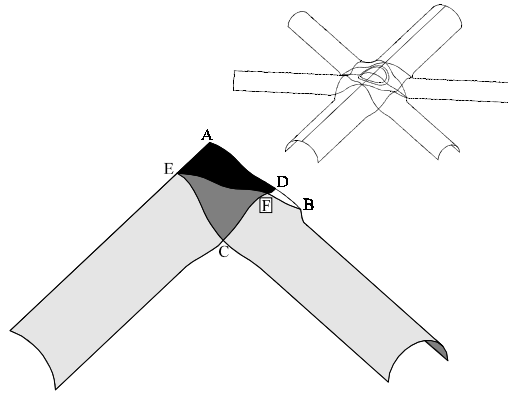


Fig 10. Conventional CAD geometry

The results from the stress analysis showed generally higher transverse tensile and intralaminar shear stresses, especially in the highly deformed B lay-up. At this point the peak transverse tension increased from 169MPa (for the standard lay-up manufacture-led node) to 213MPa (for this filleted tube version), an increase of 26%. The stresses in other parts of the model showed slight worsening of performance over the manufacture-led node, with the exception of the main arm. As noted previously, high transverse tensile stresses were encountered in the inside surface of the main arm under tensile load due to the flare out of the node arm. This transverse tension is purely geometry driven, and as the filleted tube version has no long sweep, the transverse tension is lower (at 157MPa cf. 205MPa for the 'good' design). It must be noted, however, that this value of 157MPa is still too high and a 90° ply would still be required. It must be emphasised that there would be considerable difficulties involved in the manufacture of defect free nodes to this design.

GENERAL DISCUSSION

The prototyping exercise reported here has been entirely driven by low cost manufacturing considerations based around the concept of designing the component and mould tool around the geometries easily available from the reinforcement. Initial test results indicate that the design can carry the required load in tension straight across the node in one pair of arms. No effort has currently been made to establish the adequacy of the design in compression across the node. Even if the design requires modification the basic concepts of laying up a prepreg preform in the flat state and deforming this onto a tool whose dimensions have been chosen for ease of forming should be retained as it is these features that lead to controllable costs and quality.

It has been assumed above that a measure of automation of the lay-up process will be required in a production environment. The symmetry of the node preform would allow several nodes to be laid up at once, either manually or by tape-layer. Simple changes to lay-up practices such as this should have major impacts on overall economics.

CONCLUSIONS

For at least some components the concept of designing the geometry to follow the characteristics of the reinforcement has been demonstrated.

1. This has been demonstrated via the manufacture of a complex composite node.
2. In this case the geometry was only fixed at the load introduction points and allowed to follow “natural” paths elsewhere.
3. The design is quick to produce and good results can be obtained with unskilled labour.
4. Testing has shown that the design is capable of carrying the required tensile end load in arms that are directly opposite across the node.
5. The performance of the node has yet to be established in terms of compressive loads or loads applied between adjacent arms.
6. The theoretical performance of the node has been seen to be lacking in strength when subjected to large tensile loads due to the flare of the main arm. It has further been demonstrated that the inclusion of a 90° ply is beneficial to the overall stress state in the node, to a point where it is capable of carrying the loads required of it.
7. The standard CAD geometry based node is seen to be inferior in stress state to the manufacture-led node, but only marginally so. The important point to remember is that the CAD part contains large deformations, and it is almost inevitable that the moulded node to this shape would contain splits and wrinkles. The manufacture led node is, by definition, extremely quick and easy to prepare as well as being superior in performance to what would have been designed without paying attention to design for manufacture.

ACKNOWLEDGEMENT

The authors would like to acknowledge the support of the UK Engineering and Physical Sciences Research Council, via contract number GRK66833

REFERENCES

1. Hart-Smith. L. (1988) *Designing with advanced fibrous composites*. Proc Australian Bicentennial International Congress in Mechanical Engineering.
2. Potter. K.D., (1979) *The influence of accurate stretch data for reinforcements on the production of complex structural mouldings. Part 1. Deformation of aligned sheets and fabrics*. Composites. July 1979. pp 161-7
3. Potter, K.D. (1980) *Deformation mechanisms of fibre reinforcements and their influence on the fabrication of structural parts*. Advances in composite materials. (eds A.R. Bunsell, C. Bathias. A. Martrenchar, D. Menkes, G.Verchery) Pergamon Press. pp 1564-79
4. Potter. K. D., & Robertson. F. C. (1987) *Bismaleimide formulations for resin transfer moulding*. 32nd International SAMPE Symposium. April.
5. Morgan. D. (1989) *Design of an aero-engine thrust reverser blocker door*. Proc 34th International SAMPE Symposium. 2358-64.
6. Varvill. R. (1995) *The Skylon spaceplane*. Proc 46th International Astronautical Congress. Oslo. Paper IAA 95-V3.07 International Astronautical Federation.
7. Bond. A & Varvill R (1995) *Skylon operations and economics*. Proc 46th International Astronautical Congress. Oslo. Paper IAA 95-IAA.1.1.07 International Astronautical Federation.
8. Potter. K.D. (1983) *High rate reforming of thermoplastic laminate into small, complex components; a process study*. Proc 4th International Conference, SAMPE European Chapter. SAMPE. pp 103-12.
9. Adams R.D., Atkins R.W., Harris J.A. & Kinloch A.J. Stress analysis and failure properties of carbon-fibre reinforced plastic/steel double lap joints, J. Adhesion (1986) 20 p.29-53

A NEW IMPREGNATION TOOL FOR ON-LINE MANUFACTURING OF THERMOPLASTIC COMPOSITES

A. Lutz, R. Funck, T. Harmia, K. Friedrich

Institut für Verbundwerkstoffe GmbH, D-67663 Kaiserslautern, Germany

SUMMARY: With a newly developed impregnation tool it is possible to produce thermoplastic intermediate composite material forms such as tapes and/or to manufacture on-line, i.e. in one processing step, thermoplastic composite components. The impregnation tool is small in size, so as to be flexible for handling in front of established manufacturing processes such as pultrusion or filament-winding. Fibers and molten polymer matrix will get in contact at the outer surface of the impregnation wheel, which is the centre-piece of the impregnation tool. The molten polymer is provided from a commercial extruder. Testing of the process is illustrated by a combination of impregnation and filament-winding, in order to produce small sized tubes.

KEYWORDS: thermoplastic matrix, fibre-bundle, on-line impregnation, melt, filament-winding, pultrusion, process-combination

INTRODUCTION

Thermoplastic composites show a different property spectrum compared to thermosetting composites, which in many applications can provide advantages, such as: high fracture toughness, possibility of post-thermoforming, fast fabrication cycles and easy recycling. One interesting and new application of thermoplastic composites is the combination of different manufacturing techniques such as filament winding and injection moulding in order to carry high loads (filament wound inner part) and at the same time realize a complex shape (injection moulded outer part) [1]. However, a basic problem in manufacturing of thermoplastic composites is the fast, void free impregnation of fibre bundles or rovings with the highly viscous matrix. Many routes, such as film stacking, impregnation with thermoplastic powder, commingling of thermoplastic fibres with reinforcing fibres, or using an additional solvent to reduce the viscosity of the thermoplastic resin exist in order to overcome this problem. All of these pre-forms were necessary while manufacturing thermoplastic composites. In order to realize economic manufacturing processes it is of interest to reduce the machinery and intermediate costs. However, with the current state-of-the-art technology it is still necessary to use pre-impregnated materials which make such processes rather expensive for high volume production of pultruded or filament wound components.

This paper reports about the combination of an impregnation and a manufacturing process which is now possible because of the development of a new impregnation tool. This impregnation tool is small of size and very flexible in handling because of an open and

accessible design. The thermoplastic melt is provided from an extruder. No solvent or other additional chemicals for viscosity reduction are necessary.

BACKGROUND

Pultrusion and filament winding employing thermoplastic matrix systems have many advantages over the traditional thermosetting systems in terms of mechanical and impact behaviour, possibility of post-thermoforming, recycling and less curing time. Many more advantages but also drawbacks exist between thermoplastic and thermoset matrix materials for composite applications. The decision which kind of matrix is the most suitable one for a special part application must be determined in connection with the global demands of the part to be realized. It is false to favorite one of both matrix materials without the background of the later application. However, many advantages are in favour for thermoplastic matrices, but also disadvantages make the manufacturing processes more demanding. The most important difficulty in manufacturing continuous fibre reinforced thermoplastic composites is to gain a high degree of impregnation. This is especially true for the connection of the highly viscous and glutinous thermoplastic melt and the very slender filaments of the reinforcing material. The viscosity of the thermoplastic melt is, depending on the selected matrix, often more than two or three orders of magnitude higher in comparison to thermosets (Fig.1) [2].

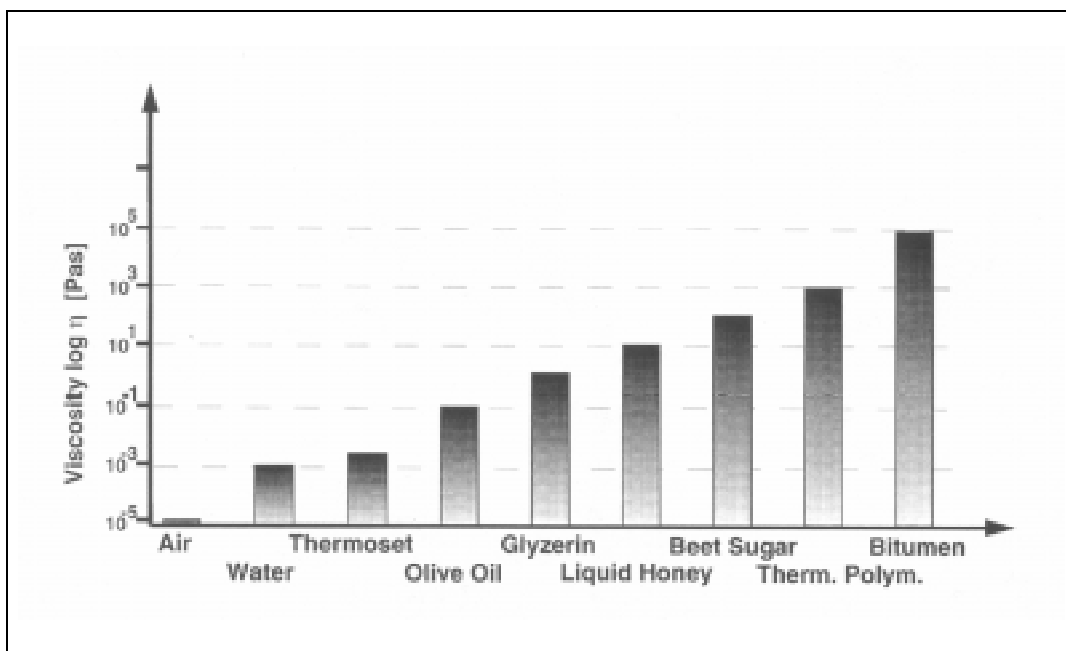


Fig. 1: Viscosity values of different liquids

While the impregnation of thermosetting composites often occurs immediately in front of the manufacturing device, e.g. in filament winding and pultrusion processes, this could not be achieved so far with thermoplastic matrices in an economic range. The reasons are not only the difficult impregnation because of the high viscosity of the melt, it is also difficult to handle the heated melt and all the machinery parts, that must be heated. To overcome these problems it is up to now state-of-the-art to separate the impregnation and manufacturing processes. The impregnation of thermoplastic composite intermediates itself is divided into many different techniques, and a few of them are described in the following: In an overview,

the totally impregnated intermediates like tapes or organic sheets and the semi-impregnated intermediates like powder impregnated fibre bundles, commingled fibre bundles or cowoven mats must be separated. The main difference between these two groups is that the impregnation step is completely finished (in the tapes and organic sheets) in contrast to the semi-impregnated intermediates which are not really impregnated. In this case only the fibres and the matrix material are mixed in such a way that the distribution of the matrix and the fibres is optimized in order to reduce the way of flow for the melt when the matrix is molten. Figure 2 gives an overview of the most important impregnation techniques.

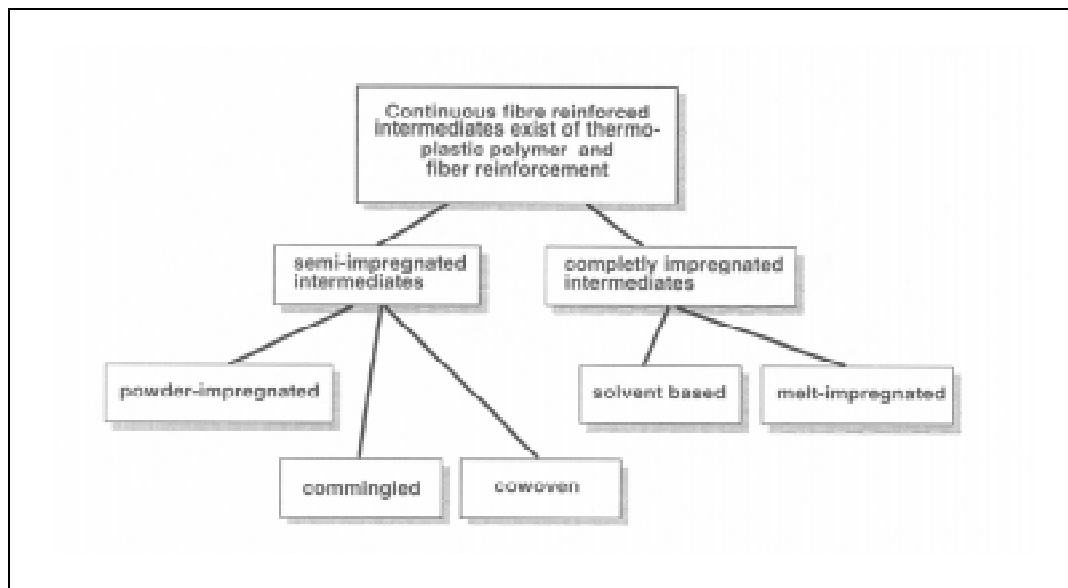


Fig. 2: Impregnation techniques

The main drawback of the semi-impregnated intermediates is that the impregnation does not occur before the part processing takes place. The consequence is that the impregnation quality is not easy to control. The degree of impregnation of the totally impregnated composite intermediates is close to those of the manufactured parts. For filament winding processes with tape e.g. it is not necessary to heat up the complete tape, but it is enough to heat the contact zone right in front of the nip-point between tape and the already wound structure [3]. Therefore it is possible to achieve higher processing speeds.

An additional drawback of the pre-impregnated intermediates is that the users are restricted to the materials which are on the market available. That means, the composition of fibre and matrix material, the fibre volume content, the colour and all the other qualities are depending on the suppliers offer. Up to now only a few different kinds of thermoplastic composite intermediates are available. This limits the application development despite the many advantages of a thermoplastic matrix. Additionally, the cost of the long fibre reinforced thermoplastic composite intermediates is higher, compared to the material costs for thermosetting composites.

The aim for this research project was to overcome these mentioned drawbacks for thermoplastic composites and to develop a new process which combines the impregnation and the manufacturing process.

DEVELOPMENT OF A SUITABLE IMPREGNATION PROCESS

To be not depend on the special offers of intermediate material suppliers, raw materials for thermoplastic composite parts should be generally available. It is possible to choose from a very large amount of suppliers of fibres and matrices when direct melt impregnation is used. Additionally, the direct impregnation via melt compared to other techniques mentioned above has the advantage, that no “preprocessing” of the matrix except of melting is necessary. To produce a high-quality composite it is important to realize a high degree of impregnation without any voids or defects. At this point the existing melt impregnation techniques are discussed, in order to find out their strengths and weaknesses:

In one commonly used melt impregnation technique for fibre rovings today, the impregnation is carried out by feeding fibre bundles alongside a number of pins which are situated in a heated bath of molten polymer matrix (Figure 3) [4].

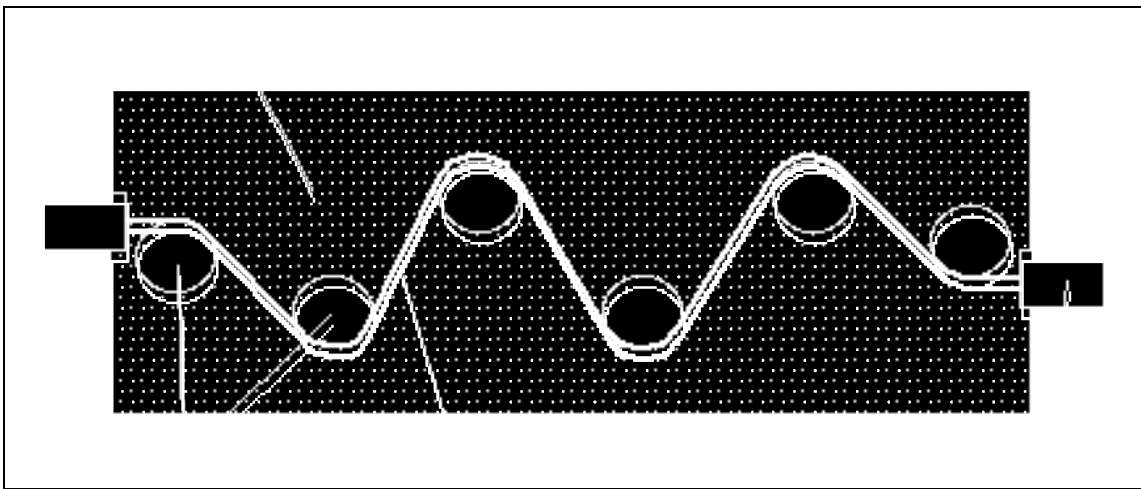


Fig. 3: The melt bath impregnation technique

However some drawbacks are connected to this technique, which are: (a) fibre damage caused by physical contact with the pins, (b) fibre tension generated by the diversion of the fibre bundle together with the high sliding friction (caused by the presence of viscous melt at the surface of the pins), and (c) that the impregnation step takes only place when the fibre bundles are in contact with the pins. This “melt bath”-technique has also been studied by several research groups and qualitative and quantitative models exist to describe the tension build up in the fibre bundles and the impregnation process in this technique [5,6]. This understanding can be used to optimize the melt bath impregnation technique, yet the basic drawbacks of this process related to the high fibre tension, the very sensitive process and the short impregnation time need further attention. Negative for a combination with a filament winding or pultrusion process is the large geometric size and weight of the melt bath. Additionally, the close design makes an easy set up (change of fibre bundles or matrix material) difficult. For a filament winding process the achievable processing speeds are low and not economic enough.

Another melt impregnation process exists of two or more dies in which a nozzle supports the melt through the fibre bundle. Also in this process the impregnation takes place in a short time step in which the fibre bundle crosses the nozzle. A high fibre tension must be generated in order to keep the fibre bundle in contact with the dies, so that the melt can penetrate

perpendicular through it. Figure 4 shows a schematic drawing of this impregnation process [7].

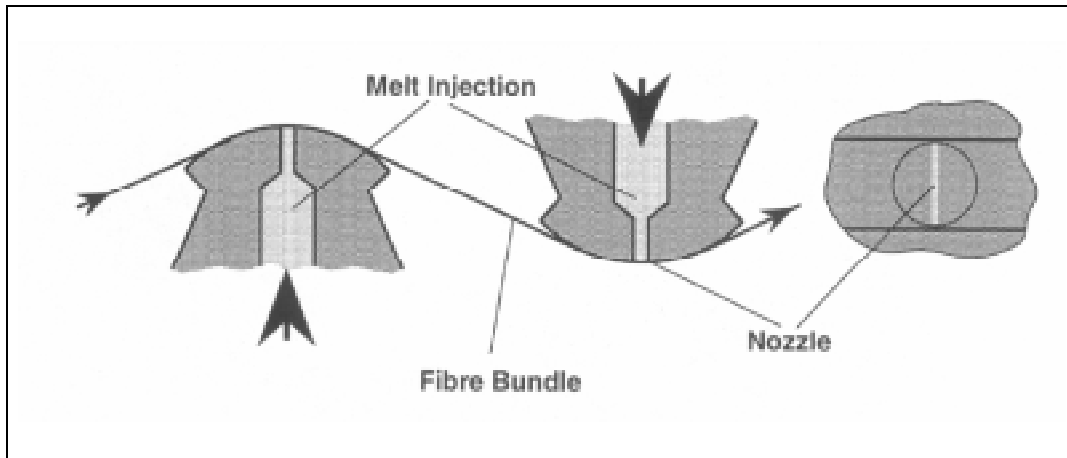


Fig. 4: The melt injection impregnation technique

The main drawback is the high fibre tension that must be adjusted in the manner that the fibre bundle is in contact with the dies. The impregnation time is very short. An impregnation can only take place when the fibres pass the nozzle. The pressure of the melt must be very high to ensure that the high flow resistance of the fibre bundle can be exceeded.

The evaluation of these melt impregnation techniques with a simple mathematical equation shows which are the most important parameters for a penetration process:

Darcy's law describes the basic parameters of a penetration process through a porous medium (such as a fibre bundle). The value of the penetration speed v_{Matrix} of a liquid medium is described as:

$$v_{Matrix} = \frac{K}{\eta} \cdot \frac{\Delta p_{FB}}{\Delta l_{FB}}$$

where Δl_{FB} is the thickness of the fibre bundle, η the viscosity of the polymer melt, K a geometric constant, and Δp_{FB} the pressure difference. The integration shows the depth of penetration z in function of these parameters: [6]:

$$z = \sqrt{\frac{K \cdot 2 \cdot t_i \cdot \Delta p_{FB}}{\eta}}$$

When all constants are combined to one constant (z is also constant and equal to the bundle thickness) only the relevant variables of penetration are shown:

$$const = \frac{t_i \cdot \Delta p_{FB}}{\eta}$$

It is now recognizable for a high value of this constant (equal to a better impregnation) that these three parameters of impregnation are the most important ones. The viscosity should be low, whereas the time of impregnation and the melt pressure should be high.

For both impregnation processes described the real time of impregnation is very short. In case of the melt bath technique it takes place only in front of the contact zone with the pins [6], while using the melt injection, impregnation occurs only in the range of the nozzle. Because of the short impregnation time, the melt pressure must be high so as to realize equal impregnation depths. Therefore the value of fibre bundle tension must also be high to keep the filaments in close contact with the nozzle. To overcome these geometric and theoretical drawbacks a new impregnation tool was developed which unites all the important conditions.

NEW IMPREGNATION TOOL AND PROCESS COMBINATION

The aims of the new tool design for impregnation of fibre bundles with a thermoplastic melt were: (a) to verify a longer impregnation time, thus allowing a higher line speeds (out-put), (b) to prevent the build up of high fibre tension, (c) to allow easy and smooth processing of the fibre bundles (no sharp diversion angles), even when a number of broken filaments exists in the fibre bundle (decreasing the sensitivity of the process), and (d) to design a simple structure of the tool in order to allow fast set up times, easy handling, and the possibility to situate it in front of a manufacturing process. All of these criteria could be met by the new tool (impregnation wheel) (Figure 5)[8].

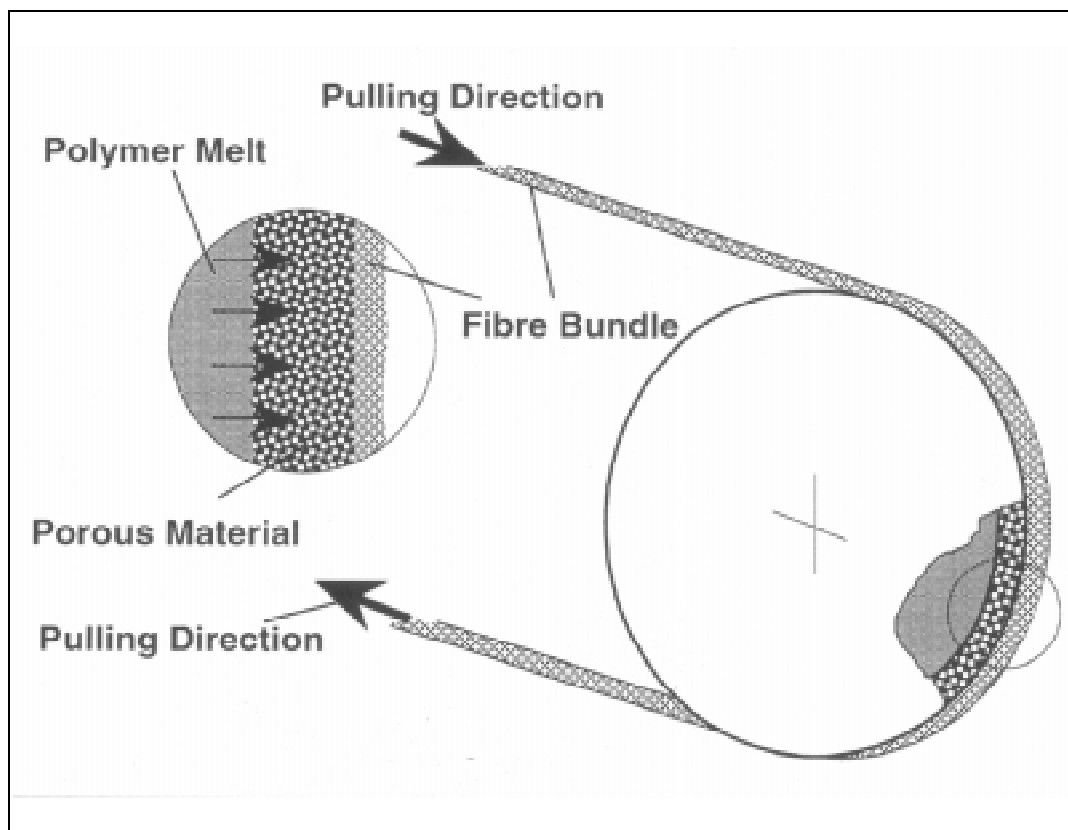


Fig. 5: The new impregnation tool (impregnation wheel)

The impregnation wheel consists of a ring, which allows the molten thermoplastic matrix to penetrate through it and through the fibre bundle, which is pulled between a supporting rail

system placed at the edges of the wheel. The fibre bundle is in physical contact with the outer surface of the ring along half of its perimeter (up to 180°), and this section of the ring is permeable. By increasing the diameter of the impregnation wheel, the duration of the impregnation step can be largely extended. This means that the effective impregnation time t_i is much longer compared to the processes described above. Because of the high shear rate while the molten polymer matrix penetrates through the porous material the viscosity η is reduced to a minimum value. Therefore, the impregnation pressure Δp_{FB} can be reduced to reach a lower fibre bundle tension which reduces fibre damages due to the impregnation step. The latter allows to produce high quality impregnated fibre bundles. As this wheel is positioned right in front of the pultrusion die or the filament winding mandrel, it is not only possible to precisely control the winding or pultrusion temperature but also to vary the fibre volume fraction within a certain range. Because of the fully molten polymer, the impregnated fibre bundle is completely welded with the surface of the wound layer manufactured before, or to the neighbouring strands during pultrusion. This design therefore promises high output due to the adjustable impregnation time, no or low fibre bundle tensioning due to its low diversion (by the large diameter of the wheel), and short set up times as well as easy handling due to the fact that there are no dies through which the fibre bundle has to be pulled through. The fibre volume fraction is adjusted by controlling the amount of molten polymer.

The station has to be placed next to a commercially available extruder that provides the molten polymer through a flexible heated tube, thus feeding the molten matrix into the impregnation tool. The impregnation head was built in a small size to allow attachment to commercial filament winding supports (Figure 6). It is very easy to change or replace the fibre bundles in short times. In addition, it will be attempted soon to adjust the impregnation tool to an existing thermoplastic pultrusion line.

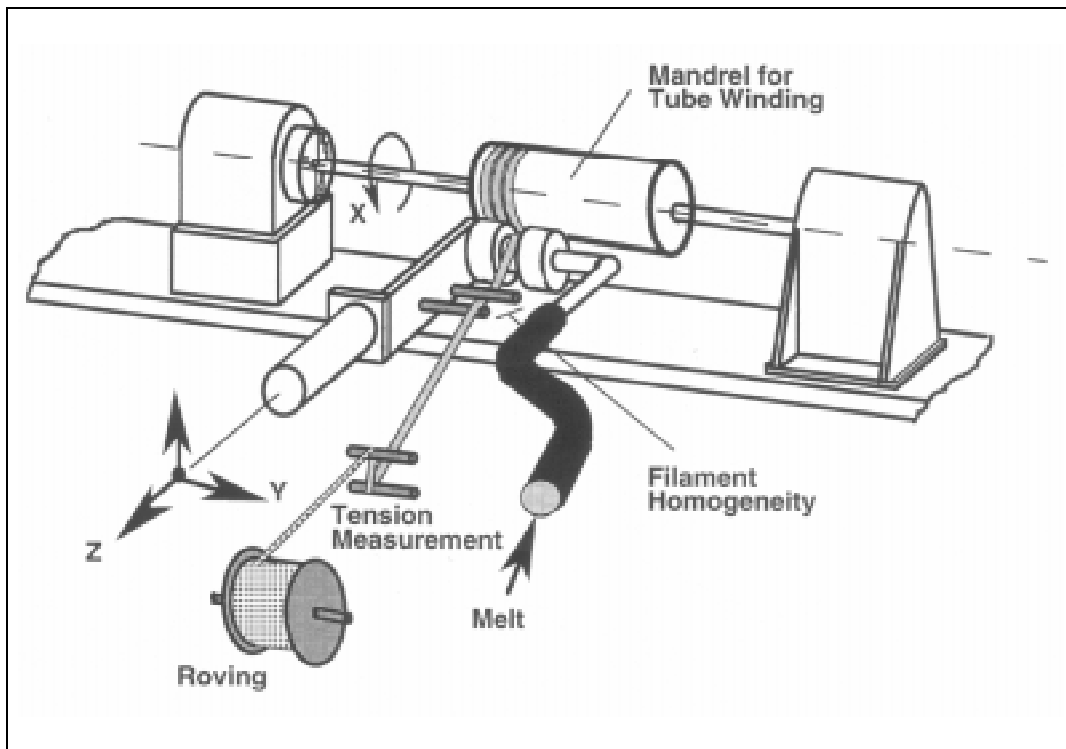


Fig. 6: Principle of the combined impregnation and filament-winding process

CHARACTERIZATION OF MANUFACTURED PARTS

All these advantages are demonstrated on the example of filament wound tubes (Figure 7).

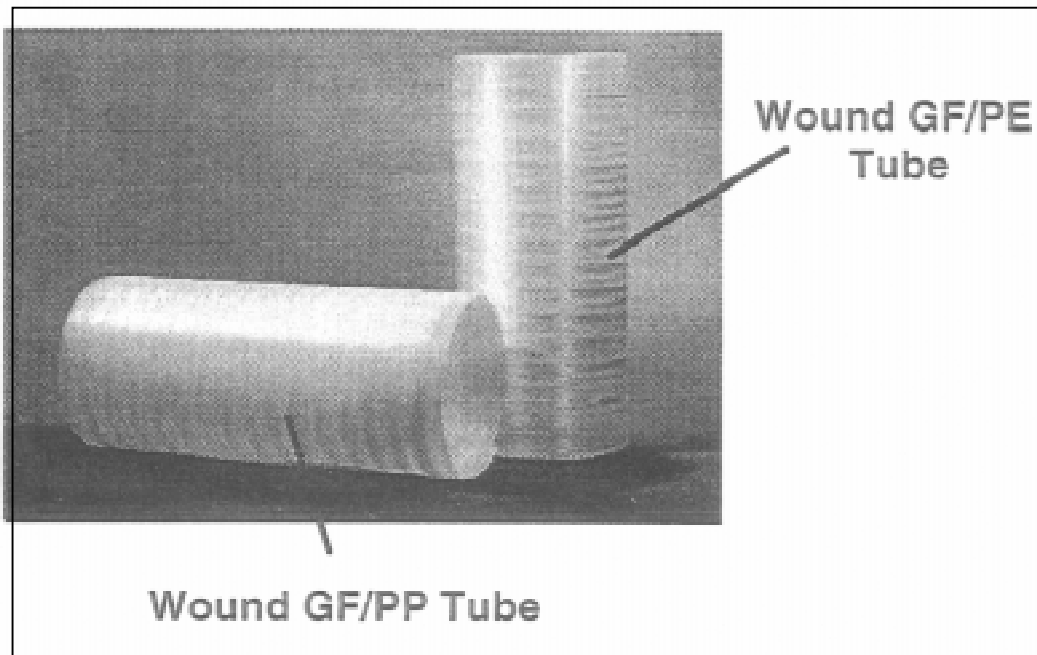


Fig. 7: On-line impregnated and wound tubes

The inner perimeter of these tubes was 70mm and the length up to 700mm. The materials used in the study were three glass fiber bundles, each with 1200 tex and different matrix polymers (e.g. PP; PE; PA12). Microscopic inspections of polished samples obtained by these winding tests showed that a satisfactory impregnation quality is achievable. However, optimisation of the governing processing parameters is expected to further improve the quality of the wound parts. In these first test runs only winding angles of 90° were realized. The determination of the degree of impregnation was carried out by embedding three samples (which were taken from different positions of the wound tube) into an epoxy resin. After curing and polishing, the degree of impregnation was determined by the ratio of the impregnated fibers to all counted fibers in the analyzed surface of a sample (cross section of the tube). One polished surface of an impregnated fibre bundle embedded in epoxy is presented in Figure 8.

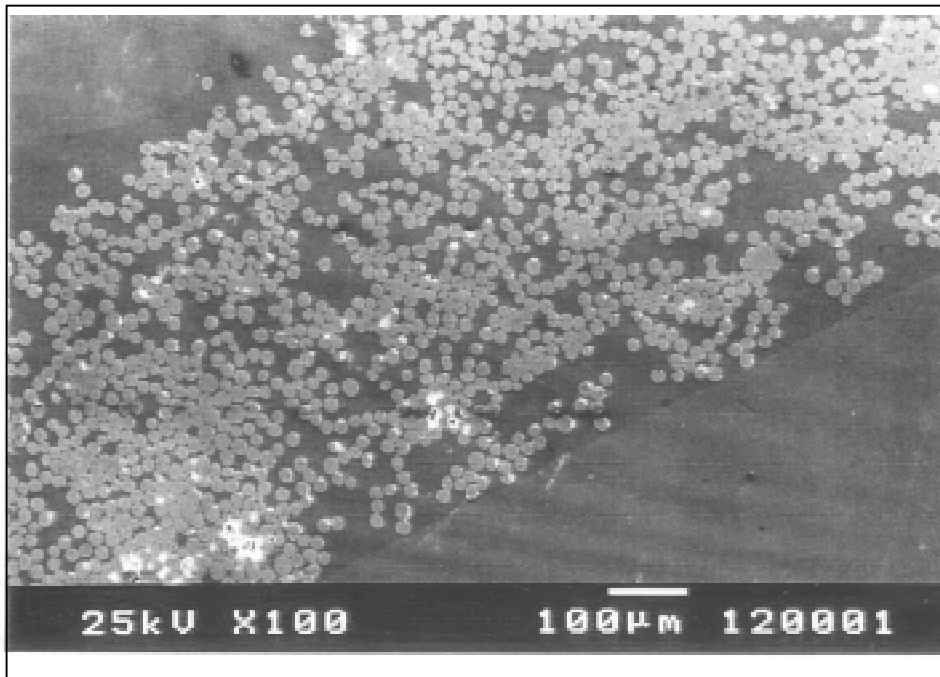


Figure 8. A cross section sample of a wound tube, manufactured with the combined impregnation and winding process (PP-GF winding speed: 5m/min)

CONCLUSIONS

A new process consisting of a new melt impregnation tool, the so called “impregnation wheel”, in combination with a common manufacturing process is presented; it shows some promising and innovative manufacturing aspects. The combination makes processing of continuous fibre reinforced thermoplastic composites in one manufacturing step possible; it is therefore very attractive from an economic stand point. Compared to other existing techniques it is now possible to save the cost for manufacturing intermediates and to be free in combining various fibre and matrix materials. Generally the measured degrees of impregnation of the wound glass fibre reinforced PP-tubes are very high. Hence the results presented here allow to speculate, that higher processing speeds together with a high degree of impregnation can be realized with further optimization of this new processing facility.

ACKNOWLEDGEMENTS

The work was financially supported by the Deutsche Forschungsgemeinschaft (DFG FR 675/23-1). Further thanks are due to the FONDS DER CHEMISCHEN INDUSTRIE, Frankfurt, for support of Professor Friedrich's personal research activities in 1997.

REFERENCES

1. F. Hauptert, C. Chen, K. Friedrich: Manufacturing of Thermoplastic Composite Parts by Combined Filament Winding and Injection Molding, in Proc. Int. Conf. Comp. Materials ICCM-10, August 13-18, 1995, Woodhead Publishing, Whistler, Canada, 1995, Vol. III, p. 381-388.
2. Pahl, M.; Gleißle, W.; Laun, H.-M.: Praktische Rheologie der Kunststoffe und Elastomere, VDI-Verlag GmbH, Düsseldorf, (1991) p. 34.
3. Hauptert, F.; Friedrich, K.: Processing Related Consolidation of High Speed Filament Wound Continuous Fiber/Thermoplastic Composite Rings; 3rd International Conference: Flow Processes in Composite Materials '94, 7th-9th July, 1994, University College Galway, Ireland; Conference Proceedings
4. ICI, New European Patent Specification, Publication Number: 82300150.8, 1982.
5. Longmuir, A.J.; Chandler, H.W.; Gibson, A.G.: Continuous Melt Impregnation of Glass Fibre Tows, in 6th. Int. Conf. on Fibre Reinforced Composites, FRC'94, March 29-31, Chameleon Press, 1994, Newcastle, England, p 23/1 - 23/10.
6. Bijsterbosch, H.; Gaymans, R.J.: Impregnation of glass rovings with a polyamide melt. Part 1: Impregnation Bath, Comp. Manufac., 4, (1993) p. 85 - 92.
7. E. I. Du Pont de Nemours and Company, United States Patent, Publication Number: 4,640,861, 1987.
8. Lutz, A.; Harmia, T.; Friedrich, K.; Halonen, E.-R.: Development of a new impregnation-tool for manufacturing void-free, melt-impregnated continuous fibre bundles; 17th International Conference & Exhibition SAMPE EUROPE, May 28 - 30, Basel, 1996

SIMULATION OF TEMPERATURE AND CURING PROFILES IN PULTRUDED COMPOSITE RODS

Basuki R Suratno, Lin Ye and Yiu-Wing Mai

Centre for Advanced Materials Technology (CAMT), Department of Mechanical and Mechatronic Engineering, The University of Sydney, NSW 2006, Australia

SUMMARY: Pultrusion is one of many composite manufacturing techniques with potential for rapid and cost-effective production. In this paper, an iterative procedure was developed to simulate the pultrusion process of polymer matrix composites, involving both heat transfer and curing sub-models. A two-dimensional finite element model was applied to simulate heat transfer and temperature profiles inside the die during the pultrusion process, which was coupled with numerical approximation of the curing kinetics for thermosetting polymer resins. Major pultrusion mechanisms (heat transfer and degree-of-curing) can be simulated for two-dimensional pultruded polymer matrix composites. The pultrusion processes of AS4/EPON-9420/9470/537 CF/epoxy composite rods were simulated and the results were compared to those in the literature. The approach developed in this study can be easily adopted to tailor two-dimensional pultrusion processes in practical applications.

KEYWORDS: pultrusion, heat transfer, degree-of-cure, finite element model

INTRODUCTION

Pultrusion is one of the most cost-effective techniques for manufacturing composite structural components with a constant cross-section, being applicable for both thermoset and thermoplastic matrix composites. A typical pultrusion system, Figure 1, consists of creels for feeding dry reinforcing fibres, a resin bath for impregnation, a heated forming die for consolidation and curing, pulling mechanisms for pulling the product at constant speed, and a cut-off saw to cut the part to the desired length.

In most practical approaches to pultrusion, a variety of means have been applied to impregnate reinforcing materials with resins. Almost all types of filamentary reinforcing materials can be used, such as rovings, tows, mats, cloth or any hybrid of these. The most widely used reinforcing material is fibreglass, e.g. E glass and S glass fibres. Pultrusion-grade resin matrices are available in a variety of systems such as polyester, epoxy, vinyl ester and phenolic resins. Unsaturated polyester resins are most commonly used because of low heat input required with faster gelation compared to other resin systems.

To produce pultruded products with consistent and high quality, it is important to tailor and control the pultrusion process. To achieve a uniform degree-of-cure in the cross section of a product, the temperature profile inside of the pultrusion die is an essential aspect. Therefore, it is important to develop mechanics models to simulate the pultrusion process, and in turn to tailor the process.

As the resin-impregnated fibre tows enter the die, the heat is transferred from the die wall to the compacted fibre-resin blend. Due to the low thermal conductivity of the blend, the temperature at the centre of the material is lower than that near the die wall. However, when the temperature in the blend reaches a critical level at which the catalyst becomes activated, the curing reaction begins and generates heat due to the exothermic reaction, which causes the temperature at the centre to be higher than that near the wall. Therefore, the temperature profile in the composite material inside the forming die is a balance of heat transfer and exothermic reaction.

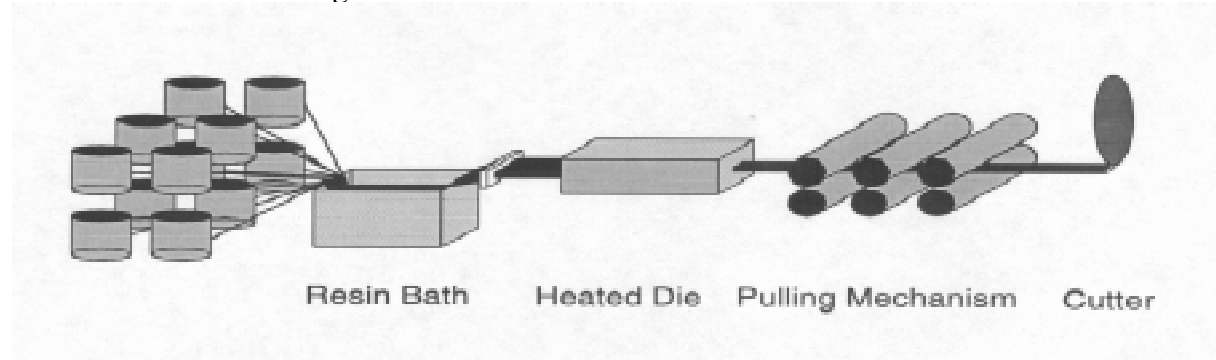


Figure 1. The diagram of the pultrusion process

Several models have been developed to gain a fundamental understanding of pultrusion process. Using a finite difference method, Han and Lee [1] applied an empirical kinetic model with a prescribed wall temperature profile in the simulation. Pultrusion characteristics were studied with variables such as resin type, fibre type, catalyst type, and the pulling speed. It was concluded that kinetic parameters need to be determined individually for each material system and each pultruded cross-section profile. Batch and Macosko [2] developed a pultrusion model based on a kinetic approach that includes a heat transfer model, a resin pressure model, and a pulling force model. The resin pressure was described assuming that the fibre-resin blend acts like an anisotropic porous media. Darcy's law was used for the fluid continuity to express the dependency of fluid pressure on the resin density, viscosity, and the volume fraction of fibres. Hackett and Prasad [3] applied a one-dimensional finite element model based on the Galerkin weighted residual method to solve the heat transfer equations, with liquid and solid sub-models to define the gelation point. This approach was later extended to predict temperature distributions and the degree-of-cure inside pultruded composites along the pultrusion line [4], and a convective boundary condition was assumed to replace the prescribed wall temperature profiles. An unsteady state model was developed by Wu and Joseph [5] to describe transient conditions for start-up or change of operation conditions, which includes the degree-of-cure, and temperature distributions in the material and die. Ma and Chen [6] developed a kinetic model for heat transfer to predict profiles of temperature and degree-of-cure in a pultruded glass fibre composite of a rectangular cross section for a block polyurethane resin using a finite difference method. It was found that the proposed kinetic model described well the curing behaviour of reinforced block polyurethane resins using appropriate kinetic parameters. Batch and Macosko [7] developed a more comprehensive model to describe the effects of radio frequency (RF) preheating, changes of thermal properties with temperature and degree-of-cure, hindered cooling due to shrinkage of the profile away from the die wall, air cooling of the profile while outside the die. The equations of transient heat transfer and reaction kinetics were solved by implicit finite difference methods. Gorthala et al [8] focused on the development of models for describing effects of velocity profiles including slip velocity as well as gelation length. Degree-of-cure, and viscosity of the resin at gelation were simulated.

In the previous studies simulations were mainly conducted using a self-developed finite difference or finite element program coupled with the curing kinetics. The main objective of this study is to develop a new procedure to simulate the pultrusion process using a commercial finite element software and numerical approximation of curing kinetics. The major principles can be applied to any other commercial finite element packages, which in turn makes the simulation of pultrusion process much more cost-effective.

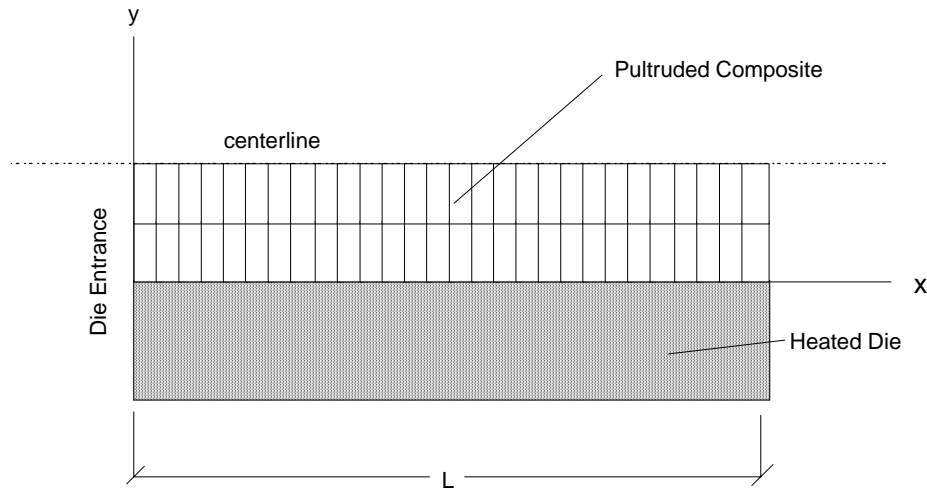


Figure 2: Pultrusion model in cartesian coordinates

PROCESS MODELING

From previous analyses, the basic assumptions of the present pultrusion model are:

- 1) the process is two-dimensional at a steady state;
- 2) the matrix and fibre have the same temperature at any point, i.e. the material is homogeneous; and
- 3) the influence of pressure on the heat of reaction is neglected.

Based on those assumptions, the equation of heat transfer can be expressed as [4],

$$\rho c u \frac{\partial T}{\partial x} - \frac{\partial}{\partial x} (k_x \frac{\partial T}{\partial x}) - \frac{\partial}{\partial y} (k_y \frac{\partial T}{\partial y}) - H_r \rho m_m \frac{\partial \alpha}{\partial t} = 0 \quad (1)$$

where

- T = temperature of the material
- k = thermal conductivity of the material
- c = heat capacity of the material
- u = pultrusion line speed
- H_r = ultimate heat of reaction
- m_m = mass fraction of matrix
- α = degree-of-cure
- ρ = density of the material

This global heat transfer model can be further divided into two basic sub-models: i.e. heat transfer defined by the first three terms and curing process by the last term. In this study, the solution of Equation 1 is approached using an iterative technique of two sub-models.

Heat Transfer

Since the top and bottom heat platens of the die are assumed to be at the same temperature, the process is symmetric about its mid-plane. Therefore, the process is only simulated for the bottom half shown in Figure 2. The boundary conditions can be expressed as,

$$T(0,y) = T_0 \quad (2a)$$

$$T(x,0) = T_D(x) \quad (2b)$$

where T_0 is the material temperature at the entrance of the die, and T_D the die wall temperature.

As a first order approach, it is assumed that for the composite within the die, thermal properties are independent of the curing state of the composite. In this case, the thermal properties of the composite can be approximated using micromechanics analysis of fibre reinforced composite

$$\rho = \rho_m v_m + \rho_f (1 - v_m) \quad (3)$$

$$c = m_m c_m + (1 - m_m) c_f \quad (4)$$

$$k_{x,y} = \frac{1}{\frac{m_m}{k_m} + \frac{(1 - m_m)}{k_{f,x,y}}} \quad (5)$$

materials from the constituent properties [9], where the subscripts m and f refer to matrix and fibre, respectively, $k_{x,y}$ the thermal conductivity in the x and y directions, c the heat capacity, v_m the matrix volume fraction, and m_m the matrix mass fraction.

Curing Model

The curing within the pultruded composite is a complex chemical reaction process that has not been clearly understood [4]. Relationships among temperature, degree-of-cure, and rate-of-cure have been established for several commercial pultruded grade resins [4,10]. Differential scanning calorimetry (DSC) was normally applied to measure the heat reaction and the rate-of-cure. The relationship between the rate-of-cure ($d\alpha/dt$) and the degree-of-cure (α) can be approximated using a modified Arrhenius type equation [10],

$$\frac{d\alpha}{dt} = K_o \exp\left(\frac{-\Delta E_A}{RT}\right) (1 - \alpha)^n \quad (6)$$

where K_o is a pre-exponential constant, ΔE_A the activation energy, R the universal gas constant, and n the order of reaction.

Numerical Simulation

From the governing differential equation (Eq. 1), it can be seen that the temperature state and the degree-of-cure are coupled, and they have to be solved simultaneously. In this case, an iteration technique is applied. Firstly, it is assumed that the degree-of-cure is zero everywhere in the composite. Then the finite element analysis is performed to obtain the initial state of the

temperature for each element. Using the temperature profile, the rate-of-cure for each element is calculated using Eq. 6. At the entrance of the die, the resin enters the die in the form of an uncured liquid such that starting from this entrance line, the degree-of-cure is equal to zero at any step of iteration, i.e.

$$\alpha(0,y) = 0 \quad (7)$$

As it was mentioned in the previous section that the process is assumed to be at a steady state, and the flow of composite is assumed to be only along the x axis of the die (the velocity in the y direction is neglected), such that time is only a function of x [4]. Therefore, the rate-of-cure can be defined by the derivation with respect to x rather than to time.

$$\frac{\partial \alpha}{\partial x} = \frac{l}{u} \frac{\partial \alpha}{\partial t} \quad (8)$$

Once the rate-of-cure with respect to x for each element is obtained, the next step is to integrate the gradient to find the degree-of-cure (α) [4].

$$\alpha(x + \Delta x, y) = \alpha(x, y) + \frac{l}{2} \left[\frac{\partial \alpha}{\partial x}(x, y) + \frac{\partial \alpha}{\partial x}(x + \Delta x, y) \right] \Delta x \quad (9)$$

where Δx is the distance between the centers of the adjacent elements.

This degree-of-cure profile will be applied to calculate the temperature profile for a new step of iteration using the finite element analysis. In general, the iteration procedure may be simply summarised as a flowchart shown in Figure 3. The criterion for convergence is set such that the difference in temperatures at each node obtained between two consecutive iterations is not greater than 1°C.

EVALUATIONS AND DISCUSSION

Simulations were performed for pultruded composite rods with a diameter of 0.95 cm, using the data obtained by Valliappan et al [10] for a AS4/EPON 9420/9470/537 graphite/epoxy system. This reference was chosen since it provides experimental and numerical results for verification. The die length was 91.4 cm with three different pulling speeds of 20, 30 and 40 cm/min, respectively. The thermal properties of the system and kinetic parameters for the epoxy are given Tables 1 and 2, respectively. The typical profile of die wall temperature and the simulation of centerline temperature distribution are presented in Figure 4. In the region near the entrance of the die, the die wall temperature is higher than that of the centerline, with the die releasing heat to the composite during the curing reaction. The length of this zone depends on the pulling speed; the higher the pulling speed is, the longer this zone [4]. The temperature of the composite

beyond that zone is higher than that of the die wall due to accumulation of heat generated by the exothermal curing process. In evaluations, the solution of the heat transfer sub-model was obtained using an ABAQUS FEM package, and the curing sub-model was approximated using numerical solutions, based on the procedure in Figure 3.

Table 1. Thermal Properties of AS4/EPON 9420/9470/537 Composite Material [10]

Material	Density (g/cm ³)	Specific Heat (J/g.K)	Thermal Conductivity (W/m.K)
Fibre	1.790	0.712	k _{fy} = 11.6 k _{fx} = 66.0
Matrix	1.260	1.255	0.2

Table 2. Kinetic Parameters of Shell EPON 9420/9470/537 epoxy resin [10]

Parameters	Symbol	Value
Pre-exponential constant	K_0	19.14 x 10 ⁴ [s ⁻¹]
Activation energy	E_A	60.5 x 10 ³ [J/mol]
Heat reaction	ΔH	323.7 [J/g]
Order of reaction	n	1.69

Effect of Mesh Discretization

Since the heat is transported from the die to the composite by two mechanisms (convection and conduction), the relative amount of heat transferred is expressed by the Peclet Number (Pe) [11] defined by,

$$Pe = \frac{\rho c u L}{k} \quad (10)$$

where L is the length of the element along the direction of the flow. Because the nature of finite element method is the central difference [11], it yields a reasonable solution only when the value of Pe is low (should be less than 2 theoretically) [12]. However, when Pe is too large (convection dominates the system), false oscillations are generated, which may conceal the true solution[11].

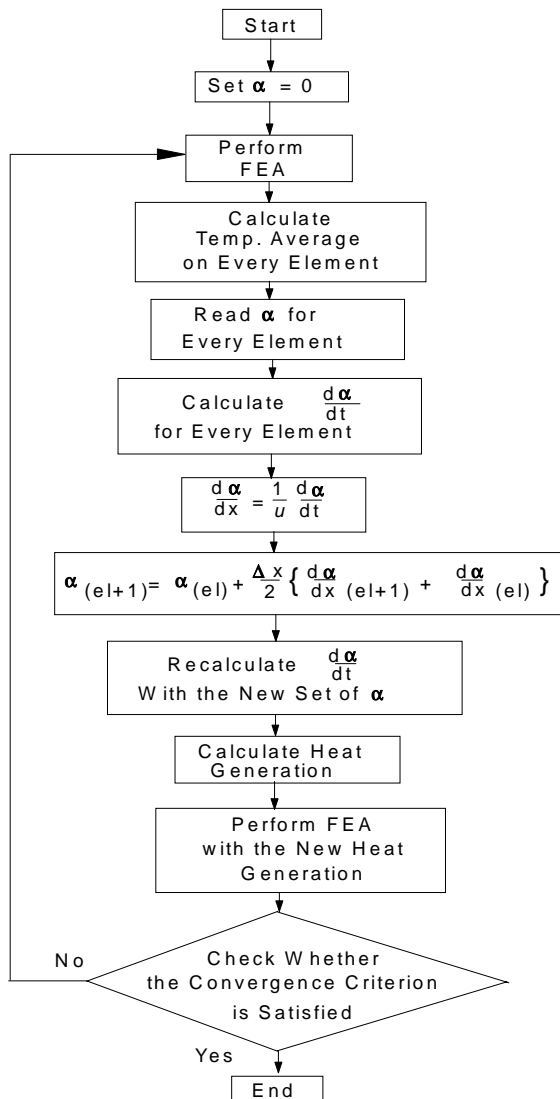


Figure 3. Iteration procedure to solve temperature and degree-of-cure.

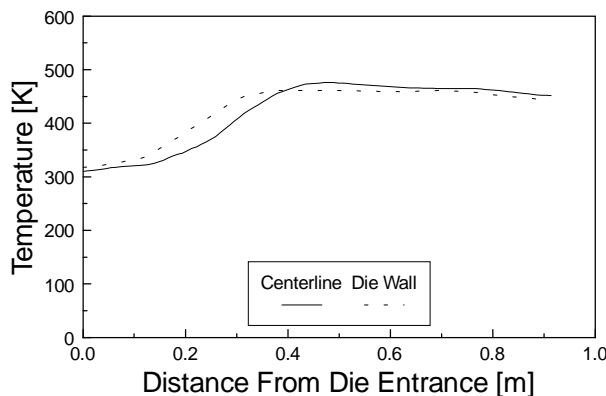


Figure 4. A typical centerline temperature profile of the pultrusion process.

In this study, the small Peclet Number was obtained by refining the element size in the direction of the flow. Three different meshes were created uniformly using four-node elements, producing Peclet Number of 96, 12 and 3 at a pulling speed of $u = 30$ cm/minute. The element number for each mesh along the centerline was 99, 792, and 3168, respectively (with two rows of the element along the y axis for every mesh) and the boundary conditions of Eqs 2a and 2b were applied to each mesh. Figure 5 shows the effect of Peclet Number on temperature profiles at the centerline. For Peclet Number = 96, the result shows a sharp increase in the middle of the die length to a value of above 600 °K. This divergence is caused by the coarse mesh being used. The results for Peclet Number = 12 or 3 show a good agreement with that obtained by Valliappan et al [10] (prediction and experimentation). Figure 6 presents the effect of Peclet Number on degree-of-cure. Since the degree-of-cure is dependent on temperature, the results are correlated to the temperature distributions. For Peclet Number = 96 the curing process is already complete at the middle of the die, which is not realistic. For the cases of $Pe=12$ and $Pe=3$ the results are in agreement with those obtained by Valliappan et al [10].

Effect of Initial Boundary Condition

Before entering the die, the temperature of the material (fibre and resin) was assumed to be close to the ambient temperature (300 °K). This assumption was then applied to the finite element model for heat transfer with Peclet Number of 96 at a pulling speed of 30 cm/min. The results are presented in Figures 7 and 8 together with those obtained from the finite element model for Peclet Number = 3 but without the initial condition. It can be seen that both results show the same temperature distribution along the die length.

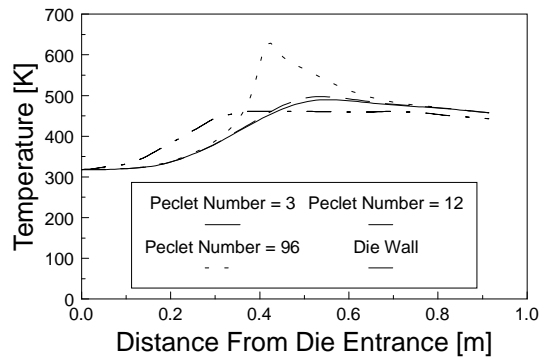


Figure 5. Effect of Peclet Number on centerline temperature profiles at pulling speed of 30 cm/min.

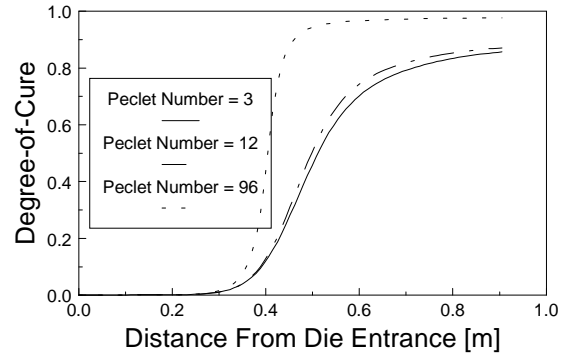


Figure 6. Effect of Peclet Number on centerline degree-of-cure at pulling speed of 30 cm/min.

This phenomenon is caused by the iterative starting point of the FEM analysis. If the initial condition for temperature is not specified, the finite element program assumes that the initial condition is 0 °K. It was found that the initial boundary condition does not have a visible influence on the results if Peclet Number is small. Furthermore, it can be seen that coarser mesh can still achieve accurate results by adding the initial boundary condition to the model. However, some commercial FEM packages do not provide the initial boundary condition which means that application of the fine meshes to avoid inaccuracy of the results becomes necessary.

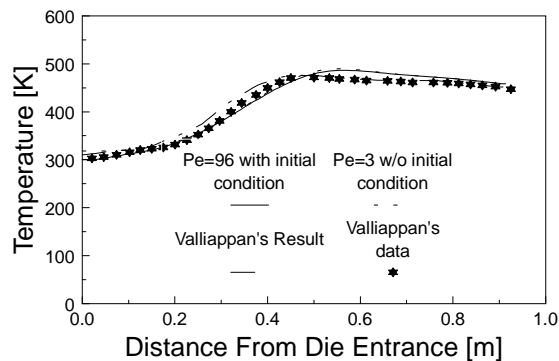


Figure 7. Centerline temperature profiles obtained with and without initial boundary conditions.

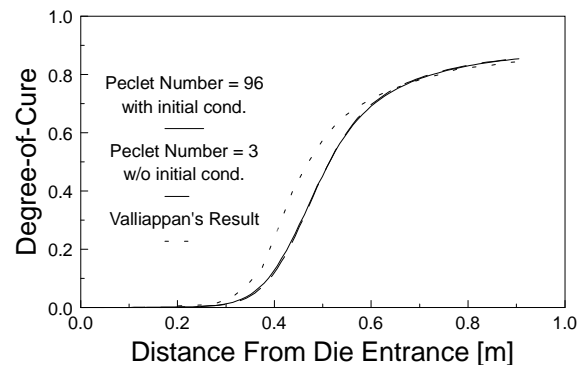


Figure 8. Centerline degree-of-cure profiles obtained with and without initial boundary conditions.

Effect of Pulling Speed

Three different pulling speeds were applied in the simulations with $Pe = 96$ and the initial boundary condition. Figure 9 shows centerline temperature distributions with different pulling speeds but with the same die wall temperature. It can be seen that when the pulling speed is increased, the initial lag of the centerline temperature increases. This is caused by the fact that as the pulling speed is raised, the time available for heat transfer to the center of the composite becomes shorter, which causes the centerline temperature of the composite to be less than that at a low pulling speed. On the degree-of-cure profiles, it can be seen that when the pulling speed is increased, the degree-of-cure at the die exit decreases. To obtain a sufficiently cured product at a high pulling speed, either the die wall temperature or the die length has to be increased.

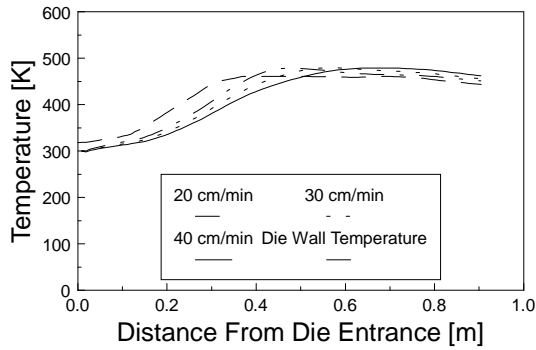


Figure 9. Effect of pulling speed on centerline temperature profiles ($Pe = 96$ with initial boundary condition).

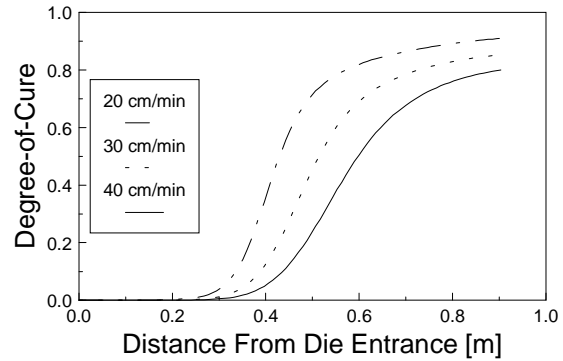


Figure 10. Effect of pulling speed on centerline degree-of-cure profiles ($Pe = 96$ with initial boundary condition).

CONCLUSION

Combining the finite element model (FEM) for heat transfer and the numerical approximation for curing kinetics, profiles of centerline temperature and degree-of-cure were simulated for a pultruded carbon/epoxy composite. Effects of finite element mesh, initial temperature condition for FEM analysis and pulling speed on the pultrusion process were studied. Comparisons of the results to those published by Valliappan et al [10] show good agreements. Based on the methodology used in this study, a procedure to simulate profiles of temperature and degree-of-cure of pultruded composites can be easily adopted using a commercial finite element software.

ACKNOWLEDGMENT

B. R. Suratno is grateful for the award of a postgraduate scholarship tenable at the University of Sydney by the Australian Agency for International Development (AusAID). L. Ye and Y. W. Mai would like to acknowledge the continuing support of this project by the Australian Research Council (ARC).

REFERENCES

1. Han, C. D. and D. S. Lee. "Development of a Mathematical Model for the Pultrusion Process," *Polymer Engineering and Science*, Vol. 26, 1986, pp. 393-404.
2. Batch, G. L. and C. W. Macosko. "Heat Transfer and Cure in Pultrusion: Model and Experimental Verification," *AIChE Journal*, Vol. 39, 1993, pp. 1228-1241.
3. Hacket, R. M. and S. N. Prasad. "Pultrusion Process Modeling," *Advances in Thermoplastic Matrix composite Materials*, G. M. Newaz, ed., ASTM STP 1044, American Society for Testing and Materials, 1989, pp. 62-70.
4. Hacket, R. M. and S. Zhu. "Two-Dimensional Finite Element Model of the Pultrusion Process," *Journal of Reinforced Plastics and Composites*, Vol. 2, 1992, pp. 1322-1351.
5. Wu, H. and B. Joseph. "Model Based and Knowledge Based Control of Pultrusion Processes," *SAMPE Journal*, Vol. 26, 1990, pp. 59-70.
6. Ma, E. M. and C. Chen. "The Development of a Mathematical Model for the Pultrusion of Blocked Polyurethane Composites," *Journal of Applied Polymer Science*, Vol. 50, 1993, pp. 759-764.
7. Batch, G. L. and C. W. Macosko. "A Computer Analysis of Temperature and Pressure Distribution in a Pultrusion Die," *42nd Annual Conference*, The Society of Plastics Industry, Inc., 1987, pp. 1-7.
8. Gorthala, R., J. A. Roux and J. G. Vaughan. "Resin Flow, Cure and Heat Transfer Analysis for Pultrusion Process," *Journal of Composite Materials*, Vol. 28, 1994, pp. 486-506.
9. Jones, R. M., *Mechanics of Composites Materials*, McGraw-Hill, New York, 1980.
10. Valliappan, M., Roux, J. A., Vaughan, J. G., and Arafat, E. S. "Die and Post-die Temperature and Cure in Graphite/Epoxy Composites," *Composites: Part B*, Vol. 27B, 1996, pp. 1-9.
11. Huang, H. C. and Usmani, A. S., *Finite Element Analysis for Heat Transfer*, Springer-Verlag, London, 1994.
12. Patankar, S. V., *Numerical Heat Transfer and Fluid Flow*, McGraw-Hill, New York, 1980.

THE USE OF A SMALL PULTRUDER FOR SPECIMEN PREPARATION

John O. Outwater

Department of Mechanical Engineering, University of Vermont, Burlington, Vermont 05405

SUMMARY: One of the difficulties in studying composite materials lies in the preparation of uniform specimens easily and quickly. It must be possible to change various characteristics of materials and the cure cycle with a minimum of "fuss". It must also be possible to test such specimens without a quantity of specialized equipment so that a small production facility can have the quality control and flexibility for quality monitoring that is characteristic of larger production units. This paper will describe a small pultruder which is compact and versatile enough to produce such specimens and also some apparatus that will test the debonding energy of the resin-fiber bond which property is, perhaps, the key item in developing reliable properties of the composite itself.

KEYWORDS: pultruder, benchtop, debonding energy in shear, property determination

INTRODUCTION

The process of pultrusion is deceptively simple: an impregnated strand is pulled through a heated die. It cures and the hard rod is pulled to a cutoff and simply severed into the correct lengths. The problems that need to be addressed include the following:

1. What is the optimum material?
2. What are its curing characteristics?
3. What is optimum pultrusion speed?
4. What kind of properties can we expect?
5. Is it possible to readily change the materials without incurring an unreasonable cost?
6. Can I use simple apparatus to determine various properties?

We have developed a small benchtop pultruder (1) to address each of these problems and believe that it is a useful production tool as well as being a splendid research apparatus.

DESCRIPTION OF APPARATUS

The benchtop pultruder consists of the following items:

1. A small temperature controlled hotplate to determine the gel times of resins at different temperatures.
2. An impregnation bath which uses disposable plastic cups.
3. A controllable speed puller.

4. A stainless steel die with two heat zones: the first zone is 0.11 m long, the second zone is 0.18 m long and each has a separate temperature controller.
5. The pultruder produces a specimen 3 mm diameter. This is large enough to show the properties of a larger section and small enough to require a minimal creel. It is also small enough to permit manual cutting so that expensive saws are not needed.
6. The overall dimensions are 1.6 m long, 0.6 m wide and 0.4 m high. The spools of fiber will sit on the floor under the bench that is supporting the pultruder so a minimal floor space is needed.
7. The die is removable so that it can be slid out of the heating elements and simply be burned out if it should jamb. It can then be rethreaded and restarted with a minimum of "fuss".
8. The fibers can be lifted out of the resin bath and run to dryness so that it can easily and cleanly be restarted after being stopped.

What we have tried to produce is equipment that is eminently simple for any experimental use. Fig. 1.

USING THE SYSTEM

There are three key items to be measured before it is possible to scale up the sections sizes:

1. The gel-time plot for various temperatures.
2. The fracture energy is shear for various combinations of materials and time-temperature relationships.
3. The shear modulus in torsion of the pultruded rod.

The temperature-time relationship for gelling and curing is determined by using the small temperature controlled hotplate. Drip some of the resin on it. Stir the resin to gel and note the time of gelling demanded at the temperatures you might expect. A typical plot is shown in Fig. 2.

This curve is the key item for determining the speed and temperature of the die.

The curve in Fig. 2 is for a typical resin system (Owens-Corning E-606 polyester resin with 1% benzoyl peroxide and 1% SP-48 Specialty Products release agent) the curve shows a sharp decrease in time as the temperature is increased. The inflection in the curve occurs here at about 150°C. This we shall refer to as the Critical Cure Temperature T_c . It will control the speed of pulling and temperature of the die. It is essential that both the surface and interior of the pultrusion reaches this temperature.

We found (2) that raising the temperature of cure to more than 25°C above T_c is deleterious as the resin becomes more waxy than if cured at T_c . This can be avoided by raising the surface temperature to about 10°C below T_c . This allows the exotherm to bring the interior up to T_c .

The time needed to reach T_c is about 7 s so, with a 0.3 m die we can expect to need a pultrusion speed of about $0.3/7 = 0.04$ m/s. It should be recognized that the resin will shrink in the die. This will tend to pull the product away from the die so it will be practical to use a slightly lower pulling speed than directly calculated - or we can use a postcure oven when the product can be exposed to radiant heat, again at a controlled temperature. The ovens supplied

with the system are 0.3 m long so we can essentially double the pulling speed when we use an oven.

QUALITY CHECKING

The checking of the quality of a pultruded product is central to optimizing the pultrusion variables. The optimum way of doing this is by a measurement of the fracture energy in shear of a rod.

This parameter is exactly what we seek - a measure of the bonding of fibers to resin. The problem with doing just this is that the measurement of such properties is somewhat awkward and described in reference (1). What we also notice from (2) is that the fracture energy in shear closely parallels the shear modulus in torsion.

This is a much simpler quantity to measure and can easily be done using a small torsion tester - this can be commercial Fig. 4 or it can be made from a simple construction kit (3).

The results of such a test are shown in Fig. 3

Essentially, what we see from this test is that there is definitely an optimum dwell time in the die. This translates to an optimum speed of draw and can be determined easily and experimentally for any material combination. It also shows that there is a sharp drop-off in properties if we wander from this optimum value.

SCALE-UP TO LARGER SECTIONS

The experimental work has been done on 3 mm rod which is often not a useful pultrusion size. It is incumbent to be able to decide speeds and temperatures on a larger section. This can be done by making the assumption that the diffusivity of the specimen is a constant and about $7 \times 10^{-8} \text{ m}^2/\text{s}$ (2). Then we can calculate the time required for the center temperature to be within 10°C of the outer surface.

This is done by approximating from simple heat transfer formulae (4).

The results are that values of T_c are related by the inverse square of the diameter of the rod. So an easy scale up is possible after we have determined the T_c for the 3 mm rod.

These values of T_c will depend on many factors and must be computed on the basis of approximation when sections of unusual shape are being made. It is often desirable that a post curing oven be used to ensure complete cure and to obviate the necessity for an impractically long die.

CONCLUSIONS

The usefulness of a small pultruder lies in its ability to determine some vital parameters of the process:

1. The optimum die temperatures
2. The optimum die dwell time
3. The optimum material for your purpose
4. The expected material properties.

And this all being done in a small space and with a minimum expenditure of material and time.

ACKNOWLEDGMENTS

The author wishes to acknowledge the help of Dr. Donald V. Gaucher of Owens-Corning Fiberglas for his sound advice. The Owens-Corning Fiberglas which supplied the fiber and resin, Specialty Products, the release agent, and Lucidol, the catalyst. These are gratefully acknowledged. Vermont Instrument Co., Burlington, Vermont, generously allowed the use of the Vermont Pultrusion Test System.

REFERENCES

1. Outwater, J.O., "The Fracture Energy of Pultruded Rod," *Jour. of Comp. Matls.* (Jan. 1986)
2. Outwater, J.O., "On the Mechanics of Pultrusion," 41st Annual Conference, RP/C Institute, 6-C, 1986.
3. FAC System, Transitoria Trading AB, Stockholm.
4. Carslaw, H.S. and J.C. Jaeger, *Conduction of Heat in Solids*, 2nd Ed., Oxford U.P., London, p. 102 (1959)

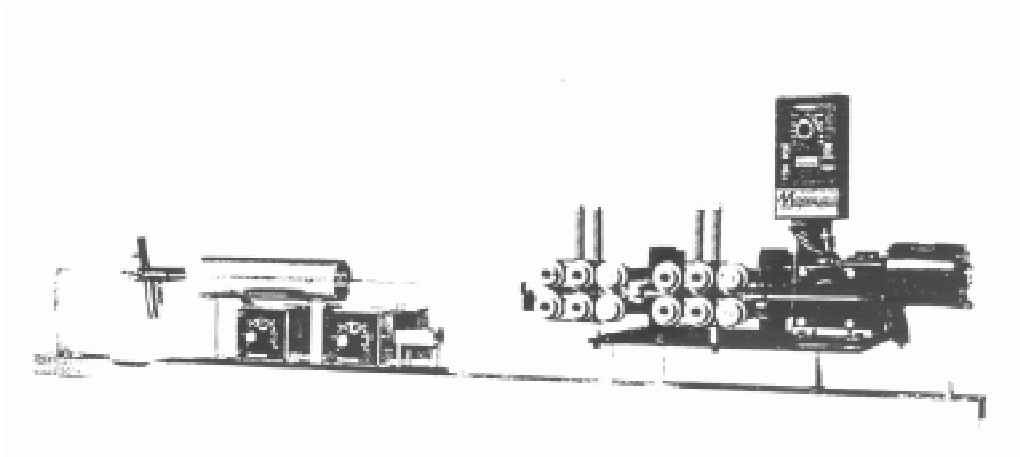


Figure 1: Bench Pultruder

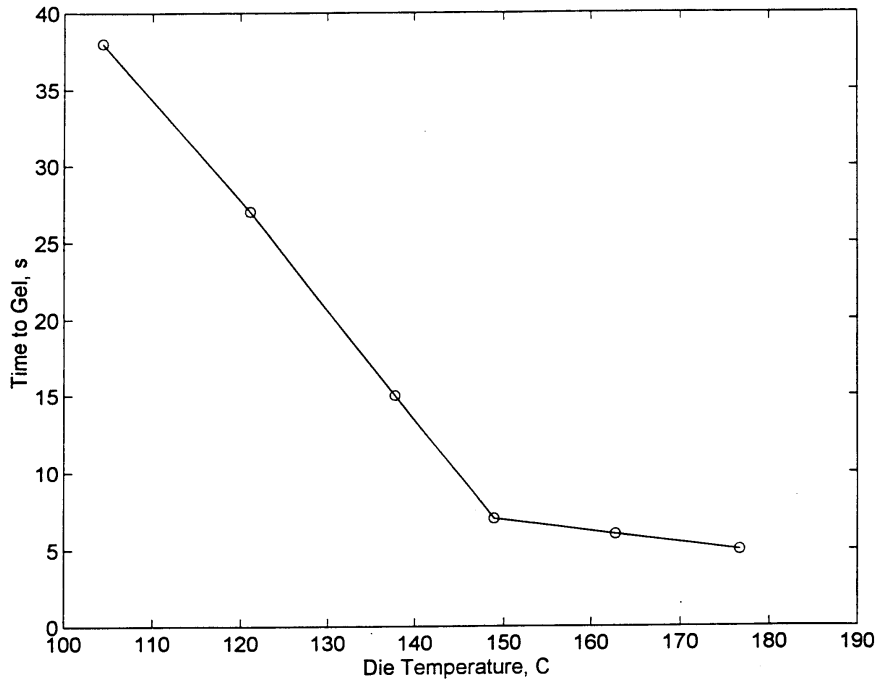


Figure 2: The time required for a resin system to gel when in contact with surfaces at various temperatures

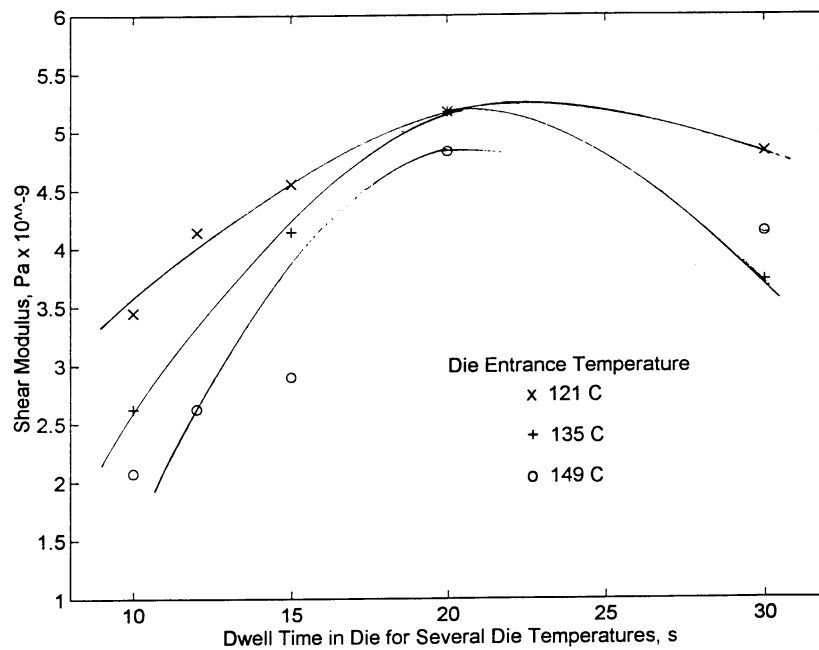


Figure 3: The shear modulus of the pultruded rod plotted against various dwell times in the die, for different die inlet temperatures, showing an optimum dwell time and die temperature exists

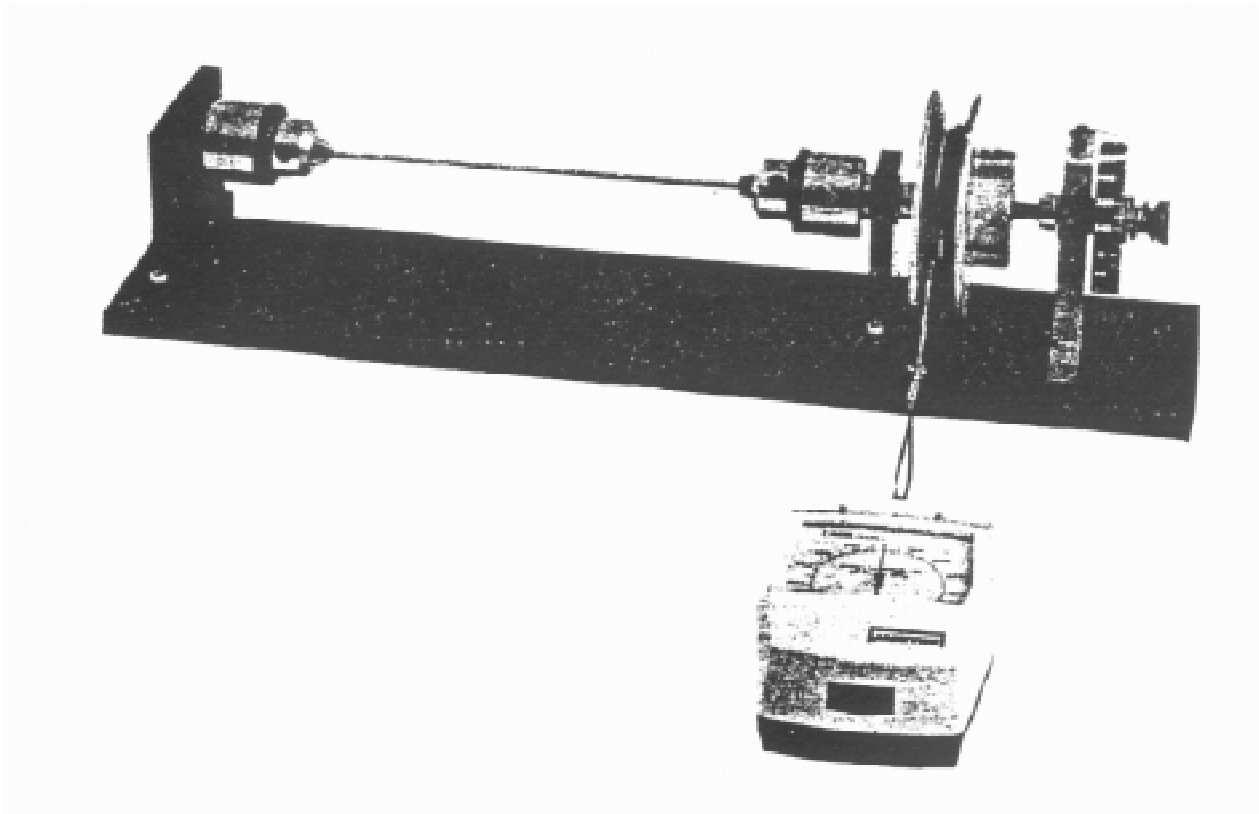


Figure 4: Mechanical torsion tester

CHARACTERISATION AND MODELLING OF THE HIGH SPEED PULTRUSION OF COMMINGLED GLASS FIBRE / POLYPROPYLENE COMPOSITES

A. Miller and A.G. Gibson

Centre for Composite Materials Engineering, Materials Division, Department of Mechanical, Materials and Manufacturing Engineering, Herschel Building, Newcastle University, Newcastle upon Tyne, NE1 7RU, UK

SUMMARY: A thermoplastic pultrusion line has been developed which is capable of pultruding polypropylene / glass fibre (PP/GF) commingled tows into flat strip and circular rod sections at line speeds up to 10m/min. A heat transfer model was used to predict the temperature profile of the composite at any point during processing allowing for accurate process conditions to be evaluated. A consolidation model has also been developed which can be used to evaluate the effect of pressure and velocity on impregnation conditions. The pultruded sections exhibit good mechanical properties and are of minimal void content. SEM microscopy is used to highlight the impregnation quality of the composites.

KEYWORDS: commingled fibres, thermoplastic composites, pultrusion, consolidation.

INTRODUCTION

For production of a thermoplastic composite it is important that its microstructure is uniformly wetted out and that it has a strong resin/fibre interface [1]. The processing of composites involves impregnating a fibrous bed with resin, then shaping and consolidating it to a high fibre volume fraction. To overcome the design restriction in the forming of complex parts, impregnation can be delayed until the material undertakes its final shape. This *mingling* operation brings the solid polymer and fibre reinforcement together to intimate contact. The aim of this is to reduce the distance the polymer melt must flow in order to fully impregnate the fibre bed. A high degree of intimacy can be achieved by providing the matrix in fibre form and intermingling, or coveaving, polymer fibres with reinforcing fibres. These commingled fibres should ideally be combined in the same strand to minimise the flow distance for impregnation.

Continuous commingled tows are produced when the matrix is spun into a fibre yarn and combined with the reinforcement to produce a commingled hybrid tow. A problem incurred in this route is that intimate mixing is difficult to achieve and may lead to resin rich and unwetted areas of the composite [2]. Therefore, to assure a good distribution of the polymer and reinforcing fibres, it is essential that the matrix fibre diameter is matched as closely as possible to that of the reinforcement [3].

Some workers have recently investigated the potential of commingled fibres for use in the continuous pultrusion process. Michaeli and Jürss [4], claim to have successfully pultruded sectional products such as a strip, a rod and a pipe using a pull braiding system with PP/GF

tows finding that the 'mechanical properties, surface, dimensional and impregnation quality are good, although refinable' but, due to the necessary cooling and consolidation time, high pultrusion speeds were not achieved. Larock *et al* [5], also encountered some difficulties pultruding Graphite/PPS hybrid yarns stating that 'commingled fibres offer unique problems with the initial pultrusion start up'

EXPERIMENTAL

A schematic of the process used for the continuous pultrusion of commingled polypropylene / glass fibres (PP/GF) can be seen in Fig. 1. The process was used to pultrude flat strip and rod sections at line speeds up to 10m/min. The commingled tows were manufactured by Vetrotex under the trade name "Twintex" with 70% by weight (45% by volume) of glass, with an overall tex value of 680. The fibre cheeses were stored on a creel stand and delivered to the process under controlled tension. For production of a 20x2mm rectangular strip 96 tows were used, and for the production of a 2mm diameter rod 8 tows were required. A "bar and plate" tensioning device was used to maintain even tension throughout the system during processing, with uniform pre-tension values varying between 5 and 10 Newtons with line speed.

The pre-tensioned tows then passed through an infra-red oven to preheat the polymer to its melt temperature and initiate wet-out of the reinforcement. The preheat temperatures were dependent on processing speed and thus varied accordingly. The tows were then passed over a series of impregnation pins, a widely accepted technique used to aid the impregnation of thermoplastic matrix composites [6-8]. As the tows travel over the impregnation pins, an applied pressure is generated which increases the polymer melt flow through the reinforcement and reduces the void content of the composite. The tows are then passed through a series of heated forming dies which gradually reduce the product to the required shape. The minimum die contact lengths which are employed in the process preserve a low pull force, which was measured on-line throughout processing using a data acquisition unit. The maximum pull forces measured during processing of the strip varied from 0.375 KN at a line speed of 1m/min to 1.2 KN at 10m/min. Final consolidation and finishing of the product took place in the cold forming die and the finished section consolidated to minimum void content was then spray cooled and hauled off at the end of the process.

In order to understand the cooling and product consolidation stage of the composite, a heat transfer model, derived using finite difference equations, was applied to the process. The model divides the pultruded section into a series of nodes at which the temperature at each point is calculated. This enabled the temperature at any point in the section to be predicted at any position during the pultrusion process. This and the temperature measurements taken on-line were used to define the product and die temperature range where die adhesion ceases and maximum consolidation occurs, allowing for production of composites with minimum void content.

The sections produced from the process were then tested for impregnation quality (void content) using the immersion technique ASTM D-792 and samples were also subjected to the flexural strength test, BS2782 : Pt 3 : Method 335A.

CONSOLIDATION MODELLING

A consolidation model has been developed which can be used to express the degree of consolidation (or reduction in void content) of the composite against pressure and time. This

model can be applied to the pultrusion process and used to determine the optimum pressure and die contact times required to achieve full product consolidation.

The impregnation model should allow for the pressure dependence of impregnation behaviour and the possible power law behaviour of the resin. A flow length, X , can be used to describe the distance (on a microscopic scale) that the resin must flow to achieve the required impregnation level at the end of stage 1 (Fig. 2). For stage 2 a simple model, discussed for instance by Gibson and Månson [9], relates the flow velocity (U) of the resin in the fibre bed by Darcy's law to the pressure gradient from the following equation :

$$U = \frac{dx}{dt} = \frac{SP}{\eta x} \quad (1)$$

The model does not allow for pressure dependence or power law behaviour of the resin. The power law behaviour of the impregnation process was discussed by Aström *et al* [10] who proposed the following equation :

$$\frac{dx}{dt} = \frac{k'}{Y} \left(\frac{P}{x} \right)^{\frac{1}{n}} \quad (2)$$

where n is the power law index and k' and Y are constants. If k' is a function of pressure then,

$$k' = AP^{-m} \quad (3)$$

where A and m are constants. Substituting eqn. (2) into (3) produces the following :

$$\frac{dx}{dt} = \frac{A}{Y} \frac{P^{\frac{1}{n}-m}}{x^{\frac{1}{n}}} \quad (4)$$

which can be expressed as

$$\frac{dx}{dt} = B \frac{P^{\frac{1}{n}-m}}{x^{\frac{1}{n}}} \quad (5)$$

where B is constant from A and Y .

Constant velocity conditions

A series of compaction trials were undertaken to investigate the consolidation behaviour of the commingled material. Layers of material were stacked together in a matched die mould at a temperature of 190°C and compressed at 5, 20, 50 and 100mm/min as shown in Fig. 3. The variation of pressure versus flow length was measured during each test, until the samples were consolidated to minimum void content. For these constant velocity conditions the cross head speed, V is related to eqn. (5) below,

$$V = B \frac{P^{\frac{1}{n}-m}}{x^{\frac{1}{n}}} \quad (6)$$

therefore

$$V^n x = B^n P^{(1-nm)} \quad (7)$$

Plotting P versus $V^n x$ varying n until the curves close together is shown in Fig. 4 for a value of $n = 0.25$. Taking a Log - Log plot of this gives the graph shown in Fig. 5 in which the slope approximates to 1. It can therefore be said that, to a good approximation, $m = 0$. So from this,

$$V = B \left(\frac{P}{x} \right)^{\frac{1}{n}} \quad (8)$$

The value of B can be found from the graph and is equal to 0.14.

Constant pressure conditions

Constant pressure conditions occur during the pultrusion process as the tow passes over the impregnation pins. Since $m = 0$ we know from eqn. (5) that :

$$\frac{dx}{dt} = B \frac{P^{\frac{1}{n}}}{x^{\frac{1}{n}}} \quad (9)$$

Rearranging we obtain,

$$x^{\frac{1}{n}} dx = BP^{\frac{1}{n}} dt \quad (10)$$

Integrating this expression gives

$$\frac{n}{n+1} x^{\frac{n+1}{n}} + C = BP^{\frac{1}{n}} t \quad (11)$$

and since when $x = 0$, $t = 0$ so $C = 0$, so the time for consolidation under constant pressure conditions can be expressed as :

$$t = \left(\frac{n}{n+1} \right) \frac{x^{\frac{n+1}{n}}}{BP^{\frac{1}{n}}} \quad (12)$$

where $n = 0.25$ and $B = 0.14$. The results from this model can then be compared to the experimental conditions observed during pultrusion processing, where a constant pressure is observed.

Variation of void content initial conditions

The variation of void content against impregnation level can be found from the unit volume of material described in Fig. 2. At the initial condition, before any resin flow has taken place, the flow length, x , is equal to zero. As the volume of fibres is equal to V_{f1} , the same as at the end conditions, the volume of matrix will be equal to $1 - V_{f1}$ which is also the same as the end conditions. Thus the volume of voids occupied at the initial condition will also be equal to $1 - V_{f1}$, which is the volume that will eventually be occupied by the matrix. The total unit volume can therefore be written as :

$$\text{Total unit volume} = 2 - V_{f1} \quad (13)$$

where the initial void volume fraction, V_{v0} , is given by :

$$V_{v0} = \frac{1 - V_{f1}}{2 - V_{f1}} \quad (14)$$

which, for a 45% by volume of glass commingled composite is equal to 0.35.

Variation of void content - intermediate conditions

As the resin flows a distance x (Fig.2) the degree of impregnation, x^* , is defined as x/X . The volume of voids occupied at this stage can be expressed as

$$\text{Volume of voids} = (1 - V_{f1})(1 - x^*) \quad (15)$$

Therefore the intermediate void fraction will follow this relationship :

$$V_v = \frac{(1 - V_{f1})(1 - x^*)}{1 + (1 - V_{f1})(1 - x^*)} \quad (16)$$

At the end condition $x^* = 1$, which is the condition of full impregnation, where $V_v = 0$

RESULTS AND DISCUSSION

Pultrusion processing results

The graph shown in Fig.6 represents the comparison between measured and theoretical void content reduction against impregnation time for the pultrusion of a 20x2mm commingled PP/GF strip at a line speed of 1m/min. The modelled impregnation time (solid line) was calculated from eqn. (12) in which the theoretical reduction in void content was calculated from eqn. (16).

The average pressure induced as the tows passed over the impregnation pins was constant for each line speed and calculated from

$$P = \frac{T}{2rw} \quad (17)$$

where T is the tension in the tows (measured pull force during processing), r the impregnation pin radius and w the tow width as it passes over the pins. Thus for a line speed of 1m/min the average pull force was measured to be 375N and with a pin radius of 15mm and tow width of 40mm, an average pressure over the pins of 0.312MPa was achieved. The experimental data points were taken as the tow passed over each pin and were measured using the immersion technique ASTM D-792. It can be seen from the graph that the results correlate well with the models predictions. The minimum void content achievable through pin impregnation was found to be 8%. The void content was then further reduced to a minimum value as it passed through the consolidation dies further down the process.

Mechanical properties results

The mechanical properties in relation quality and line speed were measured in terms of flexural strength for the pultruded sections of a 20 x 2mm strip and 2mm diameter rod section. Figs 7 and 8 show that the mechanical properties are slightly reduced as the line speed is increased, due to the reduction in impregnation time and increase in void content. The final void content values were found to vary between 0 and 2% for speeds 1 to 5m/min and from 1 to 4% for speeds 5 to 10m/min. The values of flexural strength for both sections are good varying between 600 - 700 MPa according to these conditions. Fig. 9 shows the SEM micrograph of a 20x2mm strip pultruded at 7m/min. The impregnation level is seen to be good, with few dark areas observed which demonstrates the minimum void content of the composite.

CONCLUSIONS

A consolidation model has been applied to commingled fibres which relates impregnation time to pressure and velocity and can be used to predict optimum conditions for pultrusion processing. The pultrusion line developed can successfully produce continuous sections of strip and rod with minimum void content and good mechanical properties at high line speeds. The results demonstrate that the pultrusion of commingled fibres is a promising technique in the development of thermoplastic composites and now that the base technology is established, more complex shapes can be attempted in the future.

ACKNOWLEDGEMENTS

This work was carried out in collaboration with PERA Technology Centre, Melton Mowbray under the DTI/LINK programme.

REFERENCES

1. Leach, David C., "Continuous Fibre Reinforced Thermoplastic Matrix Composites", *Chapter 2 of Advanced Composites*, Edited by Ivana K. Partridge, Elsevier Applied Science, 1989, pp 43-111.

2. van West, B.P., Pipes, B.R. and Advani, S.G., "The Consolidation of Commingled Thermoplastic Fabrics", *Journal of Polymer Composites*, Vol. 12, No. 6, 1991, pp 417-427.
3. Chang, I.Y. and Lees, J.K., "Recent Developments in Thermoplastic Composites: A Review of Matrix Systems and Processing Methods", *Journal of Thermoplastic Composite Materials*, Vol. 1., 1988, pp 277-296.
4. Michaeli, W. and Jürss, D., "Thermoplastic Pull-Braiding: Pultrusion of Profiles with Braided Fibre Lay-up and Thermoplastic Matrix System (PP)", *Composites Part A*, Vol. 27A, No. 1, 1996, pp 3-7.
5. Larock, J.A., Hahn, H.T., Evans, D.J., "Pultrusion Processes for Thermoplastic Composites", *Society of the Plastics Industry*, 44th Annual Conference, 1989.
6. Devlin, B.J., Williams, M.D., Quinn, J.A., and Gibson, A.G., "Pultrusion of Unidirectional Composites with Thermoplastic Matrices", *Composites Manufacturing*, Vol. 2, 3 - 4, pp 203 - 209, 1992.
7. Bijsterbosch, H. and Gaymans, R.J., "Impregnation of Glass Rovings with a Polyamide Melt. Part 1: Impregnation Bath", *Composites Manufacturing*, Vol. 4, No. 2, pp 85 - 91, 1993.
8. Miller, A. and Gibson, A.G., "Impregnation Techniques for Thermoplastic Composites", *Polymers and Polymer Composites*, Vol. 4, No.7, pp 459-481, 1996.
9. Gibson, A.G. and Manson, J.-A.E, "Impregnation Technology For Thermoplastic Matrix Composites", *Composites Manufacturing*, Vol. 3, No. 4, pp 223 - 233, 1992.
10. Astrom, B.T., Pipes, R.B., Advani, S.G., "On Flow Through Aligned Fiber Beds and its Application to Composites Processing", *Journal of Composite Materials*, Vol 26., No. 9, pp 1351-1373, 1992.

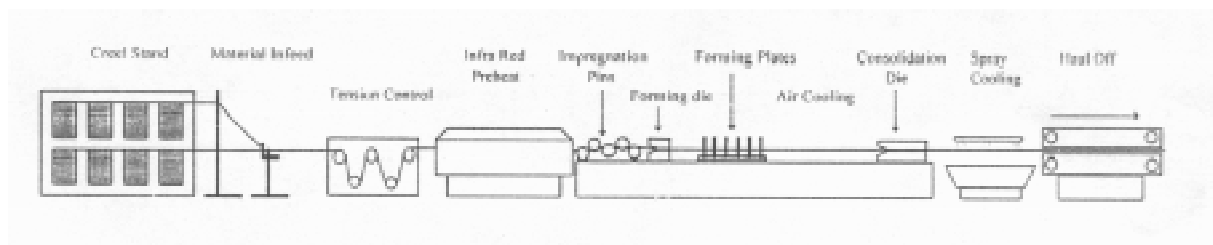


Fig. 1 : Schematic of the process used to pultrude continuous commingled PP/GF tows into product sections

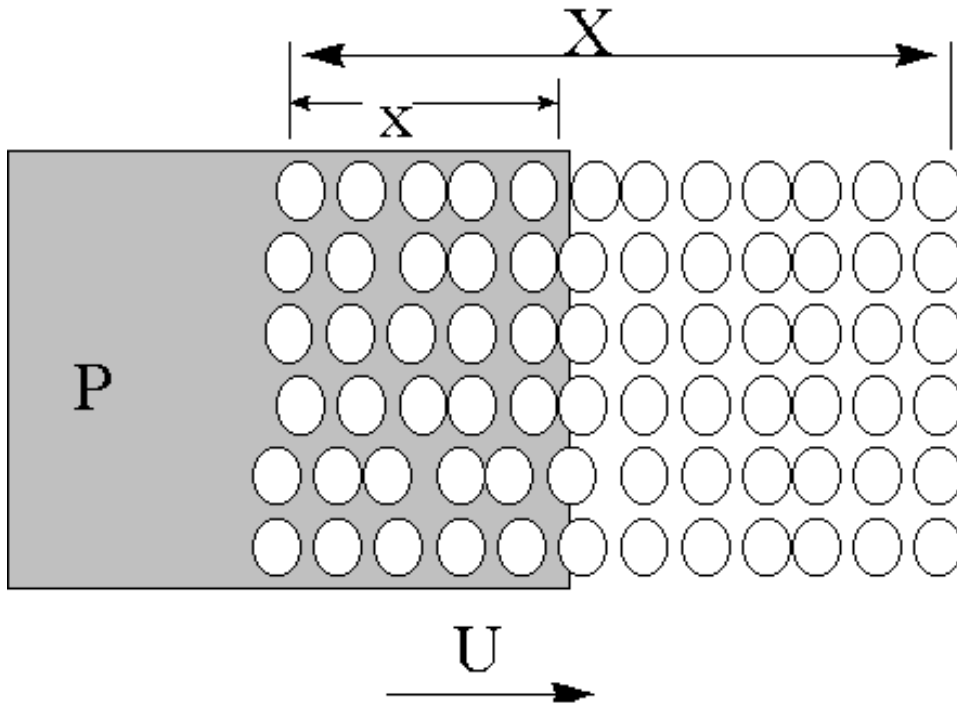


Fig. 2 : Impregnation of a porous fibre bed under an applied pressure, P .

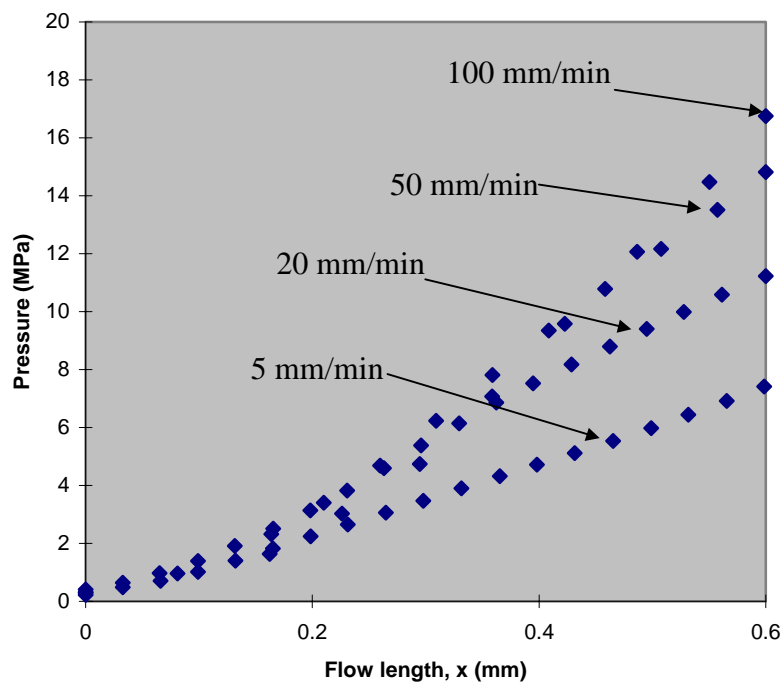


Fig. 3 : Consolidation of commingled tows at various compaction rates

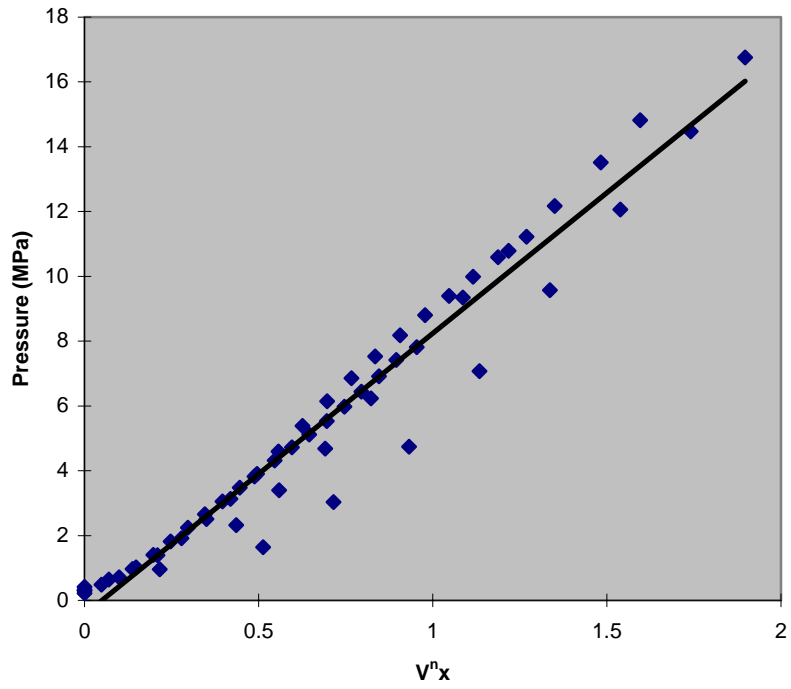


Fig. 4 : Plot of Pressure (MPa) versus $V^n x$, where $n = 0.25$

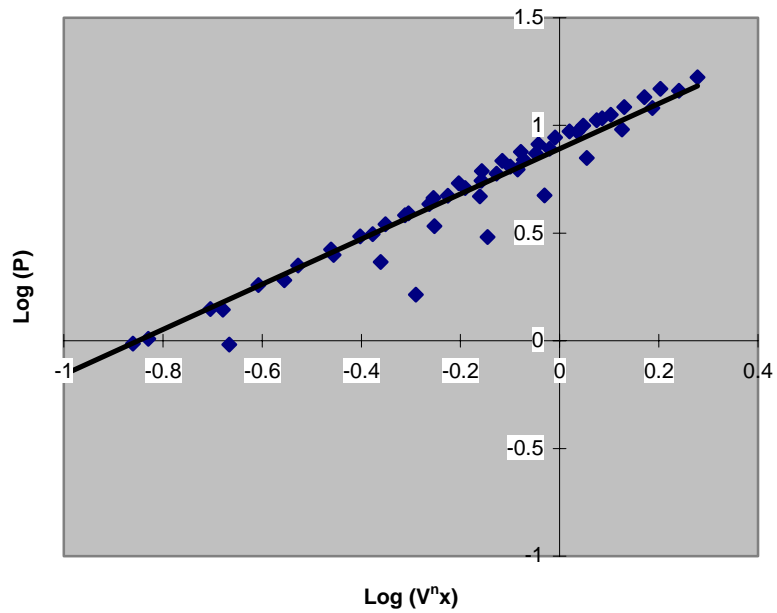


Fig. 5 : Plot of $\text{Log}(P)$ versus $\text{Log}(V^n x)$, slope ~ 1

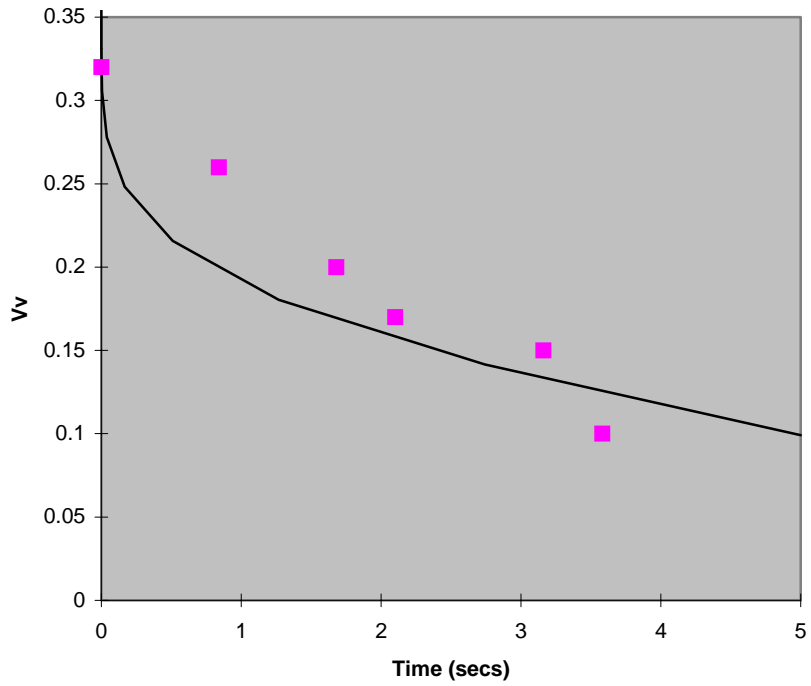


Fig. 6 : Consolidation results for a 20 x 2mm strip pultruded at 1m/min. The solid line represents the theoretical values obtained from eqn(12) and the points represent experimental data

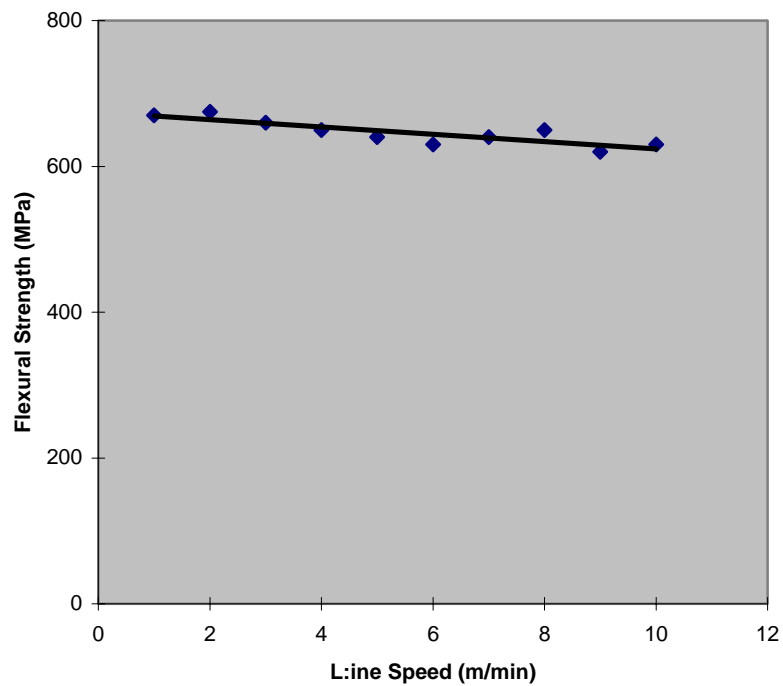


Fig. 7 : Flexural strength versus line speed for a pultruded 20 x 2mm strip

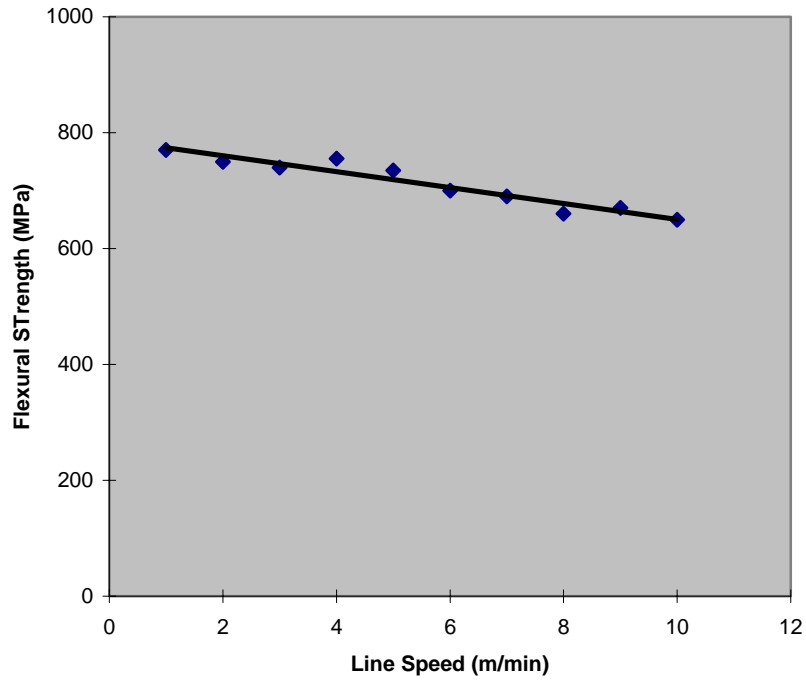


Fig. 8 : Flexural strength versus line speed for a pultruded 2mm diameter rod

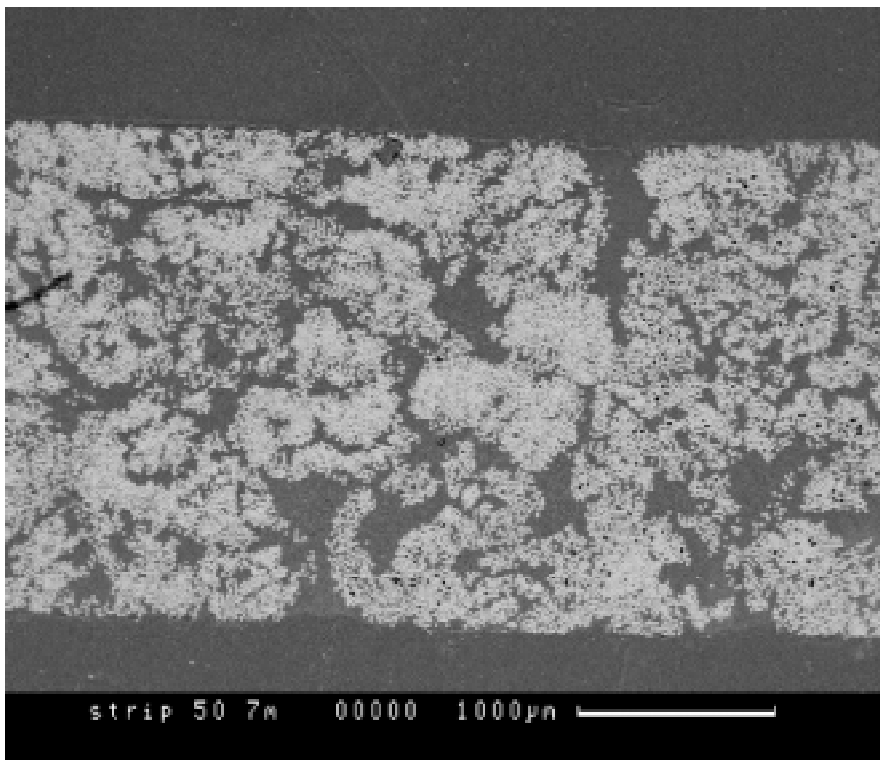


Fig. 9 : SEM micrograph of a pultruded 20x2mm strip produced at a line speed of 7m/min.

NUMERICAL MODELLING OF RESIN CURE USING A GENERAL PURPOSE FE PACKAGE

S.C. Joshi , Liu Xiao-Lin and Y.C. Lam

*Department of Mechanical Engineering, Monash University,
Clayton, Victoria 3168, Australia.*

SUMMARY: This paper proposes a procedure for using a general purpose finite element package with a transient thermal analysis facility to perform cure modelling. In the procedure, a general purpose finite element package was employed to carry out transient thermal analysis and a user program was developed to simulate the cure kinetics using nodal control volumes based on the finite element mesh. Theoretical background and numerical implementation of the procedure are described in the paper.

Application of the procedure was demonstrated by modelling the curing of a 140 layer T300/3501-6 uni-directional prepreg laminate in an autoclave as a one-dimensional as well as a three-dimensional problem. The stability of the procedure with the mesh density and length of the time step used was investigated. The temperature profiles predicted by the present approach were in excellent agreement with the available experimental data.

KEYWORDS: resin cure, finite element thermal analysis, nodal control volume

INTRODUCTION

The manufacturing of fibre reinforced composite parts are complex, require special environment and can be costly to control. This is because the composites consist of two different material systems, namely fibre and matrix systems. Most commonly used fibres are glass, aramid, boron, carbon and graphite while matrices are generally thermosetting resins. The successful production of a composite part depends mainly upon the use of a proper cure cycle that leads to complete and uniform curing. As a high exothermic reaction is a characteristics of curing of thermoset resins, the temperature profiles in the curing part depend upon not only the amount of heating power supplied to the tool but also the amount of heat generated by the resin cure reaction. The generated heat is a function of the total mass fraction of resin in the mould and the resin system used. The exothermic reaction associated with low thermal conductivity can lead to excessively high temperatures at some locations in the part and, as a consequence, result in a non-uniform state of cure. Therefore, it is desirable to study the effects of this temperature rise when setting up a cure cycle for the component.

It has been proven that the process of resin cure and the related thermal response of the component can be modelled relatively accurately by a numerical method, such as the finite element method [1-4]. However, most of the results reported were obtained using specially developed programs in which two major tasks of the cure modelling: solution of the discretised energy equations and simulation of the cure kinetics, are coupled. Development of

such a program is usually lengthy and costly, especially when a three-dimensional geometry and complicated boundary/interface conditions are to be accommodated.

This paper proposes a procedure by which a general purpose finite element package can be employed to perform cure modelling. The theoretical background and numerical implementation of the procedure are described. The application of the procedure to the cure modelling of a thick graphite/epoxy prepreg laminate with and without considering the three-dimensional heat transfer effect, is presented. The results obtained were in excellent agreement with the experimental data.

THEORETICAL BACKGROUND

Governing Equations

For simplicity, let us consider a prepreg moulding process. In this case, the resin is more or less evenly distributed in a prepreg lay-up and the convective heat transfer effect caused by the resin flow can be safely ignored. It is also assumed that the resin and fibres are at the same temperature at any point in the curing composite and form a macroscopically homogeneous material system for heat transfer purpose. Under these assumptions, the energy equation governing heat transfer in the curing product is simplified as:

$$\frac{\partial}{\partial x} \left(K_x \frac{\partial T}{\partial x} \right) + \frac{\partial}{\partial y} \left(K_y \frac{\partial T}{\partial y} \right) + \frac{\partial}{\partial z} \left(K_z \frac{\partial T}{\partial z} \right) + \frac{\partial Q}{\partial t} = \rho_c \cdot c_p \cdot \frac{\partial T}{\partial t} \quad (1)$$

where ρ_c , c_p , and K_i ($i = x, y, z$) are lumped density, specific heat and directional thermal conductivities of the lay-up material respectively.

The internal heat generation source term $\frac{\partial Q}{\partial t}$ represents the exothermic effect of the resin reaction. By ignoring the effect of resin flow on the species, it is related to the rate of cure directly by the following equation:

$$\rho_c \frac{dQ}{dt} = \rho_r V_r Q_{total} \frac{d\alpha}{dt} \quad (2)$$

where, α is the degree of cure which is defined as the ratio of the heat released to the total heat of reaction, Q_{total} is total heat of reaction and, $\rho_r V_r$ is mass content of the resin.

Cure Reaction Kinetics

The heat release rate for a particular resin system can be determined by a Differential Scanning Calorimeter (DSC) experiment. The experimental data obtained from DSC is usually fitted into some semi-empirical model representing the rate of cure as a function of temperature and the degree of cure. One of the most frequently used and simplest model is the following Arrhenius relation [5-8]:

$$\frac{d\alpha}{dt} = f(T, \alpha) = B(1 - \alpha)^C \exp(-\Delta E / RT) \quad (3)$$

where R is the universal gas constant, T is absolute temperature, B , ΔE and C are material constants to be determined by the experiment.

In some cases, it is more accurate to fit the data by two Arrhenius equations [8]. Namely, one have:

$$\frac{d\alpha}{dt} = \begin{cases} B_1 \cdot (1-\alpha)^{C_1} \exp(-\Delta E_1 / RT) & \alpha \leq A \\ B_2 (1-\alpha)^{C_2} \exp(-\Delta E_2 / RT) & \alpha > A \end{cases} \quad (4)$$

Let $B_r = B \exp(-\Delta E / RT)$, Eqn 3 can be rewritten as:

$$\frac{1}{(1-\alpha)^c} d\alpha = B_r dt \quad (5)$$

Integrating Eqn 5 produces:

$$\alpha = 1 - [1 + (C-1)S]^{\frac{1}{1-C}} \quad (c \neq 1) \quad (6)$$

where S is an integral:

$$S = \int_{t_0}^t B_r d\theta = B \int_{t_0}^t \exp(-\Delta E / RT) d\theta \quad (7)$$

Adapting an explicit scheme, the integral can be evaluated approximately as:

$$S_t = S_{t_0} + B \exp(-\Delta E / RT_{t_0}) \Delta t \quad t \in [t_0, t_0 + \Delta t] \quad (8)$$

Once S is evaluated for a time step, α , $\frac{d\alpha}{dt}$ and $\frac{\partial Q}{\partial t}$ can be calculated using Eqns 6, 4 and 2 respectively.

NUMERICAL IMPLEMENTATION

Solution Procedure

From the above presentation, it is obvious that cure modelling can indeed be considered as a transient heat transfer analysis by taking into account the effect of the resin cure reaction. Numerically, It can be divided into two sub-tasks: formulation and solution of the heat transfer equations, and simulation of the cure kinetics. Although most of the general purpose finite element packages can be used to perform the first sub-task, they usually do not provide facility to evaluate the cure kinetics.

A procedure is proposed in which a general purpose finite element package is employed to perform transient thermal analysis and a user program is developed to simulate the cure reaction using nodal control volumes based on the finite element mesh. Once the temperature field is obtained by the finite element analysis, the user program is activated to simulate the cure kinetics and heat generation at each of the nodal control volumes. These are then lumped and applied as heat sources at those nodal points for the finite element transient thermal analysis of next time step. This can easily be achieved through modification of the input data

file to the finite element package. If necessary, a few iterations can be performed to achieve higher accuracy. The procedure is repeated until the curing process completes. The modelling process is automated by executing the user program and the finite element package alternatively in batch mode. Fig. 1 illustrates the flow chart of the procedure.

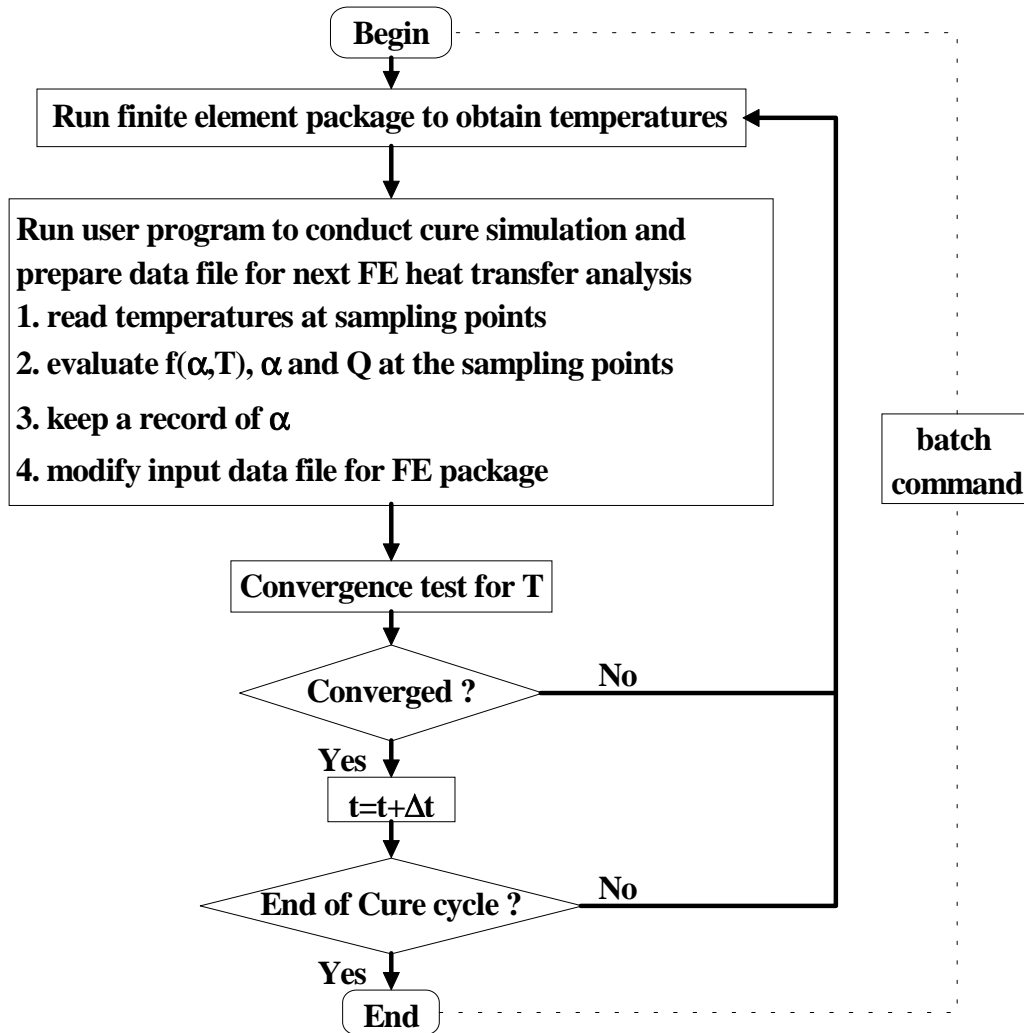


Fig. 1: Flow chart of the cure modelling procedure.

Numerical Evaluation of Nodal Heat Sources

The major computation involved in the user program is the evaluation of the equivalent nodal heat sources caused by the cure reaction. In this paper, the evaluation is conducted based on the finite element nodal control volumes.

A control volume is an/a area/volume over which the parameters such as temperature, pressure, etc., are assumed to be constant. The concept of nodal control volumes has been successfully used by investigators for the flow simulation [2,3,5]. In this technique, initially sub-control volumes are created by connecting a centroid of the finite element to the center-points of its surfaces. The boundary of each sub-control volume contains only one finite element node and that volume is assumed to be linked to that particular node. This way, all the sub-control volumes surrounding the node formulate a nodal control volume, see Fig. 2. Heat generated within the volume is then lumped as a point heat source applied at the node.

Once the finite element mesh is defined, all the geometrical data are available and can be used to calculate the area/volume of each of the control volumes.

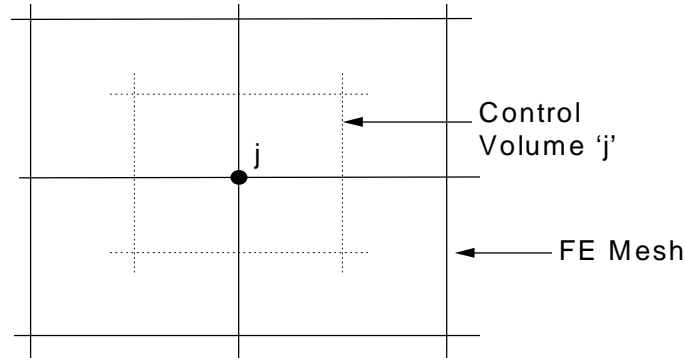


Fig. 2: Nodal control volume based on finite element mesh.

The resin content of control volume j can be determined as:

$$V_r^j = V^j V_r \quad (9)$$

where, V_r^j : resin content of control volume j , V^j : area/volume of control volume j , V_r : resin volume fraction.

Total heat generated in control volume j is:

$$Q^j = (Q_{Total}) V_r^j \cdot \frac{d\alpha^j}{dt} \quad (10)$$

This is applied as a lumped heat source at nodal point j .

CURE MODELLING OF A THICK LAMINATE

Modelling Conditions

The procedure was applied to simulate the curing process of a thick square laminate in autoclave as a one-dimensional as well as a three-dimensional problem. The same problem was analysed using CURE, a specially developed finite difference cure modelling program [8]. The laminate was made up of 140 plies of T300/3501-6 uni-directional prepreg. The bagging materials were assumed to be a combination of one layer of release film, two of breather and one of nylon. Geometric details of the tooling configuration are shown in Fig. 3. Physical properties of the tooling, prepreg and bagging materials are given in Table 1. Reaction kinetics of Hercules 3501-6 resin system can be expressed by Eqn 4 [8]. Table 2 lists the parameters in the equation.

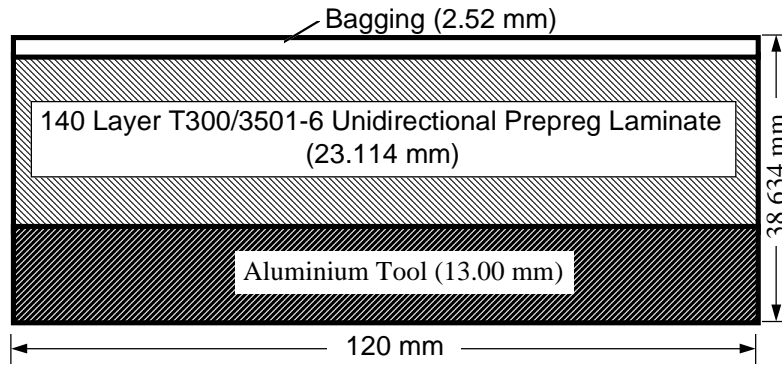


Fig. 3: Cross section of tooling configuration.

Table 1: Physical properties used in the model

Material	Aluminium	T300/ 3501-6	Bagging
Density [kg/m ³]	2692.12	1555.00	355.65
Specific Heat [J/kg. K]	916.91	909.00	1256.0
Conductivity [W/m. K]	216.30	0.556	0.069

Table 2: Parameters in cure kinetics model for Hercules 3501-6 resin system

Q_{total} (J/kg)	A	B_1	B_2	ΔE_1 (J/mol)	ΔE_2 (J/mol)	C_1	C_2
3.8×10^5	0.18	3.49×10^8	2.53×10^5	94828	73445	10	1.2

The one-dimensional model of the laminate, as shown in Fig. 4a, was created using different number of 4-noded quadrilateral field elements. The three-dimensional model of a quarter (because of 2-axis symmetry) of the laminate fabrication assembly is illustrated in Fig. 4b which consisted of 210 (49 for the tool, 80 for the laminate and 81 for the bagging), 8-noded solid field elements.

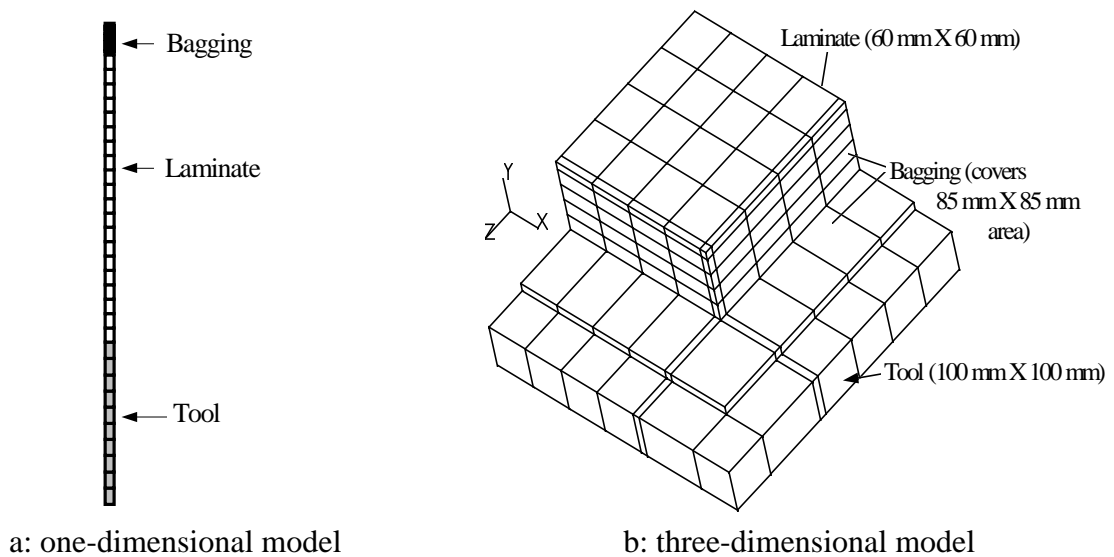


Fig. 4: Finite element models.

As reported by Vodicka [8], a heat transfer coefficient of $85\text{W/m}^2\cdot\text{K}$ was used between the autoclave air and the tool/bagging materials in the present analysis. The autoclave temperature cycle adapted is given in Fig. 5.

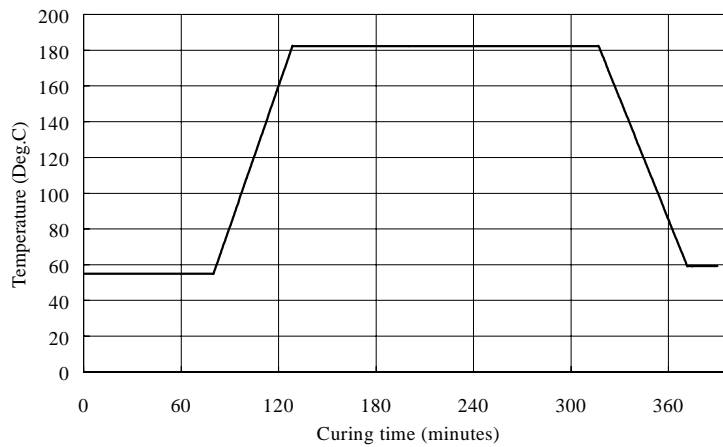
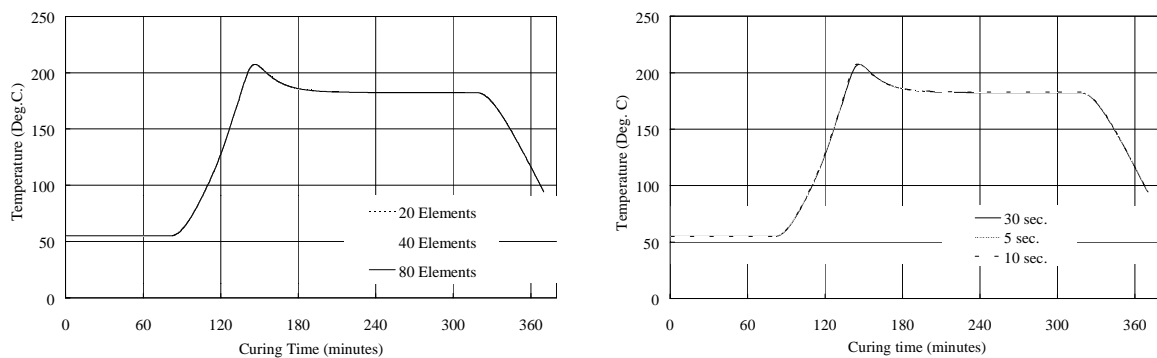


Fig. 5: Autoclave temperature cycle.

RESULTS AND DISCUSSION

To investigate the stability of the procedure, the problem was first analysed using different number of elements and different size of time increments in one-dimensional modelling. No iterations were applied in the analysis. Fig. 6 illustrates temperature response in the central layer of the laminate. Very negligible variations were observed. This suggests that the results are not sensitive to both the mesh density and the size of time increment. In the following analyses, a 30 seconds time step was used with no iteration performed.



a. different finite element mesh density.

b. different time increments.

Fig. 6: Temperature response at central lamina

Using the same computational conditions, the problem was modelled using both the present procedure and CURE. The temperature results obtained for the central layer were compared with the experimental data in Fig. 7. Also shown in the figure is the simulated temperature response without considering the exothermic effect.

The results indicated that both procedures predicted temperature responses generally in good agreement with the experimental result. However, the result obtained by CURE tended to shift away from the true response after the temperature overshoot caused by the exothermic effect. The maximum temperature predicted by the present model and CURE was 207.1°C and 210.6°C respectively while the experimental value was 205.6°C . The exothermic effect of resin cure is obvious, causing a temperature overshoot of more than 25°C in the central layer. This highlights the need for a cure modelling to be conducted for the thick laminate.

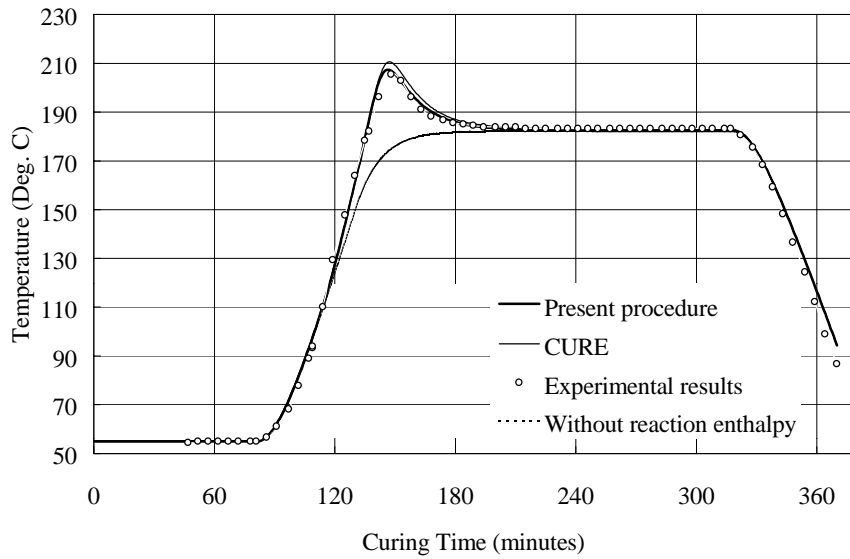


Fig. 7: Temperature response at central lamina obtained by different methods.

At the initial stage of the cure cycle, autoclave temperature was hold at 55°C for 80 minutes to allow the temperature in the tooling set-up to homogenise. Very negligible cure ($\alpha=0.0013$) was observed during this stage. Therefore, this segment of the cure cycle was ignored in three-dimensional analysis to save the computational efforts. Significant solidification was observed from 126.5 minute. The degree of cure at central lamina reached a value of 0.6 (approximate gel point) at 138.0 minute and 0.95 at 156.5 minute, see Fig. 8.

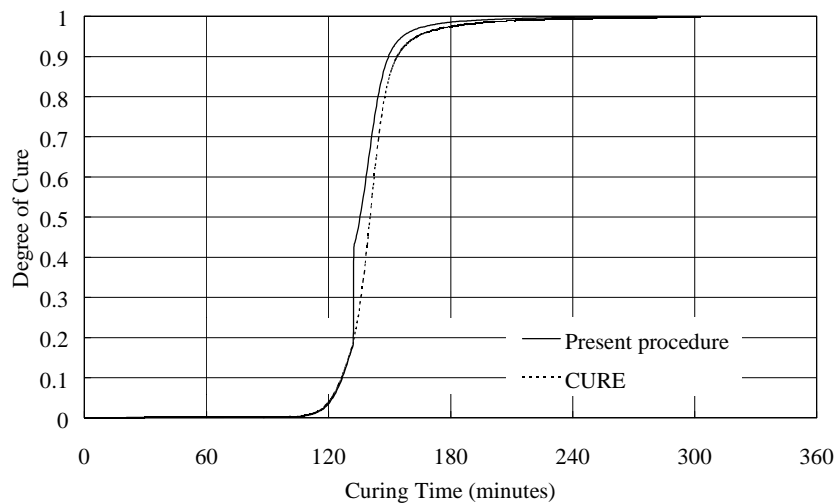


Fig. 8: Degree of cure at central lamina Vs. time (1D simulation).

Fig. 9 compares the temperature responses at the centre of the laminate predicted by one-dimensional and three-dimensional simulations respectively. The two predictions were generally in good agreement, giving the highest temperatures of 207.1°C and 207.0°C respectively. The temperature predicted by one-dimensional analysis had a slower rate of decrease after the temperature overshoot as compared to the three-dimensional result. This is because that in one-dimensional analysis heat could only be dissipated into the air from the top and bottom surfaces, while in three-dimensional analysis additional dissipation was allowed from the edges.

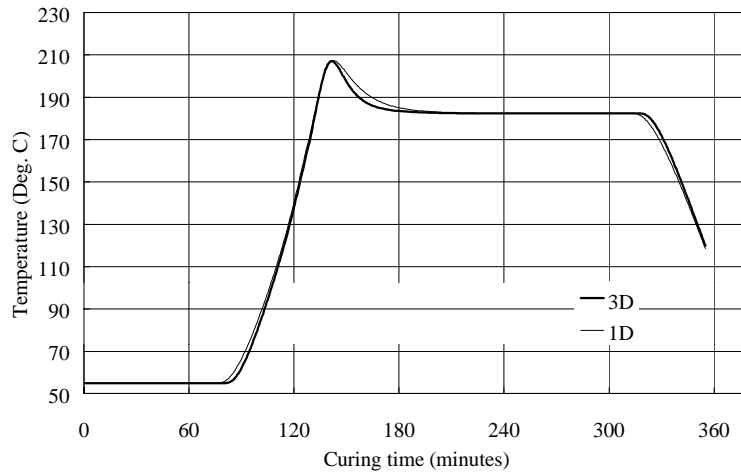


Fig. 9: Temperature response by 1D and 3D Cure Modelling using present procedure

To further investigate the edge effect which can only be considered by three-dimensional analysis, temperature contours of the central lamina at two different timings are illustrated in Fig. 10. At the early stage of curing, there was little reaction and heat was transferred from the autoclave air into the laminate through the tooling/air interface. Therefore, temperatures at central locations were lower than those of the positions close to the interface. At the later stage, significant exothermic effect of curing caused higher temperature in the laminate than that of the autoclave air and heat was dissipated from the laminate to the air. Temperature was then decreasing from the centre of the laminate to the interface. Maximum temperature difference observed for the central lamina was 8°C.

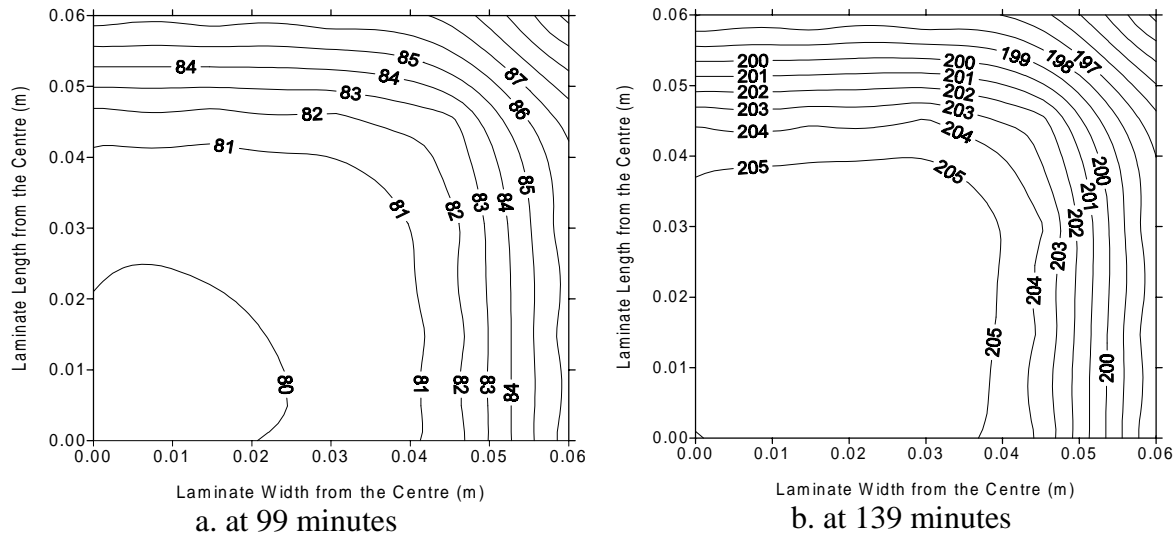


Fig. 10: Temperature contours in the central lamina.

Fig. 11 shows temperature distribution in thickness direction at 139 minutes. Since the bagging materials have very low thermal conductivity, heat was very difficult to dissipate from the top surface. This resulted in a temperature difference of about 20°C in thickness direction. Such a significant difference in temperature would affect the uniformity of the cure. Fig. 12 gives the distribution of α at the corresponding sections. A 10% difference in the degree of cure was observed.

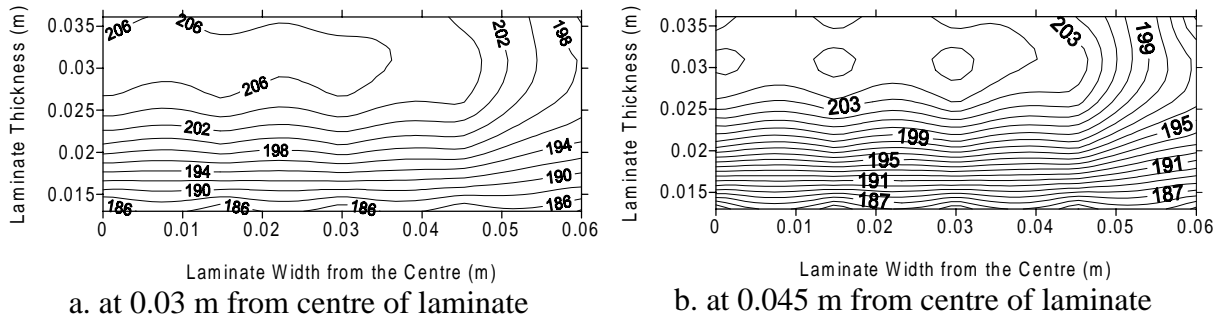


Fig. 11: Temperatures after 139 minutes of curing.

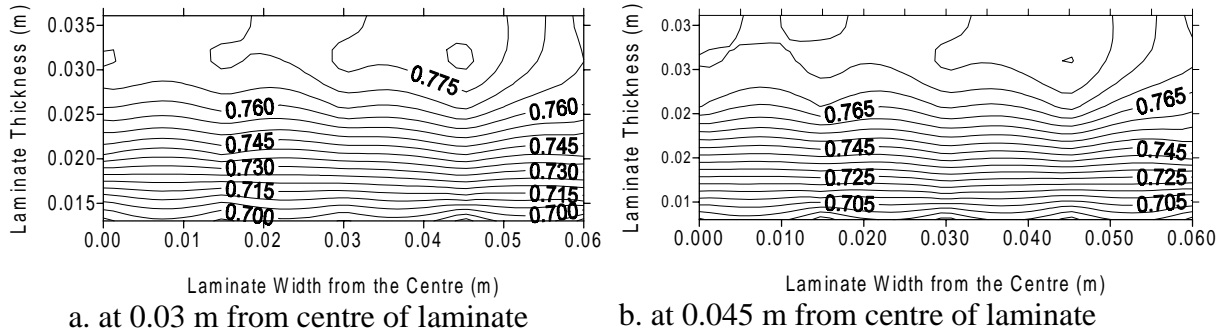


Fig. 12: Degree of cure after 139 minutes of curing.

CONCLUSIONS

A procedure was proposed to employ a general purpose finite element package in cure modelling for composite manufacturing. Thus, the costly development of a numerical thermal analysis program can be avoided. The procedure was validated by the simulation of the curing process for a 140 layer T300/3501-6 laminate. It can be concluded that

1. The procedure is numerically stable and produces more accurate results than the specially developed finite difference cure modelling program CURE.
2. The procedure can make use of all the features pertaining to the finite element package used. Therefore, cure modelling for composite parts with complicated geometry and material properties can be conducted by the procedure. In particular, it can perform three-dimensional cure modelling.
3. The results of cure modelling for the thick laminate indicate that the one-dimensional simulation can only predict the temperature and the degree of cure along the central axis of the laminate. A three-dimensional simulation should be performed if more accurate and comprehensive results are required.

ACKNOWLEDGMENTS

Various supports from the Cooperative Research Centre for Advanced Composite Structures Limited, Australia, are appreciated. The first author gratefully acknowledges the financial assistance received from Monash university and the Australian government.

REFERENCES

1. Loos A.C., MacRae J.D., "A Process Simulation Model for the Manufacture of a Blade-stiffened panel by the Resin Film Infusion Process", *Composites Science and Technology*, Vol. 56, 1996, pp. 273-289.
2. Young W.B., "Thermal Behaviour of the Resin and Mold in the Process of Resin Transfer Molding", *Journal of Reinforced Plastics and Composites*, Vol. 14, 1995, pp. 310-332.
3. Young W.B., "Three-Dimensional Non-isothermal Mould filling Simulations in Resin Transfer Moulding", *Polymer Composites*, Vol. 15, 1994, pp. 118-127.
4. Bruschke M.V., Advani S.G., "A Numerical Approach to model Non-isothermal Viscous Flow through Fibrous Media with Free Surfaces", *International Journal for Numerical Methods in Fluids*, Vol. 19, 1994, pp. 575-603.
5. Bogetti T.A. and Gillespie Jr. J.W., "Two-Dimensional Cure Simulation of Thick Thermosetting Composites", *Journal of Composite Materials*, Vol. 25, 1991, pp. 239-273.
6. Kim C., Teng H., Tucker C. III, "The Continuous Curing Process for Thermoset Polymer Composites. Part 1: Modelling and Demonstration", *Journal of Composite Materials*, Vol. 29, 1995, pp. 1220-1253.
7. Vergnaud J.M. and Bouzon J., *Cure of Thermosetting Resins: Modelling and Experiments*, Springer-Verlag, London, 1992, pp. 105-107.
8. Vodicka R. and Evans N., "User's Manual for Cure, A Computer Simulation of the Autoclave Curing Process for Composite Lay-Up", *CRC-AS report*, Restricted Circulation, 1994.

CURING OF COMPOSITE PREPREG LAMINATES BY RESISTANCE HEATING OF INTERNAL CARBON VEILS

Charles E. Bakis and Frank J. Bantell

*Department of Engineering Science and Mechanics, 227 Hammond Building,
Composites Manufacturing Technology Center
The Pennsylvania State University, University Park, PA 16802, USA.*

SUMMARY: The goal of this investigation is to assess the feasibility of using internal carbon fiber resistance heaters with temperature feedback to cure laminated composites comprised of either S2 glass or IM7 carbon fiber reinforced epoxy prepreg. Internal temperature distributions and cumulative energy consumptions were measured in unidirectional laminates with 6.4 mm (50 ply) and 38.1 mm (300 ply) thicknesses. The temperature distributions revealed a lack of deviations in temperature from the manufacturer's recommended cure cycles commonly seen in thick laminates cured by conventional means, although a means of improving temperature uniformity is needed. Volumetric energy usage was five to ten times greater in the thin laminates than in the thick laminates cured with internal heaters. This difference was attributed to incomplete curing in certain areas and a higher volume to surface ratio in the latter.

KEYWORDS: processing, thick laminates, internal heating, resistance heating

INTRODUCTION

During the cure process of fiber reinforced epoxy laminates, a phenomenon known as temperature overshoot or spiking has been known to occur. Temperature overshoot occurs when the thickness and thermal diffusivity of a volume of material are such that the heat generated by the exothermic curing process cannot be transferred to the external surfaces of the material at a rate which will prevent the interior of the material from reaching dangerously high temperatures. Scott and Beck [1] measured temperature overshoots in 128-, 64-, and 32-ply carbon/epoxy laminates processed in an autoclave. In the 128-ply carbon/epoxy laminate, the maximum temperature overshoot was 60°C. Kenny [2] observed 30°C temperature overshoots in an 8-mm-thick carbon/epoxy laminate cured in a standard autoclave process. Butler and Engel [3] observed a 70°C overshoot due to the exotherm of 50-cm-thick glass/epoxy composites made by resin transfer molding. Overshoot temperatures of these magnitudes could possibly cause thermal damage in certain epoxy resin composites.

In terms of the potential for temperature overshoot, Kenny et al. [4] defined a thick composite based on material properties. The idea of a half thickness, h_{AD} , of the material was introduced, where the total thickness of a part would be twice its half thickness. Equation 1 is the expression for h_{AD} ,

$$h_{AD} = \{k / [\rho C_p K_0 \exp(Q / RT_c)]\}^{1/2} \quad (1)$$

where k is the composite thermal conductivity, ρ is the composite density, C_p is the specific heat of the composite, K_0 is a frequency factor used in describing the kinetic rate constant derived from a thermokinetic model for nonautocatalytic reactions, Q is the activation energy for cure of the resin, R is the universal gas constant, and T_c is the processing temperature. The half thickness reported by Kenny [2, 4] for carbon epoxy prepregs is approximately 1 cm. It is indicated in Eqn 1 that materials with higher thermal conductivity and processing temperature and lower density, specific heat, frequency factor, and cure activation energy will have a greater half thickness and therefore less tendency for temperature spiking for a given thickness of material. Since composites composed of glass or carbon fiber are differentiated in these terms by higher thermal conductivity, lower density, and lower specific heat in the carbon composite, it can be expected that carbon composites are less likely than glass composites to undergo temperature spikes during cure — all else being the same.

There have been methods developed for dealing with temperature spiking due to the exothermic reaction in fiber reinforced epoxy composites. Among these are the manufacturer's thick part processing cycle, continuous curing or simultaneous lay-up and *in-situ* cure process [5], staged curing [6], and embedded resistance heating [3].

The objective of this investigation is to evaluate the internal heating method developed by Butler and Engel [3] for resin transfer molding applications as it applies to carbon and glass reinforced epoxy laminates of thicknesses of 6.4 and 38.1 mm. New contributions of the present work include the following: the incorporation of a single-zone, internal temperature feedback loop; the calculation of real-time power and cumulative energy used during the cure cycle; the application of the method to prepreg material systems; the comparison of two material systems with identical resin types and resin volume fractions but different fiber types; and the comparison of thin and moderately thick parts. Thermocouples were embedded at various locations through the thickness of the laminates and monitored continuously. Temperature distributions in laminates cured by two different methods — computer controlled hot press curing and internal resistance heating element curing — were compared.

EXPERIMENTAL METHODOLOGY

The material systems used in the present investigation were Hercules MAGNAMITE[®] carbon prepreg tape IM7/8551-7A and Hercules MAGNAMITE[®] S2-glass[®] prepreg tape S2/8551-7A. These zero-bleed prepregs were chosen due to their availability and also due to their having the same volume fraction and type of resin, thereby allowing a controlled comparison of the effect of fiber type on curing characteristics. The laminates used were nominally either 50- or 300- plies thick. The manufacturer's cured ply thickness were 0.140 mm for the carbon prepreg and 0.127 mm for the glass prepreg. Hence, the nominal thicknesses of the thin and thick laminates were assumed to be 6.4 and 38.1 mm, respectively. As will be described below, all laminates were essentially unidirectionally reinforced. Two layers of 102 by 76 mm carbon veil with randomly oriented chopped fibers were used for each internal resistance heater, also called the heating patch. A single veil had an average areal density of 16 g/m². Copper wires which had 76 mm of insulation stripped at the end were placed across opposite ends of the veil so that current passed along the 102 mm dimension. The two wires thus sandwiched between two veils comprised a heating patch. The thin laminates used one heating patch at the mid-plane location and the thick laminates used three heating patches connected in series as shown in Fig. 1.

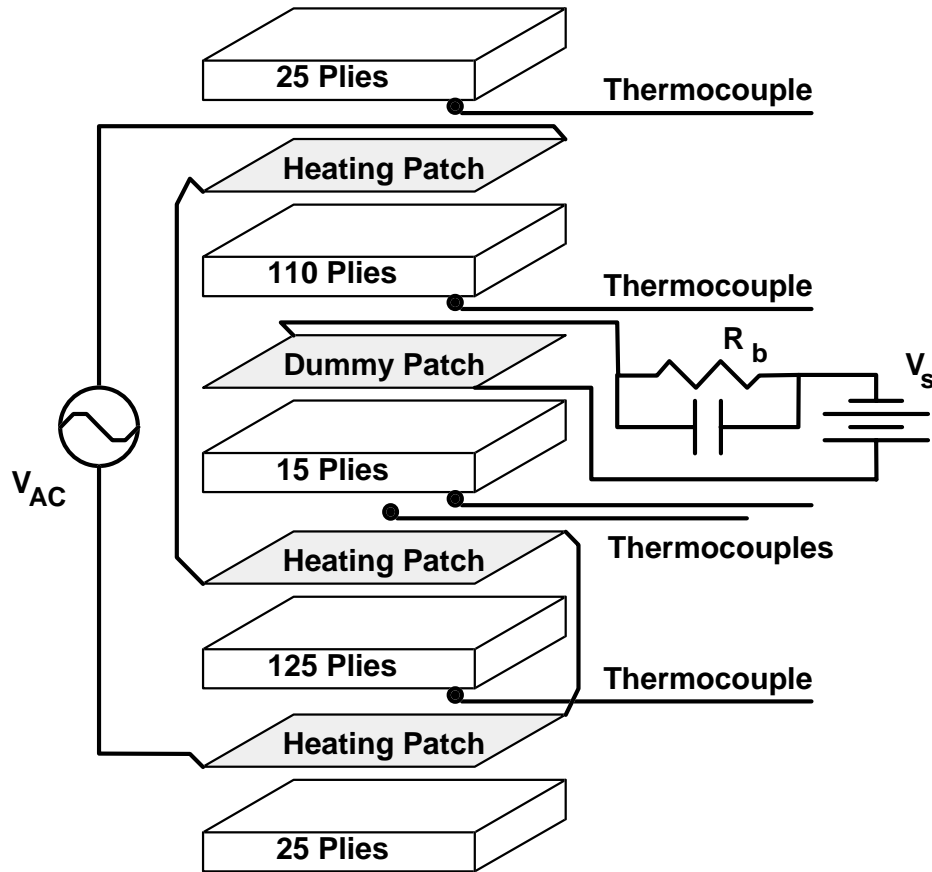


Fig. 1: An exploded view of the internal resistance heating setup for a 300 ply, 38-mm glass/epoxy laminate

In order to determine the resistance and, hence, power dissipation of the patches throughout the cure cycle, a dummy carbon patch was used in a separate DC voltage divider circuit. A low (0.5 - 1 V) DC voltage source introduced current to the circuit while an 8 Ω ceramic resistor was used as the ballast resistor across which voltage was recorded (Fig. 1). A 220 μF capacitor was placed in parallel with the ballast resistor to eliminate electrical noise that resulted from the proximity of the relatively high AC voltage heating patches to the low DC voltage dummy patch. The dummy patches were located 7 and 15 plies from the middle surface of the thin and thick laminates, respectively. If the ballast resistor voltage is V_b , the DC source voltage is V_s , and the ballast resistance is R_b , then the dummy patch resistance, R_p , is given by Eqn 2.

$$R_p = R_b(V_s / V_b - 1) \quad (2)$$

The *average* power dissipated by the series-connected patches, P , was calculated using Eqn 3,

$$P = (V_{AC})^2 / 2R_H \quad (3)$$

where V_{AC} is the *peak* voltage output of the AC source and R_H is the sum of the resistances of all the heating patches in the specimen. At any time during the cure cycle, each heating patch was assumed to have a resistance equal to that continuously measured with the *in-situ* dummy patch, thereby accounting for, in an approximate sense, the effects of contact pressure between patches and wires, liquid epoxy infusion, degree of cure, and process temperature on

patch resistance. To ascertain the internal temperature distribution, at least one type J thermocouple was inserted near the center of all four patches in the case of the thick laminates (Fig. 1) and at four comparable locations (scaled for the number of plies) in the thin laminates.

To manufacture the thick laminates, a rectangular aluminum mold was fabricated with inner dimensions of 127 by 102 mm by up to 76 mm thick. A variable thickness, 127 by 102 mm caul plate was manufactured to fit snugly into the mold and was used to transfer compaction pressure from press platens to the laminates. Near the center of one of the 127 mm sides of the mold, several small holes were made to allow passage of thermocouple and electrical wires. The thin laminates were manufactured using a pair of 330 by 304 by 13 mm aluminum caul plates with putty material used to confine the planar dimensions of the prepreg to 127 by 102 mm. The laminates were made with all their fibers oriented in the 102 mm direction, except for the carbon/epoxy laminates which were cured by internal patch resistance heating. In these exceptions, a $[0/90]_s$ laminate of glass/epoxy prepreg was added above and below each carbon patch to prevent an electrical short circuit with the surrounding carbon prepreg material. To account for the added thickness of the glass/epoxy insulation, eight plies of carbon epoxy prepreg were subtracted for each carbon patch present in the thick carbon specimen. No such correction was made in the thin carbon specimen, resulting in added thickness in comparison with the thin glass specimen. Attempts were made to minimize heat loss from the molds to the surrounding environment when using internal patch resistance heating by wrapping glass wool insulation around the sides of the molds and by placing 13-mm-thick plywood sheets between the mold and the upper and lower platens of the press.

Two curing methods were investigated: hot press curing and internal carbon patch curing. The hot press was a Tetrahedron model MTP-14 with 35.6 cm square platens and computer controlled force and temperature. The internal patch curing was done with a 120 VAC (peak), 10 A (peak) variable autotransformer as the power source and the MTP-14 for compaction force only. An on/off type temperature controller was used to control the temperature as measured by a separate thermocouple placed on the center-most heating patch (Fig. 1).

During a typical experiment, a stopwatch and analog voltmeter were used to manually record, every few minutes, the peak voltage output of the AC source for the heater patches. Power source peak voltages for the thin and thick laminates were held constant at values of approximately 25 and 40 VAC, respectively, throughout an experiment. Time, thermocouple readings, the DC dummy source voltage and DC dummy ballast resistor voltage were all recorded every 50 sec with a computer. Elapsed time that the AC power was applied to the heating patches was measured against real time by periodically recording the time from an analogue clock powered by the same on/off temperature controller which energized the power patches. Hence, based on Eqn 3, the cumulative energy dissipated in the specimen, E , was determined by multiplying the averaged average power during each interval, P_i , by the respective clock time increment during that interval, Δt_i , and summing as in Eqn 4.

$$E = \sum_i P_i(\Delta t_i) \quad (4)$$

RESULTS

Temperature profiles for a hot-press cured 38.1-mm-thick glass/epoxy laminate shown in Fig. 2 reveal some inaccuracy in the tracking of the temperature versus the MRC cycle, particularly during temperature ramps. The two middle thermocouples in this experiment were located at the middle and at the quarter point along the length of the laminate. One of these recorded the maximum temperature spike of 10°C after the beginning of the 177°C dwell. The deviations from the MRC were even less in the 38.1-mm-thick carbon/epoxy laminate and in thinner laminates of either type cured in the hot press (data not shown here). These data suggest that the materials tested here, in conjunction with the high thermal conductivity mold and good thermal coupling between the mold and temperature-controlled platens of the hot press, do not develop dangerous temperature spikes during the standard cure process. Based on visual inspection, these specimens appeared to be well-consolidated and fully-cured.

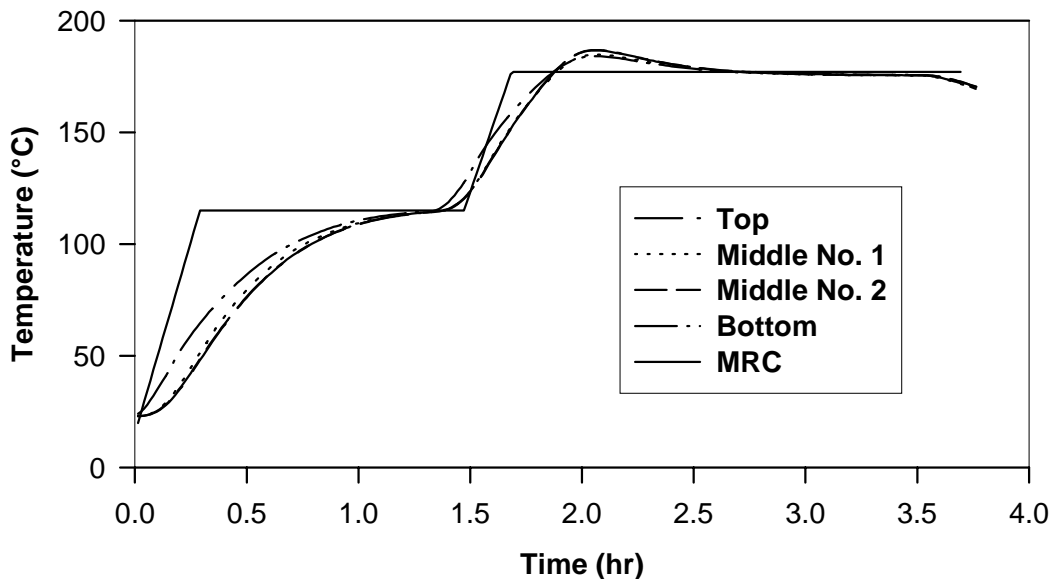


Fig. 2: Temperature profiles in a 38.1-mm glass/epoxy laminate cured in a hot press

Representative dummy patch resistance data from two internally heated 6.4-mm laminates shown in Fig. 3 indicate a decrease from approximately 3 to 2 Ω shortly after the application of consolidation pressure. Dummy patch resistance data for the 38.1-mm laminates were essentially identical to those shown in Fig. 2. The 33% drop in resistance attributed to contact pressure is important from the standpoint of the power dissipation calculation (Eqn 3) as well as the physical interpretation that liquid epoxy infusion, temperature change and degree of cure did not significantly affect patch resistance in these experiments.

Temperature profiles in the 6.4-mm internally-heated glass/epoxy and carbon/epoxy laminates are shown in Figs. 4 and 5, respectively. Temperature ramps were rather course due the manual stepwise increase in settings of the temperature controller, but neither specimen exhibited any significant temperature overshoot. In both figures, the middle thermocouple did not measure exactly the same temperature as the nearby but separate controller thermocouple

which was also located at the midplane of the specimen. These variations of up to 15°C could be due to variations in power input across the plane of the middle heating patches, possibly related to the visually apparent density variations in the patch material from point to point.

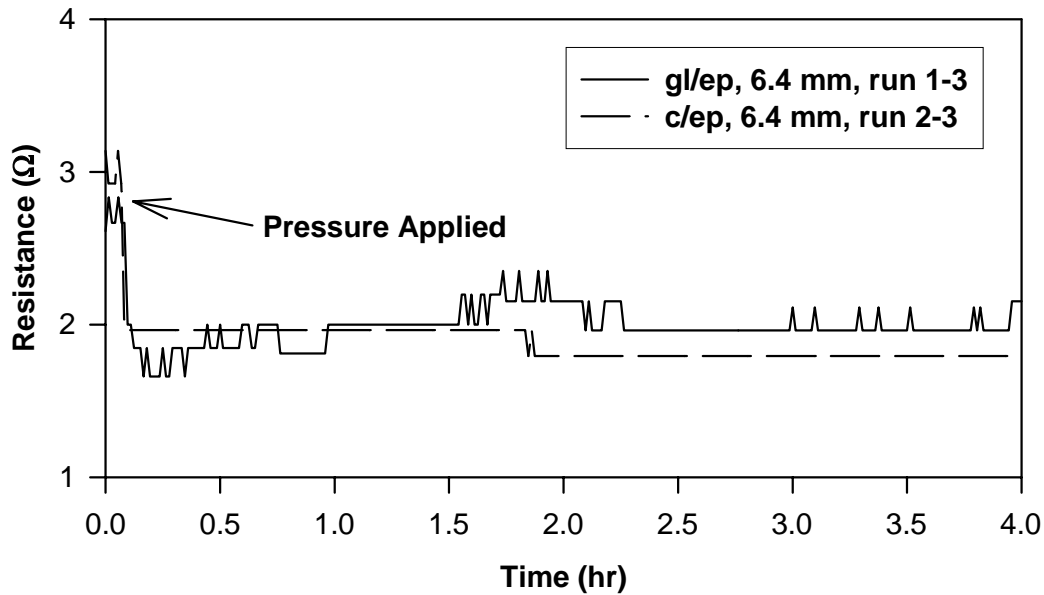


Fig. 3: Dummy carbon patch resistance during the cure cycle

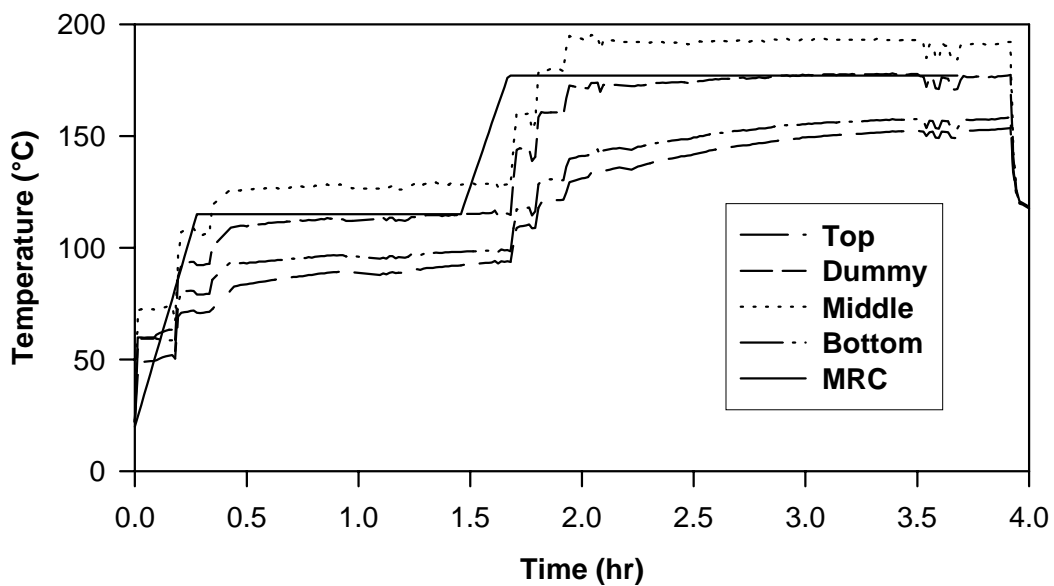


Fig. 4: Temperature profiles in a 6.4-mm glass/epoxy laminate with one heating patch

The instantaneous average power dissipated by the single heating patch of a 6.4-mm carbon/epoxy specimen is shown in Fig. 6 to vary from 90 W at the outset to 160 W during the final dwell due to the decrease in resistance of the heating patch shown in Fig. 3. The integrated value of cumulative average energy is also shown in Fig. 6, but it should be kept in mind that this value is arrived at not by integration of average power along the real time axis but, rather, along the actual heating time axis (the time the heating patch is energized), which is not shown in Fig. 6. Average power dissipation while the internal heater was energized in the 6.4-mm glass/epoxy specimen was approximately 170 W.

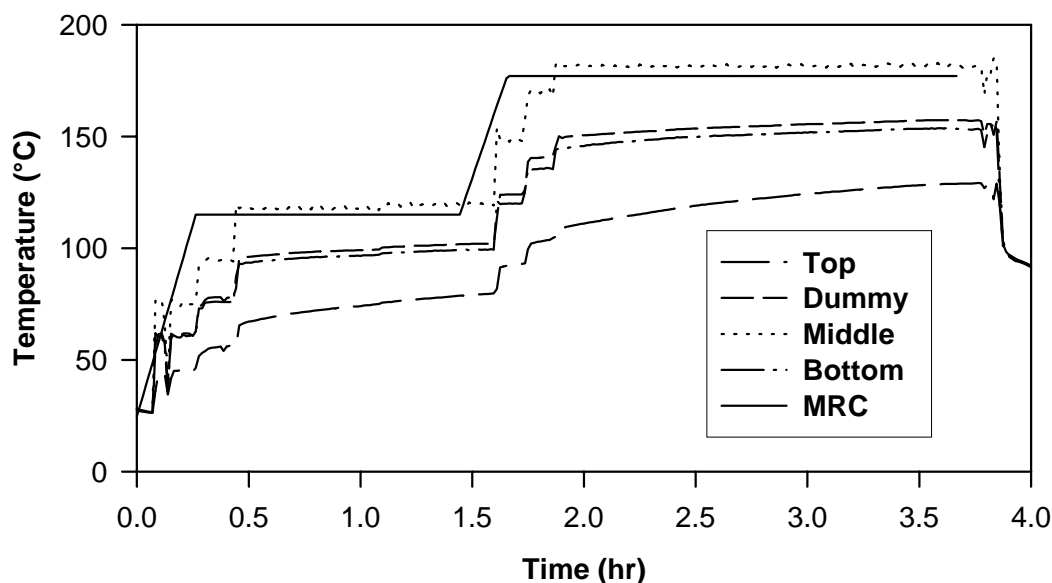


Fig. 5: Temperature profiles in a 6.4-mm carbon/epoxy laminate with one heating patch

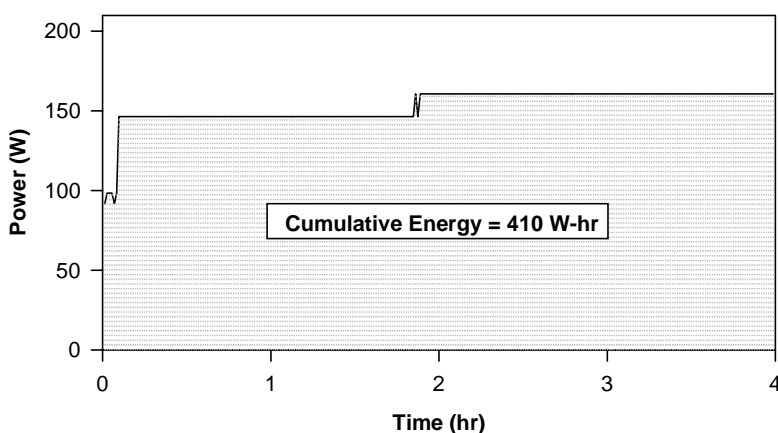


Fig. 6: Average power in a 6.4-mm carbon/epoxy specimen with one heating patch

The temperature profiles of 38.1-mm specimens indicated spatial temperature deviations of up to 60°C from the MRC cycle, mainly in the top and bottom regions of the material (Figs. 7 and 8). However, no evidence of temperature spiking was seen in any region. It is apparent that relatively more power needs to be put into the thicker materials near the extreme top and bottom of the laminates to overcome their natural tendency to become hotter near the midplane during cure. Based on visual inspection, it was observed that the 38.1-mm laminates did not fully cure near the outer extreme positions in the mold due to the cooler temperature there.

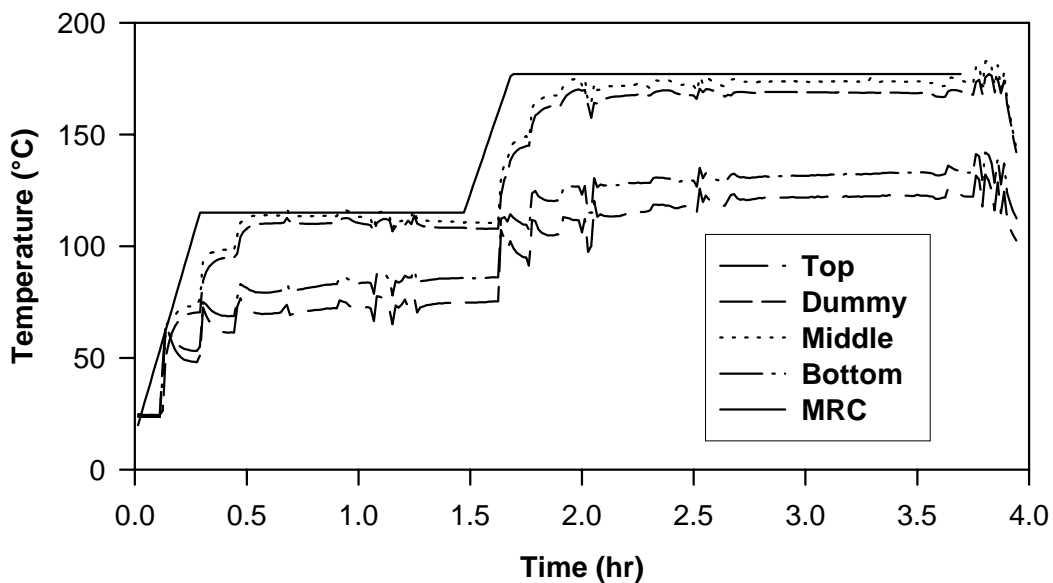


Fig. 7: Temperature profiles in a 38.1-mm glass/epoxy laminate with three heating patches

The average power dissipation of the three internal heaters when energized in either 38.1-mm specimen was approximately 150 W. The cumulative average energy dissipations of the 38.1-mm specimens are compared to those of the 6.4-mm specimens in Table 1. Cumulative energies of the 38.1-mm specimens are similar to each other and five to ten times less than those of the thinner specimens, regardless of material type. The results therefore do not indicate a strong link between fiber type and energy required to cure. There is, however, a strong indication that thinner laminates take more energy per unit volume to cure than do thick laminates.

CONCLUSIONS

In this investigation of 6.4- and 38.1-mm-thick laminates composed of glass/epoxy and carbon/epoxy prepreg, minor temperature undershoots and overshoots were recorded in specimens cured in a hot press according to the manufacturer's recommended cure cycle, particularly in the thickest glass/epoxy laminate. These results suggested that material type and thickness play a role in the ability to control temperature uniformly in a hot press.

Resistance of the carbon veil (patch) material used to promote curing by internally heating the laminates while compaction pressure was applied by a press dropped by approximately 33% due to the application of pressure. No other factors such as resin infusion, temperature change, or degree of cure affected patch resistance. Variations of up to 15°C in temperature across the plane of a typical carbon patch during cure were attributed to areal nonuniformities of patch composition.

Typical values of average power dissipated in all specimens when the internal heaters were energized were between 150 and 170 W. This amount of power was unable to fully cure the 38.1-mm glass/epoxy laminate in certain regions, but all other specimens appeared to be fully cured and well consolidated. Cumulative energies used were somewhat lower in the thicker specimens (240-320 W·hr) than in the thinner specimens (410-470 W·hr). The energy per unit volume applied to the thin specimens was 5-10 times that applied to the thick specimens, which may be related to the higher surface-to-volume ratio of the thin specimens and the higher resulting heat loss to the environment. However, the differing thermal characteristics of the carbon and glass fibers did not correlate with significantly different energy consumptions per unit volume of material. No temperature spikes were observed in the internally-heated specimens, although it is clear that more energy needs to be applied near the exterior regions of thicker specimens due to their tendency to become hottest in the interior regions during cure.

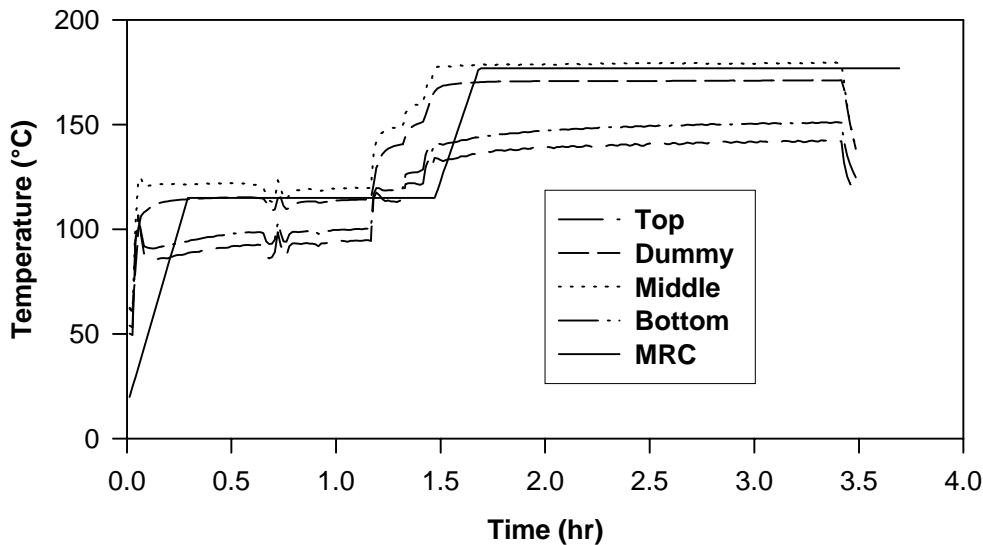


Fig. 8: Temperature profiles in a 38.1-mm carbon/epoxy laminate with three heating patches

Table 1: Dimensions and energy values for carbon/epoxy (c) and glass/epoxy (g) specimens

Specimen	No. Plies	Actual Thickness (mm)	Volume (cm ³)	Energy (W·hr)	Energy/Volume (W·hr/mm ³)
6.4-mm c	66	8.4	108.2	410	3.8
6.4-mm g	50	6.1	78.7	470	6.0
38.1-mm c	300	35.6	458.8	320	0.70
38.1-mm g	300	35.6	458.8	240	0.52

ACKNOWLEDGMENTS

The authors would like to thank McDonnell Douglas Aerospace Corporation of St. Louis, MO, for donating prepreg and the Composites Manufacturing Technology Center for providing processing supplies and equipment to carry out this work. Prof. Renata S. Engel provided many useful suggestions and much advice during the course of this work. Mr. Chris Congdon, Dr. Chris Gabrys, Mr. Ryan Emerson, Mr. Mike Croyle, and Mr. Steve Weller provided valuable technical assistance in the laboratory.

REFERENCES

1. Scott, E.P. and Beck, J.V., "Estimation of Thermal Properties in Carbon/Epoxy Composite Materials during Cure," *Journal of Composite Materials*, Vol. 26, No. 1, 1992, pp. 20-36.
2. Kenny, J.M., "Application of Modeling to the Control and Optimization of Composites Processing," *Composite Structures*, Vol. 27, Nos. 1,2, 1994, pp. 129-139.
3. Butler, D. and Engel, R.S., "On the Use of Embedded Graphite Patches for Cure in Resin Transfer Molding," *Proceedings Tenth International Conference on Composite Materials*, Whistler, British Columbia, Canada, August 14-18, 1995, Vol. III: Processing and Manufacturing, Poursatip, A. and Street, K., Eds., pp. 269-276.
4. Kenny, J.M., Apicella, A., and Nicolais, L., "A Model for the Thermal Chemorheological Behavior of Thermosets. I: Processing of Epoxy-Based Composites," *Polymer Engineering and Science*, Vol. 29, No. 15, 1989, pp. 973-983.
5. Kim, C., Teng, H., Tucker, C.L. III, and White, S.R., "The Continuous Curing Process for Thermoset Polymer Composites. Part 1: Modeling and Demonstration," *Journal of Composite Materials*, Vol. 29, No. 9, 1995, pp. 1222-1253.
6. White, S.R., and Kim, Y.K., "Effects of Staged Curing on Mechanical Properties of Thermosetting Matrix Composites," *Proceedings American Society for Composites, Seventh Technical Conference*, University Park, Pennsylvania, October 13-15, 1992, pp. 69-77.

OPTIMIZED CURE CYCLE TO MINIMIZE FIBER STRESSES IN POLYMER MATRIX COMPOSITES

Mohamed S. Genidy¹, Madhu. S. Madhukar¹ and John D. Russell²

¹*Department of Mechanical, Aerospace and Engineering Science
The University of Tennessee, Knoxville, Tennessee 37996, USA*

²*Wright Laboratory, Materials Directorate (WL/MLBC B654), 2941 P St. Ste 1
Wright Patterson Air Force Base, Dayton OH 45433-7750, USA*

SUMMARY: A technique for the cure cycle optimization for a thermoset polymer matrix composites is developed. In this technique, a given polymer is cured around a pretensioned fiber. As the curing continues, the volume of polymer changes due to its thermal expansion and polymerization shrinkage. The matrix volume change occurring after the point in the cure cycle when fiber-matrix interface has developed enough shear strength affects the fiber tension. An automated feedback system is developed to change the heating rate proportional to the change in fiber tension so as to produce the minimum fiber tension change. Such a cure cycle is defined as the optimum. The volumetric dilatometer is also used to independently monitor the matrix volume change during the standard and the optimum cure cycles. The comparison between the two techniques show that the cure cycle that produces minimum change in fiber tension also produces minimum change in polymer volume.

KEYWORDS: cure cycle, cure shrinkage, thermal expansion, residual stresses, polymerization

INTRODUCTION

Several studies have been conducted to understand the cure kinetics of thermoset resins [1,2]. One of the main objectives of these studies has been to understand how the chemical and thermal changes encountered during curing of these resins lead to the residual stresses in composites [3,4]. The effect of residual stresses generated during curing is reflected in the mechanical properties of cured composites [5]. In calculating the thermal residual stress in composites, a stress-free state at the highest temperature in the curing cycle is commonly assumed. Thus the attention is focused on the optimization of the cooling path so as to minimize the residual stresses in composites. However, before the cooldown begins, the matrix undergoes significant volume changes [6,7]. These volume changes also produce residual stress in composites. This residual stress is then relieved by several mechanisms such as fiber waviness, warping, delamination, and microcracking. The volume change during the cure of a conventional polymer resin is displayed in Figure 1 [7]. Cure shrinkage of the thermosets can be divided into polymerization and thermal shrinkage. Thermal expansion is seen in region 1 as the polymer is heated. Polymerization shrinkage (region 2) occurs during crosslinking and depends on the chemical composition and polymerization reaction (i.e. addition versus condensation reactions) [8]. A polymer is more dense than its monomer, and the resulting shrinkage upon polymerization can reach 10 to 20% [9]. In region 3, the system

has equilibrated after the completion of polymerization. In region 4, thermal contraction is seen as the polymer cools.

The technique used in this study relies on utilizing the fiber tension change when a polymer is cured around the fiber to determine the optimum cure cycle. A typical result of fiber tension change during the standard cure cycle for a carbon/ epoxy composite is shown in Figure 2 [10]. When the temperature is increased from the first dwell to the second dwell period, the fiber tension drops because of matrix thermal expansion. During the second dwell period the fiber tension begins to increase because of matrix shrinkage produced by its crosslinking. Then, the fiber tension remains unchanged suggesting that the system has reached equilibrium and the matrix polymerization is complete. Finally, during the cooldown the matrix thermal shrinkage produces an increase in fiber tension. The fiber tension change profile (Figure 2) correlate quite well with the matrix volume change curve (Figure 1).

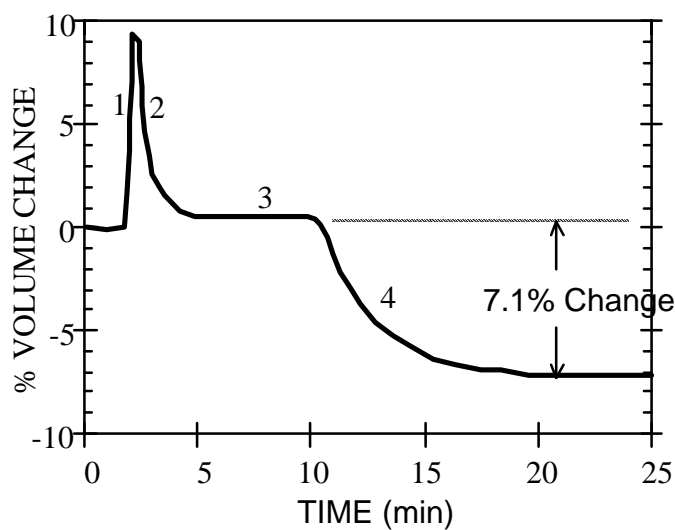


Figure 1: Volume change during cure of a conventional polyester resin (data from ref. 7).

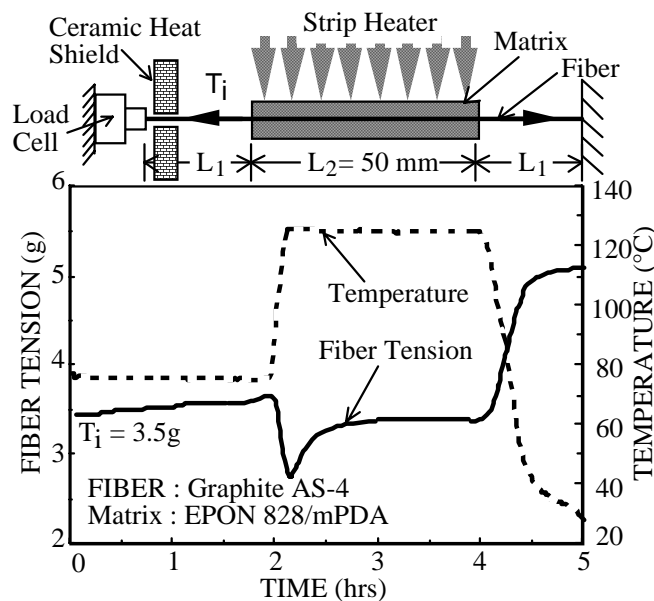


Figure 2: Change in fiber tension during the standard cure cycle of a single fiber gr/ep composite.

This paper presents a method to obtain an optimum cure cycle for a given fiber-matrix system. The optimum cure cycle has been considered to be the one which produces minimum change in fiber tension during the cure cycle. The results are independently verified by determining the matrix volume change using volumetric dilatometry.

EXPERIMENTAL METHOD

Material

The materials used in this study were AS4 graphite fiber and 3501-6 epoxy resin, both obtained from Hercules.

Cure Cycle Optimization Procedure

The procedure involves applying a known tension to a fiber having fixed ends, and then monitoring the change in the fiber tension when the matrix around the fiber is subjected to a given temperature-time curing cycle. One end of the fiber is fixed to a rigid support. The other end of the fiber is passed through a cavity in a silicone mold and glued to a load cell. The thickness of the base and sides of the silicone mold were kept as small as possible (about 0.3 mm) to minimize the effect of silicone mold volume change on experimental results. A predetermined tension is applied to the fiber. The silicone cavity is filled with the degassed polymer and the cure cycle is applied by a strip-heater (see the top insert of Figure 2). The temperature is controlled by a computer. A ceramic plate is placed between the heated zone and the load cell to prevent heating of the load cell. The temperature is monitored by means of a thermocouple placed beside the specimen. The output from the load cell and the thermocouple is recorded during the entire curing process. A fiber pretension of 5 g was applied in all experiments.

A closed-loop feedback control system is developed which is based on the assumption that it is possible to find a cure cycle in which the polymer thermal expansion is simultaneously canceled by its cure shrinkage. The flow chart of the feedback system is shown in Figure 3. In this system, the polymer is heated to a temperature when the fiber tension begins to change. At this point, the polymer crosslinking has reached a state when the polymer volume changes affect the fiber tension. At this instant, the feedback system is turned on. The computer program automatically changes the heating rate once every minute proportional to the fiber tension change. An increase in fiber tension implies that the polymer is shrinking. Hence, the heating rate is increased to minimize the shrinkage with the thermal expansion. Similarly, when fiber tension decreases, the heating rate is decreased to allow cancellation of the thermal expansion part of polymer volume change with polymer cure shrinkage. The feedback system turns off the heat when there is no change in the fiber tension during a 30 min. temperature hold. The constant fiber tension implies that there is no polymer volume change hence the cure is complete.

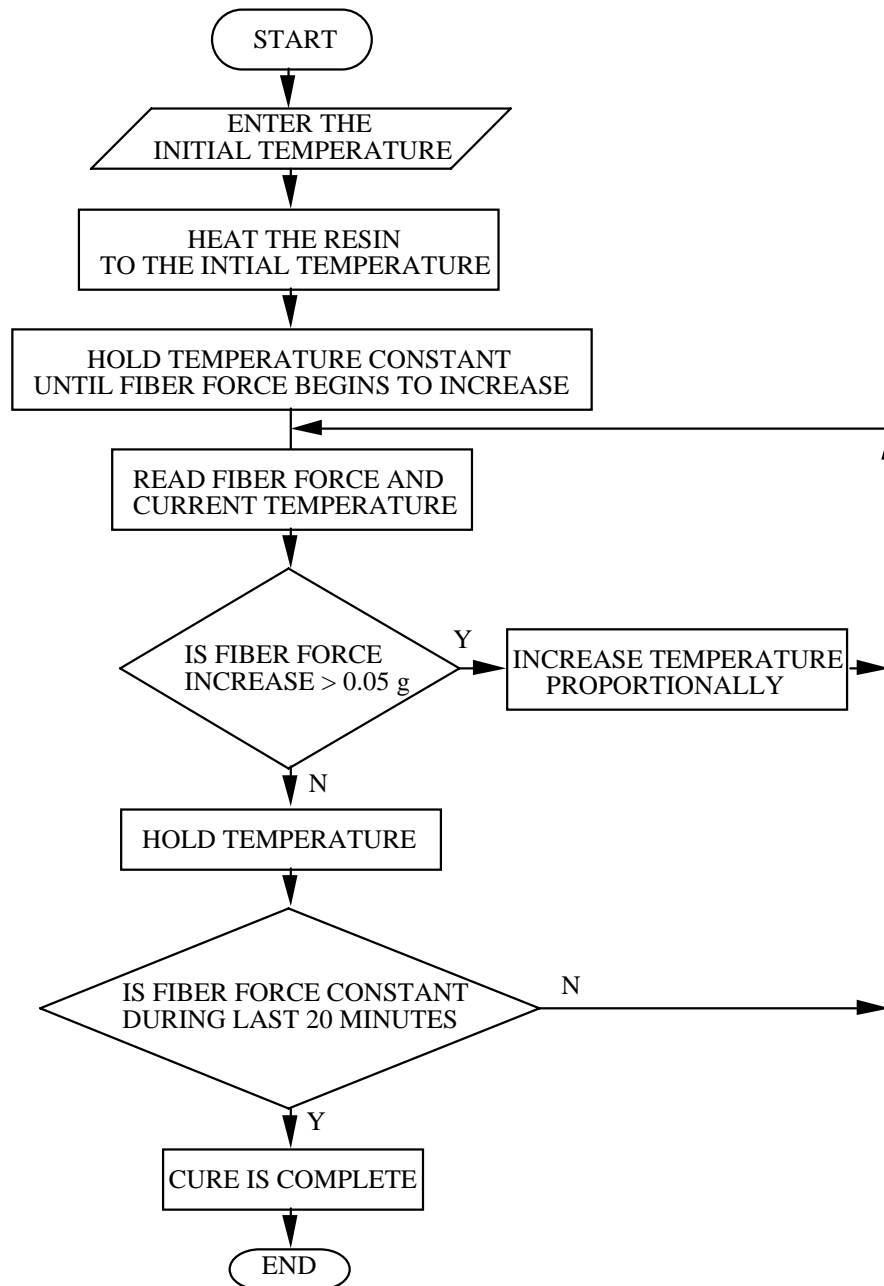


Figure 3. The flow chart of the closed-loop feedback system for obtaining the optimum cure cycle for a given fiber-matrix system.

Volumetric Dilatometry

The volumetric dilatometer used was the GNOMIX, Inc. PVT Apparatus. This equipment has been described in detail in ref. [11]. Samples from 0.5 to 1.0 g of 3501-6 resin were used. Samples were cured using the same cure cycle as used in the fiber tension experiments. A constant pressure of 10 MPa was always maintained on the sample to prevent any evaporation of mercury, which boils at 357°C (675°F) at atmospheric pressure. The sample volume was recorded once every minute.

RESULTS AND DISCUSSION

Standard Cure Cycle

The standard cure cycle for the 3501-6 epoxy resin consists of: heating the sample from room temperature to 116°C (240°F) in 30 minutes; hold the temperature at 116°C (240°F) for 60 minutes; raise the temperature from 116°C (240°F) to 177°C (350°F) in 25 minutes; hold the temperature at 177°C (350°F) for 240 minutes; cool the sample to room temperature in 60 minutes.

Figure 4 shows fiber force profile when the standard cure cycle is applied. During temperature increase from room to the first dwell at 116°C (240°F), the fiber force does not change significantly because the polymer is still able to freely flow around the fiber. As the heating starts again to raise the temperature to the second dwell at 177°C (350°F), a drop in the fiber tension is noticed. At this stage the matrix has polymerized to the point that matrix volume change can now affect the fiber tension. During this period both thermal expansion and crosslinking shrinkage of polymer occurs. However, the thermal expansion part of the matrix dominates over its crosslinking shrinkage because of the rapid heating rate. Hence, the net effect is a drop in the fiber load during this temperature increase. During the temperature hold at 177°C (350°F), the matrix thermal expansion stops, however, the volume shrinkage due to its crosslinking continues resulting in an increase in fiber force until it has reached a constant value. At this point, the resin cure is believed to be completed which results in an almost flat curve for the fiber force. During the cooldown, a decrease in matrix volume produces an increase in fiber load. The test was repeated three times using the same cure cycle and similar results were obtained.

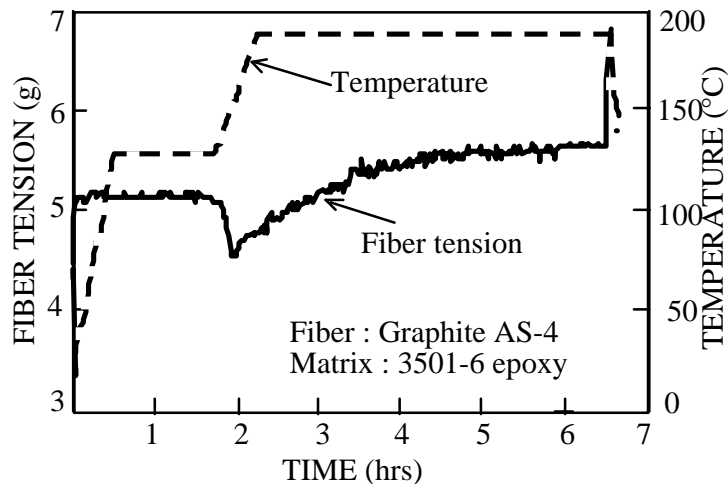


Figure 4: Fiber tension profile during the standard cure cycle.

Figure 5 shows the volume change of the resin using the volumetric dilatometer during the standard cure cycle. The results correlate well with the proposed mechanisms that produced fiber load change (Figures 4 and 5). The only difference is that while the volumetric dilatometry can detect the matrix volume change at all instances of the cure cycle, the fiber tension experiment is able to respond to the matrix volume changes only after matrix polymerization has reached a critical point when fiber-matrix interface has developed enough shear strength. This critical point occurs towards the end of the first dwell period. That is why the matrix volume change detected by the volumetric dilatometer during the first temperature increase does not correspond with the fiber tension plot. However, during the

second temperature increase and the subsequent temperature hold, both techniques provide the same conclusion in regard to matrix volume change, that is, a net volume increase of matrix during the temperature increase from 116°C (240°F) to 177°C (350°F) followed by polymerization induced volume shrinkage during the temperature hold. Also, as the polymerization is completed (after about 4 hours), both fiber tension and volume change curves reach a plateau (Figures 4 and 5) until cooldown begins at which point the matrix volume begins to decrease.

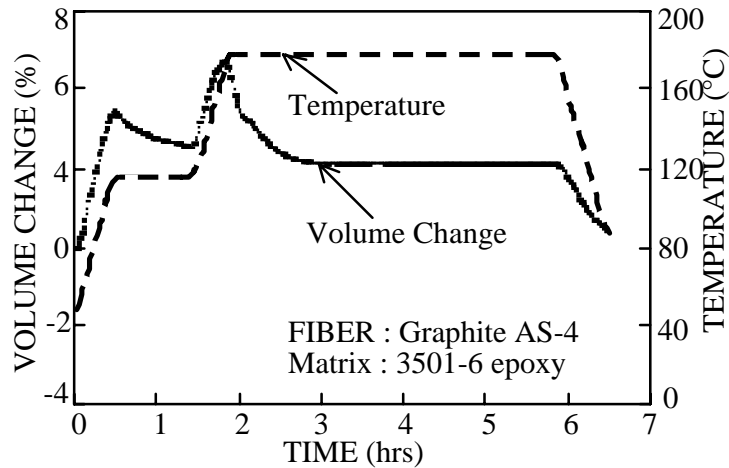


Figure 5: Polymer volume change during the standard cure cycle.. A significant volume change occurs during the standard cure cycle.

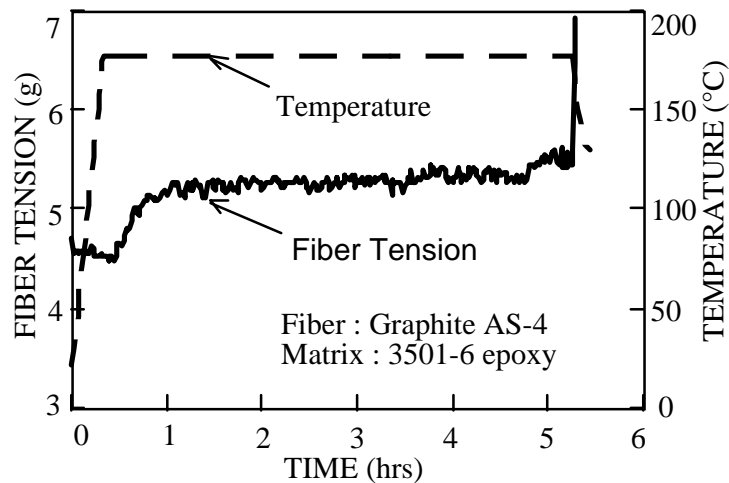


Figure 6: Fiber tension profile during temperature hold period. The increase in fiber load is due to cure shrinkage of the matrix.

To further verify the proposed mechanism that produce change in fiber tension, another cure cycle was applied in which the first temperature hold at 116°C (240°F) was eliminated and the temperature was rapidly raised to the second dwell at 177°C (350°F), and then held constant, Figure 6. In such heating cycle since all the thermal expansion occurs when matrix is still able to flow around the fiber, it is believed that the only source of volume changes during the temperature hold that can be detected by the pretensioned fiber is the cure shrinkage. In such case, the fiber force is expected to increase with the degree of cure until the cure is completed

at which point there should be no change in the fiber force. Figure 6 shows the results obtained for this cure cycle which agree with the results expected with the proposed volume change mechanisms.

Optimum Cure Cycle

The matrix volume changes that occur during that standard cure cycle are undesirable as they produce curing induced fiber stresses which may cause fiber fracture [10] and fiber waviness [12]. The situation can be corrected by finding an optimum cycle that produces the minimum amount of matrix volume change. Using the fiber tension experiment, two approaches were adopted to find such a cure cycle, namely a trial-and-error approach and a feedback control system. These two methods and the results are described below.

Trial-And-Error Approach

A trial-and-error approach was first taken to find a cure cycle in which there is a simultaneous shrinkage due to cure and expansion due to thermal expansion of the same magnitude. For such a cure cycle the matrix volume and hence the fiber force will remain constant. Several different cure cycle experiments were conducted in which each cure cycle was modified based on the results obtained from the previous cure cycles. In all these cure cycles the curing was considered to be complete when there was no change in fiber tension during a 30 minute temperature hold period. The tests were continued until the cure cycle that produced the minimum matrix volume change was obtained. It usually took about four to five iterations to find an optimum cure cycle. Figure 7 shows the load and temperature profile for what is believed to be an optimum cure cycle for this particular type of resins. In this cycle the temperature is first increased linearly room temperature to 138°C (280°F) in 30 minutes and then again increased linearly to 177°C (350°F) in 210 minutes followed by a 30 minute hold at 177°C (350°F). It is believed that during the first 100 minutes of curing, the matrix is still able to freely flow around the fiber. As a result, any matrix volume change during this period is not detected by the fiber. After that time, matrix thermal expansion produced by the slow temperature increase is simultaneously canceled by its cure shrinkage which produces almost no net volume change and hence no fiber tension change.

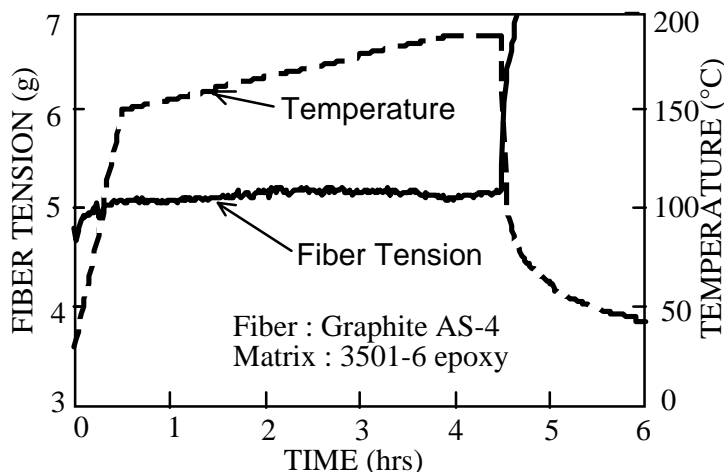


Figure 7: The optimum cure cycle obtained using trial-and-error approach. The flat fiber tension curve indicates minimum matrix volume change.

The cure cycle obtained using the trial-and-error method was also used in volumetric dilatometry studies. The results are shown in Figure 8. It should be noted that the initial changes in polymer volume (during the first 100 minutes) do not affect the fiber force since the bond between the fiber and the resin is not fully developed yet. One more interesting observation that can be made from the comparison of the net matrix volume change in the standard and optimized cure cycles is that just prior to the start of cooldown the standard cure cycle produces larger net volume change (about 2%) compared to almost 0% net volume change in the optimum cure cycle (Figures 5 and 8). This may have important implication in the residual stresses developed in closed-mold processes.

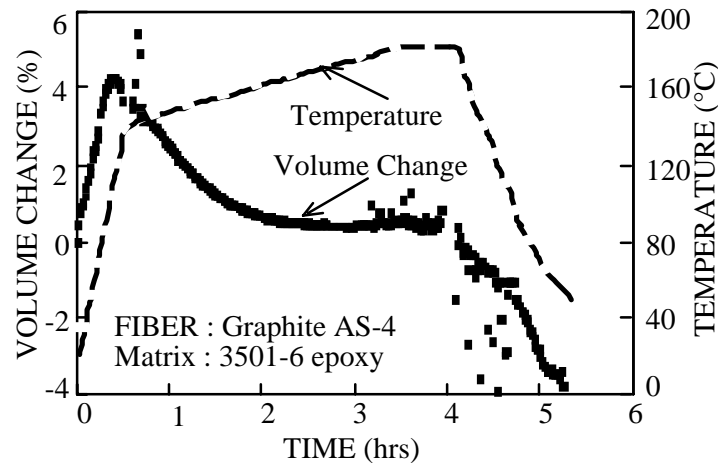


Figure 8: Polymer volume change during the optimum cure cycle. The volume change profiles correlates well the fiber tension change during the same cure cycle (Figure 7).

Feed-back Control System

In another approach to finding an optimum cure cycle for a given fiber-matrix system, a computerized closed-loop feedback control system was developed. The details of the procedure are described in Experimental Method section.

Figure 9 shows results obtained using the feedback system for the same resin used in the trial-and-error approach. It can be seen that the fiber tension plot is almost completely flat. Also the heating rate is not linear as was used in the trial-and-error approach. The instantaneous correction in the heating rate to maintain a constant fiber tension allows the determination of an optimum cure cycle where there is almost complete cancellation of the matrix thermal expansion by its cure shrinkage.

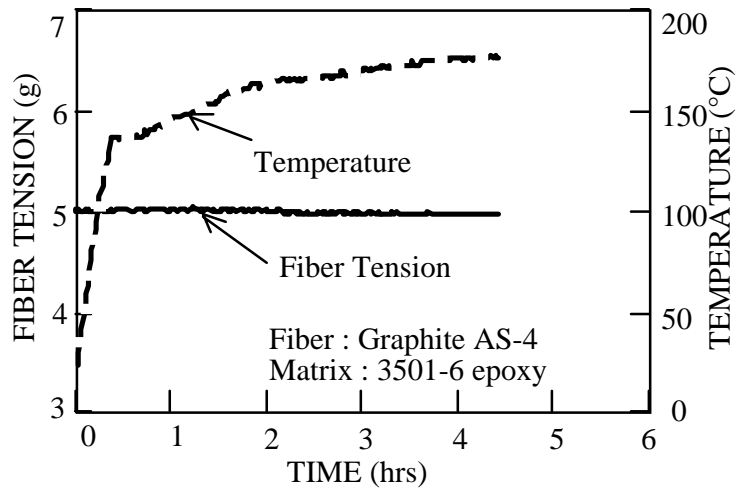


Figure 9: The optimum cure cycle obtained using feedback control system. The flat fiber tension curve indicates minimum matrix volume change

Mechanical Properties

Some preliminary 3-point flexure experiments were also conducted on resin samples cured using the standard and optimum cure cycles. 3 specimens were tested for each case. The average flexural moduli of specimens cured using the standard the optimized cure cycles were 4.9 GPa, and 5.3 GPa, respectively. Considering the experimental scatter, these difference are not considered statistically significant. Hence, it was concluded that modifying the cure cycle did not change the polymer mechanical properties. Additional work on the effect of cure cycle on polymer glass transition temperature, and its strength and toughness is currently underway.

CONCLUSIONS

A new method is developed to understand mechanism of polymer resin cure in composite materials. The method is based on an observation that when a polymer matrix is cured around pretensioned fiber, it causes a change in fiber tension. The method was used to obtain a cure cycle that is considered to be optimum in the sense that it results in minimum change in the fiber stresses during cure. The fiber tension data is correlated with independent experiments on volumetric dilatometry. The volumetric dilatometer experiments show that there is a significant matrix volume change when a standard cure cycle is used. The optimized cure cycle results in minimum matrix volume change by allowing the matrix thermal expansion and cure shrinkage to occur simultaneously thus cancel each other out. Composite materials cured using such optimum cycles may have better dimensional stability and less likelihood of fiber failure, fiber waviness, etc. The developed procedure can also be used to detect the completeness of the resin cure which may result in a shorter cure cycle.

ACKNOWLEDGMENTS

The authors wish to thank Wright Laboratory, Materials Directorate for the majority of the support for this research (contract # F49620-96-1-0085). The assistance of Chad Davis, undergraduate research assistant throughout this study is gratefully acknowledged.

REFERENCES

1. Loos, A. C. and Springer, G. S., "Curing of Epoxy Matrix Composites", *Journal of Composite Materials* Vol. 17, 1983, pp. 135-169.
2. Hodges, J., Yates B., Darby, M. I., Wostenholm, G. H., Clemmet, J.F., and Keates, T.F., "Residual Stresses and Optimum Cure Cycle for an Epoxy Resin", *Journal of Materials Science*, Vol. 24, 1989, pp. 1984-1990.
3. Pagano, N. J. and Hahn, H. T., "Evaluation of Composite Curing Stresses", *Composite Materials: Testing and Design (Fourth Conference)*, ASTM STP 617, American Society for Testing and Materials, 1977, pp. 317-329.
4. White, S. R. and Hahn, H. T., "Process Modeling of Composite Materials: Residual Stress Development During Cure. Part II. Experimental Validation", *Journal of Composite Materials*, Vol. 26, 1992, pp. 2423-2453.
5. Lee, S. and Springer, G. S., "Effects of Cure on the Mechanical Properties of Composites", *Journal of Composite Materials*, Vol. 22, 1988, pp. 15-29.
6. Russell, J. D., "Cure Shrinkage of Thermoset Composites", *SAMPE Quarterly*, Vol. 24, No. 2, 1993, pp. 28-33.
7. Kroekel, C.H. and Bartkus, E.L., "Low Shrink Polyester Resins: Performance and Application", *Annual Conference, Reinforced Plastics/Composites Institute*, 1968, Brookfield Center CT: SPI.
8. Daniel, I.M., Wang, T.M., Karalekas, D. and Gotro, J.T., "Determination of Chemical Cure Shrinkage in Composite Laminates", *Journal of Composites Technology and Research*, Vol. 12, No. 3, 1990, p. 172.
9. Rodriquez, F., *Principles of Polymer Systems*, 3rd ed. New York: Hemisphere, 1989.
10. Madhukar, M.S., Kosuri, R. P., and Bowles, K.J., "Reduction of Curing Induced Fiber Stresses by Cure Cycle Optimization in Polymer Matrix Composites", *Proceedings of Tenth International Conference on Composite Materials*, Whistler, British Columbia, Canada, August 14-18, 1995, Vol. III: Processing and Manufacturing, Poursartip, A. and Street, K.N., Eds. pp. 157-164.
11. Russell, J.D., "Analysis of Viscoelastic Properties of High-Temperature Polymers Using a Thermodynamic Equation of State", *M.S. Thesis*, 1991, University of Dayton, Ohio, USA.
12. Madhukar, M.S. and Dutta, P.K., "Effect of Matrix Stiffness on Wavy Fiber Behavior in Single-Carbon-Fiber-Epoxy Composites", *Special Report 94-10, April 1994, U.S. Army Corps of Engineers, Cold Regions Research & Engineering Laboratory (CRREL)*, Hanover, New Hampshire, USA.

BISALLYLOXYIMIDES- NEW CO-REACTANTS FOR BISMALEIMIDES

T. C. Morton and B. Dao

CSIRO, Division of Chemicals and Polymers, Private Bag 10, Clayton South MDC, Victoria 3169, Australia

SUMMARY: This paper describes investigations on a new class of reactive monomer which can be used as a co-reactant in thermosetting polyimide matrix resins. The new materials offer a number of advantages over the commonly used co-reactants for bismaleimides including improved thermal stability, higher T_g and in some cases better resin flow properties. When these new materials are mixed with suitable bismaleimide monomers and applied to suitable reinforcing fibres such as carbon, they can be cured into useful composites having substantially improved thermal stabilities as judged from thermal weight loss at 204_C and 250_C. The preparation of polyimide oligomers with N-allyloxyimide end-caps for use as co-reactants or flow and toughness modifiers in other polyimide resins is also described.

KEYWORDS: Bisallyloxyimides, bismaleimide co-reactants, thermally stable polyimides

INTRODUCTION

Bismaleimide terminated compounds are well known resin types used in the preparation of thermosetting polyimides [1]. Compared with other polyimide thermosets, bismaleimides offer the advantage of having processing and curing requirements closest to those of high performance epoxy systems. In view of their generally higher thermal stability compared to epoxies, they have been attractive for advanced composite, and other applications, requiring higher temperature capability. The versatile chemistry of the maleimide moiety permits reaction with a range of other groups to make co-polymers of great value as resin matrices with special properties.

The maleimide double bond is electron deficient and highly reactive to nucleophiles. Thus amines, hydrazides and thiols readily undergo a Michael type addition across the double bond to give substituted succinimides. Dienes can undergo Diels-Alder addition with the maleimide double bond to give fused six member ring structures which can often be aromatized [1]. However the most commonly used co-reactants are carbon substituted bisallyl compounds, the allyl groups of which undergo an ene reaction with the maleimide to form styrene derivatives which react with additional maleimide to form a complex cross-linked, partially aromatized structure. The nature of this cure structure appears to limit the thermo-oxidative stability of the matrix and makes conventional bismaleimides unsuitable for really high temperature applications. Typically, a laminate made from such a system will lose from 4-10% of its weight on thermally aging at 204_C for six months. These allyl co-reactants can be as simple as 3,3'-diallylbisphenol A (MATB) as used in the Matrimid™5292 commercial bismaleimide system or larger molecular weight materials such as the bis[2-allylphenoxy]phthalimides developed by Stenzenberger and Konig [2]. The present work was

initiated as an investigation into alternative cure chemistries for bismaleimides as it was believed that given the right chemistry the above thermal stability limitations could be overcome.

Simple allyloxyimides have been studied as initiators in free radical polymerization. Thus Druliner [3] reports the use of N-allyloxyphthalimide as an initiator in acrylate polymerization. However most of the allyloxyimides reported in the literature have either been used as synthetic intermediates in the preparation of allyloxyamines or have been synthesised for biological screening programs. Diallyloxyimides do not appear to have been described previously in the scientific literature.

Some preliminary experiments with N-allyloxyphthalimide and N-phenylmaleimide showed that a reaction took place on heating these two materials which appeared to involve the formation of a polymer. Therefore the previously unknown bisallyloxyimides (Fig.1) were synthesized and investigated as potential co-reactants for bismaleimides. These compounds are the subject of Patent application [4].

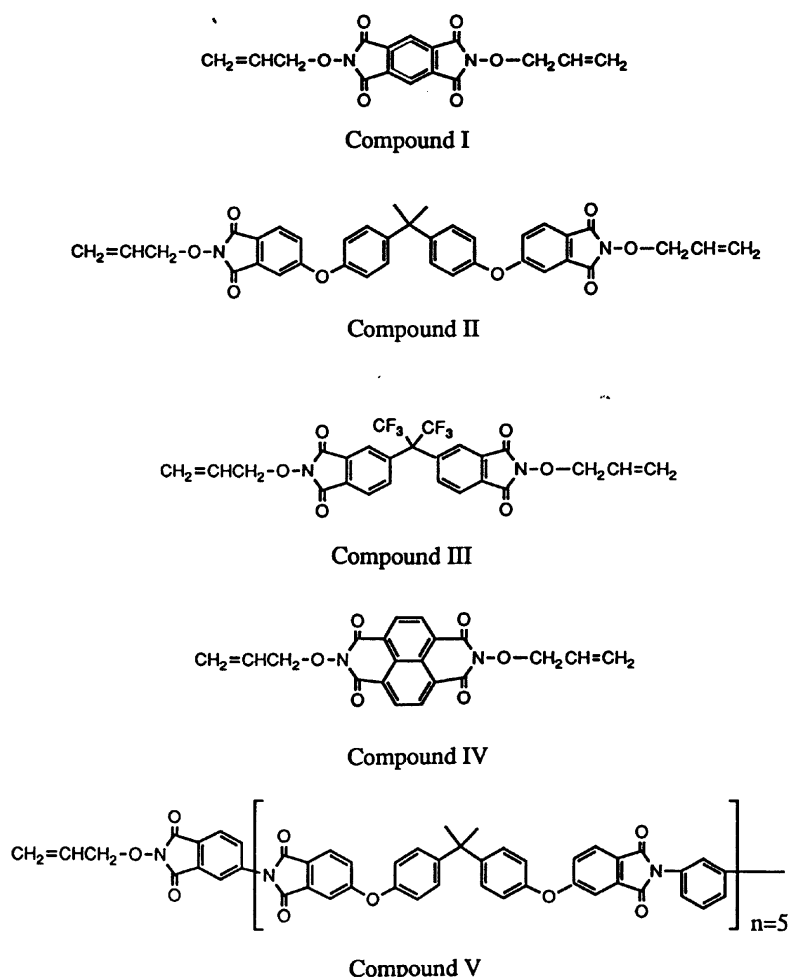


Figure 1: Structures of the new compounds

EXPERIMENTAL DETAILS

Characterization

All bisallyloxyimides were characterized by NMR, IR and MS, and also by GPC if they were soluble in THF. FTIR spectra were obtained by a variety of techniques ranging from films to reflectance methods using either a Bomem Michelson Series or a Mattson high-resolution FTIR instrument. NMR spectra were recorded in either CDCl₃, CDCl₃ containing a trace of MeOH-d₄ or in DMSO-d₆ using Bruker AC200, 250NMR or DRX500 spectrometers. Mass spectra were obtained on a Jeol JMS-DX303 mass spectrometer, using Fast Atom Bombardment or Field Desorption techniques. GPC analysis was carried out at 30°C using a Waters 150-C GPC with Ultrastaygel columns. Molecular weights were calibrated with respect to polyimide standards. HPLC analyses were performed using a Shimadzu LC-4A instrument fitted with an Altex Ultrasphere octadecyl silanized (ODS) reverse phase column using gradients of methanol/water. Mettler TA3000 and TA4000 thermal analysis instruments were used for differential scanning calorimetry (DSC) and thermal gravimetric analysis (TGA). DSC experiments were carried out under nitrogen at a scan rate of 10°C/min. Dynamic mechanical thermal analyses (DMTA) were run on a Polymer Laboratories Mk2 instrument. Fracture toughness data was obtained following the approach of Hinkley [5] or alternatively by a Double-Torsion method [6]. Neat resin static compressive properties were determined according to ASTM D695M-85, or indirectly from the laminate in-plane shear modulus using a micromechanical calculation. Flexural modulus was determined using ASTM D790M Method 1 procedure A.

Synthesis

The title compounds were made by first reacting the dianhydride with hydroxylamine in pyridine, followed by allylation. In the case of bis N-allyloxyimide end capped oligoimides, the oligomers were made by standard procedures [7] and then end-capped by a variation of the procedure described below.

2,6-diallyloxybenzo[1,2-c:4,5-c']-dipyrrole-1,3,5,7(1H,6H)-tetrone.
Compound I (DAPMI)

A solution of hydroxylamine hydrochloride (107g, 1.54 mole) in pyridine (1l) in a three necked flask fitted with thermometer, mechanical stirrer, reflux condenser and blanketed with argon was cooled to 30°C and pyromellitic anhydride (152.7g, 0.7 mole) was added. The mixture was stirred at room temperature for 10-15 minutes during which the exotherm raised the temperature rose from 30 to 45°C. The mixture was then heated to 90°C for 45 min. At the end of this time, the reaction mixture was cooled and the fine precipitate filtered off, washed with water (the red anion is present in basic aqueous medium), dilute acetic acid and then finally with water to yield the dihydroxy compound as a cream powder, mp 300-303°C, 111.7g (64.3%).

The dihydroxy compound (74.4g, 0.3 mole) in a mixture of dry DMF (300ml) and triethylamine (0.6 mole, g, 83.7ml) was stirred at room temperature. Allyl bromide (87.12g, 62.33 ml, 0.72 mole) was added in one lot and a solution was attained while the temperature rose to 45°C. The initial red colour of the anion was dispelled after about 10 minutes and a fine precipitate formed. The mixture was stirred at room temperature for 24h and then poured into water. The precipitated product was filtered off and then washed twice with methanol and

then dried (64g, 67%). Recrystallization from dichloromethane/light petroleum yielded Compound I as colourless needles, mp 222-223°C. Mass spectrum (c.i.) 329 (M+1), 357 (M+29). ¹H nmr (CDCl₃): 4.73, m, 4H; 5.34, m, 2H; 5.42, m 2H; 6.11, m, 2H; 8.26, s, 2H. ¹³C nmr 79.14, 118.64, 123.27, 130.81, 134.81, 134.25, 161.36.

The functionality of the oligomers was obtained by consideration of ¹H NMR data and the molecular weight.

Cured Neat Resin Bars

The bismaleimides used in this study (apart from the reference material Matrimid 5292A (MAT A)) were experimental materials and their preparation and properties are described fully in reference [8]. The procedure described here is only one of a number of alternative procedures used: Two experimental bismaleimides M/pPDA/UIDA/pPDA/M (M, maleimide; pPDA, p-phenylene diamine; UIDA, ultem anhydride, called CBR330) and M/Ethacure208/M (CBR328) were preheated separately at 220°C under vacuum for 30 min to remove strongly bound solvent. CBR328 (11.2g) was then placed in a resin flask and heated to 220°C where it formed a melt, a low molecular weight thermosetting polyimide (PAB, 11g) was then added, followed by the bisallyloxyimide compound I (DAPMI) (12.43g). While there is always the chance of a run-away exotherm in these blending operations this was never experienced using the quantities described here. When a full melt had been obtained, CBR330 (20.4g) was added in portions to obtain a perfect melt which was degassed under oil pump vacuum (1-2mm) for 10 min. The melt was either transferred directly into a preheated mould or cooled, ground to a powder and compressed into a mold on the hot press. The cure was carried out in three stages: 1h at 220°C; 2h at 250°C and 2h at 280°C to give a neat resin product with T_g (by DMTA) 286°C (1Hz). Some skill and attention to detail was needed to obtain cured neat resin slabs entirely free of voids by this technique.

Preparation of Laminates

A melt was produced as above, then ground up in a mortar and pestle and the micropulverized with dichloromethane to give a suitable mixture for prepregging. SP Systems RC200P plain weavcarbon fibre cloth or equivalent was coated at a rate of 1.1g of resin/g of cloth. The prepregs were dried in warm air for 60 min and "B" staged at 110°C for 2-5 min. A 10x10cm coupon for DMTA use was typically made by aligning 5 plies of prepreg in the warp direction and hot pressing between caul plates under a low initial pressure of a few psi until the platens reached 220°C, followed by 46psi at 220°C for 1h, increasing to 115psi as the temperature is raised to 250°C for 2h and then finally 280°C for 2h.

Alternatively the laminate could be partially cured under epoxy conditions: heating 180°C for 2h, followed by 200°C for 6h, and could then be removed from the press and given a free standing post-cure of 230°C for 6h. Satisfactory laminates up to 200X150mm and 12 plies were made by these procedures.

RESULTS AND DISCUSSION

Thermal Studies

All of the bisallyloxyimides were shown to self-polymerize. When the cure of Compound I was studied DSC it showed a bimodal exotherm with individual peaks at 256 and 318°C, the total energy of which represented 200 kJ/mole of allyl group. Compound II melted at 150°C and had an exotherm peaking at 292°C (180 kJ/mole of allyl group) and Compound III, mp 58°C developed a cure peak at 313°C and yielded a cure exotherm of 255 kJ/mole for the allyl group. The N-allyloxyimide endcapped oligomer CBR371 (Mn 5493) showed an exotherm peaking at 326°C corresponding to 134 kJ/mole of allyl group.

When the blend of bismaleimides and Compound I described in Section 2.4 was run on the DSC a melting endotherm was observed at 195°C followed by the onset of a large exotherm at 230°C, peaking at 285°C. The energy yield corresponded to 195 kJ/mole of maleimide. This result is typical of those obtained with all of the allyloxyimide/bismaleimide blends; that is an exotherm peaking at lower temperature than for the bisallyloxyimide alone with about the same energy yield per mole as self-polymerization.

Neat Resin Characteristics

The bisallyloxyimides tend to have considerably lower melting points than other imide derivatives derived from the same dianhydrides and this helps significantly in processing the materials into laminates. In contrast the low minimum viscosities reached with some of these systems caused difficulty in making void-free, cured neat resin samples. The voids were generated when the low viscosities reached during cure reduced the hydraulic pressure developed within the resin inside the die thus preventing the process of squeezing out the last traces of volatiles. Table 1 summarizes some of the data obtained for selected systems. When DAPMI was used the neat resin was of comparable toughness to the commercial MATA/MATB system. The use of oligomer Compound V gave a product with higher toughness, comparable Tg and improved thermal stability. The compressive moduli that were determined by the indirect method were comparable to the values obtained for MATA/MATB by the same method.

Figure 2 shows the DMTA traces obtained from the neat resin bar made by the procedure described in Section 2.3 taken (a) immediately after cure and (b) after 14 days aging in air at 250°C. The modulus in both samples shows a marked temperature dependence. On aging there is a decrease in modulus as well as a decrease in its temperature dependence and an increase in Tg. Similar trends were observed for the other systems.

Some physical properties of cured 5 ply laminates

Table 1 summarizes properties found for some of the systems when processed into prepregs and cured into laminates. It can be seen that the oligomer CBR368 showed the best thermal stability characteristics. The Tg measured after a 7 day soak in water at 71°C is not altered significantly for the DAPMI containing system. More detailed thermal weight loss data for laminates using formulations based on Compound I (DAPMI) with the experimental bismaleimides CBR330 and M/TriMe/UIDA/TriMe/M (TriMe, 2,4,6-Trimethyl-1,3-phenylene diamine; UIDA, ultem anhydride, called CBR331), is shown in Figures 3 and 4.

The thermal aging figures of laminates at 204°C (Figure 4) showed that the CBR330/DAPMI system is superior in the long term to CBR331/DAPMI and far superior to the commercial MAT A/MAT B. Although the two former systems behave similarly for the first 6-8 weeks of aging, the weight losses on CBR331 then accelerate, whereas CBR330 maintains the steady rate. This difference is thought to be due to oxidative susceptibility of the methyl groups of backbone amine (TriMe) in CBR331 over the long term. Subsequent work on oligomeric materials is aimed at eliminating this amine.

Minimum conditions for cure

The CBR330/DAPMI system could be cured under epoxy conditions (a factor of great importance in the industry) so long as cure is completed in a free standing post cure. When two laminates were prepared from the same prepreg and one was cured according to the standard method and the other as described above, T_g values were 292 and 295°C (1Hz) respectively and the shapes of the two curves were very similar. The latter laminate did not distort on post cure and did not show any voidage.

Studies on the mechanism of the curing reaction

A number of model systems have been examined to obtain an insight as to the nature of the interaction between bismaleimides and allyloxyimides during cure. As expected, an addition to the maleimide double bond is involved because succinimide species are produced. This was demonstrated by the observation of succinimide H3 and H4 protons in the ¹H NMR spectrum in the reaction product from N-n-butylmaleimide and N-allyloxyphthalimide. There is also evidence from this model system for an exchange reaction involving migration of the amine of the maleimide into the phthalimide ring. We have shown in an ESR study [9] that the onset of cure in a maleimide /DAPMI system is associated with the generation of vastly increased amounts of free radical species at around 250°C. Further work is in progress.

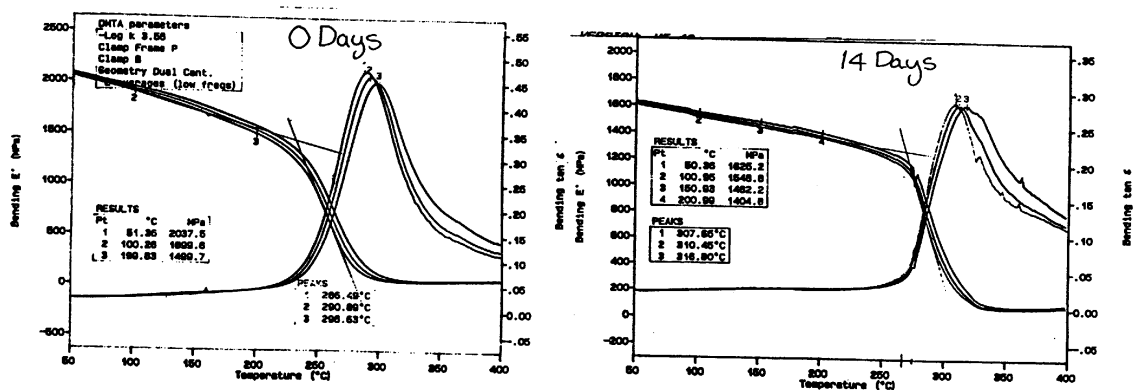


Figure 2. Changes observed in the DMTA curves obtained for cured neat resin on 14 day aging at 250°C. System: CBR330/CBR328/DAPMI/PAB see text.

Table 1. Summary of all Properties of Selected Experimental Bismaleimides With the best all round properties

	CBR330/ MATB	CBR330/ DAPMI	CBR331/ MATB	CBR331/ DAPMI	CBR330/ CBR368	MATA/ MATB
Tg neat resin°C	251 (220)	286 (235)	263 (225)	309 (250)	279 (240)	305
Fracture Toughness Kg MPa.m ^{1/2}		0.69			0.98	0.71
Compressive Modulus GPa			2.08±0.32			4.02±0.13
Compressive Modulus Indirect GPa		2.36+0.03	2.34±0.05			2.50±0.04
Flexural Modulus GPa	4.12+0.11		3.33 ±0.09			
Thermal Stab Wt. loss @ 250°C 1D, 7D, 14D	-1.17, 3.25, 4.68	0.3, 1.51, 2.33			0.02, 0.32, 0.77	
LAMINATE						
Tg °C (aver.)	269 (226)	265 (222)	283 (256)	304 (272)	280 (245)	299 (272)
Tg (wet) 7D at 71°C	246-241 (170)	275-269 (233)	270-263 (235)	na		307-293 (270)
Thermal Stab Wt. loss @ 250°C 1D, 7D, 14D	0.51, 1.62, 2.40	0.32, 0.73, 1.11	0.22, 1.53, 2.52	na, 0.85, 2.37	0.19, 0.24, 0.61	0.29, 1.74, 2.75
Thermal Stab Wt loss@ 204°C 1M, 3M, 6M	0.82, 1.89, 3.67	0.16, 0.77, 1.63	0.85, 3.87, 9.22	0.14, 1.63, 5.81		1.00, 3.62, 11.60
Water uptake % @71°C 1D, 7D, 14D	1.04, 1.53, 1.63	0.99, 1.35, 1.43	1.04, 1.23, 1.43			1.77, 2.27, 2.42
MEK uptake 1D, 7D, 14D	0.28, 0.65, 0.89	0.43, 0.67, 0.78	2.17, 6.76, 10.0			0.31, 0.80, 0.87
JET FUEL uptake 1D, 7D, 14D	0.11, 0.25, 0.38	0.26, 0.53, 0.73	0.51, 0.94, 1.00			0.42, 1.05, 1.33
Shear Modulus GPa		4.39 +0.06	3.86±0.11			3.70±0.07

Notes on Table

In many cases values were determined for these parameters on several laminates. In these cases the value quoted is the average value obtained.

The limits shown for mechanical properties are ± one standard deviation.

Tg is measured at 1Hz in a Polymer Labs DMTA, Tb (point of break in Modulus) is given in parenthesis values are averages where multiple determinations were available.

250°C Stabilities are quoted as weight losses after 1,7 and 14 days.

204°C Stabilities are quoted as weight losses after 1,3 and 6 months.

Indirect determination of Neat Resin Compressive modulus was via micromechanics from laminate in-plane shear modulus.

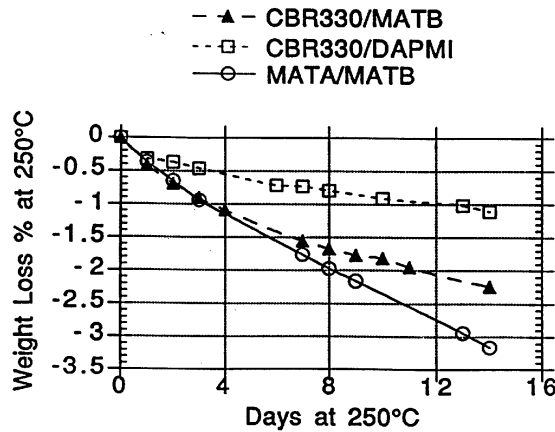
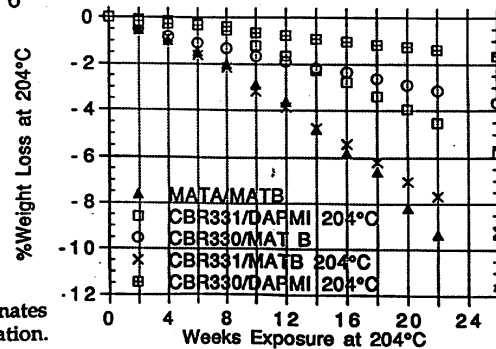


Figure 3. Comparison of weight loss data on aging of laminates at 250°C. See text for abbreviation identification.

Figure 4. Comparison of weight loss data on aging of laminates over 6 months at 204°C. See text for abbreviation identification.



CONCLUSIONS

A new class of reactive monomer with unique end groups has been developed which can be used as a co-reactant in thermosetting matrix resins for advanced composite materials. These materials offer a number of advantages over the commonly used co-reactants for bismaleimides including substantially improved thermal stability, higher T_g , in some cases better resin flow properties, and yet initial cure can still be carried out under epoxy conditions (typically 180-200°C). The new end-groups have also been incorporated into oligoimides which are still easily processible. The synthetic chemistry involved in incorporation of this end group into polyimide precursors is low cost, straight forward, high yielding and clean.

Thermal stabilities of the materials reported lie intermediate between state of the art bismaleimides and the current most highly thermally stable polyimides. Further work is in progress to improve these materials even further.

ACKNOWLEDGEMENTS

The authors wish to thank R.Varley for DMTA analysis, G. Heath for the mid- and near-IR work, I Vit and K. Smith for the mass spectral data, particularly in obtaining spectra from the very high molecular weight low volatility materials; I. Willing for high resolution NMR data, and P.Warden (CSIRO Division of Forest Products) for some of the mechanical testing and the micromechanical estimation of compressive modulus.

REFERENCES

1. Stenzenberger, H. D., "Addition Polyimides", Polyimides, Ed., Wilson, D., Stenzenberger, H. D. and Hergenrother, P. M., Blackie, Glasgow., 1990, pp 79-128.
2. Stenzenberger, H. D. and Konig, P., "Bis[3-(2-Allylphenoxy)phthalimides: A New Class of Comonomers for Bismaleimides", *High Perform. Polym.*, Vol.1, 1989, pp. 133-144.
3. Druliner, J. D., "Living Radical Polymerization Involving Oxygen-Centered Species Attached to Propagating Chain Ends", *Macromolecules*, Vol. 24, 1991, pp.6079-6082
4. Dao, B. and Morton, T. C., "Bisallyloxyimides" , US Patent Application (1995) 08/550153.
5. Hinkley, J. A., "Small Compact Tension Specimens for Polymer Toughness Screening", *J. Appl. Polym. Sci*, 32, 1986, pp. 5653-5655.
6. Pletka, B. J., Fuller, Jr., E. R., and Koepke B. G., "An Evaluation of Double Torsion Testing-Experimental", *Fracture Mechanics Applied to Brittle Materials. ASTM STP 678*, Freiman, S. W., Ed., American Society for Testing Materials, Philadelphia, 1979, pp. 19-37.
7. Hawthorne, D. G., Hodgkin, J. H., Jackson, M. B., Loder, J. W. and Morton, T. C. , "Preparation and Characterization of some new diamino-bisimides" *High Perform. Polym.* 6, 1994, pp. 287-301.
8. Dao, B., Hawthorne, D. G., Hodgkin, J. H., Jackson, M. B. and Morton, T. C., "Preparation and characterization of some novel bismaleimide monomers and polymers based on diaminobisimides", *High Perform. Polym.* , Vol. 8 , 1996, pp. 243-263.
9. Hawthorne, D. G. and Morton, T. C. , unpublished ESR study .

CURING AND DEFORMATION ANALYSIS IN SMC COMPRESSION MOLDING

Hiroyuki Hamada¹, Keigo Futamata² and Hajime Naito³

¹ Faculty of Textile Science, Kyoto Institute of Technology,
Matsugasaki, Sakyo-ku, Kyoto 606, Japan

² Graduate School, Kyoto Institute of Technology, Matsugasaki, Sakyo-ku, Kyoto 606, Japan

³ Sekisui Chemical Co., Ltd., Kamitoba, Minami-ku, Kyoto 601, Japan

SUMMARY: Cure and flow behavior of SMC during compression molding are rather complicated due to heat generation, heterogeneous material and so on. This paper describes numerical analysis method for both cure and flow behavior of SMC in order to establish total CAE system for SMC compression molding. Analytical method of cure behavior was combined between numerical and experimental method. The heat generation was determined by both data and defined as function of temperature inside of SMC. This heat generation function was used in the unsteady heat conduction analysis. The most important flow behavior which was clarified by experiment was slippage flow. The slippage flow occurs in both interlamina and intralamina, and this flow behavior influence on distribution of fiber content fraction in products, that leads to scattering for the mechanical properties of products. In order to understand slippage flow behavior three-dimensional large deformation elastic-plastic analysis was used. The calculated results were in good agreement with the experimental results. These analyses proposed were included into total CAE system for SMC compression molding.

KEY WORDS: SMC compression molding, curing, heat generation, initial deformation, slippage flow, hybrid experimental-numerical approach, elastic-plastic analysis, CAE system

INTRODUCTION

SMC (Sheet Molding Compound) is typical fiber reinforced plastics for high volume processing and has been used in structural parts of transportation vehicles, water tank, bathtub and so on. They have high surface appearance, so that exterior applications are also attractive. In order to obtain high strength of molded products long fiber and/or high volume fraction SMC has been developed. Although recycle problems for protecting the earth environment are appeared, SMC will be still major fiber reinforced plastics in terms of volume of productions. Accordingly, there have been many research works related to SMC product from both academia and industry. The publish works were roughly divided into three categories; one is the material aspects such as resin, low profile additives, and the effects material system on properties of molded products [1-5]. The second one is the fabrication system including CAE system [6-14]. The third one is some defects appeared in the products [15-17].

However for designing of SMC products and compression mold, there is no unified approach. The reasons are concentrated to two points; one is material flow and the other is curing

behavior. SMC flow pattern during compression molding is very complicated because reinforcing fibers move together with matrix. As mentioned in the former paragraph Tucker made very practical work for flow pattern of SMC and developed software [18], however essential or characteristics flow behavior can not be solved because it did not consider the effects of reinforcing fibers and also laminated materials. The second point is curing behavior that affects post-deformation state of products after the products removed from the mold. The analysis of curing process is difficult due to heterogeneous materials containing many different components. Fiber orientation state of SMC moldings also greatly affects on post-deformation. Another difficulty of curing analysis is that final curing state is determined through temperature distribution from the beginning of compression process and material thermal properties. Basically SMC material changes their state from liquid to solid because of curing phenomenon, so that the thermal properties such as heat conductivity, thermal expansion and so on are changed abruptly. The material data base for these properties is not establishes and these are changed easily by changing their contents. On the other hand a set of mold would be expensive, so that changing mold design according to try and error method is inconvenient. In order to overcome these problems, CAE system is required for a mold design.

In this paper we propose total CAE system shown in Fig.1. The CAE system was constructed by several parts. In each part numerical analysis methods were developed by using commercial numerical software and/or original program that were mainly finite element method. The establishment of the CAE system is based on following process. First, once material is set into the cavity, and later temperature inside the material increases because of heat transfer from hot mold to material. Next, the upper mold moves downward and material is deformed with slippage flow at interlamina and intralamina of SMC. After initial deformation of material, resin with fibers flows and the mold cavity is filled with them. At then, it is necessary to consider anisotropy of viscosity that affects on the flow pattern. At the curing process, we need to understand distribution of degree of cure and temperature that affect on occurrence of thermal stress and post-deformation. Especially we have to consider thermal history during process. Finally, above analysis results apply to design of stiffness and strength of products.

This paper describes usefulness of the total CAE system. Particularly, a new original method was introduced to analysis of curing process, which enable to understand curing profile during flow stage and curing stage.

HEAT GENERATION AND CURING ANALYSIS

Analysis

Three dimensional heat conduction analysis was performed, in which heat generation due to chemical reaction was included. The curing phenomenon was considered through the heat generation term in the equation of three dimensional heat conduction and the construction method for this term was the most important in this analysis. The basic equation was:

$$\rho c \frac{\partial T}{\partial t} = k_x \frac{\partial^2 T}{\partial x^2} + k_y \frac{\partial^2 T}{\partial y^2} + k_z \frac{\partial^2 T}{\partial z^2} + Q \quad (1)$$

where ρ is the density, c is the specific heat, k_x , k_y and k_z are thermal conductivity for x-, y- and z-direction respectively. In order to create the heat generation term the difference of increase of temperature between system with and without heat generation was paid attention. The first system was performed by actual materials and the numerical analysis was used for latter system. We assume that material is set in a heated mold and then heat is conducted from the mold into the material. Temperature inside material increases and reaches to the temperature of heated mold eventually in the case of system without heat generation, whereas the temperature increases rapidly and exceeds the heated mold temperature in the case of system with heat generation. Typical examples are shown in Fig.2 for both cases.

Fig.3 shows finite element division for three dimensional heat conduction analysis in which solid elements were used. Boundary conditions are follows; temperature is fixed on planes-ABCD and -KLM because of mold surface, and planes-ABK and -ADM are symmetrical plane, so that adiabatic boundary conditions are applied. The increase of temperature for system without heat generation as shown in Fig.2 was obtained from the center point by using this analysis. The differences between the analysis and the experiment were caused by the heat generation, so that calorific value was obtained as following equation.

$$\rho c \frac{\Delta T_2 - \Delta T_1}{\Delta t} - Q = 0 \quad (2)$$

where ΔT_1 and ΔT_2 are temperature increment in time variation Δt of the experiment and analysis respectively, and the derivation of the above equation was mentioned in Appendix part briefly.

First calorific value was calculated as function of time corresponding to temperature-time curve and also cumulative calorific value was defined through time as well. The relation between calorific value and time was rewritten to that between calorific value and temperature at the center. Accordingly, heat generation term was defined by the temperature inside material. When temperature reaches a specific value, material emits heat stepwise. The degree of cure was defined as the ratio of sum of heat generation, ΣQ , to total heat generation, $[\Sigma Q]_{Total}$, as follows.

$$\alpha = \frac{\Sigma Q}{[\Sigma Q]_{Total}} \quad (3)$$

Furthermore, curing was completed when α was 0.8 in the analytical region[19]. The curing profile could be practical by using this assumption.

This analytical method was combination between numerical and experimental method, and recently this method was called Hybrid Experimental-Numerical approach for a determination problem.

Results

Fig.2 shows temperature-time curves obtained by experiment and numerical analysis without heat generation. The heat generation occurred from about 130. Using these results, calorific value calculated as function of time and also cumulative calorific value defined through time

as well are shown in Figs.4 and 5 respectively. Total calorific value could be calculated and was estimated about 7.010^{-5} kcal/mm³ as shown in Fig.5. The relation between calorific value and time was rewritten to that between heat generation and temperature at the center. Fig.6 shows this relation. Consequently, heat generation term could be defined by the temperature inside of material. In order to confirm the validity of this method the heat generation function obtained was introduced into heat conduction analysis. Fig.2 also shows result of this analysis. Temperature-time curve obtained by numerical analysis was good agreement with the experimental result.

Curing profile of cross section through thickness direction obtained by numerical analysis is shown in Fig.7. At holding time 210 sec, curing of the bottom layer was completed firstly. At holding time 250 sec, curing of the top layer was also done. Then, curing have progressed toward the center at holding time 315 sec, curing of all region was completed finally. Where 'holding time' was defined as time kept material surface in contact with closing upper mold until start of compression.

In this way, cure behavior in the initial process stage was asymmetry through thickness direction due to considering with the upper mold closing time. Consequently, it seemed that practical curing profile could be obtained by this numerical analysis method.

DEFORMATION ANALYSIS

Analysis

As mentioned in Introduction part the flow pattern is very complicated aspects in SMC compression molding due to effects of fiber and cure state. Particularly, at the initial stage a characteristic flow/deformation states appears as shown in Fig.8. Fig.8 shows side view of the initial stage in the case of three layered SMC. (a) shows that upper and lower layers deforms precedent to the middle layer, on the other hand (b) shows the preceding middle layer. The slippage flow was common phenomena that occur at the inter- and intra-lamina. Normally, decrease of viscosity or elastic modulus of materials due to heat conduction creates the case of (a), and cured upper/lower layers tend to make the cases of (b).

Basically viscosity or elastic modulus of materials decreases with increase of temperature due to thermal diffusion. This situation does not consider the chemical reaction and chemical diffusion; that is $\dot{\epsilon} = 0$. Once chemical reaction occurs these material constants would depend on the degree of cure and increase dramatically as shown in Fig.9. The dependence of material constants on temperature could be easily measured, however the dependence on degree of cure hardly be measured. In this paper an appropriate assumption was made for analyzing deformation state that was affected by both thermal and chemical diffusion.

Fig.3 shows finite element division for the initial deformation analysis of three layers. Boundary conditions are follows; nodes on the plane-KLM were fixed for x-, y- and z-direction, nodes on the plane-ADM and the plane-ABK of neutral planes were fixed for x- and y-direction respectively. Nodes on the plane-ABCD were fixed for x- and y-direction and were given prescribed displacement -0.1 mm every one step for z-direction.

After heat conduction analysis with heat generation term described in the previous section was performed, material constants were determined according to the former discussion. In order to

express slippage flow double nodes were set between not only interlamina layers but also intralamina layers. When the difference of shearing strain adjacent elements exceeds a critical value, it was assumed that separation of the double nodes was initiated. The material model used in this analysis was elastic-plastic relations.

Results

Fig.10 shows deformation state in the case of uniform material constants. The material constants are same in all the elements, so that frictional effects were appeared at the top and bottom surface. The separation occurred at the interlamina. Fig.11(a) shows the actual cases in which heat conduction analysis was performed and also dependence of material constants on temperature was considered. The lower layer was heated by the mold until upper mold touched the upper layer and the period of this time was 30 seconds. The slippage flow was initiated between lower layer and middle layer and therefore lower layer deformed precedent to the middle layer. Fig.11(b) shows another example in which more 6 seconds have passed since deformation state was above state. It was easy to imagine that both upper and lower layers were heated up and material constants were decreased due to thermal diffusion in both layers. The deformation state was very similar to the case as shown in Fig.8(a).

Fig.12 shows the case of extreme long keeping time in which the change of material constants due to curing was considered. After upper mold touched the materials 100 seconds were kept at the same condition. At both upper and lower layers cure occurred and therefore material constants were dramatically increased. The slippage flow initiated both sides of middle layer and finally middle layer was squeezed out. This result was similar to the case as shown in Fig.8(b).

The initial deformation state including slippage flow would affect greatly flow behavior of materials and also fiber orientation of reinforcing fibers, and further post deformation behavior would be caused. According to cure state the initial deformation was changed drastically and this phenomenon indicates an importance of analysis for cure state, so that analytical method proposed in this paper were very useful technique and enable determine molding condition such as mold temperature, closing speed of press machine that related to time to touch the materials and so on. Practically these molding conditions could be determined considering into material characteristics, because different composition of materials made different thermal properties. As shown in previous section the analytical method was suitable for actual material system, therefore proposed method could select molding conditions corresponding to each material.

CONCLUSION

This paper described analytical method for cure state and initial deformation state of SMC during compression molding. The most important result was that database for heat generation due to chemical reaction could be established by Hybrid Experimental-Numerical approach and further the degree of cure was calculated. The initial deformation state was calculated by three dimensional finite element analysis and particularly slippage flow between inter- and intra-lamina was considered. The cure state was very delicate because keeping time of mold affected dramatically and accordingly the initial state was also changed.

REFERENCES

1. Atkins, K.E., "Advances in Pigmentation of Low Profile Composites", *Proceedings the 51st Annual Conference on The Society of the Plastic Industry*, Cincinnati, Ohio, U.S., February 5-7, 1996, Session 13-D.
2. Kan, W.-M.J., Lee, L.J., "LPA Performance in Low Temperature BMC/SMC", *Proceedings the 51st Annual Conference on The Society of the Plastic Industry*, Cincinnati, Ohio, U.S., February 5-7, 1996, Session 2-A.
3. Kinkelaar, M., Muzumdar, S., Lee, L.J., "Analysis of LPA Mechanism by Dilatometry Study", *Proceedings the 49th Annual Conference on The Society of the Plastic Industry*, Cincinnati, Ohio, U.S., February 7-9, 1994, Session 5-C.
4. Young, J.J., Lucas, R.L., Wade, C.B., "A New Versatile Class A SMC Resin", *Proceedings the 51st Annual Conference on The Society of the Plastic Industry*, Cincinnati, Ohio, U.S., February 5-7, 1996, Session 22-D.
5. Kia, H.G., Viscomi, P.V., "High-Pressure/High-Temperature Dilatometry", *Proceedings the 49th Annual Conference on The Society of the Plastic Industry*, Cincinnati, Ohio, U.S., February 7-9, 1994, Session 5-F.
6. Barone, M.R., Caulk, D.A., "A Model for the Flow of a Chopped Fiber Reinforced Polymer Compound in Compression Molding", *Journal of Applied Mechanics*, Vol.53, 1986, pp361-371.
7. Sun, E.M., Davis, B.A., Osswald, T.A., "Modeling and Simulation of Thick Compression Molded Parts", *Proceedings the 50th Annual Conference on The Society of the Plastic Industry*, Cincinnati, Ohio, U.S., January 30-February 1, 1995, Session 15-B.
8. Twu, J.-T., Hill, R.R., Wang, T.J., Lee, L.J., "Numerical Simulation of Non-Isothermal SMC (Sheet Molding Compound) Molding", *Polymer Composites*, Vol.14, No.6, 1993, pp.503-514.
9. Chang, S.-H., Osswald, T.A., "Predicting Shrinkage and Warpage of Fiber-Reinforced Composite Parts", *Polymer Composites*, Vol.15, No.4, 1994, pp.270-277.
10. Fan, J.D., Lee, L.J., "Optimization of Polyester Sheet Molding Compound. Part II: Theoretical Modeling", *Polymer Composites*, Vol.7, No.4, 1993, pp.250-260.
11. Xu, J., Kim, J., Ho, T., Lee, L.J., "Compression Molding of Sheet Molding Compounds in Plate-Rib Type Geometry", *Polymer Composites*, Vol.14, No.14, 1993, pp.51-52.
12. Hirai, T., "A New Continuous Fabrication System for SMC-Roll Forming", *Proceedings the 51st Annual Conference on The Society of the Plastic Industry*, Cincinnati, Ohio, U.S., February 5-7, 1996, Session 2-C.
13. Collister, J.E., Butler, K.I., Rinz, J.E., "Hydraulically-Assisted Compression Molding Material and Process Development", *Proceedings the 51st Annual Conference on The Society of the Plastic Industry*, Cincinnati, Ohio, U.S., February 5-7, 1996, Session 2-B.
14. Richey, T.A., "Development of a Modular, Automatic SMC Charge Pattern Cutter", *Proceedings the 49th Annual Conference on The Society of the Plastic Industry*, Cincinnati, Ohio, U.S., February 7-9, 1994, Session 18-A.

15. Atkins, K.E., Seats, R.L., Montagne, M.H.P., Behar, G., “Advances in Thermoset Injection Molding Part IV: Knitline and Elevated Temperature Properties in Thermoset Composites”, *Proceedings the 48th Annual Conference on The Society of the Plastic Industry*, Cincinnati, Ohio, U.S., February 8-11, 1993, Session 12-D.
16. Yamada, H., Mihata, I., Tomiyama, T., Walsh, S.P., “Investigation of the Fundamental Causes of Pinholes in SMC Moldings”, *Proceedings the 47h Annual Conference on The Society of the Plastic Industry*, Cincinnati, Ohio, U.S., February 3-6, 1992, Session 1-B.
17. Halvarsson, S., Petterson, J., Nilson, P., “Critical Molding Conditions for Blistering During Compression Molding of Sheet Molding Compound (SMC)”, *Proceedings the 48th Annual Conference on The Society of the Plastic Industry*, Cincinnati, Ohio, U.S., February 8-11, 1993, Session 17-C.
18. Tucker, C.L., “Compression Molding of Polymer and Composites”, *Injection and Compression Molding Fundamentals*, Isayev, A. I., ed., Marcel Dekker Inc., New York and Basel, 1987, pp481-565.
19. Barone, M.R., Caulk, C.A., “Effect of Deformation and Thermoset Cure on Heat Conduction in a Chopped Fiber Reinforced Polyester During Compression Molding”, *Int. J. Heat and mass Transfer*, Vol.22, 1979, pp1021-1032.

APPENDIX

The heat conduction equation without the heat generation was shown by equation (a-1).

$$\rho c \frac{\partial T}{\partial t} = k_x \frac{\partial^2 T}{\partial x^2} + k_y \frac{\partial^2 T}{\partial y^2} + k_z \frac{\partial^2 T}{\partial z^2} \quad (\text{a-1})$$

where ρ is the density, c is the specific heat, k_x , k_y and k_z are thermal conductivity for x-, y- and z-direction respectively.

Boundary conditions were shown by following equation.

$$\begin{cases} T = T_0 & (\text{the boundary } S_1) \\ q = q_0 & (\text{the boundary } S_2) \end{cases} \quad (\text{a-2})$$

Equations (a-1) and (a-2) were applied to the principle of virtual work, then following equation could be obtained.

$$\int_v \left\{ \delta T \rho c \frac{\partial T}{\partial t} - k_x \frac{\partial \delta T}{\partial x} \frac{\partial T}{\partial x} - k_y \frac{\partial \delta T}{\partial y} \frac{\partial T}{\partial y} - k_z \frac{\partial \delta T}{\partial z} \frac{\partial T}{\partial z} \right\} dv = 0 \quad (\text{a-3})$$

It was considered that the internal energy, Q , was caused by a chemical diffusion and depended on material temperature, moreover, this was given every step of each temperature. Then following equation could be obtained.

$$\int_v \left\{ \delta T \rho c \frac{\partial T}{\partial t} - k_x \frac{\partial \delta T}{\partial x} \frac{\partial T}{\partial x} - k_y \frac{\partial \delta T}{\partial y} \frac{\partial T}{\partial y} - k_z \frac{\partial \delta T}{\partial z} \frac{\partial T}{\partial z} \right\} dv + \sum_i Q_w \Delta_i \delta T = 0 \quad (\text{a-4})$$

where Q_w and Δ_i represent the energy at the point x_i and the delta function (1 : at the coordinate of the point x_i , 0 : at the coordinates except the point x_i) respectively. System 1 and system 2 were named by systems for equation (a-3) and (a-4) respectively. Here some assumptions were written as follows.

1. Some property values were constant independent of both systems and material temperature.
2. The heat generation at minute region without temperature distribution occur uniformly.
3. The heat conduction terms of temperature gradient for both systems were equal in minute time.

The internal energy $Q (=Q_w\Delta_i)$ which was given by the differences between systems 1 and 2 could be shown by the equation (a-5).

$$\rho c \left(\left[\frac{\partial T}{\partial t} \right]_2 - \left[\frac{\partial T}{\partial t} \right]_1 \right) - Q = 0 \tag{a-5}$$

It could be considered that the internal energy represents heat generation due to the chemical diffusion. Equation (a-5) could modify following equation for finite time Δt .

$$\rho c \frac{\Delta T_2 - \Delta T_1}{\Delta t} - Q = 0 \tag{a-6}$$

ΔT_1 is temperature increment for system 1 without heat generation

ΔT_2 is temperature increment for system 2 with heat generation

The heat generation per unit time and volume could be obtained by equation (a-6).

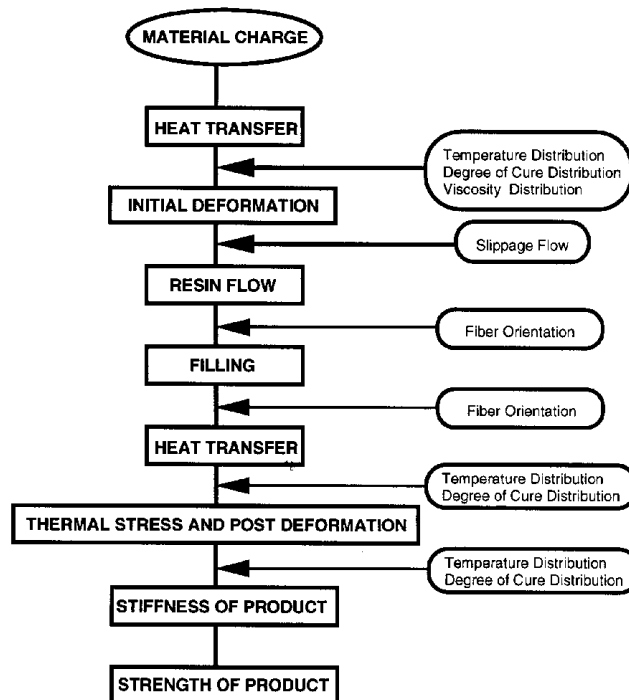


Figure 1: Total CAE system for SMC compression molding.

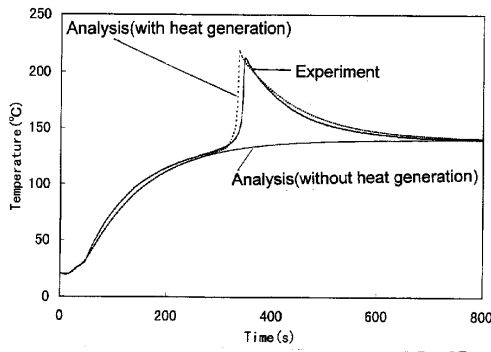


Figure 2: Temperature-time curve.

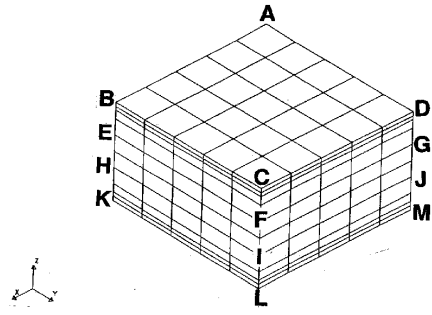


Figure 3: Finite element division.

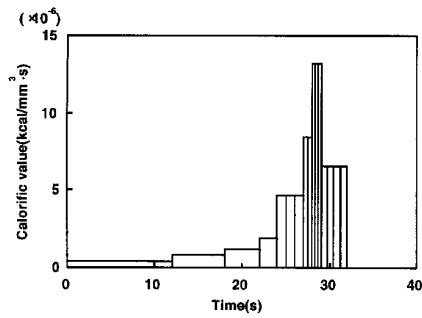


Fig.4 Relation between heat generation during cure and time.

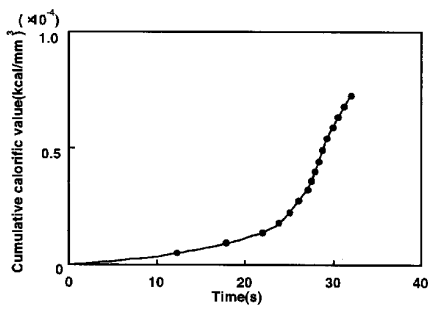


Figure 5: Cumulative heat generation versus time.

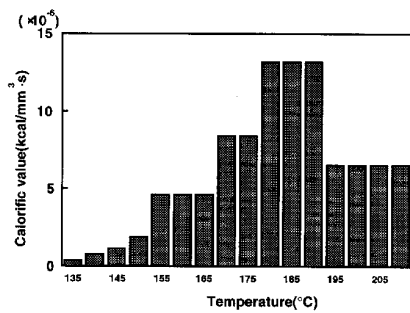


Figure 6: Relation between heat generation during cure and temperature.

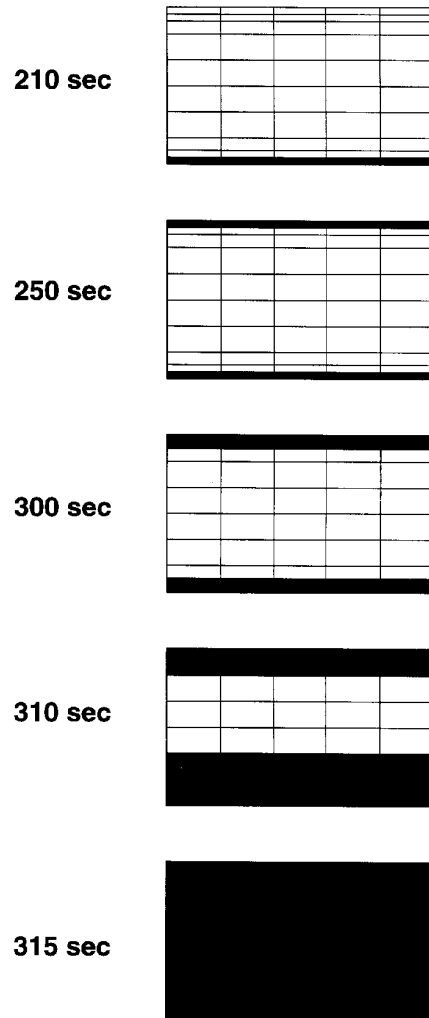


Figure 7: Curing profiles obtained by numerical analysis.

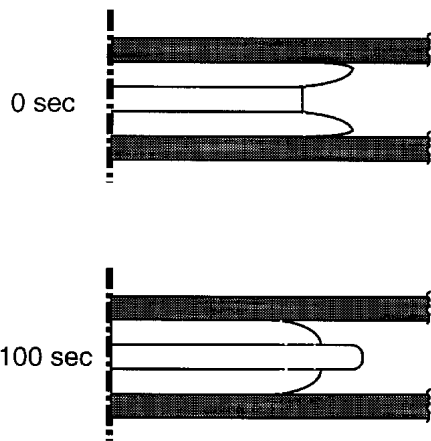


Figure 8: Schematic drawing of a characteristic flow/deformation states at the initial stage.

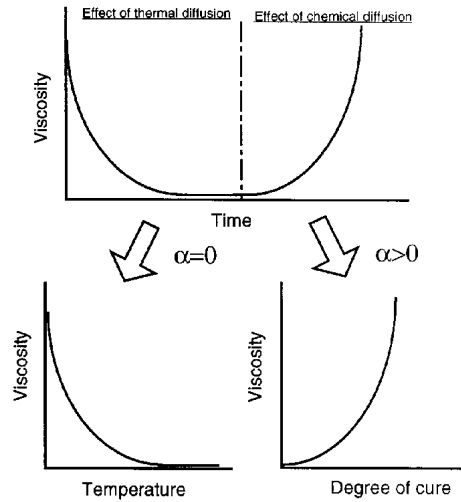


Figure 9: Typical viscosity variation during SMC compression molding.

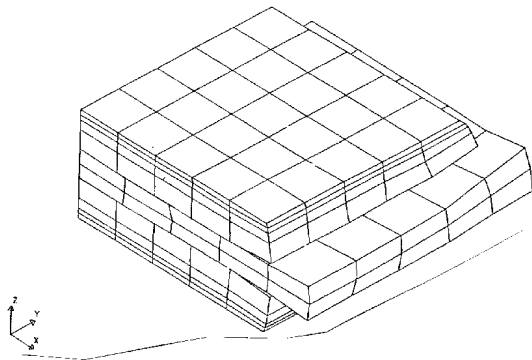


Figure 10: Deformed mesh in the case of uniform material constants.

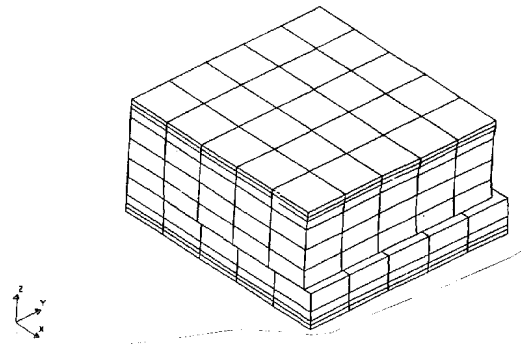


Figure 11a: Deformed mesh in the case of holding time 0 sec (10th step).

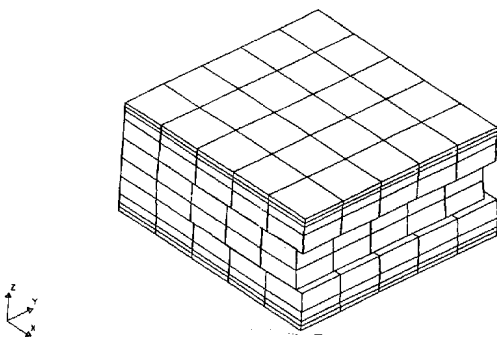


Figure 11 b: Deformed mesh in the case of holding time 0 sec (20th step).

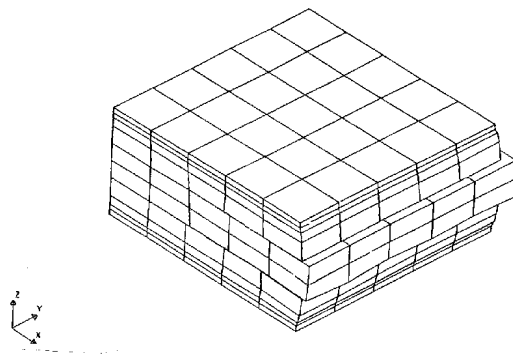


Figure 12: Deformed mesh in the case of holding time 100 sec (20th step).

INFLUENCE OF FILLER ON SMC ROLL FORMING

Tsutao Katayama¹, Kazumasa Kurokawa¹, Masahiro Shinohara²,
Yuuzou Hayakawa³ and Masahiro Hakotani³

¹ *Department of Mechanical Engineering, Doshisha University,
Tanabe-cho, Tsuzuki-gun, Kyoto, 610-03 Japan*

² *Maizuru National College of Technology,
234 Shiraya, Maizuru, Kyoto, 625 Japan*

³ *TAKADEA CHEMICAL INDUSTRIES, LTD.,
Juso-honmachi, Yodogawa-ku, Osaka, 532 Japan*

SUMMARY: We proposed to apply roll forming to SMC, expecting the decrease of a forming energy, a short production time and a controllability of the fibre orientation.

In this paper, we tried to find out the suitable materials for roll forming. The experiments were carried out in consideration of the amount of the filler and the filler diameter. By varying the amount of the filler and the filler diameter, we can control the flow resistance of the material. And we can find out the suitable materials using hybrid laminated materials to form the flange part in channel shaped products. This means that Roll forming by using hybrid laminated materials has a controllability of the fibre orientation in SMC comparing with extrusion.

KEYWORDS: SMC, roll forming, hybrid laminated materials, controllability of fibre orientation.

INTRODUCTION

SMC (Sheet Moulding Compound) has some excellent characteristics such as a surface brilliance, a formability and excellent mechanical properties, and is used in a wide range of automobile parts, housing equipments and so on. SMC is usually formed by compression moulding. This method can make production time short, but it requires large-sized and expensive press forming machines and a huge energy for the forming because of a growing of a hydrostatic stress domain generated in the mould. And with this method, it is difficult to form long-sized products which is usually used as structural members, because of the limitation of the size of a forming machine and a mould.

In the field of metal forming, roll forming is usually used to form long-sized products. This method is the processing of the continuous micro-reduction given by driven upper and lower rolls. When this method is applied to SMC forming, there are some advantages compared with compression moulding. During roll forming, the almost of forming load works as the deviatoric stress, so it is possible to reduce the forming energy. [1],[2] As a result, it is possible to minify and simplify the forming machine. Moreover, because roll forming is continuous forming, it is easier for roll forming to form long-sized products than for compression moulding.

In the previous study, the influence of the reduction and the tension between roll stands has been investigated.[3] However, the materials for SMC Roll Forming are only empirically chosen, so it is not clear what characteristics of the material are suitable for SMC Roll Forming. In this paper, we consider the filler, which is one of the components of SMC material. The influence of the amount of the filler and the filler diameter on the load-displacement properties and the formability of SMC is investigated. And then, using the laminated materials with various flow resistance, the influence of the laminate pattern on the formability of SMC is investigated, especially paying attention to forming the flange part of channel shaped products. And fibre orientations are checked on.

SMC ROLL FORMING

Concept of SMC Roll Forming

SMC Roll Forming is to deform gradually SMC with multiple roll stages and to form into various cross-sectional shapes in long products. After forming, deformed materials are cured by the curing oven. Though the method is same as that in metallurgical technology, the materials have heterogeneous and anisotropic and the production shape requires the lateral spread of materials. So we must consider the deformation characteristics of these materials.

SMC Used in This Study

The contents of SMC used in this experiment is shown in Table 1. This SMC is cut into 75 x 600 mm and 5 SMC sheets are laminated. The thickness of laminated materials is 9 mm.

Table 1: Contents of SMC.

Components (wt %)		Relative density
Resin (UP, TP, etc.)	31.3	1.10
Glass fibre	28.0	2.54
CaCO ₃ (filler)	40.7	2.70

Roll Forming Machine

Roll forming machine shown in Fig. 1 is used in this experiment. The reduction and the roll velocity that will influence the formability are set up at each stand. The cross section of roll is also shown in Fig. 1.

Forming Method And Measurement of Experimental Parameters

The product with channel shaped cross section is formed by continuous roll forming. The shape of product has the cross section of 75 x 20 x 4 mm (= width x flange height x web thickness). Laminated materials are inserted into the arrow direction as shown in Fig. 1 and we form repeatedly until the web thickness becomes 4 mm. Elongation, flange height and forming load are measured during forming. And fibre orientation angle of the products is also measured. Elongation at the web part is measured to observe the longitudinal deformation of materials during forming. To obtain the elongation after laminating, the lines in 300 mm are marked at the centre of materials surface. And the length of the marked lines are measured at each insertion

into the machine. Elongation is calculated by next formula,

$$Et = \ln (eln / el0) \tag{1}$$

where, Et is the total strain of elongation after n-th pass, eln is the length of the marked lines after n-th pass, and $el0$ is the initial length of the marked line.

And to observe the lateral deformation of materials during forming, flange height is also measured. Flange height is calculated as follows,

$$Ft = \ln (fln / fl0) \tag{2}$$

where, Ft is the total strain of flange height after n-th pass, fln is flange height after n-th pass, and $fl0$ is the initial flange height (same as the thickness of laminated materials = 9 mm).

Forming load is measured by strain gauges which are attached to the support bars shown in Fig. 1.

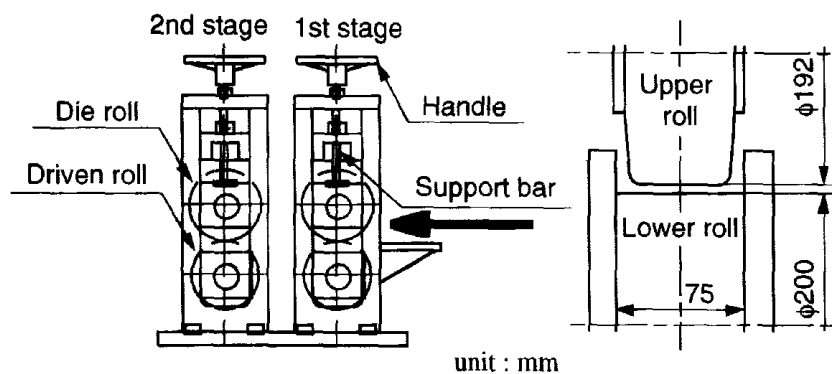


Fig. 1: Roll forming machine and cross section of roll.

Fibre orientation angles at the web part of the products are measured. Fibre orientations are relative to the material flow during forming, so the measurement of fibre orientations are the way to estimate the deformation of the material during forming.

After curing, the specimen (50 x 50 mm) is cut off from the web part of products and fibre orientation angles are measured at the 3 areas of the specimen as shown in Fig. 2. The directions of the orientation angle are also shown in Fig. 2.

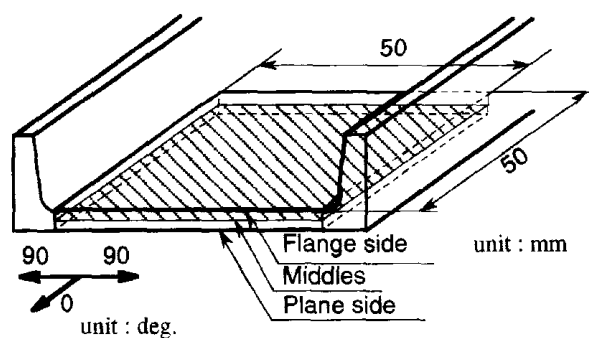


Fig. 2: Sampling planes of fibre orientation angle and the direction of orientation.

INFLUENCE OF FILLER IN SMC ON LOAD-DISPLACEMENT PROPERTIES AND FORMABILITY

The study on SMC Roll Forming has been carried out until now, but the choice of the materials for SMC Roll Forming was only empirical. In this section, we consider the filler, which is one of the components of SMC material. The influence of the amount of the filler and the filler diameter on forming load and the deformation of the materials is investigated.

Materials for Experiments

In this section, we use 3 types of SMC materials as follows;

- Material A : standard SMC material whose contents is shown in Table 1
- Material B : with larger amount of the filler than in Material A
- Material C : with smaller filler diameter than in Material A

Larger amount of the filler and smaller filler diameter in SMC are expected to make the viscosity of SMC higher because of larger surface area of the filler.

Compression Test

In order to know the properties of these 3 materials in the above, 10 SMC sheets are laminated and compression tests using Instron 4206 universal testing machine are carried out. Crosshead speeds are 30, 50, 70, 90, 110, 130, 150 mm/min.

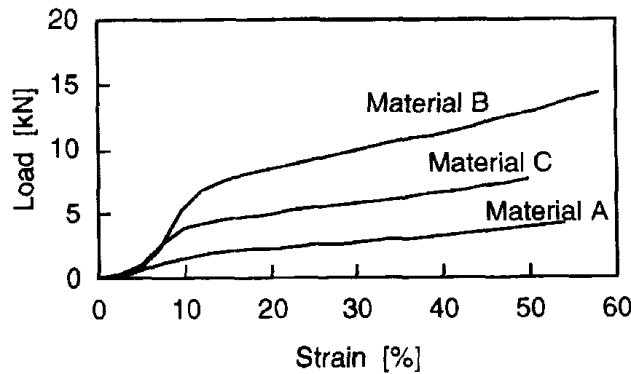


Fig. 3: The result of compression test. (Crosshead speed = 90 mm/min.)

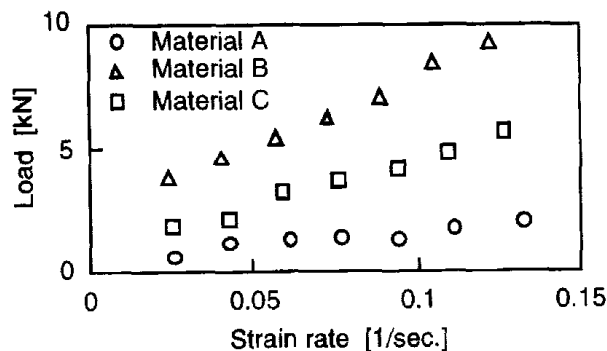


Fig. 4: Relation between load at plastic deformation and strain rate.

Fig. 3 shows the load-strain curve of 3 types of materials under compression test and Fig. 4 shows the relation between the load when plastic deformation occurs and strain rate. In these figures, Material B shows the highest load value and Material A shows the lowest.

Roll Forming Test

Using 3 types of materials, roll forming tests are carried out under the forming condition shown in Table 2.[3] This condition shows constant reduction ratio at 7% and considers the elongation of products between roll stands. The initial thickness of the materials is 9.0 mm and final thickness of the products at the web part is 4.2 mm.

Table 2: Forming condition.

Stage	Reduction (mm)	Roll velocity (m/min.)
1	0.630	1.00
2	0.586	1.07
3	0.545	1.14
4	0.507	1.21
5	0.471	1.26
6	0.438	1.31
7	0.408	1.36
8	0.379	1.41
9	0.353	1.46
10	0.328	1.51
11	0.305	1.56
12	0.284	1.59

Results and Discussion

Fig. 5 shows the relation between the forming pressure and the reduction in thickness. The forming pressure, Y axis, is determined by dividing the forming load by the contact arc length between the roll and the material. The contact arc length L is calculated by Eq.(3).

$$L = R \cdot \cos^{-1} \{ 1 - \Delta h / (2R) \} \quad (3)$$

where R and Δh is roll radius and the reduction at each stage respectively.

Under every forming conditions, the contact width between the roll and the material is constant, so we can consider this value in the Y axis as forming pressure.

The value in the X axis denotes the total reduction in thickness, r determined as follows;

$$r = (h_0 - h_n) / h_0 \times 100 \quad (4)$$

where h_0 is the initial thickness of the material and h_n is the thickness of the materials after n-th pass.

In this figure, Material A shows the lowest forming pressure and Material B shows the highest in 3 types. Comparing with the compression test, the influence of the filler condition in SMC on the forming load is similar to the results of compression test. So we can estimate the forming load by the results of compression test.

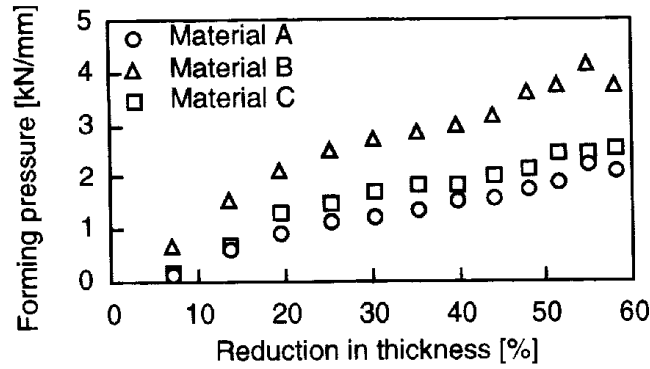


Fig. 5: Relation between forming pressure and reduction in thickness.

Fig. 6 show the relation between the total strain of elongation and the reduction in thickness. In this figure, it is shown that elongation of Material A is the largest and elongation of Material B is the smallest. But these difference is very small.

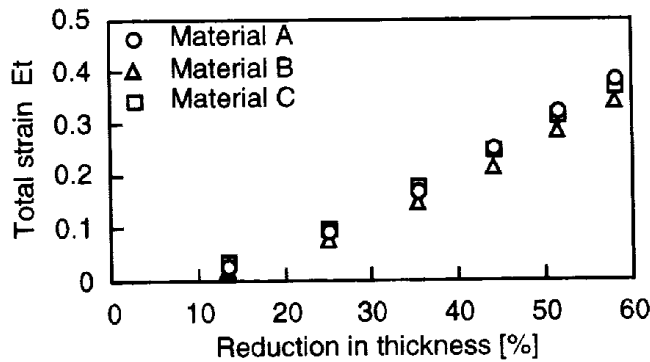


Fig. 6: Relation between total strain of elongation and reduction in thickness.

Fig. 7 shows the relation between total strain in the flange height direction and the reduction in thickness. In this figure, it is shown that the flange height of Material B is the highest and the flange height of Material A is the lowest. Generally in the case of roll forming, material deforms mainly to the longitudinal direction because of the friction between roll and material. However, Material B shows higher flow resistance than other materials, so it seems that the deformation to the longitudinal direction is arrested by the existence of material itself. Instead of deforming to longitudinal direction, the material deforms in the lateral direction to the rolling direction because of lower deformation energy to the free edge, and the flange height of Material B becomes larger due to higher viscosity.

Fig. 8 shows the fibre orientation angle of each material in each sampling plane. In every material, the fibre orientations at the flange side and the plane side, which are near the surface of the products, trend to turn to the longitudinal direction. It seems to be caused by the friction between roll and material. At middles of Material B and C, the fibre orientations shift from longitudinal direction to lateral direction. This tendency is remarkable in the case of Material B. Average fibre orientation angle before forming is almost equal in all material. (See Fig. 9) The difference of fibre orientation among each material seems to be caused by the difference of deformation behaviour due to the viscosity.

As a result, Material B with larger amount of the filler is suitable for forming the products with the channel shaped cross section and parallel flange part, and we can get the lateral fibre orientation to the rolling direction with higher viscous materials.

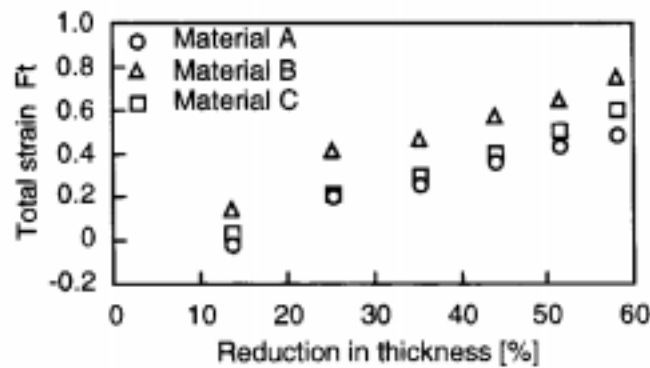


Fig. 7: Relation between total strain in flange height and reduction in thickness.

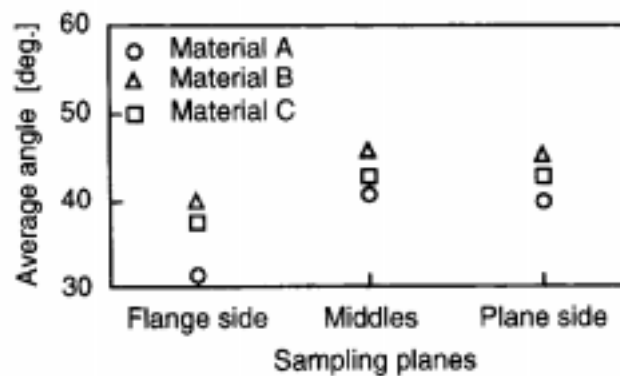


Fig. 8: Average fibre orientation angle.

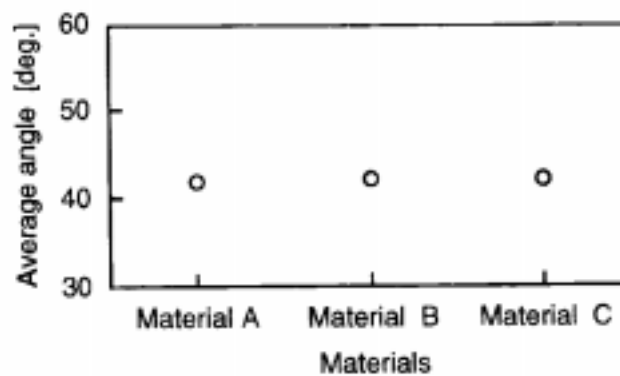


Fig. 9: Average fibre orientation angle before forming.

FORMABILITY OF HYBRID LAMINATED MATERIALS

SMC is usually used by laminating by several sheets. In this section, using Material A and Material B, which are used in the former section, we make hybrid laminated materials and investigate the influence of the laminating construction on the formability of materials.

Forming Condition and Laminating Construction

Forming condition is the same as that in the former section, and the laminating construction is shown in Fig.10.

Material D : outer layers are Material B and inner 3 layers are Material A
 Material E : outer layers are Material A and inner 3 layers are Material B

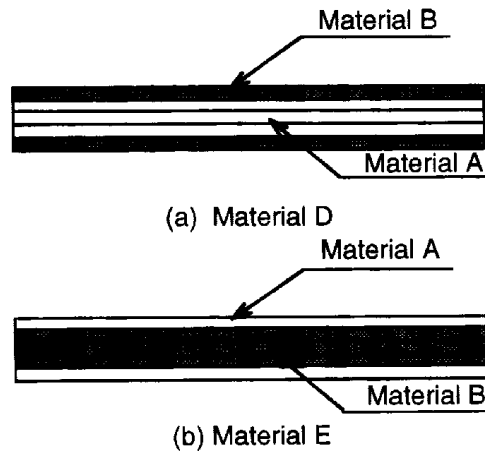


Fig.10: Laminating construction of Material D and Material E.

Results and Discussion

Fig.11 shows the relation between the forming pressure and the reduction in thickness. In this figure, Material D and Material E show lower forming pressure than Material B because these materials contain Material A which shows lower flow resistance. Comparing Material D with Material E, Material D shows higher forming pressure. In roll forming, outer layers mainly deform. The outer layers of Material D are Material B which shows higher flow resistance, so Material D shows higher forming pressure than Material E.

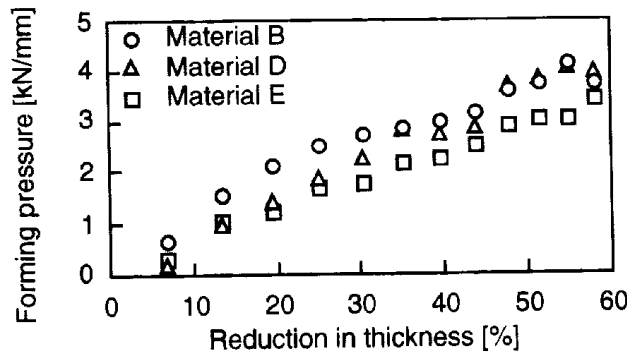


Fig.11: Relation between forming pressure and reduction in thickness.

Fig.12 shows the relation between the total strain of elongation and the reduction in thickness and Fig.13 shows the relation between the total strain in the flange height and the reduction in thickness. In these figures, it is shown that elongation of Material D is smaller and the flange height of Material D is higher. And Fig.14 shows the fibre orientation angle in each material at

each sampling plane.

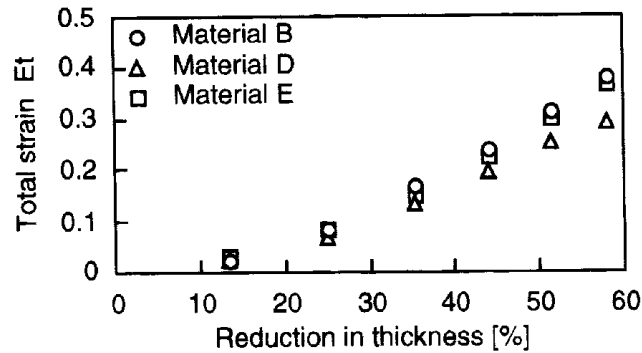


Fig.12: Relation between total strain of elongation and reduction in thickness.

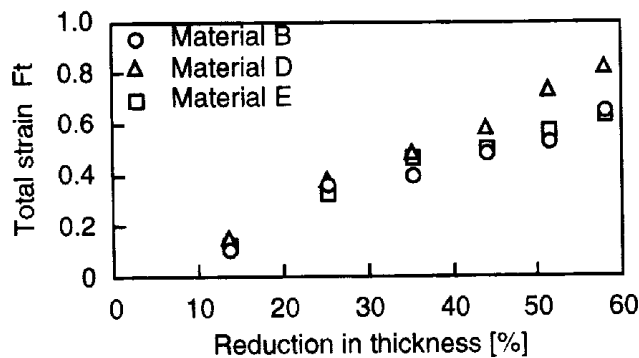


Fig.13: Relation between total strain in flange height and reduction in thickness.

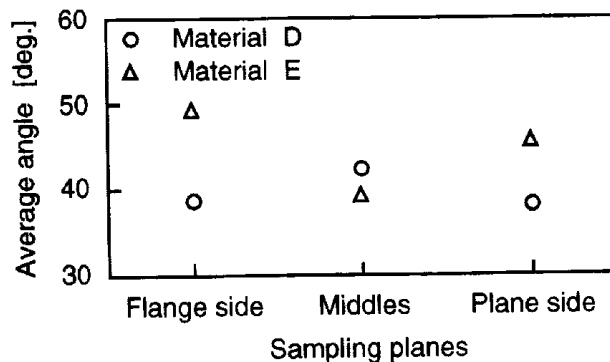


Fig.14: Average fibre orientation angle.

In the case of Material D, because the outer layers, Material B, don't deform so well, the deformation concentrates in the inner layers, Material A. The inner layers tend to deform to the longitudinal direction and the lateral direction, but the deformation to the longitudinal direction is arrested by the outer layers. So the inner layers deform to the lateral direction to the rolling and the flange height becomes higher.

In the case of Material E, the outer layers tend to deform to the longitudinal direction, but the inner layers don't deform and arrest the longitudinal deformation of the outer layers. So the outer layers don't deform to longitudinal direction, but deform to lateral direction. These are shown in Fig.14. However, the volume fraction of Material A in Material E is smaller than that

in Material D, then the flange height of Material E doesn't become higher. Consequently, Material D, where outer layers are Material B and inner layers are Material A, is suitable for forming the products with the channel shaped cross section and the parallel flange part.

CONCLUSIONS

We tried to find out the suitable materials for forming the flange part, that is, suitable materials for deforming to the longitudinal direction to the rolling direction. The experiments were carried out in consideration of the amount of the filler and the filler diameter in SMC. The following results were obtained;

- 1) Needless to say, larger amount of the filler makes the flow resistance higher. In the case of same contents in SMC, smaller diameter of the filler makes the flow resistance higher.
- 2) Higher flow resistance results in the tendency to flow the lateral direction to the rolling direction. This is suitable to form the flange part in channel shaped products.
- 3) By using hybrid laminated materials with high and low flow resistant materials, we could make the material flow to the lateral direction to the rolling direction in keeping lower working load.

REFERENCES

- 1 Hirai, T., Hayakawa, Y. and Hakotani, M., *Materials and Technologies*, 1, 295, 1994 Woodhead Publishing
- 2 Hirai, T., "Roll Forming of SMC Considering the Boundary Effects Caused by Heterogeneous Properties", *Journal of JSPP*, Vol.6, No.12, 1994 pp.922-933.
- 3 Katayama, T., Kurokawa, K., Hayakawa, Y. and Hakotani, M., "The Influence of Roll Velocity and Reduction on Formability in SMC Roll Forming", *Proc. of seventh European Conference on Composite Materials*, pp 347-352, 1996.

IMPREGNATION OF THERMOPLASTIC COMPOSITES MANUFACTURED BY DOUBLE BELT PRESS TECHNIQUE

Xiaoming Wang, Christoph Mayer and Manfred Neitzel

*Institut für Verbundwerkstoffe GmbH (IVW), Erwin-Schrödinger-Str., Geb.58
D-67663 Kaiserslautern, Germany*

SUMMARY: The manufacturing of thermoplastic composites by continuously running double belt press has become one of the most effective techniques for high quantity production. The combination of thermoplastic materials and fabric layers during the manufacturing implies impregnation phenomena of the fabric layers distinct from one in RTM that has been frequently discussed in many previous papers. Here, the work is focused on the clarification of the impregnation phenomenon which occurred in the continuous manufacturing process. Results were presented by the observation of samples that were fabricated at different process velocity to determine the impregnation time. Meanwhile, further analysis and experiments revealed that variation of mechanical properties of thermoplastic composites could be realized by using different process velocity and temperature boundary conditions to change the impregnation degree of the reinforcing fabrics.

KEYWORDS: thermoplastic composites, manufacturing science, impregnation, double belt press

INTRODUCTION

A timesaving manufacturing process to produce composites with expected performance and as low cost as possible is always a subject to be pursued by industries. The fabrication of thermoplastic composites by means of a continuously running double belt press is one of the most effective manufacturing methods for high quantity production. During the process, thermoplastic materials will melt and then penetrate into the fabric layers under pressure applied by the double belts. It is evident that the penetration process of the thermoplastic flow into fabric layers is directly relevant to the impregnation of the fabrics which have dominant effects on mechanical properties of thermoplastic composites if the fabrics and matrix has been determined.

As known, the impregnation of fabrics as reinforcement in thermoset composites has become one of the focused problems since resin transfer molding (RTM), one of favorite methods to fabricate structural composite, is basically a process of preform mould filling with liquid resins. Analysis on the impregnation was set up on the basis of Darcy's theory [1, 2] which has been introduced to analyze mass and energy transfer in porous materials [3], and it concluded the complicated relation between seepage velocity and pressure drop in fabrics into a parameter — permeability [4, 5, 6, 7, 8].

It is certain that the supposition and application of the permeability lead to simplification of analysis and scaling of fabric impregnation process. But it is necessary to point out that the

permeability described in the Darcy's theory only indicates an overall ability of resins penetrating into porous preform in macro-scale during the RTM process. Thus the theory can be applied only when dimensions of pores and reinforcements are many orders of magnitude less than one in the flow direction. On such basis, the permeability can be determined by experiments [9, 10, 11, 12].

In the continuous manufacturing processing the double belt press, the impregnation of fabrics is developed along the direction of thickness rather than in plane usually in RTM. Thus the dimension in flow direction is comparable with the diameter of the roving constituting fabric layers. As a result, the impregnation of the fabric layers is estimated to be considerably distinct from impregnation phenomena in RTM.

This paper was devoted to clarify the impregnation phenomenon of composite sheets manufactured by using the double belt press with the aid of observation of samples fabricated under the same pressure and temperature boundary conditions in different process period or velocity. Meanwhile, it is also intended that the different degree of impregnation of the fabrics was obtained by applying appropriate process conditions to alter mechanical properties of thermoplastic composites.

OBSERVATION OF THE IMPREGNATION PROCESS

The utilization of the double belt press technique is actually a process of combining fabrics and thermoplastic materials along with the penetration of the molten thermoplastic materials into the fabric layers by pressure. As shown in Fig.1, the thermoplastic materials are processed by heat transfer and conduction originated from heating and cooling plates under pressure produced by a hydraulic system and imposed on the continuous laminates by steel belts. The resident time of the polymer in the high temperature and heating zone will directly have an impact on the molten polymer percolating into the fabric layers. The impregnation process will finally be completed in this zones.

It is no doubt that the completion of the impregnation process should take some time. As a consequence, the abasement or extension of the process period will lead to the decrease or increase of the impregnation degree of fabrics before the impregnation falls into saturation. By using an experimental layup as depicted in Fig.2, the completion of impregnation process could be approximately simulated by the impregnation states of samples produced by the different process period. To control the process period, it is a simple way to apply different process velocity in the manufacturing process.

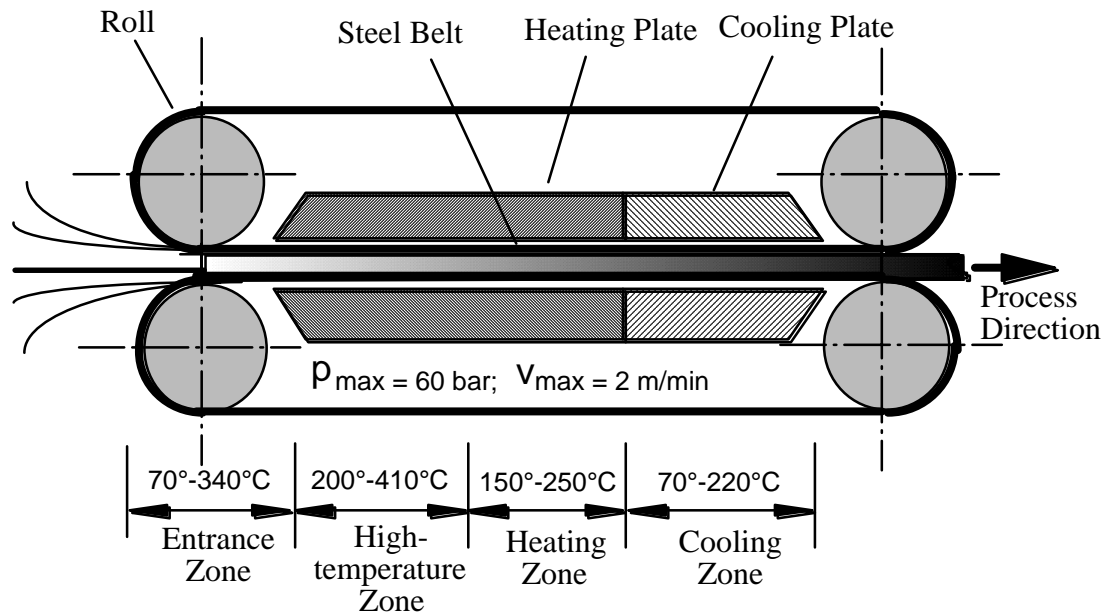


Fig.1 Manufacturing using the double belt press

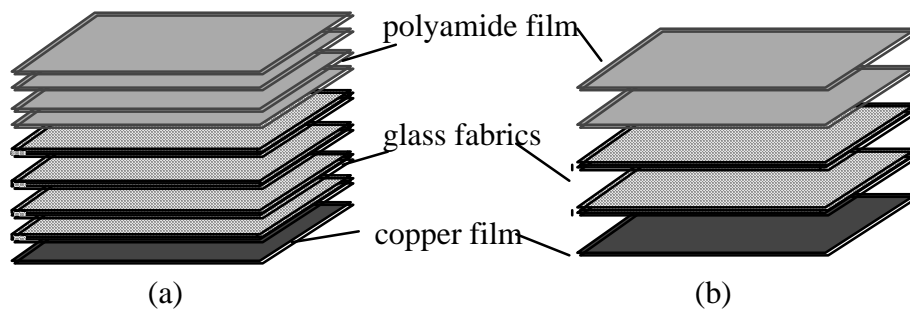


Fig.2 Experimental layout of polymer films and fabrics for samples

On the basis of the same pressure and temperature boundary conditions in the four zones depicted in Fig.1, two kinds of samples (1) and (2) with two and four glass fabric layers, shown as in Fig.2, are fabricated at the process velocity of 1.7, 1.3, 0.9, 0.5 and 0.2m/min. Different from common alternative layout, two or four layers of polyamide films are all mounted on the upper surface of the glass fabrics to increase the penetration distance of the molten polyamide. The fabricated samples are then cut into pieces and fixed in epoxy for optical microscope analysis.

As shown in Fig.3, (a)-(c) are pictures of cross sections of the sample (1) produced at the process velocity of 1.7, 0.9 and 0.2 m/min respectively. The ellipses embracing many fibres are cross sections of rovings, where the local white areas inside and outside the rovings are filled by epoxy and indicate fibres not being impregnated. It can be found that, in Fig3-(a), due to the limit resident time to stay in molten state, the polyamide flow infiltrate almost only into the second fabric layer, whereas the fibers inside the rovings of the layer were almost unimpregnated. After that, polyamide filled the whole fabric structure, and fibres inside the rovings lying at the upper layers were gradually partially impregnated at the same time, as shown in Fig.3-(b). This phenomenon may ascribe to the large difference in permeability between the fabrics structures and the fiber bundles. The impregnation process is ultimately

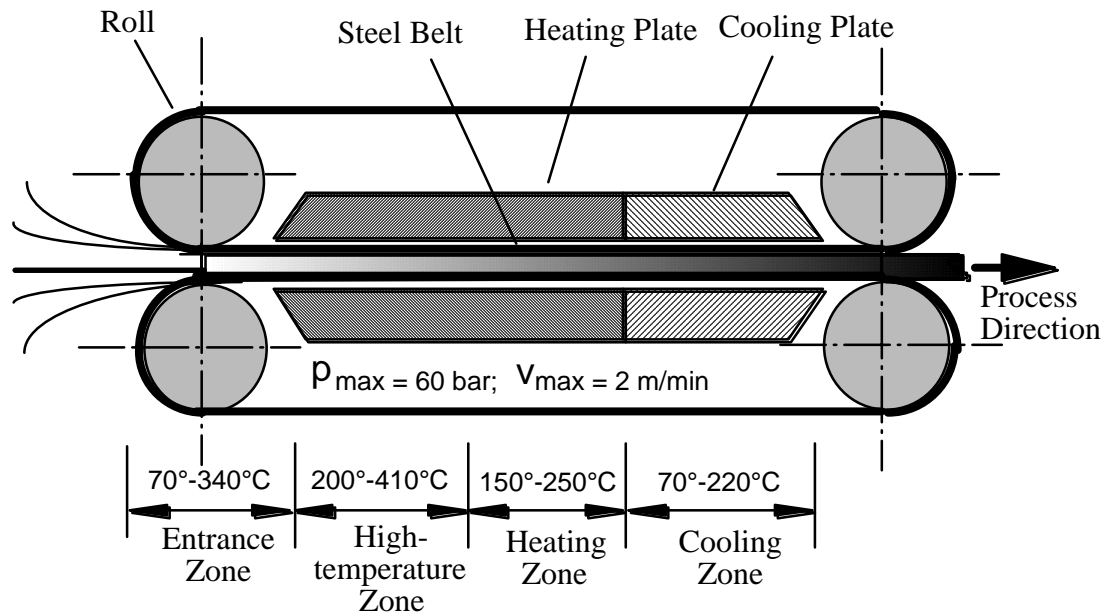


Fig.1 Manufacturing using the double belt press

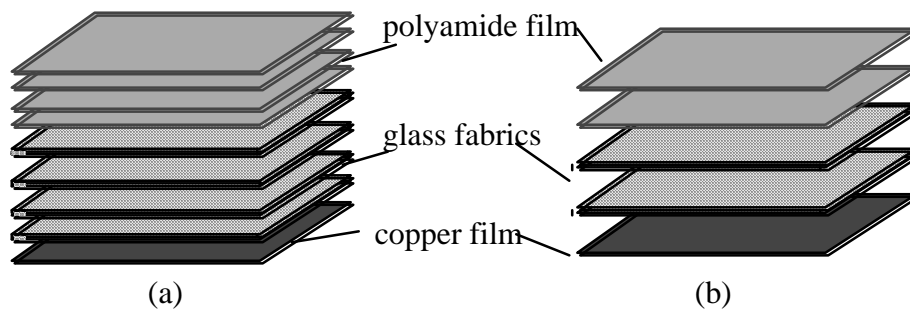


Fig.2 Experimental layout of polymer films and fabrics for samples

On the basis of the same pressure and temperature boundary conditions in the four zones depicted in Fig.1, two kinds of samples (1) and (2) with two and four glass fabric layers, shown as in Fig.2, are fabricated at the process velocity of 1.7, 1.3, 0.9, 0.5 and 0.2m/min. Different from common alternative layout, two or four layers of polyamide films are all mounted on the upper surface of the glass fabrics to increase the penetration distance of the molten polyamide. The fabricated samples are then cut into pieces and fixed in epoxy for optical microscope analysis.

As shown in Fig.3, (a)-(c) are pictures of cross sections of the sample (1) produced at the process velocity of 1.7, 0.9 and 0.2 m/min respectively. The ellipses embracing many fibres are cross sections of rovings, where the local white areas inside and outside the rovings are filled by epoxy and indicate fibres not being impregnated. It can be found that, in Fig3-(a), due to the limit resident time to stay in molten state, the polyamide flow infiltrate almost only into the second fabric layer, whereas the fibers inside the rovings of the layer were almost unimpregnated. After that, polyamide filled the whole fabric structure, and fibres inside the rovings lying at the upper layers were gradually partially impregnated at the same time, as shown in Fig.3-(b). This phenomenon may ascribe to the large difference in permeability between the fabrics structures and the fiber bundles. The impregnation process is ultimately

completed with the full fill of all space outside and inside the rovings as displayed in Fig.3-(c).

A more detailed impregnation process is described in Fig.4. The investigated samples were produced with the experimental layout as described in Fig.2-(2) at a process velocity of 1.7, 1.3, 0.9, 0.5 and 0.2 m/min respectively. It may be discovered that the polyamide first infiltrated the space outside the roving as shown in Fig.4-(a). After that, it began to penetrate into the roving as illustrated in Fig.4-(b), later gradually spread over the roving (see Fig.4-(c,d)) and finally impregnated all fibres in the roving as depicted in Fig.4-(e). Obviously, the white region filled with epoxy became smaller and smaller inside the rovings, thus it manifested that the samples had the impregnation degree increased. Simultaneously, the thickness of thermoplastic sheets became thinner and thinner during the process because the polyamide imposed on the top, as shown in the pictures, gradually penetrated into the roving, impregnated the fibres and squeezed out air at the same time.

The complete impregnation process illustrated above exhibits the strong inhomogeneity of flow pattern in the fabric layers. As described, macro-flow frequently described in the percolation of polymer and impregnation of fabrics in RTM has already lost its meaning since the completion of the impregnation process is not marked by the infiltration of flow through the fabric layers, but determined by the time required to penetrate into the roving. In this regard, the use of permeability given in Darcy's theory to describe an ability of polymer penetrating into the fabrics is inappropriate, and thus the impregnation process through the thickness of the fabrics cannot be predicted by Darcy's theory any more.

It may be concluded that the relative small distance along the infiltration direction of flow extremely magnified the influence of the micro-flow during the impregnation of fabrics, and the micro-flow into the rovings has a dominant effect on the actual impregnation of the fabrics. Such a strong effect of micro-flow on the impregnation is essentially different from one in RTM. Therefore, the description of the impregnation should also be distinct from one in RTM, where macro-flow prevails during the impregnation process and Darcy's theory could consequently be used.

One should pay attention to a case where the micro-flow will gradually lose its dominant position with the increase in thickness of fabric layers. As shown in Fig.3-(b), partial fibres in the rovings of the first and second layer had been impregnated to a different degree when the polyamide reached the bottom of the fabrics. It is logical to think that the micro-flow and inhomogeneous impregnation along the direction of thickness of the fabrics will be too small to have influence on the global flow and impregnation when the thickness is large enough, and the impregnation process will be as same as one in RTM.

Finally, it is emphasized that the special impregnation phenomena in the manufacturing of thermoplastic composites by using a double belt press may give an advantage in obtaining the thermoplastic composites with different impregnation degree by the control of process velocity.

EFFECTS OF IMPREGNATION ON MECHANICAL PROPERTIES

To some extent, the impregnation degree shows a degree of combination between polymer matrix and reinforcements, and must have a deep influence on mechanical properties of composites. As a consequence, variation of mechanical properties of thermoplastic

composites may come true by means of the manufacturing process design of composites featured with different degree of impregnation.

As discussed in the preceding sections, the process velocity in the manufacturing process has a conclusive effect on the impregnation degree of fabrics in thermoplastic composites. Additionally, it can also be easily understood that temperature boundary conditions are also related to the impregnation degree.

By choosing process velocity V_0 , $2V_0$, $3V_0$ and $4V_0$, where V_0 is a reference process velocity, and different process temperature, differently impregnated samples were fabricated by alternately stacking glass fiber fabrics and polyamide films. Their flexural mechanical property was then examined by using a three-point bending test to investigate the effect of impregnation on the mechanical property.

As shown in Fig.5-(a), the relationship between stress (load/area of cross section) and transverse displacement at the loaded point of a beam was obtained from the tests. It is obvious that the samples fabricated at a lower process velocity and thus a longer resident time in the high temperature zone exhibited brittle failure whereas the samples produced at a higher process velocity presented ductile fracture, where the step damage might be seen clearly for the samples at higher process velocity. Meanwhile, as displayed in Fig.6, the flexural modulus and strength was reduced with the increase of process velocity, while the deformation endurance was considerably enhanced for the relative high process velocity. Additionally, a character similar to plastic flow of metal — ductility was first achieved by increasing the process velocity from V_0 to $2V_0$ (see Fig.5-a) even if the deformation endurance held almost unchanged. The similar case could be also observed by decreasing the process temperature from $1.3077T_0$ to $1.0769T_0$ at a process velocity as shown in Fig.5-(b), where T_0 is a reference temperature.

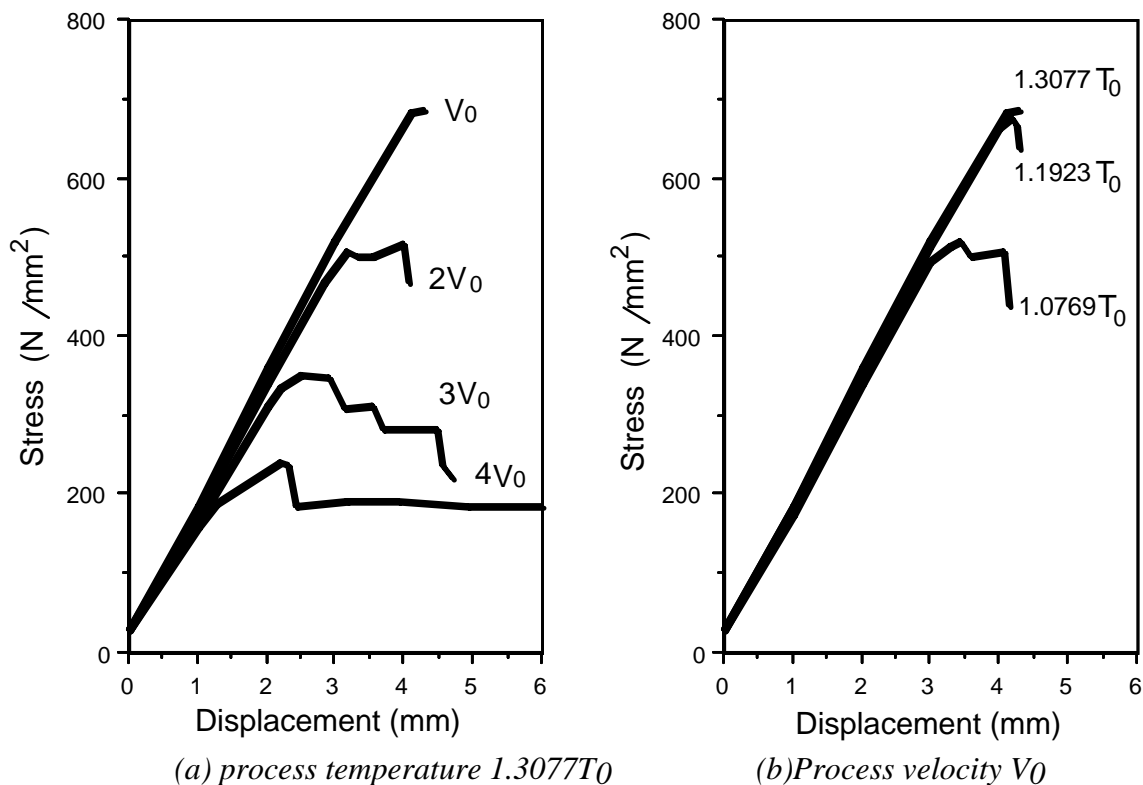


Fig.5 Flexural behavior of samples fabricated at different process velocity and temperature

It is necessary to understand that all phenomena observed in Fig.5 and Fig.6 were results mostly in response to the variation of impregnation no mater what parameters such as process velocity , temperature boundary conditions or others in the manufacturing process are employed to change mechanical properties of thermoplastic composites. Evidently, controlling impregnation would be a way to vary mechanical properties and optimize the manufacturing process of thermoplastic composites by using continuously running a double belt press.

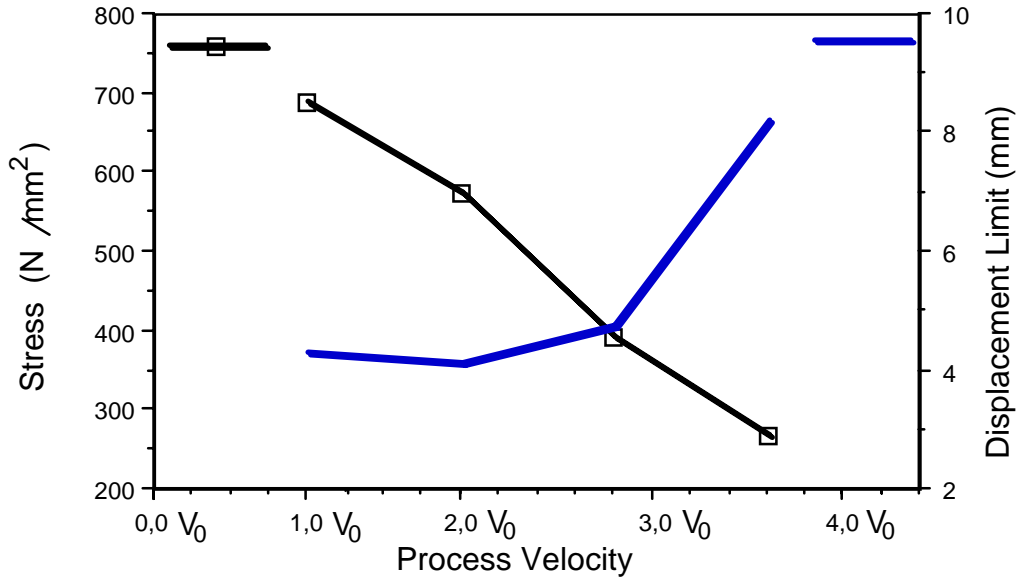


Fig.6 Flexural strength and deformation endurance of samples

CONCLUSION

Results from experiments showed that melted polymer promptly penetrated the fabric layers during the manufacturing process. The high resistance to the polymer flow into the roving produced strong inhomogeneity of flow pattern in fabric layers and considerably delayed the impregnation inside the rovings. Therefore, polymer first filled the space outside the rovings before fibres inside were gradually impregnated. On the other hand, thermoplastic composites with different degree of impregnation could be obtained by appropriately controlling the impregnation process resulting from the design of process velocity as well as temperature boundary conditions in the manufacturing process. Then mechanical properties of thermoplastic composites could be varied.

ACKNOWLEDGMENT

The authors are very grateful to the Alexander von Humboldt Foundation and also thank the German Federal Ministry of Education and Research (BMBF) for its support of the project 03V-3008.

REFERENCES

1. B. Liu, S. Bickerton and G. Advani, 'Modelling and simulation of resin transfer moulding (RTM) - gate control, venting and dry spot prediction', *Composites: Part A*, Vol.27A, 1996, pp135-141.
2. D. R. Calhoun and S. Yalvac et al., 'Mold filling analysis in resin transfer molding', *Polymer Composites*, Vol.17, 1996, pp251-264 .
3. M. Kaviany, *Principles of Heat Transfer in Porous Media*, Spinger-Verlag, New York, 1991.
4. F. R. Phelan Jr., 'Modeling of microscale flow in fibrous porous media', *Advanced Composite Materials: New Developments and Applications Conference Proceedings*, Detroit, Michigan USA, Sept.30-Oct.3, 1991, pp175-185.
5. M. V. Brusckhe, 'A predictive model for permeability and non-isothermal flow of viscous and shear-thinning fluids in anisotropic fibrous media', *CCM Report 92-56*, 1992.
6. F. R. Phelan Jr., 'Analysis of transverse flow in aligned fibrous porous media', *Composites: Part A*, Vol.27A, 1996, pp25-34.
7. J. V. Westhuizen and J. P. D. Plessis, 'An attempt to quantify fibre bed permeability utilizing the phase average Navier-Stokes equation', *Composites: Part A*, Vol.27A, pp263-269.
8. S. Ranganathan, F. R. Phelan Jr. and S. G. Advani, 'A generalized model for the transverse fluid permeability in unidirectional fibrous media', *Polymer Composites*, Vol.17, 1996, pp222-230.
9. R. S. Parnas and J. G. Howard et al., 'Permeability characterization. Part 1: A proposed standard reference fabric for permeability. Part 2: Flow behavior in multiple-layer preform', *Polymer Composites*, Vol.16, 1995, pp429-458.
10. C. Lekakou and M. A. K.Johari et al., 'Measurement techniques and effects on in-plane permeability of woven cloths in resin transfer moulding', *Composites: Part A*, Vol.27A, 1996, pp401-408.
11. E. J. Kart and A.W.Fell et al., 'Data validation procedures for the automated determination of the two-dimensional permeability tensor of a fabric reinforcement', *Composites: Part A*, Vol.27A, 1996, pp255-261.
12. V. Shafi and M. Neitzel, 'Effects of fabrics architecture on the longitudinal permeability in resin transfer moulding', *Proceedings of 7th European Conference on Composite Materials*, London, UK, 14-16 May, 1996, pp279-284.

USE OF OPTICAL FIBER SENSORS IN AUTOCLAVE MOLDING OF GFRP LAMINATES

Jianye Jiang¹, Katsuhiko Osaka², Takehito Fukuda²
Shinya Motogi², Hisashi Tsukatani³ and Shintaro Kitade⁴

¹ Graduate School of Engineering, Osaka City University
3-3-138, Sugimoto, Sumiyoshi-ku, Osaka, 558, Japan

² Department of Mechanical Engineering, Osaka City University
3-3-138, Sugimoto, Sumiyoshi-ku, Osaka, 558, Japan

³ Under Graduate School of Engineering, Osaka City University
3-3-138, Sugimoto, Sumiyoshi-ku, Osaka, 558, Japan

⁴ Composite Laboratory Research Institute, Ishikawajima-Harima Heavy Industries Co., Ltd
Shinnakahara 1, Isogo, Yokohama, 235, Japan

SUMMARY: A real-time measurement of internal and residual strains in GFRP laminates with an optical fiber strain sensor is performed in an autoclave molding. An Extrinsic Fabry-Perot Interferometric (EFPI) type optical fiber strain sensor is embedded into prepreg sheets before the molding. The ion viscosity and the temperature of the epoxy resin matrix are also simultaneously measured with the internal strain measurement. The results of the experiments shows that the internal and the residual strain of GFRP laminates during the molding can be monitored by the optical fiber sensor. It is also found that the circumstances around the embedded optical fiber strain sensor should be taken into account for the interpretation of the measured internal and residual strain.

KEYWORDS: internal strain, residual strain, autoclave molding, optical fiber strain sensor, cure process, GFRP laminate, ion viscosity

INTRODUCTION

Advanced composite materials are usually cured by autoclaves. Mechanical properties of molded products strongly depends on the molding conditions. The cure conditions such as temperature, pressure and their timings and rates etc. in the autoclave molding are empirically determined by some trial-and-error tests. Such process might be time consuming if products have varieties of e.g., their shape and thickness, of matrix materials and reinforcing fibers. Therefore it is strongly desired to establish a way of determining an optimum cure condition which can be automatically adapted to varieties of moldings. For this purpose, the optimum cure condition has to be determined based on the data of the degree of matrix cure, void content and residual stress and/or strain etc. within products manufactured under various molding conditions. Among them, the degree of matrix cure is most important, and residual stress data are also needed for they considerably affect the mechanical properties of products. Real-time monitoring during the molding is expected to be the best way to obtain their data. Recently studies of real-time monitoring of matrix cure with optical fiber sensors have been performed. Druy et al. have reported a cure monitoring with infrared-transmitting optical fiber sensors[1]. An ultrasonic detection technique with optical fibers has been applied to a cure monitoring by Ohn et al.[2]. Myrick et al. have reported a cure monitoring using Raman

spectrum measurement with optical fibers[3]. Their works have shown that the real-time cure monitoring at any position in the laminates is possible using optical fiber sensors which have the same shape as reinforcing fibers. Wang et al. determined residual stresses by curled shape of unsymmetric laminates after molding[4]. Analysis of residual stresses due to cool-down from the post cure for the symmetric cross-ply composites has been performed by Chen et al., but the experiment has not yet been done[5]. A paper on real-time monitoring of residual stresses and/or strains has not been found until now.

In the present study, a real-time monitoring method of internal strains is investigated with embedded optical strain sensors in GFRP laminates during autoclave molding process. In the experiment, ion viscosity and temperature of the epoxy resin matrix are simultaneously measured with the internal strains. Comparing their results, the relationship between internal strains and the cure process is investigated.

OPTICAL FIBER STRAIN SENSOR

In the measurement of internal strains, Fiber Optic Strain Gage System II (FOSS II) (Fiber & Sensor Technologies) was used. It had an optical fiber sensor whose sensing type was an Extrinsic Fabry-Perot Interferometric (EFPI) one. A schematic diagram of the EFPI strain sensor is shown in figure 1. FOSS II detects small changes of the length of air gap and converts them to strains using a gage factor of each strain sensor. The strain is measured by the following process. FOSS II transmits laser beam into the input/output optical fiber, and detects the intensity of the beam reflected by the reflector in the sensor. The operating temperature and resolution of the EFPI strain sensor in this experiment are -272 to $+350$ °C and $10,000 \mu\epsilon$ in the full scale. The gage size of the EFPI strain sensor was $350 \mu\text{m} \times 4 \text{mm}$.

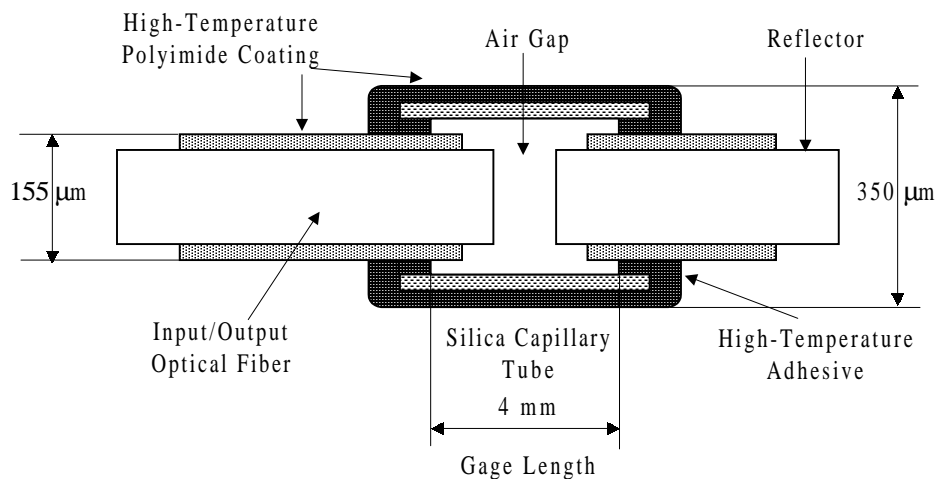


Fig.1 Schematic diagram of the EFPI strain sensor

DIELECTRIC CONSTANT MONITORING

The electric property of thermoset resins is in general dielectric from its liquid to solid phases. The dielectric response under AC field is the sum of contributions from dipole moments and

ionic charges. Development of the gelation and polymerization reduces the mobilities of dipoles and isolated ions. Therefore dielectric response can be an indicator of solidification of high-polymers, in particular the loss part of dielectric constant is convenient to estimate the solidification.

Let the complex specific dielectric constant be ϵ under AC electric field. ϵ is written as, by definition,

$$\epsilon = \epsilon' - i\epsilon'' \quad (1)$$

where ϵ' , and ϵ'' are the specific dielectric constant and the loss factor respectively. The latter is closely related to the solidification process of polymers. The loss factor ϵ'' can be expressed as

$$\epsilon'' = \frac{\sigma}{\omega\epsilon_0} + \frac{(\epsilon_l - \epsilon_h)\omega\tau}{1 + \omega^2\tau^2} \quad (2)$$

where

- σ = ionic conductivity,
- ω = angular frequency of the applied AC field,
- ϵ_0 = permeability of the vacuum,
- ϵ_l = relaxed permeability,
- ϵ_h = unrelaxed permeability,
- τ = relaxation time.

When the frequency is not very high ($\omega\tau \ll 1$), the loss factor is reduced to the ionic contribution only, i.e.,

$$\epsilon'' = \frac{\sigma}{\omega\epsilon_0} \quad (3)$$

Therefore the conductivity measurement gives the loss factor in the low frequency approximation. The reciprocal of conductivity $1/\sigma$ i.e., the electric resistance, is particularly convenient to estimate the solidification since its minimum (maximum) corresponds to the maximum (minimum) mobility of ions in polymers. The resistance $1/\sigma$ is also called the ion viscosity since it has a clear correspondence with the usual viscosity measured by a rheometer. The ion viscosity measurement by dielectric monitoring is more convenient than usual viscosity because the ion viscosity can be continuously measured through all phases of polymers. On the other hand, the rheometer can only measure the liquid viscosity [6].

EXPERIMENT

In the autoclave molding experiment, GFRP laminates were used. The prepreg used was GF Scotch-ply 1009-36 by 3M and the matrix resin was high temperature type epoxy. Their stacking configurations were $[0_8]$ and $[0_2/90_2/0_2]$. Different cure patterns corresponding to their stacking configurations were adopted. Two EFPI strain sensors were embedded in the middle plane of the laminates in stacking process of prepreps. Location of two EFPI strain sensors embedded within composite layers is shown in Figure 2. The dielectric sensor was also set up within prepreps in stacking process. A schematic diagram of monitoring system in the experiment is shown in figure 3. The signal cables of EFPI strain sensors (effectively optical fibers) and a dielectric sensor were connected to measurement apparatus out of the

autoclave. The way of pulling the cables out of the autoclave were devised in order to keep sealing up it. The strain responses of GFRP laminates from the EFPI strain sensor were measured by the FOSS II system, being saved in a personal computer by an AD converter. The dielectric responses and temperature of resin were measured by Eumetric 100A of Micromet Instruments, being saved in a personal computer by a RS232C interface.

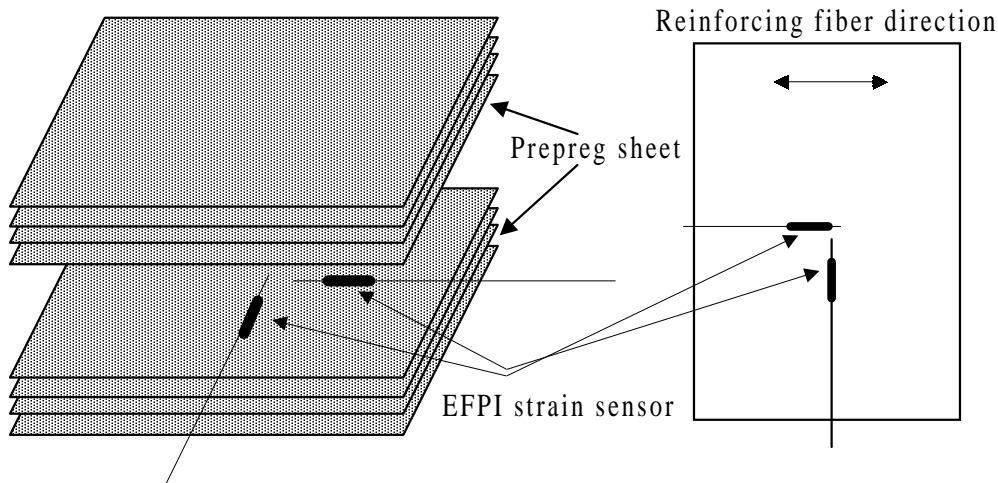


Fig.2 Location of EFPI strain sensors within a UD laminate

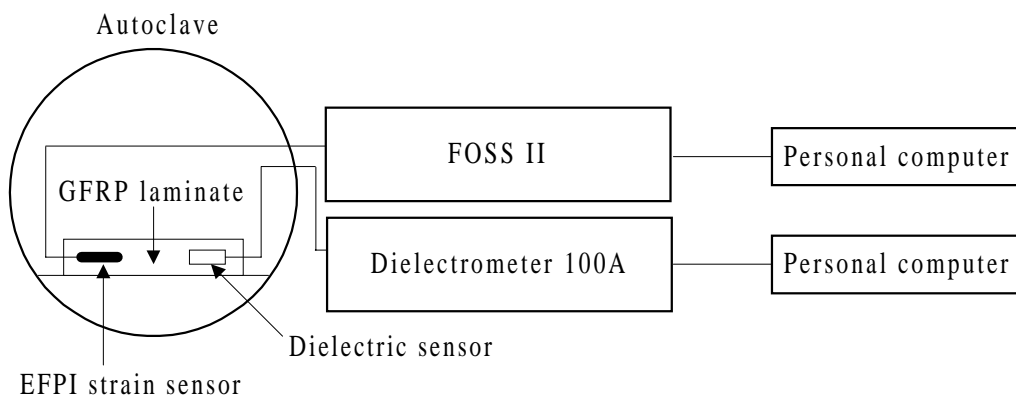


Fig.3 Schematic diagram of monitoring system

RESULTS AND DISCUSSION

Unidirectional Laminate

The curing pattern in the autoclave molding for unidirectional laminate is shown in figure 4. Figure 5 shows the measured results of change in ion viscosity of epoxy matrix and temperature of the material. The magnitude of change in the ion viscosity is indicated by $\log(1/\sigma)$. The abscissa of the figure shows the molding time. The ion viscosity rapidly decreases at the first temperature increasing stage. This corresponds to melting of the epoxy matrix. From this change of the ion viscosity, it is found that all matrix have finished to melt at about 50 min of the molding time. Then the ion viscosity slightly changes at the constant temperature stage. At the post cure stage, it gradually approaches to a definite value, namely, the cure is almost completed. At the last cooling stage, the ion viscosity rapidly increases.

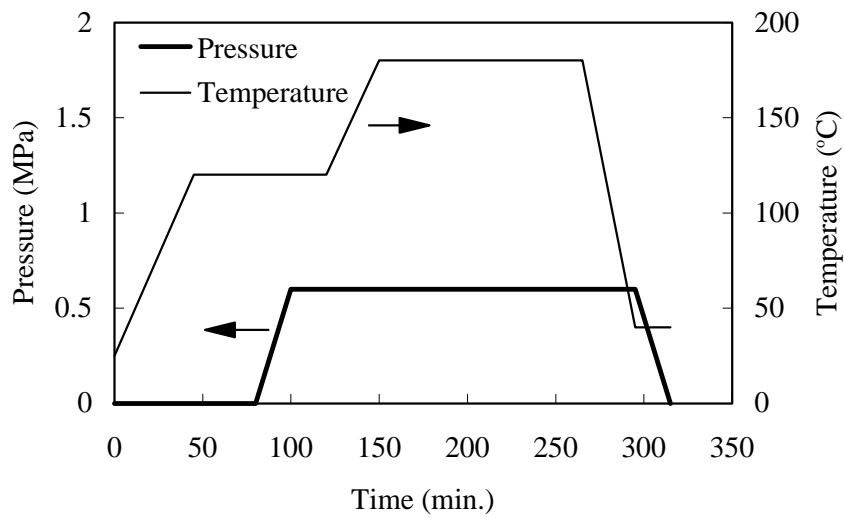


Fig.4 Curing pattern in autoclave molding

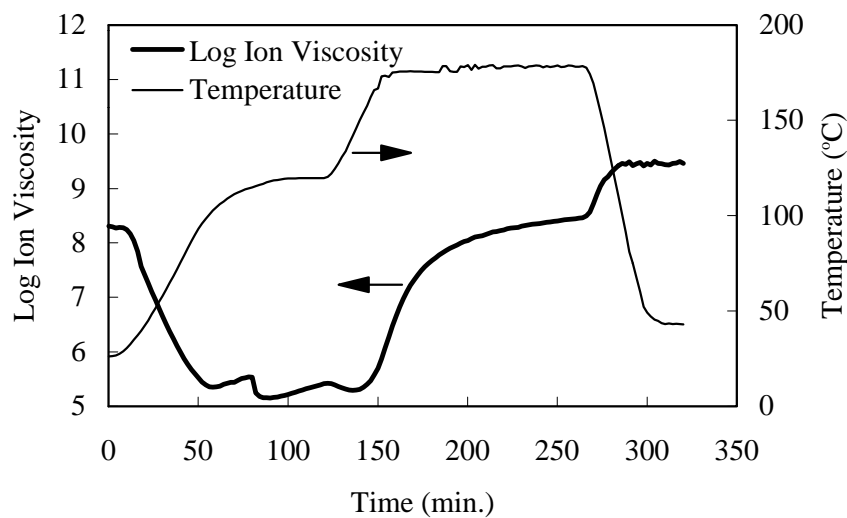


Fig.5 Change in ion viscosity and temperature

Figure 6 shows the experimental results of internal strains by two EFPI strain sensors. In the figure, A is the strain obtained by the EFPI strain sensor embedded in the same direction with the reinforcing fiber of unidirectional laminates. B shows the strain obtained by the strain sensor embedded perpendicularly to the fiber direction. The strain A gradually increases at the first temperature increasing stage. It shows the maximum value before the ion viscosity shows the minimum. And then it begins to gradually decrease. It changes from the tensile strain to the compressive one and it increases until the molding is completed. In the same way as the result of A, B rapidly increases at the first temperature increasing stage and shows the maximum value before the ion viscosity denotes the minimum. It changes from the tensile to the compressive and shows the maximum compressive value at the second temperature increasing stage. In the same way as the change of the ion viscosity, it gradually approaches to a definite value. At the last cooling stage, it rapidly increases.

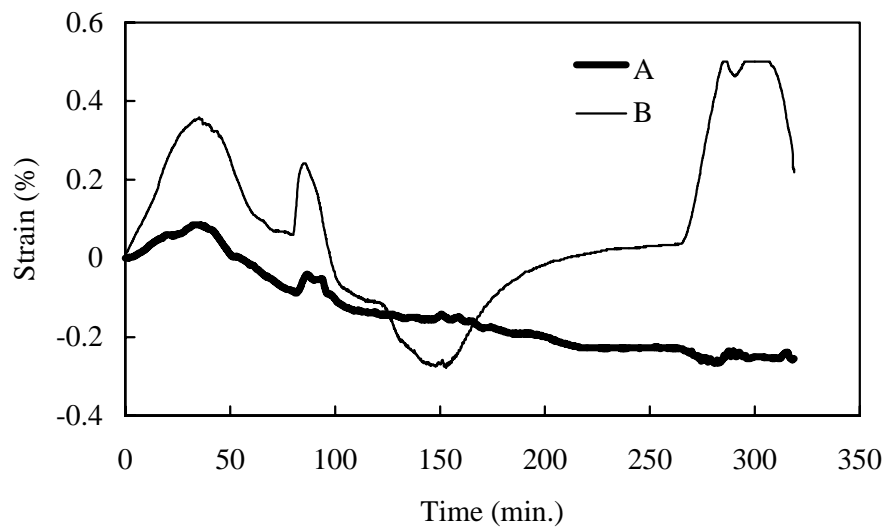


Fig.6 Internal strain responses of GFRP UD laminate

Crossply Laminates

Figure 7 shows the cure pattern in the autoclave molding for crossply laminates. In the figure, two kinds of molding conditions with different cooling rates at the last molding stage are shown. One is the rate of 4.6°C/min and another is that of 2.3°C/min.

Figure 8 shows the measured results of change in the ion viscosity of epoxy matrix and temperature within the autoclave. They show the same change as those of the unidirectional laminate do with the change of temperature and pressure in the autoclave molding. The ion viscosity increases abruptly at the molding time of about 140 min., when the gelation of the epoxy matrix begins.

Figure 9 shows the internal strains measured by the EFPI strain sensors embedded in the same direction with the reinforcing fibers in central laminae of the crossply laminate. In the figure CL1 represents the result of the laminate molded with the cooling rate of 4.6°C/min and CL2 represents that of 2.3°C/min. In spite of the same molding conditions except for the last cooling rates, the strain responses of CL1 and CL2 show the very different change till 200 min of the molding time. After 200 min, the strain of CL1 keeps the same value till 270 min

when the cooling stage begins and then it decreases. In the cooling stage, it changes uniformly and to the compressive strain. CL2 shows the same tendency to change.

Figure 10 shows the internal strains measured by the EFPI strain sensors embedded in the perpendicular direction to the reinforcing fibers in central laminae of the crossply laminate. In the figure CT1 represents the result of the laminate molded with the cooling rate of 4.6°C/min and CT2 represents that of 2.3°C/min. The strain responses of CT1 and CT2 show the very different change till 200 min. After 200 min, they are constant till 270 min at the beginning of the cooling stage. This tendency of change is the same in CL1 and CL2. After 270 min, their strains increase uniformly.

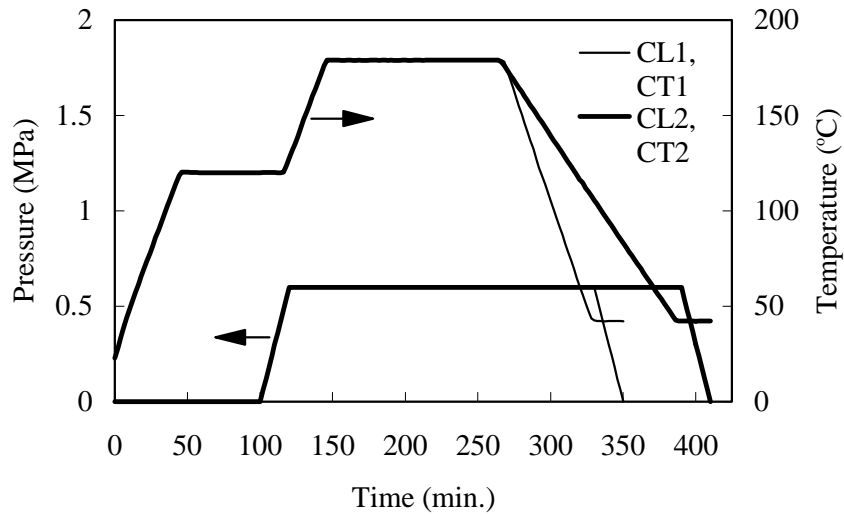


Fig.7 Curing pattern in autoclave molding

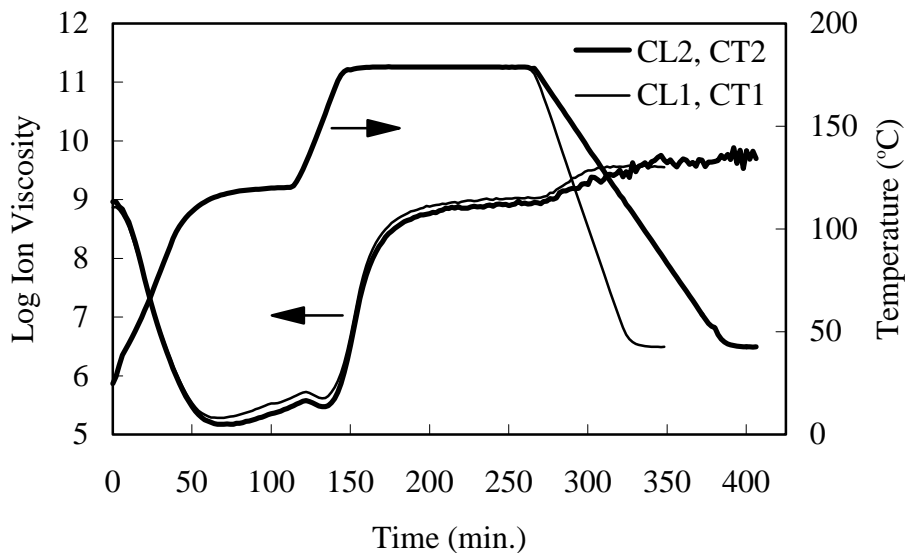


Fig.8 Change in ion viscosity and temperature

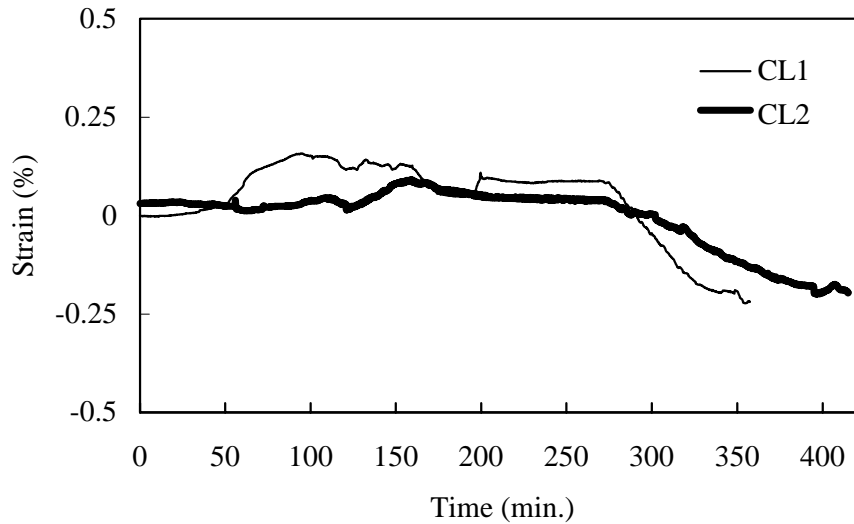


Fig.9 Strain responses of CL1 and CL2

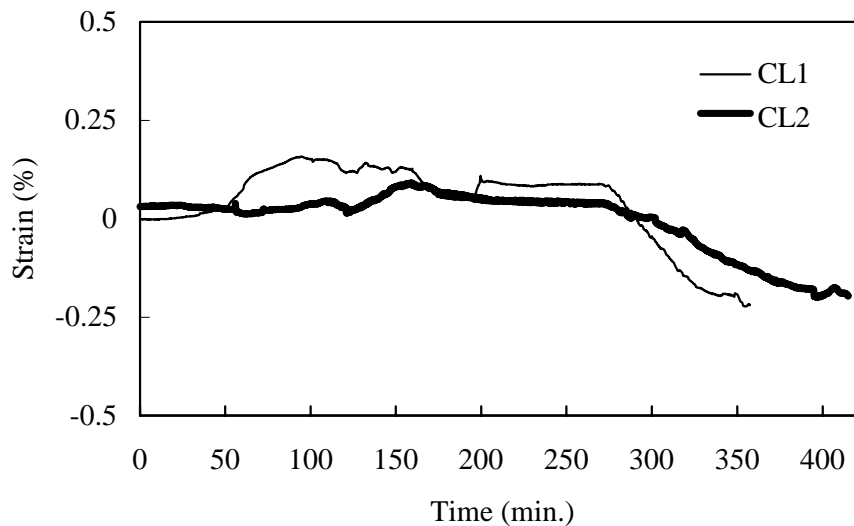


Fig.10 Strain responses of CT1 and CT2

The residual strain of the laminate in which the EFPI strain sensor was embedded in the same direction with the reinforcing fibers is the compressive one. On the other hand, the residual strain of the laminate in which the EFPI strain sensor was embedded in the perpendicular direction to the reinforcing fibers is tensile. The compressive residual strain is generally expected to develop in the laminate by the shrinkage of the epoxy matrix at the cooling stage in the molding. But the contradictory result was obtained in the measurement of the residual strain in the laminate which contained the strain sensors embedded in the perpendicular direction to the reinforcing fibers. The reason why the tensile residual strains took place is investigated below.

As the EFPI strain sensor is very large in comparison with the reinforcing glass fibers, the strain measured by the sensor can be different from that of the reinforcing fibers. Therefore the state of the embedded strain sensor within the laminate can influence the result measured by it. In order to examine, the micrographs of the state of the embedded strain sensor were

taken. Figures 11 and 12 are the micrographs of the cross-section of the part in which the strain sensors were embedded in the perpendicular direction to the reinforcing fibers. Figure 11 shows the cross-section which was made by cutting along the same direction with the EFPI strain sensor. Figure 12 shows the cross-section which was made by the cutting along the perpendicular direction to the EFPI strain sensor. The diameter of the sensing part of the EFPI strain sensor is very large in comparison with the reinforcing fibers. The embedding the strain sensor into the laminate gives rise to the resin rich region neighboring to the sensor. From this figure, it is known that the sensing part of the sensor is loaded with the transverse compression. In the case of the sensor embedded in the same direction with the reinforcing fibers, the resin rich region was not found. It is thought that the different result of the residual strain is due to such different surrounding conditions of the sensor. However this explanation is not yet confirmed, so it is necessary to be validated.

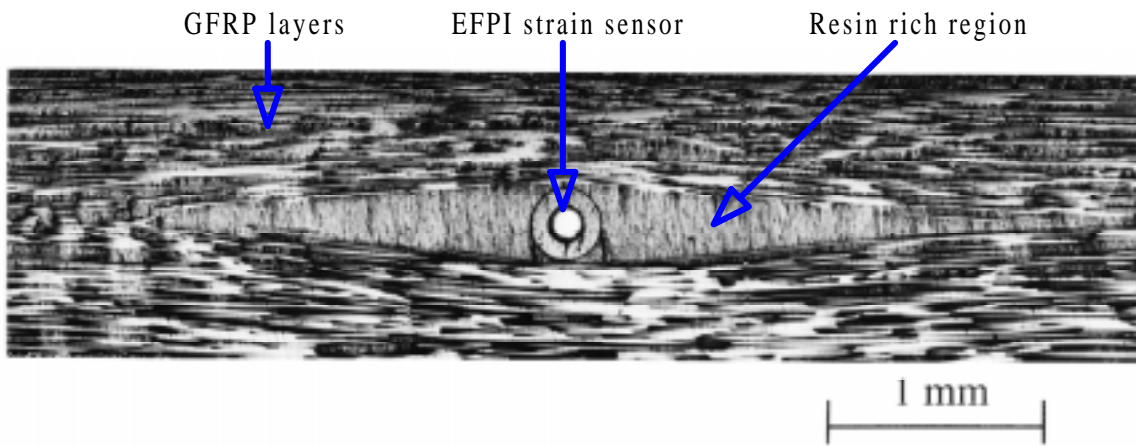


Fig.11 Micrograph of the EFPI strain sensor embedded in the crossply laminate (the cross-section perpendicular to the sensor)

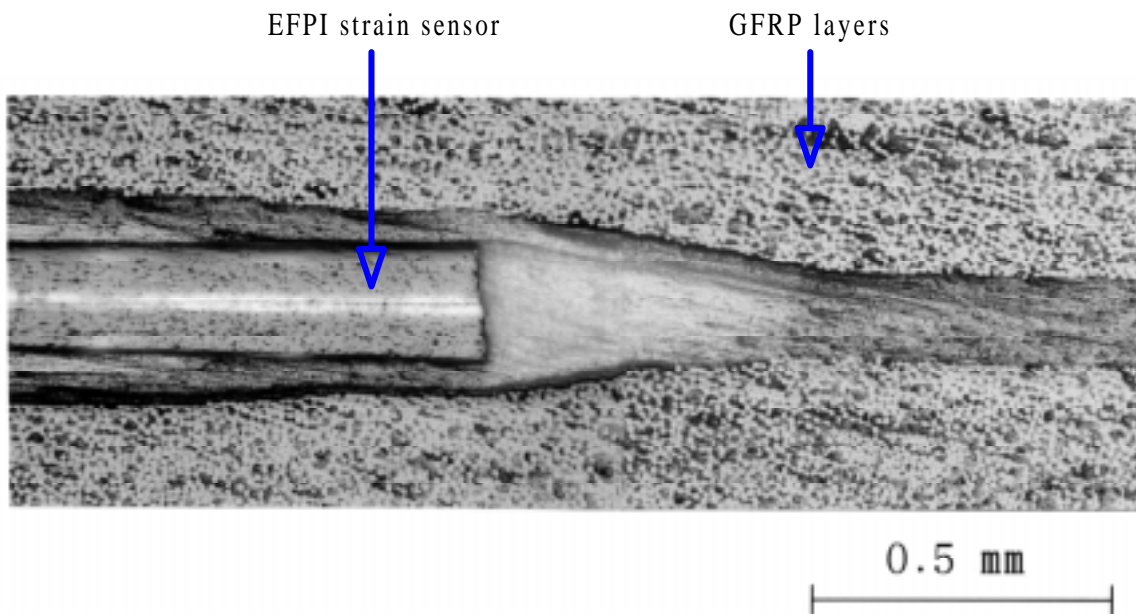


Fig.12 Micrograph of the EFPI strain sensor embedded in the crossply laminate (the cross-section along the sensor)

CONCLUSION

In this paper, the applicability of optical fiber sensors to real-time measurement of internal and residual strains in GFRP laminates was investigated in an autoclave molding. In the measurement an EFPI strain sensor was used. The results of experiments showed that the internal strain of GFRP laminates during the molding can be monitored by the EFPI strain sensor and the residual strains of the laminates can be estimated from the internal strains measured at the end of the molding. But it was found that the measured data by the EFPI strain sensor do not directly indicate the internal strain of the reinforcing fibers or matrix resins. Therefore it was recognized that the measured strain data by the EFPI strain sensor should be converted to the true internal strain taking account of the embedded circumstances of the sensor in the laminates.

REFERENCES

1. Mark A. Drury, Lucy Elanjian and W.A. Stevenson, "Composite cure monitoring with infrared optical fiber", *SPIE Vol. 986 Fiber Optic Smart Structures and Skins*, 1988, pp. 130-134.
2. Myo M. Ohn, Andrew Davis, Kexing Liu and Raymond M. Measure, "Embedded fiber optic detection of ultrasound and its application to cure monitoring", *SPIE Vol. 1798 Fiber Optic Smart Structures and Skins*, V 1992, pp. 134-143.
3. M.L. Myrick, S.M. Angel, R.E. Lyon, and T.M. Vess, "EPOXY CURE MONITORING USING FIBER-OPTIC RAMAN SPECTROSCOPY", *SAMPE Journal*, Vol. 28, No. 4, July/August 1992, pp. 37-42.
4. T.-M. Wang, I. M. Daniel and J.T. Gotro, "Thermoviscoelastic Analysis of Residual Stresses and Warpape in Composite Laminates", *Journal of Composite Materials*, Vol. 26, No. 6/1992, pp. 883-899.
5. Rong-Sheng Chen, Chen-Yi Tu & Guey-Shin Chen, "The residual thermal stresses due to cool-down of post cure for the symmetric cross-ply TCM composite material", *Composite Structures*, 26 (1993) 155-166.
6. Johnny R. Gentry, "Automotive/Aerospace Synergism in Computer-Aided Composite Processing", *SAE TECHNICAL PAPER SERIES*, No.911120, 1991.

PERMEABILITY OF FIBER REINFORCEMENTS AFTER SHEAR DEFORMATION

Chyi-Lang Lai and Wen-Bin Young

*Department of Aeronautics and Astronautics
National Cheng-Kung University
Tainan, Taiwan 70101, ROC*

SUMMARY: In liquid composite molding processes such as resin transfer molding and structural reaction injection molding, fiber reinforcements usually experience some deformation in order to conform to the complex shape of the mold cavity. Deformation of the fiber reinforcement is characterized by factors as the local surface curvature of mold and the type of reinforcements. For woven fabrics, shear deformation is the major mechanism to conform to the complicated mold cavity during the preforming process. The structure of the woven fiber mat after deformation is rearranged, resulting in variation of local fiber content. This may cause some significant effects on the fiber permeability and result in quite different mold filling pattern from expected. Incomplete wetting of the fiber preform during the mold filling stage may occur. Therefore, study of the permeabilities for deformed fiber reinforcements are quite important. In the flow simulation of the filling process, success of the prediction highly depends on the correct values of in-plane permeabilities. Change of in-plane permeability of the fabric after shear deformation must be well understood. This article investigated the permeability of woven fiber mats under different shearing angles. Several flow experiments were conducted on bidirectional woven roving fabrics in different shear angles. Two relevant factors, the ratio of principal permeabilities and the direction of principal axes with respect to the orientation of the fabric, are studied to investigate their variations with respect to shear deformation of the fiber reinforcements. It is found that the shifted angle of the principal axes is increasing with the increase of the shearing angle. At the same time, in-plane permeability ratio may decrease as increasing the shearing angle.

KEYWORDS: Permeability, resin transfer molding, polymer composites, fiber deformation

INTRODUCTION

In the fabrication of polymer composites, an important step is to homogeneously bring the polymer matrix and the fiber reinforcements together. Several manufacturing processes accomplish this step by injecting the fluid resin into the dry fiber reinforcements inside a close cavity. Among those, resin transfer molding (RTM) and structural reaction injection molding (SRIM) are becoming increasing popular composite processes because of their fast cycle time, low labor requirements and low equipment cost. In the RTM process, the pre-mixed resin is injected under pressure into a closed mold preplaced with fiber reinforcements. During this process, resin flows around and through the fiber bundles until the entire fiber reinforcements are saturated. In a reaction injection molding pultrusion (RIM pultrusion) process, resin is forced into a die to wet out the incoming dry fibers. This process differs from the traditional wet bath approach in that resin is injected into the die under a pressure. Therefore, the

pultrusion speed and the product quality are both increased. Also, the types of resin materials that can be used are less limited.

Among those processes, the most common defect encountered is the poor wetting of the fiber reinforcements, which leads to the distributions of micro-voids in the final products. The appearances of voids in the final product can be attributed to the problems of inappropriate fiber bundle wet-out and the resin filling path. Voids can appear as the resin flows unevenly and encloses air into a large dry spot or as the wetting of the fiber bundle is not complete. Researchers had conducted numerical and experimental analysis of resin filling in the RTM process in order to understand the filling flow patterns. The results can help to estimate the formation of voids due to the uneven filling flow. Permeabilities which characterize the ability of the fluid to penetrate the fiber reinforcements are the fundamental material properties used in the study of the resin filling process. Theoretical and experimental works had been conducted to study the permeabilities of different fiber reinforcements [1~36].

In the experimental measurements of the in-plane fiber permeabilities, two types of techniques were reported. For the one-dimensional case, a uniform flow from a line source is forced to penetrate through the fiber reinforcements [1~8]. The flow rate is kept constant while the injecting pressure is measured as the fluid passing through the fiber reinforcements. Based on Darcy's law, the in-plane permeabilities can be obtained from the measured injection pressure. The major drawback of this method is the leakage flow at the edges of the fiber reinforcements during the measuring process, which is called the edge effect[21, 21]. For woven fiber mats, the edge effect is more server due to the loose fiber structure near the edges. Therefore, some extra sealing at the edges of the fiber reinforcements is necessary in conducting the one-dimensional line source measurement. However, due to the difficulty of edge sealing, the repeatability of experiments using this method is quite poor. One other experimental method utilizes a two-dimensional flow [9, 10, 17]. Fluid is injected from the center of a circular fiber reinforcement and the inlet pressure and flow front positions are measured. A complicated analytical solution of the flow in a circular field is solved based on Darcy's law. Then, the measured flow front position and the inlet pressure are used to determine the permeabilities.

All of the above mentioned measurements were conducted on measuring the undeformed bi-directional and unidirectional fiber reinforcements. In liquid composite molding processes such as RTM and SRIM, fiber reinforcements usually experience some deformation in order to conform to the complex shape of the mold cavity. Deformation of the fiber reinforcement is characterized by factors as the local surface curvature of mold and the type of reinforcements. For woven fabrics, shear deformation is the major mechanism to conform to the complicated mold cavity during the preforming process. The structure of the woven fiber mat after deformation is rearranged, resulting in variation of local fiber content. This may cause some significant effects on the fiber permeability and result in quite different mold filling pattern from expected. Incomplete wetting of the fiber preform during the mold filling stage may occur. Therefore, study of the permeabilities for deformed fiber reinforcements are quite important. In the flow simulation of the filling process, success of the prediction highly depends on the correct values of in-plane permeabilities. Change of in-plane permeability of the fabric after shear deformation must be well understood.

There are few reports addressing the variation of permeability after deformation of the fiber reinforcements. Hammami [35] measured the directional permeability of unidirectional fiber mat after shear deformation. Rudd [36] reported the permeability of random and aligned fiber

mats under shear deformation. This article investigated the permeability of woven fiber mats under different deformed angles. Several flow experiments were conducted on bi-directional woven roving mats. Two relevant factors, the ratio of principal permeabilities and the direction of principal axes with respect to the orientation of the fabric, are studied to investigate their variations with respect to the shear deformation of the woven fiber mats.

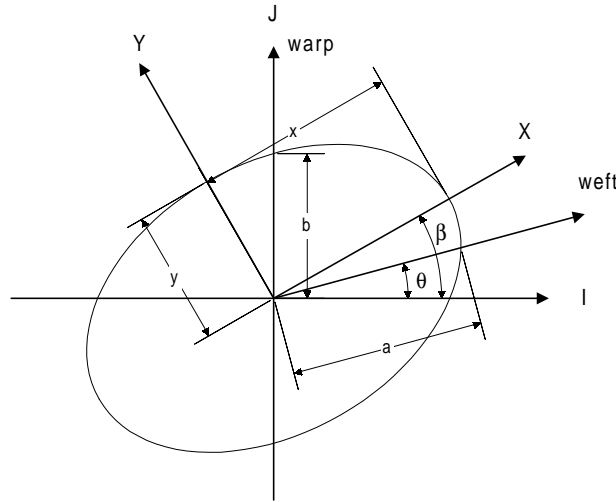


Fig. 1: Description of the shearing angle and the deformed fabric

BASIC CONCEPTS

Deformation of woven fiber mat under forming process has been discussed by many researchers. The primary deformation mode is the shear deformation of the fiber roving. Fig. 1 illustrates the woven fiber roving under deformation angle θ and the resulting main axis that has an angle β with respect to the original axis. In this diagram, the warp direction is kept aligned with the original J direction, and the weft direction is sheared in an angle θ with respect to the original I direction. Due to the change of the fiber structure, the resulting principal direction of the permeability will shift to the X direction. Based on the assumption that the flow rate along the weft and warp directions are kept at the same ratio, the following relation can be devised:

$$\left(\frac{b}{a}\right)^2 \approx \alpha = \frac{k_2}{k_1} \tag{1}$$

where k_1 and k_2 are the principal permeabilities of the undeformed fiber fabric. It is further assumed that the flow front shape of the deformed fiber fabric remains elliptic. The permeability ratio ($\bar{\alpha}$) of the deformed fabric can be expressed as:

$$\bar{\alpha} = \left(\frac{Y}{X}\right)^2 = \frac{k_y}{k_x} \tag{2}$$

where k_x and k_y are the principal permeabilities of the deformed fabric. The flow front shape of the deformed fabric shown in Fig. 1 can be described by the following Equ.

$$A I^2 + B I J + J^2 + D = 0 \tag{3}$$

From Fig. 1, the ellipse passes two points, $(a\cos\theta, a\sin\theta)$ and $(0, b)$. For the undeformed fabric, the tangent of the flow front in the warp direction parallels to the weft direction, and vice versa as shown in Fig. 2. It is assumed that, for the deformed fabric, the tangent of the flow front in the warp direction still parallels to the weft direction (also shown in Fig. 2). Based on this assumption, the slope at point $(0, b)$ can be expressed as:

$$\left(\frac{dJ}{dI}\right)_b = \tan\theta \quad (4)$$

Substituting Equ 4 and the two points, $(a\cos\theta, a\sin\theta)$ and $(0, b)$, into Equ 3, the constants A , B , and D can be evaluated. The resulting Equ of the ellipse is

$$\frac{1}{\cos^2\theta} \left(\frac{b^2}{a^2} + \sin^2\theta\right) I^2 - 2\tan\theta J + J^2 - b^2 = 0 \quad (5)$$

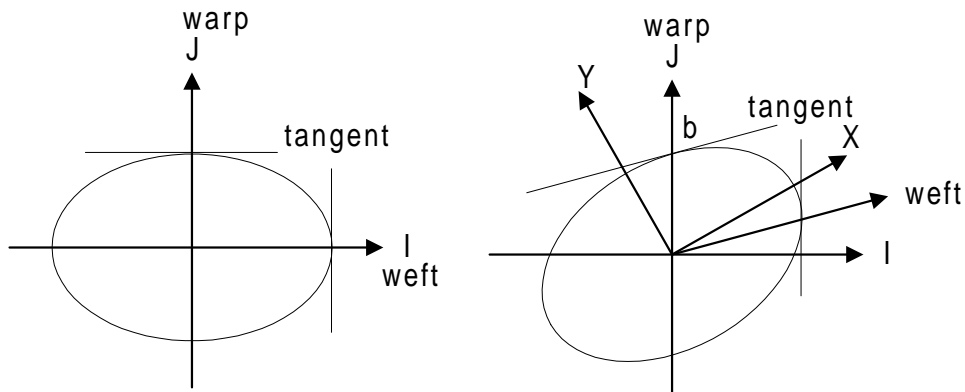


Fig. 2: Tangent of the flow front along the weft and warp directions for deformed and undeformed fabric

By formula of the ellipse Eqs, we have

$$\tan 2\beta = \frac{B}{A-1} \quad (6)$$

and

$$\beta = \frac{1}{2} \tan^{-1} \frac{\sin 2\theta}{\cos 2\theta - \alpha} \quad (7)$$

If the ellipse Equ is described in X and Y coordinates and the relations that it passes the points $(a\cos(\beta-\theta), -a\sin(\beta-\theta))$ and $(b\sin\beta, b\cos\beta)$ are applied, the permeability ratio, $\bar{\alpha}$, is found to be

$$\bar{\alpha} = \frac{\sin^2(\beta-\theta) - \alpha \cos^2\beta}{\alpha \sin^2\beta - \cos^2(\beta-\theta)} \quad (8)$$

The above relation is based on the assumption that the tangent of the flow front along the warp direction always parallels to the weft direction. For the case of unidirectional fiber mat,

this is close to the reality since the fiber will form a barrier for the transverse flow perpendicular to the fiber. For the woven fiber fabric, the crimps of fiber roving create some vacancy between the fibers. Therefore, the weft roving only has a partial barrier effect on the flow along the warp direction. It is, thus, reasonable to modify the relation in Equ 4 to the form as:

$$\left(\frac{dJ}{dI}\right)_b = m \tan\theta \quad (9)$$

where m is a correcting factor between 0 and 1 depending the structure of the fiber network. It is assumed to be a material constant of the fiber reinforcement. The resulting ellipse equation becomes:

$$\frac{1}{\cos^2\theta} \left(\frac{b^2}{a^2} + (2m-1)\sin^2\theta\right)I^2 - 2m \tan\theta IJ + J^2 - b^2 = 0 \quad (10)$$

and

$$\beta = \frac{1}{2} \tan^{-1} \frac{m \sin 2\theta}{1 - \alpha - 2m \sin^2 \theta} \quad (11)$$

$$\bar{\alpha} = \frac{\sin^2(\beta - \theta) - \alpha \cos^2 \beta}{\alpha \sin^2 \beta - \cos^2(\beta - \theta)} \quad (12)$$

Equs 11 and 12 are used to predict the shift angle of the permeability axis and the permeability ratio for the fiber fabric that is sheared to an angle, θ . For the limit case of $\alpha = 1$, Eqs 11 and 12 become:

$$(\beta)_{\alpha=1} = \frac{\pi}{4} + \frac{\theta}{2} \quad (13)$$

$$(\bar{\alpha})_{\alpha=1} = \frac{m \sin\theta (\sin\theta - 1) + \cos^2\theta}{m \sin\theta (\sin\theta + 1) + \cos^2\theta} \quad (14)$$

As the value of m is equal to 1, Eqs 11 and 12 reduced to Eqs 7 and 8. For the case of $\beta = \theta$ (i.e., the principal permeability axis is always along the fiber roving), m has a minimum value that can be derived from Equ 11.

$$m = 1 - \alpha \quad (15)$$

Therefore, the value of m must be located in between $(1-\alpha)$ and 1 to ensure that β is always greater than θ .

EXPERIMENTAL MATERIALS AND APPARATUS

Fiberglass (E-glass) is the most commonly used reinforcement in RTM process, especially for automotive body panels. The bi-directional woven roving fiberglass mats were used in this study. A Newtonian liquid, hydraulic oil R68 with room temperature viscosity of 159 cp, was used with the woven roving fiber mat (TGFW-600 glass fiber mats from Taiwan Glass Co.,

Ltd.). The surface density of the glass fiber, which is defined as the weight per unit surface area, is equal to 600 g/m^2 .

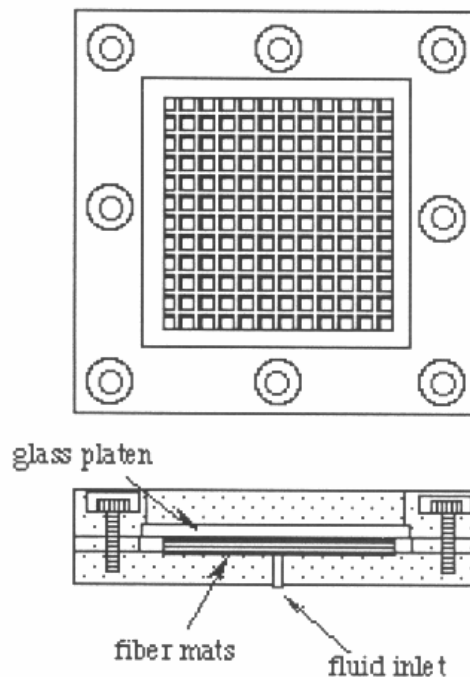


Fig. 3: Apparatus for measuring the flow shape in deformed woven fiber mats

The flow shape in deformed fiber mats were measured using the mold filling apparatus shown schematically in Fig. 3. A pressure pot was constructed by connecting a steel cylinder to the high pressure nitrogen cylinder. The steel cylinder was filled with a non-reactive fluid by means of a gear pump and driven at a constant pressure by the high pressure source. The filling pressure can be varied by adjusting the pressure regulator.

The 30 cm by 30 cm platens of the mold were constructed from 2.5 cm thick aluminum plates. A 6.35 mm diameter inlet was drilled into the center of the lower platen. The upper platen was cut a 20 by 20 cm opening at the center, which was fitted into a hardened transparent glass. The mold cavity was formed by inserting eight pieces of rectangular 2 mm or 5 mm thick aluminum blocks between the upper and lower molds. The entire assembly was clamped together by screw bolts. Measurements were made by placing in the mold cavity with a 18x18 cm fiberglass stack containing a 1.8 cm hole in the center. The fiber reinforcements were first sheared to the desired angle and, then, cut into the size to fit in the mold. As fluid was injected from the center gate, the flow shape was recorded.

RESULTS AND DISCUSSIONS

TGFW-600 glass fiber mats were used to check the first assumption done in the previous analysis. The fiber fabric was first sheared to the desired angle, then the fluid was injected into fiber fabric. Until a developed ellipse shape was formed, the injection was stopped. The wet distances along the weft and warp roving from the inlet to the flow front were measured. Fig. 4 shows plot of the ratio, (b/a) , with respect to different shear angles. Although, the data scatters a lot, the mean value seems to keep unchanged with respect to the shear angle.

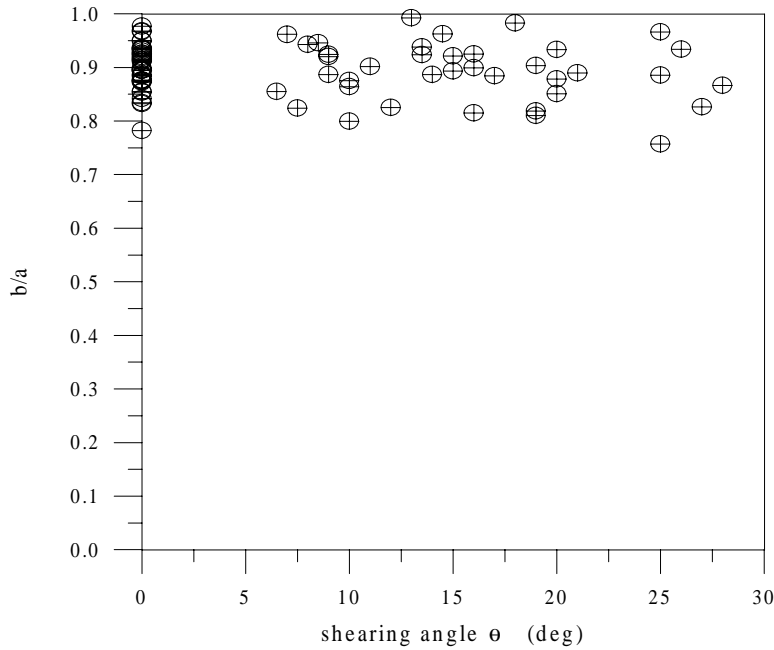


Fig. 4: Ratio (b/a) for fiber fabric with different shear angle

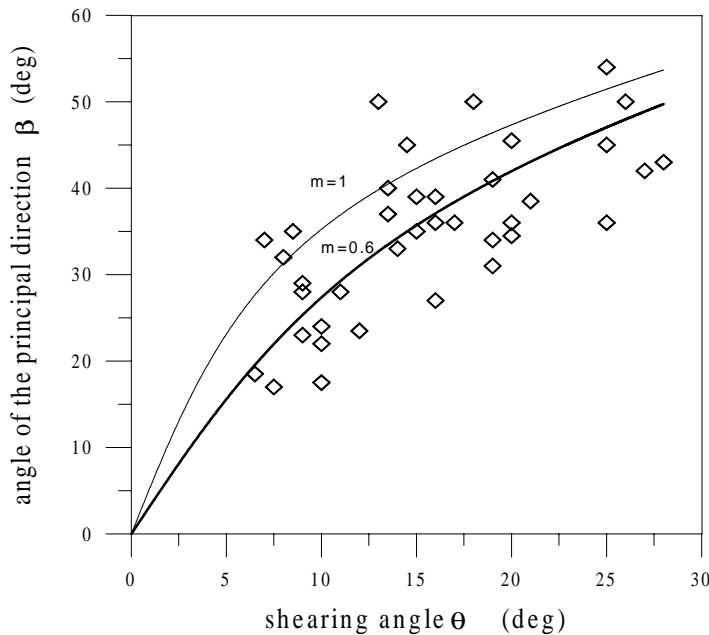


Fig. 5: Principal direction angle for fiber fabric with different shear angles

The principal directions of the fiber fabric after shear deformation were also measured. The image of the flow front was first scanned into the computer, then a best fit ellipse to the flow front image was found to define the principal direction. The principal direction angle for TGFW-600 glass fiber mat is plotted against the shear angles as shown in Fig. 5. It shows a gradually increase for the principal direction angle that is always larger than the corresponding shear angle. The predictions from Equs 11 and 12 are also shown in Fig. 5 with m equaling to 0.6 and 1. For this type of fiber fabric, $m = 0.6$ gives a better prediction of the principal angle. The permeability ratios for fiber fabric after deformation are shown in

Fig. 6 together with the prediction with $m=1$ and $m=0.6$. Again, the prediction for $m=0.6$ gives a better prediction.

From the experimental observation of measuring other type of fiber fabric, it could be concluded that, as α is less than 0.4, the value of m is close to $(1-\alpha)$. This is for the types of fiber reinforcements with strong flow preference in one direction than the other, such as unidirectional fiber mat. As mentioned before, for this type of fiber mats, the principal direction always follows the roving direction, and the value of m will approach its minimum. For woven roving bi-directional fiber mats, the value of m found in the laboratory is close to 0.6~0.7 for $\alpha > 0.6$. However, it is a function of α , which is unable to be defined theoretically in the current status.

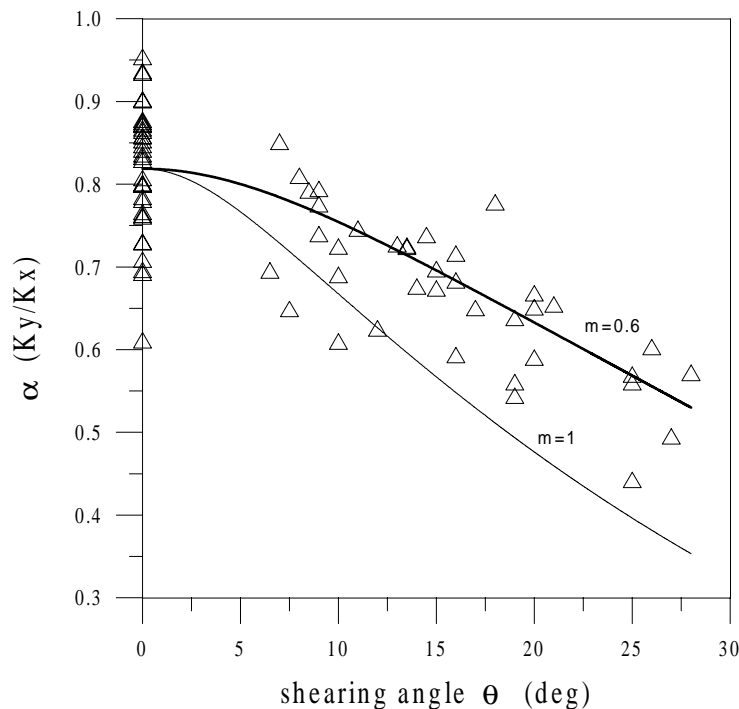


Fig. 6: Permeability ratio for fiber fabric with different shear angles

CONCLUSIONS

This article investigated the permeability of woven fiber mats with shearing angles. Several flow experiments were conducted on bidirectional woven roving fabrics in different shear angles. Two relevant factors, the ratio of principal permeabilities and the direction of principal axes with respect to the orientation of the fabric, are studied to investigate their variations with respect to shear deformation of the fiber reinforcements. It is found that the shifted angle of the principal axes is increasing with the increase of the shearing angle. At the same time, in-plane permeability ratio may decrease as increasing the shearing angle. A theoretical model was proposed to predict the principal direction angle and permeability ratio after the fiber fabric was deformed.

REFERENCES

- 1 R. Gauvin and M. Chibani, " The Modeling of Mold Filling in Resin Transfer Molding", Intl. Polym. Proc., 1,42 (1986).
- 2 J.A. Molnar, L. Trevino, and L.J. Lee, Polym. Comp., 10, 414 (1989).
- 3 R. Gauvin and M. Chibani, " A study of Permeability of Non-woven Reinforcements in Composite Molding", SAMPE Quarterly, April, 52 (1990).
- 4 K.L. Ahn and J.C. Seferis, " Simultaneous Measurements of Permeability and Capillary Pressure of Thermosetting in Woven Fabric Reinforcements", Polym. Comp., 12(3), 146 (1991).
- 5 L. Trevino, K. Rupel, W.B. Young, M.J. Liou and L.J. Lee, "Analysis of Resin Injection Molding in Molds with Preplaced Fiber Mats I : Permeability and Compressibility Measurements", Polym. Comp., 12(1), 20 (1991).
- 6 R.S. Parnas and F.R. Phelan Jr., " The Effects of Heterogeneous Porous Media on Mold Filling in resin Transfer Molding", SAMPE Quarterly, January, 53 (1991).
- 7 B. Gebart, P. Gudmundson, L. Strombeck and C. Lundemo, "Analysis of the Permeability in RTM Reinforcements", Intern.Conf. of Comp. Materials , 15E (1991).
- 8 Y.R. Kim and S.P. McCarthy, " Resin Flow Through Fiber Reinforcements During Composite Processing", SAMPE Quarterly, April, 16 (1991).
- 9 K.L. Adams, B. Miller, and L. Rebenfeld, "Forced In-Plane Flow of an Epoxy Resin in Fibrous Networks", Polym. Eng. Sci., 26(20), 1434 (1986).
- 10 K.L. Adams, W.B. Russel and L. Rebenfeld, "Radial Penetration of a Viscous Liquid into a Planar Anisotropic Porous Medium", Int. J. Multiphase Flow,14(2)., 203 (1988).
- 11 K.L. Adams and L. Rebenfeld, "Permeability Characteristica of Multilayer Fiber Reinforcements Part I : Experiment Observations", Polym. Comp., 12(3), 179 (1991).
- 12 K.L. Adams and L. Rebenfeld, "Permeability Characteristica of Multilayer Fiber Reinforcements Part I : Theoretical Model", Polym. Comp., 12(3), 186 (1991).
- 13 B.R. Gebart, "Permeability of Unidirectional Reinforcements for RTM", J. Compo. Materials, 26(8), p1100, 1992.
- 14 L. Skartsis, B. Khomami, and J.L. Kardos, " Resin Flow Through Fiber Beds During Composite Manufacturing Processes. Part II: Numerical and Experimental Studies of newtonian Flow Through Ideal and Actual Fiber Beds", Polym. Eng. Sci., 32(4), p231, 1992
- 15 R. Parnas and A.J. Salem, "A Comparison of the Unidirectional and Radial In-plane Flow of Fluids Through Woven Composite Reinforcements", Polym. Compo., 14(5), p383, 1993.
- 16 J. Summerscales, "A model for the Effect of Fiber Clustering on the Flow Rate in Resin Transfer Moulding", Compo. Manufacturing, 4(1), p27, 1993.
- 17 A.W. Chan, D.E. Larive and R.J. Morgan, "Anisotropic Permeability of Fiber Preforms: Constant Flow Rate Measurement", J. Compo. Materials, 27(10), p996, 1993.
- 18 A.L. Berdichevsky and Z. Cai, "Preform Permeability Predictions by Self-Consistent Method and Finite Element Simulation", Polym. Compo., 14(2), p132, 1993.
- 19 Z. Cai and A.L. Berdichevsky, "An Improved Self-Consistent Method for Estimating the Permeability of a Fiber Assembly", Polym. Compo., 14(4), p314, 1993.
- 20 Z. Cai and A.L. Berdichevsky, "Numerical Simulation on the Permeability Variations of a Fiber Assembly", Polym. Compo., 14(6), p529, 1993.

- 21 C.H. Wu, T.J. Wang, and L.J. Lee, "Trans-Plane Fluid Permeability Measurement and Its Applications in Liquid Composite Molding", *Polym. Compo.*, 15(4), p289, 1994.
- 22 T.J. Wang, C.H. Wu, and L.J. Lee, "In-Plane Permeability Measurement and Analysis in Liquid Composite Molding", *Polym. Compo.*, 15(4), p278, 1994.
- 23 CD Rudd, JP Chick, DJ Morris, and NA Warrior, "In-Plane Permeability Characterization of Mats and Fabrics Using SRIM", ICCM-10, pp. III-181-III-188 Canada, 1995.
- 24 JR Weitzenbock, RA Sheno, and PA Wilson, "Characterization of Resin Flow Through Thick Laminates in Resin Transfer Molding", ICCM-10, pp. III-301-III-308 Canada, 1995.
- 25 S.H. Ahn, W.I. Lee, and G.S. Springer, "Measurement of the Three-Dimensional Permeability of Fiber Preforms Using Embedded Fiber Optic Sensors", *J. of Composite Materials*, 29(6), pp. 714-733, 1995.
- 26 T.S. Lundstrom and B.R. Gebart, "Effect of Perturbation of Fiber Architecture on Permeability Inside Fibre Tows", *J. of Composite Materials*, 29(4), pp. 424-443, 1995.
- 27 W.B. Young and S.F. Wu, "Permeability Measurement of Bidirectional Woven Glass Fibers", *J. of Reinforced Plastics and Composites*, 14(10), pp. 1108-1120, 1995.
- 28 P. Ferland, D. Guittard, and F. Trochu, "Concurrent Methods for Permeability Measurement in Resin Transfer Molding", *Polymer Composites*, 17(1), pp. 149-158, 1996.
- 29 B.R. Gebart and P. Lidstrom, "Measurement of In-Plane Permeability of Anisotropic Fiber Reinforcements", *Polymer Composites*, 17(1), pp. 43-51, 1996.
- 30 R. Gauvin, F. Trouchu, Y. Lemenn, and L. Diallo, "Permeability Measurement and Flow Simulation Through Fiber Reinforcement", *Polymer Composites*, 17(1), pp. 34-42, 1996.
- 31 F.R. Phelan Jr. And G. Wise, "Analysis of Transverse Flow in Aligned Fibrous Porous Media", *Composites Part A*, 27A(1), pp. 25-34, 1996.
- 32 C. Lekakou, MAK Johari, D. Norman, and MG Bader, "Measurement techniques and effects on in-plane permeability of woven cloths in resin transfer moulding", *Composites: Part A*, 27A, pp. 401-408, 1996.
- 33 E.J. Carter, A.W. Fell, P.R. Griffin, and J. Summerscales, "data validation procedures for the automated determination of the two-dimensional permeability tensor of a fabric reinforcement", *Composites: Part A*, 27A, pp. 255-261, 1996.
- 34 S. Ranganathan, F.R. Phelan Jr., and S.G. Advani, "A Generalized Model for the Transverse Fluid Permeability in Unidirectional Fibrous Media", *Polymer Composites*, 17(2), pp. 222-230, 1996.
- 35 A. Hammami, F. Trouchu, R. Gauvin, and S. Wirth, "Directional Permeability Measurement of Deformed Reinforcement", *J. of Reinforced Plastics and Composites*, 15(6), pp. 552-562, 1996.
- 36 C.D. Rudd, A.C. Long, P. Mcgeehin, and P. Smith, "In-Plane Permeability Determination for Simulation of liquid Composite Molding of Complex Shapes", *Polymer Composites*, 17(1), pp. 52-59, 1996.

WETTING AND CONSOLIDATION OF NYLON 6 POWDER COATED CARBON FIBER TOW

M. Rammoorthy¹ and J. Muzzy²

¹ *Technical Center, AlliedSignal Inc.,*

P.O. Box 31, Petersburg, Virginia 23804, U.S.A.

² *Composites Manufacturing Research Program, School of Chemical Engineering
Georgia Institute of Technology, Atlanta, Georgia 30332-0100, U.S.A.*

SUMMARY: An attractive means for combining continuous reinforcing fibers with thermoplastic matrices entails powder coating spread fiber tows. After fusing the powder to the tow it is quenched, creating a flexible but bulky towpreg. When nylon 6 is the powder coating on carbon fiber tow, significant debulking of the towpreg occurs while the towpreg is being heated. Surprisingly, most of this debulking occurs before the nylon 6 is completely melted. For an oven setting of 260 °C the void content of a powder coated 12,000 filament tow dropped from over 90 % to under 20 % in less than 20 seconds even though the temperature inside the tow does not reach 225 °C, the final melting point of nylon 6, until 30 seconds in the oven. A capillary flow model was developed which effectively represents this wetting behavior.

KEYWORDS: nylon 6, carbon fiber, wetting, consolidation, powder coating, prepreg, towpreg, thermoplastic.

INTRODUCTION

A schematic of a powder coating process for producing flexible thermoplastic towpreg is shown in Figure 1. By spreading the multifilament tows to expose virtually all the fibers and then powder coating the exposed filaments, the difficulty of forcing molten polymer with a high viscosity into a packed bed of fibers is avoided. After powder coating the thermoplastic is melted to fuse the polymer to the fibers. The hot towpreg is quenched before the spread towpreg is condensed in order to obtain a flexible towpreg comprised of multiple plies of partially wet out fibers. Both this process and product form have been patented [1,2] and commercialized [3]. This flexible towpreg is well suited for making textile preforms by braiding and weaving

For processes like filament winding and advanced tow placement it is preferable to have a well consolidated, fully wet out, void-free towpreg with well defined dimensions. The primary objectives of this research were to develop a process as well as the attendant processing parameters to convert flexible unconsolidated towpreg into well consolidated towpreg. In earlier work on this subject [4,5] both roll consolidation and pultrusion were found to be inadequate for this task because dry fibers would hang up in the die or rollers, break, and accumulate during operation, ultimately disrupting the process. In this study non-contact heating is emphasized as a means of wetting out these dry fiber sections. Following

this thermal wetting and debulking it is possible to make well consolidated and shaped towpreg without incurring process disruptions

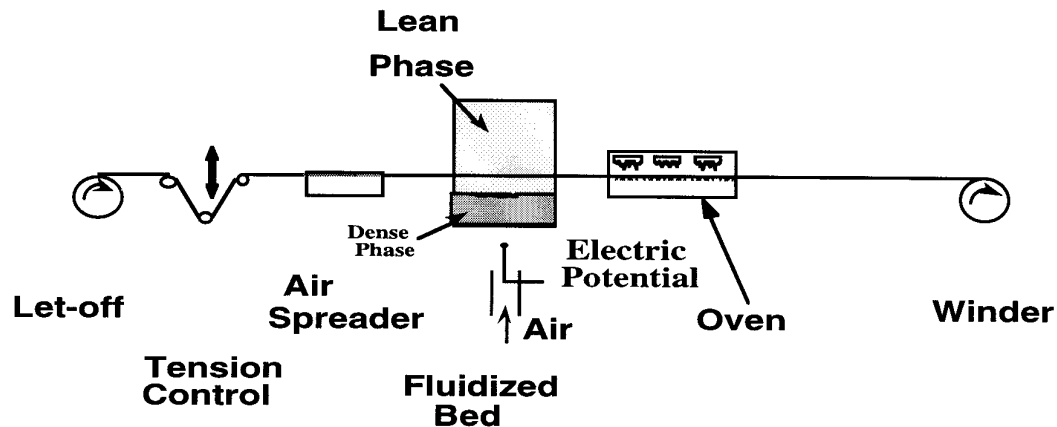


Fig. 1: Process for producing powder coated tow using an electrostatically charged fluidized bed

EXPERIMENTAL

The towpreg used for this research was made using 12,000 filament carbon fiber tow, Celion G30-500, from BASF and later Toray Industries. The powder coating was performed by Custom Composite Materials, Inc., now Applied Fiber Systems, Ltd [3]. The towpreg was served with nylon fiber to improve the bundle integrity. This nylon fiber was less than 1 % of the towpreg. The towpreg contained 60 % fiber by volume. The cross-sectional area of this towpreg is 8 mm² whereas the same towpreg after complete consolidation has a cross-sectional area of 0.91 mm². Thus, the flexible towpreg is quite bulky due to the incomplete melting and flow of nylon powder within the towpreg.

The apparatus for investigating wetting in an oven is shown in Figure 2. The towpreg was tied to a steel rod which was anchored at one end. The towpreg was tensioned using pressure rollers. The tension was set and measured using an ALPHACELLTM tension measuring device from Alpatron, Inc. The oven, a ThermolyneTM Type 21100 tubular furnace, was placed on rails. The oven was heated to a preset temperature while in position over the steel rod. After reaching steady state the oven was rolled over the towpreg section. The towpreg temperature was continuously recorded by computer from a thermocouple embedded in the towpreg. The experiments were repeated for different residence times, oven temperatures and towpreg tensions.

The cross-sectional areas of the towpregs were obtained from SEM at 60X magnification. The outline of the towpreg cross-section was traced using transparent paper which was then photocopied, cut and weighed. A calibration curve for the paper weight versus magnified area was used to obtain the towpreg cross-sectional area.

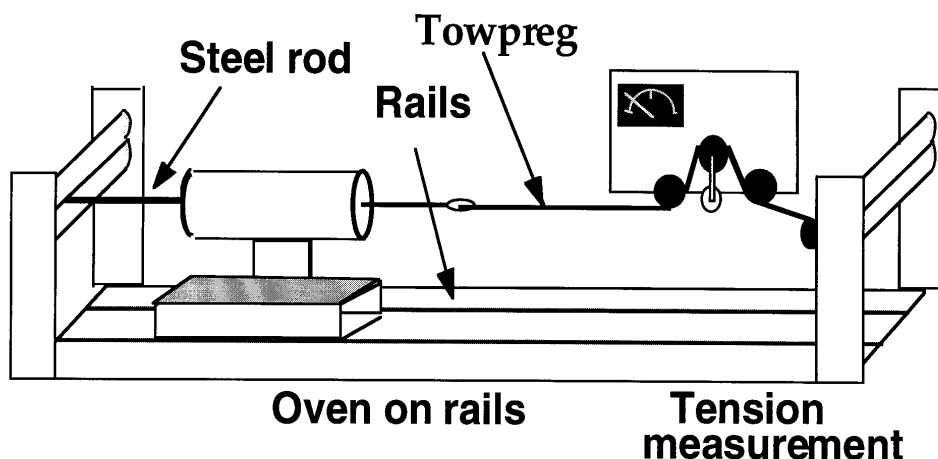


Fig. 2: Apparatus for studying towpreg wetting versus time, tension and oven temperature

WETTING EXPERIMENTS

Figure 3 shows the towpreg temperature and cross-sectional area for an oven setting of 260 °C. The cross-sectional area of the towpreg starts to drop rapidly once the towpreg reaches 180 °C. It stops shrinking rapidly around 20 seconds when the towpreg is at 210 °C. There is a gradual further shrinkage to about 1 mm², close to the void-free cross-sectional area of 0.91 mm².

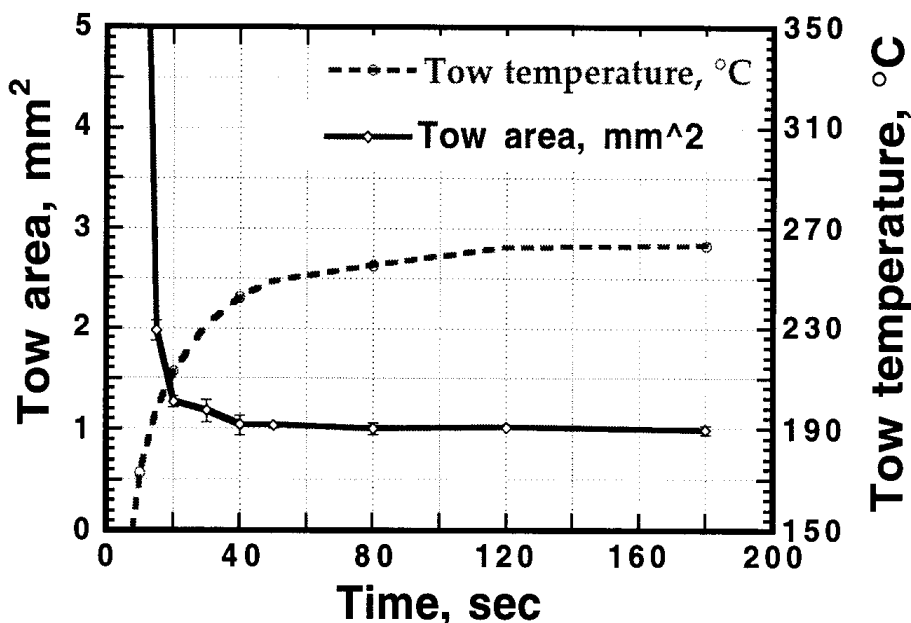


Fig. 3: Towpreg cross-sectional area and temperature versus residence time in oven.

Similar responses were seen at oven settings of 332 and 386 °C. Due to the higher temperatures, the residence times to approach 1 mm² were reduced. Also, at 386 °C the towpregs expanded after 40 seconds due to degradation of the nylon. For all three oven settings most of the towpreg cross-sectional shrinkage occurred before the towpreg reached 225 °C, the reported melting point for nylon 6.

The rapid shrinkage still occurred with only nominal tension. Better overall reduction in void content was achieved with a tension of 4 lb_f (1.8 kg_f). Increasing tension further led to no further reduction in void content.

Since so much wetting occurred below the apparent melting point for nylon 6 sections of towpreg were videotaped in a hot stage microscope. The extent of fiber wetting started to increase around 180 °C, as in the oven experiments. Most of the wetting was completed by the time the towpreg reached 225 °C.

Figure 4 shows a DSC scan of this nylon 6 towpreg. There is evidence of melting starting near 180 °C. It is highly likely that considerable melting and recrystallization occurs in this nylon 6 at low temperatures since the towpreg is quenched extremely rapidly in production - on the order of 100 °C per second. This melting of metastable crystals is sufficient to permit substantial fiber wetting to occur before the nylon 6 recrystallizes. This virtually concurrent melting and recrystallization is not evident in Figure 4 because the latent heat effect of overlapping melting and recrystallization is virtually zero. The hot stage microscopy does support this basis for the low temperature wetting.

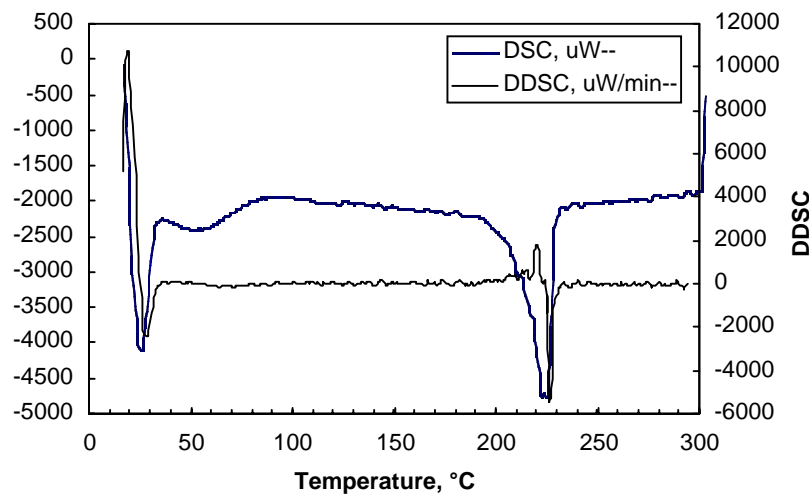


Fig. 4: DSC trace of towpreg melting at 10 °C/min showing melting beginning near 180 °C.

WETTING MODEL

A capillary flow model was developed for the wetting observed in the oven. The derivation of the model is presented elsewhere [6]. The area of the tow, A_{tow} , is:

$$A_{tow} = k_1 \left(\frac{\exp\left(\frac{E_a}{RT}\right)}{\left(1 - \frac{T}{k_2}\right)^{\frac{11}{9}} t} \right) \quad (1)$$

where k_1 depends on material and system properties, E_a is the activation energy for viscous flow, R is the gas constant, T is temperature, k_2 is a material constant and t is time. The constant k_1 is:

$$k_1 = N_{tow} \frac{4\sqrt{3}}{9} \left(\frac{R_m}{R_f} \right)^3 R_m^3 \left(\frac{v_{fl}}{v_{ml}} \right) \left(\frac{\eta_o}{\gamma_o \cos \theta} \right) \quad (2)$$

where the parameters in equation 2 are defined in Table 1.

Table 1 Parameters Used to Estimate k_1 in Capillary Flow Model

R_m	Particle Radius	5.5 Microns
R_f	Fiber Radius	4 Microns
θ	Contact Angle	42°
v_{fl}	Final Fiber Volume Fraction	0.6
v_{ml}	Final Matrix Volume Fraction	0.4
η_o	Viscosity of Nylon 6 at 232 °C	422 Pa•s
γ_o	Surface Tension at 0 K	264 Dyne/cm
N_{tow}	Number of Filaments in Tow	12,000

The first parameter in Table 1, R_m , is the mean particle size. The mean particle radius of the nylon 6 powder was determined to be 72 microns. However, this radius is before the powder was fused to the fiber. Furthermore, such large particles bridge multiple fibers and multiple flow channels. The approach used to obtain R_m equal to 5.5 microns is based on the initial hydraulic radius of the flow channel. Using the initial tow cross-sectional area of the towpreg of 8 mm and assuming 12,000 channels, equal to the number of filaments in the tow, a hydraulic radius was calculated for each channel, assuming each channel was equivalent in size. Then the hydraulic radius was set equal to R_m . Additional parameters in Table 1 readily determined from the initial towpreg include the number of filaments in the tow, the fiber radius, the fiber volume fraction and the matrix volume fraction. The volume fractions were calculated from the measured weight fractions assuming no voids in the fully consolidated towpreg.

No data was available for the contact angle for nylon 6 on carbon fiber. An angle of 42° was selected based on measurements for related polymers on carbon fiber [7]. The surface tension at absolute zero, γ_o , was calculated using the Guggenheim equation [8],

$$\gamma = \gamma_o \left(1 - \frac{T}{k_2} \right)^{\frac{11}{9}} \quad (3)$$

a known surface tension for nylon 6 of 35 dyne/cm at 265°C [9], and an empirical estimate of k_2 obtained by fitting equation 1 as discussed below. The viscosity, η_o , was measured by capillary viscometry at a low apparent shear rate of 46 s⁻¹.

The value of k_1 obtained using these parameters is 1.3 x 10⁻⁴ mm²•s. This value is fairly close to the empirically determined value of 3.88 x 10⁻⁵ mm²•s. The value of k_1 is very

sensitive to the choice of R_m since k_1 depends on R_m raised to the sixth power. For example, using the measured powder radius of 72 microns leads to a very high estimate of k_1 equal to $650 \text{ mm}^2 \cdot \text{s}$.

Unfortunately, the second constant, k_1 , in Equation 1 cannot be estimated in advance. Based on the Guggenheim Equation k_2 is the imaginary critical temperature of the polymer. For polymers in general, estimates of k_2 have ranged from 600 K to 900 K [8]. Thus, the value of 663 K obtained by fitting the data appears reasonable.

Figure 5 presents a simulation of A_{tow} versus time for an oven setting of $260 \text{ }^\circ\text{C}$ along with the experimental results. The empirically determined values of k_1 and k_2 were used in this simulation. Since the temperature of the towpreg changes while the fibers are wet out, it was necessary to use time-temperature superposition to establish equivalent incremental residence times at a reference temperature. Equation 1 was used as a basis for conducting this time-temperature superposition. Equation 4 shows the resulting expression.

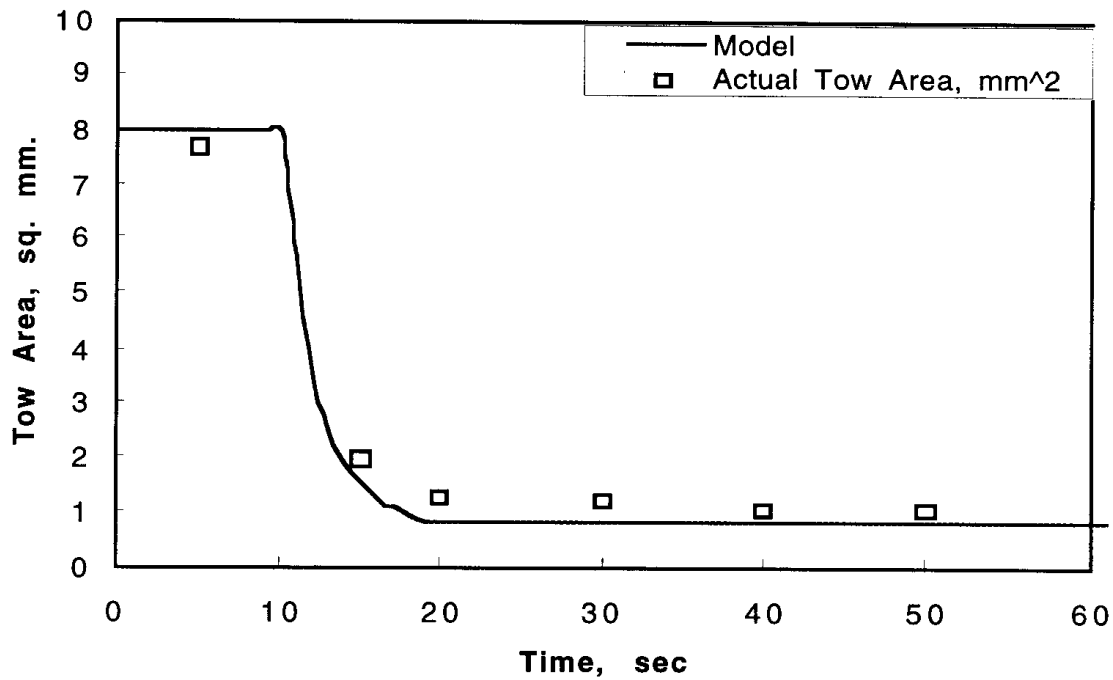


Fig. 5: Simulation of towpreg cross-sectional area versus residence time in oven.

$$dt_{\text{ref}} = dt \left(\frac{k_2 - T}{k_2 - T_{\text{ref}}} \right)^{\frac{11}{9}} \exp \left(\frac{E_a}{R} \left(\frac{1}{T_{\text{ref}}} - \frac{1}{T} \right) \right) \quad (4)$$

The temperature dependence of the contact angle, which is unknown, has been ignored in this superposition expression. In the simulation shown in Figure 5 the reference temperature time increments have been converted back to real time. Based on the observation of no flow below $180 \text{ }^\circ\text{C}$, dt_{ref} was set equal to zero until $180 \text{ }^\circ\text{C}$ was attained. No further change in towpreg area was permitted once the simulation reached an area of 0.91 mm^2 , representing a void free towpreg.

The simulation shown in Figure 5 represents the experimental trends well. Once the threshold temperature of 180 °C was reached both the model and the experimental results show rapid wetting. Experimentally, complete wetting is not achieved. This discrepancy between the model and experiment is attributed to the somewhat random distribution of the powder in the towpreg, the large size distribution of the powder, and the considerable variability of the cross-sectional areas of the actual flow channels. While some flow channels have excess resin, others are starved of resin. Hence, not all the voids are removed until external pressure is applied.

CONTINUOUS CONSOLIDATION

Based on these wetting experiments a new process for converting the flexible towpreg into consolidated ribbon was developed and tested. Figure 6 presents a schematic diagram of this process. The towpreg is tensioned since this improves wetting. The oven reduces the void content of the towpreg to below 25%. The hot towpreg enters a circular die with a cross-sectional area of 1.4 mm² in order to induce some pressure driven resin flow. Then the emerging towpreg is pressed by steel rollers with a gap setting equal to the thickness sought for the ribbon. At the same time these rollers quench the towpreg.

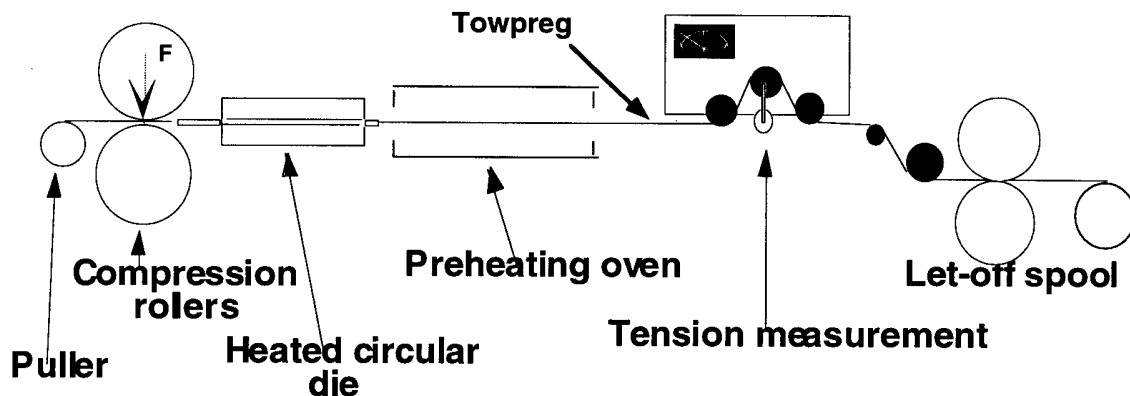


Fig. 6: Apparatus for continuous conversion of unconsolidated powder coated tow into consolidated flat towpreg.

Processing conditions for continuous consolidation have not been optimized. Following is an example of conditions which led to a well consolidated ribbon with less than 2 % voids. The tension was set at 1.8 kg_f. The oven and die were set at 260 °C and 275 °C respectively. Samples were collected at different line speeds. Surprisingly, towpreg with the lowest void content was collected at the highest speed attempted, 6 m/min.

Since this process incorporates a die, as in pultrusion, it is informative to compare this experimental line speed with pultrusion speeds. For both thermosets and thermoplastics pultrusion speeds are typically less than 3 m/min. The high speed achieved in this trial run is quite promising. By extending the length of the oven and possibly the length of the die, successful consolidation at even higher speeds is expected.

DISCUSSION

The rapid wetting and ease of consolidation of nylon 6 coated carbon fiber towpreg may not occur in other systems. Nylon melt has a low viscosity compared to most polymer melts. Also, nylon wets and bonds to the oxidized carbon surface very well. Thus, research is in progress at Georgia Tech to examine the wetting and consolidation of other combinations of polymers and fibers.

It is common practice to ignore contributions due to wetting in analyzing the consolidation of thermoplastic composites [10]. This research clearly shows that wetting without the application of external pressure can lead to substantial debulking and reduction in void content. Frequently in processing thermoplastic composite preforms the preform is heated above its melt temperature in an oven before shaping and consolidating it in a mold below the solidification temperature of the matrix. For nylon 6 powder coated carbon fiber preforms extensive debulking of the preform occurs before the preform is inserted in the mold. Thus, these unconsolidated preforms can be molded virtually as quickly as fully consolidated sheets are stamped.

CONCLUSIONS

Nylon 6 powder coated carbon fiber tows are rapidly wet out and debulked by heating the towpreg above 180 °C. The nylon 6 behaves like a melt above 180 °C even though the final melting temperature for nylon 6 is 225 °C. By treating the nylon 6 as a melt above 180 °C a capillary flow model represents the wetting and debulking of the towpreg well. By combining an oven, die and roll consolidator in line this flexible towpreg can be converted into consolidated towpreg rapidly.

ACKNOWLEDGEMENTS

Fellowship support from the McLain Foundation for M. Rammoorthy and the donation of towpreg from Custom Composite Materials (now Applied Fiber Systems, Ltd.) is gratefully appreciated.

REFERENCES

1. Muzzy, J.D. and Varughese, B., U.S. Patent 5,171,630, Flexible Multiply Towpreg, 1992
2. Muzzy, J.D. and Varughese, B., U.S. Patent 5,094,883, Flexible Multiply Towpreg and Method of Production Therefor, 1992
3. Custom Composite Materials, Inc., Atlanta, GA, now Applied Fiber Systems, Ltd., 14201 Myerlake Circle, Clearwater, FL 34620
4. Rammoorthy, M., On-line Consolidation of Powder Coated Filaments, Georgia Institute of Technology, Masters Dissertation, 1993
5. Rammoorthy, M. and Muzzy, J.D., On-line Consolidation of Powder Fusion Coated Filaments, *International Sampe Symposium*, Vol. 26, 450, 1994

6. Rammoorthy, M., Consolidation of Nylon 6 Powder Coated Graphite Fiber Tows, Georgia Institute of Technology, PhD Dissertation, 1996
7. Andersson, C-H., Dartman, T., Wahlberg, J., and Klasson, C., Wetting and Adhesion of some Thermoplastic Materials to Fibers, *Interfacial Phenomena in Composite Materials*, Butterworth-Heinemann, UK, p. 61--64, 1991
8. van Krevelen, D. W. , *Properties of Polymers : Their Correlation with Chemical Structure, their Numerical Estimation and Prediction from Additive Group Contributions*, Elsevier, Amsterdam, 3rd, 1990
9. Hybart, F. J. and White, T. R., The Surface Tension of Viscous Polymers at High Temperatures, *Journal of Applied Polymer Science, III*, Vol. 7, p. 118--121, 1960
10. Connor, M., Toll, S. and Manson, J-A. E., A Model for the Consolidation of Aligned Thermoplastic Powder Impregnated Composites, *Journal of Thermoplastic Composite Materials*, Vol. 8, No. 2, p.138--162, 1995

MANUFACTURE OF THERMOPLASTIC TOWPREGS BY USING THE AQUEOUS FOAM TECHNIQUE

Manoj Kashiramka And Youqi Wang

*Department of Mechanical Engineering
Kansas State University, Manhattan, KS 66506 U.S.A.*

SUMMARY: The quality of prepregs is a critical aspect towards the manufacture of high quality composites. In this paper, the aqueous foam technique is employed to produce thermoplastic prepregs. In this process, a suspension is made from resin powder and water. A surfactant is added. Then the suspension is sent to a foam generating system, where suspension and pressured air are mixed, generating foam. The foam acts as the diluent of matrix. The aqueous matrix foam is then applied onto a fiber tow. Then, the fiber tow moves through a furnace and the prepreg is produced. Three kinds of prepregs were made by using this process. Carbon fibers and glass fibers were incorporated with a polyimide thermoplastic resin or a polyester thermoplastic resin. The quality of prepregs was evaluated.

KEYWORDS: prepregging process, thermoplastic resin, fiber reinforced composite, aqueous foam, matrix impregnation

INTRODUCTION

The manufacturing process for the laminated composite involves two steps. During the first step, a mixture of resin and curing agent is coated onto fibers, forming a thin sheet or a biconstituent fiber tow, called the “prepreg” or “tow-prepreg”. During the second step, prepregs are stacked and bonded together within a vacuum bag inside a high pressure, high temperature autoclave.

The solution/ slurry coating technique is commonly employed in industry to coat matrix onto fibers. With solution coating, the polymer is dissolved in a solvent and the fiber is impregnated with the resulting solution. This method was developed for liquid thermoset resins. Later, several thermoplastic resins were developed. These resins are not in a liquid state. Also, it is often difficult to find a suitable solvent to create a low viscosity liquid. Thus, the resin solution coating was replaced by a resin suspension[1-2]. However, it is difficult to achieve complete impregnation because of the high viscosity of the thermoplastic resin. In order to overcome this problem, several new thermoplastic prepregging processes were

developed. They include various dry powder coating methods[3-7], a hot melted coating process[8] and an aqueous foam prepregging process[9]. In this paper, the aqueous foam method is employed to produce thermoplastic prepregs.

The aqueous foam prepregging method evolved from the foam finishing technology used in the textile industry. This technology was developed to apply coatings and finishes to fabrics. In the past, the coating process involved spraying a solution of chemicals onto the fabric. A huge amount of energy is required to evaporate large quantities of water. Research was then directed towards developing a less energy intensive process. The foam-finishing technology was thus generated.

In the foam finishing process, foaming agent is added into a concentrated finish formulation, generating foam. The foam is then applied onto the fabric. Whereas water was used in the earlier process as the primary diluent, foam is the primary diluent in the foam finishing process. Because the concentration of liquid forming foam in the new process is much greater than the concentration of chemical solution used in the old method, much less water is required. This reduces the energy consumed and the chemical discharge; meanwhile, the drying process is speed up.

The foaming technology was employed in the prepregging process at Clemson university. Foam acts as a carrier medium for the matrix powder. Compared to the traditional solution/slurry method, this process reduces the chemical discharge. In addition, difficulties created by the high viscosity of the thermoplastic resin can be avoided. Compared to the dry powder method, the aqueous foam method does not create dust hazard.

The purpose of this paper is to broaden the scope of the aqueous foam prepregging process by utilizing different fibers and resin. A foam prepregging process system has been developed at Kansas State University. Three kinds of fibers and two kinds of resins were incorporated by this process. The quality of the tow-prepregs manufactured was evaluated.

AQUEOUS FOAM PREPREGGING SYSTEM

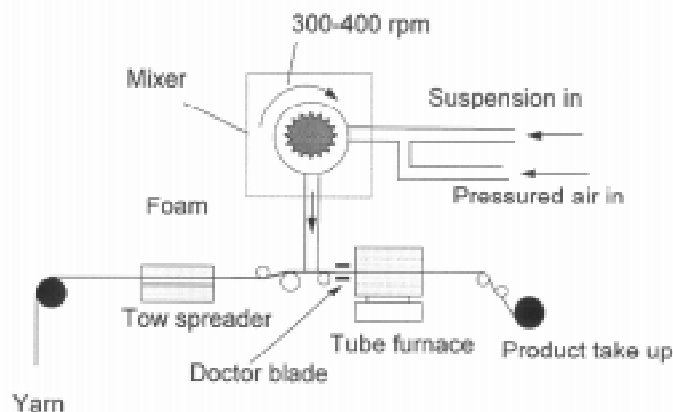


Fig.1 The prepregging Process

Fig.1 is an illustration of the system. First, the fiber tow moves through a tow spreader and is spread to a width of 2-3 inches. Then aqueous foam, as a carrier medium, is applied to the moving tow. The moving tow passes through a tube furnace and is then taken up by a rotating spool. The system includes four major devices: a pneumatic yarn spreader, a foam generating and supplying system, a tubular furnace and a product-take-up system. The prepregging process can be divided into four sub-processes: spreading yarn, applying matrix onto fiber, drying and curing the prepreg, and taking-up the final prepreg.

Spreading Yarn

Spreading the yarn helps achieve an adequate impregnation. Yarn is spread before the impregnation stage. It becomes possible to coat matrix onto every individual fiber. The structure of the yarn spreader is shown in the Fig.2. The spreader consists of three pieces: a cover plate, a middle plate with several air slots and an air box. The yarn is placed between the cover plate and the middle plate. During the operation, pressured air enters the air box from the pneumatic tubes connected to two sides of the box. Then, air is forced to pass through slots on the middle plate, and then flows parallel with the yarn path. Consequently, the yarn is spread as shown in Fig.2.

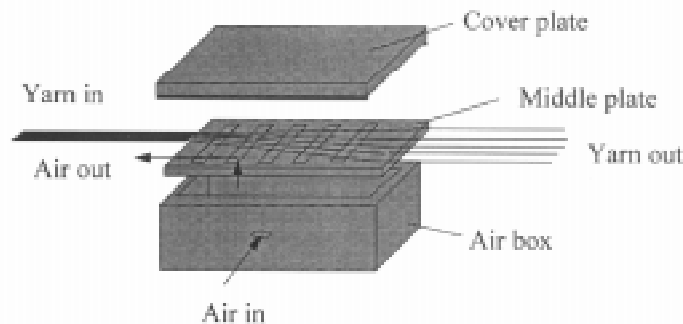


Fig.2 Yarn Spreading Process

Applying Matrix onto Fiber

An aqueous foam, which carries the matrix powder, is then applied onto the spread yarn. The aqueous foam is produced by the following procedure: Firstly, a suspension is made from resin powder and water. A surfactant is added. Then the suspension and the pressured air are simultaneously sent to a high speed mixer, generating foam. The matrix powder sticks onto the foam's surface. Foam, acting as carrier medium, is coated on the spread tow. A doctor blade is placed in order to control the fiber volume fraction.

Drying and Curing

The yarn then moves through a tube furnace. The temperature inside the furnace is kept slightly higher than the melting point of the matrix. The water and most of the surfactant within the suspension are removed in the tube furnace. The aqueous foams collapse. The resin powder melts and uniformly distributes onto the fiber. Thus, the towpreg is produced inside the furnace.

Taking Up Product

The product take-up system includes two speed control motors. One is to control the linear motion of the spool and the other the rotating rate of the spool. The tow-prepreg is wound on the spool uniformly.

The quality of tow-prepreg is determined by several factors, such as the concentration of the suspension, the selection of the surfactant, the particle size of the matrix powder, the processing temperature and the processing speed.

MANUFACTURE OF THERMOPLASTIC TOW-PREPREGS

The objective of this research was to study the foam generation process and to make this process more broadbased. There were three types of fibers which were used and two thermoplastic resin systems which were employed to manufacture tow-prepregs. The fibers used were E-glass, IM-7 and T-650/32. The resin systems used were E-250-5 polyester and PIXA. The quality of towpregs made is being evaluated by finding the fiber volume fraction and by SEM(Scanning Electron Microscope) photographs.

Three kinds of tow-prepregs were produced. We started with a low temperature fiber-resin system and then went to a high temperature resin system, which would help us enormously in understanding thermoplastic prepregging process. These three prepregs were: E-glass fibers/E-250-5 polyester tow-prepregs, IM7 carbon fiber /E-250-5 polyester tow-prepregs and T-650/35 carbon fibers/PIXA resin tow-prepregs.

Preparation of Suspension

The first step to make the prepreg is to prepare the suspension. The quality of suspension is critical for the quality of the towpreg. The quality of suspension is determined mainly by three factors: the size of the particles of matrix powder, the surfactant selection and concentration, and the concentration of the suspension.

We started with the E-250-5 polyester resin. The average particle size of the resin powder (as received from the company) was 200 micros. Using the as-received-resin, towpregs with a fiber volume fraction ranging from 20% to 40% were produced. The particle size was perceived to be a hindrance in getting higher fiber volume fractions and in getting uniform quality impregnation, as the large particle can not uniformly stick onto the surface of the foam. In addition, the powder will form large matrix drops when the particle size is much greater than fiber's diameter. Thus, the powder was grounded in order to reduce its particle size. The average particle size was reduced to 16-17 microns. The foam quality was improved dramatically. The particle size of the PIXA resin was in the range of 10-20 microns. It might be better if the particle size could be reduced to the order of the fiber's diameter.

The selection and concentration of surfactant affects the foaming process. Emcol LO, manufactured by Witco Corporation, Oleochemicals/Surfactant Group, Houston, TX was first selected. The chemical name is lauramine oxide. This nonionic surfactant was used for making suspension with the E-250-5 polyester resin. Then, Emcol K-8300, manufactured by the same company, is used for a making suspension of PIXA thermoplastic resin powder. The

chemical name is sodium oleoylsopropanolamide sulfosuccinate. The concentration of the surfactant ranges from 0.4-0.6%.

The concentration is the third factor which determines the quality of foam. Because the foam can carry only a limited amount of powder, the concentration can not be too high. On the other hand, it is easy to remove the surfactant and water from the tow-preg as the high concentration suspension is used. In our practice, the concentration ranges from 15%-20%. The air pressure ranges from 20-30psi.

Processing Temperature

After the matrix foam is applied onto the fiber, the fiber tow moves through a tube furnace. The temperature of the furnace determines the curing process. There are two approaches. The first approach is to set the temperature of the furnace slightly higher than the melting point. Thus, the matrix melts inside the furnace and coats the fiber. The second approach is to set the furnace temperature slightly lower than the melting point. Thus, the matrix does not melt inside the furnace and only water evaporates. Eventually, we get a biconstituent yarn. The advantage of the second approach is that the tow-preg is flexible, which thus reduces the possibility for fiber damage in the next manufacturing step. The disadvantage is the matrix powder may fall from the tow-preg. Uniformity of fiber volume fraction of the towpreg might be affected. The advantage of the first approach is that it is easy to control the quality of tow-preg and to examine the fiber volume fraction of the tow-preg. The disadvantage is the tow-preg is so stiff that the fiber might be damaged during the take-up process.

Fiber Volume Fractions

The control of the fiber volume fraction is an important aspect to determining the quality of the tow-prepreg. The fiber volume fraction is controlled by a doctor blade. It was found that the finer the powder, the easier to control the fiber volume fraction. For example, both the 200 micron and 17 micron polyester powders were coated onto a 12K E-glass fiber tow. By using the 200 micron powder, the fiber volume fraction was dispersed and big matrix drops could be seen under the microscope. However, the fiber volume fraction could be controlled to the level of 50-70% after a grinding process.

Scanning Electron Microscope Photograph(SEM)

SEM photographs were taken to inspect the quality of the tow-prepreg samples. The photographs were compared with SEM photographs of commercially available prepreg samples.

Fig.3 is an SEM photographs of an E-glass fiber/Polyester towpreg sample. The fiber volume fraction of the sample is 50 %. It can be seen that fibers are parallel to each other and there are few globules of matrix on fibers. Fig.4 is the SEM photograph of a T-650-5/PIXA. The fiber volume fraction is 51%. Fibers seen in the photograph are less parallel compared to the first sample. The photograph also shows that the matrix has melted and there is adhesion between the matrix and fibers. However, the matrix distribution is not so uniform compared to the first sample. There are two reasons for this situation. First, the diameter of the carbon fiber is much smaller than the glass fiber. It is difficult to reconverge fibers after the yarn is spread. Thus, it is difficult to return the alignment of the fibers to the original. The alignment of yarn is difficult to return to the original. Second, the diameter of carbon fiber is less than half of the

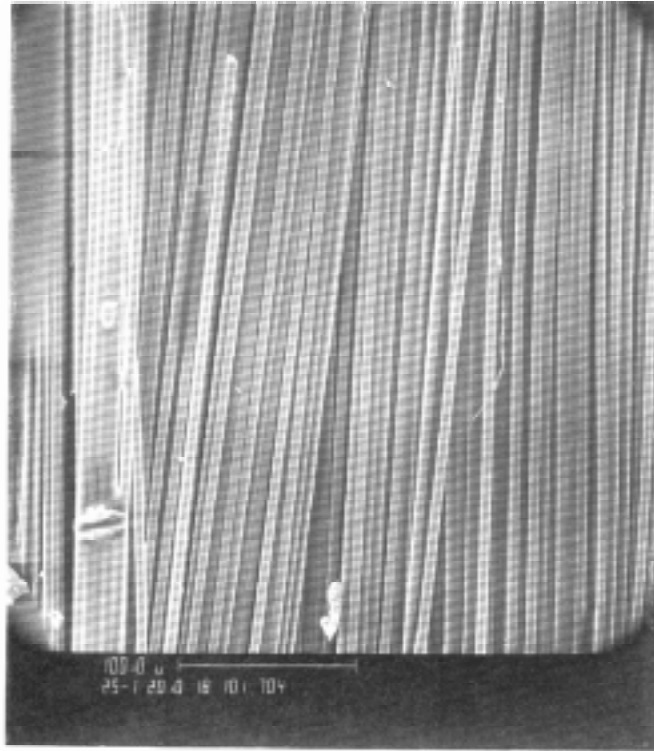


Fig.3 SEM photograph of E-glass fiber /polyester thermoplastic resin tow-preg sample

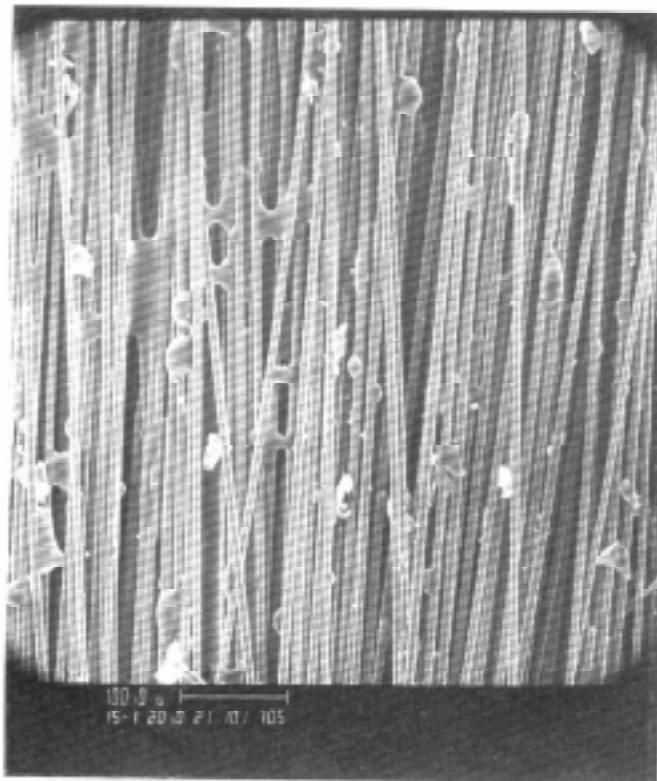


Fig.4 SEM photograph of T-650 carbon fiber/PIXA matrix tow-preg sample

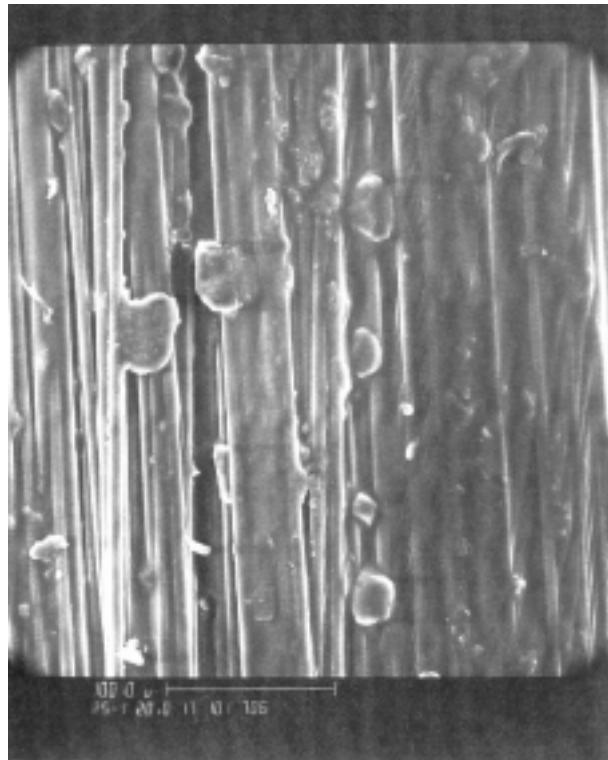


Fig.5 SEM photograph of commercially available carbon fiber/epoxy resin prepreg

particle size of the matrix powder. As such, the size of the droplet of the matrix is greater than the fiber diameter. This creates a difficulty of uniformly coating of matrix onto fibers. The droplet of matrix is more visible. Fig.5 is the SEM photograph of a commercially available carbon fiber/epoxy resin prepreg sample.

CONCLUSIONS AND RECOMMENDATIONS

It has been proved from our practice that the foam generation process can be used with different fibers and thermoplastic resin systems to produce quality towpregs. Also, it is possible to employ it in the manufacture of certain thermoset resin tow-pregs if the resin powder is available. However, certain research and certain improvements have to be made so that the process can be widely used.

Yarn Spreading

Yarn is being spread before coating such that the matrix can be coated onto fibers equally. Although the fibers were spread, equal distribution of fiber along the width of the tow spreader was not achieved. This affects uniform coating quality. In order to solve this problem, the shape of the pneumatic tow spread should be redesigned. The spreading process should be more gradual to avoid yarn damage.

Selection of Surfactant

Surfactant determines the quality of foam. For each resin-fiber system, there corresponds one or more possible surfactants which could be used. A thorough study is needed to determine: 1. effect of surfactant on the quality of foam, 2. removal of surfactant, 3. the affect of residual surfactant in the matrix on the quality of tow-preg and 4. the affect of surfactant on the fiber strength and the fiber-matrix interface bonding strength.

Processing Temperature

The process temperature will affect the flexibility of the prepreg. If the processing temperature is too high, the prepreg becomes stiff. The fiber might be thus damaged during the next step of manufacturing process. If the temperature is too low, the matrix powder will not stick on the fiber. Consequently, some powder may fall away from the prepreg, affecting the fiber volume fraction of the prepreps.

Compared to the commonly used solution/slurry method, the aqueous foam method can achieve a better impregnation because resin powder can be coated to every individual fiber. Compared to the dry powder impregnation method, the foam process avoids a dust hazard. Because the foam is water based, the process is environmentally friendly.

ACKNOWLEDGEMENT

This work was supported by a NASA EPSCoR research grant.

REFERENCES

1. Towell, T.W., Hirt, D.E. and Johnston, N.J., "LARC-TPI1500 composites fabricated using an aqueous slurry process", *22nd International SAMPE Technical Conference*, November 6-8, 1990, pp. 1156-1169.
2. Ramani, K., Tryfondis, M., Hoyly, C. and Gentry, J., "thermoplastic powder composite manufacturing using a wet slurry method", *Processing and Fabrication and Manufacturing of Composite Materials*, ASME, 1992, pp.115-129.
3. Muzzy, J., Varughese, B., Thammongkol, V. and Tincher, W., "Electrostatic prepregging of thermoplastic matrices", *SAMPE Journal*, Vol. 25, No.5, 1989, pp.15-21.
4. Throne, J. L. and Sohn, M. S., "Electrostatic dry powder prepregging of carbon fiber", *35th International SAMPE Symposium*, April 2-5, 1990.
5. Iyer, S., R. and Drzal, L.T., "Manufacture of powder-impregnated thermoplastic composites", *Journal of Thermoplastic Composite Materials*, Vol.3, 1990, pp.325-330.
6. Edie, D.D., Gantt, B.W., Lickfield, G.C., Drews, M.J. and Ellison, M.S., "Thermoplastic coating of carbon fibers", *Advances in Thermoplastic Matrix Composite Materials, ASTM STP 1044*, G.M. Newaz, Ed., ASTM, Philadelphia, 1989, pp. 50-61.

7. Baucom, M., and Marchello, J. M., "Powder curtain prepreg process", *Journal of Advanced Materials*, Vol.25, No.4, July,1994, pp.31-35.
8. Donald M. Bigg, "Producing thermoplastic matrix sheet composites: two processes", *Plastic Engineering*, October 1990, pp.33-45.
9. Chary, R.R. and Hirt, D.E., "Coating carbon fibers with a thermoplastic polyimide using aqueous foam", *Polymer Composites*, August, 1994, pp. 306-311.

THE ELASTIC STRESS IN A FIBRE NETWORK IMPREGNATED WITH MOLTEN POLYPROPYLENE

Colin Servais¹, Staffan Toll² and Jan-Anders E. Månson¹

¹ *Laboratoire de Technologie des Composites et Polymères, Ecole Polytechnique Fédérale de Lausanne, CH-1015 Lausanne, Switzerland.*

² *Department of Polymeric Materials, Chalmers University of Technology, S-41296 Göteborg, Sweden*

SUMMARY: A constitutive equation was previously derived for disperse planar fibre networks under transverse compression and validated for *non-impregnated* fibre networks. In this work we apply the equation to a fibre network which has been *impregnated* with a molten polypropylene. Low velocity compression experiments show that the pressure contribution of the fibre network is unchanged by the presence of the liquid polymer and hence that the above equation is applicable to this important case without modification. At sufficiently slow compression rates the fibre network is undisturbed by the liquid which merely flows through it. The limits for this behaviour are also established. The equation successfully predicts the loading response for compression speeds ranging from 10^{-3} to $5 \cdot 10^{-3}$ mm/s. The viscous contribution of the resin used becomes significant at compression rates above 10^{-3} mm/s, and below $2 \cdot 10^{-4}$ mm/s exceedingly low responses are observed, possibly due to fibre slippage and rearrangements.

KEYWORDS: elastic stress, compressibility of fibres, discontinuous fibres, disperse planar fibre networks, segregation, fibre slippage, fibre rearrangement, concentrated fibre suspension

INTRODUCTION

Fibre networks are common in applications such as paper processing, felts, filters and reinforcement in composite materials, of which we are particularly interested in the processing of fibre/resin suspensions into composite materials. In all these cases, fibre packing is usually such that the fibre network sustains significant elastic compressive stress. The elastic stress has sometimes to be taken into account in manufacturing processes such as impregnation, consolidation and flow moulding. In these processes the fibre orientation distribution is often planar, or close to planar; and the network, compressed in the direction perpendicular to the plane of orientation, contributes to the stress state of the suspension. Many attempts have been made to model the network stress, notably by van Wyk [1] for 3D fibre networks (wads) and Gutowski [2] for the 1D case (unidirectional fibre beds). Toll and Månson [3] have derived a constitutive model for the 2D case (planar fibre beds). They found a power law relationship between the loading pressure and the fibre volume fraction, where the power law exponent was equal to five. The model successfully described compression data of a planar fibre network.

However, those experiments were all performed "dry," without any liquid resin, which might lubricate the fibre bed and thereby reduce its response. The issue addressed here is whether

the equation by Toll and Månson is valid in the presence of a liquid matrix, such as molten polypropylene in glass mat reinforced thermoplastics (GMT). In order to isolate the packing response of the fibre mat, compression experiments can be performed at low compressive rates, so that the matrix percolates through the fibre bed without inducing any in-plane fibre motion. Kim and McCarthy [4] have investigated the compressibility and relaxation of a stack of impregnated bundle mats with random orientations, and their results are a useful source of comparison to this constitutive equation.

THEORETICAL BACKGROUND

Toll and Månson [3] derived an analytical solution for the elastic compression of a disperse planar fibre network:

$$P = \frac{512}{5\pi^4} E f^4 (\phi^5 - \phi_o^5), \quad (1)$$

where P is the applied pressure, E is the Young's modulus of the fibres, f is a function of the fibre orientation distribution, defined by Toll [5], and ϕ is the fibre volume fraction. The second term, ϕ_o^5 , is a parameter that needs adjustment but tends to be negligible at realistic volume fractions, in which case

$$P = \frac{512}{5\pi^4} E f^4 \phi^5. \quad (2)$$

The derivation of this result is based on the concept that each segment of fibre acts as a bending beam supported by two neighbouring fibres and deflected by a third. Segments of fibre are deflected under a load P . As a segment deflects, it may encounter another fibre. New fibre-fibre contact points are thus continuously generated during compression, making the response highly non-linear. The following assumptions are made about the microstructure:

1. The structure is statistically homogeneous.
2. The fibres are approximately straight and all oriented in the same plane.
3. The fibres are well dispersed in space, in the sense that they do not form bundles.
4. The fibre diameter is uniform.
5. No slippage between fibres occurs.

Two additional assumptions are needed in order to obtain the closed-form result:

6. The incremental force at the fibre-fibre contact points, due to an incremental change in applied load, is uniform.
7. Contact points are randomly distributed along a given fibre.

Although these assumptions appear realistic in the case of a non-impregnated network, assumptions 5 and 6 may or may not hold in the presence of a liquid matrix, lubricating the contact points. If some slippage should occur, the model will predict a too high pressure and the P - ϕ curve will shift towards lower pressure. In addition, any viscous or viscoelastic stresses contributed by the matrix are of course not accounted for by Eqn. 1 and 2. This contribution will add to the network response, shifting the P - ϕ curve towards higher pressure. The elastic response due to the fibre network can, however, be expected to dominate at sufficiently high fibre volume fractions.

Kim and McCarthy [4] have tested various fibre mats mainly made of collimated fibres. As compression speed increases the curve shifts slightly towards higher pressure. Their conclusion was that lower speeds allows more time for fibre rearrangement to occur for non-impregnated networks, and thus requires less load to compress the fibre network. The authors also suggest that lubrication makes the fibre rearrangement easier at low pressures and reduces fibre breakage at high pressures.

EXPERIMENTAL

Experiments have been performed using a commercial thermoplastic composite from AZDEL, Inc., with disperse glass fibres and carbon black-filled polypropylene matrix. The fibre length and diameter were 12.7 mm and 12 μm , respectively. The sheets as delivered were semi-consolidated, contained up to 50% voids and had a thickness between 6.1 and 6.5 mm. The influence of air entrapment has been analysed by Leterrier [6], and significant scatter in the material properties and flow results has been mentioned by Ericsson [7]. Fibre weight fractions were obtained by ashing and weighing each specimen after testing. Specimens that deviated significantly from the average in thickness or weight were discarded. Calculations were performed using $\rho_{\text{glass}} = 2.60 \text{ g/cm}^3$ and $E_{\text{glass}} = 75 \text{ GPa}$. The in-plane fibre orientation distribution was assumed to be planar random on average, although a slight preferred orientation is known to be present in this material. Thus the value used for the orientation function was that corresponding to planar random orientation, $f = 2/\pi$.

Specimens of $33 \times 33 \text{ mm}^2$ were placed between two 25 mm diameter horizontal parallel plates of a Rheometrics RSA displacement-controlled rheometer as shown in Fig. 1. They were heated to 180°C in an oven until a uniform temperature was reached throughout the thickness; the upper fixture did not touch the specimen during the heating phase. The time of heating was 15 minutes; longer times were also tried but had no effect on the results. The upper plate of the rheometer fixture was then displaced to lightly touch the top of the preform and the initial thickness was recorded. At this moment a small pressure, 20 to 120 Pa, was applied to the sample, and the value of the unloaded fibre volume fraction ϕ_o was extrapolated from that obtained for these small pressures. This volume fraction is somewhat arbitrary since even very small loads may have a strong influence on the sample volume in the melt state, but this procedure only affects the value of ϕ_o , which is unimportant other than at low pressures.

Tests were performed at constant displacement rates ranging between $5 \cdot 10^{-4}$ and 1 mm/s and the pressure response was recorded. These speeds were sufficiently low so as to cause complete segregation, that is the matrix percolated through motionless fibres and wept out of the specimen as schematically represented in Fig. 1. As a result, the fibre mass contained between the plates was kept constant, and the volume fraction could be directly related to the plate separation.

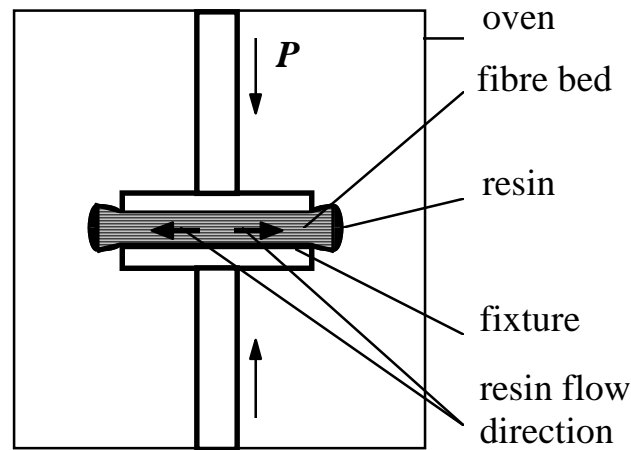


Fig. 1: The fibre bed is being compressed vertically, but does not flow horizontally, while the resin weeps out.

RESULTS AND DISCUSSION

The loading response of lubricated systems shows good correlation with that of previous experiments made on dry fibre beds. Fig. 2 shows the response of an impregnated network compressed at 10^{-3} mm/s and 180°C and that of a dry mat loaded at 0.1 mm/s at room temperature. The two curves superimpose well; so under these conditions no lubrication effect is observed. The compression speed of 10^{-3} mm/s is sufficiently small to ensure that the elastic response of the fibre network dominates. The experiments reported here were performed at 180°C . Changing the temperature to 200°C made no difference; this was also mentioned by Ericsson [7]. No fibre breakage has been detected for the investigated fibre volume fractions.

The elastic network model, Eqn. (1), successfully predicts the loading response for speeds ranging from 10^{-3} to $5 \cdot 10^{-3}$ mm/s; this is shown in Fig. 3. The experimental data also show good reproducibility. The difference between the theoretical curve and experimental data is within the uncertainty of the fibre orientation distribution. The results in Fig. 3 suggest a slight preferred fibre orientation ($f=0.53$). No effect of the displacement rate, nor of the fibre rearrangement, is detected within the scatter. The unloaded fibre volume fraction ϕ_o was estimated to 0.033, by extrapolation.

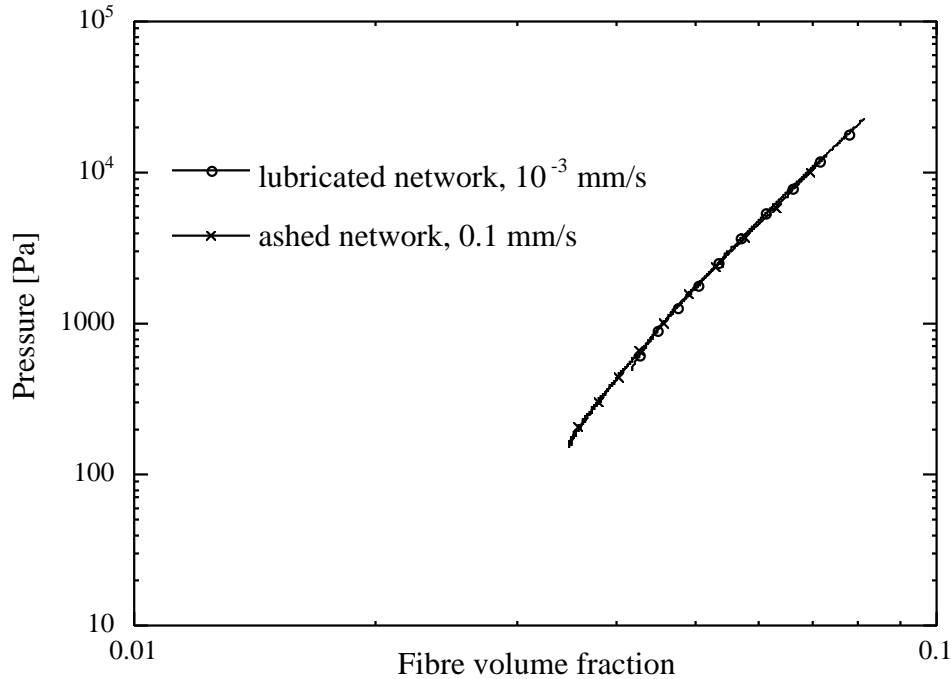


Fig. 2: Comparison of the compression behaviour between a lubricated and an ashed fibre network. The temperature is 180°C and the compression speeds are as indicated.

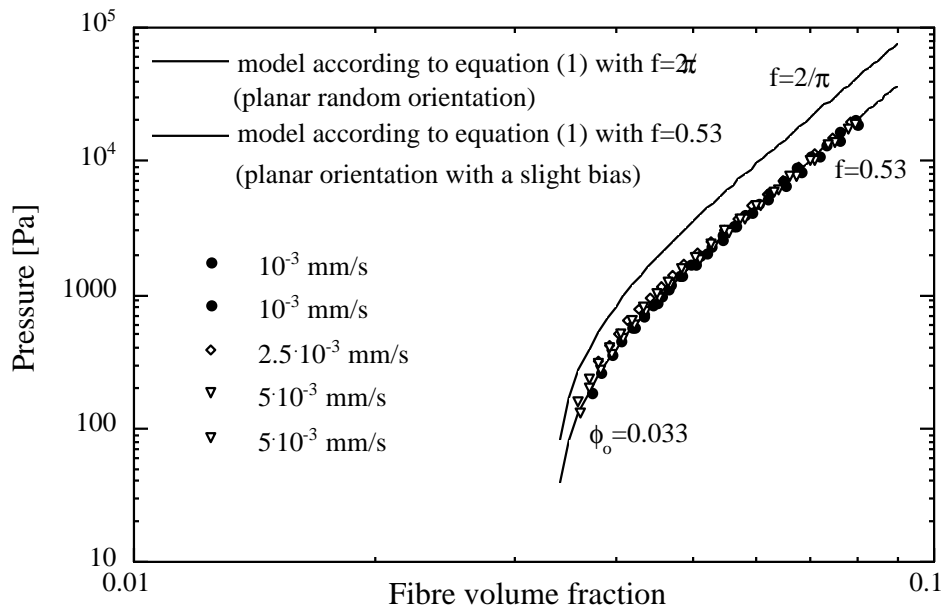


Fig. 3: Loading response of impregnated networks, for speeds ranging from 10⁻³ to 5·10⁻³ mm/s, compared to the prediction of equation (1).

Compression rate effects are detected at rates either below 10⁻³ or above 5·10⁻³ mm/s. It would thus appear that the influence of fibre rearrangement and resin response can be dissociated in this case, appearing in separate rate intervals. The viscous or viscoelastic response of the matrix while it is percolating through the fibre bed could only be detected at speeds exceeding 5·10⁻³ mm/s. This matrix response adds to the network elastic stress leading to higher pressures than for an non-impregnated network. Fibre rearrangements by slippage, on the other hand, is apparent mainly at the lower rates. It probably occurs at all compression rates,

but could only be directly detected from two types of experiment: compression at very low speeds and pressure relaxation.

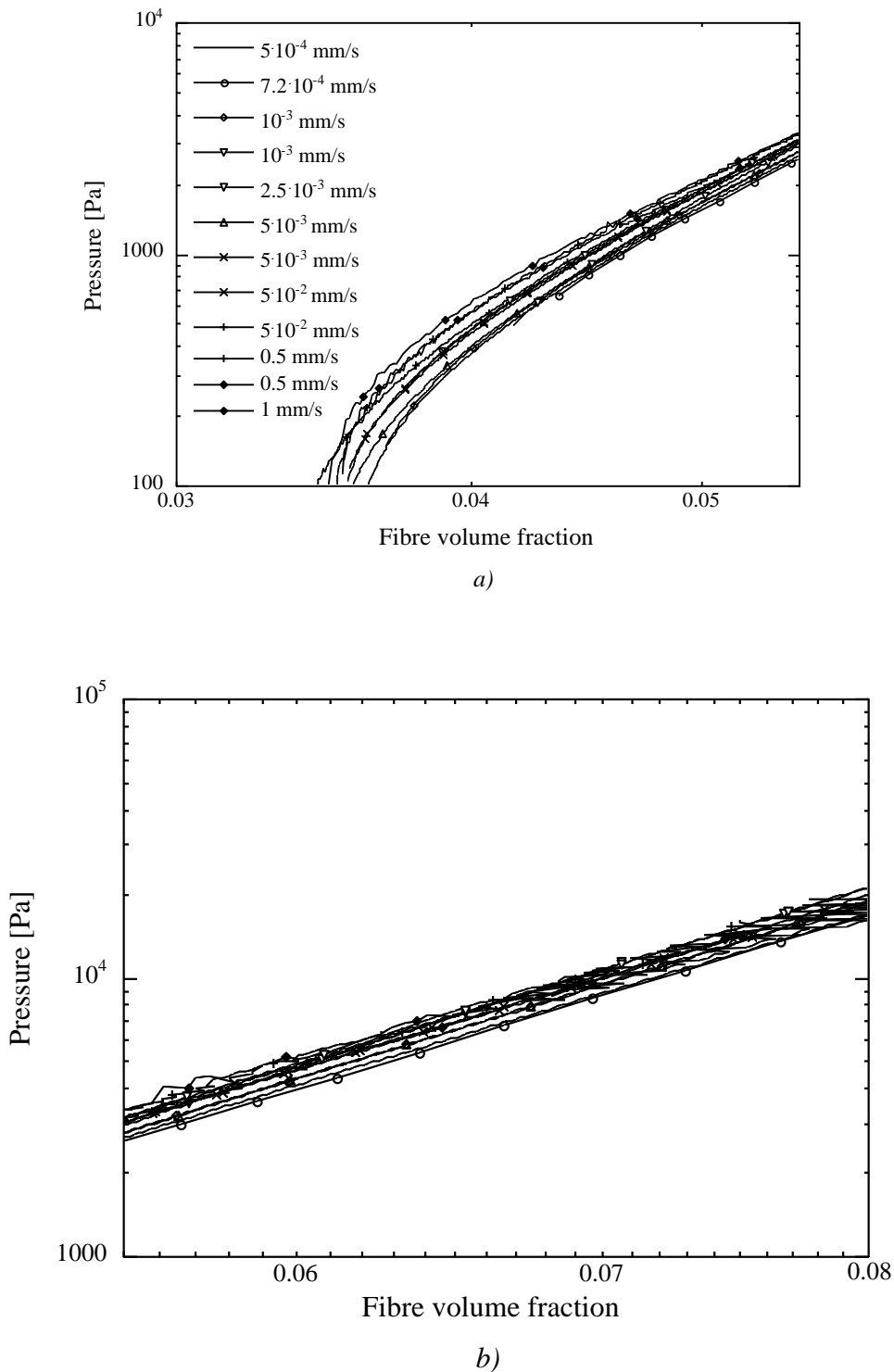


Fig. 4: Compression behaviour for different speeds ranging from $5 \cdot 10^{-4}$ to 1 mm/s at 180°C ,
 a) lower and b) higher fibre volume fractions

Fig. 4b shows displacement rate effects at compression rates exceeding $5 \cdot 10^{-3}$ mm/s. The power law exponent of the relationship between the fibre volume fraction and the packing force tends to decrease slightly as a result of significant matrix response, but is still very close

to five. Also, the pressure tends to increase with increasing speed for a given volume fraction. For reasons of accuracy 1 mm/s could not be exceeded. Fig. 4a shows an even clearer effect of displacement rate at lower fibre volume fractions: the pressure is higher for higher speeds. Differences between higher and lower fibre volume fractions are explained by the dominance of the packing force at higher volume fractions.

At the lowest speeds, $7.2 \cdot 10^{-4}$ and $5 \cdot 10^{-4}$ mm/s, the packing force is below that of non-impregnated fibre networks, as shown in Fig. 4b. This is taken as evidence of fibre rearrangement. A similar decrease in the stress response at low velocities was observed by Kim and McCarthy [4]. A general comparison between the model and the above results is presented in Fig. 5. Fibre rearrangement is also detected by pressure relaxation experiments. Relaxation can be observed by recording the pressure once the plates have stopped. A reduction of the packing force with time was also observed by Kim and McCarthy. After 20 minutes the pressure reaches a constant value. The pressure drop, recorded at the highest volume fractions, ranges between 3% and 8 %, but can reach 18% when loading has been performed at the highest speeds. Dry fibre mats do not exhibit stress relaxation. The pressure drop is likely caused by stress relaxation in the matrix and fibre rearrangement. Finally it seems that the fibre rearrangement and viscoelastic response of the matrix are coupled, the latter phenomenon increasing the first: total pressure drop of 18% at the highest speeds.

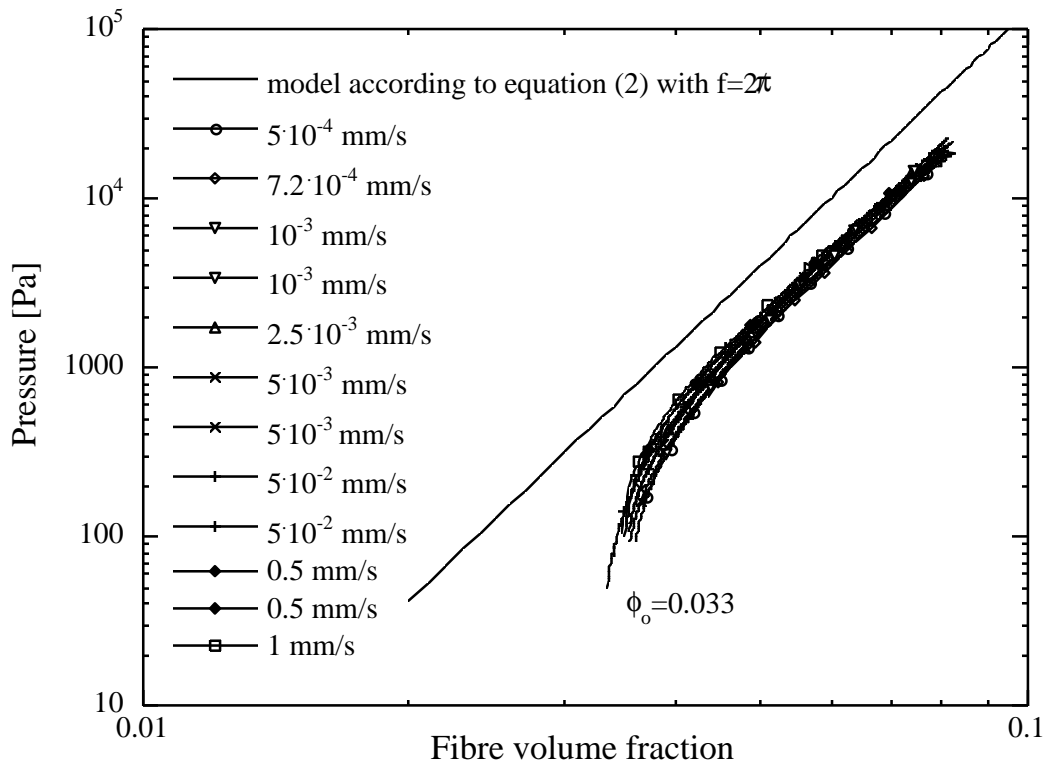


Fig. 5: General comparison between the model, according to equation (2), and experimental results for all investigated speeds.

The weak influence of the matrix on the loading response for these disperse networks may not be valid for other types of fibre beds. In disperse fibre systems the relatively large contact force at the individual contact points between fibres inhibits fibre motion and renders the characteristics of the impregnated network similar to those of the "dry" case.

CONCLUSION

The packing theory derived for dispersed dry fibre mats can also be applied to commercial lubricated fibre networks. In preform processing, for instance, this work gives a constitutive equation directly related to preform compression. The fibre network response is proportional to fibre volume fraction raised to the power five in all investigated situations. Viscous resistance due to the resin increases the instantaneous loading pressure for compression speeds exceeding $5 \cdot 10^{-3}$ mm/s, while possible fibre rearrangement decreases this pressure; this phenomenon could be detected during compression at speeds below 10^{-3} mm/s and in relaxation processes when the pressure response is below the one measured for non-impregnated fibre networks, but is thought to always be present.

ACKNOWLEDGEMENTS

This research is part of the European Research Program COST 512 'Modelling in Materials Science and Processing', which is supported by the Conseil des Ecoles Polytechniques Fédérales, Berne and by the Office Fédéral de l'Education et de la Science, Berne.

REFERENCES

1. van Wyk, C.M., "Note on the compressibility of wool", J. Textile Institute, Vol. 37, 1946, pp. T285-T292.
2. Gutowski, T.G., Kingery, J. and Boucher, D., "Experiments in composites consolidation: fibre deformation", SPE ANTEC: Technical Papers, Vol. 32, 1986, pp.1316-1320.
3. Toll, S. and Månson, J.-A.E., "Elastic compression of a fibre network", J. Appl. Mech, Vol. 62, 1995, pp. 223-226.
4. Kim, Y.R., McCarthy, S.P. and Fanucci, J.P., "Compressibility and relaxation of fibre reinforcements during composite processing", Polymer Composite, Vol. 12, No. 1, 1991, pp. 13-19.
5. Toll, S., "Note: On the tube model for fibre suspensions", Journal of Rheology, Vol. 37, No.1, 1993, pp. 123-125.
6. Leterrier, Y. and G'Sell, C., "Formation and elimination of voids during the processing of thermoplastic matrix composites", Polymer Composites, Vol. 15, No 2, 1994, pp. 101-105.
7. Ericsson, K.A., Rheology of glass mat reinforced thermoplastics, Ph.D. thesis, EPFL, Lausanne, Switzerland, 1996.

BLENDS OF POLY(ETHYLENE TEREPHTHALATE) AND EPOXY RESIN AS A MATRIX MATERIAL FOR CONTINUOUS FIBRE - REINFORCED COMPOSITES

A. Saalbrink, M. Mureau and T. Peijs

*Centre for Polymers and Composites, Eindhoven University of Technology,
P.O. Box 513, 5600 MB Eindhoven, The Netherlands*

SUMMARY: Epoxy resin is applied as a reactive solvent for poly(ethylene terephthalate) (PET) to obtain solutions with a low melt-viscosity. These solutions are cured according to two different cure schedules, the first schedule curing in the melt and the second allowing for crystallization of the PET prior to curing. Blends cured in the melt show a phase-separated morphology with a decreased epoxy particle size. The flexural strength and strain to failure show an increase with increasing epoxy content, whereas blends cured in the melt show overall lower flexural properties, indicating degradation of PET. The flexural performance of glass fabric laminates with a PET / epoxy matrix confirm that the reactive processing route yields good quality composites. The laminate in-plane shear strength is increased with increasing epoxy content, which is in agreement with the increase in the matrix flexural properties and the increase in fibre-matrix adhesion due to the presence of epoxy resin.

KEYWORDS: reactive solvent, epoxy-modified thermoplast, phase separation, in-plane shear strength, fibre-matrix adhesion, polymer blends.

INTRODUCTION

New developments in fibre-reinforced thermoplastic composites are aiming at cost-effective composites which may attract large-volume markets such as the automotive industry. Since the cost-effectiveness of a product is strongly dependent on raw material costs, these developments are mainly focusing on low-cost materials like glass fibres as a reinforcement and commodity thermoplastics such as polypropylene (PP), polyamide (PA), poly(buthylene terephthalate) (PBT) and poly(ethylene terephthalate) (PET) as a matrix.

Glass fibre-reinforced composites based on thermoplastics are often produced by way of melt- or solution impregnation routes. Because of the relatively high melt viscosities of thermoplastic polymer melts, melt impregnation is often only achieved in the case of low molecular weight polymers, resulting in poor mechanical properties in terms of stiffness, strength and impact-resistance.

In the case of solution impregnation techniques, the solution provides a low viscosity medium that can easily impregnate the fibres. After impregnation the solvent has to be removed by conventional drying operations. However, the presence of residual solvent can result in a reduction in T_g and poor interface conditions, which is widely recognized as a major problem.

In order to overcome these drawbacks in conventional solution impregnation, a new processing route based on the use of epoxy resins as reactive solvents is currently under

development in our laboratory [1-5]. An interesting aspect of this reactive processing route is that in the case of fibre-reinforced composites the epoxy resin is not only an effective solvent, lowering the viscosity (for tractable polymers) and (or) the processing temperature (for intractable polymers) of the polymer matrix and thus acting as a processing aid during impregnation. After impregnation and shaping, the reactive solvent is polymerized and converted into a non-solvent. This initiates phase separation and, depending on the composition of the blend, phase inversion. As a consequence, a dispersed epoxy phase results, which is locked up inside the continuous thermoplastic phase. In this way the cured reactive solvent provides an essential structural part of the final material and contributes to interfacial adhesion between the fibre and the thermoplastic matrix [2, 4, 5].

In this paper we describe the use of epoxy resin as a reactive solvent for PET, a semi-crystalline engineering thermoplast. Next to this, we report on the application of these PET / epoxy blends as a matrix material for continuous glass fibre-reinforced composites.

EXPERIMENTAL

PET / epoxy blends

Materials and blend preparation

The PET used in this study (BX5662, $M_n = 25 \text{ kg}\cdot\text{mol}^{-1}$, $M_w = 60 \text{ kg}\cdot\text{mol}^{-1}$) was kindly supplied by ICI. Prior to blending the PET granules were powdered and dried overnight at $150 \text{ }^\circ\text{C}$. As the reactive solvent a standard 2-functional epoxy resin, diglycidyl ether of bisphenol-A (DGEBA, Araldite LY556, Ciba Geigy), with a molecular weight of $380 \text{ g}\cdot\text{mol}^{-1}$ was used. The resin was cured with a stoichiometric amount of 4-functional amine curing agent, 4,4'-methylene bis(3-chloro-2,6-diethyl aniline) (M-CDEA), supplied by Lonza.

To study the viscosity of PET / DGEBA solutions, mixtures of PET and epoxy resin (in absence of curing agent) with a PET content of 40-100 wt.% were prepared in a miniature co-rotating twin screw extruder (6 cm^3 volume) at $260 \text{ }^\circ\text{C}$ and 40 rpm.

PET / epoxy blends (epoxy resin and curing agent) with a PET content of 50-100 wt.% were prepared by premixing the constituents and feeding this mixture into a Haake Rheomex type TW-100 twin-screw compounding extruder at $270 \text{ }^\circ\text{C}$ and 50 rpm screw-speed. After compounding the blends were compression moulded and cured to obtain 1.8 mm thick plates. Two different cure schedules were applied. In the first cure schedule (A) the epoxy was cured in the melt at $260 \text{ }^\circ\text{C}$, after which the PET was allowed to crystallize. The second cure schedule (B) allowed for crystallization of the PET at $180 \text{ }^\circ\text{C}$ prior to complete curing of the epoxy. A crystallization temperature of $180 \text{ }^\circ\text{C}$ was selected because of the maximum in crystallization rate at this temperature for unmodified PET [6]. The different cure schedules applied are shown in Table 1.

Table 1: Cure schedules for curing of the PET / DGEBA / M-CDEA blends

Cure schedule	Step 1	Step 2	Step 3
A	3 min at $260 \text{ }^\circ\text{C}$	40 min at $260 \text{ }^\circ\text{C}$	20 min at $180 \text{ }^\circ\text{C}$
B	3 min at $260 \text{ }^\circ\text{C}$	180 min at $180 \text{ }^\circ\text{C}$	

Rheology

The zero-shear viscosity of PET / DGEBA solutions at 260 °C was determined in the linear visco-elastic region using a Rheometrics type RDS-II Spectrometer. An oscillating parallel-plate test setup with 25 mm plates and a 0.8 mm gap distance was used.

Morphology

The morphology of the cured PET / epoxy blends was studied using Scanning Electron Microscopy (SEM, Cambridge Stereoscan 200). The samples for SEM observations were prepared by cryogenic fracture, etched by oxygen plasma for 10 minutes and finally coated with a thin gold/palladium layer.

Mechanical properties

The mechanical properties of the cured blends were determined by three-point bending tests on a Zwick type 1445 testing machine. The three-point bending tests were performed according to the ASTM D790-86 standard (dimensions 50 x 25 x 1.9 mm) at a strain rate of 10^{-3} s^{-1} and at span-to-depth ratios of 16.

Composites based on PET / epoxy blends

Materials and composite manufacture

Six-ply laminates were manufactured from woven E-glass fibre 8H satin-weave fabric (SS0303-8203, $300 \text{ g}\cdot\text{m}^{-2}$, Ten Cate Advanced Composites). The matrix consisted of PET / epoxy blends with a PET content of 50-100 wt.%, which were prepared as described in the previous section. The composites were manufactured by stacking six layers of fabric alternately with layers of uncured and powdered PET / epoxy blend in a mould and subsequently moulding and curing them in a hot press at a pressure of 25 bar to obtain 1.9 mm thick plates. The different cure schedules applied are shown in Table 1. The total volume fraction of fibre in all laminates was approximately 40 %.

Mechanical properties

The mechanical properties of the six-ply laminates were determined by three-point bending and in-plane shear tests on a Zwick type 1445 testing machine. The three-point bending tests were performed on 0/90° coupons (dimensions 40 x 25 x 1.9 mm) according to the ASTM D790-86 standard at a strain-rate of 10^{-3} s^{-1} . Span-to-depth ratios of 16 were used. The in-plane shear tests were performed by uniaxial tensile tests on $\pm 45^\circ$ coupons (dimensions 160 x 20 x 1.9 mm) according to the ASTM D3518-91 and D3039-93 standards at a cross head speed of $2 \text{ mm}\cdot\text{min}^{-1}$. The shear modulus (G_{12}) was measured using both a longitudinal and a transverse extensometer.

RESULTS AND DISCUSSION

Rheology of PET / epoxy resin solutions

In Figure 1 the zero-shear viscosities of homogeneous PET / DGEBA solutions at a temperature of 260 °C are presented. The viscosity of the PET used in this study (300 Pa·s at 260 °C) is low in comparison with melt-viscosities of other standard polymers commonly used ($10^3 - 10^5$ Pa·s). However, even lower viscosities are obtained for solutions of PET with epoxy resin. Upon increasing the epoxy resin content a dramatic decrease in viscosity is observed from 300 Pa·s for pure PET to a value of approximately 0.1 Pa·s at 60 wt.% epoxy resin. This low melt-viscosity is in the same range as for resins used in structural reaction injection moulding (SRIM) and in resin transfer moulding (RTM). In this way, our objective to lower the viscosity of the thermoplast in order to increase the impregnation rate and level of continuous-fibre reinforcements could certainly be achieved by using epoxy resin as a reactive solven

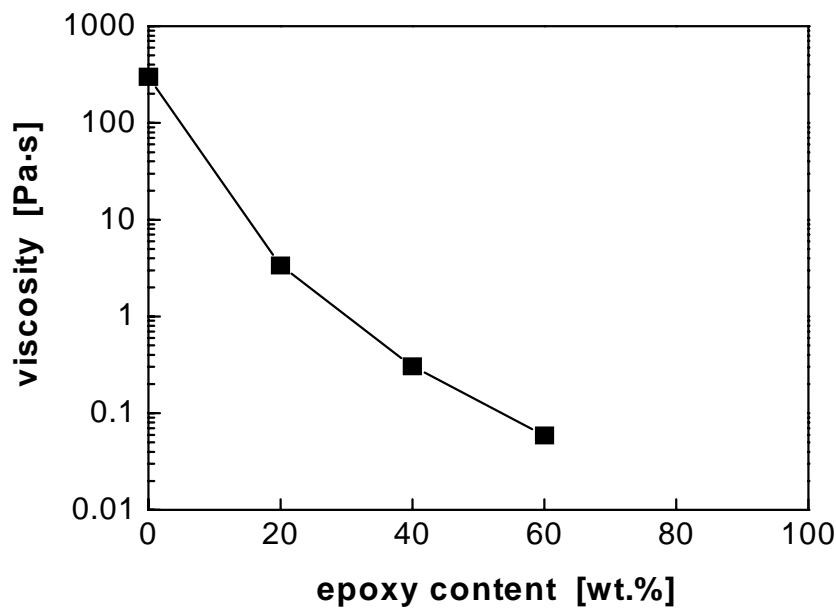


Figure 1: Zero-shear viscosities of PET / DGEBA solutions at 260 °C versus the epoxy resin content

PET / epoxy blends

Morphology

The SEM micrographs of the PET / DGEBA / M-CDEA blends cured at 260 °C and at 180 °C are presented in Figure 2. In all the cured blends a phase separated and phase inverted morphology of dispersed epoxy particles in a continuous PET matrix is observed. With

increasing PET content the dispersed epoxy-phase diameter is decreased. This decrease is a combined effect of decreasing the epoxy volume fraction and increasing the viscosity of the solutions upon decreasing the epoxy content. A high viscosity reduces the coarsening of growing epoxy droplets by coalescence effects, resulting in a smaller epoxy particle size as has been shown for other thermoplast / epoxy systems [1,7]. However, the effect of viscosity on the particle size is probably not large because of the relatively low initial viscosities of the PET / epoxy blends, see Figure 1. Next to this, a decrease in the dispersed epoxy particle size is observed with increasing initial cure temperature. Obviously, the increased rate of polymerization of epoxy decreases the time to gelation of the epoxy, at which point the morphology is set and extensive coalescence is prevented.

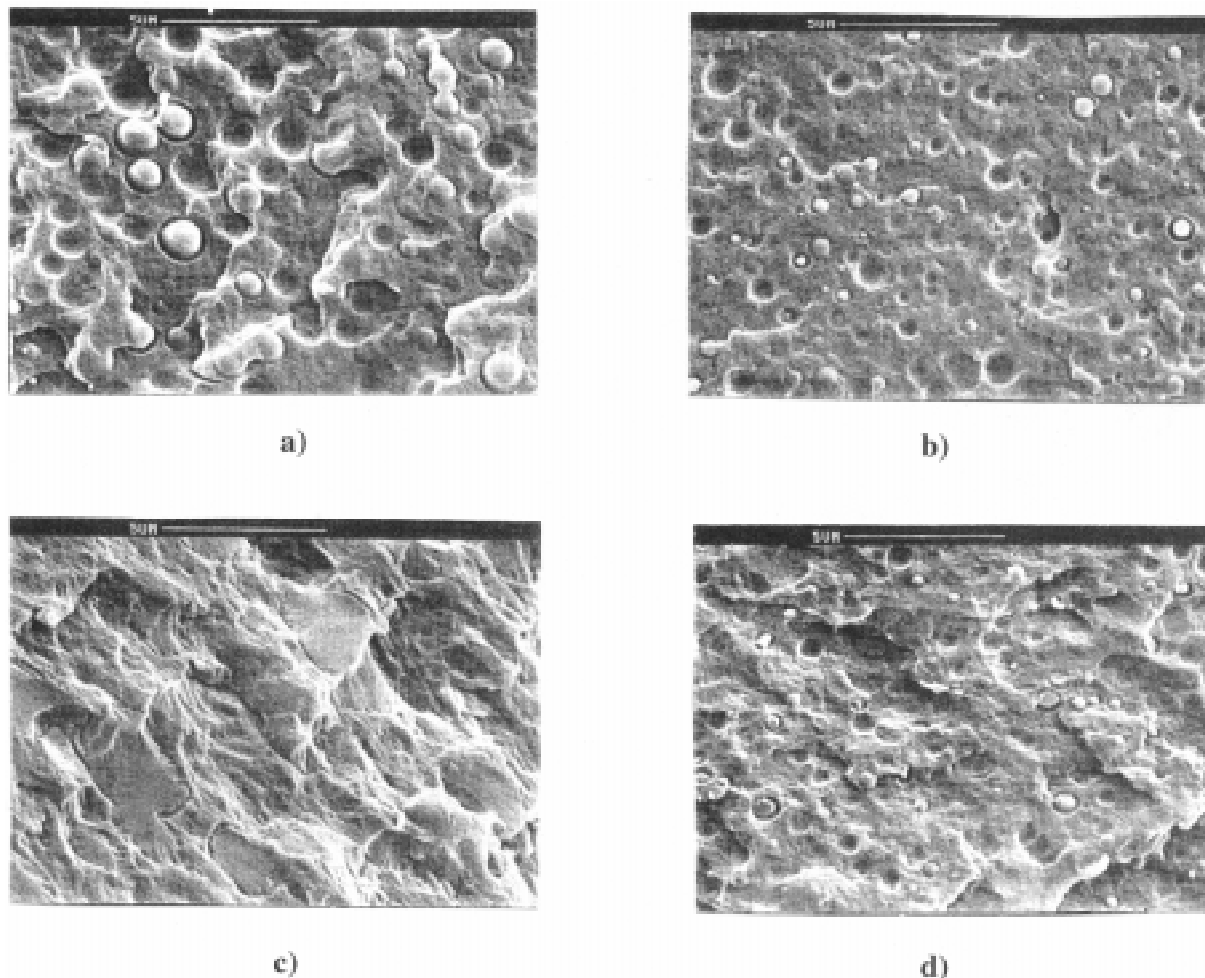


Figure 2: SEM micrographs of fracture surfaces of PET / epoxy blends cured at 260 °C containing respectively a) 50 wt.%, b) 75 wt.% PET and cured at 180 °C containing respectively c) 50 wt.%, d) 75 wt.% wt.% PET.

Mechanical behaviour

Table 2 shows the flexural properties of the PET / epoxy blends cured at 260 °C and 180 °C versus the blend composition. For the blends cured at 260 °C and for the blends cured at 180 °C the modulus, strength and strain to failure show an increase upon increasing the epoxy content. Next to this it is observed that blends cured at 260 °C overall exhibit a lower flexural strength and strain to failure. Curing at this temperature will cause more chemical degradation of PET to occur by e.g. hydrolysis or aminolysis reaction, resulting in a lower PET molecular

weight. This increase in molecular weight will decrease the mechanical properties such as strength and strain to failure.

Table 2: Flexural mechanical properties of the PET / epoxy blends cured according to cure schedule A (260 °C) and schedule B (180 °C)

PET content [wt.%]	cure schedule A (260 °C)			cure schedule B (180 °C)		
	E [GPa]	σ [MPa]	ϵ [%]	E [GPa]	σ [MPa]	ϵ [%]
50	3.7	103.9	2.8	3.6	127.4	3.6
75	3.9	91.9	2.3	4.1	118.3	2.9
100	4.2	71.0	1.7	4.2	53.9	1.3

Composites based on PET / epoxy blends

Flexural mechanical properties

In Table 3 the flexural mechanical properties of the glass fabric laminates are presented. Since the flexural properties are mainly dominated by the fibre properties, the flexural performance of the PET / epoxy based laminates does not vary much with blend composition. The level of flexural performance confirms that the reactive processing route yields good quality composites with a good impregnation, without any compromise in comparison with unmodified PET based laminates.

Table 3: Flexural mechanical properties of the glass fabric laminates based on PET / epoxy blends cured according to cure schedule A (260 °C) and cure schedule B (180 °C).

PET content [wt.%]	cure schedule A (260 °C)			cure schedule B (180 °C)		
	E [GPa]	σ [MPa]	ϵ [%]	E [GPa]	σ [MPa]	ϵ [%]
50	11.1	320	2.9	11.2	330	3.0
75	11.0	333	3.0	11.7	372	3.2
100	10.1	291	2.9	11.1	321	2.9

In-plane shear properties

In Figure 3 the in-plane shear strength of the glass fabric laminates is shown. Upon increasing the epoxy content in the PET / epoxy matrix a substantial increase in in-plane shear strength can be observed. Next to this, an overall higher shear strength is observed for laminates cured at 180 °C. Since shear properties of composites are mainly determined by the properties of the matrix and the interphase, this increase in shear strength is fully in agreement with the results obtained for the blends as has been shown in Table 2. The fibre - matrix adhesion is also improved significantly by the presence of epoxy resin, which was confirmed by SEM

observations. Next to this, the shear modulus of the laminates is about 2.2 GPa and is hardly dependent on the epoxy content in the matrix.

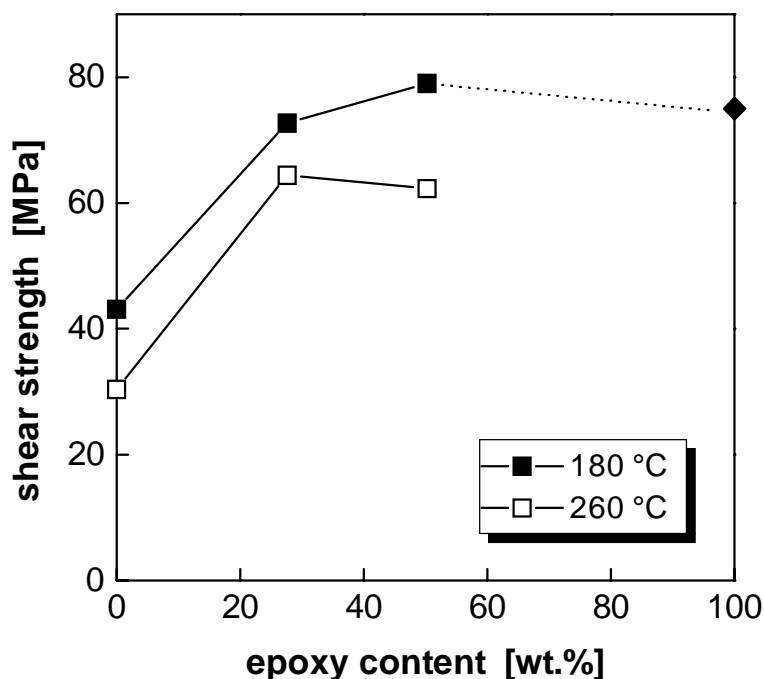


Figure 3: *In-plane shear strength of glass fabric laminates based on PET / epoxy blends cured according to schedule A: □ 260 °C and schedule B: ■ 180 °C versus the epoxy content. ♦ taken from [8].*

CONCLUSIONS

The application of PET as a matrix material for glass fabric reinforced composites has been studied using epoxy resin as a reactive solvent. Solutions of PET in epoxy resin show low viscosities, from 300 Pa•s for pure PET to approximately 0.1 Pa•s at 60 wt.% epoxy resin. This low melt-viscosity is in the same range as for resins used in SRIM and RTM techniques. In this way, an increase in the rate and level of impregnation of continuous-fibre reinforcements could certainly be achieved by using epoxy resin as a reactive solvent. Upon curing of the PET / epoxy blends phase separation and phase inversion is initiated, resulting in a morphology of dispersed epoxy particles in a continuous PET matrix. The flexural strength and strain to failure of the cured blends increase with increasing epoxy content. Blends cured in the melt at 260 °C show overall lower mechanical properties than blends which are allowed to crystallize at a lower temperature prior to complete curing, because of degradation of PET at this high temperature. The flexural performance of glass fabric laminates based on these blends confirm that the reactive processing route yields good quality composites. The in-plane shear strength of the laminates is increased significantly with increasing epoxy content in the matrix. Moreover, the fibre - matrix adhesion is improved with increasing epoxy content.

ACKNOWLEDGMENTS

The authors would like to thank dr. P.T. McGrail of ICI Middlesbrough (UK) for supplying the PET polymer, Lonza (The Netherlands) for supplying the M-CDEA curing agent and Ten Cate Advanced Composites (The Netherlands) for providing the glass fabric.

REFERENCES

1. Venderbosch, R.W., Meijer, H.E.H. and Lemstra, P.J., "Processing of intractable polymers using reactive solvents: 1. Poly(2,6-dimethyl-1,4-phenylene ether) / epoxy resin", *Polymer*, Vol.35, No. 20, 1994, pp.4349-4357
2. Venderbosch, R.W., Meijer, H.E.H. and Lemstra, P.J., "Processing of intractable polymers using reactive solvents: 2. Poly(2,6-dimethyl-1,4-phenylene ether) as a matrix material for high performance composites", *Polymer*, Vol. 36, No. 6, 1995, 1167-1178
3. Venderbosch, R.W., Meijer, H.E.H. and Lemstra, P.J., "Processing of intractable polymers using reactive solvents: 3. Mechanical properties of Poly(2,6-dimethyl-1,4-phenylene ether) processed by using various epoxy resin systems", *Polymer*, Vol.36, No. 15, 1995, pp.2903-2913
4. Venderbosch, R.W., Peijs, T., Meijer, H.E.H., and Lemstra, P.J., "Fibre-reinforced composites with tailored interphases using PPE/epoxy blends as a matrix system", *Composites - Part A: Applied Science and Manufacturing*, Vol. 27, No. 9, 1996, pp. 895-905
5. Meijer, H.E.H., Venderbosch, R.W., Goossens, J.G.P. and Lemstra, P.J., "Processing of thermoplastic polymers using reactive solvents", *High Performance Polymers*, Vol. 8, 1996, pp. 133-167
6. Palys, L.H. and Phillips, P.J., "Microkinetics of crystallization in poly(ethylene terephthalate)", *Journal of Polymer Science, Part B: Polymer Physics*, Vol. 18, No. 4, 1980, pp. 829-852
7. Yamanaka, K. and Inoue, T., " Structure development in epoxy resin modified with poly(ether sulphone)", *Polymer*, Vol. 30, No. 4, 1989, pp 662
8. Information Sheet No. FTA 46f, "Fibredux 913", Ciba Geigy, 1991

ELECTRON BEAM CURE OF COMPOSITES FOR AEROSPACE STRUCTURES

Allan S. Crasto, Ran Y. Kim and Brian P. Rice

University of Dayton Research Institute 300 College Park Ave., Dayton, OH 45469-0168, USA

SUMMARY: In this study the properties and performance of two electron beam (EB)-cured epoxy resins and their composites are compared with those of 3501-6, a thermally-cured epoxy widely used in aerospace structures. Mechanical performance of the EB-cured materials is significantly reduced under hot/wet conditions, due in part to relatively low glass transition temperatures and the susceptibility of a poor fiber-matrix interfacial bond to degradation under the influence of moisture. Both EB-cured resins undergo additional thermal cure, although this does not appear to adversely affect their performance. While EB cure offers several technical and economic advantages over conventional cure, improvements in materials are required before the full benefits of this process can be realized in aerospace structures.

KEYWORDS: electron beam-cure, epoxy composites, aerospace structures

INTRODUCTION

There are four factors that influence material selection for aerospace structures: weight, performance, the ability to fabricate components and cost. Polymeric composite structures hold an edge over metal structures in weight. Great strides have been made in improving composite performance and durability for specific aerospace environments, and a number of new and innovative processing and fabrication techniques are enabling the fabrication of large, integrated and complex composite structures. The stumbling block, however, toward more widespread composites usage in aerospace structures is their cost. This has spawned many research programs in recent years, such as the U.S. Department of Defense's Composites Affordability Initiative (CAI), aimed at reducing the cost of composite structures. While a reduction in raw material costs will help, innovative design concepts and a reduction in fabrication costs (including labor, tooling, cure, assembly, etc) provide a greater impact on overall costs. Over the years electron beams have been widely used in the coatings industry to cure polymeric coatings. In the last 10 years or so, this technology has been gaining attention for the cure of composite materials, primarily because of the potential for cost savings over conventional cure methods. Most of the research in this field has been conducted at Aerospatiale in France [1,2], at Atomic energy of Canada, Ltd. (AECL) in Manitoba, Canada [3,4], and at the Oak Ridge National Laboratory (ORNL) in Oak Ridge, Tennessee [5].

In the electron beam (EB) cure of composites, high-energy electrons from an accelerator initiate polymerization and crosslinking of the matrix resin. This process requires special resin chemistry. Most commercially-available EB-curable polymers have ethylene unsaturation and cure via a free-radical mechanism. In epoxies this unsaturation may be introduced through

acrylation or methacrylation of the terminal epoxy groups. However, conventional epoxy resins may also be EB-cured through a cationic mechanism, using the appropriate catalyst. For applications requiring a higher use-temperature, bismaleimide resins have been employed, modified with reactive diluents which make the material radiation sensitive. Electron penetration into a composite is directly proportional to the beam energy and inversely proportional to the composite density. A 10 MeV beam, for example, can penetrate about 2.5 cm of typical carbon fiber composite (density 1.5 g/cc) [6]. The beam must also penetrate any vacuum bag or pressure vessel if these are required for manufacturing the part. Products with a thickness greater than the EB penetration limit can be cured with x-rays, which are obtained from the same accelerator by placing a conversion target (such as Ta or W) in the path of the electron beam. Although the penetration limit for x-rays is about four times that for electrons, the time needed for curing may increase by a factor of about 10 to 50 since the absorption coefficients for energy from x-rays are generally lower than those from electrons. To limit the use of x-rays, the highest permissible energy level is selected - 10 MeV - above which there is a risk of activating metallic materials. The highest possible power is also used to minimize cure time.

EB-cure of composite structures offers a number of advantages over traditional autoclave cure:

- Selectable-temperature curing. Cure at ambient temperature allows the use of inexpensive tooling, while cure at the service temperature of the finished part reduces thermal residual stresses during its use. There is a temperature rise during cure, due to exothermic reactions and absorbed radiation energy; however, excessive heating can be avoided by using multiple passes to deliver the required dose.
- Reduced cure time. A 50-kW accelerator can cure about 1200 kg of composites per hour [7]. This is several times faster than conventional thermal cure in an autoclave, even though composite components are cured in batches as opposed to one at a time with EB cure.
- Improved material handling, EB-cure resins may be stored under ambient conditions and have longer shelf life than thermal-cure formulations. EB processing is a continuous operation, and components may be individually cured immediately after assembly, facilitating production scheduling and inventory control.
- Reduced solvent usage and volatile generation.
- Controllable energy input (and lower consumption) with minimal waste. Comparisons of energy required to cure specific composite parts ranging in mass from 0.3 to 16 kg showed a 10 times lower energy requirement for EB cure compared to autoclave cure [8].
- Greater design flexibility. This process allows the cure of selected areas only, the co-cure of different matrix materials, fabrication of unsymmetric and unbalanced composites, uniform cure of a range of thicknesses in the same part, and incorporation of metal inserts and fixtures prior to cure.

All these attractive features combine to create a process which is inherently less expensive than autoclave cure, particularly when high throughput is required. In addition EB cure could be a potentially enabling technology for the fabrication of very large structures such as cryogenic fuel tanks and for the processing of critical composite space structures, where reduced thermal stresses are essential for dimensional stability in the space environment. Several feasibility studies have been conducted which demonstrate the inherent economic and technical advantages offered by EB cure for aerospace composite structures; however, the success of this technology is dependent on development of the appropriate material systems and processes. When selecting a material system for a particular application, certain property

tradeoffs are necessary. For example, improved toughness is usually achieved at the expense of reduced elevated temperature performance. Keying on improvements in one property (such as glass transition temperature) as a measure of success or maturity of this technology is therefore inappropriate. A better assessment of the state of the art is obtained by selecting one or more specific structural applications and evaluating how EB-cured candidate systems meet their property/performance requirements. Alternatively, the characteristics of state-of-the-art EB-cured material systems may be directly compared with a baseline thermally-cured system already in use in aerospace structures. This last approach was the one employed in the present study to assess the status of EB-cured materials systems for aircraft and spacecraft structures.

EXPERIMENTAL

Materials

Two state-of-the-art EB-cured material systems were evaluated, RB-47 (from Aerospatiale) and CAT-B (from Applied Poleramics, Inc.), representative of free-radical and cationic curing mechanisms, respectively. RB-47 is a methacrylated epoxy resin while CAT-B is a mixture of epoxies derived from diglycidyl ether of bisphenol-A and cured with a photoinitiator. The baseline for comparison was 3501-6 (Hercules, Inc.), the thermally-cured epoxy workhorse of the aerospace industry. Composites of these resins reinforced with AS4 (unsized) and IM7 carbon fibers were also evaluated.

Processing

Both RB-47 and CAT-B were obtained as EB-cured neat resin plates for evaluation. Neat 3501-6 epoxy was fabricated into a plaque by casting the debulked molten resin between glass plates at 121°C followed by two hours at 177°C. Unidirectional AS4/CAT-B hot-melt prepreg tape was fabricated on a drum winder. A minimum resin bath temperature of 120°C was required to obtain adequate resin viscosity and tow impregnation. The prepreg was cut and layed up into laminates of $[0]_8$, $[\pm 45]_{2s}$ and $[0_2/90_2]_T$ orientations. These lay-ups were consolidated in a vacuum bag for eight hours at 70°C, and then EB-cured at Electron Beam Services, Inc. while still under vacuum. The cure was accomplished with a dose of 200 kGy delivered in four passes of the composite under the electron beam. An EB-cured $[0]_8$ panel of IM7/RB-47 was also obtained for evaluation.

Characterization

Moisture absorption of the cured neat resins was characterized after immersion in distilled water at 23°C. Thermal expansion measurements were made over the range of -100°C or 100°C using bonded strain gages. Thermal analysis was conducted on TA Instruments equipment with DSC and TGA scans (in air and nitrogen) at rates of 10°C/min. Dynamic mechanical analysis was performed on a Rheometrics RDS-II dynamic mechanical analyzer in the torsion mode at a frequency of 100rad/s and a scan rate of 5°C/min. All glass transition temperatures (T_g) reported in this paper were determined from the knee in the storage modulus curve. Isothermal aging studies were also conducted in the RDS-II (in nitrogen) in which the dynamic storage modulus was continuously monitored as a function of aging time.

Mechanical characterization of resin and composite specimens was conducted at MTS test machines. The majority of specimens were tested dry at 23°C(RTD), dry at 121°C(ETD), and wet at either 23°C(RTW) or 121°C (ETW) after boiling in water for 24 hours. Fracture toughness of the neat resins was determined under ambient conditions, after drying in a vacuum oven at 50°C and after aging at 121°C in a vacuum for 72 hours.

RESULTS AND DISCUSSION

Feasibility studies have indicated that electron beam cure of composites has some compelling economic and technical advantages over traditional thermal cure in an autoclave and is also an enabling technology for certain integrated structural designs. materials development, however, has not kept pace with improvements in hardware and process technology. A composite material system must meet some minimum mechanical property requirements under a range of test conditions to be considered for aircraft structural applications. a generic set of such tests was conducted to compare the EB-cure material systems with a baseline thermally-cured system accepted for such applications. The candidate material systems selected for this study represent the current state of the art with respect to the two major categories of EB-cure epoxies (free radical cure and cationic cure) although they are not necessarily optimized for the tests to which they were subjected. The ability to cure at ambient temperature, with consequent reduction in thermal residual stresses, makes EB-cure technology attractive for composite space structures. A key requirement for a space structure is dimensional stability over the range of operational temperatures. While it is advocated that thermal postcure of EB-cured composites (for cationically-cured systems) may be unnecessary [5], these structures will nevertheless experience elevated temperature at the upper extreme of the thermal cycles, and it is of interest to determine if the inevitable thermal postcure results in structural distortion.

Characterization of Neat Resins

Moisture absorption in the cured neat resins as a function of time is shown in Figure 1. While the initial rates of absorption for RB-47 and 3501-6 are similar, they begin to diverge after 1600 hours. Compared to these resins, moisture is absorbed at a slower rate in CAT-B. From the trends displayed to date, it appears that the thermally-cured 3501-6 will have a higher equilibrium moisture content than either of the EB-cured resins. Thermogravimetric analyses, conducted in both nitrogen and air, display excellent thermal and thermooxidative stability for all three resins up to 300°C. While the rate of mass loss from 3501-6 increases sharply at about 310°C (in nitrogen), the EB-cured resins are stable up to about 380°C. At 400°C the 3501-6 epoxy retains 74% of its weight in air and 67% of its weight in nitrogen, compared to 87% and 89%, respectively, for the EB-cured resins. Thermal expansions of the EB-cured resins over the range of -100°C to 100°C are essentially the same. The average coefficient of thermal expansion (CTE) over this range is about 20% higher for the EB-cured resins (51 ppm/°C) compared to 3501-6 (41 ppm/°C). This translates to an approximately 10% higher transverse CTE in a unidirectional ply reinforced with AS4 fiber with a fiber volume fraction of 0.6.

From a DSC scan of the EB-cured CAT-B resin (Figure 2A), there appears to be residual uncured material in the sample. Taking the ratio of the corresponding exotherm (11.5 mcal/mg) to that generated from the thermal cure of uncured liquid resin (106.6 mcal/mg) to that generated from the thermal cure of uncured liquid resin (106.6 mcal/mg), the degree of

cure of the EB-cured CAT-B panel is estimated at 89%. This is surprising, considering that an electron beam dose of 300 kGy was employed for this cure, in excess of the standard dose of 150 kGy. In comparison, the 3501-6 plaque, fabricated in-house, has a degree of cure of 97%. From a DSC scan of the EB-cured RB-47, it is unclear if there is any exotherm generated due to the uncertainty in establishing a baseline for the scan. However, when a sample of the same material is thermally postcured and then scanned in the DSC, comparison with the initial scan (Figure 2B) clearly shows that the resin cure in the original plaque was incomplete. Uncured resin, to quantify the degree of cure of the RB-47 plaque, was unavailable. From these results it appears that the application of thermal energy to an EB-cured epoxy is capable of generating exotherm through some additional chemical reaction which does not occur under electron beam irradiation. When EB-cured composites are employed in service, elevated temperature exposure may trigger such (thermally-induced) reactions, with consequent changes in shape, properties or performance of the structure.

Representative dynamic storage moduli (G') of the three resins as functions of temperature are shown in Figure 3. From this figure it can be seen that RB-47 has a relatively low T_g (115°C). The storage modulus of CAT-B starts to drop at about 110°C. However, simultaneous thermal postcure limits the rate of decline in G' until the second knee (at about 160°C), giving rise to a T_g of 160°C. The storage modulus curve for 3501-6 is relatively flat on this log scale, with a sharp knee and a corresponding T_g of 202°C. A better representation of this data is a plot of retention of storage modulus (on a linear scale) as a function of temperature, as shown in Figure 4, which allows direct comparison of the three resins. For example, RB-47, CAT-B and 3501-6 show a retention of 60% of their room-temperature storage moduli at temperatures of approximately 108°C, 133°C and 185°C, respectively; alternatively, at 121°C, RB-47, CAT-B and 3501-6 retain 42, 70 and 82%, respectively, of their storage moduli at room temperature. These data demonstrate the superiority of thermally-cured 3501-6 for elevated-temperature applications.

Tensile properties of the neat resins were determined under ambient conditions (RTD), at 121°C (ETD), and at room temperature after boiling in water for 24 hours (RTW). As expected from the poor retention of storage modulus under dynamic mechanical testing, both the EB-cured resins experience a knockdown in tensile modulus at 121°C (Figure 5), the RB-47 more so than the CAT-B, while 3501-6 retains about 75% of its room-temperature modulus.

Resin tensile strength at 121°C follows the same trend as tensile modulus (Figure 6), with strength retention of only about 25% and 55% of the corresponding room-temperature values for RB-47 and CAT-B, respectively. Absorbed moisture causes only a 15-20% drop in tensile modulus of the EB-cured resins, although the corresponding drop in tensile strength is close to 40%. Thermally-cured 3501-6, on the other hand, suffers only a 5% loss in modulus under similar conditions and a 25% loss in strength.

Composite Processing

Unitape prepreg was processed in-house on a drum winder using unsized AS4 (12K0 fiber and CAT-B resin. This resin may be processed from the melt or from a solution in methylethyl ketone. The former option was preferred, to eliminate the necessity of having to remove residual solvent prior to cure. The minimum melt temperature for satisfactory fiber tow impregnation was found to be 120°C. Cure of this cationically-cured resin system is advanced thermally, however, which limits the resin pot life. Cure advancement at elevated

temperatures is illustrated in Figure 7, where the dynamic viscosity of the resin at four different temperatures is plotted as a function of time. It is apparent that at a processing temperature of 125°C, the limited pot life of the resin requires that prepregging be completed in three hours.

The processing challenge with EB-cured materials lies in obtaining a void-free part through appropriate consolidation *prior* to cure, since the resin is immobile *during* cure. The consolidation temperature has to be carefully selected; it must be high enough to significantly reduce resin viscosity, thereby allowing compaction and the escape of trapped air, but not too high to significantly advance the thermal cure of the resin. Initially, panels were consolidated in a vacuum bag at 70°C cooled to ambient temperature, and the vacuum released prior to cure in the electron beam. This resulted in panels with large unbonded areas between plies. In the second attempt the vacuum was maintained during the electron beam cure. A vacuum bag tends to retain the heat from absorbed energy and cure reactions, resulting in an increase in panel temperature during cure. The temperature rise was limited to 50°C by delivering the required dose in four passes. Ultrasonic C-scans of the resulting panels revealed mixed results; some panels appeared to be well-consolidated, while others in the same batch were not. Only the well-consolidated panels were tested. These preliminary results indicate the need for some consolidation pressure during EB-cure and further optimization of the consolidation conditions prior to cure.

Composite Characterization

In addition to the test conditions used for neat resins, the mechanical properties of composites were also evaluated under hot/wet conditions. The results are summarized in Table 1. The longitudinal tensile modulus of IM7/RB-47 approximates the value predicted from the rule of mixtures, although the tensile strength is substantially lower than expected. The low tensile strength is due to premature longitudinal splitting of the specimen originating at the gripped ends which, in turn, arises from poor fiber-matrix bond strength. This is borne out by the relatively low 90° tensile strength for this composite system. Reduction in matrix strength at elevated temperature causes a 50% drop in 90° tensile strength. After boiling in water for 24 hours, there is a 65% drop in 90° tensile strength at ambient temperature. From a comparison with the trends observed in neat RB-47, it appears that the water boil causes a significant deterioration in the already low fiber-matrix bond strength of this composite system. This was confirmed from SEM examinations of the fracture surfaces of failed test specimens. A combination of moisture *and* elevated temperature (121°C) drastically reduces the transverse strength to a value which is less than 10% of the dry, room-temperature strength. A similar trend was observed in interlaminar shear strength measurements. Corresponding manufacturer's data for a thermally-cured IM7/epoxy composite system (IM7/8552) are also shown in the table for comparison.

Matrix-dominated properties of the AS4/CAT-B composite system are compared to those of thermally-cured AS4/3501-6 in Table 1. There is a greater drop in the in-plane shear modulus of AS4/CAT-B at 121°C (35%, compared to 15% for AS4/3501-6), while the reduction after the 24-hour water boil is 23% (compared to only 5% for AS4/3501-6). The thermally-cured composite displays fairly good retention of matrix- and interface-dominated properties, such as transverse tensile and flexural strength, at elevated temperature and under the influence of absorbed moisture. On the other hand, AS4/CAT-B displays a 23% drop in 90° flexural strength at 121°C and a 42% drop at room temperature after boiling in water for 24 hours,

suggesting significant moisture-induced deterioration of the fiber-matrix interface. This was confirmed from SEM examinations of failed test specimens.

Isothermal Aging of Resins and Composites

A possible application of EB-cure technology is in space structures, because of the potential of greatly reduced residual stresses (and hence better dimensional stability) resulting from ambient curing conditions. However, the lack of full cure in an electron beam (as evidenced from the DSC studies described earlier) raises a concern about the potential for dimensional distortion when cure advances (thermally) in the application environment. Space structures may cycle between -157°C and 121°C . Consequently, neat resin and composite specimens were isothermally aged at 121°C to simulate the upper temperature of such a space environment. The changes in dynamic storage moduli of EB-cured neat resins and composites with time are shown in Figures 8 and 9, respectively. Most of the change in storage modulus occurs within the first 10 hours of aging. dynamic storage moduli vs. temperature of EB-cured composites are compared before and after isothermal aging (for 48 hours) in Figure 10. The two knees in the baseline curve for CAT-B are more pronounced here than in the corresponding G' curve for the neat resin (Figure 3). The first knee occurs at approximately 60°C , which is the temperature at which the exotherm initiates during the DSC scan (Figure 2A). The disappearance of this knee after gain (Figure 10) suggests that it arises from additional cure during the test and not from a second toughening phase of lower T_g . The change in composite T_g with aging is more pronounced than the corresponding change in neat resin T_g , as seen from Table 2.

Possible consequences of thermal postcure and the increase in stiffness which occur during aging are a decrease in fracture toughness and an increase in residual stresses. The extent of warpage of an unsymmetrical laminate provides a measure of the built-in residual stresses. A $[0_4/90_4]_T$ unsymmetric laminate of AS4/CAT-B was fabricated, and narrow strips, 15 cm long and 6.35 mm wide, were sectioned. This narrow width limits the warpage to a single direction. Chemical shrinkage during cure resulted in a slight curvature of the strips under ambient conditions (0.7 mm, compared to 9.7 mm for a thermally-cured AS4/3501-6 laminate with the same layout). On heating, thermal expansion causes the strips to straighten out and then experience a reversal in curvature which increases out to 121°C . With the temperature maintained at 121°C , however, there is no further change in warpage (determined by monitoring the central deflection of the composite strip to the nearest 0.05 mm) over a 48-hour period, indicating no measurable increase in residual stresses with this isothermal aging. The fracture toughness of neat resin specimens aged for 72 hours at 121°C was also measured and compared with the corresponding values for unaged specimens. The results are shown in Table 2. Fracture toughness does not decrease with aging; in fact it appears to increase, possibly due to further (thermal) advancement of cure. Preliminary indications, therefore, are that the (thermal) cure advancement seen in DSC studies does not adversely affect the performance of EB-cured composites.

SUMMARY AND CONCLUSIONS

Electron beam cure offers significant technical and economic advantages over conventional autoclave cure of composite structures for aerospace applications. The key to realizing the potential of this technology is development of the appropriate composite constituents (matrix resins, fiber sizings) which will yield a cured product equivalent or superior to its thermally-

cured counterpart. The two EB-cured systems evaluated in this study (epoxy-based RB-47 and CAT-B) both display evidence of additional thermal cure, in spite of receiving an electron dose greater than that normally employed. This suggests the possibility of thermally-activated chemical reactions occurring in the composite structure in its application environment. However, sustained exposure to a temperature of 121°C reveals no adverse aging effects; there is no measurable increase in residual stress and no deterioration in resin toughness, although the dynamic storage modulus and T_g increase slightly. Cured resin thermal and thermooxidative stabilities are on par with those of thermally-cured 3501-6 epoxy; however, resin T_g is significantly lower, which translates to a significant to substantial reduction in mechanical performance at elevated temperatures. This poor performance at elevated temperature carries over to the composite and is compounded by the susceptibility of a relatively weak fiber-matrix interfacial bond to degradation in the presence of moisture. A first step toward reaping the benefits of this process in aerospace structures is to develop resin formulation with inherently high T_g and appropriate fiber sizings that will generate acceptable hot/wet mechanical properties.

ACKNOWLEDGMENTS

The assistance of the following is gratefully acknowledged: James Lute, Bill Ragland, Ron Esterline, John Camping and Ron Trejo of the University of Dayton Research Institute for fabricating and characterizing composites; Rich Moulton of applied Poleramics, Inc. and tom Knoebel of E Beam Services Inc. for providing test materials and electron beam-curing the composites, respectively; and the U.S. air Force for sponsorship of this work under Contract No. F33615-95-D-5029.

REFERENCES

1. D. Beziere and J. P. Denost, "Composite Curing: A New Process," Proc. AIAA Conference on Structures, Dynamics and Materials, AIAA-89-2868 (1989).
2. D. Beziere and B. Capdepuy, "Electron Beam Curing of Composites," Proc. Inyt. SAMPE Symp., 35, p. 1221 (1990).
3. C. B. Saunders, et al., "Radiation-Curable Carbon Fiber Prepreg Composites," Polym. Compos., 9(6), p. 389 (1988).
4. C. B. Saunders, et al., "Electron Curing of Fiber-Reinforced Composites; Recent Developments," Proc./ Int. SAMPE Symp., 38, p. 1681 (1993)
5. C. Janke, "Electron Beam Curable Cationic Epoxy Resin Systems and Composites," Proc. Electron Beam Curing of Composites Workshop, Oak Ridge, TN, Paper 8 (Sep 1996).
6. C. B. Saunders, et al., "Recent Developments in the Electron-Beam Curing of Fiber-Reinforced Composites," Proc. Int. SAMPE Symp., 37, p. 944 (1992).
7. C. B. Saunders, et al., "Characterization of Matrix Polymers for Electron-Beam-Cured Fiber-Reinforced Composites," in Irradiation of Polymeric Materials, ACS Symp. Series No. 527, E. Reichmanis, C. Frank and J. O'Donnell, eds. (American Chemical society, 1993), p. 305.
8. S. L. Iverson, et al., "Radiation Curable Composites: Environmental Advantages," Proc. Int. Symp. on Applications of Isotopes and Radiation in Conservation of the Environment, Karlsruhe, Germany (International Atomic Energy Agency, Vienna, 1992).

A NEW TECHNIQUE FOR THE PREPARATION OF POLYETHYLENE FIBRE / POLYETHYLENE MATRIX COMPOSITES AND THE RESULTING MECHANICAL PROPERTIES

F. v. Lacroix, M. Werwer, K. Schulte

*Polymer/Composites Section Technical University Hamburg-Harburg
21071 Hamburg, Germany*

SUMMARY: Different impregnation techniques for Polyethylene fibre / Polyethylene matrix composites using molten PE, PE powder and PE solution are described and discussed. Best results have been reached with the new solution impregnation method. The processing route includes an impregnation step in a saturated matrix solution. The growth of a matrix layer on the fibre surfaces in such a solution is shown by SEM micrographs. Further processing steps are the preparation of prepregs and their hot compacting to form PE/PE composites. In this work unidirectional composites were prepared at three compacting temperatures. The influence of the final processing temperature is discussed. Mechanical testing showed a high Young's modulus and a high tensile strength. The composite compressive strength is comparably low as a result of low compressive strength of the PE fibre.

KEYWORDS: polyethylene fibre, manufacturing, mechanical properties

INTRODUCTION

Ultra high modulus polyethylene (UHM PE) fibres exhibit high specific strength and stiffness combined with high strain to failure [1]. They especially improve the damage tolerance, fatigue and impact resistance and vibration damping when used as reinforcement for thermoplastic matrices. Polyethylene as matrix material is chemically resistant to most solvents, has a low coefficient of friction, is biocompatible and hydrophobe. Therefore it is widely used for biomedical application as in artificial hips or knee-joints [2]. A PE-fibre/PE-matrix composite would not only improve the mechanical properties of bulk PE but furthermore would enable to have a fully recyclable composite.

Impregnation of fibre bundles with matrix, this means the penetration of matrix into fibre bundles, the wetting of all fibres and the homogeneous distributions of the fibres in the matrix, is a very important step during composite manufacturing. Because many mechanical weak points of composites e.g. matrix rich areas or fibre contacts are founded in incomplete or imperfect impregnation. Using thermoplastic matrices the higher viscosity of the melt compared to uncured thermosetting plastics e.g. epoxy enlarged the difficulty in impregnation, because the higher viscosity leads to a reduced matrix flow.

Impregnation routes

HDPE and LDPE can potentially be used as matrix in a PE/PE-composite due to their lower melting temperatures than the UHM PE fibres [3-6]. However, the temperature window to produce the composite without damaging the fibres is rather narrow and the viscosity of the matrices in this temperature region are relatively high. Therefore impregnation of PE-fibre bundles with HDPE or LDPE matrices is rather difficult. Impregnation techniques can be classified by the condition of the matrices during the process. Figure 1 shows short results of impregnation experiments with HDPE and LDPE matrices.

	LDPE	HDPE
Melt	low penetration of matrix into bundle	
Powder	inhomogeneous powder distribution, agglomeration	
Solution	segregation and crystallisation of matrix on fibre surfaces	
	fibre volumen fraction: $V_f \geq 50\%$	$V_f \geq 85\%$

Figure 1: Results of the impregnation tests

For the melt impregnation tests UHM PE-fibre bundles (Dyneema, DSM The Netherlands) and HDPE-films are used. The fibre bundles were fixed in a mould to prevent shrinkage and stacked between HDPE-films. The mould was heated to 140°C for 15 minutes in laboratory press at a pressure of 4 bar. At the light micrograph (Fig. 2) of such a consolidated specimen, cut and polished perpendicular to fibre direction, three different areas can be seen. Outside of the bundle is the pure matrix (a). The outer part (b) of the bundle is impregnated. Fibre and matrix form a regular area, but in the middle of the bundle single fibres can be seen (c). Here, in this inner part of the bundle, isn't any matrix. The HDPE didn't flow into this inner part of the bundle caused by the high viscosity of molten matrix. Increasing the manufacturing temperature reduces the viscosity of matrix only a little, but just below melting point of fibre they melt at their surfaces, glue together and form a closed bundle. Therefore penetration of matrix into the bundle is stopped by a closed border of glued fibres. Increasing the impregnation time or using a LDPE with a lower melting point and a lower viscosity than HDPE didn't show a significant change of the Problem. However impregnation of PE / PE composites by melt impregnation technique is relatively difficult, caused by low penetration of matrix into fibre bundles (Fig. 1).

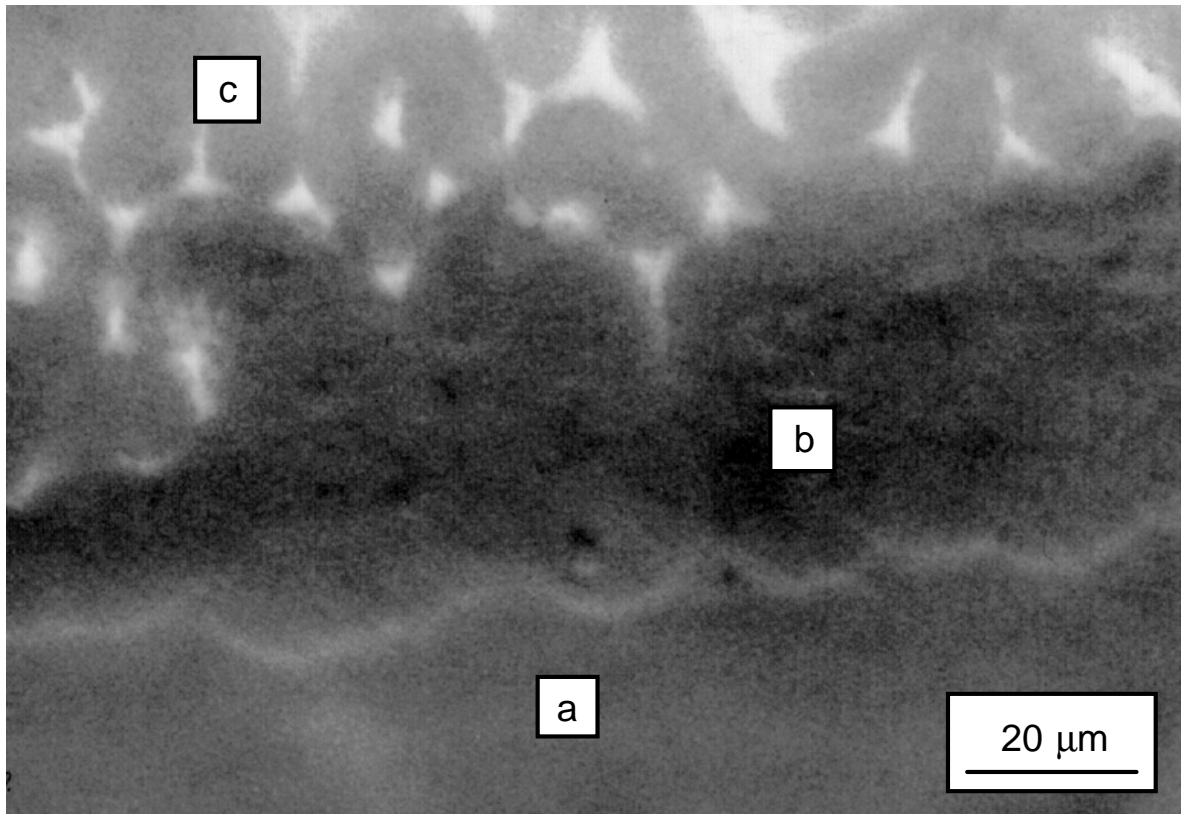


Figure 2: Melt impregnation, light micrograph of a polished crosssection

To impregnate fibre bundles with matrix powder, a very fine matrix powder is needed. The particle size of the powder should be in the range of the fibre diameter (10..25 μm). Dipping fibres in such a fine LDPE powder or shaking fibres in a box together with the powder resulted in a very inhomogeneous powder distribution with agglomerated LDPE particles (Fig. 1). Hinrichsen et al [6] published a work about continuous powder impregnation of UHM PE fibres with LDPE matrix. For Impregnation they pulled the fibre bundles through a special fluidized bed chamber, heated them in a melting oven and compacted the tape between shaped rollers. For their paper they produced only a composite tape with a low fibre volume fraction of 10.8% and the problems of impregnation are increasing with increasing fibre volume fraction. However, this continuous powder impregnation technique is on the way to be a method to produce PE/PE composites.

Crystallisation of PE in a saturated solution is a well known fact. Dipping a high oriented substrate in such a solution, crystallisation is nucleated on the fibre surface [7]. An oriented layer around the fibres is growing. The novel idea of the present work is to use this phenomenon for producing PE/PE composites. Figure 3 shows UHM PE fibres after different times in a xylene solution with a low LDPE concentration (5 weight%) at 70°C. A thin layer of LDPE on surface of the treated fibres can be seen compare (Fig. 3a) untreated fibre and (Fig. 3b) 8 minutes treated fibres. The thickness of the layer increases with increasing treatment time (Fig 3b-d). After 19,5 hours the fibres are covered with a thick layer of LDPE (Fig. 3d).

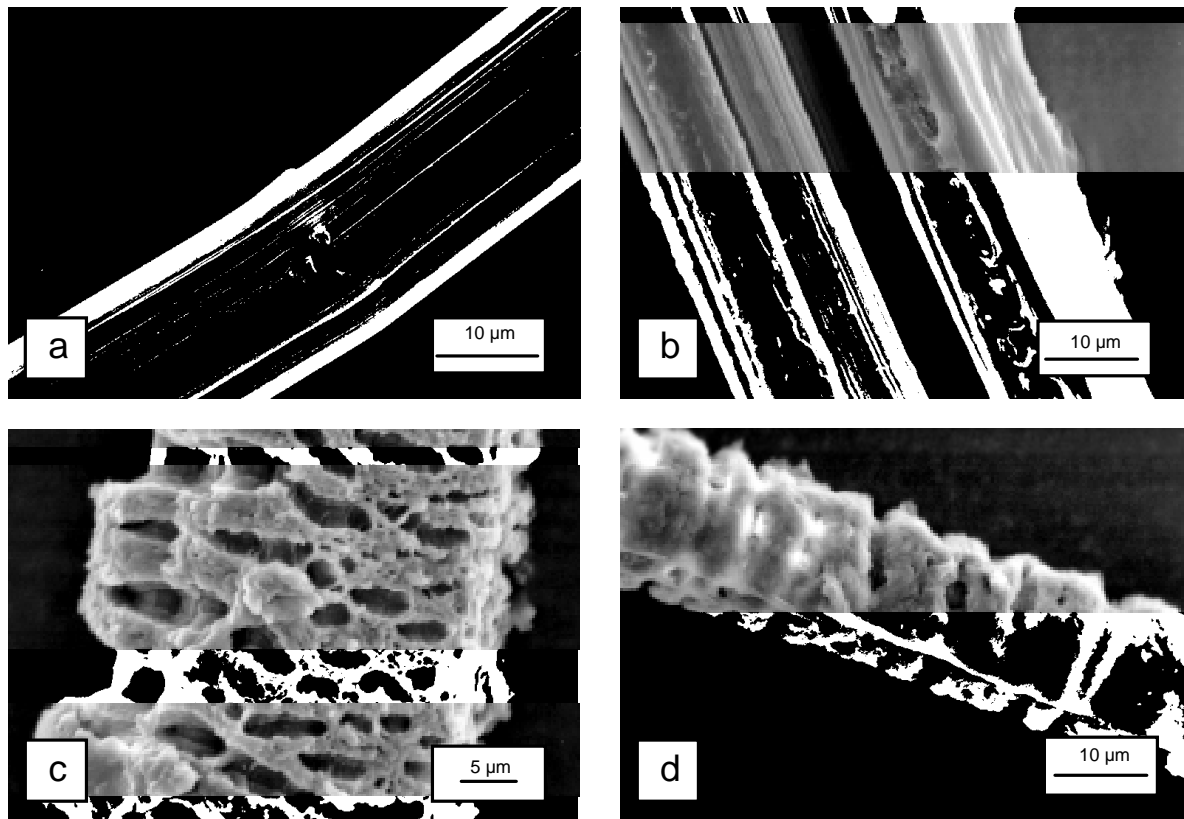


Figure 3: Scanning electron micrographs of PE-fibres: (a) untreated, after treatment in LDPE/xylene for (b) 8 min, (c) 3,25 h and (d) 19,5 h.

The coated fibres turned out to be an ideal pre impregnated material, because each fibre is surrounded by the LDPE-matrix. Heating the parallel arranged impregnated fibres or fibre bundles and compacting them above the melting temperature of the matrix material leads to a one polymer composite with well defined fibre distribution. In contrast to our investigations with melt impregnated PE/PE composites, the high matrix viscosity (below the melting point of fibres) causes no problem, because the flow paths of matrix in the solution impregnated material are neglectible short.

In principal the solution impregnation method is working although with a HDPE matrix, but due to the less solubility of HDPE compared to LDPE it is more difficult to reach a thick matrix layer on fibre surfaces. Until now only thin HDPE layers, corresponding to 15 % matrix volume fraction have been achieved.

Composite fabrication

Figure 4 shows the discharge of the new manufacturing technique for PE/PE composites. It starts with commercial UHM PE fibres, Dyneema SK 65 (DSM, The Netherlands). In the first step, the solution impregnation, UHM PE fibre rowings (1760 dTex) were wound to bundles on a frame, dipped for 10 minutes in a 12 weight% solution of LDPE in xylene at 70°C and were dried in an oven at 50°C (experimental details are given elsewhere[8]). In figure 5a a thick regular coating of LDPE on fibre surface is visible. At higher magnification (Fig 5b) single coated fibres can be recognised. The fibre volume fraction was calculated by weighing the bundles before impregnation and after drying to 55%.

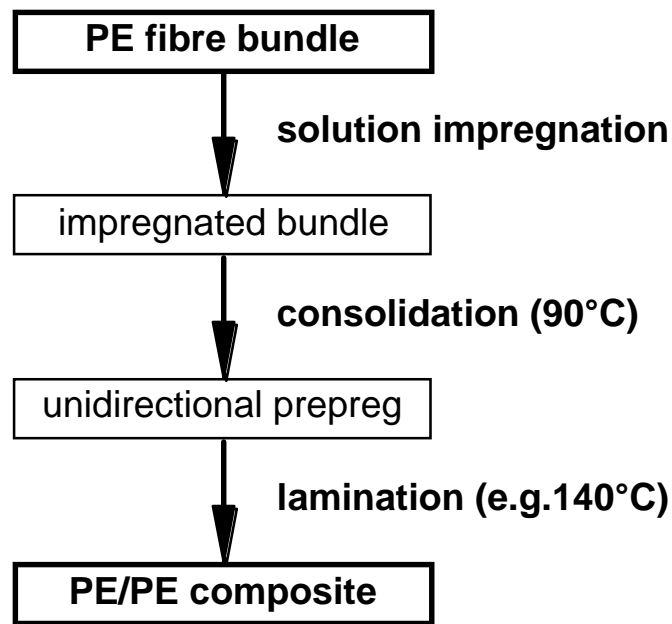


Figure 4: Discharge of the solution impregnation technique

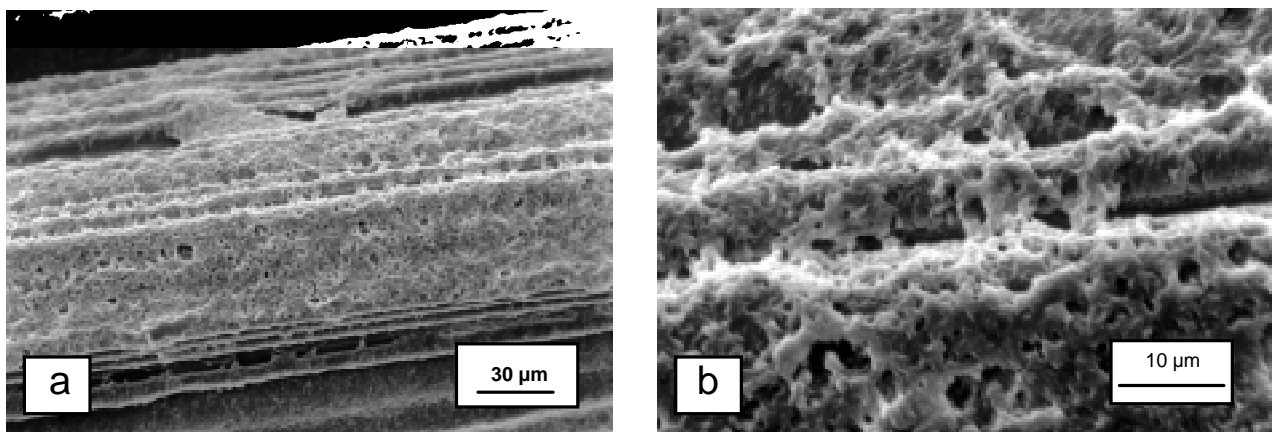


Figure 5: Scanning electron micrographs of an impregnated PE-fibre bundle (a), (b) higher magnification

In the second manufacturing step several parallel arranged impregnated bundles were consolidated at 90°C in a laboratory press to get unidirectional prepregs. In the last step these prepregs were cut, laminated and pressed at 120°C, 130°C and 140°C for 10 minutes to unidirectional compression and tensile specimens. Alternatively NOL-Rings (diameter 100 mm) were wound with the impregnated bundles and heated at the same temperatures again for 10 minutes.

Mechanical Properties

Tensile modulus and strength were measured with flat specimen and NOL-rings. The tensile test results for different manufacturing temperatures are presented in Figure 6. The composites prepared at 120°C manufacturing temperature had a relatively high Young's modulus with values of 35 GPa, but the Young's modulus decreases with increasing manufacturing temperature. The Young's modulus of specimens consolidated at 140°C decreases to 20 GPa due to thermal damage of fibres which have a melting point of 146°C. Molecular and crystalline orientation decrease and the fibres shrink while treated at 140°C.

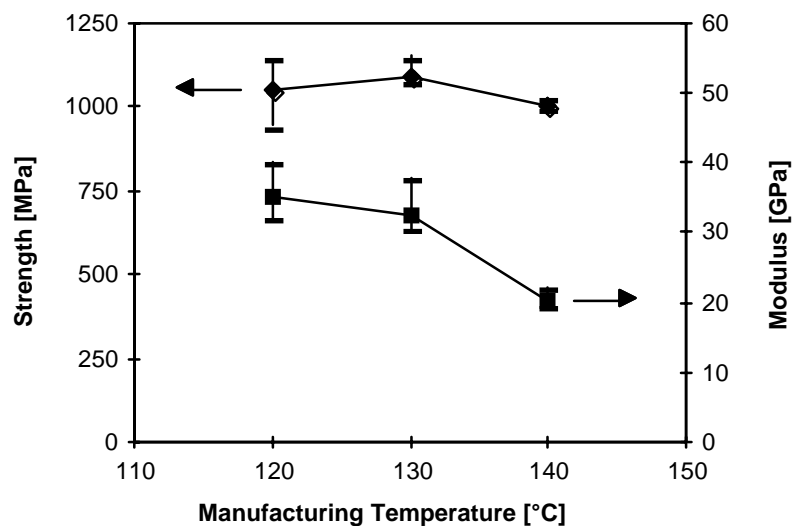


Figure 6: Tensile properties of LDPE / PE fibre composites

The tensile strength, measured with the NOL-ring specimen exceeded 1 GPa for all manufacturing temperatures (Fig. 6). An apparent maximum of strength can be observed at a manufacturing temperature of 130°C. It can be assumed that we have at this temperature a better fibre wetting and consolidation when compared to 120°C manufacturing temperature and of course no thermal damage when compared to 140°C manufacturing temperature. However, the tensile strength was nearly unaffected by the three consolidation temperatures. This was not expected, because the fibre strength is as the Young's modulus a function of fibre quality. We would expect the strength decrease also with increasing manufacturing temperature as it is the case for the Young's modulus. The rings and the flat specimens separately measuring the strength and the modulus respectively were manufactured by different techniques. The flat specimen were consolidated in a simple mould and the fibre shrinkage was only restricted by the viscosity of the melted matrix material and the consolidation pressure. The fibre shrinkage was macroscopically visible (e.g. about 10 % shrinkage at 140°C final consolidation temperature). To produce the ring specimens the

impregnated bundles were wound around a core. The ends were fixed in the mould during consolidation. Therefore fibre shrinkage was prevented and thermal damage of the fibres was lower compared to the flat specimens.

Figure 7 shows the fractured area of a NOL-ring failed in tension. The ring split into several parts (Fig. 7a). The SEM investigation shows that the bundles fibrillate into single polyethylene fibres (Fig. 7b). Figure 7c shows fibres with the for Dyneema typical not round crosssection. The fibres appear like a flat tape with axes of 10 to 25 μm (Fig. 7c). The fibres further fibrillate into macrofibrils with diameters of about 3 μm (Fig. 7d). The macrofibrils fibrillate into microfibrils with diameters of 0.5 μm (Fig. 7e). This shows that the failure mode is a hierarchically structured fibrillation with the hierarchies: microfibril, macrofibril, fibre, fibre bundle and specimen.

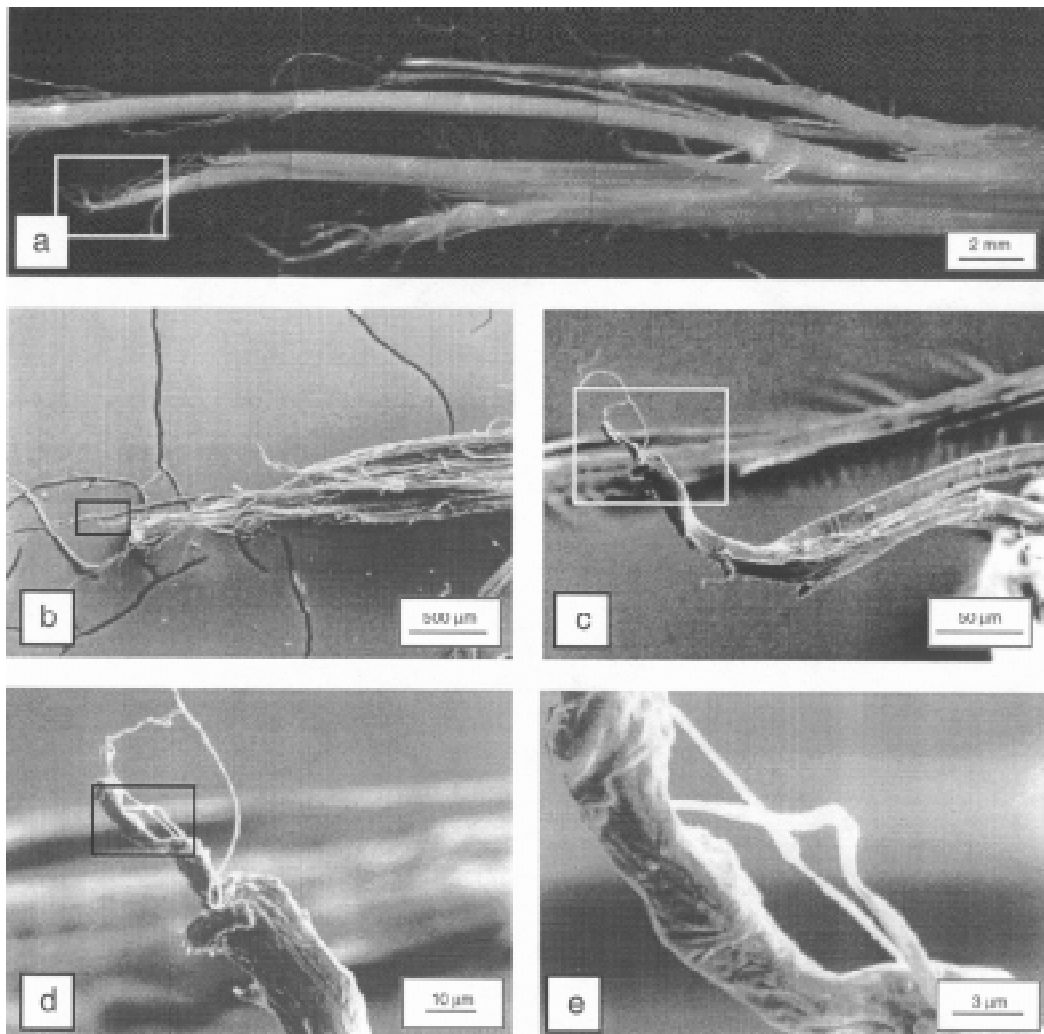


Figure 7: Light micrograph (a) and SEM micrograph (b-d) showing the different steps of fracture process

*a) hole specimen, b) fibre bundle, c) single fibre,
d) macrofibril of fibre, e) microfibril of fibre*

The results of the compression tests from the different manufacturing temperatures are summarised in Figure 8. The compression modulus showed the same decrease with increasing manufacturing temperature as the tensile modulus. Because of fibre misalignment the

Young's modulus in compression was lower as in tension. Tensile loading straightened the wavy fibres which led to a higher fibre alignment in the loading direction and an increased Young's modulus. In contrast, the fibre waviness in compression immediately leads to kinking and shear band format and thus a low Young's modulus. The low stiffness of the LDPE matrix accelerates this behaviour.

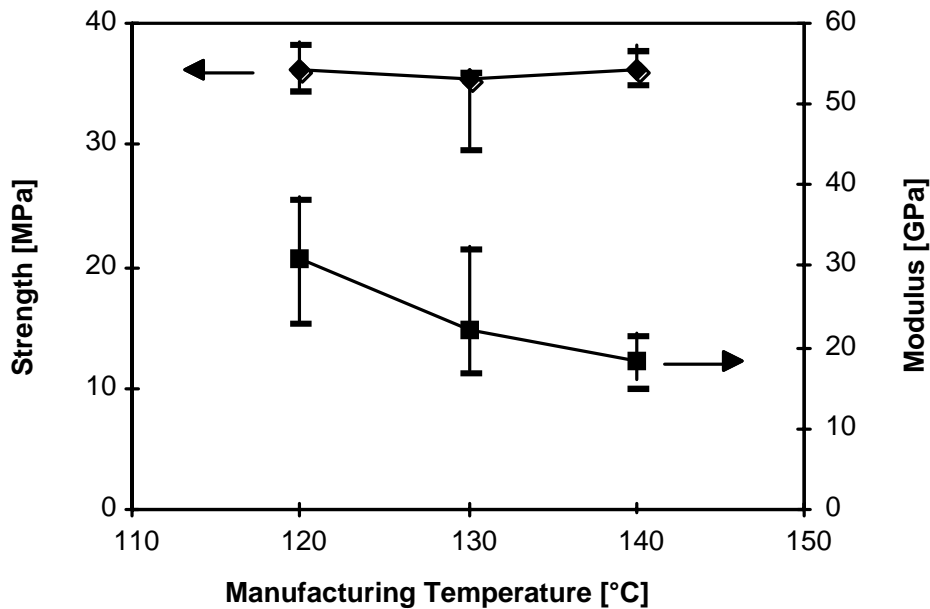


Figure 8: Compressive properties of LDPE / PE-fibre composites

The compressive strength of the PE/LDPE composites (Fig. 8) was just opposite to the high tensile strength (Fig. 6). The composite failed already at about 36 MPa. This low compressive strength was nearly unaffected by the manufacturing temperature. Figure 9 shows in a polarised light micrograph a specimen failed in compression. A kinkband through the whole specimen can be observed. This demonstrates the low compressive stability of UHM PE fibres in a LDPE matrix.

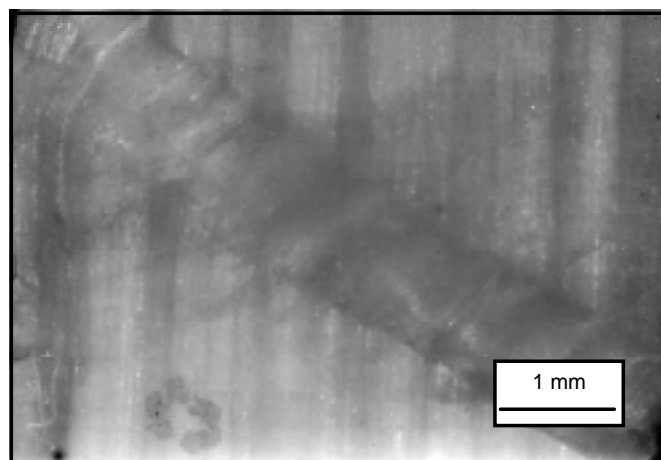


Figure 9: Polarized light micrograph of a specimen failed in compression

CONCLUSIONS

Different impregnation routes for PE/PE composites have been discussed. Melt impregnation techniques results in low penetration of matrix into bundle. Impregnation with PE powder leads to agglomeration and inhomogeneous distribution of powder particles. The new solution impregnation technique solves the impregnation problems. This manufacturing route starts with the impregnation of UHM PE fibre bundles in a LDPE / xylene solution. Further processing steps are preparation of prepregs and hot compacting to get the PE/PE composites. Mechanical testing shows a high Young's modulus and a high tensile strength. Because of their good tensile strength and further expected positive properties e.g. high energy absorption capacity, biocompatibility, and chemical resistance PE/PE composites are interesting for special applications, e.g. ballistic protection or as implant material for artificial joints.

REFERENCES

- 1 D.S. Prevorsek: Preparation, structure, properties and applications of gel-spun ultrastrong polyethylene fibres, TRIP, Vol. 3, No. 1, 1995, 4-11
- 2 T. M. Wright, D. L. Bartel: The problem of surface damage in polyethylene total knee components, Clinical Orthopaedics and Related Research, 209, 1986, 67-74
- 3 N.J. Capiati, R.S. Porter: The concept of one polymer composites modelled with high density polyethylene, J. Mater. Sci., 10, 1975, 1671-1677
- 4 A. Teishev, S. D. Incardona, C. Migliaresi, G. Marom: Polyethylen fibers - polyethylene matrix composites: preparation and physical properties, J. Appl. Polym. Sci, 50, 1993, 503-511
- 5 C. Marais, P. Feillard: Manufacturing and mechanical characterisation of unidirectional polyethylene-fibre/polyethylene-matrix composites, Compos. Sci. Technol., 45, 1992, 247-255
- 6 N. Chand, S. Kreuzberg, G. Hinrichsen: Influence of processing conditions on the tensile properties of unidirectional UHMWPE fibre/LDPE composites, Composites, 9, 1994, 878-880
- 7 E. Schulz, R. Hirte: Bildung strukturierter Polyethylen-Schichten auf hochgeordneten Polyethylen-Faeden, Acta Polymerica, 39, 1988, 177-183
- 8 F. v. Lacroix, M. Werwer, K. Schulte: Solution impregnation of polyethylene fibre / polyethylene matrix composites. Comp. Sci. & Tech., submitted

BASIC PRINCIPLES OF FILAMENT WINDING

Leng Xingwu ¹, Wo Dingzhu ²

¹Harbin FRP Institute No,100 Hongqi Ave, Harbin, China.

²Nanjing University of Aeronautics & Astronautics
c-218No.29 Yudao Street, Nanjing 210016, P.R. China

SUMMARY: Basic principles of filament winding such as winding rate ratio, overall winding pattern local winding pattern, winding angle, winding central angle, winding thickness, geometrical shape of the product to be wound, filament geometry, geodesic line winding, non-geodesic line winding, irregular section winding, concave curvature bridging winding are summarized in this paper, most of which are derived from practice [1]-[12], some are cited from the reports on special subjects. They are recommended for those engaging in the design and process of filament winding and teachers and students of the colleges.

KEYWORDS: filament winding, winding rate ratio, winding angle, bridged winding

INTRODUCTION

Principle 1. Overall winding pattern is determined by winding rate ratio, i.e. the winding rate ratio determines the geometry of filament over the surface of mandrel, the number of filament crossovers, the number of points of tangency in the circumference, or the number of parallelograms etc..

Winding rate ratio is the number of rotation of the mandrel to the number transverse of filament in axial direction of rotating mandrel, it is determined by the following formula:

$$I = K/N \quad (1)$$

Where K is the number of circles of the filament wound on mandrel and N is the point of tangency of the filament on the top of the ends in a complete winding circulation, K the filament crossover points are:

$$M = K - 1 \quad (2)$$

From formula (2) it can be seen that when M is big enough, the winding becomes "Weaving" winding, the number of parallelograms N is:

$$N = n(K - 2) \quad (3)$$

From formulas (1), (2), (3), we can see as long as the winding rate ratio is definite, the numbers of parallelograms are defined.

Ratiocination 1: Winding rate ratio can only determine the overall winding pattern, not the geometrical shape of the local pattern.

Principle 2. The local dimension of the winding product, the local winding angles and the points of tangency determine the local winding pattern.

Ratiocination 1: The local winding pattern is independent of the K circles of the rotating mandrel in a complete winding circulation, i.e. the local winding pattern is related to winding

rate ratio formula(1). Divisor N when the points of tangency are equal to a certain number, the local winding pattern bears no relation to the change of winding rate ratio.

Principle 3. Overall winding pattern is independent of the geometrical shape of the product to be wound

from formula(1) it can be seen that the winding rate ratio I is determined by relative rotating number K and the number of points of tangency. N It is not related to other factors. Parameters N and K have no relation to geometric

Ratiocination 1: The Overall winding pattern has no relation with the change of the dimension of section in mandrel axial direction. That is the theoretical basis for us successful helical winding the irregular section of toroidal.

Ratiocination 2: The overall winding pattern has no relation to the distance between the axis of mandrel and every points of circumference of the product section. That is the theoretical basis for us successful helical winding the irregular section of non-toroidal.

Principle 4. The Delivery of filament is determined by the following microratio:

$$\Delta n \leq b / n\pi D \cos\alpha \quad (4)$$

where n is microratio; b is the width of filaments; n is the number of points of tangency. if the microratio coincides with formula(4), the filament can cover the product densely. we take = for densely covering of filaments, for filaments overlapping.

Ratiocination 1: The thin and dense of the filaments delivery is determined by microratio. After the intervals of the filament delivery is substituted into formula (4), the delivery of the filament is as follows:

$$\Delta l = (b + \Delta l) / n\pi D \cos\alpha \quad (5)$$

Where l is distance between the adjacent filaments. B+ l is the distance between the central lines of the adjacent filaments. Formula(5) is used for calculating winding structures with interval filaments such as filtering pipes, porous structures.

Ratiocination 3: When $(b + l) / \cos\alpha$ is equal to round number times of circumference D, porous structure can be wound. a new filament winding structure can be wound on the basis of the ratiocination.

Ratiocination 4: The discrimination of distribution of filament of the irregular and changeable sections is:

$$\Delta_{i\pi} = b/D | \cos\alpha | \quad (6)$$

we take < filament overlapping

= for dense distribution

> for thin distribution

Ratiocination 5: When the microratio is zero, filaments must be overlapped, the overlapping place and points of tangency must divide the circumference into equal parts[3].

Ratiocination 6: The thickest place of the filament on the wound

product must be the place where $(D\cos\alpha)$ is min, while the thinnest place must be the place where $(D\cos\alpha)$ is maximum.

Principle 5. Winding rate ratio is determined by the sums of all the center angles. The relation between the winding rate ratio and The sum of the center angles is

$$I = \theta / 360^\circ \quad (7)$$

Where θ_n is the sum of the center angles of the rotating manerel when a complete winding circulation is finished, while the sum of center angle of the double path are determined by the sum of every center angel of one path.

Ratiocination: The winding rate ratio is independent of the local winding angles and the local center winding angles.

Principle 6. The filament wound along the geodesic line path is stable, because the geodesic line consists of numerous short path lines, which are stable, so the filament along the geodesic line is stable and can not slide.

Usually the relation between the formula of the winding angle of geodesic lie and the radius is

$$r |\sin\alpha| = c \quad (8)$$

where r is the radius of any section.

α is the winding angle of any section.

Rationcination; If the friction coeffecient is neglected, any deflection of the filament from the geodesic line will result in the filament sliding untill the filament slide into the position of geodesic line.

Pronciple 7. Equivalent circle".

Any section of non-rotator can be simplified to a equivalent circle circumference and calculated according to helical winding.

The circumference of the "equivalent circle" is

$$\pi D_{ec} = a + b + c + \dots + n \quad (9)$$

where D_{ec} is the iameter of the "equivalent circle", n is the length of the sides of any convex polygon.

The winding angles of the "equivalent circle" is

$$\tan \alpha_{ec} = (a + b + c + \dots + n) / L_1 \quad (10)$$

where α_{ec} is the winding angle of the "equivalent circle"

L_1 is the pitch.

By using the principle of the "eqwuivalent circle", the winding calculation of the complicated section is greatly simplified, meanwhile, the winding angle of the "equivalent circle" is typical for any irregular section, it can be used as the design parameter.

Ratiocination 1: Any product with circle section can be simplified to a non-rotatory with the equal circumference section for winding calculation. the factors of the round product is the parameters of the "equivalent circle".

Ratiocination 2: After any products with the circle section is changed into the nonrotatory with unequal circumference, the circle sectioin is no longer the "equivalent circle" of the non-rotatory, but is a "differential circle",

it is not equal to circumfrence, the winding angle of the "equivalent circle" and the "differential circle" of non-rotatory can be calculated as the following formula:

$$\tan \alpha_{c c} = W \tan \alpha_{d c} \quad (11)$$

where $\alpha_{c c}$ is winding angle of the "equivalent circle" of non-rotator.

$\alpha_{d c}$ is winding angle of the "differential circle" of non-rodatory
i.e. winding angle of the circle section.

W is the ratio of radii of "equivalent circle" and "differential circle".

Principle 8. Stability of non-geodesic line [7].

Because the friction exists in the filament layers, the filament will not slide but remains stable when the filament deflects the geodesic line to some distance. The filament stability equation of the non-geodesic line is:

$$T = 2F \sin(\Delta\alpha/2) \quad (12)$$

where T is friction force preventing the filament from sliding

F is the tension force of filament

$\Delta\alpha$ is the stable winding angle deflecting the geodesic line

Ratiocination 1: The filament deflecting from the geodesic line must slide until it slides into the position of non-geodesic line.

Principle 9. Principle of unequal winding angle.

The means equal winding angle can not be realized over the whole body of the product in one helical winding axis.

Ratiocination 1: It is impossible for any product to be wound with equal thickness by helical winding.

Ratiocination 2: The helical winding can be realized with equal thickness over the body of the cylindrical vessel of same diameter.

Ratiocination 3: The equal thickness of the equal angle winding can be realized on the body of the conic vessel coinciding to the condition of stable winding angle of non-geodesic line [8].

Principle 10. "Bridged winding" principle of winding on the concave curvature [9].

To any products with concave curvature of the rotating body, when

$\Delta h > 0$, the filament can not be wound on the curvature of the surface of the mandrel for example, on the small ends of the cone to the cylinder:

$$\Delta h = \frac{r \sin \alpha \cos \beta \sqrt{\sin(\alpha + \beta) \sin(\alpha - \beta) + 2 \cos \alpha \cos \beta \sin \alpha \sin \beta}}{\sin(\alpha + \beta) \sin(\alpha - \beta) + \cos \alpha \cos \beta \sin \alpha \sin \beta} \quad (13)$$

where r is the radius of the cylinder

α is half angle of the cone

β is the angle between the surface of the filament and the mandrel.

Ratiocination 1: In order to avoid "bridged winding" on the curvature, we increase the winding angle to 90; or make a smooth line through the top of "bridged" height h instead of the concave curvature, see formula (13).

Ratiocination 2: The height of bridged filament winding of the concave curvature of the rotating body can be calculated by using the diagram approximately.

CONCLUSION

The purpose for giving the principles summarized in the paper on the basis of filament winding practice is to present some basic guide rules, reinforce them and enrich our knowledge and orderliness of the process[11], therefore, to enlarge the extent of the application of the filament winding, develop the new products, make the efficiency and tap the potential of filament winding, open a new area of winding process.

REFERENCES

- [1].Leng Xingwu, Principles and Ratiocinations of Arrangement of filament. The first annual FRP Conference of China. P/122-128
- [2]. Basic Laws of Helical filament Winding. Journal of Technical Information of building Materials No.6901 P86
- [3].Leng Xingwu. The Principle for Calculating the filament-wound Netting Structure No.8.vol.8. Aug 1987
- [4].Leng Xingwu. Calculation of Filament winding angles of Concave and convex curvature. fiber Compositers No 3P.1
- [5].Basic Principles of Helical winding of FRP Irregular Grade. The first Annual FRP Conference of China. P.224 1975
- [6].Leng xingwu assumption of "Equivalent Circle" of Helical winding of Irregular Grade. The Third Annual FRP Conference of China 1977 P.321
- [7].Leng xingwu Basic Principle of Non-geodesic Stability in Filament winding Process. Journal of Chinese Society of Astronautics No.3 1983 P.28
- [8].Leng xingwu and Zhang Yinsheng, Calculation of filament winding of cone, Journal of application of engineering Plastics, No.3 1982 P.28
- [9].Leng xingwu solution to the "Over Surface Line" of the Concave Curvature of the rotating Body in the filament winding Process, Fiber composites 1981
- [10].filament winding FRP High Pressure Vessels. Journal of Technical Information of Building Materials. No.6901 P.12
- [11].Leng Xingwu. Design of filament winding Pattern, Journal of application of engineering Plastics, No.2 1983 P.28
- [12].Leng xingwu. Basic Theory of filament Winding, Journal of Astronautics materials, No.6, 1985, No.1, 1986.

MANUFACTURE AND EVALUATION OF CONTINUOUS FIBRE-REINFORCED METAL COMPOSITES

V.D. Scott¹, R.S. Bushby² and A.S. Chen¹

¹ *School of Materials Science, University of Bath, UK*

² *Structural Materials Centre, DERA, UK*

SUMMARY: Composite plate and tube, consisting of aluminium-magnesium-silicon alloy (6061) reinforced with continuous alumina-based fibres, have been manufactured by the method of liquid metal infiltration; the reinforcement was aligned unidirectionally in the plate and circumferentially in the tube. In both cases, the composites produced were well consolidated with a good bond between fibres and metal matrix, as evinced by 'rule of mixtures' calculations of modulus and Poisson's ratio. The tensile yield stress of plate differed in longitudinal and transverse directions due to anisotropic residual stresses generated in the matrix during manufacture, and both values were increased substantially by heat treatment. The tubes were subjected to two test methods, internal pressurisation and axial tension, in order to generate a tensile stress parallel and perpendicular, respectively, to the fibre direction. The yielding behaviour of the tube differed markedly from the plate due to the complex stresses developed during tube manufacture and the manner in which the tests were performed.

KEYWORDS: metal composites, fibres, manufacture, tube, mechanical properties

INTRODUCTION

The reinforcement of aluminium with continuous fibres offers, potentially, composites of high specific stiffness and strength but before these materials can be seriously considered for engineering application, reliable information on their mechanical properties is needed, a requirement which includes yielding behaviour as well as stiffness and strength. The provision of such a data base requires, however, access to material which is defect-free and of consistent quality, and it is only fairly recently that reliable continuous fibre-reinforced composites which meet these criteria have been produced [1,2,3]. The method which was used for manufacturing the composite materials involved liquid metal infiltration of fibre preforms and, in this paper, it is used to fabricate composite plate and tube composed of Al-Mg-Si alloy reinforced with continuous alumina-based fibres. The composites are tested in two principal directions, parallel and perpendicular to fibres, and their yielding behaviour is compared. The effect of heat treatment is also studied, and the results are discussed with reference to residual stress and fibre orientation in the two types of composite.

EXPERIMENTAL

Materials

The reinforcement was continuous fibre supplied as tows, with ~1000 filaments per tow, by Sumitomo Chemicals, Japan, under the trade name 'Altex'. The nominal diameter was ~13 μm and the composition was given as 85% Al_2O_3 :15% SiO_2 . The matrix metal was 6061 aluminium alloy containing 1.0 wt.% magnesium and 0.8 wt.% silicon.

Manufacture

The composites were manufactured by liquid metal infiltration, a casting process involving infiltration of a fibre preform with liquid aluminium alloy.

The fibre preform for composite plate was made by winding 'Altex' fibre tows onto a steel plate to 10 mm thickness (~50 layers). The assembly was then heated at ~600°C and transferred to a preheated (~450°C) cylindrical steel die of 50 mm diameter bore. Liquid aluminium alloy at ~900°C was introduced into the top of the die, and a force of ~2 kN applied via a hydraulic ram for a few seconds. The force then increased to ~100 kN and this was maintained for ~1 minute to assist consolidation of the solidifying metal. The die was force-cooled by means of a water-fed coil and the composite billet extracted when the temperature reached ~100°C. Excess metal was machined away to give a composite plate with unidirectionally aligned fibres.

The preform for the composite tube was made by winding fibre tows circumferentially onto a graphite mandrel (42 mm diameter and 300 mm long) to a thickness of 4 mm (19 layers). This was heated to 600°C and placed in a hot (500°C) split vertical steel die, of length 450 mm and bore diameter 50 mm, which contained vent holes in the bottom. Provision was made for the temperature of die and preform to be independently controlled via electrical resistance heaters. Liquid aluminium alloy was introduced into the top of the die, as with the plate, and after a few seconds a small amount of metal was seen to escape from the vent holes. At this point, the force increased to ~100 kN. After force-cooling, the die was split into halves to allow extraction of the composite/mandrel. The graphite was then removed and the outer surface of the composite tube machined to a diameter of 48 mm and ground smooth using 1200 grit SiC paper.

Samples of composite plate and tube were solution treated at 550°C. for 8 hours and quenched into cold water. They were then artificially aged at 170 C. for 4 hours to give matrix peak hardness. A diamond indenter was used to measure microhardness.

Microstructural Characterisation

Microstructural analysis was carried out on specimens prepared by mounting in cold-cure resin and surface grinding on successively finer grades of abrasive, finishing with colloidal alumina. Light microscopy and scanning electron microscopy (SEM) were performed, followed by local chemical analysis of selected features using electron-probe microanalysis (EPMA). SEM was used also to inspect the fractured surfaces of tested specimens.

Mechanical Evaluation

Tensile Tests on Plate

Plate specimens for tensile testing were parallel-sided, 65 mm long with a gauge length of 30 mm, and had cross-section dimensions of 6 mm × 3 mm. Soft aluminium end tabs were attached to minimise grip damage during testing and strain gauges were mounted at 0° and 90° to the specimen length in order to obtain values for Poisson's ratio as well as strain. Tests were conducted with the axis of applied stress either parallel ("longitudinal specimen") or perpendicular ("transverse specimen") to the fibres. An Instron 1195 machine was used, operating at a cross-head speed of 1.0 mm min⁻¹.

Pressurisation Tests on Tube

A tubular specimen, 55 mm long, was cut and fitted with rubber seals. This was placed between steel end-plates of a test rig, leaving the ends free to move and generating a tensile stress in the fibre direction (hoop direction). Three sets of rosette strain gauges were mounted around the middle of the tube at 120° and pressure was applied at rate of 15 MPa min⁻¹ by filling the tube with oil. Pressure and strain data were collected.

Axial Tensile Tests on Tube

For the axial tensile tests, both ends of a tubular specimen were fitted with a pair of collets and gripped with a circular collar. Three rosette strain gauges were mounted on the surface in the same configuration as the pressurisation test. The tests were carried out on the Instron machine using the same cross-head speed of 1.0 mm min⁻¹ as plate specimens.

Dynamic Modulus Measurements

Some dynamic modulus (E_D) measurements were carried out on the tube composite by measuring the velocity (v) of sound in a specimen and using $E_D = \rho v^2$, where ρ is specimen density. The velocity was found from the time taken for a pulse to travel between two transducers mounted on the specimen, either along the length by means of transducers in contact with smoothly-ground ends, or across the diameter via transducers in contact with diametrically-opposite curved surfaces.

RESULTS

Plate

The composite plate was found to be well consolidated, with a matrix porosity of <0.5 vol.%, and an uniform distribution of fibres of volume fraction (V_f) 0.4, see Fig. 1. Heat treatment produced an increase in the matrix hardness which reached a maximum of ~110HV after ~4 hours. TEM studies, reported elsewhere [1], revealed that the peak-hardness condition was characterised by the presence of a high density of β^1 precipitates in the matrix. A small amount of magnesium was found to have been absorbed by the fibres, EPMA showing that the magnesium content of the matrix was only slightly reduced because of this, to 0.9 wt.%.

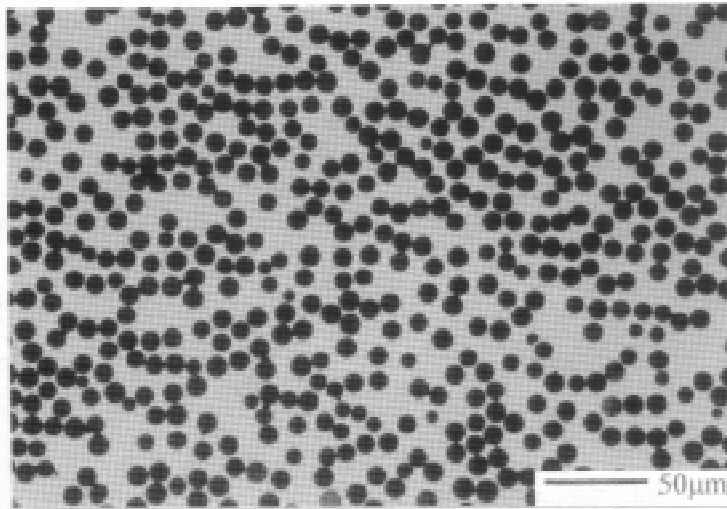


Fig. 1. Continuous fibre-reinforced plate, LM.

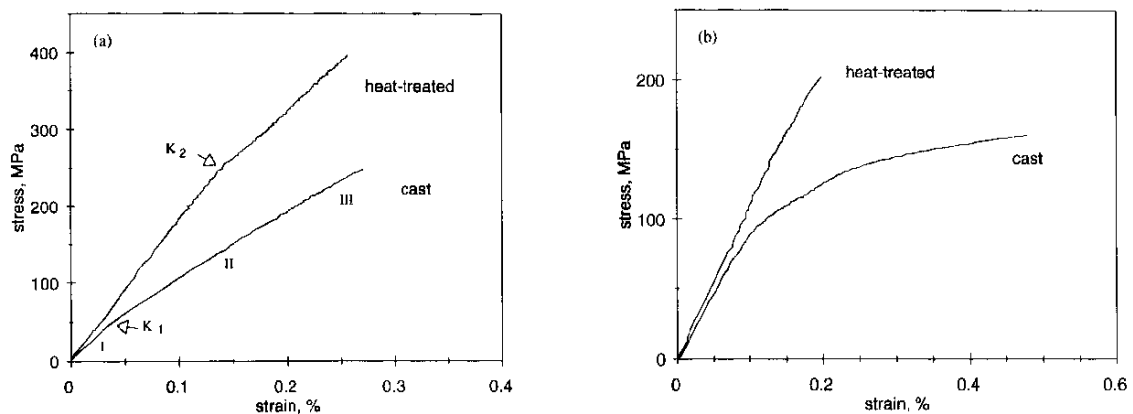


Figure 2. Stress-strain curves for tensile tests on composite plate; (a) longitudinal, (b) transverse.

Stress-strain curves for longitudinal plate are illustrated in Fig. 2a. For cast composite, the curve exhibited three stages. The first stage (I) was linear with a slope equating with 133 GPa. The slope changed at a stress of 58 MPa, usually referred as a 'knee point' (K_1), after which there was a second linear stage (II). As discussed elsewhere [1], the knee point corresponds to the start of matrix yielding and provides a value for the yield stress. Stage III was non-linear and showed a progressively decreasing slope until final failure occurred at a stress of 252 MPa. After heat treatment, the stress-strain curve was different. Stage I had, essentially, the same slope as the cast material (~ 136 GPa) but the transition to stage II (K_2) occurred at higher stress (254 MPa). Stage III was now too short to be detected and failure occurred at 396 MPa.

Stress-strain curves for transverse plate, see Fig. 2b, do not show the gradient discontinuity found in the longitudinal specimen. In the cast condition, the yield stress was estimated to be 68 MPa and the tensile strength 158 MPa. After heat treatment, these values were increased to 128 MPa and 201 MPa, respectively. Mechanical test data, including values for Poisson's ratio, are collated in table 1.

Table 1. Mechanical test results for composite plate

specimen	condition	modulus GPa	yield stress MPa	tensile strength MPa	strain to failure %	Poisson's ratio
longitudinal	cast	133	58	252	0.26	0.31*
	heat-treated	136	254	396	0.30	0.31*
transverse	cast	96	68	158	0.54	0.23**
	heat-treated	101	128	201	0.23	0.22**

* refers to v_{LT} and ** refers to v_{TL} , where the first subscript indicates the loading direction and the second the direction of Poisson's contraction; L stands for the longitudinal direction and T for the transverse direction.

Tube

Fig. 3, a section through the wall of the composite tube, shows a well-consolidated material with an even distribution of fibres of volume fraction 0.35. Matrix porosity was less than 1 % throughout the length of the tube, although a few large (~10 µm) pores were located in the

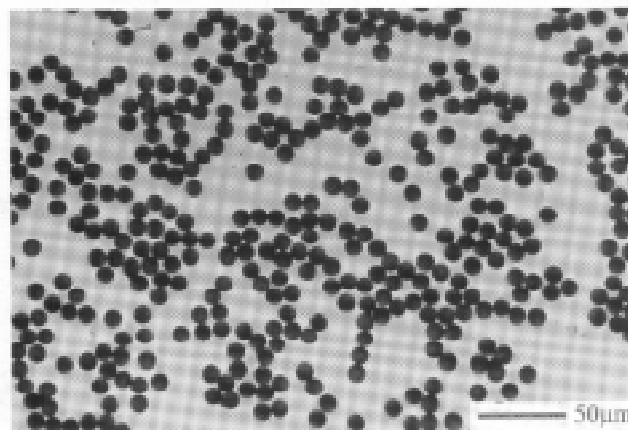


Fig. 3. Continuous fibre-reinforced tube, LM.

uppermost region. EPMA of samples cut from the opposite ends of the tube indicated that the magnesium content of the matrix was 0.95 wt% at the top and 0.80 wt% at the bottom. The matrix microhardness was much the same at the top and bottom of the tube, at 36 HV, and this was increased to 100 HV by heat treatment.

Dynamic modulus for the composite was 120 GPa in the hoop (circumferential) direction and 95 GPa in the axial direction. A stress-strain curve from the pressurisation test on cast tube, Fig. 4, shows an initial linear region, consistent with a hoop modulus of 120 GPa. A value for the yield stress was difficult to obtain because the 'knee point' (the onset of matrix yielding) was not clearly defined; the best estimate was 50 MPa. The material failed at 145 MPa. The stress-strain curve from the heat-treated tube shows an increase in yield stress, to 150 MPa, and in strength, to 260 MPa. Neither cast nor heat-treated tubes showed much tensile deformation. Each gave a failure strain of ~0.25%, with final failure being associated with axial cracking, as illustrated in Fig. 5.

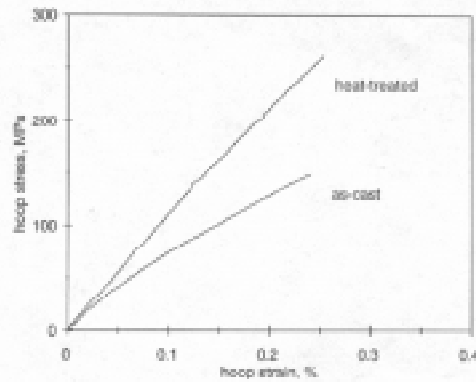


Figure 4. Stress-strain curves for internal pressure tests on composite tubes.

Stress-strain curves from axial tensile tests on composite tube are shown in Fig. 6. The initial linear region of both curves indicates an axial modulus of ~90 GPa. With cast tube, the curve departed from the linearity at 55 MPa, the axial yield stress corresponding to the onset of matrix yielding. The axial strength was ~91 MPa and final failure occurred at ~0.2% strain. The heat-treated composite tube showed an increased yield stress, ~96 MPa, and strength, ~115 MPa, but the failure strain was slightly less, ~0.12%. The fractured ends of both tested tubes exhibit a stepped appearance, Fig. 7, corresponding to hoop interfibre fracture coupled with some axial fibre cracking. Mechanical test results on tube are collated in table 2.

Table 2. Mechanical properties of composite tube.

test method	condition	modulus GPa	yield stress MPa	strength MPa	strain to failure %	Poisson's ratio
pressurisation	cast	120	50	145	0.24	0.31*
	heat-treated	120	150	260	0.25	0.33*
axial tension	cast	91	55	91	0.21	0.22**
	heat-treated	95	96	115	0.12	0.22**

* refers to ν_{HA} and ** to ν_{AH} ; H is the hoop direction and A the axial direction.

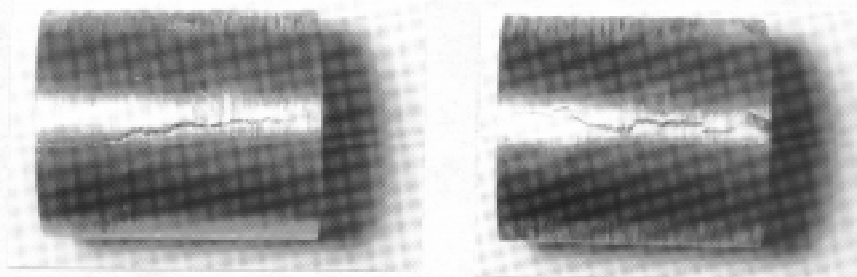


Fig. 5. Failed tubular specimens after the internal pressurisation tests.

of magnesium by fibres as the liquid metal passes down the preform, somewhat similar to a filtering mechanism. Further magnesium was probably absorbed by fibres during heat treatment but the overall reduction appeared to have little, if any, effect on the heat treatment response, as evinced by the similar matrix microhardness values ($\sim 100\text{HV}$) measured at the top and bottom of the tube.

Mechanical Behaviour

Plate

A 'rule of mixtures' (ROM) calculation for the longitudinal composite plate (fibre volume fraction of 0.4) gives a modulus of 130 GPa, matching the modulus of obtained from the stress-strain curve, see table 1, and providing evidence for a strong fibre/matrix bond. The quality of the bond has been further demonstrated by close correspondence of measured values, see table 1, and calculated values [1] of Poisson's ratio. The change of gradient of the stress-strain curve, that is the 'knee point', occurred at a stress of 58 MPa and marked the onset of matrix yield. Calculations [6] indicated that the matrix in the composite must have yielded at a stress of 30 MPa, appreciably lower than the yield stress for unreinforced alloy, 53 MPa, see [1], from which it was concluded that there was a tensile residual stress of ~ 20 MPa in the longitudinal direction due to differential contraction between fibre and matrix during composite manufacture. The reduced slope at higher stress (stage II) indicated that the modulus was now related mainly to fibre content. Yielding of the matrix continued, as has been demonstrated elsewhere [5,6] in surface replication studies, and there is evidence of matrix work hardening, with the slope of the stress-strain curve decreasing progressively (stage III) as the end of the test was approached. The increase in yield stress of composite plate caused by heat treatment, from 58 MPa to 253 MPa, was in accord with the increase in matrix yield stress brought about by precipitation hardening. The strength was also increased, to ~ 400 MPa, but the mechanism of failure remained the same, with a failure strain of $\sim 0.3\%$ and localised fibre breakage close to the fracture surface.

The absence of a 'knee point' in the stress-strain curves for the transverse specimen is consistent with the composite yield stress being determined by yielding in the matrix, with the fibres acting as discontinuous reinforcements. The higher yield stress compared with the longitudinal specimen (68 MPa and 58 MPa, respectively) is because the residual stress is compressive in the matrix and acts in opposition to the applied load. Transverse properties were also increased by heat treatment, but not to the same degree as longitudinal properties.

Tube

A ROM calculation for the hoop modulus gave 122 GPa, a value in close agreement with the dynamic modulus measurement of 120 GPa. It was also noted that the calculated axial modulus of 97 GPa was in accord with the dynamic modulus of 95 GPa. As with the plate results, the findings confirm that the composite tube was well consolidated with satisfactory fibre/matrix bonding.

Stress-strain curves obtained in the pressurisation tests, Fig. 3, did not exhibit the gradient discontinuity, or 'knee point', which characterised the onset of matrix yield in the longitudinal composite plate, see Fig. 2. This is attributed to the generation of a more complex residual stress state in the composite tube arising from differential thermal contraction between composite tube and graphite mandrel during cooling. This effect was demonstrated by

removing a small piece from a ring cut from the tube. 'Springback' then occurred and from the ring dimensions and the size of the closure gap, a residual tensile hoop stress of few MPa was deduced. However, the method of testing would also have affected the development of a knee point because yielding would have started at the inner surface, where the hoop tensile stress was greatest, and progressed towards the outer surface as the matrix strain hardened [6]. The heat-treated composite tube showed an increased yield stress from ~50 MPa to 150 MPa, in accord with matrix precipitation hardening. Evidence was not available to establish the extent to which the heat treatment process affected the state of residual stress and this needs further investigation as does the importance of cooling rate following metal infiltration. The hoop strength of the composite tube was increased by heat treatment, from 145 MPa to 260 MPa, but the mechanism of failure was the same, with axial cracking and failure at a strain of ~0.25%.

The similarity between the stress-strain behaviour of composite tube under axial tension and the transverse composite plate is because the mechanical behaviour is controlled by the matrix, with fibres having little constraining effect. Hence it is not surprising to find that the calculated modulus of 97 GPa is in close agreement with dynamic modulus measurements and with values derived from the stress-strain curve, see table 2. The difference between axial yield stress (55 MPa) and hoop yield stress (50 MPa) reflects the difference in residual stress parallel and perpendicular to the direction of fibres. The fact that the difference between the two yield stresses for the tube is much less than the difference between the transverse and longitudinal yield stresses for the plate indicates that residual stresses are smaller in the tube than in the plate. A possible reason for this is that the graphite core restricted contraction of the tube upon cooling which affected the residual stress, a possibility which requires further study. The increased axial yield stress and brittleness following heat treatment were similar to the behaviour of the transverse composite plate.

It was noticeable that the failure strength of composite tube was appreciably less than that of composite plate, see tables 1 and 2, whether measurements were made parallel or perpendicular to the fibre direction or whether the materials were in the cast or heat-treated condition. The differences can only be partly due to the lower volume fraction of fibre in tube, 0.35 compared with 0.40, and there must be some other effect. Composite integrity is not, in our view, a factor since the ratio of the hoop and axial strengths of cast tube were much the same as the ratio of longitudinal and transverse tensile strengths of cast plate, that is ~1.6. Furthermore, as mentioned earlier, the elastic moduli matched ROM calculations in both cases. It is, therefore, our contention that the lower strength of the tubular test specimen may be partly a dimensional effect, since its larger cross-section area, compared with the plate specimen, was more likely to contain a sizeable defect which adversely affected the failure process. After heat treatment, the ratio of hoop and axial strengths of the tube was increased to ~2, again similar to the effect on longitudinal and transverse strengths of plate. The reasons for this require further investigation, particularly since it could have important implications concerning engineering application of a tubular composite, as in a sealed tubular container subjected to internal pressure where the ratio of principal stresses in hoop and axial directions is 2:1. The failure mode of composite tube was similar to that seen in the composite plate. For tests carried out with the applied stress perpendicular to the fibre direction (axial test on tube and transverse test on plate), fracture mainly occurred in the matrix, with cracks running parallel to fibres and fibre breakage linking two or more matrix cracks. Where the applied stress was parallel to fibres (pressurisation test on tube and longitudinal test on plate), fibre fracture was common and appeared on the tube as axial cracks. The values of Poisson's ratio in the principal directions, as obtained from the pressurisation and axial tests on tube, were the

same as those found in the tests on longitudinal and transverse plate, respectively, and is direct confirmation of the composite quality achieved when manufacturing composites of different shapes by the method of liquid metal infiltration.

ACKNOWLEDGEMENTS

The authors thank the EPSRC and DERA for support. British Crown Copyright 1997/DERA. Published with the kind permission of the Controller of Her Britannic Majesty's Stationery Office.

REFERENCES

1. Chen, A.S., Bushby, R.S., Phillips, M.G. and Scott, V.D., A study of the mechanical properties and microstructure of fibre-reinforced aluminium alloy, *Proc. R. Soc. London, A*, **450** (1995) 537-552.
2. Deve, H.E. and McCullough C., Continuous-fibre reinforced Al composites: a new generation, *JOM* (1995) 33-37.
3. Degischer, H.P., Schulz, P. and Lacom, W. Properties of continuous fibre reinforced Al- and Mg-matrix composites produced by gas pressure infiltration. *CMMC-96 Part I*, eds. M. Fuentes, J.M. Martinez-Esnaola and A.M. Daniel (Trans. Tech. Publins.: Switzerland) (1997) pp.99-110.
4. Cappleman G.R., Watts J.F. and Clyne T.W., The interface region in squeeze-infiltrated composites containing δ -alumina fibre in an aluminium matrix, *J. Mater. Sci.*, **20** (1985) 2159-2168.
5. Chen, A.S., Bushby, R.S. and Scott, V.D., Tensile property evaluation of continuous fibre reinforced aluminium alloy, *ICCM-10, Vol II*, eds. A. Poursatip and K. Street (Woodhead Publishing Ltd: Cambridge) (1995) pp.497-504.
6. Chen, A.S., Bushby, R.S. and Scott, V.D., Deformation and damage mechanisms in fibre-reinforced metal composites under tension, *Composites A*, **28** (1997) in press.

DETERMINATION OF MANUFACTURING DISTORTION IN LAMINATED COMPOSITE COMPONENTS

D.W. Radford and T.S. RENNICK

*Composite Materials, Manufacture and Structures Laboratory, Mechanical Engineering,
Colorado State University, Fort Collins, Colorado 80523-1374*

SUMMARY: Manufacturing distortion of composites has been a problem for many years. Previous efforts have shown these distortions to be related to differences in the in-plane and through-thickness properties. Often tooling is modified to attempt to compensate for these fabrication induced distortions; however, the sources of the problem have not been clearly shown. Earlier efforts have suggested that both the cooldown from process temperature and shrinkage during cure play a role, yet no single work has measured the relative contributions of these effects. Further, researchers have suggested numerous other factors as being responsible for all, or some portion, of the measured distortion. In this work, distortion in autoclave-cured composite specimens has been experimentally measured, at temperatures ranging from 24°C to 178°C, to determine the reversible and irreversible contributions to manufacturing warpage. The measured reversible response closely matches computed distortion, based solely on the in-plane and through-thickness coefficients of thermal expansion. Further, it seems that the irreversible contributions can be separated into material dependent effects, such as cure shrinkage, and process related effects, such as part/tool interactions. Calculations indicate that both temperature change and cure shrinkage contribute significantly to manufacturing distortion; but, their contribution does not account for the total distortion. Trends in the experimentally observed distortion indicate the presence of other process related contributions.

KEYWORDS: distortion, warpage, composites manufacture, part/tool interaction

INTRODUCTION

Advanced composite materials are being used in an increasing variety of applications, ranging from sporting goods to aerospace components. However, difficulties in manufacturing and associated manufacturing costs are often strong deterrents to widespread industrial implementation. Autoclave processing is a proven source of high performance, reproducible composite parts; yet, with many years of process development, difficulties continue to arise during the creation of complex composite parts requiring a precise, specified shape. In curved composite “angle brackets”, manufacturing distortion results in a change in included angle that is often referred to as “spring-in”.

Manufacturing distortion results from the internal balancing of process-induced residual stresses [1] and can be severe, leading to out-of-tolerance dimensions and rejected parts or even difficulty extracting the part from the tooling [2]. This distortion has been suggested to be primarily related to differences in the composite material properties and responses in the

in-plane and through-thickness directions [3,4,5]. Examples of components where “spring-in” has been measured include wing leading edges [6], U-channel cross-sections [7], and waveguides [3].

Since, once cured, the resulting component geometries do not match the tooling geometry manufacturers often find it necessary to shape the tooling in an iterative fashion. This iteration of the tooling can be costly, and if material or laminate design is subsequently changed, the non-net shape tool will not generate shape correct parts. Other approaches have also been used to minimize warpage; however, many of the currently employed solutions do not directly address the causes of distortion. This can be attributed to an incomplete understanding the problem or to not recognizing the problem. Many factors enter into the final distortion; yet, little work has attempted to measure and separate the various contributions. Thus, the present project is specifically aimed at quantifying the factors that affect warpage to aid in the overall understanding, and development, of design practices which overcome manufacturing distortion, or at least that can lead to accurate predictions of required tooling geometry.

COMPONENTS OF MANUFACTURING DISTORTION

Manufacturing distortion can be seen in many types of fiber reinforced composites, with the properties of the constituent materials and the type of cure generally governing the severity. One of the worst cases is an autoclave cured carbon fiber/epoxy composite due to the low coefficient of thermal expansion (CTE) in the longitudinal direction of the reinforcing fiber, a much larger CTE in the transverse direction and a large temperature difference between cure and room temperature. Many factors must be considered in solving the problem of manufacturing distortion. Anisotropic thermal contraction and cure shrinkage of the epoxy matrix are two commonly cited factors affecting warpage. While anisotropy of the laminate coefficients of thermal expansion is generally accepted as a major contributor to warpage, acceptance of other contributions, including anisotropy of cure shrinkage, is mixed. In some studies, cure shrinkage has not been considered in warpage predictions [2,8]. In other studies, it is believed to dissipate through viscoelastic relaxation during the curing process [1,9], and in still other research cure shrinkage is considered a significant contribution [4,5,10,11,12]. Further contributing factors that have been briefly studied are tooling material properties [13] interactions between the tool and the composite [13,14], fiber misalignment [8,15], and fiber volume fraction gradients [15,16]. To satisfy an apparent need to resolve the factors affecting manufacturing distortion, an experimental approach has been taken in this work to quantify the various contributions. These contributions have been categorized into two principal components: thermoelastic (reversible) CTE contributions, and non-thermoelastic (irreversible) cure and manufacturing contributions.

Thermoelastic Component

The thermoelastic component represents the reversible thermal expansion and contraction of the angle bracket specimen, which leads to its changing included angle. This component has also been referred to as shape instability, as this thermal expansion driven phenomenon continues to affect the component shape throughout the service life [4]. Previous research efforts have shown manufacturing distortions to be related to differences between in-plane and through-thickness properties of laminated composites, and closed-form equations have been developed to predict the thermoelastic change in shape for simply curved composite

laminates [2,3,4,5]. The initial and final geometries for an angle bracket corner are depicted in figure 1 showing how a change in thickness without a change in arc length must result in a change in included angle. This distortion does not occur in conventional materials since isotropic thermal expansion results in a uniform change in size.

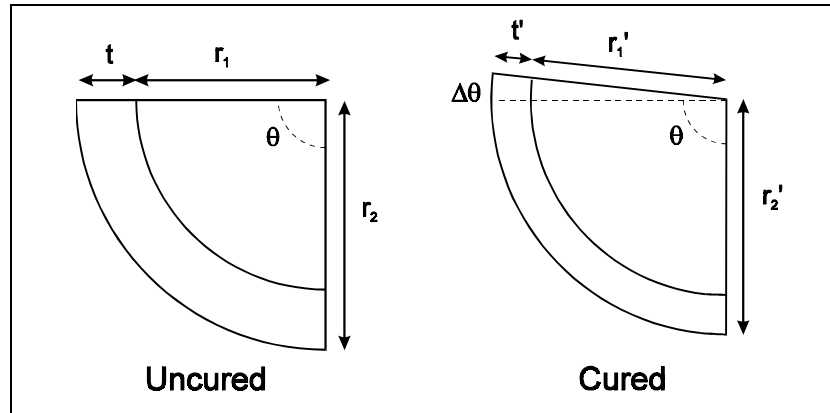


Figure 1: Composite angle bracket geometries before and after cure [17]

For an anisotropic material, such as a laminated composite, it has been suggested that this thermoelastic distortion can be predicted from a knowledge of the initial specimen geometry (included angle), the coefficients of thermal expansion and the change in temperature. The relationship that has been developed is: [5]

$$\Delta\theta = \theta \left[\frac{(\alpha_I - \alpha_T)\Delta T}{(1 + \alpha_T\Delta T)} \right], \tag{1}$$

where;

- θ = angle bracket included angle,
- $\Delta\theta$ = change in included angle,
- α_I = in-plane coefficient of thermal expansion,
- α_T = through-thickness coefficient of thermal expansion, and
- ΔT = change in temperature.

This relationship assumes that the in-plane properties are quasi-isotropic and that the through-thickness properties are uniform throughout the laminate.

Non-Thermoelastic Component

The non-thermoelastic component of manufacturing distortion is a “one time only” contribution that occurs during fabrication and is irreversible. Many factors may contribute to the non-thermoelastic component, such as cure shrinkage, tooling expansion, part/tool interactions and factors associated with the manufacturing technique. In previous work [4,5], it was suggested that fabrication shrinkage could be accounted for in an extension of equation (1) by including an additional term:

$$\Delta\theta = \theta \left\{ \left[\frac{(\alpha_I - \alpha_T)\Delta T}{(1 + \alpha_T\Delta T)} \right] + \left[\frac{(\phi_I - \phi_T)}{(1 + \phi_T)} \right] \right\}, \tag{2}$$

where; ϕ_I = in-plane fabrication shrinkage, and
 ϕ_T = through-thickness fabrication shrinkage.

If fabrication shrinkage values for the constituent materials are available, anisotropic composite fabrication shrinkage values can be obtained from a micromechanics approach. This would allow the addition of a predicted cure shrinkage induced non-thermoelastic contribution to the already developed thermoelastic prediction. This additional term can be thought of as another factor contributing to the thickness change indicated in figure 1. Again, since the reinforcing fibers constrain the in-plane displacements, the through-thickness change is the major contributor to distortion. However, additional process related effects that may be encountered, such as volume fraction gradients [16], part/tool interactions or non-uniform curing [14], are not modeled by equation (2) since phenomena control which are not directly related to differences between in-plane and through-thickness properties.

EXPERIMENTAL MEASUREMENT OF DISTORTION

Angle Bracket Specimens

Carbon fiber/epoxy angle brackets were autoclave-processed at 178°C on aluminum convex tooling. Three repetitions of each specimen, investigating stacking sequence, laminate thickness and corner radius, were produced on tooling with a 90° included angle. The stacking sequences are referenced with 0° along the angle bracket axial direction and 90° following the curvature around the angle bracket corner. Figure 2 shows two cured test specimens, of different corner radii, resting on a section of aluminum tooling.



Figure 2: Angle bracket specimens on aluminum tooling showing “spring-in”.

Experimental Procedure

A laser rotation technique is used to measure the included angle as a function of temperature. The technique requires mounting the angle bracket specimen by one arm in the heated

chamber with a small mirror attached to each arm. The laser is aimed through the chamber glass door at the mirror on one arm and the resulting reflection is aligned with the reference mark on the projection screen. The specimen is then rotated until the reflection from the second arm aligns with the reference mark. The shaft rotation is electronically measured by an encoder and the included angle is determined. This measurement is repeated in the reverse direction to bring the specimen back into its original position and allow a second check of each measured included angle. Using this approach, measurement of specimens with included angles ranging from 30° to 180° can be accomplished. One pulse of the encoder corresponds to less than 0.02° and the reproducibility of measurement is on the order of ± 1 pulse.

Angle bracket specimen measurements were made at room temperature (24°C) and then at elevated temperatures on all angle bracket specimens evaluated. Each specimen was measured with the rotation technique in roughly 14°C temperature increments to 122°C. Following this, one specimen from each group was re-measured to 178°C in a similar fashion to check the linearity of the thermoelastic response at temperatures approaching cure. Once the maximum temperature was reached, measurements were repeated back down to room temperature to observe the repeatable, thermoelastic response of the angle bracket. A complete measurement of a single specimen could be completed in 5-6 hours, with most of the time involved in temperature stabilization for each angle measurement. The rotation technique simplifies the measurement of thermoelastic response, without sacrificing precision or accuracy, and allows the included angle to be measured directly at the desired temperature. A conceptual view of a specimen prepared for measurement and a photo of an actual specimen mounted in the chamber are shown in figure 3.

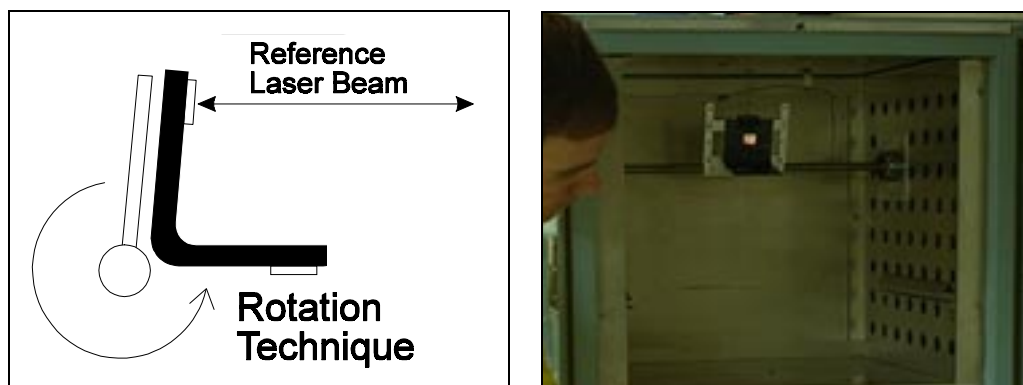


Figure 3: Rotation technique enables direct included angle measurement.

RESULTS AND DISCUSSION

Effects of stacking sequence, laminate thickness and corner radius on distortion were investigated by measuring the changing included angle, of specimens representing each variable, with temperature. Results for each effect investigated are plotted as graphs of “spring-in” angle versus temperature. The slope of the line on this type of chart is a measure of the thermoelastic contribution, while the offset from zero, at a reference temperature near the cure temperature, is essentially the non-thermoelastic contribution. Thus, the “spring-in” angle on the left side of the chart indicates the total room temperature distortion that would commonly be measured during a quality check. The value of “spring-in” on the right side of the chart is the contribution to the distortion that is not related to cooldown from cure [17].

Stacking Sequence Effects

As is seen in figure 4, both thermoelastic and non-thermoelastic components contribute to the overall warpage of angle brackets. However, their absolute and relative contributions vary, depending on stacking sequence. All specimens of this stacking sequence comparison were 8 ply and have a 6.4 mm corner radius to minimize other possible distortion variable interaction. Most of the laminates show similar thermoelastic response based on the slopes, $\Delta\theta/\Delta T$, which vary only slightly and are roughly $0.003 \text{ deg}/^\circ\text{C}$. The $[(0)_8]_T$ and $(0/+30/0/-30)_S$ laminates show much lower thermoelastic response due to large in-plane CTE's in the 90° direction, which correspond closely to the through-thickness CTE values. These more similar in-plane and through-thickness thermal expansions result in distortion behavior resembling that of an isotropic material, with a thermoelastic coefficient, $\Delta\theta/\Delta T$, of approximately $0.0005 \text{ deg}/^\circ\text{C}$. This large difference in thermoelastic response is predicted by equation (1) as both the in-plane and through-thickness CTE's are affected by changing ply orientation [4,5]. All of the laminates show a significant non-thermoelastic contribution (on the right ordinate), ranging from about 0.7 - 1.2 degrees. This large contribution to the room temperature distorted shape accounts for roughly 65% of the total room temperature distortion for the majority of the specimens. For the $[(0)_8]_T$ and $(0/+30/0/-30)_S$ laminates the contribution approaches 90% of the total. Using equation (2), the distortion related to cure shrinkage can be estimated and compared to the total non-thermoelastic distortion measured.

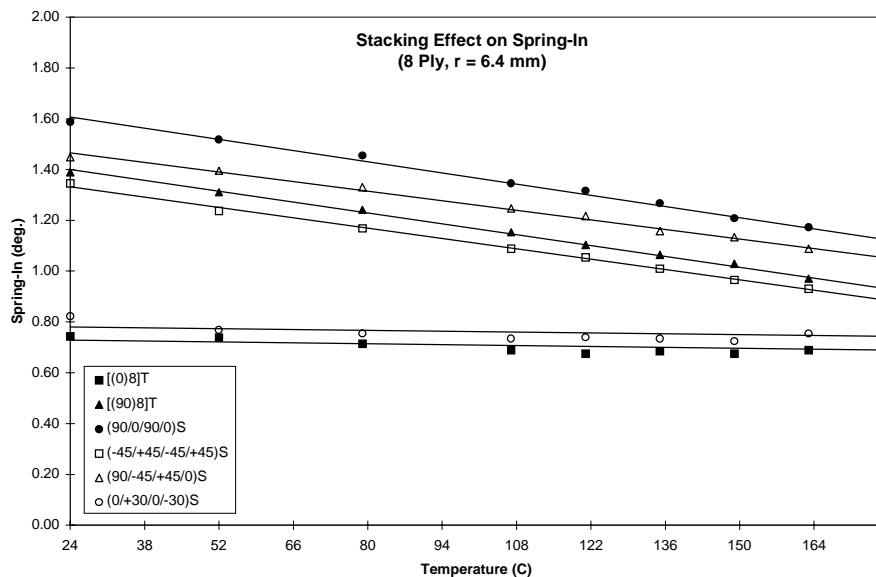


Figure 4: Experimental Stacking Sequence Effects

To investigate the relationship between predicted cure shrinkage contributions to distortion and the total non-thermoelastic distortions measured for these specimens, material properties representative of T300/934 [16] were applied in equation (2). Three dimensional (3-D) laminate properties were determined for each laminate [16], based on the T300/934 data, and the results were inserted into equation (2) along with an assumed 0.5% matrix cure shrinkage. Results for the crossply and quasi-isotropic laminates were the same, with a predicted thermoelastic contribution of $0.0036 \text{ deg}/^\circ\text{C}$, or approximately 0.56 degrees of “spring-in” at room temperature. The contribution to “spring-in” in these crossply and quasi-isotropic laminates is predicted to be approximately 0.32 degrees, based on 0.5% cure shrinkage. Thus, for these specimens, the combined predicted thermoelastic and cure shrinkage contributions sum to only approximately 50% of the total measured room temperature distortion.

Predictions of the distortion contributions, using equation (2) and the same 3-D properties, can be also be performed for the other laminates. For example, for the (0/+30/0/-30)_S laminates the predicted thermoelastic contribution is 0.0012 deg/°C, or approximately 0.19 degrees of “spring-in” at room temperature. Again, based on the 0.5% cure shrinkage, the contribution to “spring-in” for this stacking sequence is predicted to be approximately 0.11 degrees. For this stacking sequence, which is expected to respond in a more isotropic fashion due to less difference between the through-thickness and in-plane properties, the total predicted “spring-in” at room temperature is only about one third that of the crossply laminates of this investigation. Comparison of these predictions with the experimental results indicates that roughly 0.5 - 0.6 degrees of “spring-in” measured at room temperature remains unaccounted for. Matrix cure shrinkage as high as 1.5 - 2.0% would be necessary to account for the total measured non-thermoelastic distortion; however, this value of shrinkage seems extreme. Based on the measured differences in the non-thermoelastic contribution for changing stacking sequence it is believed that a significant portion of this contribution must be related to manufacturing variables. To further investigate deviations from the predictions of equation (2), which would indicate non-thermoelastic contributions other than cure shrinkage, measured effects of corner radius and laminate thickness are presented.

Radius Effects

Radius is not predicted, by equations (1) or (2), to be a contributor to either thermoelastic or non-thermoelastic distortion. No significant variation in thermoelastic response is measured, as seen by the nearly identical slopes in figure 5, which have $\Delta\theta/\Delta T$ values of approximately 0.0045 deg/°C for these 16 ply specimens. However, it is significant that while the slopes are similar for the various radii, the relative offsets vary, indicating that the measured non-thermoelastic component is radius dependent. It seems that the larger the corner radius, the less process effects other than cure shrinkage contribute to the non-thermoelastic distortion. This is consistent with a cause, such as local corner thinning during processing, which would be expected to be less severe for larger radii.

Thickness Effects

Increased thickness has often been expected to stabilize the distortion of composite parts. Results of these tests indicate that the thermoelastic component of distortion is little affected by thickness, which follows from equations (1) and (2). However, the thinnest laminates tested (8 ply, or 1 mm) show the least thermoelastic effect. This may be explained by the fact that these 8 ply specimens can also be the most difficult to measure due to their low stiffness which results in the highest potential for specimen flexure from the cantilevered mounting geometry. What does seem to match intuition is that the thickest specimens do show less total room temperature spring-in, but the experimental results indicate that the difference is primarily driven by the non-thermoelastic component of distortion. Again, this difference in non-thermoelastic contribution is not predicted by equation (2) and therefore must be assumed to be related to process effects other than shrinkage during cure.

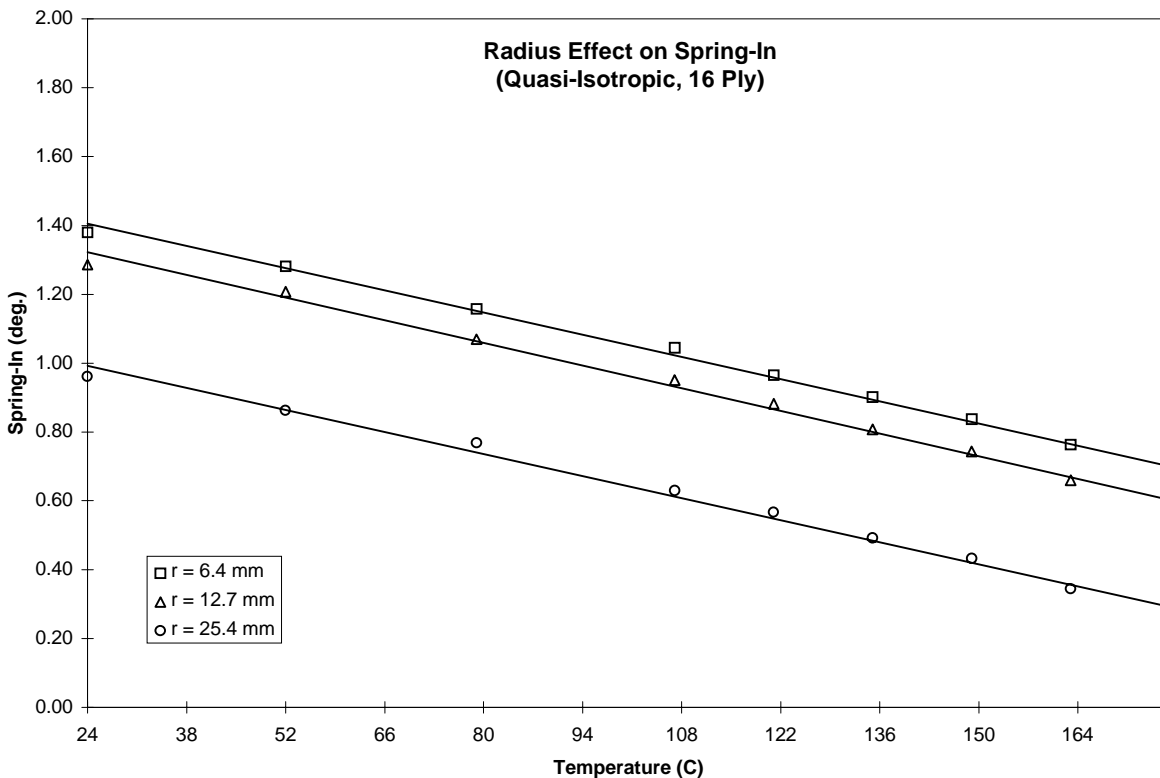


Figure 5: Corner Radius Effects on Spring-In

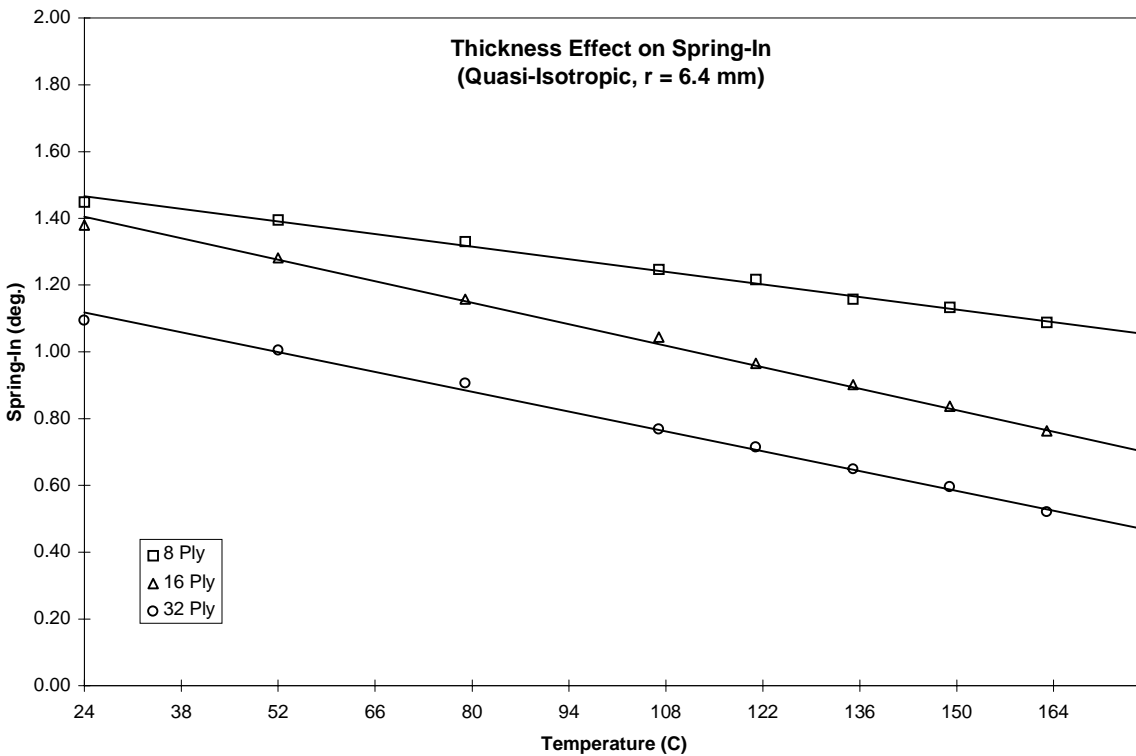


Figure 6: Effect of thickness on manufacturing distortion

General Discussion

In addition to the three variables shown in detail in figures 4 - 6, preliminary tests of included angle variations indicate a decreasing thermoelastic slope with increasing included angle. Further, these preliminary results indicate that the non-thermoelastic component also varies with included angle. These trends are both consistent with the predictions of equations (1) and (2). Overall, experimental results for these carbon fiber/epoxy angle brackets do seem to point out that the thermoelastic variations follow the trends predicted in equations (1) and (2). As predicted by equation (2), cure shrinkage should respond to the same variables as the thermoelastic component. However, from this set of experimental data it seems that the total non-thermoelastic contribution is not following the trends predicted. This leads to the belief that more than one factor determines the non-thermoelastic contribution, and that contributors other than cure shrinkage take on different functionality.

Future efforts are planned to investigate the effect of varying the fiber type while maintaining the same matrix material. This should allow further separation of some of the processing effects from the cure shrinkage. Further, tooling material comparisons are under way to evaluate the effect on part/tool interaction, and fabrication experiments are planned to attempt to continue to break down the non-thermoelastic contributions.

CONCLUSIONS

“Spring-in” of carbon fiber/epoxy angle bracket specimens has been experimentally measured to determine the thermoelastic (reversible) and non-thermoelastic (irreversible) components of distortion. A technique, incorporating a laser source, was used to obtain precise measurements of the included angle of specimens at temperatures ranging from room temperature to 178°C. The data collected indicate that all of the specimens respond linearly and in a repeatable fashion to temperature change. Differences between the measured thermoelastic contribution and the tooling geometry allow the remaining non-thermoelastic contribution to be separated. Relative non-thermoelastic contributions were computed for the stacking sequence specimens and found to range from approximately 65% to 90% of the total room temperature “spring-in”. Only the angle brackets with the largest corner radius and greatest thickness showed lower relative amounts of non-thermoelastic distortion. For an assumed matrix cure shrinkage of 0.5% the “spring-in” was predicted to be only a little more than half of the thermoelastic contribution. While this is a significant amount of the total specimen distortion, it is far less than the total non-thermoelastic contribution experimentally measured.

Trends in thermoelastic response, $\Delta\theta/\Delta T$, with stacking sequence variation were predictable, based on closed-form relationships. The measured independence of thermoelastic response on changing corner radii also matched predictions. However, the varying non-thermoelastic contributions for different radii were not predicted. As specimen geometry changed with increasing corner radius, non-thermoelastic contributions decreased, indicating sources of manufacturing distortion other than a predictable cure shrinkage induced non-thermoelastic contribution. Results related to thickness variations also indicate similar distortions not directly attributable to shrinkage during cure. Thus, these trends further suggest that process related contributions to the final distorted shape can be significant and that such other non-thermoelastic effects are not predicted by the closed-form relationships based solely on differences between in-plane and through-thickness properties. Further investigation of the

details of these other contributors is necessary to be able to fully predict distortion during cure.

ACKNOWLEDGEMENT

The authors would like to acknowledge Lockheed-Martin Tactical Aircraft Systems for support in this work.

REFERENCES

1. White, S.R. and Hahn, H.T., "Process Modeling of Composite Materials: Residual Stress Development During Cure. Part I. Model Formulation", *Journal of Composite Materials*, Vol. 26, No.16, 1992, pg. 2402.
2. Mabson, G. E., et.al., "Dimensional Stability of Curved Panels with Cocured Stiffeners and Cobonded Frames", *Third NASA Advanced Composites Technology Conference*, Long Beach, California, June, 1992.
3. Hammond, M.G. and Farrell, K., "Graphite Epoxy Composite Material Components for Communications Satellites", *Proceedings of ICCM 2*, 1978, pg. 1392.
4. Radford, D.W., "Shape Stability in Composites", PhD Thesis, Rensselaer Polytechnic Institute, May 1987.
5. Radford, D.W. and Diefendorf, R.J., "Shape Instabilities in Composites Resulting from Laminate Anisotropy", *Proceedings of the Fourth Japan-United States Conference on Composite Materials*, Washington, D.C., June 1988, pg. 439.
6. Nolet, S.C. and Sandusky, P.M., "Impact Resistant Hybrid Composite For Leading Edges", *SAMPE Quarterly*, Vol.17, No.3, 1986, pg. 46.
7. Konig, M., "Prediction of Distortion of Laminated Thermoplastics after Moulding and Cooling Down", *Proceedings of International Conference on Composites Engineering-1*, 1994, pg. 797.
8. Chamis, C.C., "Residual Stress in Angleplied Laminates and Their Effects on Laminate Behavior", *Proceedings of ICCM 2*, 1978, pg. 221.
9. White, S.R. and Hahn, H.T., "Process Modeling of Composite Materials: Residual Stress Development During Cure. Part II. Experimental Validation", *Journal of Composite Materials*, Vol. 26, No.16, 1992, pg. 2423.
10. Martin, L.P., Bogetti, T.A., and Gillespie, J.W. Jr., "Influence of Cure Shrinkage on Process-Induced Stress and Deformation in Thick Thermosetting Composites", *Proceedings of the Fifth Technical Conference of the American Society for Composites*, E. Lansing, MI, 1990, pg. 415.
11. Russell, J.D., "Cure Shrinkage of Thermoset Composites," *SAMPE Quarterly*, Vol.24, No.2, 1993, pg. 28.
12. Madhukar, M.S., Kosuri, R.P. and Bowles, K.J., "Reduction of Curing Induced Fiber Stresses by Cure Cycle Optimization in Polymer Matrix Composites", *Proceedings of ICCM X*, Vol. 3, 1995, pg. 157.
13. Pagliuso, S., "Warpage, a Nightmare for Composite Parts Producers", *Proceedings of ICCM IV*, Vol. 2, 1982, pg. 1617.
14. Hubert, P., Johnston, A., Vaziri, R. and Pourtsartip, A., "A Two-Dimensional Finite Element Processing Model for FRP Composite Components", *Proceedings of ICCM X*, Vol. 3, 1995, pg. 149.

15. Kim, P., Phillips, R., Toll, S., & Manson, J. E. "The Dimensional Stability of Composite Laminates: Sensitivity to Gradients in Fiber Content and Misalignment." International Workshop on Advanced Materials for High Precision Detectors, Archamps, France, September, 1994.
16. Radford, D.W., "Volume Fraction Gradient Induced Warpage in Curved Composite Plates", Composites Engineering, Vol. 5, No.7, 1995, pg. 923.
17. Rennick, T.S. and Radford, D.W., "Components of Manufacturing Distortion in Carbon Fiber/Epoxy Angle Brackets", 28th International SAMPE Technical Conference, Seattle, WA, 1996, pg. 189.

COMPRESSION MOULDING OF SANDWICH STRUCTURES OF GMTS AND CO-MINGLED MATERIALS FOR OPTIMISED MACRO AND MICRO MECHANICAL PROPERTIES

M.D. Wakeman, T.A. Cain, C.D. Rudd, R. Brooks, A.C. Long

Department of Mechanical Engineering, University of Nottingham, UK.

SUMMARY: To increase the usage of glass and polypropylene composites from semi-structural to structural applications, a higher and aligned glass content is needed. The co-moulding of GMTs and pre-consolidated woven co-mingled materials have been investigated to fulfill this requirement. The effects of temperature on the polypropylene were examined using gel permeation chromatography to determine preheat windows. Experimental design techniques were used to investigate the effects of processing parameters and interactions on laminates. Processing variables were ranked in order of importance for maximum flexural moduli. Statistically based processing models were generated to enable the prediction of laminate flexural moduli with varying processing conditions. Time at pressure had the greatest contribution and additional laminates were made to determine the minimum time required for full consolidation. Studies of the microstructure of the sandwich laminates were performed to investigate impregnation and removal of voidage.

KEYWORDS: co-mingled materials, glass mat thermoplastics, compression moulding, sandwich materials, voidage, experimental design techniques, gel permeation chromatography

INTRODUCTION

The major use of continuously reinforced thermoplastic composites in the automotive industry is in the production of semi-structural parts from glass mat thermoplastics (GMT). The melt impregnation of the glass mat and polypropylene in double belt laminators limits the amount of glass in standard commercial grades of GMTs to 40% by mass [1]. These materials, with typical processing cycle times of 35 seconds, offer the ability to fill large and complex moulds. GMTs are increasingly replacing steel in complex semi-structural load bearing applications, such as the VW Golf front end. In order to increase the usage of thermoplastic composites into continuously loaded structural parts the glass fibre content needs to be increased.

The glass fibre content in compression moulding materials can be increased by forming a sandwich laminate with a glass fibre fabric at the surface and a GMT core. Matrix material must impregnate the glass fibre fabric and several ways of combining fibre and matrix materials are available including co-weaving, plied matrix, inter-dispersed yarns, powder impregnation and co-mingling [2-3]. Co-mingling combines glass fibres and polypropylene filaments giving a homogeneous distribution of reinforcement and matrix, reducing the mass

transfer distance of the matrix during processing to typically 50 microns [3]. Co-mingled materials offer the potential for the manufacture of structural parts at lower moulding pressures due to the higher and aligned fibre content (compared with GMTs) and the intimate combination of reinforcement and matrix.

The complexity of components moulded from co-mingled materials is limited by geometries that the fabric will drape or conform to during processing [4]. In the sandwich laminate, flow of the GMT core between the co-mingled materials offers the potential for the production of complex geometries with a fast cycle time [5]. Co-mingled materials provide a localised higher and aligned glass fibre content and are placed locally in the tool at regions of higher operating stress. During consolidation of the sandwich laminate, the GMT core damps thickness variations between the shearing fabric but overall complexity is still thought to be restricted by the drape of the co-mingled material. Where complex features are required in the region of the co-mingled facings, the GMT has been shown to break through the co-mingled fabric to fill features such as ribs in a tool. The major difference between processing aligned materials and GMTs is that generally no bulk or large scale flow of the co-mingled structure is thought to occur.

OBJECTIVES

Given the apparent potential for increasing the use of thermoplastic composites into structural applications, assessment of the processing of material combinations was required. The specific aims of this work have been to investigate and optimise the non-isothermal compression moulding of combinations of GMTs and co-mingled fabrics and to determine the effects of processing on laminate microstructure.

EXPERIMENTAL DETAILS

Materials

The GMTs used consisted of a 40% by mass continuous random glass mat reinforced polypropylene, produced by melt impregnation in a double belt laminator. The co-mingled materials consisted of a balanced weave fabric of superficial density 650 g/m^2 woven from yarns of 60% by mass co-mingled E-glass and polypropylene. Laminates of 300mm were produced from two GMT blanks, 171 x 171mm, sandwiched between 2 blanks of co-mingled material, 198 x 198 mm, to give a nominal thickness of 4mm, as shown in Fig. 1. The co-mingled material blanks comprised two layers of co-mingled fabric which were supplied consolidated to a thickness of 0.92mm.

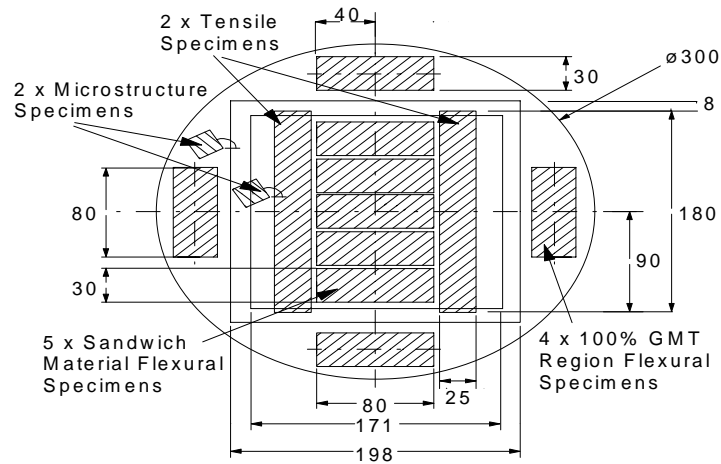


Figure 1: Laminate cutting plan nad blank locations

Processing Study

This study of the co-moulding of co-mingled materials and GMTs covered the time at moulding pressure, moulding pressure, average material pre-heat temperature, tool temperature and their interactions, as shown in Table 1. Tool temperature settings were determined from ambient to the upper range suggested by the GMT manufacturers [6]. Oven preheat temperatures were bound by the melting point and the onset of degradation of the polypropylene matrix. Moulding pressures were defined by the upper limit of the moulding press and the minimum required to fill the tool. Times at pressure were selected from recommended values of 5 seconds per mm part thickness. The maximum hydraulic press compression velocity of 12.9mm/sec was used for all experiments. Black pigmented co-mingled material and naturally pigmented GMT blanks were used to give a visual indication of flow in each laminate.

Table 1: Processing Variables

Processing Parameter	Level 1	Level 2	Level 3
Time at Pressure, (TP)	10 seconds	30 seconds	50 seconds
Moulding Pressure, (P)	50 bar	125 bar	200 bar
Material Temperature, (MT)	180°C	200°C	220°C
Tool Temperature, (TT)	20°C	50°C	80°C

Non-isothermal Compression Moulding Equipment

Infra red ovens are established technologies for preheating in compression moulding and thermo-forming, creating high flux levels for rapid material heating. A 4.5kW R-Royce infra red oven was used for heating the composite materials. A Bradley and Turnton 150 tonne hydraulic moulding press was used to generate maximum pressures of 200 bar on the laminate, with electrically heated platens used to heat the press tooling. Computer control of the press enabled fast material transfer from the oven to press, typically under 10 seconds, and the data acquisition of thermal histories. A steel compression moulding tool was designed and

produced with vertical telescoping shear edges. Fig. 2 shows the experimental moulding facility.

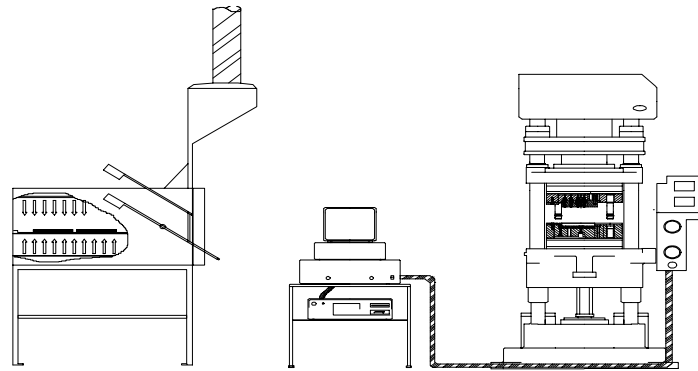


Figure 2: Hot flow compression moulding facility

Experimental Design

Experimental design was used to investigate the effects of 4 processing parameters at 3 settings. A 27 run central composite array was used, shown in Table 2, with each trial performed with levels as described in the array. The array ensured sufficient degrees of freedom to examine the linear and quadratic effects of the 4 factors together with any potential interactions in the system. Multiple linear regression (MLR) techniques were used to generate prediction equations using a second order polynomial, shown generally for two factors, A and B, in Eqn 1. The unknown parameters $\{\beta_i\}$ are the regression coefficients which were estimated by the method of least squares and the selected equation is the one for which the sum of the squares of the residuals is minimised [7].

$$y = \beta_0 + \beta_1 A + \beta_2 B + \beta_3 A^2 + \beta_4 B^2 + \varepsilon \quad (1)$$

Table 2: Central Composite Design Array

Row No.	TP (sec)	P (bar)	MT (°C)	TT (°C)	Row No.	TP (sec)	P (bar)	MT (°C)	TT (°C)
1	30	125	200	50	15	50	50	220	80
2	10	50	180	20	16	10	200	220	80
3	50	50	180	20	17	50	200	220	80
4	10	200	180	20	18	30	125	200	50
5	50	200	180	20	19	10	125	200	50
6	10	50	220	20	20	50	125	200	50
7	50	50	220	20	21	30	50	200	50
8	10	200	220	20	22	30	200	200	50
9	50	200	220	20	23	30	125	180	50
10	10	50	180	80	24	30	125	220	50
11	50	50	180	80	25	30	125	200	20
12	10	200	180	80	26	30	125	200	80
13	50	200	180	80	27	30	125	200	50

Mechanical Testing

The effects of processing parameters on the sandwich region flexural moduli and strength were measured for each laminate, with results averaged along the centre line. Specimen dimensions and locations are show in Fig. 1. Flexural tests and tensile tests were performed at 10mm/min at 5mm/min respectively.

PREHEATING FOR SANDWICH LAMINATES

Determination of Upper Processing Temperature

The high shear viscosity of polypropylene requires heating above the melt temperature to reduce the viscosity for impregnation. The onset of a thermal oxidative degradative reaction formed the maximum processing temperature for the composite under consideration. A processing window can be established as a time frame where the middle of the composite has reached the desired processing temperature but without degrading polymer at the surface. DSC trials had shown the co-mingled material polypropylene to have a reduced oxidative induction time compared with the GMT polypropylene. The effects of preheating on the weight average molar mass (Mw) of the co-mingled material polypropylene were investigated using the technique of gel permeation chromatography (GPC) to define the upper preheat thresholds for processing.

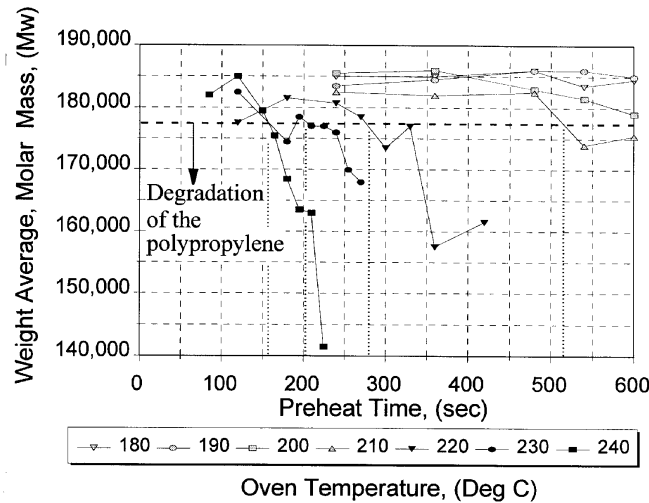


Figure 3: Effect of time and temperature on PP degradation

Samples of pre-consolidated co-mingled material were heated to oven temperatures of 180°C to 240°C in 10°C steps for 7 time intervals at each temperature. Fig. 3 shows the relations between time and temperature effects on the weight average molar mass (Mw). For temperatures of 240°C, 230°C, 220°C and 210 °C Mw reduced with an increasing time at temperature with the effect increasing with higher temperatures. For temperatures of 180°C, 190°C, 200 °C the material was stable for preheat times exceeding 600 seconds. A line at 175,500 representing the onset of degradation determined a maximum preheat time for each temperature. At the highest oven temperature of 230°C used for the sandwich laminates, the co-mingled material preheat time of 145 seconds was within the onset of degradation at 200 seconds.

Combination Material Preheating

Three average material temperatures were used to investigate effects on the consolidation of the composite. Therefore three heating profiles were determined for both composites to reach the desired processing temperature simultaneously. Co-mingled materials and GMTs have different fibre and matrix architectures resulting in disparate heat transfer characteristics. Separate studies of GMTs and pre-consolidated co-mingled materials were used to identify overlaps in processing windows. Additional experiments were used to verify and tune these predictions. The GMT was placed into the oven first and the co-mingled material added towards the end of the heating cycle. Materials were heated separately and stacked together before transfer to the tool. Table 3 summaries the preheat parameters for the three average material temperatures used in the main processing study, with Fig. 3 showing the disparate heating times.

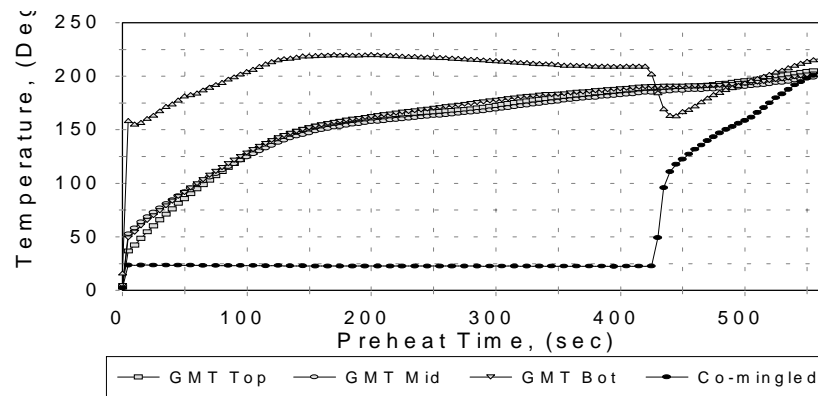


Figure 4: Preheat curves for sandwich laminates

Table 3: Combination Preheat Cycles

Oven Temp, (°C)	Average Temp, (°C)	Material	Time, (sec)
190	180	GMT	0 to 560
		Co-mingled	420 to 560
210	200	GMT	0 to 550
		Co-mingled	430 to 550
230	220	GMT	0 to 460
		Co-mingled	315 to 460

PROCESS OPTIMISATION

The 27 laminates were produced and flexural moduli were measured. Using MLR, regression coefficients were calculated with a quadratic approximation fitted to moduli data and a linear fit to the six possible interaction effects. The t ratios were calculated similarly in a spreadsheet

and used to quantify the magnitude and significance of the effect of each factor on the moduli. The percentage contributions from each significant linear factor, quadratic factor or interaction effect on the flexural moduli are shown in Table 4 (Insignificant factors labelled as '*'). Eqn 2 gives the prediction equation, where coefficients for insignificant interactions and factors were excluded.

Table 4: Processing Contributions, (%), on Flexural Moduli at 95% Confidence

Linear Effects				Quadratic Effects				Linear Interaction Effects						
TP	P	MT	TT	TP ²	P ²	MT ²	TT ²	TPxP	TPxMT	TPxTT	PxTT	MTxTT	PxMT	ε
17	11	*	15	15	10	*	*	*	*	9	*	*	9	14

$$Response = 11.2 + 0.3 TP + 0.2 P + 0.3 MT - 0.6 TP^2 + 0.5 P^2 + 0.2 TPxTT + 0.2 PxMT \quad (2)$$

To reduce error in the analysis, the levels of the four processing parameters were scaled between -1 and +1 to give a linear spacing of the original factor levels [7]. Any level of scaled processing parameter inside the range investigated can be substituted into Eqn 2 to give laminate moduli at those processing conditions.

Partial differentiation and solution of the processing equations gave maximum values for the processing factors for each laminate property. Consideration of these results with the other mechanical test data for the specimens shown in Fig. 1 resulted in optimum conditions of: a time at pressure of 50 seconds, a pressure of 200 bar, a material temperature of 220°C and a tool temperature of 80°C. Eqn 2 was utilised to generate processing response curves to show the effect of varying two variables, while the other variables were kept at the maximum level, on the

laminate flexural moduli. The domination of linear effects and exclusion of insignificant factors, without the reaching of maximum points, limited the validity of the processing models to the upper and lower levels of the processing study. Fig. 5 shows the effects of: firstly, moulding pressure and time at moulding pressure and secondly, tool temperature and material preheat temperature, on flexural moduli.

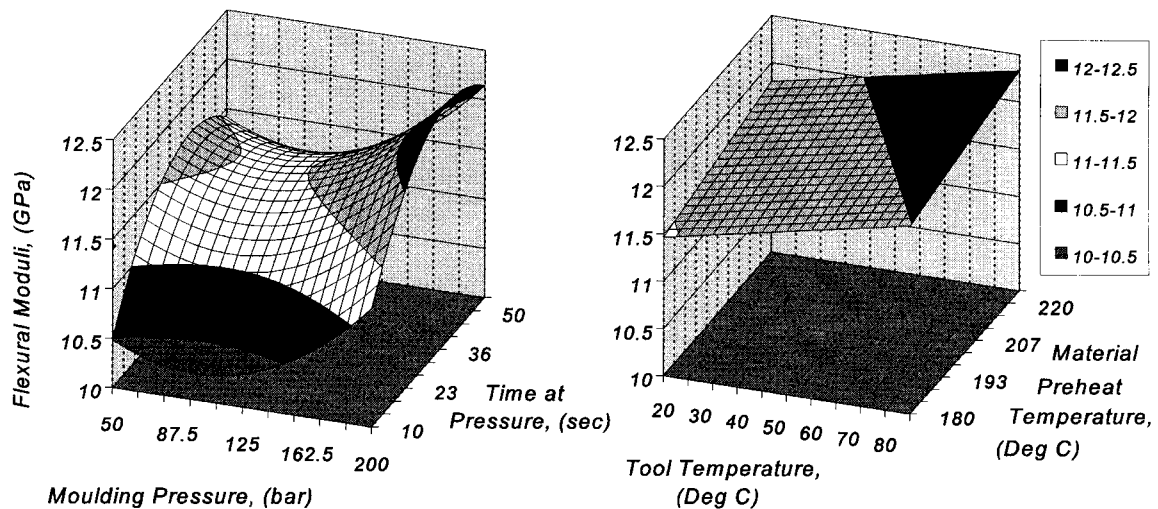


Fig. 5: Effect of Pressure and Temperature on Sandwich Laminate Flexural Modulii

Verification of Process Models and Optimum Processing Conditions

Laminates were produced at the optimised processing conditions described above. Mean and maximum moduli of 11.5 GPa and 12.5 GPa resulted. The processing model predicted moduli of 12.3 GPa at optimum conditions. Confidence limits were calculated using the upper and lower 95% limits for the significant regression coefficients which were substituted into Eqn 2, giving 13.2 GPa and 11.4 GPa respectively. The laminates produced at the optimised conditions have therefore confirmed the predictions at optimised levels.

Time at Pressure

Increasing the time at pressure from 10 to 50 seconds showed the largest effect on the laminate moduli. To investigate the effects of time at pressure further, 6 laminates were produced at optimised conditions with times at pressure of 5, 10, 20, 30, 40 and 50 seconds. Laminate mechanical properties were measured, as shown in Fig. 6, and the through thickness microstructure examined.

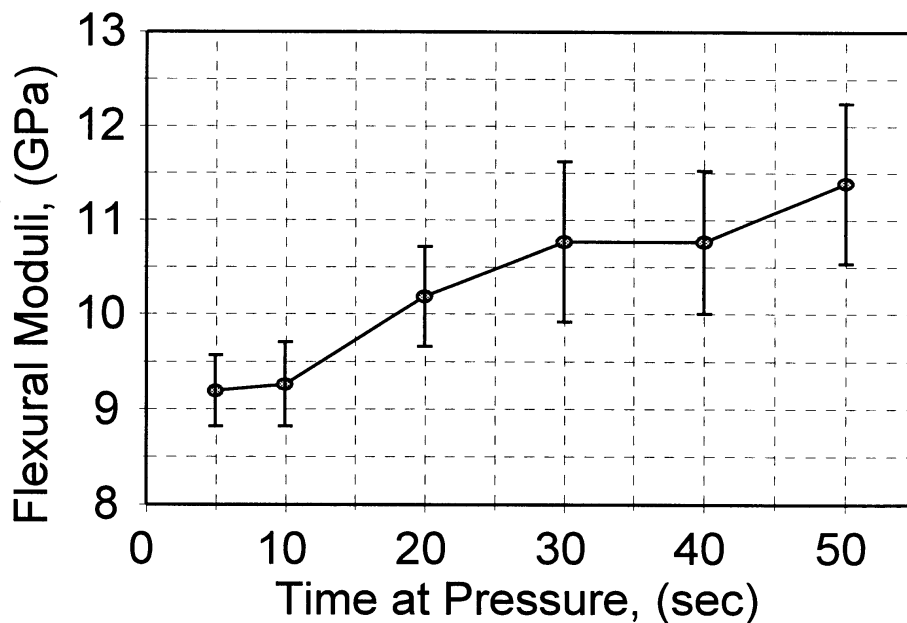


Figure 6: Effect of time at pressure on E_{Flex}

DISCUSSION

Time at Pressure

Increasing the time at pressure showed the largest effect on laminates with properties increasing with time. Through thickness micrographs of laminates produced at 10, 30 and 50 seconds of compression time are compared in Fig. 7. These show the GMT region between the co-mingled material outer layers. An increased time at pressure decreased void contents with the thickness of the mid plane void layer reducing faster in the GMT region at the laminate periphery. It was necessary to maintain the pressure to reduce the void content and to stabilise the laminate until the matrix temperature had reduced to below the onset of polypropylene crystallisation.

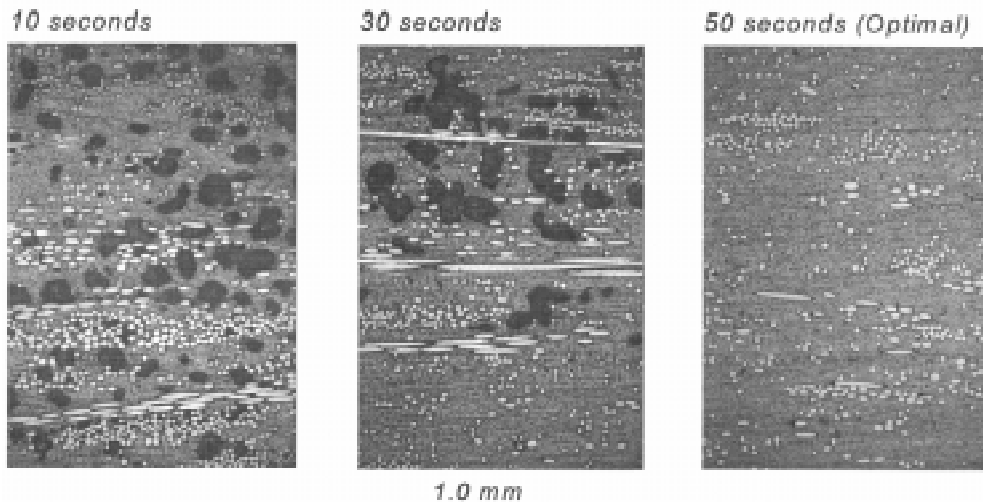


Figure 7: Effect of time at pressure on centre line microstructure

The non-isothermal compression moulding of GMT results in fountain flow through the tool cavity. The GMT freezes to the cold steel surface as it flows across the tool, with the core flowing between the cooling outer layers. With sandwich laminates, the previously consolidated co-mingled material blanks again freeze to the steel tool surface with the rapid cooling due to the higher glass content and lack of insulating air in the material structure. Fountain flow of the GMT core then results between the insulating layers of co-mingled material rather than steel, reducing the rate of heat transfer from the GMT core to the tool. The viscosity of the GMT core would therefore remain low enough for material to flow for longer time periods. In the sandwich laminate the void content, at 30 seconds compression time, of the GMT core in the sandwich region was higher than that at the laminate periphery, composed entirely of GMT. Increased time at pressure, compared with a GMT laminate, was therefore required to reduce void content in the sandwich region.

Moulding Pressure

Fig. 5 shows that increased pressure above 90 bar increased flexural moduli. The laminate mid-plane was well consolidated at 50 and 200 bar, but with increased voidage in the co-mingled material at the laminate surfaces at 50 bar. This was removed at 200 bar, as shown in a through thickness micrograph in Fig. 8 of the surface region of a laminate made at optimum conditions.

Material Preheat Temperature

An average preheat temperature of 220°C increased laminate moduli, as shown in Fig.5. A decrease in properties would result if the materials were heated to higher temperatures where the bulk of the matrix material would degrade. At preheat temperatures of 180°C the co-mingled material on the tensile face of the specimen delaminated from the GMT core during testing.

Comparison of the micrographs in Fig. 8 and Fig. 9, at 220°C and 180°C respectively, showed large areas of voidage between the glass fibres in the co-mingled material at 180°C. The increased voidage in the co-mingled material with reduced temperatures showed the importance of a rapid transfer of the hot blanks from the oven to the tool. Excessive transfer

times would reduce the material temperature, increasing the polypropylene viscosity, and the co-mingled material would not consolidate fully.

Tool Temperature

The processing model plot in Fig. 5 showed increased flexural moduli as the tool temperature increased. Voidage occurred between the co-mingled material glass tows adjacent to the tool surface at 20°C tool temperature. The number of voids in the co-mingled layers decreased towards the mid-plane of the laminate. An increased tool temperature reduced the rate of cooling of the material adjacent to the tool surface, improving the surface finish and increasing flash on laminates. Decreased cooling, reducing the rate of viscosity increase, enabled the full impregnation of the co-mingled material glass fibres to occur.

Interaction Effects

Significant interactions occurred between: firstly, time at pressure and tool temperature and secondly, pressure and material temperature. At higher times at pressure, increased tool temperatures resulted in a greater stiffness increase than at reduced times. Increased tool temperatures improved impregnation of the co-mingled blanks adjacent to the tool surface. Increased times at pressure were required to reduce voidage, which decreased mechanical properties, from the mid-plane of the laminate. At higher pressures, increased material temperatures increased moduli while at lower pressures a reduction in moduli occurred.

Processing Observations

During the compression moulding of sandwich structures, the flow of the GMT blank to the periphery of the tool was observed to drag the black pigmented polypropylene of the co-mingled materials. At optimised processing conditions this reached 28mm, indicating good mixing of the two polypropylenes. The co-mingled material blanks remained where placed in the tool.

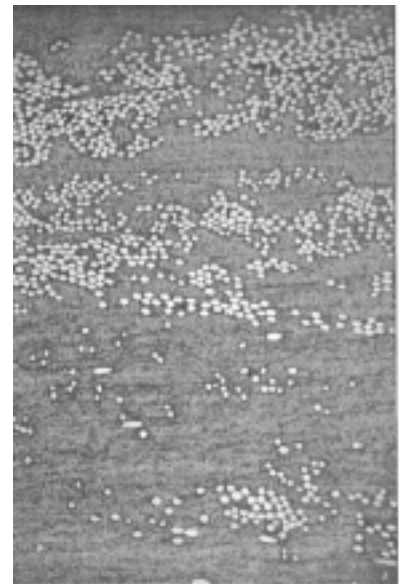


Figure 8: Surface microstructure at optimum processing conditions

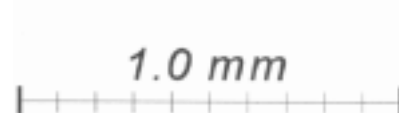
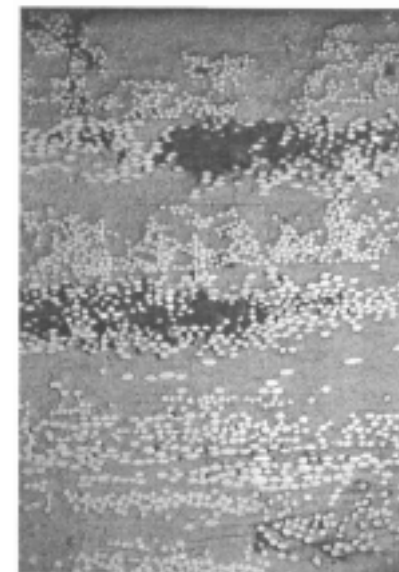


Figure 9: Surface microstructure at 180°C material preheat temperature

CONCLUSIONS

Optimum processing parameters for the production of sandwich laminates have been predicted and verified. Pressure should be maintained to eliminate mid-plane voidage. Maximum material preheat temperatures reduced matrix viscosities for impregnation of the co-mingled material glass fibres. An increased tool temperature assisted impregnation of the co-mingled materials provided that the required time at pressure was maintained. The flexural moduli were increased by 104% compared with properties for GMT laminates and were 86% of properties for co-mingled materials, for equivalent thicknesses. Substantial increases in load carrying ability resulted from the combination of the two material forms, while still offering the ability to flow the GMT between the co-mingled material blanks to fill the tool. Study of the interface of the co-mingled material and GMT regions showed that the glass fibres in the GMT moved with the flowing matrix, eliminating interlaminar voids and matrix rich areas.

ACKNOWLEDGMENTS

The authors wish to thank the: EPSRC, DTI, and the following companies for their support which made this work possible: AMM Ltd, Automold Ltd, Ford Motor Company, Jaguar Cars Ltd, MIRA, Park Hill Textiles/Carr Reinforcement, Synamit AG, Vetrotex International, Dynisco (UK). The work of RAPRA Technology Ltd is acknowledged for performing the GPC study.

REFERENCES

1. Jansz, J., "GMT: Opportunities for Glass Mat Reinforced PP in Automotive Applications." *Polypropylene'93*, Zurich, Switzerland, October 26-27th, 1993, section III, pp. 5-1 to 5-18.
2. Saint John, C., "Co-mingled Thermoplastic Prepregs Industrial Applications", *Proceedings Tenth International Conference on Composite Materials*, Whistler, British Columbia, Canada, August 14-18th, 1995, Vol. III, pp. 397-404.
3. Wakeman, M.D., Cain, T.C., Rudd, C.D., Brooks, R., Long, A.C., "Optimisation of the Flexural Stiffness of Compression Moulded Co-mingled Glass and Polypropylene Composites.", *Seventh European Conference on Composite Materials - Realising their Commercial Potential*. London, May 14-16th, 1996, Vol. 1, pp. 221-227.
4. Van West, B.P., Byron Pipes, R., Keefe, M., Advani, S.G., "The Draping and Consolidation of Co-mingled Fabrics.", *Composites Manufacturing*, Vol. 2, No. 1, 1991, pp. 10-22.
5. Schafer, J., "Thermoplastic Sandwich Sheets with Glass Fabric Reinforced Facings and Random in Plane Oriented Glass Fibre Reinforced Cores." *Proceedings Tenth International Conference on Composite Materials*, Whistler, British Columbia, Canada, August 14-18th, 1995, Vol. VI, pp. 53-60.
6. Giles, H. and Reinhard, D., "Compression Moulding of Polypropylene Glass Composites.", *36th International SAMPE Symposium and Exhibition*. San Diego, California, 1991.
7. Grove, D.M. and Davies, P.D., *Engineering, Quality and Experimental Design*. Longman Scientific and Technical, 1992.

CURING STRAINS DEVELOPED DURING THE MANUFACTURE OF GRP TUBES

J. F. Oosthuizen and W. H. Groenewald

*Department of Mechanical Engineering, Technikon Free State
Private Bag X20539, Bloemfontein, 9300, South Africa.*

SUMMARY: During the manufacture of glass reinforced plastic tubes it should be recognised that the matrix can undergo significant chemical shrinkage. It has been shown that the shrinkage due to post-cure at elevated temperatures could cause strains of significant magnitudes that could exceed the levels of stress or strain allowed for by accepted design codes and are sufficient to promote environmentally assisted cracking in certain operating environments. However, in the cases presented, no consideration was given to the strains developed during the actual lay-up of individual layers. This work provides some experimental results showing that high extension hoop and longitudinal shrinkage strains are developed during the lay-up of thick tubes layers. It is also shown that the post-cure alleviates the hoop strains to acceptable levels while the longitudinal strains are increased to possibly unacceptable magnitudes.

KEYWORDS: glass reinforced plastic, GRP, tubes, curing shrinkage, cure, post-cure

INTRODUCTION

Glass reinforced plastic (GRP) is an ideal material of choice for the manufacture of many items of chemical plant equipment. Its ability to resist degradation in aggressive chemical environments is one of the major benefits. However, the material is prone to environmentally assisted cracking (EAC) if the tensile stresses in the exposed material are not kept low. This is well recognised by codes of practice for the design of GRP equipment, which ensure specification of geometry's leading to low stresses in response to mechanical loading. Other sources of stress are also important, e.g. thermal, process induced. It has been shown that, when polyester and vinyl ester resins, typical of those used in process plant applications, are subject to elevated temperature post-cure after room temperature polymerisation, significant chemical shrinkage can occur [1, 2]. It has been presented that since this shrinkage occurs with the matrix already gelled, any restraint can give rise to large residual stresses, in particular tensile surface stresses of sufficient magnitude promote environmentally assisted cracking in many environments. However, no consideration was given to the strains developed during the actual lay-up of the individual layers. These strains are of primary importance for the determination of residual stresses and strains after manufacture. Although these shrinkage residual stresses are clearly important to designers of chemical process equipment, only limited experimental work appears to have been carried out to date. The aim of this work is to present experimental results for the shrinkage strains during manufacture, lay-up and post-cure, of typical materials and also for tubes of practical dimension. These results are compared to theoretical predictions.

CURING STRAINS DEVELOPED IN A TUBE DURING LAY-UP OF LAYERS

Two identical tubes with internal diameters of 50 mm, were manufactured on an expandable mandrel from DION 9100/CSM with a glass content of 28%. After the lay-up and cure of the surface tissue, two strain gauges were attached to each of the surface tissues to measure the hoop and longitudinal strains during lay-up of the body of the tubes. Four layers per day were applied by hand lay-up to minimise steep temperature gradients resulting from exotherm while continuously recording the strains developed due to curing. A wall thickness of ± 15 mm was obtained from sixteen layers with a tube length of 240 mm. The recorded strains were plotted to the number of layers.

Results and Discussion

The curves shown in Fig. 1 and Fig. 2 represent the strains recorded during the actual lay-up of the layers of tubes 1 and 2.

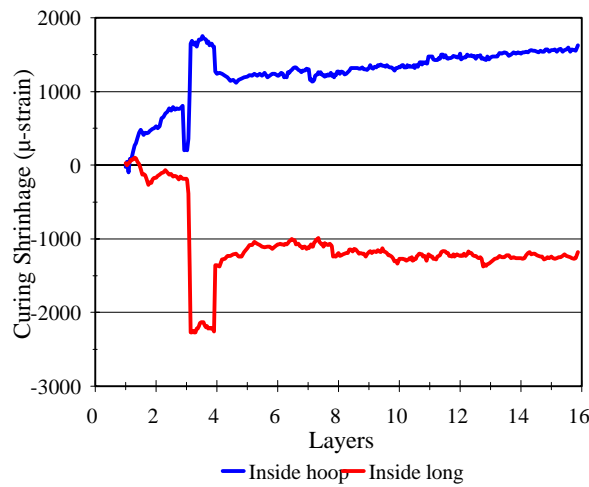


Fig. 1: Longitudinal & Hoop curing strains vs. layers for DION 9100/CSM tube (1) at inside surface

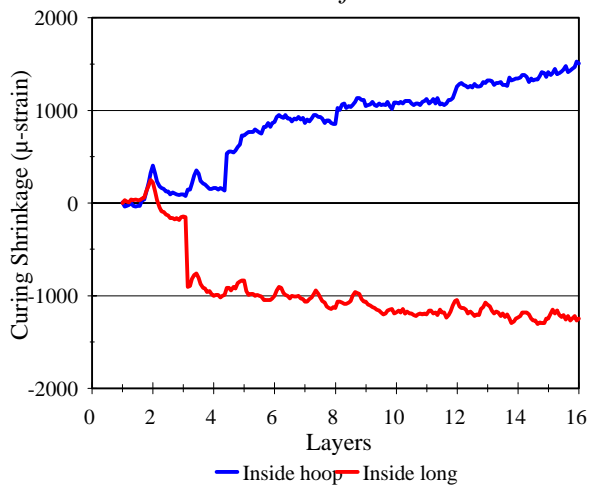


Fig. 2: Longitudinal & Hoop curing strains vs. layers for DION 9100/CSM tube (2) at inside surface

The peaks shown before layer 3 in both the figures indicate when the tubes were released from the mandrels. It can be seen that a maximum extension hoop strain of $1629\mu\epsilon$ and a longitudinal shrinkage strain of $-1181\mu\epsilon$ was attained during the lay-up of the layers for tube

1, and a maximum extension hoop strain of $1508\mu\epsilon$ and a longitudinal shrinkage strain of $-1248\mu\epsilon$ for tube 2.

Although the figures indicate that exotherm did play a role in the variation in strains, the zero and the maximum strain values were obtained at 18°C . Fig. 3 shows the temperature variation of the inner surface due to exotherm during the lay-up of the layers. It is shown that a variation of approximately 6°C is given by any layer for the given thickness of the tube. Values of curing strains for the two tubes are given in Table 1.

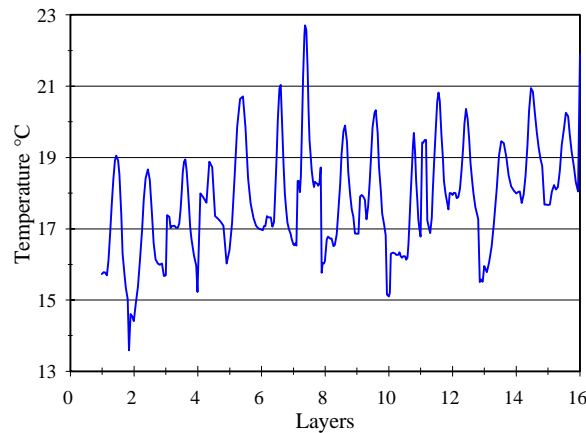


Fig. 3. Temperature variation of tube (1) inner surface due to exotherm

Table 1. Curing strains at the inner surface

Gauge Position & Direction	Strain Measured $\times 10^{-6}$	
	Tube (1)	Tube (2)
Inside Hoop (ϵ_{iz})	1629	1508
Inside Longitudinal (ϵ_{iy})	-1181	-1248

DETERMINATION OF INNER HOOP STRAIN DUE TO CURE DURING LAY-UP

Interpreting the results, in particular the “growth” of the inner circumference, the following observation is made:

1. immediately after the lay-up of layer n ($n=1, 2..16$), the laminate expands due to the heat generated by the exothermic reaction of layer n ;
2. layer n bonds to the laminate and after the exothermic reaction has been completed the whole system cools to ambient temperature;
3. as the system returns to ambient temperature, layer n prevents it to return to its original size and hence a “growth” of the inner circumference is shown and residual strains are produced.

In support of this observation calculations were made by using expressions given by Roy and Kim [3]. Material properties of the DION 9100/CSM tubes used in this study were

determined from methods given by Hoa [4] using $E_m = 3.5$ GPa, $E_f = 72$ GPa, $\nu_m = 0.35$, $\nu_f = 0.2$, $\nu_m = 0.8$, $\alpha_m = 73\mu\epsilon$ and $\alpha_f = 5\mu\epsilon$, where α_m and α_f are the coefficient of expansions (CTEs) of the matrix and the glass mat respectively. The calculated material properties are shown in Table 2 where subscripts z , r and θ indicate the axial, radial and tangential directions respectively. However, the expression for hoop thermal strains for a change in temperature does not take the change in thickness due to lay-up into account. Therefore the addition of the layers (n) were incorporated for strain calculations:

$$\begin{aligned} \epsilon_{\theta h_n} = \epsilon_{\theta c_n} = & \frac{(\alpha_r - \alpha_\theta)(k^2 - \nu_{r\theta}^2)}{(1 - k^2)(1 - c^{2k})} \left[\frac{c_n^{k+1} - 1}{k + \nu_{r\theta}} \left(\frac{r}{b_n} \right)^{k-1} + \frac{c_n^{k+1} - c_n^{2k}}{k - \nu_{r\theta}} \left(\frac{b_n}{r} \right)^{k+1} \right] \Delta T \dots \\ & + \frac{\alpha_r(1 - \nu_{r\theta}) - \alpha_\theta(k^2 - \nu_{r\theta})}{1 - k^2} \Delta T \end{aligned} \quad (1)$$

where

$$c = \frac{a}{b_n}; \quad b_n = a + n \cdot t; \quad k = \sqrt{\frac{S_{rr}}{S_{\theta\theta}}} \quad \text{and} \quad \nu_{r\theta} = -\frac{S_{r\theta}}{S_{\theta\theta}}$$

with a and b_n being the inner and outer radii of the tube, $S_{r\theta}$ and $S_{\theta\theta}$ the elements of the compliance matrix and α_r and α_θ are the CTEs of the ring in the radial and hoop directions respectively. $\epsilon_{\theta h_n}$ and $\epsilon_{\theta c_n}$ are the strains recorded resulting from the exotherm of layer n and from cooling to ambient temperature respectively and with t being the nominal thickness of each layer. Applying temperature changes due to exotherm of $\Delta T = 6^\circ\text{C}$ and a cooling temperature of -6°C , the strains are calculated for layers $n = 1, 2..16$. The strain at the inner surface of the tube, resulting from the curing of the matrix during the lay-up of the individual layers, was then calculated by:

$$\epsilon_\theta = \sum_{n=1}^{15} \epsilon_{\theta h_n} + \sum_{n=2}^{16} \epsilon_{\theta c_n} \quad (2)$$

with no usable results although the results do show that a ‘‘growth’’ actually occurs. It was, however found that if the expansion, determined for $n = 1$, is multiplied by n , reasonable results are obtained. Fig. 4 shows a linear fit of the actual hoop strain recorded and predicted results using $\epsilon_\theta = n \cdot \epsilon_{\theta h_1}$, at the inner surface. This gives a hoop strain at the inner surface of $+1432\mu\epsilon$ which corresponds well with the experimental values given in Table 1.

Table 2. Material Properties of DION 9100/CSM Laminates

Material Property	DION 9100/CSM
$E_{zz} = E_{\theta\theta}$	7120 MPa
E_{rr}	5125 MPa
$E_{r\theta}$	2337 MPa
$\nu_{z\theta}$	0.0954
$\nu_{zr} = \nu_{r\theta}$	0.32
$\alpha_z = \alpha_\theta$	16.07 $\mu\epsilon$
α_r	74.89 $\mu\epsilon$

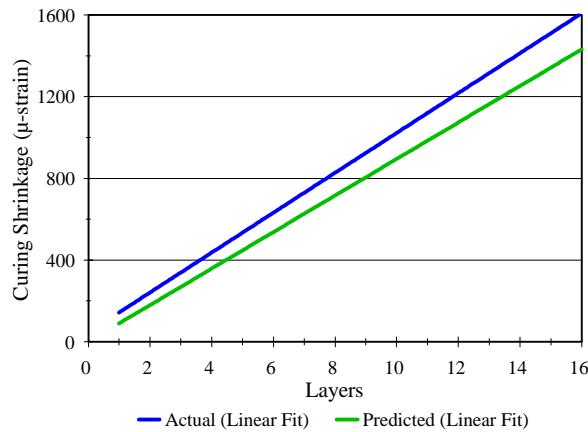


Fig. 4. Actual and predicted hoop curing strains vs. layers for DION 9100/CSM tube at the inner surface

POST-CURE SHRINKAGE OF CSM/VINYL ESTER TUBE

The two tubes were machined down to a wall thickness of 13.5 mm and prepared for post-cure by attaching two additional strain gauges, in the hoop and longitudinal directions, to the outer surface. The tubes were then placed in an oven and heated gradually to a maximum post-curing temperature of 90°C during which the strains resulting from thermal expansion and chemical shrinkage were recorded.

Results and Discussion

Fig. 5 and Fig. 6 show the strains recorded on the tubes during the post-curing process. The tubes expanded as a result of the increase in temperature until approximately 45°C at which post-cure shrinkage commenced. The tubes were maintained at maximum temperature for 2½ hours and then cooled to room temperature. The shrinkage strains measured are given in Table 3 [1, 5].

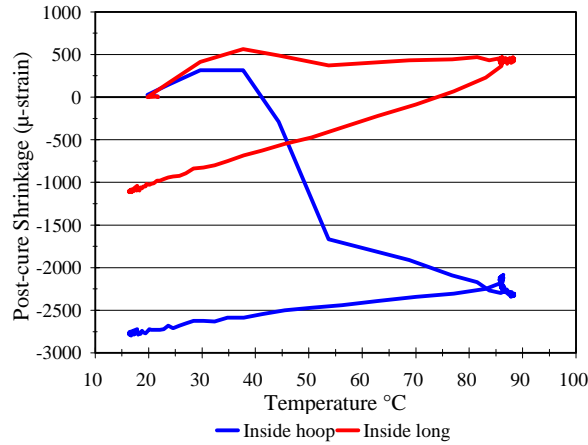


Fig. 5. Longitudinal & Hoop post-cure strains vs. temperature for DION 9100/CSM tube (1) on inside surface

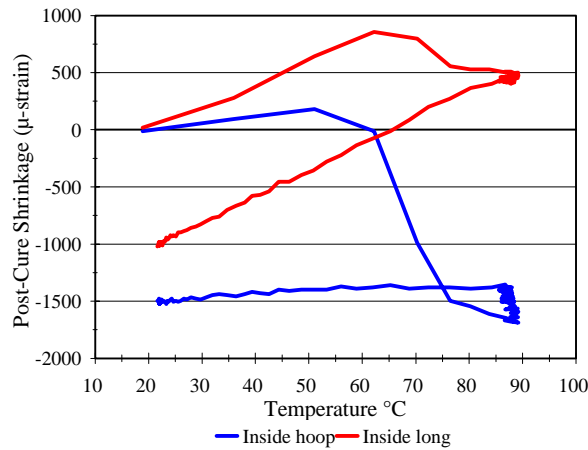


Fig. 6. Longitudinal & Hoop post-cure strains vs. temperature for DION 9100/CSM tube (2) on inside surface

However, it must be kept in mind that, since the initial strains were zeroed at commencement of the post-curing cycle, these strains are real values for the post-curing process and do not include the strains developed during the lay-up phase. Combining the post-curing strains to those obtained during lay-up, the final values obviously will be quite different, as are shown in Fig. 7 and Fig. 8.

Table 4 presents the final strains after the combination of the cure and post-cure strains. From these values a good correlation is found between the longitudinal strains. The hoop strains, however, do not compare well. This is due to the large variation found in the strains produced during the post-curing process.

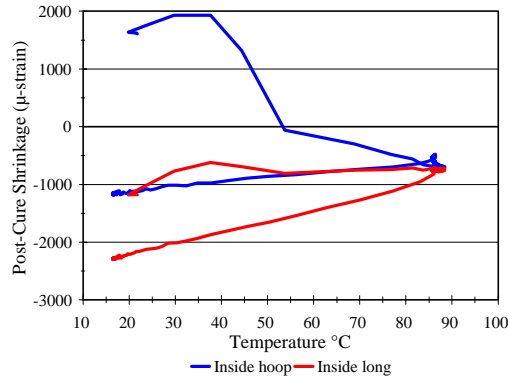


Fig. 7. Actual Post-cure Longitudinal & Hoop Strains vs. Temperature for DION 9100/CSM tube (1) on inside surface

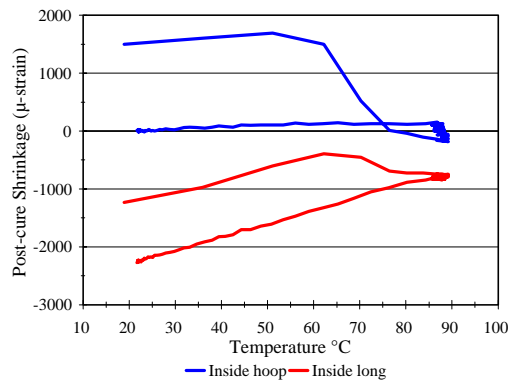


Fig. 8. Actual Post-cure Longitudinal & Hoop Strains vs. Temperature for DION 9100/CSM tube (2) on inside surface

Table 3. Post-cure shrinkage strains of the DION 9100/CSM tubes

Gauge Position & Direction	Strain Measured x 10 ⁻⁶	
	Tube (1)	Tube (2)
Inside Hoop (ϵ_{iz})	-2719	-1495
Inside Longitudinal (ϵ_{iy})	-1037	-1020

Table 4. Final shrinkage strains of the DION 9100/CSM tubes

Gauge Position & Direction	Strain Measured $\times 10^{-6}$	
	Tube (1)	Tube (2)
Inside Hoop (ϵ_{iz})	-1090	-13
Inside Longitudinal (ϵ_{iy})	-2218	-2268

CONCLUSIONS

It has been shown that significant strains are developed during the actual lay-up of individual layers of the laminate. Longitudinal strains decreased, as would be expected, but the hoop strains increased. By predicting the hoop strains, a constant temperature distribution through the laminate was assumed. However, for the material used, the temperature distribution should be linear, decreasing from the outer to the inner surface. It was also assumed that the curing shrinkage of layer n has no effect on the strain at the inner surface of the tube. These assumptions, together with the prediction of the CTEs, probably contributed to the fact that no usable results were obtained from Eqn 2.

It is also shown that post-curing of GRP tubes play an important role in the alleviation of residual hoop strains. It does however increase the residual longitudinal strains which could enhance EAC resulting from mechanical loading.

It is suggested that further experimentation of this kind is required to formulate acceptable methods to predict the strains developed during manufacture.

ACKNOWLEDGEMENTS

This work is part of an ongoing project funded by the FRD, grant GUN 2035297. The authors wish to thank Dr M. A. Stone for his guidance in the work presented, NCS Resins and AFI Reinforcement.

REFERENCES

1. Oosthuizen, J.F. and Stone, M.A., "Residual Stresses in CSM/Vinyl Ester Resin Laminates Due To Post-cure Shrinkage", *Proceedings of the 1st Intentional Conference on Composites Science and Technology*, 1996, pp 365-370.
2. Stone, M.A., Schwartz, I.F. and Chandler, H.D., "Residual stresses arising from partial in-service post-cure of GRP structures", *Composites*, **25**, 1994, pp 177-181.
3. Roy, A.K. and Kim, R.Y., "Measurement for Determining the Thermal Expansion Coefficient (CTE) of Laminated Orthotropic Rings", *Journal of Reinforced Plastics and Composites*, **12**, 1993, pp. 378-385.

4. Hoa, S. V., "Analysis for Design of Fiber Reinforced Plastic Vessels and Pipings", Technomic Publishing Company, Inc., 1991.
5. Oosthuizen, J. F., "Post-cure shrinkage stresses in GRP tubes", *Paper presented at the 9th Wits RP/Composites Conference*, Midrand, South Africa, September 1996.

MATERIAL MODELS FOR THE PROCESS SIMULATION OF THERMOPLASTIC SANDWICH FORMING

Frank Möller, Martin Maier

*Institut für Verbundwerkstoffe GmbH,
University of Kaiserslautern, 67663 Kaiserslautern, Germany*

SUMMARY: A mathematical approach describing the material behaviour for the simulation of the forming process of all-thermoplastic sandwich components is proposed. In order to account for the changing orientation of the fill- and warp fibres of the fabric-reinforced skin layers during the forming process, an oblique local coordinate system is introduced. The approach describing the thermoplastic foam core during the forming process is based on a decomposition of the foam into two parts, a skeleton and a nonlinear elastic continuum in parallel. The skeleton accounts for the foam behaviour in the elastic and plateau regime and the continuum for the lock-up of the foam due to internal gas pressure and cell wall interactions. The developed material models are implemented in the explicit FE-code CONDAT-DYNA3D¹. The models are verified by comparing the simulation results with experimental results from the forming process of flat sheets in spherical geometries.

KEYWORDS: material modelling, process simulation, thermoforming

1. INTRODUCTION

Considering lightweight structures, all-thermoplastic sandwich structures with continuous fibre reinforced skins offer several advantages compared to isotropic materials such as aluminium. By aligning the fibres of the skins in loading direction and the very light foam core, high ratios of stiffness to mass can be realised. In a similar way, other properties like thermal behaviour can be optimized. In order to design the pre-cut of the organic sheet, the changes in fibre orientation have to be determined. The simulation tasks should be the prediction of fibre orientation and distribution, areas where wrinkling occur, residual stresses and the wall-thickness distribution in the manufactured part. The simulation can also be helpful by optimizing both tool and blank holder design and judging the influence of process parameters like pressure, tool temperature and forming speed on the final part.

¹Finite Element program of the company CONDAT GmbH, Scheyern-Fernhag, Germany

The key to successful forming simulation is the mathematical description of the material behaviour. The fabric reinforcement of the skins is highly anisotropic, where the fibre stiffness may exceed 10,000 times on the scale of the shear stiffness. This fabric behaviour is overlaid by the matrix behaviour, which appears to be viscoelastic under processing conditions. On the other hand, the foam core behaves highly nonlinear and rate dependent due to air entrapped in the foam cells. With respect to the behaviour of the foam skeleton the poisson's ratios can reach very small to negative values. Under forming condition, damage of the foam cells can occur which influences the mechanical properties of the foam core.

2. MECHANICAL BEHAVIOUR OF THE FABRIC REINFORCED SKIN LAYERS

The forming mechanisms of fabric reinforced thermoplastics differ significantly from those of metal sheets. During deep drawing of metal sheets, the crucial parameter is the flowability of the material. In the case of fabric reinforced thermoplastics, such a material flow does not occur. Although the thermoplastic matrix material is able to flow the enclosed fibre net hinders large deformations in the fibre directions.

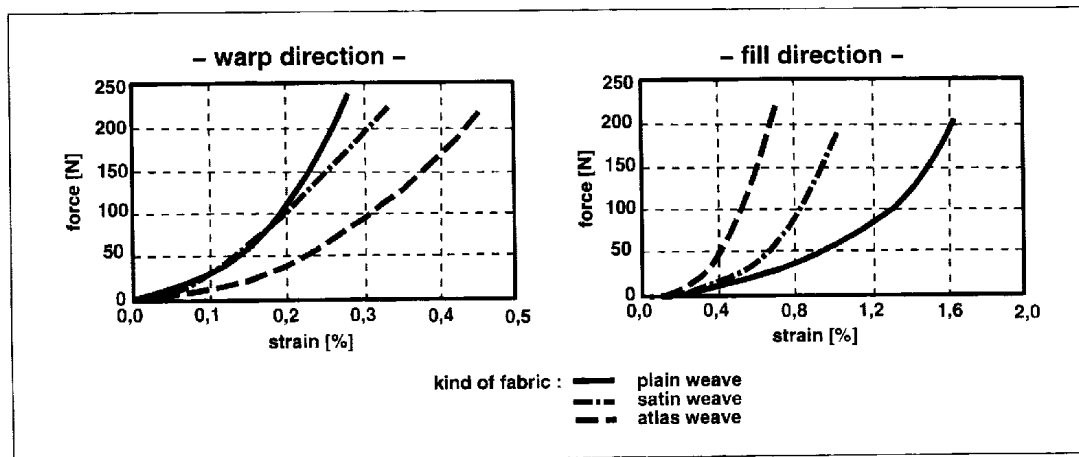


Fig. 1: Stretching potential of the fibres for different kinds fabric

However, there is a small stretching potential of the fabric due to the undulation of the yarns [1, 2]. This leads to a highly nonlinear elastic behaviour of the fabric in the yarn directions which is different in fill- and warp direction. Fig. 1 shows the force-strain-relation in the stretching area of different types of fabric, each for the fill- and warp direction. It is visible that with the increase of crossing points between the fill- and warp fibres the difference in fibre stretching between both directions becomes more significant. There is a higher stretching potential of the fill fibres compared to the warp fibres.

Because of the perpendicularly alignment of the fill- and warp fibres in the undeformed state of the fabric remarkable forming deformations can only be obtained by shearing the fabric. Because shear deformation of the fabric is the most important deformation mechanism, it was examined by a shear test where a square fabric specimen was clamped in a specially designed shear device.

The arising shear forces are shown in relation to the corresponding shear angles in Fig. 2. In this form, the relation is typical for fabrics. It can be subdivided in three characteristic

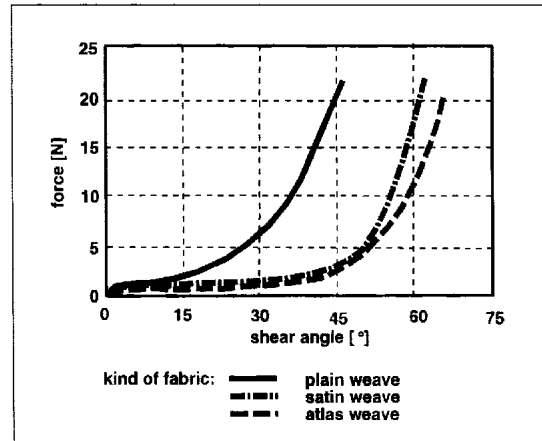


Fig. 2: shear behaviour of different kinds of fabric

sections. Responsible for the first short elastic increase in force is a bending of the yarns up to a point where the bending stresses are high enough to overcome the friction in the fibre crossing points. More fibre crossing points, dependent on the kind of fabric, increase the shear forces. The second section is characterized by a small increase in force over a wide range of the shear angle. After shear locking of the fabric, i.e. after a further shear deformation of the fabric only by rotating of the fill- and warp fibres around their crossing points is no more possible, the shear forces increase very strongly. The third section is characterized by this phenomenon. The shear angle at which the shear force increases is determined by the used kind of fabric. With a higher amount of crossing points in the fabric, it will be shifted to lower shear angles. In the shear locking region of the fabric an optically detectable wrinkling appears. But the corresponding shear angle depends on the membran load of the fabric. By loading the single fill- and warp fibres of the fabric in tension, this wrinkling can be shifted to higher shear angles. On the other hand the shear angle where the force increases is nearly uninfluenced by membran stresses. Shear tests of fabric reinforced organic sheets under forming conditions lead to the same force to shear angle relations at a slightly higher force level.

3. MATERIAL MODEL FOR THE FABRIC REINFORCED SKIN LAYERS

The mathematical description of the mechanical behaviour of fabric reinforced thermoplastics is based on a separate description of the mechanical behaviour of the thermoplastic matrix material and the fabric and the additional overlap of both contributions (Eqn. 1)[4, 5, 6].

$$\sigma(t) = \sigma_m(t) + \sigma_f \quad (1)$$

The definitions of the expressions are:

$$\begin{aligned} \sigma_m &= \text{stress contribution of the matrix} \\ \sigma_f &= \text{stress contribution of the fabric} \end{aligned}$$

The viscoelastic behaviour of the matrix material under forming temperature will be described by a combined Kelvin-Voigt / Maxwell model (Eqn. 2).

$$G(t) = G_2 + (G_1 - G_2) \cdot e^{-\beta t} \quad (2)$$

The definitions of the expressions are:

- G_1 = short-time shear modulus
- G_2 = long-time shear modulus
- B = bulkmodulus
- β = decay constant

The mechanical behaviour of the fabric is assumed to be nonlinear elastic and highly anisotropic. The coupling between the strain in fill and warp direction is neglected by setting the poisson's ratio of the fabric 0.0. Hence, a load in the warp direction does not cause a strain in the fill direction. There is also no coupling between the shear behaviour and the mechanical behaviour in the fibre directions. The stiffness formulation of the material model shows only the main diagonal occupied, but with each component as a function of the corresponding strain-component. The stress strain relation may be written as in Eqn. 3:

$$\begin{bmatrix} \sigma_{11} \\ \sigma_{22} \\ \sigma_{33} \\ \sigma_{12} \\ \sigma_{13} \\ \sigma_{23} \end{bmatrix} = \begin{bmatrix} E_{warp}(\epsilon_{11}) & 0 & 0 & 0 & 0 & 0 \\ 0 & E_{fill}(\epsilon_{22}) & 0 & 0 & 0 & 0 \\ 0 & 0 & k \cdot E_{warp}(\epsilon_{33}) & 0 & 0 & 0 \\ 0 & 0 & 0 & G(\gamma_{12}) & 0 & 0 \\ 0 & 0 & 0 & 0 & G(\gamma_{13}) & 0 \\ 0 & 0 & 0 & 0 & 0 & G(\gamma_{23}) \end{bmatrix} \cdot \begin{bmatrix} \epsilon_{11} \\ \epsilon_{22} \\ \epsilon_{33} \\ \gamma_{12} \\ \gamma_{13} \\ \gamma_{23} \end{bmatrix} \quad (3)$$

The k-factor in the stiffness description in fabric thickness direction is load dependent. It is different for tension- and compression load, which justifies a very small tension stiffness compared to the compression stiffness of a fabric in the thickness direction. In addition to the viscoelastic behaviour of the matrix, the calculation of the thickness increase under shear loading is mainly influenced by the stiffness behaviour assumed here.

During shear deformation of the fabric, the fill- and warp-fibres do not remain perpendicular to each other but surround an oblique angle which is shown in Fig. 3. As the stiffness behaviour of the fabric is known only in the fibre directions, a stress tensor can be calculated only in the oblique local coordinate system. Due to this, it is necessary to know the strain tensor in this oblique coordinate system.

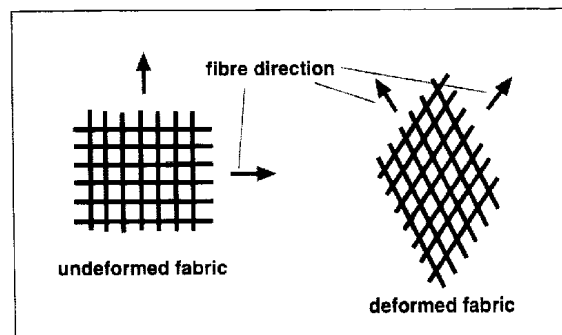


Fig. 3: Changes in fibre angle under shear deformation

Therefore, the material routine implemented in the explicit finite element code 'CONDAT-DYNA3D' uses a transformation from rectangular global coordinates into an oblique local

system whose first and second basis vector point in fibre direction of the deformed fabric and whose third basis vector is rectangular to the plain build by the first two basis vectors. This allows to calculate the stresses in the fibre directions during the entire forming process which is important to know for the process understanding and the tool and blank holder design.

At the transformation in an oblique coordinate system it is important that the covariant and the contravariant basis vectors are not identical, as in the special case of a rectangular coordinate system [7].

Assuming the covariant basis vectors to be g_1, g_2, g_3 , the contravariant basis vectors can be calculated using Eqn. 4, 5, 6.

$$g^1 = g_2 \times g_3 \quad (4)$$

$$g^2 = g_3 \times g_1 \quad (5)$$

$$g^3 = g_1 \times g_2 \quad (6)$$

Thus a covariant and a contravariant transformation matrix exists (Eqn. 7, 8).

$$T_{co} = \begin{bmatrix} g_{11} & g_{12} & g_{13} \\ g_{21} & g_{22} & g_{23} \\ g_{31} & g_{32} & g_{33} \end{bmatrix} \quad (7)$$

$$T_{cont} = \begin{bmatrix} g^{11} & g^{12} & g^{13} \\ g^{21} & g^{22} & g^{23} \\ g^{31} & g^{32} & g^{33} \end{bmatrix} \quad (8)$$

Due to the transformation the physical units will change. In order to keep the units conform, the components of the tensor will related to a unit tensor or a so called metric tensor (in oblique coordinates).

Covariant metric tensor (Eqn. 9):

$$M_{co} = T_{co} \cdot T_{co}^T \quad (9)$$

Contravariant metric tensor (Eqn. 10):

$$M_{cont} = T_{cont} \cdot T_{cont}^T \quad (10)$$

This metric tensor is necessary to calculate the physical components of the transformed tensor. Stress and strain velocity tensor are transformed in detail as follows:

Transformation of the stress tensor from global to oblique coordinates (Eqn. 11):

$$\sigma_{oblique}^* = T_{cont} \cdot \sigma_{global} \cdot T_{cont}^T \quad (11)$$

Calculation of the physical components of the stress tensor in oblique coordinates (Eqn. 12):

$$\sigma_{oblique}^{ij} = \sigma_{oblique}^{ij*} \cdot \sqrt{m_{ii} \cdot m_{jj}} \quad (12)$$

Transformation of the strain velocity tensor from global to oblique coordinates (Eqn. 13):

$$\dot{\epsilon}_{oblique}^* = T_{co} \cdot \dot{\epsilon}_{global} \cdot T_{co}^T \quad (13)$$

Calculation of the physical components of the strain velocity tensor in oblique coordinates (Eqn. 14):

$$\dot{\epsilon}_{ij\text{oblique}} = \dot{\epsilon}_{ij\text{oblique}}^* \cdot \sqrt{m^{ii} \cdot m^{jj}} \quad (14)$$

The used definitions are:

g_{ij}	=	j-th component of i-th covariant basis vector
g^{ij}	=	j-th component of i-th contravariant basis vector
T_{co}	=	covariante transformation matrix
T_{cont}	=	contravariante transformation matrix
M_{co}	=	covariant metric tensor
M_{cont}	=	contravariant metric tensor
m_{ii}	=	components of covariant metric tensor
m^{ii}	=	components of contravariant metric tensor
*	=	unnormalized tensor

4. MATERIAL MODEL FOR THE FOAM CORE

The mathematical description of the foam core is based on a decomposition of the foam in two parts: a skeleton and a nonlinear elastic continuum in parallel [8]. Therefore the total foam response of a load can be decomposed into the response of the skeleton and the response of the nonlinear elastic continuum as shown in Fig. 4.

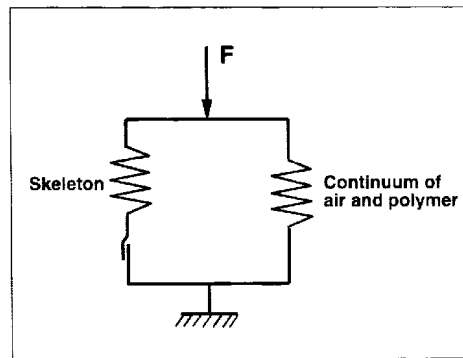


Fig. 4: Schematical description of the foam model

In the model, the skeleton behaves as nonlinear elastic-plastic and is assumed to occupy the same space as the continuum. The continuum consists of air and polymer particles which can move freely in the space the continuum occupies. Hence, the initial response of the continuum to a compression load is a slight increase of the compression stresses in the continuum, caused by the compression of the air. When the volume of the compressed continuum is occupied completely by the polymer particles, a large increase of the compression stresses occurs due to the now starting compression of the polymer particles. This corresponds to the lock up section of a foam compression curve in reality. An expression for the hydrostatic pressure in the continuum (p_{hydro}) was obtained by assuming that the air is in series with the polymer particles, the air is a perfect gas and the foam compression is an isothermal process. These assumptions indicate that the perfect gas equation (Eqn. 15) of state can be used for the air:

$$p^{air} \cdot V^{air} = p_0^{air} \cdot V_0^{air} \quad (15)$$

with:

$$\begin{aligned}
 p^{air} &= \text{current absolute air pressure} \\
 V^{air} &= \text{current air volume} \\
 p_0^{air} &= \text{original air pressure} \\
 V_0^{air} &= \text{original air volume}
 \end{aligned}$$

Where the original air volume is related to the original foam volume V_0 by Eqn. 16

$$V_0^{air} = V_0(1 - \phi) \quad (16)$$

and ϕ is the volume fraction of the polymer in the undeformed foam. The change in internal air pressure due to the loading $p = p^{air} - p_0^{air}$ is related to the change in air volume as follows (Eqn. 17):

$$\Delta V^{air} = \frac{-pV_0(1 - \phi)}{p_0^{air} + p} \quad (17)$$

The volume of the polymer, defining the cell walls will change according to the bulk modulus of the polymer K^{pol} as follows (Eqn. 18):

$$\Delta V^{pol} = \frac{-pV_0\phi}{K^{pol}} \quad (18)$$

With the engineering volume strain ε_{vol} , the internal hydrostatic pressure of the continuum can be calculated as in Eqn. 19:

$$p_{hydro} = 0.5 \cdot \frac{p_0^{air} \cdot \phi + K^{pol} \cdot (1 - \phi + \varepsilon_{vol})}{\phi} \quad (19)$$

$$-\sqrt{(0.5 \cdot \frac{p_0^{air} \cdot \phi + K^{pol} \cdot (1 - \phi + \varepsilon_{vol})}{\phi})^2 - \frac{\varepsilon_{vol} \cdot K^{pol} \cdot p_0^{air}}{\phi}}$$

Under the assumption that the continuum behaves isotropic, a bulk modulus K^{cont} and a shear modulus G^{cont} of the continuum can be calculated as shown in Eqn. 20, 21:

$$K^{cont} = \frac{p_{hydro}}{\varepsilon_{vol}} \quad (20)$$

$$G^{cont} = \frac{3K^{cont} \cdot (1 - 2\nu)}{2 \cdot (1 + \nu)} \quad (21)$$

Eqn. 22 describes the stress strain relation of the continuum:

$$\begin{bmatrix}
 \sigma_{11}^{cont} + p_{hydro} \\
 \sigma_{22}^{cont} + p_{hydro} \\
 \sigma_{33}^{cont} + p_{hydro} \\
 \sigma_{12}^{cont} \\
 \sigma_{13}^{cont} \\
 \sigma_{23}^{cont}
 \end{bmatrix}
 =
 \begin{bmatrix}
 \frac{4}{3}G^{cont} & -\frac{1}{3}G^{cont} & -\frac{1}{3}G^{cont} & 0 & 0 & 0 \\
 -\frac{1}{3}G^{cont} & \frac{4}{3}G^{cont} & -\frac{1}{3}G^{cont} & 0 & 0 & 0 \\
 -\frac{1}{3}G^{cont} & -\frac{1}{3}G^{cont} & \frac{4}{3}G^{cont} & 0 & 0 & 0 \\
 0 & 0 & 0 & G^{cont} & 0 & 0 \\
 0 & 0 & 0 & 0 & G^{cont} & 0 \\
 0 & 0 & 0 & 0 & 0 & G^{cont}
 \end{bmatrix}
 \cdot
 \begin{bmatrix}
 \varepsilon_{11} \\
 \varepsilon_{22} \\
 \varepsilon_{33} \\
 \gamma_{12} \\
 \gamma_{13} \\
 \gamma_{23}
 \end{bmatrix}
 \quad (22)$$

The mechanical behaviour of the skeleton is described as nonlinear elastic-plastic, without any coupling between the cell walls. Here elastic-plastic means that after the load has reached a certain amount the stiffness of the material decreases and the deformation after

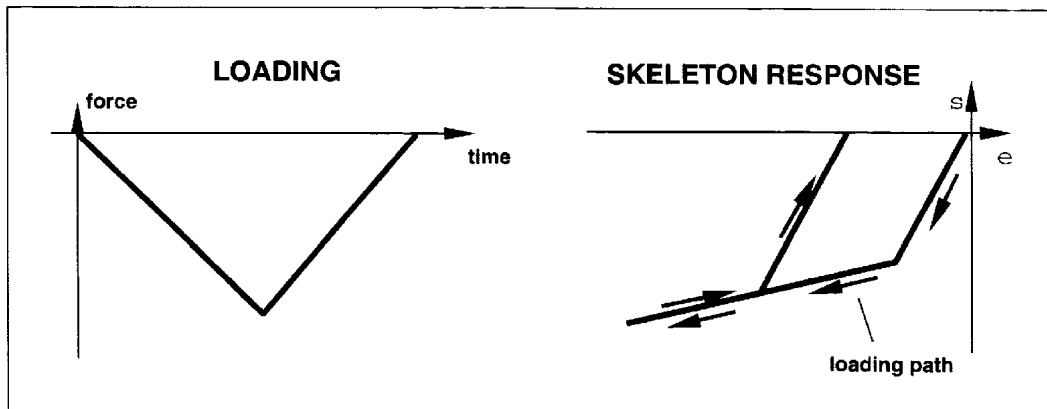


Fig. 5: Loading behaviour of the skeleton

this point is partly plastic and partly elastic weighed by a user given factor. The loading and deloading behaviour of the skeleton is shown in Fig. 5.

Eqn. 23 describes the stress strain relation of the skeleton:

$$\begin{bmatrix} \sigma_{11}^{skel} \\ \sigma_{22}^{skel} \\ \sigma_{33}^{skel} \\ \sigma_{12}^{skel} \\ \sigma_{13}^{skel} \\ \sigma_{23}^{skel} \end{bmatrix} = \begin{bmatrix} E_1(\epsilon_{11}) & 0 & 0 & 0 & 0 & 0 \\ 0 & E_2(\epsilon_{22}) & 0 & 0 & 0 & 0 \\ 0 & 0 & E_3(\epsilon_{33}) & 0 & 0 & 0 \\ 0 & 0 & 0 & G_{12}(\gamma_{12}) & 0 & 0 \\ 0 & 0 & 0 & 0 & G_{13}(\gamma_{13}) & 0 \\ 0 & 0 & 0 & 0 & 0 & G_{23}(\gamma_{23}) \end{bmatrix} \begin{bmatrix} \epsilon_{11} \\ \epsilon_{22} \\ \epsilon_{33} \\ \gamma_{12} \\ \gamma_{13} \\ \gamma_{23} \end{bmatrix} \quad (23)$$

Due to the nonlinear elastic plastic material behaviour of the cell walls the E-moduli and the shear-moduli are functions of the corresponding strains. As mentioned earlier, the stress strain relation of the complete foam is obtained by adding both contributions of the skeleton and the continuum (Eqn. 24).

$$\sigma = \sigma_{cont} + \sigma_{skel} \quad (24)$$

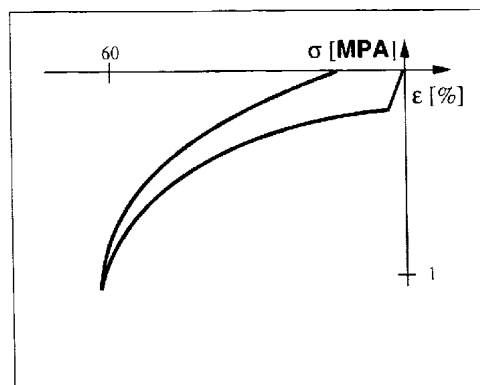


Fig. 6: Compression behaviour of a foam described by the developed model

Fig. 6 shows an example for the loading and deloading behaviour of a foam described by the mathematical model developed above.

5. RESULTS

The described material models are verified by comparing the simulation results with the experimental results from the forming process of flat sheets in spherical geometries.

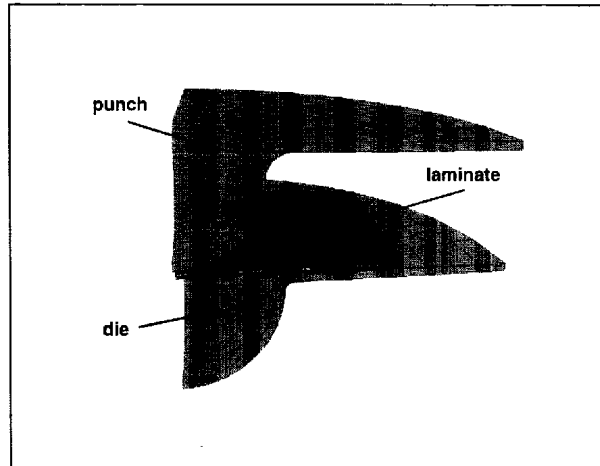


Fig. 7: Simulation model of a spherical forming process

Due to the symmetry of the problem, the simulation can be conducted for a quarter section (Fig. 7).

One important question concerning the tool design is the fissure between the punch and the die, which depends on the thickness distribution of the formed part. With the help of the proposed material models conclusions can be drawn for an optimized distribution of the width of the fissure by calculating the thickness distribution of the part after forming (Fig. 8) with respect to the stress distribution in the thickness direction.

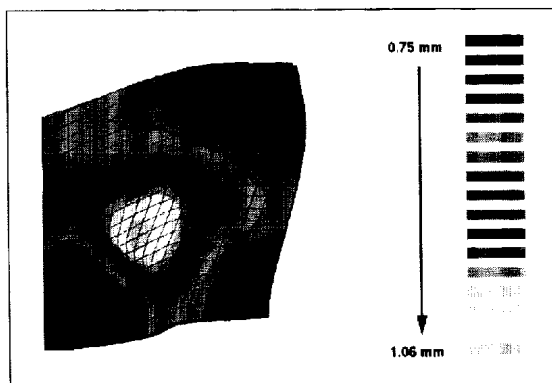


Fig. 8: Thickness distribution

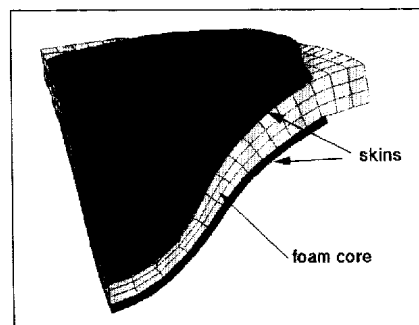


Fig. 9: Simulation of spherical forming process

The simulated deformation results of a sandwich panel during the forming process in a half-dome geometry (Fig. 9) show good agreement to the experimental results.

5. CONCLUSIONS

The developed material model for the skin layers describes the mechanical behaviour of fabric reinforced thermoplastics during the forming process. The stress distributions can be observed during the entire forming process. This is possible in the global coordinate system as well as in the oblique local coordinate system. Therefore, it is possible to draw conclusions on the loading of the fabric during the forming process. Also the thickness distribution during the entire forming process can be shown. So a tool is given to answer numerous, to the manufacturing process orientated questions like: optimized distribution of the fissure between the punch and the die of the tool; influence of different blankholder systems on the forming results; localisation of the areas where wrinkling may occur; to point out only the most serious. Predictions are possible about the influence of parameters concerning the mechanical behaviour of the fabric on the forming results.

In conjunction with the developed material model for the foam core the same questions for the forming process of sandwich panels can be answered.

REFERENCES

- [1] K"otte, R.; Mitscherling, J.; M"ullerferli, G.; Rosenbaum, U.; Specker, O.; St"oger, M.; Starke, J.; Mahlke, M.: Faserverbundwerkstoffe-Verfahrenstechnik, Me"smethoden und Proze"ssimulation; 15. IKV-Kolloquium, Aachen 1990, Seite 281-289
- [2] Biswas, A.: Gewebeverst"arkte Thermoplaste Simulation des Umformvorganges; 17. IKV-Kolloquium, Aachen 1994, Seite 330-336
- [3] Scherer, R.: Charakterisierung des Zwischenlagenabgleitens beim Thermoformen von kontinuierlich faserverst"arkten Polypropylen-Laminaten; Dissertation Universit"at Hamburg/Harburg 1992
- [4] Beaussart, A. J.: Numerical Modeling of Sheet Forming Processes for Thermoplastic Composites; Master Thesis, University of Delaware, August 1990
- [5] Pickett, A.K.; Queckb"orner, T.; De Luca, P.; Haug, E.: An explicit finite element solution for the forming prediction of continuous fibre-reinforced thermoplastic sheets; composites manufacturing; Volume 6; Number 3-4; 1995; Page 237-243
- [6] O' Braidaigh, C.M.; Pipes, R.B.: Finite Element analysis of Composite Sheet Forming Process; composites manufacturing; Volume 12, Number 3-4; 1991; Page 161-170
- [7] Klingbeil, E.: Tensorrechnung f"ur Ingenieure; Bibliographisches Institut Mannheim / Wien / Z"urich; Hochschultaschenb"ucher-Verlag; 1966
- [8] Neilsen, M.K.; Krieg, R.D.; Schreyer, H.L.: A Constitutive Theory for Rigid Polyurethane Foam; polymer engineering and science.; Volume 35; Number 5; mid-march 1995; Page 387-394

PREDICTION OF DAMAGE WIDTH IN LASER DRILLING OF PRINTED WIRING BOARD USING FEM

Toshiki Hirogaki¹, Eiichi Aoyama², Hisahiro Inoue³, Hiromichi Nobe⁴
Keiji Ogawa⁵, Youji Kitahara⁶, and Tsutao Katayama²

¹*School of Eng. The Univ. of Shiga Pref. Shiga 522, Japan*

²*Faculty of Eng. Doshisha Univ., Kyoto 610-03, Japan*

³*Faculty of Eng., Osaka Pref. Univ., Osaka 590, Japan*

⁴*Akamatu Froging Syst. Co. Ltd., Osaka 573-01, Japan*

⁵*Graduate Student, Doshisha Univ., Kyoto 610-03, Japan*

⁶*Tech. Res. Inst. of Osaka Pref., Osaka 590-02, Japan*

SUMMARY: The temperatures are measured at the various positions from the drilled hole wall during laser drilling of PWB using the thermocouples. It is found that these temperatures are dependent on the individual values of materials in the composites. Moreover, we pay attention to the properties of the glass fiber as an analytical model of FEM in order to predict the carbonized damage widths after laser drilling in PWB. The measured temperature is substituted for the boundary condition at the inside diameter of drilled hole, and the other boundaries are insulated against the heat transfer. As results, the damage widths defined as carbonizing on an experiment are good agreement with calculated ones.

KEYWORDS: GFRP, printed wiring board, CO₂ laser, damage, drilling, laser drilling, FEM

INTRODUCTION

The printed wiring board (PWB) has been smaller, because the demand for reducing the size of the electric devices has become to increase. Therefore, laser drilling has been considered as an effective method to machine the smaller through holes (less than diameter 0.3 mm) in PWB. In the case of PWB made of composite materials, it is necessary to improve the heat affect zone (carbonized zone) at the hole wall for application of laser drilling. However, there has been few studies[1,2,3] which dealt with the hole quality of laser drilling of GFRP. So, this paper describes the damage due to the heat influence in laser drilling in PWB, which is made of GFRP (epoxy / glass woven cloth, thickness 1.6 mm), using a CO₂ source.

First, the temperatures are measured at the various positions from the drilled hole wall using the thermocouples in order to research the distributions of temperatures around the hole during laser drilling of PWB. On the other hand, the heat affected damages around the hole are observed using the optical microscope. The relations between the damages and the temperatures of the hole wall are investigated from these results.

Second, the heat transfer is analyzed to predict the damage width at drilled hole wall after laser drilling using FEM. Specially, we pay attention to the properties of the glass fiber as an analytical model. The measured temperature is substituted for the boundary condition at the

inside diameter of the drilled hole, and the other boundaries are insulated against the heat transfer. The calculations are carried out to compare the experimental results under various laser irradiation times.

Finally, the carbonized damage widths on the calculated model are defined as the distances from the inside diameter at the minimum temperature in the area where the epoxy resin is carbonized on experiments. It is shown that the model with these boundary conditions based on this experiment is effective on predicting the carbonized damage widths after laser drilling in PWB.

EXPERIMENTAL EQUIPMENT AND MATERIALS

The maximum attainable power of a CO₂ laser is 250 W. The drilling is performed on the conditions of 150W, 75 W and 35 W in this study. The spot diameter is 0.3 mm on the just focus, and the lens is 5 inches. N₂ is used as the assisting gas in laser drilling.

GFRP is the type of glass (39 in mass) /epoxy-resin, plain woven cloth and thickness 1.6 mm. The workpiece is the copper clad laminate for PWB. The properties of the glass and the epoxy resin are shown in Table 1.

Fig.1 shows the diagram of measuring the temperatures during laser drilling. The thermocouples (0.1 mm) are inserted between GFRPs of thickness 0.8mm. In other words, measuring points are 0.8 mm from the surface. The signals from the sensors are recorded by the memory recorder with the signals of the shutter of a laser beam. The workpiece is mounted on the X-Y table. The distances from the hole wall are determined by observing the workpieces using the microscope after laser drilling.

Table 1: Properties of GFRP

Glass	E-glass		Composition (wt%)			
	Diameter	10 μ m	SiO ₂	54	MgO	5
Tensile strength	3.43 GPa	Al ₂ O ₃	14	B ₂ O	8	
Young's modulus	73 GPa	CaO	18			
Epoxy	Bending modulus of elasticity		19 GPa			
	Bending strength		130 MPa			

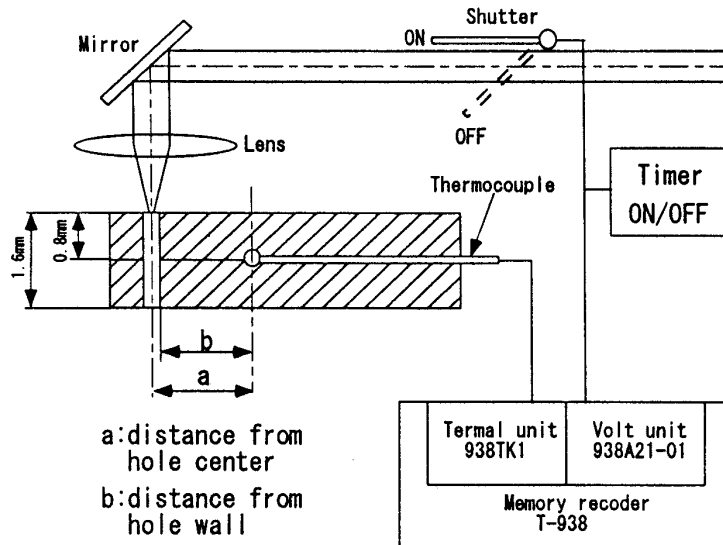


Fig.1: Experimental equipment

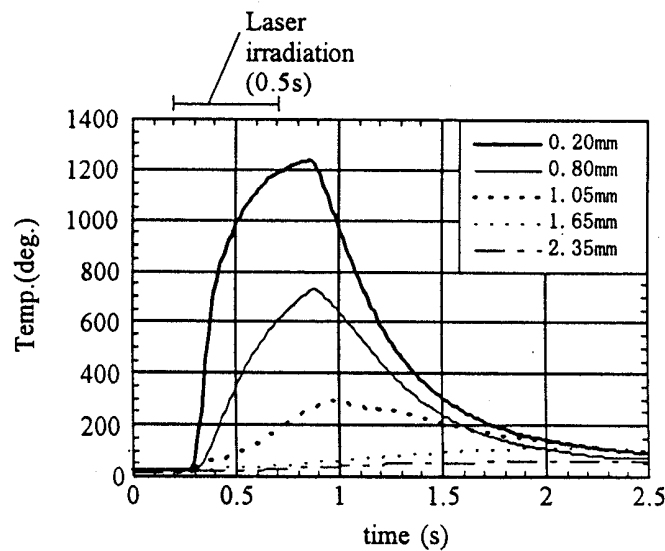


Fig.2: Temperature and time (Laser output power 150W)

RESULTS AND DISCUSSION

Measured Results of Temperature in Laser Drilling

Fig.2 shows the relations between time and the temperatures at various distances from hole wall during laser drilling. The laser irradiation time is in the case of 0.5 s. The inclination of increasing the temperature is higher at the measuring point near the drilled hole wall during the laser irradiation period. The maximum temperatures are indicated earlier at this measuring point, too. It is found from these results that the heat transfer from the hole wall causes an increase of the temperature around the hole. At the distance of 0.2 mm from the hole wall, the maximum

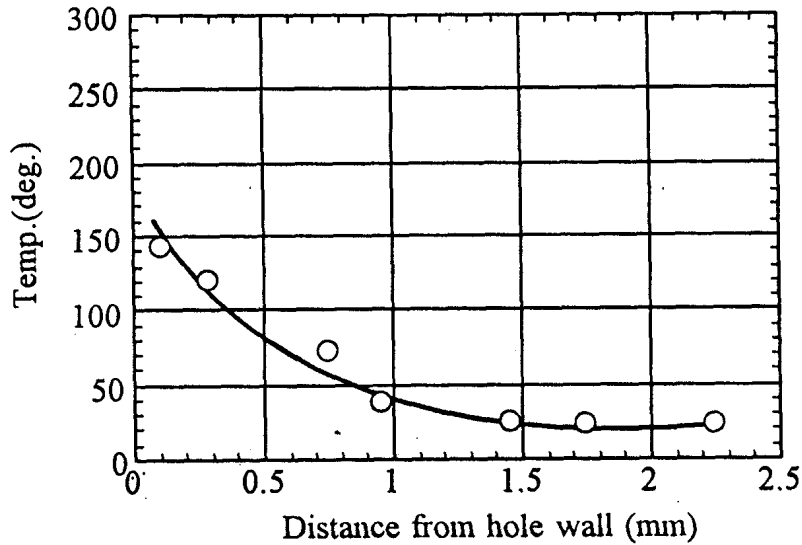


Fig.3: Maximum temperature and distance from hole wall (In the case of the epoxy resin, Laser output power 150 W)

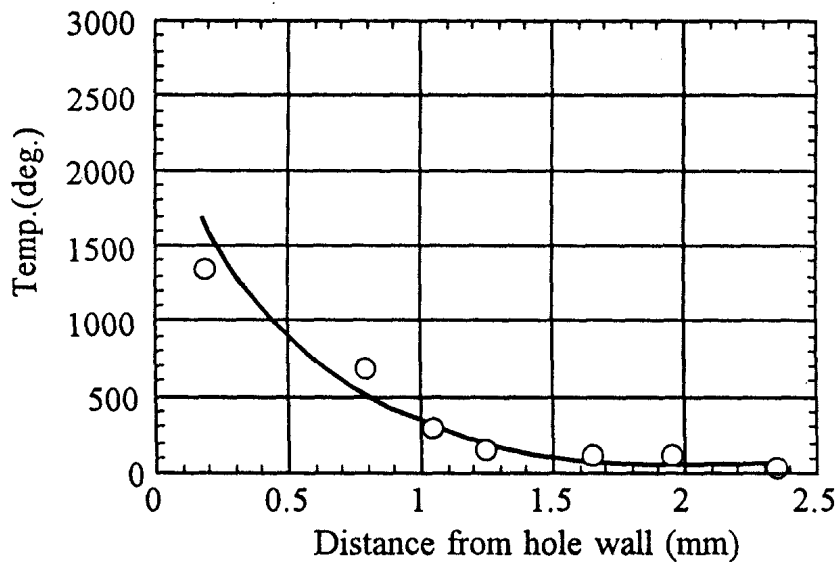


Fig.4: Maximum temperature and distance from hole wall (In the case of GFRP, Laser output power 150 W)

temperature indicates more than 1000 (1273 K). It is shown near the hole wall that the temperature is very high during laser drilling of GFRP.

Maximum Temperature in Laser Drilling

Fig.3 shows the relations between the maximum temperatures and the distances from the hole wall in laser drilling of the epoxy resin (in the case of the irradiation time 0.1s). Fig.4 shows the relations between the maximum temperatures and the distances from the hole wall in laser

drilling of GFRP (in the case of the irradiation time 0.5s). In the case of laser drilling of the epoxy resin , the thermal decomposition (pyrolysis) and the complete combustion of the epoxy resin are carried out in a moment and the heat affected damage hardly appears at the drilled hole wall [3]. From Fig.3, it is found that the maximum temperatures are low values nearest the hole wall, and the heat input is small from the hole wall in laser drilling of the epoxy resin. On the other hand, it is found from fig.4 that the temperatures are very high values near the hole wall, and the heat input is very large from the hole wall in laser drilling of GFRP. Moreover, the maximum temperature estimated from fig.4 nearest the drilled hole is approximately from 2500 to 3000 (from 2773 K to 2273 K) in drilling.

Damage after Laser Drilling

Fig.5(a) shows the microscope photograph of the hole entrance of GFRP after laser drilling in the case of the irradiation time 0.5s, and Fig.5(b) shows the glass cloth in drilled GFRP whose resin is vaporized at 600. This damage is hardly dependent on the fiber direction, because we can see the circle damage zone in Fig.5. By comparison of Fig.5(a) with Fig.5(b), we can see that the black substance in the heat affected damage is separated into the carbon (vaporization at 600) and others (no vaporization). The width of the former from hole wall is 0.8 mm and that of the latter is 0.3mm. Furthermore, by comparison of these widths with the maximum temperatures in Fig.4, it is found that the former area is from 500 to 1300 (from 773 K to 1573 K), and the latter area is more than 1300 (1573 K).

Details of the heat affected zones follow: the epoxy resin (low resolution point) is decomposed by the thermal conduction of the glass fibers at 500 (773 K), and then the pyrolytic carbon deposits on the glass fibers. Thus, the surface of the glass fibers turns to black. Additionally, the temperature of the glass fibers near the hole wall rises to more than melting point of the glass. At more than 1200 (1473 K) SiO_2 (glass fiber) is reduced to SiC by the carbon, and at more than 1500 (1773 K) the carbon varies to the graphite. As results, the carbon on the glass fibers varies to the graphite and SiC . This is the black zone in Fig.5(b). In other words, it is clear that these temperatures during drilling are dependent on the individual values of the material in the composites.

PREDICTION OF DAMAGE WIDTH

The heat affected zone is an important factor to consider the laser drilling as the new smaller diameter drilling method for the through hole. Therefore, it is necessary to estimate the distributions of the temperatures around the hole wall in various drilling conditions. So, the heat transfer analysis is carried out by FEM using boundary conditions based on above experiments.

Analytical Model

From experimental results, it is found that the heat transfer are more affected by the glass fibers than the epoxy resin in laser drilling of GFRP. So, we attract attention to the maximum temperatures at the hole wall during laser drilling, and to the properties of E glass as the material properties. In this model, the anisotropy of material properties is taken into no account, because the damage can be seen as the circle damage zone, and is hardly dependent on the fiber direction from Fig.5. The temperatures at the drilled hole wall is the sublimation temperature of SiC (2800) (3073 K) from Fig.4 . Other boundaries are insulated against the heat transfer, because the laser irradiation time is very short in laser drilling of PWB. The

specific gravity is 2.54, the thermal conduction rate is 1.04 W/mK, and the specific heat is 800 J/kgK. The radius of the drilled hole wall at the model is the radius of the spot diameter of a laser beam. The heat transfer analysis of the non-steady heat conduction is carried out by FEM on these boundary conditions.

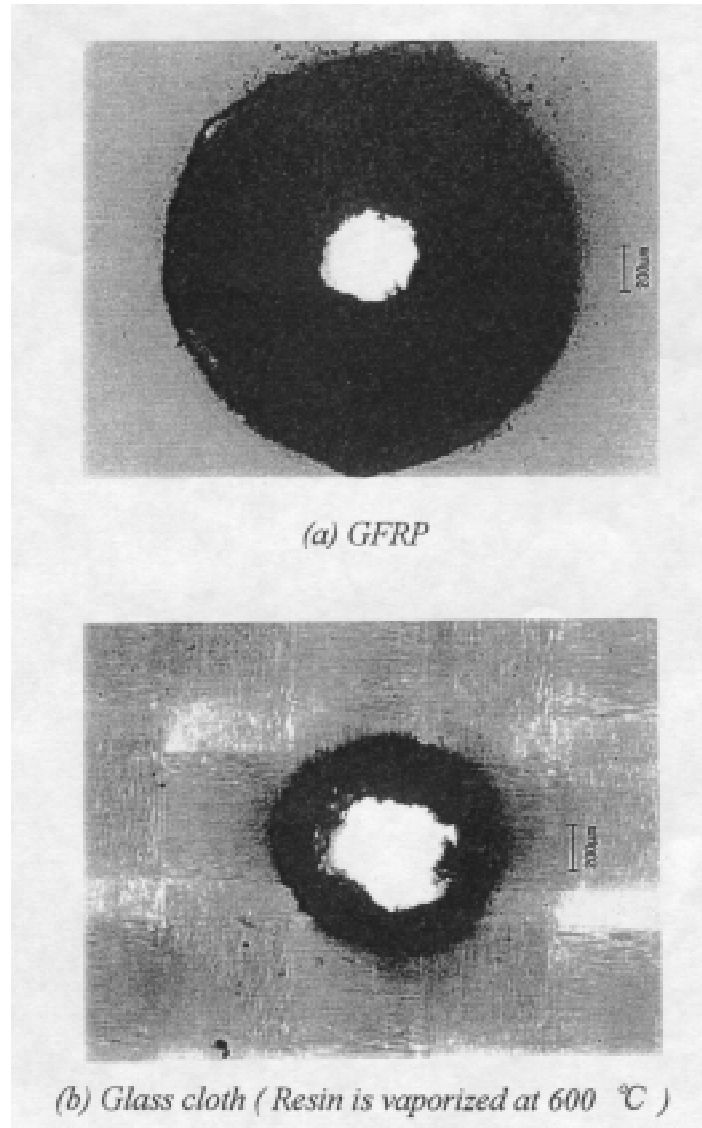


*Fig.5: Microscope photograph of hole entrance
(Laser output power 150 W, Irradiation time 0.5 s)*

Distributions of Temperatures

Fig. 6 shows the calculated results of the relations between the distances from the hole wall and the temperatures after 0.1s , 0.5s and 1.0s. Comparing Fig.4 and a calculated result after 0.5s, it is found that a calculated result is in good agreement with the experimental one. From these results, this model is effective to estimate the distributions of the maximum temperatures in laser drilling of GFRP.

Prediction of Damage Width

The black zone (carbonizing zone) in Fig.5(a) is an important area where the epoxy resin is decomposed, because this is an uneven area along the thickness of GFRP and a change in quality by the heat affect. Accordingly, this width has the influence on the reliability of the through hole plating of PWB. So, the prediction of heat affect damage widths is carried out using the calculated temperatures by this method.

That is: the areas more than 500 (773 K) are defined as the black zone (carbonizing zone) at calculated results in laser drilling. Fig.7 shows the calculated result and the microscope photograph of a experimental result in the same scale (irradiation time 0.5s and calculated after 0.5s). Fig.8 shows the relations between the irradiation time and the damage widths in the case of various laser output powers. From these figures, it is found that the damage widths after drilling of GFRP under various irradiation time can be predicted using the threshold of this temperature in this model.

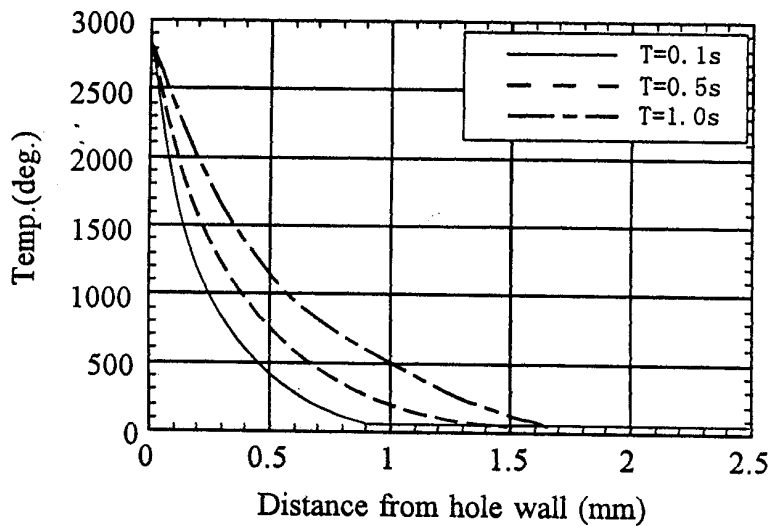


Fig.6: Calculated temperature and distance from hole wall

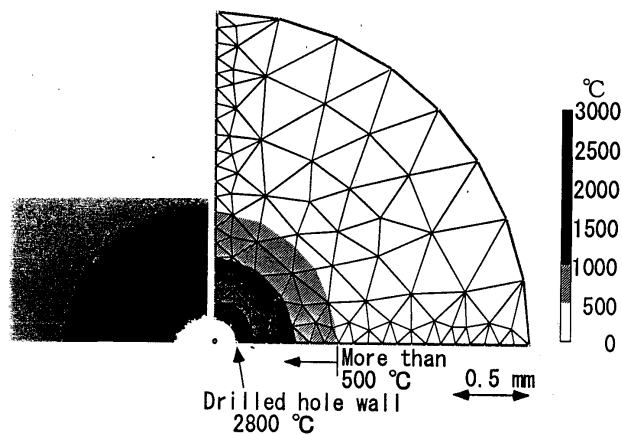


Fig.7: Comparison between experimental result and calculated one

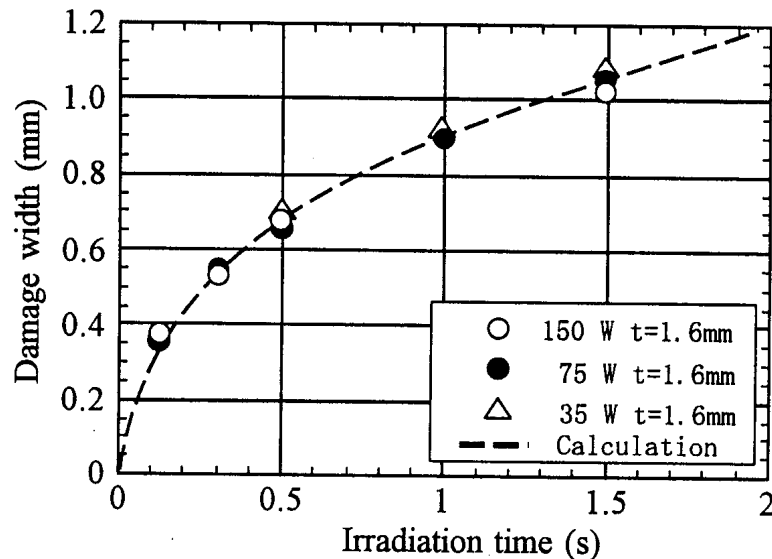


Fig.8: Damage widths and irradiation times

CONCLUSION

1. From measuring the temperatures in GFRP during laser drilling, it is found that the heat transfer from the hole wall causes an increase of the temperature around the hole. The temperatures are low values nearest the hole wall, and the heat input is small from the hole wall in laser drilling of the epoxy resin. On the other hand, the temperatures are very high values near the hole wall, and the heat input is very large from the hole wall in laser drilling of GFRP. The drilled hole temperature is approximately from 2500 to 3000 (from 2773 K to 2273 K) during drilling of GFRP.
2. Details of the heat affected zones become clear from the view point of the temperatures in laser drilling of GFRP: the epoxy resin (low resolution point) is decomposed by the thermal conduction of the glass fibers at 500 (723 K), and then the pyrolytic carbon deposits on the glass fibers. So, the surface of the glass fibers turns to black. Additionally, the temperature of the glass fibers near the hole wall rises to more than melting point of the glass. At more than 1200 (1473 K) SiO₂ (glass fiber) is reduced to SiC by the carbon, and at more than 1500 (1773 K) the carbon varies to the graphite.
3. The heat transfer is analyzed to predict the damage width (carbonizing zone) at the drilled hole wall using FEM. Specially, we attract attention to the maximum temperatures at the hole wall during laser drilling, and to the properties of E glass as the material properties. The temperature at the drilled hole wall is fixed at the sublimation temperature of SiC (2800) (3073 K) . Other boundaries are insulated against the heat transfer. As results, it is found that this model is effective to estimate the distributions of the maximum temperatures in laser drilling of GFRP. The damage widths after drilling of GFRP under various irradiation times can be predicted using the threshold of 500 (773 K) in this model.

REFERENCES

1. M. Dell'Erba, L.M. Galantucci and S. Miglietta, "An Experimental Study on Laser Drilling and Cutting of Composite Materials for the Aerospace Industry using Excimer and CO₂ Sources", *Composites Manufacturing*, Vol.3, No.1, (1992), 14-19
2. E.Aoyama, et al., "Study on Small Diameter Drilling in GFRP", *Composite Structures*, Vol.32, No.4, (1995), 567-573
3. H.Inoue, et al., "Study on Laser Drilling in PWB (Small Diameter Drilling in GFRP)", *Proceedings Tenth International Conference on Composite Materials*, Whistler, British Columbia, Canada, August 14-18, (1995), Vol.: Processing and Manufacturing , 573-580.

NUMERICAL ANALYSIS OF SHAPE FIXABILITY OF CONTINUOUS FIBRE REINFORCED THERMOPLASTICS

R.J. Dykes, D.P.W. Horrigan, D. Bhattacharyya

*Composites Research Group, Department of Mechanical Engineering,
University of Auckland, Private Bag 92019, New Zealand.*

SUMMARY: Continuous fibre-reinforced thermoplastic (CFRT) sheet materials have enjoyed a steady rise in popularity over recent times which can be largely attributed to the way they lend themselves to low-cycle-time manufacturing applications. In many of these rapid forming operations the actual process cycle is dominated by the time required to cool the moulded component to an appropriate final temperature. In such processes, the applied surface cooling rate can have a significant influence on the geometric conformance of the component as well as its internal stress state. This paper examines the applicability of the finite element (FE) method to predict the effects of a number of different cooling scenarios on the distortion incurred during the most commonly encountered deformation process in sheet forming, bending. A finite element model is developed to investigate the springforward phenomenon in composite sections which are subject to various cooling rates. The model goes some way toward accounting for the temperature dependent material property variation during cooling. Finally the results obtained from the numerical model are compared to those achieved from experiments. The implications of these results are discussed in the context of real manufacturing processes, such as deep drawing and roll forming.

KEYWORDS: springforward, shape fixability, cooling rate, continuous fibre reinforced thermoplastic, finite elements, roll forming.

INTRODUCTION

Continuous fibre-reinforced thermoplastic composites have established themselves as tough, reliable, cost effective alternatives to various other traditional structural materials such as aluminum and even their thermosetting cousins. Their most significant advantage lies in their ability to undergo rapid curing cycles from the melt which are largely dependent on the temperature and only moderately dependent on any chemistry effects. This unique characteristic has provided the opportunity to apply rapid and economical manufacturing methods along the same lines as those used in one of the most pervasive of all manufacturing industries - sheet metal forming.

Already a good deal of success has been achieved in the development of fast, efficient, processing methods which go some way to realising the full benefits of thermoplastic composite materials [1,2]. An example of one of these processes is roll forming [3], which is presently in the early stages of development, but has already demonstrated the potential for continuous production at relatively high line speeds. Figure 1 demonstrates some of the possible profiles which may be achieved ranging from simple open sections to more complex closed sections. One key area of concern though in a process like roll forming is the development of residual stress and distortion in a formed components as they cool from the forming temperature. The elevated processing temperatures, and the large differences which exist between the thermoelastic properties of the matrix and fibres in directional polymeric composites leads to an inevitable build up of residual stress and subsequent distortion during cooling. The deviation from a components intended shape can render it useless, while the residual stress state can act to severely limit both the static and dynamic strength of the part. The accurate prediction of the final shape of a formed part and its residual stress state are therefore essential to the design and performance of composite structures.

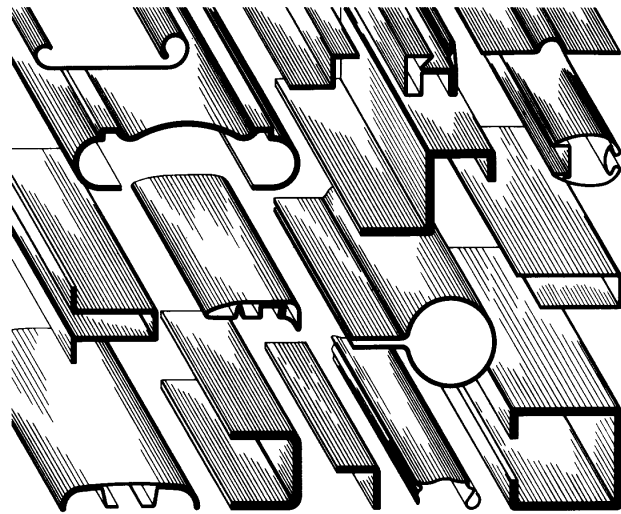


Fig. 1: Typical roll formed profiles.

Generally, models of forming processes for thermoplastic composite systems only consider one phase of the material. In the case of forming the matrix remains in a molten state and the material behaviour is considered to be viscous [4,5], or more generally viscoelastic [6]. On the other hand, models which are developed to account for the distortion of a formed component as it cools from its molten state often assume thermoelastic behaviour [7]. Analytical two phase models have been suggested by Ruddock [8] and more recently by Ruddock and Spencer [9] who have developed a model which accounts for the solidification front through a cylindrical channel section in plane strain. As expected, their analysis suggests that the residual stresses and distortion may be minimised by allowing the cooling rate to tend to zero.

The present study is primarily concerned with the concept of *shape fixability*, a generic term used to define how well a component conforms to its intended geometry after deformation. To facilitate this investigation, a set of simple bending experiments has been performed. The effect of various cooling rates on the final shape of the formed strips is examined by measuring the deviation from the part's intended geometry, or *springforward*. It is to be noted that the term '*springforward*' used in this study refers to a decrease in the enclosed part angle, as opposed to '*springback*' which is commonly associated with metallic sheet. In addition to the experimental study, a numerical analysis has been undertaken in an attempt to model the effect of cooling rate on the distortion encountered during solidification and cooling. The numerical model has been formulated to account for the material property variation during cooling. Although the model makes a number of bold simplifying assumptions regarding the

material behaviour at elevated temperatures, it does serve as a useful basis for further two phase modelling using numerical techniques.

DESCRIPTION OF MODEL

The first part of the modelling to be undertaken was that of a simple thermoelastic analysis which was formulated along the same lines as the model of Zahlan and O'Neill [7]. In this analysis a 4mm thick bend region (formed to an inner radius of 10mm) was modelled as a transversely isotropic elastic solid. In keeping with their approach, the part was constructed in a cylindrical coordinate (r, θ) reference frame with supports applied along the vertical face for which $\theta = 90^\circ$. For this model the thermal loading was applied in the form of prescribed initial and final element temperatures. It should be noted that this type of loading case assumes homogenous cooling and thus ignores any thermal gradients which would be present in an actual cooling process.

In addition to the model described above, a more rigorous analysis was undertaken, involving both a transient description of the temperature variation as well as a structural analysis to compute the thermally induced stresses and strains as a function of time. The model was divided into two parts, the first dealing with the transient temperature variation in the formed part as it cooled, and secondly, an incremental stress strain analysis to compute the part's response to the applied thermal loading. The heat flux associated with the deformation was assumed to be negligible so that the transient field analysis could be performed independently. The coupling of both the field and structural analyses was performed by way of a data transfer file (DTF) as illustrated in Figure 2.

Cooling was applied to the outer surfaces of the formed part at various rates which roughly corresponded to (i) quenching, $h = 100 \text{ W/mm}^2\text{K}$, (ii) rapid cooling, $h = 50 \text{ W/mm}^2\text{K}$, and (iii) slow cool, $h = 10 \text{ W/mm}^2\text{K}$.

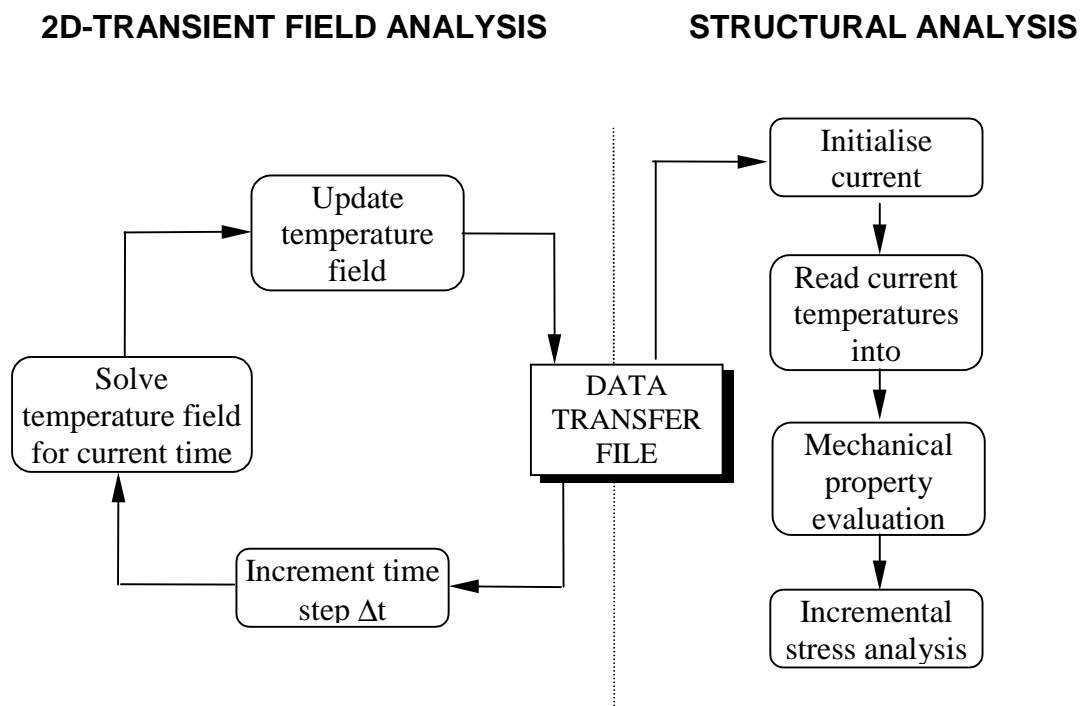


Fig. 2: Coupling of the transient field analysis and the structural analysis.

In order to model the two phase nature of the composite as it cooled from the melt, a number of simplifying assumptions has to be made regarding its constitutive behaviour. Ideally, the

numerical model would be formulated along the same lines as that of Ruddock and Spencer's [9] two phase model which idealises the molten phase as an 'anisotropic thermoelastic liquid'. Unfortunately this type of material definition is unavailable using many of the commercially available FE packages, including the LUSAS FE system used in this study. This meant that certain simplifying assumptions had to be made regarding the material response at elevated temperatures. It was decided that the closest approximation to the behaviour could be achieved using an anisotropic plastic hardening material model. While this assumption casts some doubts over the legitimacy of the results, particularly the development of stress in the part, it does address some of the issues regarding temperature dependent material property variation. More importantly, the model provides a basis from which further numerical modelling may be developed.

EXPERIMENTAL DETAILS

The experimental program consisted of a set of simple single axis, 90° bending tests which were performed using PLYTRON[®], a continuous glass fibre/polypropylene thermoplastic composite with a nominal fibre volume fraction of 35%. The single curvature bending specimens were constructed from 8 plies of prepregged sheet material giving a nominal thickness of 4mm. Figure 3 illustrates the dimensions of the samples and the intended geometry after deformation. The bending experiments were conducted over a variety of forming temperatures ranging from 180 to 140°C. In each case the same heating sequence was adopted; namely the samples were heated initially to 180°C and held for a period of 10 minutes. Once a stable environment had been reached each sample was cooled in a controlled manner to the desired forming temperature. After the specimen was formed to 90°, the strip was cooled using one of three cooling rates: i) slow (~2 °C/min) ii) moderate (~15 °C/min) iii) rapid (~60 °C/min). The cooling rate in each sample was monitored by a K-type thermocouple embedded within laminate.

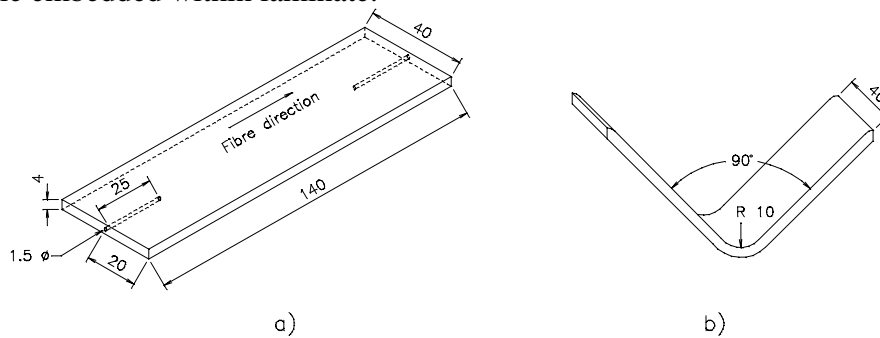


Fig. 3: a) Test sample dimensions, b) Intended geometry of deformed sample.

RESULTS AND DISCUSSION

The result of the thermoelastic analysis is illustrated in Figure 4 where the springforward effect is demonstrated as the bend region cools from a forming temperature of 180°C to room temperature. Since the formed part is not constrained by any tooling and consists entirely of unidirectional plies, the solution is independent of any of the specified elastic material parameters. The numerically predicted result is a change in the enclosed part angle of approximately 1.5° which is well short of the experimentally observed results detailed in Table 1. Somewhat surprisingly, the springforward in these experiments was found to be largely independent of the forming temperature. On the other hand the applied surface cooling rate was found to significantly influence the final shape, suggesting that the majority of the

distortion was incurred as the material underwent a phase change and subsequently cooled to room temperature.

The relationship commonly used to predict the springforward in anisotropic materials formed to angle θ can be simply written as

$$\Delta\theta = (\alpha_r - \alpha_l)\theta\Delta T \quad (1)$$

where ΔT is the temperature range over which cooling takes place and α_r and α_l are the coefficients of thermal expansion in the radial and longitudinal directions respectively. The poor agreement between the experimental results and equation (1) raises some interesting questions, particularly in light of the results of Zahlan et al. [6] who achieved good correlation with CF/PEEK material. Two interesting differences to note when comparing PP and PEEK composites are the respective temperatures at which they are processed, and also the material behaviour as they cool. PEEK is typically processed at around 400°C and exhibits a viscous type of behaviour over a relatively short temperature range when cooling from the melt. In other words the material remains essentially elastic over the majority of the cooling stage. On the other hand, PP composite materials have a relatively wide forming window and can be processed at temperatures as low as 110°C during cooling before they begin to solidify [2]. Only during a relatively short proportion of the cooling stage does the material behave like an elastic solid. It is therefore suggested that for the class of composite used in this study, a thermoelastic model by itself may be insufficient to predict the distortion incurred during cooling. The material property variation, a result of transient temperature field, necessitates a more complex model which can account for the transitional behaviour between the molten and solid phases.

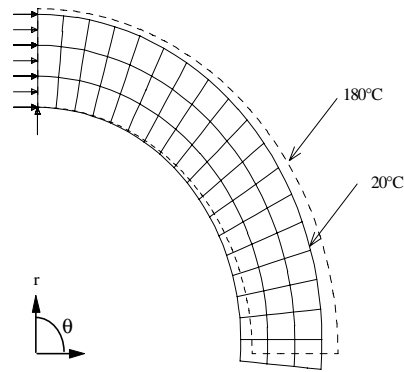


Fig. 4: Springforward predicted by the thermoelastic model upon cooling.

Table 1: Springforward of formed parts for various forming temperatures and cooling rates.

Cooling Rate	Forming Temperature				
	140°C	150°C	160°C	170°C	180°C
Slow	6.0°	5.9°	5.4°	5.3°	5.5°
Moderate	-	-	-	-	6.3
Rapid	-	-	-	-	7.4

From the results detailed in Table I, it is clear that the cooling rate has a significant influence on the magnitude of the springforward. With this in mind a thermo-mechanically coupled analysis was undertaken in an attempt to model this effect. The results of this analysis are presented in Figure 5. The distortion, or springforward $\Delta\theta$, has been plotted against the applied surface cooling rate. As the cooling rate is increased, it can be seen that the model begins to describe the response more effectively than the thermoelastic model. Although the trend is favorable, the magnitudes of the distortions are still considerably lower than what was observed experimentally. In light of the assumptions made regarding the material behaviour, this is understandable and a revised description of the thermorheological response may well give better correlation to the experimental results.

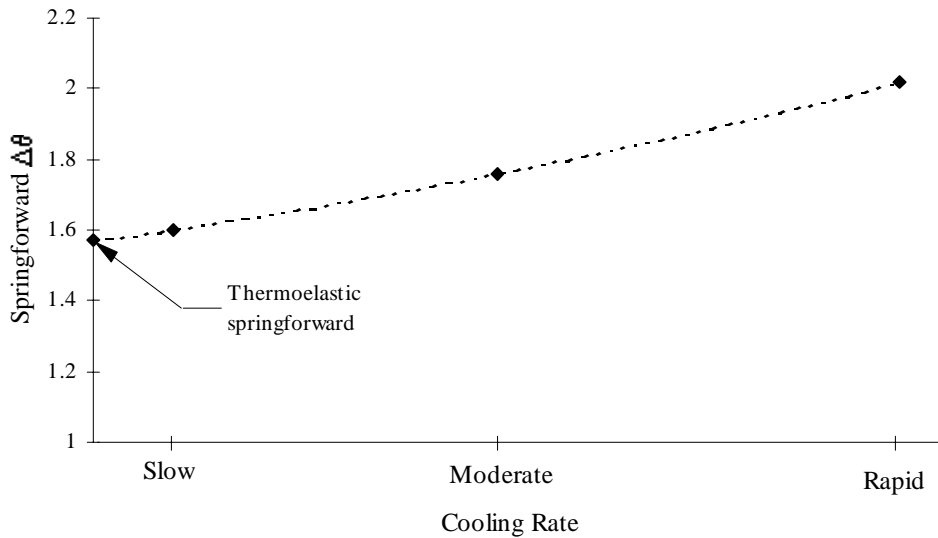


Fig. 5: Effect of cooling rate on spring forward in PLYRON sections formed to 90°.

The emphasis of this paper has been on modelling the springforward phenomenon which represents a physically measurable quantity. The residual stress state of a part is also an important quantity which affects the integrity but is infinitely more difficult to measure in a practical sense. While no attempt has been made here to characterise the stress state of the parts formed in these experiments, the residual stresses have been shown by others to be relatively slight in comparison to those values reported for carbon fibre/PEEK [10]. Cuff suggests that this might well be a result of the glass transition temperature T_g of PP being well below room temperature [10]. It is interesting to note that over three quarters of the residual stress in CF/PEEK is developed between T_g and room temperature [11]. It could be argued that realisation of the intended shape of a component manufactured from PLYTRON may be more of a concern than the internal stresses within the actual part.

Distortion of formed parts is something that cannot be avoided due to the elevated processing temperature requirements of thermoplastic composites. However, with the clever use of numerical modelling tools it can be predicted and accounted for at the design stage of a process. This is very important and could significantly reduce the time and expense associated with trial and error approaches. Like other processes, roll forming must address the issue of shape fixability if quality profiles, which meet strict tolerances are to be produced. As in standard die forming operations, the rolls, like the dies, may be exactly designed to account

for the distortion, or springforward incurred during cooling. For instance a set of rolls may be designed to underbend a particular section, as shown in Figure 6, in anticipation that it would adopt its desired shape upon cooling. In addition, the cooling rate may be conveniently managed by applying external heating or cooling devices between each forming station to alleviate large thermal gradients which have been shown in this study to also significantly influence the final shape of a component.

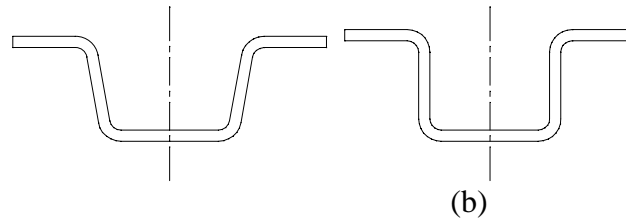


Fig. 6: Distortion of channel section (a) underbent shape prior to cooling, (b) final shape after cooling.

The implications of these results are extremely important from a manufacturing perspective as they indicate that increased conformance of a shaped component may be achieved by allowing it to cool at a relatively slow rate during the solidification period. Accepting that a cooling rate which approaches zero is both practically and economically unfeasible, the key issue that faces producers of real parts would seem to be how fast can a component be cooled without compromising its integrity. While the answer to this depends on the particular circumstances, it seems appropriate to point out, that for the class of material investigated in this study, the thermorheological behaviour has a significant bearing on the final shape of the part. Lastly it is important to note that the results presented here should not detract from the obvious benefits these materials possess, however they do point towards the need to consider very carefully the effect that cooling rate has on the shape fixability.

CONCLUSIONS

A set of simple bending tests have been performed on strips of directional glass fibre/polypropylene composite to determine the effect of forming temperature and cooling rate on the resulting distortion. The springforward in each strip was observed to be largely independent of forming temperature but highly dependent on the applied cooling rate. Samples cooled at a rapid rate were found to distort to a greater extent than samples which were allowed to cool slowly.

A finite element analysis has also been performed in an attempt to model the experimentally achieved springforward results. The first analysis idealised the formed part as a thermoelastic orthotropic solid. Unlike the results obtained for carbon fibre/PEEK, the correlation between the model and experimental results was unacceptably poor with an under prediction of around 3.5° . This has been attributed to the material property variation, a result of the transient temperature field, around the solidification period. Further modelling was then undertaken in an attempt to account for the temperature and material property variation in the part. The results of this analysis proved to be more effective in terms of modelling the cooling rate dependence although the magnitudes obtained failed to match with those achieved experimentally. It should be noted that this type of analysis appears to be extremely difficult

to tackle using many of the commercially available FE packages. However the model presented here does provide a useful basis for further work to be undertaken in this area.

The results indicate the use of slower cooling might be beneficial in producing parts with greater conformance to that of their intended geometry. This has to be acknowledged by manufacturers using materials such as PLYTRON which possess many other advantages, including lower melt temperature and a significantly large processing window.

REFERENCES

1. Offringa, A. R. 'Industrial Report: Thermoplastic composites - rapid processing applications', *Composites: Part A*, 27A, pp. 329-336 (1996).
2. Martin, T.A., Bhattacharyya, D., 'Rapid manufacturing of thermoplastic composite section by roll forming', *Australasian Conference on Technology for Manufacturing*, Massey University, Palmerston North, New Zealand, February, 1997.
3. Mander, S. J., Bhattacharyya, D., 'Roll forming of fibre-reinforced thermoplastic composites', *Proceedings of ICCM-10*, Vol. III: Processing and Manufacturing, Whistler, B.C. Canada, pp. 413-420, 1995.
4. Martin, T.A., Bhattacharyya, D. and Collins, I.F. 'Bending of fibre-reinforced thermoplastic sheets', *Composites Manufacturing*, 6, pp. 177-187, 1995.
5. Dykes, R.J., Martin, T.A., Bhattacharyya, D., 'Determination of longitudinal and transverse shear behaviour of continuous fibre reinforced thermoplastics from vee-bending', *Proceedings of Flow Processes in Composite Materials*, Aberystwyth, Wales, 1996.
6. Mander, S.J., Bhattacharyya, D., Collins, I.F., Watson, P., 'Linear visco-elastic characterisation of transverse flows of fibre-reinforced thermoplastic composites, submitted to *Composites Manufacturing*, 1995.
7. Zahlan, N., O'Neill, J.M., 'Design and fabrication of composite components; the spring-forward phenomenon', *Composites* 20, Num. 1, January 1989.
8. Ruddock, G.J., 'An elasticity approach to the solidification of fibre-reinforced shells, Submitted to the *Journal of Elasticity*, 1995.
9. Ruddock, G.J., Spencer, A.J.M., 'Effect of cooling rate on the solidification of a cylindrical channel section', *Proceedings of Flow Processes in Composite Materials*, Aberystwyth, Wales, 1996.
10. Cuff, G., 'Fibre-reinforced industrial thermoplastic composites', Woodhead Publishers Ltd., Cambridge, UK, 1995.
11. Nairn, J.A., Zoller, P., 'Residual thermal stresses in semicrystalline thermoplastic matrix composites', 5th International Conference on Composite Materials ICCM-5, pp. 931-946. 1985.

SECONDARY STRUCTURE EFFECTS ON THE PROCESS-INDUCED RESIDUAL STRESS DEVELOPMENT OF CYLINDER STRUCTURE

Yeong K. Kim¹ and Scott R. White²

¹*Korea Institute of Aeronautical Technology, Korean Air,
Jonmin-Dong 461-1, Yoosung-Gu, Daejun 305-390, Korea*

²*Dept. of Aeronautical and Astronautical Engineering, University of Illinois,
306 Talbot Lab, Urbana, Il 61801, U. S. A.*

SUMMARY: In this paper the viscoelastic analysis on the process-induced residual stresses of cylindrical structure by filament winding process is presented. The focus was on the effects of the secondary structures such as teflon tape and mandrel on the final residual stress. The material used in this study was Hercules AS4/3501-6 prepreg system. The material behavior of 3501-6 epoxy during cure was modeled by a series of stress relaxation tests for the viscoelastic constitutive equations of the composite during cure. A finite element method was used to calculate the residual stresses, and the results at the selected time during cure cycle are shown to understand the mechanism of stress development. It was found that small final residual stresses are developed when the material with high Young's modulus and thermal expansion coefficient is used for the mandrel structure .

KEYWORDS: filament winding, thermoset composites processing, residual stresses, viscoelasticity, stress relaxation

INTRODUCTION

The stress free states at cure temperature has been widely assumed for the process-induced residual stress analyses of polymer matrix fiber-reinforced composite structures. Figure 1 shows dynamic mechanical analysis on fully cured Hercules AS4/3501-6 composite. In this Figure, the glass transition temperature of fully cured specimen is 213°C. Reflecting the fact that the cure temperature of this material is 177°C, it is questionable that full stress relaxation of the residual stress occurs at the cure temperature. Recent studies on the viscoelastic residual stress analyses of AS4/3501-6 laminated plates [1-5] showed that the temperature-degree of cure-dependent relaxation behavior as well as the resin shrinkage during cure had a great influence on the final residual stress development. In the case of cylindrical structures manufactured by filament winding, the interaction between the mandrel and the composite structure makes the residual stress development problem much more complex.

The filament winding process is commonly composed of the three steps: 1) winding the composite tows onto a mandrel structure, 2) curing, 3) cooldown and removing the mandrel. After winding, the composite and the mandrel structure is placed in an oven or autoclave to cure the composite structure. The cure processing is very similar to the laminate case except for the additional constraints due to the mandrel structure. Numerous studies have examined process-induced residual stresses of cylindrical structures [6-14]. However, their solutions

were based on the elastic approach. When the entire cure cycle was considered, assumption of either a simple linear relationship between degree of cure and the mechanical properties of composite [11,12], or a step function to describe the increase in composite material properties after gelation was taken [13,14]. For the case of cylindrical structures, apparently no viscoelastic analysis of process-induced residual stresses including the mandrel effect has been attempted.

In this study viscoelastic process-induced residual stresses in cylindrical composite structures are analyzed. The thermorheologically complex model for AS4/3501-6 prepreg system developed in the previous works [1-5] was used for the constitutive equation. The residual stress development of the cross-ply cylinder structure by autoclave cure process was investigated. The slip effect of teflon film between mandrel and composite structure was taken into account. Young's modulus and the thermal expansion coefficient were changed to examine the mandrel property effect. The results were compared to each other to find the condition for small final residual stresses in the composite structure.

During consolidation fibers move inward in the radial direction and resin percolates outward. There is a loss of fiber tension as this process occurs. In the following analysis the effect of winding tension is assumed to be negligible.

VISCOELASTIC CONSTITUTIVE EQUATION

In the previous study [1,4], the most general expression for the constitutive relationship of an anisotropic viscoelastic material during cure in matrix form was presented such that

$$\sigma_i(t) = \int_{-\infty}^t Q_{ij}(t, \tau) \frac{\partial}{\partial \tau} (\varepsilon_j(\tau) - \tilde{\varepsilon}_j(\tau)) d\tau \quad (1)$$

Here, σ_i is the stresses and ε_j and $\tilde{\varepsilon}_j$ are total strains and non-mechanical strains, respectively. The present and past times are t and τ , respectively. The time dependent effects in the stiffness matrix Q_{ij} can be temperature, moisture, degree of cure and all other factors which have influence on the material property during cure. If the cure process is spatial dependent, Q_{ij} is also a function of location.

The non-mechanical strains $\tilde{\varepsilon}_j$ in the polymer matrix composite cure process can be described as

$$\tilde{\varepsilon}_j(\tau) = \phi_j(\alpha, T, M) \Delta T(t) + \beta_j(\alpha, T, M) \Delta M(t) + \gamma_j(\alpha, T, M) \Delta \alpha(t) \quad (2)$$

ϕ_j = effective thermal expansion coeff.

β_j = effective moisture expansion coeff.

γ_j = effective chemical expansion coeff.

ΔT = change in temperature

ΔM = change in moisture concentration

$\Delta \alpha$ = change in degree of cure

Equation (1) can be simplified to time-superposition integration form if the material shows thermorheologically simple behavior to temperature and moisture at a constant degree of cure α_c . With this assumption and if there is no strain history before $t=0$, equation (1) can be rewritten as anisotropic linear viscoelastic constitutive equation such that

$$\sigma_i(t) = \int_0^t Q_{ij}(\alpha_c, \xi - \xi') \frac{\partial}{\partial \tau} (\varepsilon_j(\tau) - \tilde{\varepsilon}_j(\tau)) d\tau \quad (3)$$

where,

$$\xi = \int_0^t \chi[\alpha_c, T(s), M(s)] ds \quad (4)$$

$$\xi' = \int_0^\tau \chi[\alpha_c, T(s), M(s)] ds \quad (5).$$

In equations (4) and (5), χ is the shift function and is a function of degree of cure, temperature and moisture, and s is the time integration variable. This research is based on equation (3), which implies that the material is assumed to be thermorheologically simple at constant degree of cure.

For simplicity, the following notation is adopted such that

The caret on the variables signifies the principal axes condition. The principal axes r , θ and l of the cylinder are shown in Figure 2. If the cylinder structure is axisymmetric and each layer is transversely isotropic, equation (6) is expressed as the matrix form such that

$$\begin{Bmatrix} \hat{\sigma}_l \\ \hat{\sigma}_\theta \\ \hat{\sigma}_r \\ \hat{\sigma}_{l\theta} \end{Bmatrix} = \begin{bmatrix} \hat{Q}_{11} & \hat{Q}_{12} & \hat{Q}_{12} & 0 \\ \hat{Q}_{12} & \hat{Q}_{22} & \hat{Q}_{23} & 0 \\ \hat{Q}_{12} & \hat{Q}_{23} & \hat{Q}_{22} & 0 \\ 0 & 0 & 0 & \hat{Q}_{44} \end{bmatrix} \begin{Bmatrix} \hat{\varepsilon}_l \\ \hat{\varepsilon}_\theta \\ \hat{\varepsilon}_r \\ \hat{\varepsilon}_{l\theta} \end{Bmatrix} \quad (8)$$

where,

$$\begin{aligned} \hat{Q}_{11} &= \frac{1 - v_{r\theta}v_{\theta r}}{\Lambda} \hat{E}_l \\ \hat{Q}_{12} &= \frac{v_{lr} + v_{rl}v_{r\theta}}{\Lambda} \hat{E}_l \\ \hat{Q}_{22} &= \frac{1 - v_{rl}v_{lr}}{\Lambda} \hat{E}_\theta \\ \hat{Q}_{23} &= \frac{v_{r\theta} + v_{l\theta}v_{rl}}{\Lambda} \hat{E}_\theta \\ \hat{Q}_{44} &= \hat{G}_{12} = \hat{G}_{13} \\ \Lambda &= 1 - v_{rl}v_{lr} - v_{l\theta}v_{\theta l} - v_{r\theta}v_{\theta r} - 2v_{l\theta}^2v_{r\theta} \end{aligned} \quad (9).$$

Therefore, the independent time-dependent engineering properties are

$$\hat{E}_l, \hat{E}_\theta = \hat{E}_r, v_{l\theta} = v_{lr}, v_{\theta r}, \hat{G}_{l\theta} = \hat{G}_{rl} \quad (10).$$

In the previous studies [1,3,4], the stress relaxation behavior of 3501-6 epoxy resin system during cure was modeled in a thermorheologically complex manner by a series of stress relaxation tests. On the basis of this model the stress relaxation model of AS4/3501-6 graphite/epoxy composite was developed. For AS4/3501-6 graphite/epoxy composite, it was assumed that the material behavior was thermorheologically simple at constant degree of cure,

and the effective time-dependent stiffnesses were modeled using a series of exponential function such that

$$\hat{Q}_{ij}(\alpha, \xi) = \hat{Q}_{ij}^{\infty} + \sum_{\omega=1}^N \hat{Q}_{ij}^{\omega} \exp\left(-\frac{\xi(\alpha, T)}{\eta_{\omega}(\alpha)}\right) \quad (11)$$

where $\hat{Q}_{ij}^{\omega} = \hat{Q}_{ij}^u - \hat{Q}_{ij}^{\infty}$ and \hat{Q}_{ij}^u is elastic stiffness and \hat{Q}_{ij}^{∞} is equilibrium stiffness. η is discrete relaxation time, and is a function of degree of cure. The reduced parameter ξ was modeled as a function of degree of cure as well as temperature. The layer was assumed as transversely isotropic, and the four independent elastic stiffness are listed in Table 1. Each stiffness was modeled by ten term exponential series, and the equilibrium stiffness was calculated using partition factor $R = 1/7$ based on the stress relaxation test result of fully cured AS4/3501-6 composite [1]. Since the properties in the fiber direction are essentially time-independent, \hat{Q}_{11} and \hat{Q}_{12} in Table 1 were assumed to be constant. The remaining stiffnesses were assumed to relax according to the same shift function.

FINITE ELEMENT FORMULATION

In previous works [3,4], a finite element model was developed for the AS4/3501-6 laminate cases. Similar formulation was used in the cylinder structure case .

A recursive formulation presented by Taylor et al. [15] was applied to account for the degree of cure effect as well as to overcome large memory storage problem in solving the time superposition integration equation (3). To adopt the method, the derivative of the global displacement and the thermal-chemical strains were assumed to be piecewise linear during each time interval. Additionally, the degree of cure α is assumed constant during each time interval so that

Table 1: Elastic stiffness, thermal and chemical expansion coefficient of fully cure AS4/3501-6 cylinder in the principal directions

Q_{11} (GPa)	127.4
Q_{12} (GPa)	3.88
Q_{22} (GPa)	10.0
Q_{44} (GPa)	2.57
ϕ_i ($\mu\epsilon/^{\circ}\text{C}$)	0.5
$\phi_r = \phi_{\theta}$ ($\mu\epsilon/^{\circ}\text{C}$)	35.3
γ_i ($\mu\epsilon$)	-167
$\gamma_r = \gamma_{\theta}$ ($\mu\epsilon$)	-8,810

Table 2: The material properties of aluminum, teflon film and steel

	E (GPa)	ν	ϕ ($\mu\epsilon/^{\circ}\text{C}$)
Aluminum	72.4	0.3	23.6
Steel	200	0.3	11.3
Teflon Film	same with mandrel	0.3	same with mandrel

Here, $\alpha(\bar{t}_k)$ is obtained separately through thermo-chemical model of the composite. The detailed formulation is presented in reference [1].

Since the cylinder structure is assumed to be axisymmetric, the strains in this case are calculated from

$$\begin{aligned}\varepsilon_r &= \frac{\partial u}{\partial r} \\ \varepsilon_l &= \frac{\partial w}{\partial l} \\ \varepsilon_\theta &= \frac{u}{r} \\ \varepsilon_{rl} &= \frac{\partial u}{\partial l} + \frac{\partial w}{\partial r}\end{aligned}\quad (13).$$

To consider the mandrel effect, the elastic response of the mandrel material must be combined with the composite structure. In addition, a thin teflon film is used to separate the composite structure and mandrel after cure. Since the film material allows slip to occur in the l -direction, a stress discontinuity is introduced in this direction. Slip elements were inserted between the mandrel and composite structure to simulate the effects of the film.

The mandrel and film materials are assumed to be composed of elastic materials with the constitutive equations such as

$$\begin{Bmatrix} \sigma_l \\ \sigma_\theta \\ \sigma_r \\ \sigma_{lr} \end{Bmatrix} = \begin{bmatrix} d_{11} & d_{12} & d_{13} & 0 \\ d_{12} & d_{22} & d_{23} & 0 \\ d_{13} & d_{23} & d_{33} & 0 \\ 0 & 0 & 0 & d_{44} \end{bmatrix} \begin{Bmatrix} \varepsilon_l \\ \varepsilon_\theta \\ \varepsilon_r \\ \varepsilon_{lr} \end{Bmatrix}\quad (14).$$

The stiffnesses are expressed as

$$\begin{aligned}d_{11} = d_{22} = d_{33} &= \frac{E(1-\nu)}{(1+\nu)(1-2\nu)} = d_1 \\ d_{12} = d_{13} = d_{23} &= \frac{E\nu}{(1+\nu)(1-2\nu)} = d_2 \\ d_{44} &= \frac{E}{2(1+\nu)} = d_3\end{aligned}\quad (15)$$

where E and ν are Young's modulus and Poisson's ratio, respectively. All properties of mandrel and teflon film were assumed to be constant throughout the cure cycle. A thin teflon film covers the surface of the mandrel and this film, in general, is viscoelastic. However, since the thickness of the teflon in r -direction is negligible compared to the mandrel, the stress relaxation behavior of the teflon can be neglected. Additionally, the thermal expansion coefficient of the teflon is assumed to be same as that of the mandrel material. In the analysis, only d_{33} in equation (14) is given a non-zero value for the teflon elements. All the material properties used in the finite element analysis for the mandrel and teflon film are listed in Table 2. Whenever the radial stress at the interface between the composite cylinder and the

mandrel structure became tensile ($\sigma_r \geq 0$), the value of d_{33} was reduced to 10^{-9} GPa in order to simulate the separation effect between the mandrel and cylinder.

In this analysis, the moisture effect is neglected and the effective thermal and chemical expansion coefficients are assumed to be constant during cure. The effective thermal expansion coefficients for the composite cylinder are listed in Table 1.

To consider the chemical shrinkage effect, the volume shrinkage is modeled by a linear expression as

$$V_{ch}(\alpha) = V_{ch}^T \alpha \quad (16)$$

where V_{ch}^T is total volumetric shrinkage of the resin. A typical value of 5% for V_{ch}^T for epoxy was assumed for the chemical shrinkage strain. The corresponding effective chemical shrinkage coefficients are calculated by a self-consistent micromechanical model [16], and they are listed in Table 1.

In the reference [1], the effect of the cure dependent equilibrium modulus was studied for thin laminate cases. It was found that the cure dependency of the equilibrium stiffness did not have significant effect on the final residual stress. Therefore, it was assumed that the equilibrium stiffnesses were constant during cure in this study.

NUMERICAL STUDIES

In the results which follow the stacking sequence for the cylinder structure in Figure 2 was $[mandrel/teflon\ film/0^\circ/90^\circ]_T$. The thickness of the mandrel structure (mandrel and teflon) was chosen to be equal to 1/3 of the total cylinder structure thickness. In this case $h=3h_m$. The thickness of the teflon film was 1% of the mandrel structure thickness. The structural geometry considered is a thickness to mean diameter ratio of $r_c/b=13$ with an aspect ratio a/b of 3. Due to the symmetry of the cylinder structure, only a quarter of the section was analyzed, and the following results are at $l=0$.

Figure 3 shows the temperature cycle and corresponding degree of cure history for the MRC cycle. The temperature of the first dwell is 116°C for one hour. In the second dwell, the temperature is 177°C for 2 hours. $2.5^\circ\text{C}/\text{min}$ was equally applied to the increase and the decrease rate of the temperature of the cure cycle. With this temperature cycle, degree of cure advancement was calculated on the basis of the thermo-chemical cure kinetic models for AS4/3501-6 composite in the references [17]. It was assumed that the temperature and degree of cure are changed uniformly through the thickness of the composite structure during cure. The corresponding stress distributions are shown at nine specific times (37, 96, 121, 181, 240, 256, 274, 290 and 302 minutes) throughout the cure cycle in the figures which follow. These times are overlaid on the cure cycle in Figure 3.

Figures 4-9 represent the stress developments during cure cycle. In this case the mandrel material is aluminum. Figures 4 and 5 show the radial stress profile developments during cure. To the start of cure temperature at 121 min, the stress distribution in the cylinder structure is compressive. During cure from 121 min to 181 min, the compressive stress is slightly changed due to the resin shrinkage effect. As the temperature is decreased during cooldown stage, the stress distribution is changed from compression to tension. After the

separation is occurred between the mandrel and the composite structure at about 46°C, the stress at the mandrel remains zero while the stress at the composite structure is tensile. The maximum stress after cooldown is found to be 1.17 MPa at the 0°/90° interface. The axial stress distributions are shown in Figures 6 and 7. Since the displacement discontinuity between the mandrel and the composite structure exists, there is no stress development in the mandrel. Immediately before cooldown the 0° layer is in compression and the 90° layer is in tension. After cooldown the stress magnitudes are all elevated significantly. The final axial stress at the inner radius is -35 MPa. The hoop stress distributions are shown in Figures 8 and 9. The stress distributions in the mandrel and 90° are significant in the magnitude due to the mandrel expansion at the cure temperature. After the mandrel is separated during cooldown, the final residual stress in 0° layer is tensile while the stress in 90° layer is compressive. It was found that the radial and hoop stress magnitudes during cure temperature are very large compared to the final residual stresses due to the mandrel expansion.

To investigate the influence of mandrel material properties on the final residual stress, the aluminum mandrel is changed to steel mandrel. The material properties are listed in Table 2. The stress profile developments during cure are similar to the previous cases. And only the final radial stresses are considered. Figure 10 shows the comparison of the final radial stress distributions for both cases under the same cure cycle in Figure 3. The maximum stress with steel mandrel shows slightly higher value. To investigate the material property effects further, three cases of Young's modulus of mandrel materials are compared in Figure 11. The thermal expansion coefficient was kept constant as $2.36\mu\epsilon/^\circ\text{C}$. The results show that the final radial stress is increased as Young's modulus decreases. To examine the thermal expansion coefficient effect, three different cases with constant Young's modulus of 72.4 GPa are compared in Figure 12. In this case, the final radial stress is increased as the thermal expansion coefficient is decreased.

CONCLUSION

In this research, the residual stress in the cylinder structure by cure process is analyzed. The stress profile developments during cure were presented to understand the stress development mechanism. The finite element method was used with axisymmetric assumption on the cylinder structure, and slip elements were inserted to simulate the slip effect and separation effect by teflon between the composite structure and mandrel. Parametric studies such as Young's modulus and thermal expansion coefficient of the mandrel on the final residual stresses were performed to investigate the effects of the mandrel material properties. It was found that the residual stresses at the cure temperature were very high in magnitude due to the thermal expansion of the mandrel compared to the final residual stress. And the usage of high Young's modulus and high thermal expansion coefficient of the mandrel material showed low final residual stresses in the case of AS4/3501-6 composite. In summary, the stress developments over full cure cycle with accurate information about material properties has to be analyzed to find the reason of damages of the composite structure by the residual stresses.

REFERENCES

1. Kim, Y.K., "Process-induced Residual Stress Analysis of Graphite-Epoxy Composite Structures," *Ph. D. Thesis*, Dept. of Aero. & Astro. Eng., Univ. of Illinois, Urbana, IL, 1996

2. Y. Kim and S. R. White, "Process-Induced Stress Relaxation Analysis of AS4/3501-6 Laminate," *Journal of Reinforced Plastics and Composites*, in press.
3. Y. K. Kim and S. R. White, "Stress Relaxation Behavior of 3501-6 Epoxy Resin During Cure," *Polymer Engineering and Science*, in press.
4. Y. K. Kim and S. R. White, "Stress Relaxation During Cure of 3501-6 Epoxy Resin," *Proceedings of the 1995 ASME International Mechanical Engineering Congress and Exposition*, San Francisco, CA, Nov. 12-17, 1995, pp. 43-56.
5. S. R. White and Y. K. Kim, "Processing-Induced Residual Stress Analysis of Thick Composite Laminates," *ASME 1996 International Mechanical Engineering Congress and Exposition*, Atlanta, GE, November 17-22, 1996, MD-Vol. 74, Advanced Materials: Development, Characterization, Processing, and Mechanical Behavior, T. Nicholas, Ed., pp. 69-70.
6. Cohen, D. and Hyer, M. W., "Residual Stresses in Cross-Ply Composite Tubes," VPI-E-84-16, Virginia Polytechnic Institute and State University, Blacksburg, Virginia, 1984,
7. Caluis, E. P., Lee, S. Y. and Springer, G. S., "Filament Winding Cylinders: II. Validation of the Process Model," *J. of Composite Materials*, Vol. 24 , 1990, pp. 1299-1243.
8. Cirino, M., "Axisymmetric and Cylindrically Orthotropic Analysis of Filament Winding," *Ph. D. Thesis*, University of Delaware, Newark, DE, 1989.
9. Caluis, E. P., Lee, S. Y. and Springer, G. S., "Filament Winding Cylinders: II. Validation of the Process Model," *J. of Composite Materials*, Vol. 24 , 1990, pp. 1299-1243.
10. Lee, S. Y. and Springer, G. S., "Filament Winding Cylinders: I. Process Model," *J. of Composite Materials*, Vol. 24, 1990, pp. 1270-1298.
11. Lee, S. Y. and Springer, G. S., "Filament Winding Cylinders: II. Validation of the Process Model," *J. of Composite Materials*, Vol. 24, 1990, pp. 1299-1343.
12. Aleong, C. and Munro, M., "Effect of Winding Tension and Cure Schedule on Residual Stresses in Radially-Thick Fiber Composite Rings," *Polymer Engineering and Science*, Vol. 31, 1991, pp. 1344-1350.
13. White, S. R. and Zhang, Z., "The Effect of Mandrel Material on the Processing-Induced Residual Stresses in Thick Filament Wound Composite Cylinder," *J. of Reinforced Plastics and Composites*, Vol. 12, 1993, pp. 698-711.
14. Yi, S., Ahmad, M. F. and Hilton, H. H., "Manufacturing Process Induced Residual Deformation and Stresses in Filamentary Polymer Matrix Composites," *36th AIAA/ASME/ASCE/AHS/ASC Structures, Structural Dynamics and Materials Conference*, New Orleans, LA, April 10-12, 1995, AIAA 95-1476.
15. Taylor, R. L., Pister, K. S. and Goudreau, G. L., "Thermomechanical Analysis of Viscoelastic Solids," *Int. Journal for Numerical Methods in Eng.*, Vol. 2, 1970, pp. 45-59.
16. Whitney, J. M. and McCullough, R. L., "Micromechanical Materials Modeling," *Delaware Composites Design Encyclopedia*, Vol. 2, Technomic Pub. Co., Inc., 1990
17. Lee, W. I., Loos, A. C. and Springer, G. S., "Heat of Reaction, Degree of Cure, and Viscosity of Hercules 3501-6 Resin," *J. of Composite Materials*, Vol. 16, 1982, pp. 510-520.

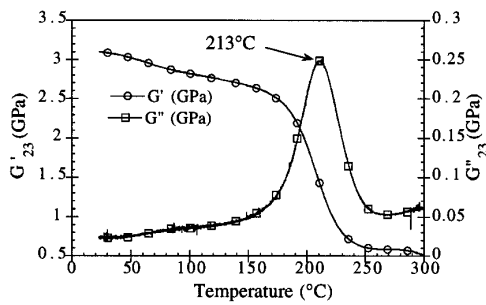


Fig. 1: Storage and loss shear moduli versus temperature for fully cured [0]₁₀ AS4/3501-6 laminate

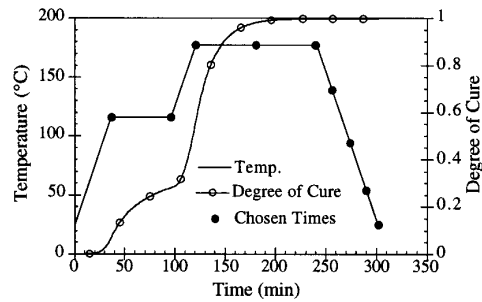


Fig. 3: Temperature and degree of cure history of AS4/3501-6 during MRC cycle

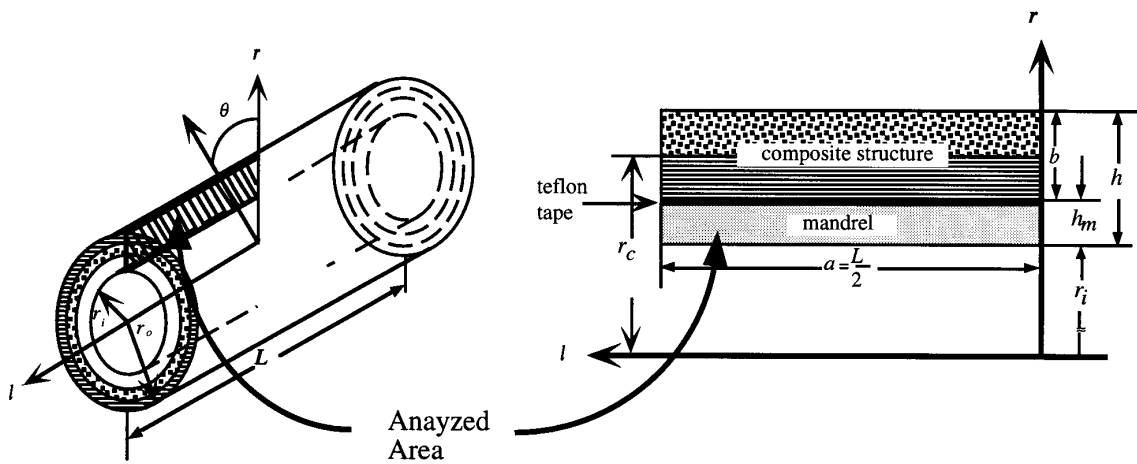


Fig. 2: Geometry of the cylinder structure.

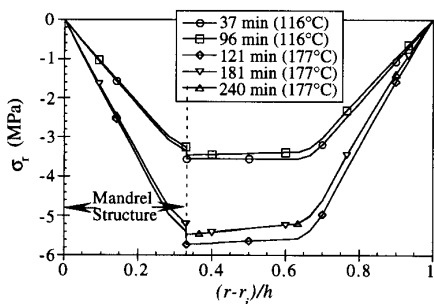


Fig. 4: Radial stress distributions during cure of a [0/90]_T composite cylinder up to the start of cooldown. The mandrel material is aluminum.

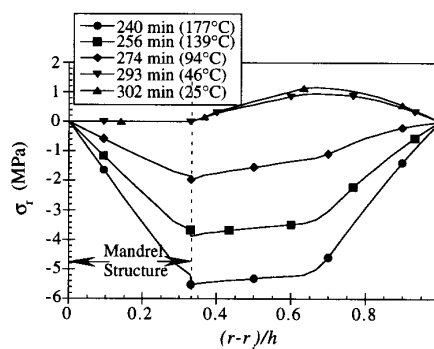


Fig. 5: Radial stress distributions during cooldown of a [0/90]_T composite cylinder. The mandrel material is aluminum.

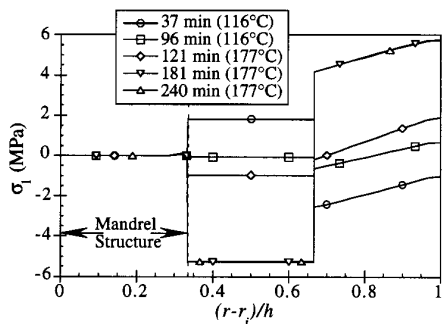


Fig. 6: Axial stress distributions during cure of a $[0/90]_T$ composite cylinder up to the start of cooldown.

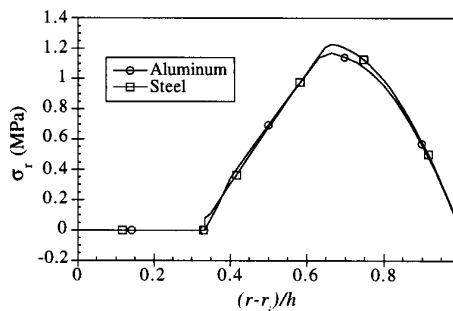


Fig. 10: Final residual stress in the radial direction using aluminum and steel mandrels

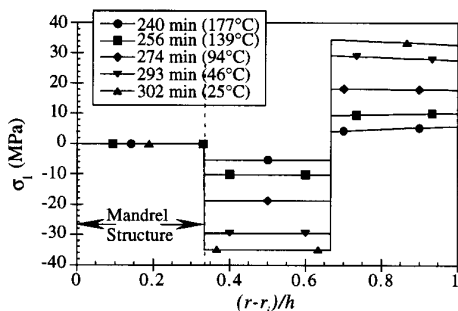


Fig. 7: Axial stress distribution during cooldown of a $[0/90]_T$ composite cylinder.

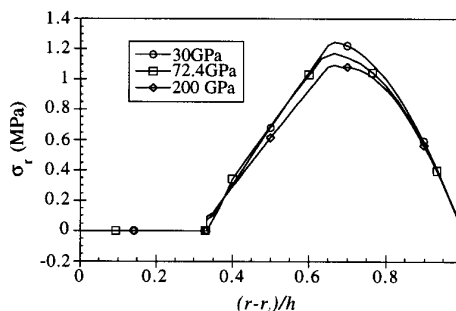


Fig. 11: Comparison of final radial stresses using different mandrel structures. The thermal expansion coefficient is kept constant as $2.36 \mu\epsilon/^\circ\text{C}$ for all cases.

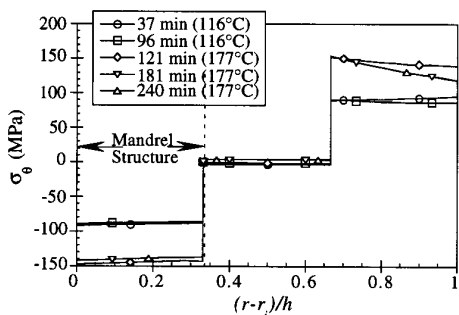


Fig. 8: Hoop stress distributions during cure of a $[0/90]_T$ composite cylinder up to the start of cooldown.

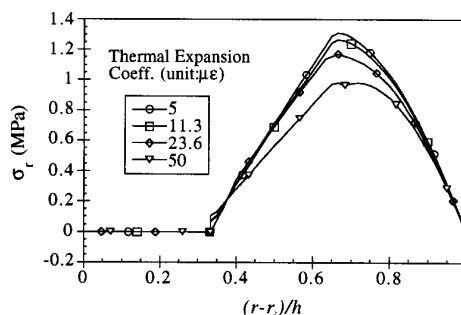


Fig. 12: Comparison of final radial stresses using different mandrel structures. The Young's modulus is kept constant as 72.4 GPa for all cases.

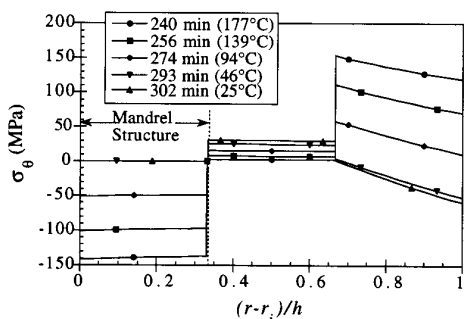


Fig. 9: Hoop stress distributions during cooldown of a $[0/90]_T$ composite cylinder.

SIMULATION OF MECHANICAL ALLOYING IN A SHAKER BALL MILL WITH VARIABLE SIZE PARTICLES

Dmitri Gavrilov, Oleg Vinogradov and William J.D. Shaw

*Department of Mechanical Engineering
University of Calgary, Calgary, Alberta, T2N 1N4, Canada*

SUMMARY: The problem of grinding in a shaker ball mill is considered as a statistical process of particles refinement caused by collisions. Based on the assumption that particles are uniformly distributed in space, the probabilities of them being caught between two colliding balls are formulated and used to assess the probability of transition to a system with different particle sizes. Two approaches are developed: one, based on the random sampling from all possible system states, and another, on the mass flow equation. The first approach results in a discrete Monte Carlo simulation model, while the second one in a continuous model. Both approaches give similar distribution of particle sizes after a specified number of ball collisions, and compare favorably with the corresponding experimental results. The numerical results are obtained by using an object-oriented software developed to simulate the dynamics of granular-type materials.

KEYWORDS: computer simulation, mechanical alloying, shaker ball mill

INTRODUCTION

Mechanical alloying has been around since the late 1960's and the principles have been explained and established by Benjamin [1]. However, little information currently exists with respect to the design and efficient operation of grinding equipment for the production of this material [2]. Commercial ball mills of a number of different types have been constructed and used, but most design and operating information is obtained by trial and error. Many of the attritor designs are based on the original work by Szegvari [3]. Some pilot attritor equipment has been used to generate experimental operating information [4] which is a starting basis but is specific to that equipment. Other studies in terms of applying theoretical analysis techniques are currently evolving [5,6]. Models put forth for different processing equipment are based upon energy principles combined with kinematics [7-10]. However, due to the simplifying assumptions, these models are and will always be quite limited in application. A computer simulation approach does not have many limitations of simplified analytical models and as such

can be a powerful tool in studying and optimizing the grinding processes in shaker ball mills. Such an approach is the subject of this paper.

The simulation procedure comprises two steps. The first deals with the determination of the number of collisions in a specified time for given shaker geometry, number and sizes of balls, and frequency and amplitude of shaking. This part has been developed and validated previously [12]. The present work deals with the second step, namely, the investigation of the grinding process in terms of the distribution of particles radii during the milling process. Two approaches are developed: one, based on the random sampling from all possible system states, and another, on the conservation of mass after each event of collision. The first approach results in a discrete Monte Carlo simulation model, while the second one in a continuous model. Both approaches give similar distribution of particle sizes after a specified number of ball collisions, and compare favorably with the corresponding experimental results. The numerical results are obtained by using an object-oriented software developed to simulate the dynamics of granular-type materials. The experimental results presented in the paper concern a composite material made out of two components: polyamide and polyethelene milled together from the initial 4 mm size to the final 3 micron one. The powder produced in this way is then compressed at some temperature below the melting point to obtain a composite material.

STATISTICAL MODEL

The shaker ball milling is simulated in a 3-D space. The mill is represented by a cylinder with plain or spherical lids. The system oscillates in a vertical direction with a specified amplitude and frequency. The cylinder is filled with balls, which move inside it, colliding with each other, as well as with the cylinder walls. At all times, all parameters of moving balls, including their positions and velocities, are accessible. Thus, it is possible to predict when collisions occur between the balls and between the balls and the cylinder. The time of each collision is recorded, as well as the amount of energy lost in the collision due to friction.

In a straightforward approach, one could try to simulate the system of material particles and steel balls as one system in which the number of material particles (modeled by spheres) grows in time. The split of a material particle takes place every time it is caught between the two colliding balls. However, in this scenario the number of particles becomes so large with time (i.e., one 1-mm particle can be split into one million 0.01-mm pieces during first seconds of shaking), that it becomes computationally inefficient to keep track of position and velocity of each particle. In this respect, a statistical model offers an alternative way of describing the distribution of particles radii during the milling process.

The random process of grinding can be represented by a directed graph with system states represented by the vertices, and transition states by the edges. Each edge is weighted with the probability of transition to another state, and the sum of weights of all edges going out of a vertex is always equal to 1. This is demonstrated on a simple example shown in Fig.1, where the numbers indicating the probabilities are given as illustrative.

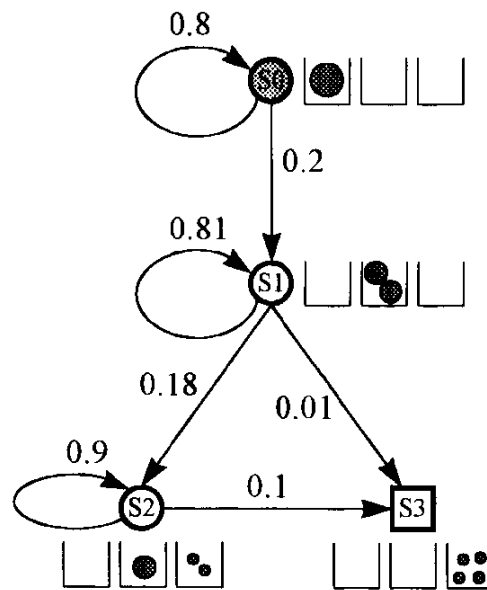


Fig. 1 An illustrative example of the graph describing the grinding process

In this example a single particle in the state S_0 is transformed into a two-particle system in the state S_1 , and then into a three-particle system (different particle sizes) in the state S_2 , and eventually into a four-particle system in the state S_3 (final particle size in this example). Note, that different particle sizes are placed in different “baskets”. In this example there are only three baskets: B_0 , B_1 and B_2 . Thus the initial state S_0 has 1 particle in the basket B_0 , and no particles in baskets B_1 and B_2 . When a collision occurs, the particle in B_0 may break up into two smaller ones with probability 0.2, and then the system will move into the state S_1 with 0 particles in basket B_0 , 2 particles in basket B_1 , and none in B_2 . The other possibility is to stay in the same state S_0 , i.e. the particle was not involved in the collision. The probability of the latter event is 0.8.

When the system is in the state S_1 with 2 particles in basket B_1 , there are three possible outcomes of a collision. In the first scenario, both particles are broken and moved into the basket B_2 . The probability of this is 0.01. With this transition the system is moved into the final state S_3 , when all particles are in the last basket B_2 . The second possible outcome is when only one of two particles in basket B_1 is broken. The probability of this is 0.18, and with this transition the system moves into the state S_2 with 1 particle in basket B_1 and 2 particles in basket B_2 . The third outcome is when no particles are broken due to a collision, and the system stays in the state S_1 . The probability of this is the remaining 0.81. Finally, for the state S_2 , which has one particle in B_1 , there are two possible outcomes: one, when the particle is broken (with probability 0.1) and the system is moved into the final state S_3 , or, second, when the particle is not broken (with probability 0.9), and the system stays in the state S_2 .

The above example represents a graph of all possible outcomes during the grinding process from the initial to the final state. It is clear that if the initial particle is to be reduced by many orders of magnitude (f.e. from 4mm to $1\mu\text{m}$), the graph becomes very complicated, and the

determination of all intermediate states time consuming. Instead, a random sampling technique can be used to obtain a statistically representative sample of outcomes after a specified number of transitions from the initial to the final state. A single simulation run then represents a random path from the initial (S0) to the final state (SN). The probabilities of transition from state to state can be found using the Monte Carlo simulation technique.

The statistical approach is based on the assumption that the distribution of particles is uniform in space for each particle size. It is also assumed that the condition for a particle to be split is associated with the possibility of its location between the colliding balls within the so-called “grinding volume” (see Fig.2, where the grinding volume is shaded). It follows then from these two assumptions that the probability of a particle of a specific size r_A to be inside the grinding volume is equal to the ratio of this volume V_{gr} to the total volume occupied by the particles in the shaker $V_{avail} = V_{shaker} - V_{balls}$, where V_{shaker} is the volume of the shaker, and V_{balls} is the total volume of balls moving inside the shaker. The grinding volume can be calculated approximately by the following formula

$$V_{gr} \approx 4\pi \frac{R_1 R_2}{R_1 + R_2} r_A^2 \quad (1)$$

where r_A is the radius of the particle A , and R_1 and R_2 are the radii of two collided balls.

Then, since it is assumed that the particle can be located at any point of the available volume V_{avail} with equal probability, the probability that the particle A is located inside the grinding volume is

$$P_{gr} = \frac{V_{gr}}{V_{avail}} \quad (2)$$

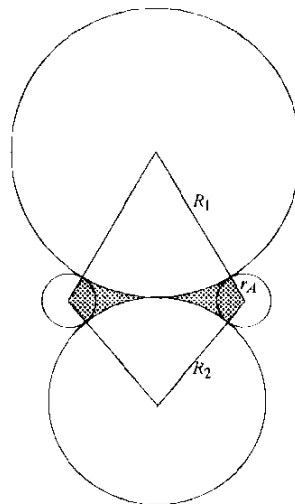


Fig.2 The grinding volume

Equation 2 is used to calculate the probability of grinding for each particle in the system. One can see that the probability of grinding decreases as the square of particle radius. This conforms to the experimental fact that the milling rate is greatly reduced when particles become small (see Numerical Results section below).

We will assume that if a particle with radius r_A participates in a collision, then it is split into two equal particles with radii $\frac{r_A}{\sqrt[3]{2}}$ (so that the total volume is conserved). Assuming that initially all particles have equal radii r_0 , it is sufficient to keep track only of the number of particles N_i for each of the radii

$$r_i = r_0 2^{-i/3}, \quad i = 0..k \quad (3)$$

Here r_k is the minimum particle radius, such that the particles with this radius do not break into smaller particles anymore. Usually, this radius is about $1\mu\text{m}$ [13].

As in the example of Fig. 1, the distribution of particles according to their radii can be viewed as their placement in the corresponding baskets so that each basket B_i holds particles of radius r_i . Initially, all particles have radius r_0 and are placed into the basket B_0 . Let us denote the number of particles in a basket B_i as N_i . If a particle from basket B_i was involved in a collision, then one particle is removed from basket B_i and two particles are added into basket B_{i+1} (see Fig. 3).

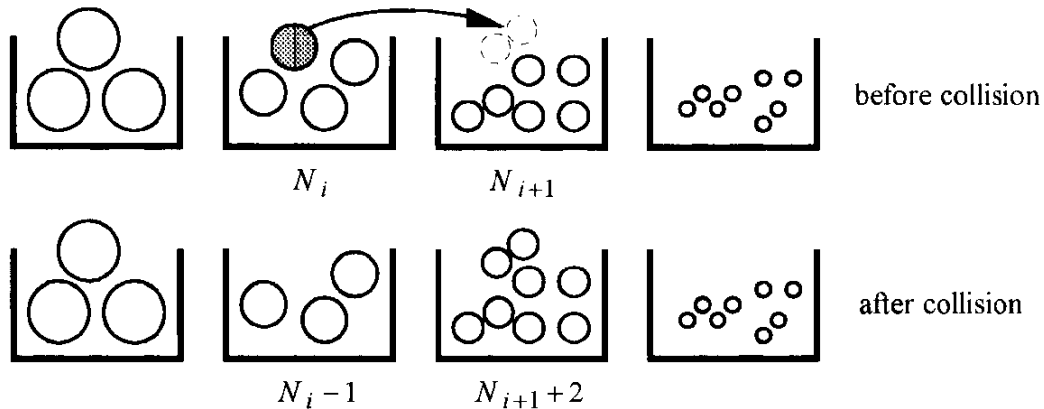


Fig.3 Effect of collision on redistribution of particles in baskets

Since all particles in a basket have the same radius, the probabilities of grinding are calculated by the same formula (Eqn 2). Then, the number of particles from the same basket involved in the collision is described by the binomial distribution. Thus, the number N_i^c of particles with radius r_i participated in a collision is distributed as

$$P(N_i^c = x) = \binom{x}{N_i} p_i^x (1 - p_i)^{N_i - x}, \quad x = 0..N_i \quad (4)$$

where p_i is the grinding probability $P_{gr}(r_i)$ (see Eqn 2) for a particular particle radius r_i . Note, that the volume required for the number of crashed particles N_i^c can exceed the

grinding volume V_{gr} . However, for the binomial distribution the probability of this event decreases with the number of particles.

In summary, when a collision between two balls takes place, the particles are redistributed in baskets. For each basket B_i , $i = 0..k-1$, a random number of particles $0 \leq N_i^c \leq N_i$ involved in collision is determined, and then N_i^c is deducted from N_i , and $2N_i^c$ is added to N_{i+1} . N_i^c is a discrete random variable distributed by the binomial law with parameters (p_i, N_i) . The process is stopped when all particles are in the last basket B_k , i.e. all material is grinded. The number of collisions, as well as the distribution of particle sizes during the grinding, are the objectives of the simulation.

ANALYTICAL MODEL

Although the model described above is much more efficient compared with the analysis of the complete graph of grinding events, it is still quite slow. In a usual run, the number of collisions required to grind the material can be as large as 10^{12} . Since each collision must be handled separately, the run times could be quite long even on a supercomputer. To solve this problem, a continuous analytical model is introduced, which represents the average-case behavior of the statistical model.

The analytical model also considers baskets containing balls with similar radii. However, instead of recording the number of particles in a basket, the total mass of particles in each basket is considered. Then the incremental mass balance equation for a single basket is derived, which leads to a differential form of the mass flow equation.

Let us denote the mass in a single basket by X_i , $i = 0..k$. Clearly, if a mass of one particle with radius r_i is m_i (which is proportional to r_i^3), then $X_i = N_i m_i$. Let us consider how masses of particles in baskets are redistributed after a collision. Since N_i^c is a discrete random variable distributed according to the binomial law with parameters (p_i, N_i) , its mean value is $p_i N_i$, i.e. on average that many particles from basket B_i are broken due to collision. Then the mass transferred from basket B_i into basket B_{i+1} is

$$p_i N_i m_i = p_i X_i, \quad i = 0..k-1 \quad (5)$$

The mass transferred from the last basket B_k is zero, since particles in this basket did not break. Now we will obtain a differential equation describing the change of mass of the material in baskets in time. Let us assume that collisions occur in the system with frequency λ . Then during the time interval dt there will be λdt collisions. The mass transferred from basket B_i into basket B_{i+1} can be represented as $\lambda p_i X_i dt$. At the same time, the mass $\lambda p_{i-1} X_{i-1} dt$ is transferred into basket B_i from basket B_{i-1} for all $i = 1..k$ (no mass is transferred into the first basket B_0). Then the total change of mass in basket B_i during the time dt is

$$dX_i = \lambda(p_{i-1} X_{i-1} - p_i X_i) dt, \quad i = 1..k-1 \quad (6)$$

Basket B_0 does not have any mass transferred into it, and therefore, $dX_0 = -\lambda p_0 X_0 dt$. The last basket B_k does not have any mass floating out, thus, $dX_k = \lambda p_{k-1} X_{k-1} dt$. The resulting differential system describing the average-case behavior of the grinding process is

$$\dot{\mathbf{X}} = \lambda \mathbf{P} \mathbf{X} \quad (7)$$

where $\mathbf{X} = \{X_i\}^T$, $i = 0..k$, and

$$\mathbf{P} = \begin{bmatrix} -p_0 & 0 & 0 & \dots & 0 & 0 & 0 \\ p_0 & -p_1 & 0 & \dots & 0 & 0 & 0 \\ 0 & -p_1 & p_2 & \dots & 0 & 0 & 0 \\ \dots & \dots & \dots & \dots & \dots & \dots & \dots \\ 0 & 0 & 0 & \dots & -p_{k-2} & 0 & 0 \\ 0 & 0 & 0 & \dots & p_{k-2} & -p_{k-1} & 0 \\ 0 & 0 & 0 & \dots & 0 & p_{k-1} & 0 \end{bmatrix} \quad (8)$$

The initial conditions are set as

$$X_0(0) = M, \text{ and } X_i(0) = 0, i = 1..k \quad (9)$$

This linear differential system has analytic solution:

$$X_m(t) = M \prod_{i=0}^{m-1} p_i \sum_{i=0}^m \frac{e^{-\lambda p_i t}}{\prod_{j=0, j \neq i}^m (p_j - p_i)}, m = 0..k \quad (10)$$

The numerical results (see below) confirm that the continuous analytical model provides a very good approximation of the discrete statistical model. Moreover, by the law of large numbers, the average values of statistical model parameters calculated for a large number of runs converge to the analytical solution. Equation 10 gives an explicit dependence of the outcome of the grinding process on the system parameters.

NUMERICAL RESULTS

An object-oriented library developed to simulate the dynamics of granular-type materials [11, 12] was used to simulate the shaker ball mill. The above library allowed to create a needed application very quickly by defining only application-specific properties of objects, such as laws of motion and collision rules.

The software system consists of two parts: the first part is used to simulate the dynamics of ball motion in the shaker ball mill and measure system parameters, such as frequency of collisions. A special “energy dissipation cut-off” value was used to exclude low-velocity collisions from consideration. This parameter becomes particularly important for the simulations with high filling ratios, when velocities of balls are comparatively low and many low-velocity collisions occur. The point is that when two balls collide with a low relative velocity, the energy dissipated in a collision may not be enough to break any particles. The

value of the energy cut off parameter must be determined experimentally for materials to be ground.

The second part of the program deals with the simulation of grinding. It inputs the results of the shaker simulations and uses them in subsequent runs of the grinding process model. The program outputs particles radii distributions at specified moments of time. The program implements both statistical and analytical models for the grinding simulation. Both programs are written in Object-Oriented Pascal in Borland Delphi environment. They run in Windows 95 operating system on PC.

A number of tests was run for the following system parameters: ball-to-ball coefficient of restitution = 0.980, ball-to-wall coefficient of restitution = 0.950, shaker radius = 31.5 mm, shaker height = 103.0 mm, shaker frequency = 52.6 Hz, shaker amplitude = 10.9 mm, productive collision cut off = 0.0001 Joule, ball radius = 3.200 mm, balls number = 125, ball density = 7850.0 kg/m³ (steel). For this set of parameters approximately 100,000 collisions/sec. was obtained. This number becomes quite stable after 0.1 sec (i.e. it does not change after that). For this reason the simulation time to determine the number of collision was 1 sec, and $\lambda = 100,000$ collisions/second.

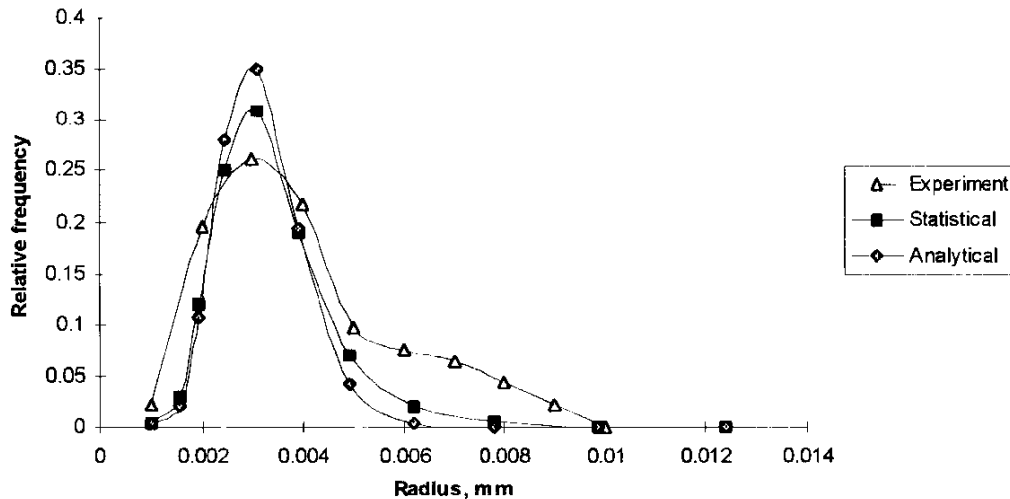


Fig. 4. Particle radii distribution

The distribution of radii of particles after 24 hours of milling are presented in Fig. 4. The effective rate of collisions for the simulation was set to 100,000 collisions per second, i.e. the resulting distribution is obtained after approximately $8.64 \cdot 10^9$ collisions. The experimental data in Fig.4 is taken from [13]. The close correspondence between both simulation and experimental results is clearly seen. The solutions obtained from statistical and analytical models are almost equivalent.

Another validating result is that the distribution of radii is almost independent from the initial particle radius, i.e. the milling rate is significantly higher for larger particles, and they are very quickly ground to the smaller ones. Another very interesting result, which is also in

correspondents with the experiments, is that the milling rate is independent from the amount of material put into the mill.

CONCLUSIONS AND FUTURE WORK

A software tool based on the object-oriented approach has been developed which allows to design more efficient shaker ball mills by numerically investigating such system parameters as energy losses, ball velocities, and particles radii distributions during the grinding process. An analytical model of particles refinement developed in this paper gives an explicit dependence of the process in terms of system parameters and thus allows optimization of the milling process. The experimental results confirm the validity of both numerical and analytical models of the grinding in a shaker ball mill.

The simulation program will be further verified in the near future with experimental measurements taken on an existing shaker ball mill after which the model was originally configured.

REFERENCES

1. J.S. Benjamin, "Dispersion Strengthened Superalloys by Mechanical Alloying", *Metallurgical Transactions*, V1, 1970, p. 2943-2951.
2. *Milling of Brittle and Ductile Materials*, Metals Handbook, Ninth Edition, Powder Metallurgy, V7, ASM, 1984, p.57-70.
3. A. Szegvari and M. Yang, "Attritor Grinding and Dispersing Equipment", *Seminar on Dispersion of Pigments and Resins in Fluid Media*, Kent State University, Ohio, May 9, 1984, p. 1-7.
4. H. Kimura, M. Kimura and F. Takada, "Development of an Extremely High Energy Ball Mill for Solid State Amorphizing Transformations", *J. of the Less-Common Metals*, V140, 1988, p. 113-118.
5. B.N. Babich and V.A. Djatlenko, "A Mathematical Model for the Process of Mechanical Alloying", *Structural Application of Mechanical Alloying*, ed's. F.H. Froes and J.J. deBarbadillo, ASM, 1990, p. 287-292.
6. T.H. Courtney and D.R. Maurice, "Some Fundamental Physics of the Mechanical Alloying Process", *Solid State Powder Processing*, ed's. A.H. Clauer and J.J. deBarbadillo, TMS, 1990, p. 3-19.
7. A.S. Lazarev, A.A. Kolesnikov, and V.A. Korol, "Mass and Energy Transfer During The Mechanical Alloying of Powder in an Attritor", *Soviet Powder Metallurgy and Metal Ceramics*, V 25, N8, 1986, p. 613-617.
8. A.N. Streletskii, "Measurements and Calculation of Main Parameters of Powder Mechanical Treatment in Different Mills", *Proc. of the 2nd International Conference on Structural Application of Mechanical Alloying*, Vancouver, B.C., September 20-22, 1993, p. 51-58.
9. P.G. McCormick, H. Huang, M.P. Dallimore, J. Ding and J. Pan, " The Dynamics of Mechanical Alloying", *Proc. of the 2nd International Conference on Structural Application of Mechanical Alloying*, Vancouver, B.C., September 20-22, 1993, p. 45-50.

THE EFFECT OF THERMOFORMING ON THE TENSILE STRENGTH OF UNIDIRECTIONAL DISCONTINUOUS ALIGNED FIBER COMPOSITES

Jens Schuster

*Fachhochschule Kaiserslautern, Site Pirmasens
Lemberger Str. 63, 66955 Pirmasens, Germany*

SUMMARY: Specimens made of uni- and bidirectional Discontinuous Aligned Fiber (DAF) composite materials were elongated to different states of deformation by thermoforming. Tensile tests were performed using pre-stretched specimens. Thermoforming behavior was modelled using the Herschel-Bulkley model. The effect of fiber orientation during thermoforming was described by applying the Jeffrey-Equation. A combination of both the Herschel-Bulkley-Model and the Jeffrey-Equation enabled, under consideration of thermal stresses, the determination of the ultimate tensile strength of thermoformed uni- and bidirectional DAF-materials. These results were in good agreement with those of the experimental tensile tests.

KEYWORDS: composites, PEK-matrix, discontinuous aligned fiber composites, thermoforming, Herschel-Bulkley-Model, Jeffrey-equation, ultimate tensile strength

INTRODUCTION

Over the last decade, a large number of rapid and cost effective manufacturing methods have been developed suitable for processing of continuous fiber reinforced thermoplastic materials [1]. Utilizing related processes known from thermosetting composites and neat thermoplastic materials and adopting sheet forming techniques typical to those used with metallic materials fabrication techniques such as thermoforming were developed [2, 3]. In comparison with traditional processing of thermosetting composites into complex geometries, thermoforming of advanced continuous fiber reinforced thermoplastic composite sheets offers several advantages such as in-situ consolidation, and faster processing cycles. However, some important processing issues have to be resolved before this can become a viable economical process. E.g. when transferring a flat continuous fiber reinforced laminate into a 3-D shaped component, a number of different deformation mechanisms have to be taken into account [3, 4]. Unlike isotropic metallic sheets, continuous fiber reinforced thermoplastics are inextensible in the fiber direction. For these material systems, the dominant mode of the deformation parallel to the fiber direction during forming is thus shearing within the individual plies and between them, i.e. intra- and interply shear [3]. Besides these two mechanisms, three others (fiber rotation, resin percolation, and transverse

fiber flow) are also active with less importance. These slipping processes depend strongly on the laminate lay-up, the fiber/matrix combination used, and the processing conditions such as pressure, temperature, and forming speed; all of them have a great influence on the final part quality [5, 6].

In order to avoid buckling problems whilst retaining acceptable processing times, a Discontinuous Aligned Fiber (DAF) composite material which provides a "drawable" feature was recently developed by DuPont to overcome the thermoforming limitations encountered with continuous fiber systems [7]. DAF consists of aligned carbon fibers, having an average length of $L = 5$ cm, in a thermoplastic polyetherketoneketone-matrix (PEKK), with a fiber volume fraction of $\phi_F = 58\%$. Due to the fiber discontinuity, a sixth deformation mechanism, the longitudinal fiber slip, is allowed. Concerns about the strength and stiffness properties of undeformed DAF-material can be neglected due to the high degree of efficiency of 0.95 based on high fiber length and their nearly perfect alignment.

MATERIAL AND THERMOFORMING PROCEDURE

The material used in this study was a discontinuous but highly collimated carbon fiber polyetherketoneketone (CF/PEKK) system described above. Platens with a thickness of approximately 2 mm and lay-up sequence of $[0^\circ]_{16}$ were cut into specimens with a width of 27 mm and a length of 400 mm. In order to generate the desired states of deformation in the specimens prior to mechanical tests, they were subjected to a thermoforming procedure. The forming process of the DAF-samples was realized by employing a particular stretch-forming technique. The stretch-forming was carried out using a setup consisting of a tensile testing machine providing the tensile force F and a laboratory hot press integrated into the testing machine (Fig. 1).

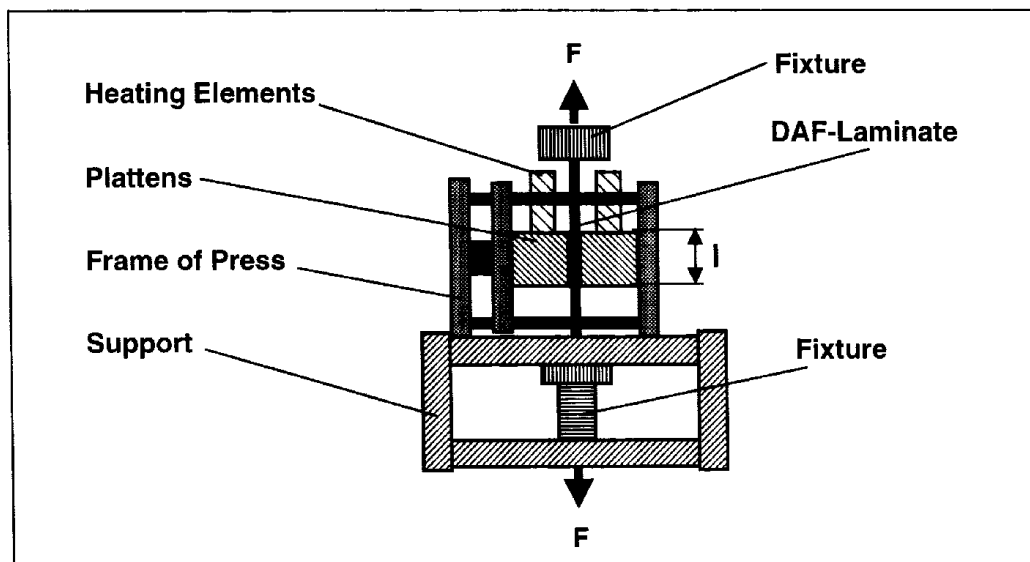


Fig. 1: Device for thermoforming

Previous experiments have shown that the use of a press tool was necessary in order to apply a sufficiently high pressure (13.6 MPa). This press tool, width 28 mm and length of l

= 160 mm, was placed between the heated plates. Before thermoforming, the heating plates had to be coated with a thin film of a release agent and covered with a sheet of polyimide foil in order to ensure easy demolding. It was aimed to generate plastic elongations ϵ_{plast} of 3%, 6%, 9%, and 12% of the 160 mm specimen length. Fig. 2 depicts the temperature-pressure course of the deformation process. After preheating the sample to 390 °C, it was deformed without external pressure. Once the desired elongation (speed of deformation = 1 mm/s) was reached, a consolidation pressure of 13.6 MPa was applied and the sample was cooled down. It was then removed after the temperature had dropped below crystallization temperature of the PEKK-matrix (255°C). Although the consolidation pressure was as high as 13.6 MPa, the 12%-deformed unidirectional samples could not be fully consolidated due to local necking effects.

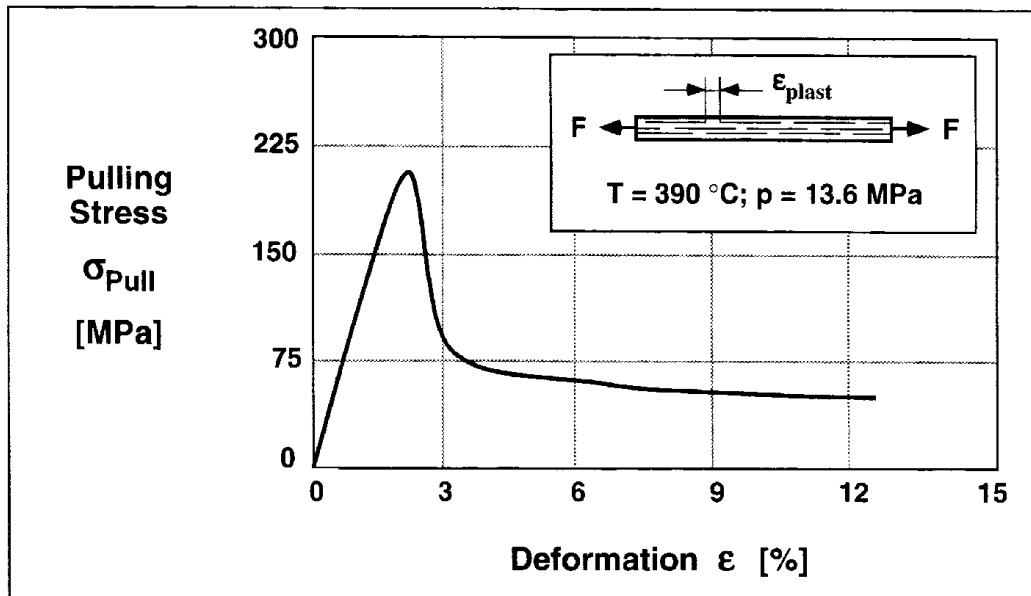


Fig. 2: Stress-deformation-curve during thermoforming of unidirectional DAF

TENSILE TESTS

The tensile tests on the unidirectional samples were performed according to ASTM 3039 employing a Zwick 1485 universal tensile testing machine. Fig. 3 shows that the state of pre-deformation has an obvious influence on the tensile strength of unidirectional laminated DAF-samples. with the 3%-elongated specimens having the highest tensile strength. This can be explained by the initial straightening of the approximately 95% aligned fibers in the original DAF-sheet, which up to a certain strain value leads to stiffening and higher loading efficiency. In addition, residual compressive stresses were induced in the DAF-material during stretch-forming by clamping it in fixtures until its removal from the forming device. Thus, the sample was still under tensile loading which turned into a compressive inner stress state after releasing the clamps so that an elastic redeformation could occur. The drop in the tensile properties of the 12%-deformed unidirectional samples is due to the insufficiently consolidated sections [8].

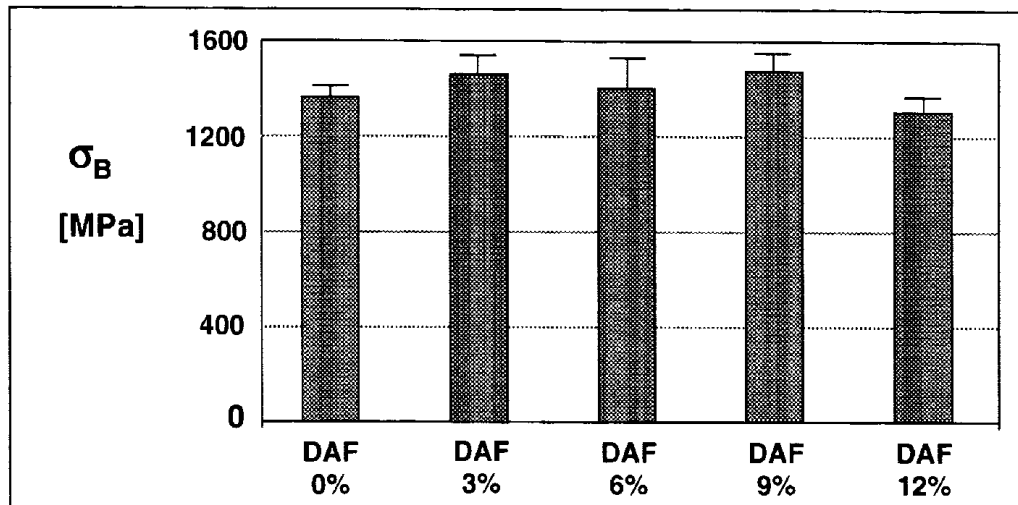


Fig. 3: Tensile strength of thermoformed uni- and bidirectional DAF-samples

MODELLING

In general, the ultimate tensile strength σ_B as a function of the deformation ε can be calculated by considering changes in fiber orientation ($\sigma_{B\eta}$) and by taking into account the residual compressive stresses σ_{Com} , which increases the ultimate tensile strength :

$$\sigma_B(\varepsilon) = \sigma_{B\eta} + \sigma_{Com} \quad (1)$$

with the modified rule of mixture for long fibers .

$$\sigma_{B\eta} = \sigma_F \phi_F \eta_F + \sigma_M (1 - \phi_F) \quad (2)$$

where η_F represents the fiber orientation, ϕ_F the fiber volume fraction, and σ_F as well as σ_M the tensile strength of the fibers and the matrix, respectively. Therefore, the modelling of the mechanical properties is divided into two parts:

- Modelling of the thermoforming behavior and thus the residual compressive strength
- Modelling of the improvement in fiber orientation.

The residual compressive strength is an output of forces applied during thermoforming which are due visco-plastic properties of the molten DAF-material (Fig. 4) [9]. In order to describe the visco-plastic behavior of unidirectional DAF, a mechanical-rheological model has to be applied fulfilling two requirements: 1) a description of the increasing pulling stress until a maximum is reached and 2) a description of the following stress relaxation. One model being excellently suitable for this task is the Herschel-Bulkley-Model (Fig. 5). It consists of the well-known Maxwell-Model combined with the ideal plastic Saint Venant Element situated parallel to the damping element. For stresses lower than a certain limit, the Saint Venant Element acts as a mechanical friction related blockade of the damper leading to

an exclusive loading of the spring. As soon as the adhesive strength σ_{Ad} of this element is exceeded, a stress equilibrium between damper and spring will be achieved.

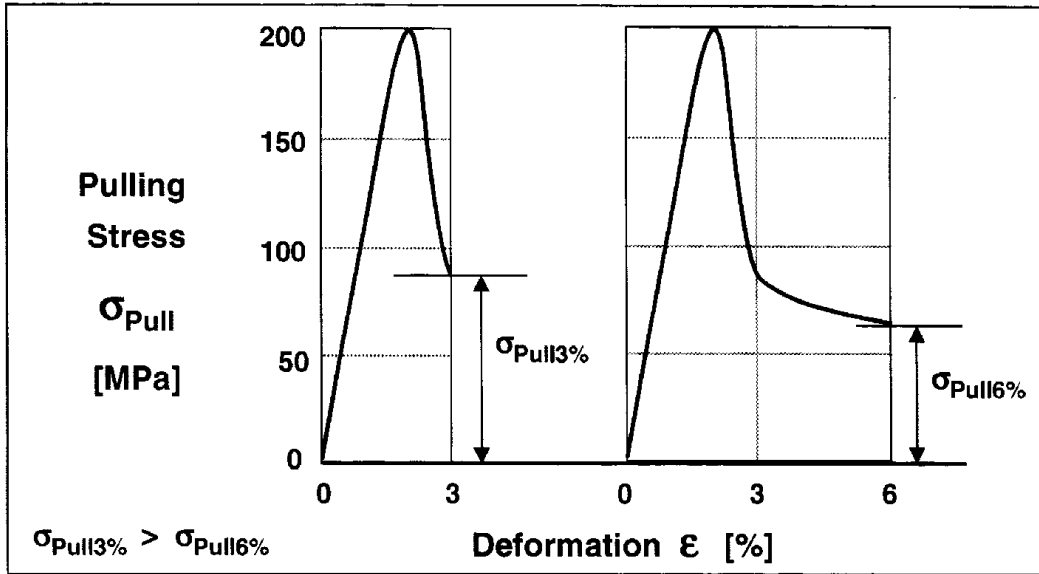


Fig. 4: Residual strength of unidirectional DAF after thermoforming

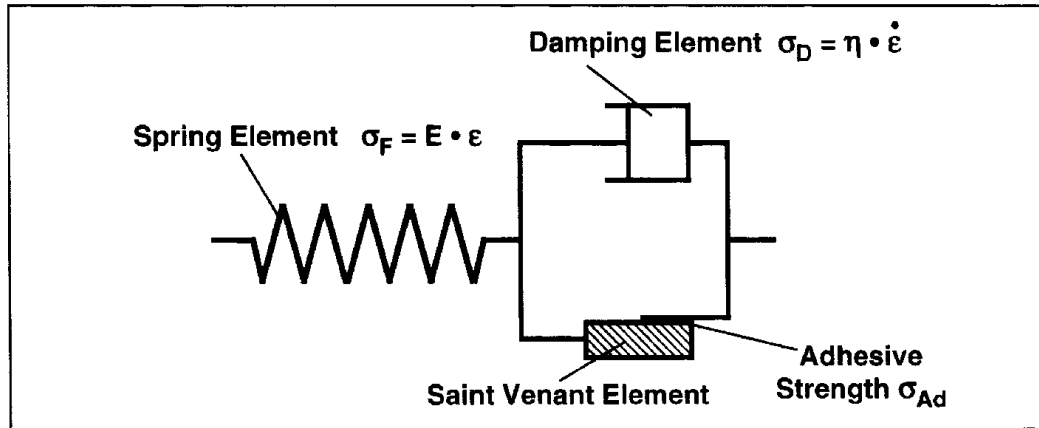


Fig. 5: Herschel-Bulkley-Model

Thus, the increase in pulling stress until maximum (Case I) can be described accordingly to Hook's law with the Young's modulus of the molten DAF in fiber direction [9]:

$$\sigma_{Pull} = E_{melt} \epsilon \tag{3}$$

where $E_{melt} = 8000 \text{ MPa}$ can be assumed as a realistic measure for the modulus of the molten 0° -layers [10, 11]. In case of a pulling stress σ_{Pull} larger than σ_{Ad} (Case II), the Herschel-Bulkley-Model converts into the Maxwell-Model. The total deformation ϵ can thus be written as

$$\epsilon = \epsilon_{spring} + \epsilon_{damper} \tag{4}$$

The deformation rate can be calculated accordingly:

$$\dot{\epsilon} = \dot{\epsilon}_{\text{spring}} + \dot{\epsilon}_{\text{damper}} = \frac{\dot{\sigma}}{E} + \frac{\sigma}{\eta} \quad (5)$$

where E ($E = E_{\text{melt}}$) represents the Young's modulus and η the viscosity of the molten material in fiber direction. In order to calculate the response of the model at a constant deformation rate, an inhomogeneous differential equation of the first order consisting of a homogeneous and a particular part (σ_h and σ_p , respectively) has to be solved. As a boundary condition, the time t is defined 0 when σ_{Ad} is reached. Thus, the following expression for σ_{Pull} can be derived

$$\sigma_{\text{Pull}} = \left(\sigma_{Ad} - \eta \frac{v}{l} \right) e^{-\frac{Et}{\eta}} + \eta \frac{v}{l} \quad (6)$$

where v/l (v = deformation rate, l = tool length) equals to the deformation velocity $\dot{\epsilon}$. The viscosity η can either be obtained experimentally by evaluating the stress-deformation curve for $\sigma(t \rightarrow \infty)$ or via a theoretical approach. In the first case, a $\sigma(t \rightarrow \infty)$ of 48 MPa leads to a viscosity of $4.6 \cdot 10^{11}$ Pa s. A theoretical solution was developed by Coffin and Pipes [12]:

$$\eta = \eta_{11} = \frac{\eta_0 A_T (1-\mu) \phi_F}{2\mu} \left(\frac{L}{D} \right)^2 \left[1 + \frac{A_T^2 (1-\mu)^2}{4\mu^2} \left(\frac{L}{D} \right)^2 (\lambda \dot{\epsilon})^2 \right]^{\frac{(n-1)}{2}} \quad (7)$$

where ϕ_F is the fiber volume fraction, L the length, and D the diameter of the fiber. The temperature shift factor, A_T , is defined as:

$$A_T = e^{-\frac{\eta}{\eta_0} \left(\frac{T}{T_0} - 1 \right)} = \frac{\bar{\eta}_0}{\eta_0} \quad (8)$$

where $\bar{\eta}_0$ and η_0 represent the zero-shear viscosity and normalized zero-shear viscosity, respectively. Note, that the temperature shift factor is normalized so that at a given reference temperature, T_0 , the shift factor equals zero. The factor μ is defined as

$$\mu = 1 - \sqrt{\frac{\phi_F}{\pi}} \quad (9)$$

The power law exponent, n , determines the degree of nonlinearity. The value of $n = 1$ corresponds to a Newtonian fluid, and as the exponent decreases the fluid exhibits increased shear thinning. It can be determined as follows:

$$\eta = \eta_0 A_T \left[1 + (\lambda A_T \dot{\gamma})^2 \right]^{\frac{(n-1)}{2}} \quad (10)$$

where λ determines the onset of nonlinearity. The missing values for the equations 8 and 9

were determined using additional data on PEKK material published by Chang et.al. [25, 26] thus determining the parameters for a temperature of 390 °C as follows:

$$\eta_0 = 2500 \text{ Pa s}, \lambda = 1,78, n = 0.584, \xi = 5.04, A_T = 0.53$$

The effective viscosity η_{11} of the medium (molten DAF in fiber direction) can be calculated using Equation 7. However, the fiber aspect ratio L/D is not precisely known. The fiber diameter of AS-4 carbon fibers is about 7 μm . The fiber length distribution of this material with an average fiber length of 54 mm was measured from Chang and Pratte [13]. Nevertheless, it has to be taken into account that the measurement of the length of long fiber is a difficult task to be solved; because it is often accompanied by fiber breakage that leads to fiber shortening and to falsifying of the test result. Therefore, the real average fiber length is higher than measured whilst the number of shortened fibers is unknown. In order to provide a sufficient accurate solution, the effective viscosity η_{11} is calculated for different L/D -ratios (Table 1). These calculated results in Table 1 correspond well with the viscosity of $4.6 \cdot 10^{11}$ Pa s which was reached via the experimental approach explained before.

Table 1: Effective viscosity of DAF at 390 °C as a function of the L/D -ratio

L/D [10^4]	0.75	1	1.25	1.5
η_{11} [10^{10} Pa s]	10.2	16.3	23.3	31.2

The residual compressive stress is due to the pulling stress at a certain state of deformation. However, cooling down the DAF-material below crystallization temperature (i.e. at $\Delta\vartheta = 89$ K) reduced the applied stress of the unidirectional material by 10 MPa due to the thermal expansion of carbon fibers and PEKK-matrix. The alteration in thermally related stresses (σ_{Therm}) in fiber direction can be calculated for a given temperature $\Delta\vartheta$ as follows [14]:

$$\sigma_{\text{Therm}} = (E_F \alpha_F \phi_F + E_M \alpha_M (1 - \phi_F)) \Delta\vartheta \quad (11)$$

where α_F and α_M are the thermal expansion coefficients of fiber and matrix [24]. The residual compressive stress can therefore be approximated as

$$\sigma_{\text{Com}} = \sigma_{\text{Pull}} + \sigma_{\text{Therm}} \quad (12)$$

A model for determining the angle of orientation θ of fibers immersed in a flowing viscous fluid (flowing velocity v) was developed by Folgar and Tucker and is based on the Jeffrey-equation [15, 16]:

$$\dot{\theta} = -\sin\theta \cos\theta \frac{\partial v_x}{\partial x} - \sin^2\theta \frac{\partial v_x}{\partial y} + \cos^2\theta \frac{\partial v_y}{\partial x} + \sin\theta \cos\theta \frac{\partial v_y}{\partial y} \quad (13)$$

For a one-dimensional flow in x-direction under consideration fiber interactions by introducing an interaction factor K_i and an integration along the tool length l leads

$$\dot{\theta} = -\frac{1}{2} K_i \frac{v}{l} \sin 2\theta \quad (14)$$

The solution of this differential equation can be simplified to

$$\theta = \arctan\left(C e^{-K_i \frac{v}{l} t}\right) = \arctan\left(C e^{-K_i \epsilon}\right) \quad (15)$$

The parameters C and K_i were determined by using boundary conditions measured in a scanning electron microscope:

- (1) $\theta (\epsilon = 0 \%) = 7^\circ$
- (2) $\theta (\epsilon = 3 \%) = 3.63^\circ$

Therefore, the equations to describe fiber orientation during stretch-forming of DAF are

$$\theta = \arctan\left(0.122 e^{-21.84\epsilon}\right) \quad (16)$$

The fiber orientation angle θ can be turned into the fiber orientation factor η_F (Eqn. 2) which equals to coefficient a_{33} of the fiber orientation tensor [29 - 31]:

$$\eta_F = a_{33} = \cos^2 \theta \quad (17)$$

RESULTS

The Herschel-Bulkley-Model expressed in Eqn. 3 and Eqn. 6 allows a precise determination of the stresses needed to deform unidirectional orientated DAF-material by stretch-forming. The comparison between measured and calculated values is exemplarily shown in Fig. 6.

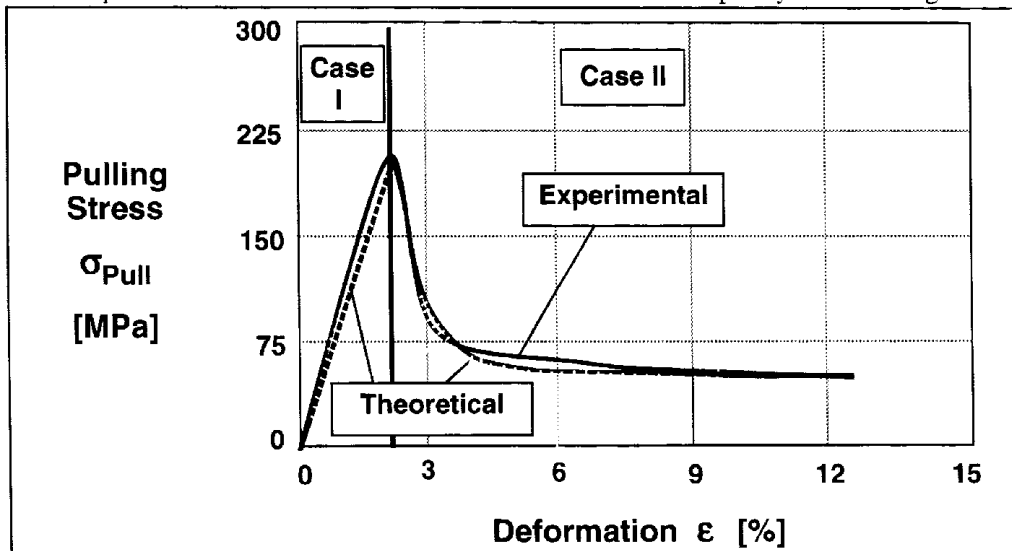


Fig. 6: Comparison of experimental and model results of the pulling stress

In addition, the outcome of modelling the ultimate tensile strength of thermoformed DAF is depicted in Fig. 7 collectively with the experimental data (see also Fig. 3). Based on the tensile test results of the undeformed sample the modelled values correspond well to the measured values for elongation from 3% to 9%. In case of the 12%-deformed sample, the correlation between experiment and calculation is inferior. This is due to the previously discussed consolidation problems which have not been taken into account in the model introduced.

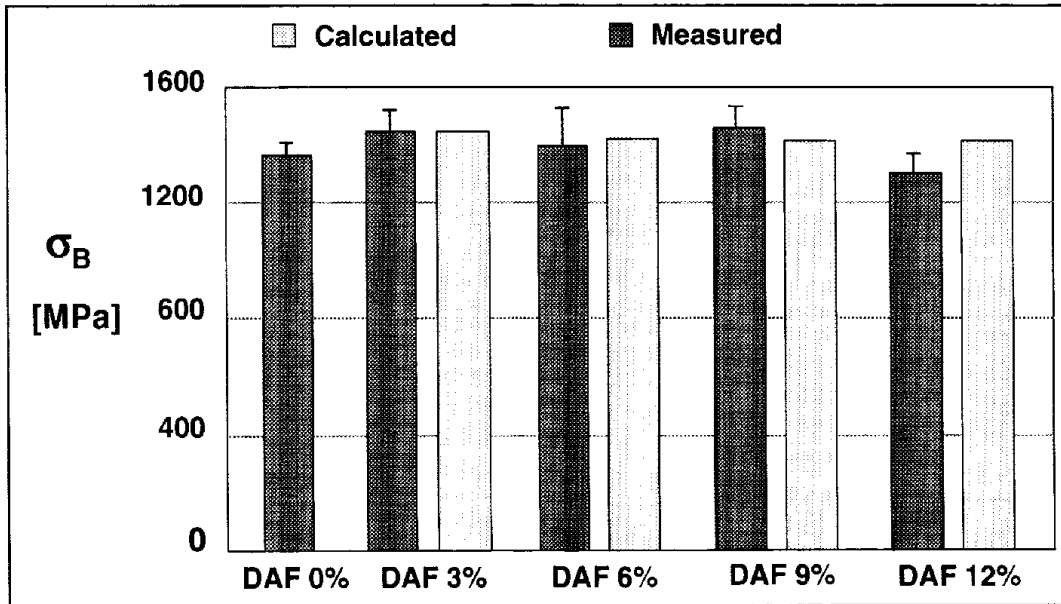


Fig. 7: Comparison of experimental and model results of the ultimate tensile stress

CONCLUSIONS

It is possible to describe the thermoforming behavior of unidirectional discontinuous aligned fiber composites by using the Herschel-Bulkley-Model. It allows under consideration of thermal stresses introduced to the material during cooling, the determination of internal residual stresses. Besides fiber orientation in deformation direction, the residual stresses are a major factor to increase the ultimate tensile strength, which can be realistically concluded by a combination of the Herschel-Bulkley-Model and a modified expression of the Jeffrey-Equation.

ACKNOWLEDGEMENT

Thanks are due to DuPont, Wilmington, USA for providing the LDFTM-composite material. In addition, financial support for "thermoforming experiments with thermoplastic composites" by the Deutsche Forschungsgemeinschaft (DFG FR 675-7-2) is gratefully acknowledged.

REFERENCES

1. Cogswell, F.N. 'Thermoplastic Aromatic Polymer Composites' *Butterworth-Heinemann Ltd*, Oxford (1992)
2. Månson, J.-A.E. 'Processing of Thermoplastic-Based Advanced Composites' in: *Advanced Thermoplastic Composites: Characterization and Processing* (Eds.: Kausch, H.-H. and Legras, R.), *Carl Hanser Verlag, Munich, Vienna, New York, Barcelona* (1993)
3. Friedrich, K., Hou, M. and Krebs, J. 'Stamp Forming of Continuous Fibre/Thermoplastic Composite Sheets' in: *Composite Materials, Vol. 12, Thermoplastic Sheet Forming*, (Ed.: Bhattacharyya, D.) *Elsevier Science Publisher, Amsterdam* (1997)
4. Okine, R.K.: 'Analysis of forming parts from advanced thermoplastic composite sheet materials', *SAMPE Journal* 25 3 (1989) pp. 9 - 19
5. Hou, M. and Friedrich, K. 'Thermoforming of High-Performance Composites with Thermoplastic Matrix' *Engineering Plastics* 5 2 (1992) pp. 86 - 100
6. Scherer, R. and Friedrich, K. 'Inter- and Intraply-Slip Processes during Thermoforming of PP/CF-Laminates' *Composites Manufacturing* 2 2 (1991) pp. 92 - 96
7. Medwin, S.J., Pratte, J., Effing, M. and Beyeler, E. 'LDF - Reinforcement: The Revolution Making Cost-Effective Complex Shaped Thermoplastic Composite Structures' *Werkstoffe & Konstruktion* 6 1 (1992) pp. 23 - 30
8. Schuster, J. and Friedrich, K. 'The Fatigue Behaviour of Thermoformed Discontinuous Aligned Fiber Composites' *Proceedings "The Tenth International Conference on Composite Materials"*, Whistler, Kanada (1995) pp. I-593 - I-600
9. Schuster, J. and Friedrich, K. 'Modelling of Mechanical Properties of Discontinuous Aligned Fiber Composites after Thermoforming' *Journal of Thermoplastic Composite Materials*, accepted for publication
10. Scherer, R. 'Charakterisierung des Zwischenlagenabgleitens beim Thermoformen von kontinuierlich faserverstärkten Polypropylen-Laminaten' *VDI-Verlag GmbH, Düsseldorf* (1993)
11. Scherer, R., Zahlan, N. and Friedrich, K. 'Modelling the Interply-Slip Process during Thermoforming of Thermoplastic Composites Using Finite Element Analysis' in: *Composite Materials - Design and Analysis* (Eds.: W.P. de Wilde and W.R. Blain) *Computational Mechanics Publications, Southampton* (1990) pp. 39 - 52
12. Coffin, D.W. and Pipes, R.B. 'Anisotropic Viscosities of an Oriented Fiber Assembly with Temperature and Strain Rate Dependence' *Proceedings "International Conference on Composite Materials VIII"*, Hawaii, USA (Eds.: Springer, G.S. and Tsai, S.W.), Stanford, CA (1991) pp. 10-I-1 - 10-I-9
13. Chang, I.Y. and Pratte, J.F. 'LDF™ Thermoplastic Composites Technology' *Journal of Thermoplastic Composite Materials* 4 3 (1991) pp. 227 - 252
14. Schuster, J. and Friedrich, K. 'Modelling of the effect of thermoforming on the mechanical properties of discontinuous aligned fiber composites' *Proceedings "The First International Conference on Composite Science and Technology"*, Durban, South Africa (1996) pp. 463 - 469
15. Folgar, F. and Tucker III, C.L. 'Orientation Behavior of Fibers in Concentrated Suspensions' *Journal of Reinforced Plastics and Composites* 3 2 (1984) pp. 98 - 119
16. Jeffrey, G.B. 'The Motion of Ellipsoidal Particles Immersed in a Viscous Fluid' *Proceedings "Royal Society of London"*, London, U.K. 102 (1923) pp. A-161 - A-161

ELECTROSTATIC POWDER SPRAY MANUFACTURE OF LONG FIBER COMPOSITE MATERIALS FOR INJECTION MOLDING

Mark S.Duvall , Nana Tzeng and Karthik Ramani

School of Mechanical Engineering, Purdue University, West Lafayette, IN 47907, USA

SUMMARY: An electrostatic powder spray impregnation process developed at Purdue University has been applied to the problem of manufacturing long fiber reinforced pellets for thermoplastic injection molding. By using a combination of powder impregnation and an intermediate impregnation and fiber wet-out stage, this process could potentially produce long fiber injection molding materials more effectively and economically than current pultrusion compounding methods. Both glass and carbon fibers were impregnated with polycarbonate powder and formed into long fiber pellets. These materials were injection molded into ASTM specimens and tested for tensile and flexural properties.

KEYWORDS: long fiber, injection, molding, powder, impregnation, thermoplastic, glass, carbon, polycarbonate

INTRODUCTION

Injection molded thermoplastic composites are widely employed to produce complex parts with good mechanical properties and environmental resistance. Fiber reinforced plastics generally fall into two categories, long fiber and short fiber composites. Short fiber pellets are produced by extrusion compounding chopped fibers with a thermoplastic resin. The process is economical but causes severe fiber attrition, resulting in parts with shorter fiber lengths and lower mechanical properties. Long fiber pellets are produced by pultrusion compounding, where melt-impregnated fibers are pulled through dies to impregnate the fibers and then chopped into pellets on the order of 12.5 mm in length. Parts produced from this material exhibit greater fiber lengths and better overall mechanical properties than short fiber composites. Due to the high melt viscosities of the thermoplastic resins and the high pulling forces involved in pultrusion, long fiber pellet manufacture is generally more costly. In addition, large-scale commercial pultrusion machines have costly tooling issues.

Powder impregnation has been proposed by many researchers as a method of overcoming thermoplastic resin viscosity and increasing process speed. A thorough review of thermoplastic impregnation techniques, including powder impregnation, was presented by Gibson [1]. Electrostatic powder spray impregnation has proven a viable technique for impregnating continuous fibers with thermoplastic polymer powders [2]. Further development of a versatile ribbonizing method [3] has enabled this process to coat and manufacture long fiber injection molding materials without pultrusion compounding.

PROCESS OVERVIEW

In Figure 1, continuous fibers are pulled off a fiber tensioner and through a air knife pneumatic spreading area. The fibers are spread to expose the individual filaments and moisturized to provide electrical conductivity. An electrostatic powder spray gun draws thermoplastic powder into an air stream, charges the powder particles, and directs them at the moving fiber tow. The powder coated towpreg then travels through a radiant oven to evaporate the small quantity of moisture and coalesce the particles onto the fibers. At this stage, the towpreg still requires additional fiber wet-out before processing into pellet form. An intermediate impregnation stage, shown in Figure 2, uses a flexible steel spring against a flat, heated metal die to complete the impregnation of the fibers with the thermoplastic resin. The flexible spring distributes the consolidation pressure over the towpreg in the processing area, minimizing fiber damage and reducing the pulling force on the towpreg. After this impregnation, or ribbonizing, stage, air jets cool the material before it reaches a high speed cutter that chops the towpreg into 12.5 mm pellets. A visual comparison of these powder-coated long fiber pellets with other fiber-reinforced injection molding pellets is shown in Figure 3.

Materials

Continuous glass and carbon fibers were coated with polycarbonate powder for this study. Polycarbonate pellets were ground to a 100 μm average diameter. The properties of the reinforcing fibers used are shown in Table 1. The AS4 12k carbon was unsized, while the 12k S2 glass was packaged in a multi-ended, sized form. The carbon reinforced polycarbonate pellets were made in two initial lengths, 6.2 mm and 12.5 mm, both with a fiber mass fraction of 40%. The S2-glass filled polycarbonate used a fiber mass fraction of 50% and an initial length of 12.5 mm.

Impregnation and Ribbonizing of Coated Fiber Tow

After coating, the powder laden tow passes through the radiant oven. The high resin fraction of the tow requires higher oven temperatures to melt the extra powder. The tow leaves the oven and cools slightly before reaching the first spring-die ribbonizing unit. Allowing the tow to cool after the powder melts keeps the polycarbonate resin from sloughing off onto the ceramic guides or at the entrance to the spring-die. The first stage uses low pressure to evenly and gently distribute the resin without damaging the fibers. The second stage is set at a higher pressure to improve impregnation and fiber wetout. Table 2 contains the key parameters for the ribbonizing stage. After the second ribbonizing unit, a slotted pulley forms the towpreg to a constant width of 0.4 mm.

After coalescing in the tunnel oven, a typical cross-section of AS4/polycarbonate towpreg looks like Figure 4. The powder particles are fused onto the fibers, but most of the surface area of the fibers in the tow remains dry. Figure 5 shows a cross-section of ribbonized AS4 carbon/polycarbonate towpreg. The unsized packaging of the carbon tow allows for excellent dispersion of the powdered polycarbonate during spray coating, and also facilitates transverse fiber wet-out during ribbonizing.

Coated S2-glass/polycarbonate towpreg is shown in Figure 6. The bundled, sized treatment of the raw S2-glass prevents the powder from completely impregnating the bundles of fibers. The ribbonizing stage helps to impregnate these bundles, as shown in Figure 7.

Unlike the carbon towpreg, the S2-glass retains its bundled nature, and discrete fiber-rich and resin-rich areas are seen throughout the towpreg. The ribbonizing parameters used were not sufficient to completely impregnate the tow and disperse the fibers uniformly. For injection molding, this may actually be an advantage. Bailey proposed that discrete fiber bundles have a greater chance of surviving the injection molding process intact [4].

This impregnation method has a number of potential advantages over pultrusion for ribbonizing thermoplastic towpreg. It reduces the amount of time the polymer spends in the melt state. Pultrusion dies generally force the tow into a rigid cross-section, and then force the molten polymer through the packed fiber bed. This has the effect of reducing the permeability of the fibers to the transverse resin flow. The spring-die apparatus flattens the tow, reducing both the flow distances for the polymer and the fiber packing effects. The movable upper spring and the simple flat die alleviates the need for extensive tooling dies to create the pellet shape, reducing the costs of implementing the design. Finally, multiple spring-die units can be used with different setting to achieve a desired impregnation rate for any combination of fiber, resin, and resin fraction with easy control over the heating and pressure parameters at each stage.

Experimental Injection Molding Setup

ASTM tensile and flexural specimens were injection molded on a 55 ton Cincinnati Milacron general purpose injection molding machine at the processing conditions shown in Table 3. The pellets were dried in an oven for 4 hours at 120 °C to remove any moisture absorbed by the polycarbonate which could affect the injection molding process. The injection molding parameters used were similar to many published strategies for long fiber materials ([5],[6]). An inverse temperature scheme for the Zones 1 through 3 on the extruder barrel was used for heating the pellets. Zone 3 is closest to the pellet entrance, while Zone 1 is closest to the mold. By heating the pellets quickly to the melting point and using a low extruder screw RPM to minimize shear heating, researchers believe that fiber damage can be reduced. A minimum of ten specimens from each material were made during molding. The tensile and flexural specimens on opposite sides of the mold, were made simultaneously.

RESULTS AND DISCUSSION

The ASTM specimens were tested in a Q-Test electromechanical tensile testing machine in accordance with ASTM D638 (tensile) and D790 (flexural) specifications. Figure 8 shows the tensile testing results. Flexural test results, in this case three-point bending, are shown in Figure 9. Pieces of the broken samples were polished for microstructural analysis. Others underwent solvent dissolution and fiber length determination. Results from all the tests are contained in Table 4.

The effect of initial pellet length on the strength of carbon fiber samples was not readily apparent. The half inch pellets demonstrated 3.4% higher tensile strength and 5.9% higher flexural strength than the quarter inch pellets, but further experimentation is required to support this observation. When compared with commercial 40% carbon-filled short fiber pellets, the AS4/polycarbonate pellets tested 9.1% higher in tensile strength and 13.6% higher in flexural strength. These are encouraging results, as long fiber composites can be weaker than their short fiber counterparts in tension [7].

The 50% mass fraction S2/polycarbonate pellets presented a little more difficulty during molding. The large loading of glass caused slight mold flow problems. This caused the tensile specimens to be slightly weaker at the end furthest from the entrance gate, and resulted in many of the specimens breaking outside the gauge length of the sample. The 179 MPa tensile strength reported is 6.7 MPa higher than one commercial 50% glass-filled material. A common problem with tensile tests which place the specimen under constant stress along its entire length. A single flaw anywhere in this region can result in failure. Flexural specimens reach a peak stress only under the middle plunger, therefore the test results show less deviation. Flexural bending strengths averaged 296 MPa. The commercial 50% glass-filled material advertised a flexural strength of 262 MPa.

Fiber length determination is an important indicator of the success of any injection molding material or technique. Residual fiber length in an injection molded part is an indicator of the degree of fiber attrition that occurred. Small samples from core and skin areas in a part were immersed in methylene chloride to dissolve the polycarbonate matrix. The raw fibers were washed with more solvent to remove any residue and dried. To measure fiber lengths, a sample of the fibers was mixed with a volatile solvent and drops of this mixture were placed on microscope slides. Once dried, they were examined under an optical microscope with a CCD camera using NIH Image software. This program allows calibration of screen pixels to a standard. A representative selection of 250 were counted, measured and averaged to obtain a number average fiber length.

Initial fiber length results for this set of experiments were lower than expected. Carbon fibers are brittle, and experience severe fiber attrition during molding. Glass is more resilient, but still only showed average lengths of 328 microns. Many researchers have reported lengths ranging from 300 microns to over 2.0mm [5]. Many factors affect fiber length, including pellet geometry, matrix and fiber type, and molding machine setup and parameters. A true comparison between long fiber materials would have to occur on the same machine with identical processing parameters.

SUMMARY

An electrostatic powder impregnation process developed at Purdue University has successfully been applied to the manufacture of long fiber injection molding materials. This method is presented as an alternative to the commonly employed technique of pultrusion compounding these materials. The relatively good impregnation achieved by the powder coating technique, when combined with the spring-die ribbonizing method developed, could potentially produce these materials at higher line speeds and at a lower cost.

A basic preliminary comparison of these materials with commercially produced pellets showed favorable performance. A valid comparison of properties would require combining equivalent polymers and fibers to the materials found in the commercial pellets, then molding them on the same machine. Future research will focus more on this type of comparison, but current results demonstrated the viability of powder impregnation for producing long fiber injection molding pellets.

REFERENCES

1. Gibson, A.G. and J.-A.E. Manson, "Impregnation technology for thermoplastic matrix composites", *Composites Manufacturing*, 3(4): p. 223-233,1992.
2. Ramani, K., D.E. Woolard, and M.S. Duvall, "An electrostatic powder spray process for manufacturing thermoplastic composites", *Polymer Composites*, 16(6): p. 459-469,1995.
3. Duvall, M.S., K. Ramani, M. Bays, and F. Caillat, "In-situ composite manufacture using an electrostatic powder spray process and filament winding", *Polymers and Polymer Composites*, 4(5): p. 325-334,1996.
4. Bailey, R. and H. Kraft, "A study of fibre attrition in the processing of long fibre reinforced thermoplastics", *Intern. Polymer Processing*, 2: p. 94-101,1987.
5. Cianelli, D.A., J.E. Travis, and R.S. Bailey, "How to process long-fiber reinforced thermoplastics", *Plastics Technology*, : p. 83-89,1988.
6. Cattanach, J.B., G. Guff, and F.N. Cogswell, "The processing of thermoplastics containing high loadings of long and continuous reinforcing fibers", *Journal of Polymer Engineering*, 6(Nos., 1-4): p. 346-362,1986.
7. McClelland, A.N. and A.G. Gibson, "Rheology and fibre orientation in the injection moulding of long fibre reinforced nylon 66 composites", *Composites Manufacturing*, 1: p. 15-,1990.

TABLES

Table 1 Pellet reinforcing fiber properties

Pellet Material	Fiber Type	Fiber Count	Fiber Package	Density (g/cm ³)	Tow Yield
PC/Carbon	Hercules AS4	12k	single ended, unsized	1.80	1230 m/kg (1700 ft/lb)
PC/Glass	OCF S2-glass	12k	multi-ended, sized	2.49	520 m/kg (240 yds/lb)

Table 2 Oven and Spring-Die parameters

Pellet Material	Oven Temperature (°C)	Spring-Die Temperature (°C)	Spring Pressure P1, P2 (kPa)	Post Forming
PC/Carbon	500	450	35, 140	line tension only
PC/Glass	550	430	35, 140	tension, slot roller

Table 3 Injection Molding Processing Conditions

Nozzle Temperature	260 °C (500 °F)
Zone 1 Temperature	288 °C (550 °F)
Zone 2 Temperature	302 °C (575 °F)
Zone 3 Temperature	316 °C (600 °F)
Mold Temperature	93 °C (200 °F)
Back Pressure	0.7 MPa (100 psi)
Pack Pressure	4.1 MPa (600 psi)

Table 4 Results

Material	Pellet Length mm (in.)	Average Tensile Strength MPa (kpsi)	Average Flexural Strength MPa (kpsi)	Number Average Fiber Length μ m
PC/Carbon	6.2 (0.25)	176 (25.5)	263 (38.1)	218
PC/Carbon	12.5 (0.50)	182 (26.4)	279 (40.5)	224
PC/Glass	12.5 (0.50)	179 (26.0)	296 (42.9)	328

FIGURES

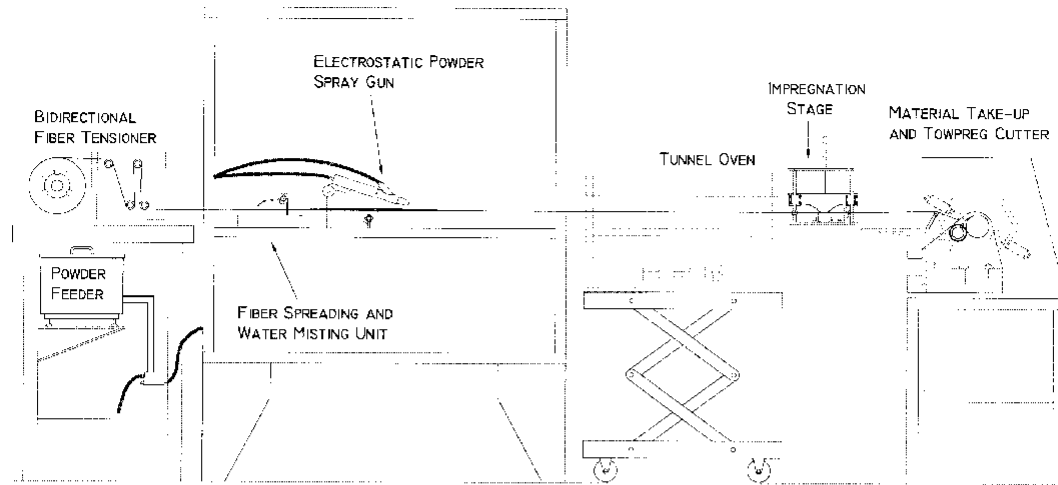


Figure 1 Electrostatic powder spray coating process applied to long fiber pellet manufacture

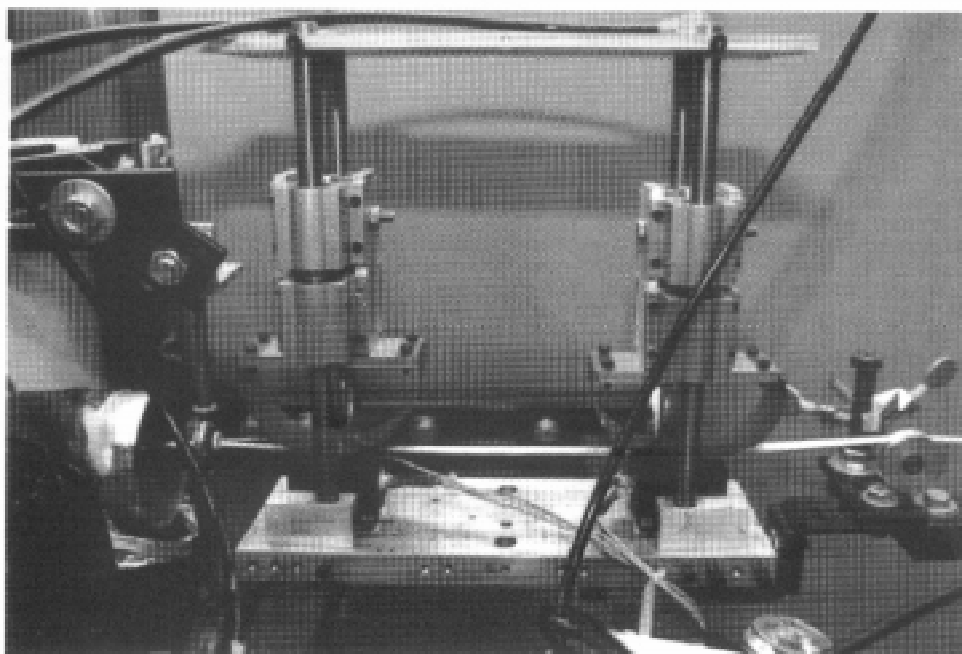


Figure 2 Ribbonizing and impregnation stage with two heated spring-die stages

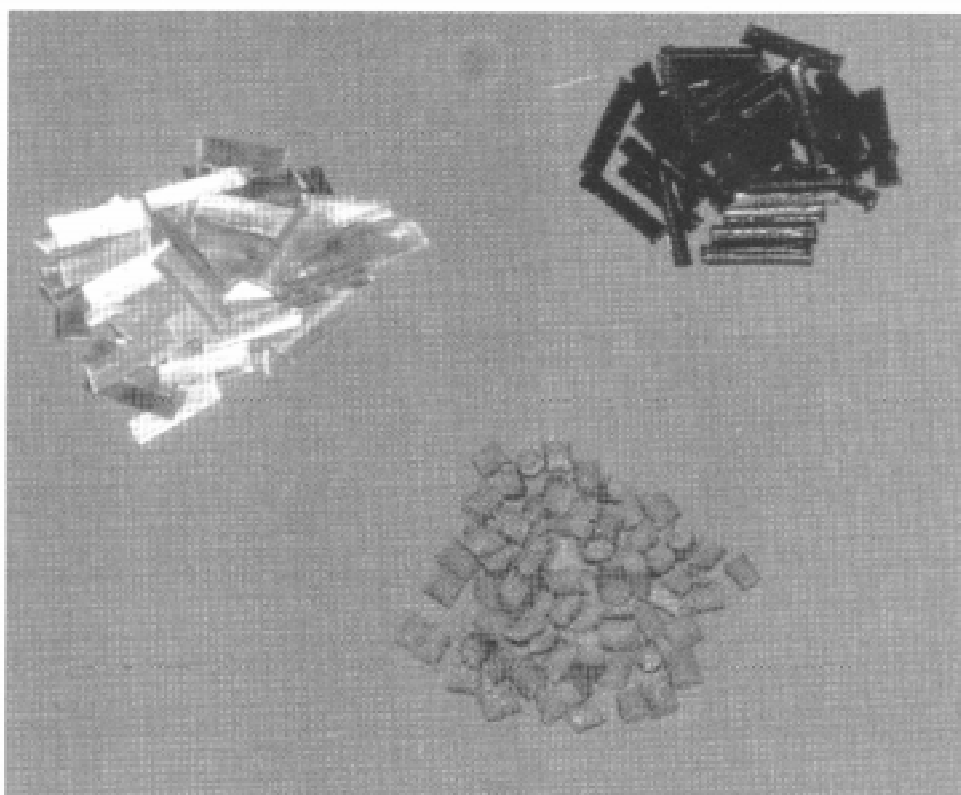


Figure 3 Clockwise from upper right: commercial long-glass pellets, commercial short-glass pellets, powder-coated long-glass polycarbonate pellets

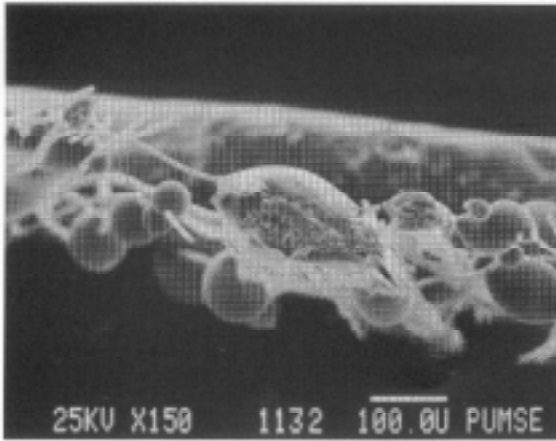


Figure 4 Cross-section of AS4/PC tow after powder coating and oven coalescence

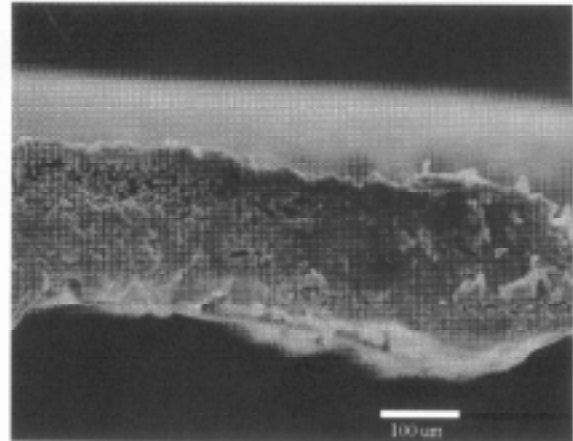


Figure 5 Cross-section of AS4/PC tow after ribbonizing

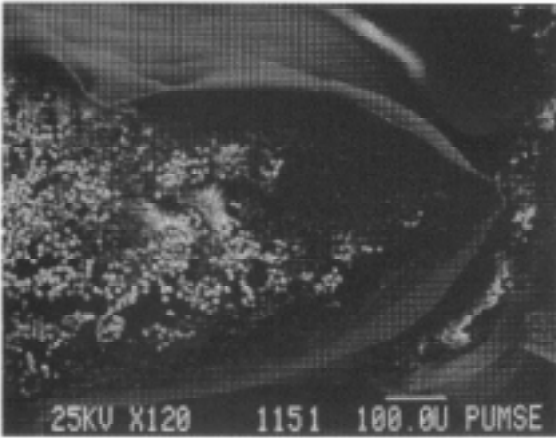


Figure 6 Cross-section of S2 glass/PC tow after powder coating and coalescence in radiant oven (120x)

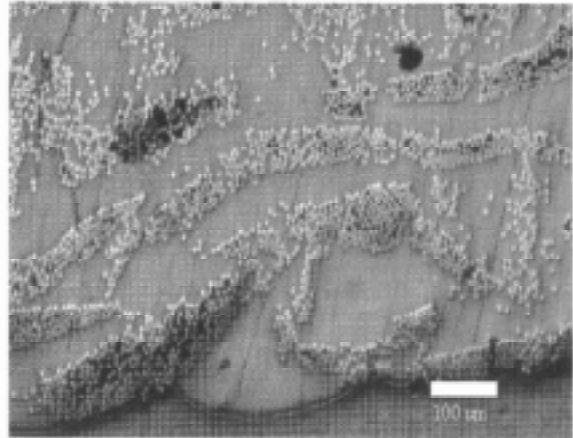


Figure 7 Cross-section of S2 glass/PC tow after ribbonizing with almost complete fiber wetout (240x)

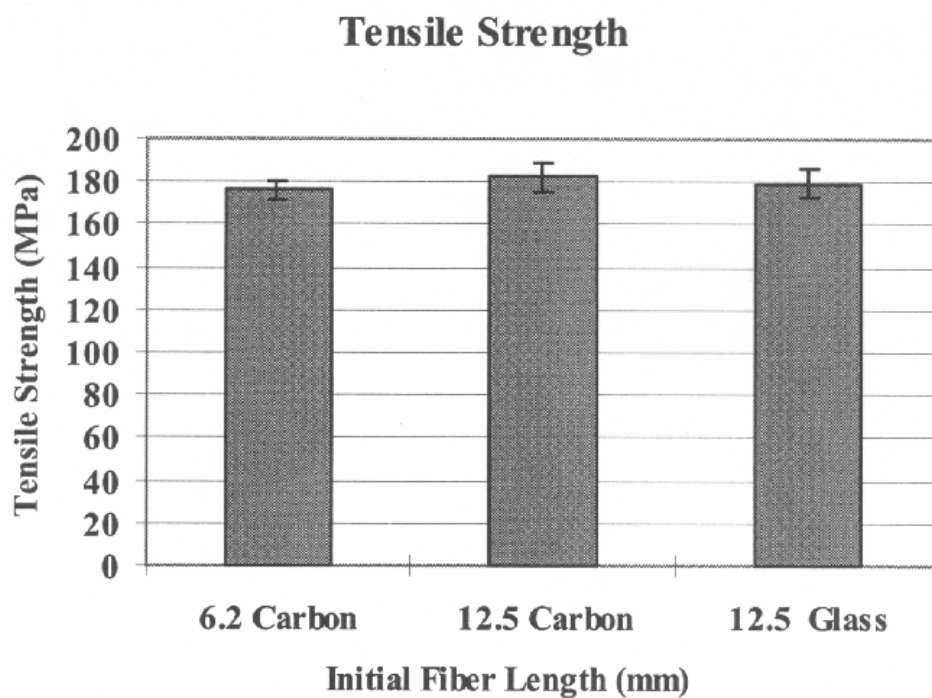


Figure 8 Tensile strengths of powder-coated long fiber pellets

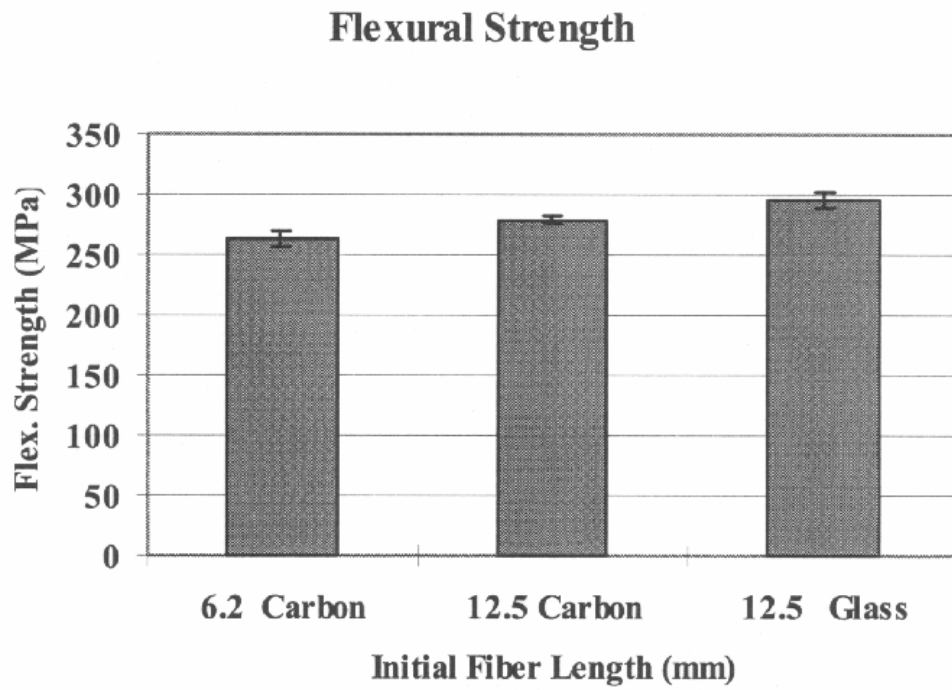


Figure 9 Flexural strengths of powder-coated long fiber pellets

SQUEEZE FLOW TESTING OF POLYPROPYLENE AND GLASS MAT THERMOPLASTICS AT COMPRESSION MOULDING STRAIN RATES

J. H. Bland¹, H. E. N. Bersee² and A. G. Gibson³

^{1,3} *Centre for Composite Materials Engineering, Materials Division, Dept. of Mechanical, Materials and Manufacturing Engineering, Herschel Building, University of Newcastle, Newcastle upon Tyne, U.K.*

² *Shell Research and Technology Centre, Amsterdam, Badhuisweg 3, 1031 CM Amsterdam, The Netherlands.*

SUMMARY: Axisymmetric biaxial squeeze flow tests have been carried out on continuous fibre Glass Mat Thermoplastic (GMT) and also on samples of the unfilled polypropylene matrix. Tests were carried out at constant squeezing rates representative of conditions in the compression moulding process. Lubricated squeeze flow was also used to study biaxial extensional flow. The results of lubricated and unlubricated tests on similar samples are compared and the flow characteristics identified. Unlubricated squeeze flow of GMT can be characterised by three regions: 1) a short 'start-up' period of elastic material compression, 2) predominantly extensional flow over the majority of the squeezing range and 3) shear-dominated flow at small plate separations. Results from lubricated and unlubricated tests on GMT under the same conditions are very similar for the first half of the total deformation, with the squeezing force in the unlubricated condition rising rapidly after further flow as shear flow effects become more significant.

KEYWORDS: Glass Mat Thermoplastic, GMT, polypropylene, rheology, lubricated squeeze flow, biaxial extensional flow

INTRODUCTION

The compression moulding of Glass Mat Thermoplastics (GMTs) has become a popular route for the high-volume production of complex semi-structural parts, especially for the automotive industry. There is, however, a relative lack of knowledge of the flow behaviour of GMT during moulding, which prevents a full understanding of the process and hinders the development of mould-filling predictions. The squeeze flow technique, shown schematically in Fig. 1, has received much interest as a study technique for compression moulding materials since the biaxial flow field generated is broadly representative of the flow mechanism found in the moulding process. In this technique, a disc-shaped sample of molten material is squeezed between heated parallel plates which move together under a controlled approach. The material response in terms of the squeezing force and plate separation is measured throughout the test.

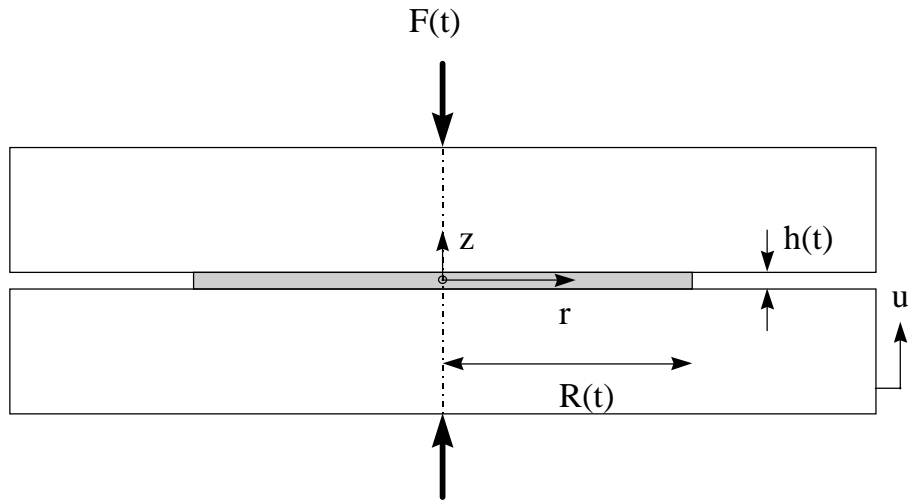


Figure 1: Schematic diagram of constant volume squeeze flow

In this work, a constant velocity squeezing condition is imposed with the fastest squeezing rates used representative of those found in the moulding process. Samples of the unfilled polypropylene matrix material with a similar geometry to the GMT samples used were tested to examine the effect of the mat reinforcement on flow behaviour.

The squeeze flow technique may be operated under lubricated or unlubricated conditions. Unlubricated squeeze flow of polymer melts creates a shear flow field in the test material and the technique can be used to measure shear viscosity [1,2] under certain conditions. The effect of lubrication is to change the gapwise velocity profile from a near-parabolic shape (Fig. 2(a)) to that of a ‘plug flow’ (biaxial extension) with complete material slippage at the plate surfaces, as shown in Fig. 2(b). There should, then, be a significantly different material response between the two conditions for tests on unfilled materials.

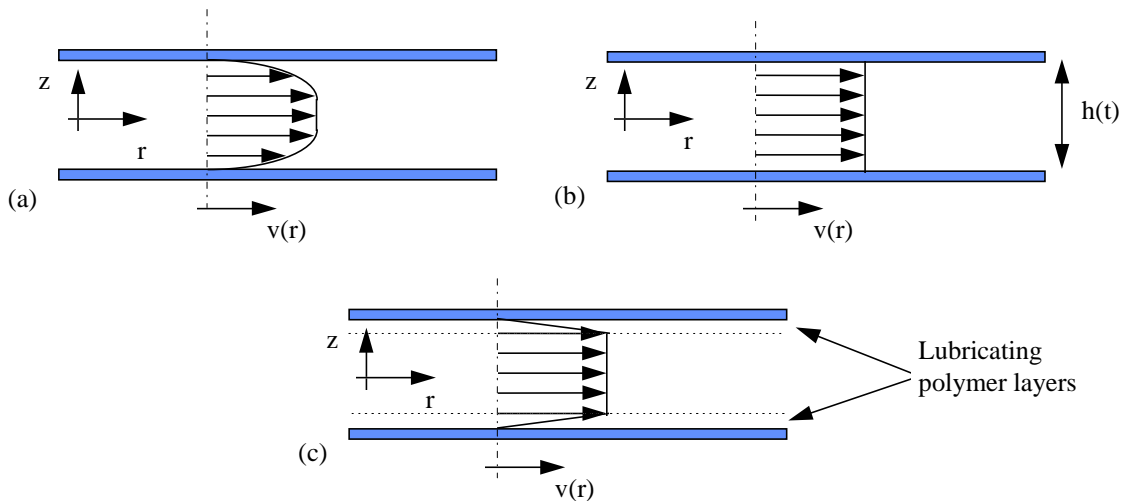


Figure 2: Velocity profiles in squeeze flow

However, previous work [3,4] on the *unlubricated* squeeze flow of GMT has demonstrated the predominance of extensional flow during squeezing. It was suggested, however, that the flow mechanism involved a thin shearing layer of polypropylene matrix acting as a lubricant at the plate surface while the bulk material underwent biaxial extension as shown in Fig. 2(c). Also, it is probable that the flow field was shear-dominated at small plate separations.

Lubricated squeeze flow, in which the flow mechanism is pure biaxial extension, should be a useful comparison with which to test these conclusions.

THEORY

The constant volume squeeze flow technique is shown schematically in Fig. 1. A molten disc-shaped sample is squeezed between two parallel heated plates under a constant squeezing rate. The sample thickness decreases as the plates approach one another and the sample radius increases as the material flows. Power law constitutive equations are used to model the flow behaviour and the squeezing force is strongly dependent on the flow boundary conditions at the plate surfaces.

Unlubricated Squeeze Flow

Under unlubricated conditions, a ‘no-slip’ condition is imposed at the surfaces of the plates. For unfilled polymer melts, this results in a pure shear flow field with a near-parabolic gapwise velocity profile. The power law constitutive equation for shear flow gives the shear stress as

$$\tau = A_s \dot{\gamma}^m \quad (1)$$

where A_s is the shear flow power law constant, m the power law index and $\dot{\gamma}$ the shear rate. The Scott equation [5] describes the variation of squeezing force with plate separation for a power law fluid;

$$F_{ca} = \left(\frac{2m+1}{m} \right)^m \left(\frac{2\pi A_s R^{m+3}}{m+3} \right) \left(\frac{u^m}{h^{2m+1}} \right) \quad (2)$$

where u is the squeezing velocity, h the instantaneous plate separation and R the sample radius. This equation is derived for constant area tests (sample diameter equal to plate diameter) and may be modified for application to constant volume tests to give

$$F_{cv} = \left(\frac{2m+1}{m} \right)^m \left(\frac{2VA_s R_o^{m+1}}{m+3} \right) (h_o)^{\frac{m+1}{2}} \left(\frac{u^m}{h^{\frac{5m+5}{2}}} \right) \quad (3)$$

where V is the sample volume and R_o and h_o the initial sample radius and thickness respectively.

Lubricated Squeeze Flow

The ‘no-slip’ condition is eliminated if a layer of lubricant is applied to the surface of the plates and to the sample, which has the effect of causing complete wall slip and eliminating the shear component of flow. In the absence of a shear contribution to the flow field, the material flows in biaxial extension with the radial velocity proportional to the radial position, r , but constant with respect to vertical position, z , between the plates (Fig. 2(b)).

From the power law constitutive equation, the strain rate-dependent extending stress is given by

$$\sigma = A_e \dot{\epsilon}^n \quad (4)$$

where A_e is the extensional flow power law parameter and n is the power law index. For the squeeze flow geometry, $\dot{\epsilon}$, the strain rate, is given by

$$\dot{\epsilon} = \left(\frac{u}{h} \right) \quad (5)$$

where u is the squeezing rate and h the instantaneous plate separation. An expression for the squeezing force during the test may be obtained directly from Eqn (4) and, using the constant volume assumption to describe the increasing sample radius, yields

$$F_{cv} = \left(\frac{V}{h} \right) A_e \left(\frac{u}{h} \right)^n \quad (6)$$

In order to determine power law parameters, we rearrange this expression and, taking logarithms, obtain

$$\log(Fh) = \log(VA_e) + n \cdot \log(\dot{\epsilon}) \quad (7)$$

A double logarithmic plot of (Fh) vs. $(\dot{\epsilon})$ should therefore give a straight line of slope n with A_e being calculated from the intercept of the line with the vertical axis corresponding to unity strain rate. It should be noted that A_e is often found to be strain-dependent [6], as in the case of a strain-hardening material.

MATERIALS

Both polypropylene (Shell grade XS-6500-S) and GMT samples were made with the same nominal geometry. Pure polymer samples were made by melt pressing 85 g of polymer granules in a simple plate mould and yielded samples with an average diameter of 148 mm and a 4.5 mm thickness.

The GMT material used in this work was based on the continuous swirled fibre mat produced by Symalit of Switzerland. Commercial grades of GMT, however, contain some ground recycled material between mat layers and have a comparatively large variation in glass content over a given area (around $\pm 4\%$ by weight variation). In order to be able to determine volume fraction more accurately, maintain consistent sample quality and to vary glass content in future studies, samples were manufactured by compression moulding. The manufacture of samples 'in-house' also reduces the effects of data scatter due to the variation in commercial material specification from batch to batch. A simple 150 mm diameter closed circular mould was used and samples manufactured by film stacking and hot pressing. The polypropylene matrix is the same as that used in the pure polymer samples. Samples were inspected individually after moulding to ensure good quality test specimens. The final average dimensions of the samples were 149.9 mm diameter with a 3.9 mm thickness and an average glass content of 30% by weight.

SQUEEZE FLOW EQUIPMENT AND TEST PROCEDURES

Fig. 3 shows the equipment used. The 395 mm x 395 mm squeeze flow plates are supported by four sliding columns to provide lateral stability and the whole apparatus is mounted in a 500 kN servohydraulic testing frame. Electrical heating elements and water cooling channels are incorporated beneath each plate.

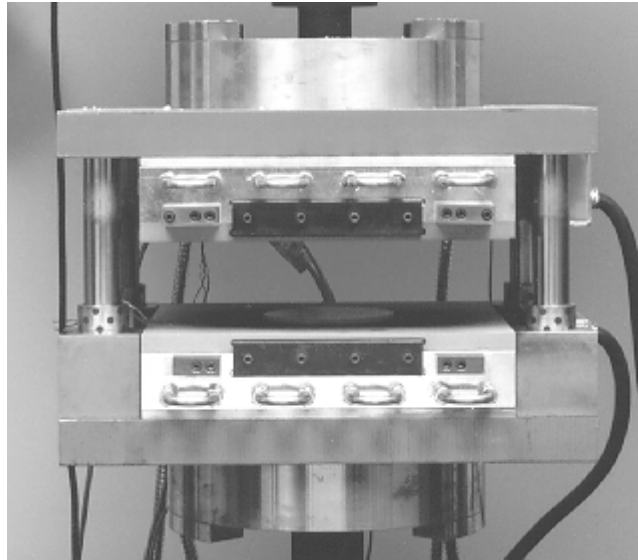


Figure 3: Photograph of Squeeze Flow Plates

Before testing, the plates are heated up with a separation of a few millimetres to allow for thermal expansion. Once the temperature had stabilised, the test programme opened the plates and the sample was placed in the centre of the lower plate. The plates are then closed to a separation of 5 mm and left for 10 minutes to allow the sample temperature to stabilise at 190°C. At the start of heating, the upper plate is not in contact with the GMT sample. This condition is imposed to allow for data correction due to the effects of internal friction and machine inertia at the start of machine movement. During heating, however, the GMT ‘lofts’ and contacts the upper plate. The initial movement of the plates reconsolidates the material and only squeezing in the final 3.9 mm is regarded as valid data. Once the sample is uniformly heated, the plates are driven together at the required velocity to a plate separation of 1 mm. The squeezing velocities used were 0.3, 1, 5, 10 and 20 mm/s. The same procedure is used for testing polypropylene samples, although lofting does not, of course, occur.

The most critical experimental factor in the lubricated squeeze flow technique is obtaining complete material slip at the plate surfaces. Silicon oils of various viscosities were used and the most effective lubricant determined by trial and error. The *quantity* of lubricant used was also found to be critical: too much and/or too high a viscosity of oil created an uneven lubricant layer and caused flow instabilities. A distorted sample shape resulted. With too little or too low a viscosity, incomplete wall slip occurred and pure extensional flow could not be achieved. In this work, tracers on the surfaces of the samples were used to assess the extent of slippage. Tracers were made from 5 mm lengths of thin carbon fibre/PEEK composite tape and were placed in shallow grooves in the sample surface as shown in Fig. 4. The position of the tracers after testing gives an indication of whether complete wall slip has been achieved. If complete wall slip is achieved, the tracers should remain at the outermost radial position on the sample. It was found that GMT was less sensitive to the lubrication method than was the

unfilled polypropylene, presumably due to the higher viscosity of the material. In all the tests, oil with a viscosity of 0.5 Pa.s was wiped on to the plates with a clean cloth prior to plate heating, with care being taken to apply as even a coating as possible. The surfaces of the test sample were also coated. After the test, when cooling was completed, the plates were degreased with acetone to ensure no residual oil build-up in subsequent tests.

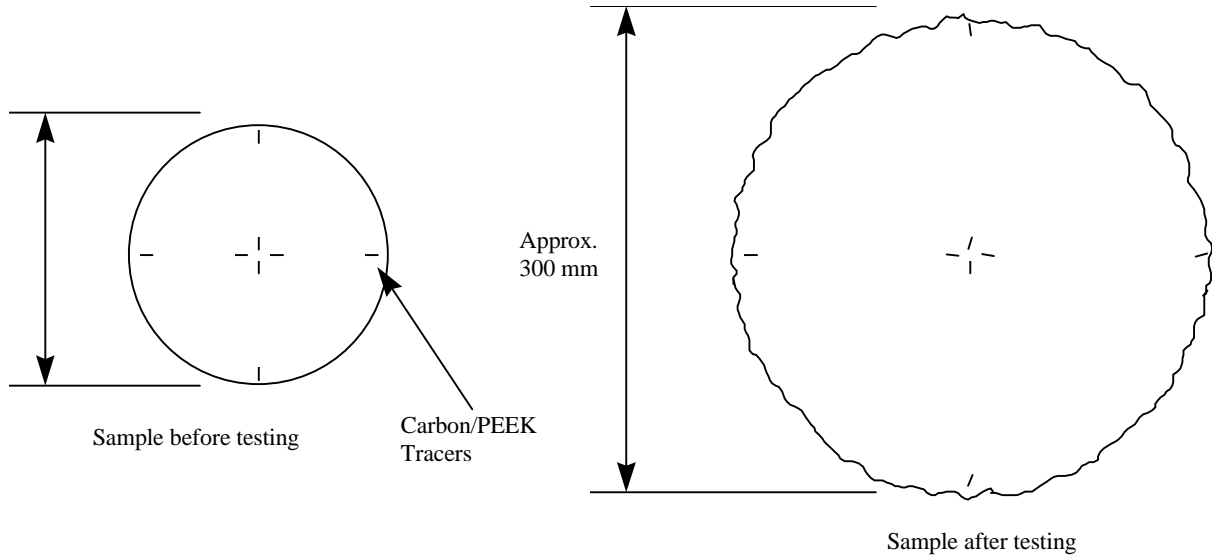


Figure 4: Positioning of Tracers on Sample Surface to Assess Extent of Wall Slip

RESULTS

Polypropylene

Fig. 5 shows squeezing force vs. plate displacement plots for squeeze flow tests on polypropylene. Lubricated and non-lubricated tests are shown on the same plot for squeezing rates of 1, 10 and 20 mm/s. It can be seen that lubrication lowers the required squeezing force by around 50% for the whole range of squeezing.

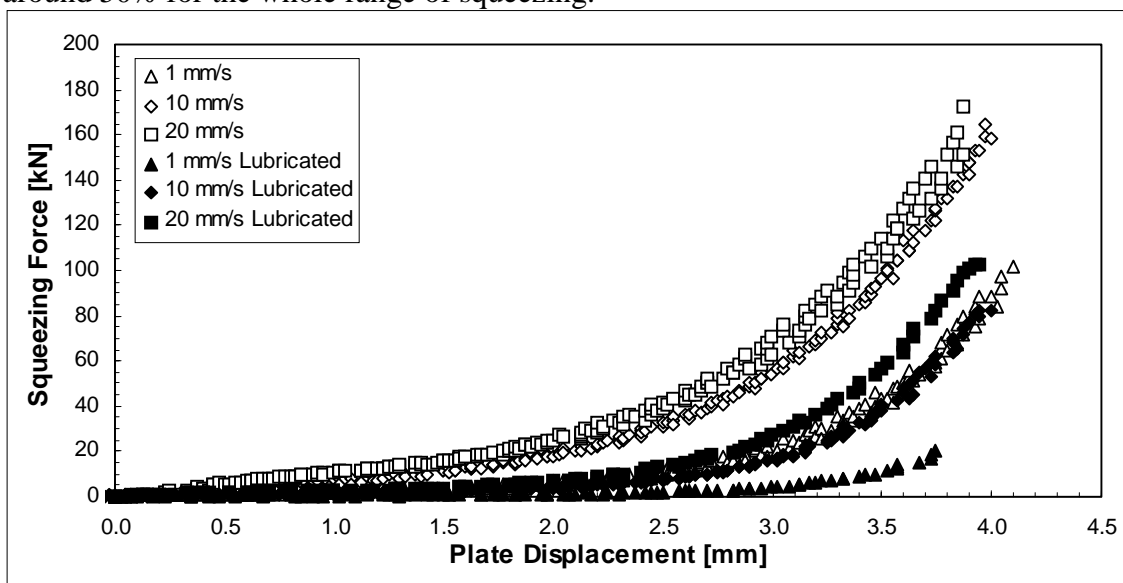


Figure 5: Squeezing Force vs. Plate Displacement for Polypropylene Tests

Other workers have used the unlubricated and lubricated squeeze flow techniques to generate shear and extensional viscosity data for polymer melts [1,7]. It should be noted, however, that a state of approximately steady flow must be achieved for this purpose. With the squeezing rates used in this work, which are chosen to be representative of the compression moulding process, it is not possible to achieve a steady state (or a 'quasi-steady state', as is most often assumed) and the calculation of viscosity data would not be valid.

Glass Mat Thermoplastic

Experimental data from lubricated and unlubricated tests on GMT at three different squeezing rates are compared in Fig. 6. Again, lubrication lowers the squeezing force, but to a much lesser extent than in tests on pure polypropylene.

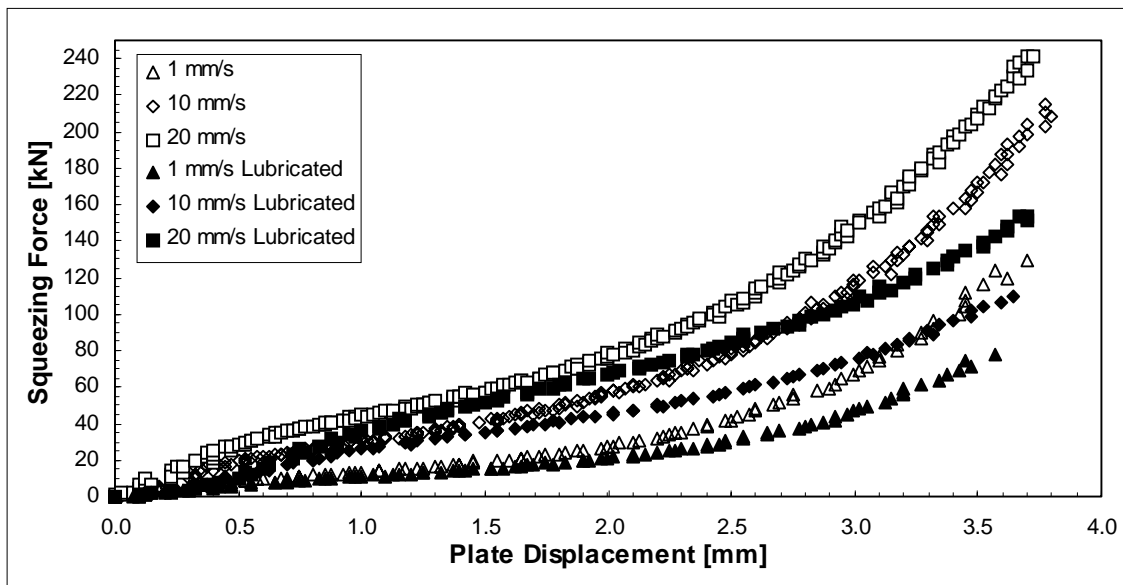


Figure 6: Squeezing Force vs. Plate Displacement for GMT

Squeezing force is similar for unlubricated and lubricated cases for about the first half of the test, with the force in the lubricated tests only slightly less than that for the unlubricated tests. At plate separations of less than about 2 mm, however, the force in the unlubricated tests increases much more sharply than that in the lubricated tests and the difference between the two becomes much larger.

A double logarithmic plot of $(F_x h)$ vs. $\dot{\epsilon}$ may be constructed (see Eqn 7) for the lubricated test data as shown in Fig. 7. Here, a linear relation exists for each value of plate separation plotted. These lines have slope n and their intercept with the vertical axis shown can be used to calculate A_e .

There is a small variation of A_e with increasing strain, as shown in Fig. 8. In fact, a slight decrease in A_e occurs as plate separation decreases and the variation may be approximated with a polynomial relationship. The resulting equation may be substituted into Eqn 5 to describe the squeezing force in power law terms. A typical test is compared with this model in Fig. 9. It should be noted that the 'start-up' flow region, corresponding to elastic compression of the sample, at the beginning of the test is not described by this model.

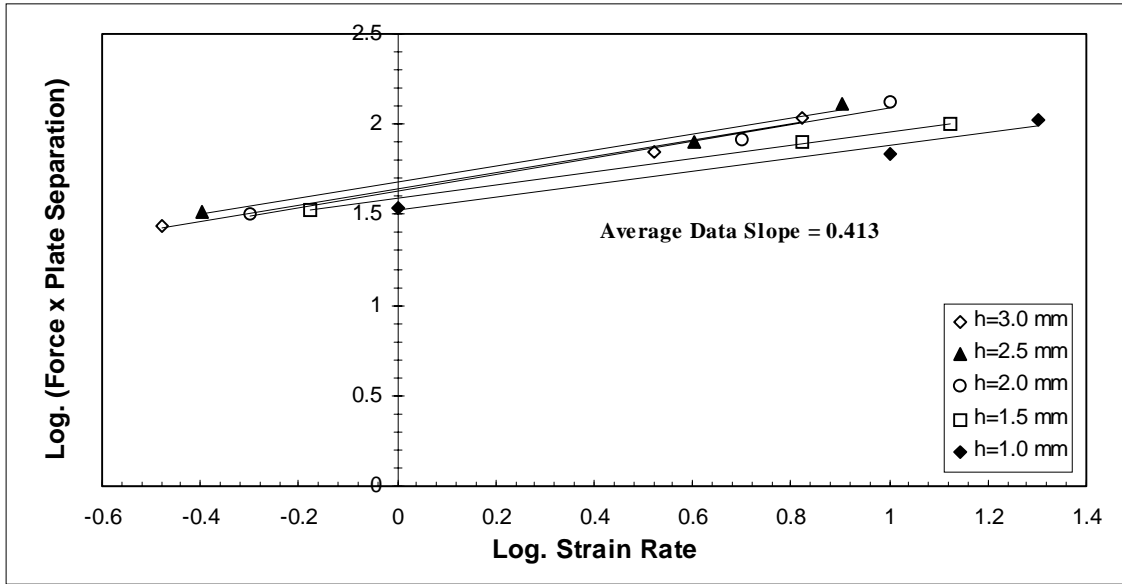


Figure 7: Log. (Squeezing Force x Plate Separation) vs. Log. Strain Rate for Lubricated GMT Tests

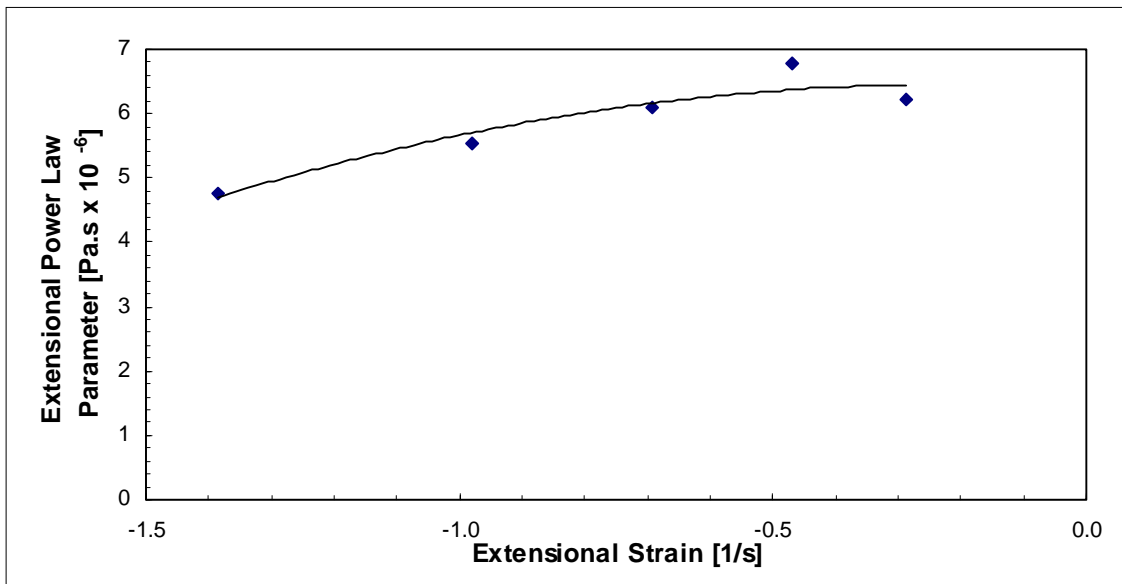


Figure 8: Variation of Extensional Flow Power Law Parameter with Strain Rate for Lubricated Tests on GMT

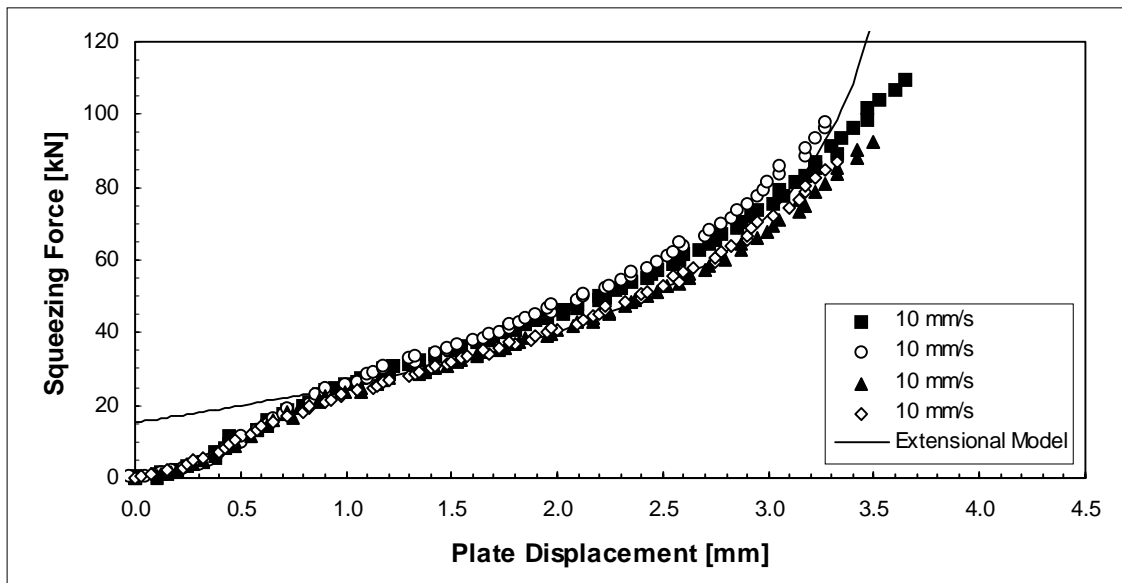


Figure 9: Comparison of Extensional Flow Model with Experimental Results

DISCUSSION

The unlubricated squeeze flow tests on GMT in previous work [3] showed that the flow could be modelled as biaxial extension over a portion of the total range of plate separation. This region occurred after the initial elastic compression and before the flow became shear-dominated at small plate separations. In this region, the squeezing forces found in *lubricated* squeeze flow are very similar to, although slightly lower than, those with unlubricated conditions. It was also suggested that a thin polypropylene layer, acting as a lubricant, may exist at the plate surfaces in unlubricated squeeze flow, and the small discrepancy between unlubricated and lubricated results may be due to the force required to shear this thin polymer layer. This behaviour supports the evidence for the biaxial extension of GMT in unlubricated squeeze flow.

At small plate separations, the squeezing force in unlubricated tests rises much more rapidly than that in lubricated tests. This is to be expected if the flow field in unlubricated tests becomes increasingly dominated by shear at small plate separations. Lubricated GMT, conversely, continues to undergo extensional flow throughout the test, as indicated by the final position of the surface tracers.

As may be expected, the flow behaviour of the polypropylene matrix material is different. The absence of the glass mat reinforcement reduces squeezing forces by around 25% at the highest loads in unlubricated tests. The forces in these tests are significantly higher than those under lubricated conditions throughout the range of plate displacement. This discrepancy in force represents the two extremes of material flow: shear flow under unlubricated conditions, with biaxial extension occurring in lubricated tests.

CONCLUSIONS

The unlubricated squeeze flow of unfilled polypropylene is shear-dominated. This behaviour has been modelled using power law shear flow constitutive equations [1,2] and also used to generate shear viscosity data under condition of steady flow. The effect of lubricating the plate surfaces during testing is to lower the required squeeze force throughout the test as the material undergoes biaxial extension with a negligible shear flow contribution.

Flow of GMT in squeeze flow appears to consist of three regions: 1) a 'start-up' flow of elastic material compression, 2) biaxial extension over the majority of the squeezing range and 3) a shear-dominated flow at small plate separations. This is confirmed by results from lubricated squeeze flow tests. For the range of squeezing attributed to extension in unlubricated squeeze flow, the forces are similar to those seen in lubricated squeeze flow. In the shear-dominated region at small plate separations under unlubricated conditions, the forces are much higher than in lubricated flow.

This work has attempted to simulate conditions in the compression moulding process if conditions were isothermal. Flow of GMT under these conditions is predominately extensional and can be described to a good approximation by simple power law relations. During flow in thin sections, however, flow behaviour changes and shear flow becomes increasingly important, causing a sharp rise in squeezing force. A purely extensional model may underestimate actual pressing forces under these conditions and an accurate model of compression moulding must cater for these changes in flow conditions.

ACKNOWLEDGEMENTS

Mr. J. H. Bland would like to thank Shell Research and Technology Centre, Amsterdam for partial funding in this work under the Co-operative Award in Science and Engineering scheme. In addition, many useful discussions with Professor S. Toll of Chalmers University, Gothenburg, Sweden are gratefully acknowledged. Further funding from the Engineering and Physical Sciences Research Council was also gratefully received.

REFERENCES

1. Laun, H. M. "Rheometry Towards Complex Flows: Squeeze Flow Technique" *Makromol. Chem., Macromol. Symp.*, Vol.56, 1992, pp.55-66.
2. Winther, G., Almdal, K. and Kramer, O., "Determination of Polymer Melt Viscosity by Squeezing Flow with Constant Plate Velocity", *Jnl. of Non-Newtonian Fluid Mech.*, Vol.39, 1991, pp.118-136
3. Kotiskos, G., Bland, J. H. and Gibson, A. G., "Squeeze Flow Testing of Glass Mat Thermoplastic Materials" *Composites A*, Vol.27A, No.12, 1996, pp.1195-1200.
4. Bland, J. H., Bersee, H. E. N. and Gibson, A. G., "Squeeze Flow of Polypropylene and Glass Mat Thermoplastics at Compression Moulding Strain Rates. Part II: Squeeze Flow of Glass Mat Thermoplastics" *Submitted to Composites A*.

5. Bird, R. B., Armstrong, R. C. and Hassager, O., *Dynamics of Polymeric Liquids; Volume 1*, 2nd Edition, J. Wiley & Sons, New York, 1987.
6. Collyer, A. A. and Clegg, D. W. (Eds.), *Rheological Measurement*, Elsevier Applied Science, London, 1988.
7. Hoover, K. C. & Tock, R. W., "Experimental Studies on the Biaxial Extensional Viscosity of Polypropylene" *Poly. Eng. & Sci.*, Vol.16, No.2, Feb.1976, pp.82-86.
8. Hsu, T. C. & Harrison, I. R., "Measurement of the Equibiaxial Elongational Viscosity of Polystyrene Using Lubricated Squeezing" *Poly. Eng. & Sci.*, Vol.31, No.4, Feb.1991, pp.223-230.

THE DRAPE FORMING OF A RUDDER TIP PREFORM

Paul Andrews¹, Rowan Paton¹ and John Wang²

¹ *Cooperative Research Centre for Advanced Composite Structures Limited (CRC-ACS),
506 Lorimer Street, Fishermens Bend, Victoria, 3207, Australia.*

² *CRC-ACS, School of Mechanical Engineering, University of NSW, Sydney, 2052, Australia.*

SUMMARY: This paper describes the development of a drape forming method for a rudder tip preform. Shear characteristics of the glassfibre fabric were investigated using three different test methods, and a fabric lock angle was defined and measured. Simple fabric shear tests performed by hand were sufficient to define fabric shear limits for subsequent computer drape simulation trials.

Drape forming experiments and computer drape simulations showed good agreement overall. Drape simulation was found to be a very useful tool for designing preform manufacturing processes. In the drape forming of a rudder tip, it was demonstrated that a simple adjustment of the orientation of the forming tool was effective in distributing fabric shear more evenly over the part, eliminating wrinkling. Successful drape forming of $0/90^\circ$ and $\pm 45^\circ$ plies was achieved.

KEYWORDS: Drape simulation, fabric draping, fabric shear, intersection angle, preform.

INTRODUCTION

The CRC-ACS has made a number of advanced composite demonstrator components to showcase its preforming and liquid moulding technology. One of these components is a fibreglass/epoxy rudder tip, currently made by Aerospace Technologies of Australia from a fibreglass/epoxy prepreg, laid up by hand on a male mandrel, and cured in an autoclave. The CRC-ACS demonstrator component has been made by RTM; an important part of the success of this demonstrator component was the ability to drape the fibreglass fabric into the “deep draw” preform shape quickly and easily, without wrinkles or other defects. In particular the ability to shape the preform without the use of any ply drop-offs or internal splices was very desirable.

The paper first describes an investigation into the draping characteristics of the selected fibreglass fabrics. A very simple bench test was used, as well as mechanical tests on fabric samples. The second part of the paper discusses tests to determine how the fabric can be draped over the component mould shape. This section reports both experimental and computer simulation trials.

CURRENT PRODUCTION METHOD

The lay-up for the Rudder Tip fairing under investigation consists of eight plies of 302 gm/m², 8 harness satin, 1581-style prepreg and two plies of 107gm/m², 4 harness satin, 120-style glassfibre prepreg. The two 120-style prepreg plies are positioned on the part surfaces. This rudder tip part is 800 mm long, weighing 1300 gm and is currently laid up on a male mandrel. No orientation is specified for the prepreg lay-up. Debulking is required for after every two plies of prepreg. Considerable cutting and splicing is required to form the plies around the tight double curvature of the leading edge radius of the part, which makes the part expensive to produce. The very tacky nature of the prepreg used also causes problems in layup.

FABRIC SHEAR TESTS

Initial hand draping trials on the Rudder Tip mould showed that the double curvature of this part would test the limits of shear in the 1581 and 120 glass fabrics. To understand this aspect of draping, a very simple fabric shear limit test was performed. This involved laying the fabrics on a smooth flat surface and marking a 50mm square grid on the fabric along warp and weft directions. The fabric was then stretched by hand on the flat surface, until the fabric “locked”, with further stretching producing wrinkles and local lifting of the fabric off the surface. At this point load was removed and the “intersection angle”, α , between the grid in the warp and weft directions, was measured using a protractor. The shear deformation of the fabric, β , was then calculated from $\beta = 90^\circ - \alpha$. The intersection angle at which wrinkles appeared was defined in this study as the “fabric lock angle” α^* . The limit value of fabric shear, β^* , can be obtained from $\beta^* = 90^\circ - \alpha^*$. The simple method used here to measure the fabric shear limit produced results consistent with those of Skelton [1], who fully explains the mechanics of fabric shear.

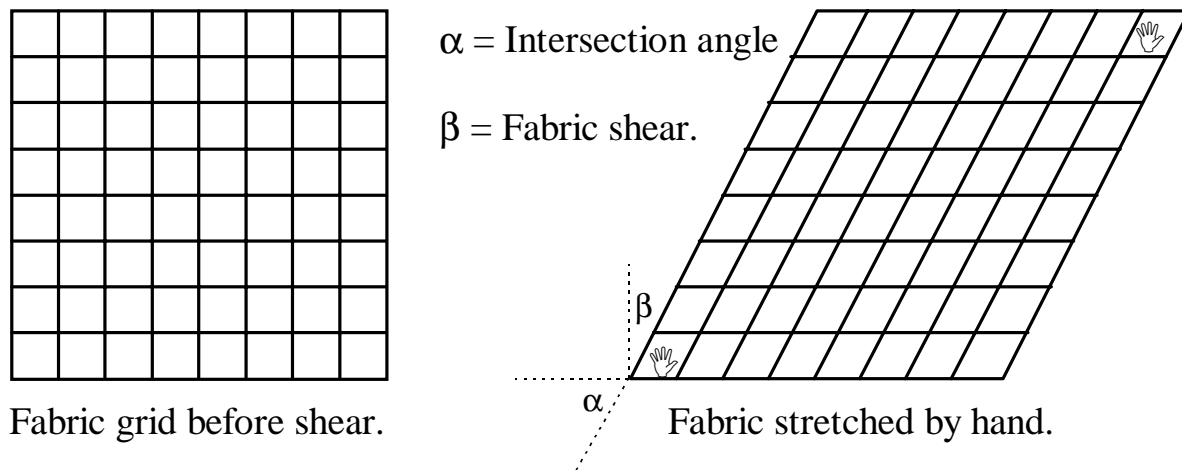


Figure 1: A simple fabric shear limit test to measure lock angle, α^ .*

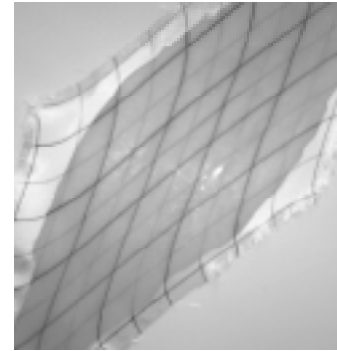


Figure 2: Shear limit test of 1581 fabric: α is 40° .

Figure 3: Wet 1581 fabric: α is 30° .

The test result for the 1581 style fabric is shown in Fig. 2. For 1581, an angle α of 40° was measured, while for the 120 fabric, an angle α of 30° was measured. A third test, with the 1581 cloth wetted by a low viscosity (room-temperature-curing) polyester resin, was also carried out. In this case, the fabric showed a significantly reduced α of 30° , as seen in Fig. 3. This improvement in fabric shear may be due to the lubrication effect of the resin, acting at tow crossovers, and also allowing easier reshaping of the tows for a tighter nesting of the fabric. The resin also provides tack, making the formation of wrinkles more difficult.

Two other sets of shear limit tests were carried out, with results made available for this study [2]. Simple bias extension tests were carried out on strips of fabric 120mm wide gripped in 80mm-wide jaws. A total fixed weight of 400gm on the lower jaw provided the only force. The fabric specimens were long enough to allow unrestrained deformation in the “gauge length”. Limit intersection angles were found to be 36° for the 1581 fabric and 35° for the 120 fabric. With fabrics wet with glycerine oil, the corresponding figures for α were 28° and 26° respectively.

Finally, dynamic testing using an Instron 1122A tensile test machine was carried out. The maximum capacity of the load cell used was 9.8N and the test speed used was 10mm/min. The test arrangement is shown in Fig. 4. In order to ensure correct installation of the specimen in the fixture, the fabric specimen with marked lines was mounted on the fixture on the bench, then the top half and bottom half of the fixture were rigidly connected using a connecting bar. The whole fixture was then installed in the jaws of the Instron machine and the connecting bar removed. The total length of the specimen was 320mm, with 220mm between two jaws (gross gauge length), 38mm clamped inside each jaw and 12mm projecting out from one side of each jaw. The width of the specimen was 100mm. Five specimens of each fabric were tested.

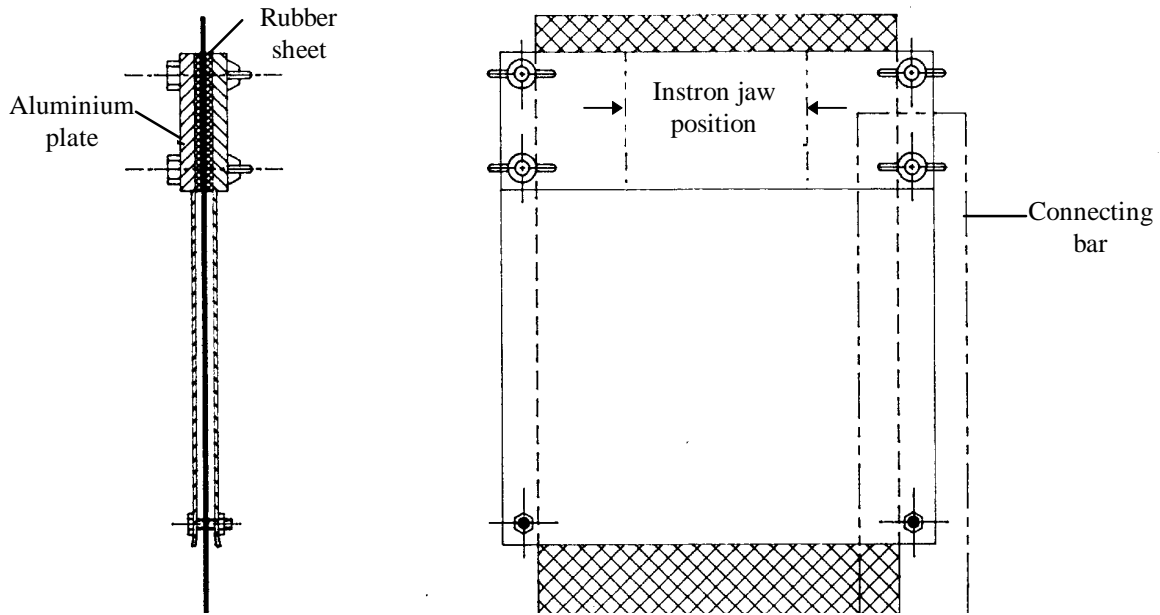


Figure 4: The clamping arrangement for the bias extension test.

Bias extension measurements in the gauge length were converted to intersection angles, and load was measured as force per unit width. The results are shown in Fig. 5. They indicate, as found previously, that 120-style fabric appears to drape more easily than 1581-style fabric, although this may be only because the 120 fabric is much lighter. The bias extension force for both fabrics increases substantially below $\alpha = 40^\circ$, but it is difficult from this test to define a precise lock angle α .

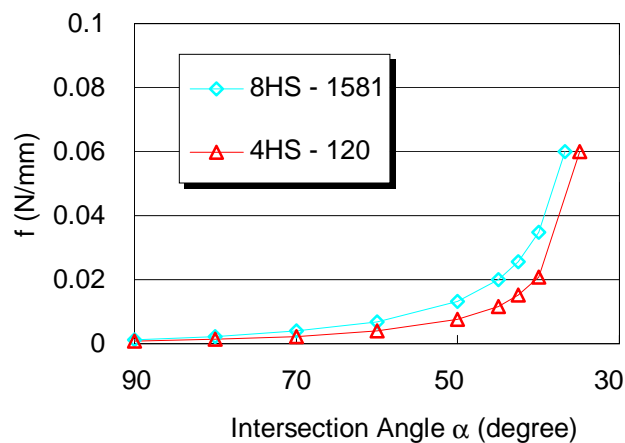


Figure 5: Results of dynamic bias extension test.

HAND DRAPING TRIALS

Drape forming trials for the Rudder Tip were carried out on a forming mould which was a full-scale replica of the production male mandrel. The 1581 fabric was cut in $0/90^\circ$ and $\pm 45^\circ$ orientations, and a 50 mm square grid pattern was marked on the fabric to identify warp and weft directions. No drape trials were carried out on the 120 style fabric, as it was considered that this material was more easily formed than the 1581 fabric.

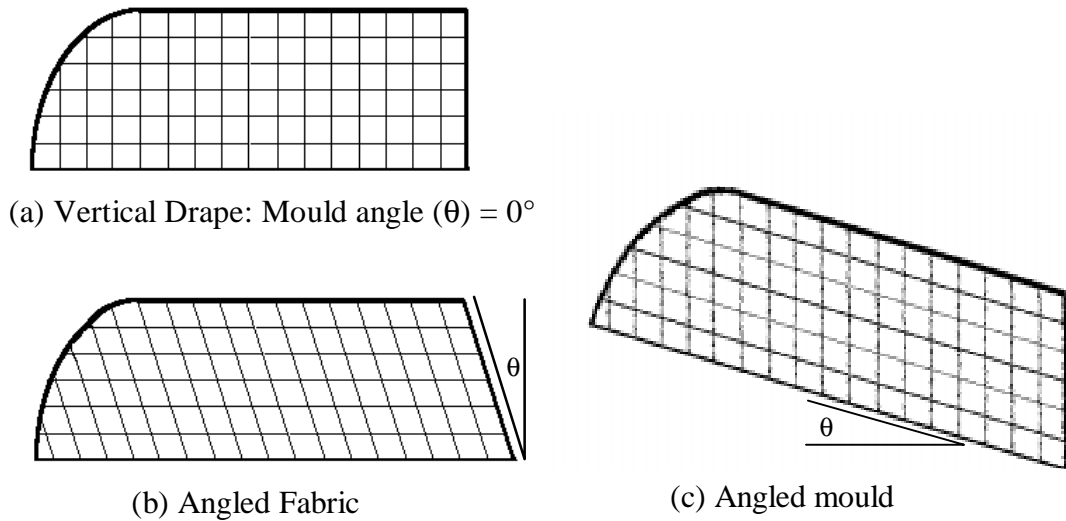


Figure 6: Mould drape angle, θ , achieved by angling either the fabric or the mould.

Initial drape trials using a 0/90° ply draped vertically, as in Fig. 6(a), showed a large amount of excess fabric at the front of the part, where the surface curves through an arc of 180°. It was found that this excess fabric could best be accommodated by sweeping the fabric on the side of the part rearward as shown in Fig. 6(b). In this way, the excess fabric at the front of the part was “shifted” to the rear of the part. The change in angle of the previously vertical fabric tows from the vertical is defined here as the mould drape angle, θ . (In this particular case only θ is also the shear angle of the fabric along the sides of the part).

In later trials, it was found that although the fabric could be swept back by hand to a measured angle θ , it was easier to raise the forming mould to the required angle θ , and allow the fabric to drape vertically, as shown in Fig. 6(c). The effect was identical. $\theta = 10^\circ$ was tried first. Bunching and wrinkling of fabric around the front of the part was greatly reduced, with most of the excess fabric moved along to the back of the part, past the trim line. However Fig. 8 shows that a few small wrinkles were present in the fabric around the front of the part, where intersection angles of 38° to 40° were measured, indicating that the fabric was at the limits of its ability to drape this shape.

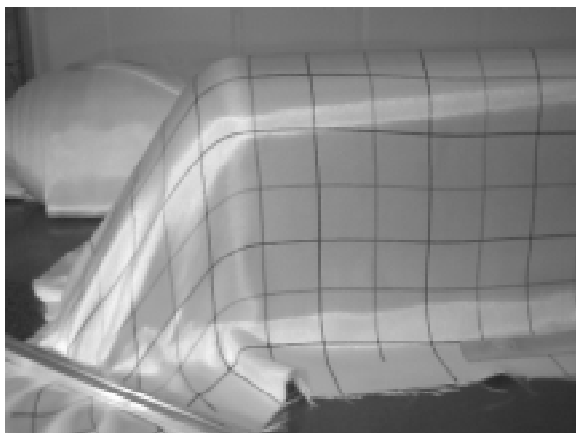


Figure 7: 0/90 ply, $\theta = 0^\circ$: Excess fabric at the front of the part.

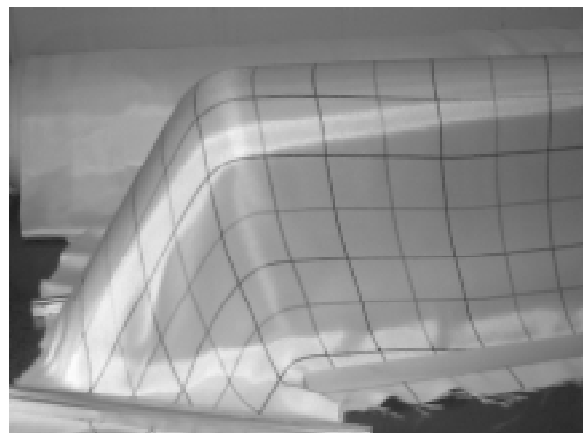


Figure 8: 0/90 ply, $\theta = 10^\circ$: Some minor wrinkles at the front of the part.

The mould drape angle was increased to $\theta = 20^\circ$, as shown in Fig. 9. This significantly reduced fabric shear at the front of the part, with more of the excess fabric being moved to the back of the part, past the trim line. The wrinkling problem was no longer evident and intersection angles measured were greater than 50° , even in the most highly stretched areas of the draped fabric.

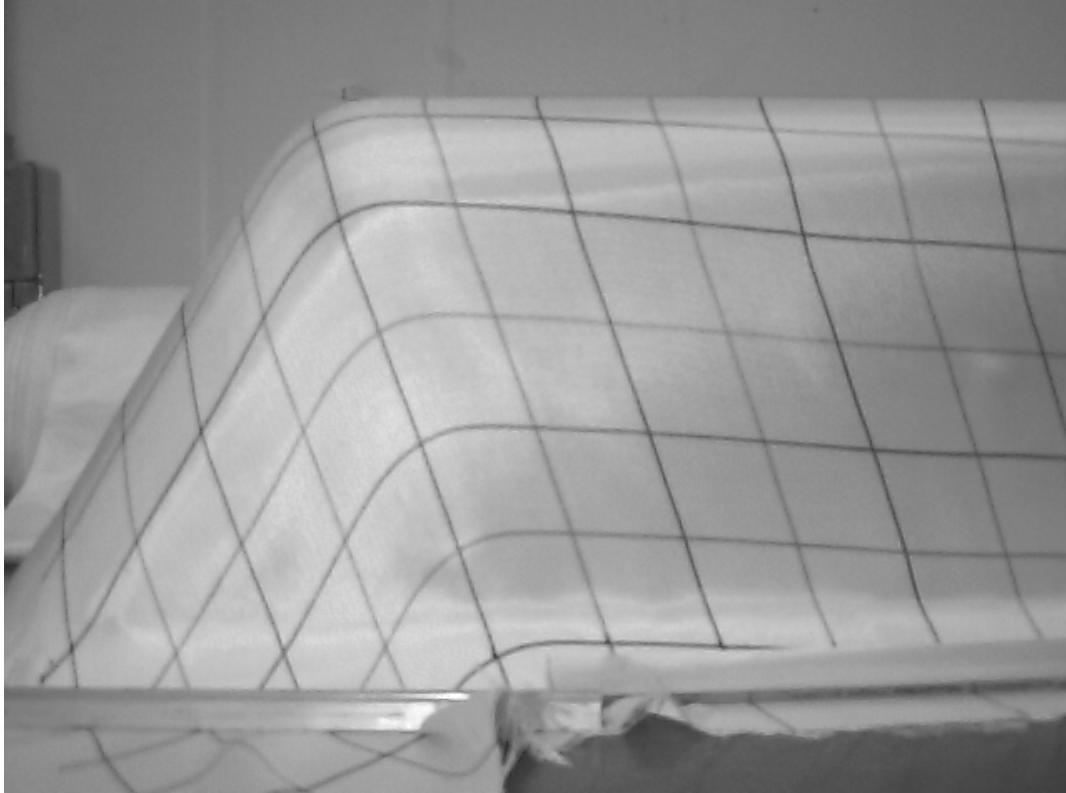


Figure 9: 0/90 ply, $\theta = 20^\circ$: Successful draping, no wrinkles.

Similar trials were carried out, again using a single ply of 1581 fabric, with the ply orientation at $\pm 45^\circ$. Fig. 10 shows the symmetrical placement of the $\pm 45^\circ$ ply on the forming mould, which is horizontal (mould drape angle of 0°). A large excess of fabric was again found to accumulate around the front of the part. The amount of excess material in this case appeared to be greater than for the $0/90^\circ$ ply (see Fig. 7) at a 0° mould drape angle.

Again, an angling of the forming mould on which the $\pm 45^\circ$ ply was draped, resulted in a “redistribution” of the excess material around the front of the part, and the wrinkling problems were overcome. Figs. 11 & 12 show that with a drape angle of 10° , redistribution of the excess fabric occurred by a diagonal stretching of the fabric in three directions. Originating at the top of the leading edge (the point where the fabric first contacted the angled forming tool), lines of maximum stretch occurred along the centreline at the front, and symmetrically down the left and right sides of the forming tool. This redistribution of excess fabric occurred in a different manner to that observed with the $0/90^\circ$ plies, where the excess fabric was moved uniformly along the length of the part, past the rear trim line.

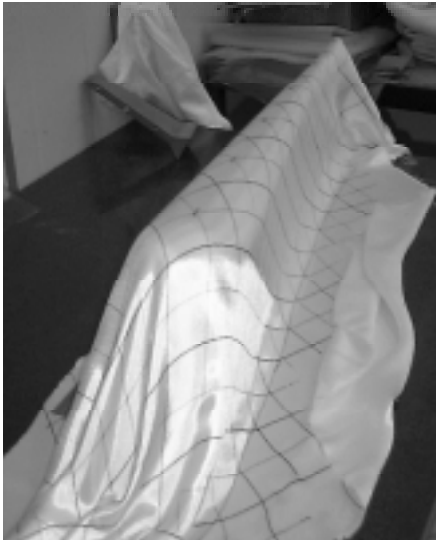


Figure 10: $\pm 45^\circ$ ply, $\theta = 0^\circ$; Excess fabric at the front of the part.



Figure 11: $\pm 45^\circ$ ply, $\theta = 10^\circ$; The excess fabric is redistributed.

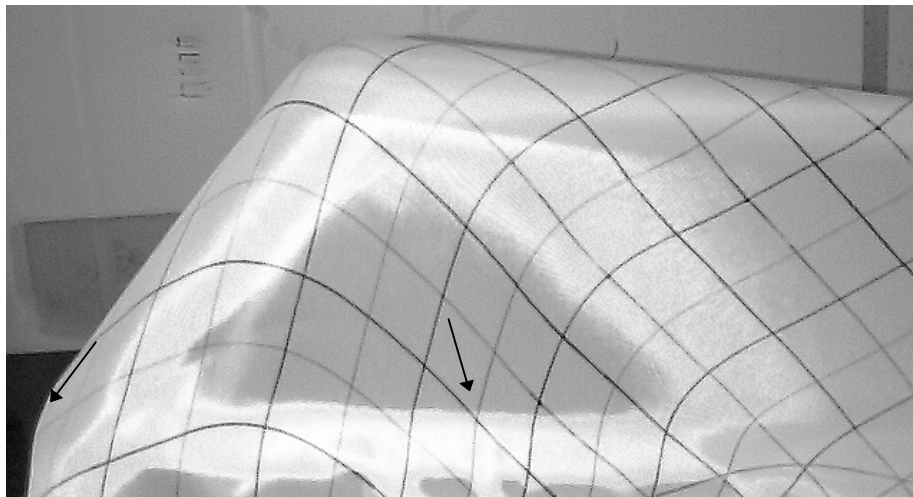


Figure 12: $\pm 45^\circ$ ply, $\theta = 10^\circ$; another view.

Mould drape angles of 6.5° and 20° were also tried (see Table 1), with very similar results to those obtained using 10° . Maximum fabric shear results showed little variation (ie. $40-41^\circ$) for the range of tool angles trialed ($6.5-20^\circ$).

DRAPE SIMULATION

A computer drape simulation of the Rudder Tip shape was performed using the Patran 3 Laminate Modeller analysis package. This computer program fits a simulated fabric onto a finite element mesh of a part shape to produce a drape simulation. Laminate Modeller is based on the pin-joint net idealisation of a fabric which was first proposed by Mark and Taylor in 1956 [3]. This software model is based on the assumptions that: (i) tows are inextensible, and tow crossover points act as pin-joints with no relative slippage; and (ii) that tow segments are always straight between crossover points. Fabric shear is the only deformation mechanism allowed, and the fabric is fully in contact with the surface.

To simulate draping over a surface, it is necessary to show two intersecting lines on the part surface to simulate the tows in the fabric. This software package has some options for “globe draping” ie. draping on a highly curved surface. The option selected here was “geodesic,” which corrects for assumption (ii) by allowing curvature of the lines drawn from the starting point, (at the high point of the part) through the crossover points along geodesic paths on the surface. This method of draping control is most useful for an arbitrary three dimensional surface with double curvature.

The Patran3/Laminate Modeller simulations are shown below, in Figures 13 and 14. These simplified representations indicate warp and weft directions, from which can be found the intersection angles (α). Where shear in the fabric is predicted to be higher than the limit value (ie. areas where wrinkles may occur), the warp and weft lines are omitted for clarity. A limit value of shear deformation $\beta^* = 50^\circ$ was specified for this study, in line with the hand drape test results mentioned previously. The maximum predicted fabric shear, β_{max} , required to drape the Rudder Tip surface for the mould drape angles specified is summarised in Table 1.

Table 1: Predicted and measured maximum shear angles

Ply Orientation	Mould Drape Angle(θ)	Predicted β_{max}	Measured β_{max}
0/90°	0°	62.8°	>50°: Wrinkling
	10°	54.0°	52°: Small wrinkles
	20°	45.8°	40°
	26°	40.3°	No result
±45°	0°	70.0°	>50°: Wrinkling
	6.5°	42.9°	41°
	10°	46.0°	40°
	20°	45.5°	40°

Table 1 shows that the drape simulation predictions and the results of the hand draping experiments agree very well. For the 0/90° plies, the drape simulation predicted that β is well beyond the fabric shear limit β^* for the mould drape angle (θ) of 0°, and just beyond β^* for $\theta = 10^\circ$. This agrees well with the hand draping results, where draping was found to be impossible at $\theta = 0^\circ$, and marginal at $\theta = 10^\circ$, with only a few minor wrinkles.

For the ±45° plies, the simulation predicted that draping is not possible at $\theta = 0^\circ$; the hand draping experiments verified this, with a considerable excess of material at the front of the rudder tip at this angle. Draping was predicted to be possible, however, at $\theta = 6.5^\circ$, 10° and 20° ; hand draping confirmed this. Interestingly, draping was predicted to be slightly easier at 6.5° than 10° or 20° ; this could not be confirmed by the hand draping experiments.

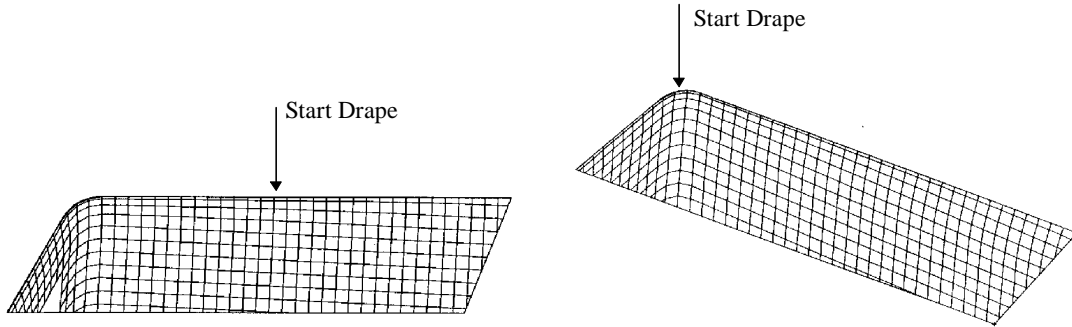


Figure 13(a) & (b): 0/90° drape simulation.

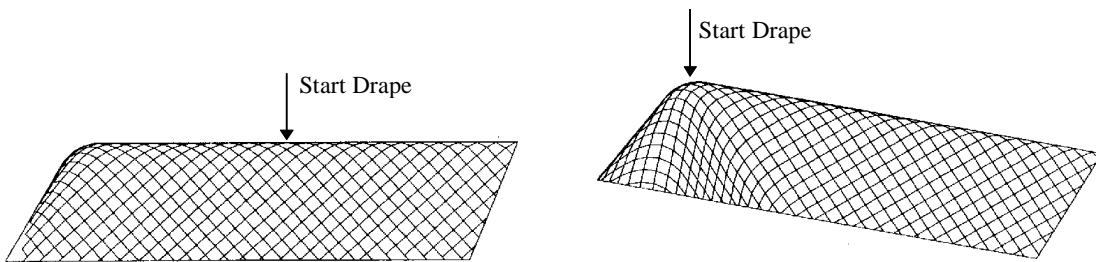


Figure 14(a) & (b): ±45° drape simulation.

Comparison of Figures 10, 12 and 14 show that the general arrangement of the fabric is quite similar in simulation and experiment. In all cases the predicted β_{\max} was found to be from 2° to 6° higher than the measured β_{\max} in this shape. This may indicate that fabric shear is not the only mechanism operating, and that yarn slippage may also be occurring.

Significant differences can be noted in the way the 0/90° and ±45° plies drape around the rudder tip shape. Fig. 15 suggests the different deformation required. The 0/90° ply is stretched in the two “bias” directions at ±45° to the rudder tip leading edge, forming two highly-sheared fabric “ears”. Moderate shearing also occurs along the sides of the mould. The ±45° ply is stretched in three fabric bias directions at 0°, +90° and -90° to the mould leading edge, forming the ears mentioned above, but is not stretched appreciably along the sides or spine of the mould. The availability of three bias directions at the mould front for the ±45° ply gives it a wider arc of highly sheared fabric, apparently allowing it to fit the shape with a lower β_{\max} than the 0/90° ply. This improved ease of forming for the ±45° ply was evident in drape trials, where a small θ of 6.5° produced successful draping. For the 0/90° ply, it was necessary to increase mould drape angle to 20° to achieve successful draping.

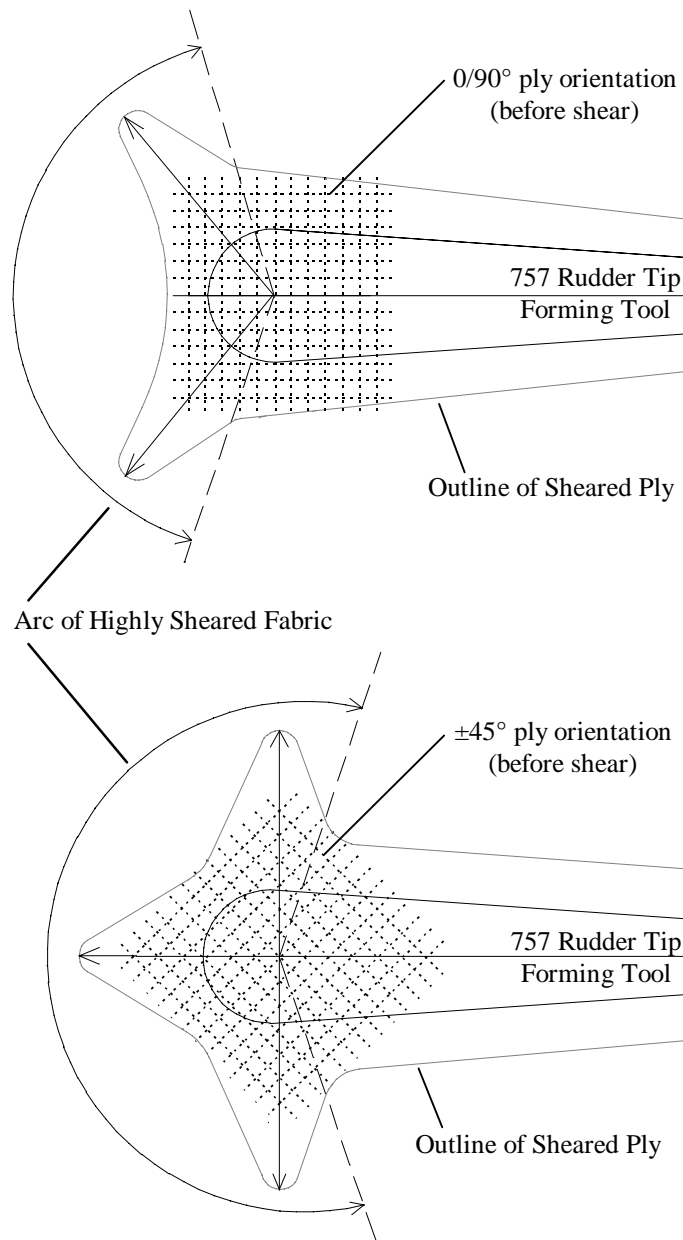


Figure 15: Schematic of fabric shear for $0/90^\circ$ and $\pm 45^\circ$ plies.

CONCLUSIONS

Three types of test were used to establish the effective limit intersection angle for reinforcement fabrics. A very simple test performed by hand on a flat surface was the easiest of the three and was found to be sufficiently accurate for computer drape simulation trials.

It was demonstrated that the rudder tip geometry can be draped from one piece of fabric for both $0/90^\circ$ and $\pm 45^\circ$ ply orientations. The two fabric orientations differed in the characteristic way in which drape forming was achieved around the highly curved front of the rudder tip part. The methods developed using single fabric plies, are expected to facilitate the production of a multi-ply rudder tip preform.

Comparison of drape simulation predictions and hand draping experiments indicated good agreement overall. Drape simulation is therefore a useful tool, particularly when the mould/tool is not available for draping experiments.

ACKNOWLEDGMENTS

ASTA cell leaders Mr. Peter Lazaro and Mr. Peter Maxwell kindly allowed use of a production tool and provided glass fabrics for draping trials. Mr Chris Granatir of CRC-ACS helped with the hand draping experiments.

REFERENCES

1. Skelton, J. Fundamentals of Fabric Shear. Textile Research Journal. Dec. 1976, pp 862 - 869.
2. Wang, J. Report on Test of Draping Properties of Fabric Preforms. School of Mechanical and Manufacturing Engineering, University of New South Wales, Sydney, Australia, October 1995.
3. Mark, C. and Taylor, H.M. The Fitting of Woven Cloth to Surfaces. Journal of Textile Institute, 47: T477 - T488, 1956.

THE EFFECT OF AGED MATERIALS ON THE AUTOCLAVE CURE OF THICK COMPOSITES

Evan A. Kempner¹, H. Thomas Hahn¹ and Hoon Huh²

¹ *Mechanical & Aerospace Engineering Department,
University of California, Los Angeles, CA 90095-1597, USA*
² *Korea Advanced Institute of Science and Technology, 373-1,
Kusong-Dong, Yusong Gu, Taejon 305-701, Korea*

SUMMARY: In order to control the quality of composites fabricated from prepreg, specifications are available for shelf life and out time for various material systems. Once the shelf life has been exceeded, the prepreg must either pass acceptance tests or be disposed of. The objective of this work is to determine the lifetime of prepregs by evaluating the effect of aging on the curing of thick composites. The investigation is carried out by applying numerical simulations of the curing process for graphite/epoxy AS4/3501-6 composite laminates of 3cm thickness. The results indicate that fairly uniform compaction can be achieved in 3cm laminates when using prepreg with up to 10% initial curing. However, large nonuniformity in fiber volume fraction occurs when using prepregs with initial curing of 20% and 30%. In addition, the incomplete compaction that occurs when using initially cured prepregs causes large temperature overshoot during cure despite the lower heat of reaction.

KEYWORDS: prepreg aging, cure simulation, thick composites

INTRODUCTION

Manufacturing composite parts from prepreg requires careful storage of the materials in order to produce laminates that meet desired performance specifications. Since prepreg materials contain resins that cure continuously, they are usually stored in a freezer to slow the curing reaction. Although industry practice and requirements vary, large rolls of prepreg may be thawed and refrozen many times as material is needed. Every time the material is thawed to room temperature, the state of cure will advance somewhat. Subsequently, age and out time of these materials may affect the quality of laminates produced.

In order to control the quality of composites fabricated from prepreg, specifications are available for shelf life and out time for various material systems. In production facilities, a careful history of the time out of the freezer is maintained for each roll of prepreg. Once the recommended shelf life or out time has been exceeded, the material can not be used unless acceptance criteria is met. Since requalification of these materials is not feasible, they must be disposed of if they do not pass the acceptance tests. Since disposal costs sometimes exceed material costs, this can become very expensive in situations where material is not used regularly. Therefore, composites manufacturers have tried to determine the usefulness of aged prepregs.

To identify the effects of aging, several studies have been published which describe the changes in physical properties of composites fabricated from advanced prepregs. These include methods to detect aging such as dielectric measurements, dynamic mechanical analysis and differential scanning calorimetry as well as the determination of the effects of aging on mechanical properties [1-5]. These studies have been conducted on a variety of material systems including graphite/epoxy, polyimides, and bismaleimide modified epoxy/graphite prepreg. In this paper, the discussion will be limited to graphite/epoxy composites.

Sanjana [6] studied the aging behavior of Hercules AS4/3501-6 graphite/epoxy prepreg under ambient and various other heat and humidity conditions. Prepreg tack was found to deteriorate before any other property. A prepreg is defined as tacky when its glass transition temperature is lower than the ambient temperature. The loss of tack makes it difficult to fabricate composite components with complicated shapes. However, Sanjana found that mechanical properties did not deteriorate until much after tack had been lost. Scola [7] found similar results from aging tests performed on AS4/3501-6. Mechanical tests on composites fabricated from prepreg aged under humid conditions indicated that the properties were unaffected by this conditioning. However, tackiness was found to increase in prepregs conditioned at higher humidity due to plasticization of the resin.

Prepreg tack is a relative term and is therefore difficult to measure. Several tests are available that can be used for semi-quantitative measures of tackiness. These include tests which measure the distance a metal ball can roll across the surface of a prepreg. Other tests measure the adherence of a prepreg to a metal surface. Probably the most common method of determining the flow properties of prepreg is a squeeze flow test, which is described in an ASTM standard [8]. This test measures the amount of resin squeezed from several layers of prepreg at the approximate processing temperature. The results of this test are usually used to compare lots of material and determine if the prepreg is acceptable for producing parts.

While prepreg tack is necessary to layup complex geometry parts, the flow properties of the prepreg will also affect the ability to achieve complete compaction during cure. As curing proceeds, compaction occurs such that the outer plies, adjacent to the bleeder, are compressed first. Eventually compaction occurs in the interior layers. However, in thick composites, gellation of the resin sometimes occurs before compaction of all of the layers can be achieved. This was demonstrated for thick graphite/epoxy laminates by Campbell et al. [9]. Composite laminates were cured using different consolidation pressures. Tang et al. [10] quantified these results by measuring ply thicknesses from photo micrographs. The results indicated that for 60 ply laminates, full compaction was only achieved in the outermost layers, and even the laminates cured at the highest pressure contained uncompacted plies near the tool surface.

The problem of temperature overshoot and incomplete compaction during the cure of thick composites was studied through numerical simulations by Hojjati and Hoa [11]. The simulations were based on the curing model developed by Loos and Springer [12] and the squeezed sponge model for one-dimensional consolidation proposed by Dave et al. [13]. Several common cure cycles were applied to AS4/3501-6 composites ranging in thickness from 2.5 cm to 30 cm. The prepreg was initially considered to be unreacted. Nevertheless, the results showed that the maximum thickness for which the manufacturer's recommended cure cycle could achieve complete compaction was 3.0 cm. Application of a cure cycle that has been recommended for thick composites resulted in reduced temperature overshoot, but did not improve the compaction behavior.

Twardowski et al. [14] addressed the effect of using somewhat advanced prepregs on the processing characteristics of thick composites. Poor correlation in temperatures predicted by simulation with experimental results prompted the consideration that some initial aging of the prepreg could have led to lower heat generation during the curing reaction. Therefore, heat transfer simulations were performed for 5 cm laminates with initial degree of cure varying up to 40%. Compaction behavior was not considered in these simulation. The results showed that the magnitude of temperature overshoot decreased with increasing initial degree of cure.

Studies on prepreg aging available in the literature have determined that little effect on the mechanical properties result in thin laminates produced from advanced prepregs. However, the effect of aging on compaction of thick composites has not been addressed. Therefore, the goal of this work is to examine the effects of initial prepreg aging on the curing behavior of thick graphite/epoxy composites. Curing simulations will be used to evaluate the variation in processing characteristics due to the advanced state of prepreg.

ANALYSIS

Consider a fiber preform that is fully saturated with viscous resin and subject to uniform compressive loading and varying temperature boundaries as shown in Fig. 1. The applied temperature will cause the resin viscosity to drop and resin flow to occur. As the matrix material is displaced, compaction of the laminate will occur in the thickness direction. When curing large composite structures, most of the heat and resin flow will occur in the z direction only. Therefore, only the one-dimensional case is treated here.

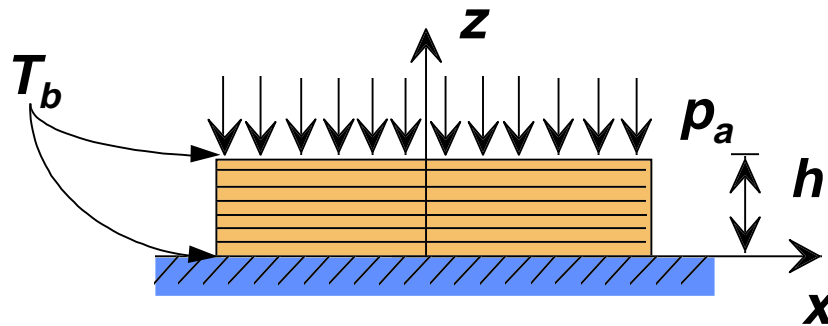


Fig. 1: Schematic of a composite laminate subject to a compaction pressure, p_a , and cure temperature, T_b

The heat transfer analysis used for the composite during curing was developed by Loos and Springer [12]. This model assumes heat transfer to occur due to conduction through the thickness of the laminate. Heat is also generated inside the laminate as curing proceeds. The one-dimensional heat balance for the laminate is given by

$$\frac{\partial T}{\partial t} = \alpha_z \frac{\partial^2 T}{\partial z^2} + \frac{1}{c_p} \dot{H} \quad (1)$$

where α_z and c_p are the thermal diffusivity and heat capacity of the composite and \dot{H} is the rate of heat generation.

The rate of heat generation is determined by

$$\dot{H} = V_m H_{Rm} \frac{\rho_m}{\rho} \frac{d\alpha}{dt} \quad (2)$$

where H_{Rm} is the heat of reaction of the resin, α is degree of cure, V_m is matrix volume fraction, ρ_m is resin density, and ρ is the composite density. An expression for the rate of change of degree of cure was developed for AS4/3501-6 prepreg [15] as given by

$$\frac{\partial\alpha}{\partial t} = \begin{cases} (K_1 + K_2\alpha)(1-\alpha)(.47-\alpha) & \alpha \leq 0.3 \\ K_3(1-\alpha) & \alpha > 0.3 \end{cases} \quad (3)$$

where

$$K_i = A_i \exp\left(-\frac{\Delta E_i}{RT}\right) \quad (4)$$

for $i = 1$ to 3 and R is the universal gas constant. A viscosity relation was also proposed

$$\mu = \mu_\infty \exp\left(\frac{U}{RT} + \kappa\alpha\right) \quad (5)$$

where μ_∞ and κ are constants and U is the activation energy for viscosity.

The governing equation for one-dimensional compaction and one-dimensional resin flow is essentially the same as that proposed by Dave [13]

$$-\frac{\partial p_a}{\partial t} + \frac{\partial p}{\partial t} = \frac{V_f}{S_z^f \mu} \left[\frac{\partial}{\partial z} \left(K_z \frac{\partial p}{\partial z} \right) \right] \quad (6)$$

where p_a is the external pressure applied to the laminate, p is resin pressure, V_f is fiber volume fraction, and S_z^f and K_z represent the compressibility and permeability of the fiber preform, respectively.

The fiber compressibility relates the change in fiber volume fraction to the effective fiber stress as given by the relation

$$S_z^f = \frac{\partial V_f}{\partial \sigma_z^{fe}} \quad (7)$$

where σ_z^{fe} is the effective stress carried by the fiber preform. Several empirical relations have been developed between fiber volume fraction and effective fiber stress based on experimental results. The following expression was used by Hojjati and Hoa [11]

$$V_f = \begin{cases} -6.915 \times 10^{-7} \sigma_z^{fe} + 0.53 & 0 \leq -\sigma_z^{fe} \leq 68.7 \text{ kPa} \\ 0.1094 \log_{10}(-\sigma_z^{fe}) + 0.0486 & 68.7 \leq -\sigma_z^{fe} \leq 1030 \text{ kPa} \end{cases} \quad (8)$$

Therefore, S_z^f will change nonlinearly during compaction. Permeability will also change during compaction. One common relation for permeability as a function of fiber volume fraction is the given by the Carman-Kozeny equation,

$$K_z = \frac{r_f^2}{4C_z} \frac{(1-V_f)^3}{V_f^2} \quad (9)$$

where r_f is the fiber radius and C_z is the Kozeny constant [16].

The initial conditions for the cure simulation are given by

$$T = T_\infty, \quad z \in \{0, h\} \quad (10)$$

$$p = p_a, \quad z \in \{0, h\} \quad (11)$$

where T_∞ is the ambient temperature. The boundary conditions are specified as

$$\frac{\partial p}{\partial z} = 0, \quad z = 0 \quad (12)$$

$$p = 0, \quad z = h \quad (13)$$

$$T = T_b, \quad z = [0, h] \quad (14)$$

where T_b is obtained from the applied cure cycle.

The above equations were solved numerically using a Crank-Nicholson finite difference scheme in which all calculations are based on the variables at their average value between the current and past time steps. Eqns 1 and 6 were solved simultaneously. Since S_z^f and K_z change during the cure, they must be updated continuously. Therefore, an iterative approach was used. Good accuracy and convergence was found using a time step of one second and position steps of 0.1 cm.

RESULTS AND DISCUSSION

The aging that will occur due to exposure of AS4/3501-6 graphite/epoxy prepreg to ambient conditions can be calculated from the cure kinetics relations described above. The out time specified by Hercules for this prepreg is 10 days, but much longer out times have been considered in aging studies [17]. Assuming room temperature to be 25°C, consider the case of 30 days at this temperature. Using the input parameters listed in Table 1, the extent of reaction that could result during the out time was calculated to be 0.06 after 10 days and 0.16 after 30 days. Note, however, that the cure kinetics parameters were measured at very high temperatures. Since they are based on empirical data fitting, it is not clear how reliable they are at room temperature.

Table 1: Input parameters for cure kinetics calculations

Exponential factor, A_1 (min^{-1})	2.101×10^9
Exponential factor, A_2 (min^{-1})	-2.014×10^9
Exponential factor, A_3 (min^{-1})	1.96×10^5
Activation energy, ΔE_1 (J mol^{-1})	8.07×10^4
Activation energy, ΔE_2 (J mol^{-1})	7.78×10^4
Activation energy, ΔE_3 (J mol^{-1})	5.66×10^4
Heat of reaction, H_{Rm} (J kg^{-1})	4.73×10^5

In [11], it was determined that 3 cm is the maximum laminate thickness that can be produced with complete consolidation using conventional cure cycles. The recommended cure cycle for this material system consists of a 70 minute dwell at 116°C and a 130 minute dwell at 177°C with temperature ramp rates of 2°C/min. Modified cure cycles are available for thick composites which were found to reduce temperature overshoot. However, these cure cycles do not have a significant effect on the compaction behavior.

To determine the effect of prepreg aging on the cure of thick composites, simulations were performed for laminates with initial thickness of 3 cm and initial degree of cure ranging from 0.01 to 0.3. The input properties used for the simulation model are listed in Table 2. The manufacturer's recommended cure cycle was used throughout. Fig. 2 shows the change in thickness during cure for four different initial conditions. The results indicate that the maximum thickness change is obtained using an initial degree of cure of 0.01. The final laminate thickness obtained with $\alpha_{init} = 0.1$ is only 1.3% greater than that obtained with uncured material. However, the final thickness achieved with $\alpha_{init} = 0.2$ and 0.3 is found to be 6.3% and 18% greater than that obtained with new material.

Table 2: Input properties for simulation

Resin density, ρ_m (kg m^{-3})	1.26×10^3
Specific heat of resin, c_{pm} ($\text{J kg}^{-1} \text{K}^{-1}$)	1.26×10^3
Thermal conductivity of resin, k_{zm} ($\text{W m}^{-1} \text{K}^{-1}$)	0.167
Fiber density, ρ_f (kg m^{-3})	1.79×10^3
Specific heat of fiber, c_{pf} ($\text{J kg}^{-1} \text{K}^{-1}$)	7.12×10^2
Thermal conductivity of fiber, k_{zf} ($\text{W m}^{-1} \text{K}^{-1}$)	26
Fiber radius, r_f (m)	3.5×10^{-6}
Kozeny constant, C_z	6
Initial fiber volume fraction, V_{fi}	0.53
Activation energy for viscosity, U (J mol^{-1})	9.08×10^4
Viscosity constant, μ_∞ (Pa s)	7.93×10^{-14}
Viscosity constant, κ	14.1

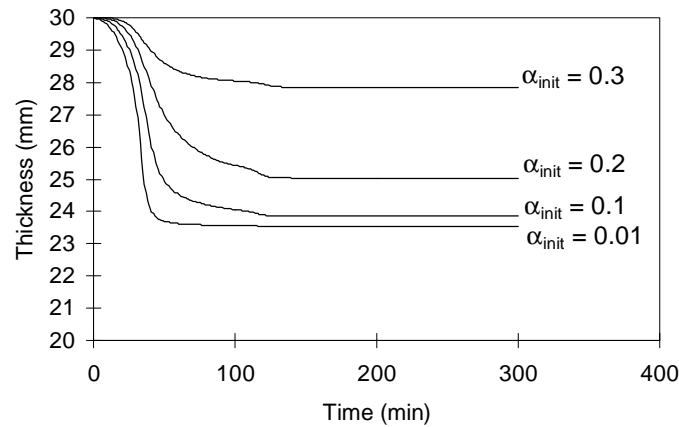


Fig. 2: Change in thickness during cure for laminates with initial aging

The nonuniformity of consolidation through the thickness of the laminate is shown in Fig. 3. As expected, uniform consolidation was achieved with $\alpha_{init} = 0.01$. The small difference in final thickness achieved with $\alpha_{init} = 0.1$ results in only small inhomogeneity in fiber volume fraction through the thickness. The fiber volume fraction distribution for the laminate cured with $\alpha_{init} = 0.2$ indicates a variation between 0.6 and 0.68 throughout the entire laminate while $\alpha_{init} = 0.3$ resulted in approximately one quarter of the laminate remaining unchanged from the initial fiber volume fraction. While incomplete consolidation will affect mechanical properties by reducing fiber volume fraction, part performance will be more significantly affected by the nonuniform compaction and subsequent nonuniform properties.

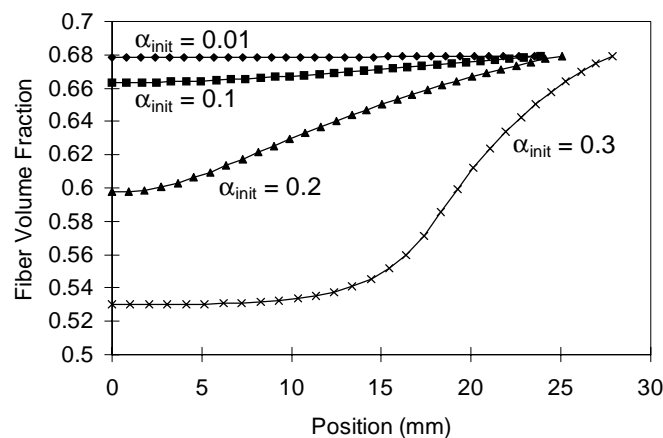


Fig. 3: Distribution of fiber volume fraction after cure of laminates with initial aging

The effect of initial prepreg aging on temperature overshoot is examined. Fig. 4 shows midplane temperatures during cure for the 3 cm laminates. Comparison of maximum temperature overshoot obtained during simulations with $\alpha_{init} = 0.3$ and $\alpha_{init} = 0.01$ indicates a 10°C higher result for the aged prepreg. This behavior contradicts the results found in Ref. 14, where heat transfer simulations showed reduced temperature overshoot in laminates produced from aged prepreps. The reason for this difference is that compaction was neglected in the simulations of Ref. 14. Although less heat is generated by the curing reaction with initially aged materials, the laminate is 4.3 mm thicker than the initially uncured materials at the time that the maximum overshoot occurs. Therefore, the low thermal conductivity of the composite appears to be more significant than the heat of reaction of the resin.

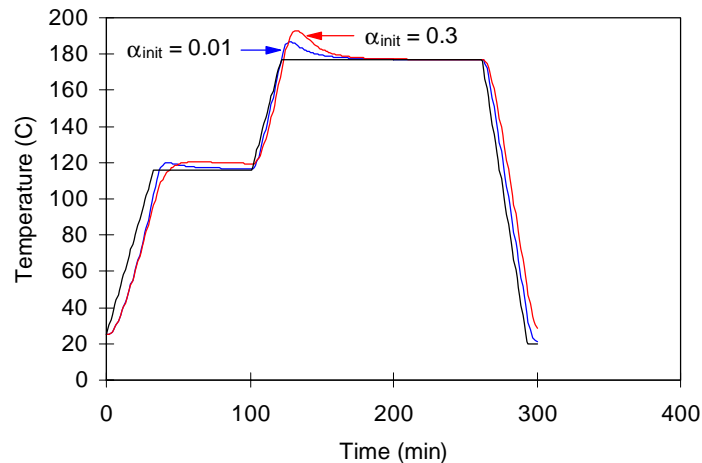


Fig. 4: Midplane temperatures during cure for laminates with different initial aging

CONCLUSIONS

Storage recommendations provided by the material manufacturer do not provide a direct indication of the limitations of aged materials. Therefore, a study was conducted in which simulations were performed for autoclave curing of composite laminates with various thicknesses and with materials of different conditions. A numerical code was implemented to solve the one-dimensional heat transfer as well as the resin flow and fiber deformation during cure. The results showed that fairly uniform compaction can be achieved in 3cm laminates when using prepreg with up to 10% initial curing. However, by applying a 30 day out time, it was shown that resins in prepreg can advance to 16% when kept at conditions of 25°C. When prepreps with initial curing of 20% and 30% were used, large nonuniformity in fiber volume fraction was found. Also, large temperature overshoot occurred during cure with partially cured prepreg due to the poor compaction. This shows that partially curing prepreg is not a viable approach to controlling temperature overshoot in thick composites.

ACKNOWLEDGMENTS

The present paper is based on work supported in part by the Office of Naval Research under Grant N00014-92-J-1846 and in part by the Department of Energy Integrated Manufacturing Engineering Predoctoral Fellowship (EAK). The authors would like to thank Yapa Rajapakse, ONR Scientific Officer, for his interest in the work.

REFERENCES

1. Dunn, D.A., Hagnauer, G.L. and Doherty, J.E.B., "Aging Effects on Prepreg Composition and Laminate Properties", ANTEC Proceedings, 1989, pp. 1142-1146.
2. Vuong, T., "An Out Time Study on PMR-15 Polyimide Resin", *Proceedings of 32nd International SAMPE Symposium*, 1987, pp. 839-852.

3. Scola, D.A., Vontell, J., and Felsen, M., "Effects of Ambient Aging of 5245C/Graphite Prepreg on Composition and Mechanical Properties of Fabricated Composites", *Polymer Composites*, Vol. 8, No. 4, 1987, pp. 244-255.
4. Shepard, D.D., "PMR-15: Aging Detection Using Dielectric Sensors", Proceedings of the 35th International SAMPE Symposium, 1990, pp. 1499-1506.
5. Akay, M., "Effects of Prepreg Ageing and Post-Cure Hygrothermal Conditioning on the Mechanical Behaviour of Carbon-Fibre/Epoxy Laminates", *Composites Science and Technology*, Vol. 38, No. 4, 1990, pp. 359-370.
6. Sanjana, S.N., "Overage Indicators for Prepreg Products", *SAMPE Journal*, Vol. 16, no. 1, 1980, pp. 5-11.
7. Scola, D.A. "The Effects of Humidity Exposure on AS/3501-6 Prepreg Material", 15th National SAMPE Technical Conference, 1983, pp. 9-20.
8. Standard Test Method for Resin Flow of Carbon Fiber-Epoxy Prepreg, ASTM Standard D3531-76, 1989.
9. Campbell, F.C., Mallow, A.R. and Amuendo, K.C., "Computer Aided Curing of Composites", McDonnell-Douglas Corporation, St. Louis, Missouri, Report No. IR-0355-4, 1985.
10. Tang, J., Lee, W.I. and Springer, G.S., "Effects of Cure Pressure on Resin Flow, Voids, and Mechanical Properties", *Journal of Composite Materials*, Vol. 21, No. 5, 1987, pp. 421-440.
11. Hojjati, M. and Hoa, S.V., "Curing Simulation of Thick Thermosetting Composites", *Composites Manufacturing*, Vol. 5, No. 3, 1994, pp. 159-169.
12. Loos, A.C. and Springer, G.S., "Curing of Epoxy Matrix Composites," *Journal of Composite Materials*, Vol. 17, No. 2, 1983, pp. 135-169.
13. Dave, R., "A Unified Approach to Modeling Resin Flow During Composite Processing," *Journal of Composite Materials*, Vol. 24, No. 1, 1990, pp. 22-41, 1990.
14. Twardowski, T.E., Lin, S.E. and Geil, P.H., "Curing in Thick Composite Laminates: Experiment and Simulation", *Journal of Composite Materials*, Vol. 27, No. 3, 1993, pp. 216-250.
15. Lee, W.I., Loos, A.C. and Springer, G.S., "Heat of Reaction, Degree of Cure, and Viscosity of Hercules 3501-6 Resin," *Journal of Composite Materials*, Vol. 16, No. 6, pp. 510-520, 1982.
16. Terzaghi, K. and Peck, R.B., *Soil Mechanics in Engineering Practice*, Wiley, New York, 1967.
17. Hercules Product Data Sheet, Hercules Advanced Materials & Systems Co., Magna, Utah.

ISSUES IN MODELING DISCONTINUOUS RANDOM FIBER SRIM COMPOSITES

O. Ochoa and T. Eason

*Center for Mechanics of Composites, Texas A&M University,
College Station, Texas, 77840-3123, USA*

SUMMARY: The performance of SRIM (Structural Reaction Injection Molded) composites with thermal spray preform is simulated with finite element analysis and compared to experimental data. The finite element method is used in conjunction with an idealized representative volume element (RVE) to develop an understanding of the fiber/fiber and fiber/matrix behavior. A one dimensional transient heat transfer analysis is used to simulate the thermal gradient through the thickness of the RVE to simulate the processing stresses. Once the residual stresses are introduced into the RVE model, the tangent tensile modulus is calculated for the RVE. The emphasis is placed on the thermomechanical response and the accompanying degradation in strength and stiffness. The RVE methodology will be used to understand the effects of the fiber/fiber interaction and matrix behavior on the static properties of the composite. Initial results indicate that the approach taken provides a realistic avenue to access the micro and macro aspects of this material system.

KEYWORDS: discontinuous fiber, residual stresses from processing, structural reaction injection molding, thermomechanical modeling, damage initiation and progression

INTRODUCTION

Adequate analysis of the processing effects on the mechanical performance becomes of increasing importance as more economical manufacturing options are sought for composites. Randomly oriented discontinuous fiber (RDF) composites provide one avenue for reducing manufacturing cost by combining high production rates with low material cost and scrap rates. Empirical relations for the modulus of RDF composites work well for predicting the mechanical response in the initial region. However, experimental evidence suggests that SRIM composites display a non-linear stress-strain response. The experimental observations may be validated by investigating the interaction among neighboring fibers and between the fiber and matrix under thermomechanical loading. This is accomplished by using a finite element model with non-linear matrix properties and damage progression capability to characterize the non-linear response of the composite and identify of the failure mode. Improvements in material performance can then be obtained by adjusting the influential material parameters for improved performance of the composite system.

Experiments to understand the influence of the fiber structure have concentrated on parametric studies to determine the influence of chop length, strand size and binder type on the permeability of the preform and structural performance of the composite. From these studies, the important fiber parameters are identified as binder type and number of filaments per a strand. Chop length (when varied well above the critical length) and filament diameter

appear to have little influence on the modulus and strength of the composite. The important matrix properties are coefficient of thermal expansion, modulus and yield strength. Matrix ductility has been shown to have little influence on the performance of the composite system .

The prediction of modulus and strength using a laminate analogy is adequate for predicting the response of the composite at the macro level. Early work formed the quasi-isotropic laminate analogy which provided a good approximation for the initial linear modulus. Current research in random fiber composites continues to rely on laminate analogy but addresses fiber orientation and progressive failure to capture the nonlinear response. This type of development is limited because fiber/matrix interface and fiber/fiber interaction are only accounted for in a smeared manner. The micro-mechanical aspects of the fiber/matrix interface and fiber/fiber interaction appear to be the most promising in developing a complete picture of the RDF SRIM composite's behavior. A shear lag approach to investigate the stresses around a short fiber imbedded in a matrix has contributed to the understanding of the load transfer within discontinuous fibrous composites. This approach works well for aligned fiber composites. However for fibrous assemblies where the fibers come into contact with one another, the axial fiber stress and the interfacial shear stress at the outer fiber surface is difficult to predict. The most promising path in developing a thorough understanding of the failure behavior of the RDF SRIM composite's behavior is to account for the constituents distinctive structure within the micromechanics frame.

The micromechanics approach introduces higher order stress or strain gradients to account for heterogeneity in the material system. Internal strain energy of the system can be used to obtain average of the stress-strain variations in the composite leading to the stiffness or compliance evaluation. It is extremely important to describe the structure of the heterogeneity as closely as possible to generate accurate results. Improved bounds for the moduli can be obtained using information beyond that contained in the volume fraction as in rule of mixtures. Komori and Makishima developed a general expression for the average number of contacts per unit fiber length in randomly oriented fibrous assemblies which was later improved by Pan. These contacts are believed to be essential in the understanding of the structural heterogeneity in the material for RDF composite systems.

PROCESSING AND EXPERIMENTAL OBSERVATIONS

The thermal spray/SRIM process begins by manufacturing a near net shape fiber preform. The fiber preform is constructed on a wire screen with an exhaust fan connected to one end. A continuous roving spool is used to deliver the strand to the chopper gun where the roving is cut into two inch lengths. As the two inch strand leaves the chopper gun, the strand crosses paths with a flame gun and a stream of binder melting the binder to the strand before being delivered to the preform screen. The binder quickly solidifies and holds the fiber to the preform. The exhaust fan is used to pull air over the fibers to hold them in place while the binder cools. The preform is then removed from the screen and ready for injection molding. After the fiber preform is constructed, the preform is inserted into a mold cavity. The mold cavity is closed and the preform is injected with a fast reacting two part polyurethane system at a mold temperature of 93°C. After the panel is cured for approximately 90 seconds, the mold is opened and the composite panel is removed and cooled down to room temperature. As the surface begins to cool, it takes on a tensile in-plane stresses while the warmer interior assumes a compressive state of in-plane normal stress. As the center reaches room temperature, the in-plane normal stress at the surface changes sign becoming compressive

while the stresses in the interior becomes tensile. Large in-plane tensile stresses develop due to the mismatch in the thermal coefficients of expansion between the glass fiber reinforcement and the urethane resin during cooling giving rise to areas that will favor yielding and microcracking.

Photoelastic results verify that residual stresses in the plane of the fibers are of a substantial tensile magnitude within the resin. Estimates of the difference between the in-plane stress and the through the thickness stress range from 6.4 -12.7 MPa at points in the matrix away from the fibers. If the through the thickness stress is assumed to be negligible, the in-plane stress in the matrix becomes 6.4- 12.7 MPa. The worst case occurs if the resin is not allowed to contract in the through the thickness direction implying that the in-plane stress in the matrix could be as high as 18.8-24.8 MPa which is about 30% of the yield stress in the matrix.

SPATE 9000 (interferometry) observations during tensile-tensile fatigue testing indicates that the damage displayed in the test coupon originates from localized region within the specimen. The regions appear as low stress areas and grow as fatigue cycles accumulate as shown in Fig. 1. Notice the region between 40 to 45 mm where the spot at 7 thousand cycles grows as the number of cycles increases. This is the location where the test specimen failed. The rest of the test specimen shows a variation of stresses that increases as cycles accumulate. The lower portion (0-10 mm) shows the influence of the bottom grip. When the specimen was measured with a non-contact thermometer, the temperature was higher at the 40 to 45 mm location than other regions within the specimen. This indicates the hysteresis in the material was greater at the damage sites. It is believed the heat production at the 40 to 45 mm region indicates the presence of yielding, microcracking and interphase damage.

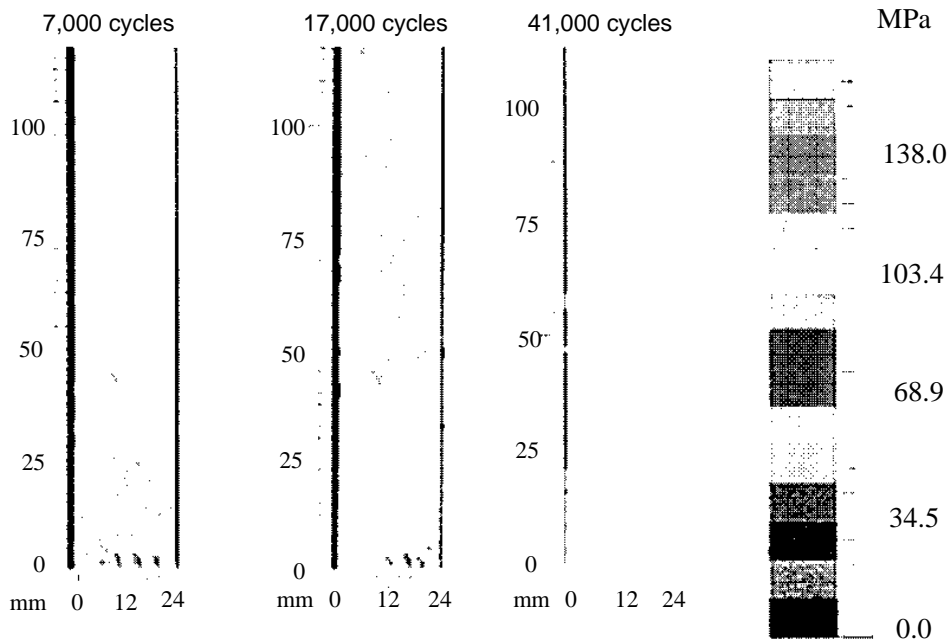


Fig. 1: Progressive failure of a tensile fatigue specimen using SPATE (40% ult. R=.1)

The stress-strain response of the static tensile specimen displays two moduli at room temperature as shown in Fig. 2. The initial modulus is 12.1 GPa with the secondary modulus at 7.89 GPa. Even though the initial part of the curve appears to be linear, a slight softening is present at lower stresses. This is attributed to matrix yielding and microcracking at localized regions in the specimen that is verified by photoelastic observations. These localized regions

are initiated during processing as the composite cools from 200°F to 70°F and influence the mechanical performance of the composite.

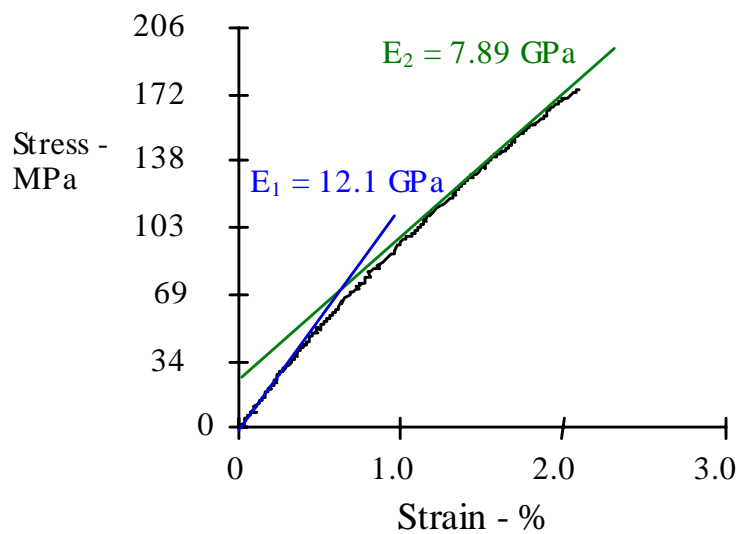


Fig. 2: Static tensile response of RDF SRIM composites at room temperature

EXPERIMENTAL METHODOLOGY

Mechanical properties for the neat resin were determined as a function of temperature. Static testing for the neat resin followed ASTM D3039 for tensile and ASTM D3410 for compression. The yield stress for the neat resin was determined using Considere's method where the tangent point to the true stress versus extension ratio curve is found that passes through zero extension ratio. The material displays an elastic perfectly plastic behavior. Data obtained from uniaxial tension and compression tests at four temperatures are tabulated in Table 1. The modulus of the resin in Fig. 3 was determined using a Rheometrics RSAII Solids Analyzer with a temperature sweep conducted at 1 Hz. Variations in the coefficient of linear thermal expansion in Fig. 3 were found using a Rheometrics TMA.

The thermal properties of the composite were required for the transient heat transfer analysis to predict the residual stresses from processing. A Mettler DSC 30 was used to obtain specific heat as a function of temperature. The average value between the mold temperature and room temperature was found to be $1.01 \text{ J}/(\text{gram}\cdot\text{K})$. The thermal conductance of the composite material was determined to be $431.5 \text{ Jm}/(\text{Hr}\cdot\text{m}^2 \cdot \text{°C})$ using a Dynatech Rapid-K with the upper plate set at 40 °C and the lower plate set at 6 °C .

Static tensile test for the composite followed ASTM D5083. The primary modulus, E_1 , was obtained from the initial linear portion of the stress versus strain curve as per ASTM D5083. The secondary modulus, E_2 , was obtained by linear regression through the last half of the stress strain curve.

Table 1: Yield stress for tensile and compression tests at various temperatures

Temperature °C	Tensile MPa	Compressive MPa
-40	98.6	101.3
21	77.1	77.8
49	53.0	54.3
78	35.3	34.2

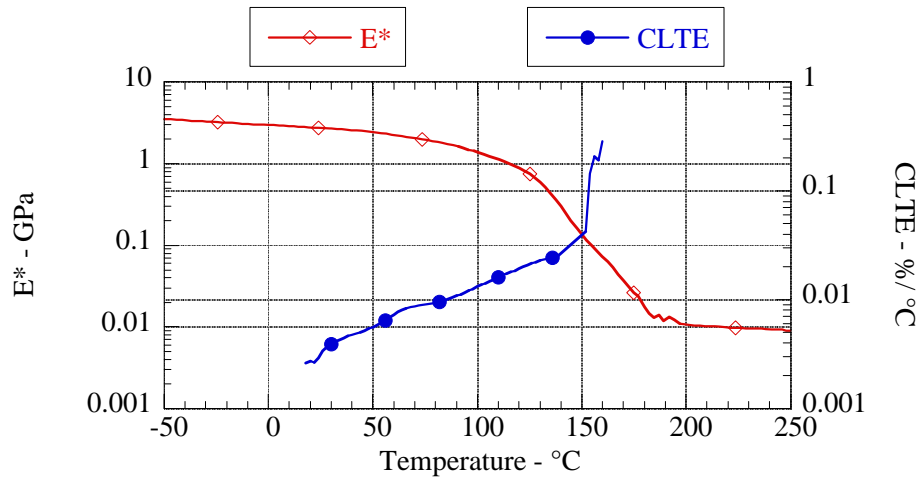


Fig. 3: Modulus and coefficient of linear thermal expansion of the resin as a function of temperature

COMPUTATIONAL MODELING

Finite element method is used in conjunction with an RVE to predict the performance of the composite. Residual stresses from processing are modeled using a one dimensional transient heat transfer analysis to simulate the thermal gradient through the thickness of the part. Constant strain boundary conditions are applied to the RVE so that the average constitutive response for the composite can be determined with and without residual stresses. The model uses one dimensional continuum elements to simulate the fibers and three dimensional continuum elements to represent the resin. The glass fibers are assumed to remain linearly elastic until failure. The resin is modeled as a nonlinear isotropic material within ABAQUS. The Hencky-Mises criterion is used as the matrix yield criteria for elastic perfectly plastic behavior. A model of this type is extremely useful due to its simplicity and computational efficiency while still providing an approximation to the variation in the microstructure.

MESH/DISCRETIZATION

The finite element model of the RVE consists of three layers of fibers representing one tenth of the thickness of the panel thickness. The RVE mesh is constructed by first generating the resin region and then adding the fibers. Three dimensional continuum elements, C3D8 in ABAQUS, are used to represent the resin system and one dimensional continuum elements, C1D2 in ABAQUS, are used to represent the fiber. The fiber angles and locations are randomly assigned within planes orthogonal to the Z axis. Multi-point constraints are used to attach the fibers to the resin. If the fiber node occupies the same location as a resin node, *TIE is used within ABAQUS. This makes the resin node the master node while the fiber node becomes the slave node as shown in Fig. 4 as Case I. If the fiber node is in-between two resin nodes, *LINEAR is utilized within ABAQUS. This requires the displacements for the fiber node to be linearly interpolated from the two resin nodes as shown in Fig. 4 as Case II. If the angle between the fiber and the x-axis is greater than 45° , the interpolation is accomplished between the adjacent x-nodes as shown for fiber C in Fig. 4. Fibers that are oriented less than 45° with the x-axis are interpolated between adjacent y-nodes as shown for fiber B. This insures that the maximum discrepancy between the largest possible element length is less than the square root of two times the smallest fiber element length.

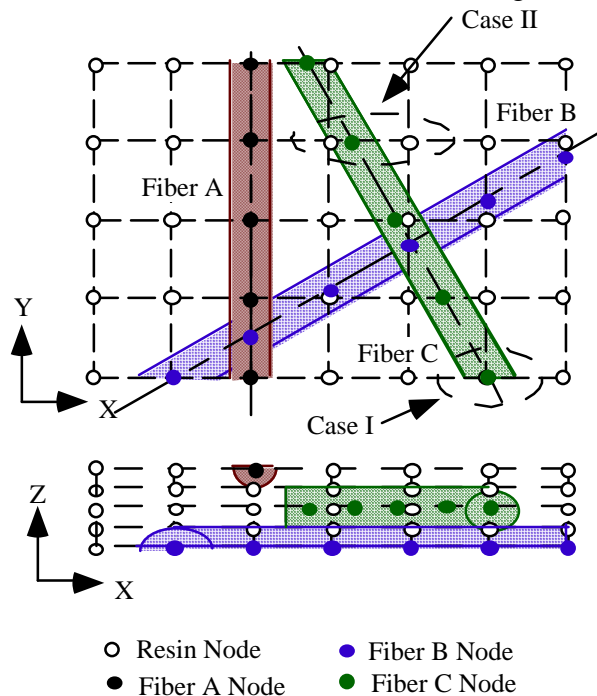


Fig. 4: Fiber and resin node arrangement in mesh

BOUNDARY AND LOADING CONDITIONS

The boundary conditions are applied to the mesh in Fig. 5 are zero displacement along;

- X-axis in the Y direction,
- Y-axis in the X direction,
- and the bottom in the Z direction,

to simulate the boundary conditions for the RVE. The remaining sides in Fig. 5 are constrained using multi-point constraints to allow the;

- XX side to move in a uniform X direction,

- YY side to move in a uniform Y direction,
 - top side to move in a uniform Z direction,
- to simulate the boundary conditions for the RVE. For the thermal cool down, no other boundary conditions are applied. Thus the RVE is allowed to contract freely in a uniform fashion. The thermal gradient through the thickness is governed by a one dimensional transient heat transfer model. The RVE is assumed to be in the horizontal position with respect to the X-Y plane with convection cooling only. The composite panel is assumed to be stress free before the RVE begins to cool. A prescribed displacement is applied to the XX-side to simulate mechanical loading. For the combined analysis of processing stresses followed by mechanical loading, a two step loading procedure is used where the RVE is cooled to room temperature and followed by the mechanical loading.

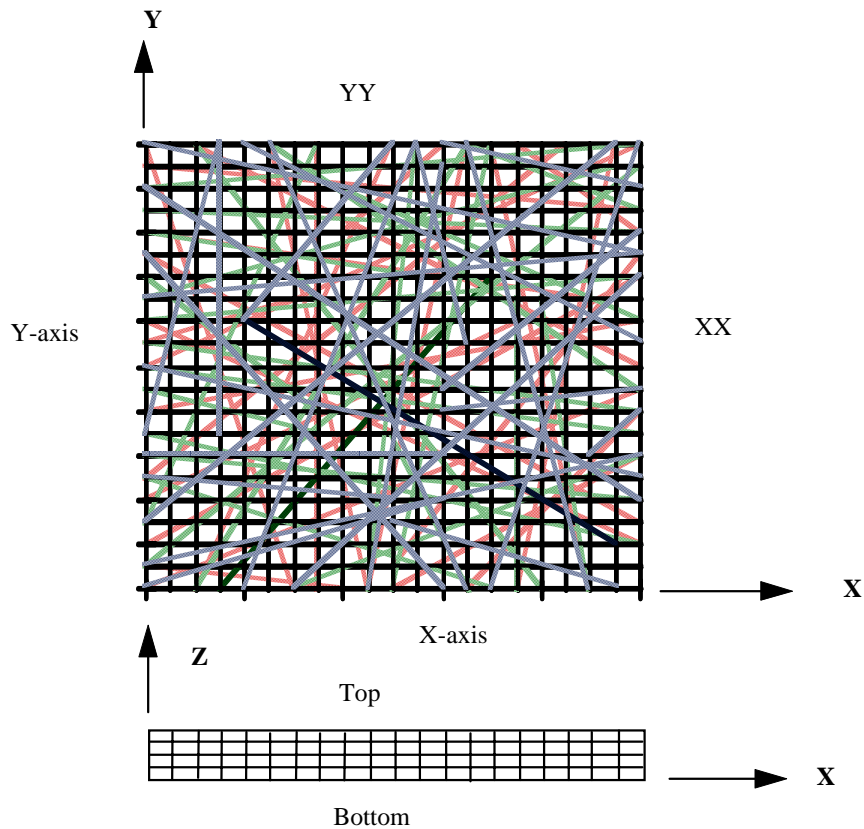


Fig. 5: Boundary conditions for the model

RESULTS

The middle layer of the mesh is shown in Fig. 6 where a fiber of interest is shown in bold with element numbers 50402-50415. The stresses shown in Fig. 7 are from thermal loading from 93 °C to 21 °C for a single fiber and multi-fiber case. The single fiber case is for the entire RVE model to contain only the fiber of interest. The multi-fiber case is when all the fibers are present in the RVE. The axial stress is obtained from the FEM analysis and is displayed as a solid line. The average interfacial stresses were calculated from the axial stress using the relationship;

$$\tau_i = -\frac{D}{4} \frac{d\sigma_f}{dx} \quad (1)$$

and is shown as a dotted line. Where $d\sigma_f/dx$ was taken to be the slope of the axial fiber stress

with respect to an incremental length of fiber and D is the diameter of the fiber. The assumption is made that there is no stress transferred at the fiber ends. Notice that the single fiber model over predicts the axial stress in the fiber by a factor of three and the shear stress at the ends of the fiber by a factor of four. This is due to the constraint from neighboring fibers in the multi-fiber case which keeps the resin from contracting and the fiber from developing the stresses shown in the single fiber case.

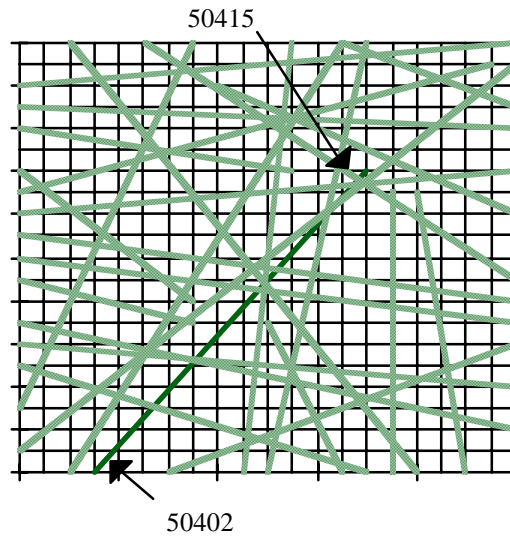


Fig. 6: Middle layer of the mesh with a fiber of interest shown in bold

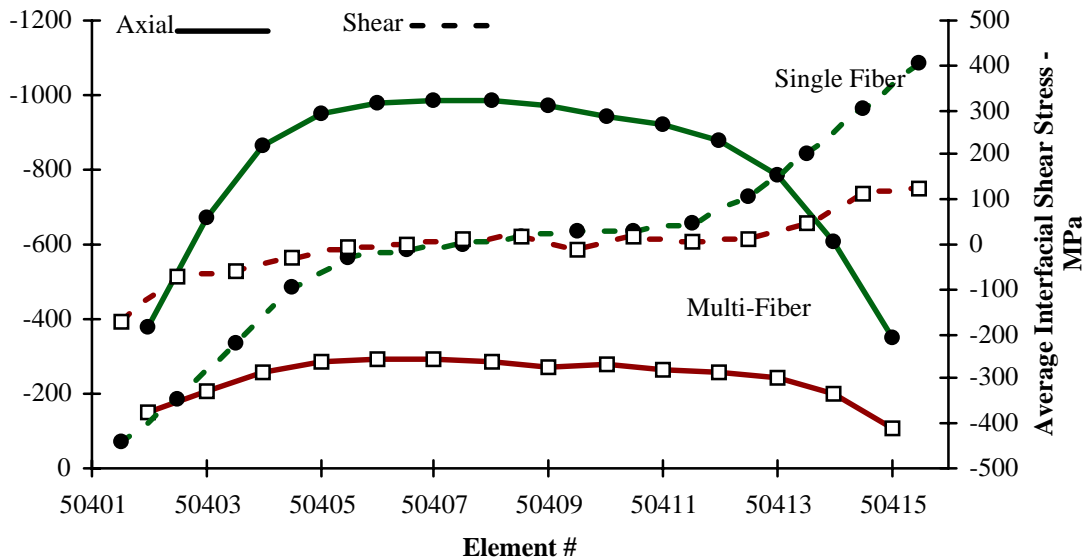


Fig. 7: Fiber stress from single fiber and multi-fiber model with thermal loading (□ multi-fiber • single fiber)

The Mises stress for the resin from the middle layer of the multi-fiber with thermal loading only is shown in Fig. 8. For the single fiber model the Mises stresses in the resin are less than 1 MPa. When mechanical loading is applied to the model after cool down, approximately 50% of the resin is yielding at .6% strain. At 1.1 % strain more than 90% of the resin is yielding. The influence of yielding is seen in the stress versus strain curve for the RVE in Fig.

9. Notice that the FEM model without processing stresses greatly over predicts the stresses as compared to the test data and displays 48% difference in the secondary modulus with a 3% difference in the initial modulus. The FEM model with processing stresses comes closer to the actual test data with a 18% difference in the secondary modulus and a 1.6% difference in the initial modulus. The point where the stress-strain curve transitions from the initial modulus to the secondary modulus is close to .4% strain in the test data. The FEM model with processing stresses and no processing stress transitions at .5% strain. This may be attributed to flaws from processing that initiate yielding at a lower strain than is seen in the current FEM models. Current efforts are focused on developing methods to introduce processing flaws into the model to statistically simulate the distribution seen in the SRIM composite.

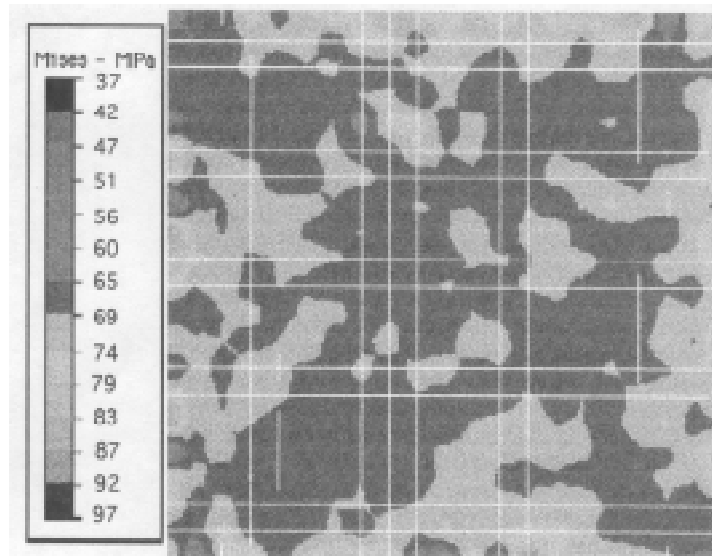


Fig. 8: Mises stress in the composite as processed (only resin elements shown)

CONCLUSIONS

The finite element model developed to understand RDF SRIM composites predicts large residual tensile stresses in the matrix from the processing temperature. This creates localized areas favorable to yielding within the matrix. The model is able to capture the overall non-linear response of the composite as well as fiber/fiber and fiber/matrix interaction in RDF composites. The modeling procedure appears to be realistic to investigate the thermomechanical performance of the RDF SRIM composite.

ACKNOWLEDGMENTS

The author wishes to acknowledge the financial support of The Dow Chemical Company. Particular thanks are extended to K. Fielder, J. Barron, and the B1608 Composite Test Lab for their patience and assistance.

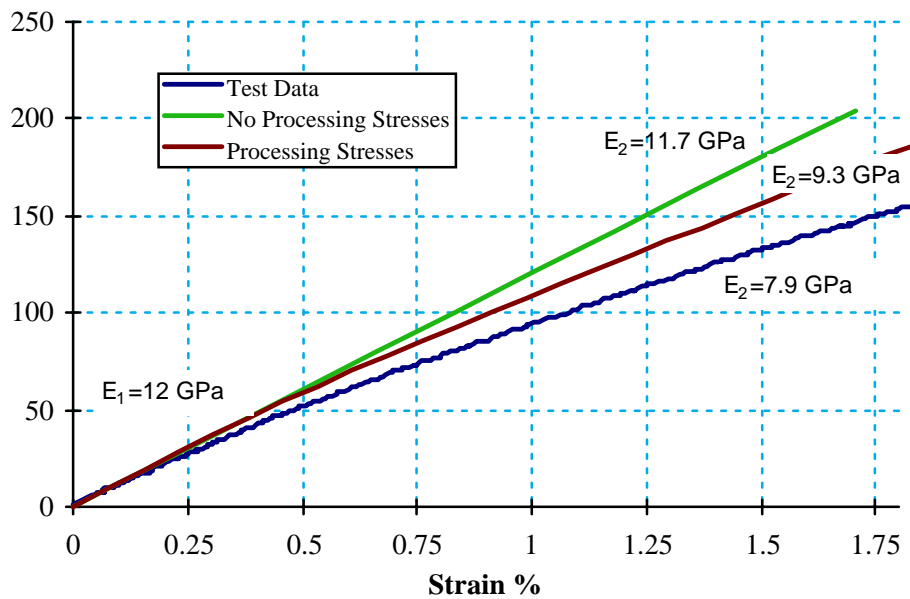


Fig. 9: Comparison between FEM model and testing data.

REFERENCES

1. Corum, M., H. McCoy, M. Ruggles, and W. Simpson, "Durability of a Continuous Strand Mat Polymeric Composite for Automotive Structural Applications", Proceedings of the 11th Annual ESD Advanced Comp. Conf., Dearborn, MI, Nov. 1995, pp. 401-412.
2. Schell, P. L. and J. M. DiMario, "Fiber Directed Preform Reinforcement: Factors That May Influence Mechanical Properties in Liquid Composite Molding", 46th Annual Conf., Comp. Inst., The Society of Plastics Industry, February 18-21, 1991, pp. 1-7 Session 14-F.
3. Agarwal, B. D. and L. J. Broutman, Analysis and Performance of Fiber Composites, 2nd ed., John Wiley & Sons, New York, 1990. pp. 136-140.
4. Halpin, J. C. and N. J. Pagano, "The Laminate Approximation for Randomly Oriented Fibrous Composites", J. Comp. Mat., 3 pp. 720-724
5. Giurgiutiu, Victor, Kenneth Reifsnider and Ronald Kriz, "Advanced Models for Strength of Quasi-Random Fiber Composites", AIAA/ASME/ASCE/AHS/ASC 35th Structures, Structural Dynamics, and Materials Conf., April 18-22, 1994
6. Young, R. J., C. Galotis, and D. N. Batchelder, "Measurement of Fibre Strain in All-Polymer Composites, 6th Int. Conf. on Deformation, Yield and Fracture, Cambridge, UK.
7. Torquato S. 1992. "Connection Between Morphology and Effective Properties of Heterogeneous Materials," ASME, AMD-Vol. 147, pp. 53-65.
8. Komori, Takashi and Kunio Makishima, "Numbers of Fiber-to-Fiber Contacts in General Fiber Assemblies", Textile Res. J. 47, (1977)
9. Pan, Ning, "A Modified Analysis of the Microstructural Characteristics of General Fiber Assemblies", Textile Research Journal, 63, 6, (1993)

KEY FACTORS AFFECTING THE PERMEABILITY MEASUREMENT IN CONTINUOUS FIBER REINFORCEMENTS

M. L. Diallo, R. Gauvin and F. Trochu

*Center for Applied Research on Polymers
Mechanical Engineering Department, École Polytechnique de Montréal
P.O. Box 6079, Station "Centre-Ville", Montreal, Que., H3C 3A7, Canada*

SUMMARY: Good permeability data are essential to any valuable flow simulation of Liquid Composite Molding Processes. Since there is no standard procedure to do it, every laboratory interested in the subject has developed a set-up and a measuring technique. We have done the same in our laboratory. We conducted experiments for in-plane permeability with various fluid / reinforcement combinations over a range of injection conditions. Testing conditions investigated include the type of fluid, the pressure gradient and the porosity. Measurements in the transient and the saturated mode were done. Fiber architecture was also investigated. It was found that reinforcements having the same structure but manufactured with fibers of different tex have different permeability. It shows that the diameter of the fiber bundles has an effect. We also investigated the pressure gradient. It was found that at high cavity pressure, the permeability computed with the Darcy's law is increased. This increase in permeability may be attributed either to channeling effects due to a geometric change in the preform or compressibility of the fiber preform as the pressure increases. In literature, studies of fabric permeability have employed fluids such as silicon oil, motor oil, corn oil, corn syrup, tap or distilled water, etc. To evaluate the fluid effects, permeability experiments were conducted with four fluids: water diluted corn syrup, Dow 200 silicon oil, HETRON 922 vinyl ester resin and glycerin.

KEYWORDS: Permeability, Liquid Composite Molding, Fabric, Reinforcements, RTM, SRIM, Flow simulation, Preform.

INTRODUCTION

Continuous fiber reinforcement thermoset polymeric composites can be produced by injecting a reactive liquid resin into a mold with preplaced reinforcement. The two best known liquid composite molding (LCM) processes are Resin Transfer Molding (RTM) and Structural Reaction Injection Molding (SRIM). In these processes the reactive liquid is pumped into the mold where fiber reinforcement has been preplaced. After the cure cycle of the injected resin is completed, the mold is opened and the composite part can be removed. Typically, in RTM, resin reactivity is lower than for SRIM and viscosity higher. In these processes, injection pressure could be as low as 0.1 MPa and as high as 3 MPa. In many cases, low cost fiberglass-polyester or epoxy tools are used. In these processes, the reinforcement could take several forms, for instance, it could be a stitched preform, a continuous strand mat or any type of fabrics such as a woven roving, a non-crimp stitched (NCS) fabric, a woven fabric or a combination of two or more of these reinforcements.

In addition to the necessary pressure to compress the reinforcements into the mold, the resin pressure generated during mold filling is an important parameter in mold design and equipment selection. The major variables controlling the resin pressure developed in the mold are the permeability of the fiber reinforcement, viscosity of the resin, and flow rate. The flow rate can be directly controlled by the injection equipment. The viscosities of the resins can be measured by commercially available viscometers. In order to successfully predict the pressure gradients within the mold, accurate permeability data must be available for all reinforcements used. The permeability is also of interest for the prediction of fill times. However a substantial amount of permeability data have appeared in the literature [1-10]. Since there is no standard procedure for permeability measurement, every laboratory interested in the subject has developed a set-up and a measuring technique. Usually, permeability data are obtained from experiments based on Darcy's law. This law states that the macroscopic velocity of the flow is related to the pressure gradients through the following equation:

$$v = \frac{[K]}{\mu} \nabla P \quad (1)$$

where v is the macroscopic flow velocity, ∇P is the pressure gradient, $[K]$ is the permeability tensor and μ denotes the resin viscosity.

This paper presents the results of an extensive study to evaluate the influence of several parameters on permeability measurement.

EXPERIMENTAL

Reinforcement

Four different reinforcements were used for the tests. These are:

1. JB Martin NCS 81053: a non-crimp, stitch bonded, bi-directional material consisting of high tex fiber bundles and is balanced with 48,9% of its weight in both weft and warp directions. The remainder of its weight 2.2% comprised two stitching polyester threads in the warp layer (1.5%) and a third one (0.7%) in the weft layer. The overall surface density is 618 g/m².
2. JB Martin NCS 82675: it has the same weave as the JB 81053 but with lower tex fiber bundles. Its overall fabric weight is 315 g/m².
3. Thermoformable glass fabric from Brochier, the EB 315-E01-120, which has an anisotropic permeability and a surface density of 315g/m². It is named the Injectex fabric by the company. To facilitate the flow in the weft direction it is stitched with polyester threads allowing high permeability in this direction, the Injectex direction, and a relatively low one in the warp direction. Permeability was measured as received and after thermoforming.
4. Injectex GB 390 E02 -107: a thermoformable balanced carbon fabric from Brochier. Its surface density is 390 g/m².

Schematics of these materials are shown in figure 1.

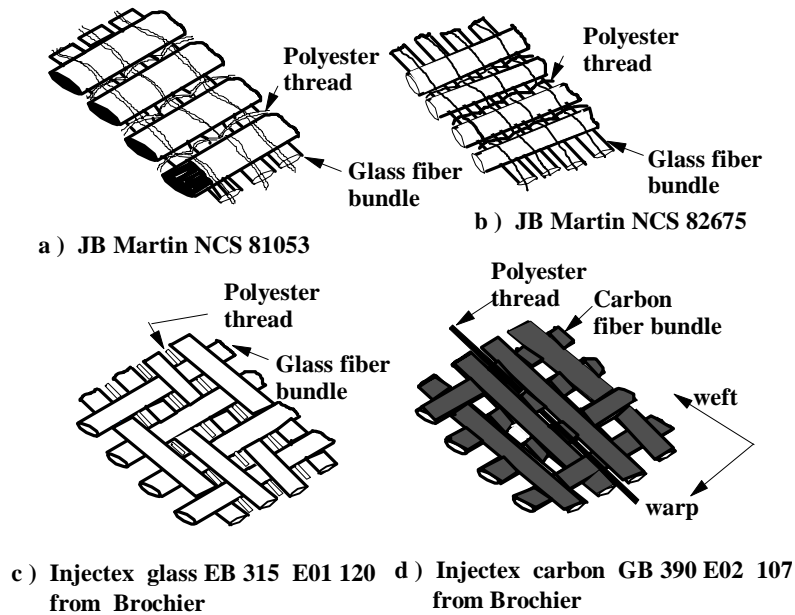


Figure 1. Schematics of the reinforcements used

Test fluids

Four fluids, water diluted corn syrup, Dow 200 silicon oil, HETRON 922 vinyl ester resin and glycerin were used. The viscosities are about 100 centipoise (Cp), 102 Cp, 360 Cp and 865 Cp, respectively. Viscosity at room temperature was measured using a Brookfield LVT-DV1 digital viscometer. Both the corn syrup and the silicon oil are widely used in the literature and their Newtonian behavior is excellent. Also the corn syrup has the advantage to be easy to handle and to wet the glass fabric very well. To ease the flow front visualization, the corn syrup was colored green prior to testing. For a better conservation, 2000 PPM of sodium azide are added to aqueous corn syrup to insure a bactericidal effect.

Apparatus

A rectangular mold filling apparatus is used for unidirectional permeability measurement. The mold assembly is made of two tempered glass plates of 93 cm x 13 cm x 1.9 cm.. Tempered glass is used instead of plexiglass to minimize plaque deflection. The mold cavity is formed with a 2.4 mm thick picture frame. Silicone sealant is used to prevent edge effects. A diaphragm pressure transducer 0 - 500 Kpa is mounted near the inlet port and a constant inlet flow rate is obtained with a cylinder mounted on a tensile testing machine.

Care was taken to remove all air bubbles from the tubing lines before each experiment. The JB Martin NCS reinforcements were sprayed with a very thin line of glue before cutting the specimen from the roll to reduce the fraying of the materials. Initial tests without the glue line showed a very high by-pass flow along the edges due to the reduction in glass volume fraction where the material had frayed.

The necessary precaution was taken to assure a plug flow. Each reinforcement layer was weighed before the experiments. Fiber volume fraction was determined by the following equation:

$$V_f = \frac{n\zeta}{h\rho_f} \quad (2)$$

where V_f is the volume fiber fraction, n is the number of layers, ζ is the layer surface density, h is the cavity thickness and ρ_f the density of the fiber. The density of fiber is taken from published literature (for E-glass, $2.56 \times 10^6 \text{ kg/m}^3$; carbon fiber, $1.77 \times 10^6 \text{ kg/m}^3$).

RESULTS AND DISCUSSIONS

To measure the transient in-plane permeability, so called dry permeability, the elapsed time t is recorded at every 2 centimeters during the mold filling and the inlet pressure $P_0(t)$ is also collected. From the experimental data, plot of permeability vs front position is constructed. Example of permeability plot is shown in figure 2. It can be observed that during the first few cm of mold filling, the flow appears to be in transition, and the figure shows that it takes some distance for the flow to stabilize. This results in a higher permeability at the beginning. This phenomenon was observed earlier [10,11] and was mainly attributed to the relative significance of the capillary effects at the beginning of the filling. This lead us to suggest a minimum length for the permeability measurement in a unidirectional flow experiment [12].

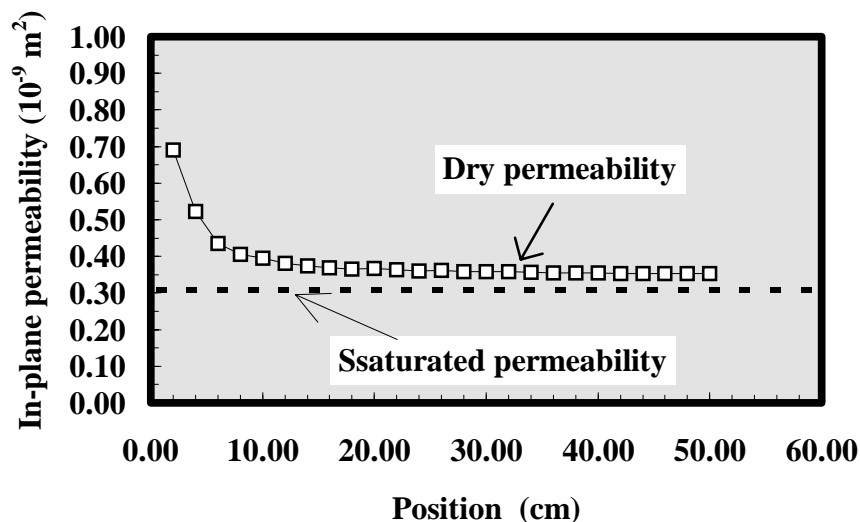


Figure 2. Permeability convergence of a typical run
JB 82675 (weft), $V_f = 41\%$

Figure 3 shows the pressure traces during a typical run. As expected, the initial part of the curve is almost linear. As it can be seen, the inlet pressure reaches its maximum after the flow front has exited the reinforcement. While the pressure continues to rise, air bubbles flow out the reinforcement. This steady value corresponds to the pressure used to calculate the saturated permeability. It is worth remembering that Darcy's law is defined for a saturated porous media.

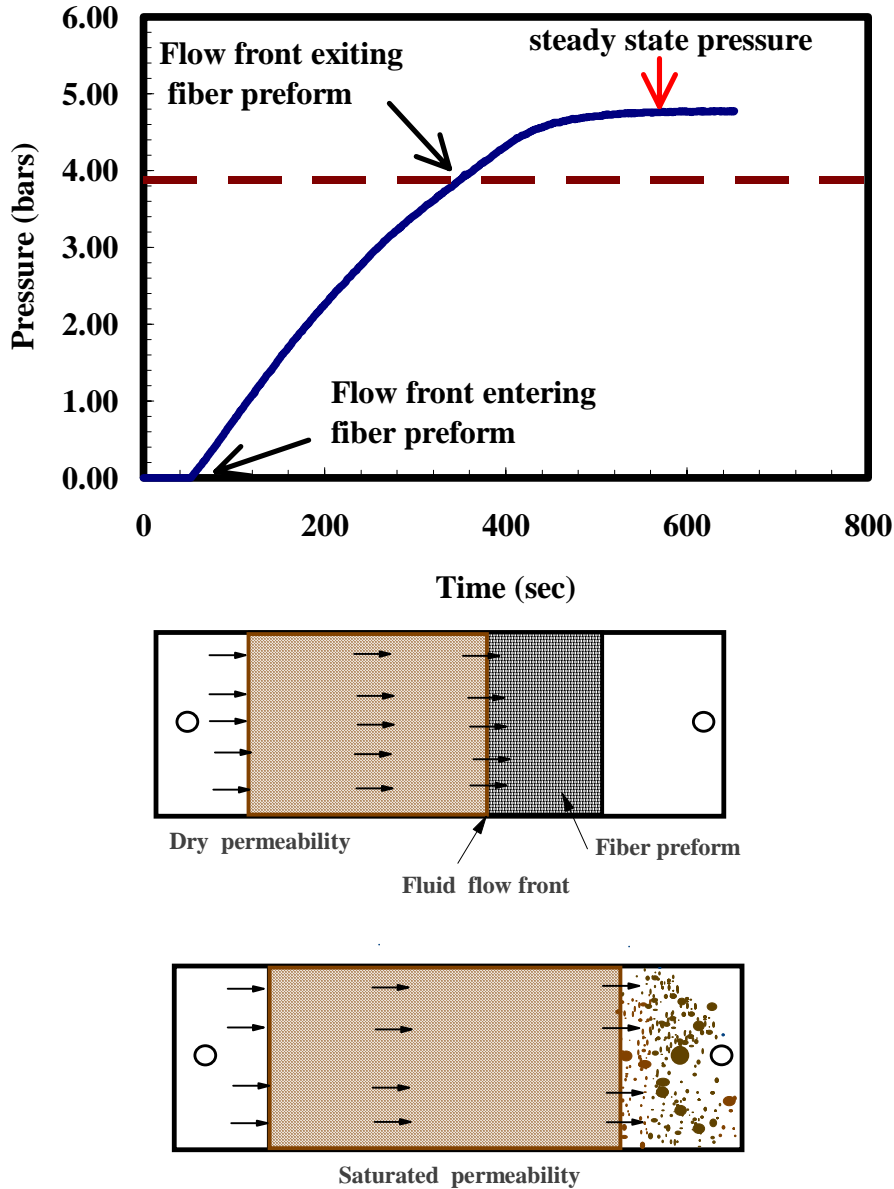


Figure 3. Pressure versus time during filling

A series of experiments was performed at various fiber volume fractions V_f with the different reinforcements. The permeability of each reinforcement as a function of V_f is presented in figures 4, 5 and 6. One can see on figure 5 that when a preform was used rather than a layered bed, the material permeability was found slightly smaller.

With the carbon fabric, we observed scatter in the permeability values when the permeant fluid is corn syrup (see figure 6). This is probably because the corn syrup does not wet out the carbon fibers well. In fact, a qualitative inspection of the fabric after each permeability experiment revealed that the carbon fiber tows are not evenly wet by the corn syrup.

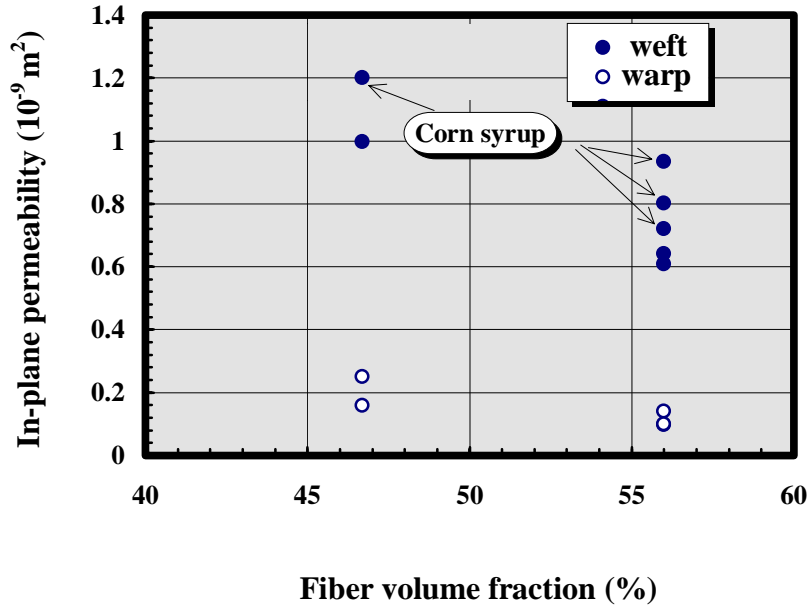


Figure 6. In-plane permeability of Injectex carbon GB 390. Measurements were done using Dow 200 silicon oil 100 Cst, except for the points indicated otherwise

As noted in previous work [13] and by other groups [5, 9, 14], the relationship between permeability and fiber volume fraction is not linear and it can vary significantly. Smaller air bubbles exiting the preform were observed for higher fiber volume fraction. The size and the amount of bubbles were also influenced by the fabric orientation, weft or warp. This phenomenon was also observed by Wang et al. [15] and Carman [16] who mentioned that the size of air bubbles seems to be related to pore structure. We agreed on the influence of pore structure but we should add the pore structure with respect to the flow direction. To study the effect of the air bubbles on the permeability measurement, the fluid was allowed to flow continuously for a certain period of time at a constant flow rate. The air bubbles were flushed out and pressure became steady as indicated above. The permeability was then measured in this saturated regime. It decreased as much as 5 to 10% after complete removal of trapped air.

In our experiments, first the transient permeability is computed point by point with Darcy's law during cavity filling. The value reported here corresponds to the stabilize value as shown in figure 2. Then, with the same sample still sitting in the cavity, the pressure gradient is recorded for each constant flow rate. These experimental points are plot on a graph of (Q/A) versus pressure. The saturated permeability is computed from a least square fit of these data points. An example of such a graph is given in figure 7 for the JB 82675 in the weft direction.

It can be observed that for steady flow experiments, the fabric showed a slight increase in permeability at high pressure gradients. The departure from linearity was also observed by other authors [1,17,18,19,20]. It has been proposed that this effect might be related to fiber movement, which could cause changes in pore structure and result in channeling effect due to higher pressure. Even if a higher pressure increases slightly the saturated permeability, it is always lower than the dry permeability. This is consistent with the experimental results presented in [11,19,21]. One physical explanation for the fact that dry permeability is higher than steady state permeability is provided by consideration of the mechanism by which the air bubbles between adjacent fiber bundles (tows) are displaced as the fluid front advances[22].

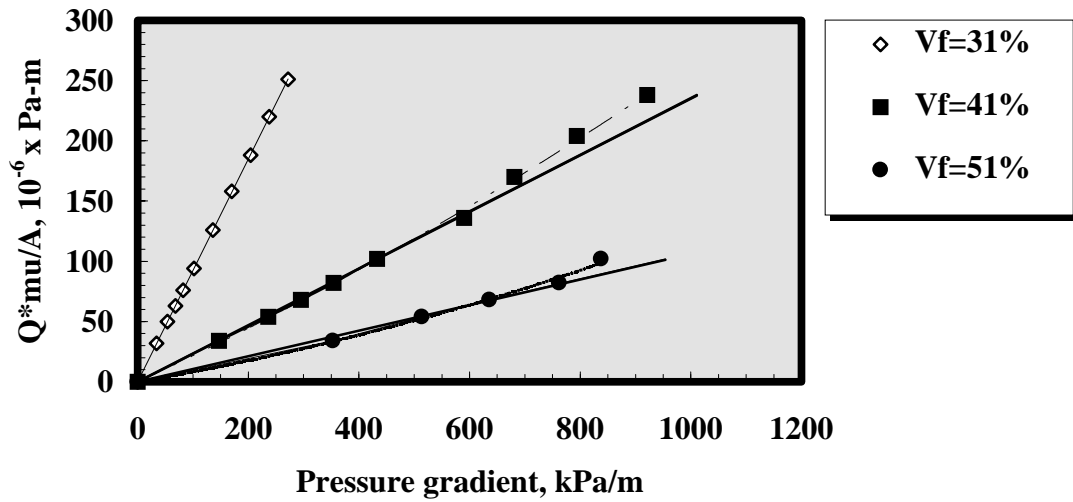


Figure 7. Flow as a function of pressure gradient for the JB 82675 (weft);
 $\mu = 0.102 \text{ Pa}\cdot\text{s}$; $K_{sat} = 0.924 * 10^{-9} \text{ m}^2$ ($V_f = 31\%$);
 $K_{sat} = 0.235 * 10^{-9} \text{ m}^2$ ($V_f = 41\%$); $K_{sat} = 0.106 * 10^{-9} \text{ m}^2$ ($V_f = 51\%$)

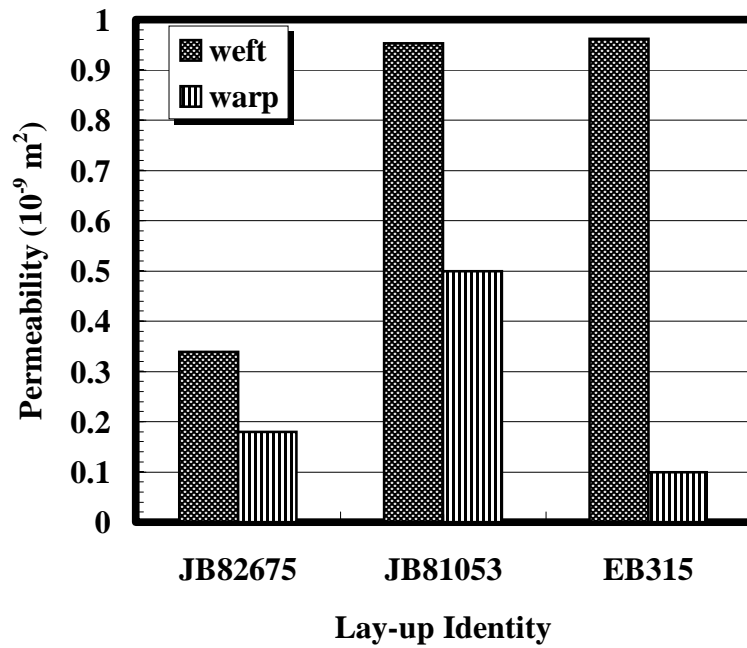


Figure 8. Effect of fiber structure on permeability. $V_f \approx 40\%$.
 Values were obtained using Dow 200 silicon oil 100 Cst.

As can be seen in figure 8, the permeability is closely related to fiber architecture and fiber orientation even if the fiber volume fraction is the same. Even if each material investigated had similar tex fibers in both directions, the magnitude of the permeability is much higher in the weft direction. This is attributed to the thread stitches that hold the layers together and run in the weft direction. Both of the JB Martin NCS fabrics had the same architecture but were

manufactured with fiber bundles of different tex. It is likely that the wider fiber tows in the JB 81053 also provide larger inter-tow spaces and hence increase the permeability. The results also indicate that the fiber bundle diameter has an effect on the permeability.

The anisotropy index of the fabrics which is the ratio between the two dry in-plane permeabilities as a function of the fiber volume fraction is given in figure 9. This index is relatively constant for all fabrics tested, except for non thermoformed Brochier EB 315, for which the increase is tremendous.

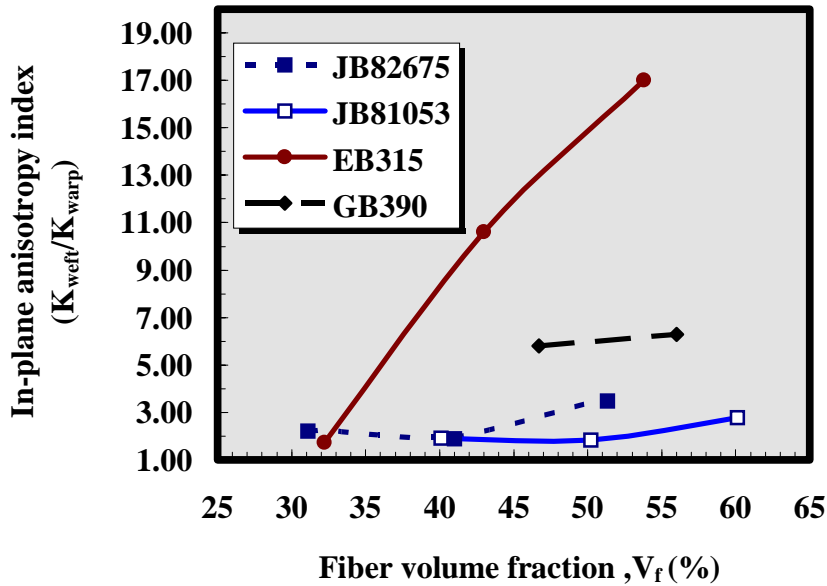


Figure 9. In-plane anisotropy index as a function of fiber fraction V_f

Figure 10 displays the dry in-plane permeability of the non thermoformed Brochier Injectex EB 315 at 41% of fiber volume fraction for the four fluids selected. Furthermore, a non filtered corn syrup was used to see the influence of filtering on permeability. One can see that it is lower with the non filtered corn syrup. Since there are solids in suspension in the non filtered syrup, this results in blocking effects and the computed permeability is reduced. The highest permeability in both directions corresponds to the use of the glycerin and the lowest to the use of non filtered corn syrup.

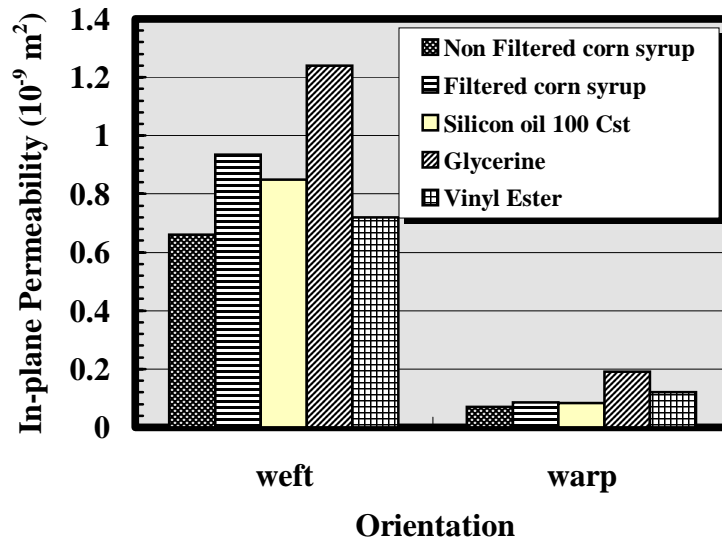


Figure 10. Permeability for non thermoformed Brochier EB 315 as a function of permeant fluid. Fiber volume fraction = 41%

CONCLUSION

Fluid flow through continuous fiber reinforcements has been studied. It was found that in addition to the porosity several other parameters influence the permeability measurement. These parameters include 1) type of fluid, 2) cavity pressure level, 3) fiber structure, and 4) resin saturation. By comparing the results in the wrap and weft directions, it is clearly show that not only the fiber structure or its image, the pore geometry, that influence the permeability but also the orientation of this structure with respect to the flow direction. Also the study shows that there is considerable differences between different types of reinforcement, even at the same fiber volume fraction. Finally, since the fluid can influence significantly the computed permeability, it is advisable to use the resin for the permeability values to be used in simulation code.

ACKNOWLEDGMENTS

The authors would like to thank the NSERC of Canada and the Fond FCAR du Québec for their financial support. The RTMFLOT user's Club members, Aérospatiale, ETH-Zurich, Ford, Matra, Hispano-Suiza, INSA de Toulouse and ISITEM de Nantes are also acknowledged. We also thank J.B. Martin and Armkem for providing free materials.

REFERENCES

1. Kim, Y.R., McCarthy S.P., Fanucci, J.P., Nolet, S.C. and Koppernaes C., 22nd SAMPE Technical Conference, pp.709-723(1990).
2. Hayward, J.S. and Harris, B., Sampe Journal, **26**, 3, pp. 39-46(1990).

3. Steenkamer, D.A., Wilkins, D.J., Karbhari, V.M., J. Mater. Sc. Let., **12**, 971-973(1993).
4. Greve, B. N. and Soh, SAE transaction, **99**, 5, pp. 331-343, 1990.
5. Molnar, J. A. , Trevino, L. and Lee, L. J. , Polym. Compo., **10** , 6, pp.414(1989).
6. Fracchia, C.A., Master thesis, Mech. Eng., Univ. of Illinois, Urbana-Champaign(1990).
7. Verhus, A.S. and Peeters, J.H.A., Compos. Manufact., **4**, 1, pp 33-37(1993).
8. Gauvin, R., Trochu, F., Lemenn, Y. and Diallo, L., Polym. comp., **17**(1):34-42 (1996).
9. Coulter J.P., Smith B. and Guceri S., Proc. of the Am.Soc. for Compo., **2**:209(1987)
10. Luce, T.L., Advani, S.G., Howard, J.G. and Parnas, R.S.,with the permission of the authors, submitted to Polymer Composites.
11. Williams, J.G., Morris, C.E.M. and Ennis, B.C. Poly. Eng. Sci., **14**, 413(1974).
12. Ferland, P. Guittard, D. Trochu, F., Polym. Comp., **17**(1):149-158(1996).
13. Gauvin, R. and Kerachni, A., J.E.C., Août 1992.
14. Cai, Z. Compos. Manufact., **3**, 4, pp 251-257(1992).
15. Wang T.J., Perry M.L. and Lee L. J., Antec, pp.756-760(1992)
16. Carman, P. C., Trans. Am. Inst. Chem. Eng., **15**, 150(1937)
17. Gauvin, R., Chibani, M. and Lafontaine, L., 41st Ann. Conf., Compos. Inst., Soc. Plas. Ind., 19-B(1986).
18. Mishra, S. and Jayaraman, K., SAE, International Congress and Exposition, N.930174, Detroit, Michigan, March 1-5 , 1993.
19. Martin, G. Q., and Son, J. S., ASM Conference on Advanced Composites, **2**, pp. 149(1986)
20. Dave R. and Houle S., Proc. of the Am. Soc. for Compo., **4**, pp. 539(1990).
21. Foley M.F., Gutowski T., 23rd SAMPE Technical Conference, pp.326-340(1991).
22. Parnas, R. S. and Phelan, F. R., SAMPE Q., **22**, 6, pp.53(1991).

PREPARATION OF SHORT CARBON FIBER REINFORCED POLYPHENYLENE SULFIDE COMPOSITES BY IMPREGNATION IN SUSPENSION

Xiao Wang, Jiarui Xu, Bingyuan Xie and Hanmin Zeng

Materials Science Institute, Zhongshan University, Guangzhou, 510275, China

SUMMARY: A new method based on impregnation in suspension has been developed to prepare short carbon fiber reinforced polyphenylene sulfide composites. It is shown that the new method can overcome effectively the difficulties generally experienced in preparing the composite by melt extrusion. In this paper, the influence of the processing parameters and the processing modes on the preparation of the fiber granular compounds have been investigated and evaluated. With proper suspension concentration and processing conditions the fiber volume fraction of the fiber granular compounds is able to achieve values as high as 0.75. Satisfactory mechanical performance of the composites made of the injection granulates by using this technique is obtained.

KEYWORDS: suspension impregnation, short carbon fiber reinforced, polyphenylene sulfide, composite processing

INTRODUCTION

Short carbon fiber (CF) reinforced polyphenylene sulfide (PPS) composite is one of the high performance materials which can be shaped, like ordinary thermoplastics, by injection, extrusion or compressive molding [1-3]. However, some characteristics of the resin, such as the thermal-crosslinking nature upon heated at elevated temperature and its high melting point make the preparation of short CF/PPS composites difficult. Extruders that can operate at high temperature are generally needed. During extrusion, the resin staying at the extruder die may gradually become solidified by crosslinking, forming small blocks to stop up the extruder die or cut off the yarns, resulting in interruption of the flowing process. If the residual material is not well removed after preparation, the resin left inside the extruder cylinder may also crosslink to form unmelted coatings on the screws. Additionally, the volume fraction of reinforcement in the composite prepared by melt extrusion is relatively low, restraining the further enhancement of the mechanical properties.

We have recently developed an aqueous impregnation process to prepare short glass fiber reinforced PPS composites [4], showing that the new processing method can overcome effectively the above mentioned difficulties in preparing the composites. In this paper, the

application of the new technique to prepare short carbon fiber reinforced PPS composites is outlined. The influences of the processing parameters and the processing modes of the fiber granular compounds on the performances of the composites made of the injection granulates are investigated and evaluated in order to obtain short CF/PPS composites with satisfactory properties.

EXPERIMENTAL

Materials

The PPS powder is a product of Changshou Chemical Plant, Chongqing, China. The melt viscosity given by the factory is 524mPa·s.

The carbon fiber used is a product of The Jilin Carbon Materials, China. The tensile strength of the 1K yarns is reported to be 3,355 MPa.

The Preparing Process

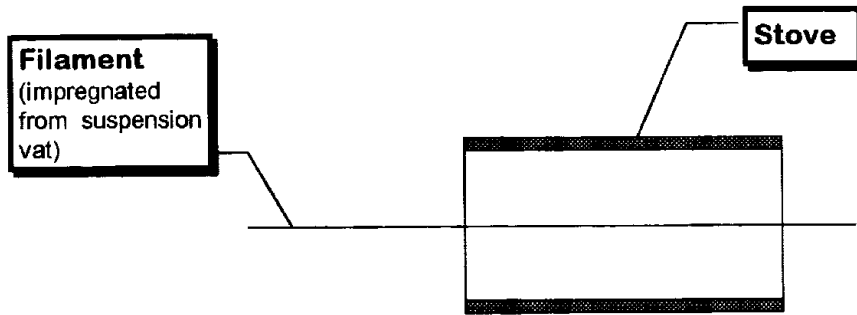
The preparing process is similar to that of short glass fiber reinforced polyphenylene sulfide composites as described in detail elsewhere [4]. The main ingredients of the suspension include water, PPS powder and other additives which are used in order to improve the dispersity and stability of the suspension. The device consists of a set of tow guides, a suspension vat, a heating stove and a cutter, which is relatively uncomplicated and inexpensive. The carbon fiber yarns are introduced into the vat and impregnated by powdered PPS resin dispersed in the suspension. The heating stove is divided into three sections with different temperatures: the stoving section, the melting section and the post-heating section. The water in the yarns is sufficiently volatilized at the first section. At the second section, the powdered resin in the yarns is melted and combined closely with the carbon fibers. Pre-crosslinking is carried out while the yarns pass the third section. The extension of crosslinking can be controlled by changing the temperature at the section. To obtain good mechanical performances of the materials, pre-crosslinking of the PPS resin has been shown to be necessary [5]. The long yarns stuck by the resin are cut immediately after coming from the heating stove to obtain the fiber granular compounds in designed length. The short carbon fiber reinforced PPS composites can be obtained from this kind of fiber granular compounds by using injection or compressive moulding.

Three processing modes of the manufacture of the fiber granular compounds have been developed in this study, namely Mode I, Mode II and Mode III. Mode I is the simplest one, where only one filament as one yarn passes through the stove. In Mode II, several filaments are used at the same time. The individual filament is respectively impregnated in the suspension vat and then concentrated by tow guides to form one yarn which passes through the stove. A great number of filaments are used at the same time in Mode III, where each filament as one yarn respectively enters the suspension vat and the stove.

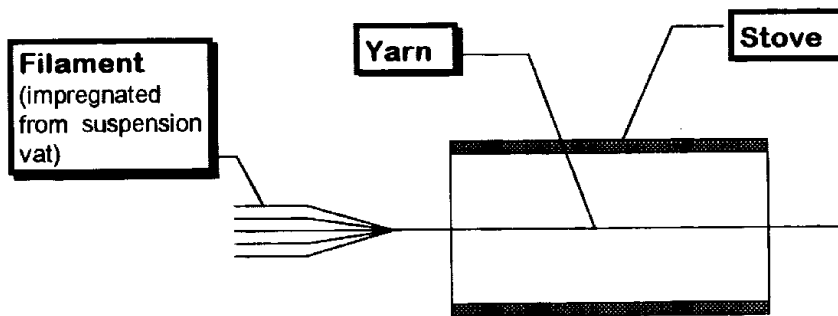
Determination of Fiber Fraction

A simple and efficient computer-aided method has been developed [6-7] to determinate the content of carbon fiber in the fiber granular compounds in terms of fiber volume content V_{cf} , fiber weight content W_{cf} , resin volume content V_{pps} or resin weight content W_{pps} . The weights of

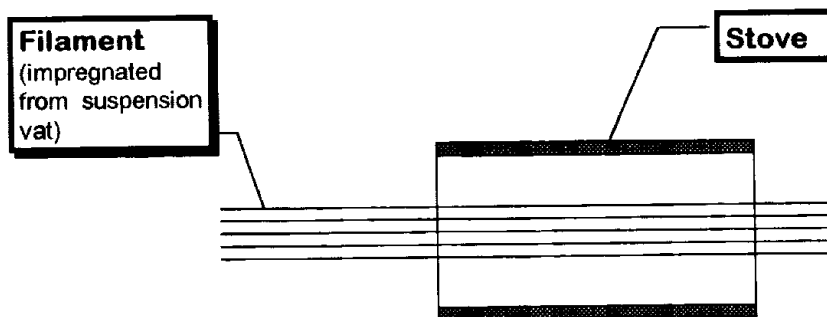
fiber and resin and the densities of fiber and resin of the samples are measured to calculate the four parameters.



(a) Mode I



(b) Mode II



(c) Mode III

Figure 1. Processing Modes of the Suspension Technique

Measurement of Mechanical Properties

The mechanical tests were conducted according to *the Standard Testing Method of China* (GB1040-79, GB1042-79 and GB1043-79), which are similar to the corresponding ASTM testing methods. The test specimens of the short GF/PPS composites are made of the fiber granular compounds by using injection moulding.

RESULTS AND DISCUSSION

Effects of Suspension Concentrations on the Fiber Contents

In the aqueous impregnation process it is very important to control the relative amount of resin and carbon fiber in the fiber granular compounds, which can be indicated by one of the following parameters: the carbon fiber volume content V_{cf} , the carbon fiber weight content W_{cf} , the resin volume content V_{pps} or the resin weight content W_{pps} . These parameters are known to give great influence on the mechanical properties of composites manufactured by the fiber granular compounds. In order to achieve desired performances of the CF/PPS composites, the relationships between these parameters and the processing conditions of the fiber granular compounds should be investigated systematically. It is found that the suspension concentration is one of the key factors which have great influence on the above parameters.

The effects of the suspension concentration on the magnitudes of V_{cf} , V_{pps} , W_{cf} and W_{pps} of the fiber granular compounds are shown in Table 1. It is in evidence that the higher the resin content in the suspension, the greater the amount of the resin in the fiber granular compounds. Therefore, the four parameters can be controlled by changing the suspension concentration. It can also be seen that with proper suspension concentration and processing conditions the fiber volume fraction of the fiber granular compounds is able to achieve values as high as 0.75 which is impossible by melt extrusion process.

Table 1 Influence of Suspension Concentration on the Fiber Content of the Fiber Granular Compounds

Suspension Concentration (g/ml)	10%	20%	30%
V_{cf}	0.748	0.616	0.497
V_{pps}	0.252	0.384	0.503
W_{cf}	0.794	0.673	0.551
W_{pps}	0.206	0.327	0.449

Processing mode: Mode I

Effects of Processing Modes on the Fiber Contents

The values of V_{cf} , V_{pps} , W_{cf} and W_{pps} of the fiber granular compounds obtained from various processing modes are shown in Table 2. It appears that Mode I and Mode III have similar

influence on the four parameters. Mode I is suitable for laboratory tests while Mode III is advantageous to raise the output rate so it can be applied to bulk production. On the other hand, the values of the four parameters by Mode II differ apparently from those by other modes. The resin content increases greatly by using Mode II. This suggests that the spaces and cavities among the filaments can hold powdered PPS to increase effectively the amount of resin deposited on the filaments. Therefore, it can be deduced that variation of the resin content of the fiber granular compounds depends on the number of the filaments in one yarn when using Mode II.

Table 2 Influence of Processing Modes on the Fiber Content of the Fiber Granular Compounds

Processing Modes	Mode I	Mode II	Mode III
V_{cf}	0.497	0.335	0.479
V_{pps}	0.503	0.665	0.521
W_{cf}	0.551	0.392	0.539
W_{pps}	0.449	0.608	0.461

Suspension concentration: 30%

Effects of Fiber Contents on the Tensile Strength of the Composites

In the melt extrusion method, it is rather difficult to raise the value of V_{cf} of the granulates of the composites because it needs sufficient amount of resin to keep good fluidity in the cylinder of the extruders. This may restrict the further improvement of the performances of the composite made of the fiber granular compounds. The difficulty may be overcome by the new method as it permits a large variation of the value of V_{cf} of the fiber granular compounds as shown in Table 1 and Table 2. The suspension impregnation method can produce a fiber granular compounds with a fiber volume content as high as 75%, extending significantly the reinforcement efficiency of the carbon fibers in the CF/PPS composites made of the granulates. Experimental results show that the tensile strength of the composites increases with the raise of the carbon fiber volume content of the injection granulates, as shown in Fig 2.

It can be found that when the carbon fiber volume content of the fiber granular compounds is less than 20%, poor reinforcement efficiency in the composites made of the injection granulates is found. At the level of 30% of V_{cf} the tensile strength of the composite begins to rise remarkably. The fiber granular compounds with 40% of carbon fiber volume content, which is difficult to obtain by extrusion technique, gives twice as much as the tensile strength of the composites with 20%. When the fiber volume content of the granulates is raised up to 60%, the tensile strength of the composite goes up 4.5 times as high as that of net resin.

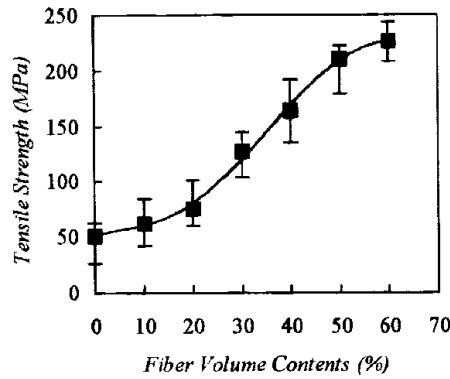


Figure 2 Influence of the Fiber Volume Contents of the Fiber Granular Compounds on the Tensile Strength of the Composites (Testing Method: GB1040-79)

Mechanical Properties of the Composites

Using the suspension impregnation method, short CF/PPS composites with satisfactory properties can be obtained. The mechanical properties of both net PPS and the carbon fiber reinforced PPS composites are shown in Table 3. The fiber volume content of the fiber granular compounds used is 40%. The injection granulates are manufactured by Mode III with suspension concentration 35%. It can be seen that remarkable reinforcement efficiency was obtained by the suspension impregnation method. The mechanical properties of the short CF/PPS composite are greatly raised. The tensile modulus of the composite exceeds three times that of the net PPS. The flexural strength and the impact strength of the composites rise to about four times as much as that of PPS. Particularly, the flexural modulus and the notched impact strength of the composite increase more significantly. It is evident from Table 3 that the flexural modulus of the composites goes up nearly ten times and the notched impact strength jumps up to sixteen times as high as that of net PPS. Usually, PPS gives relatively low notched impact strength. Products made of PPS alone are generally brittle upon impact. The addition of carbon fiber can greatly raise the tenacity of the material and make the composite become a kind of high performance materials.

Table 3 Mechanical Properties of the Short CF/PPS Composites

Mechanical Properties	Testing Method	PPS	CF/PPS
Tensile Strength (MPa)	GB1040-79	51.1	164.7
Tensile Modulus (GPa)	GB1040-79	2.06	5.74
Flexural Strength (MPa)	GB1042-79	96.6	415.2
Flexural Modulus (GPa)	GB1042-79	2.63	25.8
Impact Strength (kJ/m ²)	GB1043-79	7.43	28.7
Notched Impact Strength (kJ/m ²)	GB1043-79	0.84	13.6

V_f of the injection granulates used: 40%

Processing mode of the injection granulates used: Mode III

CONCLUSIONS

The new processing method based on impregnation in suspension is practicable for preparing short carbon fiber/PPS composites. The carbon fiber contents can be controlled by changing the concentration of the suspension. Processing modes give remarkable influence of the fiber content of the fiber granular compounds. The tensile strength of the composite increases with the increasing of the fiber contents of the injection granulates used. With proper suspension concentration and processing conditions, satisfactory mechanical performances of short CF/PPS composites can be obtained by the suspension processing technique.

Acknowledgment The financial supports of the Natural Science Foundation of Guangdong Province and Research Foundation of Zhongshan University are gratefully acknowledged. Jiarui Xu would also like to acknowledge the support of the National Natural Science Foundation of China (Grand # 59625307). The work is also supported by The Opening Laboratory of Polymeric Composites and Functional Materials, The State Educational Commission of China.

REFERENCES

1. Zeng, Q., *J. Guangzhou Chemical Engineering* (Chinese), No.1, 1986, pp.37.
2. Luo, H., Xie, B., Wang, X., *J. New Carbon Materials* (Chinese), Vol. 1, No.2, 1992, pp.31.
3. Luo, H., Xie, B., Wang, X., and Zeng, H., *J. Fiber Composites Materials* (Chinese), Vol.9, No.3, 1992, pp.15-17.
4. Wang, X., Xu, J., Mai, K., & Zeng, H., submitted to *Plastics, Rubber and Composites Processing and Applications*
5. Hawkins, R. T., *Macromolecules*, Vol.9, No.2, 1976, pp.189-194.
6. Wang, X., Xu, J., Zhang, W., & Zeng, H., *Advancement in Composite Materials* (Proc. of 8th National Conference on Composite Materials), Ed. S. Li, Aero-industrial Publishing House, Nanjing, 1994, pp.617-623 (ISBN: 7-80046-735-X)
7. Wang, X., Xu, J., Mai, K., & Zeng, H., Proc. 9th National Conference on Composite Materials, Ed. Z. Zhang, Vol. 2, World Book Publishing Co. Beijing, 1996, pp.615-620. (ISBN: 7-5062-2951X/TB.17)

THE FABRIC COWOVEN WITH PEEK AND CARBON FIBRE AND THEIR COMPOSITE

Lou Kuiyang, Zhu Bo and Chen Xiangbao

*National Key Lab. of Composites, Institute of Aeronautical Materials
PO Box 81-3, Beijing 100095, P.R. CHINA*

SUMMARY: Polyetheretherketone (PEEK) was made into filaments, and cowoven into unidirectional fabric with T300 carbon fibre. The fabric was cut into pieces and stacked. When the PEEK filaments in them melted and wet the carbon fibre in hot press at 380 °C and 3.0 MPa, unidirectional laminates were formed. Some of their mechanical properties were tested. Short beam shear, longitudinal flexure strength were 112 MPa and 1747 MPa, respectively, equivalent to the laminate converted with prepreg made by powder coating. The work of the paper showed a special process for thermoplastic prepreg with flexibility and drapeability which required for structure with complex contour but were not possessed by most other thermoplastic prepregs.

KEYWORDS: peek, cowoven fabric, fibre hybrid, commingle

INTRODUCTION

In the recent research, thermoplastic prepregs have been made with powder coating, in-situ polymerization and some other process[1], converted into composite parts and applied in aeronautical fields[2-3]. Compared with thermosetting composites, they have higher toughness and damage tolerance, better hot/wet resistance, ability to be remelted and remolded, and potency of low cost[4]. But because the prepregs have no drapeability and flexibility, it is very difficult to make complex contour parts with them. Thus it is very important to develop a new process to make prepregs with flexibility and drapeability. Fabric cowoven with polymer filaments and reinforcing fibre is such a kind of product[5]. In the process for it, thermoplastic polymer is required to be spun into filaments and cowoven with carbon fibre. Its advantages include flexibility and drapeability, precise control on resin

content, uniform resin distribution among fibre. In addition, when the diameters of matrix fibre are small enough, it could be commingled with carbon fibre into one yarn, which could be woven, or braided, or knitted, or stitched into 3-D near net shape preform. It is a new process which could reduce the wastage and cost, enhance the through thickness properties by the thickness directional fibre and good designability and processability[10].

In this paper, PEEK was made into filaments with average diameter of 94.2 μ m, cowoven with T300-3k carbon fibre into unidirectional fabric. The laminates made of them had good properties.

MATERIALS

PEEK was supplied by Jilin University, CHINA, with reduced viscosity of 0.65 dl/g, density of 1.32g/cm³. It was desiccated at 160 °C for 4 hr. T300-3K carbon fibre was got from Torayca Co. JAPAN and used without treating.

EXPERIMENTS

PEEK Fibre

Filaments of PEEK was made by melt spinning without drawing so that it would not shrink too much when heated up to the forming temperature. The average shrinkage of them was 2.5% at 100 °C and 5% at 200 °C. There were six holes in the spinning jet so each tows consisted of six filaments. Their diameters were measured for the importance on the quality of hybridization. It was showed that the diameters of different points along a filament were very uniform, but the diameters of various filaments had much difference. The properties of PEEK fibre were listed in table 1.

Table 1 The properties of PEEK fibre

Item	Unit	Value
Density	g/cm ³	1.32
Numbers in a tow		6
Average diameter	$\times 10^{-6}$ m	94.2
Elongation	%	>40
Shrinkage at 100 °C	%	2.5
Shrinkage at 200 °C	%	5

Unidirectional Fabric

There are two kinds of 2-D fabric of thermoplastic fibre and reinforcing fibre. One is called cowoven fabric which was woven without hybridizing the reinforcing fibre and polymer fibre into a tow, the two yarns are interwoven separately. The other is called as commingled woven fabric, which was cowoven with commingled yarn of reinforcing fibre and polymer fibre. For the thermoplastic fibre and reinforcing fibre are hybridized at individual filament level in the commingled woven fabric which led to more uniform resin distribution and better wet out. It is preferred for composites. But it needs the diameter of polymer filament as small as that of carbon fibre to optimize the effect of commingle. When their diameters differ too much, there will be only several filaments of PEEK in a 3-k carbon fibre, thus it need higher resin flowability so that the resin could flow transversely to wet the carbon fibre.

For the average diameter of PEEK filaments in the study was more than 10 times higher than that of carbon fibre, it was very difficult to guarantee good fibre distribution and wet-out when they were commingled into one tow for composites. Thus the unidirectional fabric was made by cowoven of the two kinds of fibre, with PEEK as weft yarn, 7 ends each 10 mm, carbon fibre as warp yarn, 6.5 ends each 10 mm. The style of the fabric was plain weaving. The fabric interlaces one warp reinforcing fibre over and under one filling PEEK fibre. Before the coweaving, three tows of PEEK were made into ply yarn to decrease the work of weaving. The procedure for cowoven fabric was shown in Fig. 1. Some of their properties were tested and shown in table 2.

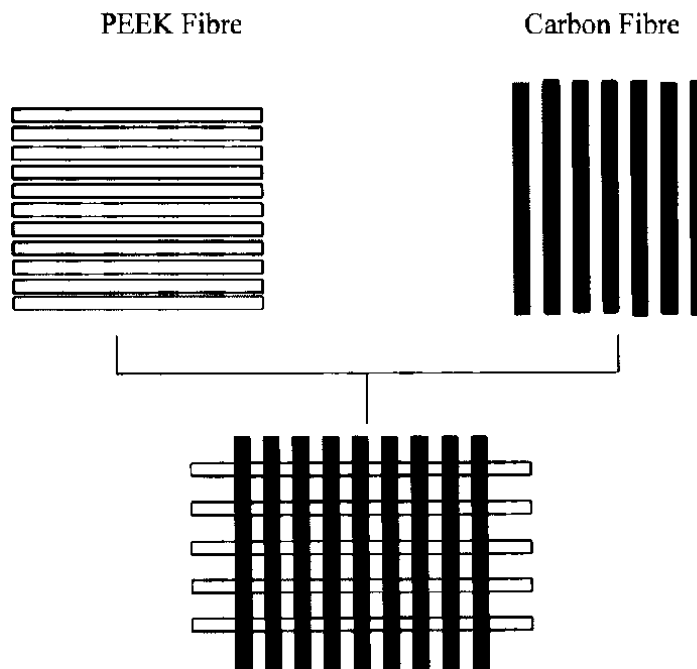


Fig.1 The process of making cowoven fabric.

Table 2 The parameters of the fabric

Item	Unit	Value
Density	g/cm ³	1.6
Length	mm	continuous
Width	mm	150
Thickness	mm	0.4
Numbers of PEEK fibre (weft)	ends/10 mm	7
Numbers of carbon fibre (warp)	ends/10 mm	6.5
Fabric weight	g/m ²	239.2
Fibre weight fraction	%	54.4
Weaving type		plain

Manufacturing of The Laminates

The unidirectional fabric was cut into pieces of plies and stacked for laminates. They were heated to 380 °C in a fully automatic vacuum hot press at the rate of 10 °C/min and 100 KPa vacuum to reduce the degradation of PEEK in air. To avoid the fibre shrinkage which may disturb the orientation of reinforcing fibre. Pressure of 1.5 MPa was applied at 150 °C before forming, and 3.0 MPa at 380 °C for shaping. The temperature of 380 °C was held for 40 min to achieve good wet-out. Then the laminate were cooled to room temperature with pressure. Fig.2 was the changes of parameters in the process.

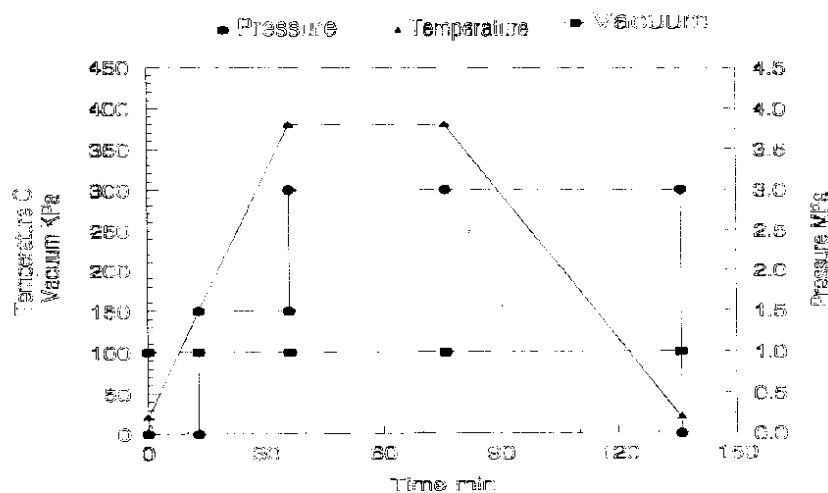


Fig.2 The processing parameters in hot press for PEEK laminate

Properties of The Laminate

To investigate the feasibility of using the fabric as prepreg and the combination of fibre and resin, short beam shear and longitudinal flexure test were conducted and compared with laminate made of prepreg by powder coating. Table 3 showed the average results of 10 short beam shear specimens and 5 longitudinal flexure specimens. It could be seen the properties of laminate made by unidirectional fabric were equivalent with that of laminate by powder coating prepreg .

Table 3 The properties of T300/PEEK composites with different prepregs

Prepreg	Testing standard	Flexure strength MPa	Short beam shear MPa
Fabric	GB3356-82 *	1747	112
Powder coating prepreg**	GB3357-82	1500	100

* National testing standard of CHINA.

**Which was also produced by ourselves.

CONCLUSION

With PEEK fibre as weft yarn and carbon fibre as warp yarn, unidirectional fabric could be manufactured with drapeability and flexibility and fibre volume fraction easy to be controlled. It is a new process for "prepreg" of thermoplastic polymer.

Unidirectional laminate could be formed by hot press molding with the T300/PEEK fabric at 380 °C, 3.0 MPa. Their short beam shear and longitudinal flexure strength were 112 MPa and 1747 MPa respectively, equivalent to that of the laminate made by powder coating prepreg, showing the success of process and the feasibility of using cowoven fabric as prepreg.

REFERENCE

1. Li Yuanzhen, Lou Kuiyang, "Powder Coating Process for Thermoplastic Prepregs", *41st SAMPE International Symposium*, 1995, pp1724.
2. Leonard E.Stanton and Stephen D.Levin, "Development and Fabrication of an Autoclave Molded PES/Quarts Sandwich Radome", *SAMPE Journal*, Vol.29, No.2, 1993, pp33.

3. Groffoths G.R. Hillier W.D. and Whiting J.A.S. "Thermoplastic Composite Manufacturing Technology for a Flight Stand Tailplane", *SAMPE Journal*, Vol.25, No.1, 1989, pp17.
4. Johnston, N.J. and Hergenrother P.M., "High Performance Thermoplastic: A Review of Neat Resin and Composite Properties", *32nd International SAMPE Symposium*, 1987, pp1400.
5. Mikiya Fujii and Hirokazu Inoguchi, "Good wettability of cowoven unidirectional Fabrics", *21st SAMPE International Technical Conference*, 21, 1989, pp496.
6. S.R.Clemans et.al, "Thermoplastic Hybrid yarns for High-Performace Composites", *Materials Engineering*, 1988, pp27.
7. Mikael Epstein, Salme Nurmi, "Near Net Shape Knitting of Fibre Glass and Carbon Fibre Composites", *36st SAMPE International Symposium*, 1991.
8. Ted Lynch, "Thermoplastic/Graphite Fibre Hybrid Fabric", *SAMPE Journal*, Vol.25, NO.1, 1989, pp17
9. Cam T. Hua, Frank K.Ko, "Properties of 3D Braided Commingled PEEK/Carbon Composites", *21st SAMPE International Technical Conference*, 1989.
10. J.Brandt, K. Drechsler,H.Richter, "The Application of 2-D and 3-D Woven Thermoplastic Fibre Preforms for Aerospace Components". *36st SAMPE International Symposium*, 1991, pp92.

LOCAL AND NONLOCAL RHEOLOGICAL EQUATIONS FOR FIBRE REINFORCED POWER LAW MELTS

Staffan Toll¹ and A. Geoffrey Gibson²

¹*Department of Polymeric Materials,
Chalmers University of Technology, S-41296, Gothenburg, Sweden*

²*Centre for Composite Materials Engineering,
University of Newcastle upon Tyne, Newcastle NE1 7RU, Great Britain*

SUMMARY: A generalisation of the traditional class of constitutive equations for fibre suspensions in slow flows is proposed. The drag force on an individual fibre strand is described by a simple power law function of its velocity relative to the bulk motion. Anisotropic power law constitutive equations are thus obtained by integration over the fibre length and proper averaging over the orientation distribution. Moreover, nonlocal action due to a non-uniform distribution of fibre centres in the flow domain is allowed for. The latter is exemplified by axisymmetric squeeze flow of a continuous strand-mat suspension.

KEYWORDS: fibre suspensions, nonlocal constitutive equations, rheology, non-newtonian, squeeze flow, GMT, thermoplastics, fibre orientation

INTRODUCTION

An important class of fibre suspensions appears in the various moulding processes for polymer composite materials, such as compression moulding and injection moulding, and there is an ongoing development of constitutive models for this kind of system. However, the vast majority of the equations proposed are limited to Newtonian suspending fluids, while many of the matrices used are thermoplastic melts, which tend to be better described as power law fluids.

An example of power law suspension flow is the squeezing flow of fibre mat reinforced polymer melts. These composite materials are known as glass mat thermoplastics (GMT), among others. Their flow behaviour at strain rates within the region of commercial interest can generally be characterised by a power law relationship between applied stress and strain rate [1-4], as demonstrated, for instance, by the GMT experimental results of Kotsikos et al. [1,2], shown in Fig. 3. These results were obtained in a constant-area squeeze flow geometry, shown in Fig. 1, using a range of plate closure speeds with a swirl mat GMT, approximating in structure to Fig. 2c. Pressure transducer measurements, Fig. 3, made during the tests show the existence of a pressure variation over the surface of the plates. This pressure distribution cannot be explained as shear induced pressure build up, as that would require unrealistically high values of the shear

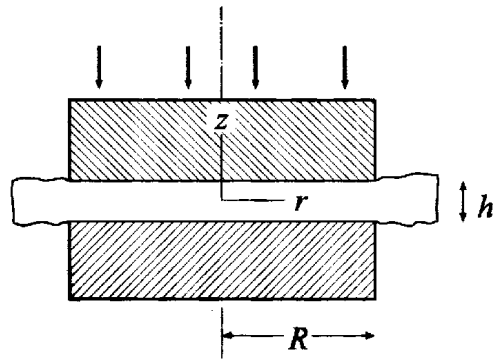


Fig. 1: Constant-area squeeze flow geometry

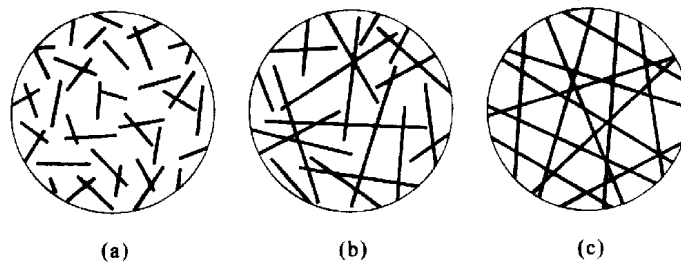


Fig. 2: Different types of structures: (a) short fibres; (b) long discontinuous fibres; (c) continuous fibres.

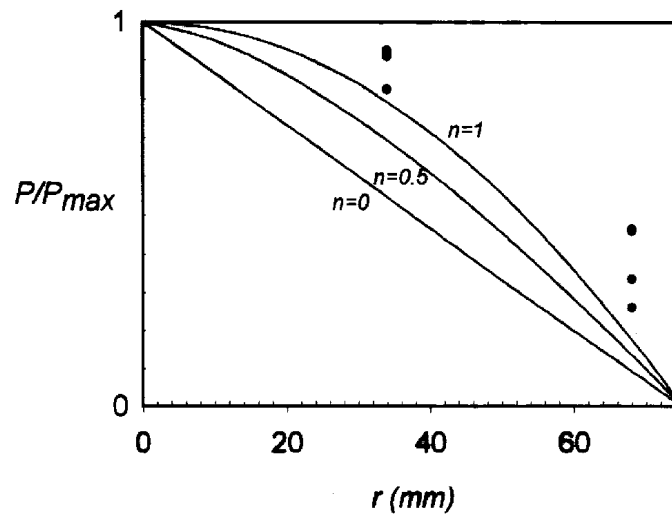


Fig. 3: Radial Pressure distribution. The data points are pressure transducer measurements by Kotsikos et al. on a polypropylene/glass GMT material with 40 weight-% random-in-plane continuous strands (Symalit AG). The radius R of the plates was 75 mm.

viscosity. Instead we suggest that this is a nonlocal effect peculiar to the structure in Fig. 2c

Power law models for fibre suspensions have previously only been published for the case of aligned fibres [5]. In this work we develop equations for more general anisotropic fibre orientation distributions.

Nonlocality in fibre suspensions is rarely considered. The type of nonlocality considered here is the long range interference between the microstructure and the location of boundaries. The problem of squeezing flow of GMT provides an intriguing example of non-local effects being central to understanding the flow behaviour. These suspensions are usually approximately planar containing fibres or fibre strands ranging, as illustrated in Fig. 2, from case (a) where the fibre length is much shorter than the domain size through to the other extreme (c) where the effective length is entirely determined by the domain geometry. Clearly, in the latter case the reduction in the effective strand length near the edge of the flow domain should diminish the local viscous response.

In this presentation we produce a constitutive equation for the effective anisotropic power law medium based on a phenomenological drag law for the individual fibre and the assumption of affinely rotating fibres. The theory allows a non-local analysis of an axisymmetric squeeze flow problem. In this way we capture the effects of the statistical heterogeneity that occurs in suspensions of continuous fibres in finite size domains.

The term strand will be used, instead of fibre for greater generality, since the effective flowing elements in planar moulding materials are frequently not single cylindrical fibres but bundles of fibres, often of non-circular cross-section.

POWER LAW DRAG

The analysis will be based on a phenomenological drag law, a relationship between the hydrodynamic drag force per unit length of strand acting on a strand segment and the velocity of the strand segment relative to the bulk motion. Considerable simplicity will be gained by postulating that the strands rotate affinely, i.e., with the bulk motion. A consequence of such a rotation is that there is no rotational component in the relative motion between a strand segment and the bulk. The relative motion consists entirely of translation along the strand axis, and there is no transverse motion. This would appear to be justified, since in a highly concentrated fibre suspension transverse motion of a strand will be greatly hindered by a large number of neighbouring strands.

The velocity of a strand segment relative to the bulk, U , can be calculated using the equation for affine fibre rotation,

$$\dot{p}_i = v_{i,j} p_j - p_i v_{j,k} p_j p_k,$$

where p is an orientation unit vector, Fig. 4, v is the bulk velocity field and commas denote differentiation. The relative velocity is

$$U_i = u_i^{\text{fibre}} - u_i^{\text{bulk}} = s \dot{p}_i - v_{i,j} s p_j = -s p_i p_j p_k v_{j,k},$$

where s is the distance from the fibre centre, Fig. 4. Introducing the rate of deformation tensor, $d_{ij} = \frac{1}{2} (v_{i,j} + v_{j,i})$, the relative velocity now becomes

$$U = U p, \tag{1}$$

$$U = -s p \cdot d \cdot p,$$

which is seen to be parallel to p , i.e., purely longitudinal.

Because of this purely longitudinal motion, a strand segment will be subjected to a force,

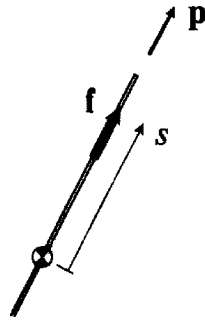


Fig. 4: Strand segment

exerted by the surrounding liquid, which is also longitudinal:

$$\mathbf{f} = -g(U)U\mathbf{p}, \quad (2)$$

where \mathbf{f} , indicated in Fig. 4, is the force per unit length of tow (in the ensemble average sense) and g is a scalar function of U . For a Newtonian fluid the following relation would apply:

$$\mathbf{f} = -\xi\eta U\mathbf{p}, \quad (3)$$

where η is the Newtonian viscosity and ξ is a non-dimensional drag coefficient which depends on the fibre orientation distribution, cross-sectional shape and volume fraction. In the case of a power law matrix with power law constant and exponent k and n , we may write

$$\mathbf{f} = -\xi^n \lambda^{1-n} k |U|^{n-1} U\mathbf{p}, \quad (4)$$

where λ is the perimeter of the fibre tow cross-section. This, of course, includes Eqn 3 as a special case when $n = 1$.

Power law drag can now be described by combining Eqns 4 and 1:

$$\mathbf{f} = \xi^n \lambda^{1-n} k |s\mathbf{p} \cdot \mathbf{d} \cdot \mathbf{p}|^{n-1} s\mathbf{p} \cdot \mathbf{d} \cdot \mathbf{p}.$$

But, as

$$|s\mathbf{p} \cdot \mathbf{d} \cdot \mathbf{p}|^{n-1} = |s|^{n-1} |\mathbf{p} \cdot \mathbf{d} \cdot \mathbf{p}|^{n-1}$$

then

$$\mathbf{f} = \xi^n \lambda^{1-n} k s |s|^{n-1} \mathbf{p} \cdot \mathbf{d} \cdot \mathbf{p} |\mathbf{p} \cdot \mathbf{d} \cdot \mathbf{p}|^{n-1} \mathbf{p}. \quad (5)$$

The present analysis will assume that the drag coefficient, ξ , of a fibre is independent of its orientation, \mathbf{p} . This is correct for certain orientation distributions, such as fully aligned, 3D random or planar random orientation (as in our example), but is otherwise an approximation of as yet unverified validity.

NONLOCAL CONSTITUTIVE EQUATION

One problem, as can be seen from Fig. 2, is that when long, or even continuous strands are dispersed in the polymer phase the material properties cannot be treated locally or separately from the geometry of the flow regime. In the most general case the length and location of

the strands depend on the position of the squeeze flow domain boundaries. Even if the flow field were uniform the material response in terms of extra stress would be neither uniform nor local, since the stress at any given point depends on interactions occurring at distant locations in the flow domain. It is necessary, therefore, to develop a non-local relationship for the stress generated in a planar suspension of strands where the interactions are governed by the drag law, Eqn 4. For simplicity the strands will be considered straight, although they may well not be so in some of the real (swirl mat) materials considered.

The particle extra stress at some bulk point, $\mathbf{x} = \mathbf{x}'$, can be defined as the ensemble average of the stress at all possible dispositions of a strand passing through that point.

$$\boldsymbol{\tau}^{(p)}(\mathbf{x}') = \phi \oint \int_{-\infty}^{\infty} \mathbf{T}(\mathbf{x}' \cdot \mathbf{p}) \psi(\mathbf{p}) \phi(s', \mathbf{p}) ds' d\mathbf{p}. \quad (6)$$

The stress, $\mathbf{T}(\mathbf{x}', \mathbf{p})$, in the strand is

$$\mathbf{T} = \frac{1}{a} \mathbf{p} \mathbf{p} \int_{s'}^{l/2} \mathbf{p} \cdot \mathbf{f} ds, \quad (7)$$

where a is the effective cross-sectional area of the strand, i.e., the sum of the cross-sectional areas of the fibres in a strand. Introducing Eqn 5 into Eqn 7 gives

$$\mathbf{T} = \xi^n \frac{\lambda^{1-n} k}{a} \mathbf{p} \mathbf{p} \mathbf{p} \cdot \mathbf{d} \cdot \mathbf{p} |\mathbf{p} \cdot \mathbf{d} \cdot \mathbf{p}|^{n-1} \int_{s'}^{l/2} s |s|^{n-1} ds,$$

and putting this expression into Eqn 6 leads to a non-local equation for the extra stress:

$$\boldsymbol{\tau}^{(p)}(\mathbf{x}') = \phi \xi^n \frac{\lambda^{1-n} k}{a} \oint \int_{-\infty}^{\infty} \left(\int_{s'}^{l/2} s |s|^{n-1} ds \right) \mathbf{p} \mathbf{p} \mathbf{p} \cdot \mathbf{d} \cdot \mathbf{p} |\mathbf{p} \cdot \mathbf{d} \cdot \mathbf{p}|^{n-1} \psi(\mathbf{p}) \phi(s', \mathbf{p}) ds' d\mathbf{p}. \quad (8)$$

SPECIAL CASES—LOCALITY

Earlier equations for fibre suspensions found in the literature are local, i.e., the stress at a material point depends only on the rate of deformation at that same point. This is justified for homogeneous flows of statistically homogeneous suspensions. We can reduce Eqn 8 to its local counterparts [5–8] by assuming statistical homogeneity or, equivalently, by letting l and s' be uncorrelated with \mathbf{x}' . For simplicity we also assume that l is uniform. Thus,

$$\boldsymbol{\tau}^{(p)} = \phi \xi^n \frac{\lambda^{1-n} k}{a} \frac{1}{n+2} \left(\frac{l}{2} \right)^{n+1} \langle |\mathbf{p} \cdot \mathbf{d} \cdot \mathbf{p}|^{n-1} \mathbf{p} \mathbf{p} \mathbf{p} \mathbf{p} \rangle : \mathbf{d}, \quad (9)$$

which is a local model for a fibre suspension of a power law fluid. Specialising further to a Newtonian suspending liquid, $n = 1$, one obtains

$$\boldsymbol{\tau}^{(p)} = \phi \xi \eta \frac{l^2}{12a} \langle \mathbf{p} \mathbf{p} \mathbf{p} \mathbf{p} \rangle : \mathbf{d}, \quad (10)$$

where η is the Newtonian viscosity of the suspending liquid. To our knowledge Eqn 9 is new, but probably of limited computational interest due to the awkward appearance of the rate-of-deformation tensor inside the orientation integral. Eqn 10, is the usual "quasi-Newtonian" form for fibre suspensions of a Newtonian fluid. With a suitable choice of the Newtonian drag

coefficient ξ , Eqn 10 coincides with, e.g., the Dinh-Armstrong equation [6] or the Shaqfeh-Fredrickson equation [7].

Eqn 9 can also be specialised to the case of elongational flow of an aligned suspension of a power law fluid,

$$\tau_{11}^{(p)} = \phi \xi^n \frac{\lambda^{1-n} k}{a} \frac{1}{n+2} \left(\frac{l}{2}\right)^{n+1} d_{11}^n, \quad (11)$$

where d_{11} is the rate of elongation and $\tau_{11}^{(p)}$ is the tensile extra stress due to the particles. For a Newtonian liquid, $n = 1$, this reduces further to

$$\tau_{11}^{(p)} = \phi \xi \eta \frac{l^2}{12a} d_{11}.$$

All these results have only one parameter that needs to be determined: the drag coefficient ξ .

The Goddard model [5] assumes a flow in an annular region surrounding a fibre of radius R_0 , with a no-slip tubular boundary of radius R_1 , concentric with the fibre. The result for cylindrical fibres is Eqn 11 with the drag coefficient

$$\xi = \frac{2\pi(1-n)/n}{1 - (R_0/R_1)^{\frac{1-n}{n}}}. \quad (12)$$

The corresponding result for a Newtonian fluid is obtained by taking the limit of Eqn 12 as $n \rightarrow 0$:

$$\xi = \frac{2\pi}{\ln \frac{R_1}{R_0}}.$$

The latter result is equivalent to Batchelor's model [8].

SQUEEZE FLOW WITH CONTINUOUS STRANDS

In the continuous fibre version of the problem, Fig. 2c, there will be no net motion along the axis of any strand. Instead the motion of each strand will be characterised by a steady radial drift towards the plate periphery. The effective length of tows, in terms of contributing to the generation of stress, will decrease considerably as their centre points approach this boundary, so the extensional viscosity may be expected to vary over the plate surface in a manner similar to that in Fig. 4. In this situation, s' and the orientation, \mathbf{p} , will uniquely determine the length and centre point location of each strand, and hence the stress distribution within it.

In Fig. 2c all fibre tows start and end on the circular boundary. As depicted in Fig. 5, this means that any strand that passes through a given point \mathbf{x} is uniquely defined by \mathbf{x} and the orientation α :

$$\begin{aligned} s' &= r \cos \alpha, \\ (l/2)^2 &= R^2 - r^2 \sin^2 \alpha. \end{aligned} \quad (13)$$

We assume here a random-in-plane orientation distribution, so that

$$\psi(\alpha) = \frac{1}{2\pi}.$$

Then it is sufficient to carry out the orientation integral in the first quadrant, so that s and \mathbf{p} are

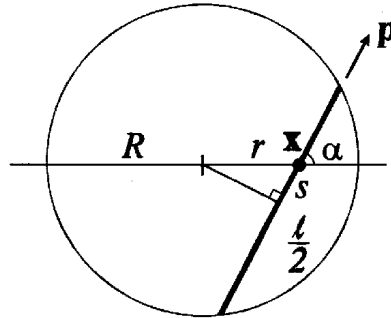


Fig. 5: Geometry of continuous squeeze flow with continuous strands

positive. It is further assumed that $d_{rr} = d_{\theta\theta} \geq 0$ and $d_{r\theta} = 0$. Thus Eqn 8 can be written

$$\tau^{(p)}(r) = \frac{2}{\pi} \phi \xi^n \frac{\lambda^{1-n} k}{a} \int_0^{\pi/2} \mathbf{p} \mathbf{p} (\mathbf{p} \cdot \mathbf{d} \cdot \mathbf{p})^n \int_{s'}^{1/2} s^n ds d\alpha.$$

Evaluating the last integral and using $p_r = \cos \alpha$ and $p_\theta = \sin \alpha$, along with the Eqns 13 one obtains

$$\tau^{(p)}(r) = \frac{2}{\pi} \phi \xi^n \frac{\lambda^{1-n} k}{a} d_{rr}^n \frac{R^{n+1}}{n+1} \int_0^{\pi/2} \mathbf{p} \mathbf{p} \left[\left(1 - \frac{r^2}{R^2} \sin^2 \alpha \right)^{\frac{n+1}{2}} - \left(\frac{r}{R} \cos \alpha \right)^{n+1} \right] d\alpha. \quad (14)$$

This integral must be evaluated numerically. In the special case $n = 1$, Eqn 14 reduces to

$$\tau_{rr}^{(p)} = \tau_{\theta\theta}^{(p)} = \eta \phi \xi \frac{R^2 - r^2}{4a} d_{rr}.$$

We shall finally illustrate the result 14 in terms of the normal pressure distribution acting on the platens. The total stress is

$$\boldsymbol{\sigma} = -\Pi \boldsymbol{\delta} + \boldsymbol{\tau}. \quad (15)$$

Here $\boldsymbol{\tau}$ is the extra stress, which consists of a fluid contribution and a particle contribution, $\boldsymbol{\tau} = \boldsymbol{\tau}^{(f)} + \boldsymbol{\tau}^{(p)}$. We have focused on the particle contribution because most often it will dominate the total stress when the aspect ratio of the fibre strands is large. This will not be true in a narrow region close to the edge of the disc, but it is assumed to be valid otherwise. In this analysis $\boldsymbol{\tau}^{(f)}$ is thus neglected. Hence

$$\boldsymbol{\sigma} \approx -\Pi \boldsymbol{\delta} + \boldsymbol{\tau}^{(p)}.$$

For the same reason, and with the same reservation, the normal pressure is

$$P = -\sigma_{zz} \approx \Pi.$$

Using equilibrium and Eqn 15 we obtain

$$P_{,r} = \tau_{rr,r} - \frac{\tau_{\theta\theta} - \tau_{rr}}{r}. \quad (16)$$

Using Eqn 14 in 16 we obtain the following expression for the radial gradient of the normal

pressure distribution:

$$P_r = \frac{2}{\pi} \phi \xi^n \frac{\lambda^{1-n} k}{a} d_{rr}^n R^n \int_0^{\pi/2} \left\{ -\cos^2 \alpha \sin^2 \alpha \frac{r}{R} \left(1 - \frac{r^2}{R^2} \sin^2 \alpha \right)^{\frac{n-1}{2}} - \cos^3 \alpha \left(\frac{r}{R} \cos \alpha \right)^n + (\cos^2 \alpha - \sin^2 \alpha) \frac{R/r}{n+1} \left[\left(1 - \frac{r^2}{R^2} \sin^2 \alpha \right)^{\frac{n+1}{2}} - \left(\frac{r}{R} \cos \alpha \right)^{n+1} \right] \right\} d\alpha.$$

This can be integrated numerically for the pressure distribution. Such pressure distributions are plotted in Fig. 3 for the experimental squeeze flow plate radius of 75 mm.

DISCUSSION AND CONCLUSIONS

The anisotropic power law equation that results from averaging fibre stresses due to non-Newtonian drag under affine fibre rotation is in appearance only marginally more complicated than its Newtonian reduction. However, the usual separability of orientation and kinematic variables into separate tensors is a strictly linear attribute and not possible in general. This is likely awkward from a computational point of view, but is bound to happen as nonlinear fluid behaviour is introduced. The only way of achieving separability would seem to be the construction of an altogether phenomenological rather than mechanistic model, stating the separability in advance. Going beyond the phenomenological drag law to describe the hydrodynamic drag is hardly useful. At high concentrations and without the luxury of a Stokesian suspending medium, a detailed model that removes the one adjustable parameter, ξ , involved here, is certainly far away.

Constant-area squeeze flow of a continuous strand-reinforced polymer melt produces a normal pressure distribution due to the interaction between strand length and boundary geometry which is very similar to that which would result from pressure build-up due to gap-wise shear. In fact it is identical in the extremes of n : for the ideal plastic case, $n = 0$, the radial distribution of P is linear, and for the Newtonian case, $n = 1$, it is parabolic. The pressure distributions in Fig. 3 are entirely due to the nonlocal coupling between the boundary geometry and microstructure. For fibres much shorter than the disc radius (Fig. 2a, or local case), the pressure distribution would be flat throughout, and for intermediate fibre lengths it would be flat at the top. The discrepancy between the theoretical curves and the data by Kotsikos et al. can be explained partly by the fact that their fibre mats were needled, reducing the effective fibre length and thus flattening the radial pressure distribution at the top, but also by our neglect of the fluid stress, $\tau^{(f)}$, which would contribute a small constant pressure.

A variety of widely used composite moulding materials, such as many GMTs, are of the swirled continuous strand type. These are invariably cut into pieces before moulding and will therefore behave as described above: their rheology is tightly linked with the size and geometry of the blanks used.

REFERENCES

1. G. Kotsikos, J.S. Bland and A.G. Gibson, "Squeeze flow mechanics for glass mat thermoplastics", *ECCM-7, 7th European Conference on Composite Materials*, Vol. I, London, 14–16 May 1996, Woodhead Publishing, pp. 213–219 (also Composites A, in press).
2. G. Kotsikos, J.S. Bland and A.G. Gibson, "Squeeze flow characterisation of glass mat thermoplastics", *FPCM-4, 4th Conference on Flow Processes in Composites*, Aberystwyth, 9–11 September 1996.

3. K.A. Ericsson, *Rheology of Glass Mat Thermoplastic*, Thesis No. 1472, LTC-EPFL, Lausanne, 1996.
4. K.A. Ericsson, S. Toll and J.-A.E. Manson, "Sliding plate rheometry of a concentrated fiber suspension", *Rheologica Acta*, submitted.
5. J.D. Goddard, "Tensile stress contribution of flow-oriented slender particles in non-Newtonian fluids", *J. Non-Newt. Fluid Mech.*, Vol. 1, 1976, pp. 1-17.
6. S.M. Dinh and R.C. Armstrong, "A rheological equation of state for semiconcentrated fibre suspensions", *J. Rheology*, Vol. 28, No. 3, 1984, pp. 207-227.
7. E.S.G. Shaqfeh and G.H. Fredrickson, "The hydrodynamic stress in a suspension of rods", *Physics of Fluids A*, Vol. 2, No. 1, 1990, pp. 7-24.
8. G.K. Batchelor, "The stress generated in a non-dilute suspension of elongated particles by pure straining motion", *J. Fluid Mech.*, Vol. 46, No. 3, 1971, pp. 813-829.

AN AIR-JET COMPACTION SYSTEM FOR DRAPING AND CONSOLIDATION IN THE AUTOMATED MANUFACTURE OF COMPOSITE COMPONENTS

Li Ma¹, Rodney A. Peck², Israel Herszberg² and Sabu John¹

¹*Department of Manufacturing Systems Engineering, Royal Melbourne Institute of Technology (RMIT), Bundoora East Campus, POBox 71, Bundoora, Vic. 3083, Australia.*

²*The Sir Lawrence Wackett Centre for Aerospace Design Technology, Department of Aerospace Engineering, Royal Melbourne Institute of Technology, GPO Box 2476V, Melbourne, Vic. 3001, Australia.*

SUMMARY: An automated system was developed for the design and manufacture of fibre reinforced plastic structures to substitute the high cost of labour in the current manual layup processes. This paper discusses a servo-controlled air-jet compaction system, which was designed and manufactured for use as a robot end effector to complete the fifth degree of freedom for an automated manufacturing system to lay-up composite components made from prepreg and dry fabric. This air-jet unit is computer controlled for precise vectorial and spatial positioning with respect to the tool used in the manufacture of a composite component. This enables the unit to be directed normal to the surface of a wide range of geometries of tools. The consolidation of each ply is effected by heated air whose temperature may be varied. The path of the compactor is guided to follow pre-determined computer generated lay-up trajectories, so as to achieve predetermined ply draping.

KEYWORDS: automated manufacture, fibre reinforced plastic composites, robotic end-effector, ply consolidation.

INTRODUCTION

The use of fibre reinforced plastic structure has been limited by their high manufacturing cost due to their labour intensive manual layup processes which are inherently costly and which attract additional costs because of the extensive inspection required for quality control. These issues have been addressed by developing automated flexible manufacturing systems for advanced composite structures. A number of such systems, reported in the open literature, are presently in various stages of development [1 - 4]. A major difficulty identified in all these programs is associated with the consolidation of prepreg and dry fabric tows on the tool, particularly for components with double curvature.

The development of the airjet end-effector for ply consolidation, which is described in this paper is part of larger research program to develop a low cost system for the automated manufacture of high quality composite components from prepreg and dry fabric[5]. This automated layup system uses concurrent design for manufacture in order to simplify the overall process so as to make it more amenable to automated manufacture. The basic system involves generating a draping finite element (FE) model using an FE computer package. The layup in the FE model is defined using a protocol in which the draping sequence of the ply is

defined as part of the design process. The information relating to draping is used to control the automation[5]. The system was designed for cost effective manufacturing by maximising flexibility, minimising human intervention during manufacture and maximising exploitation of a unified computer database.

One of the essential elements of such a system is the process of consolidating each ply into its appropriate position in the tool. An air-jet compactor driven by a servo motor has been developed to use compressed air to consolidate prepeg and tackified dry fabric plies. The orientation of the nozzle at the end of the compactor enables the unit to work on most surface used in creating composite parts, including those with complex curvature..

DESIGN CONSIDERATIONS

Often composite parts involve laying up fabric over curvature that cannot be consolidated using just one roller. Using air to apply the consolidation force enables layup on tools with complex curvature. A part can have some difficult small radius joggles close to complex curved areas and no change in tool will be needed. The air simply conforms to the curvature of the tool. Although the air jet is best suited to parts with complex curvature, it is also able to lay up efficiently onto flat or singly curved tools.

Critical issues

A number of critical issues were considered during the design phase.

1. The unit was required to function in sharp female corners or in small tools where there is limited space. Therefore, the overall size of the airjet end-effector was a critical issue.
2. The control of the nozzle path and velocity was a critical feature. For effective consolidation, it was essential to ensure that, at all phases of the consolidation process, the air-jet was aligned with the normal vectors generated from the CAD process. The starting torque and holding torque required for correct operation needed to be determined at the design stage.
3. The diameters of the high pressure air lines had to be carefully chosen so as to achieve the necessary force to consolidate the plies.
4. Simplicity of construction and operation were major considerations in the design stage.

Force applied

One essential element determining the end effector size was the force applied to the plies, which required a certain diameter of nozzle and channel pressure air. From human hand operating experiments, a force of approximately 20 N[1] was placed on the plies. The pressure obtained from the laboratory compressed air system(Ps) was 700 kPa.

Force required for draping: $F = 20 \text{ N};$
 Pressure obtained from lab system: $P = 700 \text{ kPa};$
 Square of nozzle: $S;$
 Diameter of nozzle: $D;$

$$F = P * S$$

$$S = \pi * (D/2) * (D/2)$$

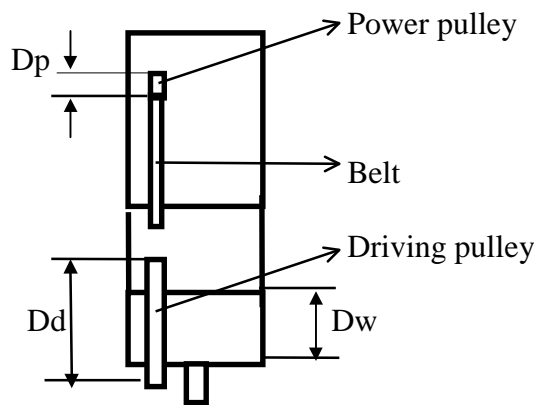
$$D = 2 * \sqrt{S/\pi} \therefore D = 2 * \sqrt{F/(p*\pi)}$$

$$D = 6 \text{ mm}$$

Therefore, 6 mm inter diameter of nozzle was chosen.

ROTATION

The speed of the nozzle turning had to be compatible with that of the robot's movement so as to complete the movement in approximately the same time or sooner. Calculations were applied for adopting a motor with its gear box and a pair of pulleys as shown in *Figure 1*.



Robot moving speed: $V_r;$
 Nozzle vectorial speed: $V_n;$
 Diameter: $D;$

 Angle rotating speed: $\omega;$
 Nozzle radius: $R_n;$

 Subscripts:
 Nozzle n
 Robot r
 Driving pulley d
 Power pulley p

Figure 1: End effector rotation mechanism

The nozzle vectorial speed (V_n) needs to be similar to the robot arm moving speed (V_r), this was expected in most of applications to be approximately : $V_n = V_r = 1 \text{ m/s}.$

$$V_n = \omega_n * R_n;$$

$$\omega_n = V_n / R_n = V_r / R_n;$$

To avoid the motor hitting the tool but still allow the nozzle to access sharp corners in limited space, a pair of pullies and a belt have been introduced to keep the motor away from rotation wheel.

The pair of pulleys chosen were:

Driving pulley: 40 teeth;

Power pulley: 10 teeth;

$$\omega_p = (R_d / R_p) * \omega_d;$$

$$\therefore \omega_p = (40 / 10) * (1000 / 22.5);$$

$$\omega_p = 177.7 \text{ degrees/sec};$$

$$\therefore \text{Its spinning speed is } 1698 \text{ rotation per minute .}$$

This range of rotation speed from the motor gear box can be adopted to drive the unit.

CONTROL

The control of the unit was performed using software developed to read draping data generated and converted from an FE model. It consisted of two sections:

1. Software to read the draping data and send the command to drive the motor using the converting card.
2. Automated error correcting system.

A servo motor control card was employed to convert the commands to pulses which were increased by a transformer before driving the motor. The motor was then calibrated to identify the number of pulses required to rotate the nozzle one degree while the compressed air was being ejected.

Since a small amount of error occurs during the process of position movement each time, a feed back system was necessary. It helped correct the error in order to obtain the precise draping position. The motor used allowed the addition of the feedback so as to produce a servo motor. A potentiometer installed in the servo generate the voltage signal which was sent back to the servo motor controller. This then terminated the motor rotation after the feedback signal matched the pulse signal sent from computer.

OVERALL AIR-JET COMPACTOR UNIT

The overall control system schematic is depicted in *figure 2*. The diagram of the air-jet compactor unit is presented in *figure 3*. These include three parts: Movement mechanism, Air-jetting and Control of motion and jet.

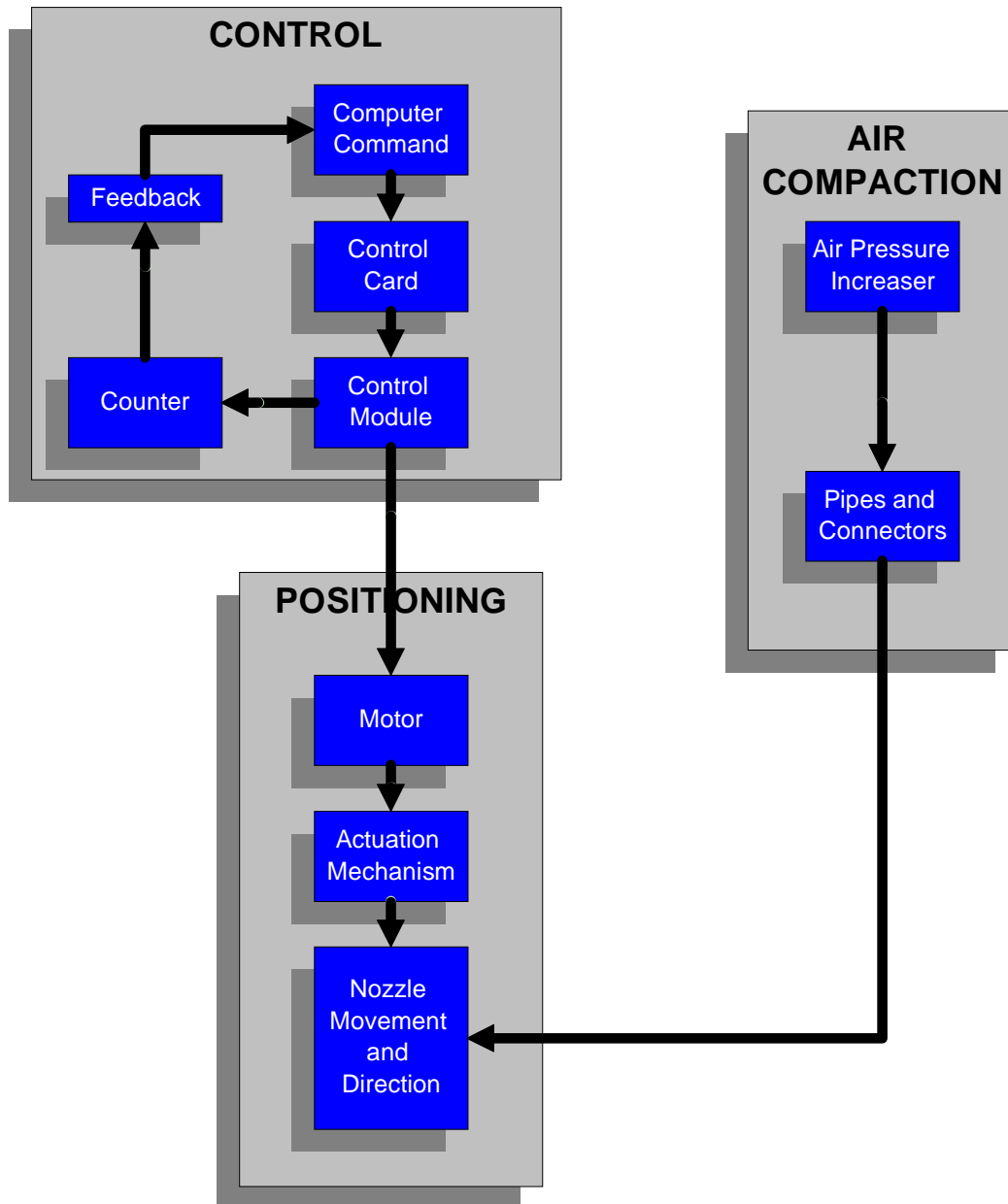


Figure 2: Schematic diagram of the air compaction control system

The reason for installing the transmission inside the tube, that supports the wheel and is held by robot, come about for two main reasons. First, it could reduce the overall size of the unit, enabling the unit to work in small space. Second, it contributes to safety considerations.

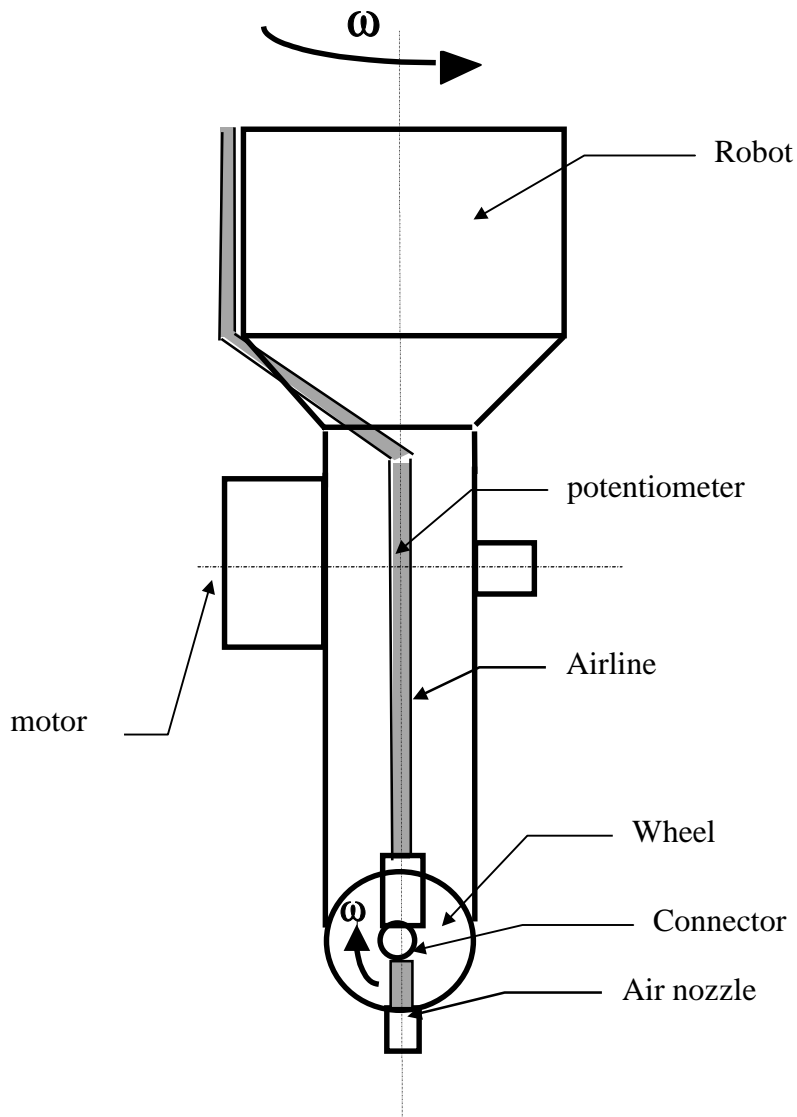


Figure 3: Diagram of air-jet end effector

Moving parts

The nozzle at the end of the wheel is driven by the motor via pulleys and a belt, after the speed had been reduced and torque had been increased by a gear box at end of the motor. It can rotate up to 100 degrees on each side, which ensures the nozzle is able to point normal to any curved surface when used with a vertical rotational axis from robot. All moving parts were kept small to ensure the final end effector was able to access small radius and parts with deep sections. Further reduction in size was impractical as a certain airflow was needed using standard airline thus dictating the size of the overall dimensions used.

Air-jetting parts

After the command was given by the software the compressed air was turned on by a solenoid switch and the air was ejected out from nozzle by passing through a pipe situated internally to the rotating cylinder the nozzle was attached to.

Controlling parts

Following the given computer command, a servo motor controller received the pulse sent from a computer control card. This pulse was then increased to allow it to drive the motor step to its position. The potentiometer at the end of gear box generated the feed back voltage from the motor rotation back to the controller so as to modify the nozzle to the correct position.

TEST OF CONCEPT

Calibration of the nozzle controller was performed by finding what pulse corresponded to what angle. This following relationship was found;

$$\text{Pulses} = 21/9 \times \text{Angle (in degrees)}$$

The unit has been fully calibrated and basic tests performed using the system software. However, final testing of the end effector will require the integration of all hardware and control by the software in order for it to be fully tested..

The draping force, although enough to consolidate ply onto simple curved tools, would not be adequate for shape corners. These, however, could be consolidated by introducing an air pressure increaser (pneumatic air ejector) in the air line. Heating the compressed air would also help press the plies into sharp corners, as a result of the prepreg softening tack increasing. Dry fabric with binder (B staged resin) could also be influenced by such heating. The air heating system is being developed.

CONCLUSION

An air-jet compactor unit has been designed for use in an automated composite manufacture layup cell which enables plies to be layed onto various types of complex curved tooling.

A prototype airjet compactor has been constructed, calibrated and its operational aspects successfully tested.

The control system required to operate the compactor has been designed, constructed and successfully tested.

REFERENCES

1. R.O. Buckingham, and R.O. Buckingham, "Automating the Manufacture of composite Broadgoods," Composites Part A, vol. 27A, pp. 191-200, 1996.
2. J. A Chestney and M. Sarhadi, "Control and integration techniques in a fully automated manufacturing cell for carbon composites", presented at IEEE Proc. -- Control Theory Appl. 1996.
3. D. G. Johson and J. J. Hill, "A Sensory Gripper For Composite Handling", pp 409 - 415.
4. D. E. Ruth and P. Mulgaonkar, "Robotic Lay-up of Prepreg Composite Plies", presented at IEEE International Conference on Robotics and Automation, 1990.
5. R.Peck, I.Herszberg and S. John, "A system for the design and automated lay-up for the manufacture of composite components.", ICCM-11, Gold Coast, Australia, July, 1997

PRESS FORMING OF GLASS MAT REINFORCED THERMOPLASTIC SHEET

Yasunori Nakamura, Yoshikazu Kontani

*Department of Mechanical Engineering, Osaka Sangyo University,
3-1-1 Nakagaito, Daito, Osaka, 574, Japan*

SUMMARY: Experimental study of deep drawing of glass mat reinforced thermoplastic sheet is carried out for the purpose of obtaining a cup shaped container which has thin wall and uniform fiber distribution by using the cheap conventional sheet metal forming die. At 120 °C, close to melting temperature, both flat head and hemispherical punch can form a cup without any wrinkling. Larger blank holding force reduces the both flange and body wrinkling by both flat head and hemispherical punch. But excess blank holding force makes breakage at the side wall. It is possible to find out the optimum blank holding force which can form a cup without wrinkling or breakage. Smaller thickness of blank and higher blank holding force make a large stretch deformation especially by hemispherical punch.

KEYWORDS: sheet forming, deep drawing, thermoplastic, glass mat

INTRODUCTION

Flow molding of Stampable sheet in a closed die is used generally as a forming method of thermoplastic composites. In this method, the forming a shallow container having thick wall is easy, but the forming a deep container having thin wall is difficult. When long fiber is used in high fiber content material, as the flowability of fiber in a matrix is insufficient, resin rich portion occurs often, which makes the mechanical strength degraded.

On the other hand, press forming of cloth reinforced sheet is done when a product requires more strength. [1,2] But, because freedom of deformation of cloth is low, deformation is limited to shear deformation in particular direction in 45° to fiber direction of cloth. [3,4] As wrinkling occurs easily in a principal direction of cloth, the forming is difficult. Therefore, the experimental studies of deep drawing of glass mat reinforced thermoplastic sheet are carried out for a purpose to get a container having thin wall and uniform fiber density distribution of high fiber content material. Both flat head and hemispherical punch are used. The effect of forming temperature, punch shape and other forming conditions upon the formability of sheet are examined.

Table 1: Physical Properties of Nylon sheet

Name	ELEPHAN NT 120 (NITTO BOSEKI CO.,LTD)
Glass transition temperature/°C	about 0
Melting temperature/°C	120-130

Table 2: Specifications of Glass Mat

Name	Glass chopped roving mat (NIHON MATAI CO.,LTD)
Filament diameter/μm	13
Weight/(g/m ²)	264

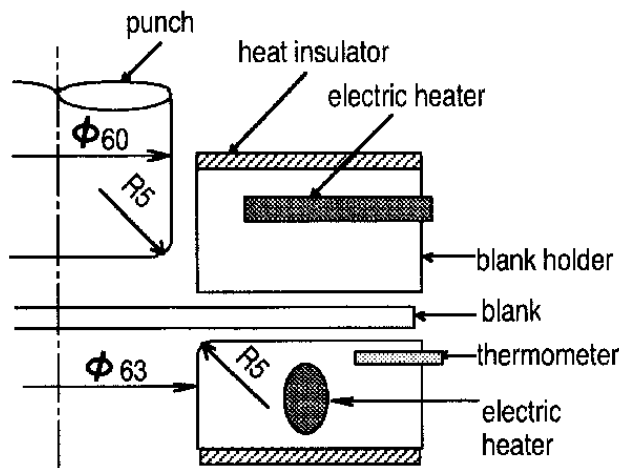


Fig. 1: Forming tools

Table 3: Impregmate Conditions

Temperature/°C	170
Holding time/min	40
Pressure/kN	9.6

Table 4: Specifications of FRTP sheet

Number of mat	2	3	4
Thickness/mm	0.4	0.6	0.8
Fiber content/wt%	46	64	60

Table 5: Specifications of forming tools

Tool	Flat head punch	Hemispherical punch	Die
Diameter/mm	60	60	63
Shoulder radius/mm	5	--	5

EXPERIMENT

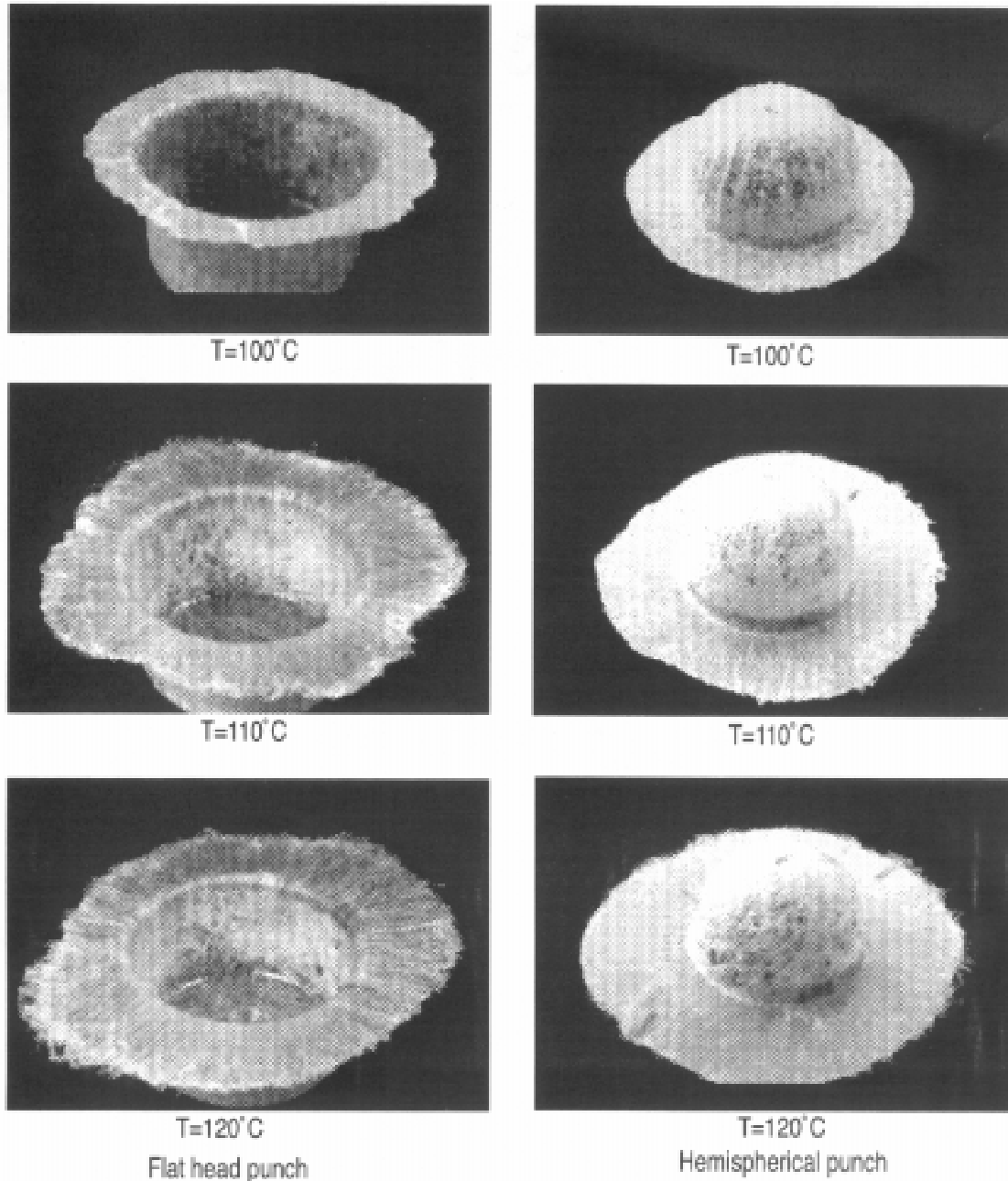
Fabrication of FRTP sheet

The material for a matrix is a low melting temperature nylon sheet. The reinforcement used is a chopped strand glass mat. Physical properties of the nylon sheet and specifications of the glass mat are shown in Table 1 and 2.

FRTP sheet is prepared by film stacking method. A certain number of the mat, such as 1, 2 and 3, is stacked with nylon films to obtain different thickness FRTP sheet. The number of the nylon sheets is chosen to acquire 55 wt% fiber content. The impregnate process is performed by using a vacuum hot press. Table 3 shows the impregnate conditions of FRTP sheet. Table 4 shows the thickness of impregnated sheet and the actual fiber content of each kind of FRTP sheet.

Deep drawing test

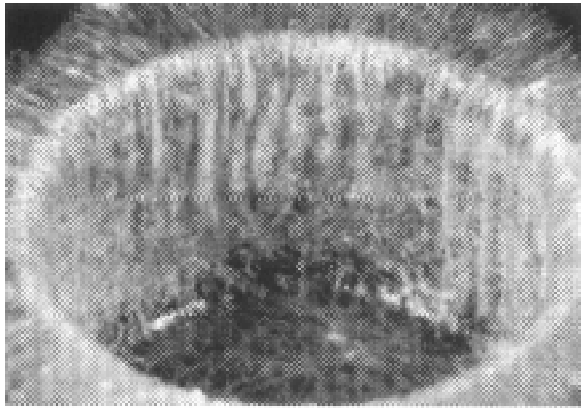
Fig. 1 shows the scheme of forming tools. These are exactly same as sheet metal forming tools except heating. Hemispherical punch and flat head punch are used. Table 5 shows the specification of forming tools. The flange surface of the die and the blank holder are heated upto forming temperature by electric cartridge heaters but punch is not.



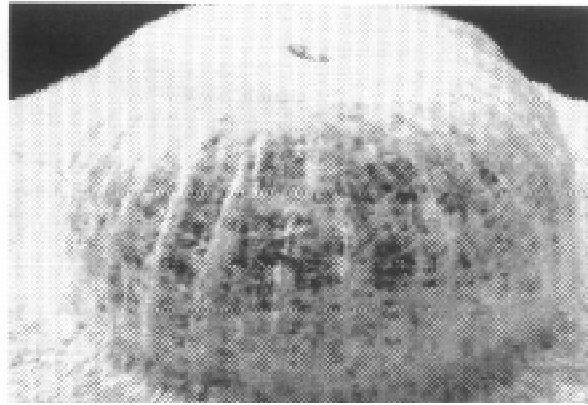
Thickness 0.4mm, Blank holding force 3.8kN, Depth 40mm

Fig. 2: Effect of forming temperature T

FRTP sheet is cut into circular blanks with 150 mm diameter. A blank is kept in a heated oven to become forming temperature for 5 minutes before forming process. Heated blank is placed onto the die and blank holding force is engaged. Then, the blank is drawn into die as the manner of conventional sheet metal deep drawing. Forming is done under such condition as blank holding force are 1.9, 3.8, 7.7, 11.5, 15.4 kN and forming temperature are 100, 110, 120 °C.



Thickness 0.4mm, Forming temperature 100°C, Blank holding force 11.5kN



Thickness 0.4mm, Forming temperature 100°C, Blank holding force 3.8kN

Fig. 3: Wrinklings on flat head punch

Fig. 4: Body wrinklings on hemispherical punch

EXPERIMENTAL RESULTS

Effect of forming temperature

Fig. 2 shows formed cups with 40 mm in depth. Blanks with 0.4 mm initial thickness are formed under the condition as blank holding force is 3.8 kN, and forming temperature are 100, 110, 120 °C.

In the case of forming at 100 °C, there are countless wrinklings in both flange and side wall of formed cup by using flat head punch. The close up of wrinklings on side wall is shown with Fig. 3. Matrix at this temperature is in solid state, which has good plastic deformability but has poor flowability. When the matrix deforms compressively in circumferential direction, compressive stress acts on glass fibers and make small size bucklings because of poor flowability of matrix. When the hemispherical punch is used, there are small size wrinklings in flange. But larger size body wrinklings instead of small size wrinklings occur in the side wall and hemispherical part. Fig. 4 shows the close up of body wrinklings on hemispherical cup.

Forming at 110 °C reduces the both flange and body wrinklings because matrix fallibility increases. But small size body wrinklings still remain at the top of hemispherical cup.

As matrix has enough fallibility at 120 °C, sheet can be compressed without fiber buckling. Both flat head and hemispherical punch can make a cup without wrinkling. As the forming temperature becomes higher, the amount of material flowing into die hole from blank holder decreases and elongation in the meridian direction increases. It is considered that better flowability of matrix and larger stretch deformation in the meridian direction reduces the wrinkling. Following test is carried at forming temperature 120 °C.

Effect of blank holding force

Fig. 5 shows cups formed by flat head and hemispherical punch. These initial thickness is 0.4 mm, forming temperature is 120 °C, cup depth is 40 mm, blank holding forces are 1.9, 3.8, 7.7, 11.5 kN. In the case of blank holding force 1.9 kN, there are wrinklings on both flat head cup and

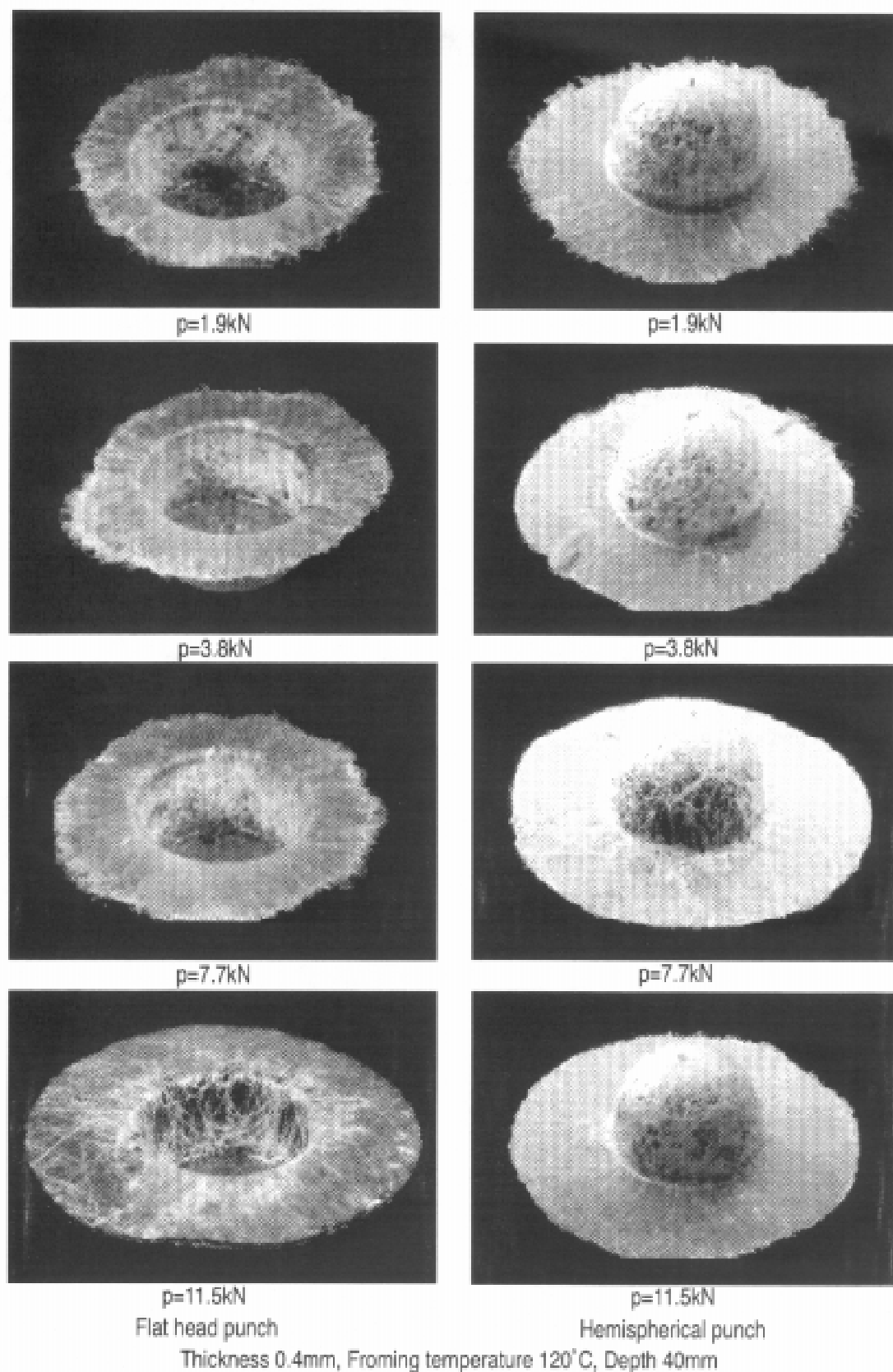
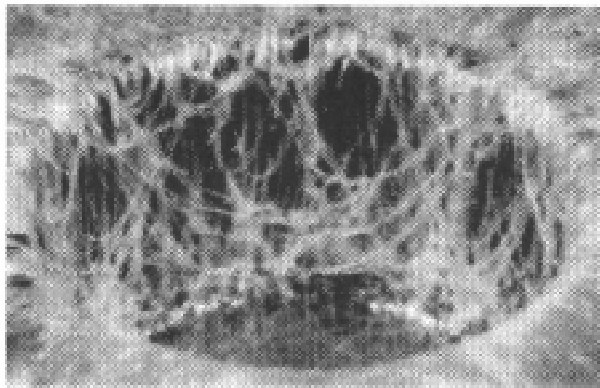


Fig. 5: Effect of blank holding force p



Thickness 0.4mm, Forming temperature 120°C,
Blank holding force 11.5kN

Fig. 6: Breakage on flat head punch

hemispherical cup. Larger holding force reduces the wrinklings because large holding force keeps more material remained on flange, and reduces the amount of material which moves into the die hole from blank holder. This makes elongation of side wall large. Therefore, the amount of wrinkling become small. But in case of flat head punch with blank holding force 11.5 kN, more elongation occurs on side wall and a part without fiber or resin is caused. Fig. 6 shows the close up of this part. Also, in the case of hemispherical punch with blank holding force 7.7, 11.5 kN, it shows similar phenomena. This phenomenon is regarded

as a stretch breakage of side wall and is similar to material breakage in sheet metal deep drawing. Therefore, blank holding force has an optimum value to form a cup without wrinkling or breakage as similar as sheet metal deep drawing. In case of hemispherical punch, the value of optimum blank holding force is lower than that of flat head punch.

Density distribution

As the fiber bundles in glass mat make unevenness on cup surface, measuring the thickness distribution is difficult. So, density per unit area is used to examine the state of deformation of material instead of thickness change. Fig. 7 shows the measuring points. Fig. 8 and 9 show density distributions in meridian direction. Forming temperature is 120 °C, and initial thickness are 0.4 and 0.6 mm.

Fig. 8 shows the case of flat head punch. The upper part of side wall, where large circumferential compression is caused, has higher density per unit area. This is equivalent to increasing of thickness. The larger initial thickness and the lower blank holding force make higher rate of increasing density. This means increasing the draw deformation in circumferential direction and decreasing the stretch in meridian direction. This is because the larger thickness and the lower

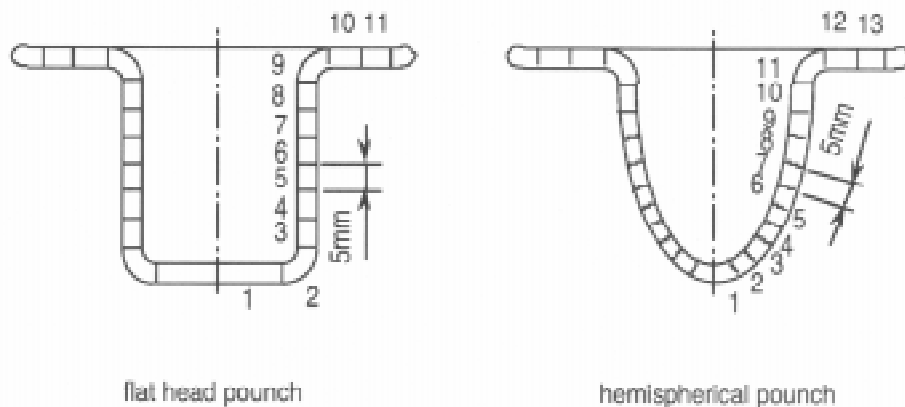
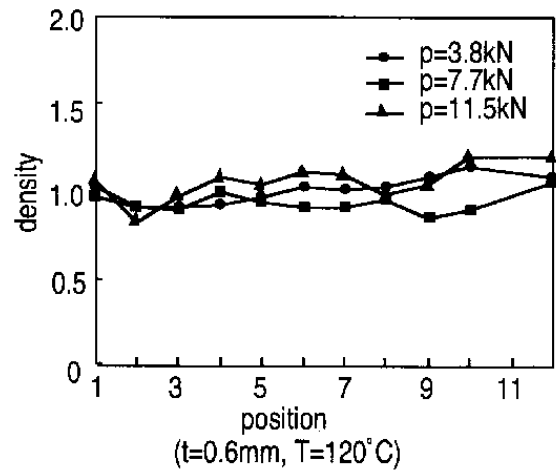
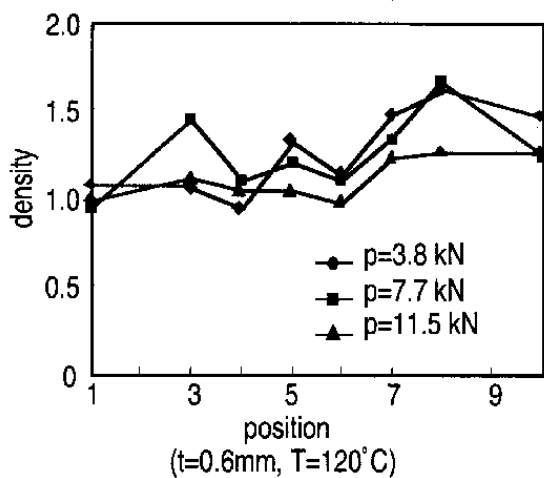
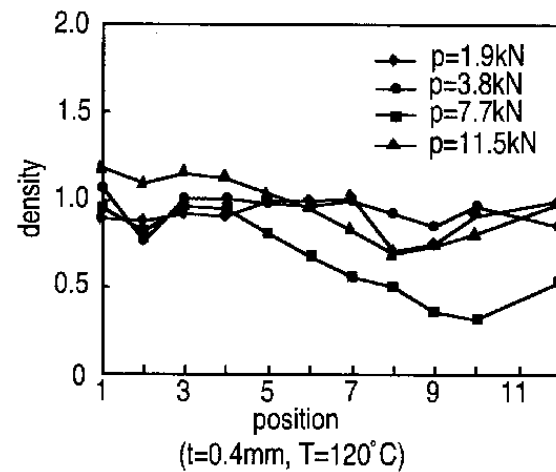
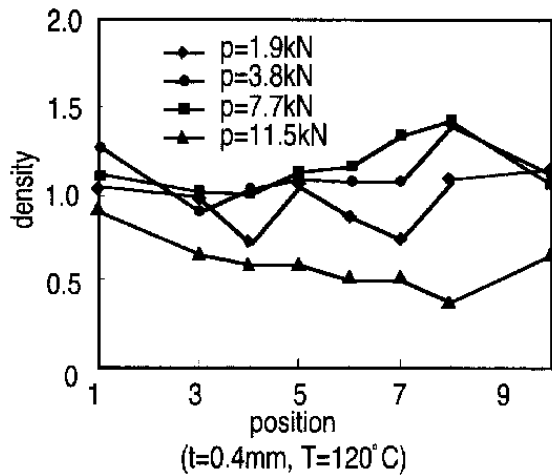


Fig. 7: measuring points



p: Blank holding force, t: Thickness of blank, T: Forming temperature

Fig. 8: Density distributions
(flat head punch)

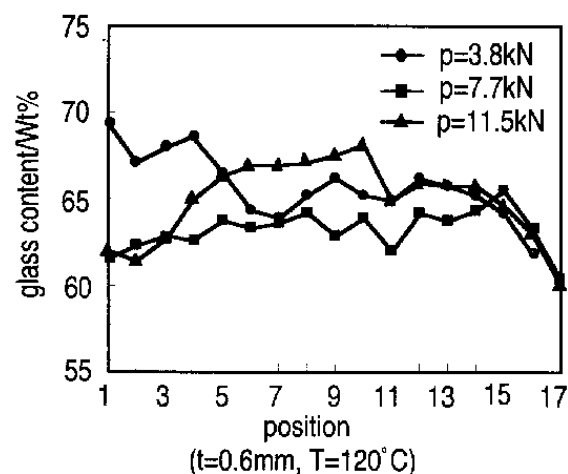
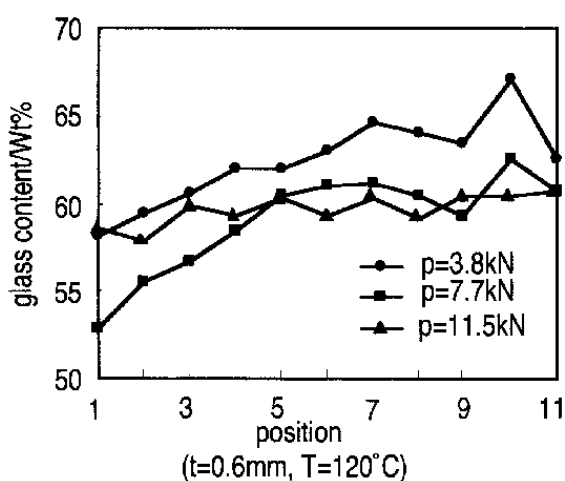
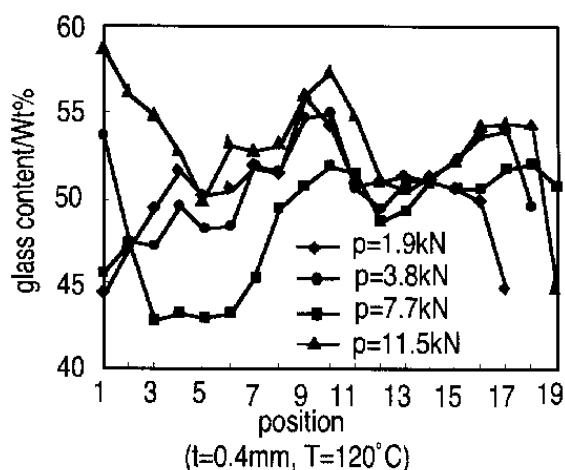
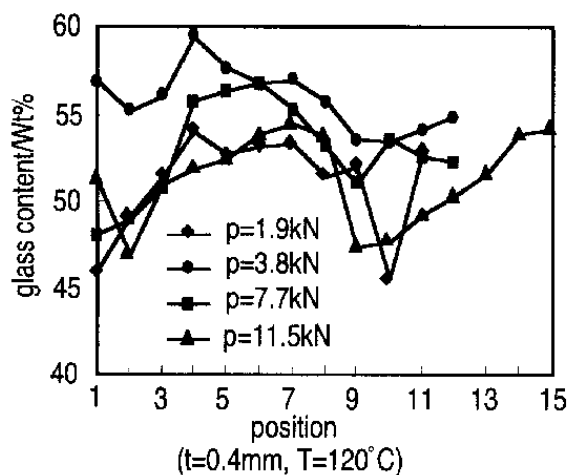
Fig. 9: Density distributions
(hemispherical punch)

blank holding force increase the amount of material flow into die hole from blank holder.

Fig. 9 shows the case of hemispherical punch. There is no increase of density of per unit area at upper part of side wall, where density increase can be seen with flat head punch. Even with a larger thickness - 0.6 mm -, thickness remains almost uniform. But, the density becomes small at side wall close to die shoulder with lower thickness - 0.4 mm -. This shows stretch in meridian direction becomes large and shrinkage in circumference direction is small. It is easy to stretch the material with hemispherical punch and decrease the amount of material flow into die hole from blank holder. Most thin part is seen at the side wall close to die shoulder. This can be seen also with flat head punch. The breakage would come out at this point as can be seen in Fig. 6.

Fiber content distribution

The forming is carried out at temperature close to melting point of resin. It is thought that drawing traction force transferred by fiber itself and viscosity of resin. Fiber weight content distribution is measured to exam the behavior of fiber and resin. Fig. 10 and 11 show fibefr content distributions in meridian direction with forming temperature 120 °C, initial thickness 0.4, 0.6



p: Blank holding force, t: Thickness of blank, T: Forming temperature

Fig. 10: Fiber content distributions (flat head punch)

Fig. 11: Fiber content distributions (hemispherical punch)

mm.

Fig. 10 shows the case of flat head punch. Glass content is minimum at side wall close to punch shoulder and becomes maximum at flange. Then, it becomes small at the edge of flange again. A portion with large compressive deformation has high fiber content. It is thought as compressive deformation makes compaction of fibers. As increasing the thickness is limited, excess resin flows out and move outward to edge of flange.

Fig. 11 shows the case of hemispherical punch. It shows similar result as with flat head punch. The ratio of increase of fiber content is small on the contrary to flat head punch. This is because the stretch in meridian direction is large and circumference compressive deformation becomes small at the bottom of cup and side wall in case of hemispheric punch. Therefore, amount of resin flow out would decrease.

CONCLUSIONS

Glass reinforced thermoplastic sheet can be formed into cup shape by deep drawing operation as the manner of conventional sheet metal deep drawing. Forming at relatively low temperature - 100, 110 °C, as the resin is solid state - makes many small size wrinklins on both side wall and flange of cup. Both flat head and hemispherical punch can draw a cup without wrinkling in forming at the temperature close to melting point of resin. Higher forming temperature reduces the material flow from flange into the die hole and makes larger stretch deformation in side wall. This is why higher forming temperature reduces the wrinkling. Larger blank holding force also reduces material flow from flange into the die hole and reduces the wrinkling. But, excess blank holding force makes breakage at the side wall close to die shoulder. Therefore, it is possible to find the optimum blank holding force which can form a cup without wrinkling or breakage. The optimum blank holding force in the case of using hemispherical punch is smaller than one with flat head punch. The portion of side wall close to die shoulder has a larger drawing deformation because of thickness increase and fiber content increase in this portion. Thickness increase rate and fiber content increase during the forming with hemispherical punch are small in comparison with flat head punch. Smaller thickness of blank and higher blank holding force make a large stretch deformation especially by hemispherical punch.

REFERENCES

- (1) K.D.Potter., "The Influence of Accurate Stretch Data for Reinforcements on the Production of Complex Structural Moulding. Part 1: Deformation of Aligned Sheets and Fabrics", *Composite*, July 1979, pp.161-167.
- (2) R.Scherer, N.Zahlan and K.Friedrich., "Modelling the Interply-Slip Process during Thermoforming of Thermoplastic Composites using Finite Element Analysis", *Proceedings of the 2nd Int. Conference on Computer Aided Design in Composite Materials Technology*, Brussels, April, 1990, pp.25-27.
- (3) P.Boisse, J.C.Gelin and H.Sabhi, "Forming of Glass Fiber Fabrics into Complex Shapes Experimental and Computational Aspects", *Annals of the CIRP*, Vol. 41, 1, 1992, pp.327-330.
- (4) B.P.V.West, R.B.Pioes, M.Keefe and S.G.Advani., "The draping and consolidation of commingled fabrics", *Composite Manufacturing*, Vol. 1, No. 1 1991, pp.10-22.

THE DEVELOPMENT OF FIBER-REINFORCED THERMOPLASTIC POLYSTYRENE COMPOSITES FOR PULTRUSION (1)

Chin-Hsing Chen and Wen-Si Wang

*Institute of Chemical Engineering,
Chinese Culture University, Yang-Ming-Shan, Taipei, Taiwan, ROC*

SUMMARY : A feasibility study on the pultrusion of a fiber-reinforced thermoplastic polystyrene (PS) composites has been conducted using a proprietary method. The PS prepolymer synthesized in this study was prepared from blends of styrene monomer and benzoyl peroxide(BPO).The process feasibility and the effects of the processing parameters on the mechanical properties of the fiber-reinforced PS composites by pultrusion has been investigated. From the investigations of the long pot life of styrene prepolymer, the high reactivity of styrene prepolymer, and excellent fiber wet-out, it was found that the PS resin showed excellent process feasibility for pultrusion. The processing parameters investigated include pulling rate(in-line speed), die temperature, and postcure temperature and time. It was found that the mechanical properties increase with increasing die temperature, and with decreasing pulling rate. The mechanical properties increase at a suitable postcure temperature and time.

KEYWORDS: pultrusion, polystyrene, prepolymer, process feasibility, processing parameter, properties, composite

INTRODUCTION

Pultrusion process has been grown very rapidly in the past decades due to the development of materials and processing technique¹. However, the pultrusion process has been associated almost exclusively with thermoset polymers such as unsaturated polyester, vinyl ester, phenolic and epoxy resin²⁻⁴ from the early 1950s. Material handling of thermoset materials is very tedious since these materials inherited a limited shelf life and are often stored at low temperature. Quality control is another cost factor to thermoset resin since each batch from manufacturer must be inspected before mixing and each formulation must be matched to previous batches⁵. Consequently, composite fabricators are searching for thermoplastic matrix materials as replacements .

Thermoplastic material show the potential for high-speed, low tooling cost, and short cycle time process. Substantial cost reductions can also be realized due to their unlimited shelf life, reduced scrap and waste (owe to the recyclability of the materials), ease of repair

ability to be welded or fused together⁶⁻¹⁰. Thermoplastic composite material provides the opportunity for developing an entirely new area of pultruded composite profiles and structures¹¹.

In this study, thermoplastic polystyrene (PS) pultrusion has been investigated. Styrene monomer was used directly, and polymerized in the die. It provides a new concept for in-situ thermoplastic pultrusion¹². This paper presents the process feasibility and the effects of the processing parameters on the mechanical properties of the fiber-reinforced PS composites by pultrusion.

EXPERIMENTAL

Materials

The styrene monomer was a purified industry grade and was supplied by the Taiwan Styrene Co., Taiwan. The initiator benzoyl peroxide (BPO) used was a guaranteed reagent and was supplied from the Kanto Chemical Co., Japan. The continuous E-glass fiber roving was TGFR-P2200 which was obtained from the Taiwan Glass Co., Taiwan. Two fillers were used in this study, namely, kaolin and talc and was supplied by Cheng Shin Co., Taiwan. The styrene prepolymer synthesized in this study.

Preparation of styrene prepolymer

In this study, the styrene prepolymer was synthesized by heating the inhibitor-free monomer in a water bath at 75 °C until it became noticeably. In order to remove the reaction heat, the synthesized prepolymer was immersed in an ice bath for 30min, then was stored at low temperature, below about 10 °C.

Apparatus

- (1) A pultrusion die with multiple heating zone of dimensions of 0.319x1.27x82.0 cm (thickness x width x length) was self-designed. The surfaces of the stainless steel die have been treated by chrome plating, as shown in Fig. 1.
- (2) Viscosities were measured with a Brookfield RVF model viscometer during the synthesis of polystyrene prepolymer.
- (3) A universal material testing machine, an Instron 1123, Instron Co., USA.
- (4) The SEM (Scanning Electron Microscope) used was a S-570, Hitachi Co., Japan.
- (5) The GPC (Gel Permeation Chromatography) used was a Unical 3-02, Viscotek Co., USA.
- (6) The DSC (Differential Scanning Calorimetry) used was a Model 910, Du pont Co., USA.
- (7) The GPC (Gel Permeation Chromatography) used was a Unical 3-02, Viscotek Co., USA

RESULTS AND DISCUSSION

Properties of styrene prepolymer

The viscosity of styrene prepolymer was measured by a Brookfield viscometer as shown in Fig. 2. An optimum temperature at 75 °C was found. When the temperature is lower than 75

°C, processing time will be too long. However, when temperature is high than 75 °C, the viscosity of styrene prepolymer can not be controlled easily. Table 1 summarizes the physical properties of styrene monomer and its prepolymer.

Process feasibility study

The thermoplastic resin used for *in-situ* pultrusion process must possess the following characteristics : (1) long pot life in the impregnation tank; (2) high reactivity; and (3) good wet-out between fiber and resin.

In order to provide a sufficient time for pultrusion processing, the pot life of styrene prepolymer must be prolonged. Fig. 3 shows the viscosity versus reaction time of styrene prepolymer at various temperatures. One can observe the viscosity of styrene prepolymer rises only 120 cps after 10 hr at 30 °C. This results indicate that the pot life of styrene prepolymer are longer than 10 hr when the impregnation tank is set at 30 °C, which provides a sufficient time for subsequent processing.

In the pultrusion process, the styrene prepolymer must have high reactivity, otherwise, they cannot be fabricated in a short time in the die. Generally, when the polystyrene was polymerized, the IR spectrum that the absorption peaks C=C disappear at 1630 cm^{-1} . Fig. 4 shows the IR spectra of (a) styrene prepolymer and (b) polystyrene. From the figure, one can observe that when the styrene prepolymer polymerized at 160 °C for 60 sec, the C=C peaks at 1630 cm^{-1} disappear clearly. From these observation of these peaks, the thermoplastic polystyrene resin can be polymerized in a short time; thus the composites can be fabricated in a short time in the pultrusion die.

In order to obtain composites with the best mechanical properties, adequate fiber wet-out is very important. The morphology phenomena can be observed by SEM photographs. The cross-section and fracture surfaces of pultruded glass fiber reinforced thermoplastic polystyrene composites were investigated by SEM micrography as shown in Fig. 5. From (a) of figure one can observed that the fiber bundles are distributed evenly in the polystyrene matrices, and from figure (b), the excellent wet-out of fiber by polystyrene resin can be observed.

Processing parameters study

Pulling rate--Since pultrusion is an automatic and continuous process for fabricating fiber reinforced plastics, the proper pulling rate is a critical parameter in the optimization of the production rate and the mechanical properties of the composites.

In general, the mechanical properties increase with the decreasing of pulling rate. For a lower pulling rate, the residence time of the resin in the pultrusion die will be longer; hence, the degree of polymerization will be higher and the wet-out of fibers will be better. Figs. 6 and 7 show the effect of pulling rate on the flexural strength and flexural modulus of the pultruded glass fiber reinforced thermoplastic polystyrene composites at die temperatures of 160, 180 and 200 °C, respectively. From these figures, one can observe that when the die temperature was set 160~200 °C, the lower the pulling rate, the higher the mechanical properties. When the pulling rate is lower than 20 cm/min, the production rate will be too low to be utilized in an industrial application. However, when the pulling rate is higher than 80 cm/min, the mechanical properties will be reduced due to poor polymerization. From the above explanations, the optimum pulling rates are 20~80 cm/min in this study.

Die temperature--The operating die temperature was determined by a Differential Scanning calorimetry(DSC). Five to ten mg of styrene prepolymer sample was placed on the DSC cell. The dynamic scanning at 10 °C/min is shown in Fig. 8. From this figure, it was found that the exothermic peak start temperature, peak onset temperature, peak maximum temperature and peak end temperature are 64.5, 105.3, 138.6 and 274.2 °C, respectively, and the total heat generated during the polymerization is 349.1 J/g. The conversion of reaction (extent of reaction) versus temperature for a dynamic DSC scanning at 10 °C/min is shown in Fig. 9. From this figure, a high conversion of reaction (>70%) was measured when reaction temperature was higher than 160 °C. The isothermal scanning at 140 °C, 150 °C, 160 °C and 170 °C is shown in Fig. 10. These DSC curves summarize the comparison of four processing temperatures, from which the polymerization rate (time) can be obtained. When the temperature were set higher than 160 °C, the resin polymerization can be completed under 1.5 minutes. Therefore, in order to obtain the high conversion and fabricate in a short time in the pultrusion die, the die temperature should be higher than 160 °C.

Figs. 6 and 7 show the flexural strength and flexural modulus of pultruded glass fiber reinforced polystyrene composites versus pulling rates at various die temperatures, From these figures, one can observe that the higher the die temperature, the better the mechanical properties will be obtained, due to the higher the die temperature, the higher the degree of polymerization. The die temperature cannot be higher than 200 °C, otherwise the composites might be degraded. The die temperature cannot be lower than 160 °C, otherwise, the styrene prepolymer are not polymerized completely, hence, the mechanical properties decrease sharply.

From the DSC diagram, and from the study of mechanical properties, it may be concluded that the suitable die temperatures range are between 160 and 200 °C in this study.

Postcure temperature and time—The main purpose of postcuring is to ensure complete reaction and to drive off volatility from the composites. In the pultrusion process, the resin polymerizes in a short time in the die and the polymerization cannot be completed. Postcuring will encourage the unreacted prepolymer to react to a higher degree. Hence, postcuring the pultruded glass fiber reinforced composites will increase the degree of polymerization and improve the mechanical properties of composites.

Figs. 11 and 12 illustrate the flexural strength and flexural modulus of pultruded glass fiber reinforced polystyrene composites versus postcure time at various postcure temperatures. From these results it can be seen that the mechanical properties of pultruded composites were improved by postcuring at 80, 100, and 120 °C. Although the postcuring can improve the mechanical properties, from these figure one can observe that the pultruded composites begin to degrade after 12 hr at postcuring temperature 80 °C, 8 hr at 100 °C, and 4 hr at 120 °C, and the flexural strength and modulus was reduced. It was found the optimum postcure temperature and time are 120 °C and 4 hr, respectively.

CONCLUSIONS

In this study, a suitable thermoplastic polystyrene resin system was developed for the pultrusion process. The styrene prepolymer was synthesized by styrene monomer with initiator. It was found from viscometer, GPC and ¹H-NMR spectra tests, the viscosity, weight average molecular weight and conversion of styrene prepolymer can be observed.

The feasibility of the pultrusion of glass fiber reinforced thermoplastic polystyrene

composites have been demonstrated. From viscosity study that the optimum temperature of styrene prepolymer in the impregnation tank was 30 °C, and long pot life of styrene prepolymer can be confirmed at 30 °C. The high reactivity of prepolymer was observed from IR spectra at elevated temperature. From the morphological study of SEM photographs that good fiber impregnation by the thermoplastic polystyrene resin was observed. The styrene prepolymer was suitable for a thermoplastic polystyrene pultrusion process.

The effect of processing parameters on the mechanical properties of glass fiber reinforced thermoplastic polystyrene composites by pultrusion has been studied. The optimum pulling rates obtained in this study are 20~80 cm/min. From DSC diagrams and the mechanical properties tests that the suitable pultrusion die temperature is in the range of 160 °C to 200 °C. The postcuring process can improve the mechanical properties of pultruded product, it was found the optimum postcure temperature and time are 120 °C and 4 hr, respectively.

REFERENCES

1. Meyre, R. W., "Handbook of Pultrusion Technology", Chapman and Hall Ltd., 1985, pp.271-272.
2. Florentine, R. A., "Low-Cost High Performance Composites-MAGNAWEAVE Reinforcements for Pultrusion", 37th Annu Conf., RP/C, SPI, 10-A, Sheraton Washington, USA, 1982.
3. Hindersinn, R. R., "Pultruded Reinforced Phenolic Resin Product," U.S. Patent 4,419,400 Dec., 1983.
4. Hwang, J. S., "Research on the Pultrusion Polymer Composites—Processing Parameters", Master Thesis, National Tsing Hua University, Taiwan, Republic of China, 1986.
5. Hill, S.G., House, E. E., and Hoggatt, J. T., Boeing Aerospace Company for Naval Air Systems Command, Contract N00019-77-C0561, 1979.
6. Beck, D. E., "Continuous Graphite/Polysulfone RP Thermoforming for Large Space Structure Construction", 38th Annu. Conf., RP/C, SPI, 20-C, 1983.
7. Madenjian, A. R., Tessier, N. J. and Schott, N. R., "Effect of Significant Processing Various on Thermoplastic Matrix Pultruded Composites", 40th Annu. Conf., RP/C, SPI, 11-F, 1985.
8. Ishida, H and Rotter, G., "RIM-Pultrusion of Thermoplastic Matrix Composites", 43rd Annu. Conf., RP/C, SPI, 6-A, 1988.
9. O'Connor, J. E. and Beaver, W. H., "Polyphenylene Sulfide Pultruded Type Composites Structure", 42nd Annu. Conf., RP/C, SPI, 1-D, 1987.
10. David, E. B., "New Processes and Prospects in Pultrusion", 38th Annu. Conf., RP/C, SPI, 4-D, 1985.
11. Goldsworthy, W. B., "Thermoplastic Composites : The New Structural", *Plastics World*, ug., 1984, p.56.
12. Hwang, J. S. and Tong, S. N., "Development of ABS Resins for In-situ Pultrusion", 43rd Annu. Conf., RP/C, SPI, 6-E, 1988.
13. Ishida, H. and Rotter, G., "RIM-Pultrusion of Thermoplastic Matrix Composites", 43rd Annu. Conf., RP/C, SPI, 6-A, 1988.
14. Rolston, J. A., "Process and Economic Factors for Pultrusion", *Polymer Plastic Technology Engineering*, Vol.13, No.1, 1979, pp.65-82.

Table 1. Physical properties of styrene monomer and its prepolymer.

Properties	Unit	Styrene monomer	Styrene prepolymer
Specific gravity	—	0.9045	1.03
Molecular weight	—	120	1000-1300
Conversion	%	0	5.23
Viscosity (25 °C)	Pa.s	0.01	0.8-1.2

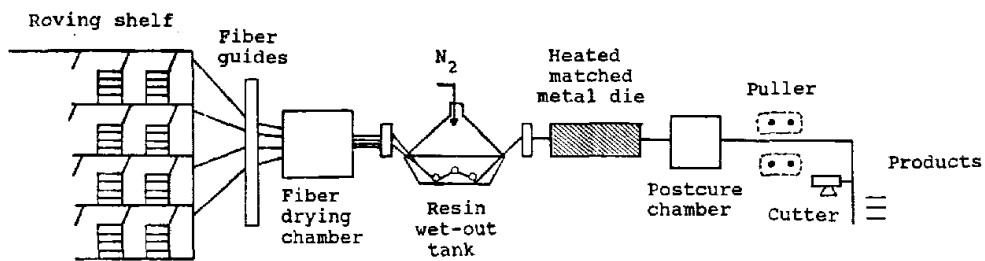


Fig. 1. Flow chart of pultrusion machine.

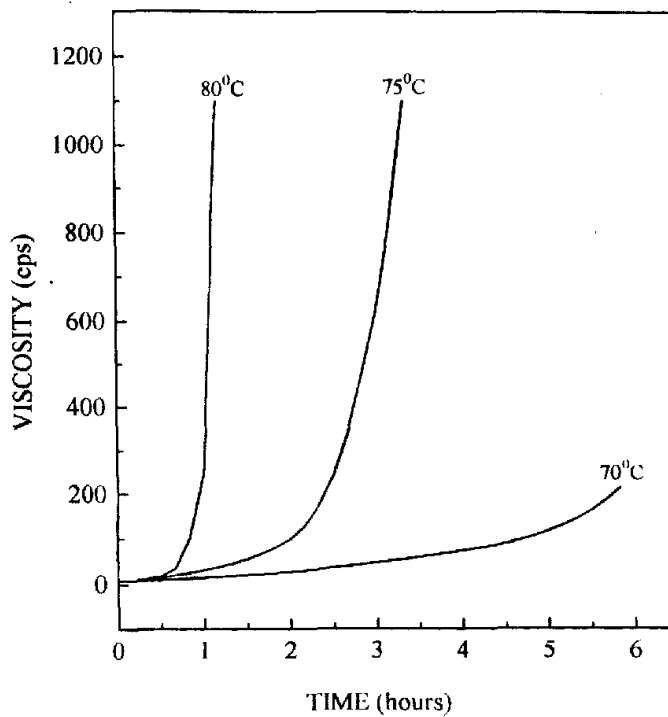


Fig. 2. Viscosity of synthesized styrene prepolymer versus various temperatures.

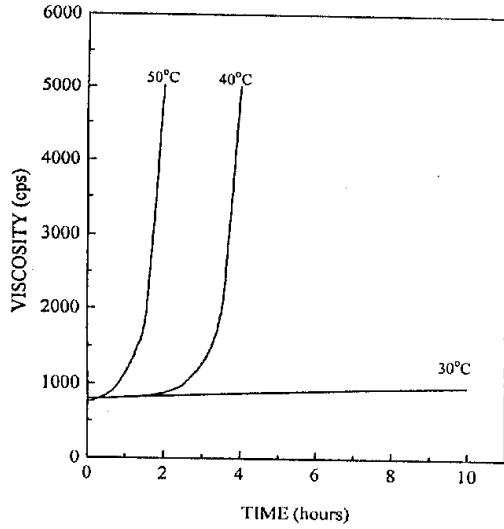


Fig. 3. Viscosity versus time of synthesized styrene prepolymer at various temperatures.

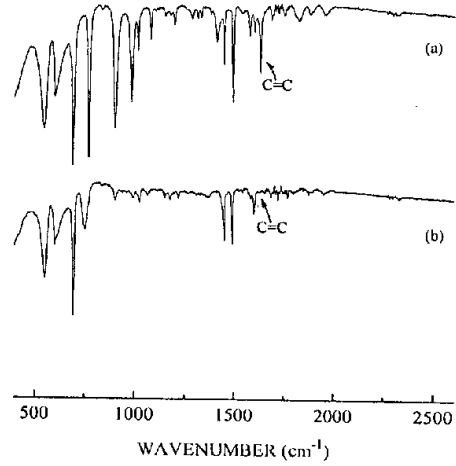
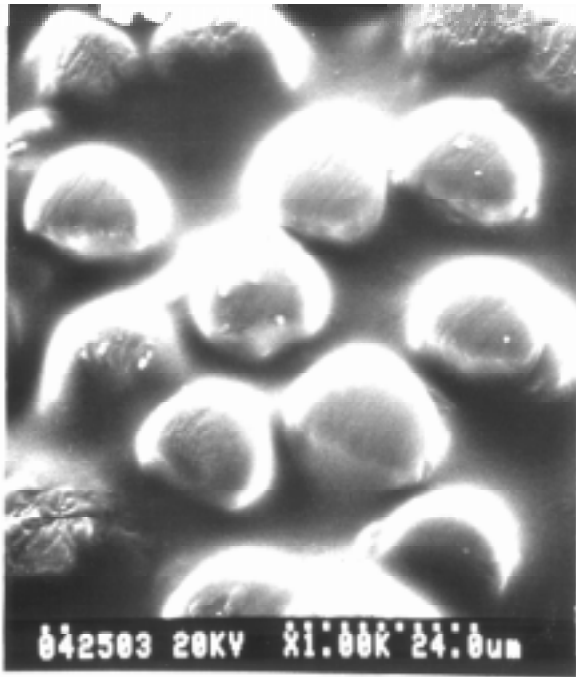
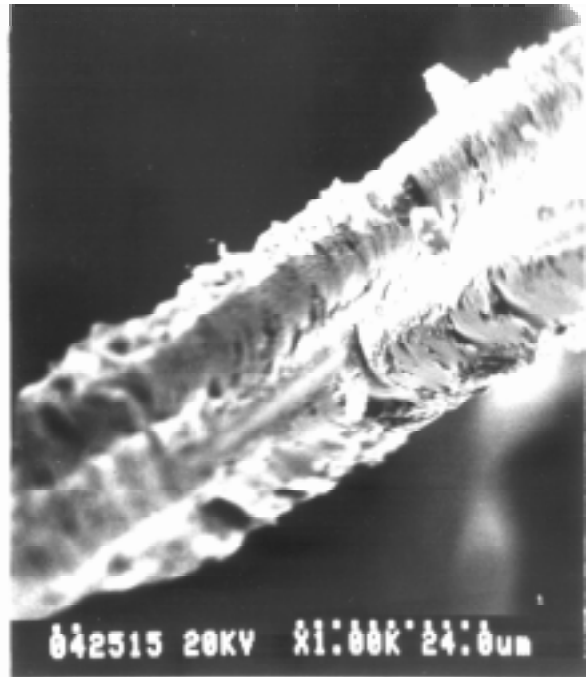


Fig. 4. The IR spectra of (a) styrene prepolymer; and (b) polystyrene.



(a)



(b)

Fig. 5. SEM microphotographs of pultruded glass fiber reinforced polystyrene composites : (a) cross-section; and (b) fracture surface.

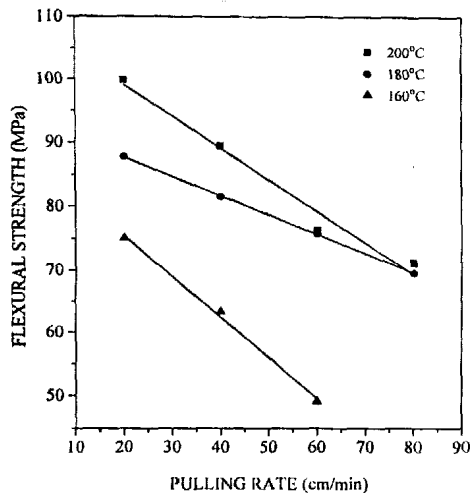


Fig. 6. Flexural strength of pultruded glass fiber reinforced polystyrene composites versus pulling rate at various temperatures.

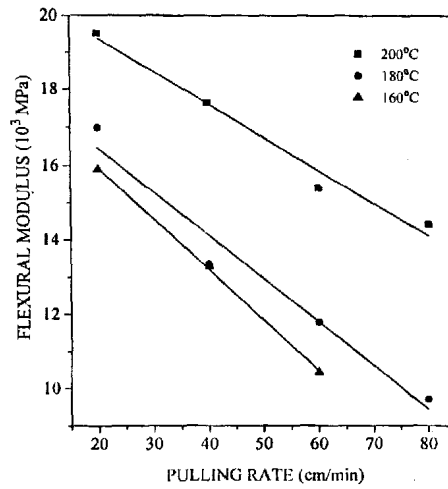


Fig. 7. Flexural modulus of pultruded glass fiber reinforced polystyrene composites versus pulling rate at various temperatures.

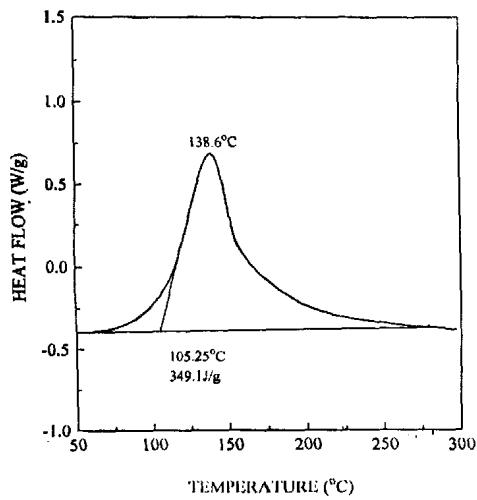


Fig. 8. DSC thermograms of styrene prepolymer by dynamic scanning at 10 °C/min.

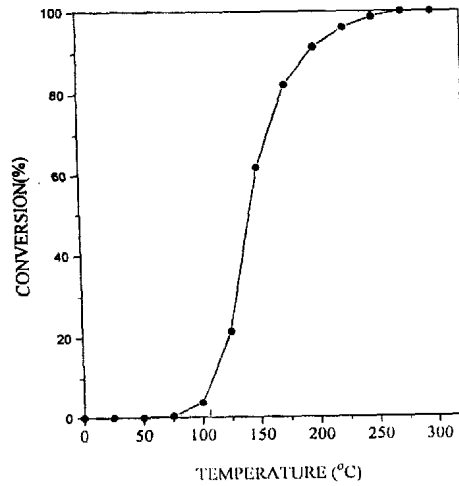


Fig. 9. Conversion versus temperature of styrene prepolymer for dynamic DSC at 10 °C/min.

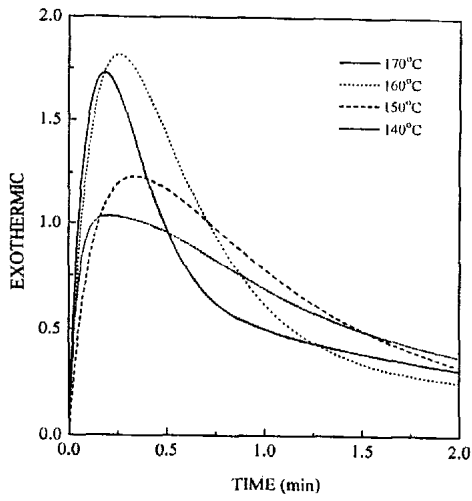


Fig. 10. DSC thermograms of styrene prepolymer by isothermal scanning.

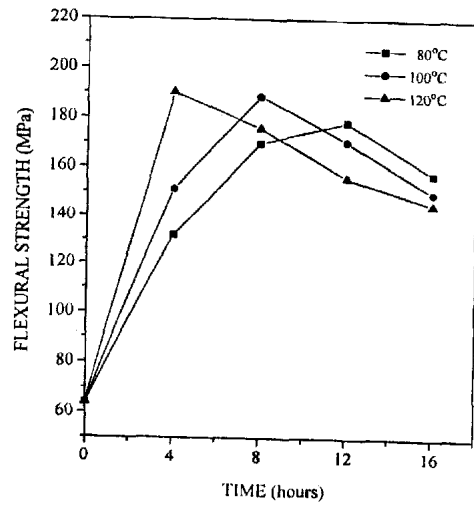


Fig. 11. Flexural strength of pultruded glass fiber reinforced polystyrene composites versus postcure time at various post-cure temperatures.

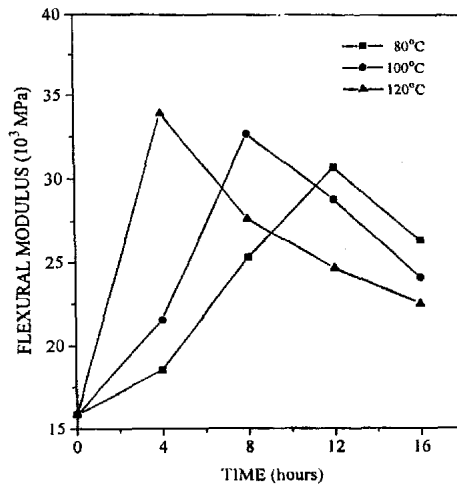


Fig. 12. Flexural modulus of pultruded glass fiber reinforced polystyrene composites versus postcure time at various post-cure temperatures.

POROSITY CALCULATION OF MIXTURES OF FIBROUS PARTICLES

R. P. Zou ¹, A. B. Yu ¹, and D. L. Xu ²

¹ *School of Materials Science and Engineering, The University of New South Wales
Sydney, NSW 2052, Australia*

² *Department of Materials Engineering, Xi'an University of Architecture and Technology
Xi'an 710055, P. R. China*

SUMMARY: The initial forming of fibre blend to high green density, i.e. the packing of fibrous particles, is important to the reinforcement of composite materials. It is very useful to develop a general predictive method for the optimum selection of particle mixtures for the property control of ceramic or composite products. This paper presents such a mathematical model developed on the basis of the similarity analysis between the spherical and non-spherical particle packings and assesses its applicability to the packing of fibrous particles with discrete and/or continuous length distributions. The results indicate that the model can predict this packing system well and hence provides an effective way to solve various packing problems in the composite materials processing.

KEYWORDS: packing, porosity calculation, fibrous particles, mixtures

INTRODUCTION

Among the many variables governing the packing of particles, particle size distribution is most important. Many efforts have therefore been made to understand the relationship between packing density (equal to one minus porosity) and particle size distribution, as summarised by German [1]. Generally speaking, previous work is mainly based on experimental measurement and recent studies are more concerned with mathematical modelling. In the past decade or so, significant progress has been made in the modelling of the packing of spherical particles [2-7]. The resulting mathematical models have significantly enhanced our quantitative understanding of the dependence of packing density on particle size distribution and provide an effective means for solving various packing problems. However, particles involved in practice are usually not spherical, and particle shape strongly affects particle packing. In the past, little systematic effort has been made to model the packing of nonspherical particles, mainly because of the complexity of the problem. Recently, to overcome this gap, on the basis of the similarity analysis between spherical and non-spherical particle packings, a mathematical model has been developed for predicting the packing of non-spherical particle mixtures [8].

Of particular interest here is the packing of fibrous particles. It has been known that the reinforcement of ceramic or composite materials using high strength fibres can yield high temperature structural materials with increased toughness. Understanding the initial forming of fibre blend to high green density is important to the involved processes. The packing of fibres or fibrous particles has therefore been a subject of research for years, aiming at

developing a predictive method for the optimum selection of particle mixtures for the property control of ceramic or composite products. Simple packing systems, involving mono-sized or fibre-fibre or sphere-fibre binary mixtures, have been studied in detail [9-14]. In contrast, to date very limited efforts have been given to complicated but more realistic packing systems involving multi-sized fibres [15,16].

This paper will present a study of the packing of fibrous particles by use of the modified linear packing model [8]. In particular, its applicability to the packing systems encountered in the composite materials processing will be assessed in detail. It will be shown that the model can predict the packing of these systems well and hence provides a convenient way to study the packing of fibrous particles.

THEORETICAL WORK

Mathematical Model

The system considered is assumed to be composed of n components of constant particle density, with each characterised by its (initial) porosity ϵ_i and effective (packing) diameter d_{pi} ($i=1, 2, \dots, n$). In general, the porosity of this system ϵ can be expressed as

$$\epsilon=f(X_1, X_2, \dots, X_n, d_{p1}, d_{p2}, \dots, d_{pn}, \epsilon_1, \epsilon_2, \dots, \epsilon_n) \quad (1)$$

where X_i is the fractional solid volume of the i th component. For convenience, d_{pi} are so ordered that $d_{p1} \geq d_{p2} \geq \dots \geq d_{pn}$.

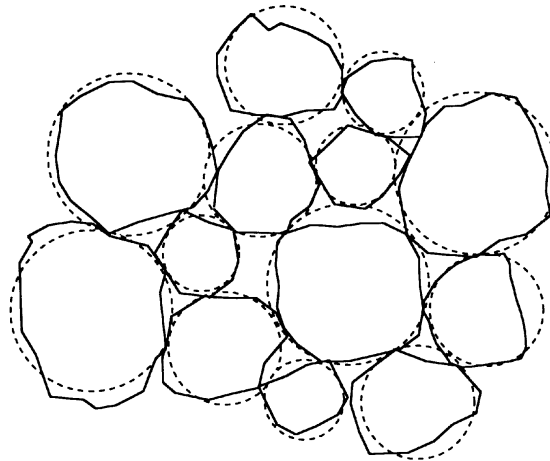


Fig. 1: A two-dimensional diagram illustrating a packing of non-spherical particles and its equivalent packing of spherical particles.

Eqn 1 implies that the particle characteristics, such as size and shape, affects the packing porosity through its effect on equivalent packing diameter and initial porosity. When particles of different sizes are mixed and packed, the volume occupied by a unit volume of solid particles, commonly referred to as the specific volume V [$=1/(1-\epsilon)$], will decrease as compared with that of mono-sized particles as a result of the mixing-interaction between two components. It is known that the mixing-interaction between two components is dependent on

their relative size which, as discussed elsewhere [17], should be quantified in terms of equivalent packing diameter resulting from the similarity analysis between spherical and non-spherical particle packings. This concept is schematically illustrated in Fig. 1 in which a packing of non-spherical particles is represented by its corresponding packing of spheres.

Technically speaking, knowing X_i , d_{pi} and ε_i allows ε to be predicted by means of a mathematical model which calculates porosity based on the same information. However, if there is a significant difference in initial porosity, the situation often found in the packing of non-spherical particles, the previous models [2-7] can not be satisfactorily used. The only model that can overcome this deficiency is the modified linear packing model. Yu et al. [8] have described this model in detail. The following just lists the model equations for porosity calculation.

According to the modified linear packing model, specific volume V can be determined by the following equations [8]:

$$V = \text{Max.} \{V_1^T, V_2^T, \dots, V_n^T\} \quad (2a)$$

where

$$V_i^T = \sum_{j=1}^{i-1} [V_j - (V_j - 1)g(r_{ij})]X_j + V_iX_i + \sum_{j=i+1}^n V_j [1 - f(r_{ij})]X_j \quad (2b)$$

where V_i are the initial specific volumes which can be determined from ε_i by definition. Eqn 2a means that V equals the maximum of v_i^T ($i=1, 2, \dots, n$). $f(r_{ij})$ and $g(r_{ij})$ are referred to as the interaction functions and only dependent on r_{ij} , the small-to-large ratio of equivalent packing diameters between components i and j , and can be determined as

$$f(r_{ij}) = (1 - r_{ij})^{3.33} + 2.81r_{ij}(1 - r_{ij})^{2.77} \quad (3)$$

and

$$g(r_{ij}) = (1 - r_{ij})^{1.97} + 0.36r_{ij}(1 - r_{ij})^{3.67} \quad (4)$$

Packing Characteristics of Mono-sized Fibres

Use of the above equations in porosity calculation requires the information of packing characteristics such as ε_i and d_{pi} a priori. It has been established that initial porosity is constant for coarse spherical particles, generally taking the value of 0.4 for the loose random packing or 0.36 for the dense random packing [1]. However, initial porosity varies with particle shape and, if particle size is smaller than a certain value, particle size as well. If the particle size and shape of component i are, respectively, represented by its equivalent volume diameter d_{vi} and sphericity ψ_i , this gives

$$\varepsilon_i = f(d_{vi}, \psi_i) \quad (5)$$

Similar arguments apply to effective diameter d_{pi} , so that

$$d_{pi} = f(d_{vi}, \psi_i) \quad (6)$$

The effect of particle size becomes important when the weak forces such as van der Waals and electrostatic forces are dominant, which will give packing behaviour different from that of coarse particles [1,18]. However, the use of a mechanic force, eg tapping/vibration or compaction, will significantly reduce this effect and give a packing matching the packing of coarse particles. In this case, the effect of particle size can be ignored. The present work only deals with such packing systems.

The packing characteristics of mono-sized non-spherical particles has been studied by Zou and Yu [19]. Fig. 2 shows their measured porosity results as a function of aspect ratio L_i (length to diameter) for fibrous particles, which can be fitted by the following equation:

$$\ln \varepsilon_i = \psi_i^{5.58} \times \exp[5.89 \times (1 - \psi_i)] \times \ln 0.40 \quad (7a)$$

for the loose random packing, and

$$\ln \varepsilon_i = \psi_i^{6.74} \times \exp[8.00 \times (1 - \psi_i)] \times \ln 0.36 \quad (7b)$$

for the dense random packing; where ψ_i depends on L_i , given by

$$\psi_i = \frac{2.621L_i^{2/3}}{1 + 2L_i} \quad (8)$$

Different experimental conditions may change Eqn 7, which in turn affects porosity. On the other hand, for a given packing system, ε_i or V_i can be readily measured, and these measured values can be used directly in a model calculation, which usually improves the prediction accuracy. In fact, this treatment has been used for most of the application examples presented in this paper.

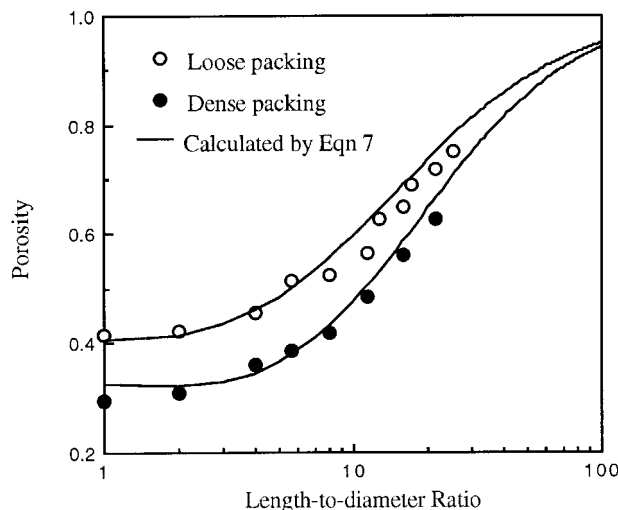


Fig 2: Initial porosity vs. particle shape for fibrous particles

The similarity between spherical and non-spherical particle packings has led to the development of the concept of equivalent packing diameter. In particular, for convex non-

spherical particles, the dependence of d_{pi} on ψ_i has been empirically established, given by [19]

$$d_{vi}/d_{pi} = \psi_i^{2.785} \times \exp[2.946(1 - \psi_i)] \quad (9)$$

By definition, d_{vi} should be related to the diameter of a fibrous particle D_i , in addition to its aspect ratio, as given by

$$d_{vi} = 1.145 L_i^{1/3} D_i \quad (10)$$

Incorporation of Eqns 7-10 into the above model allows the packing porosity of a mixture of fibrous particles to be predicted. Its accuracy will be discussed in the section below.

MODEL VALIDATION

The validity of the modified linear model can be examined by comparing the calculated and measured porosity results. For convenience, this comparison is here made for three cases: (1) the packing of fibres with a discrete length distribution; (2) the packing of fibres with a continuous length distribution; and (3) the packing of mixtures of fibres and other shaped particles.

Packing of Fibres with a Discrete Length Distribution

The first example considered here is the binary packing of fibrous particles. Milewski [9] has carried out a detailed study of this system. Fig. 3 shows one set of his measured results, and the predictions. It is obvious that the predictions are in good agreement with the measurements. Such good agreement can also be observed for the packing of multi-component mixtures. As an example, Fig. 4 shows the results for a quaternary system recently studied by Lin [20]. Note that the results are presented in triangular diagrams by fixing the fractional solid volume of a component at pre-set values, this giving the so-called pseudo-ternary packings.

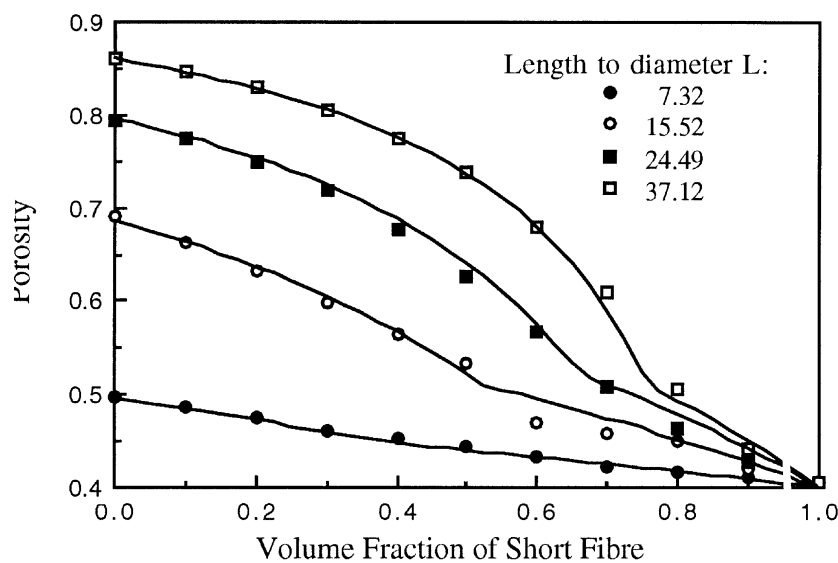


Fig. 3 Porosity results of binary mixtures of short ($L=3.91$) and long fibres of different L values, $D=2.09$ mm for all fibres: points, measurements; solid lines, predictions.

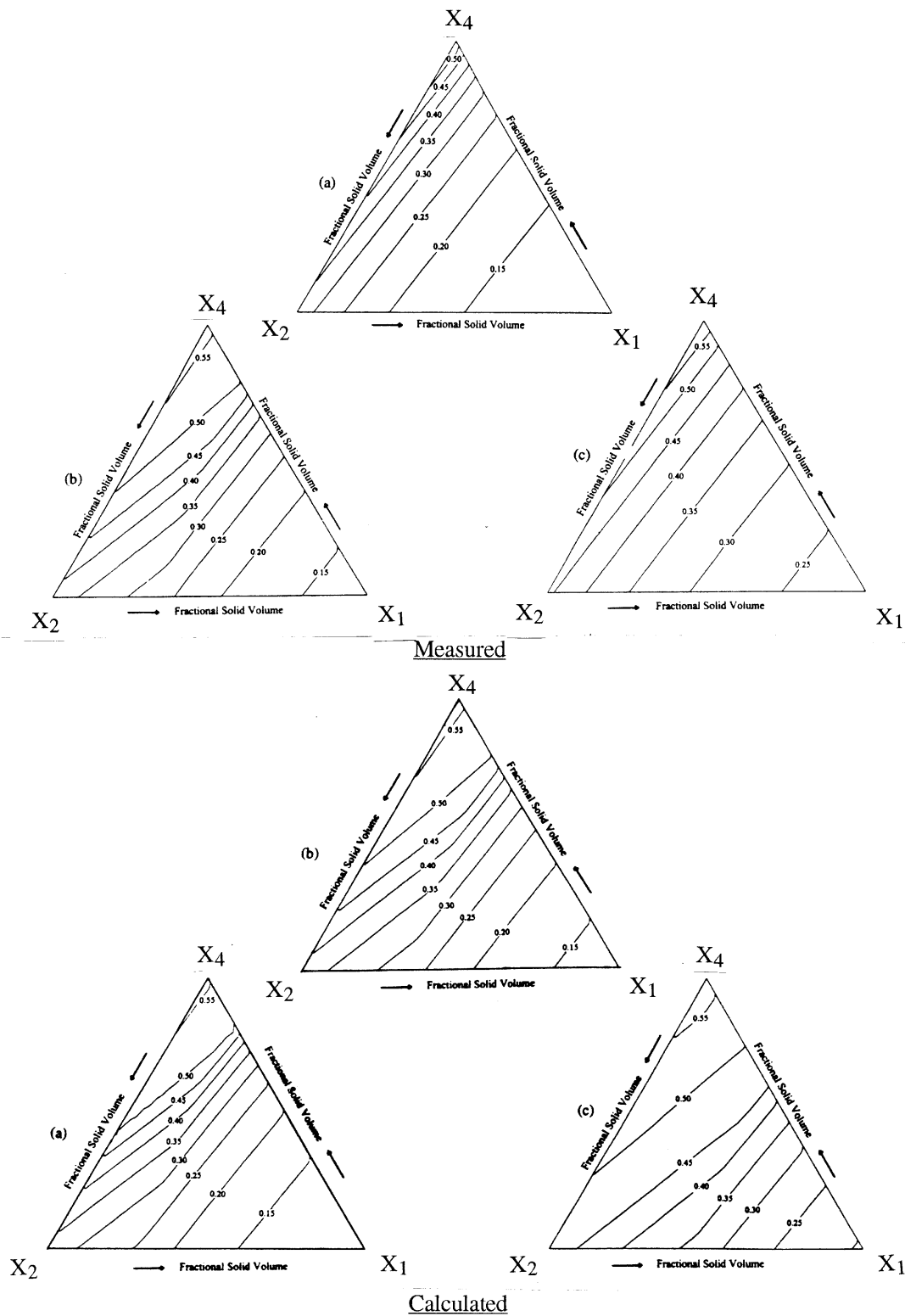


Fig. 4 Comparison between the measured and calculated packing density, ie. 1-porosity, for a quaternary system of fibrous particle of sizes: $D=2.62$ mm, $L_1=45.0$, $L_2=15.9$, $L_3=3.9$ and $L_4=1.4$ when: (a), $X_3=0$; (b), $X_3=0.20$; (c), $X_2=0.50$.

Packing of Fibres with a Continuous Length Distribution

Practical problems often involve the packing of fibrous particles with a length distribution. This packing system was recently experimentally studied by Zou et al. [16]. In particular, in their study, the fibres were assumed to be of the same diameter D , with their dimensionless lengths, ie, aspect ratios, distributed according to the modified power law length distribution:

$$f_v(L) = \frac{mL^{m-1}}{L_{\max}^m - L_{\min}^m} \quad (L_{\min} \leq L \leq L_{\max}) \quad (11)$$

or the log-normal length distribution:

$$f_v(L) = \frac{1}{\sqrt{2\pi}} \times \frac{1}{L} \times \frac{1}{\ln \sigma_g} \times \exp \left[-\frac{1}{2} \left(\frac{\ln L - \ln L_{0.5}}{\ln \sigma_g} \right)^2 \right] \quad (12)$$

Eqn 11 is similar to the modified Gaudin-Schuhman distribution using particle diameter rather than length. Obviously, for a given D , porosity should be dependent on the length range, i.e. $[L_{\min}, L_{\max}]$, and exponent m . On the other hand, for Eqn 12, porosity depends on median length $L_{0.5}$ and geometric standard variation σ_g . Zou et al. [16] found that: porosity increases with the increase of m or length range for Eqn 11, or with the increase of $L_{0.5}$ or σ_g for Eqn 12. Figs. 5 and 6 show their experimental results, together with the model predictions obtained under their experimental conditions. The good agreement between predicted and measured porosities suggests that this packing system can be well predicted by the proposed model.

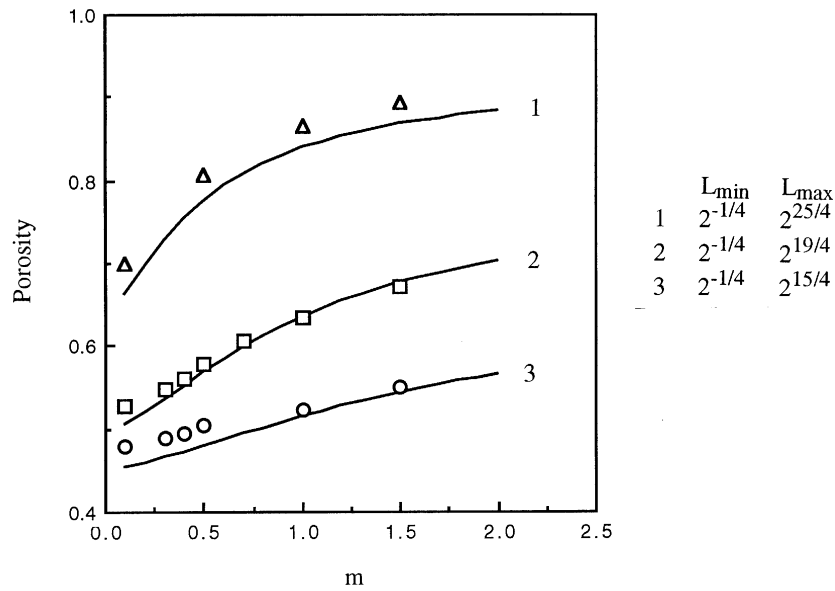


Fig. 5 Porosity of cylinders with the modified powder law length distribution for various length ranges for the loose random packing: points, measurements; —, predictions.

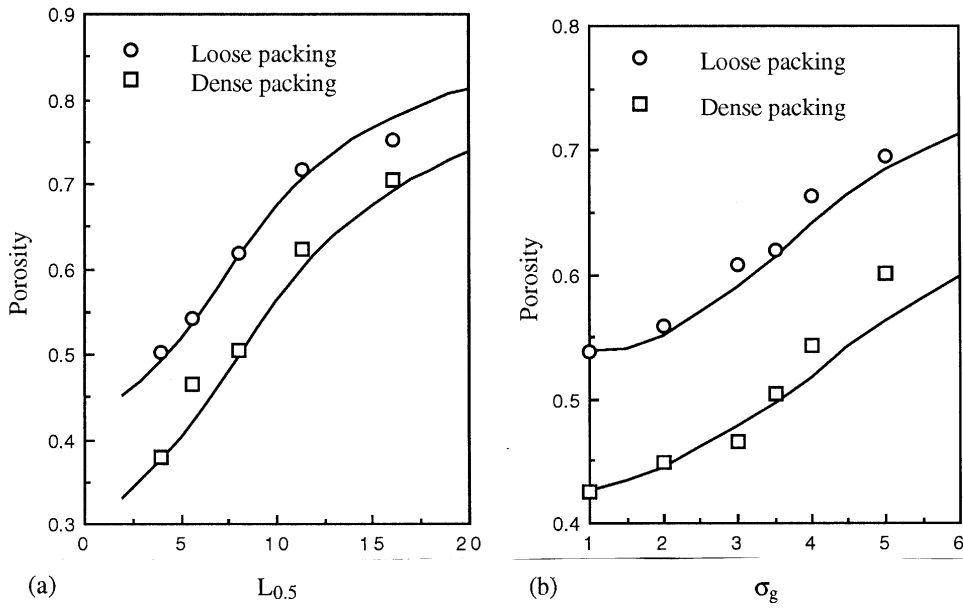


Fig. 6 Porosity of fibrous particles with the log-normal length distribution under various conditions: (a), $\sigma_g = 3.5$; (b), $L_{0.5} = 8.0$; points, measurements; —, predictions.

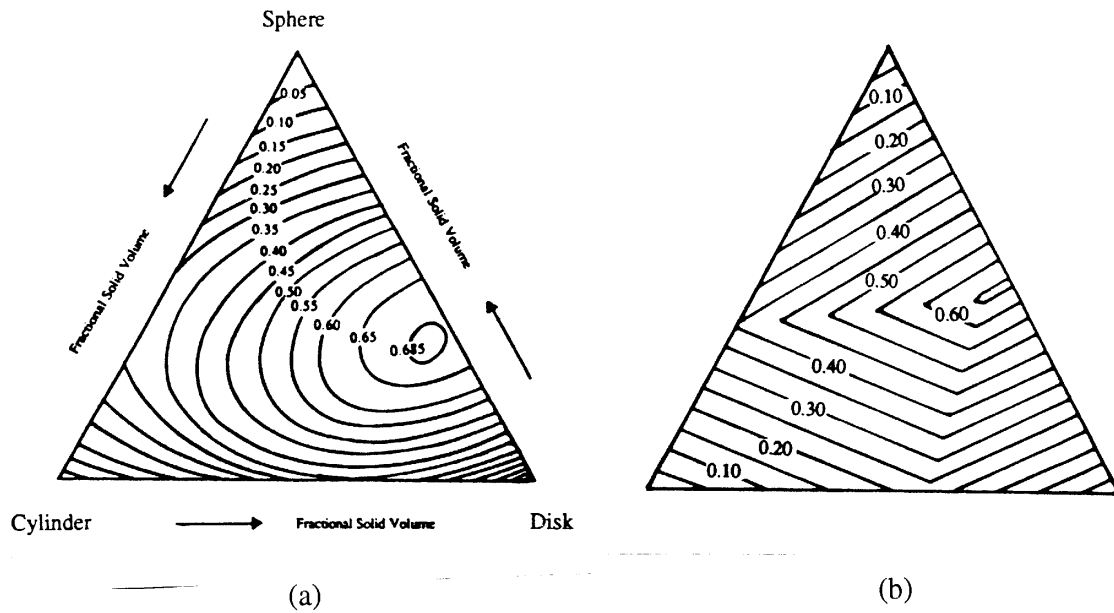


Fig. 7 Comparison between the measured (a) and calculated (b) specific volume variations for a disk-cylinder-sphere ternary system: disk, $d_{p1} = 20.59$ mm, $V_1 = 2.653$; cylinder, $d_{p2} = 10.95$ mm, $V_2 = 2.155$; sphere, $d_{p3} = 3.00$ mm, $V_3 = 1.639$.

Packing of Mixtures of Fibres and Other Shaped Particles

The proposed model may be used for predicting the porosity of non-spherical particle mixtures which include mixtures of fibres and other shaped particles, as long as ϵ_i and d_{pi} have been properly evaluated. This can be seen from the example given below.

The packing of ternary mixtures of non-spherical particles has been experimentally studied by Yu et al [15] using well defined particles such as disk and/or cylinders. To depict the similarity between spherical and non-spherical particle packings, these authors used the so-called specific volume variation ΔV in their analysis, which is defined as the difference in specific volume between unmixed and mixed states. That is

$$\Delta V = \sum_{i=1}^n V_i - V \quad (13)$$

The so-called mixed state corresponds to the present V , and the unmixed state the specific volume obtained when different types of particles are placed layer by layer without mixing. As shown in Fig. 7, their measurements can be predicted by the proposed model satisfactorily.

CONCLUSIONS

Fibrous particles are widely used in composite materials manufacturing. However, various industrial needs require various mixtures, which give various packing features as seen from the results presented in this paper. Development of a predictive method for the optimum control of such mixtures has been an important research subject. In this paper, extensive examination has been made of the application of the modified linear packing model of Yu et al. [8] to the packing of fibrous particles. The results indicate that the model can predict this packing system well and hence provides a convenient and cost-effective way to solve various packing problems.

ACKNOWLEDGEMENT

This work is partially supported by Australian Research Council (ARC), Energy and Research Development Corporation (ERDC) and Department of Industry, Science and Tourism (DIST).

REFERENCES

1. German, R. M., Particle Packing Characteristics, Metal Powder Industries Federation, Princeton, New Jersey, 1989.
2. Dodds, J. A., "The Porosity and Contact Points in Multicomponent Random Sphere Packing Calculated By a Simple Statistical Geometric Model," J. Colloid Interface Sci., Vol. 77, 1980, pp. 317-327.
3. Ouchiyama, N. and Tanaka, T., "Porosity Estimation from Particle Size Distribution," Ind. Eng. Chem. Fundam., Vol. 25, 1986, pp. 125-129.
4. Stovall, T., De Larrard, F. and Buil, M., "Linear Packing Density Model of Grain Mixtures," Powder Technol., Vol. 48, 1986, pp. 1-12.

5. Marshall, J. S. and Dhir, V. K., "On the Prediction of Porosity of Beds Composed of Mixtures of Spherical Particles," *Chem. Eng. Commun.*, Vol. 48, 1986, pp. 261-285.
6. Yu A. B. and Standish, N., "An Analytical-Parametric Theory of the Random Packing of Particles," *Powder Technol.*, Vol. 55, 1988, pp. 171-186.
7. Yu A. B. and Standish, N., "Estimation of the Porosity of Particle Mixtures by a Linear-Mixture Packing Model," *Ind. Eng. Chem. Res.*, Vol. 30, 1991, pp. 1372-1385.
8. Yu, A. B., Zou, R. P. and Standish, N., "Modifying the linear packing model for predicting the porosity of non-spherical particle mixtures," *Ind. Eng. Chem. Res.*, Vol. 35, 1996, pp. 3730-3741.
9. Milewski, J. V., "The Combined Packing of Rods and Spheres in Reinforcing Plastics," *Ind. Eng. Chem. Prod. Res. Dev.*, 17, 363-366 (1978).
10. Starr, T. L., "Packing Density of Fiber/Powder Blends". *Am. Ceram. Soc. Bull.*, Vol. 65, 1986, pp. 1293-1296.
11. Evans, K. E. and Gibson, A. G., "Prediction of the maximum packing fraction achievable in randomly oriented short-fibre composites", *Composites Sci. and Tech.*, Vol. 25, 1986, pp. 149-162.
12. Milewski, J. V., "Packing Concepts in the Utilisation of Filler and Reinforcement Combinations", *Handbook of Fillers and Reinforcements for Plastics*, Milewski, J. V. and Katz, H. S., Eds., Van Nostrand Reinhold, New York, 1987, pp. 14-33.
13. Evans, K. E. and Ferrar, M. D., *J. Phys. D.* 22 (1989) 354.
14. Yu, A. B., Standish, N. and McLean, A., "Porosity Calculation of Binary Mixtures of Nonspherical Particles", *J. Am. Ceram. Soc.*, Vol. 76, 1993, pp. 2813-2816.
15. Yu, A. B., Zou, R. P. and Standish, N., "The Packing of Ternary Mixtures of Non-Spherical Particles", *J. Am. Ceram. Soc.*, Vol. 75, 1992, pp. 2765-2772.
16. Zou, R. P., Lin, Y. X., Yu, A. B. and Wong, P., "The packing of cylindrical particles with a length distribution," *Am. Ceram. Soc.*, 1996 (in press).
17. Yu, A. B. and Standish, N. "Characterisation of Non-Spherical Particles from Their Packing Behaviour," *Powder Technol.*, Vol. 74, 1993, pp. 205-213.
18. Yu, A. B., Bridgwater, J. and Burbidge, A., "On the modelling of the packing of fine particles", *Powder Technol.*, 1997 (in press).
19. Zou, R. P. and Yu, A. B., "Evaluation of the packing characteristics of monosized non-spherical particles", *Powder Technol.*, Vol. 88, 1996, pp. 71-79.
20. Lin, Y. X., "*The Packing of Fibrous Particles*", M. Appl. Sci. Thesis, Univ. of NSW, Feb. 1996.

FLOW CHARACTERISATION OF SHEET MOULDING COMPOUNDS (SMC)

G. Kotsikos, A. G. Gibson

*Centre for Composite Materials Engineering, University of Newcastle upon Tyne,
Herschel Building, Newcastle upon Tyne, NE1 7RU, United Kingdom*

SUMMARY: The compression moulding flow of SMC has been investigated by squeeze flow testing between parallel circular plates at room temperature and a modestly elevated temperature of 30°C. A model based on the upper bound theory was adopted to characterise the squeeze flow of SMC. The present results indicate that the squeeze flow of SMC at 30°C is predominantly extensional with shear becoming significant at very small plate separations. Measurements of the pressure distribution across the plate also indicate that the flow is predominantly extensional. The presence of edge effects due to fibre length is also evident. The strong dependence of the compression moulding flow characteristics of SMC with temperature is demonstrated by the different behaviour of SMC tested at room temperature.

KEYWORDS: sheet moulding compound, squeeze flow, modelling

INTRODUCTION

One of the most common composite materials to be processed by compression moulding is Sheet Moulding Compound (SMC). Most applications are found in the automotive industries where high volume production of strong stiff lightweight parts is needed. The unmoulded composite is produced in sheets which are typically 3 to 6 mm thick. It has a complex composition consisting mainly of a thermosetting, unsaturated polyester resin, a particulate filler and glass fibre reinforcement with random in plane orientation and length of the order of 25 mm. The glass content is typically 20-30% by weight. The complexity of the composition of SMC and its difficult to interpret rheological behaviour have triggered many investigations of SMC including rheological investigations [1,2], flow visualisation of mould filling [3] and simulations of mould filling [4,5]. Most of the experimental evidence so far indicate that biaxial extension is the dominant flow form and the present work aims to further investigate the squeeze flow of SMC by developing a model which allows the flow form to vary from pure biaxial extension to pure shear, based on the upper bound theory and provide a possible quality control route for SMC production.

EXPERIMENTAL

The material used throughout this work has been industrial SMC supplied by Autopress Mouldings - UK in the form of 3 mm thick sheets with a glass content of approximately 30% by weight. The glass fibre reinforcing mat had a random in plane orientation with an average fibre length of 25 mm. The material was one month old when tested.

Isothermal axisymmetric squeeze flow testing was carried out using a set of 150 mm diameter flat plate dies, Fig. 1, mounted on a 100 kN capacity Instron screw type testing machine. Both dies could be heated by means of cartridge heaters inserted at various positions in the dies connected to a temperature controller. The temperature across the die surface was controlled by thermocouples inserted at various points in the dies. One of the dies incorporated pressure transducers flush mounted on the surface at three radial positions to enable the investigation of the pressure distribution across the dies during squeeze flow testing. Samples of SMC of 150 mm diameter were cut and placed in double layers (i.e. 6 mm total thickness) between the dies and squeezed to 25% of the initial thickness at a constant squeeze rate. Tests were carried out for a wide range of squeeze rates from 0.1 mm/s to 3 mm/s. At least three tests were carried out per squeeze speed. Tests were carried out at room temperature (18°C) and 30°C.

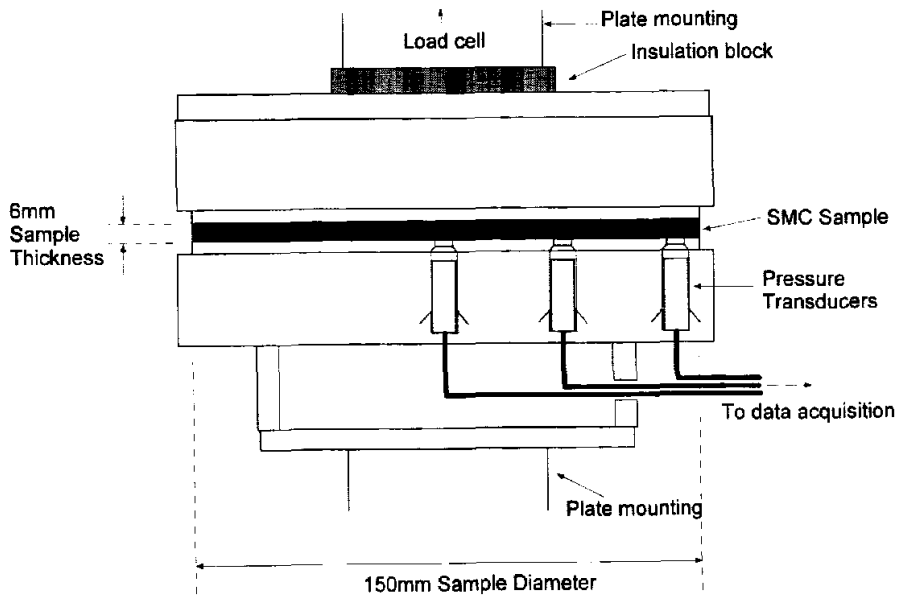


Fig. 1: Squeeze flow die

The squeeze force, die separation and the pressure transducer outputs were monitored via a data acquisition unit.

THEORY

Mathematical models based on power law equations have been used successfully in the past [6,7] to model short fibre reinforced injection moulded thermoplastic materials. Their advantage is that whilst taking account anisotropy and non-Newtonian flow effects they avoid other complicated constitutive equations. The power law equations for shear and extensional viscosities are:

$$\eta_s = A_s \cdot \dot{\gamma}^{m-1} \quad (1)$$

and
$$\eta_e = A_e \cdot \dot{\epsilon}^{n-1} \quad (2)$$

respectively. The extensional flow power law constant is often found to be strain dependent which gives an expression of the form:

$$\eta_e = A_e(\epsilon) \cdot \dot{\epsilon}^{n-1} \quad (3)$$

For the case of squeeze flow of a power law fluid between parallel plates, the squeeze force for pure shear flow is given by the Scott equation [8]:

$$F_{shear} = \left(\frac{2m+1}{m} \right)^m \left(\frac{2\pi A_s R^{m+3}}{m+3} \right) \left(\frac{\dot{h}^m}{h^{2m+1}} \right) \quad (4)$$

For this case the through thickness material velocity profile assumes a near parabolic shape, Fig. 2a and the corresponding radial pressure distribution has the form shown in Fig. 2b where maximum pressure occurs at the centre of the sample falling to zero at the edge.

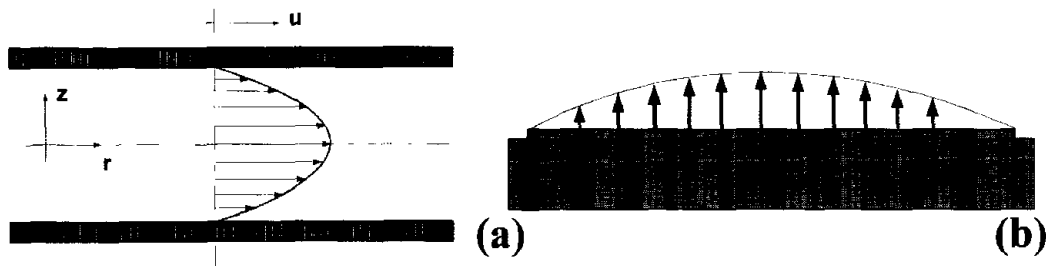


Fig. 2: a) velocity profile for a pure shear flow, b) pressure distribution profile across a flat plate die for pure shear flow

For the case of pure biaxial extension, the squeeze force is given by:

$$F_{ext} = \pi R^2 A_e(\epsilon) \left(\frac{\dot{h}}{h} \right)^n \quad (5)$$

The through thickness velocity profile corresponds to pure plug flow, Fig. 3a, with no radial variation of pressure resulting to a flat pressure distribution as shown in Fig. 3b.

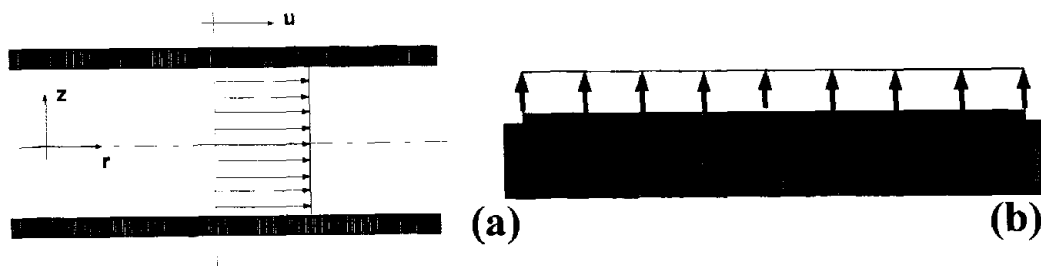


Fig. 3: a) velocity profile for pure biaxial extension, b) pressure distribution profile across a flat plate die for pure biaxial extension

It is possible that the squeeze flow may be described by an additive model which takes account of the contributions of shear and extension. Therefore:

$$F_{total} = F_{shear} + F_{ext} \tag{6}$$

Upper Bound Theory

A more exhaustive approach to the summation model would be the use of the Upper Bound Theory. This is similar to the additive model for the pressure contributions due to shear and extensional flow, but the relative contributions are allowed to change during the squeezing process thus allowing for a change in boundary conditions and velocity profiles as squeezing progresses.

In general terms the upper bound theory relates the work done by the unknown surface tractions to the rate of internal energy dissipation in a velocity field. Applying this to the squeeze flow experiment a solution of the form shown below is obtained:

$$P_{squeeze} = \Phi 1 \cdot A_e \cdot \dot{\epsilon}^n + \Phi 2 \cdot A_e \dot{\epsilon}^n \cdot X \cdot \left(\frac{2}{n+3}\right) \cdot \left(\frac{2n+1}{n}\right)^n \tag{7}$$

where $X = \frac{A_y}{A_e} \cdot \left(\frac{R}{h}\right)^{n+1}$ and 'n' is the power law index which is determined from experiment.

Here $\Phi 1$ and $\Phi 2$ are functions of 'X' normally being close to unity and change with plate separation. The functions $\Phi 1$ and $\Phi 2$ are numerical integrals which are evaluated for a number of valid and kinematically admissible profiles, the actual solution for the overall squeezing pressure being the one that corresponds to the velocity field which minimises overall pressure. Identifying the actual solution, then, requires an optimisation process. Equation 7 has two asymptotes, one for a predicted behaviour of pure biaxial extension corresponding to low values of 'X' and one for a behaviour of pure shear flow which corresponds to large values of 'X', Fig. 4.

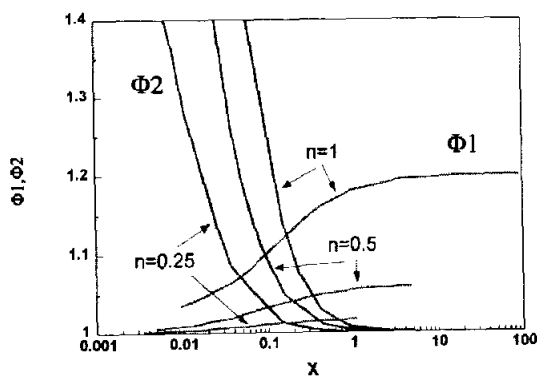


Fig. 4: Variation of functions $\Phi 1$ and $\Phi 2$ with X for different values of power law index 'n'

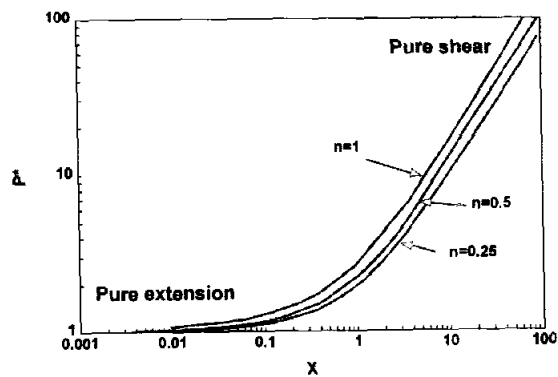


Fig. 5: Variation of Pressure with parameter X for different values of power law index 'n'

It can be seen from Fig. 5 that the power law index 'n' makes very small difference to the overall solution.

RESULTS

The data of squeeze stress against die position for various squeeze rate are given in Fig. 6 for tests at room temperature (RT) and Fig. 7 for tests at 30°C.

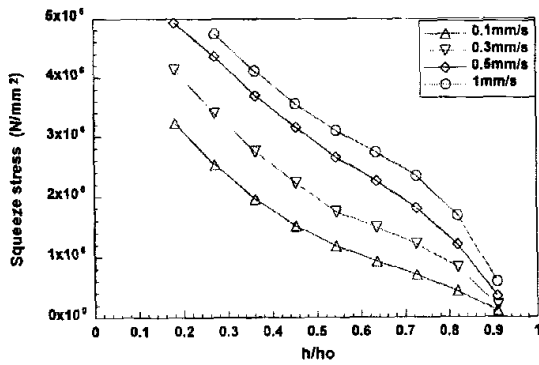


Fig. 6: Plot of squeeze stress vs plate separation during squeeze flow tests of SMC at room temperature

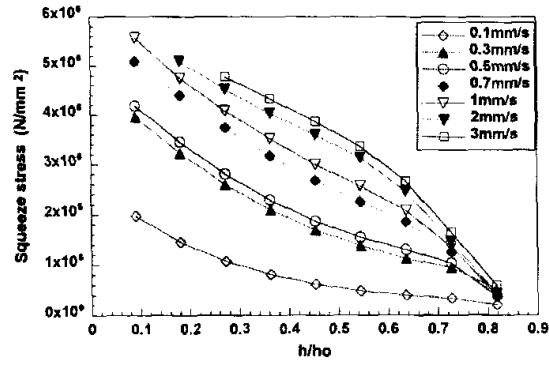


Fig. 7: Plot of squeeze stress vs plate separation during squeeze flow tests of SMC at 30°C

It can be seen from these graphs that increasing the squeeze rate increases the squeeze load. If the results are presented as logarithmic plots of squeeze stress vs strain rate at certain plate separations, Fig. 8 and Fig. 9 (RT and 30°C respectively) a difference in the behaviour of SMC at RT and 30°C is evident. The plot for the RT test yield a series of straight lines with decreasing slopes of 0.7 at the start of the squeezing to 0.2 at the end. In contrast for the tests at 30°C the slope is the same for all plate separations and equal to 0.24.

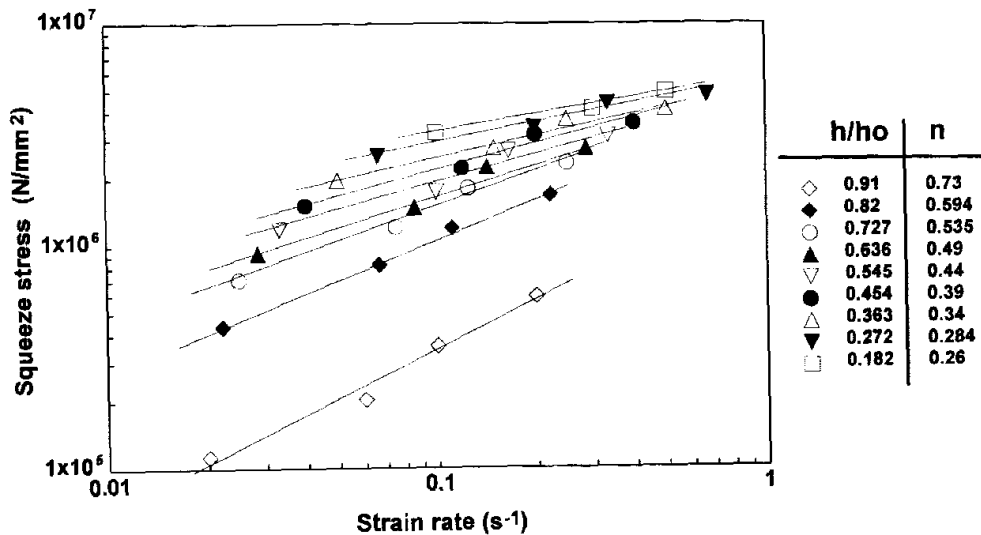


Fig. 8: Logarithmic plot of squeeze stress vs strain rate during squeeze flow of SMC at room temperature

The upper bound theory analysis was carried out for the squeeze flow of SMC at a squeeze rate of 1 mm/s and the resulting P* vs X curve is shown in Fig. 10. The analysis was carried

out for a power law index $n=0.2$ which is close to the value derived by Han and White [10] from rheological studies of SMC at various temperatures. Shear viscosity values were also obtained from their studies. The experimental results for the 1 mm/s squeeze rate are also plotted for comparison.

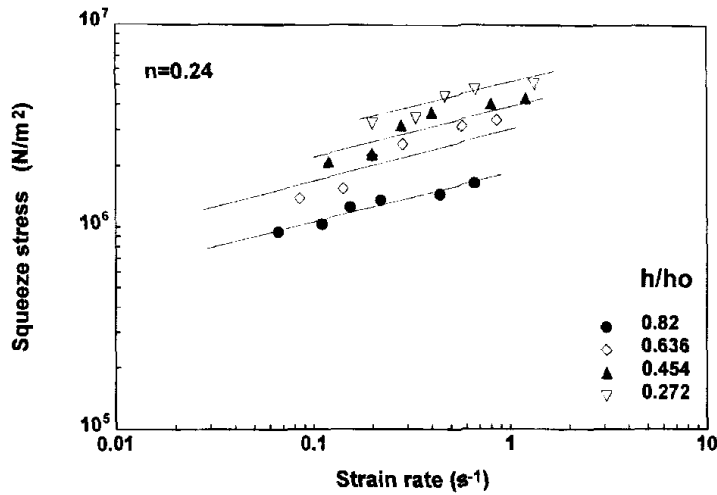


Fig. 9: Logarithmic plot of squeeze stress vs strain rate during squeeze flow of SMC at 30°C

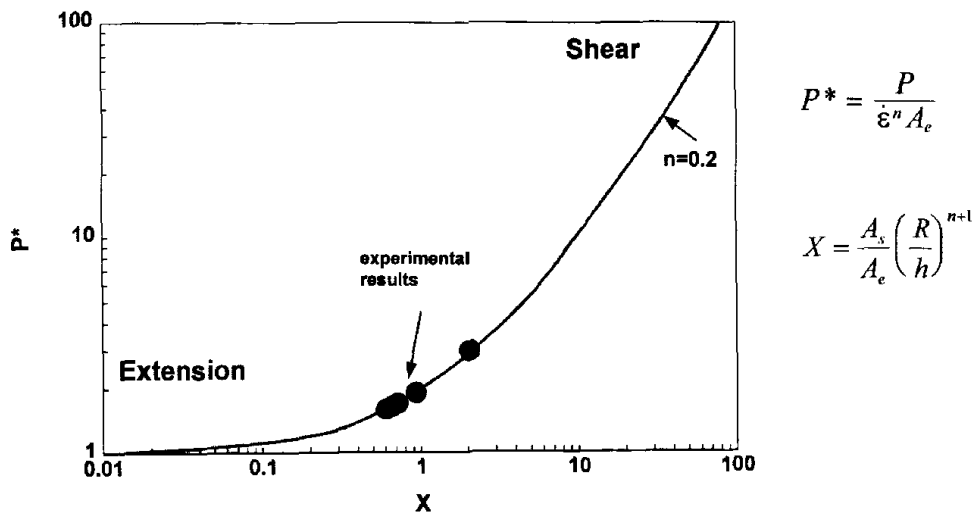


Fig. 10: Variation of pressure P^* with parameter X as obtained from the upper bound theory analysis (solid line) for a squeeze speed of 1 mm/s. The experimental results for the 1 mm/s squeeze speed tests are also shown (symbols)

Typical pressure distributions observed during squeeze flow across the plate radius are shown in Fig 11a,b and Fig 12a,b for tests at RT and 30°C respectively. These show a pressure distribution profile which is not associated to either an extensional or a purely shear flow

regime. It should also be noted that the pressure levels are lower for the tests at 30°C at all speeds tested compared with tests performed at room temperature.

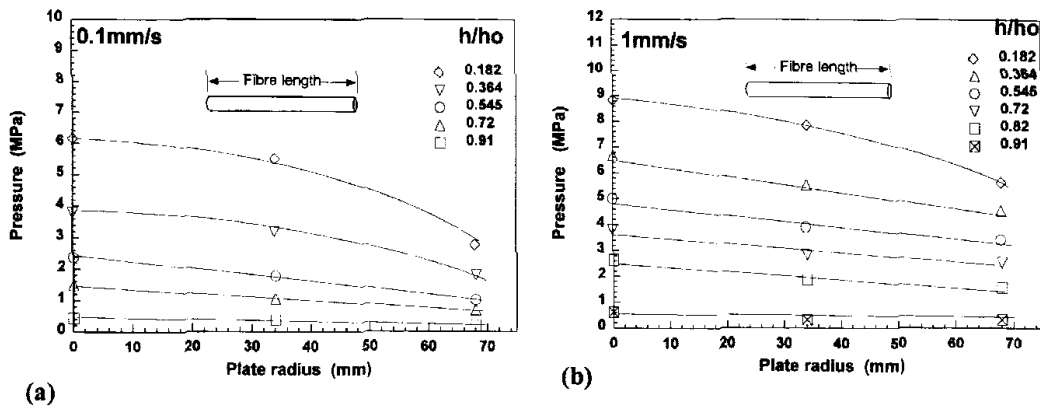


Fig. 11: Pressure distribution along plate radius during squeeze flow of SMC at room temperature. a) 0.1 mm/s squeeze rate, b) 1 mm/s squeeze rate

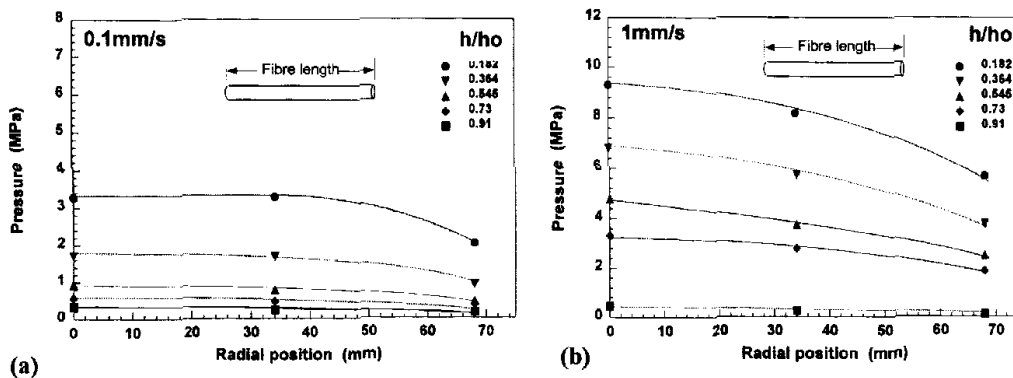


Fig. 12: Pressure distribution along plate radius during squeeze flow of SMC at 30°C. a) 0.1 mm/s squeeze rate, b) 1 mm/s squeeze rate

DISCUSSION

The mechanisms involved in the moulding flow behaviour of SMC have been discussed in the literature. Barone & Caulk [3] testing multilayer charges of SMC at 150°C have reported that at high squeeze speeds uniform extension takes place at all stages of flow, while at slow speeds the material adjacent to the hot mould undergoes greater deformation than the core material and slip occurs between layers of charges. They have thus described the flow to be a combination of slip and uniform extension. This effect was seen to diminish with reduced charge thickness and disappeared for charges three layers thick. Lee, Marker and Griffith [2] carrying out similar tests attributed this behaviour to a combination of biaxial extension and transverse shearing.

In the present work the squeeze flow behaviour of SMC is expected to be different from the one described above since the SMC moulding flow is strongly influenced by temperature.

Squeeze Flow Testing at 30°C

For these tests a logarithmic plot of squeeze stress vs strain rate (Fig. 9) at different strain levels shows a series of parallel lines with a slope of 0.24. This suggests the presence of a strain hardening effect due to the flattening of fibre bundles as squeezing progresses. This has been observed before on squeeze flow of GMT [10]. A model based on the upper bound theory which was developed previously [11] to characterise the moulding flow behaviour of GMT has been applied here for SMC. The plot in Fig. 10 shows the variation of squeeze pressure for a wide range of X values (or plate separations) with the experimental values superimposed. These show that the flow of SMC lies in the intermediate region between pure shear and pure extensional flow but closer to the extensional flow region. Further support for a predominantly extensional flow regime during squeeze flow of SMC can be obtained from the measurements of the pressure distribution across the plates during testing. These indicate that the predominant flow form is extension. The pressure drop at the edge of the plate is attributed to 'edge effects' due to the presence of the fibres. It has been shown in earlier work for continuous fibre GMT [11], which was based on the work of Batchelor [12] and Goddard [13], that the pressure distribution profile is greatly influenced by the presence of the fibre mat. This change in pressure arises from the sum of the stresses generated along individual reinforcing elements (fibres or bundles of fibres) moving in an extensional flow field. The magnitude of that effect depends on the length of the fibres. Therefore at the edges part of the length of the fibres would lie outside the plates resulting in lower pressure contribution.

Squeeze Flow Testing at Room Temperature

Logarithmic plots of squeeze stress vs strain rate at increasing strain levels, Fig. 8, show a linear relationship and the presence of strain hardening, as above, but the slope of these lines is also strain dependent and decreases from 0.73 at large plate separations to 0.26 at small plate separations. The reason for this is not completely clear but is thought to arise from the break-up of the gel structure of the thickened matrix. For such a behaviour the upper bound model cannot be easily applied and further development of the model is needed to characterise SMC at room temperature.

CONCLUSIONS

Squeeze flow testing between parallel plates can be successfully used to characterise the moulding flow behaviour of SMC. The squeeze flow behaviour of GMT is strongly influenced by temperature given that a modest increase of the test temperature from room temperature to 30°C can dramatically alter the behaviour of the material. The flow of SMC is found to be predominantly extensional. The upper bound theory can be successfully used to characterise the squeeze flow of SMC at 30°C.

ACKNOWLEDGEMENTS

The authors would like to thank Dr Paul Corscadden of Autopress Mouldings - UK, for his invaluable assistance on this project.

REFERENCES

1. Silva-Nieto, R.J., Fisher, B.C. and Birley A.W., "Rheological Characterisation of Unsaturated Polyester Resin SMC", *Polymer Engineering and Science*, Vol. 21, No. 8, 1981, pp. 499-506.
2. Lee, L.J., Marker, L.F. and Griffith R.M., "The Rheology and Mould Flow of Polyester SMC", *Polymer Composites*, Vol. 2, No. 4, 1981, pp. 209-218.
3. Barone, M.R. and Caulk, D.A., "Kinematics of Flow in Sheet Moulding Compounds", *Polymer Composites*, Vol. 6, No. 2, 1985, pp. 105-109.
4. Lee, C.C., Folgar, F. and Tucker, C.L., "Simulation of Compression Moulding for Fibre-Reinforced Thermosetting Polymers", *Transaction of ASME*, Vol. 106, May 1984, pp. 114-125.
5. Barone, M.R. and Osswald, T.A., "Boundary Integral Equations for Analysing the Flow of a Chopped Fiber Reinforced Polymer Compound in Compression Molding", *Journal of Non-Newtonian Fluid Mechanics*, Vol. 26, 1987, pp. 185-206.
6. Gibson, A.G., *Rheological Measurement*, ed. Collyer & Clegg, Elsevier, London, 1988.
7. Gibson, A.G., "Die Entry Flow of Reinforced Polymers", *Composites*, Vol. 20, No. 1, 1989, pp. 57-64.
8. Bird, R.B., Armstrong, R.C. and Hassager, O., *Dynamics of Polymeric Liquids*, 2nd Ed., Vol. 1, Wiley, New York, 1987.
9. Han, P.K. and White, J.L., "Experimental and Theoretical Studies of the Rheological and Compression Molding Characteristics of Sheet Molding Compounds", *Society of Plastics Engineers Annual Conference ANTEC 91*, 1991, pp. 1198-1169.
10. Kotsikos, G., Bland, J.H. and Gibson, A.G., "Squeeze flow testing of Glass Mat Thermoplastic material", *Composites*, Vol. 27A, No. 12, 1996, pp. 1195-1200.
11. Kotsikos, G., Bland, J.H. and Gibson, A.G., "Characterisation of Flow Behaviour of Glass Mat Thermoplastics (GMT) by Squeeze Flow Testing", *Proceedings 4th International Conference on Flow Processes in Composite Materials, FPCM '96*, Aberystwyth, Wales, UK, September 9-11, 1996.
12. Batchelor, G.K., "The Stress Generated in a Non-dilute Suspension of Elongated Particles by Pure Straining Motion", *Journal of Fluid Mechanics*, Vol. 46, Part 4, 1971, pp. 813-829.
13. Goddard, J.D., "Tensile Stress Contribution of Flow Oriented Slender Particles in Non-Newtonian Fluids", *Journal of Non-Newtonian Fluid Mechanics*, Vol. 1, 1976, pp. 1-17.

A QUANTITATIVE INVESTIGATION INTO THE EFFECT OF PROCESSING CONDITIONS AND MOULDING THICKNESS ON FIBRE ORIENTATION IN SHORT FIBRE-REINFORCED THERMOPLASTICS

C. Y. Hsu and R. Brooks

*Department of Mechanical Engineering, University of Nottingham,
University Park, Nottingham, NG7 2RD, UK*

SUMMARY: This paper reports on work which is being done to develop & use automated procedures for measuring 3D fibre orientation distribution (FOD) quantitatively in short fibre reinforced thermoplastics (SFRTPs). Through-thickness images comprising about 3000 fibres from polished sections are acquired using a CCD camera mounted on an optical-reflective microscope. Orientation is described in the form of weighted second order tensor components, in which the measurement errors, mainly resulting from the misalignment of the specimen, are included to provide upper & lower bounds. The whole process is automated and allows large numbers of images to be processed and analysed rapidly. The effects of mould geometry and processing conditions on FOD in 20% GFPP(Glass fibre reinforced polypropylene) mouldings have been studied. Results are shown of the variation of fibre orientation through the thickness at specific positions, and for complete cross-sections, the latter incorporating more than 150,000 fibres. Final orientation distribution is complex and depends on such factors as relative dominance of divergent or shear flow conditions, rate of flow and cooling effects.

KEYWORDS: injection moulding, short fibre, fibre orientation distribution, polypropylene, image processing, injection speed, moulding thickness

INTRODUCTION

Many experimental studies [1,2] have shown that fibre orientation distribution (FOD) in short fibre-reinforced thermoplastics (SFRTPs), and consequent mechanical properties, depend on the flow conditions in the mould. In order to design with SFRTPs more effectively, a thorough understanding of FOD in a quantitative way is paramount. One aim of this paper is to describe the use of an automated image processing and analysis system for the accurate quantitative measurement of FOD. A second aim is to develop a greater understanding for the effects of position, injection speed and moulding thickness on FOD. The paper presents results from FOD measurements through the cross-section of 20%GF/PP rectangular plaques and discusses these results in terms of the complex flow field generated in such plaques.

EXPERIMENTAL

Test Plaque Production

The material used in this study is 20 wt% glass filled polypropylene, injection moulded in a specially designed mould with inserts to allow different geometries and thicknesses. Nominal rectangular plaques, 150 mm x 50 mm in size and of 2 mm and 4 mm thicknesses have been moulded as shown in Fig. 1. Each plaque is fed through a 2 mm x 2 mm pin gate. Typical processing temperatures are given in table 1 and cavity fill times of 1, 3 and 10 seconds have been studied, corresponding to nominal injection speeds of 150, 50 and 15 mm/s respectively.

Table 1 : Processing temperatures for the moulding of 20% GF/PP rectangular plaques

Mould Temperature	Barrel Temperature		
	Front	Middle	Rear
50° C	260° C	240° C	230° C

Although the development of orientation in other more complex geometries has been studied [3], simple rectangular plaques were chosen to focus on the effect of processing conditions.

Measurement Positions and specimen Preparation

Detailed through-thickness fibre orientation distribution (FOD) has been measured at two primary positions, A and B, as shown in Fig. 1. Position A is 25mm from the gate at the centre of the plaque, whereas position B is half way along the plaque, i.e. 75 mm from the gate, again at the centre. Specimens for measurement are cut from the plaque at the relevant position and cast in polyester resin. Careful grinding is then performed in an automatic machine using water-proof silicon carbide papers through grades of 250, 400, 800, 1200 and 4000. Finally, the specimen is polished using 1µm aluminium paste.

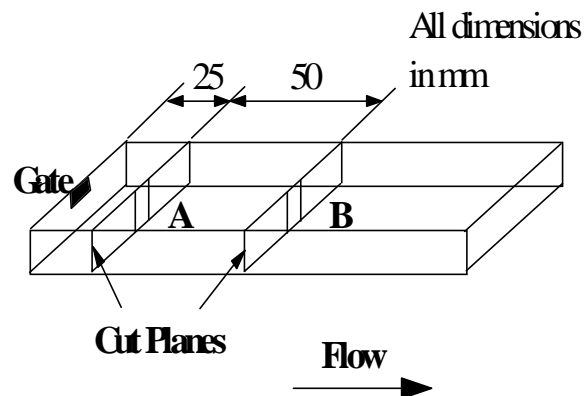


Fig. 1 Pin-gated plaque and positions where fibre orientation distribution is measured.

Image Acquisition

A Vickers microscope equipped with a 768x512 array CCD camera coupled directly to a PC is used for image acquisition. The magnification should be such that the smallest fibre diameter can be resolved and yet still present a sufficiently large field of view. A magnification of 100 is selected, giving a maximum resolution of 1.124 µm per pixel. For detailed measurements through the thickness of a 4mm plaque at each position two columns of 13 frames, each 0.860x0.287mm, are captured, amounting to at least 3000 fibres. In some cases, data from a full cross-section of the plaque is obtained where there may be in excess of 100,000 fibres.

IMAGE PROCESSING AND ANALYSIS

Image Processing Algorithms

Image processing is conducted using the function libraries of a proprietary package, Visilog®, in conjunction with purpose developed algorithms. Details are given in [4,5,6]. A top-hat transformation, based on grey-scale morphological operations, is used to separate the peak (white-grey fibre) from the valleys (dark-grey matrix), at the same time dealing with uneven illumination and poor contrast. The process involves eroding and dilating the image for N iterations, in which N is in the range $D-1.4D$, where D is the nominal fibre diameter in pixels. The resulting image is finally subtracted from the original image. After the subtraction, an Entropy function is used to threshold the image to a binary format. The connected fibres are then separated by producing a Distance Map on which a Watershed algorithm operates. The Distance Map is a map of the image, in which the brightness of a grey pixel is a measure of the distance of the corresponding binary pixel from the outer periphery of the feature. This creates a grey scale image of peaks and valleys and watershedding can separate these into distinct features. Different watersheds are set for identifying isolated particles and for segmentation of connected particles. Finally, all the separated fibres are labelled and assigned a number. The whole process is fully automated.

Pattern Recognition

Fibre cross-sections appear as circles and ellipses in the image. The three-dimensional orientation state, as defined by the two angles, θ (in-plane), and ϕ (out-of-plane), is calculated from the length of the major and minor axes of each ellipse, in addition to the angle the major axis makes with the x-axis in the image co-ordinate system. The length of the major and minor axes are derived from the second moments of area of each individual ellipse using Visilog® area moment functions. The in-plane angle θ is given by, minor

$$\frac{\text{Length of the minor axis}}{\text{Length of the major axis}} = \frac{I_{min}}{I_{max}} = \frac{\frac{I_{xx} + I_{yy}}{2} - \sqrt{\left(\frac{I_{xx} - I_{yy}}{2}\right)^2 + I_{xy}^2}}{\frac{I_{xx} + I_{yy}}{2} + \sqrt{\left(\frac{I_{xx} - I_{yy}}{2}\right)^2 + I_{xy}^2}} \quad (1)$$

where I_{xx} , I_{yy} and I_{xy} are the second moments of area of the ellipse about the x and y axes.

The out-of-plane angle ϕ is calculated from the angle the major axis of the ellipse makes with the x-axis, and is given by the following expression,

$$\tan(2\phi) = -\frac{2I_{xy}}{I_{xx} - I_{yy}} \quad (2)$$

This equation leads to two values of ϕ , 90 degrees apart. The correct value is found by back substituting into the expressions for the principal second moments and checking for consistency with the values above.

Tensor Representation of Fibre Orientation Distribution (FOD)

The orientation tensor has been shown to be a concise method of describing the average orientation state of a number of fibres [7]. The orientation angles are used as input to form the tensor components. In addition, it is necessary to weight the contribution of each fibre to the average tensor component, according to its ellipticity [7]. This takes into account the probability of cutting each fibre. The weight average second order orientation tensor components are then given by,

$$a_{ij} = \frac{\sum (a_{ij})_n \frac{I}{\cos \theta_n}}{\sum \frac{I}{\cos \theta_n}} \quad (3)$$

a_{11} & a_{22} are measures of the in-plane orientation in the flow direction & transverse to the flow direction respectively, whilst a_{33} is an indication of out-of-plane orientation.

Bounds on the Results

The major source of measurement error arises from misalignment of the section plane of the specimen. For a misalignment angle α , denoting a clockwise rotation about the 3 axis, the actual orientation angles can be computed from measured angles [8] using the following transformation expressions,

$$\begin{aligned} \cos \theta &= -\sin \alpha \sin \theta_\alpha \cos \phi_\alpha + \cos \alpha \cos \theta_\alpha \\ \cos \phi &= (\cos \alpha \sin \theta_\alpha \cos \phi_\alpha + \sin \alpha \cos \theta_\alpha) / \sin \theta \end{aligned} \quad (4)$$

where α = misalignment angle; $\theta_\alpha, \phi_\alpha$ = measured values; θ, ϕ = actual values

The specimen preparation procedure should align the section plane to within 2 degrees. A conservative estimate of the upper and lower bounds on the orientation tensor components has therefore been made by assuming the misalignment angle to be $\alpha = \pm 2.5$ degrees. These bounds are included in the graphical results presented in the following sections.

RESULTS

Effect of Position in the Plaque

Fig. 2 and Fig. 3 show through-thickness photographs taken at position A (gate) and position B (centre) of a 2mm plaque moulded at 1 second fill time i.e. high speed. Fig.4 shows the corresponding quantitative measure of through-thickness FOD at these two positions. It is clear from the photographs that there is a significant reduction in the thickness of the transversely aligned core layer at position B, a fact confirmed by the measurements shown in Fig. 4. The high values of a_{11} in layers 2-3 and 11-12 ($a_{11} > 0.6$), also shown in Fig. 4, are indicative of shear alignment in the high shear region adjacent to the frozen layers. By contrast, in these outer frozen layers, the value of a_{11} reduces as a result of the rapid cooling of the melt and corresponding increase in viscosity, which limits the amount of shear alignment that can take place. Throughout the thickness, at both positions A and B, a_{33} remains low, showing that the flow is largely in-plane in all layers. However, a_{33} values are

marginally higher away from the central core layers, possibly indicating the drag affect of the frozen layer causing some fibres to move out of plane.

As the polymer melt enters the cavity through the constricted pin gate, divergent flow will tend to align the fibres in the transverse direction giving the observed wide core region at position A. As the melt moves down the plaque the shear forces take affect on the outer layers causing greater alignment in these regions and the observed narrower core. Without the influence of shear forces, the transverse alignment in the central core is retained even at position B.

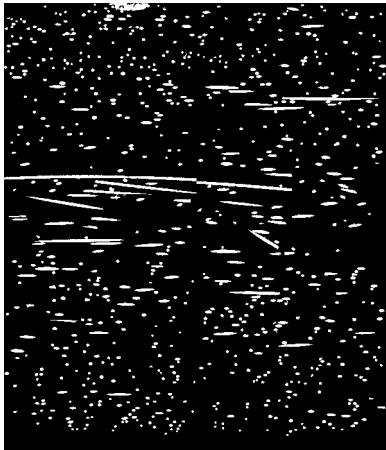


Fig.2 A through-thickness image of the 2mm plaque at position A.

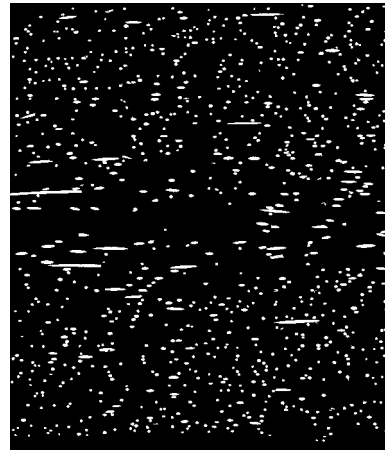


Fig.3 A through-thickness image of the 2mm plaque at position B.

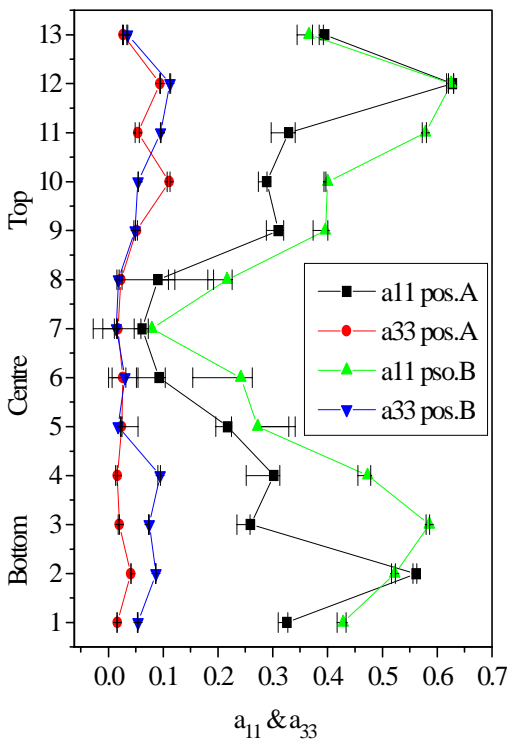


Fig.4: Measured through-thickness orientation tensor components near the gate (position A) and at the centre (position B) of the 2mm plaque at 1s. injection time.

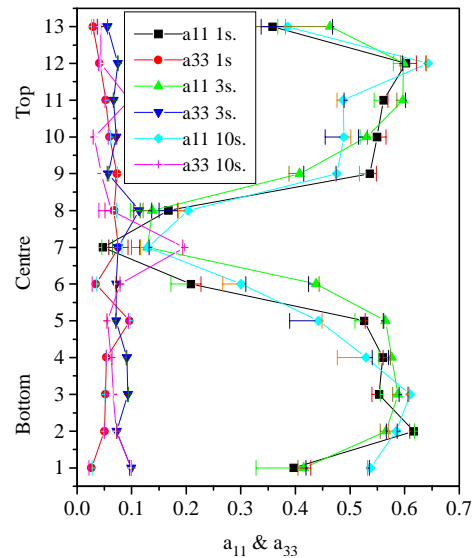


Fig. 5: Measured through-thickness orientation tensor components for the 4mm plaque at position B for different injection speeds (1s, 3s and 10s fill times)

Effect of Injection Speed

4 mm Plaque

Fig.5 shows the variation of tensor components, a_{11} and a_{33} , at position B (middle) in the 4 mm plaque, for three injection times; 1, 3, and 10 seconds. In general, the results show that injection speed over this range has little effect on the FOD. There is some evidence of a greater transverse alignment in the core region at high injection speed and a more abrupt change from high skin values to low core values at this speed. These observations may be a consequence of the blunter velocity profile arising from greater shear thinning in this case. The a_{33} values remain low throughout the thickness, again indicative of very little out-of-plane alignment apart, that is, from an increase in the core region at slow filling time. The origin of this out-of-plane alignment is uncertain.

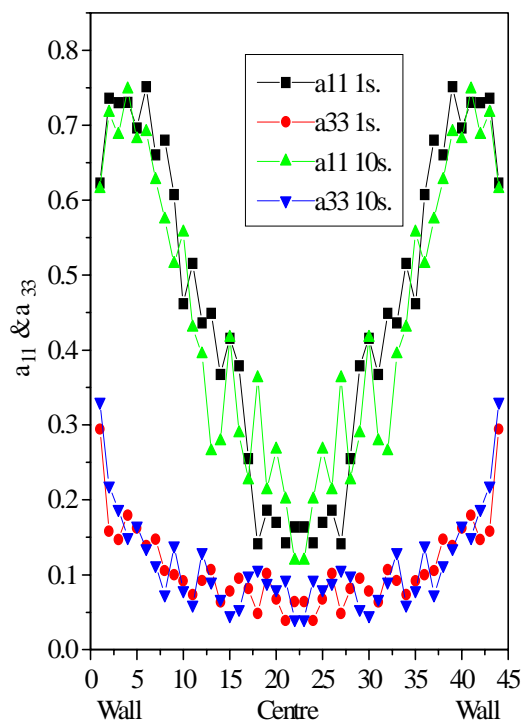


Fig.6: Measured orientation tensor components across the width of the 4mm plaque at position B for 1s and 10s injection times

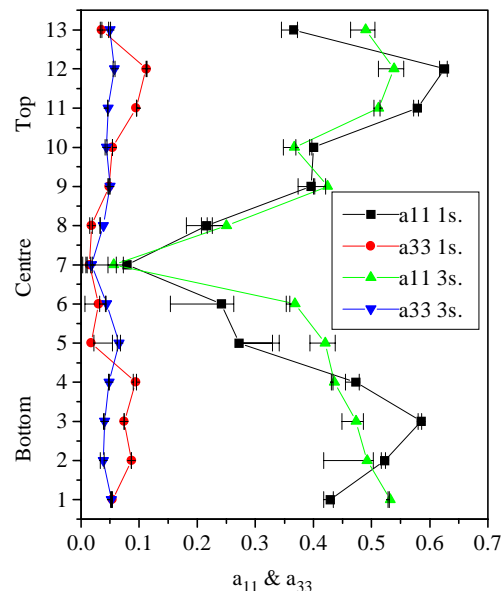


Fig.7 Measured through-thickness orientation tensor components for the 2mm plaque at position B for 1s injection times.

A further study of the effects of processing speed has been made by measuring the orientation in the two central through-thickness layers, i.e. 2/13th of the plaque thickness, across the full width of the 4 mm plaque at position B. The results are shown in Fig. 6 for two injection fill times (1s and 10s). Although there is some scatter in the measurements, it is clear that a similar pattern of FOD occurs across the width to that already seen through the thickness. Low a_{11} values occur at the centre of the plaque width, rising gradually to high values at the edges. The pattern appears to reflect the curved nature of the flow front across the width. It is also interesting to see that the a_{33} component remains low for much of the width, indicating in-plane flow, but rises to quite a high value (~ 0.3) near the plaque edges. This out of plane

alignment is likely to be caused by the fountain flow freezing onto the walls in these regions where the proximity of three mould surfaces increases the cooling rate.

As with the through-thickness results, injection speed only has a marginal effect on the cross-width results, however, a pattern is discernible. At high injection speed (1s fill time) there appears to be more of a distinction between the a_{11} values near the edge and those in the centre than there is at low injection speeds. There is a clear cross over of the a_{11} lines for the two speeds in the regions of column 17 and 27 in Fig. 5. One explanation for this is that at the higher speed the cross width flow front may be blunter due to the greater shear thinning. However, it should be pointed out that any such differences in flow front geometry have yet to be measured.

2 mm Plaque

Fig. 7 shows the through thickness FOD at position B for the 2 mm plaque at two injection speeds; 1 and 3 second fill times. At the higher injection speed (1s) a_{11} is higher in the skin regions which is a consequence of the higher shearing in this case. It is also apparent that the core region is wider for the high speed injection which could be related to the degree of cooling. At the low injection speed (3s), by the time the melt has reached the middle of the plaque (point B), it will have cooled more than it does under high speed injection conditions. This will result in a wider frozen layer, a shear region closer to the mid plane and a consequent reduced core region. In contrast to the 4 mm plaque, because of these cooling effects, the effect of injection speed is more pronounced in the thinner 2 mm plaque.

Effect of Thickness

Fast Injection Speed (1s fill time)

Figs. 8 and 9 show detailed contour plots of the a_{11} tensor component for full cross-sections at position B for both the 4 mm and 2 mm plaques. Both plaques have been moulded at high injection speed. It is important to note the complexity of the orientation.

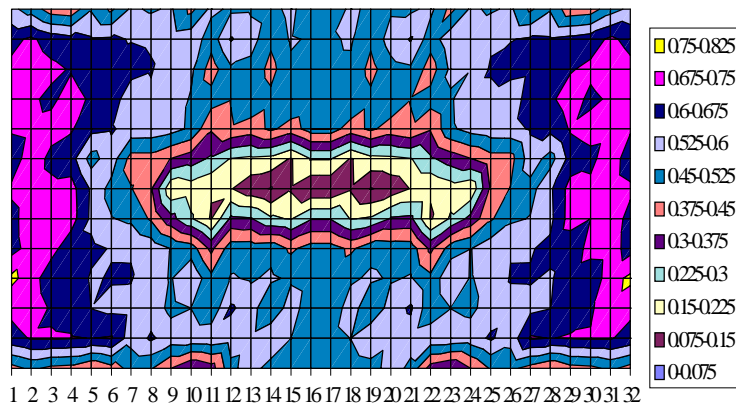


Fig.8 Cross-sectional Contour plot of a_{11} halfway along the 4mm plaque (X-width Y-, thickness); 1 second injection time.

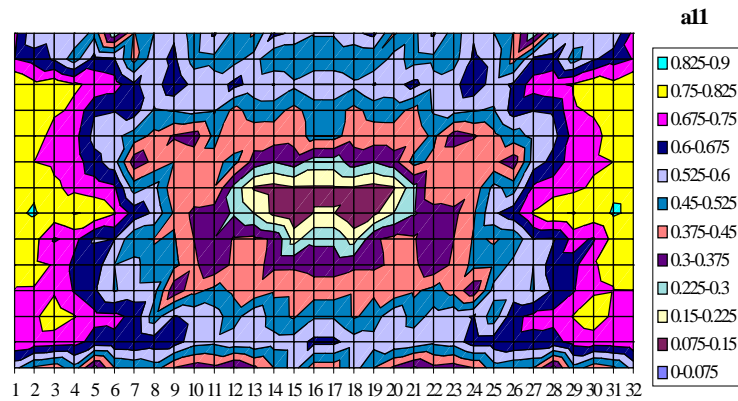


Fig. 9 Cross-sectional contour plot of a_{11} halfway along the 2mm plaque (X-width, Y-thickness); 1 second injection time.

The general skin-core structure extends throughout the cross-section of both plaques, both through the thickness and across the width. Although the low orientation contour ($a_{11} = 0.15 - 0.225$) indicates a relatively smaller core for the 2 mm plaque, particularly across the width, the mid range contour ($a_{11} = 0.375 - 0.45$) tells a very different story. This contour, which is more indicative of the transition from longitudinal to transverse alignment, shows that the 2 mm plaque has a wider through-thickness core in the central region of the cross-section. Furthermore, the 2 mm plaque shows greater a_{11} values in the upper and lower skin regions. Both of these observations can be explained by a blunter through-thickness flow front arising from greater shear thinning in the 2 mm plaque.

Slow Injection Speed (3s fill time)

Fig. 10 shows the through-thickness FOD for the 2 and 4 mm plaques at a slower injection speed and corresponds to the centre lines in the contour plots in Figs 8 and 9. In direct contrast to the high speed injection results, the 4 mm plaque now has higher a_{11} values near the upper and lower walls. As discussed in the previous section on the effect of injection speed, it is likely that in the 2 mm plaque cooling will become important at the slower speed. The shear driven alignment mechanism will be overtaken by the cooling of the melt and freezing in at lower orientation.

CONCLUSIONS

This paper has reported on the use of automated image processing & analysis methods for the quantitative measurement of 3D fibre orientation distribution in 20%GF/PP injection moulded plaques. Using these techniques it has been possible to characterise in detail the complex through-thickness FOD including full cross-sectional information. The results of the measurement of FOD at positions near the gate and middle of the plaque, at different injection speeds, have been presented. A relatively thick transverse core region near the gate, resulting from divergent flow, reduces further down the plaque as the shearing forces take effect. The effect of injection speed is minimal in the thicker 4 mm plaque, whilst clear differences were observed in the thinner 2 mm plaque. The difference between FOD in 2mm and 4mm plaques can be explained by shear thinning behaviour at fast injection speed and cooling effects at slow injection speed. A full cross-sectional comparison of the 2mm and 4mm plaques reveals the complexity of FOD showing both through-thickness and cross-width variations. The

powerful methods reported in this paper should enable a greater understanding of the important interaction between processing and fibre orientation to be achieved.

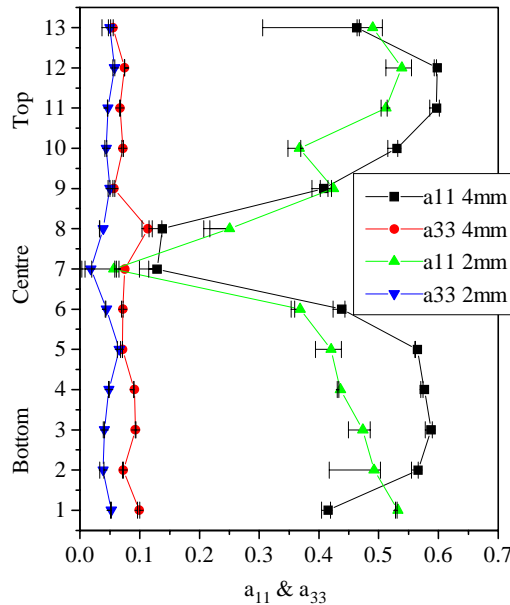


Fig.8: Measured through-thickness orientation tensor components for the 2mm and 4mm plaques at position B for 3 second injection time.

REFERENCES

1. Bright, P. F., and Darlington, M. W., 'Factors Influencing Fibre Orientation and Mechanical Properties in Fibre Reinforced Thermoplastics Injection Mouldings', *Plastics and Rubbers Processing and Application*, Vol. 1, No. 2, 1981, pp. 139-147.
2. Folks, M. J., *Short Fibre-reinforced Thermoplastics*, Chapter 6, Research Student Press, 1982.
3. Hsu, C. Y., Brooks, R., 'Experimental Determination of Orientation in Short Fibre Reinforced Thermoplastics using Image Processing and Analysis', *the 7th European Conference on Composites Materials*, 1996, London, pp.261-266
4. Visilog 4 Manual, *IPE Programmer's Guide*, NOESIS S.A. France, 1993.
5. Hsu, C. Y., *PhD thesis*, Chapter 4, University of Nottingham, 1997 (to be published).
6. Gonzalz, R., Woods, R., *Digital Image Processing*, Chapter 8, Addison-Wesley, 1992.
7. Bay R. S., and Tucker C. L., 'Stereological measurement and Error Estimates for Three-Dimensional Fibre Orientation', *Polymer Engineering and Science*, 1992, Vol. 32, No. 4, pp. 240-253.
8. Hine, P., Duckett, R. A., Davidson, N., Clarke, A. R., 'Modelling of The Elastic Properties of fibre Reinforced Composites. I: Orientation Measurement', *Composites Science and technology*, 1993, Vol. 47, pp.65-73

CURE SIMULATION MODEL FOR RESISTANCE CURED COMPOSITES

Renata S. Engel and Steven A. Weller

*Engineering Science and Mechanics Department, The Pennsylvania State University,
University Park, Pennsylvania, 16802, USA*

SUMMARY: The resistance heating method for curing thermoset composites has been developed as an alternative to oven, autoclave or hot press curing. The composite interior is heated by passing current through embedded carbon fiber patches. These internal energy sources present a new form of applied thermal loads not found in the traditional cure simulation models, which typically are limited to external boundary conditions. The paper presents a numerical method for predicting temperature, degree of cure, and cure rate for thermoset resin/fiber composites. Finite difference formulas describe the temporal and spatial derivatives of the energy equation. Heat generation terms are linearized over each time interval to ensure compatibility of cure rate and degree of cure with the corresponding temperature. Internal heating, via resistance heating, and external temperature or flux can be applied. Numerical simulations are presented to demonstrate the sensitivity to various input parameters.

KEYWORDS: numerical model, cure simulation, resistance heating, finite difference method

INTRODUCTION

Resin transfer molding and other closed mold thermoset composite manufacturing methods require a cure stage whereby heat is added through devices such as an autoclave, smart press, oven, hot plate or thermal strips. Considerable research has been conducted to develop simulations that describe the temperature profile in composites using boundary conditions appropriate for the particular curing device. For example, a finite element model [1] and implicit finite difference model [2] of an autoclave cure cycle, and a one dimensional ADI (alternating direction implicit) finite difference model for a heated tool plate cure cycle [3] illustrate the use of numerical simulations to predict temperature, degree of cure and rate of cure through the thickness of composites.

Simulations perform another valuable service in that they are used to evaluate the effects of certain processing parameters before manufacturing. For example, a one-dimensional finite difference model was employed to investigate variations in temperature response when fiber and resin properties were altered [4]. The researchers isolated the influence of one resin property without creating a new resin that exactly retained all other properties. Another study simulated the effects of boundary conditions for curing thick composites. Their results suggested thermal spikes can develop at the center of the composite when thick parts are cured with external heat sources [5]. These results were later substantiated with experiments

conducted for closed-mold, thick, fiberglass/epoxy composites cured in an oven [6]. The inability to cure thick parts in an oven initiated the development of a resistance heating method for curing thermoset composites using carbon fiber patches [7].

Unlike the simulations with externally applied heat sources, the resistance heating method requires specification of an interior source of energy. In the resistance heating method the composite is cured by passing current through an embedded carbon fiber patch. Local resistance heating acts as an internal heat source; the resin catalyzes and generates more heat. The combination of the exothermic reaction and thermal conduction drives the cure of the remaining resin. The work presented here describes the numerical model for predicting the temperature and cure profiles when internal resistance heating is applied in a closed mold composite manufacturing method.

NUMERICAL MODEL

Energy Equation

The most general form of the two-dimensional energy equation for the stationary system shown in Figure 1 is

$$\rho C_p \frac{\partial T}{\partial t} - k_x \frac{\partial^2 T}{\partial x^2} - k_y \frac{\partial^2 T}{\partial y^2} = Q \text{ for } (x, y) \in A_c \quad (1)$$

where ρ is the density, C_p is the specific heat, k_x and k_y are thermal conductivities in the x and y directions, respectively, T is the temperature, and Q represents an internal heat source, such as a chemical reaction. The properties, k_x , k_y , ρ , and C_p , for both the resin and fiber are assumed constant through the cure cycle. The energy evolved during the cure of the resin can be obtained using differential scanning calorimetry (DSC) and is characterized by the heat of reaction of the resin H_r and the degree of cure α ,

$$Q = H_r \frac{\partial \alpha}{\partial t}. \quad (2)$$

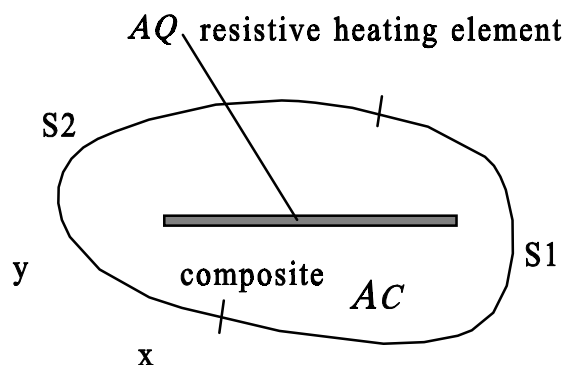


Figure 1: Composite cross-section

The DSC output is used to construct an empirical cure kinetic model of Arrhenius-type. For example, the autocatalytic kinetic model for epoxy reactions has the form.

$$\frac{\partial \alpha}{\partial t} = (k_1 + k_2 \alpha^m)(\alpha_f - \alpha)^n \quad (3)$$

where m and n are reaction orders, α_f is the final degree of cure in isothermal DSC scans, and

$$k_i = K_i \exp[-E_i / RT], \quad i = 1, 2, \quad (4)$$

such that K_i is a pre-exponential factor, E_i is the activation energy, and R is the universal gas constant. Table 1 shows cure kinetic values from two separate studies for diglycidyl ether of bishpenol-A (DGEBA) epoxies--both obtained using DSC [8], [9].

The effects of the resistive heating element shown in Figure 1 are included in the model as an internal condition specified at the location of the carbon fiber patch. At the patch, the rate of energy conducted perpendicularly away from the patch is assumed to be balanced by the power, q per unit volume, V_{patch} supplied by an external voltage source.

$$-k_y \frac{\partial^2 T}{\partial y^2} = Q_r = \frac{q}{V_{patch}} \quad \text{for } (x, y) \in A_Q. \quad (6)$$

Along with the energy balance in the x-y plane defined by equations (1) and (6), boundary conditions are needed for a complete model description. Although other forms of conditions involving heat transfer coefficients can be specified, this model restricts the application of boundary conditions to temperature and flux:

$$T = T_0, \quad \text{on } S_1 \quad \text{and} \quad \frac{\partial T}{\partial x} = q_0, \quad \text{on } S_2. \quad (7)$$

Table 1. Kinetic Parameters for DGEBA resins.

	EPON 9302 [7]	EPON 826 [8]
K_1 (sec ⁻¹)	25.1×10 ³	144×10 ³
K_2 (sec ⁻¹)	668×10 ⁶	20.8×10 ³
E_1 (kcal/mol)	13.3	15.7
E_2 (kcal/mol)	17.8	10.3
m	1.6	1.68 - 2.042×10 ⁻³ T(°K)
n	1.4	0.32 + 2.042×10 ⁻³ T(°K)
α_f	- 0.437 + 2.39×10 ⁻³ T(°K)	1

The complete boundary value problem, equations (1) and (6) with boundary conditions (7) are approximated using finite differences in conjunction with a linearization scheme over the time interval.

Linearization Model

The finite difference formulas for the spatial and temporal derivatives on the left-hand side of (1) and (6) are given as a first order backward difference and second order central differences,

$$\frac{\partial T}{\partial t} = \frac{T(t) - T(t - \Delta t)}{\Delta t} \quad (8)$$

$$\frac{\partial^2 T}{\partial x^2} = \frac{T(x - \Delta h_x) - 2T(x) + T(x + \Delta h_x)}{\Delta h_x^2} \quad (9)$$

$$\frac{\partial^2 T}{\partial y^2} = \frac{T(y - \Delta h_y) - 2T(y) + T(y + \Delta h_y)}{\Delta h_y^2} \quad (10)$$

where Δt , Δh_x , Δh_y are the time and space intervals. Using these difference formulas throughout region $A_C + A_Q$ yields the generalized form

$$[K] \{T\}^i = f_1 \{T\}^{i-1} + f_2 \{Q\}^i + f_2 \{Q_r\} \quad (11)$$

where $[K]$ includes the coefficient matrix for temperatures, f_1 and f_2 are constants based on resin and fiber material properties, and the superscript i represents the current (i th) time step. $\{Q_r\}$ does not vary with time; therefore, no superscript is shown. Notice that $\{Q\}$, the energy evolved from the chemical reaction, is evaluated in the current time step. The term is linearized based on the previous rate of cure and the rate of cure with respect to the temperature.

$$\{Q\}^i = H_r \left\{ \frac{\partial \alpha}{\partial t} \right\}^i = H_r \left\{ \frac{\partial \alpha}{\partial t} \right\}^{i-1} + H_r \frac{d}{dT} \frac{\partial \alpha}{\partial t} \Big|_{-i-1} (\{T\}^i - \{T\}^{i-1}). \quad (12)$$

Even though equation (11) can be expressed in terms that are dependent on times, i and $i-1$, further linearization over the interval is recommended, particularly since the load or source vector contains terms that vary exponentially [9].

Consider a simplified form of (11) at an arbitrary generalized time step, θ

$$[K]^\theta \{T\}^\theta = \{F\}^\theta \quad (13)$$

where θ is a dimensionless quantity that ranges from 0 to 1 such that

$$\theta = \frac{t - t^n}{t^{n+1} - t^n} = \frac{t - t^n}{\Delta t}. \quad (14)$$

The assumption that the resin and fiber properties, (conductivity, heat capacity and density) do not vary with time means the linearization scheme need only be applied to $\{T\}$ and $\{F\}$.

$$\{T\}^\theta = (1 - \theta)\{T\}^{i-1} + \theta\{T\}^i \quad (15)$$

$$\{F\}^{\theta} = (1-\theta)\{F\}^{i-1} + \theta\{F\}^i \quad (16)$$

At the limits $\theta=0$ or $\theta=1$, the form is identically a forward or backward difference, respectively. Since the backward difference formulation is unconditionally stable, all results presented here will be obtained with $\theta=1$. Once the linearizations are applied, the final form of the model is

$$[K_r]^i \{T\}^i = F_2 \{T\}^{i-2} + F_1 \{T\}^{i-1} + f_2 H_r \left\{ \frac{\partial \alpha}{\partial t} \right\}^{i-1} + f_2 \{Q_R\} \quad (17)$$

where

$$[K_r] = \theta [K]^i - f_2 H_r \frac{d}{dT} \frac{\partial \alpha}{\partial t} \Big|_{-i-1} [I] \quad (18)$$

$$F_2 = (1-\theta) f_1 \quad (19)$$

$$F_1 = (1-\theta) [K] + \theta f_1 [I] - f_2 H_r \frac{d}{dT} \frac{\partial \alpha}{\partial t} \Big|_{-i-1} [I]. \quad (20)$$

NUMERICAL SIMULATIONS

The numerical model was checked for convergence for element size and time interval. The model is more sensitive to the time step. This is primarily a result of the cure kinetic model containing exponential terms. An adaptive time step would be desirable; however, for the work presented here a constant time step was chosen for the entire cure cycle. For consistency in reporting and comparing a variety of temperature versus time and degree-of-cure versus time results, the same time step was used for all simulations regardless of whether that particular level of refined time step was needed.

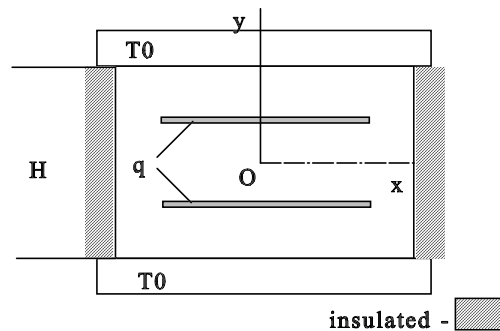


Figure 2: Schematic of cross-section for numerical simulations.

Parametric Study

A series of numerical simulations was conducted to evaluate a variety of parameters-either material properties, mold thickness or boundary conditions. The results presented focus on the latter two since they pertain to internal resistance heating in combination with, or compared to, external heating sources such as a hot press or hot plate. The model will have the geometry as shown in Figure 2 and will use the resin model for Shell EPON 826.

Figures 3, 4 and 5 illustrate the effects of varying the boundary conditions: heat source and magnitude of thermal loads. For example, consider the arrangement shown in Figure 2 with $q=0$, i.e., no carbon patches. Heat is applied in the form of an external source applied at the top and bottom of the composite. When that source input varies, even slightly, i.e., by 5°C , the exothermic reaction can cause a significant change in the temperature profile at the center of the composite. Seventy-five percent of the cure occurs at the peak of the exothermic reaction when $T_0=40^{\circ}\text{C}$, whereas only 60% of the cure occurs at the peak of the reaction for $T_0=35^{\circ}\text{C}$. This same effect of thermal spiking was observed in experimental work with 50 mm thick fiberglass/epoxy (20% fiber volume fraction) when cured in an oven [7] and also by simulation of thick carbon/epoxy laminates cured under pressure and temperature [5].

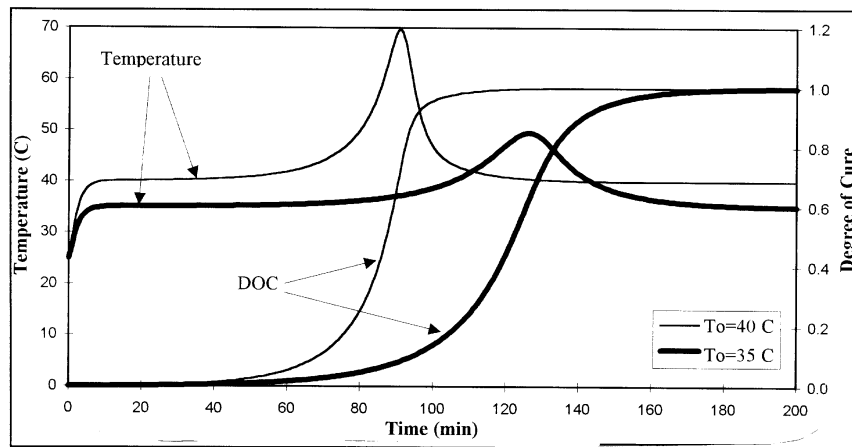


Figure 3: Temperature and Degree of Cure versus Time for $T_0=40^{\circ}\text{C}$, 35°C , with $q=0$, $H=25.4\text{ mm}$.

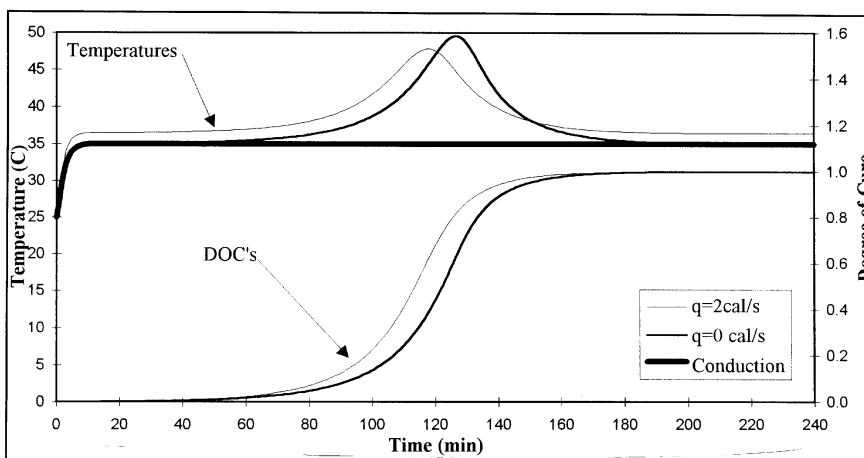


Figure 4: Temperature and Degree of Cure versus Time for conduction only, external heat source only, and resistive heating with external heat source. $H=25.4\text{ mm}$. $T_0=35^{\circ}\text{C}$

The use of resistant heating in conjunction with external heating sources can reduce the effect of thermal spiking as shown in Figure 4. The curve marked conduction is a temperature plot at the center of the specimen if the heating is due only to conduction, i.e., no chemical reaction or internal heating. The other curves represent the temperature and degree of cure when the same external heat source is applied but in one case the resistant heating patches are activated by a power source. The degree of cure at the peak exotherm is approximately 10% lower (0.67 degree of cure versus 0.60 degree of cure) when the combined method of heating is employed. This is due in part to the initial heating at the center of the composite due to the heating patch. The exothermic peak temperature is also lowered when including the additional power source. This may be due to initiating cure earlier with a more gradual release of the exothermic energy. Even though the steady state temperature is slightly increased due to the additional heat source, the cure cycle profile has been improved--a lower peak temperature is reached in less time.

At this point, one may think that by increasing the power to the patch, the maximum temperature will continue to decrease and the time to peak will be reduced. In fact, as shown in Figure 5, this is not the case. For a given external source, a small amount of internal power can decrease the time to reach peak temperature and lower the peak temperature; however, additional internal heating will cause the peak temperature to increase, and the time to reach peak temperature to decrease. The amount of cure at peak temperature is not significantly affected. An optimum combination of external and internal heating could produce the desired rate of cure and length of cure cycle. Other options involve the use of feedback whereby the manufacturers recommended cure cycle is controlled by cycling the power to the patch as needed [11].

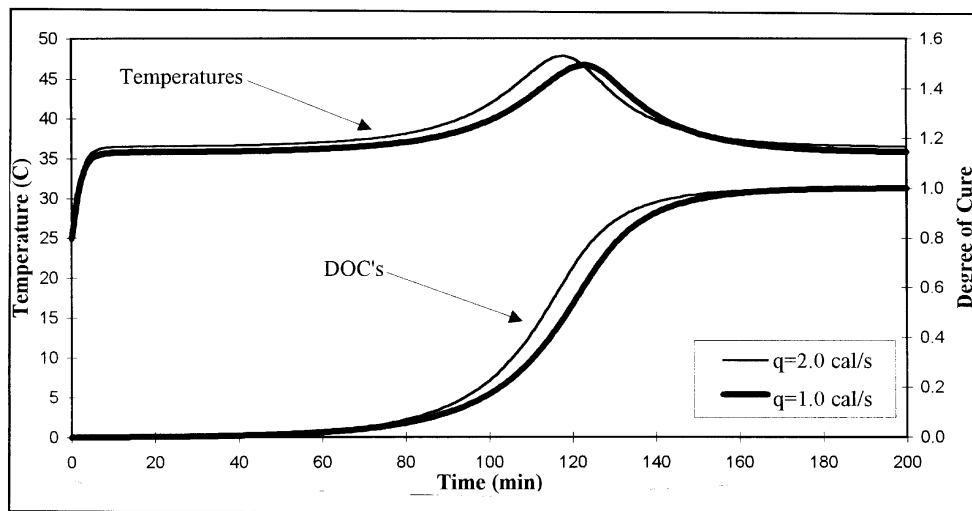


Figure 5: Temperature and Degree of Cure versus Time for resistant heating power ($q=2$ cal/s, 1 cal/s) supplied to the heating patches. $H=25.4$ mm. $T_0=35^\circ\text{C}$

Finally, the effect of internal heating was investigated for composites of varying thickness. Figure 6 shows that as the part becomes thinner, the application of resistance heating becomes less significant. Thick parts regardless of how they are cured are subjected to the same difficulty--an exponential increase in peak temperature as the thickness increases linearly; however no appreciable increase in the degree of cure at peak temperature occurs.

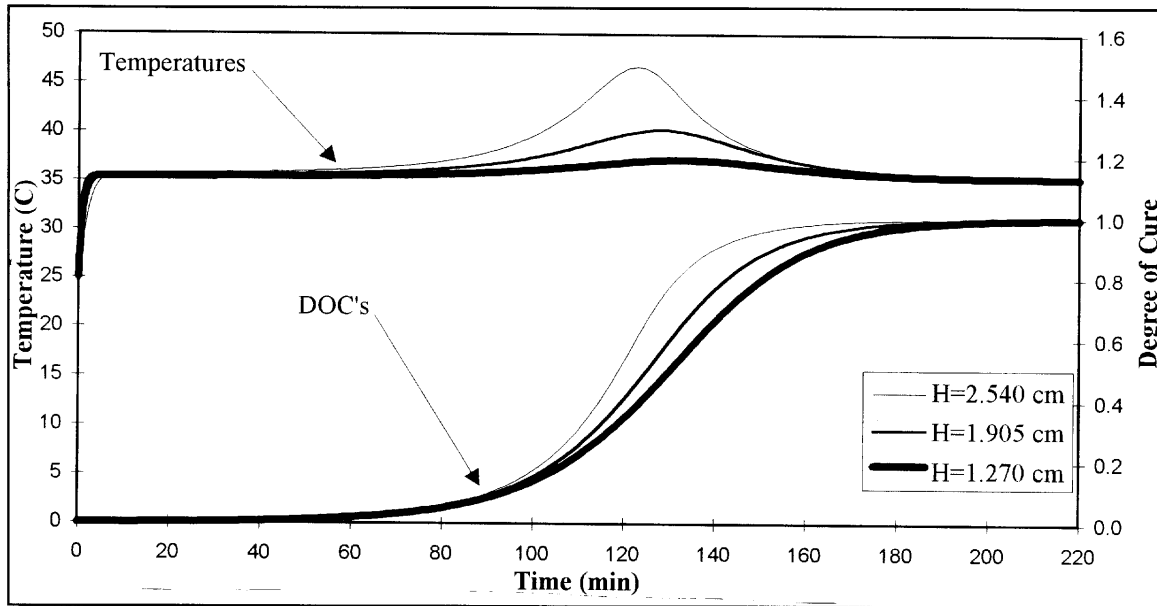


Figure 6: Temperature and Degree of Cure versus Time for $H=12.7$ mm, 19.1 mm and 25.4 mm with $q=1$ cal/s, $T_0=35^\circ\text{C}$

CONCLUSIONS

The resistance heating method of cure can be modeled using a two-dimensional finite difference scheme with an internal source term that is directly related to the power per unit volume supplied by the external electric circuit. Simulations conducted to study the influence of a variety of processing parameters indicated that a combination of external heating and internal heating can reduce thermal spiking in thick parts. Furthermore a gradual increase in temperature at the center of composites is recognized as a means of minimizing thermal spiking and thereby reducing the degree of cure achieved at the peak temperature.

As composites manufacturing moves further into markets that require mass production of thick section parts, or parts with large geometries that do not lend themselves to oven, hot press or autoclave curing, resistance heating may become more prevalent. The current simulation model addresses the need to simulate processing conditions and investigate placement of internal heating elements. To date, the model is restricted to two internal resistance heating elements; however, work is ongoing to develop more flexibility in the input parameters and boundary specification.

ACKNOWLEDGMENTS

The authors thank the National Science Foundation (DDM-9309317) and The Pennsylvania State University for supporting this work.

REFERENCES

1. Bogetti, T. A. and Gillespie, J. W., Jr., "Two-Dimensional Cure Simulation of Thick Thermosetting Composites," *Journal of Composite Materials*, Vol. 25, 1991, pp. 239-273.
2. Mijovic, J. and Wang, H. T., "Modeling of Processing of Composites Part II - Temperature Distribution During Cure," *SAMPE Journal*, March/April 1988, pp. 42-55.
3. White, S. R. and Kim, C., "A Simultaneous Lay-Up and In Situ Cure Process for Thick Composites," *Proceedings American Society for Composites - Seventh Technical Conference*, University Park, Pennsylvania, USA, October 13-15, 1992, pp. 80-89.
4. Vergnaud, J.-M. and Bouzon, J., *Cure of Thermosetting Resins: Modelling and Experiments*, Springer-Verlag, New York, 1992.
5. Twardowski, T. E., Lin, S. E., and Geil, P. H., "Curing in Thick Composite Laminates: Experiment and Simulation," *Journal of Composite Materials*, Vol. 27, No. 3, 1993. pp. 216-249.
6. Butler, D. and Engel, R. S., "On the Use of Embedded Graphite Patches for Cure in Resin Transfer Molding," *Proceedings Tenth International Conference on Composite Materials*, Whistler, British Columbia, Canada, August 14-18, 1995, Vol. III: Processing and Manufacturing, Poursartip, A. and Street, K. N., Eds., pp. 269-276.
7. Butler, D., *Curing Thick Resin Transfer Molded Composites by Resistance Heating*, Masters Thesis, The Pennsylvania State University, University Park, PA. August 1995.
8. Trivisano, A, Maffezzo, A., Kenny, J. M. and Nicolais, L., "Modelling of the Thermorheological Behavior of High Performance Composites," *35th International SAMPE Symposium*, April 2-5, 1990, pp. 590-603.
9. Mijovic, J. and Lee, C. H., "A Comparison of Chemorheological Models for Thermoset Cure," *Journal of Applied Polymer Science*, Vol. 38, 1989, pp. 2155-2170.
10. Lee, S., *Coupled FEA of Decomposing Poroelastic-Polymeric Composites and Structures with Subsequent Thermal and Gas Diffusion*, Ph.D Dissertation, The Pennsylvania State University, University Park, PA. December 1993.
11. Bakis, C. E., Bantell, F. J., "Curing of Composite Prepreg Laminates by Resistance Heating of Internal Carbon Veils," (these proceedings)

SURFACE MODIFICATION OF INORGANIC ULTRAFINE PARTICLES BY THE GRAFTING OF POLYMERS

Noria Tsubokawa¹, Kazue Kawatsura², and Yukio Shirai²

¹ *Department of Material Science and Technology, Faculty of Engineering, Niigata University, 8050 Ikarashi 2-nocho, Niigata 950-21, Japan*

² *Graduate School of Science and Technology, Niigata University, 8050 Ikarashi 2-nocho, Niigata 950-21, Japan*

SUMMARY: To modify the surface of carbon black and inorganic ultrafine particles, the radical grafting of polymers onto these surfaces was investigated. The radical polymerization of vinyl monomers was found to be initiated by the azo groups introduced onto carbon black and the corresponding polymer was grafted onto the surface. In the polymerization, grafting efficiency (proportion of grafted polymer to total polymer formed) was about 50% at the initial stage of the polymerization, but immediately decreased at middle and last stage of the polymerization because of preferential formation of ungrafted polymer. In addition, the polymerization of vinyl monomers was initiated by the system consisting of trichloroacetyl groups and Mo(CO)₆ to give the polymer-grafted ultrafine particle. In the polymerization, the grafting efficiency was about 60% and scarcely decreased even at the last stage of the polymerization. The tensile strength of polystyrene film compounded with polymer-grafted carbon black was examined.

KEYWORDS: carbon black, ultrafine silica, titanium oxide, surface grafting of polymer, azo group, radical polymerization, dispersibility

INTRODUCTION

In general, dispersing inorganic particles uniformly into a polymer matrix or an organic solvents is very difficult. In addition, mechanical properties of inorganic powder-polymer composites are considered to depend not only on the mechanical properties of the polymer matrix, but also on the properties of interfacial regions between the particle surface and the matrix polymer.

Therefore, the chemical and physical modification of inorganic powder surfaces have been extensively studied. To improve the surface properties of carbon black and ultrafine inorganic particles, such as silica and titanium oxide, the surface grafting of polymers is effective [1-4]. Polymer-grafted carbon black and ultrafine particles can be dispersed easily in organic solvents,

and recrystallized from methanol. Trichloroacetyl isocyanate, $\text{Mo}(\text{CO})_6$ and 3-aminopropyltriethoxysilane obtained from Aldrich Chemical Co. Inc. were used without further purification. *N*-Isopropylacrylamide (NIPAM) and *N,N*-diethylacrylamide (DEAM) were obtained from Kojin Co. Ltd., Japan: NIPAM and DEAM were purified by distillation and recrystallization from acetone, respectively. Styrene (St), acrylic acid (AC), *N*-vinylcarbazole (NVC), methyl methacrylate (MMA), glycidyl methacrylate (GMA), and acrylamide (AAm) were used after ordinary purification. Toluene 2,4-diisocyanate (TDI) and tetrahydrofuran (THF) was distilled just before use.

Introduction of Azo Groups onto Carbon Black

The introduction of azo groups onto carbon black surface was achieved by the reaction of ACPA with isocyanate groups, which were introduced by the treatment of carbon black with TDI. The detailed procedures were described in the previous paper [5].

Introduction of Trichloroacetyl Groups onto Inorganic Particles

The introduction of trichloroacetyl groups onto the surface of silica and titanium oxide was achieved by the reaction of trichloroacetyl isocyanate with amino and alcoholic hydroxyl groups on these surfaces, respectively. A typical example was as follows. Into a flask, 5.0 g of inorganic particle, 1.0 g of trichloroacetyl isocyanate, and 150 ml of toluene were charged and the mixture was refluxed with stirring at 80°C for 8 h under nitrogen. After the reaction, the resulting particle was centrifuged at 10⁴ rpm and supernatant solution containing unreacted trichloroacetyl isocyanate was removed. The particle precipitated was dispersed in THF and centrifuged again. The procedures were repeated until no more trichloroacetyl isocyanate could be detected in the supernatant solution.

Graft Polymerization

Into a polymerization tube, 0.30 g of carbon black having azo groups and 10.0 ml of vinyl monomer were charged. When trichloroacetyl groups/ $\text{Mo}(\text{CO})_6$ initiating system was used, 0.10 g of inorganic particles having trichloroacetyl groups, 0.01 g of $\text{Mo}(\text{CO})_6$, and 10.0 ml of vinyl monomer were charged. When NVC was used as a monomer, the polymerization was carried out using 3.00 g of NVC and 10.0 ml of benzene as a solvent. The tube was cooled with a liquid nitrogen bath, thawed three times, and sealed under high vacuum. The polymerization was conducted at 70°C with shaking. After a definite time, the reaction mixture was poured into a large excess of methanol to precipitate the polymer-grafted particle and ungrafted polymer. The precipitate was filtered, washed with methanol, and dried in vacuo at 45°C. The conversion was calculated by the following Eqn 4.

$$\text{Conversion (\%)} = (A/B) \times 100 \quad (4)$$

where *A* is weight of total polymer formed (weight of precipitate minus ultrafine particle charged) and *B* is weight of monomer charged.

Percentage of Grafting and Grafting Efficiency

To separate the polymer-grafted carbon black and inorganic particles from the reaction mixture, the product was dispersed in good solvent of grafted polymer and the dispersion was centrifuged at

10⁴ rpm. The supernatant solution containing ungrafted polymer was removed and the particles precipitated was dispersed again and centrifuged. The procedures were repeated until no more polymer could be detected in the supernatant solution. The percentage of grafting and grafting efficiency were calculated by the following Eqns 5 and 6.

$$\text{Grafting (\%)} = (C/D) \times 100 \quad (5)$$

$$\text{Grafting efficiency (\%)} = (C/E) \times 100 \quad (6)$$

where C is weight of polymer grafted, D is weight of carbon black and inorganic particle, and E is weight of total polymer formed. The weight of polymer grafted onto particle, C , was determined from the weight increment of the particle after graft polymerization.

Stability of Polymer-Grafted Ultrafine Particles

Polymer-grafted carbon black and inorganic particle (0.10 g) were dispersed in 100 ml of good solvent for grafted polymer and allowed to stand at room temperature. After a definite time, 5.0 ml of dispersion liquid was taken out with a pipet and these particle dispersed was determined. The stability of dispersion was estimated by the following Eqn 7

$$\text{Particle dispersed (\%)} = (F/G) \times 100 \quad (7)$$

where F is weight of particle dispersed after standing and G is weight of particle dispersed before standing.

RESULTS AND DISCUSSION

Graft Polymerization Initiated by Azo Groups on Carbon Black

The introduction of azo groups onto carbon black surface was achieved by the reaction of ACPA with isocyanate groups on the surface, which were introduced onto the surface by the reaction of carboxyl and phenolic hydroxyl groups on the surface with TDI.

The introduction of ACPA groups onto carbon black surface was confirmed by DSC curves of TDI-treated and TDI-ACPA-treated carbon black. TDI-ACPA-treated carbon black shows exothermic peak at about 110-120°C, but TDI-treated carbon black shows no peaks below 150°C. This suggests the introduction of azo groups onto the surface.

The amount of azo groups introduced onto the surface was estimated to be 0.33 mmol/g by elemental (nitrogen) analysis.

The result indicate that about 50% of surface functional groups are converted to azo groups. The carbon black having azo groups was abbreviated as CB-Azo.

The polymerization of MMA was carried out in the presence of CB-Azo at 70°C and the initiating activities of the azo groups on the surface were examined.

Table 1: Initiating ability of azo groups introduced onto carbon black surface

Run	Carbon black	Conversion (%)	Grafting (%)
1	None	0.7	-
2	Untreated	0	-
3	ACPA-adsorbed	0	-
4	CB-Azo	4.6	40.0

CB-Azo, 0.30 g; MMA, 10.0 ml; 70°C; 6 h.

The results are summarized in Table 1. As shown in Table 1, thermal polymerization of MMA proceeded even in the absence of initiator, although the rate of the polymerization was small (Run 1). In the presence of untreated carbon black (Run 2) and ACPA-adsorbed carbon black (Run 3), the initiation of the polymerization and grafting of polyMMA onto the surface were hardly observed. On the contrary, the polymerization of MMA was successfully initiated by CB-Azo to give polyMMA-grafted carbon black (Run 4).

Table 2 shows the results of the graft polymerization of various vinyl monomers in the presence of CB-Azo.

It became apparent that CB-Azo has an ability to initiate the radical graft polymerization of vinyl monomers to give the corresponding polymer-grafted carbon black.

These results indicate that, in the presence of CB-Azo, the polymerization is considered to be initiated by the radicals formed by the decomposition of the azo groups and grafted polymer chains are propagated from the carbon black surface.

Figure 1 shows the relationship between conversion and grafting efficiency in the polymerization of MMA initiated by CB-Azo. It is interesting to note that the grafting efficiency is very high, i.e., about 50%, at the initial stage of the polymerization, but quickly decreased to few percent with progress of the polymerization.

These results are explained as follows: the polymerization of MMA is initiated by both radicals on the carbon black surface and initiator fragments formed by the thermal decomposition of azo groups on the surface. The radicals formed on the carbon black surface initiate the graft polymerization and grafted chains are propagated from the surface (Eqn 1). On the other hand, the fragment radicals initiate the polymerization to produce ungrafted polymer (Eqn 2). Therefore, in the initial stage of the polymerization, grafting efficiency become to be about 50%. However, the propagation of grafted polymer from the surface radicals is considered to be gradually inhibited by neighboring grafted polymers and the formation of ungrafted polymer becomes to preferential reaction in the middle and last stage of the polymerization, which decreased the grafting efficiency.

Table 2: Graft polymerization of various vinyl monomers initiated by CB-Azo

Vinyl monomer	Conversion (%)	Grafting (%)
Styrene	2.0	28.5
AAm	1.7	24.0
MMA	4.7	40.0
Acrylic acid	6.2	64.8
NIPAM	5.6	35.9
Styrene / Acrylic acid	13.1	76.2

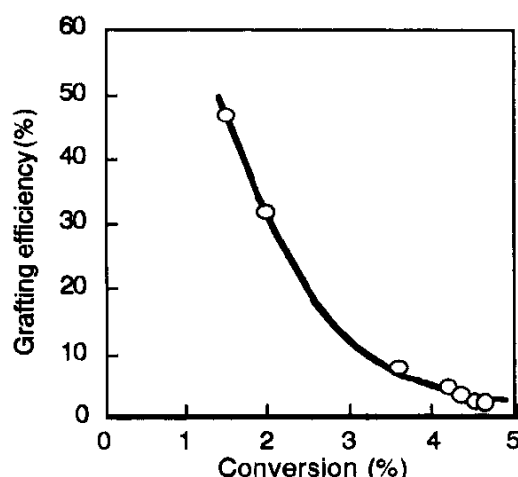


Fig. 1: Relationship between grafting efficiency and MMA conversion in the polymerization by CB-Azo

Table 3: Polymerization of MMA initiated by silica / Mo(CO)₆ systems

Run	Silica	Mo(CO) ₆ (g)	Conversion (%)	Grafting (%)
1	Untreated	-	0	-
2	None	0.01	0	-
3	Untreated	0.01	0	-
4	Silica-R-COCCl ₃	-	0	-
5	Silica-R-COCCl ₃	0.01	7.0	393.8

Silica, 0.10 g; MMA, 10.0 ml; 70 °C; 30 min.

Graft Polymerization Initiated by the System Consisting of Trichloroacetyl Groups on Inorganic Particle and Mo(CO)₆

Bamford and his coworkers have reported that the system consisting of haloalkyl compounds and transition metal carbonyl derivatives, such as Mo(CO)₆, has an ability to initiate the radical polymerization of vinyl monomers [6]. The grafting of vinyl polymers onto glass beads (particle size, 10-50 μm) initiated by the system consisting of trichloroacetyl groups on the surface has been reported by Eastmond et al. [7]. Therefore, the grafting of polymers onto ultrafine silica and titanium oxide by the polymerization initiated by system consisting of trichloroacetyl groups on the surface and Mo(CO)₆ was examined.

The introduction of trichloroacetyl groups onto ultrafine silica surface was achieved by the reaction of trichloroacetyl isocyanate with amino groups, which were introduced by the reaction with 3-aminopropyltriethoxysilane. On the other hand, trichloroacetyl groups were introduced onto titanium oxide modified with alcoholic hydroxyl groups by the direct reaction of trichloroacetyl isocyanate with hydroxyl groups. The amount of trichloroacetyl groups introduced onto ultrafine silica and titanium oxide was determined to be 0.59 mmol/g and 0.09 mmol/g, respectively. The ultrafine silica and titanium oxide having trichloro-acetyl groups were abbreviated as Silica-R-COCCl₃ and TiO₂-R-COCCl₃, respectively.

The polymerization of MMA initiated by Silica-R-COCCl₃/Mo(CO)₆ system was investigated. The results are shown in Table 3. No polymerization of MMA was initiated in the presence of

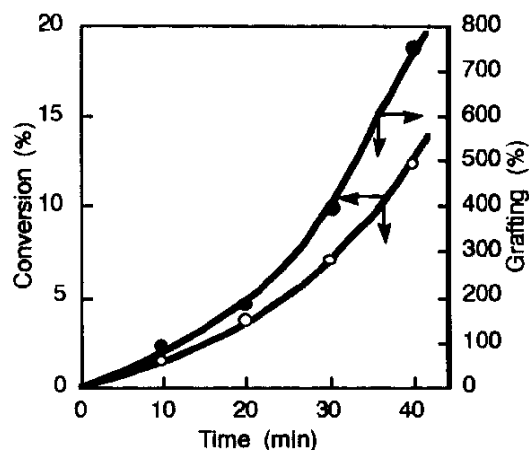


Fig. 2: Polymerization of MMA initiated by Silica-R-COCCl₃/Mo(CO)₆ system. Silica-R-COCCl₃, 0.10 g; Mo(CO)₆, 0.01 g; MMA, 10.0 ml; 70 °C

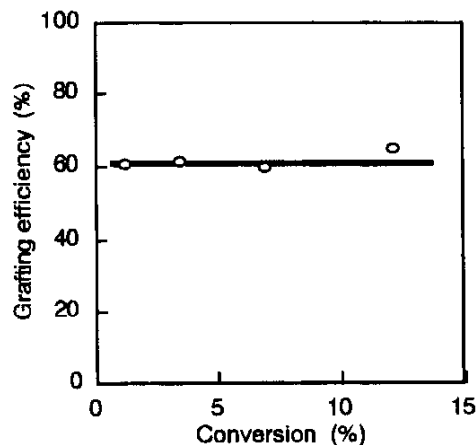


Fig. 3: Relationship between conversion and grafting efficiency in the polymerization shown in Fig. 2

Table 4: Graft polymerization of vinyl monomers initiated by Silica-R-COCCl₃ / Mo(CO)₆ and TiO₂-R-COCCl₃ / Mo(CO)₆ system

Inorganic Particle	Monomer	Time (min)	Conversion (%)	Grafting (%)
Silica-R-COCCl ₃	Styrene	120	9.0	150.5
	MMA	40	12.7	741.4
	NVC	120	78.5	35.4
	NIPAM	40	15.4	99.5
TiO ₂ -R-COCCl ₃	Styrene	60	4.4	39.2
	MMA	30	10.8	302.7
	NIPAM	30	3.9	50.1
	DEAM	6	7.6	295.3

Particle-R-COCCl₃, 0.10 g; Mo(CO)₆, 0.01 g; monomer, 10.0 ml; 70 °C.

untreated silica (Run 1). Molybdenum hexacarbonyl (Run 2) and Silica-R-COCCl₃ (Run 4) alone have no ability to initiate the polymerization. In addition, no polymerization was initiated by the system consisting of untreated silica and Mo(CO)₆ (Run 3). On the contrary, the polymerization of MMA was successfully initiated in the coexistence of Silica-R-COCCl₃ and Mo(CO)₆ and polyMMA was grafted onto the surface (Run 5).

Figure 2 shows the time-conversion and time-percentage of grafting curves in the graft polymerization of MMA initiated by Silica-R-COCCl₃/Mo(CO)₆ system at 70°C. It was found that conversion and percentage of grafting increase with progress of the polymerization and percentage of grafting exceeded 700% after 40 min. The value was extremely higher than that obtained from the graft polymerization initiated by azo groups introduced onto carbon black (as shown in Table 2) and ultrafine silica surface [8].

The relationship between grafting efficiency and conversion in the graft polymerization was shown in Figure 3. It is interesting to note that the grafting efficiency was very high, about 60% and scarcely decreased even in the last stage of the polymerization. As mentioned above, the grafting efficiency in the graft polymerization initiated by azo groups on carbon black is about 50% at the initial stage of the polymerization, but immediately decreases to few percent at the middle and last stage of the polymerization.

This indicates that in the initiating system consisting of trichloroacetyl groups and Mo(CO)₆, the propagation of polymer chain from the surface was preferentially proceeded because of no formation of initiator fragments which produce ungrafted polymer (Eq.3). The formation of ungrafted polymer is considered to be based on the chain transfer reaction of growing polymer radicals from the surface.

Table 4 shows the results of the graft polymerization of various monomers onto ultrafine silica and titanium oxide initiated by the system consisting of surface trichloroacetyl groups and Mo(CO)₆. It was found that the graft polymerization of vinyl monomers is successfully initiated by the systems and the corresponding polymers are effectively grafted onto these surfaces.

Based on the above results, it is concluded that the system consisting of silica and titanium oxide

having trichloroacetyl groups and $\text{Mo}(\text{CO})_6$ has an ability to initiate the polymerization of vinyl monomers to give the corresponding polymer-grafted particles with high percentage of grafting. In the polymerization, grafted polymer is considered to propagate from the surface radicals formed by the interaction of surface trichloroacetyl groups with $\text{Mo}(\text{CO})_6$.

Dispersibility of Polymer-Grafted Particles

Figure 4 shows the comparison of dispersibility of polyAAm-grafted carbon black in water with that of polyAAm-adsorbed carbon black and untreated carbon black. Untreated carbon black completely precipitated within 1 day. The stability of the carbon black dispersion was scarcely improved by adsorption of polyAAm. On the contrary, polyAAm-grafted carbon black gave a stable colloidal dispersion in water, which is good solvent for grafted polyAAm. About 80% of carbon black remained dispersed in water even after 30 days.

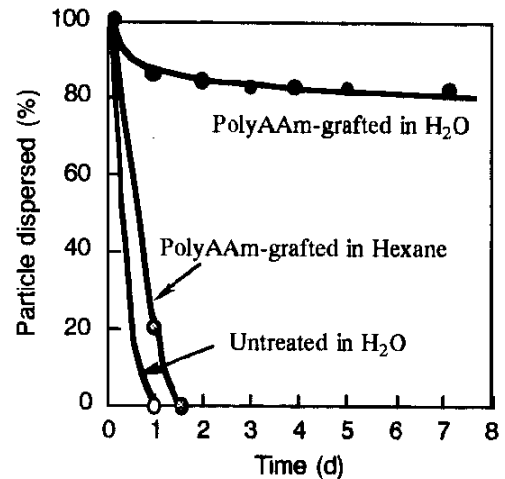


Fig. 4: Dispersibility of polyAAm-grafted silica in water and hexane

However, even the polyAAm-grafted carbon black precipitated in hexane, which is non solvent of polyAAm as shown in Figure 4. This suggests that polymer chains grafted onto carbon black lose the ability to interfere with the aggregation of carbon black when the carbon black is dispersed in a poor solvent for the grafted polymer.

Accordingly, it seems that grafted polymer chains spread out from the carbon black surface in a good solvent for the grafted polymer, but shrink onto the surface in a poor solvent.

Mechanical Properties of Films Compounded with Polymer-Grafted Carbon Black

The tensile strength of polystyrene films compounded with polystyrene-grafted carbon black was measured and compared with that of films compounded with untreated carbon black. The results are summarized in Table 5.

Table 5: Tensile strength of polystyrene films compounded with polystyrene-grafted carbon black

Carbon black	Grafting (%)	Carbon black content (%)	Tensile strength (N/mm ²)
None	-	-	26.2
Untreated	-	10	7.2
Untreated	-	20	5.3
Polystyrene-grafted	9.5	10	9.3
	9.5	20	7.4
	28.5	10	22.5
	28.5	20	19.5

When untreated carbon black was compounded into polystyrene films, the tensile strength markedly decreased with increasing content of carbon black. This may be due to the fact that untreated carbon black particles form aggregates in the polystyrene matrix. Although polystyrene-grafted carbon black with a low percentage of grafting dispersed in polystyrene film uniformly, it failed to prevent the decrease of the tensile strength of the film.

On the contrary, this large decrease of tensile strength was not observed, even at high carbon black concentrations when the polystyrene film was compounded with polystyrene-grafted carbon black with 28.5% grafting. This is probably the case because the polymer-grafted carbon black particles disperse uniformly in polystyrene matrix, and the polystyrene grafted on the carbon black gives the carbon black higher compatibility with, and adhesion to, the matrix.

CONCLUSIONS

1. The radical graft polymerization of various vinyl monomers was successfully initiated by azo groups introduced onto carbon black surface and the corresponding polymers were grafted onto the surface.
2. The system consisting of $\text{Mo}(\text{CO})_6$ and trichloroacetyl groups introduced onto inorganic particle surface, such as ultrafine silica and titanium oxide, has an ability to initiate the radical graft polymerization of vinyl monomers to give the corresponding polymer-grafted particles.
3. Polymer-grafted carbon black gave a stable colloidal dispersion in solvents for grafted polymer chain.
4. The decrease of tensile strength was scarcely observed, even at high carbon black concentrations when the polystyrene film was compounded with polystyrene-grafted carbon black with 28.5% grafting.

ACKNOWLEDGEMENTS

The authors wish to Wako Pure Chemical Ind. Co., Ltd. for providing ACPA, to Kojin Co., Ltd. for providing NIPAM and DEAM, and Shiseido Co., Ltd. for providing titanium oxide modified with alcoholic hydroxyl groups.

REFERENCES

1. Tsubokawa, N., "Functionalization of Carbon Black by Surface Grafting of Polymers", *Prog. Polym. Sci.*, Vol.17, 1992, 417-470.
2. Tsubokawa, N., "Surface Modification by Polymer Grafting", *Handbook of Carbon Black*, Carbon Black Association, Japan, Ed., Carbon Black Association, Japan, Tokyo, 1995, pp.167-175.
3. Tsubokawa, N., "Functionalization of Inorganic Powder Surface by the Grafting of Polymers", *Kobunshi (High Polymers, Japan)*, Vol.45, 1996, 412-417.

4. Fujiki, K., Tsubokawa, N. and Sone, Y., "Radical Grafting from Carbon Black. Graft Polymerization of Vinyl Monomers Initiated by Azo Groups Introduced onto Carbon Black Surface", *Polym. J.*, Vol.22, 1990, 661-670.
5. Tsubokawa, N., "Carbon Black (Graft Copolymer)", *Polymeric Materials Encyclopedia (Second Volume)*, Salamone, J.C., Ed., CRC Press, New York, 1996, pp.941-946.
6. Bamford, C.H., Eastmond, G.C. and Maltman, W.R., "Mechanism of Free Radical Formation by $\text{Mo}(\text{CO})_6 + \text{CCl}_4$ ", *Trans Faraday Soc.*, Vol.62, 1966, 2531-2543.
7. Eastmond, G.C., Nguyen-Huu, C. and Pirett, W.H., "Graft Polymerization from Glass Surfaces", *Polymer*, Vol.21, 1980, 598-603.
8. Tsubokawa, N., Kogure, A., Maruyama, K., Sone, Y. and Shimomura, M., "Graft Polymerization of Vinyl Monomers from Inorganic Ultrafine Particles Initiated by Azo Groups Introduced onto the Surface", *Polym. J.*, Vol.22, 1990, 827-833.
9. Heskins, M. and Guillet, J.E., "Solution Properties of Poly(*N*-isopropylacrylamide)", *J. Macromol. Sci. -Chem.*, Vol.A2, 1968, 1441-1455.

ELASTOPLASTIC FINITE-ELEMENT ANALYSIS OF HEAT-SEALED AREA IN LAMINATED PLASTIC FILM USED FOR LIQUID PACKAGING BAGS UNDER DIFFERENT TEMPERATURES

E. Umezaki¹, Y. Kubota¹, A. Shimamoto² and K. Futase³

¹ *Department of Mechanical Engineering, Nippon Institute of Technology
4-1 Gakuendai, Miyashiro, Saitama 345, Japan*

² *Department of Mechanical Engineering, Saitama Institute of Technology
1690 Fusaiji, Okabe, Saitama 369-02, Japan*

³ *Taisei Lamick Co. Ltd., 873-1 Shimoohsaki, Shiraoka, Saitama 349-02, Japan*

SUMMARY: In this study, stress and strain on a cross section of a heat-sealed area in laminated plastic film used for liquid packaging bags under different temperatures were analyzed using the elastoplastic finite-element method upon application of static load to dynamically investigate the cause of bursting of the bags. Prior to the analysis, Young's moduli, Poisson's ratios and stress-strain curves of the components constituting the film, which were necessary in the analysis, were measured using a grid method. In addition, the force acting on an area was determined by measuring the pressure in the bags. The shapes of cross sections obtained by the analysis of their material properties and the force were in good agreement with those obtained by cutting frozen bags under compressive loads. As a result, characteristic distributions of equivalent stress and strain, which depend on temperature, were found in the area.

KEYWORDS: finite element analysis, stress, strain, liquid packaging bag, plastic film, grid method, heat sealing

INTRODUCTION

The use of plastic containers for packing foods is steadily increasing recently. However, since the majority of these containers are not recycled but used in the one-way mode, plastic garbage has become a serious environmental problem. Under such circumstances, the reduction of volume and thickness of these wastes is required to minimize their total quantity. Attracting attention in this respect are flexible packages which not only facilitate reduction of volume and thickness but can also be folded into compact volumes for easy recovery. Particularly advantageous among them are liquid packages made of laminated film in which the quantity of plastic used can be reduced to 1/5-1/10 that used for hard packages.

However, the disadvantage is that, since a thin laminated film is used, it can readily cause possible bursting of packages due to temperature changes or shock during transportation. To overcome this disadvantage, knowledge of the dynamic mechanism of bursting is necessary.

Until now, very little has been known about this mechanism, and there have been only a few experimental studies on bursting[1]-[3].

In this study, stress and strain on a cross section of a heat-sealed area, at which most bursting occurs, in a laminated plastic film used for liquid packaging bags under different temperatures were analyzed using the elastoplastic finite-element method upon application of static load, to dynamically investigate the cause of bursting of the bags. Prior to the analysis, Young's moduli, Poisson's ratios and stress-strain curves of the components constituting the film, which were necessary in the analysis, were measured in tension tests using a grid method. In addition, the force acting on an area was determined by measuring the pressure in the bags. The shape of the cross section obtained by the analysis of their material properties and force was compared with that obtained by cutting frozen bags under compressive loads. The analytical results for equivalent stress and strain are discussed.

LIQUID PACKAGING BAG

Structure of Laminated Film

Figure 1 shows the liquid packaging bags used in this study, which were made of laminated film and contained about 17ml of water. Three sides of these bags were heat-sealed by an automatic packaging machine (NT-Dangan, Nippon Seiki) under the same sealing conditions, which were determined based on the plastic film test (JIS-Z-1707-1975, Japanese Standards Association) for food packages.

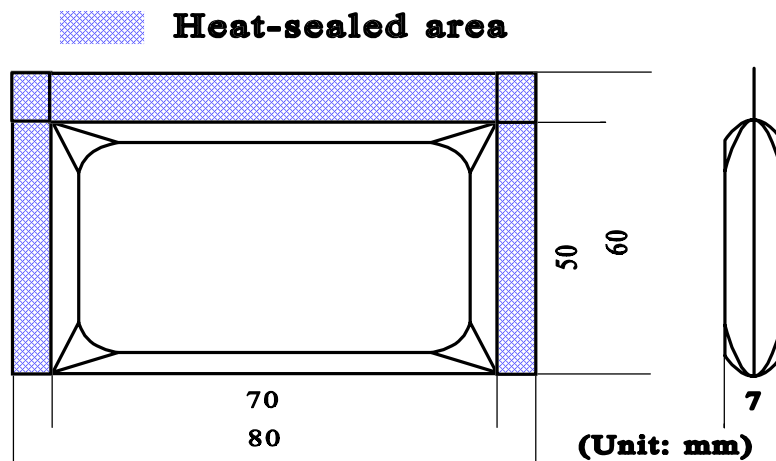


Fig. 1: Shape and dimensions of liquid

The laminated film consisted of nylon, NY, (15 μ m in thickness), polyethylene, PE, (25 μ m in thickness) and ethylene vinylacetate copolymer, EVA, (25 μ m in thickness) used in common, as shown in Fig.2. Two films, PE and EVA, were combined into one film, called a seal layer, PE-EVA, during heat sealing.

Shape of Cross Section of Heat-Sealed Area

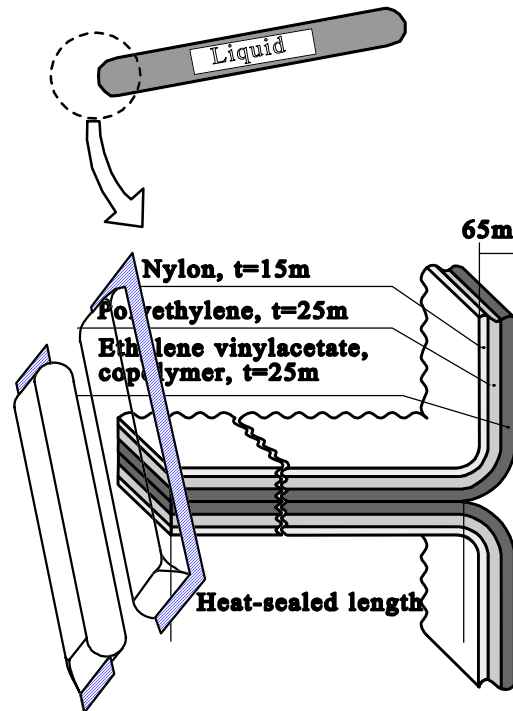


Fig. 2: Cross section of laminated plastic film used for liquid packaging bag.

Liquid packaging bags were frozen at a temperature of -20°C in a thermostatic oven in order to investigate the shape of the cross section of the heat-sealed area of the bags under compressive loads, F , between 0 and 1kN, as shown in Fig.3. The frozen bags were cut in the longitudinal direction, as shown in Fig.3. The cross sections were observed using a microscope before thawing.

Figure 4 shows two examples of the sections observed at loads, F , of 0N and 400N. Figure 4(a) was used to model a cross section of the heat-sealed area of the bags for the finite-element analysis.

MATERIAL PROPERTIES OF LAMINATED FILM

Young's moduli, E , Poisson's ratios, ν , and stress-strain curves of NY and PE-EVA, which were necessary in the finite-element analysis, were measured in tension tests using a grid method. Generally, laminated plastic film used for liquid packaging bags is made by together rolling NY film, which is formed beforehand, and PE and EVA films, which are formed from powder materials by heating and extraction in the manufacturing process of the laminated film. NY, PE and EVA films are difficult to completely separate from the laminated film. In this study, NY and PE-EVA films were separated from the laminated film by using ethyl acetate solution immediately after the manufacture of the laminated film.

Figure 5 shows the shape and dimensions of the specimens, which were based on JIS-K-6734, used for obtaining E , ν and stress-strain curves of NY and PE-EVA. Cross grids with 2mm

pitch were printed on the surface of the specimens using a simple printing technique, as shown in Fig.6. The specimens were set in an electric furnace equipped with a universal test machine (RTM-1T, Orientech) with 10kN capacity, as shown in Fig.7, and subjected to tensile loads at a rate of 5mm/min at temperatures of -10, 0, 20 and 40°C.

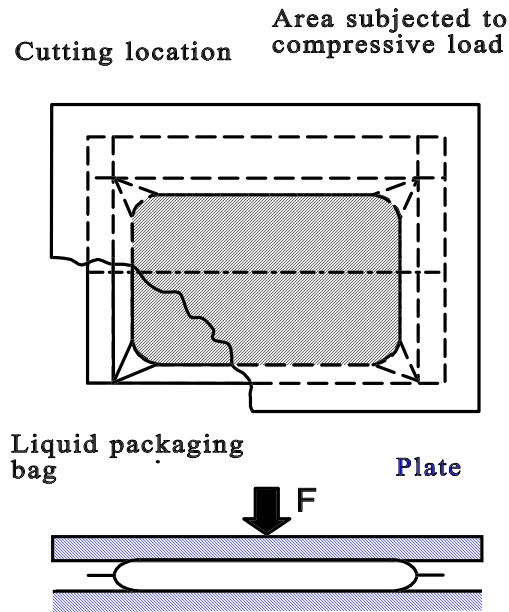


Fig. 3: Compression of liquid packaging bag used to investigate cross section shape of heat-sealed area.

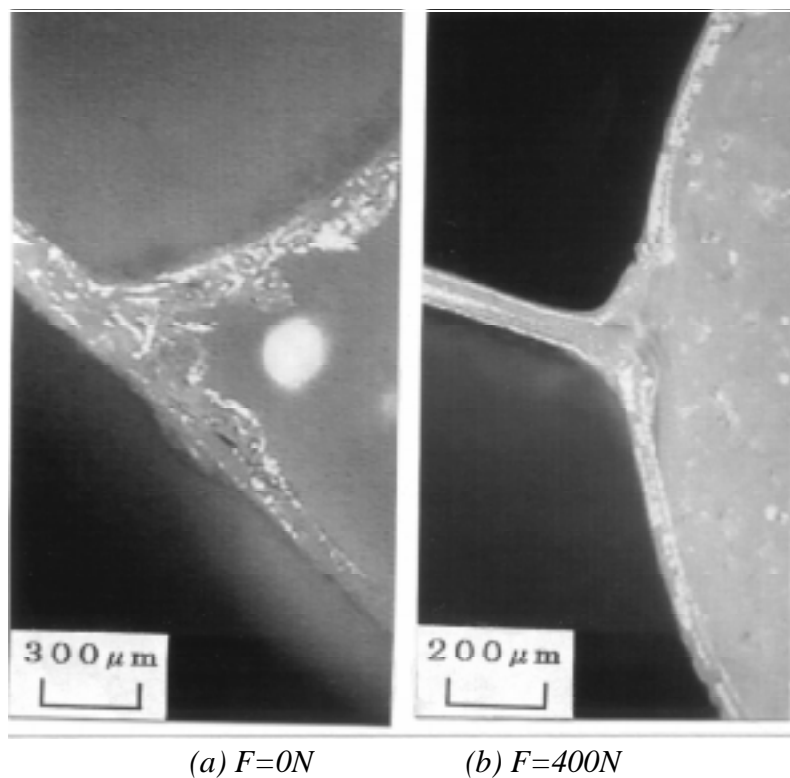


Fig. 4: Cross section of heat-sealed area cut from bags frozen under compression load, F .

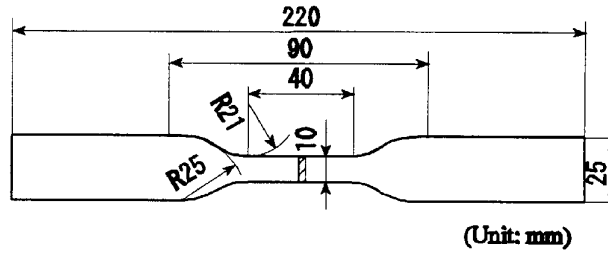


Fig. 5: Specimen for measuring material properties

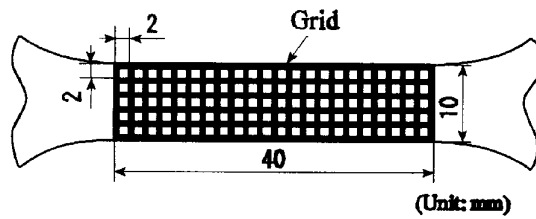


Fig. 6: Grid printed on specimen surface.

The images of the specimen surfaces with the grids were recorded using an 8mm video camera via a CCD camera, in tension tests, as shown in Fig.7. The amounts of tensile loads at which the images were recorded were read off from a load counter photographed using another 8mm video camera.

The stress, σ , was obtained by dividing axial load by the initial cross-sectional area of the film specimen. The longitudinal and lateral strains, ϵ_L and ϵ_T , which were measured in the directions parallel and normal to tensile load, were obtained by measuring the deformations, δ_L and δ_T , in the original lengths, D_L and D_T , between two line segments, which were selected from the line segments forming grids drawn on the specimen surface, and dividing δ_L and δ_T by D_L and D_T , respectively.

In order to measure δ_L and δ_T , images output by a video printer were used. δ_L and δ_T in the range of elasticity were difficult to accurately measure because they were small. Hence, images enlarged 400 times by a digital duplicating machine were used.

Young's modulus, E , is defined as the ratio of σ to ϵ_L . Poisson's ratio, ν , was obtained from the ratio of ϵ_T to ϵ_L . Young's moduli, E , and Poisson's ratios, ν , obtained are given in Table 1. Figure 8 shows the stress-strain curves. Young's moduli of all films decreased and Poisson's ratios increased as temperature increased.

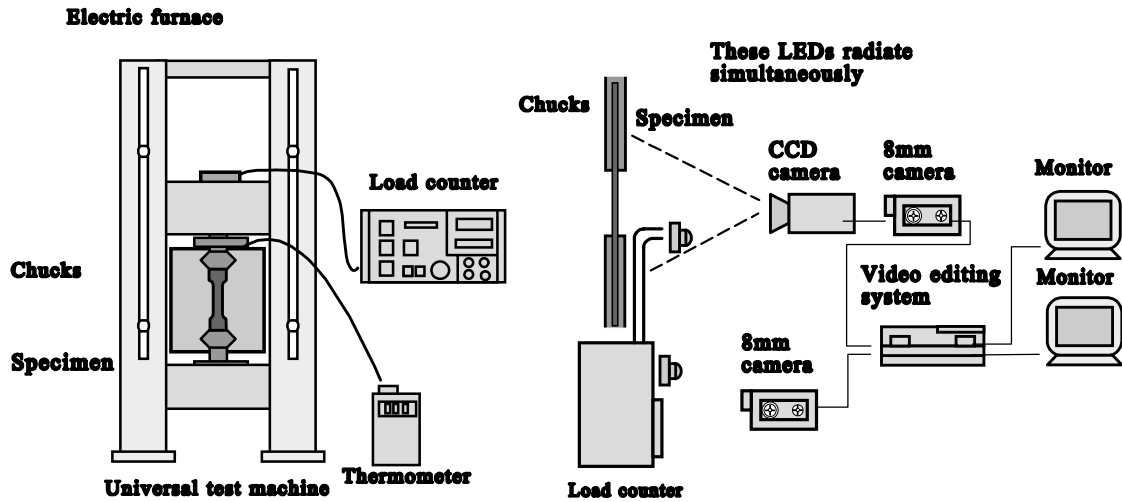
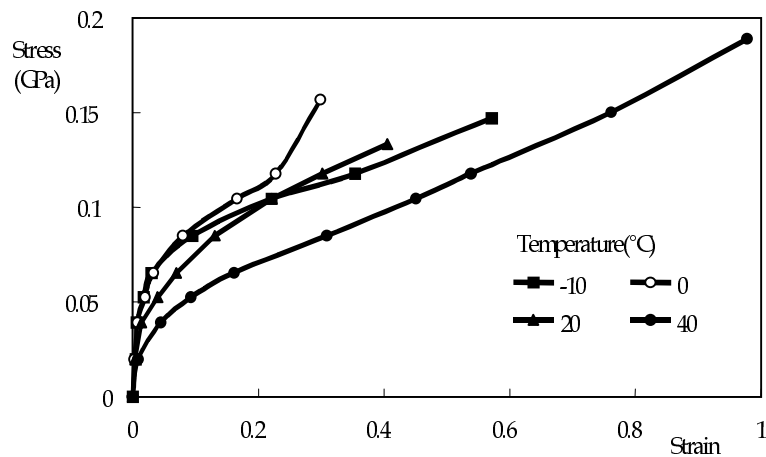


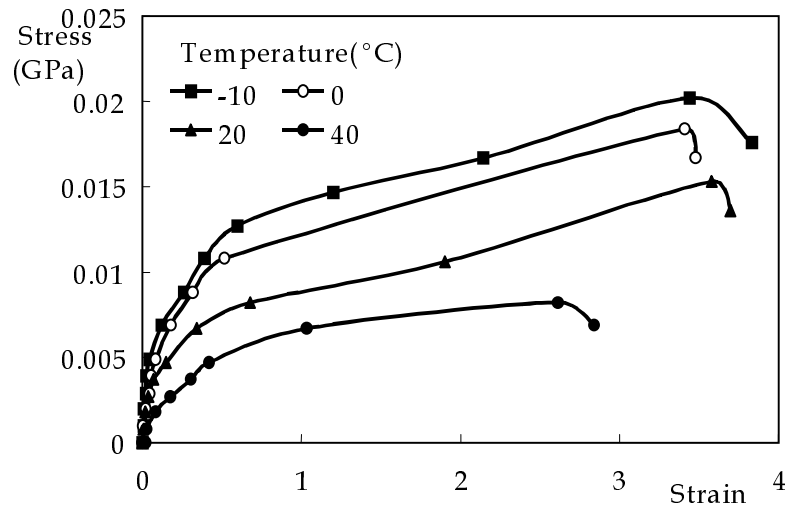
Fig. 7: Setup for measuring material properties

Table 1: Mechanical properties of NY and PE-EVA

Young's modulus, E (GPa)				
Component	-10°C	0°C	20°C	40°C
NY	6.75	4.00	4.06	1.92
PE-EVA	0.122	0.115	0.092	0.044
Poisson's ratio, ν				
Component	-10°C	0°C	20°C	40°C
NY	0.21	0.36	0.39	0.39
PE-EVA	0.21	0.34	0.36	0.42



(a) NY



(b) PE-EVA

Fig.8: Stress-strain curves

FORCE ACTING ON HEAT-SEALED AREA

The force acting on a heat-sealed area of liquid package bags, which is necessary in the finite-element analysis, was estimated from pressure, p , measured in the bags under static compression, F , in the manner similar to that shown in Fig.3. The internal pressure was measured using a pressure gage (PS-2KA, Kyowa). The gage was wrapped in polyethylene film to keep out the moisture contained in liquid packaging bags and was inserted into bags from a heat-sealed area which was partly opened. Then, the opened area was heat-sealed, using a simple heat-sealing equipment, to prevent the leakage of water.

The electrical signal, voltage, obtained from the gage was measured using a digital oscilloscope via a dynamic strain meter. The pressure was determined from the voltage using the relationship between the voltage obtained from the same gage under a given pressure in a pressure container with a pressure regulator and the pressure.

Consequently, the internal pressure, p , was proportional to the external load, F , as expressed by

$$p = F/A , \tag{1}$$

where A is the area in which the load acts, as shown in Fig.3. In this study, an area of $A=2709\text{mm}^2$ was used, which was obtained experimentally.

Figure 9 shows an example of the relationships among F , p and tension, T , acting on a cross section of film, which is encountered over a wide range of p , except in the initial stage at

which p is low. From this figure, T was found to be proportional to p . Hence, T is expressed by

$$T = rbp, \quad (2)$$

where r is the radius of parts not subjected to F and b is the depth of the bag.

In this study, $r=3.5\text{mm}$, which was determined in experiments described in the above section, and $b=10\text{mm}$ were used. Hence, the relationship between T and p used in the finite-element analysis was expressed by $T(\text{N})=35p(\text{MPa})$.

The mean bursting load for 20 bags was about 1kN.

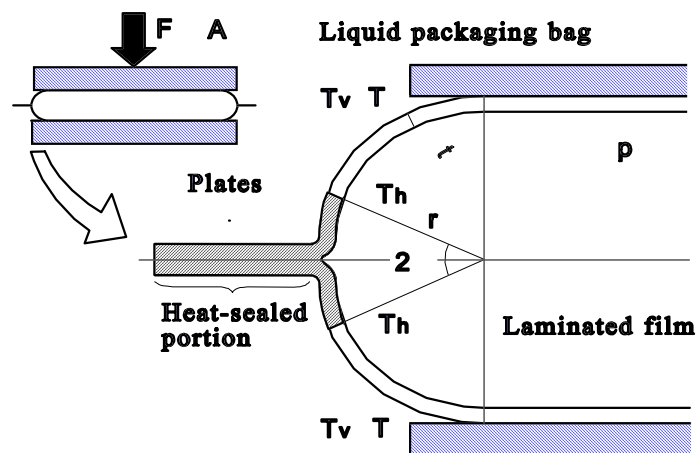


Fig. 9: Force acting on heat-sealed area

STRESS AND STRAIN IN HEAT-SEALED AREA

To analyze stress and strain in the heat-sealed area under static load, the elastoplastic finite-element method was used. MARC was used as the analytical software.

The models of packaging bags used for this analysis were approximately Y-shaped under the no-load condition, as shown in Fig.10. The shape of the models was determined with reference to cross sections of heat-sealed areas of the bags under the no-load condition, as shown in Fig.4(a). Only the upper half was used because the models showed symmetry between the upper and lower halves. At the midpoint between points C and D , only the displacement in the x direction, u , was fixed, and between points A and B , only the displacement in the y direction, v , was fixed. In order to keep line segment $C-D$ at the load points straight, a material with Young's modulus of 400GPa and Poisson's ratio of 0.3 was used for elements in the neighborhood of line $C-D$. Figure 11 shows a typical mesh in which plane strain elements were used.

Incremental loading was used for this analysis. In this analysis, an incremental load, ΔT , of 0.09N ($\Delta\sigma_{ap}=0.14\text{MPa}$) was applied from $T_{min}=0\text{N}$ to $T_{max}=18\text{N}$, which was determined from

Eqns 1 and 2 with reference to the mean burst load, as described in the above section. From Eqn 2, the incremental pressure, Δp , was given as $\Delta p(\text{MPa}) = \Delta T / rb = \Delta T(\text{N}) / 35$.

Failure, which was defined as when the maximum stress or strain in the model became equal to that at the fracture point on the strain-stress curve of NY or PE-EVA, at temperatures of -10, 0, 20 and 40°C occurred at $\sigma_{ap} = 20.6, 15.5, 12.2$ and 7.0 MPa. The strength of the bags under static load decreased as the temperature increased. The strength at 40°C was about one-third and half of those at -10°C and 20°C, respectively.

Figure 12 shows the equivalent stresses, σ_{eq} , at temperatures of -10, 0, 20 and 40°C under an applied load, σ_{ap} , of 7.0MPa. In this figure, σ_{eq} is shown on models deformed by σ_{ap} . The black regions were assigned values below $\sigma_{eq} = 7\text{MPa}$ and the white ones, above $\sigma_{eq} = 7\text{MPa}$. The color of the regions changes from black to white as the value of σ_{eq} increases from 7MPa to 70MPa.

The larger stresses were obtained at the concave part in NY and at point B, shown in Fig.10, in PE-EVA. This indicates that most of the applied load was transmitted from NY to PE-EVA near point B. The stress at point B, which was considered as the most important one from the fact that the failure occurred near this point in experiments[2], decreased as the temperature increased.

Figures 13, 14 and 15 show the equivalent strains, ϵ_{eq} , under applied loads, σ_{ap} , at temperatures of -10, 20 and 40°C, respectively. Figure 16 shows ϵ_{eq} at temperatures of -10, 0, 20 and 40°C under $\sigma_{ap} = 7.0\text{MPa}$. In these figures, ϵ_{eq} is shown on models deformed by ϵ_{ap} . The black regions are assigned values below $\epsilon_{eq} = 0.1$ and the white ones, above $\epsilon_{eq} = 0.1$, in which the plastic zones in NY and PE-EVA were obtained.

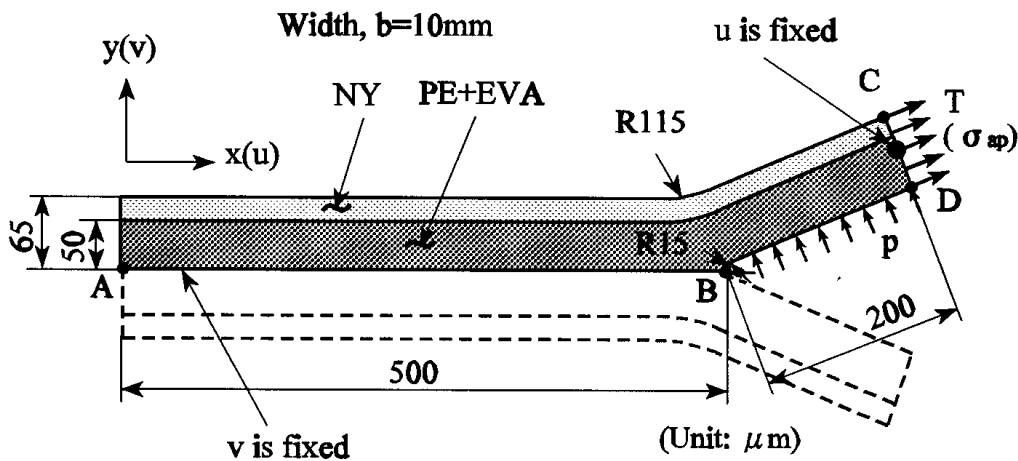


Fig.10: Model used for finite-element analysis

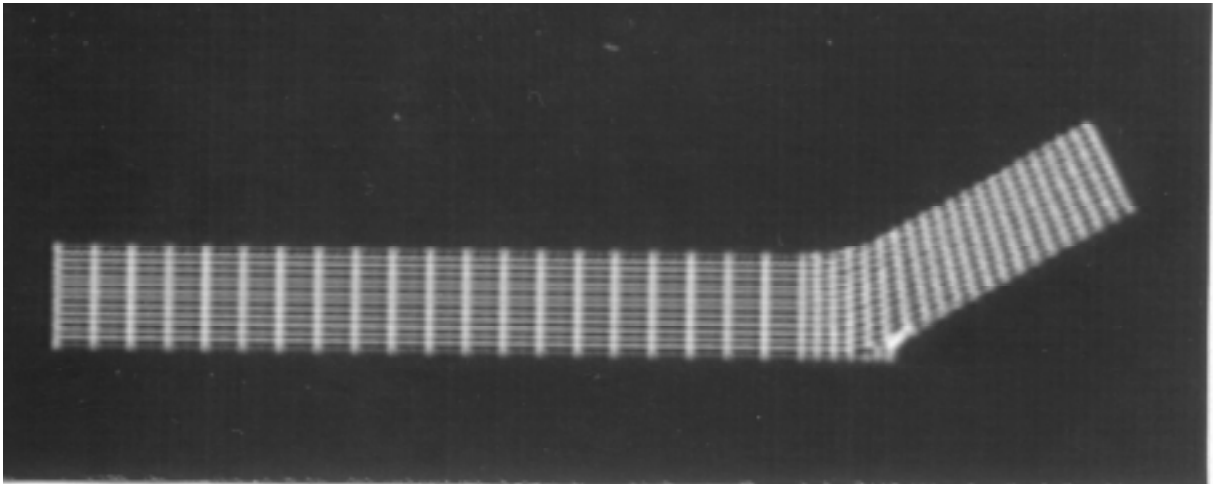


Fig.11: Typical mesh: 528 nodes, 584 elements

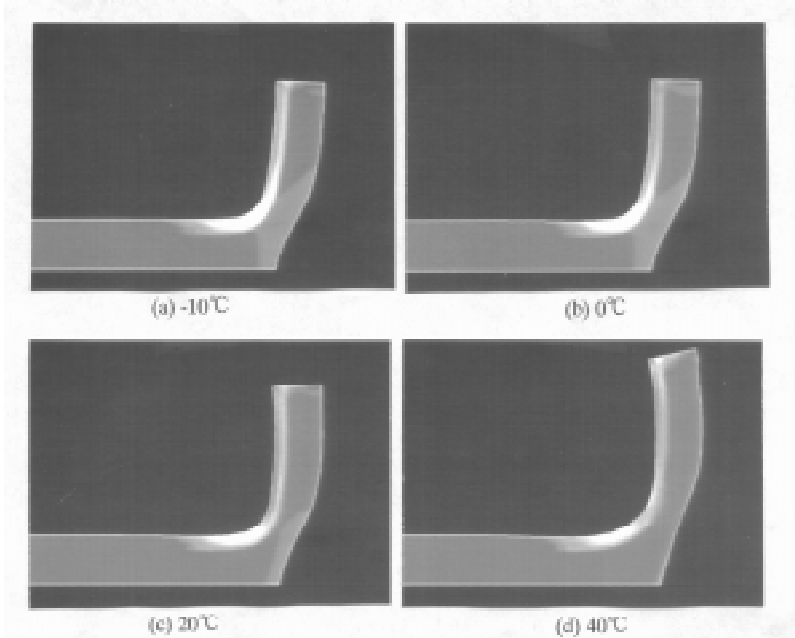


Fig.12: Effects of temperature on equivalent stress under $\sigma_{ap} = 7.0\text{MPa}$

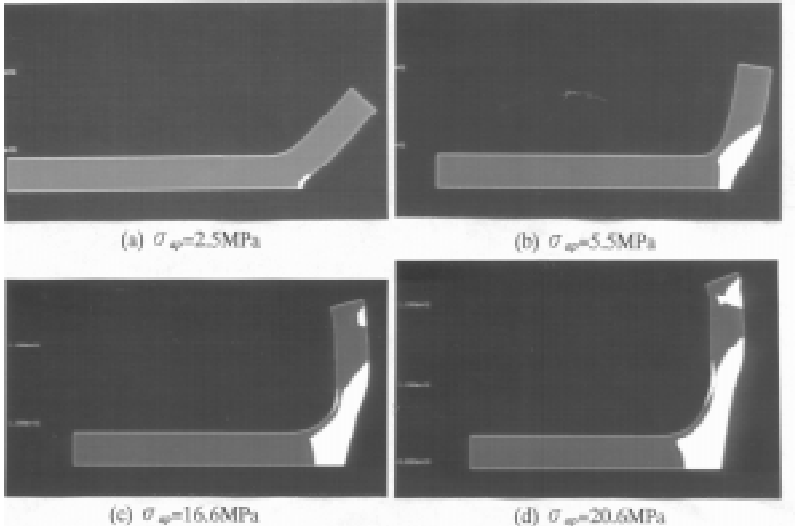
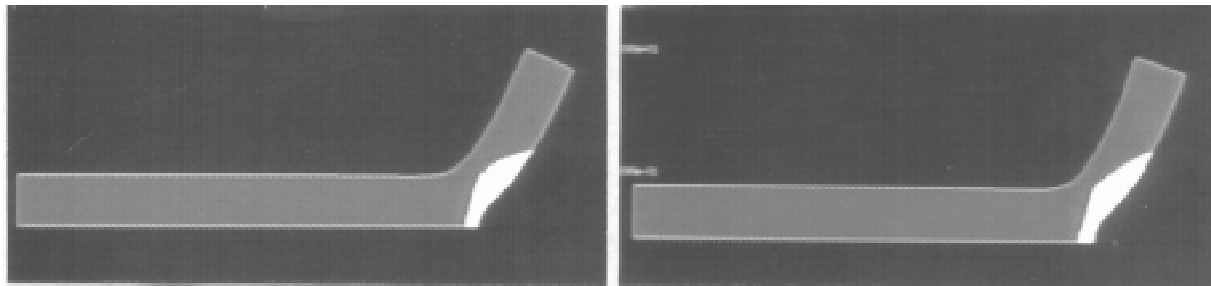


Fig.13: Effects of applied load, σ_{ap} , on equivalent strain at -10°C

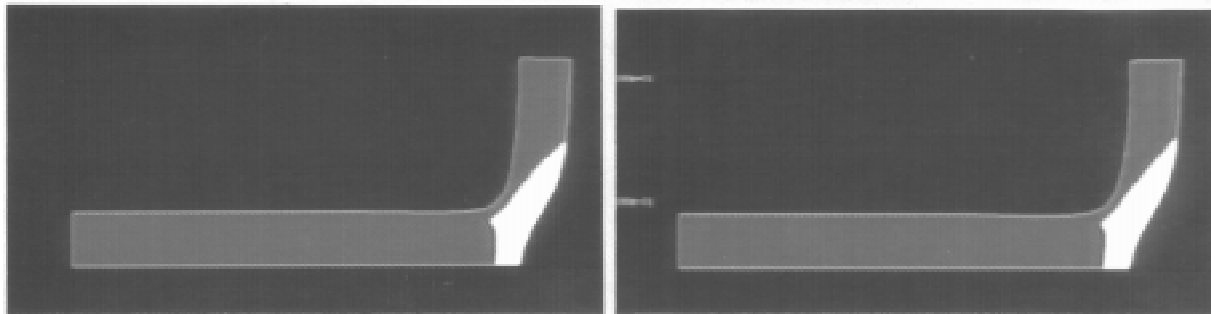
The deformation at -10°C under $\sigma_{ap}=5.5\text{MPa}$ which corresponds to about $F=280\text{N}$ is similar to that obtained experimentally and shown in Fig.4(a). The maximum equivalent strain, $\epsilon_{eq(max)}$, at each temperature occurred at point B and increased as the applied load increased. The plastic zones, in which high equivalent strains of over 0.1 exist, spread from point B toward load points in the seal layer as the applied load increased. The increase of temperature caused the increase of $\epsilon_{eq(max)}$ at point B and of the area of the plastic zone.

The above results showed that bursting of bags occurred more easily as the temperature increased. Furthermore, the fracture mode of tension rather than tearing was inferred.



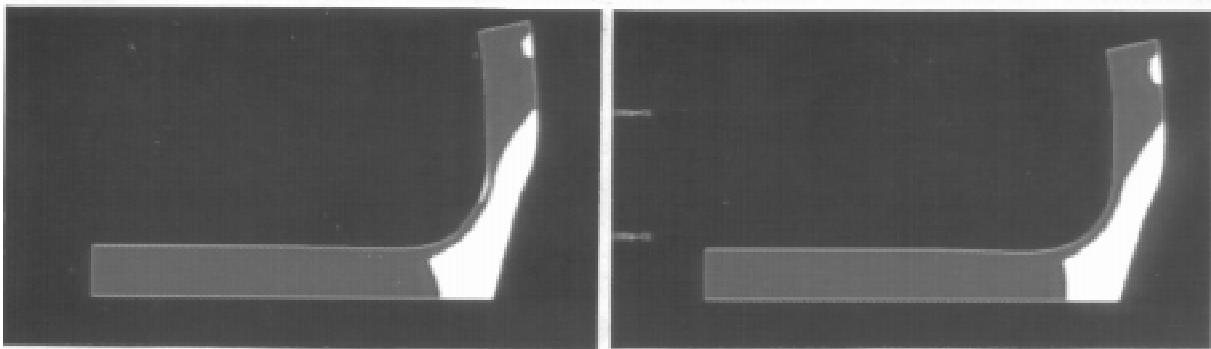
(a) $\sigma_{ap}=2.5\text{MPa}$

(a) $\sigma_{ap}=1.7\text{MPa}$



(b) $\sigma_{ap}=5.5\text{MPa}$

(b) $\sigma_{ap}=3.7\text{MPa}$

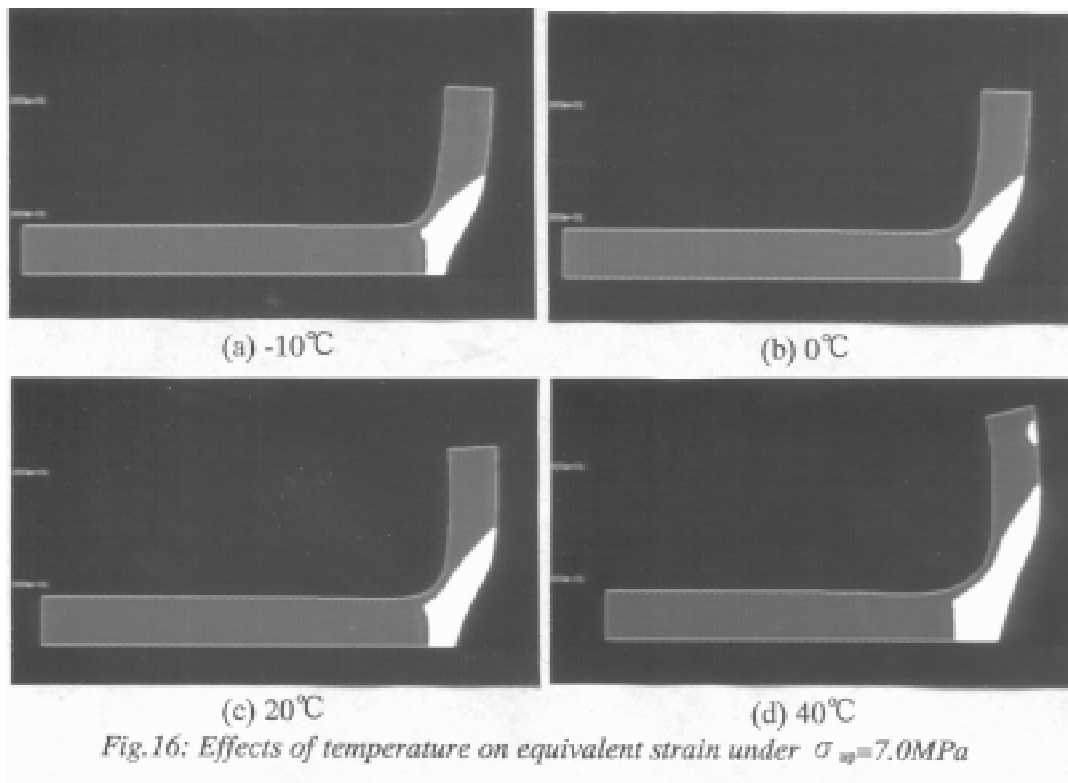


(c) $\sigma_{ap}=12.2\text{MPa}$

(c) $\sigma_{ap}=7.0\text{MPa}$

Fig.14: Effects of applied load, σ_{ap} , on equivalent strain at 20°C

Fig.15: Effects of applied load, σ_{ap} , on equivalent strain at 40°C



CONCLUSIONS

Stress and strain on a cross section of a heat-sealed area in laminated plastic film used for liquid packaging bags under different temperatures were analyzed using the elastoplastic finite-element method for the force acting on the area and material properties of the components constituting the film, which were obtained experimentally. The results indicated the following.

- (1) Most of the applied load was transmitted from NY to PE-EVA near the internal boundary point of the heat-sealed cross section.
- (2) The maximum equivalent strain occurred at the internal boundary point, and increased as the applied load increased.
- (3) The increase of temperature caused the increase of the maximum equivalent strain at the internal boundary point.

REFERENCES

1. Futase, K, Shimamoto, A., Takahashi, S. and Aoki, H., '(Study of impact-tensile strength of heat sealing in laminated film used for liquid package bag (effect of material change of base film)', *Proc. Nondestructive Testing & Stress-Strain Measurement, FENDT'92 (Tokyo)*, 1992, pp.632-637.
2. Futase, K, Shimamoto, A. and Takahashi, S., '(Impact strength test on a heat sealed portion of laminate film used for a liquid-filled bag)', *Trans. Jpn. Soc. Mech. Eng.* (in Japanese), Vol.60, No.580,A,1994, pp.2891-2896.
3. Futase, K, Shimamoto, A. and Takahashi, S., '(Changes in internal pressure of composite film packages by their drop impact)', *Trans. Jpn. Soc. Mech. Eng.* (in Japanese), Vol.60, No.580, A,1994, pp.2897-2902.

CHARACTERISING THE HOT DRAPE FORMING PROCESS AND THE EFFECT OF FIBRE SHEARING ON THE MECHANICAL PROPERTIES OF HIGHLY DRAPED COMPOSITE COMPONENTS

D. Standley

British Aerospace Airbus Limited, Filton, Bristol, BS99 7AR, England

SUMMARY: The hot drape forming process has been identified as a potential method of reducing manufacturing costs. This process consists of forming flat laminates into components incorporating complex curvature. Intra-ply shearing occurs during the forming process which has a detrimental effect on the mechanical properties of the final component. This paper outlines development trials conducted to identify the most significant parameters affecting the forming process. These were shown to be: vacuum rate, laminate geometry and forming temperature. The effect of intra-ply shearing is demonstrated through structural testing of hemispherical formed components. Two techniques are used to predict the effect of intra-ply shearing; Classical laminate theory and modified rule of mixtures. These methods are incorporated into a finite element analysis which is compared to the experimental data from the hemisphere tests. The modified rule of mixtures produced the most accurate results, however, further refinement of the finite element model is required.

KEYWORDS: hot drape forming, intra-ply shearing, mechanical properties, classical laminate theory, rule of mixtures, finite element analysis

INTRODUCTION

Composite materials consisting of continuous aligned fibre reinforcement are widely used for structural applications due to their high specific strength and stiffness. Manufacture of composite components within the aerospace industry is generally accomplished through low volume labour intensive manufacturing strategies based upon vacuum bagging and autoclaving. Hot drape forming of composite materials has been identified as a potential method of reducing the manufacturing costs of components with complex geometry. During the forming process, shearing of the fibres changes the directional properties of the material. This can have adverse effects on the structural properties of the final component.

Whilst a considerable degree of work has been performed in simulating the fibre deformation during forming, there has been little effort to characterise the forming process and the effect of fibre shear experimentally. The purpose of this paper is to establish the variables that have the greatest effect on the hot drape forming process. Experiments are performed using a hemispherical tool to investigate the effect of vacuum rate, test piece geometry and forming temperature. Two alternative models are proposed to predict the effect of intra-ply shearing; classical laminate theory and a modified rule of mixtures. The models are validated by

comparison with experimental results obtained from flat panels of sheared material. A finite element structural analysis is performed for the hemisphere which incorporates the effect of the fibre shearing. Comparisons are then made with the results of structural tests on the hemispheres.

DEFORMATION MODES OCCURRING DURING FORMING

Several two dimensional modes of deformation can occur during the forming of a single ply of composite material:

Fibre stretching

Fibre stretching is caused by tensile forces on the fibre tows, as shown in Fig. 1. Strains of more than 30% can occur during the forming process, however, as aerospace materials use high stiffness reinforcements (e.g. carbon) the fibre elongation can be neglected. The maximum fibre strain generally permitted for these types of materials is approximately 1% [1].

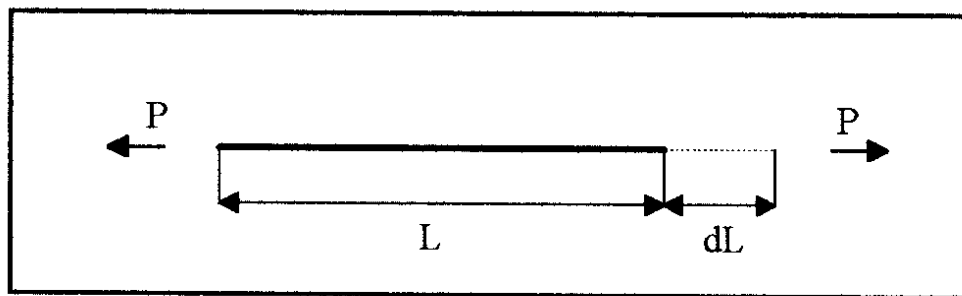


Fig. 1: Fibre stretching due to tensile forces.

Fibre straightening

This is again caused by tensile forces on the fibre tows and can result in strains of up to 10%. However, most fibre tows tend to be flat in practice which reduces the influence of the fibre straightening. As a result, this deformation mode may also be neglected.

Shear slip

Shear slip is produced by tensile forces acting perpendicular to the fibre direction, as shown in Fig. 2. However, as this mode only tends to occur at corners, it is not relevant to the hemisphere forming test used in this investigation.

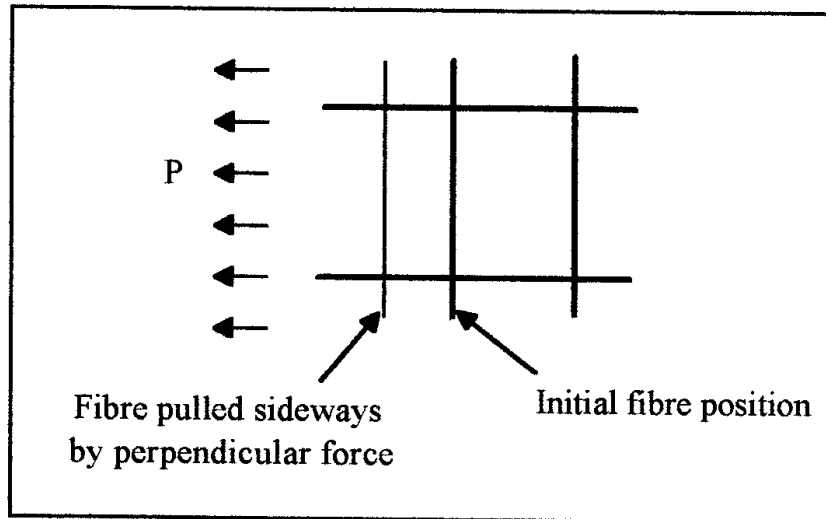


Fig. 2: Shear slip of fibre tows.

Fibre shear

Shearing of the fibres is caused by tensile forces acting in a direction other than along the fibre tows, as shown in Fig. 3. This is the major deformation mode, causing strains of up to 30% [1]. To ensure accurate predictions of the formed components behaviour, the effect of this deformation mode must be considered during the analysis stage.

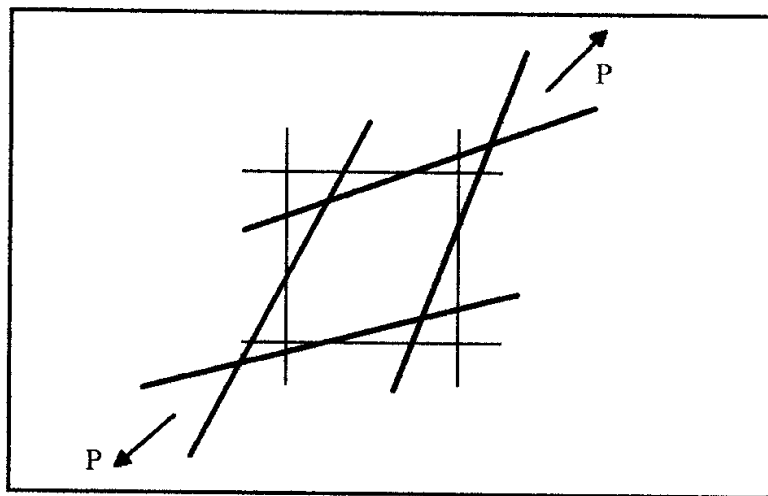


Fig. 3: Fibre shear due to tensile forces

Fibre buckling

Buckling of the fibre tows occurs as a result of compressive forces acting along the fibre direction. This can result in local wrinkles or larger global folds being formed which reduce the mechanical properties of the component. Consequently fibre buckling must be avoided during the forming process.

ANALYSIS METHODS

Classical laminate theory uses a unidirectional lamina as the basis on which to determine the stress-strain relationships for the composite laminate. At a constituent level the lamina is heterogeneous in nature, as the fibre properties differ from the matrix properties. However, classical theory adopts a macro-mechanical approach, requiring the stress and strain to be expressed as the averages of an equivalent homogenous material [2].

The modified rule of mixtures approach is derived from Krenchels work on fibre reinforced cements [3]. The material is considered to be a single lamina consisting of fibres at various orientations to the axis of loading. An efficiency factor (η) is generated for the laminate by examining the resulting strains in the fibres:

$$\eta = a_n \cos^4 \phi \quad (1)$$

Where a_n is the proportion of fibres at angle ϕ , and n is the total number of fibre groups. The efficiency factor is applied to the fibre terms of the rule of mixtures type equations to obtain the equivalent elastic modulus (E_x) and shear modulus (G_{xy}) for the laminate:

$$E_x = E_m (1-V_f) + E_f V_f \eta \quad (2)$$

$$G_{xy} = (1-V_f)G_m + E_f V_f a_n \sin^2 \phi \cos^2 \phi \quad (3)$$

This approach has the advantage of being able to allow for the changing fibre volume fraction resulting from the intra-ply shearing. This can be calculated from:

$$V_f = \frac{W N}{t \rho (\sin 2 \phi)} \quad (4)$$

Where W is the areal weight of the material (kg/m^2), N is the number of plies, t is the overall laminate thickness (m), and ρ is the fibre density (kg/m^3).

VALIDATION OF ANALYSIS METHODS

A series of 1.5 mm thick flat panels were produced to predetermined sheared fibre angles. The panels were manufactured from four plies of 5 Harness Satin weave Tenax HTA carbon fibre reinforcement with Hexcel Fibredux 6376 toughened epoxy resin. The laminates were deformed in a picture frame apparatus at 70°C with a strain rate of 1.0 mm/min. After curing, test coupons were cut from the panels as shown in Fig. 5.

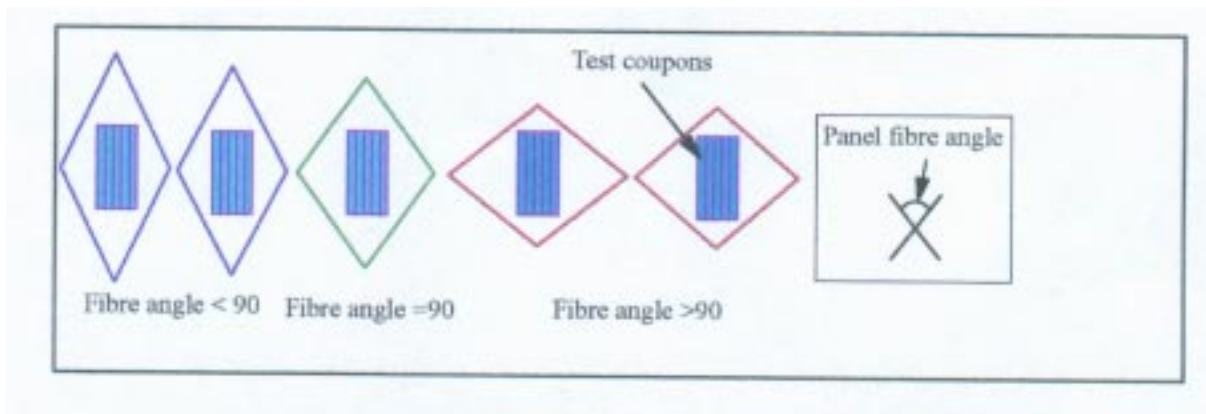


Fig. 5: Arrangement of test coupons and sheared panels

The coupons were loaded along the axis of symmetry to obtain the equivalent elastic properties. A comparison of experimental results with predictions from the rule of mixtures and classical laminate models are shown in Table 1.

Table 1: Comparison of predicted elastic modulus with experimental results

Fibre angle (degrees)	Classical laminate theory modulus value (GN/m ²)	Rule of mixtures modulus value (GN/m ²)	Experimental modulus (GN/m ²)
±35.6	33	28	29
±54.4	14	10	12

FORMING PROCESS DEVELOPMENT TRIALS

The trials were performed using 1.5 mm thick laminates of plain weave Torayca T300 carbon fibre reinforcement with Hexcel Fibredux 6376 toughened epoxy resin. The forming tool consisted of a 150 mm diameter male hemisphere form, over which the laminate was draped, together with a parallel section to allow for bridging of the test material, as shown in Fig 8. This shape has been widely used to analyse material drape [4, 5] as it represents a severe test of the materials ability to form. In addition, the varying rate of change of geometry over the hemisphere enables the material to be characterised by the distance over which it forms without wrinkling.

A single diaphragm vacuum forming process was employed in the trials, using a silicone rubber. The laminate plies were all orientated to 0° to align the areas of intra-ply shearing. This enabled the effects of the shearing to be seen more clearly. With this lay up, all intra-ply shearing occurred in the areas at 45° to the warp and weft fibres of the laminate.

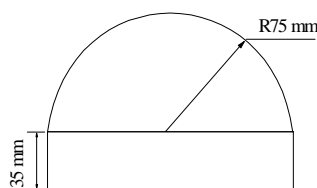


Fig. 8: Hemisphere tool geometry.

Effect of vacuum rate

The time to reach atmospheric pressure was varied from thirty seconds to four minutes to establish the optimum vacuum rate for the forming process. The minimum of fibre wrinkling occurred when the time to reach atmospheric pressure was four minutes.

Test piece shape and size

The initial laminate shape was a square of 350 mm side length. Trials performed using this laminate resulted in similar patterns of fibre wrinkling; the largest wrinkles occurred in the warp and weft directions, with smaller wrinkles forming in the areas of intra-ply shear.

The warp and weft wrinkling resulted from compressive stresses induced by the intra-ply shearing at the corners of the test piece. This fibre buckling was prevented by using an octagonal flat laminate 400 mm across flats, which equalised the amount of material around the base of the forming tool. However, the wrinkling in the areas of shear increased, as shown in Fig 9, resulting in greater wrinkling of the hemisphere section.

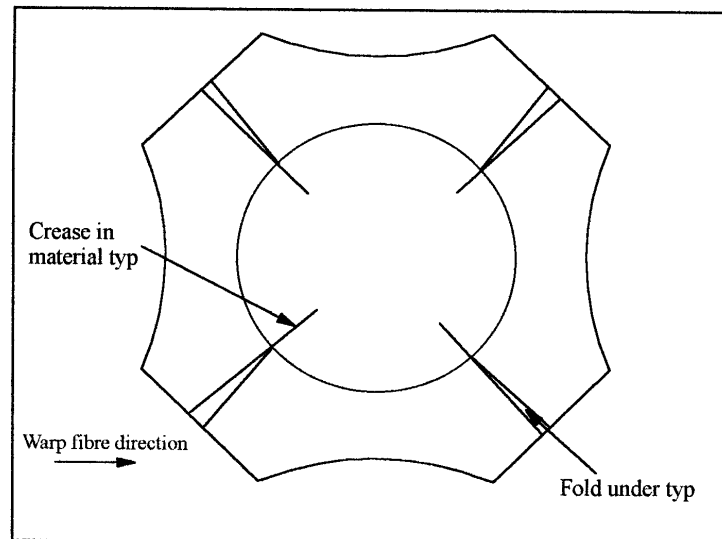


Fig. 9: Top view of formed test piece showing wrinkling.

An octagonal flat laminate measuring 375 mm across flats was used to re-introduce some warp and weft wrinkling, thereby enabling the laminate to be formed without wrinkling over the hemisphere section.

Forming temperature

Initial trials performed between 60°C and 100°C produced similar results; the largest wrinkles occurred at the corners, together with smaller wrinkles at the sides of the test piece. The similarity in the wrinkling of the formed components was related to the small reduction in resin viscosity over this temperature range [6]. Increasing the forming temperature to 130°C reduced the resin viscosity to near its minimum value. The resulting wrinkling of the formed components was reduced by 17%.

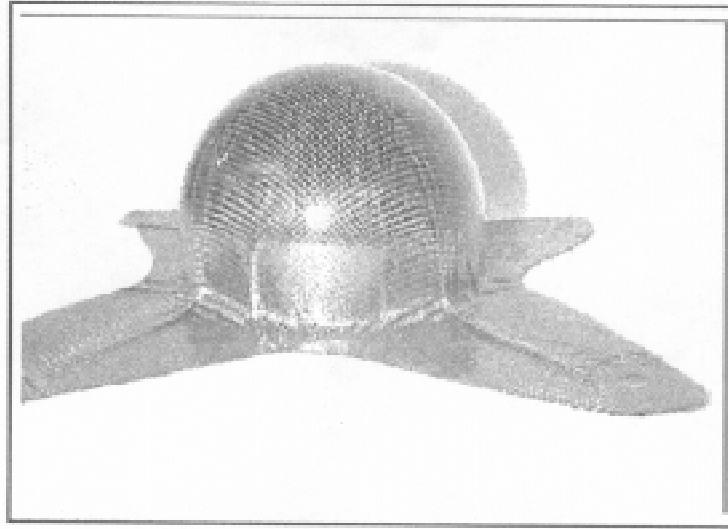


Fig. 10: Photograph of formed test piece to show wrinkling.

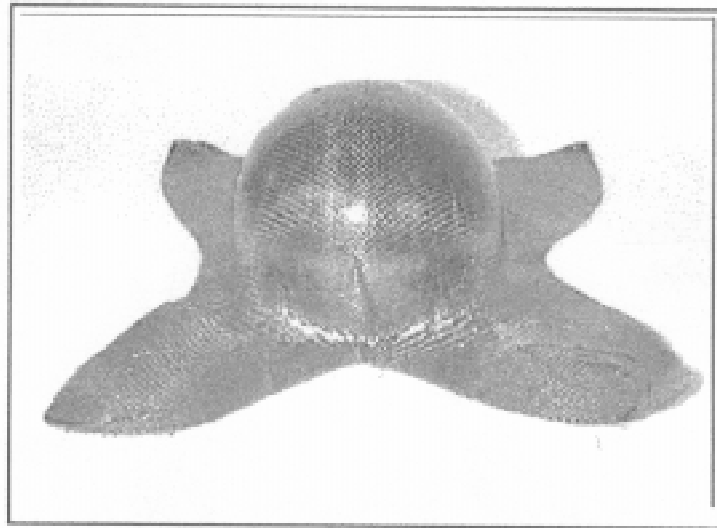


Fig. 11: Photograph of formed test piece to show reduced wrinkling.

Having established the parameters of the forming process, a hemisphere component was produced from the 5 Harness Satin material used in the manufacture of the sheared panels.

TESTING AND ANALYSIS OF HEMISPHERE COMPONENTS

The hemisphere was loaded at diametrically opposite locations across its base, as shown in Fig. 12. Resulting deflections were measured at four orientations; 0° , 15° , 30° and 45° to the warp direction to demonstrate the stiffness variation due to intra-ply shearing.

At the 45° orientation a 200 kN load resulted in a deflection of 11 mm. This was 68.4% greater than the deflection observed at the 0° orientation under the same load, as shown in Fig. 13. At 0° orientation the fibres were still aligned in the direction of the applied load as

no intra-ply shearing had occurred. Whereas, at 45° the fibres were at maximum shear, hence the reduction in material stiffness.

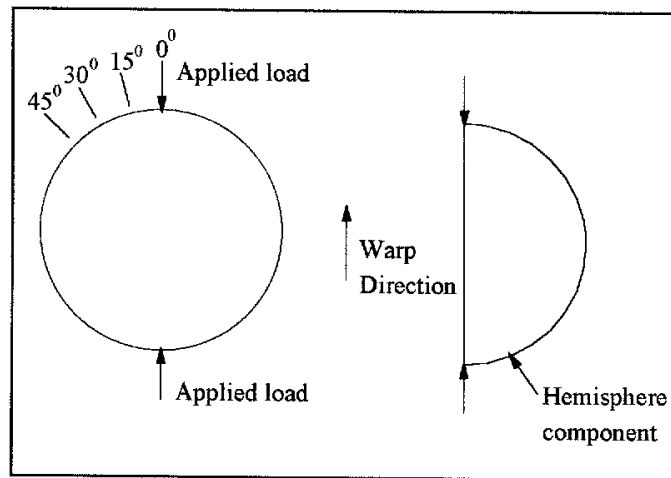


Fig. 12: Diagram of pinch test performed on hemisphere components.

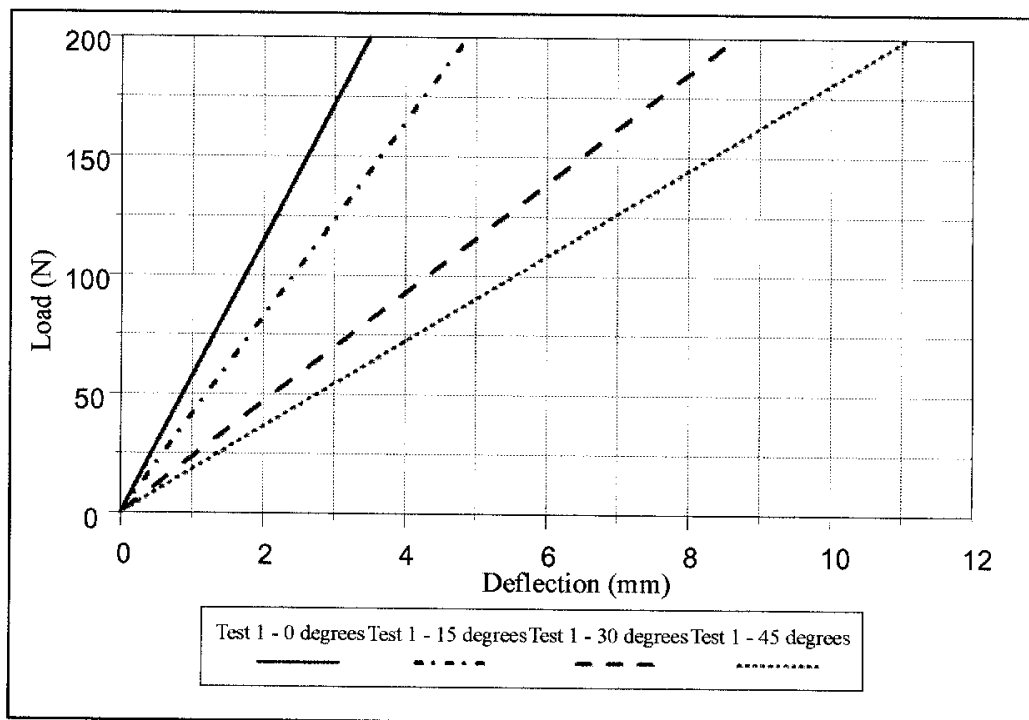


Fig. 13: Pinch test results for hemisphere component.

Two groups of finite element (FE) analysis models were produced; one using the modified rule of mixtures with the other using classical laminate theory. These groups were subdivided into models with constant and varying material properties. The varying property distribution was produced by dividing the model into eight zones, as shown in Fig. 14, based on the intra-ply shearing witnessed on the hemisphere. A different set of material properties was assigned to each zone. Predictions obtained from the models were compared with the relevant test results, as shown in Table 2.

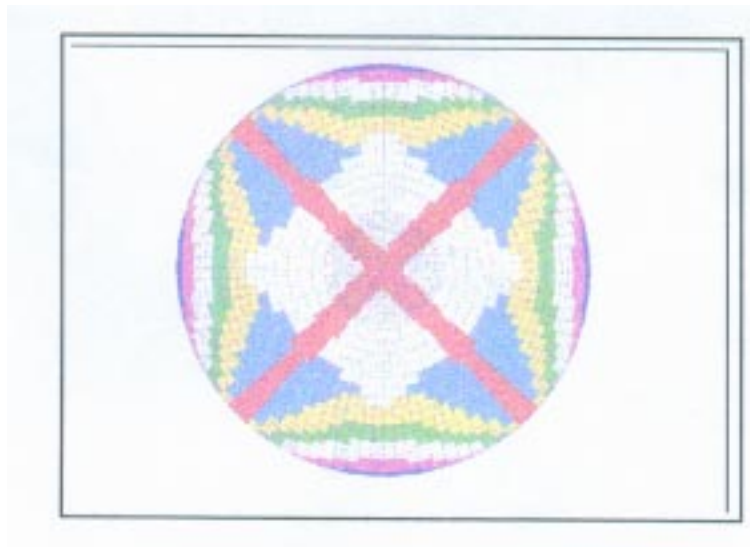


Fig 14. Zoning of material properties for FE model.

Table 2. Comparison of FE model predictions to test results.

Orientation	Classical laminate theory - No zones			Rule of mixtures - No zones			Classical laminate theory - Zoned			Rule of mixtures - Zoned		
	Deflection			Deflection			Deflection			Deflection		
	FE	Test	Error	FE	Test	Error	FE	Test	Error	FE	Test	Error
0	3	4	-25	12	4	200	3	4	-25	4	4	0
15	-	-	-	-	-	-	3	5	-40	5	5	0
30	-	-	-	-	-	-	4	9	-56	6	9	-33
45	3	11	-73	3	11	-73	4	11	-64	6	11	-45

CONCLUSIONS

The hot drape forming experiments clearly demonstrated that the forming process was affected by a number of variables:

Geometry of laminate

The degree of fibre buckling depended on the area of material undergoing intra-ply shearing. Increasing this area relative to the surrounding material reduced the amount of wrinkling.

Vacuum rate

Although the application of the vacuum was restricted by the design of the forming equipment, it was apparent that the slower vacuum rates resulted in less wrinkling.

Forming temperature

To prevent the component curing during the forming process the temperature must be restricted to between 60°C and 100°C. Experiments have shown that the degree of wrinkling is consistent over this range. Increasing the temperature to the point of minimum resin

viscosity significantly reduces the degree of wrinkling. However, the forming process cannot be completed before the component begins to cure.

The sheared panel experiments demonstrated the accuracy of both the modified rule of mixtures and classical laminate models. Simulating the effect of fibre shearing in a finite element structural analysis improved the accuracy of the predicted deflections. The modified rule of mixtures model typically produced more accurate results due to the lower shear modulus values produced with this model. Examining the FE analysis showed the shear modulus to be the critical material property governing the behaviour of the component. This was further illustrated by the large error produced when the modified rule of mixtures model was used without allowing for intra-ply shearing.

The inaccuracies in the predicted deflection values are thought to be due to the size of the material zones in the finite element analysis. These zones are necessarily large as they are produced by manually modifying the element mesh used in the analysis. The predicted deflection values could be improved by increasing the number of material zones used. Ideally, the analysis would use a separate material property set for each element in the mesh, thereby allowing for the variation in intra-ply shearing occurring throughout the component.

ACKNOWLEDGEMENTS

The author would like to thank the following for their support: British Aerospace Airbus Ltd, England. Composites Research Unit, University College Galway, Ireland.

REFERENCES

1. Horsting, K. and Wulfhorst, B., "Drapeability of textile reinforcement fabrics for composites", *Proceedings 25th International SAMPE Technical Conference*, October 26-28, 1993, pp. 876-886
2. Christensen, R. M., "*Mechanics of composite materials*", John Wiley and Sons, New York.
3. Krenchel, H., "*Fibre Reinforcement*", Akademisk Forlag, Copenhagen, 1964
4. LaRoche, D. and Vu-Khanh, T., "Modelling of the forming of complex parts from fabric composites", *Composite materials : testing and Design (Eleventh Volume)*, ASTM STP 1206, Camponeschi, E.T., Jr, Ed., American Society for Testing and Materials, Philadelphia, 1993, pp. 255-262.
5. Bergsma, O. K. and Brouwer, W. D., "Draping of fabric reinforced plastics - theory and experience from the computer to the tool", *39th International SAMPE Symposium*, April 11-14, 1994, pp. 3057-3067
6. Product data sheets, Hexcel Composites, Duxford, Cambridge, CB2 4QD, England

BLENDING EFFECT OF VINYL ESTER RESIN ON THE EPOXY MATRIX SYSTEM

Jae-Rock Lee, Soo-Jin Park and Won-Bae Park

*Advanced Materials Division, Korea Research Institute of Chemical Technology
P.O. Box 107, Yusong, Taejon, 305-600, Korea*

SUMMARY:

The room temperature (RT) curable epoxy (E) and vinyl ester (VE) resin systems with nearly same gellation times, have been selected to observe their mixing effect on mechanical properties. The studied mixing ratios of epoxy resin and vinyl ester resin were 100:0, 90:10, 80:20, 70:30, 60:40, 50:50 and 0:100 by weight. Two curing conditions were selected, only RT curing during 72 hours and RT curing during 72 hours and then post cured at 100 °C during 1 hour. The tensile, flexural, impact strength have been measured. The small addition of VE resin in E resin gave a positive synergetic effect of mixing on mechanical properties. The maximum increase of the mechanical properties were generally observed with 20wt.% of VE resin. The mixing of VE resin in E resin increased the gellation time of 50%. And this fact also changed the cross linking network to increase the flexibility, thus influenced on the final fracture surfaces.

INTRODUCTION

The development of high performance polymeric composites enables their application in large scale structural applications(1-3). In this application the economic consideration becomes one of the most important factors. The chemical modification is often revealed as too much expensive in the improvement of their properties. On the other hand, the application of simple blending of commercially available different resins can be an alternative solution. Recently there has been studied for more improved properties by this simple blending of different resins(4-8). These works were based on the simultaneously curable thermosetting materials at elevated temperature curing conditions. But these conditions are generally unable to realize in real applications.

In the common fiber reinforced industries for the large scale structural applications, they use most frequently the unsaturated polyester resin in room temperature curing conditions. The conventional unsaturated polyester resin is economically most competitive in this condition. But this cured resin is unsuitable for use in chemically

aggressive environments. To overcome this problem, VE which can be fabricated with the same process as those for conventional polyester resins was developed. VE resins are addition products of various E resins and ethylenically unsaturated mono-carboxylic acid. It combines the excellent mechanical, chemical resistance of E resins with the properties found in the unsaturated polyester resins(9,10).

But the mechanical properties of cured VE resin is generally inferior to the cured E resin which has been also known to have a good corrosion resistance. In the present work, the mixtures of room temperature curable low viscosity E and VE resin systems were prepared to study the synergetic effect of mixing. Their mixing effects on mechanical, thermal properties and fracture surface formation have been studied to give a more comprehension on the mixed network formations

EXPERIMENTAL

Materials and Sample Preparation

E resin (YD-114, low viscosity, 480cps at 21 °C by Brookfield Viscometer, diglycidyl ether of bisphenol-A, DGEBA) and hardener (triethylene tetramine, TETA) received from Kukdo-Chemical Ind. Co.(located at Seoul) were used as received. VE resin of grade SR-825L (320cps at 21 °C) was received from Seiwon Chemical Co. (Korea). Methyl ethyl ketone peroxide (MEKP, grade D-S) in the presence of 6% cobalt-octoate (grade of P-60) as accelerator (Seiwon Chemical Co.) was used as the free radical initiator for the polymerization of VE resin. The resin mixtures with the calculated amounts of initiator-accelerator and hardener poured into the vertical molds made from glass with gaps of 2 and 5mm. And then these mixture were maintained at RT during 72 hours.

Tensile and impact specimens were cut out from these cured resin castings. To know the effect of post curing the resin mixtures were poured into same type molds with the gaps of 2, 3 and 5mm and maintained at RT during 72 hours and then 1 hour at 100 °C.

The tensile, flexural and impact specimens were cut out from these resin castings.

Test Procedure

The glass transition temperature (T_g) of resin casting were measured by Differential Calorimetric Scanning (DSC).

The tensile and three-point flexural tests were done by using Instron #1125. The tensile properties of the specimens with the dimensions specified at ASTM D638 type IV were tested with the cross-head speed of 5mm/min.

The three-point flexural specimens with the dimensions specified at ASTM C393 tested with the cross-head speed of 1.3mm/min. In this case, the ratio between the thickness of the specimen and the supporting was 1:16.

The impact specimens with dimensions specified at ASTM D256 were tested by plastic impact tester (TINUS O OLSEN) at 0.25 kg_r-cm division value. In tensile test 10 specimens were used for each conditions. For the rest 5 specimens were tested.

RESULTS AND DISCUSSION

The gellation time of used E and VE resin system was nearly same as 40 minutes in RT curing condition. The addition of VE resin has lowered the viscosity but retarded the gellation time. The measured gellation time of the observed resin mixtures were always 60 minutes. The mixing of these two resins only slowed down the curing reactions until 50wt.% of VE resin. The obtained T_g values for these hardened resin mixtures were summarized in Table 1 and 2.

The post curing did not much changed their T_g values. It means that the RT curing condition gave relatively sufficient curing to this resin mixtures.

The tensile properties of RT cured specimens (during 72 hours) are presented in Figure 1. The tensile strength of cured VE resin is 49% lower than cured E resin. Small portion of VE resin added in E resin have increased tensile strength. In this cured resin mixture system, the rule of mixture cannot be sustained. The maximum increase of tensile strength was observed as 8.9% with 20wt.% of VE resin. The addition of 30, 40, and 50 wt.% of VE resin decreased the tensile strength. The tensile strength with 40 and 50 wt.% of added VE in E resin is even inferior to that of VE resin.

The results of impact strength with RT curing condition are shown in Figure 2. The impact strength of cured VE resin is 19% lower than cured E resin. The addition of 10wt.% of VE resin gave nearly same value with the cured E resin. The addition of 20 wt.% of VE resin has increased 2.5% of impact strength than cured E resin.. It was a maximum value. The addition of more vinyl ester resin content decreased the impact strength. The impact strength of 40wt.% added VE in E resin gave nearly same value of VE resin.

The image of fracture surfaces observed by Scanning Electron Microscope (SEM) can be found in Figure 3. The fracture surfaces of neat resins were mirror like. The addition of small amount induced plastic flow in some extent thus increased the fracture surfaces. The maximum increase of fracture surface by this effect was shown with 20 wt.% of VE resin . In this case, one can observe the most pronounced contrast on the fracture surfaces.

To know the effect of the post curing on the mechanical properties. The RT cured specimens were post cured at 100 °C during 1 hour. The tensile properties of post cured specimens are shown in Figure 4. One can find that the post curing improved the tensile strength in E resin dominant systems. The E resin cured system showed the increase of tensile strength more than 10%. But this effect was not observed in VE resin cured system. The total trend in tensile strength variation is as same as that of only RT cured system. It means that the maximum tensile strength was observed with 20wt.% of VE resin. The post curing has been supposed to do not give big change in the network formed by RT curing.

The flexural properties with above curing condition are presented in Figure 5 and 6. The flexural properties of only RT cured system with 30, 40 and 50wt.% of VE resin were too low for structural applications. So these results were omitted to remove the confusions. In particular, the flexural modulus of VE resin is 43% higher than that of E resin cured in the early described condition. The addition of VE in E resin has very slightly increased the flexural modulus only 1.3% with 10wt.% and 1.2% with 20wt.% of VE resin than that of E resin cured system. The more added VE resin has sharply decreased the flexural modulus. In contrast the flexural strength of VE resin is 25% lower than that of E resin. The maximum flexural strength was observed with 20wt.% of added VE resin. The increase of it was 2.2% on the basis of E resin cured system.

The results of impact strength cured RT and post cured are shown in Figure 7. The increases of impact strength by post curing were observed 3.4% for E resin and 6.3% for VE resin cured system. Anyhow the impact strength of VE resin is 17% lower than that of E resin cured system. The small portion of added VE resin again increased the impact strength of 2.4% with 20 wt.% of VE resin on the basis of the E resin cured system.

The results of observed impact fracture surfaces of the specimens cured in RT and then post cured are shown in Figure 8. The post curing in E resin has changed the fracture surfaces from mirror like to more rugged type. But the post curing effect in VE gives nearly no change on the fractures. The maximum impact strength is also observed with 20wt % of VE resin with more smooth fracture surfaces. This fact would indicate that the adequate plastic flow during impact fracture has improved the energy absorption thus increased the final failure strength. The post curing in this system would permit to have a more stress resistant through cross linking units.

CONCLUSION

The mixing of used E and VE resin has retarded the curing reactions and extended the gellation time about 50% for observed mixtures. The mechanical properties of cured

E resin is much superior to that of VE resin. But small portion of added VE resin is beneficial to improve tensile, impact and flexural strength on the basis of cured E resin system. The maximum value was generally observed with 20wt.% of VE resin. In this case the maximum positive synergetic effect of mixing was obtained. The excess content of VE resin gives the severe negative synergetic effect of mixing and resulted in the sharp decrease of thermo-mechanical properties. The post curing is effective in some extent for mechanical property improvement in E dominant systems. Only the impact strength of cured VE resin is slightly improved by post curing. The adequate portion of added VE resin induce some extent of toughness in this simultaneously crosslinking network formation and influence on the fracture surface formations. The results of present work would give the positive synergetic mixing effects in thermosetting blends.

REFERENCES

1. Kim D. H., "Composite Structures for Civil and Architectural Engineering", E & FN Spon, London, 1995.
2. Reprints, The Second Annual Wilson Forum on Existing & Potential Applications of Composite Materials in the Infrastructure, Santa Ana, CA., April 18-19, (1994)
3. Mallison J.H., "Corrosion-Resistant Plastic Composites in Chemical Plant Design", Marcel Decker Inc., New York, 1988.
4. Utracki L.A., *Polym. Eng. Sci.*, Vol. 32, 1992, p. 1801.
5. Sen A.K. and Mukherjee G.S., *Polymer*, Vol. 34, 1993., p. 2386.
6. Mukherjee G.S. and Saraf M.N., *J. Polym. Sci.: Part B*, Vol. 33, 1995, p. 855.
7. Kim D.S. and Lee J.R., *Polym.(Korea)*, Vol. 18, 1994, p. 199.
8. Lee Y.J., Lee K.J., Kim D.S. and Lee J.R., *Polym.(Korea)*, Vol. 18, 1994, p. 206.
9. Lubin G., "Handbook of Composites", Van Nostrand Reinhold Co. Inc., 1982.
10. Kroschwitz J.I., "Encyclopedia of Polymer Science and Engineering:", John Wiley & Sons, New York, 1985.

Table 1. T_g values for RT cured condition

E/VE (wt.%)	T_g (°C)
100/0	69.9
90/10	66.9
80/20	64.1
70/30	63.2
60/40	59.8
50/50	58.6
0/100	132.1

Table 2. T_g values for 100 °C, 1hr. Post-cured condition

E/VE (wt.%)	T_g (°C)
100/0	71.4
90/10	67.4
80/20	66.8
70/30	64.4
60/40	64.1
50/50	62.1
0/100	133.9

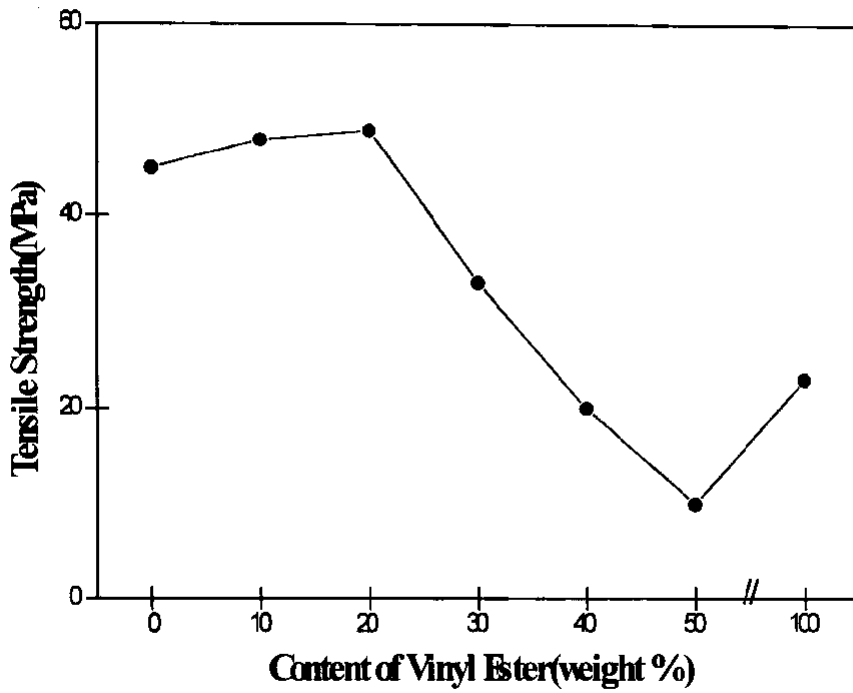


Figure 1. Effect of vinyl ester resin on the tensile strength(RT curing)

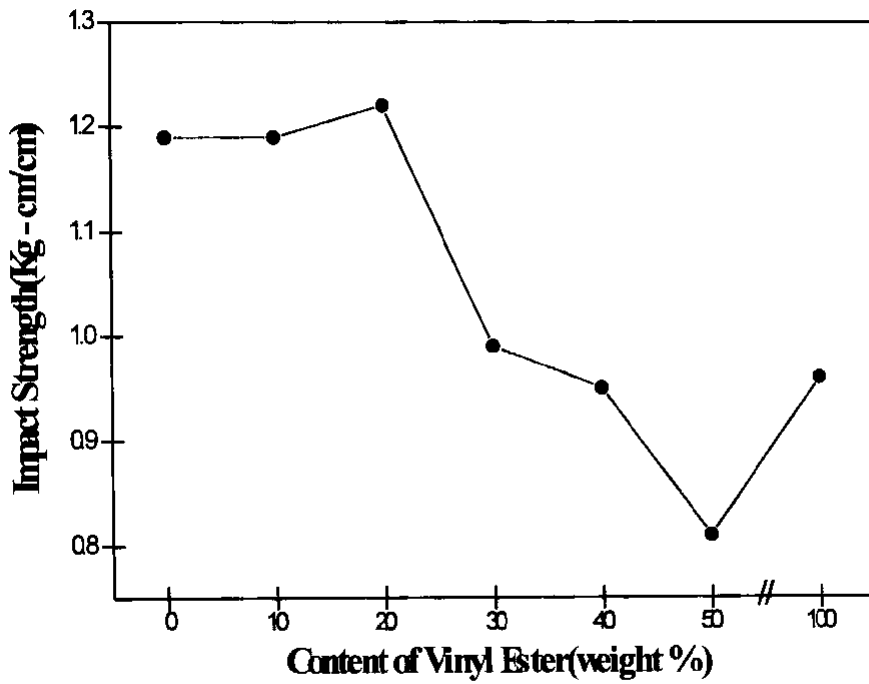


Figure 2. Effect of vinyl ester resin on the impact strength(RT curing)

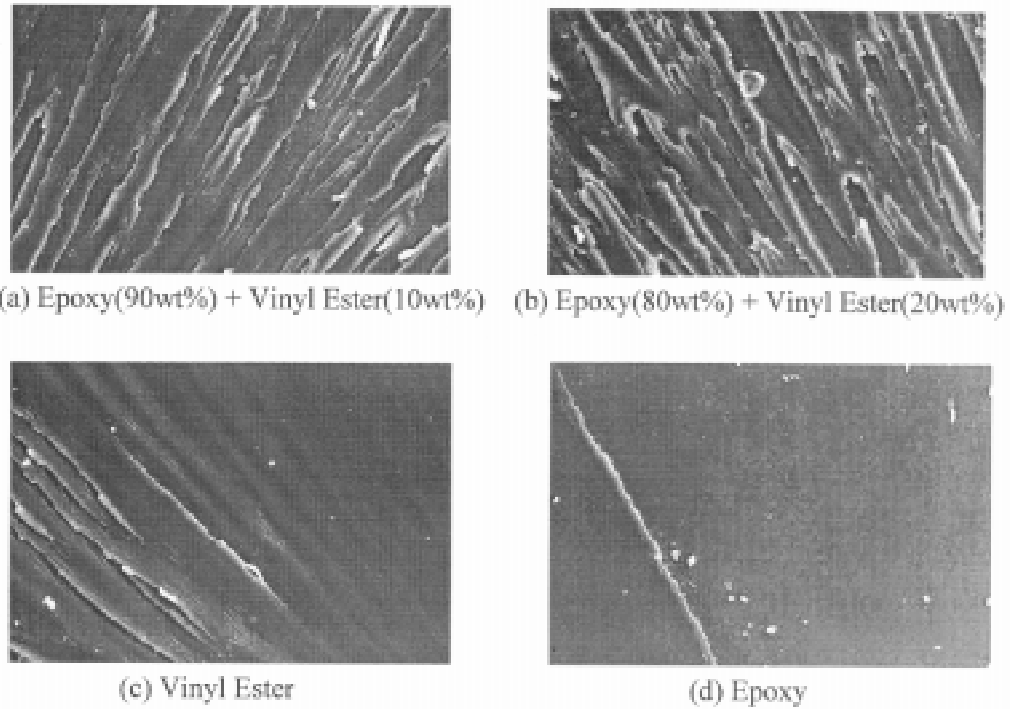


Figure 3. Effect of vinyl ester resin on the fracture surface of impact failure(RT curing)

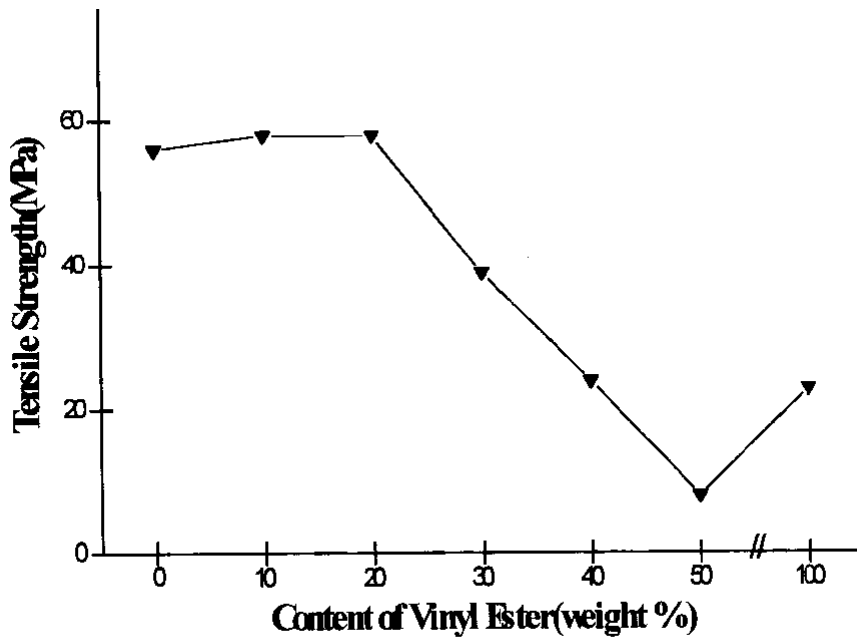


Figure 4. Effect of vinyl ester resin on the tensile strength (RT+ post curing)

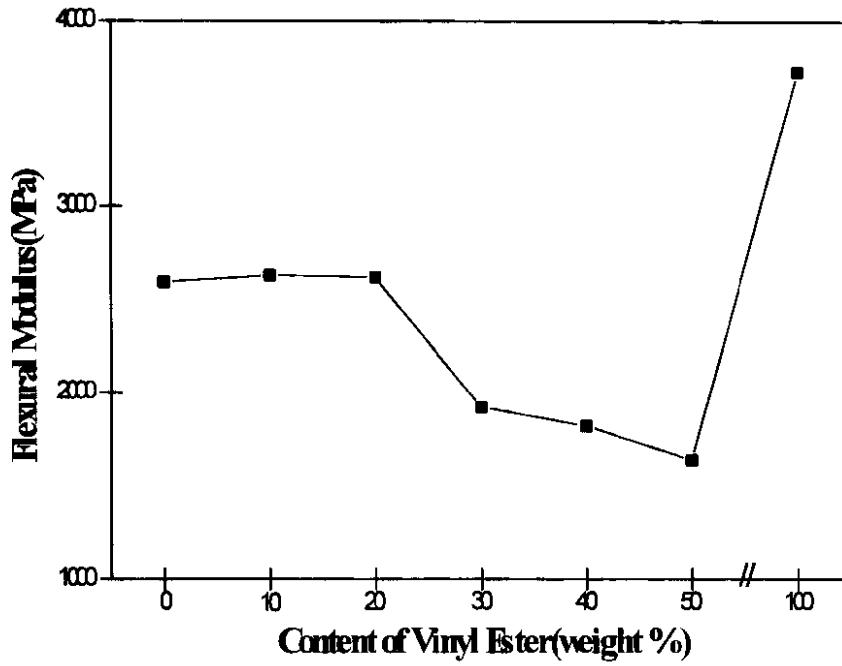


Figure 5. Effect of vinyl ester resin on the flexural modulus (RT+post curing)

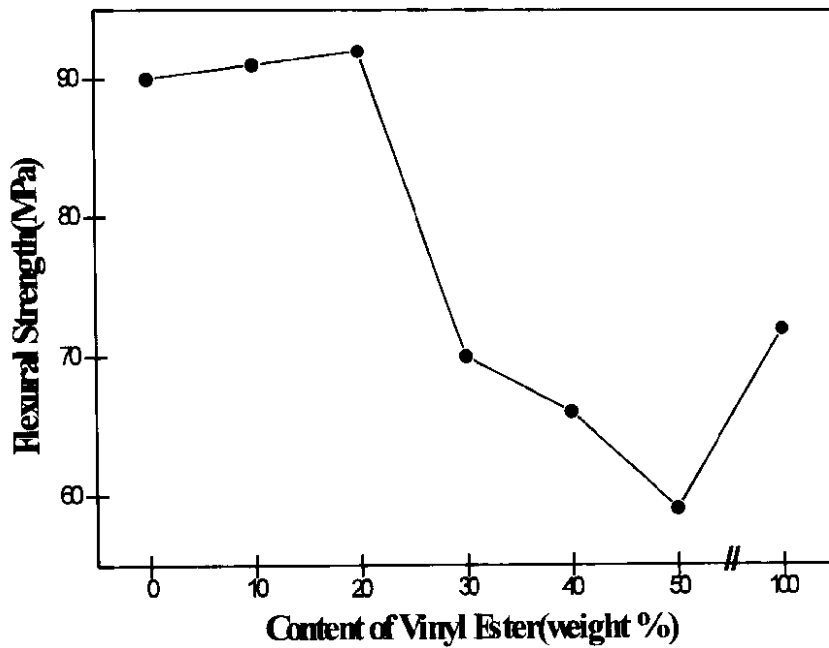


Figure 6. Effect of vinyl ester resin on the flexural strength (RT+post curing)

WEIBULL FIBRE STRENGTH PARAMETERS DETERMINED BY SINGLE FIBRE FRAGMENTATION TESTS

Shiqiang Deng, Lin Ye, Yiu-Wing Mai and Hong-Yuan Liu

*Centre for Advanced Materials Technology, Department of Mechanical & Mechatronic
Engineering, The University of Sydney, NSW 2006, Australia*

SUMMARY: Single fibre fragmentation tests of two carbon fibre/epoxy composite systems were conducted by continuously monitoring fibre fragments and applied stresses to determine the Weibull fibre strength parameters. It was shown that the measurement of the Weibull fibre strength parameters in the epoxy matrix is possible using single fibre fragmentation test. A linear relation between the logarithm of the average fibre fragment length and the logarithm of the maximum fibre axial stress was found prior to the saturation of fibre fragments. Discrepancy exists between the results obtained from the fragmentation tests and those from the extrapolation of conventional fibre tensile tests in air, which is attributed to the limitation of the Weibull weakest-link model and the fibre degradation in the specimen preparation process.

KEYWORDS: Weibull fibre strength parameters, single fibre fragmentation test, carbon fibre, epoxy, interface

INTRODUCTION

Among the micromechanical testing methods for evaluating fibre/matrix interfacial properties of fibre-reinforced composites, single fibre fragmentation test has attracted extensive attention since the method was introduced by Kelly and Tyson [1] because the fibre stress state in the test specimen is similar to that in the real composite and the fibre fragmentation phenomenon is sensitive to the level of fibre/matrix interfacial adhesion. However, for the interpretation of test results the fibre strength at the saturation state is very crucial because the direct measurement of the fibre tensile strength at the critical fibre length (commonly < 1 mm) is almost impossible using normal tensile testing methods. The value of the fibre tensile strength is usually obtained by testing a number of fibre specimens at several specified gauge lengths in air, then the results are extrapolated to the domain of the critical fibre fragment length using some statistical models such as the Weibull weakest-link model. However, the value of fibre strength at the critical fibre fragment length obtained in this way may differ from the actual *in situ* fibre strength. Therefore, the proper test methods are required to measure the *in situ* fibre tensile strength, so that more reasonable values of the interfacial properties could be obtained from the single fibre fragmentation tests. In this study single fibre fragmentation tests of two carbon fibre/epoxy composite systems were conducted by continuously monitoring the fibre fragments and the applied stresses to determine the Weibull fibre strength parameters within the range of the critical fibre length.

THEORY

The distribution function of the two-parameter Weibull model is commonly used to define the fibre strength parameters [2, 3]

$$P = 1 - \exp\left[-\left(\frac{\sigma}{\sigma_o(s)}\right)^m\right] \quad (1)$$

where P is the cumulative failure probability, σ is the applied stress, m is the Weibull shape parameter and $\sigma_o(s)$ is the local scale parameter with gauge length s . The Weibull Parameter m must be constant from one gauge length to another and the scale parameter $\sigma_o(s)$ is dependent on the gauge length s with the relation

$$\sigma_o(s) = s^{-\frac{1}{m}} \sigma_c \quad (2)$$

where σ_c is the global scale parameter for all gauge lengths. The cumulative failure probability P_i under a particular stress is approximated by

$$P_i = (n_i - 0.5) / n \quad (3)$$

where n_i is the number of fibres that have fractured at or below a stress and n is the total number of fibres tested. In practice, the plot of $\ln[-\ln(1-P)]$ versus $\ln(\sigma)$ is often used for a given fibre length to derive the Weibull shape parameter m and scale parameter $\sigma_o(s)$ from Eq. 1 since it yields a linear dependence with slope m . For different fibre lengths, the logarithmic form of Eq. 2 can be used to define m and σ_c

$$\ln[\sigma_o(s)] = \ln(\sigma_c) - \frac{1}{m} \ln(s) \quad (4)$$

Combining Eqs. 1 and 2 yields the following equation for the cumulative failure probability function

$$P = 1 - \exp\left[-s\left(\frac{\sigma}{\sigma_c}\right)^m\right] \quad (5)$$

The failure probability density function, $f(\sigma)$, can be obtained by differentiating Eq. 5 and it is given by

$$f(\sigma) = s \frac{m}{\sigma_c} \left(\frac{\sigma}{\sigma_c}\right)^{m-1} \exp\left[-s\left(\frac{\sigma}{\sigma_c}\right)^m\right] \quad (6)$$

There have been some efforts to obtain the fibre strength distribution and to study the “size effect” from single fibre fragmentation tests in recent years [4-6]. The fibre fragmentation phenomenon is viewed as a “multiple tensile test” with different gauge lengths, which obeys the Weibull weakest-link model [4, 5]. The average fibre tensile strength σ_f with a gauge length, s , is given by

$$\sigma_f = \int_0^{\infty} \sigma f(\sigma) d\sigma = \sigma_c s^{-\frac{1}{m}} \Gamma\left(1 + \frac{1}{m}\right) \quad (7)$$

where Γ is the gamma function. If the single fibre fragmentation tests are regarded as a series of tensile tests in which individual samples of various lengths are subjected to the same applied stress, the reverse form of Eq. 7 gives the relationship between the average fibre fragment length s and the fibre stress σ_f

$$s = \sigma_c^m \sigma_f^{-m} \left[\Gamma\left(1 + \frac{1}{m}\right) \right]^m \quad (8)$$

In Eq. 8, s and σ_f can be evaluated from the single fibre fragmentation tests by continuously monitoring the fibre fragments and the applied stress σ . A relationship between the fibre axial stress σ_f^z and the applied stress σ can be obtained assuming a perfect bonding between the fibre and the matrix [7]

$$\sigma_f^z(z) = \eta \left(\sigma - \sigma \frac{\cosh \sqrt{A_1} z}{\cosh \sqrt{A_1} L} \right) \quad (9)$$

where L is the half length of the fibre fragment, z is the distance from the middle point of the fibre fragment, and η and A_1 are constants related to Young's moduli and Poisson's ratios of the fibre and matrix as well as the geometry of the test specimen [7]. In Eq. 9 the maximum fibre axis stress occurs at the middle of the fibre fragment ($z=0$) where fibre breakage may happen, so that the maximum fibre axis stress is considered as the fibre fracture stress σ_f during the fibre fragmentation test.

The Young's modulus of the matrix, E_m , is normally not a constant during the whole fibre fragmentation process for most polymer resins, which was ignored in most previous studies. E_m should be dependent on the applied stress when it is used to calculate the fibre axis stress.

Based on Eq. 8, $\ln(s)$ is plotted versus $\ln(\sigma_f)$ to produce a straight line with the slope being $-m$. The Weibull scale parameter σ_c can then be calculated from the value of the intercept,

$$m \cdot \left[\ln \sigma_c + \ln \Gamma\left(1 + \frac{1}{m}\right) \right] \quad (10)$$

EXPERIMENTAL RESULTS AND DISCUSSION

Single fibre fragmentation tests of two model carbon fibre/epoxy composite systems (G34-700/Araldite-F and T700S/Araldite-F) were conducted on a Minimat testing machine (Polymer Laboratories Ltd., UK), which is installed on the sample stage of an optical microscope and controlled by a computer. G34-700 carbon fibres (Grafil Inc., USA) were supplied with two surface conditions, i.e. one without any surface treatment and the other treated using electrochemical oxidation and then coated with a thin layer of epoxy sizing (0.4% by mass). The "as received" T700S fibres were treated and sized by the manufacturer. Some of T700S fibres were washed in a methylethylketone (MEK) solution for 1 hour and then

dried for 2 hour in an oven at 200°C to remove the sizing. Fibre diameters were measured by a high resolution SEM. Test specimens, consisting of a single fibre embedded in the centre of a rubber mould filled with liquid epoxy resin, were pre-cured for 48 hours at ambient temperature and then post-cured at 120° C for 16 hours to avoid the influence of thermal residual stress produced by direct high temperature curing. The Young’s moduli of the fibre and the matrix were determined by the tensile tests. The carbon fibres used in this study have a constant Young’s modulus, but the matrix exhibits a non-linear stress-strain relationship (Fig. 1). Non-linear elastic theory was applied in this case and the stress-strain curve was divided into finite sections. A linear relation within each section is assumed and then the value of the matrix Young’s modulus, E_m , was obtained from the slope of the curve in the section.

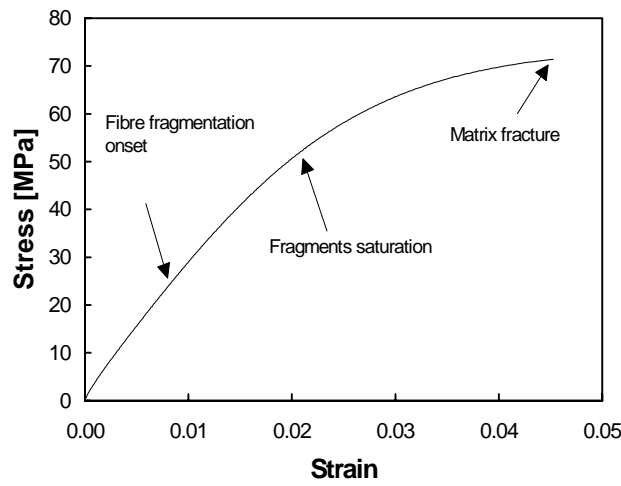


Fig. 1 Typical tensile stress-strain curve of the single fibre fragmentation test

The gauge length of all specimens was 30 mm and a cross-head speed of 0.1 mm/min was applied for the fibre fragmentation tests. The fibre breaks and the relative applied stress readings were continuously recorded during the test until the saturation of the fragments was achieved. The Weibull fibre strength parameters obtained from single fibre fragmentation tests are shown in Table 1. A typical $\ln(s)-\ln(\sigma_f)$ curve obtained using Eq. 8 for the treated/sized G34-700 carbon/Araldite-F epoxy system is shown in Fig. 2. It can be seen that the data fit reasonably well a straight line before the saturation limit is approached, but after that a great deviation from linearity occurs. The main reason for the deviation from the Weibull statistical model when approaching the saturation limit is the influence of the “ineffective length”. This length represents the fibre portion in both ends of a fibre fragment where the axial stress is built up to the value of the peak fibre stress. When the fibre fragment is much longer than the critical fibre length, the ineffective length is relative small, compared to the whole fibre segment and its effect can be neglected. However, with the increase of the applied stress, some short fibre segments cannot be broken anymore because the fibre axial stress cannot be built up to the fibre fracture strength within these segments while the fibre fragmentation in some remaining long segments still proceeds until the lengths of all segments are equal to or less than the critical fibre length. Fig. 3 shows the variation of the fibre axial stress along the fibre fragment for several different fibre lengths ($2L$), estimated by Eq. 9. It can be clearly seen that when close to the saturation limit the ineffective length is

comparable to the whole fibre fragment and thus the linear relationship between $\ln(s)$ and $\ln(\sigma_f)$ does not exist anymore.

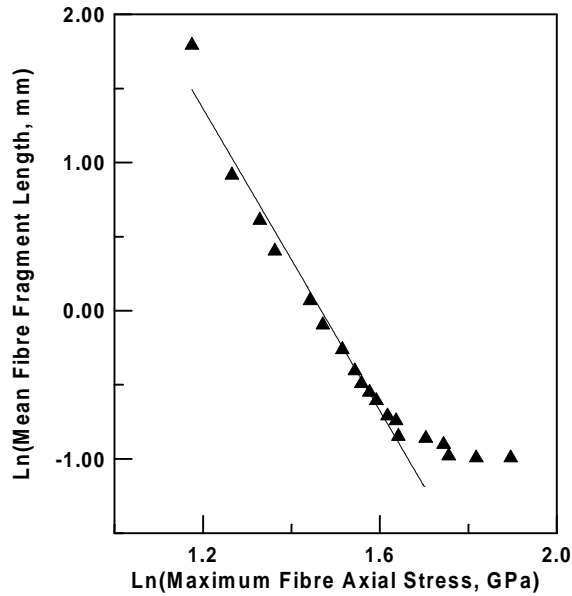


Fig. 2 A typical plot of $\ln(s)$ versus $\ln(\sigma_f)$ of single fibre fragmentation tests (treated/sized G34-700 carbon fibre/Araldite-F epoxy)

Single fibre tensile tests were also conducted for the carbon fibres based on the ASTM standard (ASTM D3379-75) and the Weibull weakest-link model was applied to analyse the results. The crosshead speed for all tests was 1 mm/min and five different gauge lengths were specified. Weibull fibre strength parameters tested in air using conventional tensile test method are listed in Table 2.

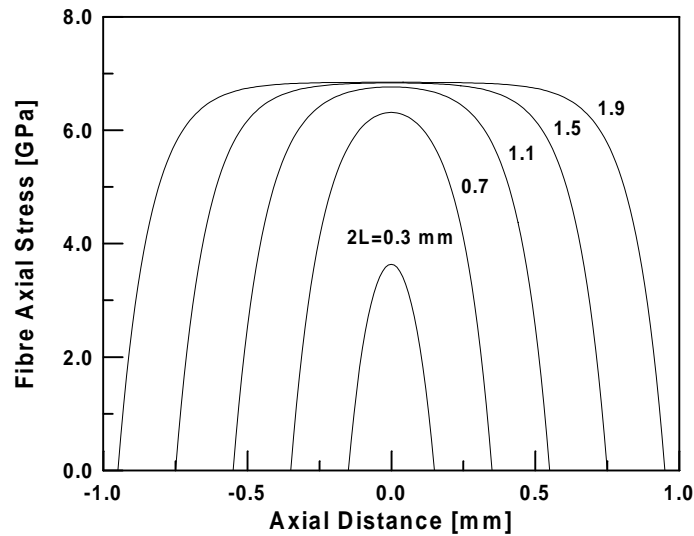


Fig.3 Plot of fibre axial stress (σ_f^z) as a function of axial distance (z) from fibre segment centre ($\sigma=50$ MPa; $E_f=240$ GPa; $E_m=1.75$ GPa)

The data obtained from six fragmentation specimens and the single fibre tensile results tested in air for treated/sized G34-700 carbon fibres are plotted together in Fig. 4. For T700S/Araldite-F systems, the similar results were obtained (Fig. 5). There is a good agreement between the values of the Weibull shape modulus obtained from the fragmentation tests and those from the conventional fibre tensile tests in air for treated/sized G34-700/Araldite-F and sized T700S/Araldite-F composite systems. However, discrepancy exists between the values of Weibull scale parameters as shown in Tables 1 and 2, Figs. 4 & 5. One of the reasons which cause the discrepancy is that the Weibull weakest-link model is only applicable over a limited length range. For long gauge lengths the chance of a low fracture stress due to accidental damage (i.e. due to rare defects which are not part of the normal defect population) becomes significant. Therefore, the size influence may be over-estimated if the extrapolation is made to a very short length as demonstrated by Dai and Piggott [8]. Another reason is considered to be the fibre degradation in the post-cure process at a high temperature. The post cure process was used in this study in the specimen preparation to reduce the influence of the matrix shrinkage during the direct curing at high temperature since extensive matrix shrinkage can cause misalignment and waviness of the fibre in the matrix. However, during the post curing at the high temperature the matrix expands much greater than the fibre does, so that a huge tensile stress (as large as 1.5 GPa) is exerted on the fibre, which increases the size of fibre flaws and even causes fibre fracture at some weak points. For untreated/unsized G34-700/Araldite-F and desized T700S/Araldite-F composite systems, discrepancy exists in both Weibull shape parameters and Weibull scale parameters between the two testing methods. This means that the assumption of perfect bonding between fibre and matrix may not be true for the two composite systems since extensive interfacial debonding may occur during the test after fibre fragmentation begins for the composite systems with weak fibre/matrix adhesion.

Table 1 Weibull strength parameters of single carbon fibres obtained from single fibre fragmentation tests

	G34-700 (Treated/ sized)	G34-700 (Untreated/ unsized)	T700S (Sized)	T700S (Desized)
Range of fibre fragments used, mm	10-0.4	10-0.8	7.5-0.7	7.5-1.0
Range of applied stress, MPa	30-50	30-45	30-58	30-55
Applied stress at saturation, MPa	53.4±1.6	48.9±3.4	59.1±1.0	56.7±3.1
Weibull shape parameter, <i>m</i>	4.8±1.2	3.2±1.2	4.8±1.4	3.3±0.6
Weibull scale parameter, σ_c GPa	4.3±0.4	5.3±0.7	8.5±1.2	9.2±1.3

Table 2 Weibull strength parameters of single carbon fibres tested in air

	Gauge length, s [mm]	Weibull shape parameter (local), m	Weibull scale parameter, $\sigma_0(s)$ [GPa]	Average tensile strength [GPa]	Weibull shape parameter (global), m	Weibull scale parameter, σ_0 [GPa]
	10	8.1	4.6	4.3±0.6		
	20	4.8	4.3	3.9±0.9		
G34-700 (Treated/sized)	30	6.4	3.9	3.6±0.6	4.3	8.1
	40	5.4	3.4	3.2±0.7		
	50	4.9	3.2	3.0±0.7		
	10	5.7	4.7	4.4±0.9		
	20	5.1	4.0	3.6±0.8		
G34-700 (Untreated/unsized)	30	5.2	3.8	3.5±0.7	5.5	7.1
	40	6.1	3.6	3.4±0.6		
	50	7.3	3.5	3.3±0.5		
	10	3.5	7.7	6.9±2.1		
	20	5.0	6.2	5.7±1.4		
T700S (Sized)	30	4.0	6.2	5.6±1.5	6.1	10.8
	40	3.7	6.0	5.4±1.6		
	50	4.0	5.8	5.3±1.4		
	10	3.8	7.0	6.3±1.6		
	20	4.0	6.3	5.7±1.6		
T700S (Desized)	30	3.4	5.9	5.3±1.5	5.9	10.4
	40	2.9	5.6	5.0±1.7		
	50	3.4	5.3	4.8±1.4		

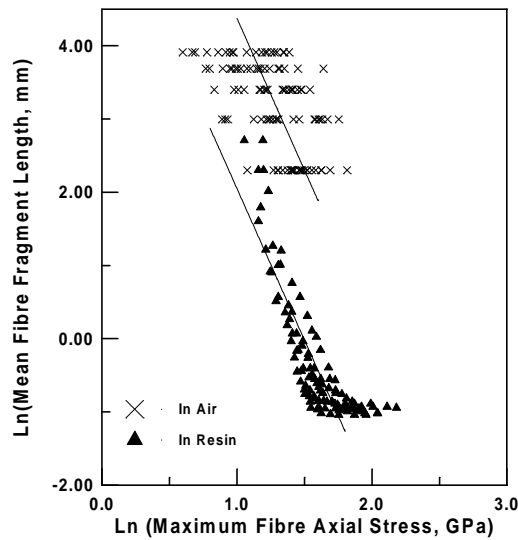


Fig. 4 Plot of $\ln(s)$ versus $\ln(\sigma_f)$ of single fibre fragmentation specimens (treated/sized G34-700 carbon fibre/Araldite-F epoxy) in comparison with results of single fibre tensile tests in air

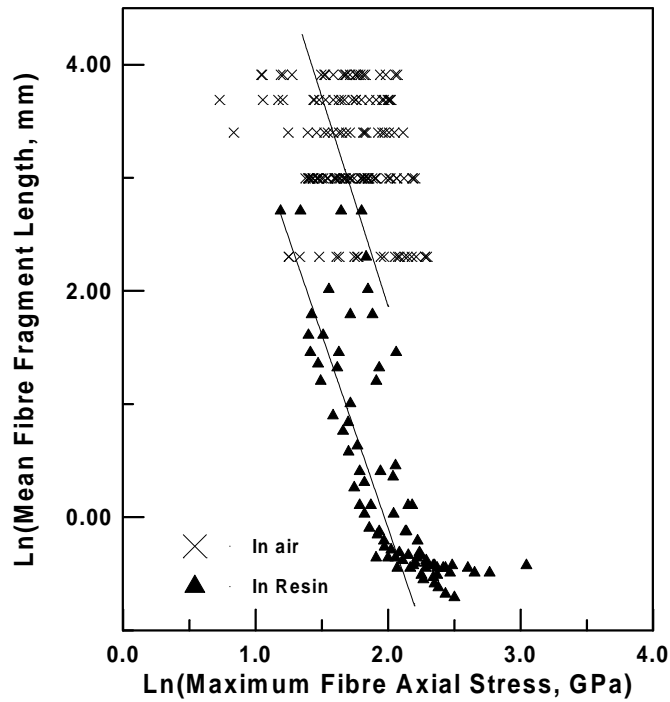


Fig. 5 Plot of $\ln(s)$ versus $\ln(\sigma_f)$ of single fibre fragmentation specimens (sized T700S carbon fibre/Araldite-F epoxy) in comparison with results of single fibre tensile tests in air

CONCLUSIONS

1. The measurement of the *in situ* fibre strength in the epoxy matrix is possible using single fibre fragmentation tests.
2. A linear relation between the logarithm of the average fibre fragment length and the logarithm of the maximum fibre axial stress is found before the saturation of fibre fragments is reached.
3. Discrepancy exists between the results obtained from the fragmentation tests and those from the extrapolations of conventional fibre tensile tests in air. This is considered to be associated with the limitation of the Weibull weakest-link model because it is only applicable over a limited length range. The fibre degradation in post-cure at the high temperature may also have a strong influence on the results.

ACKNOWLEDGEMENTS

The authors wish to thank the Australian Research Council for the continuing support of this study. Thanks are also due to Torayca Inc., Japan and Grafil Inc., USA for supplying the fibre materials. S. Deng is supported by Australian Overseas Postgraduate Scholarship (OPRS) and a Postgraduate Scholarship from the Department of Mechanical & Mechatronic Engineering at the University of Sydney.

REFERENCES

1. Kelly, A. and Tyson, W. R., "Tensile properties of fibre-reinforced metals: copper/tungsten and copper/molybdenum", *J. Mech. Phys. Solids* 13 (1965) 329.
2. Oshawa, T., Nakayama, A., Miwa, M. and Hasegawa, A., "Temperature dependence of the critical fibre length for the glass fibre-reinforced thermosetting resins", *J. Applied Polymer Science*, 22 (1978) 3203-12.
3. Watson, A. S. and Smith, R. L., "An examination of statistical theories for fibrous materials in the light of experimental data", *J. Mater. Sci.* 20 (1985) 3260-3270.
4. Wagner, H. D. and Eitan, A., "Interpretation of the fragmentation phenomenon in single-filament composite experiments", *Appl. Phys. Lett.*, 56 (1990) 1965-1967.
5. Yavin, B., Gallis, H. E., Scherf, J., Eitan, A. and Wagner, H. D., "Continuous monitoring of the fragmentation phenomenon in single fibre composite materials", *Polym. Compos.* 12 (1991) 436.
6. Goda, K., Park, J. M. and Netravali, A. N., "A new theory to obtain Weibull fibre strength parameters from a single-fibre composite test", *J. Materi. Sci.* 30 (1995) 2722.
7. Zhou, L., Kim, J. K., Baillie, C. and Mai, Yiu-Wing, "Stress transfer in the fibre fragmentation test: Part III. Effect of matrix cracking and interface debonding", *J. Compos. Materi.* 7 (1995) 881.
8. Dai, S. -R. and Piggott, M. R., "The strengths of carbon and kevlar fibres as a function of their lengths", *Composites Sci. Technol.*, 49 (1993) 81-87.

CHARACTERISATION OF NEW GENERATION SMALL DIAMETER SiC FIBRES AT HIGH TEMPERATURE

N. Hochet, M. H. Berger & A. R. Bunsell

Ecole des Mines de Paris Centre des Matériaux, BP 87, 91003 Evry Cedex, France

SUMMARY: The new generation of small diameter SiC based fibres contains markedly less oxygen than similar fibres presently in use. The effect of the oxygen content is known to create an intergranular metastable phase which limits use at high temperature and encourages creep. The reduction in oxygen in the Hi-Nicalon fibre is shown to increase the rigidity and to improve creep behaviour. In the Tyranno Lox-E fibre the reduction is still not sufficient to eliminate the effects of the intergranular phase and behaviour is seen to be similar to the previous generation of fibres.

KEYWORDS: Hi-Nicalon, Tyranno Lox-M, Tyranno Lox-E, ceramic fibre, silicon carbide, microstructure, mechanical properties, high temperature

INTRODUCTION

The development of fine and flexible fibres based on silicon carbide offers the possibility of reinforcing ceramic materials to produce high temperature structural composites. Nicalon NLM202 has been available since the early 1980s. Its microstructure has been described as consisting of β -SiC grains of 1.6 μ m diameter (55%wt) and free carbon (5%wt) embedded in an intergranular phase SiO_xC_y (40%wt) [1]. The differences between the mechanical characteristics and thermal stability of stoichiometric SiC and the SiC based ceramic from PCS are due to the existence of the intergranular phase and free carbon [2]. The Si-C-O phase allows the ceramic to creep and this is observed from 1273K. The free carbon reduces the oxidation resistance of the fibre. A fall in properties is observed associated with the decomposition of the intergranular phase and the microstructural changes.

Significant improvement of the high-temperature mechanical properties of SiC based fibres might be expected if the oxygen content could be reduced or the intergranular phase stabilised. The aim of this paper is to establish the consequences of a lower oxygen content and/or the presence of titanium on the microstructure and thermomechanical properties of the most recent polymer derived SiC based fibres.

MATERIALS

The most widely used fibres based on SiC are produced by Nippon Carbon (Nicalon fibres) and Ube Industries (Tyranno fibres) from respectively, polycarbosilane (PCS) and polytitanocarbosilane (PTC) polymer fibres. These precursor fibres are melt-spun and cross-

linked in air for the Nicalon NLM202 and the Tyranno Lox-M, or by electron beam irradiation in a helium atmosphere for the Hi-Nicalon and the Tyranno Lox-E fibres. The green fibres are then pyrolysed between 1473K and 1673K in an inert atmosphere. The main characteristics of the fibres given by the manufacturers are presented in Table 1. The precursor of the Tyranno fibres is different from that used for the Nicalon fibres, (PTC and PCS, respectively). According to Ube Industries, the presence of titanium stabilises the amorphous phase and so limits grain growth and the degradation of mechanical properties. Another effect of titanium could be the creation of Ti-C bonds, so offering better oxidation resistance, as the amount of free carbon at the interface would be reduced [4].

Table 1: Physical and chemical data on the fibres studied as given by the manufacturers [5,6]

	NLM 202	Hi-Nicalon	Tyranno Lox M	Tyranno Lox-E
Precursor	PCS	PCS	PTC	PTC
Cross linking mode	oxidation curing	radiation curing	oxidation curing	radiation curing
Diameter (μm)	15	13	8.5	11
Density (g/cm^3)	2.55	2.74	2.37	2.39
% Si wt	56.6	62.4	54.0	54.8
% C wt	31.7	37.1	31.6	37.5
% O wt	11.7	0.5	12.4	5.8
% Ti wt	0	0	2.0	1.9
C/Si at	1.31	1.39	1.36	1.64

The industrially produced Nicalon NLM202 and Tyranno Lox-M fibres, referred to here as "the present generation" have a high oxygen content (12 to 13% wt). The new generation of fibres contains less oxygen, Tyranno Lox-E (~ 5 %wt) and Hi-Nicalon (~ 0,5%wt), as the precursors have been crosslinked in the absence of oxygen. The carbon to oxygen ratio is greater in these fibres than in fibres cured by oxidation for which a part of carbon is eliminated in the form of carbon oxides during pyrolysis.

EXPERIMENTAL

The microstructures of these fibres were observed by transmission electron microscopy using an ARM working at 800 kV. Thin specimens were prepared by argon ion milling. Fracture morphologies were observed by scanning electron microscopy. The microscopes used were a Phillips 501 and a LEO Gemini 982 which was equipped with a field effect gun.

Mechanical tests were made with a mono-filamentary tensile machine equipped with a furnace allowing tests to be conducted from room temperature to 1673K in air and in flowing argon. The gauge length used for the tensile tests at room temperature was 25mm. For tests at higher temperatures, with cold jaws and in air, the gauge length was 250mm. The section heated at the maximum temperature was 30mm in length. The displacement speed for tensile tests was 0.2 mm/min. The fibres were heated for three minutes before the start of the tensile tests. As each test lasted about 5 minutes, each fibre spent an average of 8 minutes at the test temperature. Creep tests were conducted for a period of one or three days, in an argon flow.

RESULTS

Appearance of The Fibres

All the fibres had the same external appearance, they were circular in cross section , with a smooth surface and showed the same featureless morphology at the surface and core (Fig. 1).

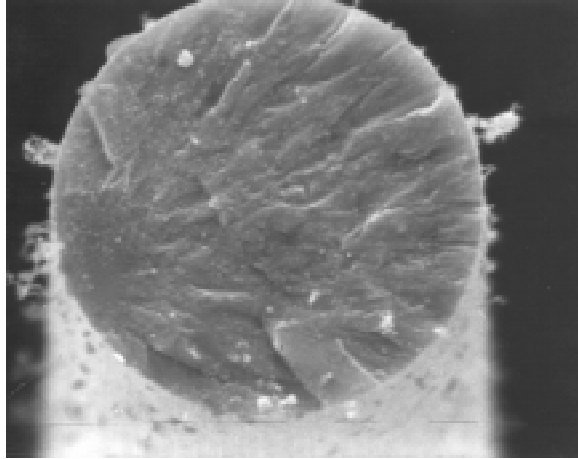


Fig. 1: Fracture morphology at room temperature

Tensile Properties at Room Temperature

All the fibres showed linear elastic behaviour at room temperature and their failure surfaces were characteristic of brittle failure (Fig. 1). The mechanical properties of these fibres at room temperature are shown in Fig 2. The fibres with a low oxygen content had elastic moduli and failure stresses which were higher than the present generation fibres. Within the same generation of fibres, the Tyranno fibres had higher failure stresses than the Nicalon fibres.

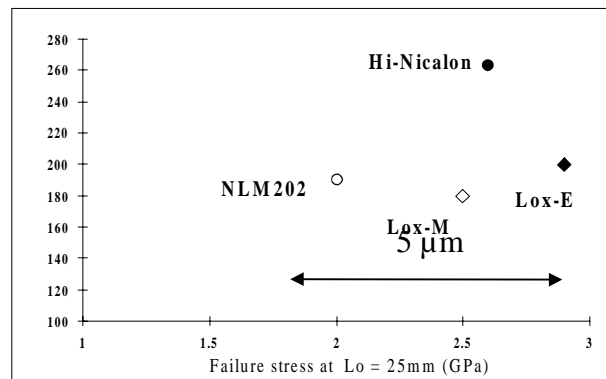


Fig. 2: Failure stress and elastic modulus of the Nicalon and Tyranno fibres

Tensile Behaviour at High Temperature

The variations of the strengths of the fibres, tested in air, as a function of temperature are presented in Fig. 3. The decrease of the failure stress was seen to occur at lower temperatures

for the Tyranno fibres. The evolution of the failure stresses of the NLM202 and Hi-Nicalon fibres were almost parallel, with higher values for the Hi-Nicalon.

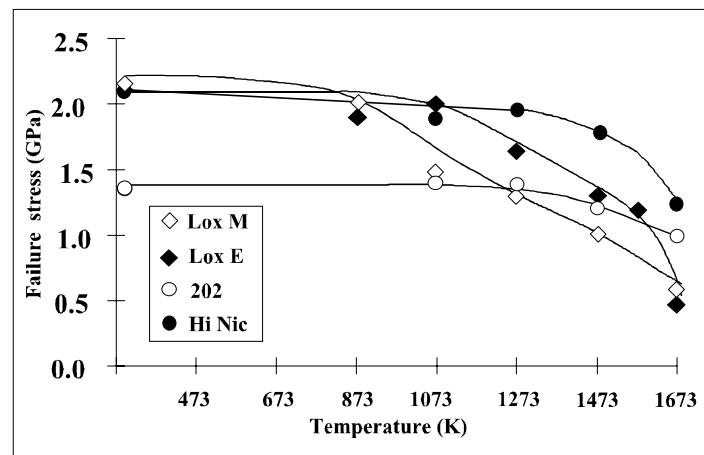


Fig.3: Evolution of tensile strengths as a function of temperature for the NLM 202, Hi-Nicalon, Lox-M and Lox-E fibres.

Creep Behaviour

Shrinkage at high temperature

Creep experiments at high temperatures and low loads revealed that negative strains were obtained at the beginning of the tests which influenced the creep curves obtained. An indication of the maximum stresses for which negative strains were detected is given in Table 2. The amount of shrinkage for a given stress increased as the temperature increased, as shown in Fig.4 but the stress for which only positive strains were obtained decreased as the temperature increased. The Nicalon fibres did not show negative deformation up to 1423K indicating no or very little shrinkage of these fibres up to this temperature. Above 1423K the Nicalon fibres began to shrink significantly. Shrinkage of the Tyranno fibres during creep experiments was observed from around 1323K and the amount of negative deformation, especially for the Lox-M fibre, were higher than that seen with the Nicalon fibres. This shrinkage during creep could be suppressed by a heat treatment of the fibres prior to mechanical testing. This is illustrated in Fig. 5 which shows results obtained with Tyranno Lox M fibres, before and after heat treatment at 1473K in argon for 5 hours (Tyranno Lox-MA). Similar stabilisation of the Hi-Nicalon could be obtained but heat treatment temperatures above 1400°C were necessary. The elastic moduli of the Lox-M fibres increased from 180 GPa to 193 GPa after heat treatment at 1473K. The effects of heat treatments on the elastic modulus of the Hi-Nicalon fibre are shown in Fig 6. It can be seen that the increase in modulus is accompanied by a decrease in strength.

Table 2: Maximum stresses σ_{max} (GPa) for which shrinkage was detected

Temperature (K)	NLM 202	Hi-Nicalon	Lox-M	Lox-E
1323	no shrinkage	no shrinkage	1.00	1.05
1423	no shrinkage	no shrinkage	0.65	0.45
1523	0.34	0.29	0.40	0.27
1623	0.18	0.20	0.08	0.20
1723	0.06	0.04	0.19	0.07

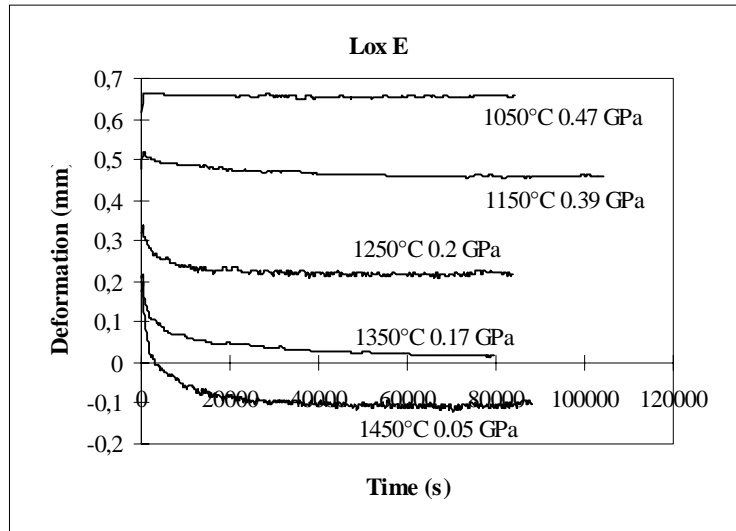


Fig.4: Shrinkage during creep increases with temperature.

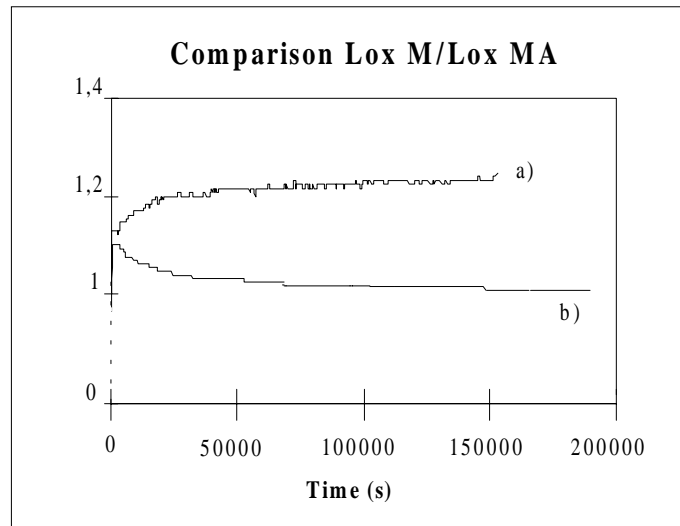


Fig. 5: Shrinkage during creep of the Lox-M b) is suppressed by a heat treatment of the fibres prior to testing a).

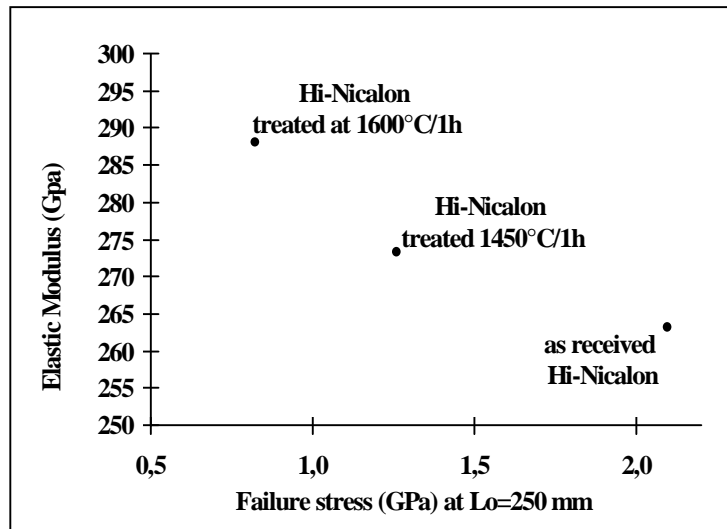


Fig.6: Variation of the rigidity and strength of the Hi-Nicalon fibre after heat-treatments.

Creep behaviour

All the fibres crept at high temperatures when under load. Their creep curves exhibited primary creep which lasted approximately five hours followed by secondary creep stages which was pseudo-stationary stage up to 1473-1573K, depending on the fibre type. Beyond these temperatures the creep rate is seen to be truly stationary. Fig.7 shows the creep behaviour of the Hi-Nicalon fibre at different temperatures subjected to approximately the same load. No third stage creep was observed.

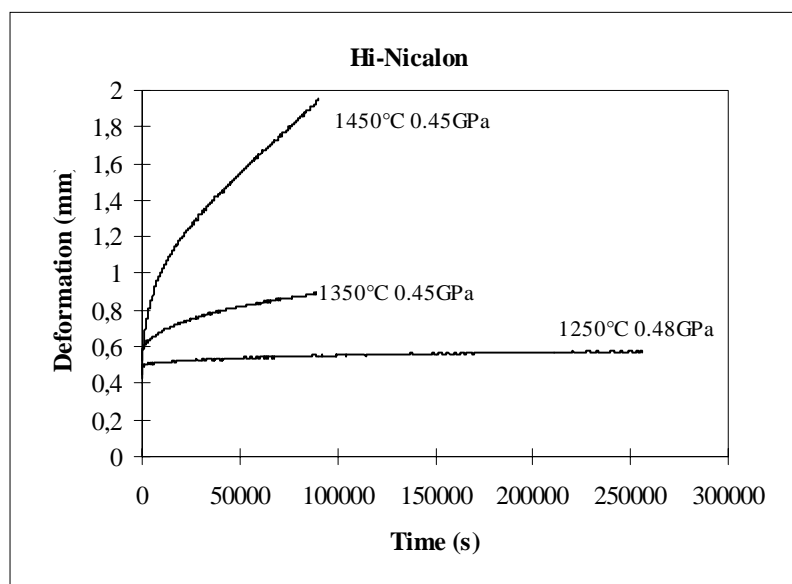


Fig. 7: Examples of creep curves for the Hi-Nicalon fibre obtained with an applied stress of ≈ 0.45 GPa

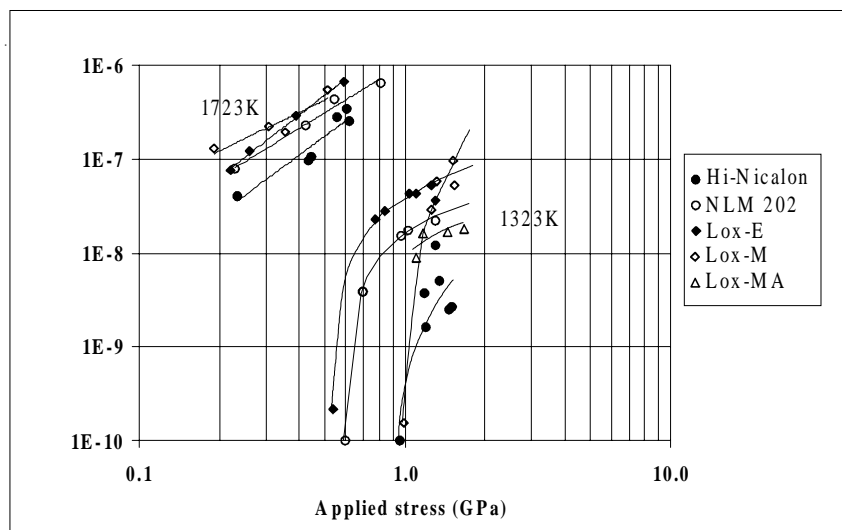


Fig.8 : Logarithmic plot of strain rates as a function of the applied stress at 1323K and 1723K for the fibres studied

Fig. 8 represents the deformation rates of the fibres respectively at 1323K and 1723K between 10 and 16 hours after the start of the creep study, for different applied stresses. Experimental limitations meant that the lowest deformation rate was 10^{-10}s^{-1} . The points shown on the curves corresponding to the threshold limit reflect therefore a rate of 10^{-10}s^{-1} . The rate of deformation, shown in Fig.8 corresponding to results obtained at 1323K, reveals the existence of creep thresholds which are high compared to the fibre failure stress. It must be noted that the Lox-M fibres show a higher creep threshold stress than the Lox-E fibres. Just above the threshold stress for the Lox-M fibre the latter creeps at a lower rate than the Lox-E fibre at the same stress. As the applied stress is increased further from the threshold level the creep rate curve for the Lox-M fibre crosses the curve for the Lox-E fibre to become greater. The creep behaviour of the NLM202 fibre can be seen from Fig.8 to be placed between that of the Lox-E and Lox-M fibres. However the Hi-Nicalon fibre possesses the highest creep threshold stress of all the fibres at 1323K and creeps at a much lower rate.

The Lox-M fibres which had been subjected to heat treatments at 1473K for 5 hours (Lox-MA) showed rates of deformation which were lower than those of the Lox-M and the NLM 202 fibres.

With increasing temperature, up to 1723K, the creep threshold stresses of all the fibres reduced. The strain rate of the Hi-Nicalon remained lower than the other fibres but the differences in creep behaviour became much less marked. Fig.8 shows the similar creep rates observed with all the fibres at 1723K.

Microstructures of the Fibres

The microstructures of the Lox-M and the Lox-E fibres, appeared similar and consisted of nanometric β -SiC grains of 2 nm in diameter and free carbon of around 1 nm in length as illustrated in Fig. 9 [7]. These microstructures were comparable to that observed with NLM202 fibres, although some larger grains up to 5 nm were found in the Lox-E fibres.

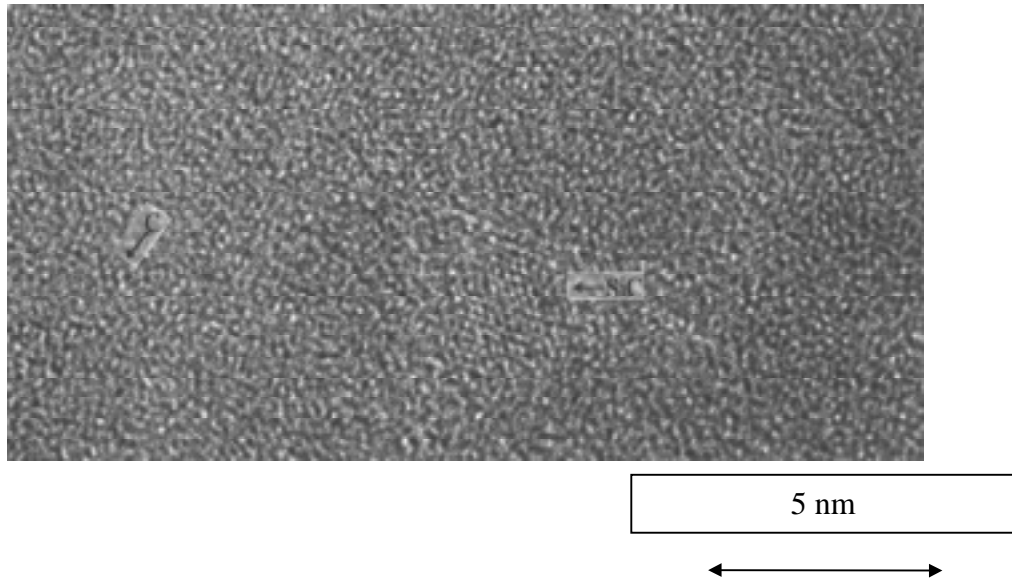


Fig. 9: Microstructure of the Lox-E fibre.

No crystallised Ti compounds were found in the as received Tyranno fibres and the titanium was assumed to be distributed inside an intergranular phase $\text{SiC}_x\text{Ti}_y\text{O}_z$ although such a phase could not be directly detected by TEM. The Hi-Nicalon fibre was distinguished from the other fibres by larger SiC grains (Fig. 10). The average grain size was about 5nm in the Hi-Nicalon but grains of up to 20nm in diameter existed, and the structure appeared to be a continuum of lattice-imaged SiC grains. Free carbon aggregates embedded in the SiC continuum exhibited better organisation in the Hi-Nicalon compared to the other fibres. They appear on lattice fringe images by the stacking of slightly distorted 5 to 10 carbon layers with a length of from 2nm up to 5nm [7].

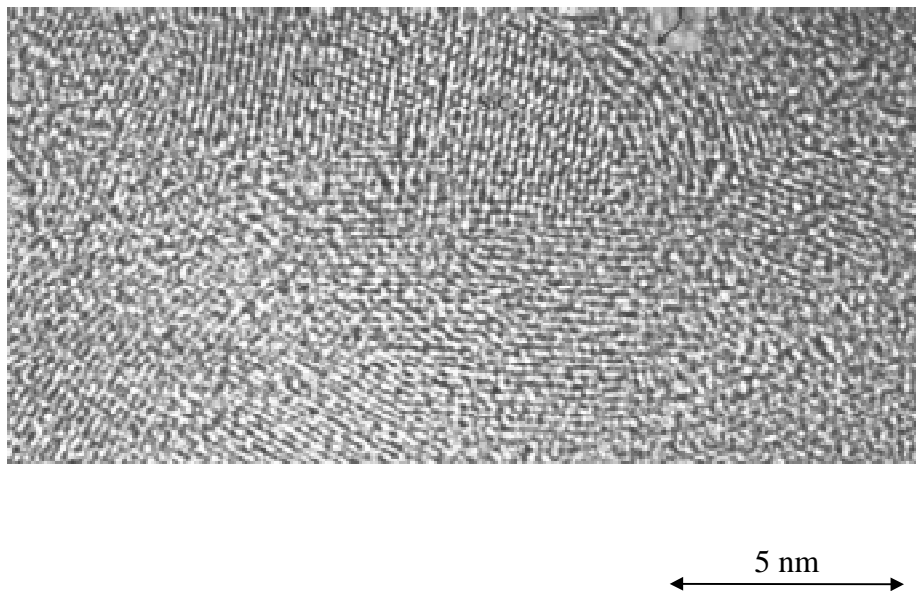


Fig. 10: Microstructure of the Hi-Nicalon fibre.

Modification of the microstructures of the fibres at high temperatures

After being heat treated for 24 hours in air above 1473K all the fibres were coated with SiO₂. At 1673K, the layer was completely crystallised into cristobalite and cracked. Some micropores could be seen in this layer and at the fibre-oxide interface (Fig. 11). A similar layer could be seen on fracture surfaces of the fibres tested at high temperatures. Fracture initiation in all the fibres tested in air was located at the SiO₂/fibre interface. The fracture morphologies at high temperatures were as brittle as those obtained at room temperature. The non oxidised part of the fibre within the silica layer can be seen from Fig. 18 to be no longer circular. The fracture behaviour of the fibres after creep in flowing argon was seen to remain brittle. A very thin SiO₂ layer could be seen on the surface of these fibres due to the presence of a low partial oxygen pressure.

Some grain growth was observed after heat treatment in air from 1373K for the Tyranno fibres and from 1573K for the Nicalon fibres. The relative grain growth for the NLM202 was 25%, for the Hi-Nicalon 55%, for the Lox-M 63% and for the Lox-E 90% after five hours at 1673K. At this temperature regions showing a continuum of SiC grains were observed in all the fibres. Growth of the free carbon aggregates was seen in all the fibres with the increase of the temperature and this carbon was frequently seen to surround SiC grains in the Hi-Nicalon fibres. The precipitation and rapid growth of grains of TiC in the Tyranno fibres was seen from 1473K [7].

After creep the fibres were seen to possess the same microstructures as after heat treatment at the same temperature with no indications of stress enhanced grain growth or anisotropy [7].

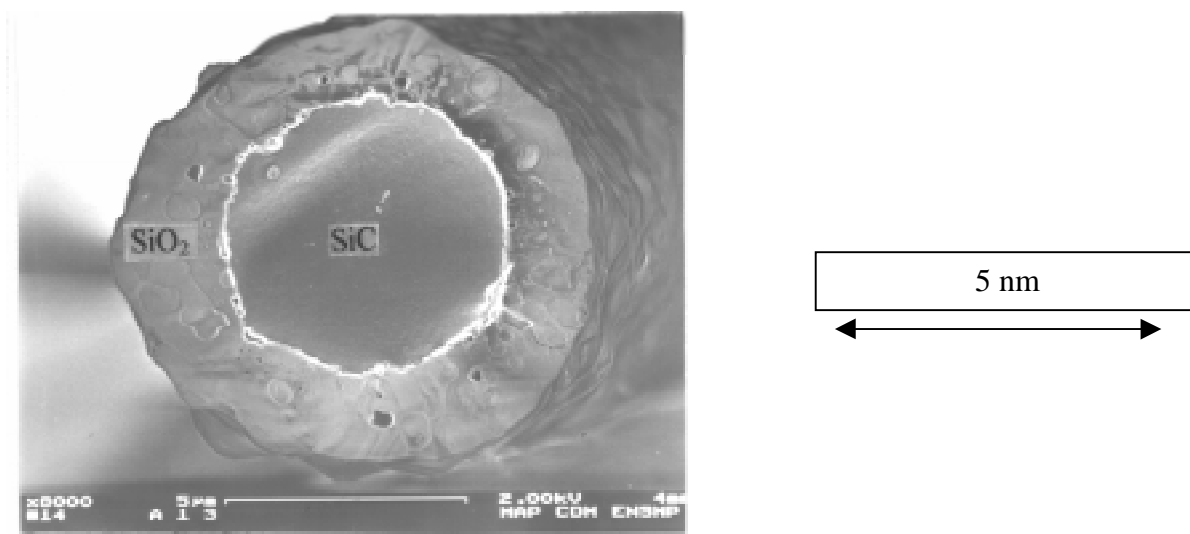


Fig. 11: Fracture Morphology of the LoxM Fibre at 1300°C.

DISCUSSION

A comparison between the microstructures and the thermo-mechanical properties of fibres with high and low oxygen contents confirms the link between oxygen content, the presence of an intergranular phase, grain size, rigidity, chemical stability and creep resistance.

The Hi-Nicalon fibre can be seen to differ markedly from the other fibres in its tensile and creep behaviour. The much lower oxygen content results in a drastic decrease of the

proportion of the low modulus intergranular phase. As a consequence, at room temperature, the Hi-Nicalon fibres show a higher Young's modulus than the other fibres. The grain sizes in the as received fibres and their growth related to their original dimensions, up to 1673K, are higher compared to those of the NLM202 fibres. The very low oxygen content in the grain boundary regions in the Hi-Nicalon does not limit the grain growth as it does in the oxygen rich fibres, but gives to the fibre better creep resistance.

The grain growth at 1673K is also more marked in the Lox-E than in the Lox-M fibre due to the reduction in oxygen content. However the presence of alkoxide groups in the PTC precursor imposes a minimum oxygen concentration at the grain boundary region in the Lox-E fibre so that this fibre behaves in creep in a similar fashion to the fibres cured by oxidation. Moreover the Tyranno fibres appear to be less stabilised as grain growth and shrinkage are seen to begin at lower temperatures than with the Nicalon fibres. The positive contribution of the titanium which was expected in the Tyranno fibres is therefore masked by the excess of oxygen and the lack of stability of the structure.

The duration of pyrolysis or the maximum temperature the fibres experience during manufacture appears to be insufficient for optimum properties to be obtained. The shrinkage seen under low loads at high temperatures is due to an increase in fibre density due to the reduction of porosity, with little contribution coming from grain growth. During the first five hours under steady loading, the deformation behaviour of the fibres is due to two mechanisms which are in competition. This effect, which is more important in the Tyranno fibres, can be reduced by a heat treatment which stabilises the fibre structure. In comparison with these fibres, the NLM202 fibre seems to be more stabilised, as shown by less grain growth and only slight shrinkage.

In passing from 1373K to 1573K, before total degradation, the microstructural changes due to the modification and reduction of the amorphous phases mean that the differences in behaviour of all the fibres become less important. As a consequence, their creep characteristics tend to converge.

CONCLUSIONS

In comparison with the earlier generation of fibres only the Hi-Nicalon fibre represents a real improvement of thermo-mechanical properties, however it still contains excess carbon which, it is reported, leads to a lower creep resistance compared to an experimental stoichiometric fibre [5]. Such modifications will not however suppress external oxidation which becomes significant above 1473K and could have a major effect at high temperatures on the fibre/matrix interface in any composites based on these fibres.

Thanks are due to Dr. A. Thorel for the realisation of the TEM pictures

REFERENCES

- [1] LE COUSTOMER P., MONTHIOUX M., and OBERLIN A. (1993) : "Understanding Nicalon Fibre", *J. Eur. Ceram. Soc.* 11, 95-103.
- [2] SIMON G., BUNSELL A.R. (1984) "Creep behaviour and structural characterisation at high temperatures of Nicalon SiC fibres". *J. Mater. Sci.* 19, 3658-3670.
- [3] OKAMURA K. (1987) "Ceramic fibres from polymer precursors". *Composites* 18 [2] 107-120
- [4] YAMAMURA T., HURUSHIMA T., HURUSHIMA T., KIMOTO M., ISHIKAWA T., SHIBUYA M., IWAI T. (1987) Development of new continuous Si-Ti-C-O fiber with high mechanical strength and heat-resistance, *High Tech Ceramics* (ed. by P. Vincenzini), pp. 737-746. Elsevier Science Publishers.
- [5] ICHIKAWA H., OKAMURA K., SEGUCHI T. (1995) "Oxygen-free ceramic fibers from organosilicon precursors and e-beam curing". *Ceramic Transactions, proceeding of High Temperature Ceramic Matrix Composites II* (edited by A.G. Evans), Vol.58, pp. 65-76.
- [6] UBE (1993) "Properties of Tyranno fiber" Technical data report n°2-001001
- [7] HOCHET N., BERGER M.H., BUNSELL A.R. (1997) "Microstructure and thermo-mechanical stability of a low-oxygen Nicalon fibre"q. Under press in *J. Microsc.* 185 [2]

MODELLING OF TIME-DEPENDENCE IN CELLULOSIC FIBRES BASED ON RAMAN SPECTROSCOPY

Wadood Y. Hamad

*Fibre Science and Technology Centre,
University of Manchester Institute of Science and Technology, Manchester, England*

SUMMARY: This paper addresses the application of Raman spectroscopic techniques to analysing the deformation micromechanics and modelling time-dependent behaviour in regenerated cellulose fibres. In addition to information obtained on the macroscopic deformation, Raman spectroscopy enables the study of changes in *internal* strain associated with creep and recovery. It is shown that the peak positions of the 1095 cm^{-1} and 895 cm^{-1} Raman-sensitive bands shift upon the application of tensile stress or strain due to the macroscopic deformation leading to direct stretching of the polymer molecules. This enables the fundamental micromechanics of deformation of the molecules within the fibre to be studied in detail; and, moreover, permits the accurate determination of the deformation of the fibres within a composite matrix where the stress and strain distribution can be mapped along individual fibres in the composite matrix and from which interfacial shear stresses can be derived. It is further indicated how the Raman-induced deformation data may be used to phenomenologically model time-dependence behaviour in these viscoelastic fibres.

KEYWORDS: raman spectroscopy, viscoelasticity, modelling, fibres, cellulose

INTRODUCTION

Raman, as well as infra-red, spectral studies of cellulosics have hitherto concentrated solely on discerning polymorphic changes in cellulose [1], and exploring the structure of cellulose [2]. Building upon the wealth of such excellent studies, successful attempts have been made [3] to characterize the deformation micromechanics in cellulose fibres. The current work is part of a large programme dedicated to explicating the molecular

deformation processes in a litany of native and regenerated cellulose fibres using Raman spectroscopic analysis; and utilizing the results thus obtained to model time-dependent phenomena in such fibres. This paper focuses on commercial grade, solvent-spun Tencel^R fibres which, in addition to their wide use in the textiles industry, are being investigated by this author as reinforcing fibres in polymer based nanocomposites whose impressive mechanical properties [4] could make them suitable candidates as load-bearing structural components.

Raman scattering is essentially the (small) portion of a beam of light that is inelastically scattered by a material — the majority of radiation which is scattered elastically at the same frequency as the incident light is the Rayleigh scattering. It is this inelastically scattered light that carries information about the molecular vibrations in the material, and hence it is useful in the characterization of non-metallic materials. Raman spectroscopy has successfully been used for the analysis of deformation processes in a variety of high-performance polymer fibres. In a number of such successful applications (see, amongst others, [5-7]), it was found that Raman bands associated with backbone groups on the polymer molecules shift in wave number on the application of stress or strain. This behaviour can be interpreted as being the result of macroscopic deformation of the polymer fibre causing chain stretching and/or crystal rotation in the polymer molecules in the fibre (for aramid fibres, for example, see [8]), and hence it can be used as a method for relating macroscopic and molecular deformation processes.

RAMAN SPECTROSCOPIC ANALYSIS OF FIBRE DEFORMATION

Materials and Instrumentation

Raman spectra were obtained for 1.6 dtex commercial grade tencel fibres (produced by solvent-spinning cellulose from wood-pulp) during deformation in a Raman microscope system. The fibre average diameter was found to be 12.3 μm . The Raman system is based upon a SPEX 1000M single monochromator with a holographic laser line filter. The 632.8 nm red line of a 7 mW He-Ne laser was used to excite the spectra to a 2 μm spot on the fibre using a modified Olympus microscope with a 50x objective. The laser beam was polarized parallel to the fibre axis for all of the measurements and the spectra were recorded using highly sensitive Wright Instruments Charge Coupled Device (CCD) camera.

Spectra were obtained from fibres during deformation in a small straining rig which fitted directly on to the stage of the microscope. Individual fibres were fixed between aluminium foil tabs which were placed on to the aluminium blocks of the straining rig using a cyanoacrylate adhesive, giving a gauge length of about 5 mm which could accurately be measured using a micrometer attachment that could be read to ± 0.005 mm. This gave a precision of ± 0.05 % for strain measurement. The fibres were loaded to failure in steps of strain of the order of 0.2% and the exposure time used to obtain a spectrum ranged from 10–30 seconds. Creep studies were performed over a period of time and the macroscopic deformation brought about by a constant load is reported in terms of the change in Raman frequency with respect to strain — as shown below. A total of 10 fibres were tested and all experiments were conducted at $23 \pm 1^\circ\text{C}$ and a

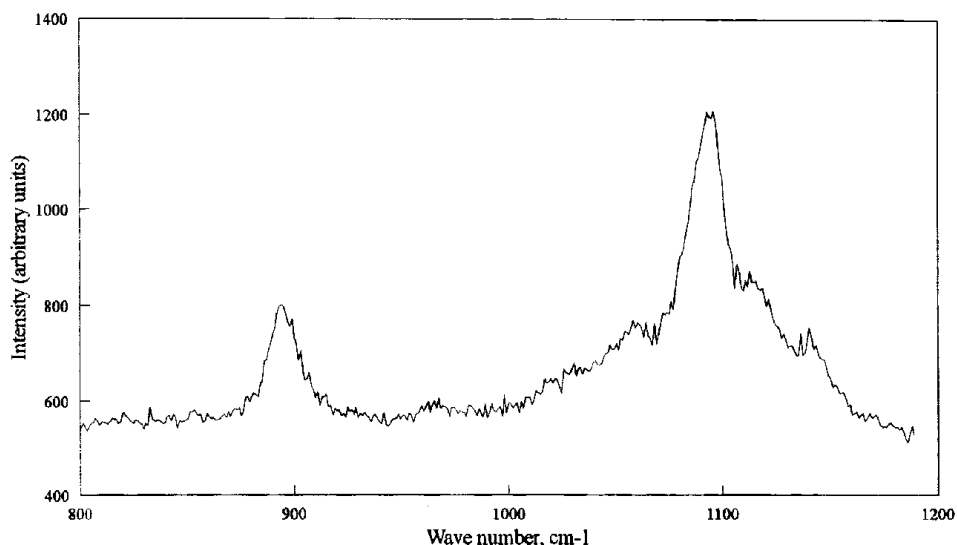


Figure 1: *Raman spectrum for a single tencel fibre in the region 850-1150 cm⁻¹ obtained using the 632.8 nm radiation from a He-Ne laser (7mW at the fibre).*

relative humidity of $50 \pm 2\%$.

Raman Deformation Studies

Results, shown elsewhere [3], indicate that exposing cellulose fibres to He-Ne laser radiation during deformation has insignificant effect on the values of strain (or stress) to failure and, hence, no fibre degradation ensues as a result.

For regenerated cellulose, the classes of internal motions associated with the different spectral features particularly fall in the regions below 1500 cm^{-1} which are the most sensitive to polymorphic change. The two peaks of Fig. 1 at 895 cm^{-1} and 1095 cm^{-1} prominently figure in the Raman spectrum for the structure of cellulose and the molecular deformation is ascertained by following these peaks as the fibres are subjected to external strain. The 1095 cm^{-1} peak is indicative of two principal modes: ring stretching together with C-O stretching motions. Whereas the 895 cm^{-1} peak indicates a contribution from angle bending coordinates involving heavy atoms only (i.e. CCC, COC, OCC), however, ring and C-O stretches and the external modes of the methylene groups may also be major contributors [9].

The effect of deformation upon the dominant Raman bands due to skeletal modes is clearly shown in Fig. 2. The bands shift to lower wave number, decrease in peak intensity and broaden somewhat upon the application of tensile strain (or stress). The shift is an indication of the straining of the fibre causing molecular deformation. The broadening, on the other hand, shows that there is a distribution of the stresses and strains over the molecules within the fibre. Fig. 3 depicts the dependence of the peak positions of the 895 cm^{-1} and 1095 cm^{-1} Raman bands, respectively, upon strain. It can be seen that the peaks shift to lower wave number and that the dependence upon strain is approximately linear.

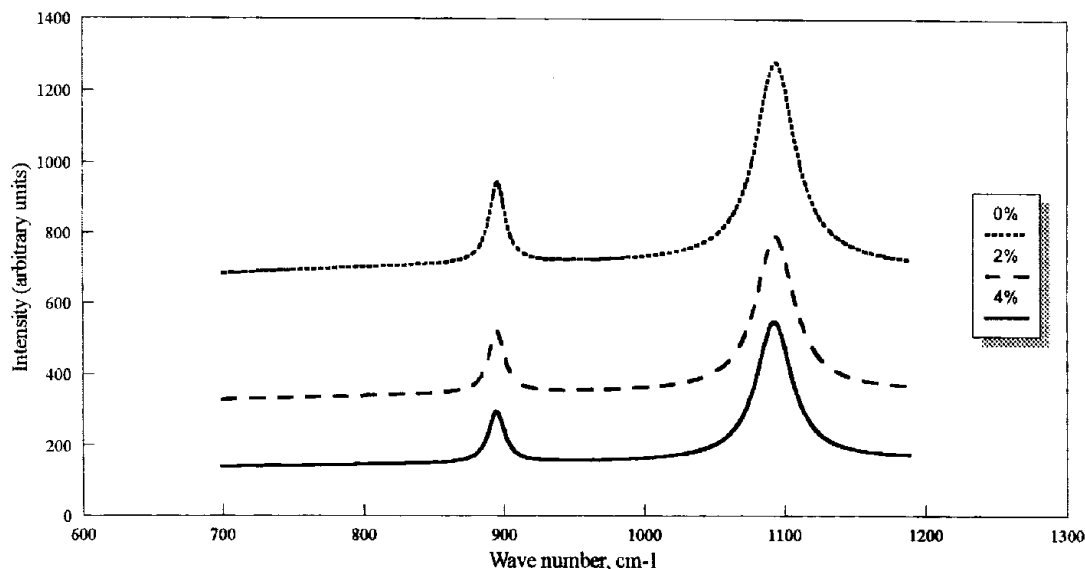


Figure 2: Shift in the position of the 895 cm^{-1} and 1095 cm^{-1} Raman band for tencel at three levels of strain.

RAMAN-MONITORED CREEP OF FIBRES

The Raman Strain Gauge

The results of the previous section clearly indicate that the macroscopic deformation of tencel is translated directly into molecular deformation; and that the deformation-induced skeletal modes most receptive to the Raman effect are those due to ring stretching together with C-O stretching motions [3, 4].

The Raman frequency versus strain plots of Fig. 3 for each of the Raman-sensitive bands may clearly be approximated by straight lines. To the extent that the Raman effect is calibrated, these straight lines serve to provide a microscopic 'strain gauge' by which internal micro-strains/stresses could be monitored. In the present work, the solvent-spun, regenerated cellulose fibres have been creep tested whilst mounted under the Raman microscope—as per details given in *Materials and Instrumentation*. The results were monitored in terms of the shifts in the 895 cm^{-1} and 1095 cm^{-1} Raman-sensitive peak positions with time. During creep under a positive external tensile stress, the macroscopic strain and strain rate must both be positive (or possibly zero). During recovery, however, the strain rate will be negative, whereas the macroscopic strain can only be positive or zero as for the loading case.

Fig. 4 depicts the variation of Raman frequency with creep time for the two Raman-sensitive bands; and utilizing the linear relationship between Raman frequency and strain for tencel fibres, corresponding plots of (micromechanical) strain versus creep time may be obtained—refer to Fig. 5. The response indicated in these figures, as detected by the Raman technique, is somewhat complex. It is evident that during the loading period, the strain components pass through a maximum, followed by a negative strain rate. It shall be demonstrated in the next section that it is possible to account for this observation in a phenomenological way.

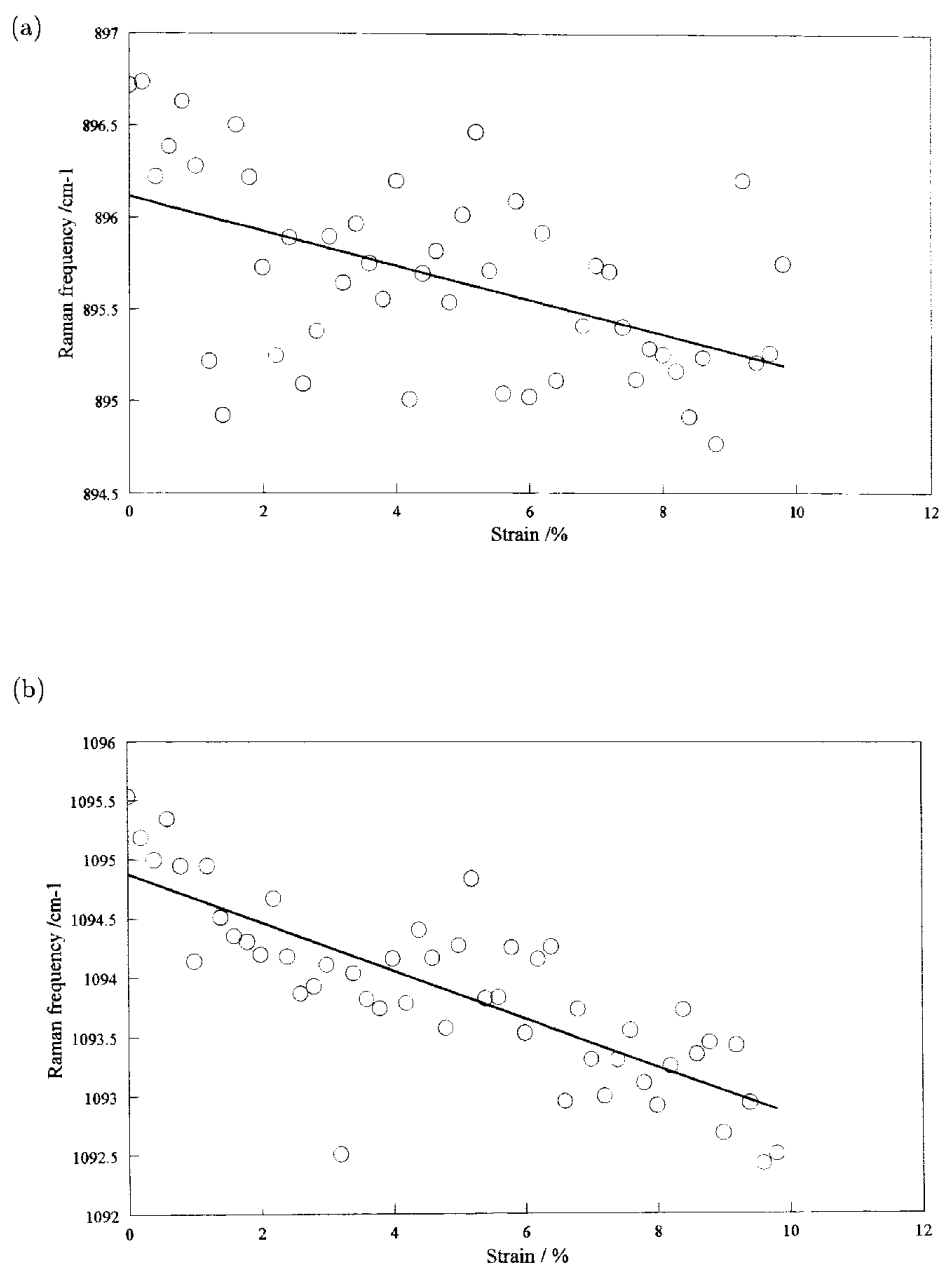


Figure 3: Dependence of the position of the 895 cm^{-1} (a) and 1095 cm^{-1} (b) Raman band peaks for tencel with strain.

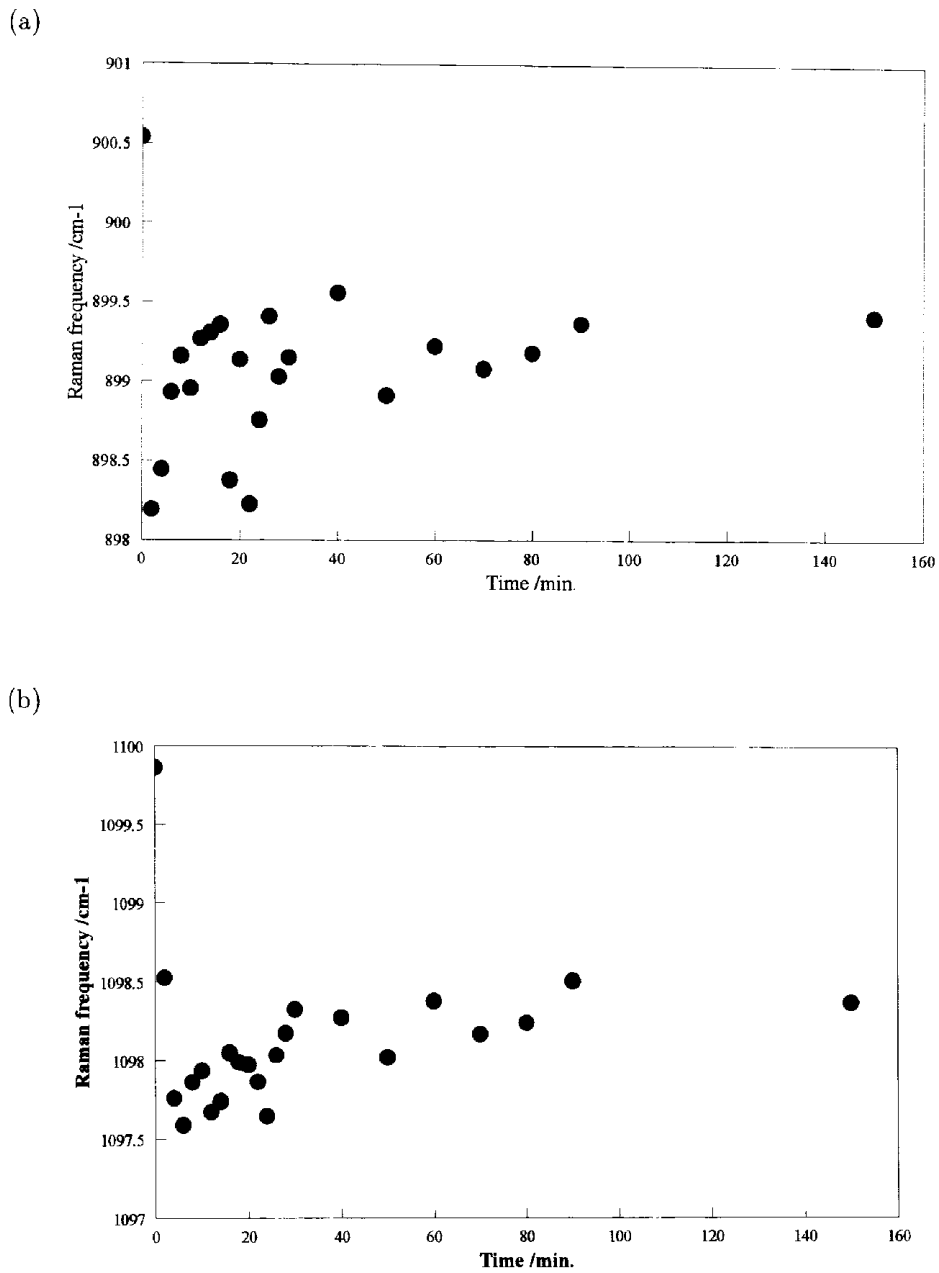


Figure 4: *Graphs of Raman shifts versus creep time data for the 895 cm⁻¹ (a) and 1095 cm⁻¹ (b) peak positions for solvent-spun tencel fibres (applied stress, $\sigma = 15844$ Pa).*

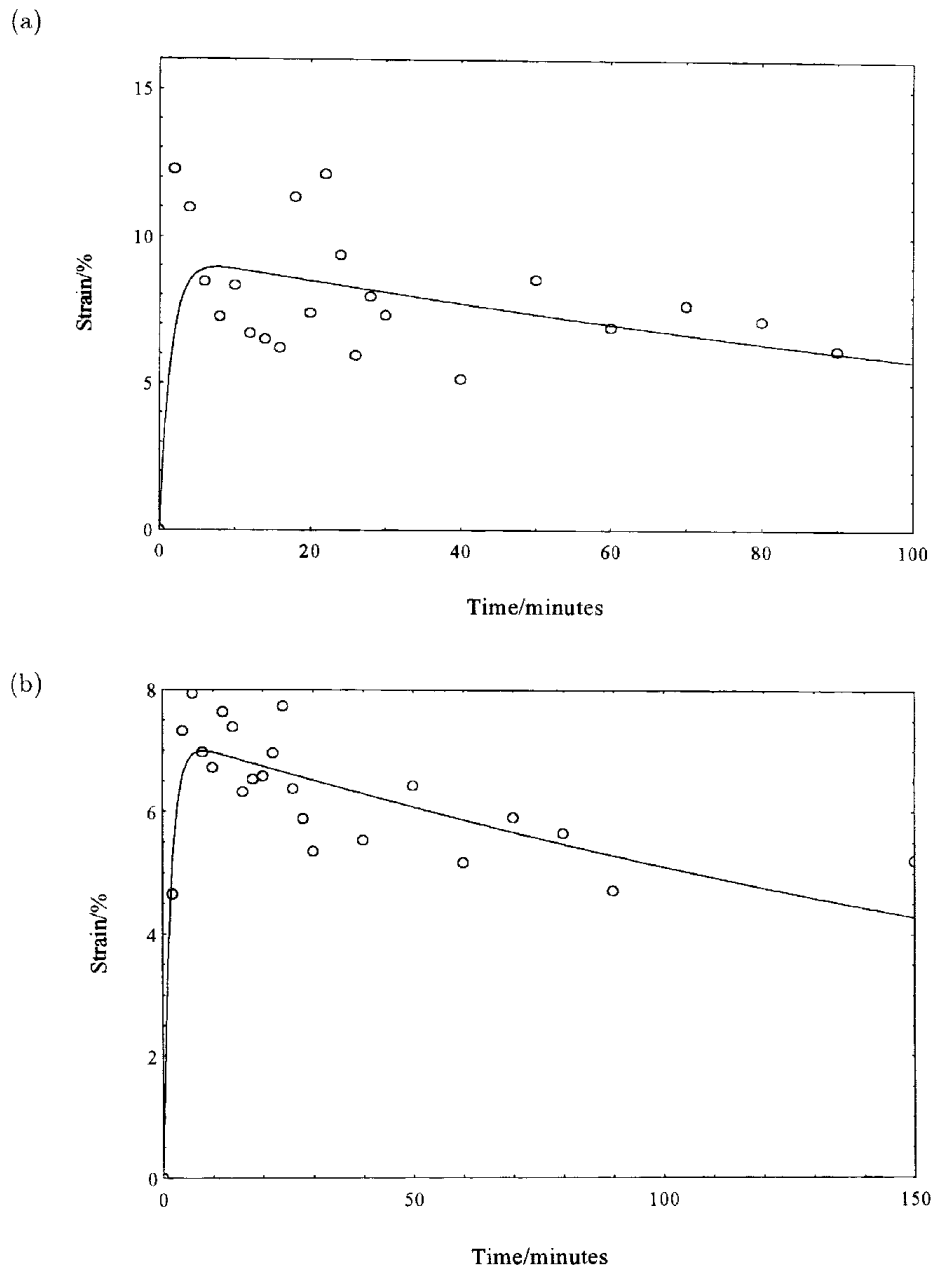


Figure 5: Corresponding graphs of (micromechanical) strain versus creep time data for the 895 cm^{-1} (a) and 1095 cm^{-1} (b) peak positions for solvent-spun tencel fibres (symbols) with simulated results (solid lines) based on the 3-phase solid model (applied stress, $\sigma = 15844\text{ Pa}$).

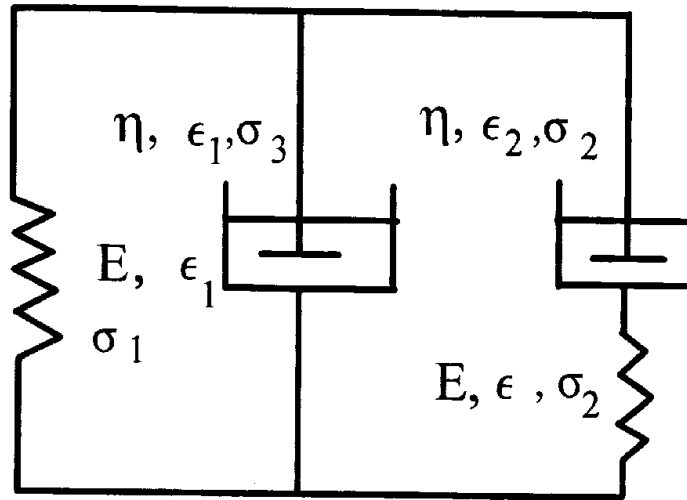


Figure 6: *The 3-phase solid model for predicting micromechanical creep in regenerated cellulose fibres.*

Creep Modelling

Based on the foregoing, it is fair to assume that the skeletal (micro)deformation of, primarily, ring stretching together with C-O stretching motions, is linearly related to the corresponding vibrational frequency (Fig. 3); and that the Raman band shift, $\Delta\nu$, versus strain sensitivity, $d(\Delta\nu)/d\epsilon$, is the same — and known — for the skeletal ring stretching modes. Thus, the relative strains in each structural region can be inferred from the Raman data; conversely, from a proposed mechanical model of creep, it is possible to simulate curves for strain versus creep time.

The proposed model, which may be referred to as a 3-phase solid model, is a modified version of the linear (Zener) solid model: with additional damping, represented by the central dashpot, however it is assumed that the two dashpots in the system are identical, as are the two springs — refer to Fig. 6. The strain in the right-hand spring predicts the micromechanical strain of the total strain in the system, and the left-hand spring should mirror the macroscopic creep/recovery strains. The model further predicts the development of negative (compressional) strain in the right-hand spring during recovery; and that the strain in the right-hand spring should pass through a maximum at some point during the creep stage.

The general differential equation that must be solved for the micromechanical strain in the system is given by:

$$\epsilon''(t) + \frac{3E}{\eta}\epsilon'(t) + \frac{E^2}{\eta^2}\epsilon(t) - \frac{\sigma'(t)}{\eta} = 0, \quad (1)$$

where ϵ , σ , E , η and t represent micromechanical strain, applied stress, Young's modulus,

damping coefficient and time, respectively — all symbols correspond to the elements of Fig. 6. Thence, applying the appropriate boundary conditions for creep, the resulting general solution for micromechanical creep in the system is:

$$\epsilon(t) = \frac{\sigma}{\sqrt{5}E} \left(\epsilon \frac{E}{2\eta} (\sqrt{5}-3)t - \epsilon \frac{E}{2\eta} (-\sqrt{5}-3)t \right). \quad (2)$$

Fig. 5 illustrates the fit of the latter equation to the Raman data. Needless to say, the agreement between the two is good and the general trend is accurately captured by the model. The corresponding constants for the depicted case of applied stress are given in Table 1.

Table 1: Constants for the 3-phase solid model, for an applied stress $\sigma = 15844$ Pa, fitted to the Raman data of Fig. 5.

Raman band (cm^{-1})	E (Pa)	η (N.s.m^{-2})
1095	979	3.4×10^4
895	759	5.0×10^6

N.B. Values were arrived at by trial and error.

CONCLUSIONS

It has been demonstrated that Raman spectroscopy is a powerful technique for explicating the deformation micromechanics of (single) regenerated cellulose fibres. Deformation has been ascertained by following the significant shifts of the 1095 cm^{-1} and 895 cm^{-1} Raman-sensitive bands under the application of mechanical stress. The Raman technique was shown to give a direct measure of molecular strain; and that it could be calibrated to provide a microscopic strain gauge by which internal micro-strains/stresses could be monitored. Indeed, this was used to shed light on the creep behaviour of these viscoelastic fibres. A phenomenological model, the 3-phase solid model, capable of predicting micromechanical strains was proposed which agrees well with the Raman results. The observed creep behaviour is adequately predicted by the model, in spite of the obvious simplicity of the model components: namely, the Newtonian dashpots for a material that is known for some considerable stress non-linearity [3]. An important result is the prediction of a strain maximum in the right-hand spring (corresponding to the micromechanical strain contribution) during the loading period. The recovery results have not been addressed in great detail at this stage, however, they will, along with investigating the application of Eyring flow processes to the case under study, be dealt with elsewhere.

ACKNOWLEDGEMENT

The author wishes to thank Professor R. J. Young of the Manchester Materials Science Centre for allowing the use of his Raman microscope facilities; and Courtaulds Fibres, Ltd., U.K. for supplying the samples.

REFERENCES

- [1] Atalla, R. H. (1976), *Applied Polymer Symp.* **28**, 659.
- [2] Marchessault, R. H. and Liang, C. Y. (1960), *J. Polym. Sci.* **43**, 71.
- [3] Hamad, W. Y. and Eichhorn, S. (1997), "Deformation Micromechanics of Regenerated Cellulose Fibers Using Raman Spectroscopy," *ASME Journal of Engineering Materials and Technology* (in press).
- [4] Hamad, W. Y., *Unpublished data.*
- [5] Andrews, M. C. and Young, R. J. (1993), *Journal of Raman Spectroscopy* **24**, 539.
- [6] Galiotis, C. and Batchelder, D. N. (1988), *J. Mater. Sci. Lett.* **7**, 545.
- [7] Yang, X., Hu, X., Day, R. J. and Young, R. J. (1992), *J. Mater. Sci.* **27**, 1409.
- [8] Young, R. J. and Ang, P. P. (1992), *Polymer* **33**, 975.
- [9] Atalla, R. H. and Nagel, S. C. (1974), *Science* **185**, 522.

THE DISTRIBUTION MODEL OF WHISKER ASPECT RATIO

Xun Zhao, Jixiang Jiang, Bing Jiang, Guang Yang

*Department of Materials Engineering and Applied Chemistry
National University of Defence Technology
Changsha, Hunan 410073, P.R.China*

SUMMARY: An investigation was undertaken to appraise the aspect ratio (l/d) of whisker materials. The study on the whisker aspect ratio involves goodness-of-fit of aspect ratio distribution model and a statistical determination of an appropriate sample size. Four kinds of whiskers such as SiCw, Si₃N₄w and 9Al₂O₃·2B₂O₃w were used. The whisker figures were taken by scanning electron microscope and the whisker aspect ratios were measured from the SEM pictures. The results of goodness of fit test indicate that the whisker aspect ratio follows Logarithm-Normal distribution at 0.99 level of confidence. An appropriate sample size is found not to be smaller than 210.

KEYWORDS: whiskers, aspect ratio, distribution model, goodness-of-fit, sample size

INTRODUCTION

Discontinuous composites are an important class of materials which have potential for utilization in a wide variety of applications. The discontinuous reinforcement can be divided into three groups, short fiber, whisker and particulate, among them the whisker has been paid attention because of its distinct reinforcing effect in composites. In recent years, many kinds of whiskers have been produced and used as reinforcement [1-5]. Discontinuous composites have several advantages that are very important for their use as structural materials. A number of composite models have been developed over the last two decades with the aim of predicting the mechanical properties of composites for given data of constituent phases (matrix and reinforcement). For example, in the case of short fiber (whisker) metal matrix composites, the strength of an composite with variable fiber lengths can be predicated by[6]

$$\sigma_{uc} = \sum_{l_i < l_c} \tau_i (V_f)_i (l_i / d_i) + \sum_{l_j \geq l_c} \sigma_f (V_f)_j \left[1 - \frac{\sigma_f}{4\tau_i (l_j / d_j)} \right] + \sigma'_m (1 - V_f) \quad (1)$$

where σ_{uc} is the ultimate tensile strength of the short fiber composites, σ'_m is the flow stress of the matrix at the failure strain of the fiber, V_f is the volume fraction of the fiber, $(V_f)_i$ and $(V_f)_j$ are the volume fraction of the fibers with $l_i < l_c$ and those with $l_j \geq l_c$, respectively. l_c is the critical fiber length. τ_i is the matrix-fiber interfacial shear strength.

It is obvious that the strength of short fiber reinforced composites depends directly and strongly upon the aspect ratio (l/d) of the discontinuous reinforcement, and it is significant to evaluate carefully the short fiber (whisker) aspect ratio. Arsenault examined the non-uniformity of aspect ratio of SiC whisker and the percentage of whisker volume fraction at various aspect ratio [7]. Sakamoto analyzed the aspect ratio distribution using Weibull distribution [8]. But the problems dealing with whisker aspect ratio distribution has not been discussed fully, due mainly to it is relatively hard to measure a great number of the aspect ratio data required for analyzing statistically such a random variable as whisker aspect ratio.

EXPERIMENT

Whisker Materials

The whiskers used in this experiment were 1) β -SiCw (TWS-100) produced by Tokai Carbon Co.Ltd, 2) α -Si₃N₄w manufactured by Tateho Chemical Co.Ltd, 3) K₂O₆·TiO₂w (HT-300, Chitan Kogyo Co.Ltd) and 4) 9Al₂O₃·2B₂O₃w (Shikoku Chemical Co. Ltd).

Measuring Whisker Aspect Ratio

By means of mixing the as-received whiskers with clean water, stirring moderately the fluid in order to disperse the whiskers as well as do not damage them, trickling the mixed fluid on a clean Aluminium foil, the specimens with dispersive whiskers for observing under scanning electron microscope were prepared. The outward appearance of different whiskers are almost the same under the observation of SEM. Making the whiskers SEM photograph into slides, the images of whiskers were projected on a white background from which the diameter and length of whiskers were measured one by one.

Goodness-of-fit Test of Whisker Aspect Ratio Distribution

The aspect ratio data were drawn to distribution histograms. On the basis of the histogram shapes, the distribution models those whisker aspect ratio population maybe follows were tentatively estimated. Then, the maximum likelihood ratio test and Kolmogorov-Smirnov test were employed to determine how well the observed aspect ratio data "fit" the specified models.

Determining the Sample Sizes

Once the distribution model of whisker aspect ratio was statistically inferred, the characteristic numbers of whisker aspect ratio samples, such as the mathematical expectation (mean) and the variances, can be obtained to describe and better understand the aspect ratio of certain whisker. In general, more accurate results can be obtained with larger sample size. Since larger samples require more time, there may be a need for a trade-off between the sample size and the specific levels of precision.

RESULTS AND DISCUSSION

Estimate of Distribution Models

The aspect ratio histograms of four kinds of whisker are shown in Figure 1. It can be found that the aspect ratio distribution is not symmetric. Comparing them with each other and with

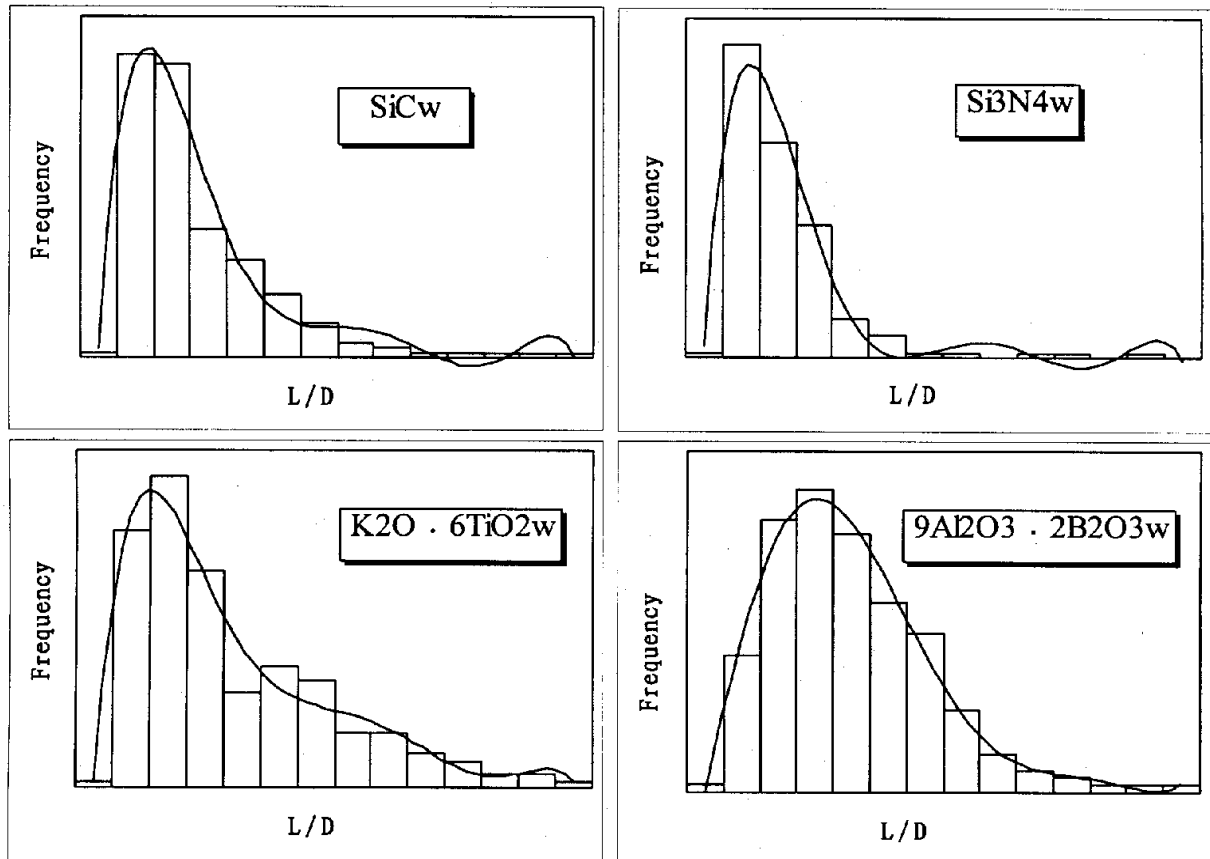


Figure 1: Histograms of Whisker Aspect Ratio

the distribution density curves of various distribution models, two inferences can be made:

- The aspect ratio of different whiskers follow the same distribution model, and
- The distribution model may be LN-Normal and Weibull distribution.

On the basis of the first inference, any whisker, for example, the Silicon Carbide whisker, could be chosen to make goodness-of-fit test and the test result should be applicable for other whiskers.

Goodness-of-fit Test

Two types of goodness-of-fit methods are considered: “maximum likelihood ratio test” and “Kolmogorov-Smirnov test”. There is detailed knowledge in literature about the fundamental and the application of these test methods.

Maximum likelihood ratio test to distinguish between LN-Normal and Weibull distribution

$$\text{Hypotheses } H_0: f_0(x; \mu, \sigma) = \frac{1}{\sqrt{2\pi}\sigma x} \exp\left[-\frac{1}{2\sigma^2}(\ln x - \mu)^2\right] \quad (x > 0) \quad (\text{LN-Normal})$$

that is, the whisker aspect ratio follows LN-Normal distribution

$$H_1: f_1(x; m, \eta) = \frac{m}{\eta} \left(\frac{x}{\eta}\right)^{m-1} \exp\left[-\frac{x}{\eta}\right] \quad (x > 0) \quad (\text{Weibull})$$

that is, the aspect ratio follows Weibull distribution

Test Statistic

$$\begin{aligned} \lambda &= \frac{\max_{m, \eta} \prod_{i=1}^n \frac{m}{\eta} \left(\frac{X_i}{\eta}\right)^{m-1} \exp\left[-\left(\frac{X_i}{\eta}\right)^m\right]}{\max_{\mu, \sigma} \prod_{i=1}^n \frac{1}{\sqrt{2\pi}\sigma X_i} \exp\left[-\frac{1}{2\sigma^2}(\ln X_i - \mu)^2\right]} \\ &= \frac{\left(\frac{\hat{m}}{\hat{\eta}}\right)^n \prod_{i=1}^n \left(\frac{X_i}{\hat{\eta}}\right)^{\hat{m}-1} \exp\left[-\left(\frac{X_i}{\hat{\eta}}\right)^{\hat{m}}\right]}{\left(\frac{1}{\sqrt{2\pi}\hat{\sigma}}\right)^n \prod_{i=1}^n \frac{1}{X_i} \exp\left[-\frac{1}{2\hat{\sigma}^2}(\ln X_i - \hat{\mu})^2\right]} \end{aligned} \quad (2)$$

where $\hat{\mu} = \frac{1}{n} \sum_{i=1}^n \ln X_i$, $\hat{\sigma}^2 = \frac{1}{n} \sum_{i=1}^n (\ln X_i - \hat{\mu})^2$ are the maximum likelihood estimation of μ and σ^2 , respectively, \hat{m} , $\hat{\eta}$ are the maximum likelihood estimation of unknown parameters m , η in Weibull distribution respectively. Substituting the maximum likelihood estimations of μ , σ , m and η into Eqn 2, the test statistic λ could be simplified to

$$\lambda = (2\pi e \hat{\sigma}^2)^{\frac{n}{2}} \prod_{i=1}^n X_i f_1(X_i; \hat{m}, \hat{\eta}) \quad (3)$$

$$\text{If assuming } E = (2\pi e \hat{\sigma}^2)^{\frac{1}{2}} \left[\prod_{i=1}^n X_i f_1(X_i; \hat{m}, \hat{\eta}) \right]^{\frac{1}{n}} \quad (4)$$

thus “ $\lambda > K$ ” is equivalent to “ $E > K$ ”, and decision rule is

$$\begin{aligned} E > E_\alpha, & \text{ reject } H_0, \text{ accept } H_1 \\ E \leq E_\alpha, & \text{ reject } H_1, \text{ accept } H_0 \end{aligned}$$

Using the measured aspect ratio data of SiCw, the maximum likelihood estimations of μ , σ^2 , m and η can be computed respectively:

$$\begin{aligned} \hat{\mu} &= \frac{1}{50} \sum_{i=1}^{50} \ln x_i = 2.3712 & \hat{\sigma}^2 &= \frac{1}{50} \sum_{i=1}^{50} (\ln x_i - \hat{\mu})^2 = 0.5863 \\ \hat{m} &= 1.2739 & \hat{\eta} &= 11.28 \end{aligned}$$

where $x_i = l_i/d_i$. Substituting these estimation values into Eqn 4, the test statistic E is equal to 0.5715. For $\alpha=0.01$, $E_{0.01}=1.054$. Since $E = 0.5715 < E_{0.01}=1.054$, the H_1 should be rejected at the 0.01 level of significance, or in other words, it should be appropriate to consider the whisker aspect ratio as following LN-Normal distribution.

Kolmogrov-Smirnov Test

In this investigation, the Kolmogrov-Smirnov Test was carried out by using a computer software of statistical inference. The test results indicate that the aspect ratio of four kinds of whisker follow LN-Normal distribution at the 0.99 level of confidence.

Determining the Sample Size Required for Evaluating Whisker Aspect ratio

It has been inferred that the whisker aspect ratio follow the LN-Normal distribution at a very high level of confidence. The researchers' interest is focused on appraising truly the nature of whiskers using statistical parameters, for example, the means and the variances of whisker aspect ratio. According to the definition of LN-Normal distribution, if a random variable X follows a LN-Normal distribution (noted as $X \sim LN(\mu, \sigma^2)$), $\ln X$ follows a Normal distribution (noted as $\ln X \sim N(\mu, \sigma^2)$). The mathematic expectation (mean) and the variance of X are

$$E(X) = \exp\left(\mu + \frac{1}{2}\sigma^2\right) \quad (5)$$

$$Var(X) = \exp[2\mu + \sigma^2][e^{\sigma^2} - 1] \quad (6)$$

where μ and σ^2 are the mean and the variance of Normal distribution population $\ln X$, respectively. Figure 2 shows the histogram of $\ln(l/d)$.

The Eqn 5 and 6 imply that the mean and the variance of LN-Normal population X depend on both mean and variance of Normal population $\ln X$. The problem of determining the sample size necessary to estimate σ^2 to within given tolerances and confidence levels is much complex. Triola gives the solution [9]:The sample variance s^2 is the best estimate of the population variance σ^2 . To be 95% confident that s^2 is within 20% of the value of σ^2 , the sample size n should be at least 210.

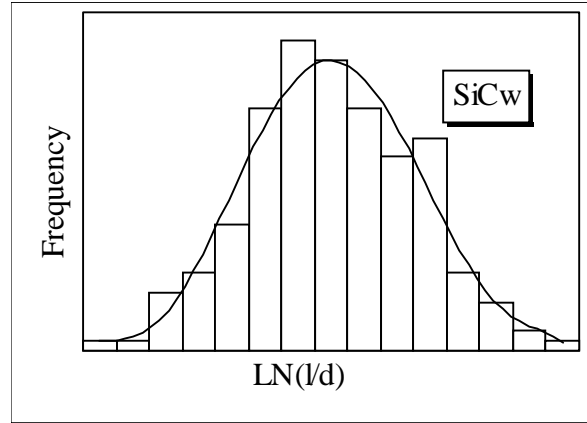


Figure 2: The histogram of $\ln(l/d)$

In terms of the means, the sample mean \bar{x} is the best point estimate of the population mean μ , and the sample size is given by

$$n = \left(\frac{Z_{\alpha/2} \sigma}{E} \right)^2 \tag{7}$$

where α is the level of significance, $Z_{\alpha/2}$ is the positive standard Z value that separates an area of $\alpha/2$ in the right tail of the standard normal distribution, σ is the standard deviation of normal distribution population and can be replaced by sample standard deviation s if $n > 30$, E is the maximum error of the point estimate \bar{x} .

The sample sizes necessary to estimate the mean and variance of whisker aspect ratio is determined according to follow schedule:

- 1) Taking the logarithm of whisker aspect ratio $(l/d)_i$.
- 2) Giving the level of confidence $1-\alpha=0.95$ ($\alpha=0.05$).
- 3) Determining the sample size n_{σ^2} for estimating the variance of $\ln(l/d)$, in this situation $n_{\sigma^2}=210$ as noted above.
- 4) Calculating the values of s^2 , s and \bar{x} with n_{σ^2} , here $s^2=0.556$, $s=0.746$ and $\bar{x} = 2.372$
- 5) For $\alpha = 0.05$, finding $Z_{\alpha/2} = 1.96$, assuming $E = 5\%$ $\bar{x} = 0.119$ and calculating n_{μ} for estimating the mean of $\ln(l/d)$:

$$n_{\mu} = \left[\frac{1.96 \times 0.746}{0.119} \right]^2 = 151.99 \approx 152$$

- 6) Taking $n_{\sigma^2, \mu} = \max(n_{\sigma^2}, n_{\mu}) = \max(210, 152) = 210$ as the required sample size.

If taking $E = 20\%$ $\bar{x} = 0.474$ instead of 5% \bar{x} , for matching with the n_{σ^2} estimate ($n_{\sigma^2} = 210$ is determined with s^2 is within 20% of σ^2), the n_{μ} is reduced from 152 to 10. This imply that n_{μ} is much smaller than n_{σ^2} at the same level of precision in the case of $\ln(l/d)$. In other words, the sample size could be determined so long as dealing with the variance.

CONCLUSIONS

1. All of the whiskers studied in this paper have the similar aspect ratio distribution density curve, the aspect ratio of different whiskers follow the same distribution model.
2. The aspect ratio of whiskers come from LN-Normal distribution population, particularly, “Kolmogorov - Smirnov Test” proves that the aspect ratio of four kinds of whiskers follow LN-Normal distribution at 0.99 level of confidence.
3. For evaluating the mean and the variance of whisker aspect ratio with 95% confidence and 20% error, 210 data should be randomly selected from the whisker aspect ratio population.

REFERENCES

1. Fukunaga, H., Pan, J. and Ning, X.G., “Squeeze Casting and Properties of Newly- Developed Whiskers Reinforced 6061 Aluminum Alloy Composites” *Proc. of the First Canadian International Composites Conference and Exhibition*, Montreal, Quebec, Canada, 4-6 September, 1991, Elsevier Science Publishers, 1992, pp.3C2-1
2. Nutt, S.K. and Carpenter, R.W., “Non - Equilibrium Phase Distribution in an Al-SiC Composite”, *Mater. Sci. and Eng.*, Vol. 75, 1985, pp169-177
3. Imai, T., Mabuchi, M., Tozama, Y. and Yamada, M., “Superplasticity in β -Silicon Nitride Whisker-reinforced 2124 Aluminium Composites”, *J. Mater. Sci. Lett.*, Vol. 9, 1990, pp255-257
4. Suganuma, K., Fujita, T., Suzuki, N. and Nihara, K., “Aluminum Composites Reinforced with a New Aluminum Borate Whisker” *J. Mater. Sci. Lett.*, Vol.9, 1990, pp.633
5. Suganuma, K., Fujita, T., Niihara, K. and Suzuki, N., “AA6061 Composite reinforced with Potassium Titanate Whisker” *J. Mater. Sci. Lett.*, Vol. 8, 1989, pp.808
6. Taya, M. and Arsenault, R.J., *Metal Matrix Composites-Thermomechanical Behavior*, Pergamon Press, 1989, Great Britain, pp.77
7. Arsenault, R.J., *Mater. Sci. and Eng.*, Vol. 64, 1987, pp. 140-156
8. Sakamoto, A., Hasegawa, H. and Minoda, Y., *Proc. of the Fifth International Conference on Composite Materials*, 1985, pp.703
9. Triola, M.F., *Elementary Statistics, 5th Edition*, Addison-Wesley Publishing Company, June 1992, U.S.A., pp.280-321

PREPARATION OF SiC COATED CARBON FIBER BASED ON RAYON USING PSI PROCESSES

**Xiaodong Li, Ping Peng, Ge Wang, Xiuying Liu, Chunxiang Feng,
Xiaozhong Huang and Yingchun He**

*Department of Material Engineering and Applied Chemistry,
National University of Defense Technology
Changsha, Hunan, P. R. China, 410073*

SUMMARY: Based on high-strength rayon fiber, continuous SiC-coated carbon fibers were prepared. A chemical treatment using an amine-containing aqueous solution enables the fiber to be pyrolyzed at much higher heating rate. Multi-step pyrolysis accompanied with polymer solution infiltration processes using polycarbosilane solution was carried out. The pyrolysis temperature is up to 1000. The kinetics of the pyrolysis was investigated and a new model was proposed, with which, the pyrolysis procedure was established. The yield of the C/SiC fibers is 35-38%. The tensile strength of the fiber is 1.3-2.0GPa, Young's modulus of 70-130 GPa and average fiber diameter of 4 to 6 μ . Since the carbon and the exterior SiC are formed from the corresponding organic precursors at high temperature, the interface of C and SiC is formed by a strong linking and in a graduation form, with SiC infiltrated into the inner part of the fiber.

KEYWORDS: rayon, polycarbosilane, polymer-solution infiltration, carbon fiber, pyrolysis, amine-containing catalyst

INTRODUCTION

The preparation of carbon fibers based on rayon have been studied extensively since decades. It has long been recognized that, due to the structure of rayon, the carbon fibers resulted are of low yield, porous, and with lower mechanical properties than PAN-based fibers. The reason that rayon remains to be one of the widely used raw materials for producing carbon fiber is that rayon comes from regenerative natural resources and the resulted carbon fibers possess some characteristic properties to various applications [1], such as in activated carbon fibers [2] and some special composites, etc. In addition, with suitable technique, rayon can be modified by coating in the process of pyrolysis, which is unavoidably followed by a high weight loss, to improve the mechanical and electromagnetic properties.

Silicon carbide can be used as a protective coating on carbon fibers by CVD [3,4] and composites for anti-oxidation applications [5,6]. The precursor of SiC, polycarbosilane, is soluble in organic solvents [7] and it would be suitable for coating on the surface of fibrils. With the coating on rayon, or partly-pyrolyzed dark rayon, the interior cellulose turns into carbon while the exterior polycarbosilane becomes SiC by pyrolysis. The porosity and the irregular and indented cross section of the dark rayon allow an amount of polycarbosilane coated onto the surface and even infiltrated into the inner part of the fiber. The carbon and SiC will be linked strongly and the interface in gradient. The amount of SiC can be varied in a

range to adjust the properties of the C/SiC fiber. Actually, this method may be easily extended into another organic precursors to form different coatings.

EXPERIMENTAL

High strength rayon was applied as the raw material, which was washed continuously with acid, water and impregnated with an amine-containing aqueous solution. After drying in hot air, the fiber was pyrolyzed in steps. Low temperature pyrolysis was at 100°C and 250°C in air and 350°C and 500°C in nitrogen through tube-furnaces. The total time required was about 3 hours. When the weight loss of the fiber was in the range of 30-50%, a process of polymer solution infiltration (PSI) of the above dark fiber was carried out using a benzene solution of polycarbosilane, surface active agents and a catalyst in ultrasonic agitation at 60°C. To keep the concentration of the polymer solution unchanged in the PSI process, the solution was continuously replenished. Multi-cycle of PSI and low temperature pyrolysis was sometimes necessary to coat as more SiC as desired on the fiber. High temperature pyrolysis was taken place at 500°C, 700°C and 1000°C in nitrogen through silica glass tube-furnaces at a higher passing rate. The total time of the pyrolysis was less than 5 hours. SiC coated carbon (C/SiC) fibers were thus obtained. The procedure is schematically presented in Fig. 1. The structure of the fibers was characterized by SEM, IR spectroscopy, DTA/TG, X-ray diffraction of fiber and powder, element analysis and XPS etc.

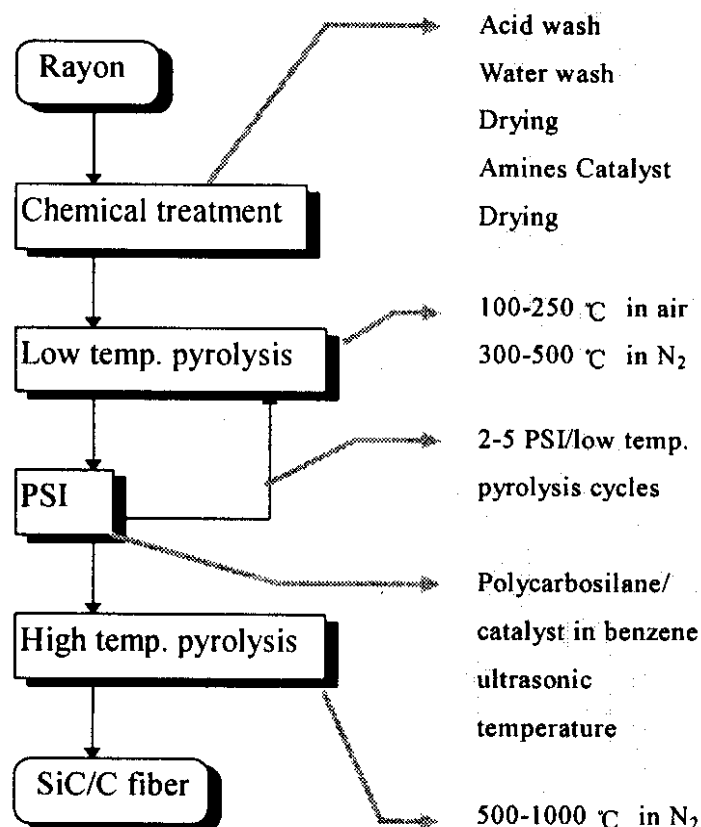


Fig. 1 Flow chart of the preparation

RESULTS AND DISCUSSION

Amines-containing Catalyst

To produce carbon fibers with high tensile strength from rayon, the low-temperature pyrolysis is usually at as low rate of heating as possible [8], due to a long time is required to moderate the chain splitting and the evaporation of the large amount of small molecules from the system. It has long been reported that the pyrolysis of rayon can be catalyzed by some chemicals, or flame retardants, such as those containing phosphorus, sulfur, halides and nitrogen etc. [9,10]. In this work, a chemical treatment using an aqueous solution containing polybasic amines and surface active agents was applied. This enables rayon to be pyrolyzed at a significantly higher heating rate, while the yield of the resulted carbon fiber is increased considerably.

It seems very complicated to explain the mechanism of the catalyst in details. What is clear is that, owing to the reactions of the amines with the primary hydroxyl group of the glucose repeat units in the fibril surface, the energy of activation of decomposition is much lower. The polybasic amines crosslink the macroradicals and a larger amount of char will be produced at lower temperature at the expense of harmful levoglucosan in the form of tar. The char in the fiber surface in turn protects the fiber from rush chain splitting and evaporation of the small molecules in the process of the next-step pyrolysis.

Fig. 2 is the TG and DTG profiles of rayon with the heating rate at 10°C/min. With the catalyst impregnation, the weight lose starts at a lower temperature (200°C) comparing with that without the treatment (290°C). DTG curve 3 shows that a new reaction takes place at low temperature, while a higher peak, which signifies the normal decomposition, appears at the same temperature with the sharp peak 4 of raw rayon. This also demonstrates that much higher residual weight of impregnated rayon left up to 600°C. This effect is somewhat equivalent to decreasing the heating rate (Fig. 3).

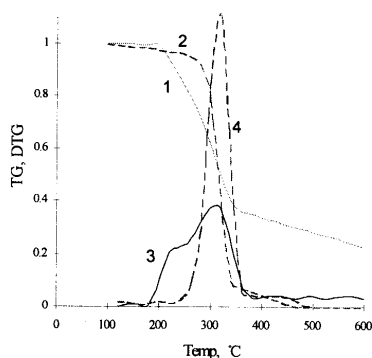


Fig. 2 The effect of the amines-containing catalyst on rayon. 1 and 2, TG with and without the catalyst; 3 and 4 DTG with and without the catalyst.

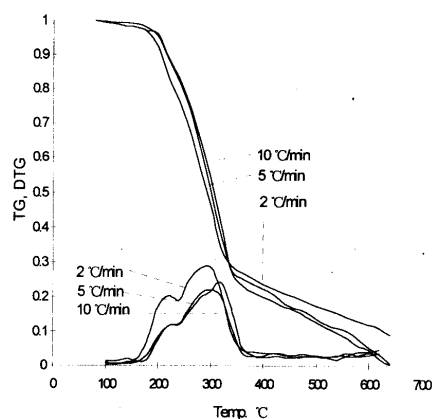


Fig. 3 The comparison of heating rate on TG and DTG profiles of rayon after impregnation.

Kinetics of the Low-temperature Pyrolysis

The kinetics of the pyrolysis, especially in low-temperature range in air, of rayon as well as the other cellulose materials has been studied by many authors [11,12]. However, there is a lot of different conclusions because of the complexity of the reactions involved. In this work, to establish the pyrolysis procedure, the kinetics was considered. As mentioned previously, the impregnation of the amines-containing catalyst accelerates the weight loss in the first-stage of pyrolysis. It would be very interesting to investigate the difference in their kinetic behaviors.

Millet [12] and Basch [13] investigated the weight loss (WI) of cellulose materials and found first-order kinetics, or

$$dWI/dt \propto -KWl.$$

However, this can hardly be used to depict the weight loss to a little longer time from the very beginning. Since the weight loss is started from the surfaced of the material, the weight loss must be a diffusion controlled reaction. The higher the weight loss, the more difficult the evaporation of the volatile components. Another term, that is similar to the diffusion from the film in surface condensation [14], should then be added to the equation, which is written as:

$$dWI/dt = K'/WI. - KWl$$

or

$$WI = (K'/K)^{0.5} (1 - e^{-2Kt})^{0.5}$$

Fig. 4 and 5 respectively show the isothermal weight loss at a few selected temperatures with and without the catalyst impregnation, and the data were emulated by the kinetic equation. The theory seems fit the weight loss of rayon studied even for a rather long time. It should be noted that the constant $(K'/K)^{0.5}$ is actually the maximum weight loss at a certain temperature.

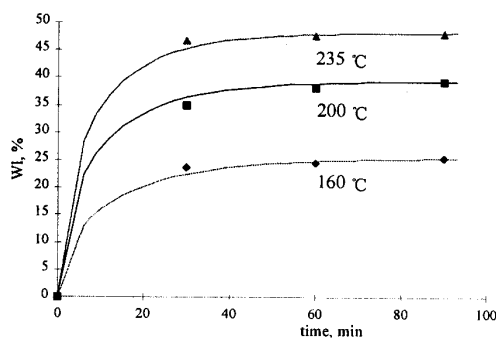


Fig. 4 Isothermal weight loss curves for the catalyst-impregnated rayon

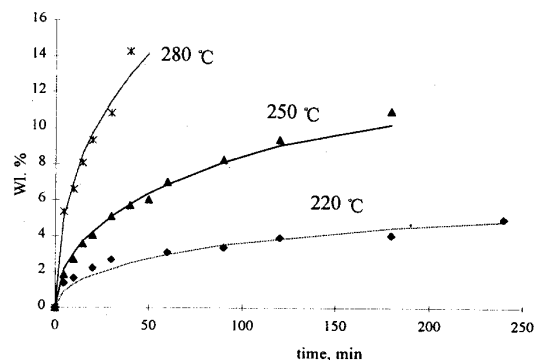


Fig. 5 Isothermal weight loss curves for rayon without catalyst-impregnation.

Fig. 6 and 7 show good linear relations which were used to the calculation of the activation energies. Table 1 summarizes the results of the kinetic analysis. With the impregnation, the two energies of activation decreased significantly.

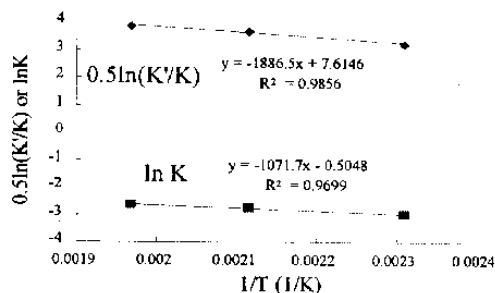


Fig.6 Calculation of activation energies of weight loss of rayon with the catalyst-impregnation.

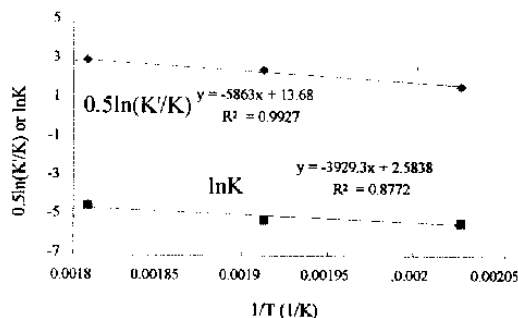


Fig. 7 Calculation of activation energies of weight loss of rayon without the catalyst-impregnation.

Table 1, The kinetics results of pyrolysis of rayon in air with and without the impregnation. (E: activation energy and A: frequency factor for K; those with prime corresponding to K')

Temp., °C	K, min ⁻¹	K', min ⁻¹	ΔE, KJ/mol	A	ΔE', KJ/mol	A'
with catalyst-impregnation						
150	0.050	32.51	8.91	0.60	42.09	4.0410 ⁶
200	0.065	100.39				
235	0.072	166.50				
without catalyst-impregnation						
220	0.005	0.168	32.67	13.25	130.16	1.0110 ¹³
250	0.006	0.953				
280	0.012	5.292				

The kinetics of the pyrolysis is a principle to establish the temperature program, passing rate and staying time of the fiber in the low temperature pyrolysis. While for high temperature pyrolysis, the temperature program were designed using a least square method.

PSI Process using Polycarbosilane Solution

After rayon fibers were pyrolyzed at low temperature, 200-300°C, the dark fibers were coated with polycarbosilane solution in benzene. The polymer solution infiltration process is very sensitive to the molecular weight and the concentration of the polycarbosilane as well as the composition of the solution used. In addition, the temperature and ultrasonic agitation of the process are also important.

To avoid the bonding between the fibrils, that will cause the fiber deteriorate in high-temperature pyrolysis, the molecular weight of polycarbosilane had to be limited to about 500°C to 1000°C and the concentration to 4-10%. In the polymer solution, surface active agents were added to disperse the polymer on the surface of fibrils. Crosslinking agent was also needed especially for low-molecular-weight polymer.

After the PSI process, the fiber was cured at elevated temperature in air for 10min and pyrolyzed at 300-400°C, followed by high temperature pyrolysis up to 1000°C. When more SiC was desired on the carbon fiber, more PSI and low-temperature pyrolysis cycles were taken. The content of SiC is about 3 to 8%.

The Structure of the C/SiC Fiber

From the SEM photograph in Fig. 8, the surface of the C/SiC fibers are smooth and no bonding between the fibrils. The X-ray diffraction patterns of the C/SiC fiber are shown in Fig. 9, there are at least three types of crystalline.

- (a) Two wide reflections belonging to carbon/graphite are found: 200 and 101. One can estimated the degree of graphite crystalline, g , by the d-spacing (in nm) of 200 reflection using equation proposed by Haraka and Warren [15],

$$d(002) = 0.3354g + 0.3440(1 - g)$$

The d-spacing is at 0.341 to 0.342nm, that means the degree of graphite crystalline is in the range of 23 to 35%.

- (b) There shows 3 reflections of β -SiC on the profiles taken on the fibers with additional non-stretch heating at 1700°C: 0.25nm (111), 0.21nm (220) and 0.15nm (311). However, for 1000°C fibers, these 3 reflections are not visible. That means the SiC crystalline is more difficult to form than polycarbosilane fiber. What is interesting is that for the commercial carbon fiber, such as T300, treated by the same PSI process and additional heating, the 3 reflections are not exist at all. This seems to be because the dense surface of the carbon fiber of T300 cannot be coated by polycarbosilane to a considerable amount, while for the dark rayon, the fiber surface is porous and rough and can hold much more polymer and shows SiC crystalline. High molecular weight in polycarbosilane is favorable for the formation of β -SiC.

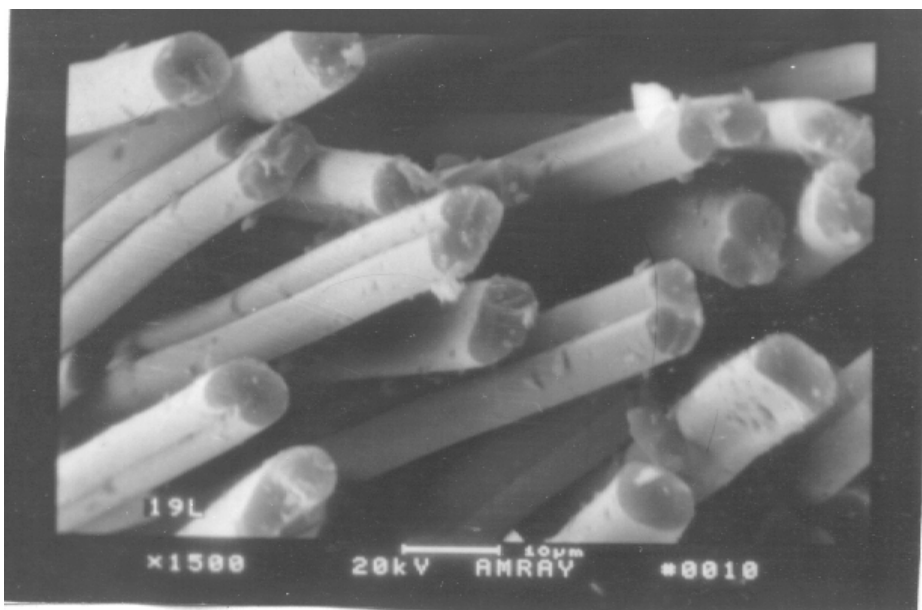


Fig. 8 SEM photograph of C/SiC fiber

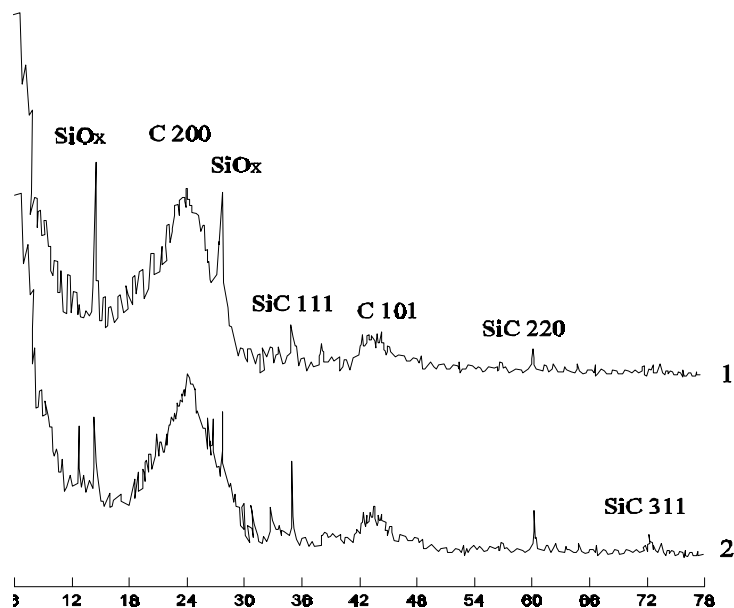


Fig. 9 X-ray diffraction patterns of C/SiC fiber.

- (c) There are 3 sharp reflections at 0.71nm, 0.64nm and 0.32nm that cannot be assigned to C/graphite or SiC. Those should belong to one of the oxides of silicon, SiO_x [16], which comes out from the oxidation of curing. But with polycarbosilane of higher molecular weight, the reflections are smaller.

Since the carbon and the exterior SiC are formed in the process of high-temperature pyrolysis, the interface of the C and SiC is not as sharp as ordinary coating of SiC on a carbon fiber by CVD method and so on. The fiber with a structure of gradient from carbon to SiC is characteristic of this process. Evidence for this was based on XPS, where Si was detected even at the center of the fibrils.

The Properties of the C/SiC Fiber

Pyrolyzed at 1000°C, the overall yield of the C/SiC fiber is 35-38% by weight related to the raw rayon. The typical average elemental contents of the fiber are made of C, 88%(w), Si, 5%, N, 3% and a certain amount of oxygen. Of the C/SiC fiber, the density is 1.55-1.60g/cm³, the tensile strength 1.3-2.0 GPa, the Young's modulus 70-130GPa, the average diameter 4 to 6 μ and the specific resistivity 10⁻² to 10⁻³ Ω cm. When the fibers were exposed at 400°C for 2 hours, the retention of the tensile strength as well as that of the weight of the C/SiC fiber is about 1.5 to 1.8 times of those of the fiber without SiC PSI treatment.

CONCLUSIONS

1. An amines-containing aqueous solution is very effective as catalyst of the pyrolysis of rayon. The impregnation of the catalyst on rayon not only accelerates the reactions, diminishing the pyrolysis time to 5 hours, but also results in a high yield, 35-38%(w), of the carbon fiber.
2. Polycarbosilane with a moderate molecular weight and concentration was coated on the surface of rayon fibrils by PSI processes. Carbon from the interior rayon and SiC from the exterior polycarbosilane are formed in the process of high temperature pyrolysis.
3. In the C/SiC fiber, carbon and SiC are linked strongly, and some SiC is infiltrated into the inner part, thus a gradient structure is assumed. The fiber after 1000°C pyrolysis contains 3-8%(w) of SiC and shows a tensile strength of 1.3-2.0 GPa and Young's modulus 70-130 GPa .
4. The weight lose kinetics of rayon is established from the experimental data that the weight lose (Wl) obeys the following relation.

$$dWl/dt = K'/Wl - KWl$$

The energies of activation were obtained.

REFERENCES

- [1] Shmidt, D. L., *SAMPE Quarterly*, Vol. 8, 1977, PP. 47.
- [2] Yoshida, A., *US. Patent*, 4814145, 1989
- [3] Wang, Y. Q., Wang, Z. M., Zhou, B. L. and Shi, C. X., *J. Mater. Sci. Lett.*, Vol. 12, 1993, PP. 817
- [4] Rooke, M. A. and Sherwood, P. M. A., *Carbon*, Vol. 33(4), 1995, PP. 375.
- [5] Sugiyama, K. and Yamamoto, E., *J. Mater. Sci.*, Vol. 24, 1989, PP. 3756.
- [6] Ma, C., Tai, N., Chang, W. and Chao, H., *J. Mater. Sci.*, Vol. 31, 1996, PP. 649.
- [7] Hasegawa, Y., Iimura, M. and Yajima, S., *J. Mater. Sci.*, Vol. 15, 1980, PP. 720.
- [8] Sittig M., *Carbon and Graphite Fibers, Manufacture and Applications*, Noyes Data Corp., Yew Jersey, 1980.
- [9] Tesoro, G. C., Sello, H. B. and Willard, J. J., *Text. Res. J.*, Vol. 39, 1969, PP. 180.
- [10] Hart, M. L., *US. Patent*, 3803056, 1974.
- [11] Basch, A. and Lewin, M., *J. Polym. Sci., Chem. Ed.*, Vol. 12, 1974, PP. 2053.
- [12] Millet, M. A. and Goedken, V. L., *Tappi*, Vol. 48, 1965, PP. 369.
- [13] Basch, A. and Lewin, M., *J. Polym. Sci., Chem. Ed.*, Vol. 11, 1973, PP. 3095.
- [14] Elias, H.-G., *Macromolecules, Synthesis and Materials*, Plenum, 1977
- [15] Haraka, C. R. and Warren, B. E., *J. Appl. Phys.*, Vol. 25, 1954, PP. 1245.
- [16] Heydemann, B., *Min. Petrog.*, Vol. 10, 1964, PP. 242

INFLUENCE OF STIFFNESS INCREASE ON A WAVY SINGLE FIBER COMPOSITE

Piyush K. Dutta¹ and Madhu S. Madhukar²

¹ *U.S.Army Cold Regions Research and Engineering Laboratory
Hanover, NH 03755-1290, USA*

² *University of Tennessee, Knoxville, TN 37996-2030, USA*

SUMMARY: Experiments were conducted by using composite specimens containing a single carbon fiber embedded in an epoxy matrix. The fibers were cast in curved geometries, and the specimens were loaded in tension. Increasing the tensile load on the single fiber-epoxy specimens broke the embedded fiber into small fragments, whose lengths were smaller in the regions where the fiber was lying parallel to the loading axis. A significant fiber/matrix interfacial debonding, observed near the broken fiber ends in all specimens, was much more pronounced when the fiber was at an angle to the loading axis. Transverse tensile stresses at the interface caused this interfacial debonding. Specimens with higher matrix stiffness had long matrix cracks at the broken fiber ends, which were perpendicular to the fiber axis. These matrix cracks tend to propagate perpendicular to the fiber axis, increasing the composite's cold sensitivity. The major conclusions are as follows: 1) When fibers are wavy, they are not loaded to their full capacity because of premature interfacial debonding started by the interfacial shear stresses and the transverse tensile stresses. The transverse tensile stresses at the interface are not present in the straight fiber specimens. 2) At higher stiffness and lower toughness values, the matrix cracks emanating at the broken fiber ends make the composite weaker. These two sources lower the strength of unidirectional composites at low temperatures.

KEYWORDS: tensile strength, interfacial bond, matrix crack, wavy fiber, low temperature, cold.

INTRODUCTION

Several past experiments on tensile loading of unidirectional composite laminates at low temperatures have shown that the longitudinal tensile strength of these composites drops at these temperatures (Dutta 1992). This research program was under taken to identify the mechanisms that are responsible for this tensile strength degradation at low temperatures.

It is generally believed that, in unidirectional composites with high fiber volume fraction, the interface properties play a significant role (Bader 1988, Madhukar and Drzal 1991). Unlike the compressive failure of uniaxial composites, which happens suddenly and which is driven by the instability of compressively loaded fibers, the longitudinal tensile failure of carbon-epoxy composites is a gradual process, i.e., the load carrying fibers start failing at well below the composite's tensile failure load. After the beginning of fiber failure, the additional tensile

load that can be applied to the composite will depend upon how the high local stresses at the broken fiber ends are transferred to the neighboring fibers. The properties of the matrix and interface govern this stress transfer mechanism and thus the tensile strength of composites.

Another factor that may affect the longitudinal tensile strength of composites is fiber waviness that may have been introduced during manufacture due to the fact that saturation has not been obtained. The wavy fiber will be nonuniformly loaded when the composite is subjected to a tensile load. In addition, the interface will also be subjected to shear as well as transverse tensile stresses near the wavy fibers. The interface is likely to fail prematurely under these combined stresses. These problems are expected to be more severe at low temperature, when the matrix has low fracture toughness. These two issues, i.e., the effects of matrix stiffness and toughness and the wavy fiber geometry on the fiber and interface failure process in single fiber composites, were investigated to understand the mechanisms that cause the strength degradation at low temperatures.

MATERIAL

The fiber used in this study was a high strength PAN-based AS4 graphite fiber. The matrix material was epoxy, which is a diglycidyl ether of bisphenol-A (EPON 828) cured with meta-phenylenediamine (m-PDA). Specimens were made with two different ratios of the m-PDA curing agent, namely 14.5 parts per hundred (phr) and 10.0 phr by weight. The epoxy was mixed, debulked in a vacuum at 75°C (167°F) for about 10 minutes and then subjected to a two-step cure cycle in air. In the first cycle, the temperature of the material was increased from room temperature 75°C (167°F) and held constant for 2 hours. Afterwards, the temperature was increased again to 125°C (257°F) and held constant for 2 hours. After the second dwell time, the heating cycle was stopped and the specimen was allowed to cool to room temperature. The purpose of the first dwell is to allow gases and other volatiles to escape matrix material and to allow the matrix to flow. The purpose of the second dwell time is to allow cross-linking of the polymer to take place. The temperature-time curing cycle was applied by means of a quartz strip heater, whose temperature was controlled by a thermostat and a power distributor. The temperature-time histories were recorded on a computer.

EXPERIMENTAL PROCEDURE

In the case of EPON 828 matrix and m-PDA curing agent, Drzal et al. (1983) have shown that both stiffness and toughness of the matrix can be changed by changing the amount of M-PDA. In this study, the matrix was cast with two different ratios of M-PDA, as mentioned in the *materials* section. The tensile stress-strain responses of these specimens were determined by mounting strain gauges to these specimens and loading them to failure. The loading rate was 0.25 mm/min (0.01 in. /min); the data were recorded and two specimens were tested for each m-PDA ratio. The average properties of these two types of matrix materials are listed in Table 1. Representative stress-strain curves for these specimens are shown in Fig. 1; the broken specimens are shown in Fig. 2.

Table 1: Effect of the m-PDA curing agent ratio on the properties of matrix material

	Young's Modulus (E) GPa (psi x 10 ³)	Failure Stress (σ_f) MPa (psi x 10 ³)	Failure strain (ϵ_f) %
EPON 828 cured with 14.5% m-PDA	4.4 (634)	50 (7.2)	2.30
EPON 828 cured with 10% m-PDA	4.7 (688)	44 (6.4)	1.27

Single-fiber composite specimens with wavy fiber geometries were cast using the two different curing-agent-to-matrix ratios. A single graphite fiber was passed through the dog-bone cavity of a silicone mold and the ends of the fiber were glued to aluminum tabs outside the mold (Fig. 3). To make specimens with wavy fiber geometries, the fiber in the mold was kept longer than the mold length. The matrix and curing agent mixture was mixed, debulked in a vacuum at 75°C (167°F) for about 10 minutes and then poured into the dog-bone cavity of the silicone mold. The single-fiber composite was then cured with the two-step cycle in air. One of the problems that was frequently encountered in fabricating the wavy specimens was that, when the matrix was poured into the cavity, the wavy fiber had a tendency to attach itself to the side walls of the mold. To stop the fiber from sticking to the walls, it was carefully pulled away from the walls by dragging it with the help of a clean pin. This process had to be repeated several times during the curing cycle until the matrix material started to gel. Once the gelation started, the wavy fiber stayed in its place. Fig. 4 shows the wavy fiber geometry produced by this method in one of the specimens that was cured with 14.5% m-PDA.

In the single-fiber composite specimens cured with 100% m-PDA, an interesting phenomenon was observed in the embedded fiber. When the cured specimens were examined under polarized light, they showed another type of highly regular waviness pattern (Fig. 5). The wavelengths of these waviness patterns were much smaller. Such waviness was always present in the 10% m-PDA specimens, but it was never seen in the 14.5% m-PDA specimens. The exact mechanisms that cause such a phenomenon is not clear but may be due to the fact that saturation has not been obtained.

The cured specimens were removed from the mold and loaded in a tensile loading fixture attached to an optical microscope. This jig allowed the real-time scanning of the specimen while it was being loaded. The loading rate was controlled by a stepper motor, which in turn was driven by a computer. As mentioned, the loading rate was 0.25 mm/min. The deformation and failure process was observed through polarized and unpolarized lights, and the images were recorded on a video cassette and on Polaroid films.

RESULTS AND DISCUSSION

During the tensile loading of all the single-fiber specimens, the fiber and interfacial failure process was continuously scanned under polarized and unpolarized light to detect the location of the first fiber failure. Generally, the first crack appeared at a lower applied load in the lower stiffness (14.5% m-PDA) samples. This is expected because, in the lower stiffness

specimens, a given applied load produces a larger strain. Fig. 6 shows polarized and unpolarized photographs of the fiber cracks observed in the 14.5% m-PDA specimens. These cracks were observed at an applied tensile stress of 35 MPa (5 Kips/in²). The polarized pictures (Fig. 6b) clearly indicate asymmetrical (with respect to the fiber axis) fringe patterns around the broken fiber ends. The fiber cracks can be seen in Fig. 6a. These cracks are perpendicular to the fiber axis and they do not extend deep into the matrix material. Fig. 7 shows fiber cracks and the fringe patterns for a 10% M-PDA specimen. These cracks were observed at an applied stress of 52 MPa (7.5 Kips/in²). Again, for the fiber cracks lying on a portion of the fiber that is at an angle to the loading axis, the polarized fringe patterns are asymmetrical at the broken fiber ends. This indicates the presence of a different stress state around the circumference of the fiber, whereas, for the crack that is lying on a portion of a fiber that is parallel to the loading axis, the fringe patterns are symmetrical. These stress patterns can be understood by examining how the interface is loaded in the two different cases. When the fiber is parallel to the loading axis, the interface carries only the shear stress. However, when the fiber is at an angle to the loading axis, it has a tendency to align itself parallel to the loading direction. As a result, the interface at the wavy fiber is subjected to shear stresses as well as the transverse tensile stresses on one side and the shear stresses and the transverse compressive stresses on the other side of the fiber. These transverse tensile and compressive stresses are schematically shown in Fig. 8.

Another interesting observation that can be made from the results shown in Figs 6 and 7 is that, for the specimens cured with 10% m-PDA, the fiber cracks extend deep into the matrix material, thus producing characteristic long, needle-shaped matrix cracks (see Fig. 7a). In the 14.5% mPDA specimens, the fiber cracks did not penetrate the neighboring matrix material (see Fig. 6a). The specimens cured with 10% m-PDA contain the matrix that has low fracture toughness or low strain to failure (Fig. 1). Therefore, when the fiber fractures inside the matrix, the high stress concentration at the broken fiber ends can easily cause the local fracture of the brittle matrix material and produce sharp matrix cracks. Since these cracks are perpendicular to fiber axis, they must contribute to the reduction of tensile strength of composites. In the case where the matrix has large strain to failure, the high stresses at broken fiber ends may be relieved by matrix deformation or by interfacial failure, or both.

When the tensile load on the single-fiber specimens continues to increase, more and more fiber fragments are created. In addition, the fringe patterns produced at the broken fiber ends are elongated and extended in the direction away from the broken end (Fig. 9). The fringe patterns indicate high shear stresses near the broken fiber ends. The high shear stresses result when the matrix prevents the fiber from springing back after it is broken. In the portions of the fiber where it is at an angle to the loading axis, there will be both shear stress and transverse tensile stress present at the fiber surface, as shown schematically in Fig. 8. The transverse tensile stress cause the premature failure of the fiber/matrix interface. As a result, when the fiber is at an angle to the loading axis, the stress are not efficiently transferred from the matrix to the fiber, and additional fiber fragments are not produced. Instead, the fiber matrix interfacial failure propagates parallel to the fiber. This interfacial failure is indicated by the narrow and much elongated fringe patterns along the fiber length in Fig. 9a.

Also seen in Fig. 9a is a long gap between the broken fiber ends. For the regions where fiber is parallel to the loading axis, such long gaps between broken fiber ends were not observed. A possible reason for such a behavior is that the extensive interfacial debonding near the fiber lying at an angle to the loading axis makes the fiber lie loosely in the matrix tunnel (the evidence of a matrix tunnel is further given below). As a result the fiber can spring back

freely after its failure. In the regions where fiber is parallel to the loading axis, the fringe patterns are much wider, suggesting much less extensive interfacial debonding. More fiber fragments are produced in these regions as the applied load is increased. In such situations the matrix surrounding the fiber prevents the fiber from springing back after its failure. This suggests that the waviness keeps the fibers from being loaded to their full capacity, thus resulting in the poor tensile properties. Generally, in the failed single-fiber specimens, there were more fiber fragments in the 14.5% m-PDA specimens than in the 10% m-PDA specimens. Such a difference can be attributed to the high stiffness and low failure strain of 10% m-PDA specimen. These specimens may have failed before the saturation of the fiber fragmentation process.

The applied tensile load on the single-fiber specimens was increased until fracture. Examination of the failed ends of the specimen under an optical microscope revealed a significant fiber pull-out in several specimens. An example of one such fiber pull-out in a 14.5% M-PDA specimen is shown in Fig. 10. Fig. 10a shows the matrix tunnel produced by the pulled out graphite fiber; Fig. 10c is the polarized photo of Fig. 10a. A comparison among Figs 10a, b and c clearly shows that when a fiber breaks during tensile loading, there is a significant fiber-matrix debonding on either side of the broken fiber ends, i.e., the fiber is loosely held in the matrix tunnel. This suggests that the elongated fringe patterns seen in Fig. 9a represent extensive fiber-matrix debonding near the broken fiber ends. Fig. 11 shows the matrix tunnel produced by fiber pull-out in the 10% m-PDA specimen. In this specimen, where the matrix material is relatively more brittle, pieces of matrix material have also been pulled out of the broken specimen. These matrix pieces are seen emanating from the needle-shaped matrix cracks Fig. 11b.

CONCLUSIONS

Experiments were conducted on specimens made of a single wavy graphite fiber in an epoxy matrix, where the matrix properties were changed by changing its ratio with m-PDA curing agent. Two ratios-10 and 14.5%-were selected. The matrix with lower m-PDA ratio was stiffer and more brittle. On the basis of observations via an optical microscope of the fiber and interface failure process during the tensile loading of these composites, the following conclusions have been made:

1. Both lower and higher stiffness samples produced fiber fragmentation during the tensile loading.
2. The tensile loading of samples with the more stiff and brittle matrix produced fewer fiber fragments. However, because of the presence of a wavy fiber, the fragment length varied significantly along the specimen length within the same specimen.
3. During the tensile loading of samples containing the low-toughness matrix, long, needle-shaped matrix cracks emanated from the fiber broken ends. Such cracks were not observed in samples in which the matrix failure strain was larger. Since the matrix toughness decreases at low temperatures, these long matrix cracks in the low-toughness matrix composites are believed to be responsible for the reduction of tensile strength at low temperatures.
4. There was significant interfacial failure near broken fiber ends in regions where the fiber was at an angle to the loading axis. The interfacial failure was much less extensive in areas where the fiber was parallel to the loading axis. In these regions, the embedded fiber broke into smaller fragments. The presence of transverse

tensile stresses at the interface in the former case is believed to be responsible for the extensive fiber/matrix interfacial failure.

5. The fractured specimens showed fiber pull-out and the corresponding matrix tunnel. This suggests that, during the tensile loading, there is extensive fiber-matrix debonding at the broken fiber end.

REFERENCES

1. Bader, M.G., "Tensile strength of uniaxial composites", *Science and Engineering of Composite Materials*, 1988, 1: 1-11.
2. Drzal, L.T., M.J. Rich, M.F. Koenig and P.F. Lloyd, "Adhesion of graphite fibers to epoxy matrices", *Journal of Adhesion*, 1983, 16:133.
3. Dutta, P.K., "Tensile strength of unidirectional fiber composites at low temperatures", *Japan-US Conference on Composite Materials*, June 22-24, 1992, pp. 782-792.
4. Madhukar, M.S. and Drzal L.T., "Fiber-matrix adhesion and its effect on composite mechanical properties: longitudinal and transverse tensile and flexure behavior of graphite/ epoxy composites", *Journal of Composite Materials*, 1991, pp. 25-29.

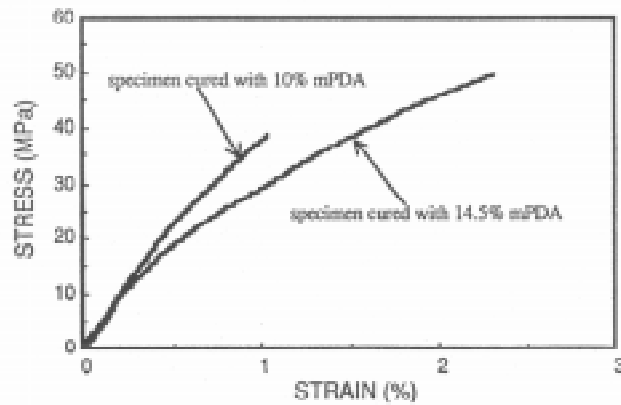


Figure 1. Effect of the hardener ratio on the stress-strain response of EPON 828 m-PDA matrix. Lowering the m-PDA ratio from its stoichiometric value (14.5% phr) results in stiffer and more brittle matrix.

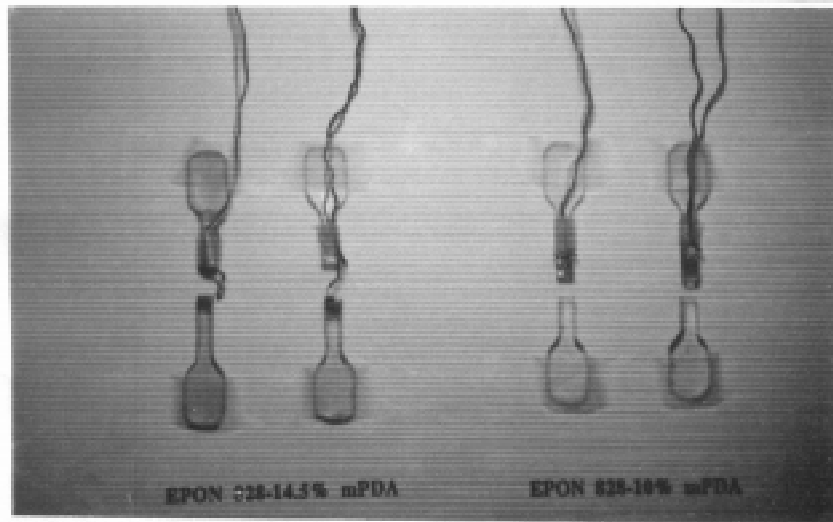


Figure 2. Fractured specimens with strain gauges.

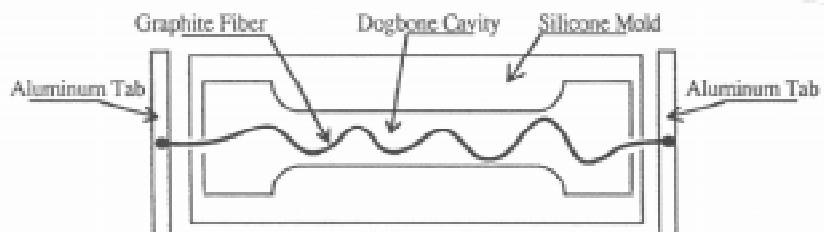


Figure 3. Arrangement used to place fiber with wavy geometry.

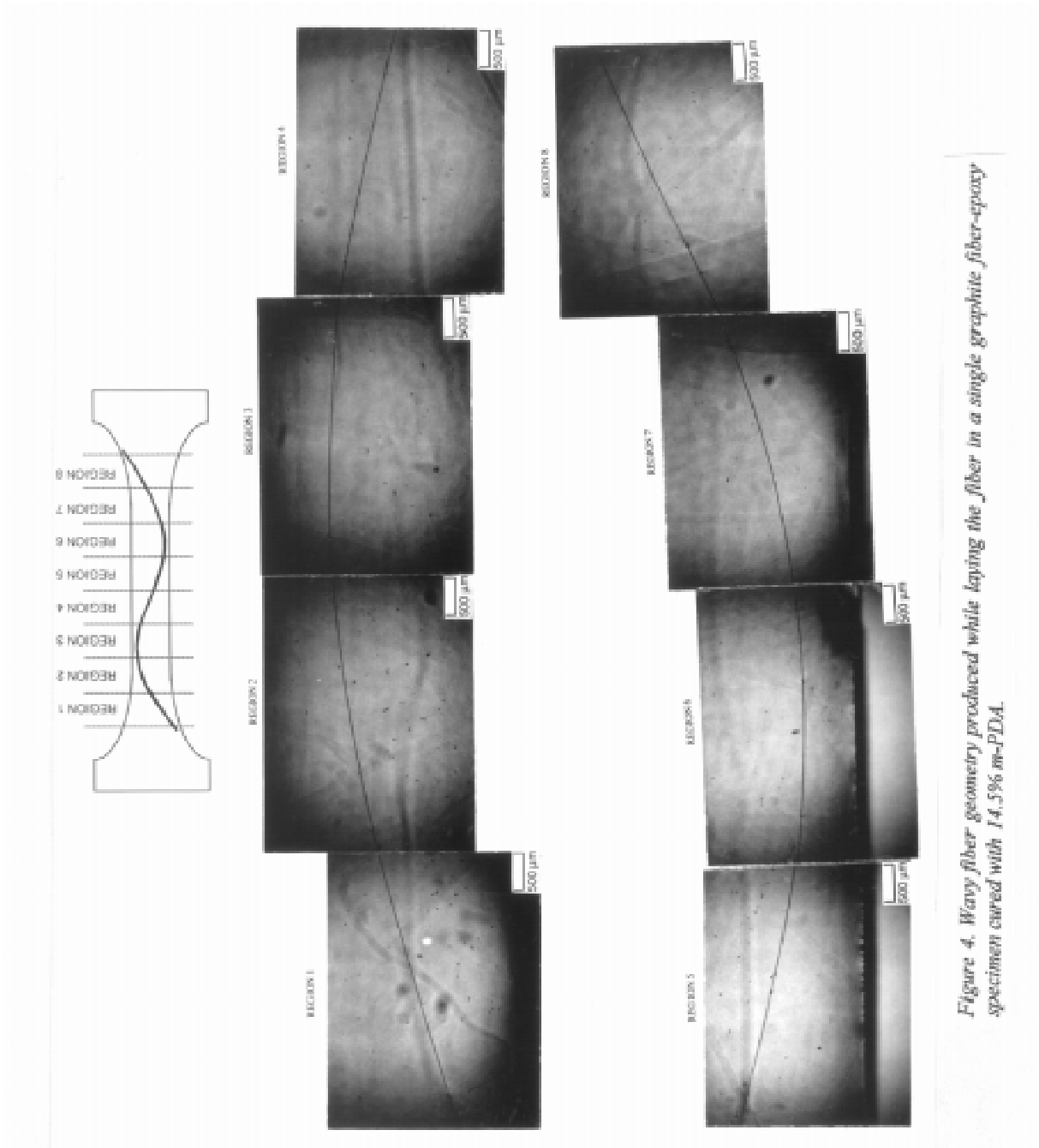


Figure 4. Wavy fiber geometry produced while laying the fiber in a single graphite fiber-epoxy specimen cured with 14.5% m-PDA.

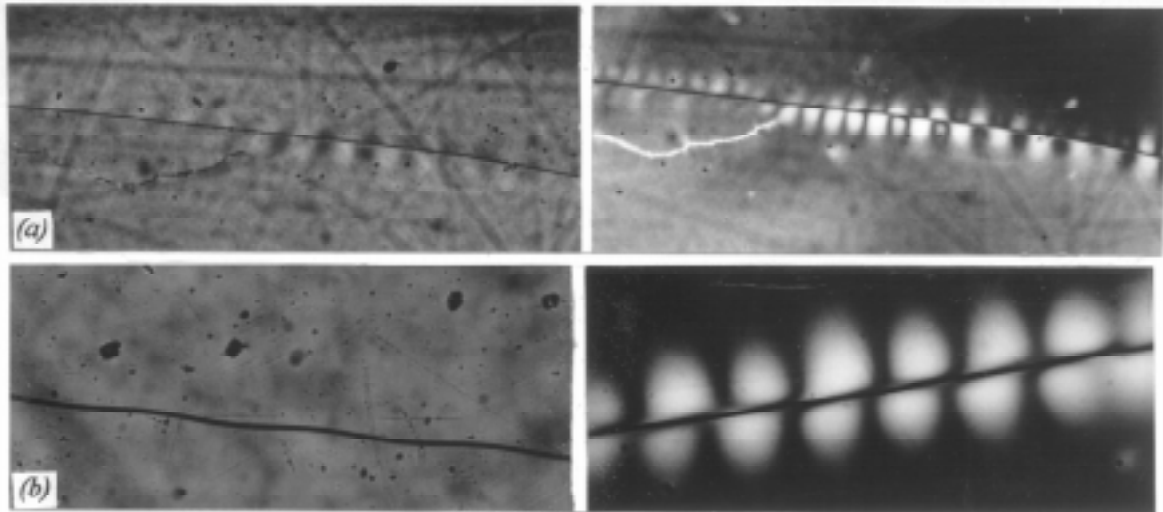
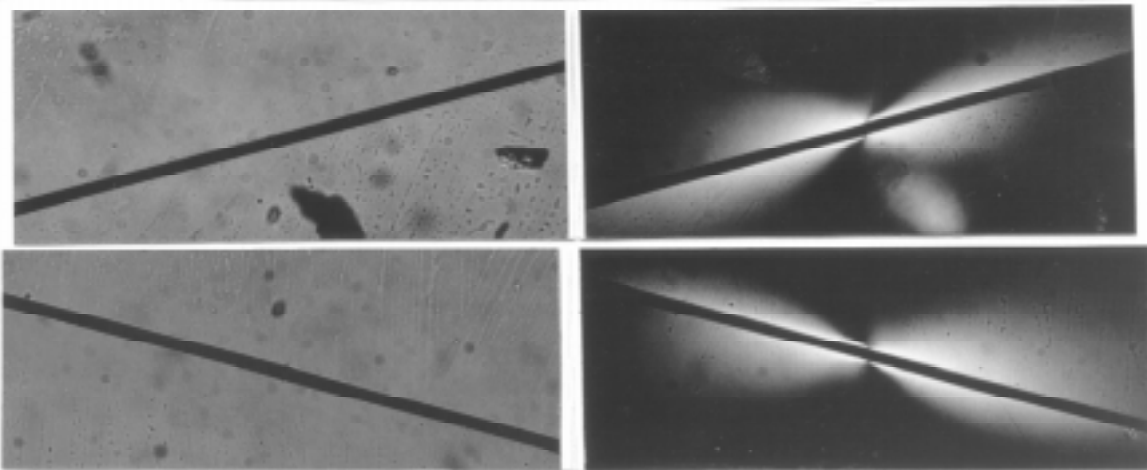


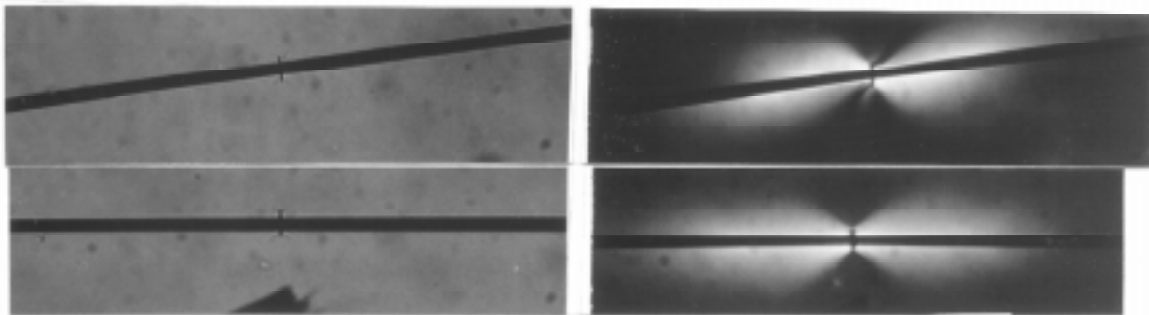
Figure 5. Fiber waviness that occurred during the curing of a single graphite-fiber epoxy specimen with 10% m-PDA. (a) Magnification 25x. (b) Magnification 100x.



(a) transmitted light, 250x,

(b) polarized light, 250x.

Figure 6. Fiber cracks and polarized fringe patterns seen during the tensile loading along the horizontal line of 14.5% m-PDA samples. Figure 6(a) shows fiber cracks that do not extend into the neighboring matrix.



(a) transmitted light, 250x,

(b) polarized light, 250x.

Figure 7. Fiber cracks and polarized fringe patterns seen during the tensile loading along the horizontal line of 10% m-PDA samples. Figure 7(a) shows the fiber cracks that extend deep into the neighboring matrix, thus producing needle shaped matrix cracks.

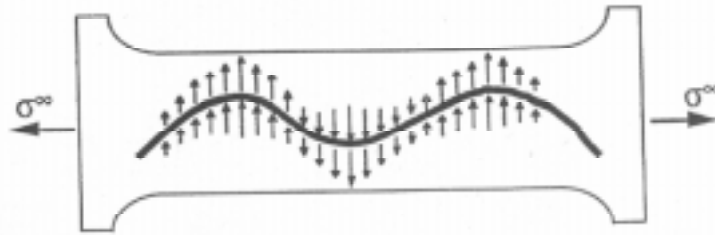
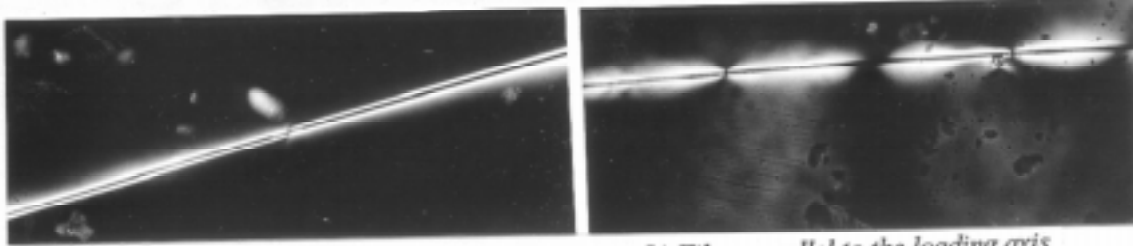


Figure 8. Interface tensile stresses around a wavy fiber.



(a) Fiber at an angle to the loading axis,

(b) Fiber parallel to the loading axis.

Figure 9. Growth of polarized fringe patterns with increasing applied load. Fringe patterns are much more elongated for the fiber section that is at an angle to the loading axis. More fiber fragments are observed when the fiber is parallel to the loading axis. The loading axis is in horizontal direction; magnification 100x.



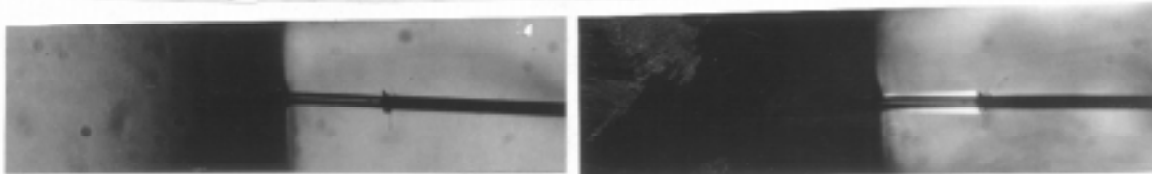
(a) Matrix tunnel,

(b) Pulled-out fiber,



(c) Polarized light.

Figure 10. Fiber pull-out and corresponding matrix tunnel formed during the fracture of a 14.5% m-PDA sample; magnification 250x.



(a) Transmitted light, 250x,

(b) Polarized light, 250x.

Figure 11. Matrix tunnel formed during the fracture of a 10% m-PDA sample.

DYNAMIC AND TRANSIENT CHARACTERIZATION OF SILICON CARBIDE FIBERS AT ELEVATED TEMPERATURES

R. C. Warren, C. D. Weaver and S. S. Sternstein

*Center for Composite Materials and Structures, Rensselaer Polytechnic Institute, 110 8th
Street, Troy, N. Y. 12180, USA*

SUMMARY: Ceramic fibers at elevated temperatures exhibit time or frequency dependent mechanical behavior, the most studied of which is creep. Several techniques for characterizing time dependent mechanical properties have been developed in this laboratory. Fibers studied to date include single crystal alumina, YAG, and seven compositions of SiC. Dynamic mechanical spectroscopy methods are used to examine short relaxation time processes associated with periodic deformation phenomena, and provide both dynamic modulus and loss factor versus temperature (to 1600°C) and frequency (from 0.1 to 25 Hz). Pulsed periodic creep and recovery tests are used to examine the longer relaxation time phenomena, and provide an accelerated means to identify and separate anelastic and inelastic creep rates. Taken together these methods provide a comprehensive understanding of the multiplicity of mechanisms and time scales that are relevant to the proper application and design of ceramic fiber reinforced composites.

KEYWORDS: silicon carbide, dynamic testing, creep of ceramics, viscoelasticity, fibers

INTRODUCTION

The analysis of the potential performance of high temperature composite materials and the design of components made from such materials requires detailed information about the constituents of the composite. It is well known that ceramic fibers exhibit high temperature behavior which is time-dependent, i.e., not entirely elastic. In order to gain a more complete understanding of the behavior of ceramic fibers at elevated temperatures and to provide a database for the engineering analysis of composites using these fibers as a reinforcement phase, this laboratory has investigated single fiber behavior using a variety of techniques. In this paper, dynamic mechanical testing and a periodic creep and recovery technique [1] are utilized for the investigation of the viscoelastic properties of ceramic fibers.

BACKGROUND

Materials scientists and engineers commonly use creep testing as a primary means to characterize long term high temperature behavior under applied loads. Generally, creep strain can include elastic, anelastic (viscoelastic) and inelastic (plastic) strain components. Refer to Fig. 1 for a schematic of a creep and recovery test. The elastic contribution to a given creep strain is readily measured by simply removing the sample load and observing the incremental

strain change. Decomposition of the remaining strain into anelastic and inelastic strains can be a challenging task, however. In general, given only a creep curve (strain vs. time) it is not possible to determine what fraction of the strain is anelastic and what fraction inelastic. This determination can be done only by performing a recovery test in which the (recovering) strain vs. time is observed following the removal of the load. The difficulty lies in the fact that as a rule, creep recovery is much slower than creep itself. Presumably, this is because creep recovery occurs with no externally applied load, and given any sort of activated rate theory for the processes involved, the reverse (recovery) process would be expected to involve a higher activation barrier than for the (forward) creep process itself. As a general rule, full recovery of anelastic strains can take as much as ten times longer than the creep itself. Thus a one month creep test might take ten months to fully recover if the strains were entirely anelastic. Clearly, the decomposition of a creep curve into anelastic and inelastic components would involve a series of creep tests for various times, each of which is followed by a longer recovery process. In this way, a long term creep curve could be decomposed into its component anelastic and inelastic strains. From both a mechanistic and design viewpoint, this decomposition is essential. As a corollary, it follows that the measurement of plastic strain rates from a single creep curve is potentially misleading since there would be no basis by which to judge the anelastic (time dependent but recoverable) strains. It is emphasized that the shape of the creep curve (e.g., constant rate) is a very misleading and poor delineator of whether the strain is inelastic or anelastic (or both), as discussed below.

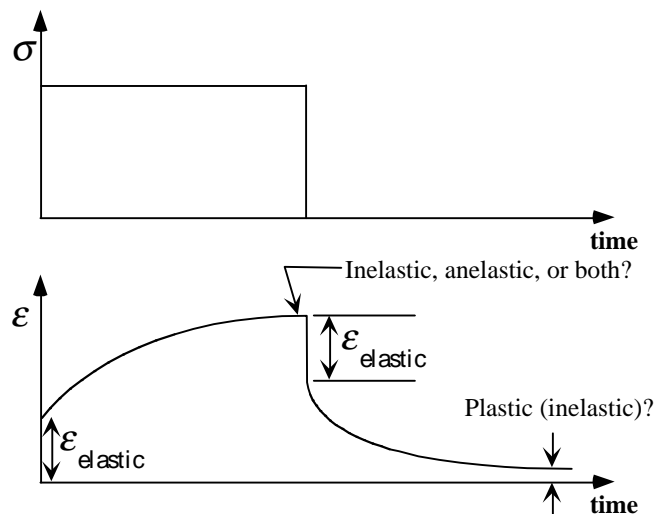


Fig. 1: Loading history and strain response for a typical creep and recovery test.

Guidance regarding the shape of a creep curve which is anelastic can be obtained directly from the theory of linear viscoelasticity (which is not to say that all anelastic processes are linear processes). Anelasticity can be represented by a series of recoverable strains each with a characteristic retardation time, or differently stated, an anelastic process can be represented by its corresponding distribution (or spectrum) of retardation times. For each retardation time, 63% of the anelastic strain component is obtained after a load application for a time equal to one retardation time. It becomes obvious then, that the shape of an anelastic creep curve is dependent on the distribution of retardation times characterizing the creep process. Without additional information, it becomes clear why the shape of the creep curve is a very poor determination of whether the creep is anelastic or inelastic. It follows that a recovery curve of 100 seconds, for example, may fully recover anelastic strains with 10 second or less retardation times, but would not recover any appreciable amount of anelastic strains having

retardation times of longer than 1000 seconds. It is for this reason that we noted earlier that the decomposition of a creep curve into its anelastic and inelastic components requires a series of recovery tests, conducted for several creep times, and not a single recovery test.

Mathematically related to the distribution of retardation times is another distribution referred to as the distribution of relaxation times, which is useful in describing anelastic processes such as stress relaxation or dynamic modulus. Initially, this laboratory engaged in dynamic mechanical testing studies on single ceramic fibers at elevated temperatures, as described elsewhere [4]. In that method a fiber is subjected to a sinusoidally varying displacement and the resulting load measured (without averaging or filtering). The load and displacement signals are then fast Fourier transformed (FFT) to obtain the component of force in-phase and out-of-phase with the displacement, ultimately providing the real (in-phase or storage or elastic) modulus and the imaginary (out-of-phase or loss or viscous) modulus, from which the loss factor can be calculated.

While the real and imaginary components of modulus provide equivalent information on the anelastic processes as does a creep/creep recovery test, they do so at a far different time scale. Dynamic measurements typically emphasize short time scale processes (e.g., relaxation times of milliseconds or less) while creep/recovery tests provide information on long time scale processes (typically retardation times of seconds to years). Thus, the two methods of measurement are complementary and provide a broad picture of material anelastic behavior over many decades of time scale. However, the dynamic modulus measurement method, being intrinsically periodic with a short time scale, quickly reaches steady state, whereas the creep/recovery method being transient, and specifically not periodic, never indicates steady state behavior. A perspective now emerges on the difficulties involved in anelastic/inelastic decomposition of creep and recovery data. The problem of reconstruction of a creep curve into its underlying component anelastic vs. time and inelastic vs. time creep curves is the basis of the test method described here.

There is evidence in the literature that ceramic fibers do exhibit surprising amounts of anelastic behavior. An important observation is given by DiCarlo [2] who performed a creep test on a silicon carbide fiber (SCS-6), followed prudently by an accelerated recovery test at a higher temperature. The creep test was done at 1275°C and 612 MPa, and followed by recovery at 1450°C. Nearly complete recovery was obtained which suggests that the creep curve was primarily anelastic. Additional creep and recovery tests for short time periods have been reported by Lara-Curzio [3]. Dynamic testing of silicon carbide fibers was conducted by Sternstein, Weaver and Beale [4] who found that both the storage and loss modulus varied with the relative amounts of carbon and silicon in the SiC sheath.

PULSED PERIODIC CREEP AND RECOVERY TESTING

One of the useful features of the dynamic test method is its periodic nature, which enables one to quickly establish steady state behavior. The test method utilized here combines the attributes of a periodic test while still offering the benefits of transient (creep) testing which emphasizes long time processes. Referring to Fig. 2, consider a test protocol in which a load is periodically applied to a sample for a period of time t_1 and then removed for some period of time $(t_p - t_1)$ and then the entire cycle repeated every t_p seconds, where t_p is the "period." Further, let the strain at the end of each loading cycle be measured, as well as the strain at the end of each recovery cycle, as shown by the arrows in Fig. 2.

This test is implemented using the apparatus described elsewhere [4] for dynamic modulus testing, but modified with a stiff closed-loop control system and computer which generates the periodic program shown in Fig. 2 and provides for automatic data acquisition. In practice, the load application or removal is done in less than 2 milliseconds without overshoot or ringing, and is made possible by a very stiff and well tuned servo. Data acquisition is done using 18 bit D/A conversion which is required for the high accuracy needed to implement the periodic pulse test. Precision timing for the pulse test history and data acquisition is done in hardware using a 6 MHz crystal, 64 bit pulse counter and interrupt generator. This provides for very precise and reproducible pulse cycles and data acquisition. Cycle periods from 0.5 seconds to days are readily obtained and the number of cycles is limitless, since the data is routinely written to hard disk. The parabolic temperature profile of the fiber testing device requires extraction of the isothermal strain data from the measured displacements by simple calculations described by Feldman and Bahder [5]. A creep activation energy of 580 kJ/mol was found for SiC by true isothermal creep testing of CVD SiC fibers by Lara-Curzio [3], and is supported by DiCarlo [2] for testing under similar conditions as used in the present study.

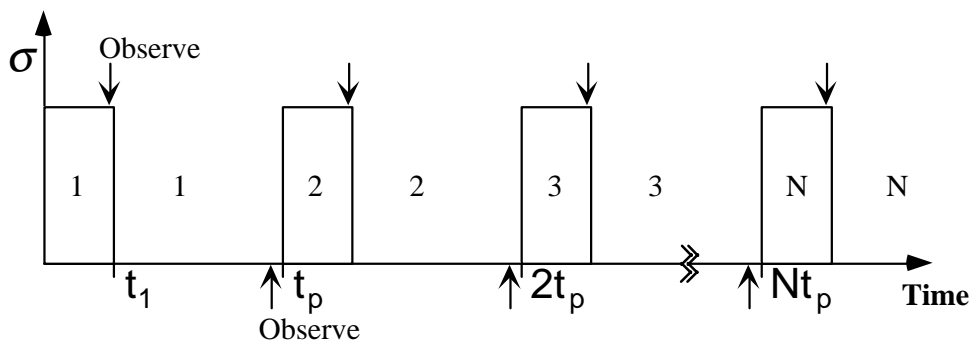


Fig. 2: Loading history and strain measurement for pulsed periodic creep and recovery testing. Strain measured at $(kt_p)^-$, $k=1\dots N$ and $(kt_p + t_1)^-$, $k=0\dots(N-1)$.

From the theory of linear viscoelasticity, it can be shown that the history described in Fig. 2 produces a slowly accumulating peak strain (the strain measured at the end of each loading cycle) and slowly accumulating recovery strain, with the rate of accumulation being strongly dependent on the ratio of the test time parameters (t_1 , t_p) relative to the retardation times of the material. The mathematics will not be presented here. Suffice it to say that anelastic creep processes having retardation times substantially longer than t_p are effectively "filtered" in that they never get activated (occur) during the loading cycle, while the processes having retardation times shorter or equivalent to t_p are largely recovered after each recovery cycle and therefore do not accumulate as they would if the load were maintained as in a single creep test (without periodic recovery). In effect, the pulsed periodic creep test will always produce less anelastic strain (for a given accumulated time under load, that is t_1 times the number of cycles) than a single creep test of the same time under load. It follows that the resultant "creep curve," that is peak strain vs. accumulated time under load will always be a better representation of the inelastic strain process (if any) than a single creep test. These predictions are fully justified by the experimental results to date, as described below.

Dynamic and pulsed periodic creep testing have been performed on several polycrystalline silicon carbide fibers provided by Textron Specialty Materials. These fibers all have roughly the same morphology (SiC sheath on a carbon core) although they vary slightly in grain size,

composition, and fiber diameter (120 to 150 micrometers). The fibers include the commercially available SCS-6 fiber and a series of five fibers of various composition, herein referred to as EF#1 - EF#5. The composition of the SiC sheath in the SCS fibers is found to vary between stoichiometric and about 1 wt% excess silicon depending on the original chemical vapor deposition (CVD) processing parameters. Additionally, dynamic testing has been performed on British Petroleum's Sigma 1240 fiber. Table 1 lists the atomic carbon / silicon ratio of the fibers used thus far in this study.

Table 1: Composition of various SCS SiC Fibers tested.

Fiber	C / Si atomic ratio
Sigma 1240	0.82
SCS-6	0.96
EF#1	0.99
EF#2	0.99+
EF#3	1.00
EF#4	0.98+
EF#5	0.98

RESULTS AND DISCUSSION

Fig. 3 shows the temperature dependence of the storage (Young's) modulus of several of the SiC fibers as determined by dynamic testing. The plot clearly shows the relationship between the amount of excess silicon in the respective fibers (see Table 1) and the retained modulus. The moduli have been normalized by their room temperature values for clarity. Only the Textron experimental fibers #3 and #5 are shown since their behavior brackets the behavior for all of the experimental fibers. Fig. 4 shows a similar behavior for the loss factor with changing composition.

Further underscoring the importance of the C / Si ratio in the SiC sheath of the fiber, pulsed periodic creep testing was conducted under identical conditions for each of the SiC fibers listed in Table 1 (with the exception of BP Sigma 1240). Fig. 5 shows that creep and recovery response of these fibers is clearly dependent upon the stoichiometry of the fiber; the greater the amount of excess silicon present, the higher the creep rate. Further testing is necessary before any statement can be made as to the mechanism by which the excess silicon so drastically controls the high temperature viscoelastic properties of silicon carbide. Again, only the Textron fibers #3 and #5 are shown as their behavior brackets that of the other experimental fibers.

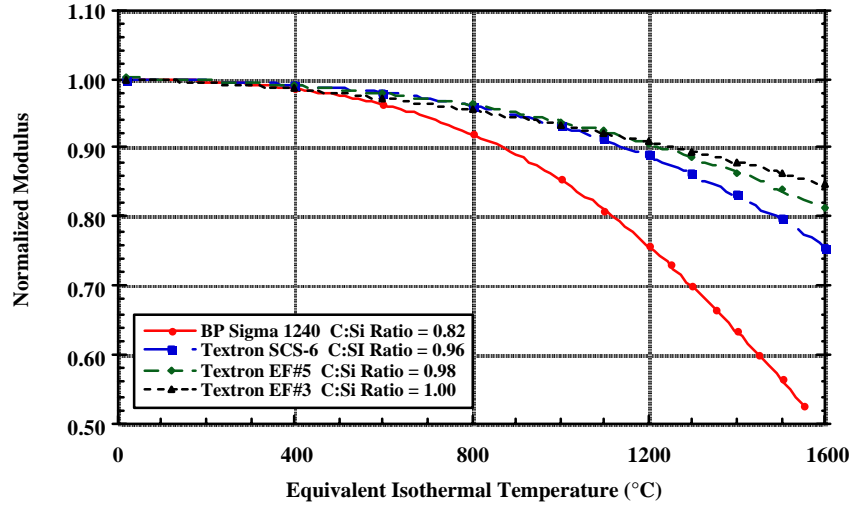


Fig. 3: Normalized Young's modulus at 1 Hz for different CVD silicon carbide fibers. Data is shown for tests conducted with a static stress of 300 MPa (200 MPa for BP Sigma 1240), dynamic stress of 100 MPa.

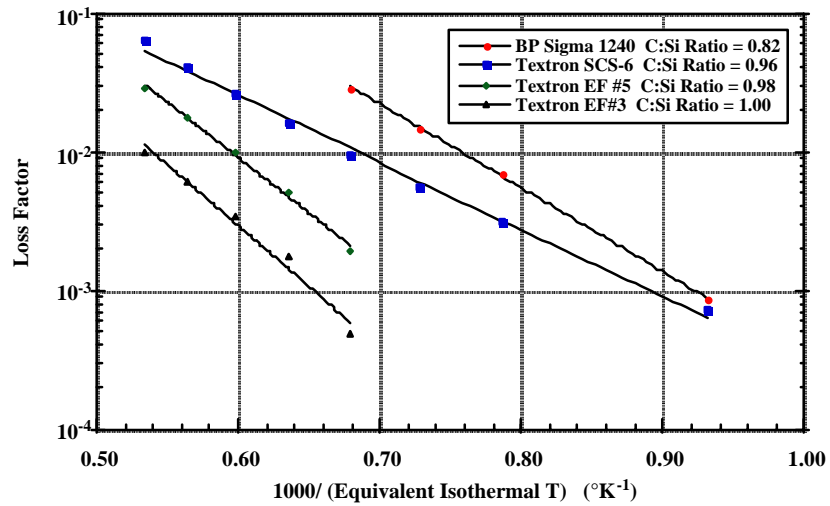


Fig. 4: High temperature loss behavior of different CVD SiC fibers at 1 Hz. All data is shown for tests performed at 300 MPa static stress, and 100 MPa dynamic stress amplitude.

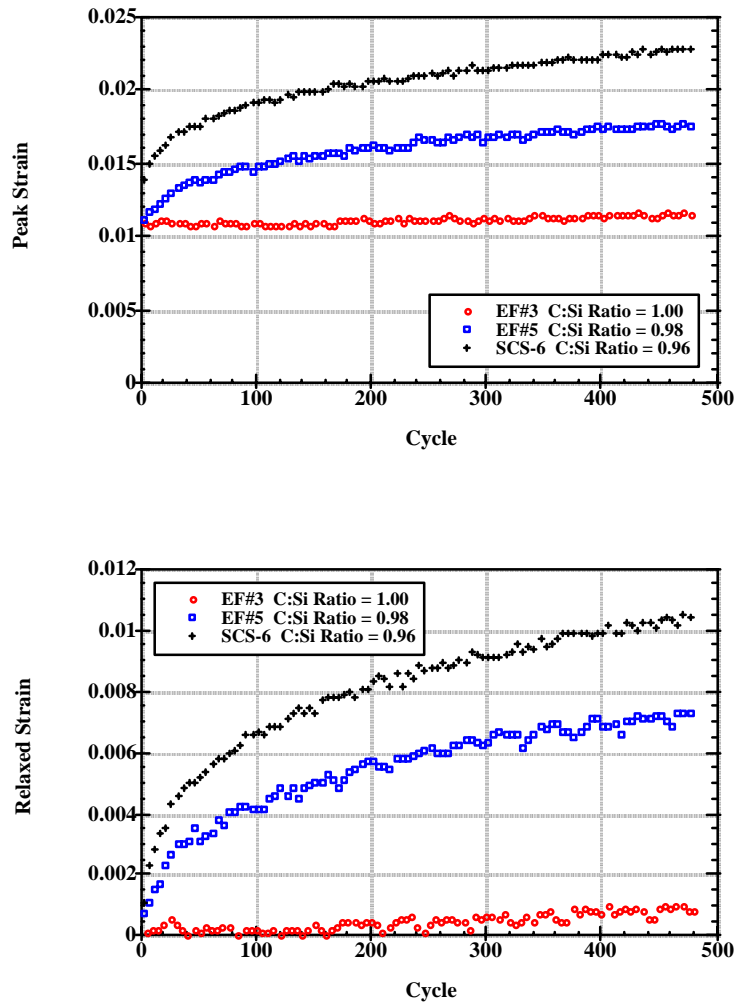


Fig. 5: Periodic Pulse Testing of SiC fibers of various compositions showing the effect of the C / Si Ratio on the high temperature viscoelastic behavior of SiC. Testing conducted at 1600°C, 200 MPa, and 480 cycles (10 sec. load on, 20 sec. load off).

Fig. 6 shows a comparison between the creep strain developed during a conventional creep test and the peak strain achieved in a pulsed periodic creep test, the latter plotted vs. accumulated time under load. The pulsed data were obtained for a duty cycle consisting of $t_1 = 10$ sec. and $t_p = 30$ sec. Also shown is a single strain point obtained after 9600 seconds of recovery for the single creep test sample. The amount of recovery is large and shows that most of the creep strain which occurred after 4600 seconds was in fact anelastic, not inelastic.

As expected, the pulsed periodic results lie between the single creep results and the recovered strain value. Additional experiments on the effects of various duty cycles (t_1 and t_p values, both as a ratio and absolute values) are currently being performed. While the recovery time to load time for the pulsed periodic test was only 2 to 1 there is still clearly a major reduction in accumulating anelastic strain. While it would be tempting to claim that the slope of the pulsed periodic creep results vs. accumulated loading time is in fact the inelastic (plastic)

strain rate, this would be premature, since other duty cycles with longer recovery to load ratios than 2/1 are required for better suppression of the anelastic strain. Nonetheless, we claim that the slope of the pulsed periodic results is closer to the true inelastic creep rate than the single creep test slope, which is clearly much larger.

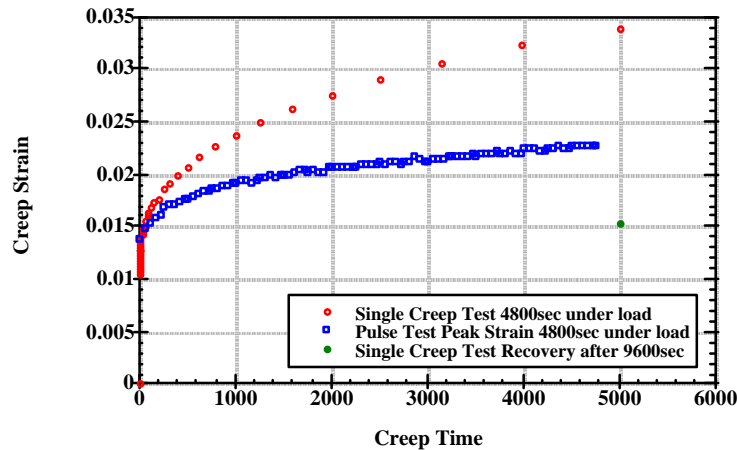


Fig. 6: Comparison of Pulse Testing with a Single Creep and Recovery test. Testing of SCS-6 conducted at 200 MPa, 1600°C, 480 cycles (10 sec. load on, 20 sec. load off) versus 4800 sec. creep, 9600 sec. recovery.

The effect of stress magnitude on the pulsed periodic creep test is shown in Fig. 7 for SCS-6 fibers at 1600°C, and it is seen that the creep process is nonlinear, as is also concluded from single cycle creep test data. Finally, the effect of cycle time at constant duty cycle ratio (2/1) is shown in Fig. 8, where it is seen that the results for 15 and 30 second periods are virtually indistinguishable.

CONCLUSIONS

In order to more fully characterize the viscoelastic behavior of silicon carbide at high temperatures it is necessary to employ multiple test methods that target specific relaxation / retardation time scales. Dynamic mechanical testing has been used to investigate the storage and loss modulus (and thus the loss factor) of several silicon carbide fibers whereby the test method only activates relaxation mechanisms with time scales in the millisecond range. Results are presented showing the effect of the carbon / silicon ratio in the SiC sheath on both the retained high temperature modulus and the loss factor.

It appears that the pulsed periodic creep test provides a method whereby the inelastic strain rate may be measured with higher accuracy and more quickly than with single cycle creep tests. Anelastic creep in ceramic fibers at elevated temperatures is surprisingly large in magnitude and covers wide time scales, and therefore significantly affects the slope of a single cycle creep curve, rendering the measurement of inelastic strain rates difficult if not impossible from such a test. The technique used in this study may provide an accelerated and more time efficient method for determining inelastic creep rates. Results are presented

showing the non-linear creep and recovery behavior displayed by SCS-6 silicon carbide fibers. Additional results show the effect of the carbon / silicon ratio in the SiC sheath on the creep and recovery behavior of several CVD fibers of varying composition.

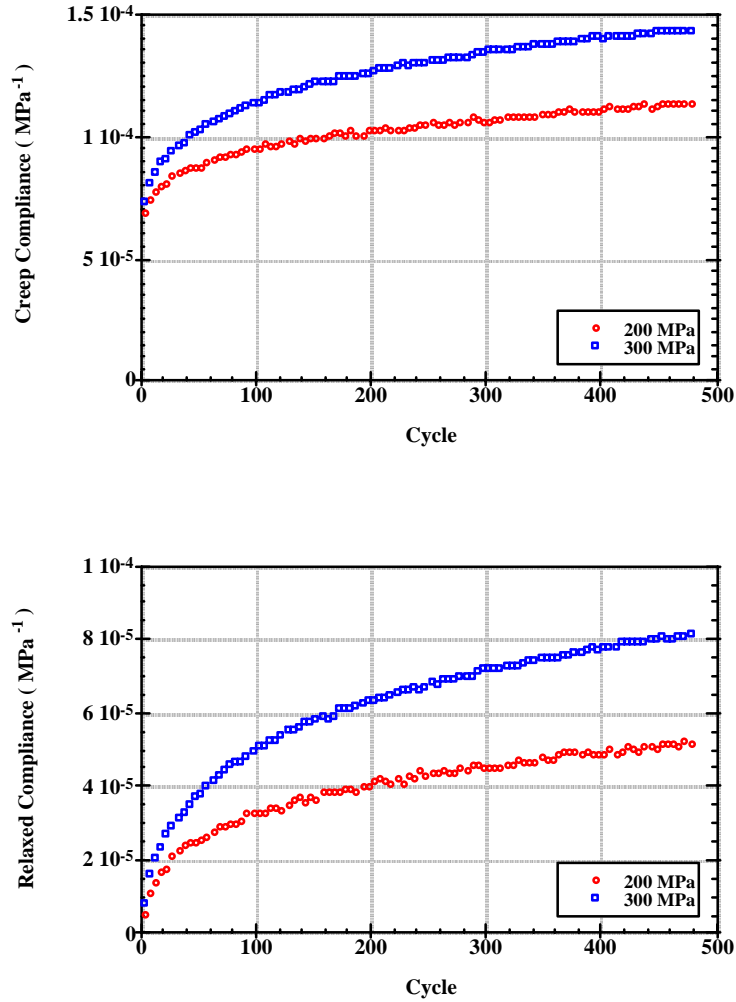


Fig. 7: Comparison of SCS-6 Pulse Testing at 200 MPa and 300 MPa stress showing non-linearity of creep behavior. Tests conducted at 1600°C for 480 cycles (10 sec. load on, 20 sec. load off).

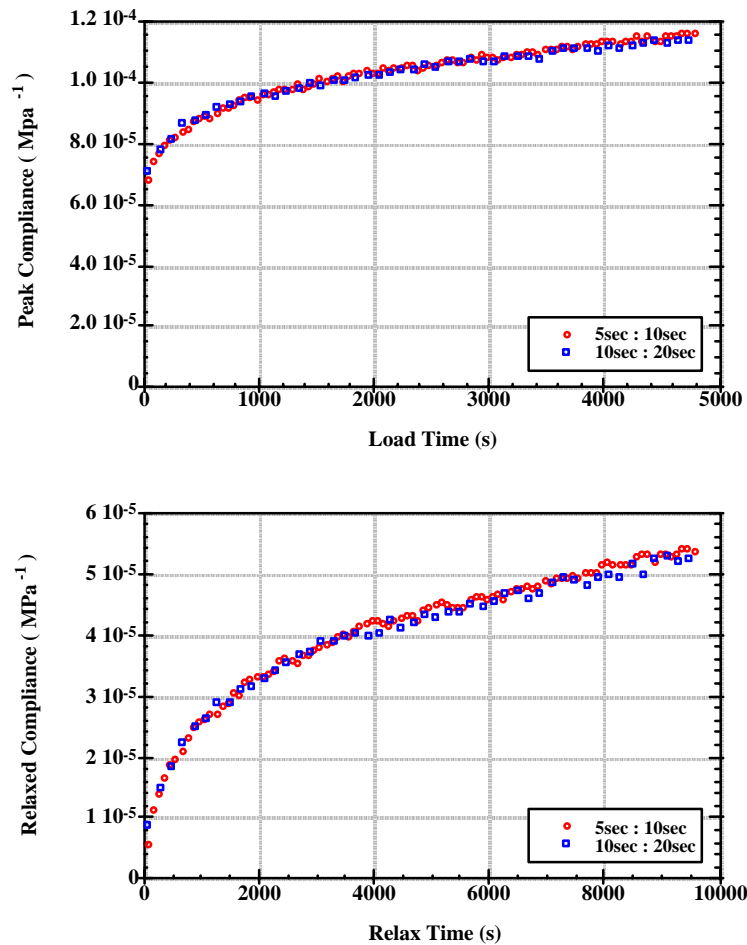


Fig. 8: Comparison of various cycle times (5 sec. load on, 10 sec. load off versus 10 sec. load on, 20 sec. load off) with 1:2 load-on : load-off time ratios. Testing of SCS-6 at 1600°C, 200 MPa, 960 cycles versus 480 cycles.

ACKNOWLEDGMENTS

This work was supported by DARPA/ONR Contract No. N-00014-86-K-0770. Previous students C. D. Weaver and J. Beale participated in the ongoing development of the fiber tester which was modified for the present study.

REFERENCES

1. Y. H. Park, J. W. Holmes, *J. Mat. Sci.*, 27 (1992) 6341
2. J. A. DiCarlo, *J. Mat. Sci.*, 21 (1986) 217.
3. E. Lara-Curzio, Thermomechanical Characterization of Silicon Carbide Fibers at Elevated Temperatures, PhD. Thesis, Rensselaer Polytechnic Institute, 1992
4. S. S. Sternstein, C. D. Weaver and J. Beale, *Materials Science and Engineering A215* (1996) 9-17.
5. L. A. Feldman, T. B. Bahder, *J. Mat. Sci.*, 8 (1989) 307

PRODUCTION OF BORON CARBIDE FIBERS USING BORIC ACID AND CELLULOSE FIBERS

Y. Bohne, H.-P. Martin, E. Müller

Freiberg University of Mining and Technology, Institute of Ceramic Materials, Gustav-Zeuner-Straße 3, Freiberg, Saxonia, D-09596, Germany

SUMMARY: This paper presents a route for producing B₄C fibers from cheap and easily available raw materials. Textile cellulosic fibers and boric acid solution are used as raw materials. It is possible to reach an optimal mixture of the primary materials by a suited soaking method. After temperature treatment between 1500°C and 1750°C under argon boron carbide fibers are obtained. The influence of the reaction temperature on boron carbide formation was investigated by IR-spectroscopy, x-ray diffraction, oxygen and carbon analysis. Almost pure boron carbide fibers of good quality were obtained at 1700°C. The shape of the raw fiber is retained during the conversion. The development of the manufacture process is still in progress and an improvement of the strength is expected. The fibers could be an alternative material to commercial available B₄C fibers.

KEYWORDS: production of boron carbide fibers, boron carbide fibers, boron carbide, cellulose fibers, boric acid, organic solvents, soaking method, carbothermic reduction

INTRODUCTION

Boron carbide fibers are very promising ceramic fibers, because they show chemical and physical properties which make them interesting. Low density (2,52 g/cm³), high strength (tensile strength: 2,1-2,5 GPa), high temperature resistance (thermal stability up to 2300°C), oxidation resistance up to 900°C and a high resistance against chemical influences make boron carbide as fiber material attractive [1]. Besides the rigid framework of strong bonded atoms corresponds to a high melting point, great hardness and appreciable electrical conductivity [2]. Boron carbide fibers are actually used for the reinforcement of special materials or inorganic materials which are exposed to highest temperatures and aggressive chemicals. A well known process of B₄C fiber preparation is a chemical conversion of a precursor fiber (CVD-process). Such boron carbide fibers are prepared by reacting of a precursor carbon yarn with a reaction mixture of H₂ and BCl₃ at temperatures around 1800°C [3]. However BCl₃ is a toxic and corrosive gas and additionally hydrogen chloride is generated [4]. The manufacture demands enormous safety care, what leads to high production costs. This paper describes a route which was firstly mentioned in the sixties [5], [6]. In our route we use cheap and easily available raw materials as textile cellulosic fibers (viscose, cotton or wool), which are used as carbon source and boric acid solution serving as boron source. The cellulosic fibers will be soaked with boric acid solution. The infiltrated fibers were treated at temperature ranges between 1500°C and 1750°C under argon. At these temperatures B₄C is formed by carbothermic reduction from boron oxide by carbon. After the conversion the shape of the raw fiber is unchanged.

PREPARATION OF FIBERS

The boric acid is dissolved in water, ethanol, butanol, hexanol or pentanol. Subsequently the cellulosic fibers (Table 1) are dipped in this solution and they soak up the boric acid solution.

Table 1: properties of raw fibers from cellulose

	fiber surface	cross-sectional form	specific surface area	density	fineness yarn
viscose (viscose type)	glossy	serrated	0,1 m ² /g	1,3	330 dtex
wool (wool type)	mat	smooth	0,1 m ² /g	1,3	328 dtex
cotton (cotton type)	glossy	smooth	0,1 m ² /g	1,3	140 dtex

It is possible to reach an optimal mixture of the primary materials and a finally dispersed distribution of boric acid through the fiber material by the soaking method. The molecular ratio of the reactants was calculated from matter amount and molar masses according to the following chemical reaction equation (Eqn. 1):



The necessary mass of boric acid for a complete formation to boron carbide must go to three times of the amount of carbon. Besides the raw fibers are soaked with water with the aim to increase the H₃BO₃ incorporation by swelling the fibers. During the drying process (air drying) the solvent evaporates, but the boric acid remains in the cellulosic frame. After this the infiltrated fibers were heated up to 1560°C, 1600°C and 1700°C under inert conditions in a tube furnace. Further more the heating rate was varied (20 K/min, 10 K/min and 0,3 K/min) and already burned samples were sintered at 1750°C (Table 2). During the annealing the cellulose

Table 2: conditions during annealing of cellulose fibers

	heating rate K/min	temperature °C	dwel time h	cooling rate K/min	sintering	closed crucible
(1)	10	1560	0,1	10		
(2)	10	1600	0,1	10		
(3)	10	1700	0,1	10		
(4)	10	1700	0,1	10		X
(5)	20	1700	0,1	10		X
(6)	0,3	1700	0,1	10		X
(7)	10	1700	0,1	10	1750°C with 20 K/min	X

decomposes into carbon, water and further volatile substances (CO₂ and CO) at temperatures between 240°C and 1000°C [7]. The decomposition of cellulose and the formation of a new structure is connected with a remarkable shrinkage. Simultaneous, the boric acid transforms into boron oxide with lost of water. At temperatures of more than 1400°C a carbothermic reaction occurs and the carbon reduces the boron oxide generating boron carbide and carbon monoxide (Eqn 1). The influence of the reaction temperature, the variation of heating rate and sintering on boron carbide formation were investigated by x-ray diffraction, IR-spectroscopy, carbon and oxygen analysis.

RESULTS AND DISCUSSION

The soak experiments show that the use of water as solvent for boric acid doesn't give satisfying results, because after soaking boric acid crystallize with crystal sizes $\geq 100 \mu\text{m}$ and the distribution of boric acid is inhomogeneous and doesn't adhere on the fiber surface. Furthermore not enough boric acid is absorbed by infiltrated into the fibers for a complete conversion to boron carbide (Fig. 1). The use of organic solvents results in increasing the H_3BO_3 -infiltration in comparison to water. All above, butanol is well suitable as solvent for boric acid, because the H_3BO_3 -infiltration is above 100% of need for all used cellulose fibers. Besides another crystallizing behaviour is observe after drying than in the case of water solvents.

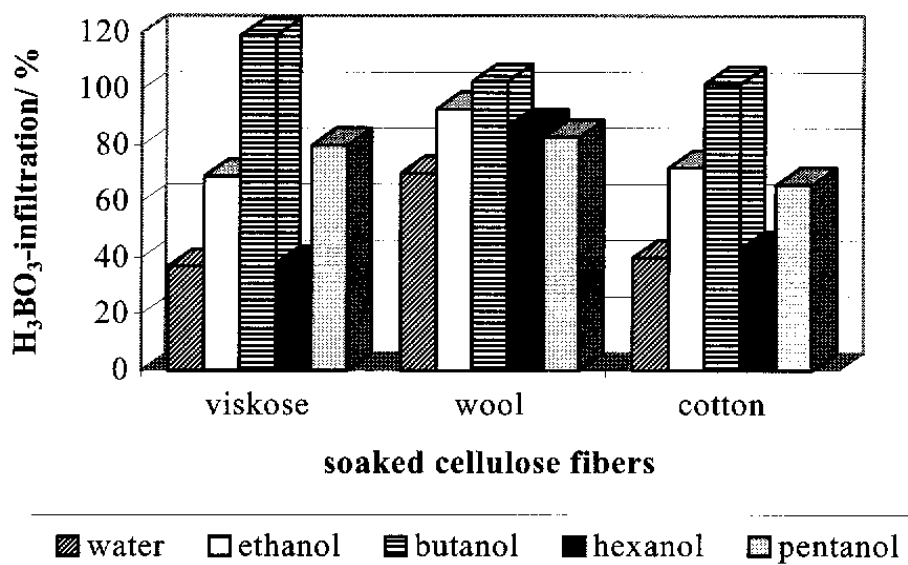


Fig. 1: H_3BO_3 -infiltration soaked cellulose fibers depend on the solvent

The boric acid crystallized finely as a layer around the raw fibers and is homogeneously distributed in them (Fig. 2). Additionally, the cellulose fibers were soaked with water before they were soaked by climbing of the boric acid/ butanol solution. That seems to be the most favourable method. As a result of water swelling the structural chain elements of the cellulose get more distant what leads to an increased cross section. Subsequently more boric acid enters into the fibers. The boric acid dissolved in alcohol get into the cavity of fibers supported through capillarity, and the alcohol promotes the volatilization of the included water, so that the boric acid remains in fine distribution.

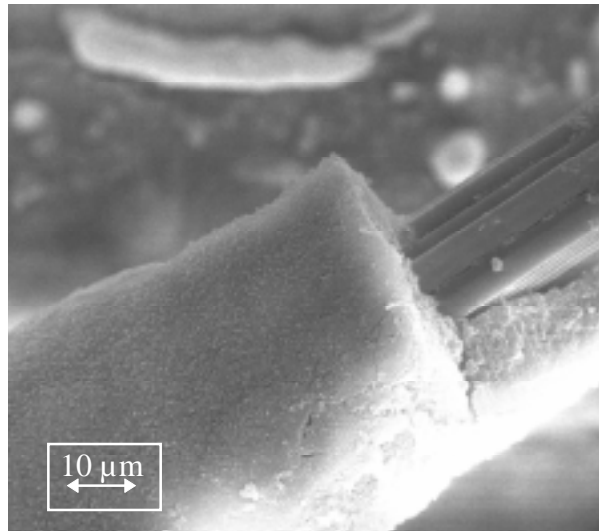


Fig. 2: SEM-photo of soaked cellulose fiber with butanol as solvent

After thermal treatment the obtained fibers were investigated by IR-spectroscopy in the wavenumber range between $2000\text{--}500\text{ cm}^{-1}$. In Figure 3 spectra of B_4C fibers of the cotton type are shown. In the IR-spectra B-C bands (around $1090\text{--}1170\text{ cm}^{-1}$) [8], [9] appears, but simultaneously with B-C bands also C-C bands (around $1600\text{--}1585\text{ cm}^{-1}$, $1465\text{--}1430\text{ cm}^{-1}$ and 700 cm^{-1}) appear, what suggest, that aromatic carbon is formed. Fibers annealed at 1560°C

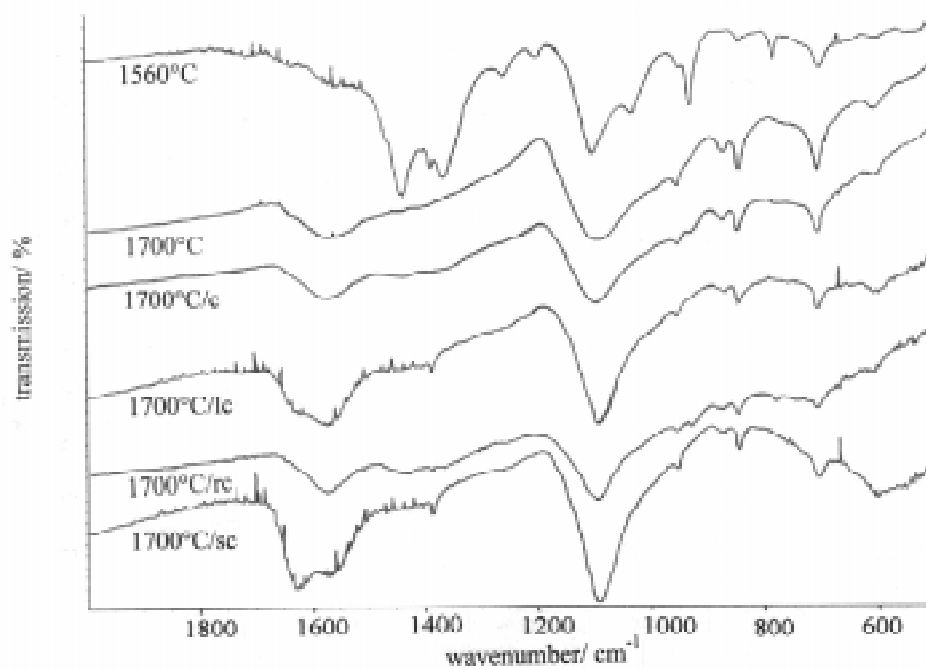


Fig. 3: IR-spectra of B_4C fibers from cotton type and different pyrolysis conditions (c ... closed crucible; lc ... low heating rate ($0,3\text{ K/min}$) and closed crucible; rc ... rapid heating rate (20 K/min) and closed crucible; sc ... sintering at 1750°C and closed crucible)

show intensive C-C bands and only a weak B-C band. But the intensity of the B-C bands grows at higher temperature and after sintering while the C-C vibrations decrease. The increasing intensity of B-C vibrations suggests an increasing crystalline amount. The obtained fibers were also investigated in regard of the carbon and oxygen content by combustions methods. Figure 4 shows the carbon and oxygen content of samples versus the pyrolysis temperature and heating rate. The B_4C fibers still contain free carbon (argement with the IR-vibrations). That results from incomplete conversion of fiber carbon to boron carbide, for instance due to a too low reaction temperature, or it was insufficient boron available due to insufficient soaking with H_3BO_3 . Moreover it is possible that boric acid or boron oxide, respectively, volatilizes during the thermal treatment. This would be connected with a loss of boron. With increasing temperature the free carbon and oxygen content decreases and the boridic carbon content increases. A rapid heating rate and a sintering at $1750^\circ C$ also improve the conversion to boron carbide. The use of closed crucible during heat treatment is also favourable for B_4C formation. The closed crucible prevents the volatilization of boron oxide. The found residual oxygen content can also result from oxide films on the boron carbide surface or incomplete decomposition of cellulose precursor. A good conversion to boron carbide was observed for fibers from viscose type which were sintered. Fibers from wool type with rapid heating rate (20 K/min) and B_4C fibers from cotton type and pyrolysis temperature of $1700^\circ C$ (10 K/min) also showed a good conversion to boron carbide.

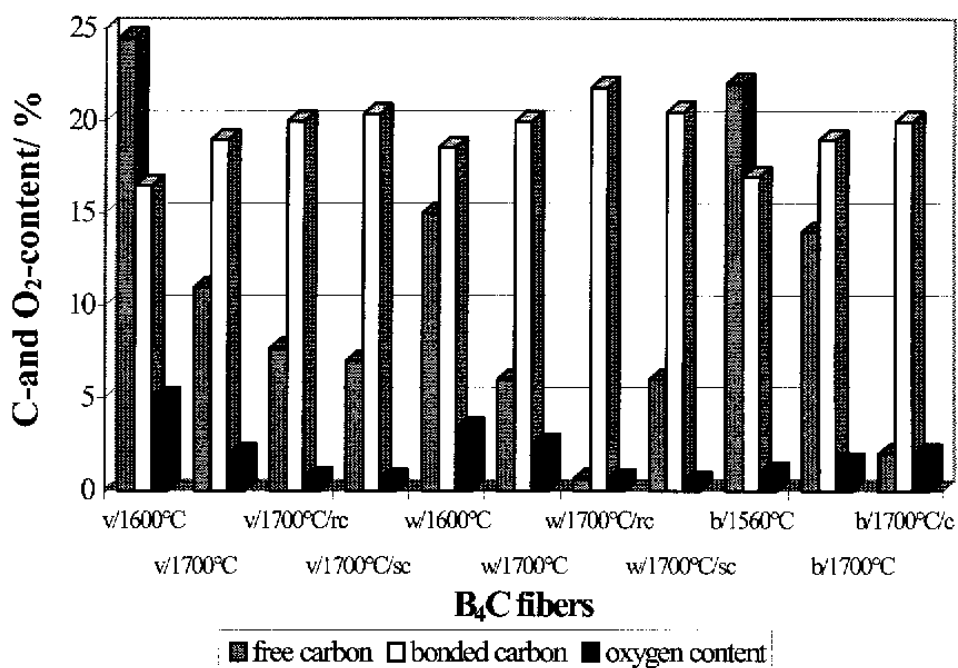


Fig. 4: carbon and oxygen content of the obtained B_4C fibers in dependence on the pyrolysis temperature and the raw fiber types: viscose type (v), wool type (w) and cotton type (c); rc ... rapid heating rate (20K/min) and closed crucible; sc ... sintering at $1750^\circ C$ and closed crucible; c ... closed crucible)

Also x-ray investigations were performed to describe the boron carbide formation. As Fig. 5 shows boron carbide is formed after thermal treatment. After a treatment at $1560^\circ C$ first B_4C peaks (marked by "•") occur and in addition carbon related peaks (marked by "x") are observed. The width of peaks and a high underground attributed to amorphous carbon is

characteristic, in particular, of samples of low reaction temperature (1560°C and 1600°C). With higher temperatures the carbon amount decreases and the peaks attributed to B₄C increase. This is characteristic for increase of crystalline phase. Almost complete boron carbide formation, according to the x-ray pattern, is obtained at 1700°C.

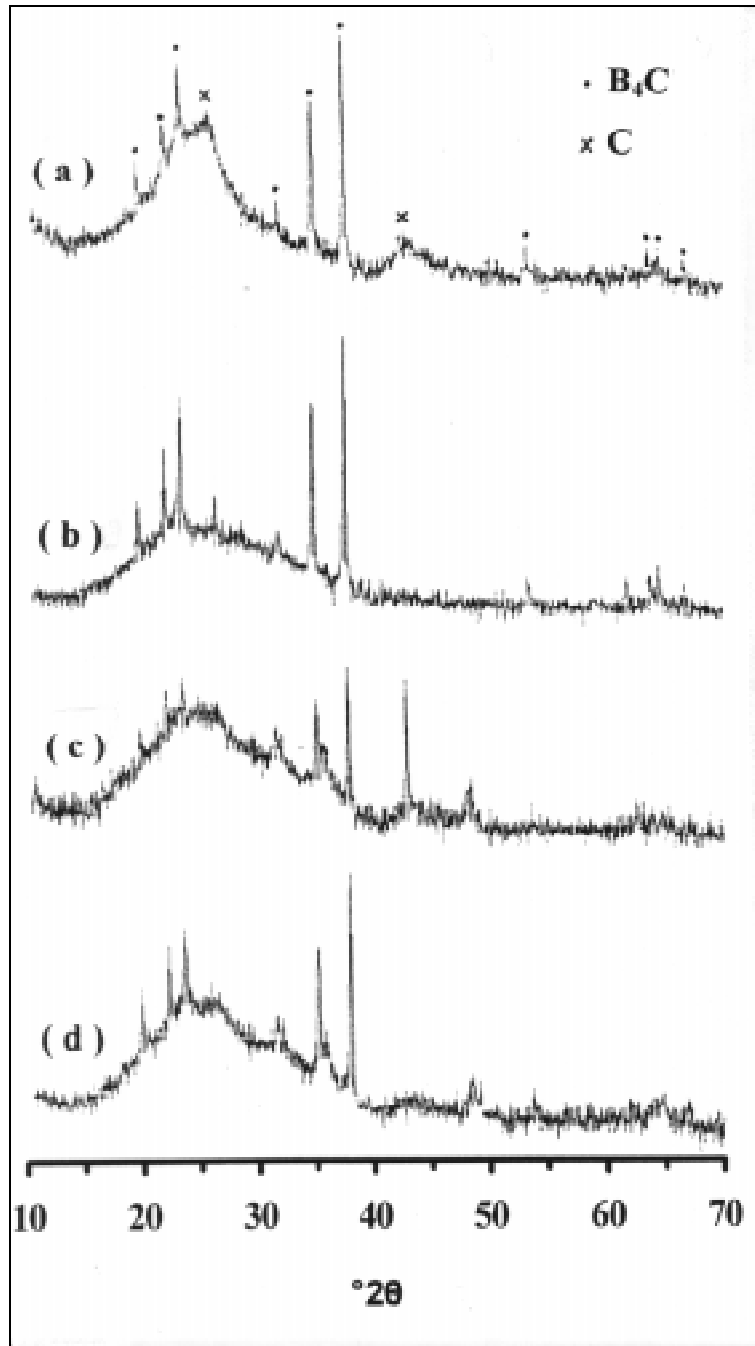


Fig. 5: x-ray patterns of produced B₄C fibers (a) cotton type/1560°C; (b) cotton type/1700°C; (c) viscose type/1600°C; (d) viscose type/1700°C

The surface area of fibers was measured by BET and the results are shown in Fig. 6. High specific surface areas of up to 16 m²/g were found. B₄C fibers of the cotton type show high specific surface areas at temperatures of 1700°C and heating rates of 20 K/min, 10 K/min and 0,3 K/min. But the surface area goes to a lower value after sintering. The fibers with wool

type show only a high specific surface area ($14 \text{ m}^2/\text{g}$) if a high heating rate was used. Only B_4C fibers from viscose type show a high specific surface area after sintering in contrast to the others. An increasing surface area indicates crystallization of fibers, which results in growth of grains and pores. The reason for coarsening is apparently surface-to-surface mass transport owing to gas formation during pyrolysis [10]. During pyrolysis volatile gases (for instance CO , CO_2 , volatile boron oxide) occur due to decomposition of the raw materials and as a product of carbothermic reduction. The weight loss of the fibers after temperature treatment was rather high (around 90%). Coarsening effects were also found by SEM investigations. The specific surface area obviously depends on the heating rate and the occurring gas forming reactions.

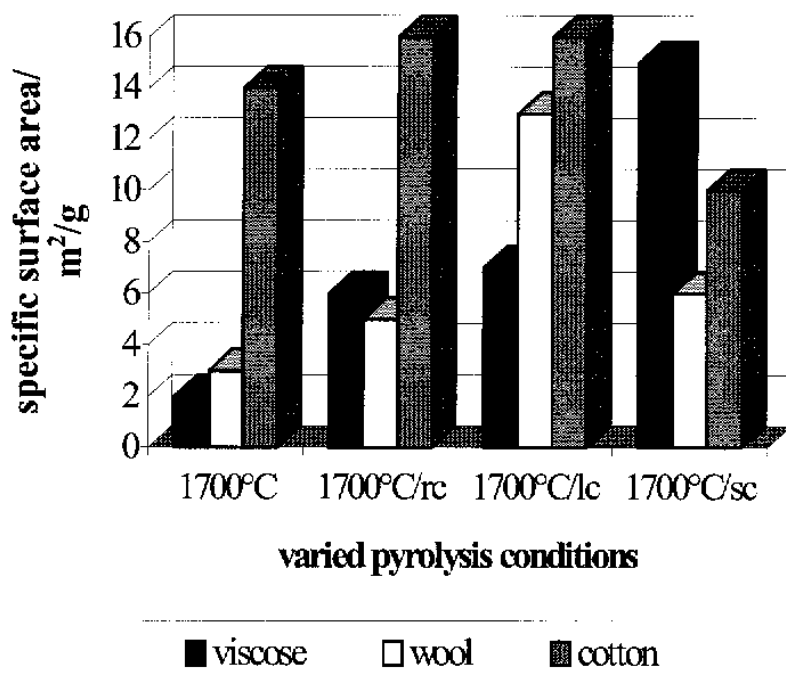


Fig. 6: specific surface area of B_4C fibers from different raw fibers and varied pyrolysis conditions (rc ... rapid heating rate (20K/min) and closed crucible; lc ... low heating rate (0,3 K/min); sc ... sintering at 1750°C and closed crucible)

SEM investigations from obtained fibers with viscose and cotton as raw fibers are shown in Figures 7 and 8. B_4C is found as main component and the shape of the raw fiber is unchanged. The surface of B_4C fibers from cotton type is smooth and fairly dense (Fig. 7). But the B_4C fibers from viscose type (Fig. 8) show submicrometer particles of relative uniform size ($\leq 1\mu\text{m}$), which are interconnected. The fibers indicate coarsening without of densification. This is a consequence of mass- transport processes, for instance by surface and vapor-phase diffusion processes [10]. However B_4C fibers as viscose raw material, sintered at 1750°C or fired at 1700°C with rapid heating rate show less tendency of coarsening.

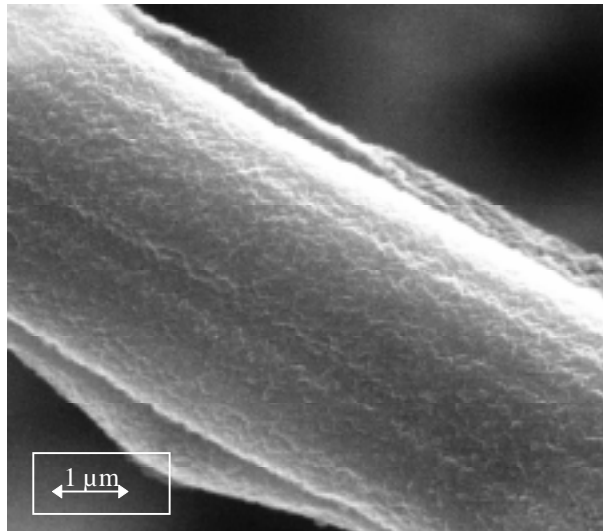


Fig. 7: SEM-photo of B_4C fibers from cotton type and a pyrolysis temperature of $1700^\circ C$

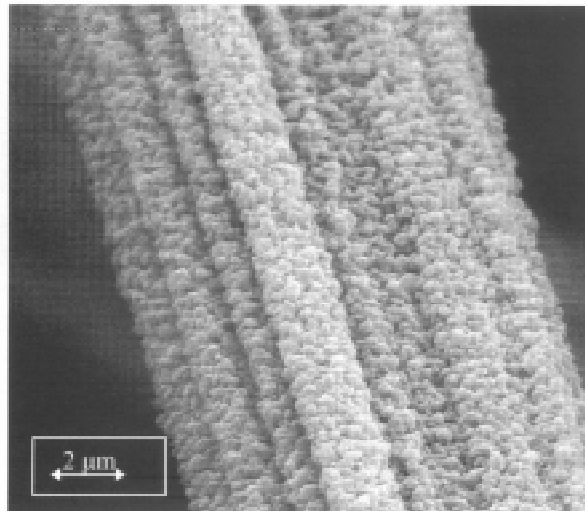


Fig. 8: SEM micrograph of B_4C fibers from viscose as raw fiber and a pyrolysis temperature of $1700^\circ C$

The coarsening of the fibergrains during pyrolysis is unfavourable regarding mechanical properties and corrosion resistance of fibers.

CONCLUSIONS

The preparation of B_4C fibers from fibers cheap and easily available materials boric acid and cellulose is simple and ecological method. Such fibers can be an alternative to commercial B_4C fibers for special applications. A good infiltration of cellulose fibers with boric acid is obtained, if butanol is used as solvent. The combination firstly water swelling and following butanol soaks is a favourable infiltration method. The investigations after temperature treatment show that boron carbide occurs at above $1500^\circ C$. But the obtained fibers still contain free carbon, whose content decreases with increasing temperature up to $1700^\circ C$ and

by sintering at 1750°C. A complete conversion to boron carbide occurs if sufficient boric acid was infiltrated. A preparation problem results from microstructural coarsening during temperature treatment. Such behavior makes the mechanical properties drop down. The effect of coarsening can be inhibited by sintering additives during pyrolysis. The idea of these additives is to activate grain boundary diffusion and volume diffusion or to inhibit surface diffusion. An improvement of strength will be still in development.

REFERENCES

1. Makarenko, G.N., "Borides of the IVb Group", *Boron and Refractory Borides*, edited by Matkovich, V.I., Springer-Verlag Berlin, Heidelberg New York, 1977, pp. 310-330
2. Gmelin-Institut für Anorganische Chemie und Grenzgebiete in der Max-Planck-Gesellschaft zur Förderung der Wissenschaften, *Gmelins Handbuch der Anorganischen Chemie*, Chemie Verlag, Weinheim, 1951, Vol. 4: Boron Compounds, pp. 427
3. Smith, W.D., "Boron Carbide Fibers from Carbon Fibers", *Boron and Refractory Borides*, edited by Matkovich, V.I., Springer-Verlag Berlin, Heidelberg New York, 1977, pp. 541-551
4. Talley, C. P., "Mechanical Properties of Glassy Boron", *Journal of Applied Physics*, New York, Vol. 30, 1959, pp. 1114
5. patent: US 3403008 (1968)
6. patent: US 399177 (1889)
7. Dawzschinsky, H., "Temperaturbeständige Faserstoffe aus anorganischen Polymeren", Akademie-Verlag Berlin, Bd. 152, pp. 16-29
8. Günzler, H., Böck, H., "IR-Spektroskopie: Eine Einführung", VCH, Weinheim, 1990, pp. 250-251
9. Deshpande, S.V., "Filament activated chemical vapor deposition of boron carbide coatings", *Journal of Applied Physics Letters*, Vol. 65, No. 14, 1994, pp.1758
10. Dole, S.L., Prochazka, S., Doremus R.H., "Microstructural Coarsening During Sintering of Boron Carbide", *Journal of the American Ceramic Society*, Vol. 72, No. 6, 1989, pp. 958-966

AKNOWLEDGEMENT

We are grateful to the Deutsche Forschungsgemeinschaft for support of this research (Mu 943/ 7-1)

CHARACTERIZATION OF MICROPHENOMENA IN COMPOSITE MATERIALS

P.F.M. Meurs, P.J.G. Schreurs, and T. Peijs

*Eindhoven University of Technology, Centre for Polymers and Composites,
P.O. Box 513, 5600 MB Eindhoven, The Netherlands*

SUMMARY: An experimental-numerical method is presented, which can be used for the characterization of microphenomena in composite materials. The method is based on the measurement of displacements of material points on the micronscale, and numerical simulations of the experiments to find material constants using an iterative procedure. Displacements of a grid of markers, created with the electron beam of a Scanning Electron Microscope, were measured during in-situ experiments in the SEM. The position of the boundary markers were used to define the geometry of the model, and their displacements were used as boundary conditions. The method has been used to estimate mechanical properties of interphases, fibre coatings, and the determination of the interfacial normal strength (INS). Based on the presented results, it can be concluded that the presented method is a suitable tool for the characterization of microphenomena in composite materials.

KEYWORDS: interphase, coating, interfacial normal strength, strain field measurements

INTRODUCTION

The mechanical properties of a composite material are determined by the properties of its constituents. Due to the strong inhomogeneity of these materials, i.e. the high stiffness ratio between fibres and matrix, and the inhomogeneous fibre distribution in a composite, the mechanical behaviour is strongly influenced by phenomena occurring at a scale of microns. For example, during transverse loading of unidirectional fibre-reinforced composites, local stress and strain concentrations around fibres determine the global macroscopic behaviour [1]. Increasing the transverse load will lead to initiation of microcracks at the fibre/matrix interface, followed by the propagation of these cracks and macroscopic failure of the composite structure. To be able to analyze these phenomena, constitutive relations for the mechanical properties of the constituents are needed. Therefore new and better methods are needed to determine these properties. Often, such methods are based on the use of field quantities, such as displacements and strains.

In recent years, increased attention to microphenomena in composite materials resulted in an increased use of microscopic techniques in a wide range of experiments. For example, optical microscopes in combination with miniature tensile stages are used to study fibre breaking and the growth of debonding cracks along fibres in single and multiple fibre fragmentation tests [2, 3]. Daniel et al. [4] use the optical microscope to study the failure process of unidirectional composites under transverse and longitudinal loading. Using such techniques a qualitative understanding of microphenomena can be obtained, but for quantitative measurements of microscopic strains Scanning Electron Microscopy (SEM) is a more suitable technique, because of its high resolution and a large depth of field. In situ observation of fracture and damage propagation in ceramic matrix composites using a tensile stage in a SEM has been performed by several researchers [5, 6]. A SEM also offers the opportunity to use the electron beam to produce line or dot patterns on the surface of specimens. The deformation of these patterns during loading of the specimen can be used as a measure for the deformation of the material [7, 8, 9].

In this study, an experimental technique has been developed for the measurement of local deformations in a composite. This technique offers the possibility to measure displacement- and strain fields, typically in an area of $20 \times 20 \mu\text{m}$, on the surface of a transversely loaded composite specimen. The experimental technique is part of a mixed experimental-numerical method, which is used to characterize the mechanical properties of interphases and fibre coatings. This method is described in the next section. Subsequently, the measurement technique is described, after which a number of applications for the characterization of microphenomena are given. Finally some conclusions are offered.

A MIXED EXPERIMENTAL-NUMERICAL METHOD

The method is based on the combination of the measurement of displacements, finite element modelling, and parameter estimation. The field quantities are measured during transverse experiments on unidirectional E-glass-fibre-reinforced epoxies. Figure 1 shows a schematic representation of the method.

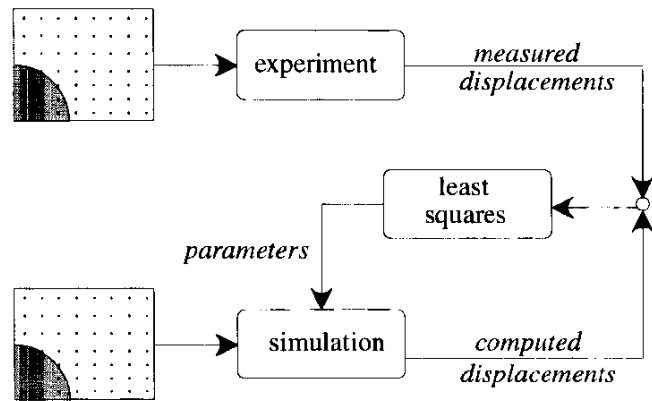


Figure 1: Schematic representation of the mixed experimental-numerical method.

Measurement of field quantities is an essential part of this study and will be discussed in detail in the next section. A grid of markers is placed on the surface of a specimen, and displacements of the markers are measured during tensile experiments in a SEM. A finite element model of the experiment is used to calculate the displacements. The geometry of this model is defined by the positions of the border markers (Figure 2) The displacements of these markers define the kinematic boundary conditions. This method offers the advantage that the numerical model gives an exact description of the local stress-strain state in the experiment. Measured and computed displacement fields are linked in order to find material parameters during an iterative procedure. The difference between measured and computed displacements is used to adjust the parameters describing the constitutive behaviour of the material.

The estimation of interphase or coating parameters comprises the comparison between the experimentally obtained displacement data of the inner markers of the grid (Figure 2) and the results of the finite element analysis [10]. This comparison reveals updated estimations of the material parameters in the simulation via a least squares algorithm. Using this estimation procedure, unknown mechanical properties of interphases and coatings can be determined, when a mathematical model of the experiment is available.

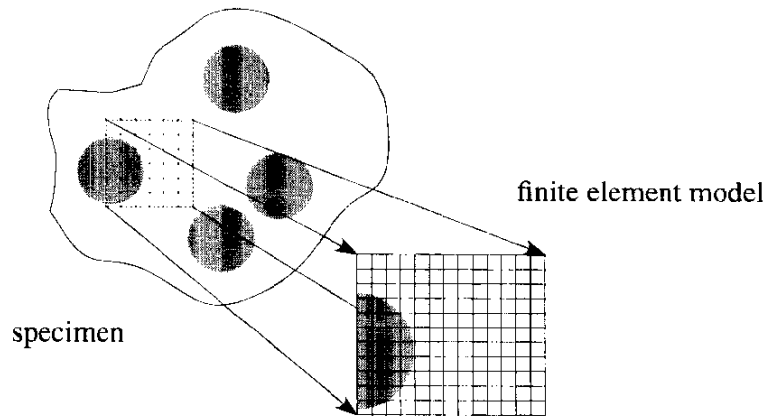


Figure 2: Local modelling of a part of a specimen.

The numerical simulation has to give an accurate representation of the stress-strain state in the experiment. Therefore orienting simulations were performed to analyze the stress-state in transversely loaded composites, and to test the influence of the marker-field position on the accuracy of the estimated material parameters .

Because displacements are measured at the surface of a transversely loaded specimen, a 3D square finite element model consisting of a quarter of a glass fibre and the surrounding polymer matrix has been used for the analysis of 3D effects. Figure 3 shows the maximum radial stress at the fibre-matrix interface, as a function of the distance to the specimen surface for three different fibre volume fractions.

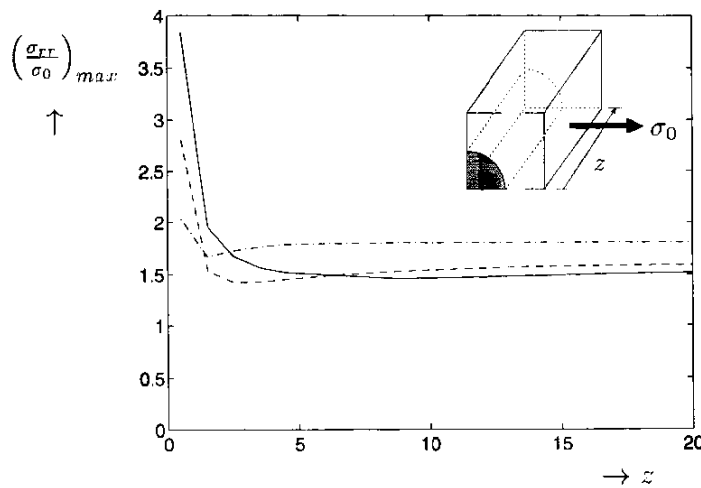


Figure 3: Maximum radial interfacial stress as a function of the distance to the specimen surface.
 · · · $V_f = 45\%$, - - - $V_f = 20\%$, — $V_f = 5\%$

The maximum radial stress increases significantly towards the specimen surface ($z=0$), showing the necessity of using 3D models for these type of experiments. At a distance of $15 \mu\text{m}$ from the surface, the stress is constant. Furthermore, the stress built-up towards the surface increases for a decreasing fibre volume fraction. When these results are translated to high volume fraction composites with a inhomogeneous fibre distribution, this would imply that the interfacial radial stresses are the highest in the matrix rich regions. Based on these numerical results, all experiments are modelled using 3D finite element models, with a thickness of $15 \mu\text{m}$.

Given a 3D-model of an experiment, numerical simulations have been performed to check the influence of changes in experimental setup and the influence of measurement noise on the estimation of parameters. Several different geometries have been analyzed (Figure 4).

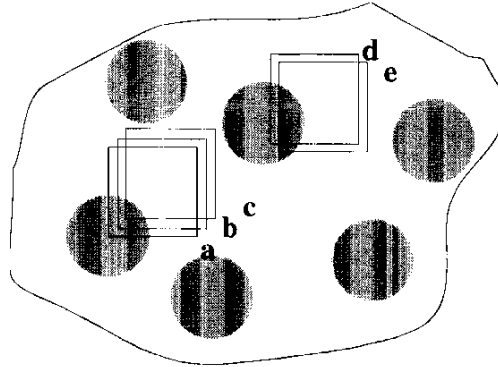


Figure 4: Numerical simulations of different marker field positions.

For all geometries (a-e), the markers are placed in a square packing, and marker distances of $1\ \mu\text{m}$ and $2\ \mu\text{m}$ have been used. In all models, the thickness of the interphase was assumed to be $1\ \mu\text{m}$, and the material properties of glass-fibre ($E=70\ \text{GPa}$), interphase, and epoxy matrix ($E=2.5\ \text{GPa}$) were modelled linearly elastic. For the interphase, a Young's modulus of $2.0\ \text{GPa}$ was taken as the 'real' value. With these values, the in-plane displacements of the markers were calculated, with prescribed displacements on the boundaries of the models. Subsequently, the marker displacement field and the boundary conditions were disturbed by random noise with an amplitude of 5% or 10% of the maximum displacement value. The disturbed displacements were used to estimate the Young's modulus of the interphase. For the initial estimate, a value of $\hat{E}_0=1.0\ \text{GPa}$ was chosen, and for each experimental setup 10 different random noise realizations were added to the calculated displacements. For the setups with a measurement noise of 5%, the average values of \hat{E}_i are close to the 'true' value of $2\ \text{GPa}$. Even for a measurement noise of 10% the maximum error was $0.2\ \text{GPa}$. The standard deviation of the 10 different estimates increases from approximately $0.3\ \text{GPa}$ to $0.7\ \text{GPa}$ for the increasing amplitude of the measurement noise.

A MEASUREMENT TECHNIQUE FOR THE MICRONS SCALE

A procedure has been developed to conduct near real-time measurements of deformations of composite materials, and to subsequently obtain measurements of displacements on the micron-scale. A grid of markers on the surface of test specimens can be generated in the SEM, as is described in this section. For analysis in the SEM, polished composite specimens were used. To avoid charging, a $\pm 100\ \text{\AA}$ thick electrically conductive gold-palladium coating was applied. Two types of markers can be obtained: raised dots and black spots.

During the observation of a specimen at high magnifications ($>5000\times$), the surface of the specimen becomes coated with a dark layer of contamination present in the vacuum chamber of the SEM. This contamination has a relatively high coefficient of thermal expansion, which can be exploited when the SEM is used in spot mode. The contamination is locally heated by the electron beam and expands, resulting in a marker, being a white spot, which represents a local raised dot on the surface. Repeating this procedure produces a marker field on the surface of a

composite (Figure 5a). The dots are placed on a part of a glass fibre cross-section and on the epoxy matrix. The diameter of the dots in Figure 5 is $0.2 \mu\text{m}$, and they are obtained with an acceleration voltage of 10KV, a magnification of 10000X, and a dwell time of 60 seconds.

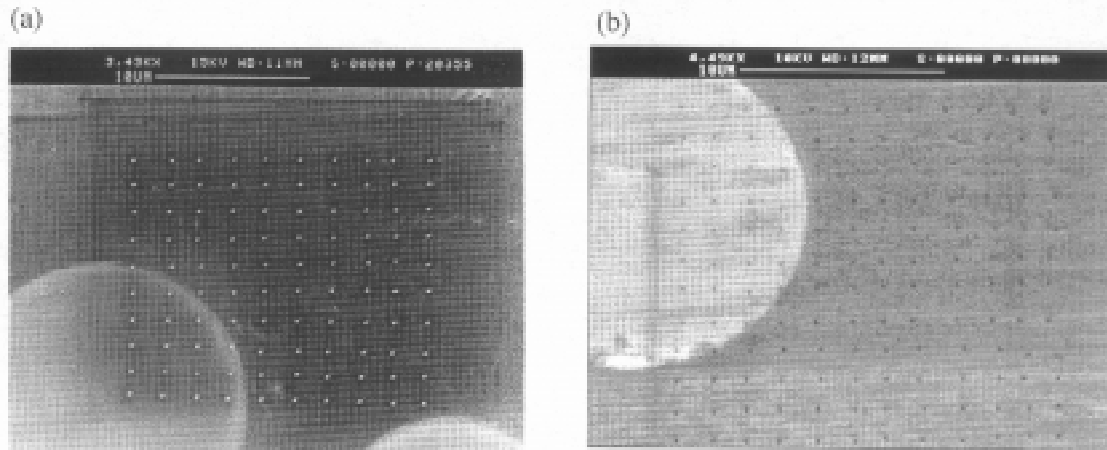


Figure 5: Two types of markers on a E-glass/epoxy composite: (a) raised dots, (b) black spots.

The second type of markers were obtained with the same settings, but with a reduced dwell time. The beam is now only used to concentrate an amount of contamination to one spot on the specimen surface. An example of a marker field consisting of these black spots is given in Figure 5b. The dwell time varied for different specimens between 5 and 10 seconds. In the characterization of microphenomena described in this paper, mostly dot maps consisting of these black spots have been used. Displacements are measured by comparing the coordinates of the dots in reference and deformed situation. The coordinates are determined from directly digitized images. After isolating the markers from the images, the coordinates were defined to be their centre of gravity.

CHARACTERIZATION OF INTERPHASE CONDITIONS

Of all composite properties, especially the properties of the interphase are difficult to determine. Up to now, most of the work to characterize these properties has been done in shear loading conditions, using experiments such as pull-out, microdebond, fragmentation or microindentation tests. However, since transverse debonding is often the first damage mechanism in composite structures, it is important that also the interphasial properties in normal loading conditions are characterized. For this purpose, glass fibre reinforced composite plates were fabricated using the filament winding technique. In order to observe microscopic displacements in-situ during experiments in the SEM, dumbbell shaped miniature specimens with a small gauge length were designed. The edges of the specimens were polished using standard metallographic procedures, to a grit size of $1 \mu\text{m}$, after which the specimens were coated with a Au-Pd sputter coating. Dot maps were placed on a part of a fibre and the surrounding matrix material in the gauge section of the specimen. Monotonic tensile tests are carried out in the SEM. The motor of the tensile stage was stopped at increasing load steps. At each load step the coordinates of the markers are determined. An example of an experiment is shown in Figure 6. The displacements shown in Figures 6b and 6c are measured near the central fibre in Figure 6a for global loads of 100 N and

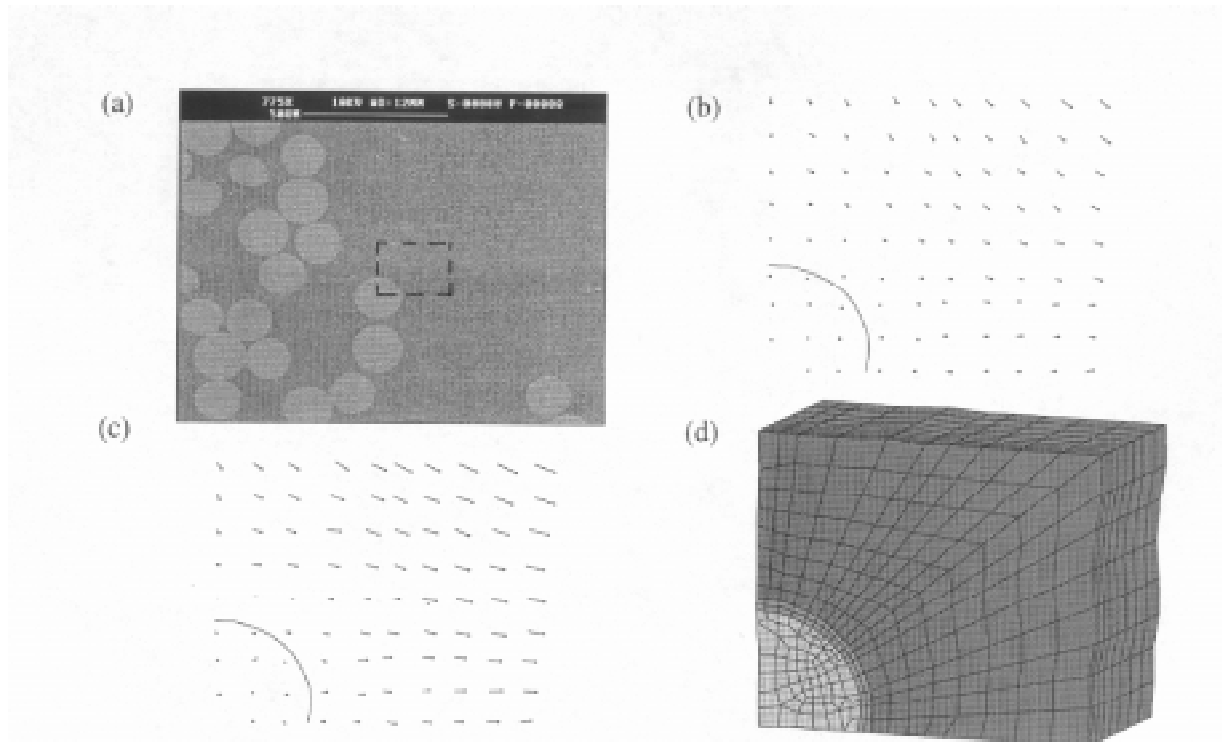


Figure 6: Experiment near a matrix rich region: (a) overview, (b) measured displacements $\times 5$ for $F=100\text{N}$, (c) measured displacements $\times 5$ for $F=150\text{N}$, (d) finite element model of the experiment.

150 N, respectively. The maximum displacements were $0.12 \mu\text{m}$ and $0.29 \mu\text{m}$ for the second load step. The finite element model of this experiment is shown in Figure 6d. The geometry is defined by the coordinates of the border markers. The displacements of these markers were used as boundary conditions for the nodes with equal in-plane coordinates, and for the boundary nodes that do not coincide with markers the displacements were interpolated. The displacements of the inner markers on the surface of the model were used to estimate the Young's modulus of the interphase. The interphase was assumed to be isotropic and having a thickness of $1 \mu\text{m}$. Table 1 shows the results for this experiment.

Table 1: Estimated interphase properties

load [N]	max. disp. [μm]	E_f [GPa]	E_m [GPa]	\bar{E}_i [GPa]	stdv. [GPa]
100	0.12	70	2.8	0.93	0.48
150	0.29	70	2.8	0.33	0.16

At each load step, 10 digital images of the marker field were stored, from which the coordinates of the markers were determined from image analysis, resulting in 10 different displacement fields with respect to the reference situation. The difference is caused by the measurement noise. For each of the 10 displacement fields E_i was estimated using the experimental-numerical method. In all cases, the estimated values E_i converged to a constant value within 5 iterations.

For the second load step, the average of E_i is lower than for the first load step. The measured displacements in the second load step lead to small plastic strains in the interphase, which can be observed in the numerical simulations. Fitting with a linear elastic constitutive model then leads to a lower value of E_i . Therefore, the first value of \bar{E}_i is closest to the true value of the Young's modulus of the interphase for this composite.

CHARACTERIZATION OF FIBRE COATINGS

Due to the significant influence of local stress-strain concentrations around fibres on macromechanical composite properties, a number of techniques have been developed to change the local stress-state. Fibre coatings and thick interphase layers with different mechanical properties than fibre and bulk-matrix can be applied to change the stress transfer from the matrix to the fibres [11, 12, 13]. The second application for which the experimental-numerical method is being used is the characterization of fibre-coatings. This was carried out with single fibre model composites reinforced with (un)coated E-glass fibres. The mechanical properties of the neat materials are given in table 2:

Table 2: Mechanical properties of the neat materials

material	E-glass fibre	epoxy matrix	epoxy coating
Young's modulus E	70 GPa	2.8 GPa	1.4 GPa
Poisson's ratio ν	0.22	0.4	0.4

Single fibres were coated by dipping them in an acetone-epoxy solution. After dipping the coated fibres were cured. Uncoated and coated fibres were positioned and fixed in the cavity of a dumbbell-shaped silicone mould, after which the epoxy matrix was added. This resulted in a microcomposite with one fibre in the centre of the gauge section. The curved edges of the specimens were polished carefully, until both fibre ends were free of surface damage.

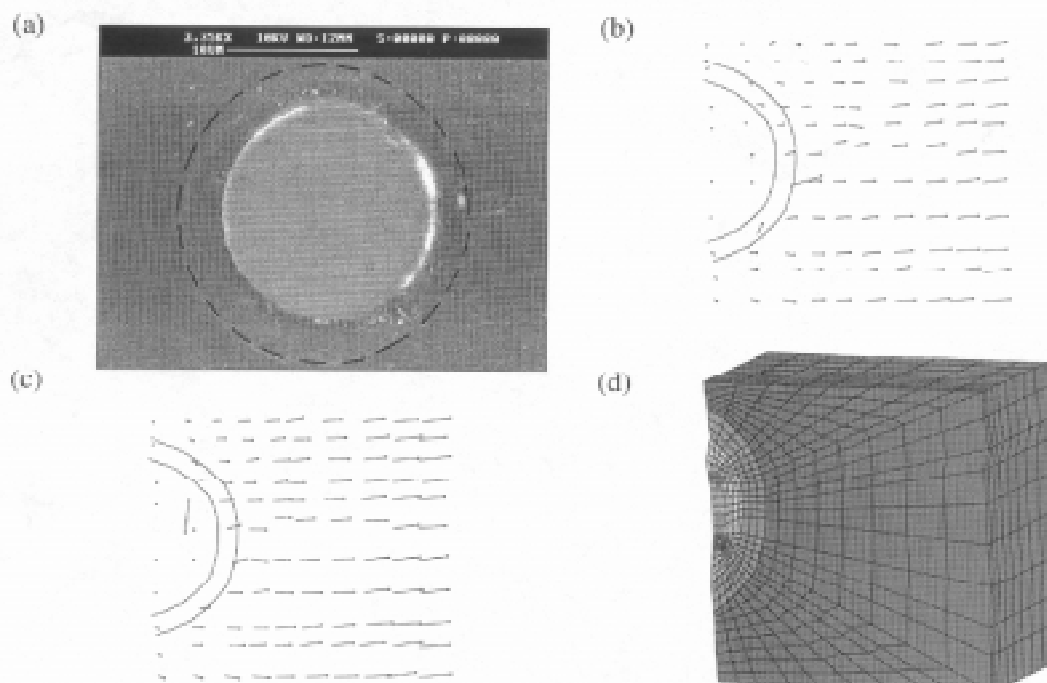


Figure 7: Experiment on a coated fibre: (a) coated fibre, (b) measured displacements $\times 5$ for $F=190\text{N}$, (c) measured displacements $\times 5$ for $F=285\text{N}$, (d) finite element model of the experiment.

An example of an experiment with a coated fibre is shown in Figure 7. Figure 7a, shows the reference configuration in which the coating can be seen. The average coating thickness was approximately $2\ \mu\text{m}$. Figures 7b and 7c, give the measured marker displacements. In the finite element model, the coating is assumed to have a uniform thickness of $2\ \mu\text{m}$. The effective mechanical properties of the coating layer will be determined by the properties of the interphase between the fibre and the coating, and the properties of the neat coating material. To compare uncoated and coated fibres, also for the uncoated fibres a layer of $2\ \mu\text{m}$ is assumed around the fibre. For both situations, the Young's moduli of these layers are estimated. In the experiments, the maximum measured displacements were approximately $0.40\ \mu\text{m}$, resulting in local plastic strains in the coating. For the uncoated fibres an average value of $0.51\ \text{GPa}$ was found, and for the coated fibres the average was $0.20\ \text{GPa}$. Because these values were estimated with an elastic model, the values are lower. However, the estimated value for the Young's modulus for coated fibres is approximately 40% of the first value, resulting in a qualitative description of the effect of the presence of a coating. In future research, these values will be estimated for experimental displacement fields that result in only elastic deformation in the coating layer.

DETERMINATION OF INTERFACIAL NORMAL STRENGTH

Transverse loading of unidirectional composites leads to initiation of microcracks at fibre-matrix interfaces, followed by propagation of these cracks leading to macroscopic failure. Therefore, the interfacial normal strength (INS) is an important material parameter. In the experiments presented here, single glass fibre model composites are used. During transverse loading of these specimens in the SEM, initiation of debonding and crack-growth can be observed. The measurement technique presented in this paper was used to measure the local stress-strain state just before crack initiation. Figure 8 shows such a measured displacement field, and the initiation of debonding just after that load step.

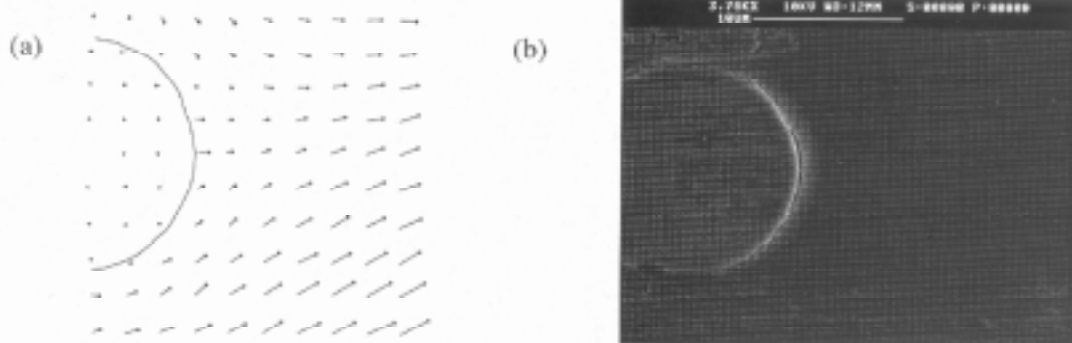


Figure 8: Experiment on a single fibre: (a) displacement field before debonding ($\times 5$), (b) initiation of debonding.

The maximum measured displacement in this experiment was approximately $0.4\ \mu\text{m}$, resulting in plastic deformations around the fibre. In the finite element model of this experiment, ideal plastic behaviour was assumed for the matrix material with a Young's modulus of $2.8\ \text{GPa}$ and a Von Mises yield stress of $66\ \text{MPa}$.

The geometry of the model was defined by the coordinates of the border markers, and the displacements of these markers were used as boundary conditions. The model with (measured) boundary conditions was used to calculate the radial and tangential stresses at the fibre-matrix interface. Because the stresses are the highest at the specimen surface, these stresses were calculated at the surface.

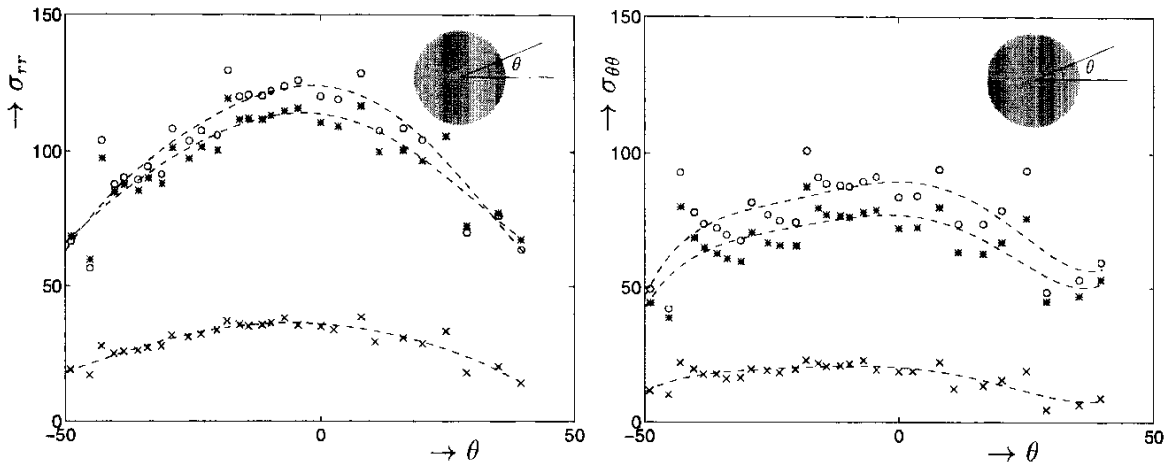


Figure 9: (a) Radial and (b) tangential interfacial stresses for increasing global load. $\times \times \times = 77 \text{ N}$, $* * * = 151 \text{ N}$, $o \ o \ o = 198 \text{ N}$.

The results are given in Figure 9, and show that the radial interfacial stress increases for increasing global loads, and that the radial stress reaches its maximum value of 125 MPa at an angle θ of -5° . Similar stress distributions were found in numerical simulations performed by de Kok et al. [14]. For all load steps the radial stresses are higher than the tangential stresses, which results in initiation of a crack along the fibre surface.

CONCLUSIONS

In this paper, an experimental-numerical method for the characterization of microphenomena in composite materials has been presented. The method is based on the measurement of field quantities during transverse experiments in a SEM. Displacements were measured on a scale of microns using markers that are produced with the electron beam of the SEM. The dot maps on the surface of specimens define the geometry and boundary conditions of a finite element model of the experiment. The advantage of this approach is that the model gives an exact description of the local stress strain state in the specimen. A number of applications for the method have been presented. Interphase conditions in high fibre volume fraction composites and the mechanical properties of coatings in single fibre model composites were estimated with an iterative procedure. An important application is the determination of the interfacial normal stress (INS). For this purpose, the measurements were used to define the local stress strain state in single fibre composites just before the moment of initiation of debonding. A finite element model was used to calculate the radial and tangential stresses at the fibre matrix interface. Based on the presented results, it can be concluded that the presented method is a suitable tool for the characterization of various microphenomena in composite materials.

REFERENCES

- [1] de Kok, J. M. M., Meijer, H. E. H. and Peijs, T., 'The influence of matrix plasticity on the failure strain of transversely loaded composite materials' *Proc. ICCM/9, 1993, pp. 242-249*
- [2] Dibenedetto, A. T. and Jones, K. D., 'The Role of Interphase Debonding on Cumulative Fractures in a Continuous Fibre-Reinforced Composite' *Comp.*, **27A**, 1996, pp. 869-879
- [3] Heuvel, P. W. J. van den, Bruggen, Y. J. W. van der and Peijs, T. 'Failure Phenomena in Multi-fibre Model Composites: Part 1. An Experimental Investigation into the Influence of Fibre Spacing and Fibre-Matrix Adhesion' *Comp.*, **27A**, 1996, pp. 855-859
- [4] Daniel, I. M. Anastassopoulos, G. and Lee, J.-W. 'Experimental Micromechanics of Brittle-Matrix Composites' *Micromechanics: experimental techniques, ASME (AMD vol. 102)*, pp. 133-146
- [5] Dalmaz, A., Reynoud, P., Rouby, D. and Fantozzi, G. 'Damage Propagation in Carbon/Silicon Carbide Composites During Tensile Tests Under the SEM' *J. Mat. Sci.*, **31**, 1996, pp. 4213-4219
- [6] Shercliff, H. R., Beaumont, P. W. R., Vekinis, G. 'Direct Observation of the Fracture of CAS-glass/SiC Composites, part II Notched Tension' *J. Mat. Sci.*, **29**, 1994, pp. 4184-4190
- [7] Corleto, C. R., Bradley, W. L. and Brinson, H. F. 'An Experimental Micromechanics Measurement Technique for Sub-micron Domains' *J. Mat. Sci.*, **31**, 1996, pp. 1803-1808
- [8] Dally, J. W. and Read, D. T. 'Electron Beam Moiré' *Exp. Mech.*, **33**, 1993, pp. 270-277
- [9] Read, D. T. and Dally, J. W. 'Electron Beam Moiré Study of Fracture of a Glass Fiber Reinforced Plastic Composite' *J. Appl. Mech.*, **61**, 1994, pp. 402-409
- [10] Meurs, P. F. M., Schreurs, P. J. G., Peijs, T. and Meijer, H. E. H. 'Characterization of Interphase Conditions in Composite Materials' *Comp.*, **27A**, 1996, pp. 781-786
- [11] Jao, S-H and McGarry, F. J. 'On the failure work and modulus of composites reinforced by thin elastomer-coated fibres' *J. Comp. Mat.*, **26**, No. 18, 1992, pp. 2632-2654
- [12] Marom, G. and Arridge, R. G. C. 'Stress concentrations and transverse modes of failure in composites with a soft fibre-matrix interlayer' *Mat. Sci. Eng.*, **23**, 1976, pp. 23-32
- [13] Venderbosch, R. W., Peijs, T., Meijer, H. E. H. and Lemstra, P. L. 'Fibre-reinforced composites with tailored interphases using PPE/epoxy blends as a matrix system' *Comp.*, **27A**, 1996, pp. 895-905
- [14] de Kok, J. M. M. van Klinken, E. J. and Peijs, T. 'Influence of fibre surface treatment on the transverse properties of carbon fibre reinforced composites' *Adv. Comp.*, 1993, pp. 427-432.

PREDICTION OF RESIDUAL STRESSES IN COMPOSITES INTERFACE BY FINITE ELEMENT METHOD

Yong-Qiu Jiang Huo-Jun Fu

Xi'an Jiaotong University, Xian, Shaanxi, 710049 P.R. CHINA

SUMMARY: Due to misfit of the elastic coefficients of fiber and matrix, the interface of fiber reinforced composites is subjected to residual stresses which have great effect on the mechanical properties of materials. Considering the model as a 3D axisymmetrical problem, the results of interfacial stresses of composites predicted by Finite Element Method agree well with the analytical method by Theory of Elasticity and Experiment Method by Laser Raman Spectroscopy. The effect of interphase on the residual stresses are analysed by Theory of Elasticity and FEM. The interfacial shearing stresses will decrease properly by considering the existence of the interface. Its effect on the interfacial radial stress is somewhat insignificant. Considering the existence of the interphase, The micromechanical model is a composite concentric cylinder with three layers: matrix, fiber and interphase.

KEYWORDS: residual stresses, micromechanical model, theory of elasticity, FEM, 3D axisymmetrical problem, interface, interphase

INTRODUCTION

Due to misfit of the elastic coefficients of fiber and matrix, the interface of fiber reinforced composites is subjected to residual stresses which can be on the order of giga-pascal, for instance, in ceramic matrix composites (CMC). The residual stresses can cause the interface debonds and allow the main crack to propagate beyond the fiber which remains intact, as shown in Fig. 1. The intact fiber then bridges the crack faces, exerting a closing traction which shields the crack tip from the stress applied to the materials. Therefore, the residual stress of the interface has great effect on the mechanical properties of materials. Hence, how to predict the residual stress is an important problem.

The effect of interphase on the residual stresses is considered. The micromechanical model is a concentric composite cylinder with three layers: matrix, fiber and interphase.

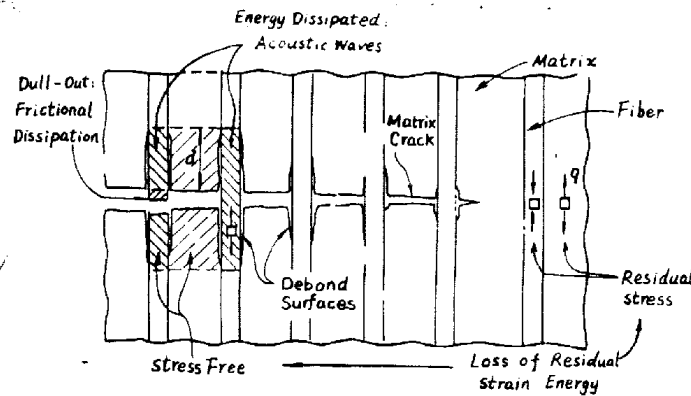


Fig. 1; Schematic representation of crack propagation through CMC

The residual stresses are analysed by Theory of Elasticity and Finite Element Method. The effect of the interphase on the residual stresses are somewhat insignificant.

ANALYSIS OF RESIDUAL STRESS BY CONSIDERRING NO INTERFACE

The micromechanical model is a composite cylinder with a fiber embedded in a concentric cylinder of matrix materials as shown in Fig. 2(a), where a and b are radii of fiber and matrix respectively. The volume fraction of the inclusion in the composite cylinder is the same as that of the entire body of fiber in the composite material.

Since this is 3D axisymmetric problem, one quarter section is considered as shown in Fig. 2 (b). The method of isoparametric elements with eight nodes is employed. The elements with constrained supports are shown in Fig 3. The composite cylinder is transversely isotropic and non-homogeneous, where as the fiber and the matrix are isotropic and homogeneous.

The analytical solution has been derived as a 3D axisymmetrical problem by Theory of Elasticity^[1].

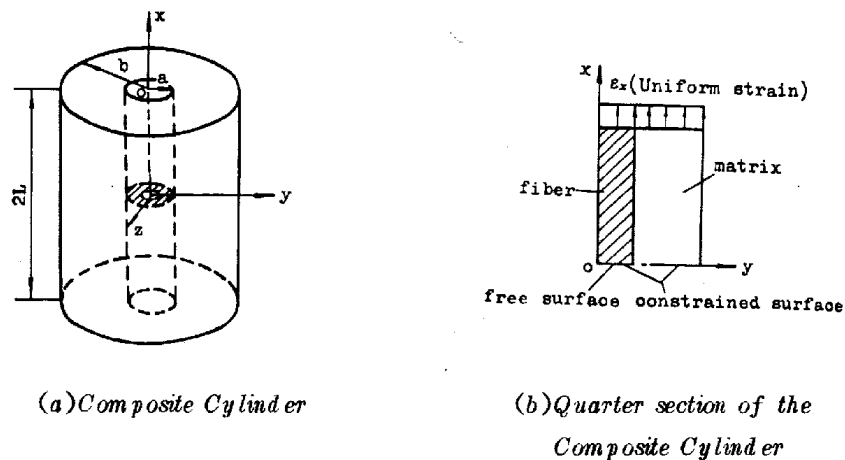


Fig. 2; Micromechanical model

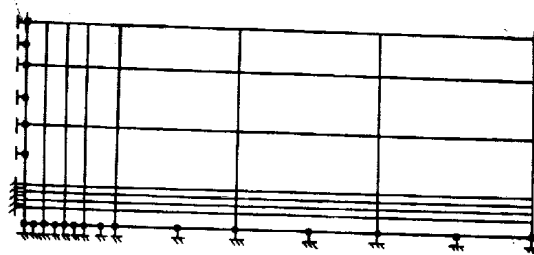


Fig. 3: Elements and constrained supports in quarter section of the composite cylinder

Numerical Example

Consider C/SiC ceramic composite. The properties are $E_f = 190 \text{ GPa}$, $\nu_f = 0.14$, $\alpha_f = 3.1 \times 10^{-6}/^\circ\text{C}$; $E_m = 400 \text{ GPa}$, $\nu_m = 0.24$, $\alpha_m = 4.7 \times 10^{-6}/^\circ\text{C}$, $\Delta T = 20^\circ\text{C} - 1200^\circ\text{C} = -1180^\circ\text{C}$. By Finite Element Method, (FEM) the distribution of residual stresses $\sigma_z^i, \sigma_r^i, \tau_{rz}^i$ along the interface of C/SiC are shown in Fig. 4. Compared with the Analytical solution which is considered as a by Theory of Elasticity, they agree pretty well.

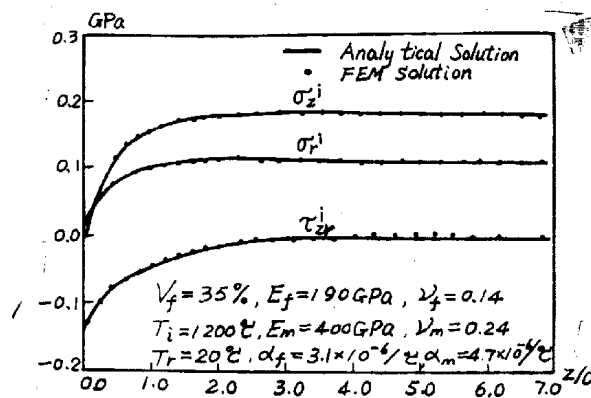


Fig. 4: Distribution of interfacial stresses of C/SiC along the axis of the fiber

ANALYSIS OF RESIDUAL STRESS BY CONSIDERING THE EXISTENCE OF INTERFACE

Analytical Solution

The micromechanical model is shown in Fig. 5, the Thickness of the interphase is h_i which is very thin, usually $5 \text{ nm} \sim 30 \text{ nm}$ for CMC. Therefore, the interphase is assumed to transfer shearing stress only^[2]. The displacement in Z-direction along the interface of the matrix and interphase is

$$U_c = U_a + \frac{\tau_{rz}^2}{G_i} \cdot h_i \quad (1)$$

where u_a is the displacement of the fiber in Z direction at $r=b$, G_i is the shearing modulus of the interphase and h_i is the thickness of the interphase. By equilibrium equation, the shearing stress along the interface of the fiber

$$\tau_{rz}^i = -\frac{a}{2} \sigma_z^i \quad (2)$$

where σ_z^i is the axial stress of the fiber. By differentiating with respect Z for both sides of Eq. (2), we have

$$\varepsilon_i = \varepsilon_a - \frac{h_i}{G_i} \cdot \frac{a}{2} \sigma_z^i \quad (3)$$

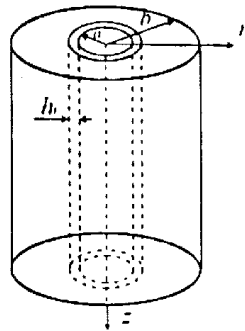


Fig. 5:

The micromechanical model of CMC with interphase

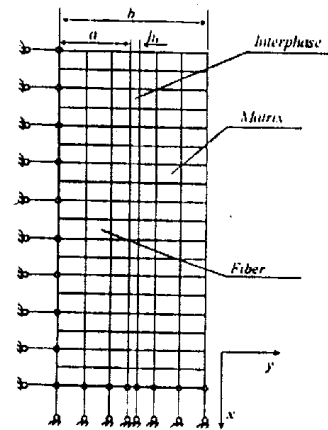


Fig 6

The quarter section of the model shown in Fig. 5 with finite elements

By the continuation of boundary interfacial shearing stress

$$\tau^{if} = \tau^{im}$$

Therefore

$$G_f \frac{2}{a} (\varepsilon_a - \varepsilon_o) = G_m \frac{\frac{b^2}{c} - c}{c^2 \ln \frac{c}{b} - \frac{1}{2}(c^2 - b^2)} (\varepsilon_c - \varepsilon_b) \quad (4)$$

Solving Equatons(3) and (4) simutaneously; We have

$$\varepsilon_c = \frac{1}{1-\lambda} \varepsilon_f - \frac{\lambda}{1-\lambda} \varepsilon_b - \frac{h_i}{G_i} \cdot \frac{a}{2(1-\lambda)} \sigma_z^i \quad (5)$$

Where

$$\lambda = \frac{G_m}{4G_f} \cdot \frac{\frac{ab^2}{c} - ac}{c^2 \ln \frac{c}{b} - \frac{1}{2}(c^2 - b^2)} \quad (6)$$

Let

$$\alpha = \frac{1}{1-\lambda}, \beta = -\frac{\lambda}{1-\lambda}, v = -\frac{h_i}{G_i} \cdot \frac{a}{2(1-\lambda)} \quad (7)$$

The Equation (6) will become

$$\varepsilon_c = \alpha \varepsilon_f + \beta \varepsilon_b + \nu \sigma_z^j \quad (8)$$

By boundary condition and equilibrium condition^[9], we have

$$\begin{cases} a_1 A_f + b_1 A_m = C_1 \cdot \varepsilon_f + d_1 + e_1 \sigma_z^j \\ a_2 A_f + b_2 A_m = C_2 \cdot \varepsilon_f + d_2 + e_2 \sigma_z^j \end{cases} \quad (9)$$

$$e_1 = -bb \cdot v, e_2 = -aa \cdot v \quad (10)$$

Where

$$\begin{aligned} aa &= \frac{E_m v_m}{(1 + v_m)(1 - 2v_m)} - \frac{E_f v_f}{(1 + v_f)(1 - 2v_f)} \\ &\quad - 4a^2 b^2 \ln \frac{a}{b} - (a^4 - b^4) \\ bb &= \frac{-4a^2 b^2 \ln \frac{a}{b} - (a^4 - b^4)}{-4b^2 \ln \frac{a}{b} - 2(a^2 - b^2)} \end{aligned} \quad (11)$$

$$\begin{aligned} a_1 &= a^2 \frac{E_f v_f}{(1 + v_f)(1 - 2v_m)} - b_0 \frac{1 - 2v_f}{v_m} \frac{a^2}{2b^2} \\ a_2 &= \frac{E_f}{(1 + v_f)(1 - 2v_f)} + \frac{E_m}{2(1 + v_m)} - (1 - dd) \cdot aa \cdot \frac{1 - 2v_m}{v_m} \frac{a^2}{2b^2} \\ b_2 &= \frac{-(1 - v_m)E_m}{(1 + v_m)(1 - 2v_m)} + (1 - dd) \cdot aa \cdot \frac{1 - 2v_m}{v_m} \left(\frac{1}{2(1 - 2v_m)} + \frac{a^2}{2b^2} \right) \\ b_1 &= \frac{E_m(b^2 - a^2)}{(1 + v_m)(1 - 2v_m)} - b_0 \frac{1 - 2v_m}{v_m} \left(\frac{1}{2(1 - 2v_m)} + \frac{a^2}{2b^2} \right) \\ c_1 &= -a^2 \Lambda_f - \Lambda_m \cdot bb \cdot dd \\ c_2 &= aa \cdot dd \\ d_1 &= \sigma_h \cdot b^2 + a^2 \frac{\alpha_f E_f \Delta T}{1 - 2v_f} + \frac{\alpha_m E_m \Delta T}{1 - 2v_m} (b^2 - a^2) - b_0 \frac{1 + v_m}{v_m} \alpha_m \Delta T \\ d_2 &= \frac{1 + v_m}{v_m} \alpha_m \Delta T \cdot (1 - dd) \cdot aa - \frac{E_m \alpha_m \Delta T}{1 - 2v_m} + \frac{E_f \alpha_f \Delta T}{1 - 2v_f} \\ e_1 &= -bb \cdot v \\ e_2 &= -aa \cdot v \end{aligned} \quad (12)$$

Here

$$\begin{aligned} b_0 &= \Lambda_m (b^2 - a^2) = \Lambda_m \cdot bb \cdot dd \\ aa &= \frac{E_m v_m}{(1 + v_m)(1 - 2v_m)} - \frac{E_f v_f}{(1 + v_f)(1 - 2v_f)} \\ &\quad - 4a^2 b^2 \ln \frac{a}{b} - (a^4 - b^4) \\ bb &= \frac{-4a^2 b^2 \ln \frac{a}{b} - (a^4 - b^4)}{-4a^2 \ln \frac{a}{b} - (2 - \frac{G_m}{G_f})(a^2 - b^2)} \\ dd &= \frac{4b^2 \ln \frac{a}{b} - 2(a^2 - b^2)}{4b^2 \ln \frac{a}{b} - (2 - \frac{G_m}{G_f})(a^2 - b^2)} \end{aligned} \quad (14)$$

$$\begin{aligned} \Lambda_f &= E_f + \frac{2E_f v_f^2}{(1 - 2v_f)(1 + 2v_f)} \\ \Lambda_m &= E_m + \frac{2E_m v_m^2}{(1 - 2v_m)(1 + 2v_m)} \end{aligned} \quad (15)$$

Solving equation (10) simultaneously, we have

$$\begin{cases} A_f = f_1 \cdot \varepsilon_f + g_1 + h_1 \sigma_f^x \\ A_m = f_2 \cdot \varepsilon_f + g_2 + h_2 \sigma_f^x \end{cases} \quad (16)$$

Where

$$\begin{aligned} f_1 &= \frac{b_2 c_1 - b_2 c_2}{a_1 b_2 - a_2 b_1}, g_1 = \frac{b_2 d_1 - b_1 d_2}{a_1 b_2 - a_2 b_1}, h_1 = \frac{e_2 b_2 - e_2 b_2}{a_1 b_2 - a_2 b_1} \\ f_2 &= \frac{a_1 c_2 - a_2 c_1}{a_1 b_2 - a_2 b_1}, g_2 = \frac{a_1 d_2 - a_2 d_1}{a_1 b_2 - a_2 b_1}, h_2 = \frac{a_1 e_2 - a_2 e_1}{a_1 b_2 - a_2 b_1} \end{aligned} \quad (17)$$

From boundary condition;

When $r=b, \alpha^m=0$ (Fig. 5),

Then

$$\varepsilon_b = f_3 \varepsilon_f + g_3 + h_3 \sigma_z^x \quad (18)$$

where

$$\begin{aligned} f_3 &= \frac{1 - 2v_m}{v_m} \left[- \left(\frac{1}{2(1 - 2v_m)} + \frac{a^2}{2b^2} \right) f_2 + \frac{a^2}{2b^2} f_1 \right] \\ g_3 &= \frac{1 - 2v_m}{v_m} \left[- \left(\frac{1}{2(1 - 2v_m)} + \frac{a^2}{2b^2} \right) g_2 + \frac{a^2}{2b^2} g_1 \right] \\ h_3 &= \frac{1 - 2v_m}{v_m} \left[- \left(\frac{1}{2(1 - 2v_m)} + \frac{a^2}{2b^2} \right) h_2 + \frac{a^2}{2b^2} h_1 \right] \end{aligned} \quad (19)$$

From the equilibrium condition, we have

$$\sigma_f = \Lambda'_f \varepsilon_f + \varphi'_f + \frac{E_f v_f h_1}{(1 + v_f)(1 - 2v_f)} \quad (20)$$

where $\Lambda'_f = \Lambda_f + \frac{E_f v_f f_1}{(1 + v_f)(1 - v_f)}$

$$\varphi'_f = \frac{E_f v f}{(1 + v_f)(1 - 2v_f)} g_1 - \frac{\alpha_f E_f \Delta T}{1 - 2v_f} \quad (21)$$

Then

$$\varepsilon_f = (\sigma_f - \varphi'_f - \frac{E_f v_f h_1}{(1 + v_f)(1 - 2v_f)} \sigma_z^x) / \Lambda'_f \quad (22)$$

From the equilibrium condition in the axis of fibre,

$$\sigma_z^x = - \frac{2}{a} \tau_{rz}$$

Then we have

$$\sigma_z^x = - \frac{8}{a^2} G_f (\varepsilon_a - \varepsilon_f) = - \frac{8\lambda}{a^2} G_f [\alpha \varepsilon_f + (\beta - 1) \varepsilon_b + v \sigma_f^x] \quad (23)$$

After simplifying, we have

$$\sigma_z^x = f_4 \varepsilon_f + g_4 \quad (24)$$

Where

$$\begin{aligned} f_4 &= \frac{-8\lambda G_f}{a^2 + 8\lambda G_f [(\beta - 1)h_3 + v]} [\alpha + (\beta - 1)f_3] \\ g_4 &= \frac{-8\lambda G_f}{a^2 + 8\lambda G_f [(\beta - 1)h_3 + v]} [(\beta - 1)g_3] \end{aligned} \quad (25)$$

By substituting equation (22) into equation (23), we have the following differential equation,

$$\sigma_z^i = a_j \cdot \sigma_f + a_i \quad (26)$$

Where

$$a_j = \frac{f_A}{\Lambda_f' + \frac{E_f v_f h_1 f_A}{(1+v_f)(1-2v_f)}}$$

$$a_i = \frac{-\phi_f' \cdot f_A + g_A \cdot \Lambda_f'}{\Lambda_f' + \frac{E_f v_f h_1 f_A}{(1+v_f)(1-2v_f)}} \quad (27)$$

Solving the differential equation (26), the residual stress in fiber is

$$\sigma_z^i = (\sigma_k + \frac{a_i}{a_j})e^{-qz} - \frac{a_i}{a_j} \quad (28)$$

Where

$$q = \sqrt{a_j} \quad (29)$$

The residual shearing stress τ_{rz}^i and radial stress σ_r^i along the interface by considering the existence of interphase are;

$$\tau_{rz}^i = \frac{aq}{2} (\sigma_k + \frac{a_i}{a_j}) e^{-qz} \quad (30)$$

$$\sigma_r^i = \frac{E_f}{1+v_f} \left(\frac{A_f}{(1-2v_f)} - \frac{B_f}{a^2} \right) - \frac{E_f}{1-2v_f} (\alpha_f \Delta T - \frac{V_f + \varepsilon_a}{1+V_f}) \quad (31)$$

where α_n is the uniformly distributed external load on fiber and matrix,

$$A_f = \frac{(b_2 c_1 - b_1 c_2) \varepsilon_f + (d_1 b_2 - d_2 b_1)}{a_1 b_2 - a_2 b_1} \quad (32)$$

$$\varepsilon_a = d d \cdot \varepsilon_f + (1 - d d) \varepsilon_b \quad (33)$$

$$B_f = 0 \text{ (Since when } r \rightarrow 0, \sigma_r^i \neq \infty \therefore B_f = 0)$$

Finite Element Method

The micromechanical model is also a composite cylinder with a fiber embedded in a concentric cylinder of matrix materials as shown in Fig. 5, where a and b are radii of fiber and matrix. The thickness of the interphase is h_i . The volume fraction of the inclusion in the composite cylinder is same as that of the entire body of fiber in the composite material.

Since this is also 3D axisymmetric problem, one quarter section is considered as shown in Fig. 6, The composite cylinder is transversely isotropic and non-homogeneous where as the fiber, matrix and interphase are isotropic and homogeneous.

Numerical Example

Consider the some numerical example with the same properties of fiber and matrix. Now the existence of the interphase is considered.

Case 1: $E_i = 335 \text{ GPa}$, $\nu_i = 0.22$, $h_i = 60 \text{ nm}$, $V_f = 35\%$, $\Delta T = 20 - 1200 = -1180^\circ \text{C}$. The distributions of residual stresses σ_z^i , σ_r^i , τ_{rz}^i along the interface by Analytical Solution and

FEM solution are shown in Fig. 7. These solutions agree pretty well. Obviously, when $Z/a \gg 2$, $\sigma_z^i = 183 \text{ MPa}$, $\sigma_r^i = 112.8 \text{ MPa}$, when $Z/a = 0$, $\tau_{rz}^i = -140.0 \text{ MPa}$; $Z/a \gg 2$, $\tau_{rz}^i \rightarrow 0$.

Case 2; $E_i = 100 \text{ GPa}$, $h_i = 60 \text{ nm}$, $\nu_i = 0.12$, $V_f = 35\%$, $\Delta T = -1180^\circ \text{C}$. The distributions of residual stresses σ_z^i , σ_r^i , τ_{rz}^i along the interface by Analytical Solution and FEM solution are shown in Fig. 8. These solutions agree pretty well. Obviously, when $Z/a \gg 2$, $\sigma_z^i = 182.3 \text{ MPa}$, $\sigma_r^i = 111.6 \text{ MPa}$, when $Z/a = 0$, $\tau_{rz}^i = -129.8 \text{ MPa}$, when $Z/a \gg 2$, $\tau_{rz}^i \rightarrow 0$.

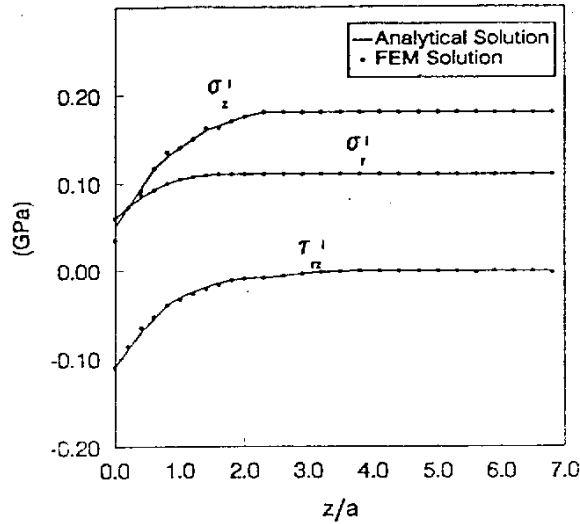


Fig. 7; Distributions of Residual and stresses of C/SiC $E_i = 335 \text{ GPa}$, $h_i = 60 \text{ nm}$, $\nu_i = 0.22$, $V_f = 35\%$

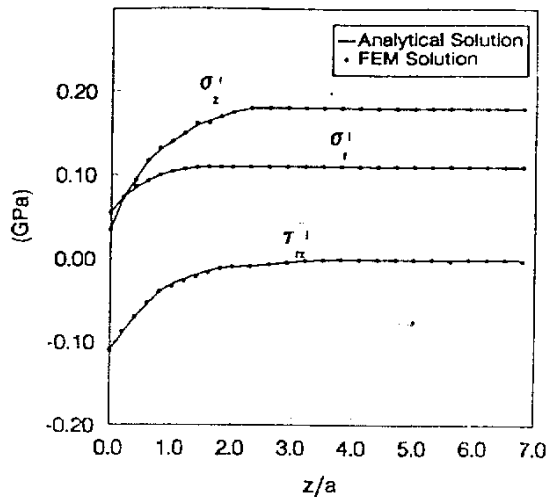


Fig. 8; Distributions of Residual Stresses of C/SiC with the properties of interphase; $E_i = 100 \text{ GPa}$, $h_i = 60 \text{ nm}$, $\nu_i = 0.12$, $V_f = 35\%$

The shearing stresses of SiC/SiC near the end of the fiber ($Z/a \rightarrow 0$) with interphase and with no interphase are quite different as shown in Fig. 9.

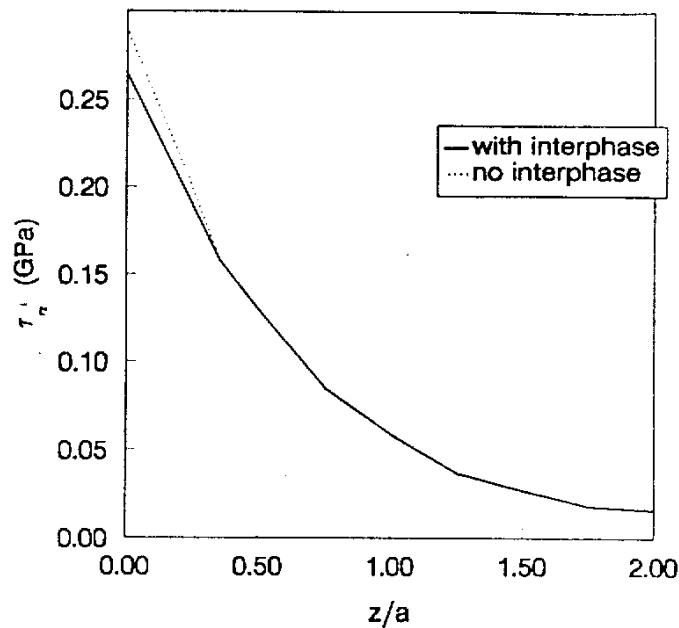


Fig. 9; The distributions of τ_{rz}^i of $\overline{\text{SiC}}/\text{SiC}$ with interphase and without interphase
 $E_f = 190 \text{ GPa}$, $\nu_f = 0.14$, $\alpha_f = 3.1 \times 10^{-6} / ^\circ\text{C}$, $V_f = 45\%$
 $E_m = 440 \text{ GPa}$, $\nu_m = 0.25$, $\alpha_m = 4.7 \times 10^{-6} / ^\circ\text{C}$,
 $E_i = 90 \text{ GPa}$, $\nu_i = 0.12$, $h_i = 20 \text{ nm}$

CONCLUSIONS

1. Considering the model as a 3D axisymmetrical problem, the results of interfacial stresses of composites predicted by FEM agree well with the analytical method by Theory of Elasticity. This conclusion is both good by considering no interphase and with the existence of interphase.
2. The Young's Modulus of the interphase E_i and the volume fraction of the fiber V_f have effect on the interfacial stresses which could be relaxed by decreasing E_i or increasing V_f appropriately, so that the strength and fracture toughness of composites will increase.
3. The interfacial shearing stress τ_{rz}^i will decrease properly by considering the existence of the interphase. Its effect on the interfacial stresses σ_r^i , τ_{rz}^i is somewhat insignificant.

REFERENCES

1. Jiang, Yong-Qiu; Li, Ge and Wang, Wei-Bo "The Analysis and Measurement of Residual stress in Ceramic Matrix Composites Interface," ICCM-10 Proceedings, 1995, pp IV 665-672.
2. Tsai Hsi-Chin, Arocho, Annette M. and Gause, Lee W., Material Science and Engineering, A 126, 1990, pp295-304.

INTERFACIAL ASPECTS OF FIBER REINFORCED BRITTLE/DUCTILE MATRIX COMPOSITES USING MICROMECHANICS TECHNIQUES AND ACOUSTIC EMISSION

Joung-Man Park¹, Sang-H Lee¹, Dong-Jin Yoon², and Dong-Woo Shin³

¹ *Department of Polymer Science & Engineering,
Regional Research Center for Aircraft Technology,
Gyeongsang National University, Chinju 660-701, Korea*

² *Failure Prevention Research Center,
Korea Research Institute of Standards and Science,
Taedok Science Town, Taejon 305-306, Korea*

³ *Department of Inorganic Materials Engineering,
Gyeongsang National University, Chinju 660-701, Korea*

SUMMARY: Interfacial bonding and microfailure modes of glass fiber reinforced brittle unsaturated polyester/modified epoxy composites were investigated via micromechanics tests and acoustic emission (AE). Various silane coupling agents were used to observe the comparative interfacial bonding and subsequent microfailure modes. In the brittle matrix layer, the number of fragments was different greatly between the silane-treated and the untreated specimens. The more the numbers of cracking was increased, the higher the interfacial bonding was improved. This might be due to the chemical and hydrogen bondings between interphases. A reasonable correlation among microdroplet, fragmentation tests and model system was found. The cracking numbers in the brittle matrix were reduced significantly after dipping for 1 hour in boiling water compared to the dry condition. The microfailure modes under a uniaxial tensile load were also investigated using AE technique by associating AE parameters including AE event, energy, and peak amplitude distribution. AE data showed the sequential occurrence of mainly three groups of AE. The first group was originated from mainly brittle matrix cracking. The second and the third group resulted from the fiber breakages and ductile matrix cracking including debonding, respectively. The micromechanical tests for the dual matrix specimens provided more reliable information on the interfacial adhesion and the microfailure modes with combining AE technique.

KEYWORDS: dual matrix composites, fragmentation test, microdroplet test, interfacial shear strength, acoustic emission

INTRODUCTION

Interfacial shear strength (IFSS) between fiber and matrix plays an important role in controlling composite properties. A relatively strong interfacial bond is needed for an efficient transfer of applied load, whereas a weak interfacial strength is desirable for toughening of fiber composite. The conventional techniques for the IFSS include single fiber pull-out, fragmentation and microindentation methods [1]. Among them, considerable attentions were drawn to the single fiber pull-out test in measuring the IFSS, since this technique showed distinct advantages over

others, i.e., a direct measure of the interfacial bond, and no limitation in the properties of fiber and matrix. In fragmentation test, However, the failure strain of the matrix should be several times larger than the fiber failure strain to cause a saturated fragmentation state.

The dual matrix composite is constructed by a single fiber, brittle inner matrix layer and ductile outer matrix. The specimen was subjected to tensile loading to result in the breaking of the embedded fiber and brittle coating layer into many fragments [2]. This specimen was designed to undergo the necessary elongation without premature failure of the matrix. Each fiber breakage could induce a fracture of the adjacent brittle layer but the propagation of crack can be stopped by the tougher support at the second interface, preventing the complete fracture.

Acoustic emission (AE) technique has been considered as a highly reliable way of detecting the active microscopic failure events in composite materials. Being subjected to the external load, AE may occur from fiber fracture, matrix cracking, and debonding at the fiber-matrix interface. The energy released by fiber fracture could be much greater than that associated with debonding or matrix cracking. In particular, AE technique is useful for opaque matrix composites being difficult to monitor optically.

In this work, the IFSS and microfailure modes of brittle/ductile dual matrix composites were evaluated using fragmentation, microdroplet methods and AE technique. The effect of the surface treatment using various coupling agents on the IFSS was also studied in details.

EXPERIMENTAL

Materials

Two kind of E-glass fibers with diameter of 14.7 μm and 30.3 μm with no sizing, and average density of 2.55 g/cm^3 were used. Tensile strength of the glass fibers was measured before fabricating composites. Various silanes including amino- and methacryloxy- functional groups were used as coupling agents. Silane coupling agents were diluted to the required concentration chosen for coating. A polymeric coupling agent increasing wettability was used for high the IFSS. The brittle matrix and microdroplet were prepared using unsaturated polyester. Benzoylperoxide and methylethylketoneperoxide were used at high temperature and at room temperature as curing agents, respectively. For outer matrix, the ductile materials was prepared using epoxy resin based on diglycidylether of bisphenol-A. Polyoxypropylenediamine were used as a curing agent of ductile matrix.

Methodologies

Single Fiber Strength Measurement and Surface Treatment: About fifty specimens in the each gauge length were tested. The gauge lengths of testing specimens were 2, 5, 10, 20 and 100 mm. Test specimens were made by centering a single glass fiber on the middle of paper frame with each gauge length, then adhering the fiber using epoxy adhesives. Coupling agent was diluted in chosen solvent for 3 hours. The fibers were coated individually in a steel frame to ensure uniform coating on the fiber surface and to avoid the complications of neighboring fiber interactions in a tow.

Preparation of Specimens and Microdroplet Test: For the four glass fibers fixed at regular distances in steel frame, microdroplets were formed on the each fiber with a specially designed micro-needle. The sizes of microdroplets were measured individually using optical microscope, and the distribution of microdroplets were in the range of 50 to 700 μm . The number of microdroplets were about 50-60 EA. Microdroplet specimen was fixed by the microvise using the micrometer. The IFSS (τ) was calculated from the measured pull-out force using

following expression: $\tau = (F_d / \pi D_f L)$, where, D_f and L are fiber diameter and length of fiber embedded in the resin, respectively, and assumed from the linear relationship between pull-out force and embedded length of fiber. A relatively large scatter in the test data was observed mainly due to the testing parameters such as the position of the microdrop in the loading fixture.

Preparation of Dual Matrix Composite and Fragmentation Test: The glass fibers fixed in the steel frame were coated with unsaturated polyester. The average thickness of brittle layers were 80 to 100 μm (Fig. 1). This brittle layer was again embedded by the ductile epoxy in a dogbone mold. The modified fragmentation test was carried out to measure the number of brittle matrix fragments and to observe failure modes under specially designed strain machine. Load was applied up to the value beyond which no further increase of matrix fragments was observed. The saturated numbers of brittle matrix cracking obtained from at least six specimens were averaged for each for statistical analysis. For the effect of moisture exposure on the interfacial adhesion, specimens were immersed in distilled water at boiling temperature for 2.5 hrs. After equilibration of the specimens for 1 hr at room temperature, then the number of brittle fragments was measured and microfailure modes were observed.

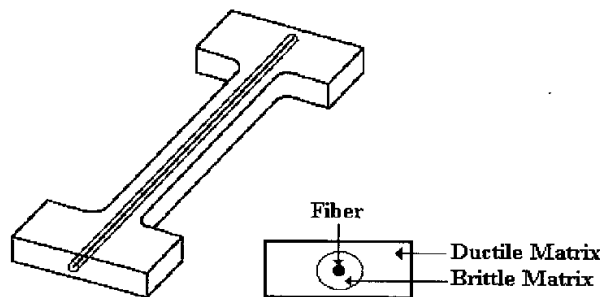


Fig. 1: Dimension of dogbone-shaped dual matrix specimen for modified fragmentation test.

Measurement of Acoustic Emission (AE): AE sensor was attached to the center of the specimen. AE signals were detected by a wideband type sensor with maximum sensitivity of -60 dB at 550 KHz. The sensor output was amplified by 60 dB at preamplifier then fed into an AE signal processing unit. Two AE parameters, peak amplitude and energy, were investigated for the time and the distribution analysis. Waveform analysis was carried out in the real time acquisition using digital oscilloscope (Fig. 2). Spectrum analysis of waveforms by fast Fourier transform (FFT) was used to analyze the characteristic frequency peaks.

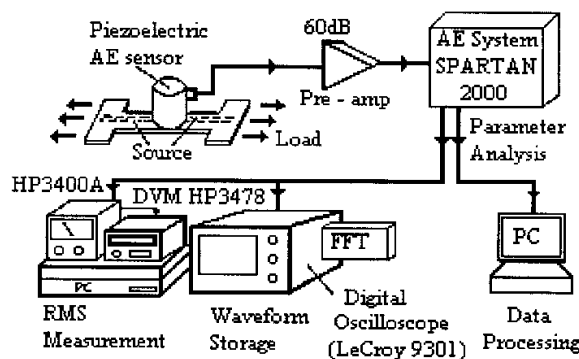


Fig. 2: Schematic illustration of AE system

RESULTS and DISCUSSION

Statistical Analysis of Tensile Strength of Fiber: Table 1 showed the tensile strength and elongation of single glass fiber depending on various gauge lengths. As the gauge length increases, tensile strength and elongation decrease as expected well from the flaw distribution.

Table 1: The dependence of tensile strength and elongation of glass fiber with diameter 14.7 μm on the gauge lengths.

Gauge length (mm)	No. of specimen (EA)	Diameter (μm)	Tensile strength (MPa)	Elongation (%)
2	38	14.7 (0.5)*	2338 (481)	7.7 (2.4)
5	40	14.4 (0.7)	1939 (360)	3.4 (1.2)
10	42	14.3 (0.6)	1774 (384)	3.2 (0.8)
20	41	14.4 (0.8)	1485 (377)	2.2 (0.6)
100	39	14.6 (0.4)	1022 (268)	1.2 (0.4)

* Standard deviation.

In Fig. 3, the glass fiber coated with amino-silane showed higher tensile strength values than the uncoated one. This might be due to the surface flaw healing effect by coated layer. Tensile strength decreased at higher concentration more than 2 wt%, because of the stress concentration at lump-shaped coating.

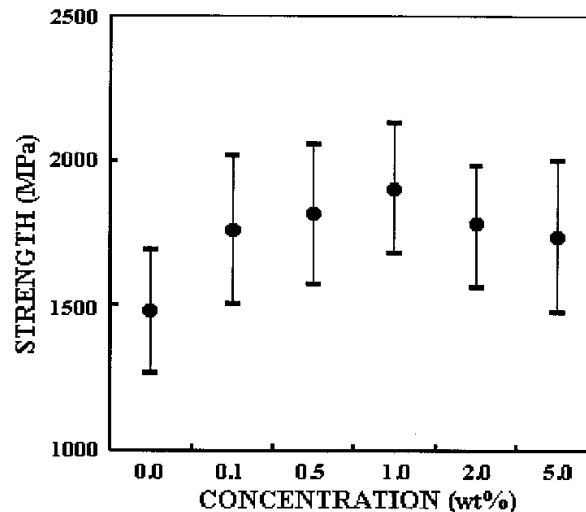


Fig. 3: Tensile strength of coated glass fiber with diameter of 30.3 μm as a function of the concentration of amino-silane coupling agent.

Interfacial Aspects by The Microdroplet and Modified Fragmentation Tests: Fig. 4 showed the embedded length *versus* pull-out force in the microdroplet test for both the amino-silane treated and the untreated one. Amino-silane treated specimens exhibited a higher pull-out force at same embedded length compared with the untreated ones. The higher the slope is, the higher the IFSS exhibits. A typical fiber pull-out from brittle unsaturated matrix during the microdroplet test is shown in Fig. 5.

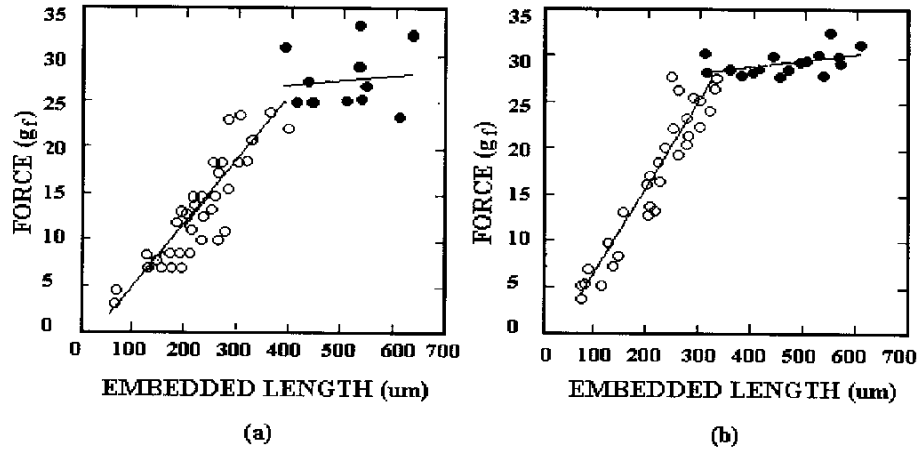


Fig. 4: Force versus embedded length curve in the microdroplet test on effective coupling agent: (a) the untreated; (b) the treated

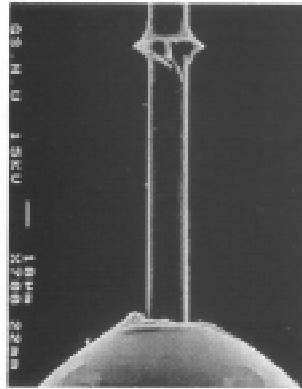


Fig. 5: Typical failure mode of glass fiber/unsaturated polyester microdroplet specimen after pulling-out

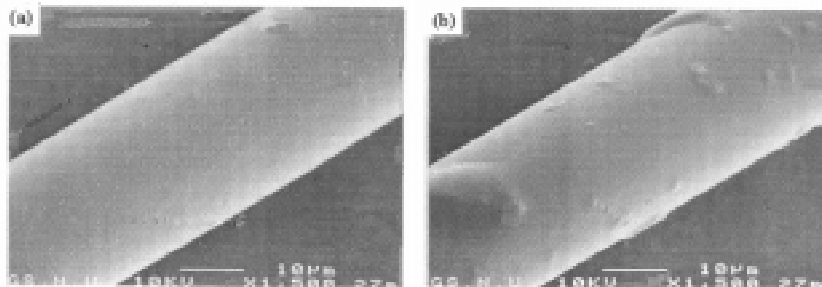


Fig. 6: SEM photographs of glass fiber surface: (a) silane treated on the glass fiber (0.5wt%, 1 min); (a) silane treated on the glass fiber (5wt%, 1 min)

Fig. 6: SEM photographs of glass fiber surface: (a) silane treated on the glass fiber (0.5wt%, 1 min); (a) silane treated on the glass fiber (5wt%, 1 min)

For uniform silane coating on a fiber surface, the silane concentration needed to be optimized. Surface morphology of fiber with coupling agent demonstrated that 0.5 wt% amino-silane solution was better than 5 wt% in the light of uniformity (Fig. 6). An uneven fiber surface at more than 5 wt% silane concentration could cause weak layer while combining with

unsaturated polyester matrix. Interfacial adhesion can be originating from chemical or physical bonding between two interphases in composites. For interphase I between the fiber surface and the silane, there can be the siloxane bonding (Si-O-Si) between an hydroxy group in glass fiber surface and silanol group in silane. And, for interphase II between silane and matrix, there can be a secondary H-bonding, covalent bonding, and physical adhesion by interdiffusion between polymer matrix and silane.

Table 2: The influence of various coupling agents on IFSS in the microdroplet test

Curing Agents	IFSS (MPa)	Improvements (%)
Untreated	12.4 (2.5)*	-
UP coating ¹⁾	16.8 (3.0)	35.9
VBAS ²⁾	15.1 (3.2)	22.0
A-174 ³⁾	14.6 (2.7)	17.5
APS	13.4 (1.6)	8.6
LiCA 38J	12.8 (1.7)	3.0

* Standard deviation.

* Optimized condition : 85 °C for 30 min.

1) Unsaturated polyester coating : UP 10 wt% styrene solution.

2) VBAS 0.5 wt% MtOH solution.

3) A-174 0.5 wt% aq. solution.

Table 3: The effect of various conditions on IFSS in the microdroplet test

Various conditions	Curing condition	IFSS (MPa)
Pot time	10 min	12.4 (2.5)*
	120 min	10.1 (2.6)
Diameter	14.7 μm	12.4 (2.5)
	30.3 μm	12.2 (2.0)
Resin type	Unsaturated polyester	12.4 (2.5)
	Epoxy	29.3 (4.9)

* Standard deviation.

* Curing condition : 85 °C for 30 min.

The effect of coupling agent on the IFSS and its improvement in the microdroplet test is given in Table 2. Polymeric coating yielded the highest improvement compared with other coupling agents because of the improved compatibility and wettability for the same kind of resin. Vinyl benzylamine silane also led to comparably high improvement. The effect of various experimental conditions such as pot time, diameter and different resins on the IFSS is shown in Table 3. The short pot time resulted in a low viscosity providing good wettability. The IFSS was high in short pot time case than the long stored case which yielded a poor wetting. Similar IFSS value was obtained in two glass fibers with very different diameters because of the same chemical composition. The brittle matrix fracture mode in the dual matrix composites was shown in Fig. 7. The treated one showed the better stress transfer through brittle matrix to fiber, and more brittle matrix fragments compared to the untreated case. The number of brittle matrix fragments under dry and wet conditions with various coupling agents were summarized in Fig. 8. The treated ones exhibited higher increment in the number of fragmentations under both dry and wet conditions.

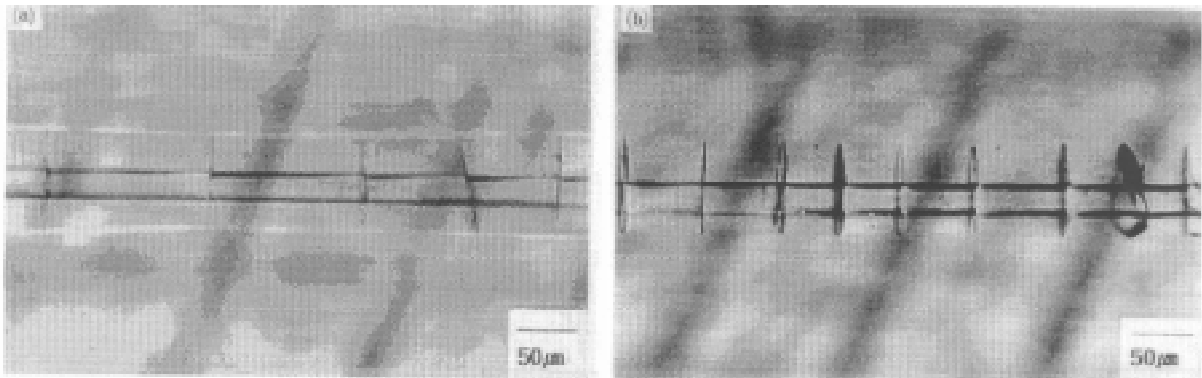


Fig. 7: Optical micrographs of brittle unsaturated polyester matrix fragmentations in dual matrix composites: (a) for the untreated; (b) for the treated without polarized-light

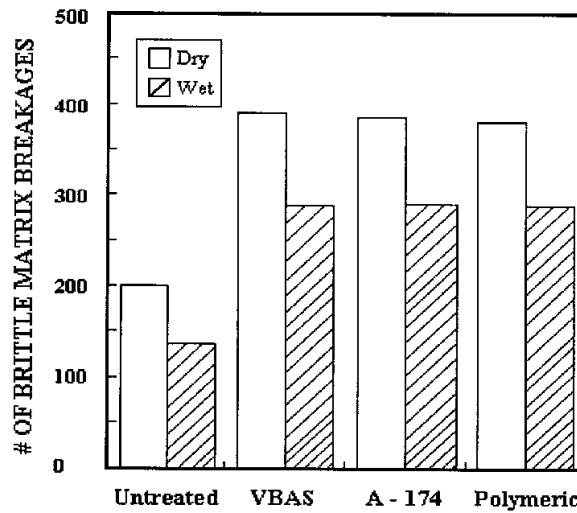


Fig. 8: Improvement % of the number of brittle matrix breakage using various coupling agents in the dual matrix composites under dry and wet conditions

Evaluation of The IFSS using Matrix Cracking Spacing: When a unidirectional, continuous fiber-reinforced composite is subjected to uniaxial tension, and if the fracture strain of the fiber is higher than that of matrix, then the first crack appears in the matrix. The crack is presumed to propagate through the matrix completely across the specimen normal to the fiber-stress axis, leaving the fibers bridging the crack.

According to the ACK model [3], once a crack forms in the matrix, the matrix region adjacent to the crack is relieved of stress and thus further cracking is inhibited. The strain in the matrix increases with distance from the crack planes at a rate determined by the maximum frictional shear stress that can be developed by the interface until it again reaches the matrix strain-to-failure at a distance X from the crack. Cracking proceeds with no increase in load until there are approximately cracks normal to the stress-fiber axis spaced between X and $2X$ apart. This crack spacing, however, can be only expected when we assume a deterministic failure stress of matrix, and a single-valued interfacial stress, as shown in Fig. 9a. The matrix crack spacing X is given by simple force balance, i.e., $2N \pi r_f \tau X = V_m \sigma_{mu}$ where N is the number of fiber per unit area, V_m the volume fraction of matrix, r_f fiber radius, σ_{mu} the stress at which the cracks begin to form, and τ is interfacial shear strength. Since $N = V_f / \pi r_f^2$ where V_f is the fiber volume fraction, X can be rewritten as follow:

$$X = \left(\frac{V_m}{V_f} \right) \left(\frac{\sigma_m r_f}{2 \tau} \right) \quad (1)$$

Eq. (1) was derived with assumption that IFSS is constant, independent of the distance from the crack surface, and the matrix has a single-valued failure stress. The equation offers a means by which the IFSS can be estimated from minimum matrix crack spacing, X , if the distribution of matrix crack spacing fall within a range X to $2X$. A deviation of crack spacing from the range of X to $2X$ has been explicitly described by Yang et. al. [4], using experimental evidence and computer simulation. Crack spacings were found to be distributed within X to $2X$ with mean value of $1.337X$ only if the Weibull modulus of matrix (m) is infinitely large.

Applying the ideal of matrix crack spacing to the model system with a brittle matrix adjacent to the single glass fiber, an IFSS can be estimated and compared with the value obtained from the direct fiber pull-out test. Multiple matrix cracking occurred in brittle matrix as shown in Fig. 9b where the fiber treated with coupling agent exhibited about one half narrower crack spacing compared to the untreated fiber system.

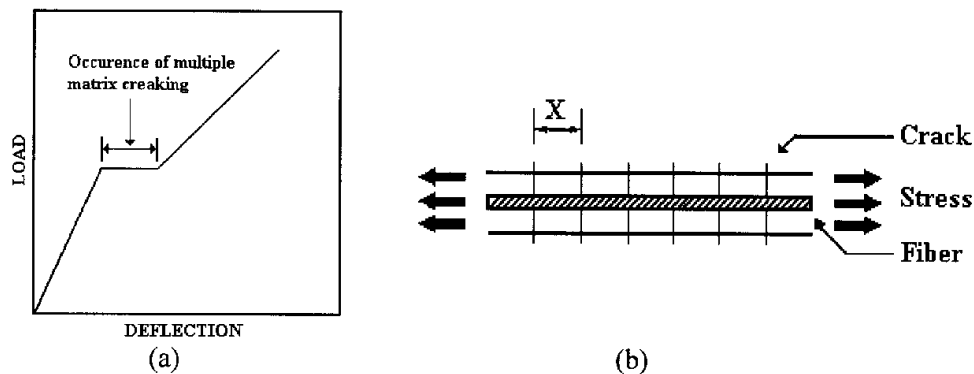


Fig. 9: Schematic of the occurrence of multiple matrix cracking ideal composite model during tensile test: (a) plot of load versus deflection; (b) composite model

Table 4: Interfacial shear strength evaluated using matrix crack spacing and matrix failure stress

Coupling Agents	Dry Condition				Wet Condition			
	No. of Matrix Cracks	Mean Crack Spacing (μm)	X (μm)	IFSS (MPa)	No. of Matrix Cracks	Mean Crack Spacing (μm)	X (μm)	IFSS (MPa)
Untreated	202.4 (19.2)	125.1 (19.2)	94.0 (8.3)	6.9 (0.7)	140.6 (9.4)*	181.4 (12.1)	135.6 (8.9)	4.8 (0.3)
Polymer	383.6 (45.0)	66.2 (6.9)	49.5 (5.1)	13.1 (1.5)	291.8 (29.6)	87.0 (7.9)	65.0 (5.9)	10.0 (1.0)
VBAS	392.2 (38.6)	64.8 (5.8)	48.5 (4.4)	13.4 (1.3)	289.0 (22.8)	87.9 (6.4)	65.7 (4.8)	9.9 (0.8)
A-174	385.2 (26.2)	65.9 (4.2)	49.3 (3.1)	13.1 (0.9)	290.6 (12.5)	87.6 (3.8)	65.5 (2.8)	9.9 (0.5)

* Standard deviation.

* Values of $V_f = 0.3$, $V_m = 0.7$, $\sigma_{mu} = 37$ MPa, $r_f = 15$ μm were used in eq. (1)

* Number of cracks within gauge length of 25.4 mm.

* Data obtained at least 6 sample were averaged.

From the configuration of a fiber with diameter of 30.3 μm and brittle matrix demonstrated in Fig. 9b, V_f of about 0.3 was obtained. The matrix failure stress σ_{mu} of 37 MPa was measured by tensile test of brittle matrix alone. For more valid value of X , the number of matrix crack within the gauge length of 25.4 mm were counted and averaged using at least 6 specimens for

each condition as given in Table 4. The system where the fiber treated with polymeric agent case yielded 383 cracks on average within 25.4 mm. Thus, average crack spacing is 66.3 μm . This in turn provides X value of 49.6 μm using the mean value of 1.337 X as suggested by Yang. Applying these data to the eq. (1), τ of 13 MPa for the polymer agent can be obtained. The IFSS of various systems evaluated using the same procedure were given in Table 4. A comparison of τ estimated from crack spacing with the value measured using fiber pull-out test shows that two values accord reasonably well while considering the standard deviation for the systems treated with various coupling agents, except the untreated.

Analysis of Acoustic Emission (AE): Fig. 10 showed the comparison of AE energy as a function of measuring time in three different specimens. In Fig. 10A and B, three groups were well separated in different ranges, whereas Fig. 10C showed only two distinct groups. Group (b) in Fig. 10A was the AE signals coming from brittle matrix cracking. The AE event numbers of group (b) in Fig. 10B were more than the number of Fig. 10A because of the effect of coupling agent.

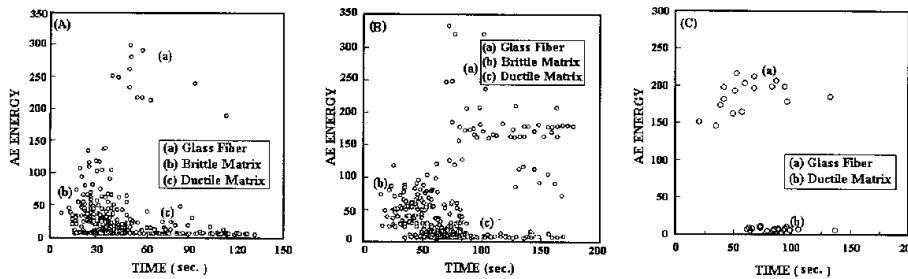


Fig. 10: Comparison of AE energy as a function of measuring time in three different specimens: (A) the untreated glass fiber/unsaturated polyester/epoxy; (B) the treated glass fiber/unsaturated polyester/epoxy; (C) the untreated glass fiber/epoxy specimen

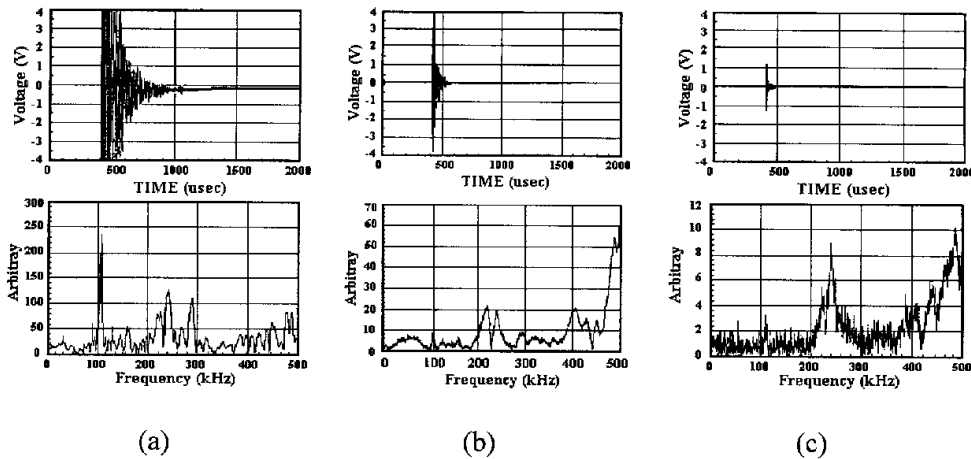


Fig. 11: AE waveforms from dual matrix specimen while straining and their fast Fourier transform (FFT) results: (a) fiber breakage; (b) brittle matrix cracking; (c) ductile matrix cracking

Fig. 11 showed typical AE waveforms generated during tensile testing and their fast Fourier transform (FFT) results. The fiber breakage caused very large AE signals compared to the signal from brittle or ductile matrix failures. The AE waveform coming from fiber breakage

was appeared at mainly about 100 KHz. The AE waveform from brittle matrix cracking was in the middle level and relatively small, whereas AE waveform from ductile matrix showed the smallest signal intensity among three failures. Characteristic peak of ductile matrix exhibited many noise signals due to low energy coming from ductile matrix fracture.

Brittle matrix fracture was observed microscopically and the subsequently accompanying AE events were observed. AE method can be correlated successfully with the modified fragmentation technique in predicting the interfacial adhesion and the failure modes. Especially, it also can be applied in the ceramic matrix composites (CMC) where are in brittle and nontransparent matrices.

CONCLUSIONS

Tensile strength and elongation decreased with increasing gauge length due to a size effect coming from heterogeneous distribution of internal or external flaws in the fiber. The silane coupling agent treated glass fiber showed higher fiber strength than those of the untreated ones because of flaw healing. High concentrated case, however, the fiber strength decreases at concentration more than 2 wt% due to the stress concentration occurred at the lumpy coating regions. In microdroplet test case, the IFSS was improved in the range of 20 to 35% when using silane coupling agents. This might be resulted from chemical and hydrogen bonding in two different interphases.

For modified fragmentation test, larger number of fragments occurred in brittle matrix layer were observed in the treated ones compared to the untreated composites under both dry and wet conditions. The relative interfacial adhesion can be obtained from the number of fragments in brittle layer. The IFSS obtained from model methods was consistent reasonably well with the experimental data predicted from pull-out test. There were three distinct AE distributions in dual matrix composites. AE waveforms and their FFT analysis provided the characteristic microfailure modes in the brittle layer cracking. Thus, AE method was useful in analyzing the interfacial and microfailure properties of the composites consisting of nontransparent matrices.

REFERENCES

1. Park, J. M., Subramanian, R. V. and Bayoumi, A. E., " Interfacial shear strength and durability improvement by silanes in single filament composite specimens of basalt fiber in brittle phenolic and isocyanate resins", *Journal of Adhesion Sci. Technol.*, Vol. 8, No. 2, 1994, pp. 133-150.
2. Favre, J. P. and Jacques, D., "Stress transfer by shear in carbon fibre model composites. Part 1. Results of single-fibre fragmentation tests with thermosetting resin", *Journal of Materials Science*, vol. 25, 1990, pp. 1373-1380.
3. Aveston, J., Cooper, G. A. and Kelly, A., *The properties of fiber composites, Single and multiple fracture*, IPC Sci. and Technol. Press, Guildford, U. K., 1971.
4. Yang, X. F. and Knowles, K. M., "The one-dimensional car parking problems and its application to the distribution of spacings between matrix cracks in unidirectional fiber-reinforced brittle materials", *Journal of Am. Ceram. Soc.*, Vol. 75, No. 1, 1992, pp. 141-147.

ACOUSTIC EMISSION INFLUENCE OF THE SIZING INTERPHASE ON THE STATIC AND DYNAMIC BEHAVIOR OF ADVANCED THERMOPLASTIC COMPOSITES

C. Mayer, M. Neitzel

*Institut für Verbundwerkstoffe GmbH, University of Kaiserslautern,
P.O.Box 3049, 67663 Kaiserslautern, Germany*

SUMMARY: In the present report, fabric reinforced thermoplastic composites based on different surface treatments were manufactured with a double belt press and examined by macromechanical evaluation using three-point bending and dynamic mechanical analysis (DMA). The influence of textile processing techniques on the composition of the coating either finish or direct sizing and thus on the mechanical property of thermoplastic composites was discussed. The application of direct sizings containing a lubricating and a coupling phase results in a reduced crosslinking density at the interfacial region due to diffusion and reaction of low molecular weight components such as lubricants and plasticizers evaporated at temperatures appropriate for thermoplastic processing.

KEYWORDS: Double belt press, fabric reinforced polyamide 6.6, finish, direct sizing, three-point bending, microscopy, dynamic mechanical analysis, energy dissipation

INTRODUCTION

Advancements in thermoplastic composites using textile reinforcements constituted a new class of composite intermediates. They can be described as tailored thermoplastic composites with UD or fabric reinforcements of glass, carbon or aramide fibers in quasi-isotropic or anisotropic arrangements to meet a variety of property and performance requirements in demanding environments. Compared with commonly available glass mat reinforced thermoplastics (GMT), they exhibit superior mechanical properties with respect to strength and stiffness. The selection of appropriate thermoplastics is another issue in customizing composite materials. Among suitable polymers are low-cost polymers (PP, ABS) as well as engineering thermoplastics (PA, PET). The manufacturing of such tailored intermediates is accomplished using a continuously running double belt press by the application of temperature, pressure and time. Afterwards, the semi-finished composite sheets can be postformed by automatized stamp-forming equipment into shell-type parts.

Besides the properties of reinforcement and matrix, the interaction of fibers and thermoplastic polymer at the interface has a strong impact on the physical behavior of composite materials. The quality of bonding at the fiber-matrix interface significantly influences the chemical performance in corrosive media, strength and toughness of composites. Therefore, an optimization of the fiber-matrix coupling with respect to both fiber wet-out and adhesion

between polymer and reinforcement is a primary requirement in manufacturing thermoplastic composites.

In numerous reports [1-3], the affinity of surface treatments on glass fibers to thermosets is well documented, whereas information on the compatibility of such interphase compositions with thermoplastic polymers barely exists [4]. Rovings with surface treatments appropriate for a number of thermoplastic polymers are commercially available. However, they are almost unsuitable for weaving purposes, since the fabrication of textile reinforcements makes specific demands on the quality of the reinforcing fibers. The aim of this report is therefore to investigate the affinity of distinct commercially available surface treatments to a thermoplastic matrix by macromechanical evaluation of samples manufactured with a double belt press.

SURFACE TREATMENTS IN TEXTILE MANUFACTURING

The fabrication of textile structures as advanced reinforcements in thermoplastic composites requires bundles of fibers either yarns or rovings to constitute a multidirectional structure. For textile fabrics or woven rovings, manufacturing is accomplished by weaving warp and weft on a loom to form a bidirectional cloth. Due to the high processing velocity, the fibers are subjected to heavy stress arising from frictional forces between the glass fibers and steel components of the loom. Hence, reduction of friction becomes a basic issue in weaving to avoid rupture of individual fibers and fluffing of the bundles and thus deterioration of the textile property.

Table 1: Comparison of finish and direct sizing

Fiber surface treatment	(i) Starch size - finish	(ii) Direct sizing
Advantages	High-speed weaving (600-900 y/min) Excellent coupling Designing of coupling agents for individual polymers	Preservation of fiber property One step manufacturing Flexible manufacturing
Disadvantages	Loss of tensile strength due to thermal treatment Additional processing step High quantity production required	Low-speed weaving (250 y/min) Size contains additional components affecting the coupling

The protection of individual fibers, textile processability and compatibility with the matrix is accomplished in two different ways: (i) A coating of size composed of starch, lubricants and cationic plasticizers is applied at the glass forming stage. For composites, the presence of these constituents negatively affects the bonding of polymer and fibers. Thus, the starch size is removed by thermal treatment at temperatures up to 600°C and substituted by coupling agents after desizing of the textile structure (finishing). The coupling agents either bifunctional silanes or chromium compounds form covalent oxane bonds or Van-der-Waals bonds with the hydroxyl groups on the glass surface and provide reactive groups to interact with the polymer [5]. (ii) A size consisting of a mixture of lubricants as well as coupling agents is applied to the glass fiber surface prior to the weaving at the glass forming stage to ensure both textile processability and fiber/matrix adhesion (direct sizing).

As listed in table 1, economical and technical benefits of two-step systems (starch size and finish) and direct sizing can be very distinct. Weaving of starch sized yarns is more efficient since the processing velocity is up to 3 times faster than that of yarns with direct sizing. However, the desizing procedure is costly and requires high quantity production to be efficient. Additionally, the thermal treatment at 600°C for a few seconds and subsequent exposure to temperatures up to 390°C for 72 hours to ensure desizing results in a loss of 10 to 15% in tensile strength of the fibers [6]. Table 2 exhibits the effect of reduced and preserved tensile strength respectively on the mechanical property of fabric reinforced epoxide and phenolic, where the number represents the change in mechanical property using direct sizing as surface treatment.

Table 2: Influence of surface treatment on mechanical property of fabric reinforced thermosets

Mechanical Property	Epoxide	Phenolic
US-style 7628, EC9-68, plain weave	Direct sizing (TD22) vs. finish (Z6040)	Direct sizing (TD22) vs. finish (A1100)
Tensile strength	+30%	+35%
Compression strength	+0%	+20%
Flexural strength	+24%	+28%
Shear strength	+30%	+30%

It is evident from above, that the deterioration of fibers due to the desizing procedure significantly affects the mechanical property of composites. Although textile reinforcements obtained from direct sized yarns exhibit superior mechanical property, the specific composition of this coating can be disadvantageous at elevated temperatures, since low molecular weight components such as lubricants and plasticizers start to evaporate at 150 to 200°C. This is not the case for finish-systems, where epoxide and amino silane based coupling agents are more durable at higher temperatures and components susceptible to volatilization were removed previously from the glass fiber surface.

Hence, it is assumed that manufacturing of thermoset and thermoplastic composites using direct sizings as surface treatments can be detrimental, since thermoplastic polymers require processing temperatures above 200°C. Components of the direct sizing may alter or deteriorate and thus negatively affect the interfacial bonding. For continuous manufacturing of engineering polymers such as polyamide processing temperatures exceed 250°C to melt the polymer and achieve viscosity low enough to percolate the fiber bundles. Therefore, investigation of the influence of pretreatment using finished textiles on the one hand and deterioration of the direct sizing at elevated temperatures on the other hand on the mechanical property of fabric reinforced thermoplastic composites becomes a necessity.

SAMPLE PREPARATION

A typical PA 6.6 matrix system, several commercial sizing systems and E-glass fabrics were selected as composite components for both microscopic observation as well as mechanical testing. The PA 6.6 matrix used in this study was supplied as 100 µm film by DuPont. E-glass yarn of 68 tex and 9 µm filament diameter was used to manufacture fabrics of 8 H satin weave US-style 7581 with 22 yarns/cm in warp and 21 yarns/cm in weft direction. Fabrics

were supplied with four commercial surface treatments either finish or direct sizing. Finished fabrics (A1100, Z6224) were manufactured by Hexcel, whereas yarns with direct sizing were provided by Vetrotex (TD22) and PPG (1383) respectively and woven by Verseidag. The coating content was 0.3 wt.-% for the finish and 0.8 wt.-% for the direct sizing. As far as known [7], the sizing composition as well as the product code and yarn supplier or weaver for each surface treatment used is listed in table 3.

Table 3: Surface treatments

Surface Treatment	Product Code	Type	Yarn Supplier/Weaver
Amino Silane	A 1100	Finish	Hexcel
Chloridfree Styrylamine Silane	Z 6224	Finish	Hexcel
Polyvinyle Acetate and Silane	TD 22	Direct Sizing	Vetrotex
Silane	1383	Direct Sizing	PPG

Thermoplastic composite intermediates were manufactured using the film-stacking technique where reinforcing fabric layers and thermoplastic films are combined alternately to a stack which is pulled continuously into the double belt press (see figure 1). Inside the press, sufficient pressure produced by a hydraulic system was imposed on the laminate. At the same time, appropriate temperature was applied in heating and cooling zones along the process direction to ensure: (i) melting of the polymer without thermal degradation, (ii) impregnation of the fabric and (iii) consolidation and downstream cooling of the laminate.

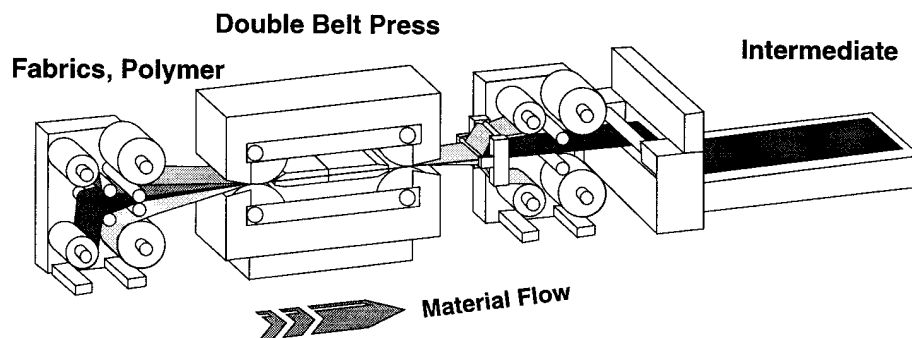


Fig. 1: Double belt press (DBP)

Using four layers of fabric style 7581 (296 g/m^2) and five layers of $100 \mu\text{m}$ PA 6.6 film laminates with a thickness of 1 mm and a fiber content of 50% by wt. were obtained.

EXPERIMENTALS

For a strong bonding of fibers and matrix to improve the mechanical property of composites two phenomenons have to be considered: (i) The work of adhesion is a strong function of the fiber wet-out and thus the real area of contact between reinforcement and polymer. Among other parameters, the difference in surface energy of polymer and fiber determines the degree and velocity of fiber wet-out during the impregnation process. Generally, the lower the surface energy of the liquid polymer compared with that of the solid fiber, the higher the

wettability of filaments. (ii) However, a perfect impregnation may result in a weak bonding of fibers and matrices since the degree of adhesion depends on the number and strength of couplings in the interphase.

Three-Point Bending

As a first approach to the compatibility of commercial sizings and PA 6.6, a three-point bending was performed. According to a novel testing method for thin thermoplastic composite samples developed by DuPont and the Institut für Verbundwerkstoffe GmbH, a span-to-depth ratio of 32:1 at a width of 25 mm was selected to evaluate the flexural property. The samples were subjected to a cross head speed of 1 mm/min. Flexural modulus was measured between a strain of 0.05 and 0.25% and strength was determined at flexural failure. As depicted in figure 2, the flexural property vary significantly.

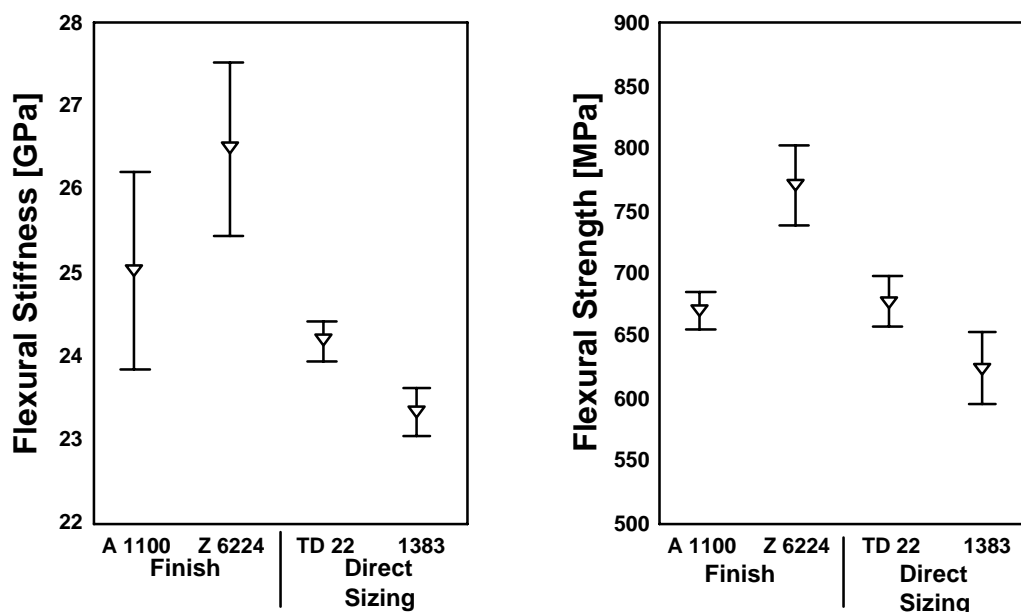


Fig. 2: Influence of surface treatment on flexural properties of fabric reinforced PA 6.6

Considering that the samples are only different by the surface treatment, this can be ascribed to: (i) the degree of impregnation, (ii) the strength of couplings in the interphase, (iii) alteration of the polymer in areas near the interphase or (iv) deterioration of the fibers due to desizing. The effect of the latter was discussed previously regarding thermoset composites. It is very interesting, that in combination with polyamide the mechanical performance of finished systems is better than that of direct sized systems. This is in opposite to the results obtained for thermoset composites where direct sized fabrics exhibited advancements by about 20 to 30%. Hence it must be assumed, that the composition of the sizings used have a much stronger impact on the mechanical property of fabric reinforced polyamide than the deterioration of fibers due to the desizing procedure.

To investigate the effect of the sizing on the compatibility of fiber and matrix, microscopic observation of polished cross-sections of as-molded samples and failure surface after flexural loading was performed.

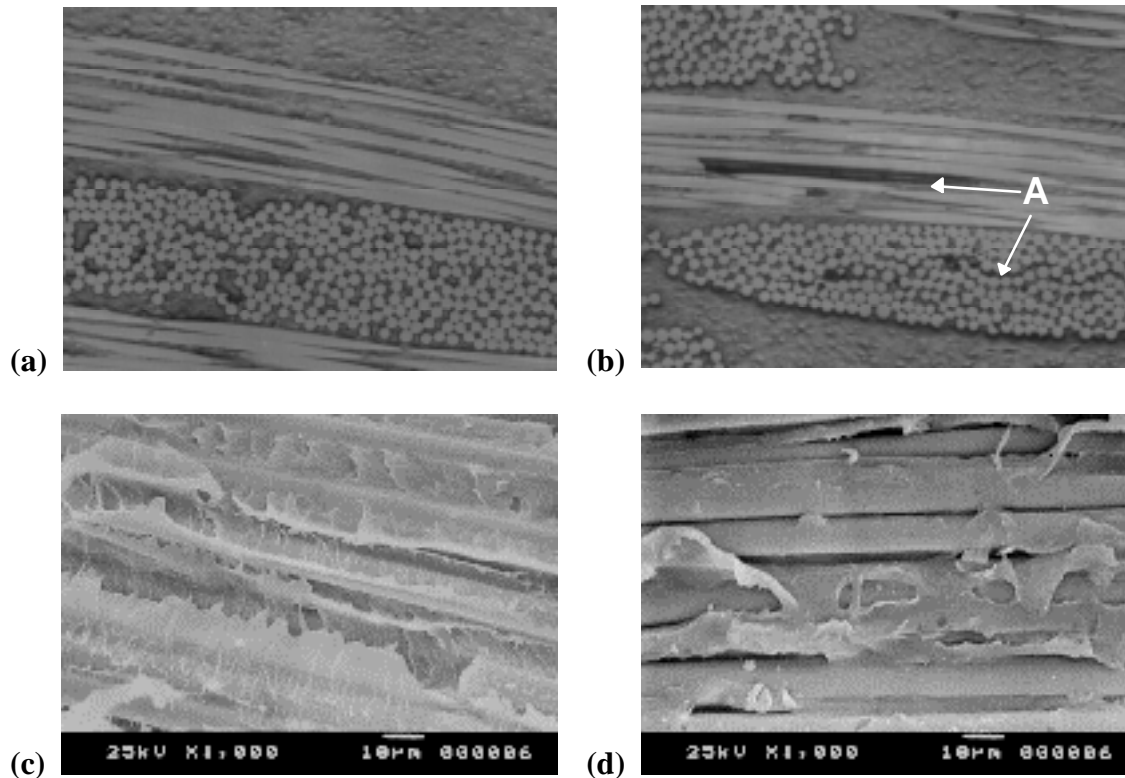


Fig. 3: Micrographs of fabric reinforced PA 6.6, showing cross-section of as-molded samples and corresponding failure surface of composites based on finish (a,c) and direct sizing (b,d). (A) displays a region of unimpregnated fibers.

Clearly from figure 3, the composition of the surface treatment as determined by the specific textile processing method plays a major role in impregnation and damage pattern of thermoplastic composites. The figures 3 (a) and (b) represent the worst case in impregnation behavior of the fabrics as a function of surface treatment. From a series of micrographs on the cross-sections of as-molded samples, direct sized yarns exhibited partial cracks in the center of fiber bundles as depicted in figure 3 (b) whereas finished fabrics tend to ensure better impregnation of the yarns as shown in figure 3 (a). Although it was difficult to distinguish the cross-sectional areas of samples different in surface coating by means of impregnation quality, it could be proved empirically that the specific composition of direct sizings penalizes polymer percolation into the yarns. Since finish and direct sizing are not only different by composition but also by weight content, the worse impregnation of direct sized yarns is either a result of low molecular weight components evaporating at 200°C or higher weight content of the coating. Looking at the failure surface via scanning electron microscopy as shown in figure 3 (c) and (d), the differences in using finished and direct sized fabrics are much more severe. Polyamide 6.6 in combination with A1100 or Z6224 exhibits cohesive failure of the polymer, whereas for both TD 22 and 1383 failure occurred at the interphase hence reflecting a change in the degree of adhesion. Accompanying above, it has to be considered that mainly the presence of gaseous evaporated components at temperatures above 200°C have a strong impact on the affinity of fibers and matrix, since the pure composition of coupling agents in finish-systems results in a fiber/matrix bonding stronger than the cohesive energy of the polymer. In contrast to microscopic evaluation of cross-sectional areas of as-molded samples, scanning electron microscopy on failed samples provided valuable insights into the damage pattern of fiber and matrix as a function of coating composition.

Dynamic Mechanical Analysis (DMA)

Among a number of techniques for interphase characterization [1], dynamic mechanical analysis provides a sensitive and nondestructive measure not only of the molecular structure and motion, phase morphology, filler addition and fiber orientation but also a detection of the interfacial region [8-11]. DMA is based on the measure of two types of response to a low-strain periodic deformation which are : (i) an elastic and (ii) a damping term. For viscoelastic materials lying between purely elastic and viscous materials, the elastic term ascribes to the fraction of deformation energy stored in the composite and thus stiffness, while the damping counts for the fraction of energy dissipated as heat. In a composite material consisting of essentially elastic fibers, a viscoelastic matrix and an interfacial region, some of the deformation energy is dissipated. Energy loss occurs either in the matrix or at the interface. Since the bulk property of the PA 6.6 matrix used remains unaffected by the processing conditions, the change in damping can mainly be ascribed to the interfacial region. Hence, a composite material with poor interfacial bonding tends to dissipate more energy than a comparable composite with good coupling of fibers and matrix. Losses in energy are determined by the complex modulus $E^* = E' + iE''$ and a mechanical loss factor $\tan\delta = E''/E'$ where E' and E'' are the storage and loss modulus, respectively. Thus any increase in damping and hence increase of molecular motion and decrease in strength of the fiber/matrix bonding is reflected by an increase in $\tan\delta$ and E'' .

Samples were subjected to a force-controlled periodic flexural loading and the complex modulus and $\tan\delta$ were measured in a dynamic mechanical thermoanalyzer, Eplexor 150N. The viscoelastic property were scanned for a temperature range from -50°C to 220°C at a heating rate of 1 K/min and 10 Hz. A static load of 40 N in combination with a dynamic load of 20 N was used to stress the composites. In figure 4 the progression of E^* and $\tan\delta$ of fabric reinforced polyamide 6.6 with surface treatments of A1100, Z6224, TD22 and 1383 is depicted as a function of temperature.

Similar to the results obtained from static flexural loading, the complex modulus E^* is considerably influenced by the surface treatment. Additionally, the course of E^* vs. temperature provides some interesting data about the flexural behavior above glass transition temperature in entropy-elastic conditions in the vicinity of the melting temperature of PA 6.6 ($T_m = 260^\circ\text{C}$). Clearly from the figure, composites based on TD22 and 1383 sized glass fibers start to fail at temperatures beyond approx. 180°C whereas the finished-systems of A1100 and Z6224 reveal a well developed plateau between T_g and 220°C .

The normalized energy dissipation $\tan\delta$ also reflects differences in the interfacial bond strength. As the figure indicates, a pronounced peak of $\tan\delta$ at approx. 50°C can be resolved thus representing a glass transition temperature. Since glass fibers do not exhibit any T_g peak below 200°C , any peak of T_g can be attributed to the coating on the glass fibers and the polymer.

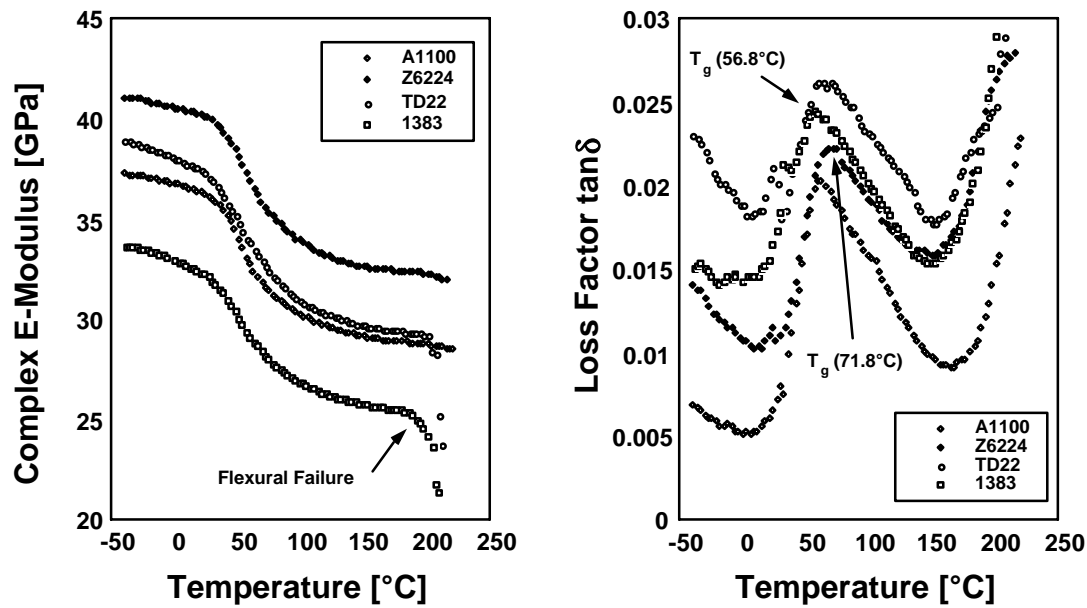


Fig. 4: Complex flexural modulus and $\tan\delta$ of fabric reinforced PA 6.6 as a function of surface treatment and temperature (static load: 40 N, dynamic load: 20 N, frequency: 10 Hz, warp direction)

Comparing the $\tan\delta$ spectra of figure 4, the degree of energy loss below and above T_g and the value of T_g may be related to the morphology of the polymer in the vicinity of the glass fiber and the relaxation behavior of the interphase. In connection with the microscopic observations on failed samples it becomes obvious, that the influence of low molecular weight constituents upon the composite property can be fairly serious. Several authors have published widely on the effect, that unreactive organic groups such as lubricants and plasticizers diffuse during the impregnation process to form an interphase with many unrestrained or free end groups, reducing the crosslinking density in the interfacial region [2,9,10]. This plasticized region of enhanced mobility of macromolecular chains then is a source of increased internal friction but reduced interfacial bond strength as it can be observed from direct sized systems (TD22, 1383). For composites based on A1100 surface treatment, a reduced $\tan\delta$ and peak amplitude indicates an improved fiber/matrix interaction. Additionally, the introduction of Z6224 results in an increased transition temperature (71.8°C) due to an increased rigidity of the interfacial zone. However, it should be emphasized, that the degree of viscoelasticity may alter from energy-elastic to entropy-elastic conditions as depicted by Z6224, where the energy loss of high modulus chloridefree styrylamine silane above T_g coincides with the damping behavior of low modulus 1383. The distinct mobility of chains above glass transition temperature suggests a difference in the ratio of covalent and hydrogen bonds for individual samples since the interfacial strength in entropy-elastic conditions is determined by the presence of covalent bonds.

CONCLUSION

The application of glass fibers for weaving purposes exhibits few characteristics which are distinct from those of reinforcing fibers used in filament winding, injection molding or pultrusion. For textile processability and compatibility with the polymer different techniques and thus specific compositions of the surface coating are employed to ensure both protection of the fibers during weaving and efficient coupling of fibers and matrix. It has been demonstrated, that the affinity of commercial surface treatments in fabrics to thermoplastic polymers can be very distinct and even contrary to the phenomenons observed among thermoset composites. For textile manufacturing a lubricating is required to protect the fibers from abrasion. However, such components start to evaporate at temperatures beyond 150 to 200°C. Since direct sizings are composed of a lubricating and a coupling phase, the temperature range required to process thermoplastic polymers penalizes the degree of crosslinking at the interfacial region due to diffusion and reaction of volatile constituents. The system of starch size and finish provides a pure lubricating composition in the weaving stage and a pure coupling composition in the composite manufacturing stage and thus excellent bonding if coupling agents are compatible with the polymer. However, this technique is limited to fabrics with a weight to area ratio below 400 g/m². Additionally, the desizing at elevated temperatures (600°C) deteriorates the fibers and provides a costly additional step. Although the utilized surface treatments are only recommended for thermoset systems, some conclusions on the composition of appropriate direct sizings for fabric reinforced thermoplastic composites can serve as guidelines to enhance the fiber/matrix bonding. In summary, the following conclusion have been made to benefit from the technique of direct sizings: (i) The content of components susceptible to volatilization at temperatures above 200°C must be reduced to such an extend where textile processability of the yarns is just ensured and thus effects on the interfacial property are minimized. (ii) Heat stabilization of lubricants in combination with (i) could further improve the interfacial bonding. (iii) Bifunctional groups either lubricants at room temperature and coupling agents at elevated temperature could diminish the problems of two-phase surface treatments.

ACKNOWLEDGMENT

The authors gratefully acknowledge the financial support of the Bundesministerium für Bildung und Forschung BMBF (Continuous Manufacturing of Tailored Textile Reinforced Thermoplastic Composites; 03N 3008)

REFERENCES

1. Dwight, D.W., Wu, H.F., "Interphase Structure-Property Relationships in Polymer Matrix Composites", Polymer Preprints, 1995, Vol. 36, No. 1, pp. 809-810
2. Lacrampe, V., Pascault, J.P., Gérard, J.F., "Physico-Chemical Characterization of Interphases created from Sizings in Glass Fibers-Dased Epoxy Composites", Polymer Preprints, 1995, Vol. 36, No. 1, pp. 813-814

3. Drown, E.K., Drzal, L.T., "Characterization of the Sizing Interphase and its Influence on the Behavior of Glass-Fiber Reinforced Epoxy Composites", Proceedings Annual Technical Conference of the Society of Plastic Engineers, 1992, pp. 239-242
4. Cinquin, J., Chabert, B., Chauchard, J., Morel, E., Trotignon, J., P., "Characterization of a Thermoplastic (PA 66) Reinforced With Unidirectional Glass Fibres, Matrix Additives and Fibre Surface Treatment Influence on the Mechanical and Viscoelastic Properties", Composites, 1990, Vol. 21, No. 2, pp. 141-147
5. Plueddemann, E., P.: Silane Coupling Agents, New York, 1982
6. Kerbrat, A., Lackmann, C., "Glasfilament-Garne mit matrixorientierten Schichten - neue Alternativen für textile Struktur-Composites", Proceedings Techtexil Symposium, Frankfurt/Main, 1993, Presentation-No. 322
7. Product Information Hexcel, Vetrotex, PPG
8. Schledjewski R., Karger-Kocsis, J.: Dynamic Mechanical Analysis of Glass Mat-reinforced Polypropylene (GMT-PP), in: Journal of Thermoplastic Composite Material, 1994, Vol. 7, S. 270-277
9. Chua, P.S., "Dynamic Mechanical Analysis Studies of the Interphase", Polymer Composites, 1987, Vol. 8, No. 5, pp. 308-313
10. Kennedy J.M., Edie, D.D., Banerjee, A., Cano, R.J., "Characterization of interfacial Bond Strength by Dynamic Analysis", Journal of Composite Materials, 1992, Vol. 26, No. 6, pp. 869-882
11. Harris, B., Braddel, O.G., Almond, D.P., Lefebvre, C., Verbist, J., "Study of Carbon Fibre Surface Treatments by Dynamic Mechanical Analysis", Journal of Material Science, 1993, Vol. 28, pp. 3353-3366

INTERFACE MOLECULAR ENGINEERING OF CARBON FIBRE COMPOSITES

D. Tripathi, A. Kettle, N. Lopattananon, A. Beck, F. R. Jones

*Dept. of Engineering Materials, The University of Sheffield
Sir Robert Hadfield Building, Mappin Street
Sheffield S1 3JD, UK.*

SUMMARY : The mechanism of adhesion of carbon fibres to epoxy and related resins results from a complex interaction of chemical functionality, microporosity and active sites at the fibre/matrix interface. The lack of an unambiguous test for the quantification of adhesion and the means of distinguishing between the roles of different adhesion mechanisms have led to much confusion. This paper reports the controlled functionalisation of untreated Type-A carbon fibres by plasma polymerisation for the evaluation of the Cumulative Stress Transfer Function (CSTF) as a measure of adhesion. Coatings prepared by the homopolymerisation of hexane and that of the octadiene are strongly hydrocarbon in nature and inhibit chemical interaction between the fibre and matrix resulting in poorer adhesion than the parent untreated fibres. The introduction of comonomers, acrylic acid, allyl alcohol and allylamine individually to the plasma feed resulted in increased levels of specific fibre surface functionalities and improvements in the degree of adhesion.

KEYWORDS: Fragmentation test, adhesion mechanisms, plasma polymerisation, CSTF methodology, Kelly-Tyson model, X-ray photoelectron spectroscopy.

INTRODUCTION

Carbon fibre reinforced composites are one of the most important composite materials and are used in a wide range of applications. The behaviour and performance of a composite material cannot be explained only in terms of the specific properties of its constituents [1]. The interphase region between the fibre and matrix is also a component which governs the mechanical and physical performance in composite systems [2].

The single fibre fragmentation test is currently considered a good method to evaluate the fibre/matrix interfacial properties because it provides simplified access to the complex phenomena that occur during composite failure, good reproducibility and simple specimen preparation. The test is particularly well suited for a study of the effects of different surface treatments or sizing on the interfacial shear strength [3-6]. In the test, a single fibre is embedded into a matrix, and a tensile stress is applied uniaxially along the fibre axis which when transferred to the fibre through the interface causes the fibre to fracture. The fibre continues to fracture into shorter lengths as the load increases, until the fragment length becomes too short to break. This situation is defined as the saturation in the fibre fragmentation process. The shortest fragment length which can break on application of stress is defined as the critical fibre length, l_c . Because of the statistical nature of fibre strength, a

single fibre does not break into the fragments of equal size and a wide variation in fragment lengths is observed. The fragment lengths for transparent matrix composites can be measured using a conventional optical microscope.

Models for Estimating Interfacial Shear Strength (IFSS)

The Kelly-Tyson model

The model first described by Kelly and Tyson is generally used to estimate IFSS from the fragmentation test and is based on a force balance [7]. It has been widely assumed that at saturation all of the fragments are debonded or nearby matrix has yielded to provide for a constant shear at the interface. The following analysis can be employed:

$$\tau = \frac{\sigma_{fu} d}{2 l_c} \quad (1)$$

Where d is the fibre diameter and σ_{fu} is the fibre strength at a length equal to the critical fibre length l_c . Early work by Ohsawa et al (1978) provided the background for the semi-empirical analysis of the test-data [8]. The critical fibre length is calculated by

$$l_c = \frac{4}{3} \bar{l} \quad (2)$$

Where \bar{l} is the average fragment length.

The fragmentation test is a very complex single embedded fibre test and several micromechanical phenomena observed in the real life composites other than fibre fracture are also observed during the fragmentation test. Shear yielding of the matrix, interfacial debonding and transverse matrix cracking have been widely reported [9,10]. In fact, the occurrence of these damage events during the fragmentation test makes the conventional data reduction technique based on the Kelly-Tyson model invalid. The limitations of the Kelly-Tyson model as well as other data reduction techniques for the fragmentation test based on the constant shear model have been the subject of several studies [9-13]. At this point, it will suffice to say that the use of the Kelly-Tyson model to calculate interfacial shear strength from the fragmentation test data is highly inaccurate.

The Cumulative Stress Transfer Function

A recently proposed data reduction technique for the fragmentation test, the cumulative stress transfer function (CSTF) technique, assumes that the quality of the interphase is dependent upon the number and length of individual fibre-fragments and that the greater stress is transferred to the embedded reinforcing fibre for the case of a good interphase in comparison to a poor interphase [14]. In this approach, the shear stress at the fibre-matrix interface associated with a fibre-fragment is calculated from the plasticity effect model and converted into a tensile stress using the balance of force argument [15]. A resultant tensile stress profile in the fibre fragment is integrated over the fragment length to estimate the stress transfer function (STF). The value of the tensile stress transferred is summed across all the fibre fragments and normalised to the total length of the fragments. This normalised value is called cumulative stress transfer function or CSTF [14] and can be defined as:

$$CSTF = \frac{\sum_{i=1}^{i=N} \int_0^{L_i} \sigma_f(x) dx}{\sum_{i=1}^{i=N} L_i} \quad (3)$$

Tripathi et al [14] have demonstrated that the values of CSTF obtained from the fragmentation test agree well with the fibre surface chemistry. For example, the CSTF value of water-sized, A1100 coupled glass fibre embedded in the epoxy resin is higher than that of water-sized, uncoupled glass fibre embedded in the same resin. In contrast to this, the interfacial shear strength, obtained from the Kelly and Tyson analysis fails to explain the influence of the glass fibre treatment and, furthermore, exceeds the shear yield strength of the matrix [16].

In this study, radio frequency induced plasma copolymerisation of acrylic acid/hexane, allyl alcohol/hexane and allylamine/octadiene gas mixtures is used to obtain a range of functionalised coatings on Type A carbon fibre surfaces. Analysis and quantification of the surface groups was determined by XPS. The single fibre fragmentation test has been employed to establish the relationship between the chemical composition of the fibre surface and the adhesion of the modified fibres to an epoxy resin. The degree of adhesion has been estimated from the Kelly-Tyson model and CSTF methodology for the single fibre fragmentation test.

EXPERIMENTAL

Fibres and Surface Treatments

Type A carbon fibres were supplied in an untreated unsized form (HTA-500) by Tenax Fibres GmbH. This is a high performance carbon fibre manufactured from a polyacrylonitrile (PAN) precursor, with high strength and standard modulus similar to the more familiar Toray T300. The 7 µm fibres are supplied as 500 filament tows, with reported values of the tensile modulus and strength of 238 GPa and 3.4 GPa respectively.

Coatings have been prepared by the direct copolymerisation of acrylic acid/hexane, allyl alcohol/hexane and allylamine 1,7-octadiene onto the untreated fibre [17]. Details of the plasma parameters are given in Table 2. The proportions of the respective monomer gases in the plasma feed were altered by varying the molar percentage of the hydrocarbon monomer, whilst maintaining a constant level of overall flow rate. This was done to deposit coherent polymer layers with variable degrees of functionalisation. The carbon fibres were then mounted individually within the plasma apparatus to ensure coating homogeneity. The details of the plasma apparatus and the polymerisation process are given elsewhere [17]. The fibre surface chemistry has been achieved by using X-ray photoelectron spectroscopy (XPS) [17].

Matrix Resin

The resin matrix has a combination of Epikote 828 (Shell Plc) with Araldite GY298 (Ciba Geigy Plc) in the ratio of 63 to 37 phr respectively. Epikote 828 is a diglycidyl ether of Bisphenol-A and Araldite GY298 is a blend of long chain aliphatic epoxy resin and Bisphenol-A. This was cured with 80 phr nadic methyl anhydride (Stag Polymers and Sealants) and 40 phr Capcure 3-800 (Henkel-Napco), a mercaptan terminated polymer. The

epoxy resin was cured at 80°C for 4 h, post-cured at 130°C for 3 h and left in the oven for natural cooling. The cured resin has an elastic modulus of 3 GPa and a tensile yield strength of 55 MPa. The shear yield strength of the resin, 32 MPa, was calculated from the measured tensile yield strength using the von Mises relationship. The details of the fragmentation test procedure and data reduction technique based on the constant shear model are given elsewhere [16,18,19]. The samples were strained to 10% applied strain. It has already been reported that carbon fibres in this matrix achieve saturation in the fragmentation process early on (typically at 5% applied strain) in the fragmentation test [6]. The mechanical properties of the resin ensure that saturation is reached [20]. At the end of the fragmentation test, the fragment lengths and debond ratios were measured using a microscope fitted with calibrated eye-piece to estimate the level of adhesion between carbon fibre and matrix of each specimen.

Table 1: Summary of coatings and plasma parameters.

Monomer mixture	Total flow rate (cm ³ (STP)min ⁻¹)	Plasma power (W)	Polymerisation time (min)
acrylic acid-hexane	1	10	10
allyl alcohol-hexane	2	1	20
allylamine-octadiene	2	2.5	10

RESULTS

The surface chemistry and morphology of carbon fibres are very complex with a mixed functionality and microporous structure [21]. The thin conformal nature of the plasma polymer deposit provides a technique for occluding the residual chemistry and structure of the as-manufactured fibres [17]. Thereby, any functionality incorporated into the film can be considered to provide the principal adhesion mechanism. The functional group concentrations obtained by XPS from the deconvolution of the C_{1s} peak are given in Table 2. The analysis shows that the thickness of the coating approximates to the XPS analysis depth (5nm) and that analysis refers percentage of surface carbon identified with that functional group. It can be seen from Table 2 that the different monomers can be used to provide specific surface functionalities on the carbon fibre surface of different concentration. Monomer feeds containing acrylic acid leads to a specific concentration of the carboxylic functionality; allyl alcohol, the hydroxyl functionality and allylamine, the amine functionality. The fraction of carbon which is assigned to a specific surface functionality decreases as the quantity of the hydrocarbon monomer is increased in the monomer feed (Fig. 1.). The CSTF and apparent interfacial shear strength values (τ_a) obtained from the fragmentation of these fibres are reported in Table 2 and are plotted as a function of fibre surface functionality in Figs. 2 and 3.

During fragment length determination, the mode of micromechanical fracture was noted and included in Table 2. Four different types of damage events in the fragmentation test specimens were observed at saturation viz. complete debonding (CD), partial debonding (PD), transverse matrix cracking (TMC) and mixed mode (MM) where transverse matrix cracking and interfacial debonding co-existed (Fig. 4.). The stress transfer across the interface in the case of complete debonding was very poor. Hence the contrast given by the polarised light was minimal which is obvious from the figure. However, stick and slip mechanism at the interface was observed which was obvious from the subtle colour difference at the fibre-matrix interface. The fibre breaks are marked on the photograph.

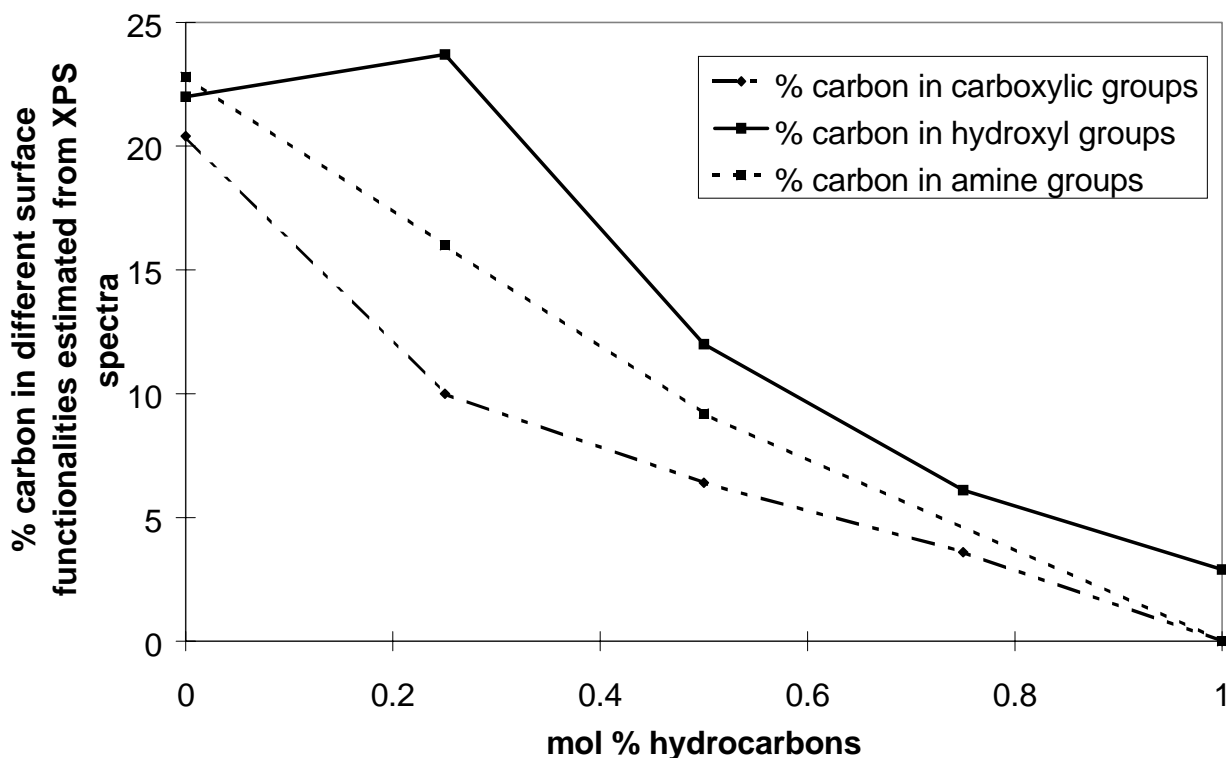


Fig. 1. Variation of the fraction of carbon assigned to specific surface functionalities as estimated from the C_{1s} peak in the XPS spectra as a function of the molar percentage of the hydrocarbon comonomer in the plasma feed.

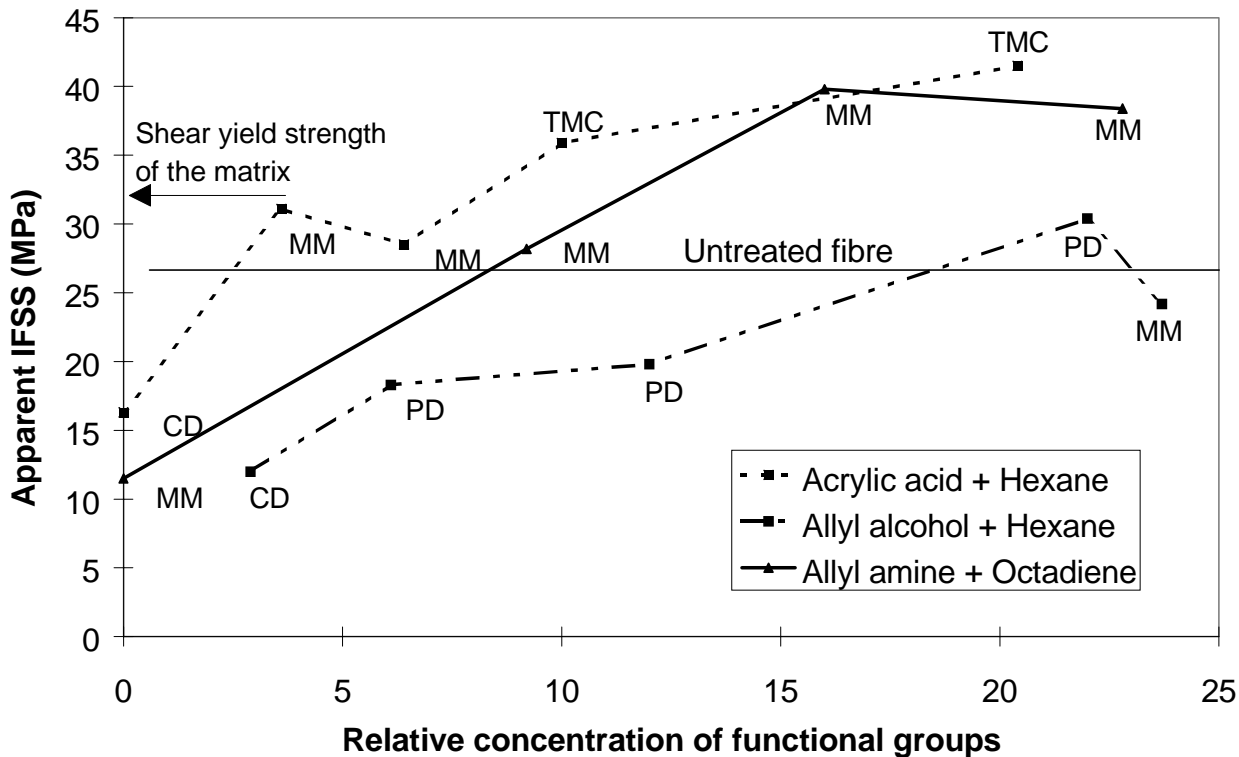


Fig. 2. Variation of apparent IFSS value as a function of the fraction of surface carbon contained in defined functional groups, deposited using a radio-frequency induced plasma polymerisation with different monomer feeds. CD, PD, MM and TMC represent fracture modes in the fragmentation test specimen (see Fig. 4.).

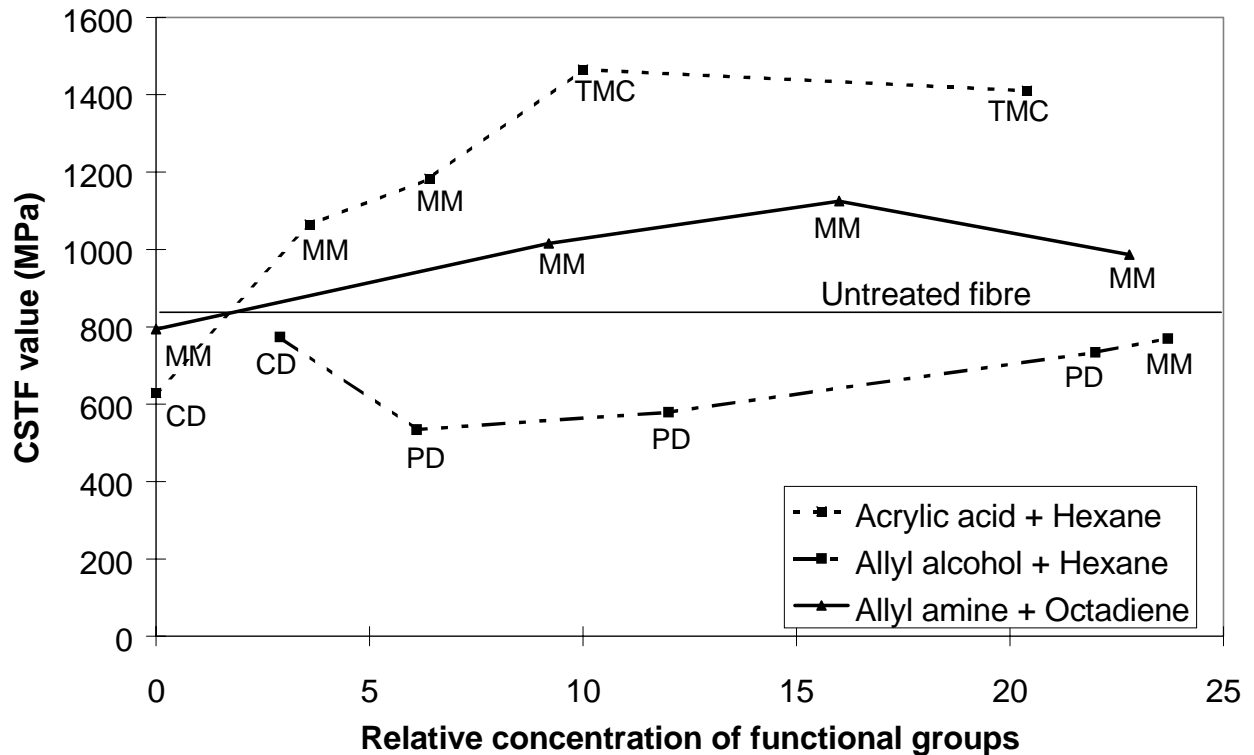


Fig. 3. Variation of CSTF value as a function of the fraction of surface carbon contained in defined functional groups, deposited using a radio-frequency induced plasma polymerisation with different monomer feeds. CD, PD, MM and TMC represent fracture modes in the fragmentation test specimen (see Fig. 4.).

Table 2 The values of apparent IFSS and CSTF as a function of the fraction of surface carbon contained in defined functional groups deposited in a plasma polymerisation. CD, MM, PD and TMC represent fracture modes in the fragmentation test specimen (see Fig. 4.).

Monomer Composition	Hydro-carbon (mol %)	Surface functionality (%)					Apparent IFSS (MPa)	CSTF (MPa)	Mode of failure
		C-CO ₂ R	C-CNR ₂	C-OR	C=O	C-H			
Untreated	-					92.1	26.9±6.0	1053	PD
Acrylic Acid + Hexane (10W)	0	20.4	-	16.2	10.9	52.5	41.5±7.5	1410	TMC
	0.25	10.0	-	15.7	8.9	65.4	35.9±6.4	1465	TMC
	0.50	6.4	-	14.6	5.8	73.2	28.5±5.1	1183	MM
	0.75	3.6	-	11.0	3.8	81.6	31.1±5.6	1064	MM
	1.00	0	-	4.9	0	95.1	16.3±2.9	629	CD
Allyl-Alcohol + Hexane (1W)	0	2.5	-	22.0	6.6	68.9	30.4±5.4	734	MM
	0.25	1.5	-	23.7	5.9	68.9	24.2±4.3	770	PD
	0.50	-	-	12.0	2.6	85.4	19.8±3.5	579	PD
	0.75	-	-	6.1	-	93.9	18.3±3.3	534	PD
	1.00	-	-	2.9	-	97.1	12.0±2.2	774	CD
Allyl-Amine + Octadiene (2.5W)	0	-	22.8	-	3.6	73.5	38.4±6.9	987	MM
	0.25	-	16.0	-	2.5	82.3	39.8±7.1	1125	MM
	0.50	-	9.2	-	0.9	89.9	28.2±5.0	1015	MM
	1.00	-	-	3.5	-	96.8	11.5±2.0	794	MM

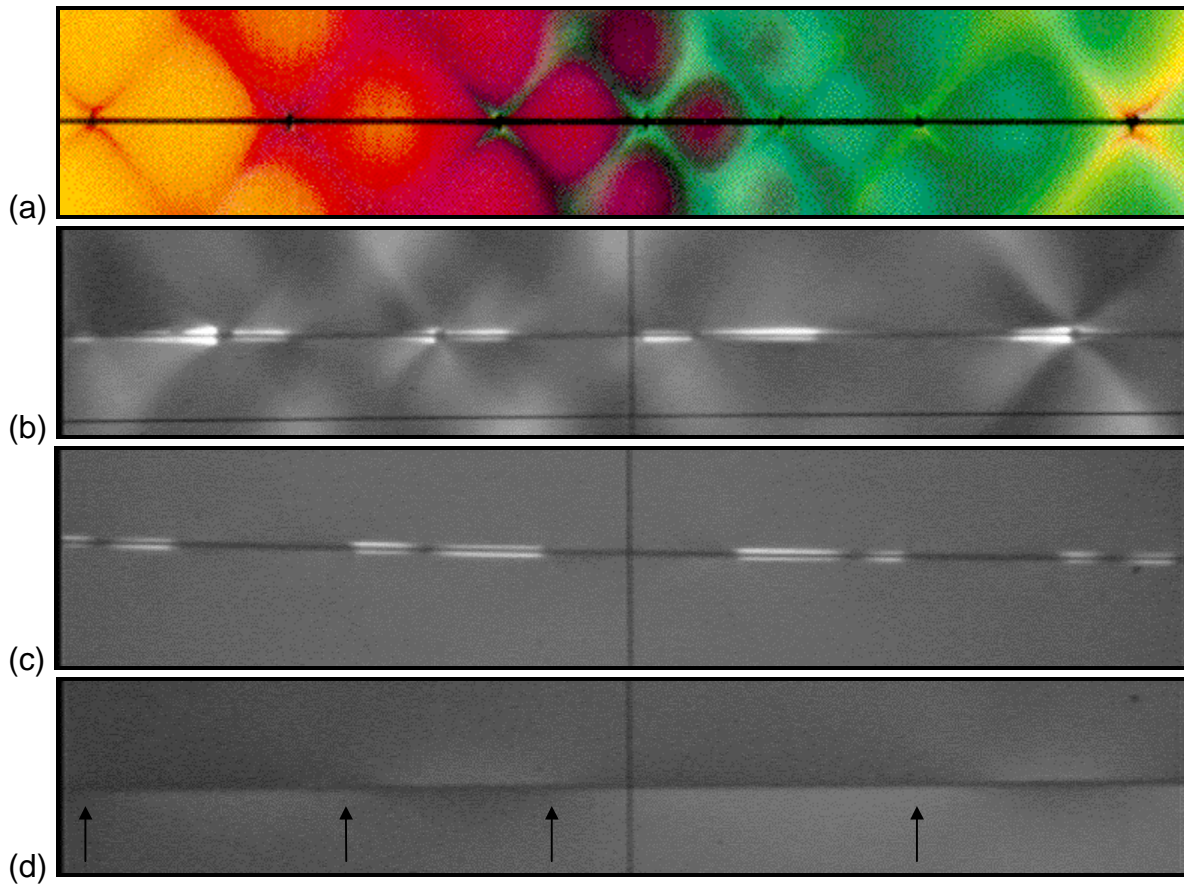


Fig. 4: The different modes of micromechanical failure observed at saturation in the fragmentation test; (a) Transverse matrix cracking (TMC), (b) Mixed mode which including transverse matrix cracking and partial debonding (MM), (c) partial interfacial debonding (PD) and (d) complete interfacial debonding (CD). Fibre breaks are shown by arrows.

DISCUSSION

It can be seen from Table 2 that the untreated unsized carbon fibre has an interfacial shear strength value of 26.9 MPa and CSTF value of 1053 MPa. Deposition of a non-functional plasma polymer coating (hexane or octadiene) onto the untreated, unsized Type A carbon fibres reduces the value of CSTF and apparent IFSS. This confirms that the residual chemistry and microstructure on the surface of the as-received fibres provide a degree of bonding to epoxy resins. However, the residual chemistry and the morphology of the as-received carbon fibre is masked by the thin coating deposited using the plasma polymerisation technique which is evident from the reduction in CSTF and apparent IFSS values on deposition of non-functional coatings. Introduction of functional monomers (acrylic acid, allyl alcohol or allyl alcohol) in the monomer feed causes an increase in values of CSTF and apparent IFSS corresponding to an improvement in interfacial adhesion of the single fibre to the epoxy resin with increasing concentration of specific surface functionalities is shown in Figs. 2 and 3.

It can be seen from Figs. 2 and 3 that an increased concentration of carboxylic and amine functionalities in the plasma polymer coating results in an increased degree of adhesion between fibre and epoxy resin matrix. This is attributable to an increased probability of covalent bond formation from the reaction of surface functionalities with the epoxide group in

the resin. It can be seen that although both data analysis methodologies (CSTF and Kelly-Tyson) show the same general trends, there are some differences. For example, the apparent interfacial shear strength and CSTF values increase with increasing surface functionality up to a point after which the CSTF values reach an apparent optimum degree of adhesion, whereas the values of apparent interfacial shear strength may increase or decrease at high concentrations of functional groups. The CSTF methodology predicts an equivalent optimum level of stress transfer whereas the apparent interfacial shear strength is much less consistent (Figs. 2 & 3). The limiting value of CSTF with fibre functionality can be attributed to an optimum interaction between the carboxylic acid groups on the fibre and the epoxide groups in the resin to provide maximum adhesion to that matrix resin, as shown by the yielding of the matrix (Figs. 2 & 3). This aspect is taken into account in the calculation of CSTF value. However, the apparent interfacial shear strength (τ_a) calculation does not take the plasticity of the matrix into account so that τ_a is invariably larger than the matrix shear yield strength [14].

An improvement in the degree of adhesion relative to the untreated fibre is observed for the acrylic acid and allylamine functionalised coatings. However, the coatings of allyl alcohol are much less effective with a value less than that for the untreated carbon fibres (Table 2). The inference from these results is that the hydroxyl groups do not bond chemically with the resin, and that the small increase in adhesion is a consequence of relatively weak dipole-dipole interactions.

Two specific trends observed in Table 2 (Acrylic acid + hexane, 0.5 and 0.75 mol %; Allyl alcohol + hexane, 0 and 0.25 mol %) highlight the superiority of the CSTF technique over the Kelly-Tyson methodology. It can be seen that the value of apparent interfacial shear strength decreases, rather than increasing, with an increase in the percentage of active surface functionalities. Although this may be attributed to the standard deviation in the interfacial shear strength measurement from the Kelly-Tyson model. However, the CSTF methodology is able to predict the logical trend. This shows that the CSTF technique is clearly more sensitive to fibre surface modification than the data reduction technique based on the Kelly-Tyson model.

It is well known that different modes of failure are observed in single fibre composites at differing degrees of fibre-matrix adhesion [17,22]. It has been previously reported that transverse matrix cracks occur at a high level of adhesion; interfacial crack growth at an intermediate level and frictional debonding at a low level [22]. We observed the same trends in this study (Fig. 4.). However, in some samples, as reported in Table 2, a mixed mode could be observed at intermediate degrees of adhesion where interfacial debonding and transverse matrix cracking co-existed. This appears to occur when the actual interfacial shear strength is close to the shear yield strength of the matrix (Fig. 2).

Transverse matrix cracking dominates the damage micromechanics when the apparent interfacial shear strength (as measured from the Kelly-Tyson model) exceeds the shear yield strength of the matrix (Fig. 2). The CSTF value (the stress transferred to the fibre) decreases with the increased surface functionality when transverse matrix cracking dominates the interfacial micromechanics. Thus the apparent maximum in CSTF value can be understood because at increased surface functionalities, the capability of the matrix to transfer stress to the fibre will be reduced in the presence of a matrix crack, despite the fact that the interfacial bond may be stronger. The influence of these transverse matrix cracks on the stress transferred to fibre end needs further investigation so that a more accurate prediction can be

made. At the moment, the plasticity effect model cannot account for these mechanisms. However, using the CSTF methodology, it is possible to identify “an optimum interface” in terms of its stress transfer capability rather than a “strong interface” inferred from the high value of apparent interfacial shear strength. This so called “strong interface” may lead to brittle fracture of high fibre volume fraction composites, leading to premature fracture without the full utilisation of fibre properties.

CONCLUSIONS

In this study, radio frequency induced plasma copolymerisation of acrylic acid/hexane, allyl alcohol/hexane and allylamine/octadiene gas mixtures is used to obtain a range of functionalised coatings on Type A carbon fibre surfaces. The single fibre fragmentation test has been employed to establish the relationship between the chemical composition of the fibre surface and the adhesion of the modified fibres to an epoxy resin. Coatings prepared by the homopolymerisation of hexane and that of the octadiene are strongly hydrocarbon in nature and inhibit chemical interaction between the fibre and matrix resulting in poorer adhesion than the parent untreated fibres. The introduction of comonomers, acrylic acid, allyl alcohol and allylamine individually to the plasma feed resulted in increased levels of specific fibre surface functionalities and improvements in the degree of adhesion. This is ascribed to the formation of covalent chemical bonds between the fibre surface functionalities and epoxide groups with the matrix resin. Within this context, carboxylic acid and amine groups are more effective than hydroxyl groups, reflecting the generally recognised reactivity of these species towards epoxides. The effectiveness of the CSTF analysis (based on the plasticity effect model) for the quantification of interfacial adhesion between Type A carbon fibres and epoxy resin has been demonstrated. A comparison with the conventional data reduction technique, based on the Kelly-Tyson model, for the calculation of apparent interfacial shear strength is also made. The results have shown that CSTF values increase with the increased concentration of surface functionalities up to an optimum degree of interfacial adhesion.

ACKNOWLEDGEMENTS

We acknowledge financial support from the Defence Research Agency (DRA), Farnborough, European Union (BRITE/EURAM BRE2-0453) and the Engineering and Physical Sciences Research Council (EPSRC), UK.

REFERENCES

1. HULL, D., An introduction to composite materials, (Cambridge Press, Cambridge, 1981), pp 38-48.
2. HUGHES, J. D. H., The carbon fibre/epoxy interface - A review, *Composites Science and Technology*, 41 (1991), 13-45.
3. DRZAL, L. T.; RICH, M. J.; LLOYD, P. F., Adhesion of graphite fibres to epoxy matrices Part 1: The role of fibre surface treatment, *Journal of Adhesion*, 16 (1982), 1-30.
4. DRZAL, L. T., Adhesion of graphite fibres to epoxy matrices: II. The effect of fibre finish, *Journal of Adhesion*, 16 (1982), 133-152.
5. CHENG, T-H.; ZHANG, J.; YUMITORI, S.; JONES, F. R.; ANDERSON, C. W., Sizing resin structure and interphase formation in carbon fibre, *Composites*, 25 (1994), 661-670.

6. CHENG, T.-H.; The role of sizing resins on the micromechanics of fibre composites, PhD thesis, The University of Sheffield, UK (1994), pp 120.
7. KELLY, A.; TYSON, W. R., Tensile properties of fibre reinforced metals: Copper/tungsten and copper/molybdenum, *Journal of Mechanics of Physical Solids*, 13 (1965), 329-350.
8. OHSAWA, T.; NAKYAMA, A.; MIWA, M.; HASEGAWA, A., Temperature dependence of the critical fibre length for the glass fibre reinforced thermosetting resins, *Journal of Applied Polymer Science*, 22 (1978), 3203-3212.
9. FEILLARD, P.; DESARMOT, G.; FAVRE, J. P. Theoretical aspects of the fragmentation test, *Composites Science and Technology*, 50 (1994), 265-279.
10. LACROIX, TH.; TILMANS, B.; KEUNINGS, R.; DESAEGER, M.; VERPOEST, I., Modelling of critical fibre length and interfacial debonding in the fragmentation testing of polymer composites, *Composites Science and Technology*, 43 (1992), 379-387.
11. TRIPATHI, D.; CHEN, F.; JONES, F. R., A pseudo-energy based method to predict the fibre-matrix adhesion using a single fibre fragmentation test, *Proceedings of the Tenth International Conference on Composite Materials*, Ed. A Poursatip and K Street (Woodhouse Publishing, Cambridge, 1995), Vol. VI, pp 689-696.
12. MELANITIS, N.; GALIOTIS, C.; TETLOW, P. L.; DAVIES, C. K. L., Interfacial stress distribution in model composites Part 2: Fragmentation studies on carbon fibre epoxy system, *Journal of Composite Materials*, 26 (1992), 574-610.
13. TRIPATHI, D.; JONES, F. R., Single fibre fragmentation test for assessing adhesion in fibre reinforced composites: A review, *Journal of Materials Science*, submitted.
14. Tripathi, D.; Jones, F. R., The load bearing capabilities of the fibre-matrix interface measured using single fibre fragmentation test, *Composites Science and Technology*, in print.
15. TRIPATHI, D.; CHEN, F.; JONES, F. R., A comprehensive model to predict the stress fields in a single fibre composite, *Journal of Composite Materials*, 30 (1996), 1514-1538.
16. TRIPATHI, D.; CHEN, F.; JONES, F. R., The effect of matrix plasticity on the stress fields in a single filament composite and the value of interfacial shear strength obtained from the fragmentation test, *Proceedings of the Royal Society A: Mathematical and Physical Sciences*, 452 (1996), 621-653.
17. KETTLE, A. P.; BECK A. J.; O'TOOLE, L.; JONES, F. R.; SHORT, F. R., Plasma polymerisation for molecular engineering of carbon fibre surfaces for optimised composites, *Composites Science and Technology*, in print.
18. CHEN, F.; TRIPATHI, D.; JONES, F. R., Determination of the interfacial shear strength of glass fibre reinforced phenolic composites by bimatrix fragmentation technique, *Composites Science and Technology*, 56 (1996), 609-622.
19. CHEN, F.; TRIPATHI, D.; JONES, F. R., The effect of the support resin on the interfacial shear strength determined by bimatrix fragmentation technique, *Composites Part A*, 27A (1996), 505-515.
20. TRIPATHI, D; JONES, F. R., The effect of matrix yield strain on the value of interfacial shear strength obtained from the fragmentation test, *Composites Part A: Applied Science and Manufacturing*, 27A (1996), 709-715.
21. ALEXANDER, M.; JONES, F. R., The effect of electrolytic oxidation upon the surface chemistry of type A carbon fibres Pts I-III, *Carbon*, 25 (1994), 698; 33 (1995), 569; 34 (1996), 1093.
22. DRZAL, L. T.; MADHUKAR, M., Fibre-matrix adhesion and its relationship to composite mechanical properties, *Journal of Materials Science*, 28 (1993), 569-610.

A STUDY OF THE TENSILE FAILURE MODE OF LASER MICRO-PERFORATED CARBON FIBRE REINFORCED THERMOPLASTICS

T.J.Matthams and T.W.Clyne

*Department of Materials Science and Metallurgy, Cambridge University,
Pembroke Street, Cambridge CB2 3QZ UK*

SUMMARY: A study has been made of the tensile failure of carbon fibre composites based on two different thermoplastic matrices. The introduction of an array of fine holes into such materials is of interest in view of the consequent improvements in formability, provided this can be achieved without unacceptable degradation of properties. It is found that a reduction in tensile strength of around 25% is induced in unidirectional composites by the presence of an array of fine holes designed to reduce the fibre length to 20 mm. The fracture path in perforated specimens runs between the holes along the fibre axis - ie parallel to the direction of loading. Lesser reductions in strength were observed with fewer holes or with other stacking sequences. The cracking parallel to the applied load was less pronounced in these specimens, although it still occurred to some degree. It has been established that this form of cracking is caused by shear stresses which peak at the surface of the holes. Computed values of these stresses are appreciably above the critical values for these systems. This information will be useful in designing hole patterns for optimisation of the microperforation process.

KEYWORDS: Thermoplastic Composites, Microperforation, Laser Processing, Tensile Strength, FEM Modelling, Failure Criteria, Shear Failure.

INTRODUCTION

A major problem with long fibre reinforced thermoplastics is that the formability is strongly impaired by the presence of the fibres. Attempts to form such material, during or after consolidation, tend to cause major microstructural defects such as wrinkling, buckling or fracturing of groups of fibres [1,2]. A promising approach to this problem is to break up the fibres in a controlled manner, such that the formability is enhanced, but leaving the average fibre aspect ratio sufficiently high for the stiffness and strength to be relatively unimpaired.

Several fibre fragmentation methods have been proposed, giving products ranging from chopped strand mat to Du Pont's Long Discontinuous Fibre™ (LDF) material [3-5]. The chopped strand mat compounds tend to have very short fibres in a planar random orientation. This limits the fibre content and results in mechanical performance well below that of the corresponding long fibre material. LDF is manufactured by a complex stretch-breaking process, prior to resin infiltration. This leads to a high volume fraction (58vol%) composite, with fibres of varyin length (typically ~50 mm). Chang [3] found that LDF materials showed excellent mechanical properties - comparable with continuous fibre composites. Schuster [6] extended the work of Chang to include mechanical testing of deformed LDF, using a hot press

integrated within a tensile testing machine. Schuster reported an increase in static strength for very small strains (up to 3%), attributed to an improvement in fibre alignment. However, there are various practical drawbacks associated with the production process which may inhibit widespread use of LDF material.

Recent studies [7,8] have outlined the development of a novel fibre fragmentation process, based on use of a laser beam to break fibres up in a controlled manner. This has certain important advantages over the LDF process, including no requirement to modify the pre-preg manufacturing process and considerable versatility with regard to the spatial distribution of fibre fracture sites. It has been shown [8] that the loads needed to deform such laser perforated material are considerably lower than those required for corresponding unperforated laminates. There is, however, concern about the effect of the arrays of fibre fracture sites produced by laser perforation on the mechanical properties of the composite. The current paper presents an investigation of the failure characteristics exhibited by microperforated carbon fibre composites under tensile loads.

EXPERIMENTAL PROCEDURES

The Perforation Process

Two composite systems have been studied. These are (a) PEEK-61vol%C (APC-2) and (b) PPS-57vol%C. Details of these systems are available in the literature [9,10]. The laser microperforation process, the principle of which was developed by Integrated Materials Technology Ltd [11], was applied to pre-pregs of these materials. This process involves moving the pre-preg past a laser head which is being fired at pre-determined intervals. Micrographs of single holes, and a schematic of the pattern of holes, produced in this way are shown in Fig.1. For the perforation operation applied to the specimens described here, the pattern parameters indicated in Fig.1(c) had the values shown in Table 1. Two fibre lengths were chosen for the current work: 20 mm and 100 mm. A small degree of overlap between adjacent holes is necessary to ensure that all fibres become cut to the selected length. However, the hole pattern was designed to ensure that the zones of stress concentration adjacent to individual holes did not overlap at all when the material was loaded parallel to the fibre axis.

Although the laser beam was circular in section (with a diameter of about 80 μm), the holes are approximately ellipsoidal as a result of the continuous relative motion between beam and specimen. (The distance travelled during the firing period of the laser was about 100 μm .) It should also be noted that the holes exhibit a considerable degree of taper - see Fig.1(b). The diameters quoted in Table 1 are average values through the thickness of the pre-preg. The severity of this taper is dependent on the thermal properties of the pre-preg and the laser firing conditions.

It can be seen in Fig. 1(b) that the hole was completely refilled with resin during consolidation. Although the filled hole will still act as a stress concentrator (since the resin is very compliant), this means that the resin will afford environmental protection to the fibres. A further point is that some fibre swelling can be seen adjacent to the hole. This is presumably due to inelastic changes in the fibre structure, or possibly entrapment of gas, induced by thermal shock and exposure to very high local temperature.

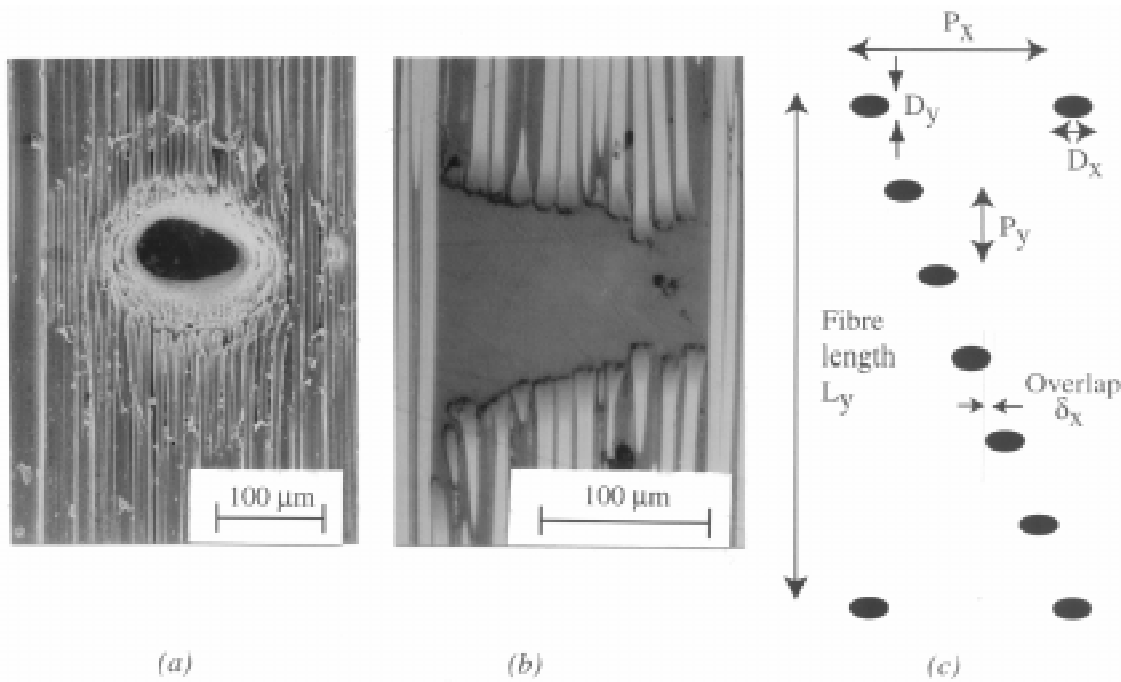


Figure 1. SEM micrographs of single holes in APC-2, showing (a) free surface of a pre-preg after perforation and (b) section through a consolidated laminate. (c) Schematic plan of an array of holes.

Table 1. Perforation pattern parameters

Pattern Code	Diameter (\perp fibre axis) D_x (μm)	Diameter (\parallel fibre axis) D_y (μm)	Pitch (\perp fibre axis) P_x (mm)	Pitch (\parallel fibre axis) P_y (mm)	Overlap (\perp fibre axis) δ_x (μm)	Fibre length L_y (mm)
L20	150	80	1.0	2.0	50	20
L100	150	80	2.2	4.54	50	100

Mechanical Testing

Once perforated, the pre-preg material was consolidated into uni-directional, UD, cross-ply ($0/90^\circ$), and quasi-isotropic ($[0/+45/-45/90]_s$), QI, laminates. These laminates were made from 8 plies of pre-preg, each being 0.125mm (APC-2) or 0.140mm (PPS-C) in thickness. Consolidation parameters were based on those recommended by the pre-preg manufacturers [9,10].

After consolidation, tensile test specimens of length 250 mm, width 20 mm and thickness ≈ 1 mm were cut from the laminates. For the UD material, off-axis specimens were produced with the long axis at selected angles to the fibre direction. Specimen dimensions conformed to those set down in the CRAG testing procedures [12]. Specimens were end-tabbed using 50 x 22 x 1.6 mm aluminium tabs, bonded using Redux 420 adhesive. This is a two-part epoxy-based adhesive, cured in a heated platen press for 2 hours. For off-axis loading, slightly smaller specimens (150 x 20 x 1 mm) were used, due to limits on material availability. Strain gauges (5 mm Kyowa) were used to obtain failure strain and modulus data.

Mechanical testing was carried out using a 100 kN Schenck screw-driven testing machine. Tensile test samples for UD, 0/90° and QI specimens were loaded at a strain rate of $5 \times 10^{-5} \text{ s}^{-1}$, load and strain data being logged on a Macintosh via a MacLab data acquisition unit. The majority of the tests were repeated about 5-8 times and appropriate average values were calculated.

RESULTS

Elastic Constants

Strain gauges placed parallel to the fibre direction were used to determine the axial Young's modulus, E_1 , of both perforated and unperforated material. This was calculated from the initial gradient of the true stress / true strain plot. Data for PPS-C laminates are shown in Table 2. It can be seen that the moduli of the perforated materials are almost identical to those of the corresponding unperforated material, even for the shortest fibres. This is hardly surprising, since the aspect ratio of the 20 mm fibres is almost 3000. With this large aspect ratio, full load transfer [13] is expected to occur, giving a stiffness similar to that for continuous fibres.

Table 2. Young's Modulus data for perforated and unperforated PPS-C Laminates.

Specimen Code	Young's modulus $E_1 \pm \sigma_n$ (GPa)	Specimen Code	Young's modulus $E_1 \pm \sigma_n$ (GPa)	Specimen Code	Young's modulus $E_1 \pm \sigma_n$ (GPa)
UD-L ∞	133.3 \pm 6.23	0/90-L ∞	67.87 \pm 2.35	QI-L ∞	45.09 \pm 0.91
UD-L100	136.3 \pm 2.77	0/90-L100	67.63 \pm 1.44	QI-L100	45.01 \pm 0.68
UD-L20	134.2 \pm 5.60	0/90-L20	60.94 \pm 3.44	QI-L20	45.00 \pm 1.77

Strength of Laminates

Failure strength data for APC-2 laminates are shown in Fig.2. The measured strengths of unperforated material (plotted at a fibre length corresponding to the specimen length) are broadly consistent with data in the literature [9,14]. It can be seen that introduction of the perforations has had a significant effect in reducing the strength of the unidirectional material, with a drop of about 25% effected by reducing the fibre length to 20 mm. The degradation on reducing the fibre length from 100 mm to 20 mm suggests that it is not simply the stress-concentrating effect of isolated holes which is responsible for the strength reduction, but rather that some interaction can occur between them which facilitates failure. This was confirmed by several experiments in which single holes of similar diameter to the laser perforations were drilled in the material. The resulting reductions in strength were small and were in all cases significantly less pronounced than in specimens with arrays of holes. It may also be noted that the observed reductions in strength on perforation are appreciably less marked for the cross-ply material, although still detectable.

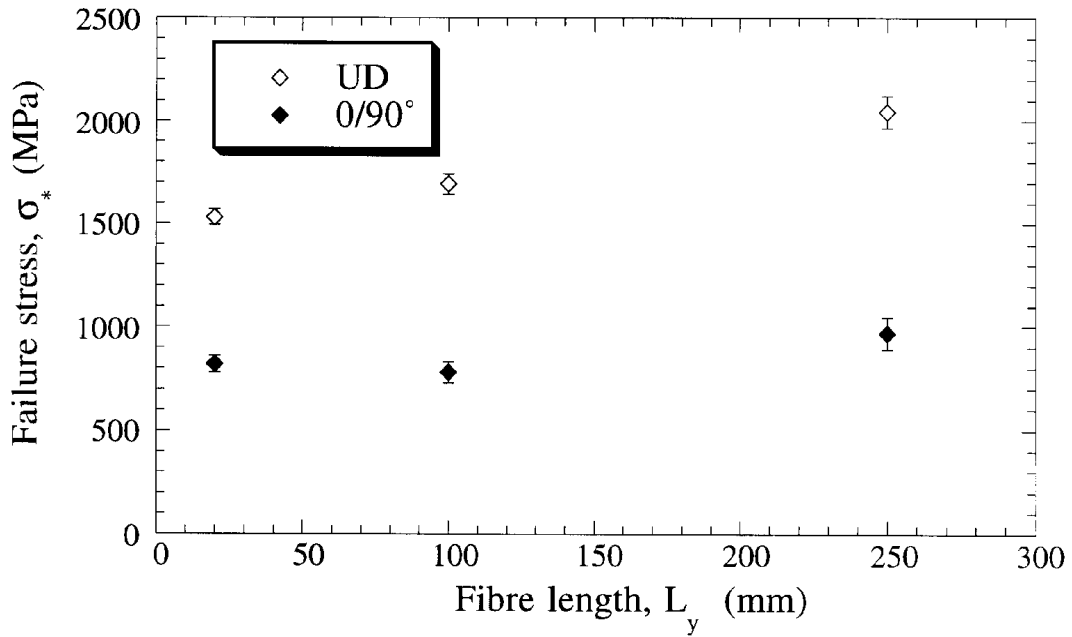


Figure 2 Failure Strengths of APC-2 Laminates. (Data for unperforated laminates have been plotted at a fibre length corresponding to the specimen length of 250 mm).

Corresponding data for the PPS-C material are shown in Fig.3. These show broadly similar trends to the APC-2 results. There is a significant reduction in the failure stress as the fibre length is reduced, ie as the density of microperforations is increased. However, it is noticeable that only a small reduction from the long fibre case is observed when the fibre length is 100 mm, particularly for the UD material. This suggests a slightly different type of interaction between the holes compared with the APC-2, possibly related to differences in interfacial bond strength or matrix properties.

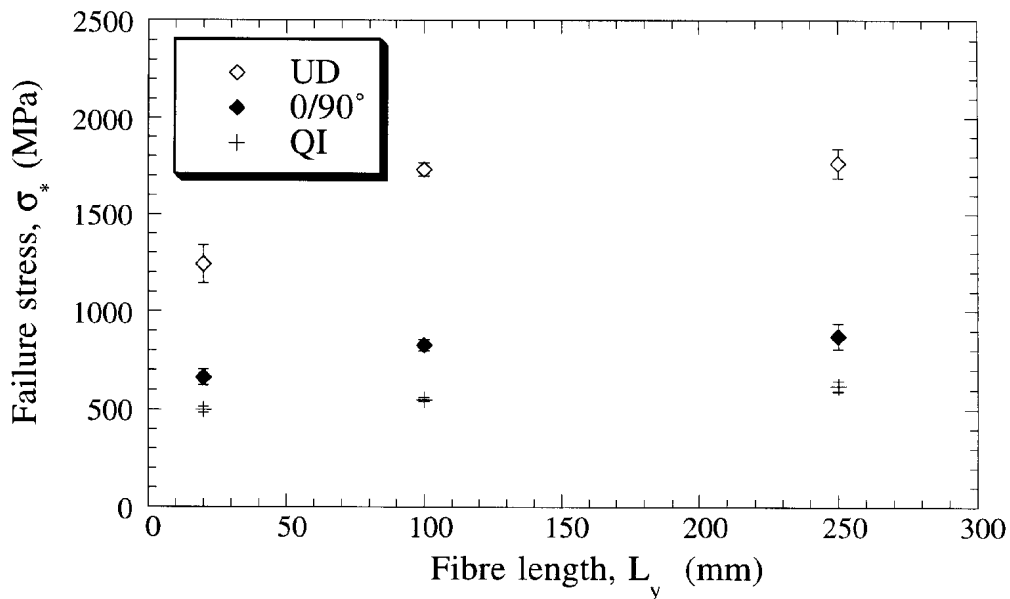


Figure 3 Failure Strengths of PPS-C Laminates. (Data for unperforated laminates have been plotted at a fibre length corresponding to the specimen length of 250 mm).

Fractography

Study of the fracture surfaces from UD specimens clearly suggested an interaction between individual holes. It is clear from SEM micrographs such as that of Fig.4(a) that there is a strong tendency for cracks to run between perforations, parallel to the applied load and fibre axis. A characteristic zig-zag crack path is thus produced, of the form shown schematically in Fig.5. Each layer of pre-preg in a laminate exhibited its own independent zig-zag pattern of this type. This involves only failure of the matrix material or fibre-matrix interface and no fibre fracture is necessary. It is not, however, immediately obvious how the applied tensile load can give rise to stresses within the specimen which could cause this mode of failure.

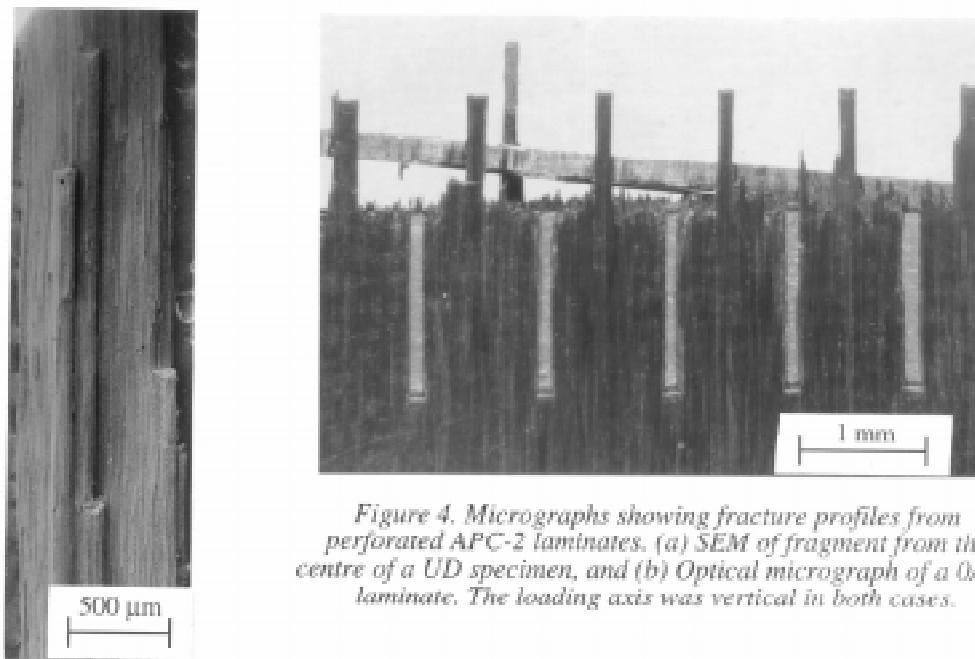


Figure 4. Micrographs showing fracture profiles from perforated APC-2 laminates. (a) SEM of fragment from the centre of a UD specimen, and (b) Optical micrograph of a 0/90° laminate. The loading axis was vertical in both cases.

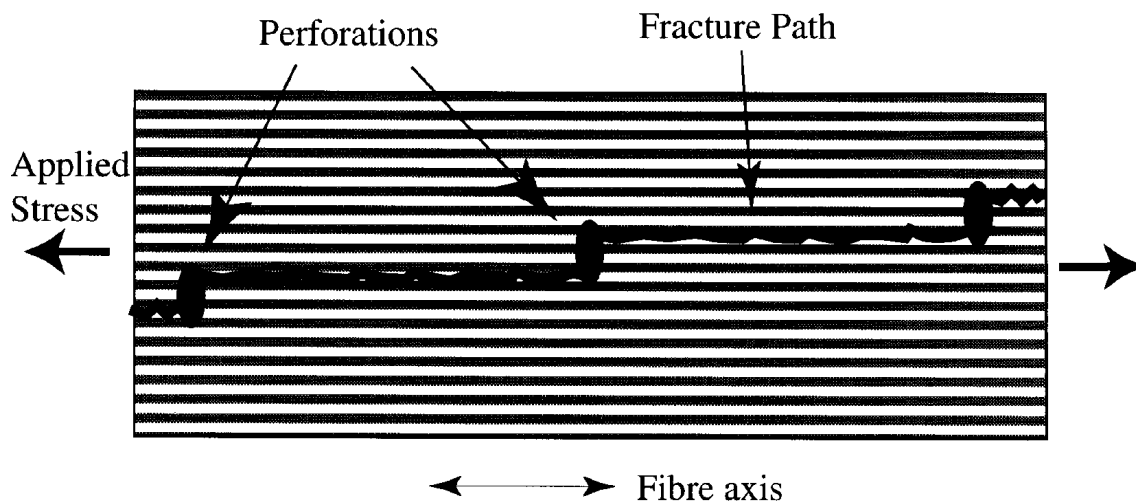


Figure 5 Schematic depiction of the fracture path followed in UD laminates, with the laser-drilled holes being linked up by extensive cracking parallel to the fibre direction.

A tendency for this mode of failure to occur was also apparent in the 0/90° and QI laminates. This can be seen in Fig.4(b). However, in these cases the cracking parallel to the loading axis in 0° plies is largely suppressed by the presence of transversely-oriented fibres in adjacent plies. The extensive fracture surface areas normal to the loading direction, seen in the UD specimens, were therefore absent in these materials, although debonded bundles of fibres, terminating in a laser-drilled perforation, could clearly be seen.

Off-Axis Testing.

To investigate the zig-zag failures seen in the UD laminates, more information was needed regarding the transverse and shear properties of the composite. A series of off-axis tests was therefore undertaken, aimed at establishing the shear and transverse strengths of unidirectional material relative to the fibre axis, τ_{12u} and σ_{2u} . A number of tensile test coupons were cut from an 8-ply laminate of unperforated UD APC-2. Specimens were cut at 0°, 30°, 60° and 90°, with at least three specimens per orientation. Specimens were end-tabbed as before, using aluminium tabs and Redux adhesive, and loaded to failure. The results are plotted in the form of measured strength against loading angle, ϕ , in Fig.6.

These data can be used to generate estimates for τ_{12u} and σ_{2u} , by using either the maximum stress or the Tsai-Hill failure criterion. In each case, a best fit curve is obtained for the experimental data. The equations [15] governing the maximum stress criterion - equations (1a), (1b) and (1c) - and those for the Tsai-Hill failure criterion - equation (2) are given below.

$$\sigma_{\phi^*} = f(\sigma_{1u}, \cos^2\phi) \quad (1a)$$

$$\sigma_{\phi^*} = f(\sigma_{2u}, \sin^2\phi) \quad (1b)$$

$$\sigma_{\phi^*} = f(\tau_{12u}, \sin\phi \cos\phi) \quad (1c)$$

$$\sigma_{\phi^*} = bbc[(f(\cos^2\phi(\cos^2\phi - \sin^2\phi), \sigma_{1u}^2) + f(\sin^4\phi, \sigma_{2u}^2) + f(\cos^2\phi \sin^2\phi, \tau_{12u}^2))^{-1/2}] \quad (2)$$

The value of σ_{2u} can be obtained directly as the measured strength at $\phi = 90^\circ$, which is about 84 MPa. Since the data for $\phi = 60^\circ$ lie almost exactly on the transverse failure curve, only the data for $\phi = 30^\circ$ can be used to estimate τ_{12u} . This leads to a prediction of $\tau_{12u} = 73$ MPa if the maximum stress criterion is used, and $\tau_{12u} = 80$ MPa if the Tsai-Hill criterion is used. A more detailed study, with many more data points in the range 10-30°, of the off-axis properties of APC-2 has been carried out by Cervenka [16] and his results led to an estimate of $\tau_{12u} = 78$ MPa; this correlates well with the results presented here.

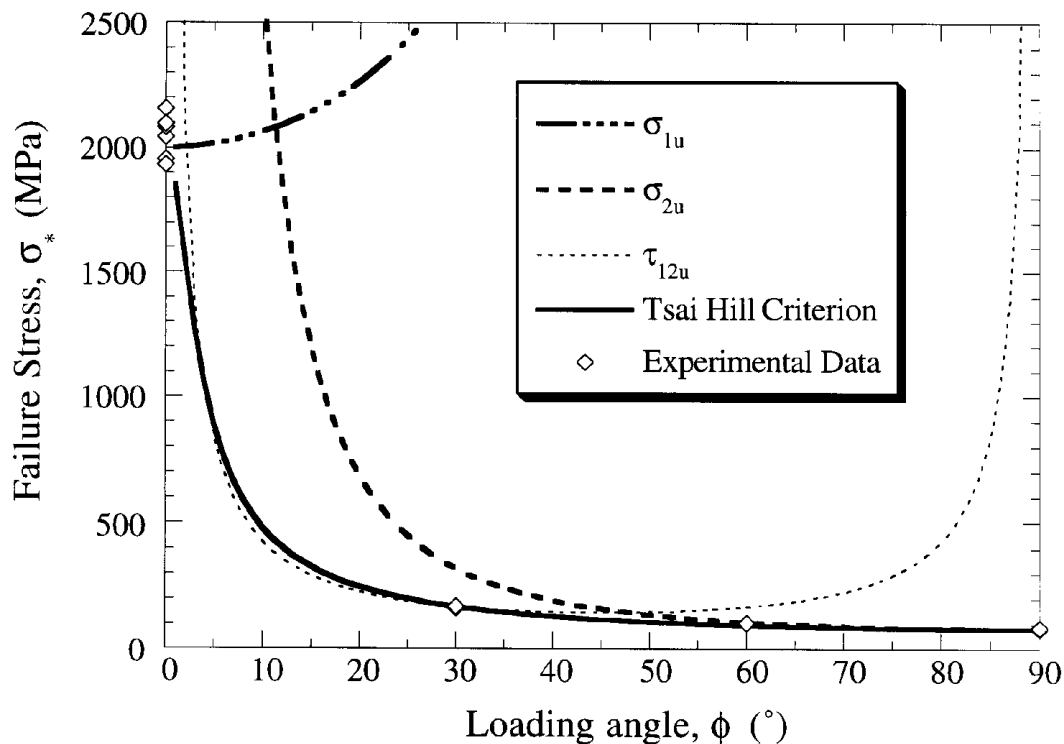


Figure 6 Measured strength data from off axis testing of APC-2 UD Laminates, together with predicted variations obtained using the maximum stress and Tsai-Hill criteria.

MODELLING OF STRESS FIELDS AROUND HOLES

Mesh Generation

An ABAQUS finite element model was set up in order to study the stress fields generated around the holes when a uniaxial load was applied in the fibre direction. Quadratic plane stress elements with 8 nodes were used for this analysis. Figure 7 shows the mesh. This represents three circular holes in an anisotropic continuum. There has been no attempt to model fibres and matrix separately. This also means that the model does not consider any differential Poisson contractions that may occur, which might give rise to transverse tensile stresses across the fibre/matrix interface. The holes have a diameter of 150 μm and are displaced from each other by 2 mm in the 1-direction and 100 μm in the 2-direction. This geometry corresponds to the perforation pattern used here for the fibre length of 20 mm. In this model, the fibre direction, i.e. the stiff direction, is the 1-direction. The left hand column of nodes was fixed, and a uniaxial tensile load of 2000 MPa was applied to the nodes on the right hand edge of the mesh in the 1-direction. The introduction of resin into the holes does not significantly affect the computed stress distributions.

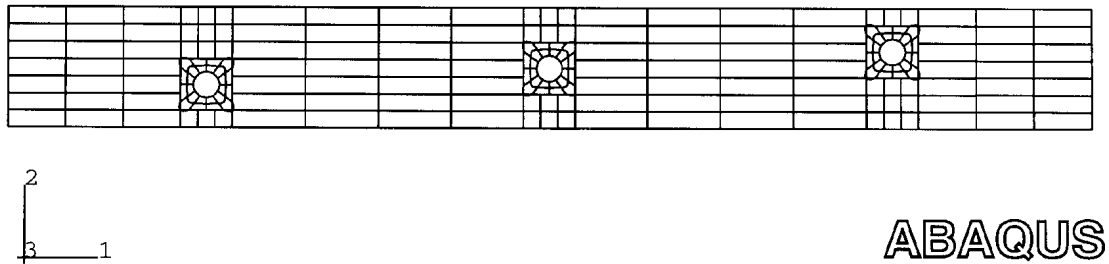


Figure 7. Mesh used for Finite Element Modelling of stress field around microperforations.

ANALYSIS OF STRESS DISTRIBUTIONS

The distributions of the σ_{22} and τ_{12} stresses are of particular interest, since they are expected to be responsible for cracking parallel to the fibres and hence to control the zig-zag failure mode seen in the perforated unidirectional composites. Study of the σ_{22} stresses revealed that they were all very low. This is expected, since there is no obvious origin for such stresses in a single ply when the composite is treated as a continuum (so that differential Poisson contraction between fibre and matrix is neglected). In practice, tensile σ_{22} stresses could arise in 0_ plies within a laminate, as a result of differential Poisson contraction between plies, but this is clearly not responsible for the observed fracture mode of the unidirectional laminates.

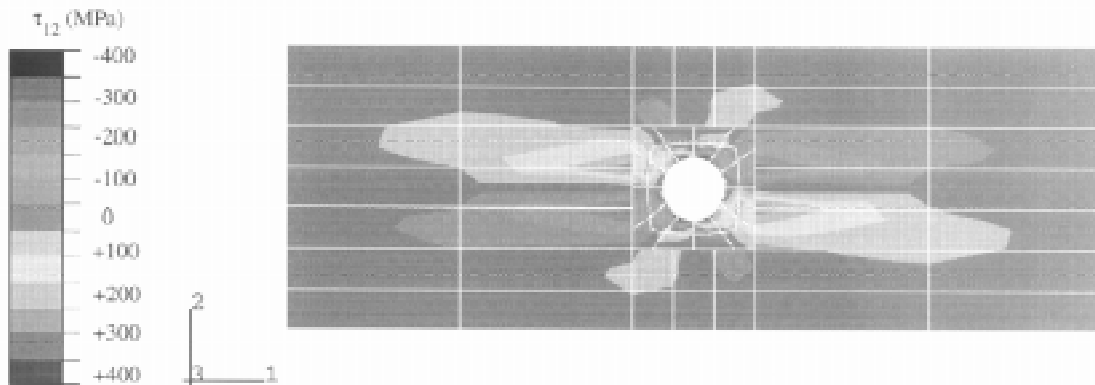


Figure 8. Distribution of τ_{12} stress around a single perforation in a UD laminate loaded parallel to the fibre axis.

The distribution of τ_{12} stresses is given in Fig.8. This shows that significant shear stresses arise on planes parallel to the applied load, particularly those which are close to being tangential to the hole. These shear stresses arise as a direct consequence of the stress concentrating effect of the hole, since the high σ_{11} stresses borne by sections passing close to the hole must fall off rapidly in sections which pass through the hole. Furthermore, the shear stresses peak at the hole surface, where they are likely to initiate propagation of the cracks which link the perforations. The predicted peak value is around 400 MPa, with values of over 100 MPa persisting to distances of about 2 hole diameters. In practice, the peak shear stress might be expected to be somewhat less than this as a result of some load sharing with adjacent plies - in which the holes would in general not be located in the same positions in the 1-2 plane. On the other hand, the actual holes are elliptical in section, with the major axis in the

2-direction, so that the σ_{11} stress concentration, and hence the peak τ_{12} stress, would be higher than for circular holes. In any event, comparison between the computed τ_{12} stresses and estimated values for τ_{12u} of around 70-80 MPa indicates that it is very likely that the observed tendency for extensive cracking parallel to the fibres in 0° plies arises in this way.

CONCLUSIONS

1. The tensile strength of two carbon fibre reinforced thermoplastic composite systems has been measured with and without arrays of fine holes produced by laser drilling, in unidirectional, cross-ply and quasi-isotropic laminates. The hole patterns were designed to break the fibres up into selected lengths, while minimising the degree to which stress concentration zones around them would overlap.
2. Significant reductions in strength resulted from incorporation of the holes, particularly when the hole density was increased so as to reduce the fibre length. This effect was more pronounced for the unidirectional composites than for the other lay-ups. There were only minor differences between the behaviour of the two composite systems.
3. The reduction in strength is largely attributed to interaction between individual holes in such a way that fracture occurred on planes parallel to the fibre axis, along the direction of loading, so as to link up the perforations without needing to fracture any fibres.
4. The stresses responsible for this mode of failure are shear stresses on planes parallel to the loading axis, which reach a peak at the surface of the hole. Computation of these shear stresses has been carried out using FEM.
5. Experimental measurements have been carried out on unperforated unidirectional composite material in order to establish the transverse and shear strengths and also to investigate the failure under mixed mode loading. Comparison between measured shear strengths and computed shear stress distributions has confirmed that these shear stresses are likely to be responsible for the observed mode of failure and hence for at least a significant proportion of the observed loss in strength of the laminates. The implications of this for optimisation of perforation patterns are currently under study.

ACKNOWLEDGEMENTS

This work forms part of the PERFORM project, which is a collaboration between The University of Cambridge, The Defence Research Agency, Integrated Materials Technology and T&N Technology Ltd. The project is funded under the DTI LINK Structural Composites Programme. Thanks are due to DRA Farnborough for providing financial support for T.J.Matthams. A number of fruitful discussions have taken place with Dr.D.J.Bray, of DRA. The authors would also like to thank Mr Jim Coleman of DRA for autoclaving the laminates used in this work.

REFERENCES

1. W. Soll and T. G. Gutowski, Forming Thermoplastic Composite Parts, SAMPE Journal, **May/June** (1988), pp. 15-19.
2. P. J. Mallon, C. M. O'Bradaigh and R. B. Pipes, Polymeric diaphragm forming of complex-curvature thermoplastic composite parts., Composites, **20(1)** (1989), pp. 48-56.
3. I. Y. Chang and J. F. Pratte, LDF Thermoplastic Composites Technology, J. Thermoplas. Comp. Mats., **4** (1991), pp. 227-251.
4. R. K. Okine, D. H. Edison and N. K. Little, Properties and Formability of a Novel Advanced Thermoplastic Composite Sheet Product., J. Reinforced Thermoplastic Composites, **8** (1990), pp. 70-90.
5. J. F. Pratte, W. H. Krueger and I. Y. Chang, High performance Thermoplastic Composites With Poly(Ether Ketone Ketone) Matrix, in 34th International SAMPE Symposium (1989), Reno, NV, USA, G. A. Zakrzewski, D. Mazenko, S. T. Peters and C. D. Dean (Eds.), SAMPE Publishing, Covina, CA, 91722, pp. 2229-2242.
6. J. Schuster and K. Friedrich, The Fatigue Behaviour of Thermoformed Discontinuous Aligned Fibre Composites, in ICCM-10 (1995), Whistler, B.C., Canada, A. Poursartip and K. Street (Eds.), Vol. 1, Woodhead Publishing Ltd, Abington, UK, pp. 593-600.
7. T. J. Matthams, D. J. Bray and T. W. Clyne, A Microperforation Process For Improving The Formability Of Long Fibre Thermoplastic Composites, and its Effect on Mechanical Properties., in ECCM-7 (1996), London, UK, Institute of Materials, Vol. 1, Woodhead Publishing Ltd, Abington, UK, pp. 229-237.
8. D. T. Steel and W. J. Clegg, The Flow Behaviour and Formability of Microperforated Composites containing Aligned Fibres, in ECCM - 7 (1996), London, Institute of Materials, Vol. 1, Woodhead Publishing Ltd, Abington, UK, pp. 239-246.
9. ICI Fiberite, APC-2. The product of High Technology - Aromatic Polymer Composites - Data Sheets. (1988).
10. Quadrax, Material Property Data Sheets, Quadrax Advanced Materials Systems, Portsmouth, RI, USA.
11. R. A. Ford, Improved Composites Materials and Method for Making Them, PCT Publication Number WO 96/01179, UK, (1996)
12. P. T. Curtis, CRAG Test Methods for the Measurement of Engineering Properties of Fibre Reinforced Plastics., Royal Aerospace Establishment, Technical Report 88012, (1988).
13. H. L. Cox, The Elasticity and Strength of Paper and other Fibrous Materials, Brit J. Appl. Phys, **3** (1952), pp. 72-79.
14. F. N. Cogswell, Thermoplastic Aromatic Polymer Composites - Appendix 17., Butterworth Heinemann Ltd, (1992).
15. D. Hull and T. W. Clyne, An Introduction to Composite Materials, Cambridge University Press, Cambridge, (1996).
16. A. J. Cervenka, PEEK/Carbon Fibre Composites: Experimental Evaluation of Unidirectional Laminates and theoretical Prediction of their Properties., Polymer Composites, **9(4)** (1988), pp. 263-270.

EFFECT OF INTERFACIAL SHEAR DEBONDING ON THE TENSILE STRENGTH AND RELIABILITY OF FIBROUS COMPOSITES: FINITE ELEMENT SIMULATION

Koichi Goda

*Department of Mechanical Engineering, Yamaguchi University
Tokiwadai, Ube 755, Japan*

SUMMARY: For the purpose of clarifying the effect of interfacial shear strength on the axial tensile strength and reliability of fibrous composites, a Monte-Carlo simulation technique based on a finite element method was developed. The results showed that the interfacial shear strength value which increased the average strength of the composites corresponded to the value which decreased their coefficient of variation. The simulated strength and reliability was closely related with the degree of damage and its type around a fiber break. That is to say, small-scale debonding promotes comparatively the cumulative effect of fiber breaks and plays a role in increasing the composite strength and reliability.

KEYWORDS: fibrous composites, tensile strength, interfacial shear strength, debonding, strength and reliability, Monte-Carlo simulation, finite element method, Weibull distribution

INTRODUCTION

It is well-known that interfacial bond properties and mechanical properties of the matrix can significantly influence the tensile strength of fiber-reinforced polymer matrix composites [1][2]. That is, a low interfacial bond promotes large-scale debonding and reduces the load-carrying capacity of the adjacent fiber. On the other hand, a high interfacial bond tends to extend cracks transversely into the matrix at fiber breaks and results in increasing stress concentrations around these breaks. The same phenomenon occurs when matrices are brittle [3]. Such large-scale debonding and matrix cracking are major factors which decrease the strengths of both polymer matrix [1][2] and metal matrix composites [4]. However, there are few reports which use analytical approaches to explain these phenomena.

The present study simulates the above phenomena to clarify the effect of interfacial shear strength on the tensile strength and reliability of fiber-reinforced polymer matrix composites, using a Monte-Carlo simulation technique based on a finite element method. A boron/epoxy monolayer composite is used as the simulation model, and five hundred simulations are carried out using various interfacial shear strengths. Additionally, this study discusses the role of interfacial debonding in increasing the strength and reliability of the composites.

ANALYSIS

Finite Element and Mesh

Microdamage following fiber breaks in a fiber-reinforced polymer matrix composite is as follows [5]:

- (i) If the interface is weak, a shear stress concentration at the fiber-matrix interface often causes interfacial shear debonding along the fiber-axis.
 - (ii) However, if the interface has a strong bond, a crack initiates at the fiber break and extends into the matrix perpendicular to the fiber-axis.
- If the matrix consists of a ductile material, it yields and the yield zone spreads along the broken fiber.

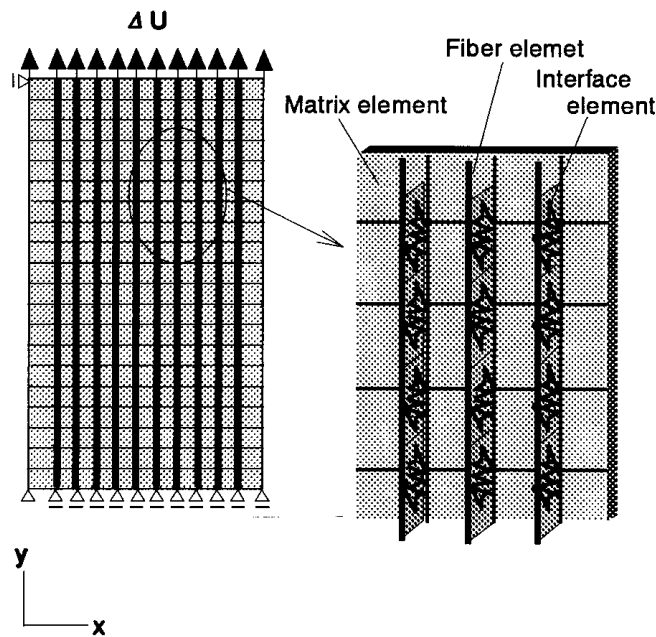
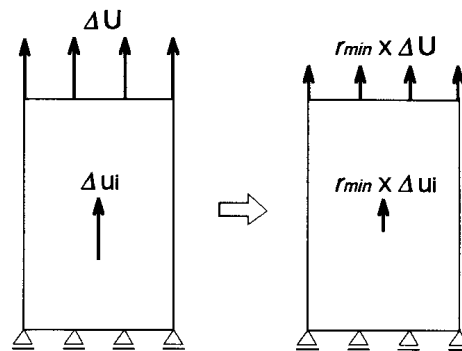


Fig.1. Finite element model and mesh.

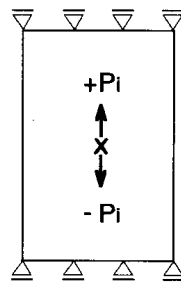
The shear-lag model [6] is widely used for estimating axial fiber stress distributions around fiber break points in a composite, simulating its axial fracture process and so on. However, the effect of (i) is not contained in the shear-lag model. Therefore, in the present study a finite element method is applied for modeling interfacial debonding and matrix cracking. The present finite element model is based on the model of a monolayer composite suggested by Mandel, et al. [7]. Figure 1 shows the model and mesh, in which a 2-node line element representing a fiber element is incorporated into the nodes along y-axis of a 4-node isoparametric element based on a plane stress condition. This plane element represents a matrix element and takes into account the multi-axial stress state of tensile and shear stresses around a fiber break. Furthermore, a shear spring element representing an interfacial bond (referred to as "interface element") connects the fiber and matrix elements. Deformation resistance of the interface element is determined by the spring constant and the relative displacement of the fiber and matrix elements. The stiffness matrix of a shear spring element is determined by the size of the bond layer and the shear modulus, similar to the formulation taken for a 2-node line element. A global stiffness matrix is constituted from the three element stiffness matrices, and therefore the whole structural analysis can be carried out following an ordinary finite element procedure. In this study a relatively brittle material such as epoxy is

used as a matrix, so that the effect of (iii) was not taken into account. Thus, it is assumed that the matrix and interface elements as well as the fiber element behave as a linear elastic body, respectively, and are statically fractured when the local stress satisfies the corresponding fracture criterion. Namely, the Young's modulus of a fiber element is changed to zero if its normal stress achieves its tensile strength. The shear modulus of an interface element is changed to zero if its shear stress achieves the so-called interfacial shear strength. For a matrix element, the Von Mises criterion is applied, in which the elastic modulus of the element is changed to zero if its equivalent stress achieves its tensile strength. In the remainder of this article, we call their fractures "damages", and individually we call them fiber break, interfacial debonding and matrix fracture, respectively.

The composite model used in this study is a boron/epoxy monolayer composite, and the finite element mesh has ten fibers of which each is divided into twenty elements. The number of nodes is 462, and the numbers of fiber, matrix and interface elements are 200, 220 and 190, respectively.



(a) Method 1



(b) Method 2

Fig.2. Calculation methods for fiber-break process.

Simulation Procedure

Occurrences of fiber breaks, matrix fracture and interfacial debonding would cause complicated stress distributions throughout a composite. Therefore, a method for estimating reasonably what type of damage occurs in each element, should be incorporated within the simulation procedure. In order to achieve such an estimation, an r -minimum method [8] is employed in this study, which was originally used in searching for yielding regions in a metal with an elastic-plastic finite element method. According to this method, a ratio of the

difference between strength and stress in each element to the stress increment is calculated, and the element giving the minimum ratio takes precedence for the damage, i.e. the fiber break, the matrix fracture or the interfacial debonding. The following is the present simulation procedure:

1. A strength of a fiber element obeys the following 2-parameter Weibull distribution:

$$F(\sigma) = 1 - \exp \left\{ - \frac{L}{L_0} \left(\frac{\sigma}{\sigma_0} \right)^m \right\} \quad (1)$$

where, m and σ_0 are the Weibull shape and scale parameters, L is an arbitrary fiber length, and in this study is equivalent to the fiber element length, L_0 is a standard gage length at which the Weibull parameters are estimated. By substituting a uniform random number into the inverse function of eqn 1, we can generate a random Weibull strength to assign to a fiber element.

2. The unknown nodal displacements Δu_i are computed under the boundary condition of displacement increment at the fiber and matrix ends, as shown in Fig.1. The computation is carried out incrementally, but the increment width is not fixed. In this study an arbitrary large increment ΔU enough to damage almost all the elements was given to the ends even at the first calculation stage. The stresses and the stress components acting in the elements are calculated from the computed displacements. Then, the ratios r are calculated for all the elements.

3. Next, a possibility of the damage occurrence and its type are determined by the r_{min} method. The outcome will change the boundary condition, as shown in Fig.2 and as follows,
 - i) If $r_{min} \leq 1$, all the stresses calculated in this stage are modified to the exact stresses by multiplying r_{min} with the stress increment in each element (see Fig.2 (a)). Then the [D] matrix components of the element giving the r_{min} are changed to zero. If this element is a fiber element or a matrix element, then in the next stage the load P_i acting in this element is released through its nodes along y-axis under the boundary condition of load increment and the fixed condition at the fiber and matrix ends (see Fig.2 (b)). If $r_{min} \leq 1$ is still satisfied, the next stage is consumed to release the load acting in the new damaged element, together with the residual load of the previous stage in the same way. This procedure is repeated until $r > 1$.
 - ii) If $r_{min} > 1$, then damage does not occur. The boundary condition of displacement increment is applied again at the fiber and matrix ends, as described in 2.

4. As the damage accumulates in a composite, the support force along y-axis begins to decrease largely at a certain strain level. It was assumed that when such behavior occurs, or when the composite stress achieves a stress level less than 80% of the maximum stress, the composite fracture criterion is satisfied.

Table 1. Material constants used in the present simulation

Young's modulus of boron fiber	397.9 GPa
Diameter of boron fiber	0.142 mm
Fiber element length	0.3 mm
Weibull shape parameter for fiber strength	7.16
Weibull scale parameter for fiber strength at 6mm	3.665 GPa
Young's modulus of epoxy matrix	3.296 GPa
Poisson's ratio of epoxy matrix	0.39
Tensile strength of epoxy matrix	45.57 MPa
Thickness of matrix element	0.371 mm
Shear modulus of interface element	1.186 GPa
Thickness of interface element	0.142 mm
Width of interface element	1.42 mm
Distance between fibers	0.259 mm

5. Following the above procedure, five hundred of simulations were carried out under different sets of random numbers. Finally the average and coefficient of variation in the simulated strengths were calculated.

The present study simulates the tensile strength and reliability of a boron/epoxy monolayer composite. In Table 1, the material constants used in the present simulation are shown. The Weibull parameters of the boron fiber (Boron/Tungsten 5.6mil, AVCO) and the tensile strength of the epoxy resin (Arardite CY230/Hardener HY2967, Ciba-Geigy Co.) were determined experimentally.

RESULTS

Effect of interfacial shear strength on the strength and reliability

Figure 3 shows typical stress-strain curves of the simulation results. In the computation, interfacial shear strengths, $\tau_1 = 11.7, 20.4$ and 35.0 MPa were used under the same set of random numbers for fiber strength. Therefore the stress levels at the first fiber break are all the same, but the behavior following the break is completely different. Figure (a) shows a similar fracture process to that of a bundle consisting of small number of fibers. That is, the first fiber break indicates the maximum stress and is followed by the other individual fiber breaks which occur at stress levels less than maximum. However in figure (b) the level of the second peak is larger than the first level and indicates the maximum stress. Figure (c) shows that the stress level drops in a moment after the first peak, though recovering slightly around 0.8% strain. These results show that $\tau_1 = 20.4$ MPa gives the highest strength, and imply that the more cumulative fiber break pattern increase the composite strength.

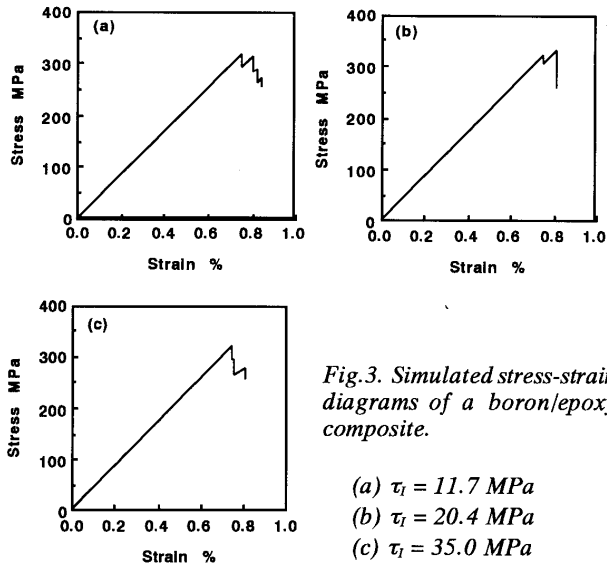


Fig.3. Simulated stress-strain diagrams of a boron/epoxy composite.

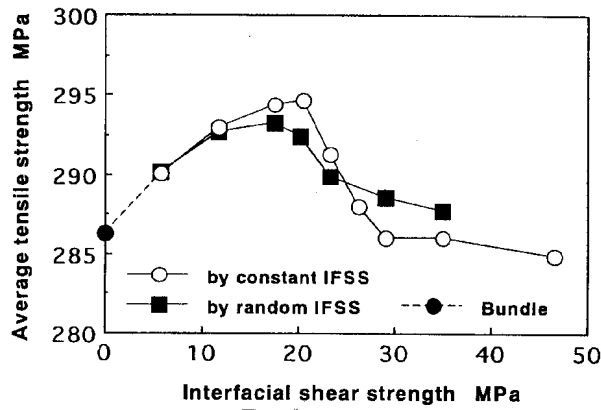


Fig.4(a) Effect of interfacial shear strength on the average tensile strength. (IFSS: Interfacial shear strength)

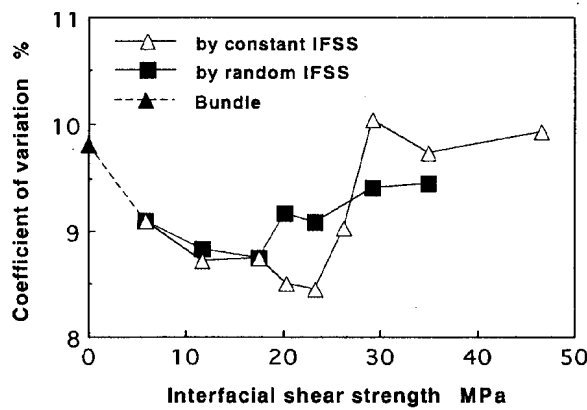


Fig.4(b) Effect of interfacial shear strength on the coefficient of variation in strength.

Figure 4 (a) and (b) shows the effect of the interfacial shear strength on the average and coefficient of variation in simulated strengths, respectively. Solid symbols at $\tau_i = 0 \text{ MPa}$ in the

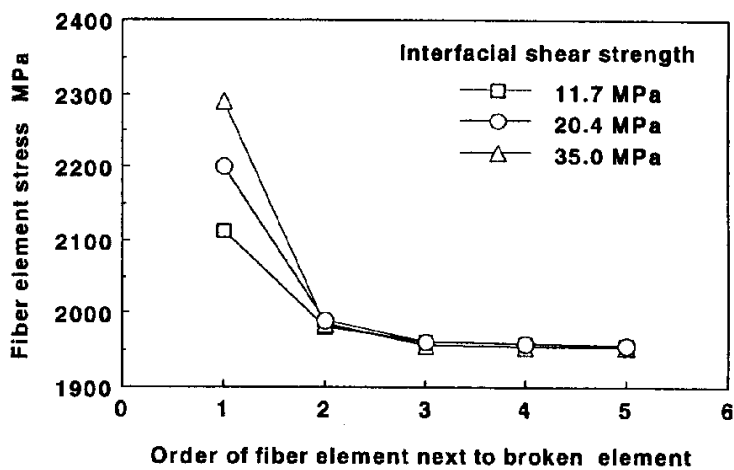
figure indicates the results of 5000 bundle simulations. The results show that the average strength shown in open circles gradually increases with increasing interfacial shear strength, but decreases after the peak at $\tau_i=20.4\text{MPa}$. The coefficient of variation shown in open triangles decreases up to $\tau_i=23.3\text{MPa}$ and then increases abruptly. It is predicted from both of the behaviors that there is an optimum interfacial shear strength which improves the strength and reliability of the composite around $\tau_i=20\text{MPa}$. The shear strength of epoxy is estimated to be 26.3MPa according to Von Mises' criterion. Figure 4 also implies that an optimal interfacial shear strength introduced in the above could be slightly less than 26.3MPa . Note that the averages and coefficients of variation result in almost the same values for levels of $\tau_i=29.1\text{MPa}$ and more. This is because matrix fracture, assumed to be a deterministic phenomenon, governs most of the damages following fiber-breaks.

In Fig.4(a) and (b) the effect of random interfacial shear strength is additionally indicated (solid squares). It is implied that the interfacial shear strength is a random variable with a relatively large variation [9]. So, random interfacial shear strengths were assigned to all the interface elements, on the condition that the interfacial shear strength obeys a 2-parameter Weibull distribution. The Weibull shape parameter was assumed to be 2.5, in order to express a large variation. As the representative interfacial shear strength value in plotting the results, 'median' was selected. Since a median is a function of the Weibull scale parameter, composite strengths with random interfacial shear strengths were simulated by changing this parameter. In Fig.4(a) the average strength shown in solid circles gradually increases with increasing the interfacial shear strength (i.e. the median, τ_M) in the similar way to that in the constant interfacial shear strength, and the peak is indicated at $\tau_M=17.5\text{MPa}$. In Fig.4(b) the minimum of the coefficients of variation is also seen in at $\tau_M=17.5\text{MPa}$. The both statistics are inferior to the peak and minimum given in the constant interfacial shear strength. However, this inferiority is reversed at $\tau_M=29.1\text{MPa}$ and 35.0MPa .

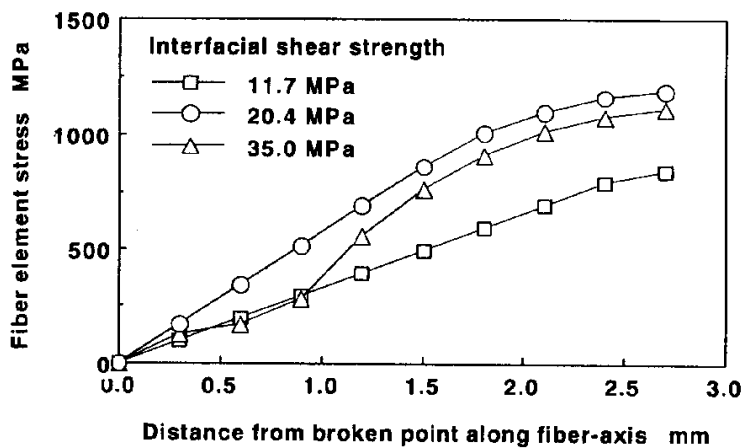
Stress distributions around a broken fiber element

It is considered that stress-strain behaviors and strengths of the composite are closely related with the degrees of matrix and interfacial damages following fiber breaks. Figure 5 shows the fiber stress distributions around a broken fiber element simulated for $\tau_i=11.7, 20.4$ and 35.0MPa , on the condition of the constant interfacial shear strength. In the figure the fiber element, fifth from the left-hand and tenth from the fiber end, was broken intentionally at the fiber stress of 1960MPa . Figure 6 shows the damage states of the matrix and interface obtained in the above simulations. The stress distributions on the fiber elements adjacent to the broken element are shown in Fig.5 (a), in which the largest stress acts on the nearest fiber element. The degree of the stress concentration depends largely on the interfacial shear strengths. That is to say, the strongest bond, i.e. $\tau_i=35.0\text{MPa}$, propagates matrix fractures into the surrounding matrix elements, as shown in Fig.6(c), and gives the largest stress concentration. On the other hand, the lowest interfacial shear strength, i.e. $\tau_i=11.7\text{MPa}$, promotes large-scale debonding, as shown in Fig.6(a), and gives the lowest stress concentration, as shown in Fig.5(a). Figure 5(b) shows the stress distributions of fiber element along the broken fiber. Since in $\tau_i=35.0\text{MPa}$ the load-carrying capacity of the broken fiber is reduced, particularly in the region where the matrix fractures occur, the stress recovery is delayed. The weakest bond, i.e. $\tau_i=11.7\text{MPa}$, yields the poorest load-carrying capacity for the broken fiber, due to large-scale debonding. The intermediate value for bond strength, i.e. $\tau_i=20.4\text{MPa}$, yields small-scale debonding and brings the highest load-carrying capacity. Figures 5 and 6 imply that there is an appropriate interfacial shear strength which can generate

a state with a relatively small stress concentration around broken fibers and a high load-carrying capacity for broken fibers. And the appropriate bond strength can possibly increase the composite strength, as shown in the previous section. Such a relation between composite strength and matrix damage is verified in the experiment in which the effect of interfacial bond on the tensile strength of a boron/ epoxy composite is investigated [2].



(a) Stress concentration on fiber elements perpendicular to fiber-axis



(b) Stress recovery of broken fiber element along fiber-axis

Fig.5. Fiber stress distributions around a broken fiber element.

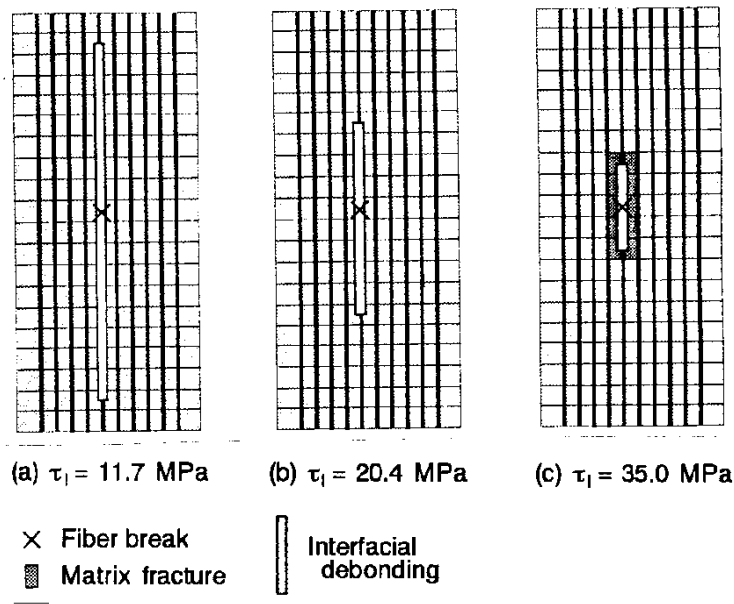


Fig.6. Damages of matrix and interface around a broken fiber element.

In Fig.4(a) and (b) random interfacial shear strengths decrease the optimum values for the average and coefficient of variation. It is predicted from the above stress distributions that the effect of large-scale debonding still remains due to its random nature, even if the median of interfacial shear strength increases. Therefore, the both statistics are not improved. Conversely, the effect of small-scale debonding still appears in the random interfacial shear strength with large medians, and therefore its averages and coefficients of variation are superior to those in the constant interfacial shear strength at $\tau_M = 29.1$ MPa and 35.0 MPa, respectively.

DISCUSSION

It was shown that the small and large interfacial shear strengths cause large-scale debonding and matrix fracture, respectively, and they both reduced the average composite strength. On the other hand, the intermediate values of interfacial shear strengths resulted in increased average strength. However why do the interfacial shear strengths increasing the average yet also produce the low coefficients of variation? The author considers that the strength and reliability of fibrous composites is closely related with damage accumulation up to the maximum stress, which in this study is equivalent to the number of broken fiber elements. For example, in Fig.3(a), (b) and (c) these numbers are 1, 2 and 1, respectively (referred to as "i-break"). Figure 7 shows the ratio of the number of broken fiber elements to the total number of simulations versus the constant interfacial shear strength. In the present simulation most of composites indicated 1-, 2- or 3-break, and four or more breaks was not a major figure (in any case approximately 1 to 3 %). The transition of the ratio is comparable to that shown in Fig.4. That is to say, the ratio of 1-break, non-cumulative failure mode, shows the minimum value at $\tau_i = 17.5$ MPa, and increases up to around 0.5 with an increase in interfacial shear strength. On the other hand, the ratio of 3-break or more, cumulative failure mode, behaves to be contrary to the case of 1-break. Namely, this ratio gives the peak at $\tau_i = 17.5$ MPa, and then decreases to

a value less than 0.2 and shows almost a constant. In the case of 2-break, intermediate failure mode, the ratio shows approximately a constant, though it keeps a slightly higher level at $\tau_i=11.7$ MPa to 23.3 MPa. Such a correspondence to Fig.7 tells us that a composite with large-scale debonding and matrix fracture yield a smaller number of fiber breaks than a composite with small-scale debonding. If failure of the weakest fiber in a composite immediately leads to composite fracture without accumulation of fiber breaks, the variability in composite strength will reflect that in fiber strength and represent an upper bound^{*1}. In other words a less cumulative failure mode will approach to this degree of scatter. Therefore both small and large interfacial shear strengths induce significant scatter in composite strength. On the other hand, more cumulative fiber breaks further increases the stress level, so that the strength distribution of survival fibers would shrink in width toward the upper side. The shrinkage might be concerned with decreasing a scatter in composite strength. Such a situation accompanied with the more cumulative fiber breaks is generated by small-scale debondings, and therefore contribute to improving the strength and reliability of composites.

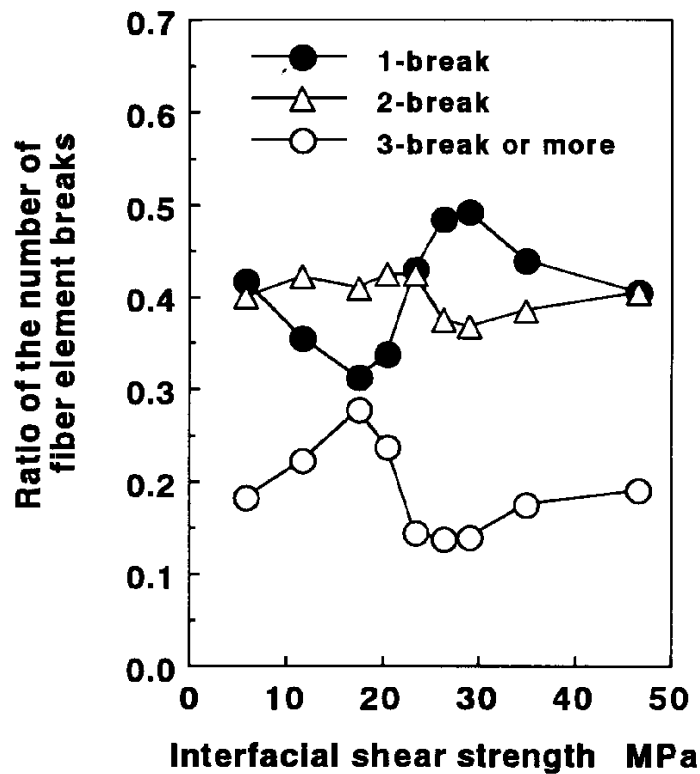


Fig.7. Ratio of the number of broken fiber elements to the total number of simulations vs. interfacial shear strength.

CONCLUSION

A Monte-Carlo simulation technique based on a finite element method was developed in order to uncover the effect of interfacial shear strength on the tensile strength and reliability of fibrous composites. In the simulation a boron/epoxy monolayer composite with ten fibers was

modeled, and five hundreds simulations were carried out using various interfacial shear strengths. The main results of this work were as follows:

(1) The interfacial shear strength value which increased the average strength of the composites corresponded to the value which decreased their coefficient of variation. This implied an existence of an optimum value of interfacial shear strength which can increase the strength and reliability. This value was estimated to be slightly less than the matrix shear strength.

(2) The simulated strength and reliability was closely related with the degree of matrix damage and its type following a fiber break. Large-scale debonding and matrix fracture reduced the number of fiber breaks accumulated up to the maximum achieved stress, and decreased the strength and reliability. On the other hand, small-scale debonding promoted comparatively the cumulative effect of fiber breaks and play a key role in increasing composite strength and reliability.

REFERENCES

1. Gatti, A., Mullin, J. V. and Berry, J. M., "The role of bond strength in the fracture of advanced filament reinforced composites", ASTM STP 460 , 1969, pp. 573-582.
2. Mullin, J. V., "Influence of fiber property variation on composite failure mechanisms", ASTM STP 521 , 1973, pp. 349-366.
3. Maekawa, Z., Hamada, H., Yokoyama, A., Lee, K. and Ishibashi, S., "Reliability evaluation on mechanical characteristics of CFRP", Proc. 6th Int. Conf. Mechanical Behavior of Materials, Vol. 1, 1991, pp. 677-682.
4. Ochiai, S. and Osamura, K., "Influences of matrix ductility, interfacial bonding strength, and fiber volume fraction on tensile strength of unidirectional metal matrix composite", Metall. Trans. A, Vol. 21A, 1990, pp. 971-977.
5. For example, Hull, D., "An Introduction to Composite Materials", Cambridge, 1981.
6. Hedgepeth, J. M., "Stress concentrations in filamentary structures", NASA Tech. Note, D-882, 1961, 1-30.
7. Mandel, J. A., Pack, S. C. and Tarazi, S., "Micromechanical studies of crack growth in fiber reinforced materials", Eng. Frac. Mech., Vol. 16, 1982, pp. 741-754.
8. Yamada, Y., Yoshimura, N. and Sakurai, T., "Plastic stress-strain matrix and its application for the solution of elastic-plastic problems by the finite element method", Int. Mech. Sci., Vol. 10, 1968, pp. 343-354.
9. For example, Netravali, A. N., Henstenburg, R. B., Phoenix, S. L. and Schwartz, P., "Interfacial shear strength studies using the single-filament-composite test", Polymer Compo., Vol. 10, 1989, pp. 226-241.

*1 If a composite consists of N fibers and the fiber strength follows a 2-parameter Weibull distribution, the distribution function for the weakest fiber strength is given as the minimum distribution of N Weibull distributions, i.e. the first order statistic. This form is also a 2-parameter Weibull distribution, and the shape parameter agrees with that in its population.

FIBRE/MATRIX ADHESION IN THERMOPLASTIC COMPOSITES: IS TRANSCRYSTALLINITY A KEY?

Andrew Beehag and Lin Ye

Centre for Advanced Materials Technology, Department of Mechanical and Mechatronic Engineering, The University of Sydney, NSW, 2006, Australia

SUMMARY: Single fibre pull-out specimens with carbon fibres (AS4, T300, T700, T800) embedded in PEEK or PPS matrix were produced using a hot stage. Transcrystallinity, or the formation of row nucleated crystalline matrix cylindrites, was induced through fibre shearing during matrix recrystallisation, resulting in the formation of a banded crystalline matrix structure. The interfacial shear strength has been evaluated to study the influence of transcrystallinity on fibre/matrix adhesion of thermoplastic composites. Transcrystallinity was found to have little or no positive influence on the interfacial shear strength of CF/PEEK systems, and a negative influence on CF/PPS systems. Under these circumstances, the merit of inducing transcrystallinity in composite systems should be reassessed.

KEYWORDS: transcrystallinity, fibre/matrix interface, matrix morphology, interfacial shear strength, PPS, PEEK, thermoplastic composite

INTRODUCTION

Studies of the region between the fibre and matrix of a composite system, known as an interface or interphase, are of major interest in the determination of composite properties. The strength of a composite is dependent on the properties of its component matrix and reinforcing fibre, but importantly it is also a product of the ability to transfer stress between the fibre and matrix. Therefore an understanding of the interaction between fibre and matrix is essential to evaluation and optimisation of composite properties. Much of the work on semicrystalline thermoplastic composite interfaces has concerned the formation of transcrystalline layers around the reinforcing fibres. These layers are created through closely spaced nucleation on the reinforcing fibre [1], creating cylindrites around the reinforcing fibre. The methods of processing that will induce transcrystalline zones around single fibres has been very well documented, particularly for GF/polypropylene composites [1-2], either with shearing of the fibre or with the fibre undisturbed [3]. However, it was evident in the literature that the effects of the transcrystalline matrix structure on stress transfer mechanisms was not clearly understood.

In the present work, the interfacial shear strengths were studied using single fibre pull-out tests for PEEK and PPS polymer with four different types of carbon fibres, namely AS4, T300, T700 and T800. The single fibre pull-out specimens were produced with and without transcrystalline layers. Effects of transcrystalline and non-transcrystalline matrix structures on pull-out strengths are investigated, and discussed in terms of their importance to bulk composite properties.

SPECIMEN PREPARATION AND TESTING METHOD

A schematic of the single fibre pull-out specimen, containing a carbon fibre (Hercules AS4, or T300, T700 and T800 from Torayca) and a semicrystalline matrix (PEEK or PPS) is shown in Fig. 1. Filaments of PEEK matrix were obtained, separating them from commingled yarn CF/PEEK (supplied by BASF), with a diameter of approximately 30 μm . PPS fibres were obtained by melting PPS powder (supplied by Phillips Petroleum), and spinning filaments of a diameter between 20 μm and 50 μm from the just-molten liquid with a scalpel blade. One matrix filament was placed on one half of a glass slide, with a single carbon fibre attached to the other half with cyanoacrylate adhesive. The two halves of the slide were then placed adjacent to one another, with the carbon fibre placed across and perpendicular to the matrix filament. A glass cover slip was then placed over the fibre and matrix. A Mettler FP82 hot stage, controlled by a Mettler FP90 central processor, was used to heat the specimen to its processing temperature, where the carbon fibre becomes embedded in the matrix which subsequently holds the fibre at its recrystallisation temperature.

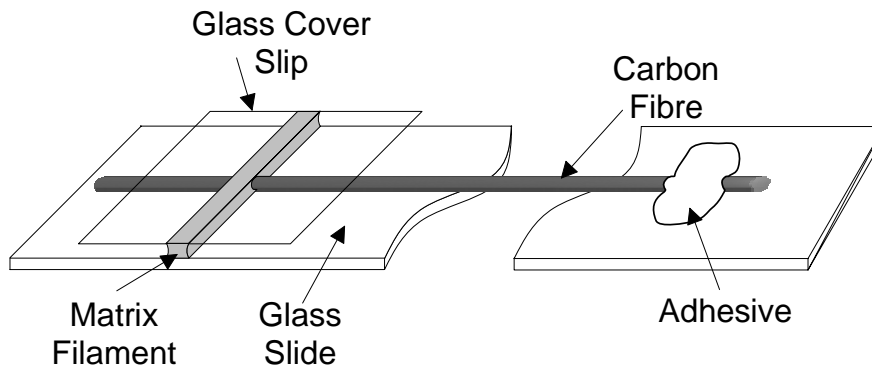


Fig. 1: Schematic of specimen for single fibre pull-out test.

Ten specimens of each fibre/matrix system were produced with or without transcrystallinity, respectively. For the CF/PEEK systems, pull-out specimens were heated to 375°C, held for 15 minutes, then cooled at 20°C/min to a recrystallisation temperature of 310°C, creating the normal matrix morphology without transcrystallinity. Specimens with transcrystallinity were produced through slightly pulling the fibre at the beginning of the recrystallisation period. Similarly the CF/PPS pull-out specimens were produced, holding at a melt temperature of 320°C for 10 mins with a recrystallisation temperature of 240°C. Transcrystalline CF/PPS pull-out specimens followed the same processing method, with a slight pulling of the fibre at 250°C during the cooling stage. After cooling the single fibre pull-out specimen to ambient temperature, the fibre was pulled out of its surrounding matrix at a speed of 0.4 mm/min using an Instron 5567 machine with a 2.5N load cell. After testing, the embedded length of the fibre was measured using an image analysis system attached to a Leica DM-RXE microscope. The interfacial shear strength (IFSS) was calculated as

$$IFSS = \frac{P}{2\pi rl} \quad (1)$$

where P is the maximum load, r the fibre radius and l the embedded fibre length.

EXPERIMENTAL RESULTS

The formation of the transcrystalline layer for an AS4/PEEK single fibre pull-out specimen is shown in partly cross-polarised light micrographs (Figs. 2a-c). Upon reaching the recrystallisation temperature of 310°C, the fibre was pulled approximately 15 µm, and a bright band appeared around the carbon fibre (Fig. 2a). The orientation of polymer chains caused by the shearing stress appears to increase the transmissibility of light, giving a whitened region in the transmission light micrograph. The transcrystalline layer then continued to grow (Fig. 2b) with time. Eventually the banded formation of the transcrystalline layer can clearly be identified, as described by Varga and Karger-Kocsis [1] for glass fibre/polypropylene systems. With increased holding time, crystalline structures began to form in the bulk of the PEEK matrix (Fig. 2c). However, in this study the formation of spherulites in the PEEK was restricted by the processing temperature of 375°C (the maximum temperature of the Mettler FP82 hot stage). Rather than the near-spherical crystalline spherulites traditionally associated with semi-crystalline polymers, the PEEK forms into highly axial, sheaf-like crystallites. Jar et al [5] found that PEEK processed at a temperature less than 395°C formed a densely nucleated matrix, and subsequently proposed that the formation of 1-2 µm sheaves of PEEK results from a melting temperature lower than 395°C, above which the self-seeding effect of PEEK matrix is removed. The cross-polarised light micrograph of the transcrystalline AS4/PEEK pull-out specimen shown in Fig. 3a clearly illustrates a prominent banded structure. However, the size of the transcrystalline layer is quite small compared to equivalent structures formed in glass fibre/polypropylene systems [1]. It is presumed that the low processing temperature of the specimen (375°C) promotes the fast formation of crystalline structures in the bulk matrix, limiting the size of growth of the transcrystalline layer.

A similar process for the formation of the transcrystalline layer for a T800/PPS single fibre pull-out specimen is shown in Figs. 2d-f. The bright band surrounding the carbon fibre after shearing (Fig. 2d) is clearer in PPS than the PEEK, due either to the darker colour of the PPS matrix or a more ordered molecular chain arrangement on shearing. Spherulites developing in the PPS matrix (Fig. 2f) are randomly nucleated ball-shaped formations, rather than the sheaf formation found in the AS4/PEEK specimens. The cross-polarised light micrograph in Fig. 3b clearly illustrates the transcrystalline layer in T800/PPS pull-out specimens. However, the transcrystalline zone in T800/PPS is less clear than the equivalent PEEK structure after processing.

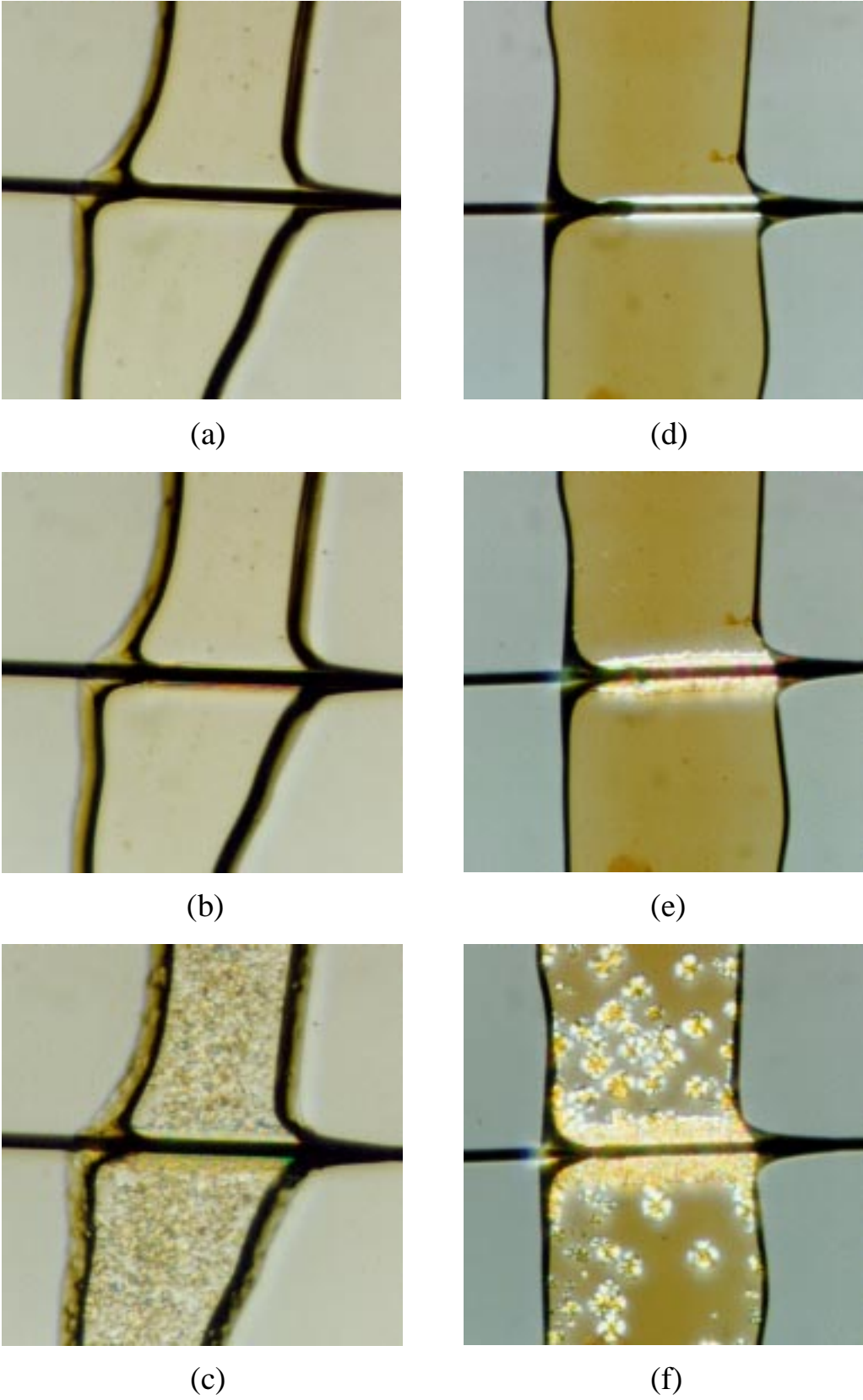
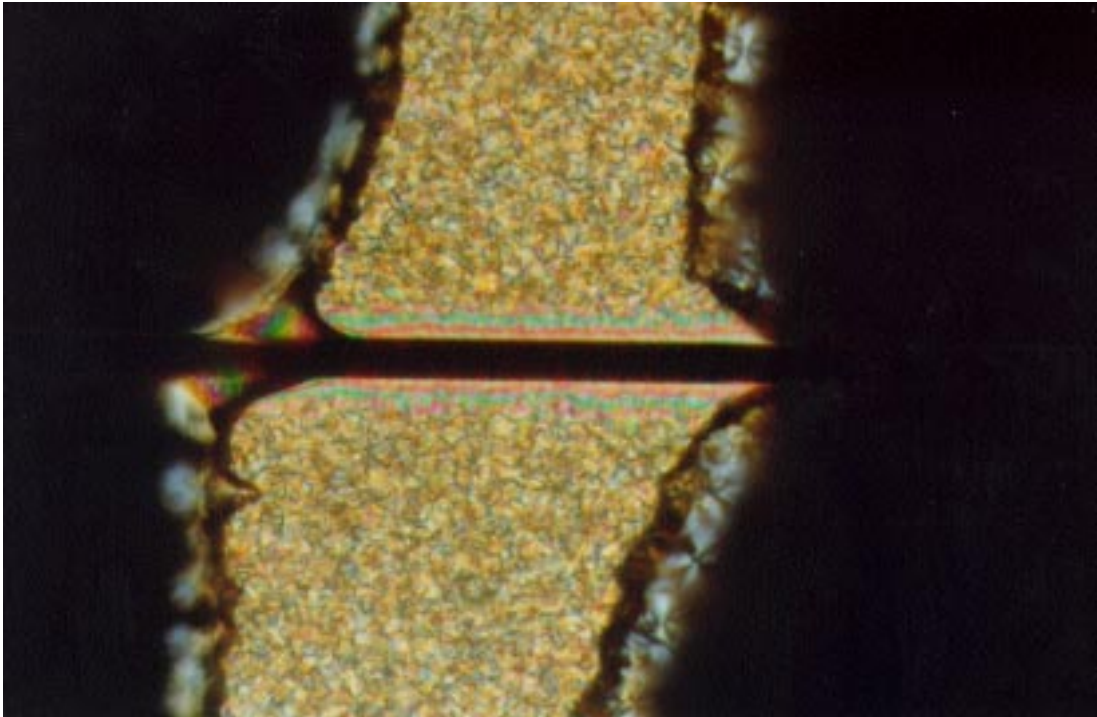
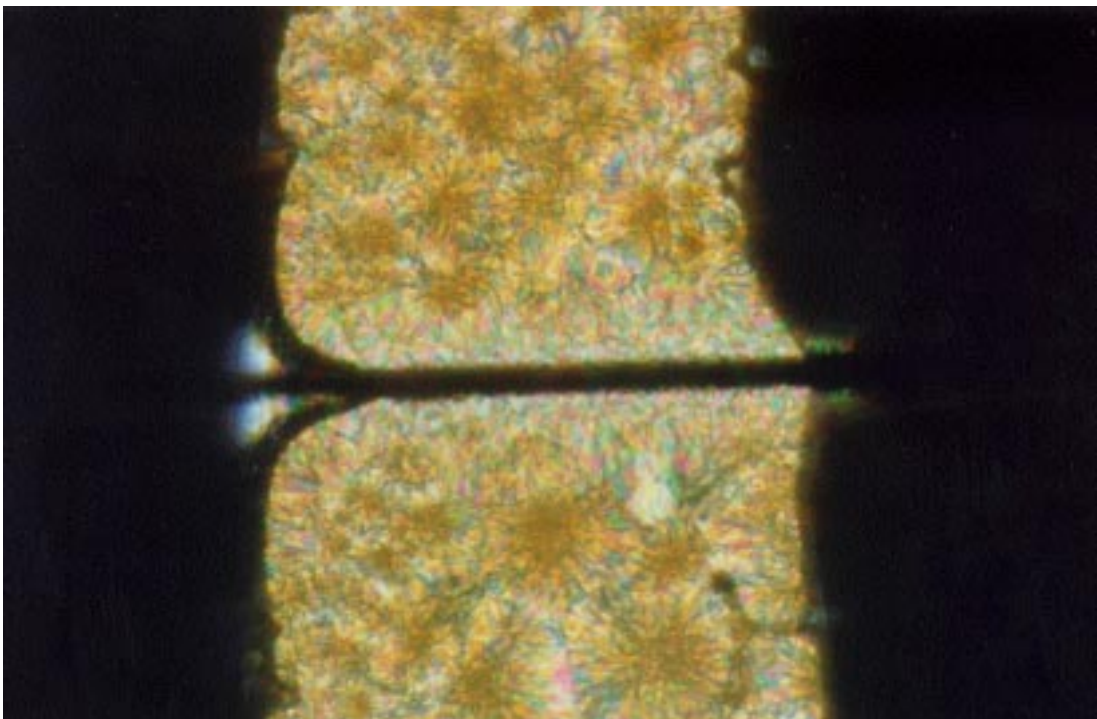


*Fig. 2: Growth of transcrystalline layer:
(a) - (c) for AS4/PEEK, and (d) - (f) for T800/PPS.*



(a)



(b)

Fig. 3: Cross-polarised micrograph of transcrystalline pull-out specimens: (a) AS4/PEEK and (b) T800/PSS.

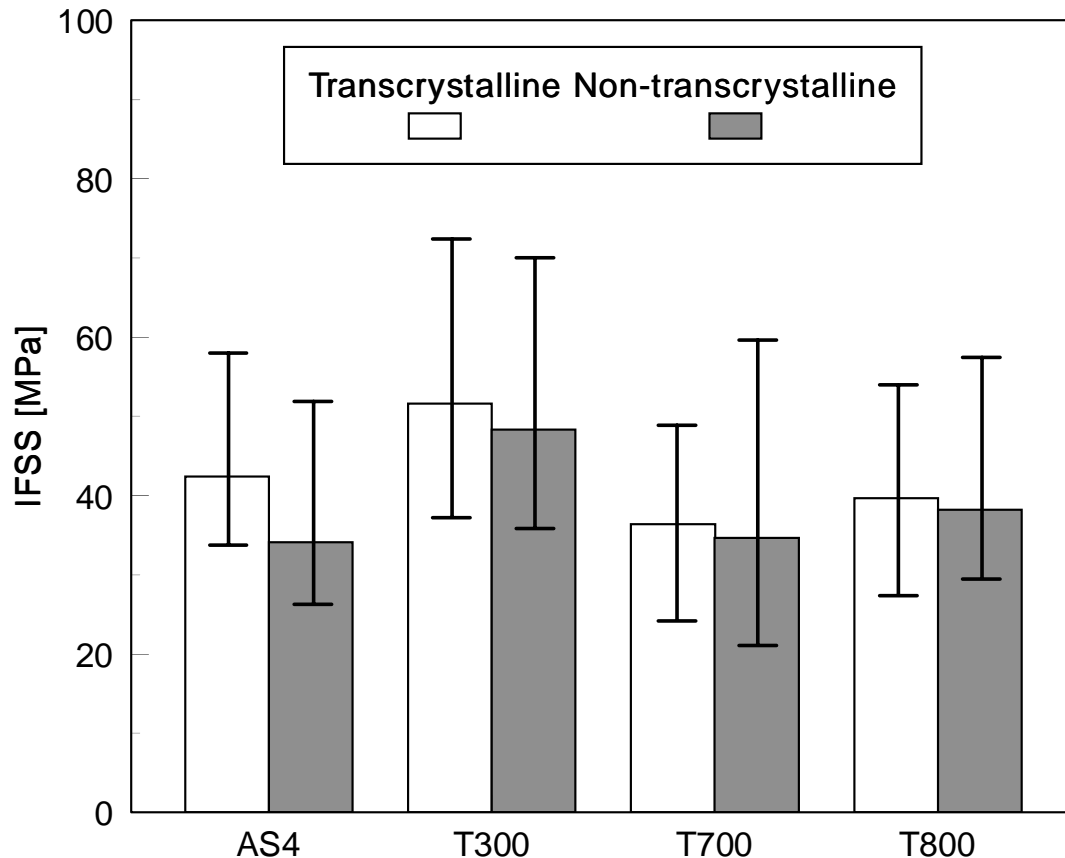


Fig. 4: Interfacial shear strength of different carbon fibres with PEEK.

The interfacial shear strengths (IFSS) of AS4, T300, T700 and T800 carbon fibres embedded in PEEK matrix with and without transcrystallinity are shown in Fig. 4. It should be noted that comparisons between specimens of different fibre types may not be valid, as an adequate control could not be maintained over variables such as humidity between fibre groups. Testing of transcrystalline and non-transcrystalline specimens was alternated for each fibre group, and therefore only comparisons between the transcrystalline and non-transcrystalline specimens should be made. The effect of transcrystallinity on the IFSS of the embedded fibre is only apparent in the AS4 fibre specimens, with transcrystalline specimens showing a higher IFSS than non-transcrystalline specimens. There appears to be some similar influence in T300 fibre specimens, but this is not significant enough to draw conclusive results. Also, while on average the transcrystalline T700 and T800 specimens had higher IFSS than the non-transcrystalline specimens, the scatter of each shows that no inference can be drawn from these results. The influence of different fibre type should also be considered. Both the AS4 and T700 are pitch-based carbon fibres, and have a very smooth fibre surface. T300 and T800 fibres, on the other hand, are PAN-based and have a ribbed surface. However, the above aspects do not favour one carbon fibre type with respect to the pull-out behaviour of transcrystalline and non-transcrystalline specimens. It is noted that AS4 fibre and T300 fibres are low in modulus compared to T700 and T800 fibres. Also, the radius of AS4 and T300 fibres, at 7 μm each, gives a higher surface area than the T700 fibre (6 μm) or T800 fibre (5 μm).

The IFSS for AS4, T300, T700 and T800 carbon fibres embedded in PPS matrix with and without transcrystallinity are shown in Fig. 5. It should again be stressed that comparisons between the IFSS of different fibre types may be invalid. However there is an overall trend to

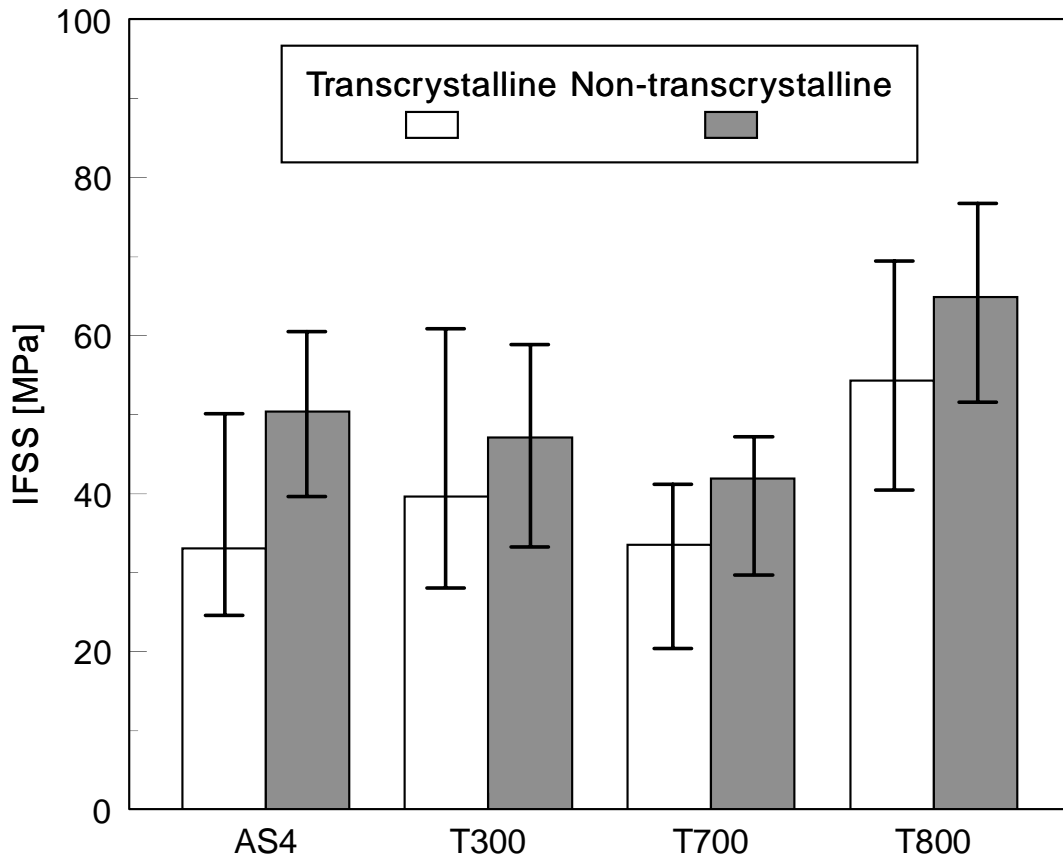


Fig. 5: Interfacial shear strength of different carbon fibres with PPS.

lower IFSS with transcrystalline formations in all fibre types. This suggests that transcrystalline formations of PPS around carbon fibres do not improve IFSS. Studies by Moon [4] suggest that differing levels of contraction stress exist around the fibre with different crystalline polymer formations. The transcrystalline zone, which forms almost immediately around the fibre, will impose a different constraint condition around the fibre to a randomly nucleated matrix, creating different levels of contraction stresses. Comparing the influence of contraction stresses on CF/PPS with CF/PEEK specimens is difficult, due to the markedly different formation of crystal structure in the PEEK matrix with the chosen processing conditions. Therefore, it not possible to verify the influence of this mechanism with the current data.

It is fair to state, given the apparent influence of transcrystalline formations on the stress transfer mechanism of model single fibre composites, the influence of transcrystallinity on the properties of bulk composites may be limited. Furthermore, special processing conditions may be required to induce transcrystallinity in bulk composites. Specifically, the requirement of inducing relative shear between fibre and matrix, when fibres in a bulk composite are very closely packed, may be very difficult to achieve, and add substantially to the processing costs, without tangible benefits. Under this circumstance, more positive properties of transcrystalline matrix structures will be required to justify a very specialised processing methodology.

CONCLUSION

The formation of transcrystalline zones around carbon fibres has been studied in PEEK and PPS matrices, and the interfacial shear strengths (IFSS) of AS4, T300, T700 and T800 carbon fibres have been evaluated for PEEK and PPS matrix, with and without transcrystallinity. The formation of the transcrystalline zone, which results from a dense concentration of nucleation sites near or along the carbon fibre surface after pulling, was shown to have a banded formation in both the PEEK and PPS matrices, being similar to GF/PP systems shown in previous studies. Pull-out testing of carbon fibres from PEEK and PPS matrices has shown that transcrystallinity is not significant in improving IFSS. In fact, pull-out specimens for PPS appear to have decreased in IFSS as a result of the presence of transcrystallinity. Special processing conditions of temperature and holding time had to be adopted to form transcrystalline zones in these model single fibre composites, and this would probably involve additional expense in processing. Also, the likelihood of transcrystalline zone formation in bulk composites is low, as relative shear may be needed between the reinforcing fibre and its surrounding matrix during processing.

In conclusion, attention to the matrix morphology at the fibre interface does not appear to be rewarded with increased interfacial shear performance, which is critical to the overall mechanical performance of the bulk composite. Further work would need to be conducted to identify more positive aspects of transcrystalline formations, before transcrystallinity is adopted as a matrix microstructure to improve the composite performance.

ACKNOWLEDGMENTS

Thanks are due to BASF, Germany, Torayca, Japan, and Phillips Petroleum, Singapore, for supplying the testing materials. Lin Ye thanks the Australian Research Council (ARC) for supporting this study with a large research grant (AB-9332172). Andrew Beehag is supported by a postgraduate scholarship from the Department of Mechanical and Mechatronic Engineering, the University of Sydney, and an ARC postgraduate supplementary scholarship.

REFERENCES

1. Varga J., Karger-Kocsis J., "Direct evidence of row-nucleated cylindritic crystallization in glass fiber-reinforced polypropylene composites", *Polymer Bulletin*, Vol. 30, 1993, pp. 105-110.
2. Gray D.G., "Transcrystallisation induced by mechanical stress on a polypropylene melt", *Journal of Polymer Science - Polymer Letters Edition*, Vol. 12, 1974, pp. 645-650.
3. Hsiao B.S., Chen J.H., "Study of transcrystallization in polymer composites", *Materials Research Society Symposium Proceedings*, Vol. 170, 1990, pp. 117-21.
4. Moon C.-K., "The effect of interfacial microstructure on the interfacial strength of glass fiber/polypropylene resin composites", *Journal of Applied Polymer Science*, Vol. 54, 1994, pp. 73-82.
5. Jar P.-Y., Cantwell W.J., Davies P., Kausch H.-H., "Effect of forming temperature on the mode I delamination resistance of carbon fibre-poly(ethylethyl ketone)", *Journal of Materials Science Letters*, Vol 10, 1991, pp. 640-42.

TIME DEPENDENCY OF MICROCRACK INITIATION AND EVOLUTION IN INTERLAYER OF COMPOSITE

Y. Q. Sun and J. Tian

Laboratory for Nonlinear Mechanics of Continuous Media, Institute of Mechanics, Chinese Academy of Science, Beijing, 100080, China Northwest Institute of Textile Sci. & Tech., Xian, 710048, China

SUMMARY: Time dependency of microcrack initiating, growing and coalescing in a microregion within interlayer of fiber reinforced composite was investigated through Mode I loading ENF sample inside SEM. The results shown; under a constant load, with the duration of loading extended, microcrack initiated due to local tensile stress in the highly stressed area; microcrack growing and coalescing proceeded through damage localization in the sites of microcrack where there existed stress concentration, the manner of the process was jumping; the strain depended on the duration of loading, the manner of the strain increasing with time of holding was also jumping which corresponded to the remarkable microcrack coalescing.

KEYWORDS: time dependency, microcrack, initiation, evolution, shear strain, interlayer, carbon/epoxy composite

INTRODUCTION

Safe design and satisfactory service life demand intimate knowledge of the properties of the material being used. It has been well recognized that many mechanical and physical properties of fiber reinforced composites depend on those of each phase^[1], and are also controlled by fiber-matrix interface or interphase^[2]. The microscopic behavior of material in a crack tip process zone during loading is closely related with the macroscopic fracture performance of composite^[3,4,5]. Therefore, it is very important to have the better understanding of the micro- or meso-scopic behavior of the material in the zone that tends to involve the formation of a damage zone, and microcrack initiation, growth and coalescence in the zone.

With respect to fiber reinforced polymer based composite materials, the micro- or meso-scopic processes of the damage depend not only upon the stress

level, but also upon the duration of loading due to the viscoelastic nature of the polymer^[6,7,8]. The influence of stress on the microcracking behavior in crack tip damage zone has been reported previously^[4,5]. The objective of current work is to investigate the effect of the duration of loading on the microcrack initiating, growing and coalescing, and the time-dependency of shear strain, through focusing on a microregion in a crack tip damage zone within the interlayer of specimen loaded inside a scanning electron microscope (SEM).

EXPERIMENTAL PROCEDURES

Test Material

The test material used in this work was one of brittle systems, carbon epoxy composite AS4/3502. The carbon fiber AS4 has an average tensile strength of 520 ksi, and the matrix material epoxy 3502 is a highly crosslinked thermosetting resin. The glass transition temperature T_g of the AS4/3502 composite is 213°C.

Specimen Preparation

The miniature ENF specimens (30mm in length, 5mm in width, and 1mm in thickness) were cut from a eight ply laminate, with the fibers being parallel to the longitudinal direction of the sample. The precrack was made by inserting a 25 μm thick strip of Teflon between the center two plies during the panel making or by razor blade notching under a stereomicroscope afterwards. To obtain a good image which can show more details on material micro-appearance the specimen surfaces to be observed by SEM were ground, polished with alumina powder to 0.03 micron finish on an automatic polisher, cleaned ultrasonically, dried, and finally sputter coated with approximate 100 angstrom of a gold-palladium alloy.

Experimental Method

The Mode II fracture test was conducted inside a SEM equipped with a tensile stage and a load-displacement measuring system. The Mode II loading condition was accomplished by using a specially designed three point bend jig. The test was performed under displacement control. With this set up of the test, any microscopic behavior of material in the crack tip damage zone in an interlayer can be monitored and recorded at any moment during the test.

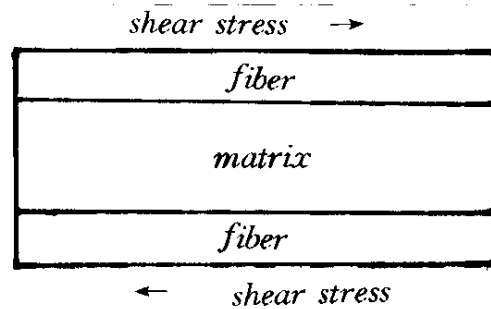
The specimen was incrementally loaded until a certain load level reached which was a little lower than the maximum level. Then the load level was kept approximately constant. A microscopic region in the crack tip damage zone was focused on which may be the location where the microcrack activi-

ties including the initiation, growth and coalescence of microcracks would be going on during the duration of loading. Several points were chosen in the microregion as reference points to measure the shear strain produced during the duration of loading. Several series of pictures showing microcracking occurred in the region of the damage zone were taken which corresponded to different span of loading.

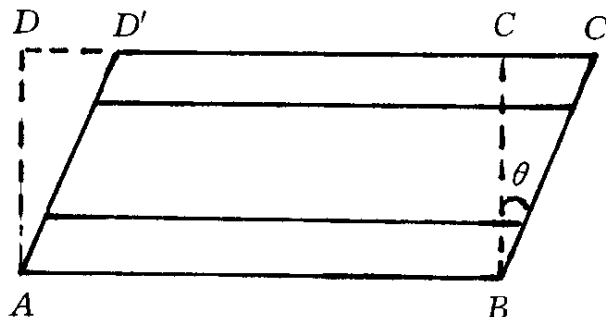
Shear Strain Measurement

The shear strain γ was calculated by measuring the displacement of the reference points. As show in Figure 1, the shear strain γ is clearly $\tan \theta$, i. e.

$$\gamma = \frac{CC'}{CB} = \tan\theta \tag{1}$$



(a)



(b)

Fig. 1: Shear strain measurement
 (a) original state, (b) after a span of duration

RESULTS AND DISCUSSIONS

Microcrack Initiating

Fig. 2 shows the microregion (or called domain) of a crack tip damage zone we had been focusing on, with the main crack tip being in the left side of the photo and between fibers. After 15 minute of holding a constant load, the first microcrack suddenly initiated in the region (Fig. 3a). As the duration of loading extended, the second and the third microcrack appeared in the right side of the first one (Fig. 3b). With the holding time further increasing, more microcrack initiated. The location and orientation of microcrack initiating are generally known to be random. But for a typical anisotropic material used here, the observation shown that the location and the orientation were depended on the local condition, i. e. , the boundary condition and the stress state. The microcracks tended to initiate in the central part of interlayer between fibers, and the preference sites were the highly stressed microarea where there was less submicrocracks generally. The orientation of microcracks initiated was about 45 degree with respect to the fibers.

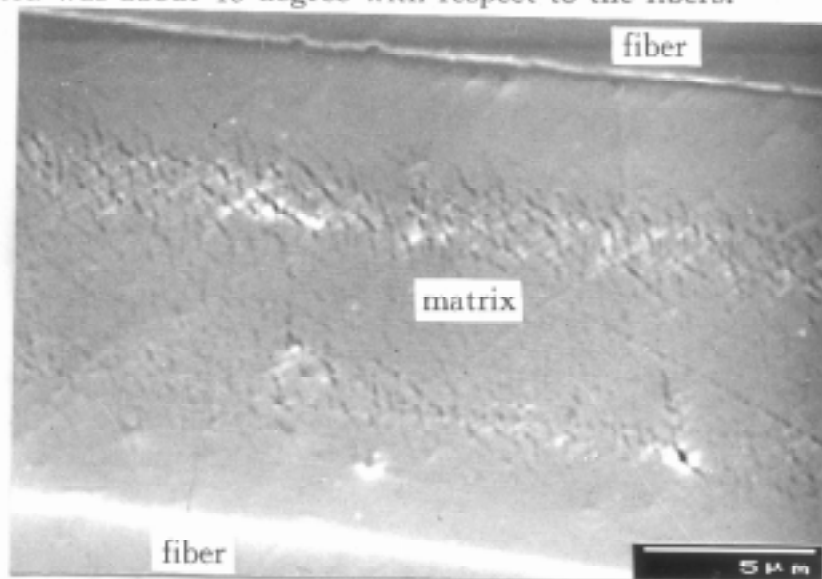


Fig. 2: Scanning electron micrograph showing a microregion of crack tip damage zone (before microcrack initiation)

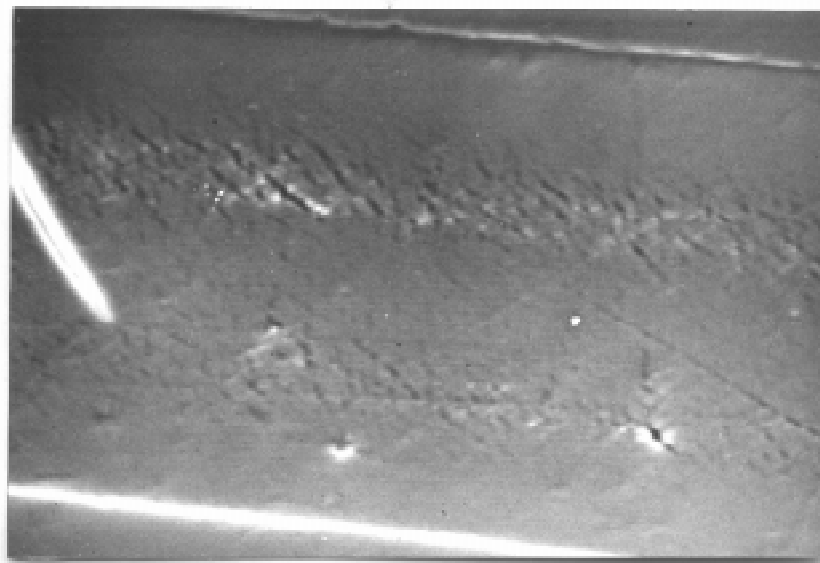
It was also noted that the tensile stress seemed to be the driving force causing the microcracks to initiate as shown in Fig. 3. Though the ENF sample sustained shear stress globally, tensile stress is locally present^[9]. When the tensile stress is equal to or higher than the bonding strength of material there, the microcrack would initiate.

From Fig. 2 and 3, it was very clear that microcrack initiation process require certain period of time. Under about a same load level, with the duration of loading increasing, the more microcrack initiated.

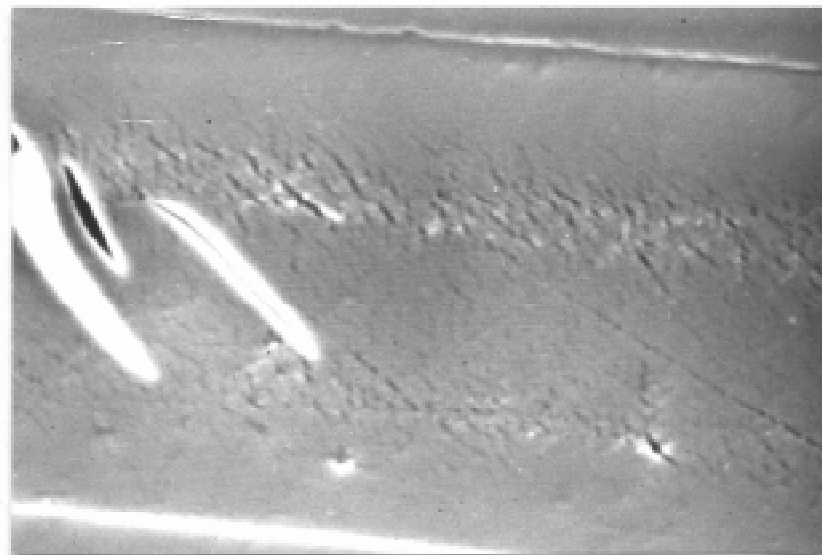
Growing and Coalescing of Microcrack

Fig. 4 through 6 show the evolution process of microcrack growing and coalescing related with duration of loading.

As indicated by the photos that with the hold time being extended (from 35 minutes to 115 minutes) the microcracks gradually grew bigger and bigger (Fig. 3 and 4) until they coalesced (Fig. 5). At the same time, new microcrack (number 4 and 5) initiated in the right side of the first 3.



(a)

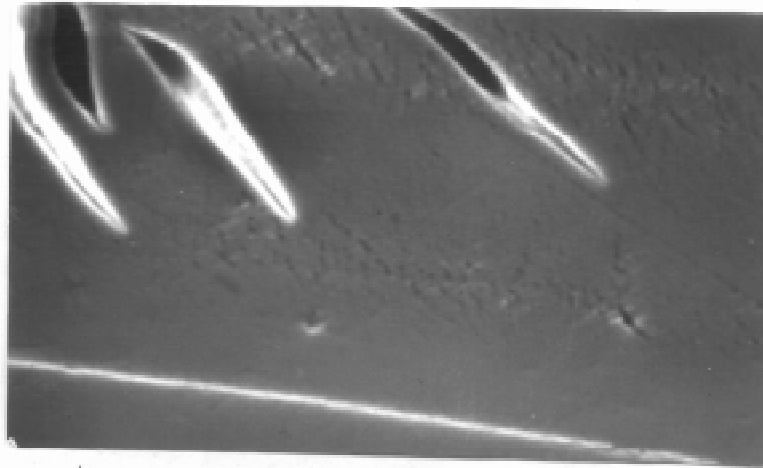


(b)

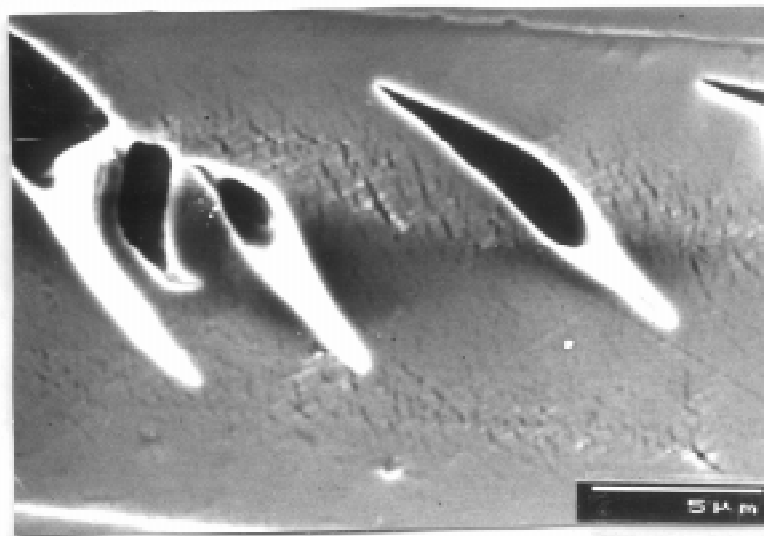
Fig. 3. Microcrack initiating
(a) after 30min, (b) after 35min

It was observed (Fig. 5, a, b and c) that the microcrack growing and coa-

lescing proceeded through damage localization in the certain portion of microcrack boundary where there existed stress concentration. It was also found that the manner of microcrack growing was jumping instead of smooth and steady.



(a)

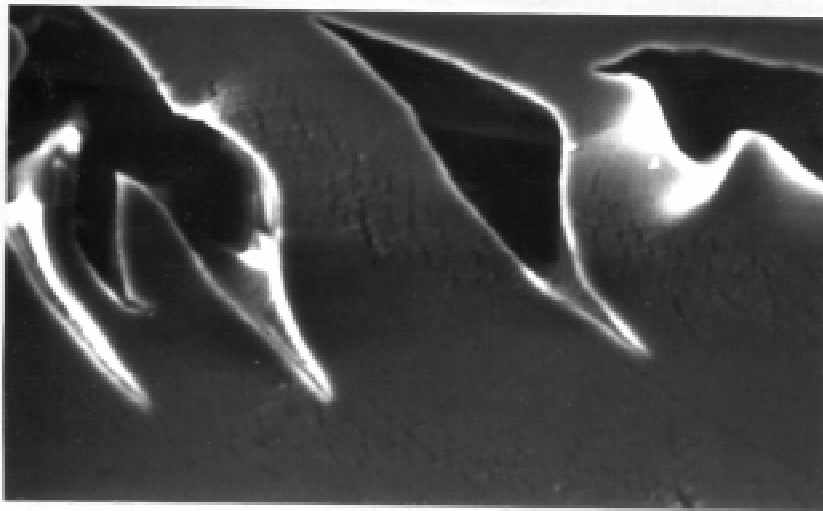


(b)

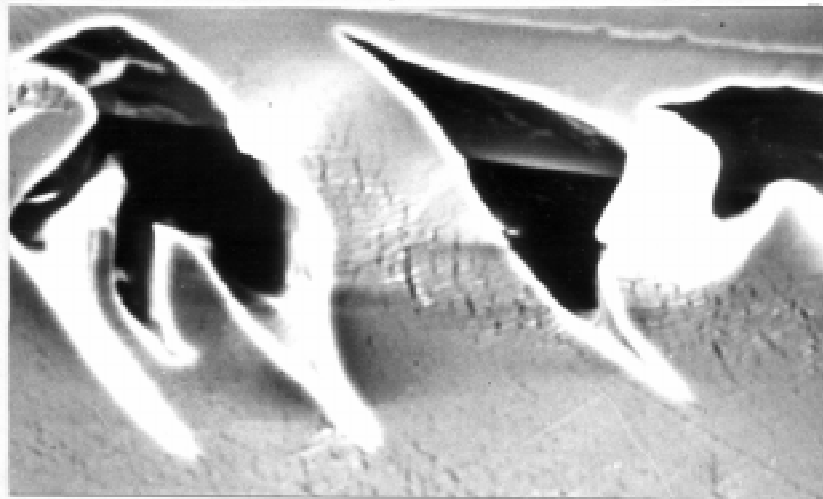
Fig. 4: Scanning electron micrographs showing the microcrack growing (a) after 45 min, (b) after 60 min

Time Dependency of Shear Strain

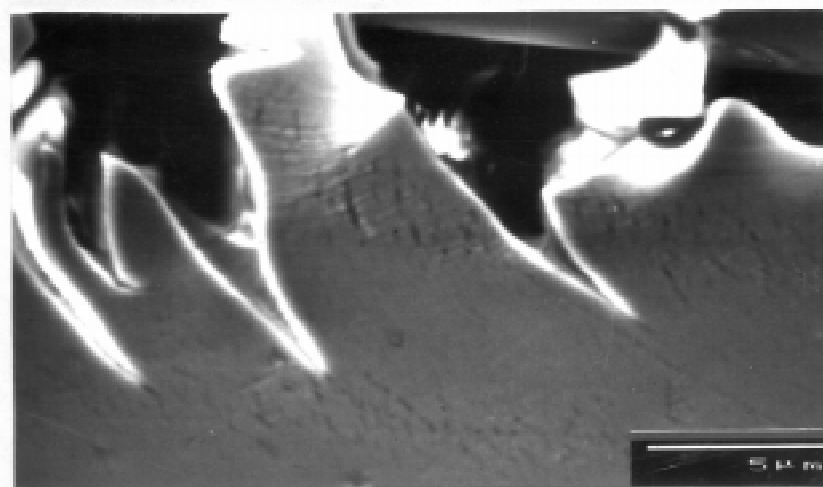
The shear strain of the material in a certain microregion depended not only on the stress level, but also on the duration of loading under a constant stress,



(a)



(b)



(c)

*Fig. 5: Scanning electron micrographs showing the microcrack coalescing
(a) after 70 min, (b) after 90 min, (c) after 115min*

the boundary condition of the region, etc., i. e.

$$\gamma = \gamma(\tau, t, b) \quad (2)$$

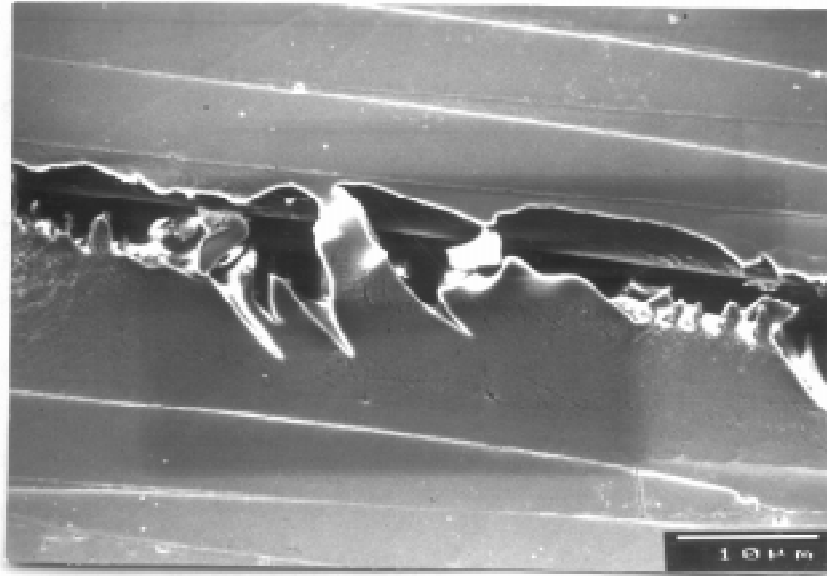


Fig. 6: Scanning electron micrograph showing the overview after the microcrack coalesced and precrack advanced

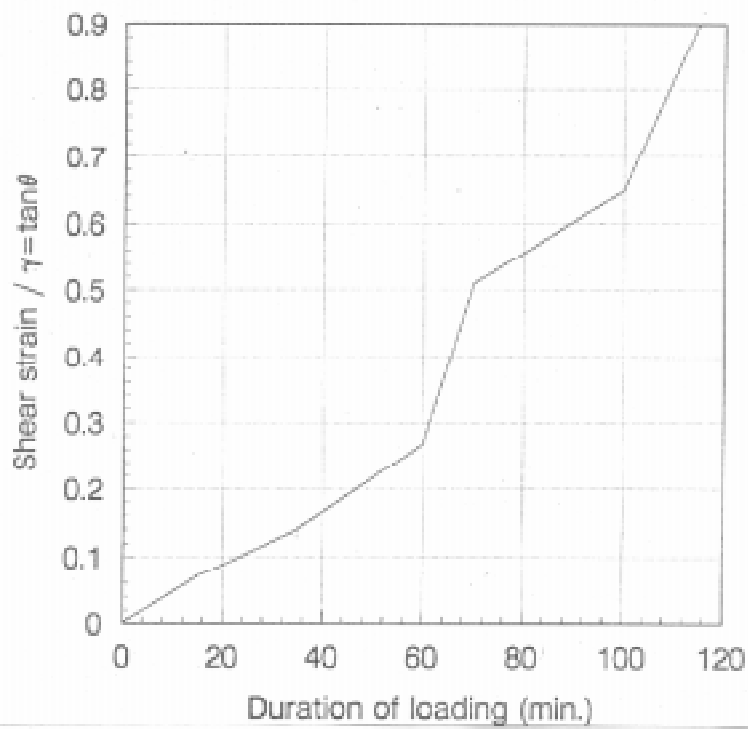


Fig. 7: The curve of duration/shear strain

Where the γ is the shear strain, and the τ , t , and b represent the shear stress, the duration of loading and the boundary condition respectively. For the polymeric material used in this work, the parameter time—the duration of loading is specially important due to the its viscoelastic nature.

The shear strains $\gamma = \tan\theta$ (Fig. 1) corresponding to each span of duration were measured based on the photos and calculated, as listed in table 1. The dependency of the shear strain on the time was illustrated in Fig. 7.

Table 1: Test data measured

code number of photo	duration of loading (min)	θ°	$\gamma = \tan\theta$
2	0	0	0
3	15	4	0
4	35	8	0.14
6	60	15	0.268
8	70	27	0.510
9	100	33	0.649
10	115	42	0.9

It can be clearly seen that the manner of strain increasing with holding time is also jumping which corresponded to the remarkable coalescing processes of the microcracks. It should be mentioned that the strains measured here actually consist of three parts; the elastic, the visco-elastic, and those caused by microcracking;

$$\gamma = \gamma_e + \gamma_{v-e} + \gamma_c \tag{3}$$

SUMMARY

Time dependency of microcrack initiation, growth and coalescence in an interlayer of fiber reinforced composite was investigated. Test results show; under a approximate constant mode II load, with the duration of loading extended,

1. the microcrack initiated due to local tensile stress in the highly stressed microarea where there less submicrocracks;
2. the microcrack growing and coalescing processes proceeded through damage localization in the location of microcracks where there existed stress concentration. The manner of the processes was jumping;
3. the shear strain depended on duration of loading under given loading and boundary conditions. The manner of strain increasing with time of hold-

ing was also jumping which corresponded to remarkable microcrack coalescing processes.

ACKNOWLEDGMENT

The financial support of the National Natural Science Foundation of China, and the Laboratory for Nonlinear Mechanics of Continuous Media, Institute of Mechanics, Chinese Academy of Science, is gratefully acknowledged.

REFERENCES

1. Krawczak, P. and Pabiot, J. , "Fracture Mechanics Applied to Glass Fiber/Epoxy Matrix Interface Characterization", *J. of Composite Materials*, Vol. 29, NO. 17, 1995, pp. 2230—2251
2. Ishida, H. (ed), "Controlled Interphases in Composite Materials" , Elsevier, New York, 1990
3. Mai, Y. W. , "Fracture Resistance and Fracture Mechanisms of Engineering Materials" , *Materials Forum*, Vol. 11. 1988, pp232—267
4. Sun, Y. Q. , Anderson, T. L. and Tian, J. , "In—situ Observatio of Delamination Fracture Text in Graphite/Epoxy Composite During Mode II Loading Inside a SEM" , *Proc. of ICCM—9*, 1993, Vol. 5, pp834—841
5. Sun, Y. Q, Tian, J. , Wang, J. B. and Anderson, T. L. , "In—situ SEM Study of Microcracking Behavior in Crack Tip Damage Zone of Polymer Matrix Composite" , *Proc. of ICCM—10*, 1995, Vol. 1, pp343—350
6. Yeow, Y. T, Morris, D. H. and Brinson, H. F. , "Time—Dependent Behavior of a Unidirectional Graphite / Epoxy Composite" , in *Composite Materials: Testing and design*, ASTM STP 674, S. W. Tsai, ed. 1982, pp 263—281
7. Crasto, A. S. and Kim, R. Y. , " Creep Behavior of High—Temperature Composites" , *Proc. of ICCM—10*, 1995, Vol. 4, pp423—430
8. Gau, U. , " Effect of Hydrothermal Aging on Bond Stress" , *Composites*, Vol. 25, No. 7, 1994, 609
9. Corleto, C. R. , Ph. D Dissertation, Texas A &. M University, 1991

INTERPHASE BETWEEN CARBON FIBRE AND THERMOTROPIC COPOLYESTER

T.W.Shyr¹, J.G. Tomka², and D.J. Johnson²

¹ *Department of Textile Engineering, Feng-Chia University, Taichung, Taiwan, R.O.C.*

² *Department of Textile Industries, Leeds University, Leeds, LS2, 9JT, U.K.*

SUMMARY : This work is concerned with the interphase between carbon fibre and vectra liquid crystal copolyester. Two grades of vectra copolyester were used. An unfilled standard vectra A950 was used as a matrix for a carbon fibre reinforced vectra copolyester model composite material. And vectra A230, containing short carbon fibres, was used for the preparation of extruded composite material. Crystallization behaviour of vectra A950 and vectra A230 was investigated by a differential scanning microscopy, and the model composite materials were prepared and observed using a hot-stage polarizing microscopy. Photographs obtained with crossed polars show that molecules of vectra copolyester in a mesophase is the tendency to be aligned along the flow direction and to be disturbed by obstacles such as carbon fibre. The fracture surface of the extruded composite material after a tensile failure was observed in a scanning electron microscopy. It reveals that a layer of vectra copolyester adheres to the pull-out carbon fibre. The layer thickness of vectra copolyester adhering to the pull-out carbon fibre is about 0.2 μ m. Transmission electron micrographs indicate that vectra copolyester is closely attached to the carbon fibre. Good adhesion between carbon fibre and vectra copolyester can be expected.

KEYWORDS: thermotropic liquid crystal copolyester, carbon fibre, interphase

INTRODUCTION

Thermotropic liquid crystal polymers can be melt-processable. HNA/HBA copolyester is an example which make the melting point in the range of 250~310 °C [1]. Therefore, they can be processed like regular thermoplastic engineering resins. Due to the advantage of easy processing using standard methods for thermoplastic polymers, low thermal shrinkage [2], low coefficient of thermal expansion, and excellent mechanical properties [1], it is anticipated that thermotropic liquid crystal polymers may possibly offer advantages as a thermoplastic matrix resin.

In the case of carbon fibre reinforcing semicrystalline thermoplastic polymers [3,4], the transcrystalline structure of the polymers is formed around the fibre at the suitable crystallization conditions. The chemical and physical structures of the thermotropic liquid crystal polymers are quite different from those of the conventional thermoplastic polymers. The interphase between fibre and thermotropic liquid crystal polymer could be different with

those between fibre and thermoplastic polymer. The work of the study was concentrated on the interaction between carbon fibre and thermotropic liquid crystal copolyester.

EXPERIMENTAL

Material

Two grades of vectra copolyesters, produced by Hoechst Celanese Company, were used. An unfilled standard vectra A950, supplied as cylindrical pellet about 2.5 mm in diameter and 3 mm in length, was used as a matrix for a single carbon fibre reinforced vectra copolyester model composite material. The inherent colour of as received polymer is uniform cream-brown. High modulus carbon fibre, HM-S Grail, supplied by Courtaulds PLC, was used to prepare model composite material. And a vectra A230 copolyester containing short carbon fibres was used for the preparation of extruded composite material. Vectra A230 is black in colour and in the form of spherical pellet about 3~4 mm in diameter. The density of vectra A950 and A230 are 1.40 g/cm^3 and 1.50 g/cm^3 , respectively.

Specimen Preparation and Characterization Techniques

Thermal properties of the materials were investigated with a Du Pont 910/990 differential scanning calorimetre (DSC). A hot-stage polarizing microscopy (HSPM) was used to make model composite materials and to observe the interaction between carbon fibre and vectra copolyester. A Leitz Laborlux 12 pol S polarized microscope with Linkam THMS 600 hot stage was used. Both DSC and HSPM were calibrated using In and Pb. Carbon fibre was placed between two films of vectra A950 as a sandwich. The model composites were made at a selected crystallization condition.

The extruded vectra A230 composite was obtained using a hydraulically operated rod spinner. The spinneret with 2 holes was used. Each hole is 0.50 mm in diameter and 5 mm in length. In this study, the extrudates produced at $305 \text{ }^\circ\text{C}$. The extrude was allowed to solidify under gravity.

The observation between carbon fibre and vectra copolyester after tensile failure was using a Cambridge stereoscan 150 scanning electron microscope (SEM) with a 300 series stage. The thickness of the specimen, which were for the observation of transmission scanning microscope (TEM), Jel 100CX TEM, is about 30~40 nm using an ultramicrotome (LKB Bromma 8800 Ultratome 3).

RESULTS AND DISCUSSIONS

Thermal Properties

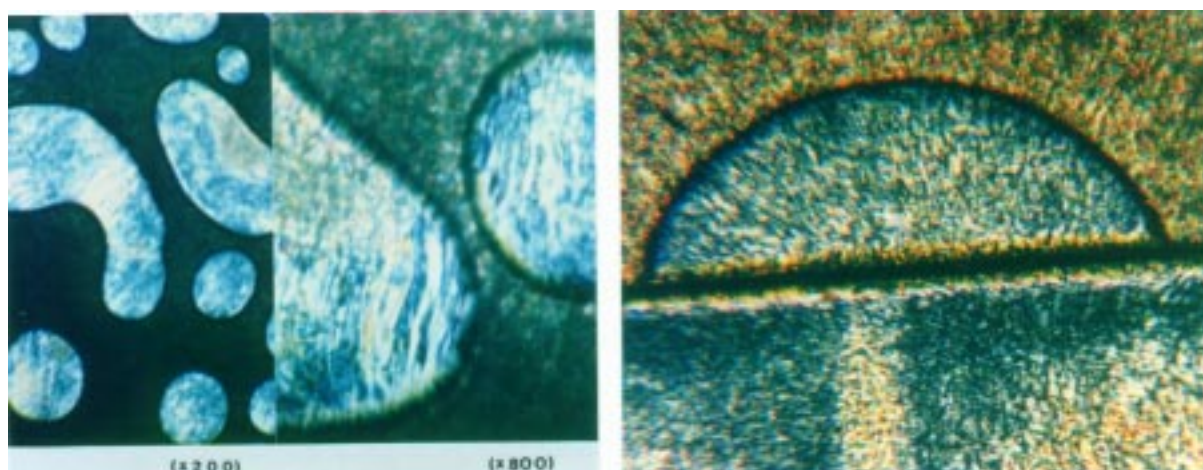
The studies of the melting and crystallization behaviour were undertaken with a DSC. From the DSC study, the peak temperature of the main endotherm of vectra A950 is $281 \text{ }^\circ\text{C}$. The end temperature of the endotherm of approximately $300 \text{ }^\circ\text{C}$. There is a smaller endotherm with a peak temperature of $182 \text{ }^\circ\text{C}$. After cooling from $350 \text{ }^\circ\text{C}$, the peak temperature remains at $281 \text{ }^\circ\text{C}$, but the end temperature is about $290 \text{ }^\circ\text{C}$. The secondary melting endotherm is absent. Crystallization behaviour was investigated by DSC after remelting at $350 \text{ }^\circ\text{C}$. At a cooling rate

of 20 °C/min vectra A950 shows an exotherm with an onset temperature of 244 °C and a peak temperature 239 °C. The melting and crystallization behaviours of vectra A230 are similar. The peak temperatures of the endotherm and the exotherm remain at 281 °C and 239 °C, respectively. The presence of carbon fibres in vectra A230 does not affect the crystallization behaviour of vectra copolyester.

Before observing single HM-S Grafil carbon fibre - vectra copolyester model composites on the HSPM, the crystallization behaviour of vectra A950 with HM-S Grafil carbon fibres was investigated by DSC technique as well. The sample was heated to 350 °C at 20 °C/min, held for 10 min, and then cooled at 80 °C/min. The DSC curve shows that the onset and the peak temperatures of the crystallization exotherm are 228 °C and 219 °C, respectively. The results are in agreement with those obtained for vectra A230 material under the same condition.

Polarizing Microscope Observations

Hot stage polarizing microscope observations of vectra A950 found that the material can be sheared at about 180 °C and flow at about 350 °C. There is no indication of any decomposition before specimen flow. Vectra A950 is deep brown from the edge of the specimen when the temperature is up to around 500 °C, which might be the starting point for decomposition. Using the above DSC results, the processing condition for a single HM-S Grafil carbon fibre - vectra A950 model composite was selected. The heating rate, remelting temperature, remelting time, cooling rate, and crystallization temperature were 20 °C/min, 350 °C, 10 min, 80 °C/min, and 230 °C, respectively. The isotherm crystallization time at 230 °C was 30 min. Photographs obtained with crossed polars are shown in Figure 1. A feature of molecules in a mesophase is the tendency to be aligned along the flow direction (see Figure 1a) and to be disturbed by obstacles such as carbon fibre (see Figure 1b). The orientation of molecules between both regions is different. The interaction between carbon fibre and vectra copolyester was not clear on the HSPM. Observations of vectra A230 also failed to reveal clearly the interaction with carbon fibre. Therefore, further observations using SEM and TEM techniques were needed. However, due to difficulty in separating a model single carbon fibre - vectra A950 composite from the glass cover slips, further studies on carbon fibre - vectra copolyester composite were made with extruded vectra A230 material.



Scanning Electron Microscope Observations

The surface of the extruded vectra A230 composite is shown in Figure 2. The diameter of the extruded vectra A230 composite exhibits considerable irregularities. Carbon fibres are not perfectly aligned parallel to the composite axis but are at a small angle to it. Carbon fibres can be observed near the composite surface or slightly protruding from the composite surface. The rough and irregular diameter of the extruded vectra A230 composite could be due to the presence of the added carbon fibres.

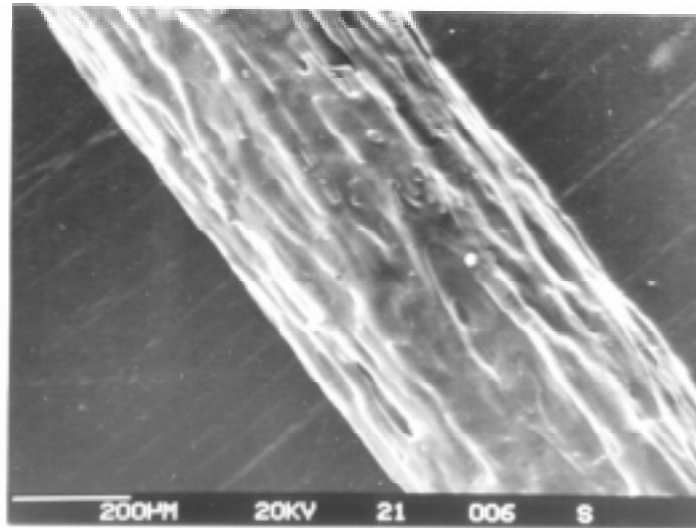
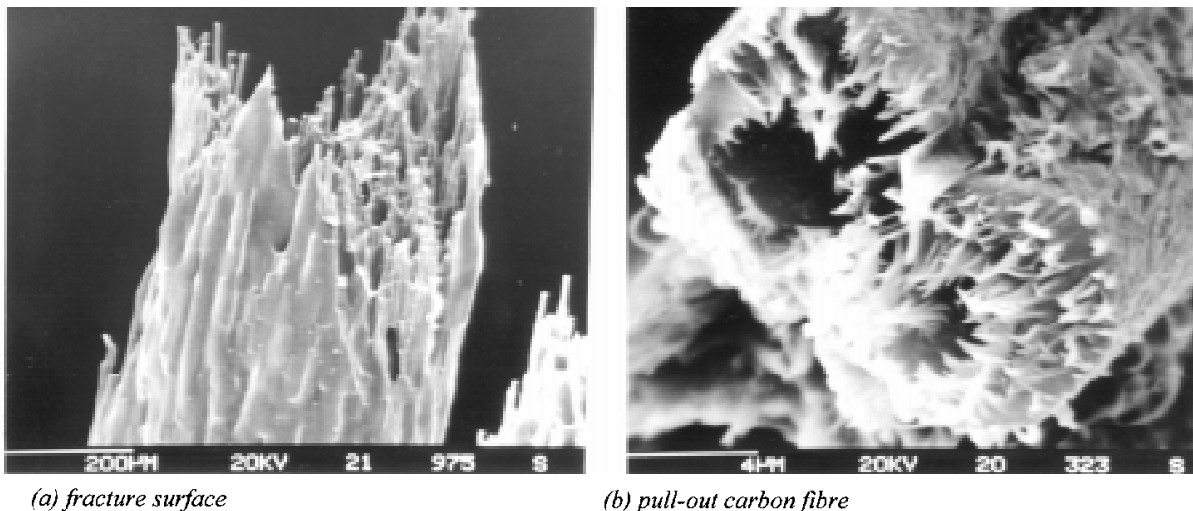


Figure 2. Scanning electron micrograph of the extruded vectra A230 composite

Tensile fractographs of the extruded vectra A230 composite are shown in Figure 3. Observations of the fracture surface of the extruded composite reveal a number of voids. A high void content, about 35 % in volume, could result from the presence of carbon fibres which interrupted the flow state of the vectra copolyester.



(a) fracture surface

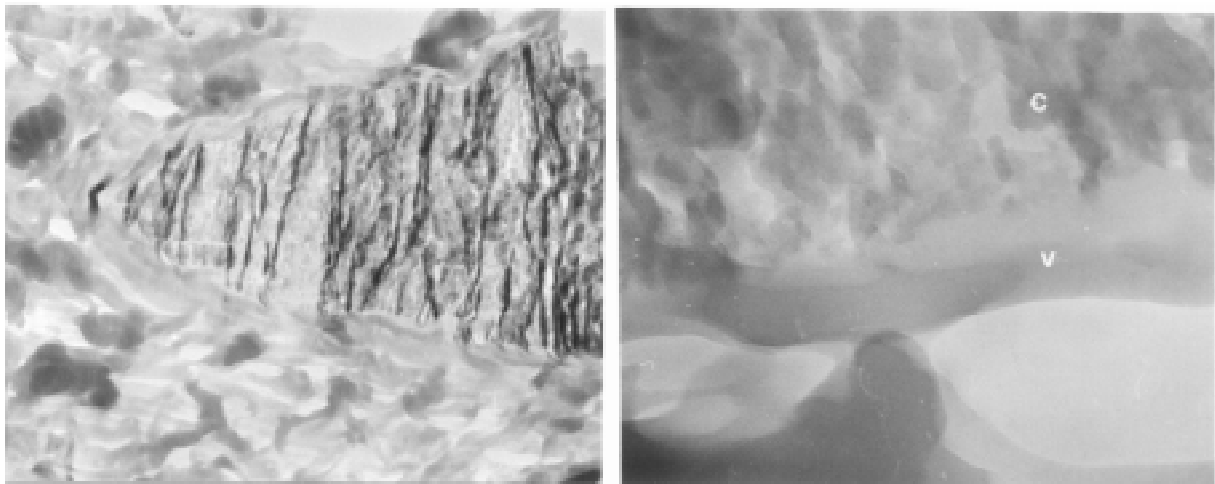
(b) pull-out carbon fibre

Figure 3. Scanning electron micrographs of tensile fracture surface of the extruded vectra A230 composite

The interaction between vectra copolyester and carbon fibre was observed, it is clear that fibre - to - matrix adhesion is quite good (see Figure 3b), as indicated by the vectra copolyester adhering to the fibre after pull out. It appears that fibre - to - vectra copolyester adhesion is better than the lateral forces between fibrils of vectra copolyester. The failure was initiated near the carbon fibre and was propagated between the fibrils. Finally, carbon fibres were pulled out and the composite was broken.

Transmission Electron Microscope Observations

Transmission electron micrographs obtained from longitudinal sections of the extruded vectra A230 composite are shown in Figure 4. The carbon fibre is embedded in the vectra copolyester, which is proved by the selected area electron diffraction pattern. In Figure 4a, it can be observed that a thin layer of vectra copolyester is closely attached to the carbon fibre. The diameter of the embedded carbon fibre is about $7\mu\text{m}$, and the thickness of the thin vectra copolyester layer is about $0.2\mu\text{m}$, which compares well with the result observed from SEM photographs that the diameter of the pull-out carbon fibre with a vectra layer is about $7.4\mu\text{m}$. A high magnification photograph shown in Figure 4b indicates that the interaction between vectra copolyester and carbon fibre is very good, since vectra copolyester sticks on the carbon fibre tightly.



(a) longitudinal section of composite (x10000)

(b) high magnification of the interaction between carbon fibre and vectra copolyester (x50000)

Figure 4. Transmission electron micrographs of extruded vectra A230 composite

CONCLUSION

The transcrystalline structure can be obtained in the fibre reinforced semicrystalline polymers under the suitable conditions. The phenomenon is not found in the carbon fibre reinforced thermotropic liquid crystal vectra copolyester. The structure of vectra copolyester near the carbon fibre is quite different with the structure in the other area of vectra copolyester. It was observed by the hot stage polarizing microscopy for a single carbon fibre model composite. The SEM photographs of carbon fibre with a layer of vectra copolyester and high magnification TEM photographs of the interphase between carbon fibre and vectra copolyester indicate that there is a very strong interaction between carbon fibre and vectra copolyester. The lateral force between fibrils is weak. Therefore the propagation of tensile

fracture is along the interface between fibrils but not along the interface between carbon fibre and vectra copolyester. Unfortunately, a higher tensile strength of extruded vectra A230 composite material was not obtained (about 103Mpa). It could be due to the length of embedded carbon fibre, in the range from 50 μ m to 300 μ m, and a number of voids on the extruded composite material.

REFERENCES

1. A. Ciferri, in "Developments in oriented polymers-2", I. M. Ward, ed., Elsevier, London, Chapter 3, 1987, P.79
2. W. J. Jackson Jr. and H. F. Kuhfuss, J. Polym. Sci. Polym. Chem. ed., 14, 1976, P.2043
3. T. W. Shyr, S. H. Yang, and J. R. Kuo, Proceedings of ICCM-9, Madrid, Spain, 1993, vol. II, P.283
4. T. W. Shyr, J. R. Kuo, and S. H. Yang, Proceedings of ICCM-10, Whistle, Canada, 1995, Vol. VI, P.487

INFLUENCE OF GRAPHITIZATION PROCESSING UPON THE CARBON-CARBON COMPOSITE INTERFACIAL PROPERTIES

Sun Wenxun¹, Huang Yudong¹, Zhang Zhiqian¹ and Wang Junshan²

¹*Department of Applied Chemistry, Harbin Institute of Technology, P.O. Box 410, Harbin 150001, P. R. China*

²*Beijing research Institute of Materials & Technology, Beijing, 100076, P. R. China*

SUMMARY: The ultimate properties of carbon-carbon (CC) composite are determined by its processing history and interfacial structure to a great extent [1,2]. As the complexity of manufacture and the difficulty to control it, The CC composite's quality varies with the fluctuation of processing condition intensely. Thus, it is essential to optimize the processing to increase and stabilize its quality by monitoring the interfacial properties during manufacture. In this paper, the author investigates the inter-bundle and outer-bundle interfacial bond strength of three dimensional woven and pierced CC composite after each graphitization treatment cycle. Results show that the inter-bundle interface has nearly reached the highest bond strength after four graphitization treatment cycles, while the outer-bundle interface does not display best interfacial performance until six graphitization treatment cycles.

KEY WORDS: carbon-carbon composites, interfacial micro-mechanical properties, push out test method, three dimensional woven structure

INTRODUCTION

Carbon-carbon material is one of the important advanced composites with many excellent properties. It does not only occupy outstanding ablation resistance, remarkable high temperature resistance and low density property(theory density is 2.2g/cm³), but also displays best wear-resisting property and dimensional stability. CC composite has been used from the primitive aero-space field such as wing leading edge, nose cap and rocket generator sprayer nozzle, etc. to transport, sport and medical fields to day [3,4]. There is evidence to belief that in the near future, the CC composite will play a more important role in a widespread range. However, two problems limit its further using now. The first case is the high cost of production, another is the fluctuation of properties. In some special field, the cost may be unimportant, but fluctuation of quality is always a fatal problem that prevents its development. One of the important reason is that the random variation in manufacture. Generally, CC processing includes five to six cycles of impregnating with resin, carbonization and graphitization treatments. Too many parameters and too long producing period result in difficulty to control the processing in uniform condition. Up to now, many researchers have engaged in studying on CC composite, and their fields can be summarized into four aspects:

1. Investigating physical structure and chemical composition in matrix and interface by scanning electron microscope(SEM), transmission electron microscope(TEM), scanning tunnel microscope (STM) and atomic force microscope(AFM), etc.[5,6,7,8].
2. Designing new weaving method and program using CAD & CAM techniques [9].
3. Analyzing mechanical performance and fracture properties through mathematics model and mechanical theory [8,10].
4. Characterizing mechanical, ablation and thermal properties, etc. based on experimental techniques [11]

Although the focus of the four aspects is much different, each of them has realized the importance of interface in CC material. The structure condition of interface directly influences CC composite's mechanical properties. And in further, it can effect on ablation resistance as well. With perfect interfacial bond state, the CC material generally appears excellent behavior of resisting airstream washing, heat shock and shear and prevents the big piece of carbon matrix peeled off composite block during ablation condition. Well, it does not mean that the stronger the interface bond strength is, the better the properties of CC composite are. For CC composite, both the fiber and matrix is brittle material that too stronger interfacial bond state can induce to brittle fracture.

In addition, during the tension test on 3-D woven CC composite, many fiber bundles are pulled out when fracture is happened and while the higher tension strength always obtained correspondingly(Fig.1). It implies that there is a new type of interfacial structure in woven CC composite besides the conventional interface that exists between the single fiber and matrix. In fact, the newer is a type of macro-interface that is between one bundle of carbon fibers and the surrounding matrix. For sake of distinguishing, the macro-interface can be termed as outer-bundle interface and the conventional can be termed as inter-bundle interface(Fig.2). The whole properties of CC composite are determined by the cooperation of them. The purpose of this paper is to investigate the different bond strength of them in different CC specimens using push-out test method. During the test, a load-displacement curve is recorded, and from the curve and through simple calculation, the interfacial shear strength can be obtained.

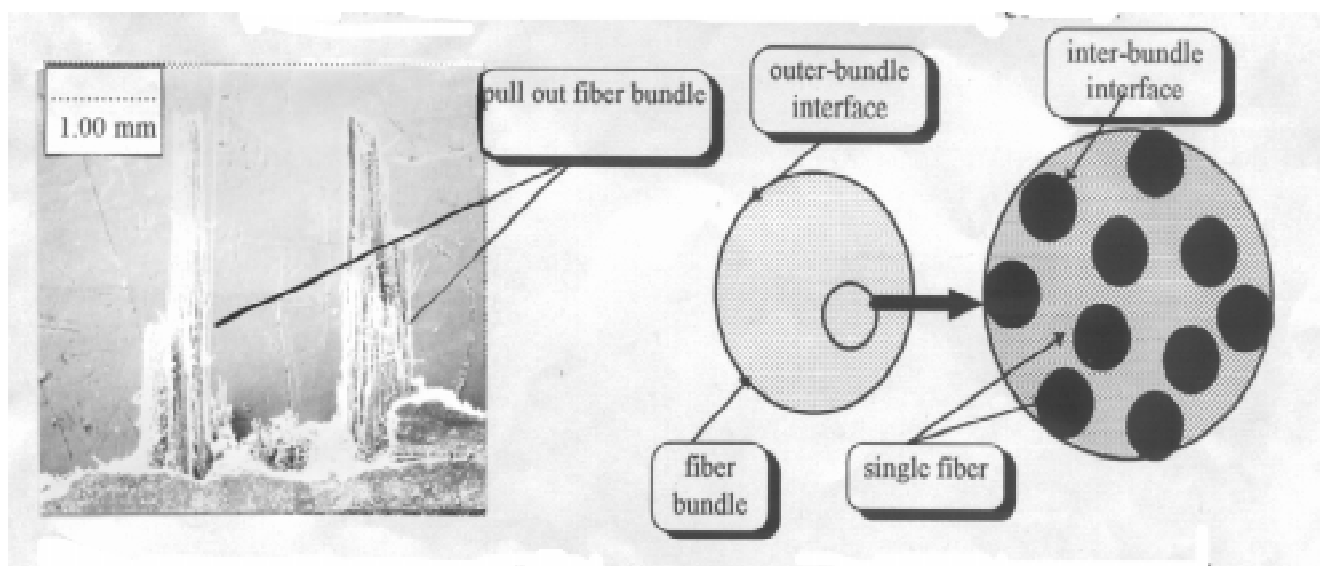


Fig.1: Tension fracture picture of 3-D CC

Fig 2: Interface in 3-D CC

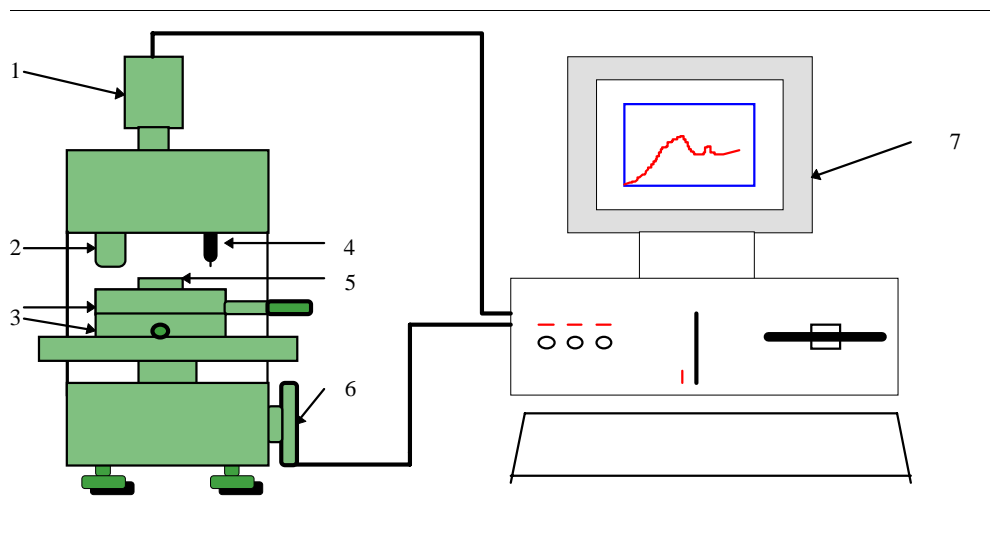
EXPERIMENT

Specimens Preparation

The experimental material is three dimensional woven pierced carbon-carbon composite made from PAN based carbon fiber and coal pitch. First, the fiber preform impregnated with pitch under 8 atm., and then impregnated under 10 atm.. The material is treated by impregnation, carbonization and graphitization for six times in total. After each cycle, a piece of specimen is cut off the block for test.

Test Instrument

The interfacial bond force is characterized by a modified push-out instrument, its diagram and the test technique are shown in Fig.3 and 4.



1-CCD camera, 2- microscope, 3-XY translation stage, 4-load and displacement cells, 5-sample, 6-loading device, 7-data acquisition system

Fig. 3 Illustration of equipment used for carbon-carbon composites push-out test

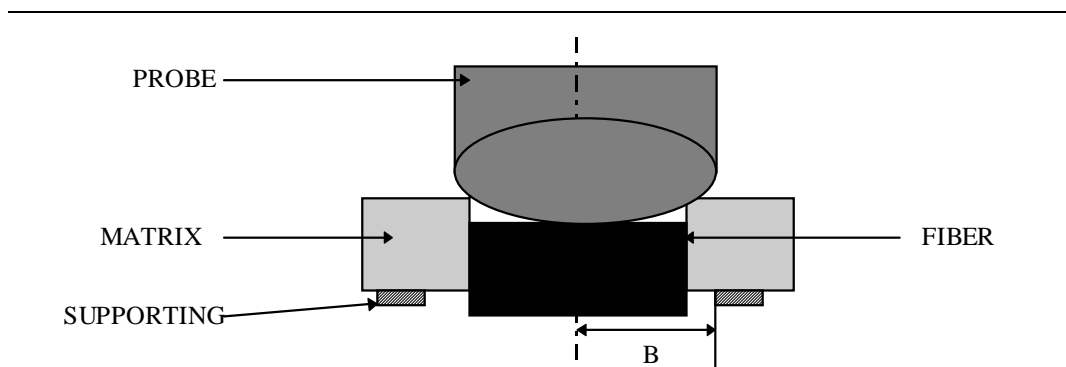


Fig. 4 Schematic illustration of push-out test

RESULTS AND DISCUSSION

Load-Displacement Curve of Push-Out

Fig. 5 gives out the SEM photographs of inter-bundle and outer-bundle interface after push-out test. In Fig. 6-7 the displacement is the relative displacement between probe tip and specimen surface. The interfacial shear strength (IFSS) is evaluated from the follows equation.

$$\tau = P/pdL \tag{1}$$

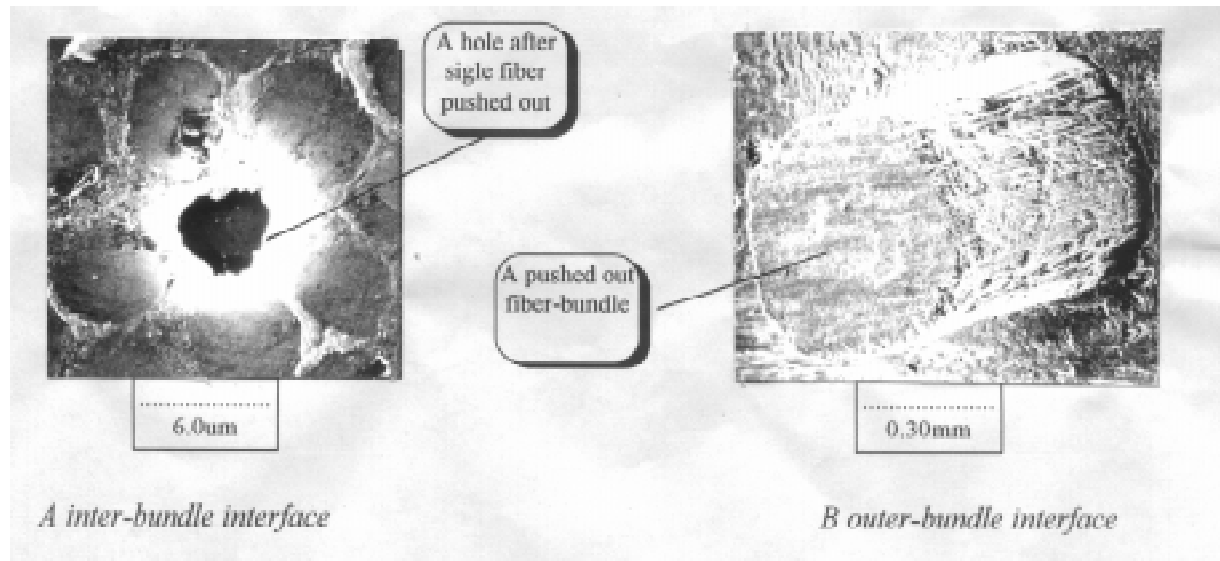


Fig. 5 the SEM picture of the push-out specimens

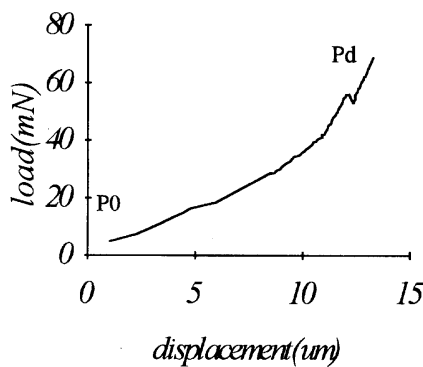


Fig.6 Inter-bundle interface push-out curve

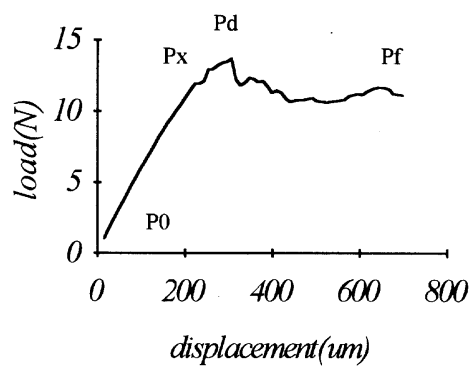


Fig.7 Outer-bundle interface push-out curve

The curves show that the push out procedures of fiber and fiber bundle are both divided into two stages. The first is interfacial debonding stage as indicated in the curves from P0 to Pd section. In this sequence, with the increase in displacement the load linearly increases until reaches the interfacial critical bonding strength, and then appears a sudden drop. The load on the moment is regarded as the maximum bond force of interface. Subsequently, the frictional sliding stage starts that fiber or fiber bundle is gradually pushed out of the matrix. But in Fig.6

the single fiber sliding stage is not distinct that the load continues to increase immediately after a small drop happened, which is because that the diamond probe tip comes into contact with the surrounding matrix surface after the fiber's axial movement (Fig.4). Whereas, in the case of fiber bundle(Fig.7), the sliding procedure is distinctly visible. Sometimes, the maximum frictional stress even surpasses the maximum bond stress(P_d) due to the roughness of debonding fiber bundle surface.

Besides, from the bundle push-out curve it can be seen that there is a small stress peak(P_x) appeared before the maximum stress(P_d) reaches. Although the small peak is not always appeared in test, its existing implies that the debonding process of fiber bundle does not happened at one time, partial debonding or inter-bundle debonding may occur before the complete debonding happens. It induces to more difficulty to analyze the failure mechanism of outer-bundle interface.

Effect of Graphitization Treatment Processing on Interfacial Strength

The specimens are divided into six groups signed as 1G#, 2G#, 3G#, 4G#, 5G#, 6G#, which expresses the different graphitization treatment times respectively. The shear strength values of inter-bundle and outer-bundle interfaces are shown in Fig. 8.

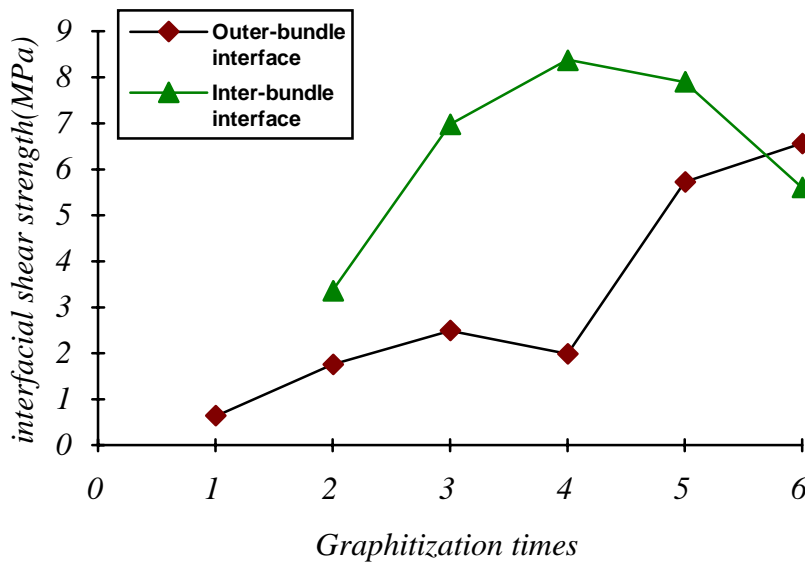


Fig. 8: The shear strength of inter-bundle and outer-bundle interfaces in different graphitization treatment

In Fig. 8, the treatment temperature of graphitization is basically similar except for the fourth cycle (2800°C) And it is shown that the two kinds of interfacial strength values have similar increase tendency with the increase in graphitization times before the fourth graphitization treatment. Whereas, after the fourth cycle, they display quite different tendency that while the inter-bundle interfacial shear strength changes to monotonically decreases, the outer-bundle interfacial shear strength continues to monotonically increase after a small drop. The reason is that the formation speeds of two kinds of interface are not equal. In other words, the matrix in the fiber bundle reaches the densified structure after the fourth cycle, and expresses high interfacial shear strength. The subsequent graphitization treatment has few effects on the densification of matrix. On the contrary, it can induce to further crystallization and

contraction of volume in matrix, which results in additional stress produced in interface and decrease of inter-bundle interfacial shear strength. At the same condition, matrices between the bundles need six cycles to reach more densified structure at least. Thus, in the whole treatment procedure the shear strength of outer-bundle interface continues to increase except for the drop that caused by temperature case.

The above phenomenon is directly related with the woven structure of CC material. In the fiber preform, fibers in the bundles are closed together while between the bundles are spaced apart. If the preform is impregnated with pitch, more pitch will fill between bundles and when the pitch is heated and sintered into carbon, big bubbles will be generated between the fiber bundles as more pitch and space exists. When the pressure in bubbles gradually increases to the critical degree, the bubbles will break into many small drops and squeeze in fiber bundles, while the resin in bundles can not generate big bubbles for the restriction of surrounding fibers and it sinters into carbon in-situ. In Fig. 8, the shear strength drop of outer-bundle interface at the fourth cycle reveals the same reason that the loose matrix and interface structure at the fourth cycle between fiber bundles is easy to produce cracks under the high treatment temperature, but in the densified fiber bundles that can not appear.

From the discussion above, clearly the adjustment of process can induce to different interfacial structure. This may provide useful information for material design.

CONCLUSION

There are two kinds of interface in multidimensional woven carbon-carbon composites that one kind is inter-bundle interface, another is outer-bundle interface. Their performance speeds during the manufacture procedure are not equal. The push-out test results show that before the fourth graphitization cycle, matrix in fiber bundles is densified faster than that out of bundles at same condition. That is to say, the inter-bundle interfacial strength increases more quickly than outer-bundle interfacial strength. The high graphitization treatment in the fourth cycle effects the outer-bundle interface more obviously than inter-bundle interface as the different densities of them.

REFERENCES

1. Schmid, T. E., AFWAL-TR-82-4159, 1982.
2. Scott, R. D, NASA CR 1658421-1, National Aeronautics and Space Administration, Washington, DC, 1982.
3. Carroll, T. J. and Connors, D. F. "Final Report for Rapid Densification of 2D Carbon-Carbon Preforms", Textron Specialty Materials Report, Dec. 1989.
4. Curry, Donald M., "Carbon-Carbon Materials Development and Flight Certification Experience From Space Shuttle", Oxidation-Resistant Carbon Carbon Composites for Hypersonic Vehicle Application. NASA CP-2051, 1988, pp. 29-50.
5. Dhama, T. L., Bahl, O. P. and Manocha, L. M. "Influence of Matrix Precursor on the Oxidation Behavior of Carbon-Carbon Composites", Carbon, Vol. 31, No. 5, 1993, pp.751-756.

6. Rellick, G. S. and Adams, P. M., "TEM Studies of Resin-Based Matrix Microstructure in Carbon/Carbon Composites", *Carbon*, Vol. 32, No. 1, 1994, pp. 127-144.
7. Huang, H. and Young, R. J. "Effect of Fiber Microstructure Upon the Modulus of PAN- and Pitch-Based Carbon Fibers", *Carbon*, Vol. 33, No. 2, 1995, pp. 97-107.
8. Kowbel, W. and Shan C. H. "Mechanical Behavior of Carbon-Carbon Composites Made with Cold Plasma Treated Carbon Fibers", *Composites*, Vol. 26, No. 11, 1995, pp. 791-797.
9. Emmerich, F. G. "Application of a Cross-Linking Model to the Young's Modulus of Graphitizable and Non-Graphitizable Carbons", *Carbon*, Vol.33, No.1, 1995, pp. 47-50.
10. Emmerich, F. G. and Luengo, C. A., "Young's Modulus of Heat-Treated", *Carbon* , Vol. 31, No. 2, 1993, pp. 333-339.
11. Anand, K. and Gupta, V. "the Effect of Processing Conditions on the Compressive and Shear Strength of 2-D Carbon-Carbon Laminates", *Carbon*, Vol. 33, No. 6, 1995, pp. 739-748.

THE MODIFICATION OF CARBON FIBER SURFACE OF 3-D WOVEN PREFORM AND ITS EFFECTS ON THE INTERFACIAL BOND PROPERTIES

Huang Yudong¹, Feng Zhihai², Sun Wenxun² and Gao Wen²

¹ *Department of Applied Chemistry 410, Harbin Institute of Technology
Harbin 150001, P.R. China*

² *Beijing Research Institute of Material and Technology, Beijing 100076, P.R. China*

SUMMARY: The air-cold plasma treatment of carbon fiber surface in 3-D orthogonal woven preforms is investigated in this paper, and the single fiber push-in (microdebonding) technique is developed to evaluate the interfacial bonding strength between fiber and matrix. It is observed that the wetting performance and the interfacial properties have been increased greatly, and the interfacial characteristic between fiber and matrix in interior region of woven is the same as that in surface region after the woven fabric is treated, The loss of tension properties due to treatment is also investigated and found to be small in the range of useful treatments.

KEYWORDS: fiber surface plasma treatment, interfacial microdebonding, 3-D woven preform, carbon fiber, interlaminar shear strength, interfacial shear strength

INTRODUCTION

In recent year, carbon woven preform has been used as the reinforced phase in the process of manufacturing high-performance resin-basic composites[1]. There are some advantages for multi-directional woven structure such as overcoming the delamination in the composite, and woven scheme being designed according to the service performance and stress condition. For the need of the service performance, however, the woven fiber makes the feature of the structure comparatively compact, which leads to the resin can not fully impregnate the fiber when it is poured into the woven. The finished product is subject to the catastrophic premature destruction due to the partial default and void, thus affecting its service performance and placing restrictions on the scope of application for the product. So it's key factor for the multi-dimensional structure to deal with the wettability and the interfacial adhesion between the fiber and matrix. To this purpose, many investigations works have been carried out[2-5] which include the improvement of resin matrix, the program designing for the woven, the analysis and calculation for resin flow model, the in-situ appraising the flow process and process improvement such as the research on the relationship between injection stress and the resin wettability. Nevertheless, the research on activation treatment on the fiber's surface has not still been reported. The research on the modification of carbon fiber surface of 3-D woven

preform with the air-cold plasma technique has been carried on in this paper, which aims at improving the wettability between fiber and resin in 3-D woven, interfacial adhesion and improving the processability of composites.

EXPERIMENTAL

The Air-Cold Plasma Treatment on the Carbon Fiber and Its Woven

The carbon fiber removed the finish and the woven are placed into the air-cold plasma treatment cavity, then treated under a certain vacuum and power for a certain time.

The Measurement of Wettability

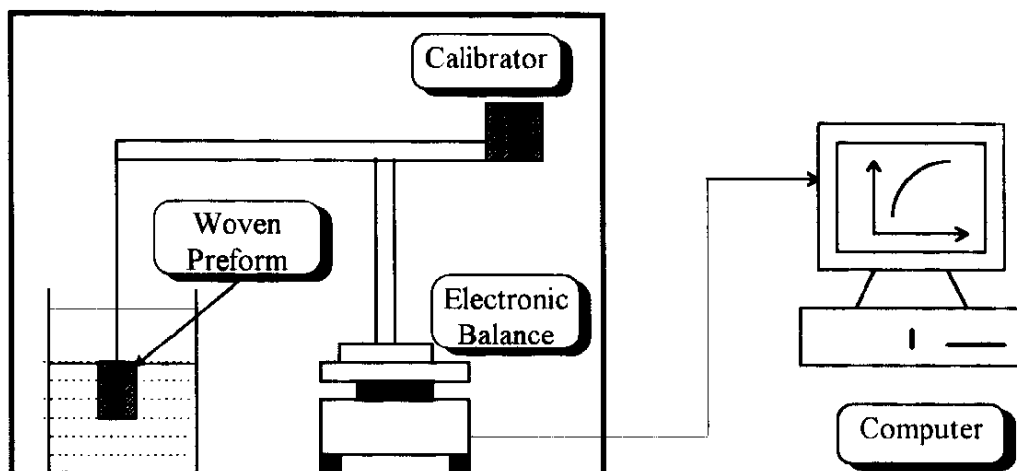


Fig. 1: dynamic measurement system of wetting speed

The wettability between the fiber and resin is indicated as the value of wetting angle and wetting speed. It's of difficulty to characterize the wetting performance using alone the wetting angle. The dynamic method is utilized to measure the wetting speed of resin in the woven, as shown in Fig.1. The approach based on the theory that the curve, weight versus time, is recorded with computer when the woven impregnated into the phenolic at a certain speed, which deduce the equation:

$$F=Wg -f \quad (1)$$

The value of force F recorded by computer is equivalent to the sum of gravity force Wg and the buoyant force f . With the increase of wetting time, the buoyant force gradually decrease due to resin impregnating the interior of woven little by little., so the F rise. The curve, force versus time, may judge the wettability between fiber and resin since the variation ratio in the buoyant force changes with the wettability.

The Fabrication of Composite Specimens

The 3-D composite is manufactured using the RTM process that the phenolic resin precatyzed is injected into the sealing die set where the reinforcement has been placed, then cured and formed.

The Measurement on the Mechanical Performance

The mechanical performances of specimen include the interlaminar shear strength (ILSS), and micro interfacial shear strength (IFSS) that is characterized with the microdebonding instrument developed by author himself[6-8].

RESULTS AND DISCUSSION

Effect of Surface Treatment on Interfacial Performance for Unidirectional laminate

The carbon fibers, divided into two groups, are treated by the air-cold plasma separately on the condition that the treatment time is controlled, then mix with the phenolic resin to model into the unidirectional laminate whose macro ILSS and micro IFSS are shown as Table 1, where the IFSS is computed by the finite element method.

Table 1: The ILSS and IFSS of unidirectional laminate

treatment time[min]	0	20	40	60
ILSS [MPa]	40.5	79	76	70
IFSS [MPa]	19.4	54.0	53.3	50.4

We can find from Table 1 that the effect of air-cold plasma on the IFSS is obvious, the maximum increase being 95 percent. At the same time, it is shown that the microdebonding test method is a means available for evaluating the interfacial bond strength between fiber and matrix.

It's generally thought why the air-cold plasma treatment can improve the interfacial adhesion performance is that the plasma may etch, clean and activate the surface of carbon fiber[9], at same time remove the inert impurity and generate the shallow gap so that the surface area in fiber is increased. On the other hand, the plasma treatment may change the chemical compound on fiber surface and engender the active group such as -OH, -COOH, -COO⁻ and -NH₂, which react chemically with the matrix resin during the cure action and produce the chemical bond so as to enhance the adhesion strength. Consequently, the air-cold plasma treatment may raise the shear strength greatly and the effect of treatment may be further demonstrated by the variation of wettability.

However, that the treatment time is too long will decrease the interfacial adhesion performance, just as the Table 1 shows: IFSS start to decline when the treatment time exceeds 20 minutes. Fig.2 displays the comparison of wetting state between untreated fiber and treated fiber, where A is wetting state between fiber untreated and resin and B is outcome at 20 minutes of treatment time. For the contact angle, it decreases from 69.5 before treating to 36.1 after treating, which shows the fitter to spread out on the surface of fiber treated.

Fig.3 shows the dynamical wetting curve for the 3-D woven, which indicates the increase of wetting speed due to treating fiber is same obvious.

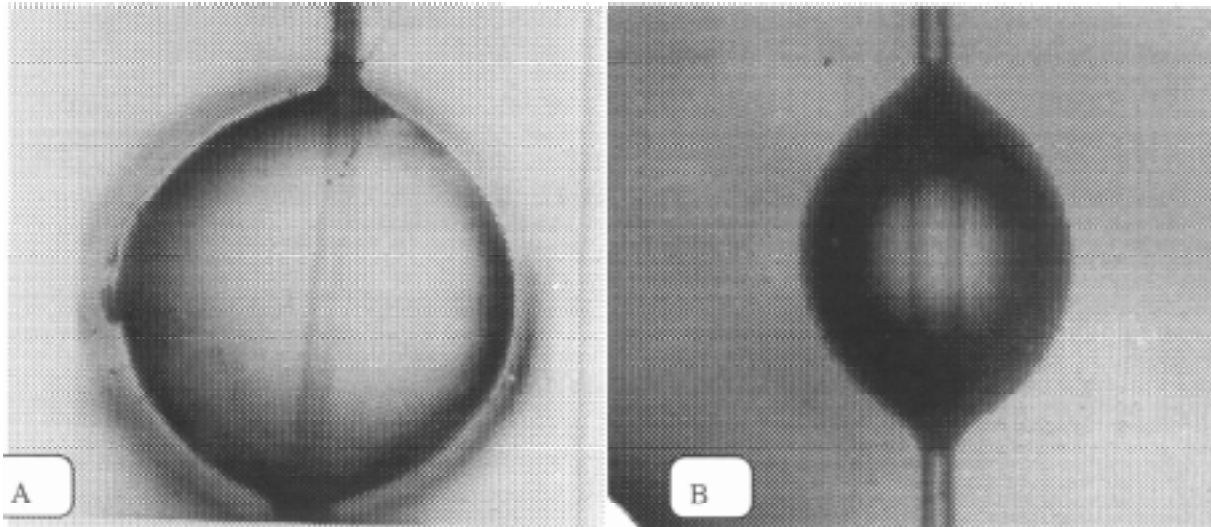


Fig.2: The wetting state of untreated fiber and treated fiber

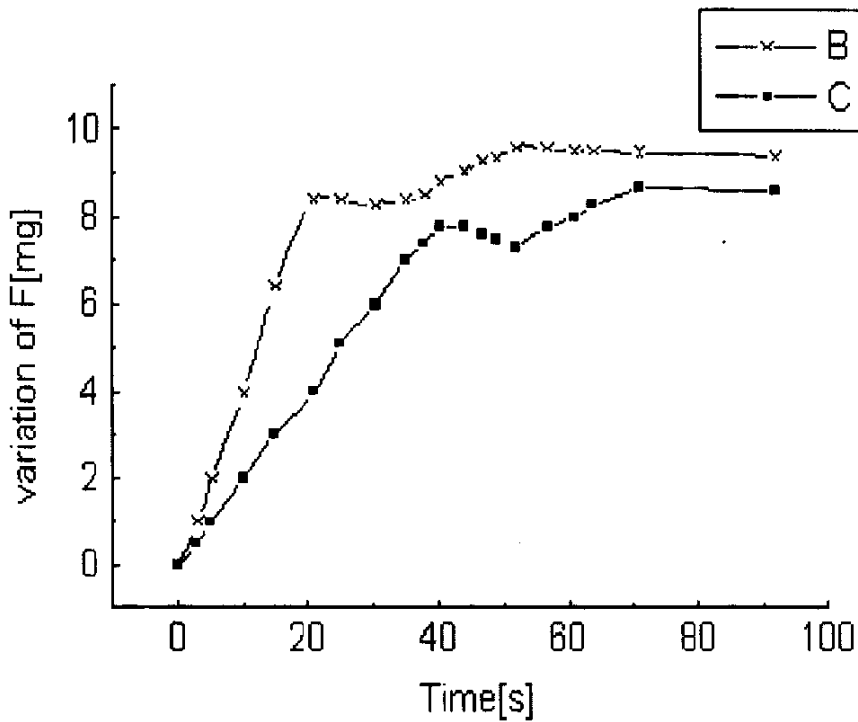


Fig 3 : The effect of air-cold plasma treatment on the wetting speed of carbon fiber woven

Effect of air-cold plasma technique on the 3-D woven

Whether the air-cold plasma technique can modify the surface of 3-D woven as multi-directional structure involves in two problems: one is whether the plasma can activate the interior fiber in the woven since structural compaction in 3-D woven and the low energy of plasma result in the failing to come into the interior fiber; another is whether the treatment outcome on the surface of fiber is same as the interior fiber. In case of the different effects, the weak region will be generated in the composite, which is unsafe factor to use this method. In order to solve both problems, the author takes advantage of the routine treatment technique to treat 3-D woven at different period of time. The results are shown in Fig.4 and Table 2, 3.

Table 2: the comparision on different treatment method

treatment method	untreated	slight oxidization	plasma treatment
IFSS(MPa)	23.4	44.7	51.2

The microdebonding of both interior and edge of woven are shown in Table 3. It indicates the IFSS of the interior fiber is same as of fiber on the edge of woven in the main. Based on discussion, that plasma has immersed the interior of 3-D woven and improved the interior fiber can be turned out.

Table 3: The comparision of IFSS with woven interior to edge

Site	IFSS [MPa]
Interior	54.5
Edge	54.1

The prevention effect is below that is imagined under the condition of minimum volume in woven though the outer fiber does hinder the plasma. Meanwhile this denotes, for 3-D woven, the micro debonding technique is superior in characterizing the IFSS inside the 3-D woven. We can make out from Table 1 and Fig.4 that the treatment is longer than the unidirectional laminate to acquire the effective treatment. Contrast with 20 minutes of treatment time for the unidirectional laminate, 30 minutes is needed for the 3-D woven to obtain the optimal shear strength. The extending time is used to set off the impedance of outer fiber. So it's essential to spend more treatment time to arrive at the optimal treatment effect.

Effect of Surface Treatment on Fiber Strength and Degeneration Effect

The Fig 5 displays the relationship curve, treatment time for the plasma versus the tension strength for single carbon fiber. The practical outcome is calculated according to Weibull statistics. Within 40min, the maximum decrease in strength by 16.6 percent mainly as a result that more plasmas etch the material and reduce the radial size. At the same time, the ditches as the result of etching will raise the stress concentration so as to result in the fiber fracture earlier.

The surface of woven become so active as to blend with resin immediately, which increase the interfacial reaction and enhance interfacial adhesion effect. However the active surface may absorb the dust, H₂O, O₂ and lose its activity gradually provided that it is exposed in the air. The effect is terminated as "degeneration effect". The degeneration effect is unavoidable in the process of manufacture due to the restriction on the process that the fibers treated have to be placed for a period of time, then blending with resin. The degeneration effect on the interfacial adhesion strength and relationship between degeneration and time may be found out from Fig.6, which demonstrates the ILSS decrease to 10 percent after the fiber treated is exposed in the air for 3 hours, however, which still enhance 73 percent comparing with the fiber untreated. In conclusion the excellent performance of composites is still maintained if the carbon fiber blends with resin within 3 hours.

CONCLUSION

Microdebonding test method is feasible as a means to measure the mechanical performance on the micro interface, which is agreement with the macro performance. Specially it is superior and cannot be substituted by other methods for the multi-directional woven.

The IFSS will rise after fibers being treated by the air-cold plasma. Moreover the treating effect on both interior and surface of fiber is same. The fracture and degeneration effect due to plasma treatment is small enough not to affect the performance of material seriously under the process condition discussed by author.

REFERENCES

1. Chan, A.W. and Hwang, S.T., "Modeling of the Impregnation Process During Resin Transfer Molding", *Polymer Engineering and Science*, Vol. 31, 1991, pp. 1149-1153.
2. Alfred, C.L. and John, D.M., "Verification of A Multidimensional Resin Transfer Molding Flow Model", *Proceedings of the 10th International Conference of Composite Materials*, Whistler, British Columbia, Canada, August 14-18, 1995, Vol. III: Processing and Manufacturing, Poursartip, A. and Street, K.N., Eds, pp. 245-252.
3. Trochu, F., Hoareau, C., Gauvin, R. and Vincent, M., "Experimental Analysis and Computer Simulation of RTM Trough Multilayer Fiber Reinforcement", *Proceedings of the 9th International Conference on Composite Materials*, Madrid, July 12-16, 1993, Vol III, pp. 481-488.
4. Weitzenbock, J.R., Sheno, R.A. and Wilson P.A., "Characterization of Resin Flow through Thick Laminates in Resin Transfer Molding", *Proceedings of the 10th International Conference of Composite Materials*, Whistler, British Columbia, Canada, August 14-18, 1995, Vol. III: Processing and Manufacturing, Poursartip, A. and Street, K.N., Eds, pp. 301-308.
5. Kwang, M.U. and Lee, W.I., "A Study on the Mold Filling Process in Resin Transfer Molding", *Polymer Engineering and Science*, Vol. 31, 1991, pp. 765-770.
6. Huang, Y.D. and Zhang, J.M., "Determination of the Interfacial Shear strength of resin Matrix Composite", *Material Science Progress*, Vol. 6, No. 1, 1992, 84-87.
7. Huang, Y.D., Zhang, Z.Q., Kong, X.R. and Wei, Y.Z., "Measurement of the In-situ Interfacial Strength in Advanced Composite Materials", *Proceedings of the International Conference on Advanced Materials*, Beijing, August 12-15, 1996, Wang T.C. and Chou T.W, Eds, pp. 892-898.
8. Huang, Y.D., Kong, X.R., Zhang Z.Q. and Wei, Y.Z., "Evaluation of In-situ Fiber/Matrix Interfacial Properties", *Acta Materiae Compositae Sinica*, Vol. 12, No. 3, 1995, pp. 83-89.
9. Huang, Y.D., Zhang, Z.Q., Wang, L., Wei, Y.Z. and Liu L.X., "Microscopic Topography Characterization of Carbon Fiber Surface", *Proceedings of the 11th*

International Conference on Textures of Materials, Xi'an, September 16-20, 1996,
Liang, Z.D. and Zuo, L., Eds, pp. 1245-1250.

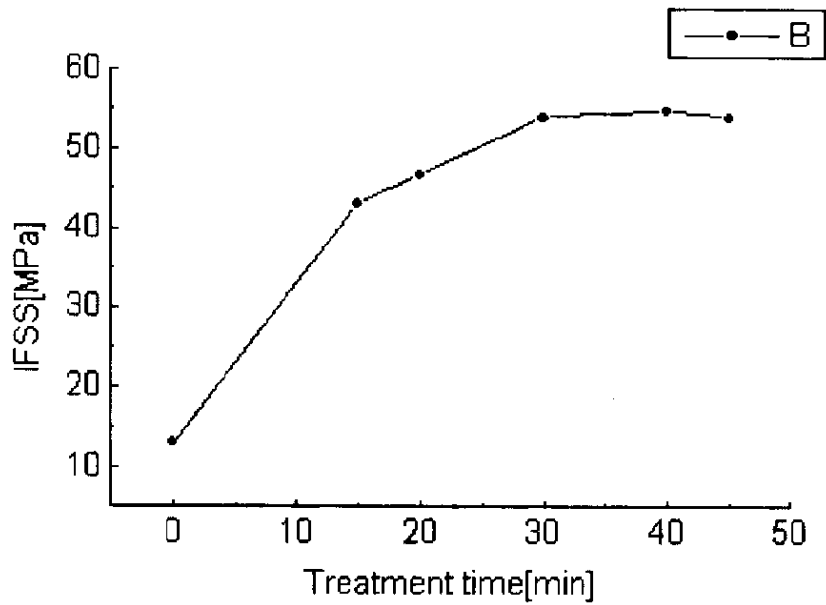


Fig 4: The relationship between air-cold plasma treatment time and IFSS

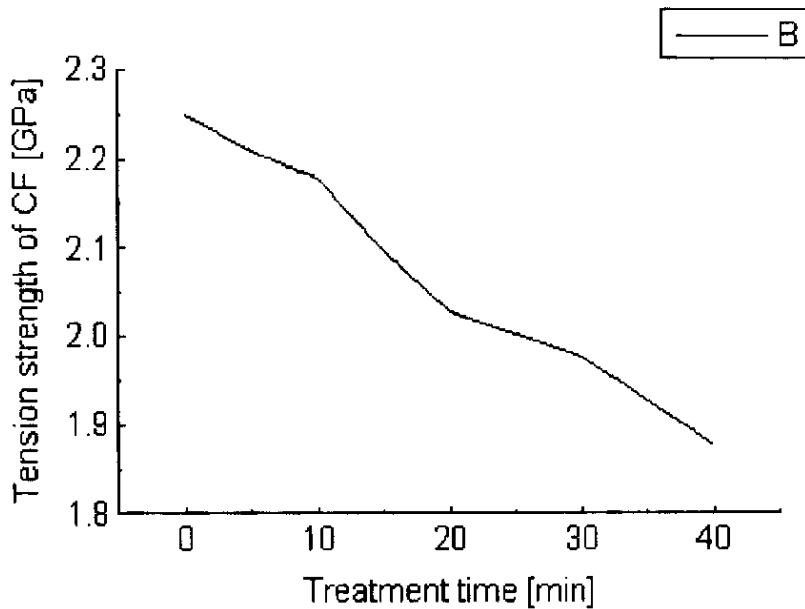


Fig 5: The effect of treatment time on tension strength

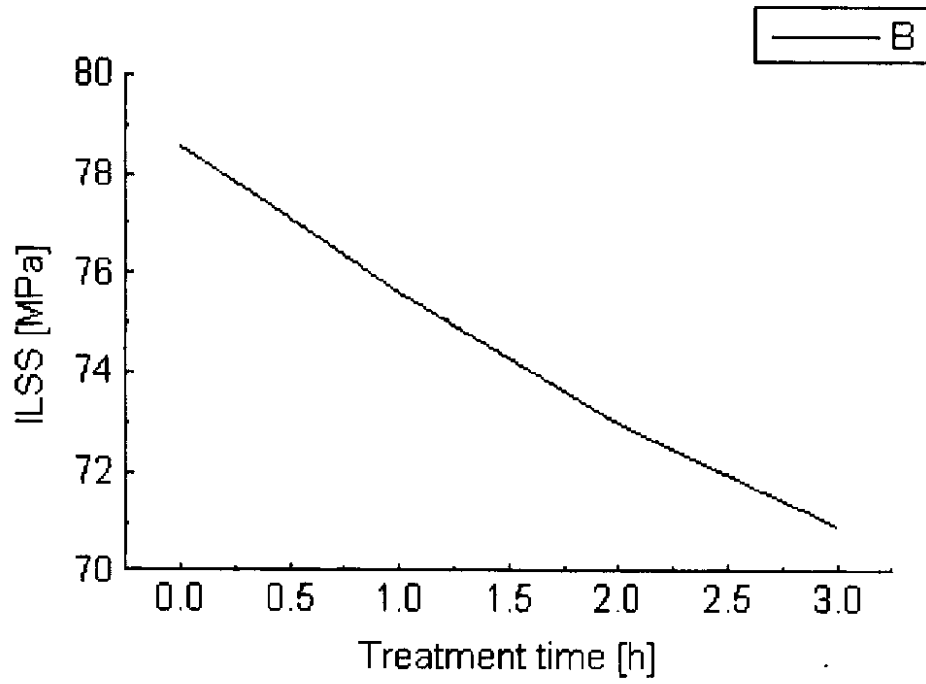


Fig 6: The relationship between degeneration and standing time

INFLUENCE OF SURFACE TREATMENT ON THE DYNAMIC-MECHANICAL PROPERTIES OF NATURAL FIBER REINFORCED PLASTICS

Jochen Gassan and Andrzej K. Bledzki

*Universität Kassel, Institut für Werkstofftechnik - Kunststoff-und Recyclingtechnik
Mönchebergstraße 3, 34109 Kassel, Germany*

SUMMARY: This paper presents investigations concerning the effectiveness of MAH-PP copolymers as coupling agents in jute-polypropylene composites. The cyclic-dynamic values, gained at the load increasing test, pointed out, that the coupling agent reduces the progress in damage at higher limit stresses. Dynamic strength of the MAH-PP modified composites is therefore raised for about 40%. SEM investigations allow to explain the increase of the characteristic values by an improved fiber-matrix adhesion, a less inclination to fiber pull-outs was determined. The improved fiber-matrix adhesion led to a decrease in impact damping-index and loss-energy.

INTRODUCTION

Natural fiber composites combine good mechanical properties with a low specific mass. But, the high level of moisture absorption by natural fibers, their poor wettability, and the insufficient adhesion between untreated fibers and the polymeric matrix, leads to debonding with age [1,4,6].

In all cases, cellulose is the main component of vegetable fibers (at jute approximately 64 wt.-%) [7]. The elementary unit of a cellulose macromolecule is anhydro-d-glucose, which contains three hydroxyls (-OH). These hydroxyls form hydrogen bonds inside the macromolecule itself (intramolecular) and between other cellulose macromolecules (intermolecular) as well as with hydroxyl groups from moist air. Therefore, all vegetable fibers are hydrophilic in nature, and their moisture content can reach 3-13 % [2].

To improve the properties of the composites the reinforcing natural fibers can be modified by physical and chemical methods. Physical methods, such as stretching [17], calendering [18,19], thermotreatment [20], and the production of hybrid yarns [21,22] do not change the chemical composition or structural and surfacial properties of the fiber.

The most important chemical modification methods are the chemical coupling methods. The coupling agent used hereby contain chemical groups, where the one can react with the fiber and the other with the polymer. The formed bonds are covalent and hydrogen bonds as well,

they improve the interfacial adhesion. Graft copolymerizates [15,16] are common methods used for natural fiber reinforcing plastics and will be described in this article. Of common usage is also the treatment with compounds which contain methylol groups [22,23], the treatment with isocyanates [8,9], triazine [6,11] or organosilanes [1,5,12] as coupling agents.

Sterzynski et al. [24] used dimethylurea (in aqueous and methanolic solutions) as coupling agent for injection molded flax-iPP composites. This treatment caused, up to a dimethylurea concentration of 12 wt.-% an 25%-increase of tensile strength and a 20%-increase of Young's modulus. Simultaneously, water repellency was improved.

Other important coupling agents for polypropylenes are silanes. The application of alkylfunctionalized silanes, according to Mieck et al. [25], does not lead to chemical bonds between the cellulose fibers and the PP-matrix. But, it seems to be realistic to assume that the long hydrocarbon chains, provided by the silane application influence the water household and wettability of the fibers and that the chemical affinity to the PP is improved.

Hydrogen bonds as well as covalent bonding mechanisms can be found in the flax-silane system. By this, Mieck et al. [25] found an 60%-increase of shear strength, using a methanolic solution of vinyltrimethoxysilane (dibutylic dilaurat of tin was added as catalyzer), depending on the silane concentration and on the type of catalyzer.

Kokta et al. [16] investigated the influence of different silane types (3% by weight of the fiber) and polymethylene polyphenylisocyanate (PMPPIC, 1% by weight of polymer) on the mechanical properties of wood pulp filled polypropylene. The strength of the silane modified composites was not changed appreciatively. Whereas, the treatment with PMPPIC led to increased strength and stiffness values, caused by chemical bonds between the isocyanate and the hydroxyl groups of the wood fiber surface.

A lot of publications [27-30] are concerned with the effectiveness of MAH-PP copolymers as coupling agent. Mieck et al. [27] determined an increased shear and tensile strength for about 100% respectively 25% at flax-polypropylene composites, whereby the coupling agent was applied on the flax-fibers before the composite was processed. These raised values are dependend on the grafting rate and on the average molar mass of the graftcopolymer.

Similarly increasing values could be attained with PP as matrix material modified with MAH. The acidic anhydride groups of the MAH-PP coupling agent are able to built both, hydrogen- as well as chemical bonds with the hydroxyl group of the flax fiber, wherby a tight anchoring of the coupling agent on the fiber surface is achieved. Besides, the long PP-chains of the MAH-PP coupling agent lead to an adaptation of the very different surface energies of matrix and reinforcement fiber, which allows a good wetting of the fiber for viscous polymers. Again an improved wetting can increase adhesion strength by an increased work of adhesion.

Scanning Electron Microscopy (SEM) investigations on MAH-PP modified cellulose fibers (filter paper) proved, according to Felix et al. [29], that this treatment improves wetting, what results in an improved fiber-PP-matrix adhesion compared to unmodified fiber matrix systems. An increase of the composite strength with increasing cellulose content was achieved, similar to Karmaker et al. [30] by the covalent bonds, which were introduced by the addition of a coupling agent.

Similarly improved mechanical properties (tensile- and impact properties) were determined by Avella et al. [28] at MAH-modified iPP composites reinforced with wheat straw fibers. The occuring reduction of moisture uptake was explained by covalent bonds between molecules of acidic maleic anhydride and the fibers.

The chemical bondings between the anhydride- and the hydroxyl groups cause a better force transfer from the matrix into the fibers, which leads to a higher tensile strength [30]. Karmaker et al. [30] determined an increasing composite strength with increasing fiber content when only the MAH-PP coupling agent was used to reinforce jute-PP (average fiber length = 2mm).

MATERIALS AND EXPERIMENTAL TECHNIQUES

Materials

The tested composites were made of tossa jute-fibers ($n_g = 2$ - woven from J. Schilgen GmbH & Co.) with a fineness of about 280 tex, which were embedded in an PP-Matrix from Vestolen GmbH Germany (Vestolen[®] P 6000F-Table 1) by using the film stacking technique.

Table 1: Technical specification of Vestolen[®] P 6000F - homopolymer³

Characteristic Value	Value
Viscosity	240 cm ³ /g
Melting Flow Index - MVR/230/2.16	7.4 cm ³ /10 min.
Melting Point	164 - 168 °C
Young's Modulus	1500 N/mm ²
Shear Modulus	800 N/mm ²
Vicat Softening Temperature	90°C

To gain a higher fiber matrix adhesion, a fiber modification with MAH-PP (®Hostaprim HC 5 from Hoechst, Germany) was applied. For this procedure the fibers first, had to be dewaxed in an alcoholic solution for 24 hours, removing the woving size (potatoe starch and waxes), subsequently the fibers were washed with distillized water. The following MAH-PP treatment similarly was carried out in an alcoholic solution. The fiber treatment was finished with a 2-hours drying process in a vacuum oven at 75°C.

Mechanical Tests

To determine the influence of the MAH-PP-coupling agent on the mechanical composite properties, the quasi-static flexural test DIN EN 63 (test speed = 2 mm/min) was used. Ten samples were investigated for each case with an standard deviation < 10%.

The load increasing fatigue tests were carried out in accordance to DIN 50 100. At the Institut für Werkstofftechnik a dynamic material testing system, called InDyMat (Intelligent Dynamic

Material Testing) was developed [31]. This system is especially qualified to be used for visco-elastic materials, because the system provides additional informations about damping, dynamic modulus and the cumulated loss-energy (according to Lazan`s definition [32]) of the material. Due to the visco-elastic behaviour of natural fiber composites, a phase shift occurs between applied stress and the material extension.

A sinus-shaped stimulation of the sample, e.g. with a hydropulser, results in a sinus-shaped extension of the sample. The two sinus curves are then separated by a phase angle from each other. Overlaying the two measured signals in a load-extension diagram, results in a hysteresis loop. InDyMat, the computer program, records the hysteresis loop at certain intervals (approximately 1000 values each time) and evaluates them.

The load increasing fatigue tests were carried out as repeated tensile stress tests, with 4 samples (geometry: $120 \times 25 \times 4 \text{ mm}^3$). Testing frequency " f_{test} " and stress ratio "R" were chosen to 10Hz and 0.1. The maximum heating of the samples did not exceed 7°C .

With the "non-penetration" falling weight impact test [31], the material can be loaded with single or multiple impacts until penetration occurs. The impact energy can be easily adjusted by varying the drop height or the drop weight. The impact testing equipment was developed according to DIN 53443 and DIN 53373. The impact force is measured with a piezoelectric sensor right behind the impactor tip. The deflection (movement of the impactor) is measured by a position sensitive detector. Impact force history and deflection are recorded and evaluated by a personal computer. If impact force is plotted against deflection, a non-penetration impact results in an open hysteresis loop defined as loss energy. The area under the hysteresis-loop is defined as strain energy. The ratio between loss and strain energy is defined as damping-index. Five samples with the dimension $60 \times 60 \times 4 \text{ mm}^3$ were tested.

RESULTS AND DISCUSSIONS

The increased characteristic values caused by the MAH-PP coupling agent (Figure 1) are mainly based [13,33] on a reduction of fiber pull-outs and less fiber-matrix debondings, which would lead to e.g. micropores in the interface [33]. The improved fiber-matrix interface leads to a lowering of the critical fiber length for a most effective stress transfer and because of that to a higher composite strength [33].

Figure 1 demonstrates that, the reinforcing effect and with this the flexural strength of the composite, increases, as a result of the improved force transfer from matrix to fiber [30], caused by the improved fiber-matrix adhesion. In comparison to the investigations of Karmaker et al. [30], where jute-fibers with an average fiber length of 2mm were used to reinforce polypropylene, and to the investigations of Felix et al. [29] at PP reinforced with filter paper, this investigations found an increase of flexural strength, through the higher fiber length, with increasing fiber content at jute reinforced PP even without an application of a coupling agent.

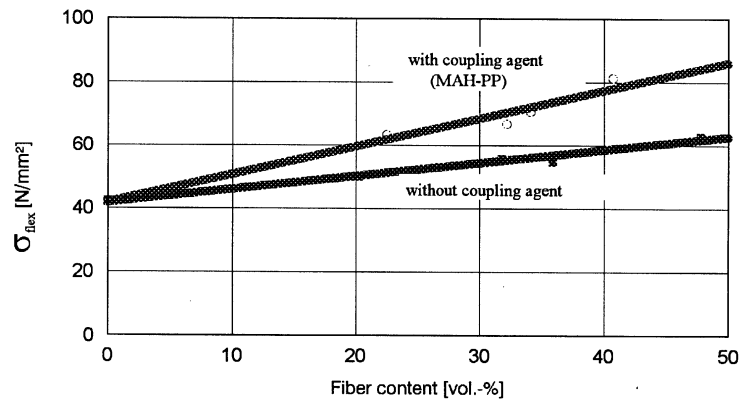


Figure 1: Influence of jute-fiber content and surface treatment on the flexural strength of jute-PP-composites

The investigations made by Mieck et al. [27] on PP reinforced with flax fibers (green flax ribbons, comb ribbon: 4.5 ktex) seem to be comparable to the here made investigations concerning the fiber length. Tensile strength of the composites is influenced similarly by the fiber content as it can be seen in figure 1. The values for flexural strength do not differ distinctly between modified and unmodified flax-PP composites up to a fiber content of about 10 vol.-%. Shear strength of the unmodified composites even decreases, after a maximum at 15% fiber content, caused by a gliding of the interface.

The improved fiber-matrix adhesion of the modified jute-polypropylene composites leads (figure 2) at comparable fiber contents to a distinctly higher dynamic strength, which is the stress at fracture measured in the load increasing test. Progress of damage (i.e. the cumulative loss-energy becomes a nonlinear function with an increasing number of load cycles [14,31]) at unmodified jute-PP composites is nearly independent of the fiber content, which results in independent maximal stresses.

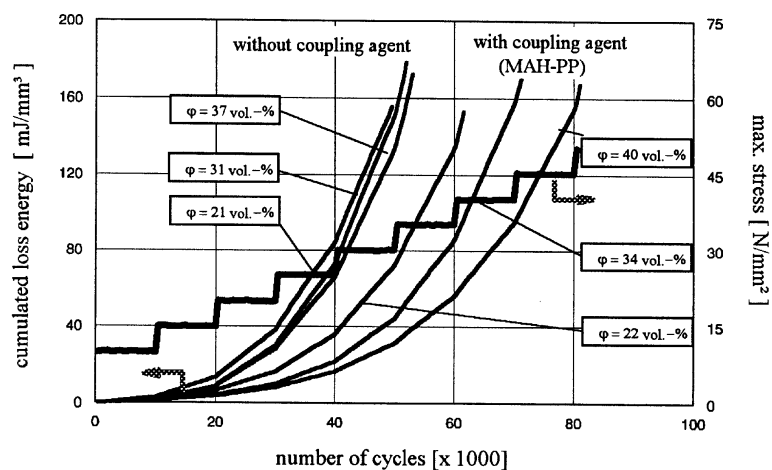


Figure 2: Influence of jute-fiber content and surface treatment on the cumulated loss energy of jute-PP-composites (test frequency = 10 Hz, R = 0.1)

It is only the improved fiber-matrix adhesion, caused by the MAH-PP coupling agent and the thereby improved force transfer, which reduces the progress of damage with increasing fiber content and leads to an increasing dynamic strength.

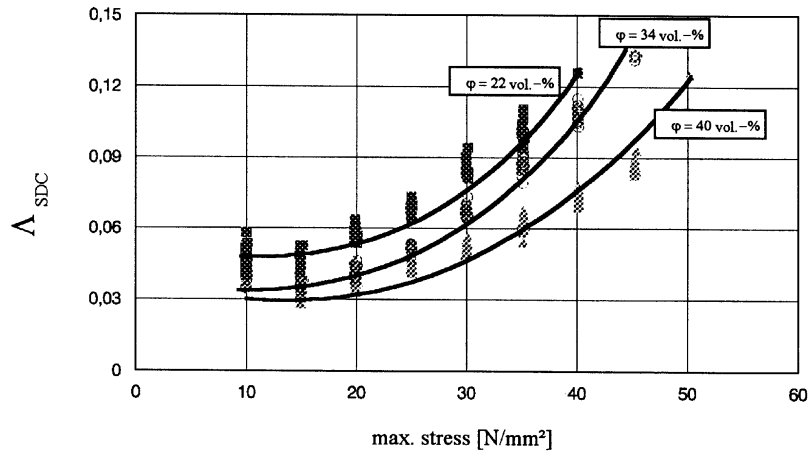


Figure 3: Influence of fiber content on the specific damping capacity (Λ_{SDC}) of MAH-PP-modified jute-PP-composites (test frequency = 10 Hz, $R = 0.1$, 10^4 number of cycles/stress levels)

Contrastingly to untreated jute-polypropylene composites, an 40%-increase of dynamic strength, at comparable fiber contents (ca. 40 vol.-%), is attained through the usage of the coupling agent. Our investigations showed furthermore (figure 3 and 4) that the damage of the jute-PP composites (modified as well as unmodified ones) does not occur spontaneously, but occurs continuously with the increasing stress. Whereby the limit stress i.e. the over proportional increase of the damping (Λ_{SDC}) [10], is moved to higher stresses (exemplarily shown for jute-PP composites modified with MAH-PP).

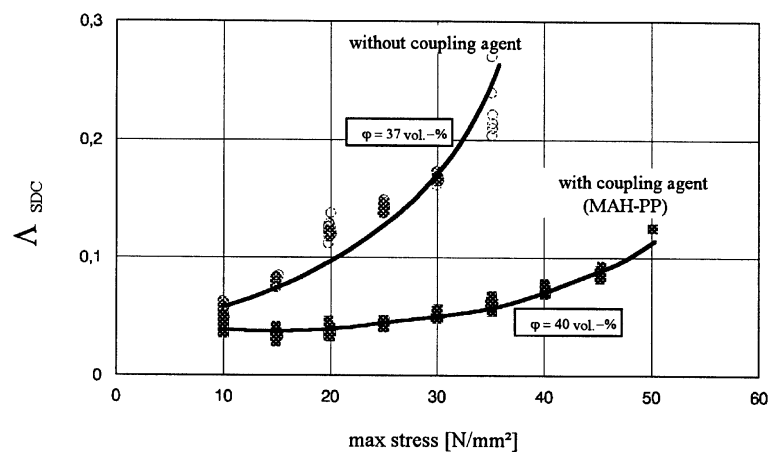


Figure 4: Influence of surface treatment on the specific damping capacity (Λ_{SDC}) of jute-PP composites (test frequency = 10 Hz, $R = 0.1$, 10^4 number of cycles/stress levels)

The damage of the composites, modified with MAH-PP, starts at distinct higher upper stress values, which were for about 20 N/mm^2 (figure 4). Whereas the unmodified jute-PP composites already show a remarkable increasing damping at the starting values of the upper stress, which was 10 N/mm^2 .

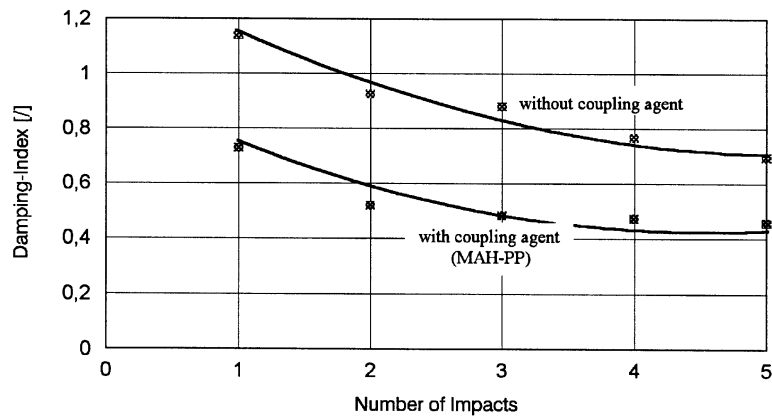


Figure 5: Influence of fiber treatment and number of impacts on the damping-index of jute-PP-Composites (impact drop height = 0.2 m, impact weight = 0,75 kg, fiber content = 36 vol.-%)

Figure 5 shows that the damping-index responds sensitive to change in fiber-matrix adhesion. At the first impact the damping ratio, i.e. damping of untreated to treated composites, is about 1.6. At the first impact, the (cumulated) loss-energy is only slightly higher for the specimens with untreated fibers (figure 6). The different slopes of the cumulated impact loss-energy curves show that due to fiber-matrix debonding more energy is dissipated by the specimen without treatment when they are subjected to repeated impact.

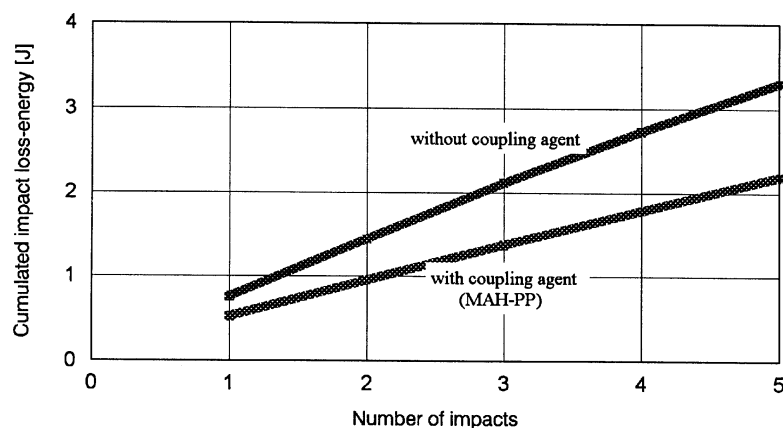


Figure 6: Influence of fiber treatment and number of impacts on the cumulated loss-energy of Jute-PP-Composites impact drop height = 0.2 m, impact weight = 0,75 kg, fiber content = 36 vol.-%

CONCLUSION

Distinct risings of the characteristic values of jute-polypropylene composites were attained with the application of MAH-PP copolymers. Flexural strength was increased for 40%, a 40%-increase was also measured for the dynamic strength in the load increasing test.

The improved fiber-matrix adhesion is caused by the chemical bonds between fiber and matrix which were provided by the coupling agent. With this, the force transfer from matrix to fiber is improved which leads to an improved reinforcing effect than in unmodified composites.

The improved fiber-matrix adhesion led to a higher damage resistance at cyclic-dynamic loadings. This was to be observed by a shift of the beginning damage towards higher maximal stresses and by a slower progress of damage with increasing load cycles respectively max. stresses. The tested composites without coupling agent independently of the fiber content (21 vol.-% to 37 vol.-%) showed a nearly identical behaviour towards constant values for the dynamic strength. With the application of MAH-PP coupling agent it was possible to reduce, with increased fiber contents, the progress of damage and with this to attain an increasing dynamic strength.

The improved fiber-matrix adhesion led to a decrease in damping-index and (cululated) loss-energy at impact loadings.

REFERENCES

1. J. Gassan, A.K. Bledzki, *Angew. Makromole. Chem.* 236, 129 (1996)
2. A.K. Bledzki, S. Reihmane, J. Gassan ; *J. Appl. Polym. Sci.* 59, 1329 (1996)
3. N.N., Technical Information about Vestolen® P 6000F, 1994
4. D.Maldas, B.V. Kokta, R.G. Raj, C. Daneault, *Polymer* 29, 1255 (1988)
5. D.S. Varma, M. Varma, I.K. Varma, *Text. Res. Inst.* 54, 821 (1984)
6. P. Zadorecki, P. Flodin, *J. Appl. Polym. Sci.* 31, 1699 (1986)
7. J. Gassan, A.K. Bledzki, 7th Interational Techtexsil Symposium, June 19 - 21, 1995 Frankfurt (Germany)
8. D. Maldas, B.V. Kokta, C. Daneault, *J. Appl. Polym. Sci.* 37, 751 (1989)
9. D. Maldas, B.V. Kokta, C. Daneault, *J. Vinyl Technol.* 11 (2), 90 (1989)
10. W. Janzen, Zum Versagens- und Bruchverhalten von Kurzglasfaser-Thermoplasten, Ph.D-thesis at the University of Kassel, Institut für Werkstofftechnik, Kassel 1989
11. P. Zadorecki, T. Rönnhult, *J. Polym. Sci. Part A Polym. Chem.* 24, 737 (1986)
12. M.H. Schneider, K.I. Brebner, *Wood Sci. Technol.* 19, 67 (1985)
13. J. Kuruvilla, Th. Sabu, C. Pavithran, *Comp. Sci. Techn.* 53, 99 (1995)
14. A.K. Bledzki, J. Gassan, K. Kurek, *Experimental Mechanics*, in press
15. S.C.O. Ugbohue, *Text. Inst.* 20 (4), 1 (1990)
16. J.I. Kroschwitz, *Polymers: Fibers and Textiles*, Wiley, New York, 1990
17. S.H. Zeronian, H. Kawabata, K.W. Alger, *Text. Res. Inst.* 60 (3), 179 (1990)
18. M.A. Semsazadeh, *Polym. Comp.* 7 (1), 23 (1986)
19. E.T.N. Bisanda, M.P. Ansell, *Comp. Sci. Technol.* 41, 165 (1991)

20. P.K.Ray, A.C.Chakravarty, S.B. Bandyopadhyay, *J. Appl. Polym. Sci.* 20, 1765 (1976)
21. A.N. Shan, S.C. Lekkard, *Fibre Sci. Technol.* 15, 41 (1981)
22. L. Hua, P. Flodin, T. Rönnhult, *Polym. Comp.* 8 (3), 203 (1987)
23. L. Hua, P. Zadorecki, P. Flodin, *Polym. Comp.* 8 (3), 199 (1987)
24. T. Sterzynski, B. Triki, S. Zelazny, *Polimery* 40 (7/8), 468 (1995)
25. K.-P. Mieck, A. Nechwatal, C. Knobelsdorf, *Angew. Makromole.Chem.* 224, 73 (1995)
26. B.V. Kokta, R.G. Raj, C. Daneault, *Polym.-Plast.Technol.Eng.* 28 (3), 247 (1989)
27. K.-P. Mieck, A. Nechwatal, C. Knobelsdorf, *Angew. Makromole.Chem.* 225, 37 (1995)
28. M. Avella, C. Bozzi, R. dell'Ebra, B. Focher, A. Marzetti, E. Martuscelli, *Angew. Makromole.Chem.* 233, 149 (1995)
29. J. Felix, P. Gatenholm; *J. Appl. Polym. Sci.* 42, 609 (1991)
30. A. Karmaker, J. Schneider, *J. Mater.Sci.Letters* 15, 201 (1996)
31. A.K. Bledzki, K. Kurek, G. Wacker, J. Gassan, *Materialprüfung* 37, 360 (1995)
32. B. Lazan, Damping of Materials and Membrans in Structural Mechanics, Pergamon Press (1968)
33. S. Dong, S. Sapiaha, H.P. Schreiber, *Polym. Eng. Sci.* 33, 343 (1993)

Notation

R	Stress ratio
Λ_{SDC}	Specific damping capacity
σ_{flex}	Flexural strength
ϕ	Fiber content

MODIFIED EPOXY RESIN MATRIX WITH CROSSLINKING STATE UNHOMOGENEITY

Shen Chao

*Beijing Institute of Aeronautical Materials,
P.O. Box 81-12, Beijing, 100095, P.R. China*

SUMMARY: The object of this paper is to modify epoxy resin matrix toughness with crosslinking state unhomogeneity. Three aromatic diamines were used to change the crosslinking structure of dicyandiamide / substituted urea / bisphenol A based epoxy resin system. By evaluation of neat resins and composites properties and Scanning Electron Microscope (SEM) analysis of fracture profile of neat resins tension and composites interlaminar fracture toughness G_{IIC} , improved epoxy resin toughness with crosslinking state unhomogeneity has been investigated. The results indicate that resin matrix hygrothermal property has been elevated when its toughness has been improved. The more unhomogeneous the crosslinking state is, the higher the resin toughness is. The service temperature of these resin matrices is up to 80 °C.

KEYWORDS: epoxy resin, modified toughness, crosslinking state unhomogeneity, hygrothermal property

INTRODUCTION

The most widely used composite materials in the aerospace industry are based on epoxy resin. In recent years, additional performance requirements have led to the development of modified epoxy resin matrices. One is to increase the toughness, the another is to enhance hygrothermal property for high temperature application^[1].

A series of different toughening techniques for thermoset resins have been developed over the last few years. Both the reduction of crosslink density and the incorporation of low molecular weight liquid rubbers can lead to a substantial increase in toughness^[2]. However this is usually achieved at the expense of the high temperature performance of the material. A variety of approaches to combine the mechanical nature of brittle high temperature thermosets and tough thermoplastics in one matrix have been successfully developed in recent years^[3]. Another promising approach to modify epoxy resin toughness with crosslinking state unhomogeneity has been reported.

In this paper, modified epoxy resin toughness with crosslinking state unhomogeneity has

been investigated by using three aromatic diamine to change the crosslinking structure of dicyandiamide/substituted urea/bisphenol A based epoxy resin system. Aromatic diamine pre-react with epoxy at high temperature to form high crosslinking structure, then dicyandiamide/substituted urea react with epoxy resin^[4] at middle temperature to form low crosslinking structure. The service temperature of these resins has been elevated when their toughness improved.

EXPERIMENTAL

Resins

The resin systems selected for this study were based on dicyandiamide /substituted urea/bisphenol A epoxy resin. Diaminodiphenylsulfone(DDS), Diaminodiphenylmethane (DDM) and 2,2'-Bis(4-aminophenoxyphenyl)-propane(BAPP) were used as modifiers respectively. After aromatic diamine react with epoxy resin at 180 °C for 2 hrs., curing agents were added at 60 °C, then the system was stirred until a homogeneous mixture was obtained.

Prepreg and Laminate Fabrication

Carbon fiber of T300B-12K was selected for prepreg fabrication. Unidirectional prepregs were produced by a hot melt process. The fiber areal weight was 130 ± 5 g/m². The resin content was $35 \pm 2\%$. Laminates were laid up and cured in an autoclave for 1.5 hrs. at 125 °C with a heating and cooling rate of 2 °C/min. The fiber volume content in the cured panels was $60 \pm 3\%$.

Neat Resin Panels Casting

The melt resin was degassed in a container under vacuum at 60 °C for 1 hrs. The sample was poured into a matched flat mold preheated to 80 °C and degassed under vacuum at 80 °C for 0.5 hrs. Then the casting neat resin panels cured at 125 °C for 1.5 hrs. with a heating and cooling rate of 2 °C/min.

Test Methods

The Differential Scanning Calorimetry (DSC) were obtained with a Perkin Elmer DSC-7 Differential Scanning Calorimeter with a heat-up rate of 10 °C/min. Curing degree was measured by a Magna-75 Fourier Transform Infrared Spectrometer. A Imass DS-I Dynamic Mechanical Analyzer was used to measure the deformation response of the cured resin. A test frequency of 1Hz and a heat-up rate of 3 °C/min (wet, 10 °C/min) was applied. All mechanical testing of neat resin panels and laminates was done by a MTS tensile machine.

Hot/Wet Performance

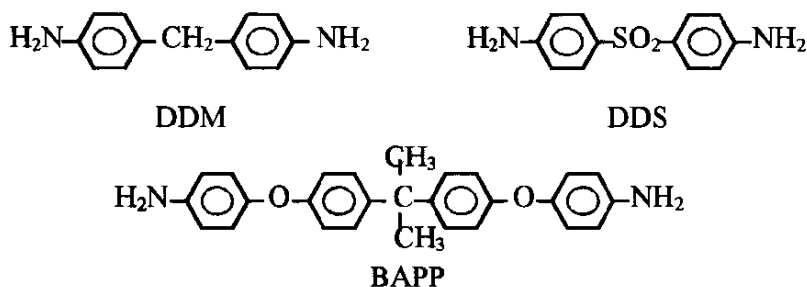
To evaluate the hot/wet performance, neat resin specimens of 4mm thickness were stored in

boil water for 7 days. The moisture uptake was monitored gravimetrically. The hot/wet resistance of neat resins and laminates was tested by Dynamic Mechanical Analysis (DMA) and interlaminar shear test after immersed in boil water for two days.

RESULTS AND DISCUSSION

Resin Reaction

The crosslinking density of aromatic diamine and bisphenol A epoxy is higher than dicyandiamide/substituted urea/bisphenol A epoxy resin system. So crosslinking state unhomogeneity can be formed when aromatic diamine was added to dicyandiamide/ substituted urea epoxy resin system. The structure of three aromatic diamines was shown as following:



The addition amount of three aromatic diamine was all 0.2 Equivalent in order to compare the influence of crosslinking state unhomogeneity while the hot-melt unidirection prepreg has middle tack and good drape. The prereaction of three aromatic diamine and epoxy was all at 180 °C for 2 hrs. in order to avoid the effect of processing parameters. Fourier Transform Infrared Spectroscopy (FTIR) and DSC show aromatic diamine is completely reaction under this condition.

DSC was used as a preliminary indicator of system reactivity. The initiation temperature T_i , the onset of reaction exotherm, and the temperature at the exothermic peak, T_p , were used to evaluate relative reactivity. Less values of T_i and T_p would indicate a higher reactive system. DSC results were summarized in table 1.

Table 1 DSC Results of Resins

	No aromatic diamine	BAPP	DDM	DDS
T_i , °C	128	124	124	125
T_p , °C	144	143	143	143
T_f , °C	191	185	186	184

Storage life also shown the same result (Table 2). The reaction for these aromatic diamine modified resin systems at room temperature was also higher than the system without aromatic diamine. Storage stability was evaluated by monitoring prepreg tack at room temperature.

Table 2 Storage life of resins

	No aromatic diamine	BAPP	DDM	DDS
Storage life, days	45	30	30	30

According to dicyandiamide/substituted urea/epoxy resin system, heating and cooling rate of 2 °C/min and dwell 1.5 hrs. at 125 °C were selected for these systems. The curing degrees tested by FTIR were outlined in Table 3.

Table 3 Curing degrees of resins

	No aromatic diamine	BAPP	DDM	DDS
Curing degree, %	96	94	94	93

Curing degree decrease is because of the high crosslinking density of aromatic diamine and restrict the curing reaction of low crosslinking density section. These parameters were then used to casting neat resin panels and laminates fabrication for performance testing.

Toughness of Resin Systems

The stress-strain curves of casting neat resin panels show a plastic deformation. (Figure 1) Aromatic diamine modified systems have larger fracture strain than the system without aromatic diamine. The fracture strain of DDM modified system was correspond to DDS modified system. BAPP modified system has lower strength and smaller fracture strain is because the casting neat resin panel has some bubbles.

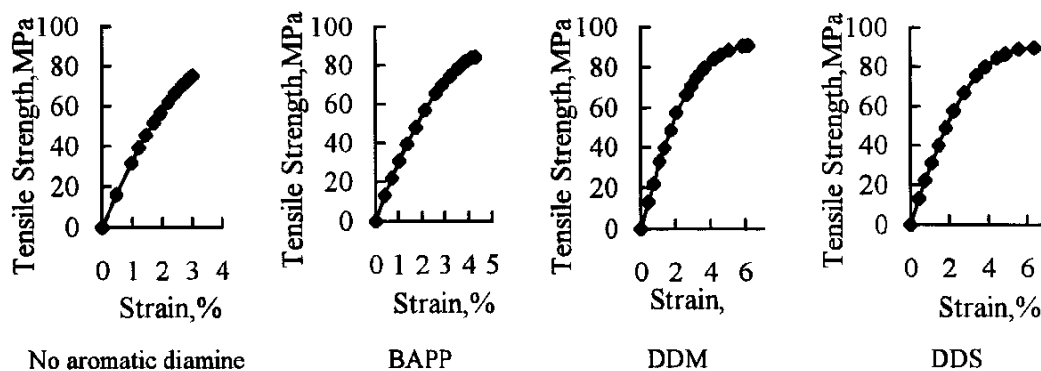


Figure 1 Stress-strain curves of casting neat resin panels

The toughness of three aromatic diamine modified systems was higher than the system without aromatic diamine. G_{IC} fracture toughness shows an increase from 184% to 283 % compared to the system without aromatic diamine. (Figure 2) BAPP system G_{IC} was lower because of BAPP longer molecular chain. The crosslinking density of high crosslinking section and crosslinking state unhomogeneity decrease. DDS system G_{IC} was the most high because of DDS short molecular chain and big stiffness.

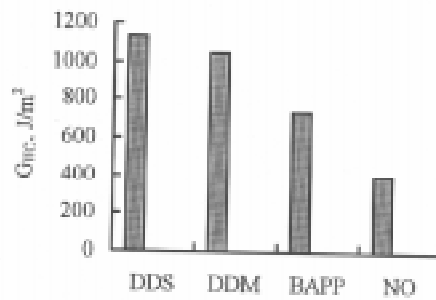


Figure 2 Interlaminar fracture toughness G_{IC} of composites

The improved toughness of three aromatic diamine modified systems was furthermore studied by SEM photomicrographs of neat resin tensile and G_{IC} fracture profile. (Figure 3, Figure 4) There was no two phases observed which means that high and low crosslinking density section didn't form separated phase. So these aromatic diamine modified systems toughness were improved by crosslinking state unhomogeneity.

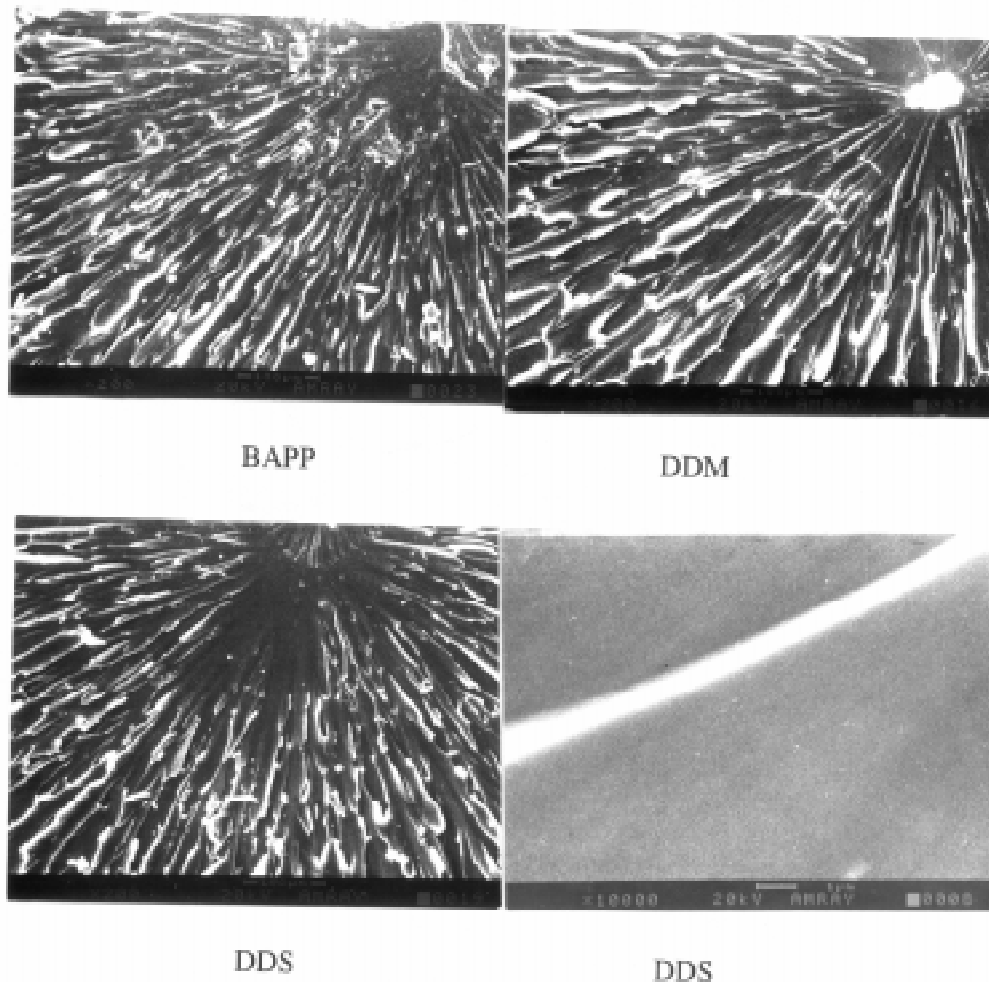


Figure 3 The tensile fracture profile of neat resins

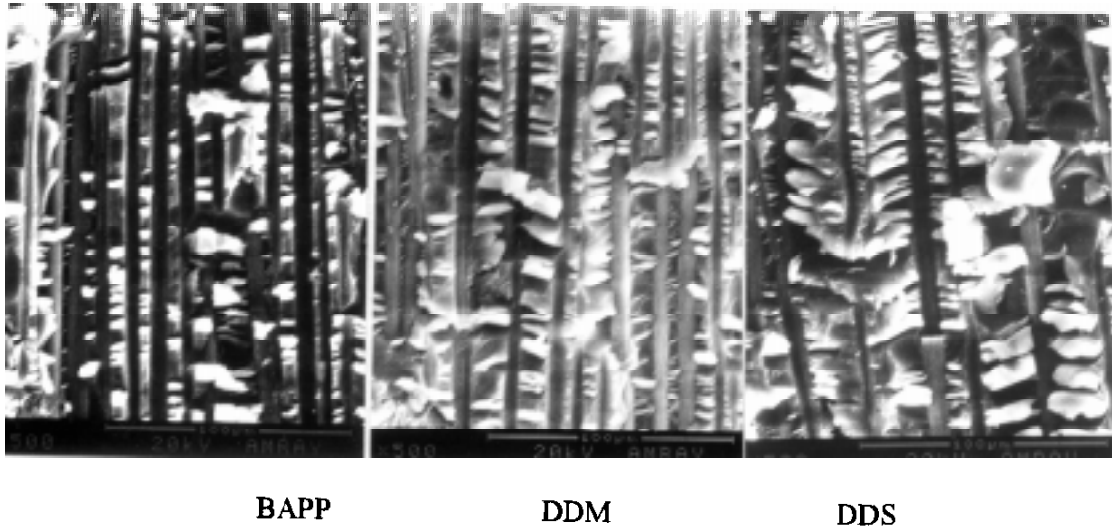


Figure 4 The G_{11C} profile of composites

Performance of Resins and Composites

Tensile strength was mainly determined by quality of casting neat resin panels and related to resin toughness. The larger the fracture strain is, the higher the tensile strength will be. Table 4 outline the tensile properties of casting neat resin panels.

Table 4 Tensile properties of neat resin

	No aromatic diamine	BAPP	DDM	DDS
Tensile strength, MPa	75.3	83.4	89.4	88.7
Tensile modulus, GPa	2.97	3.02	2.99	3.01
Fracture strain, %	3.01	4.08	5.52	5.31

Composites properties are almost the same (Table 5). Dry interlaminare shear strength (ILSS) also has little difference at room and high temperature.

Table 5 Composites properties

	No aromatic diamine	BAPP	DDM	DDS
Flexural strength, MPa	1670	1650	1640	1650
Flexural modulus, GPa	119	120	119	122
ILSS, RT, MPa	79.2	81.6	80.8	84.6
ILSS, 80 °C, MPa	57.0	58.9	58.3	61.5
ILSS, 100 °C, MPa		51.0	50.8	53.1

Excellent properties at elevated temperature can be completely sacrificed under wet conditions if a moisture pick-up of a lot. A low moisture take-up was shown in figure 5.

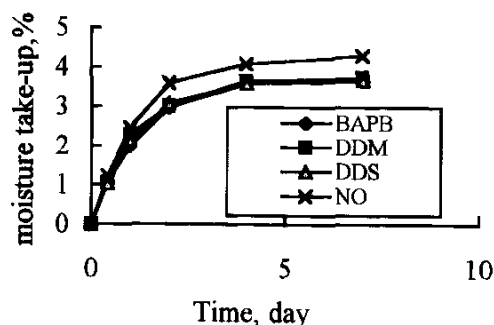


Figure 5 Moisture take-up vs time

This behavior is also reflected in the softening temperature(T_s) and glass transition temperature(T_g) of aromatic diamine modified systems as determined by DMA. While the softening temperature T_s of the system without aromatic diamine drops 29% from dry to wet condition, aromatic diamine modified systems show a loss of 21% between T_s (dry) and T_s (wet) (Table 6).

Table 6 Glass transition and softening temperature

	No aromatic diamine	BAPP	DDM	DDS
Dry T_g , °C	135	145	145	151
Dry T_s , °C	118	123	125	126
Wet T_g , °C	103	136	137	146
Wet T_s , °C	84	98	98	100

T_g maximum tan T_s tangent intercept

In order to evaluate the hot/wet properties of these resin systems, ILSS tests were conducted at both room temperature dry (RTD) and elevated temperature wet (ETW) conditions. The test results were summarized in Table 7. These results indicate that hot/wet properties of aromatic diamine modified systems are higher than the system without aromatic diamine. The retention of ILSS at 80 °C wet condition (ETW) reach to 50%, So these aromatic diamine systems can be used to 80 °C.

Table 7 Wet interlaminar shear strength

	No aromatic diamine	BAPP	DDM	DDS
ILSS, RT, MPa	60.9	65.2	64.8	67.9
ILSS, 80 °C, MPa	29.8	40.7	40.6	43.2

CONCLUSIONS

Investigations of matrix resin chemistry and mechanical properties led to the following conclusions:

The curing reaction of aromatic diamine modified systems was higher than dicyandiamide

/substituted urea resin system. Their toughness has been increased a lot because of crosslinking state unhomogeneity. Interlaminar fracture toughness G_{IIc} was as high as to 1133J/m^2 . The maximum tensile strength of casting neat resin panels was 89.4Mpa . Fracture strain was 5.52% . The normal mechanical properties was correspond to dicyandiamide/substituted urea resin system. Their hot/wet properties also have been improved and the service temperature is up to $80\text{ }^\circ\text{C}$.

REFERENCES

1. Fu Xeng-li, "Study on the Improvement of Toughness of Epoxy Resin", *Thermosetting Resin*, No.4, 1988,pp.11-17.
2. Feng Pu, "Phase Separation Theory of Systems of Epoxy Resin", *Thermosetting Resin*, No.1, 1992,pp.47-53.
3. Michael DiBerardino and Raymond Pearson, "Toughening Concepts for High Temperature Polymers", *25th International SAMPE Technical Conference*, 1993, pp.502-513.
4. Pyong-nae Son and Carl D. Weber, "Some Aspects of Monuron-Accelerated Dicyandiamide Cure of Epoxy Resins", *Journal of Applied Polymer Science*, Vol.17, 1973, pp.1305-1313.

THERMAL RESISTANT BLENDS OF BISMALIMIDE WITH POLYPHENYLENE OXIDE

Zhi-yu Xia¹, Franklin G. Shin² and Tze-chung Chan³

¹*Materials Research Centre, The Hong Kong Polytechnic University, Kowloon, Hong Kong*

²*Department of Applied Physics /Materials Research Centre,
The Hong Kong Polytechnic University, Kowloon, Hong Kong*

³*Department of Applied Biology & Chemical Technology /Materials Research Centre,
The Hong Kong Polytechnic University, Kowloon, Hong Kong.*

SUMMARY: The blends of Bismaleimide (BMI) and Polyphenylene oxide (PPO) were prepared with the aims of toughening BMI and improving PPO's thermal and chemical resistance. Good miscibility was exhibited in the BMI/PPO blends prepared by a solution method. A dispersion of the BMI phase in the blends was found with an increase in the PPO content in an optical microscopic study. In the form of filler particles, PPO affected the curing and melting behaviours of BMI. An increase in the curing temperature and a decrease in the reaction heat were observed in DSC studies, while the melting process tended to be more independent of the presence of PPO. The improvement in the PPO's thermostability was confirmed in the blends through TGA and TMA analyses, and the semi-IPN structure was verified through TGA experiments.

KEYWORDS: bismaleimide (BMI), polyphenylene oxide (PPO), blends, semi-IPN, thermal resistant material

INTRODUCTION

In less than twenty years advanced composites have been established as efficient high-performance structural materials. Among them, the polyimide matrix composites are widely used as heat-resistant polymeric materials in a variety of civil and military applications including aircraft structures, aeropropulsion, missiles and space vehicles. Although polyimides are excellent materials in thermal-oxidative stability, most of them have the drawback of poor processability and their practical applications are thus greatly restricted. However, Bismaleimide (BMI) offers a comprehensively good performance in both thermostability and processability. Its advantages over common epoxy in better thermal-oxidative stability are attributed to its high crosslink density and the aromatic and heterocyclic structures in the network. In addition to its thermal-oxidative stability, a low moisture absorption can be achieved because the imide functionality has lower capacity for hydrogen bonding than -OH or -NH₂ containing polymers. Most significantly, BMI resins can be fabricated using epoxy-like conditions and the addition polymerization mechanism gives void-free structures. Hot-melt and solution methods are commonly applied to impregnate fibres in the preparation of BMI composites. Compression moulding, autoclave moulding, filament winding and even resin transfer moulding (RTM) are all practical methods in making BMI composites [1].

Nevertheless, the inherent brittleness in BMI materials has been the major disadvantage which limits their application. They are usually high modulus materials with very low elongation at break. Other problems include the susceptibility to microcracking and the tendency of impact damage in composite laminates. Therefore, modification of BMI to improve its brittleness without a drastic sacrifice in high-temperature performance has aroused much interest in the field of material research and development. A number of methods have been explored in this aspect. One of the popular methods is through the copolymerization with reactive modifiers, such as diamine and diallyl compounds. Other chemicals including epoxy, divinyl benzene and vinyl ester resins have also been tried. Various complicated reactions are yet involved in the modification, and a lot of work still needs to be done before the chemistry and kinetics are clearly known and the microstructure and final properties of the material understood. Another convenient method in modifying BMI is blending with engineering thermoplastics. Through blending with appropriate high-performance thermoplastics, desirable thermal-mechanical properties may be imparted to the BMI to produce blends with promising behaviours. It has been concluded that the backbone chemistry, molecular weight, toughness of the thermoplastics, as well as the adhesion between the phases, influence the toughness properties of the corresponding BMI blend system [2,3]. Some authors [4-8] have also studied blends of modified BMI with thermoplastics including polysulfone, polyether sulfone, polyether imide, poly(arylene ether ketone), and encouraging results have been revealed.

As one of the commonly used engineering thermoplastics, polyphenylene oxide (PPO) has superior mechanical properties and excellent processability. Although PPO is quite adequate for certain practical high temperature applications, its thermo-oxidative stability is much worse than most polyimides. Through blending with BMI to form a semi-IPN structure, its high temperature performance is expected to be improved. Moreover, chemical resistance is also expected to be improved as a result of the semi-IPN structure.

In this paper, PPO was used as the thermoplastic modifier in the blending modification of BMI. The miscibility of the BMI with the PPO was studied. DSC, TMA and TGA were utilised in the investigation of the thermal and mechanical behaviours of the blends.

EXPERIMENTAL

Chemicals

Most chemicals were purchased from Aldrich Chemical Company (USA): 1,1'-(Methylene-di-4,1-phenylene)-bismaleimide (BMI), 95%; Poly(2,6-dimethyl-1,4-phenylene oxide); Diethylene chloromethane; trichloromethane.

Material preparation and characterization

A mixed solvent of dichloromethane and trichloromethane was used in the solution blending of PPO with BMI. After the solvent was stripped off, the samples were dried under vacuum. In order to study the morphology before curing, the blend solutions were degassed in an ultrasonic bath and applied to glass plates to obtain thin samples when dried under vacuum. The films were studied using episcopic light in a Nikon Microphot FXA microscope. A Perkin-Elmer DSC 7 was used to investigate the melting and curing behaviours of the BMI, PPO and their blends. Compression moulding was applied for the curing process. The

thermogravimetric and thermomechanical performances of the blends were evaluated using a Perkin-Elmer TGA 7 and TMA systems.

RESULTS AND DISCUSSION

Miscibility of the blends

Both cured and uncured samples of the blends with different compositions were observed under an optical microscope. The miscibility of the BMI and PPO in the blends prepared by the solution method is fairly good and the two phases are evenly distributed. The microscope photos in Fig. 1 show the change in morphology in relation to the PPO content. It can be seen from the pictures that the size of the BMI particles decreases with an increase in the PPO content. When the PPO content exceeds 50%, a continuous phase of PPO is formed, with the BMI dispersed inside it in the form of filler particles. This is more obviously shown in the picture for the sample with 45% PPO under higher magnification in which BMI spreads into very fine particles distributed in the PPO continuous phase. Upon curing, the BMI particles disappear as they first melt and then undergo the crosslinking reaction to form the semi-IPN structure where the PPO phase is confined in the BMI network.

DSC melting and curing behaviours

As a crystalline monomer with reactive polyfunctional maleimide groups, BMI melts upon heating and undergoes the curing reaction under high temperatures, even in the absence of an initiator. A three-dimensional network structure is formed as a result of crosslinking during curing. In the DSC thermogram (Fig. 2), the endothermic peak around 156 °C represents the melting of BMI, while the broad exothermic peak over the temperature range of 170 ~ 270 °C indicates the release of reaction heat during the curing process. PPO is one of the high-performance engineering plastics with stable thermal-properties over a wide temperature range: only a small endothermal peak appears around 250°C, inferring its melting at this temperature. PPO itself does not participate in the crosslinking reaction during the curing process, but it acts as a filler and affects BMI's melting and curing behaviours.

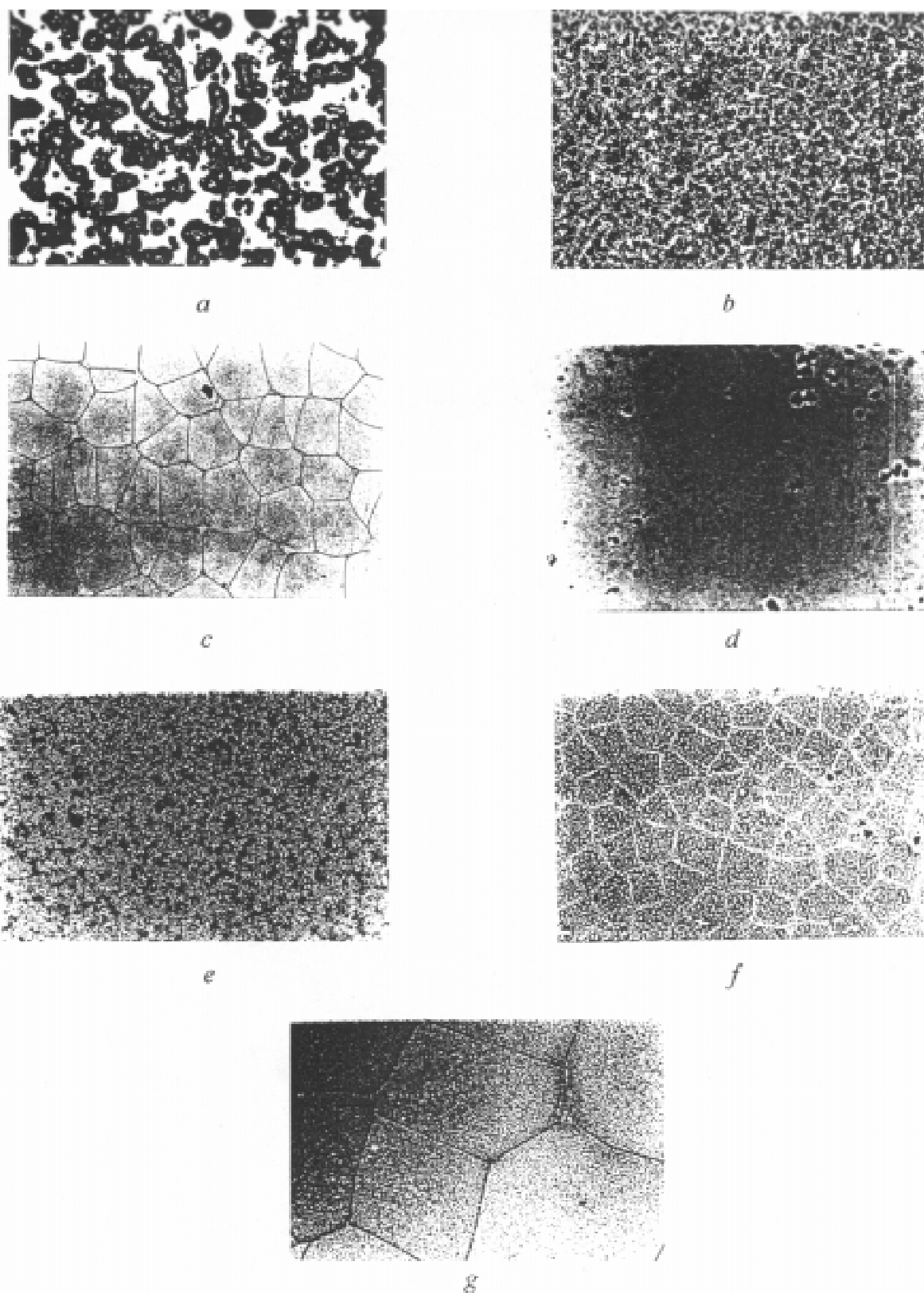


Fig. 1: Photo micrographs of BMI and BMI/PPO blends
a) BMI (x100) before curing, b) 30%PPO (x100) before curing, c) 70%PPO (x100) before curing,
d) BMI (x100) after curing, e) 30%PPO (x100) after curing, f) 70%PPO (x100) after curing,
g) 45%PPO (x400) before curing

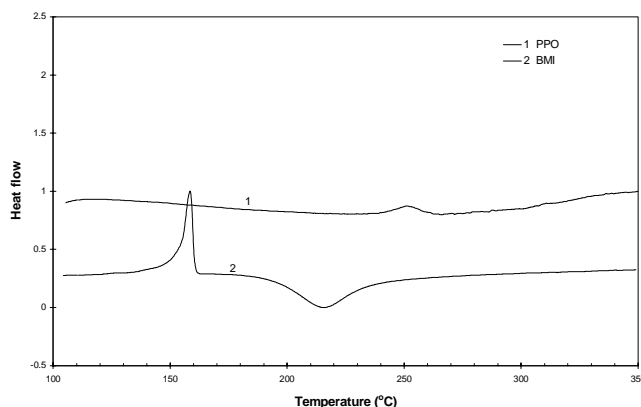


Fig. 2: DSC thermograms for BMI & PPO
($20^{\circ}\text{C}/\text{min}$, N_2)

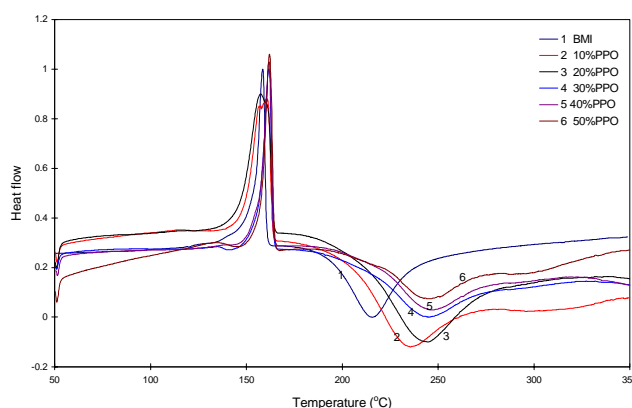


Fig. 3: DSC thermograms for BMI/PPO
($20^{\circ}\text{C}/\text{min}$, N_2)

The DSC melting and curing behaviours for the blends show different dependence on the composition. The thermograms for BMI and its blends with PPO of contents up to 50% are shown in Fig. 3. It can be seen that as the PPO content increases the curing peak shifts to higher temperature and is broadened, while the melting peak remains quite steady at its position. It is known that parameters obtained from DSC are strongly dependent upon the scanning rate used in dynamic DSC testing. In order to find the zero-scanning DSC parameters, experiments at a series of scanning rates, 2.5, 5, 10, $20^{\circ}\text{C}/\text{min}$, were performed on samples of various compositions and the data were processed by extrapolation against the scanning rate. The extrapolated curing temperature tends to increase and the reaction heat tends to decrease, even after considering the weight change of BMI in the blends of different compositions (Table 1 and Fig. 4). It is concluded that although the PPO phase in the blends brings toughness to the material through lowering the crosslinking density of the network, it increases the steric hindrance at the reactive maleimido groups in curing, and therefore shows a tendency to retard the BMI's curing reaction. On the other hand, the melting of BMI seems more independent of the composition changes in the blends. The extrapolated melting temperature fluctuates only within a narrow range and the melting enthalpy is fairly constant after correction for blend composition (broken line in Fig. 5). Part of the reason for this may be that melting is more likely a local behaviour and not prone to the influence of the environment in which BMI monomers are situated.

Table 1 DSC parameters for BMI and its blends at zero-scanning rate

PPO% (wt.)	Melting			Curing		
	T _p (°C)	ΔH (J/g)	ΔH (J/g)*	T _p (°C)	ΔH (J/g) ⁺	ΔH (J/g)*
0	155.5	61.6	61.6	182.1	-107.1	-107.1
10	157.3	56.7	63.0	203.2	-71.8	-79.7
20	157.1	51.2	64.0	208.8	-50.5	-63.1
30	158.4	47.0	67.1	208.0	-60.0	-85.7
40	157.8	43.0	71.7	208.9	-52.0	-86.7
50	158.0	34.5	69.0	205.4	-39.9	-79.8

+ Negative values of enthalpy indicate an exothermic process

* After correction for composition of the blend

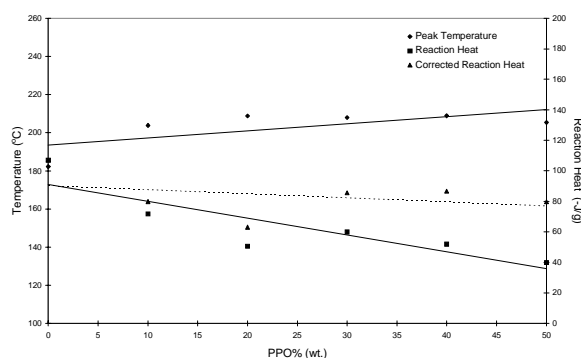


Fig. 4 Extrapolated DSC parameters in curing of BMI with different PPO contents

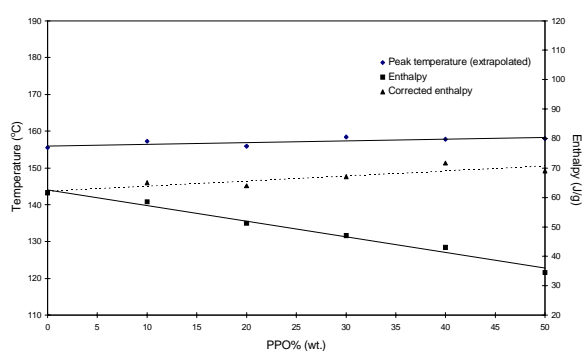


Fig. 5 Extrapolated DSC parameters in melting of BMI with different PPO contents

Kinetic study

DSC is a quick and convenient method with which to study the reaction kinetics. Compared with the Borchardt-Daniels method, which is generally used by the commercial software packaged with many DSC systems, the Kissinger method is more suitable for modelling multiple consecutive reactions [9]. It deals with the position of the peak maximum obtained under various DSC scanning rates, and it is based on the following equation:

$$\ln(\phi / T_p^2) = -E / RT_p + \ln(AR / E)$$

where ϕ is the scanning rate (K/min), T_p is the peak temperature in Kelvin, E and A are the apparent activation energy (kJ/mol) and the frequency factor respectively. A plot of $\ln(\phi / T_p^2)$ against $1/T_p$ will provide the solution to E . For the frequency factor A , Kissinger derived the following semi-empirical expression for n th-order reactions:

$$A = \frac{\phi E \exp(E / RT_p)}{RT_p^2 [n(1 - \alpha_p)^{n-1}]} \approx \frac{\phi E \exp(E / RT_p)}{RT_p^2}$$

Here, α_p is the extent of reaction at the peak exotherm. He argued that $n(1 - \alpha_p)^{n-1} \approx 1$ and is independent of heating rate.

Fig. 6 is the plot of $\ln(\phi / T_p^2)$ against $1/T_p$. The linear regression results are listed in Table 2. It is reasonable that BMI shows the lowest E and A compared with the blends, while E tends to decline with an increase in the PPO content. PPO disperses the BMI monomer in the blends, causing hindrance to the curing process, so resulting in an increase in the activation energy.

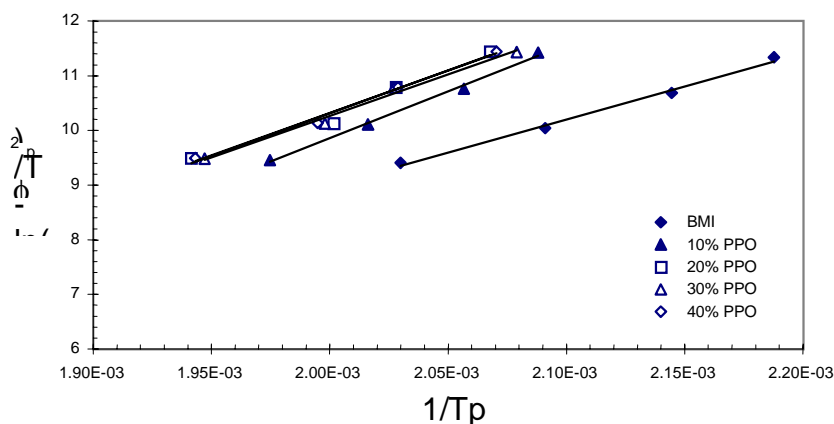


Fig. 6 Application of the Kissinger method in kinetics study

Table 2 Kinetic parameters from Kissinger analysis in curing of BMI and its blends

PPO % (wt.)	a	b	R ²	E (kJ/mol)	lnA
0	12143	15.30	0.9931	101.0	24.7
10	16215	22.59	0.9691	134.8	32.2
20	15648	20.98	0.9710	130.1	30.6
30	15137	20.01	0.9877	125.8	29.6
40	15580	20.84	0.9926	129.5	30.5

(a, slope; b, intercept; R², least-square regression coefficient)

Thermogravimetric analysis

Samples of BMI, PPO and their blends were tested in a Perkin-Elmer TGA 7. The diagrams shown in Fig. 7 exhibit the pattern of one-stage degradation for all the samples. This proves the semi-IPN structure of the BMI/PPO blends and indicates the retardance of degradation of the PPO phase when confined by the BMI network.

The relevant parameters in the decomposition of the materials are listed in Table 3. The maximum decomposition temperature (T_{max}) obtained from the first derivative analysis indicates the temperature under which a drastic decomposition and an overall break-down of the material occurs. $T_{1/2}$ is known as the temperature at 50% weight retention, and the final weight retention at the end of material decomposition is the char yield. A comparison of the onset decomposition temperature (T_{onset}) and T_{max} at different PPO contents clearly shows that both T_{onset} and T_{max} decrease with an increase in the PPO content (Fig. 8), but apparent drop is not observed until the PPO content reaches 20%. When the simple rule of mixtures (dotted

lines) is taken for comparison, it is found that the T_{onset} of the blend sample is lower than the temperature estimated from the mixing rule, while T_{max} gives higher values. The drop in T_{onset} for the blended samples may be due to the possible presence of an un-confined PPO phase which causes the early degradation of parts of the sample. Nonetheless, the overall semi-IPN structure contributes to the heat-resistance of the blend, hence raises T_{max} , which is the characteristic parameter for the heat-resistant property of the entire material. In other words, PPO's thermogravimetric resistance is improved by blending with BMI. Moreover, a decrease is observed in both $T_{1/2}$ and the char yield with the increase in the PPO content of the blends. It is expected that the char yield follows the mixing rule (dotted line in Fig. 9) since it is a mixture of the ashes of the BMI and PPO.

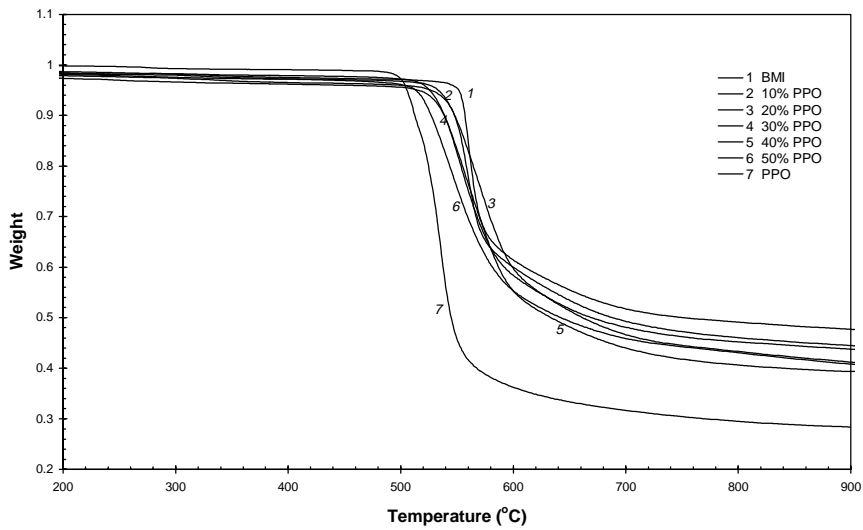


Fig. 7: Thermogravimetric analysis of BMI, PPO and BMI/PPO blends

Table 4: TGA results for BMI and its blend systems

PPO % (wt.)	T_{onset} (°C)	T_{max} (°C)	$T_{1/2}$ (°C)	Char yield (%)
0	549.9	556.6	757.8	46.7
5	550.0	562.7	692.9	43.4
10	544.9	556.5	698.8	43.7
15	545.4	559.8	695.8	42.6
20	543.7	561.0	672.3	39.7
25	535.8	551.5	685.8	42.8
30	530.1	549.4	681.7	42.7
40	526.2	553.4	638.0	38.9
50	520.6	543.2	653.9	38.9
100	513.9	531.5	541.3	28.4

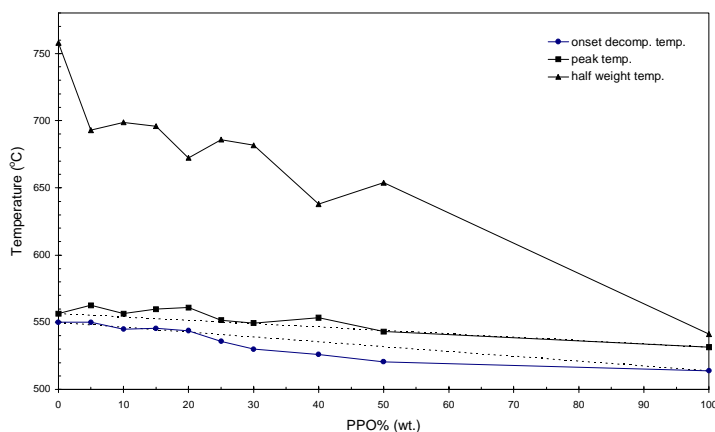


Fig. 8: TGA decomposition temperature

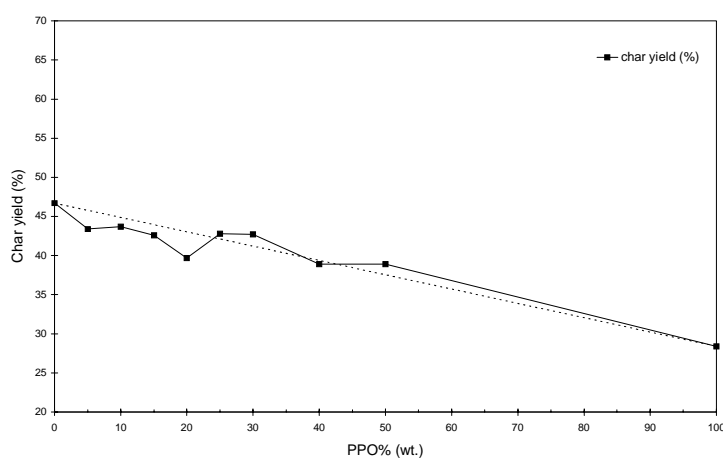


Fig.9: Char yield for BMI/PPO blends

Thermomechanical analysis

While dynamic TGA provides an indication of short-term thermal stability, TMA studies the mechanical changes during heating including the expansion of samples. Fig. 10 is the TMA thermographs for BMI material and its blends with 10-30% PPO. Apparently there is no obvious change in dimensions over the wide temperature range up to 400 °C, and the simple thermal expansion is fairly steady. None of the glass-transitions in both BMI and PPO phases can be observed from the thermographs. The high crosslink density of the network structure in the materials is believed to restrict the mobility of the molecular segments and thus suppresses the dimensional changes in the materials under test. The PPO phase is extensively distributed in the BMI network and its segmental movement is greatly restricted by the network structure. Therefore, the promising thermal mechanical stability is reflected from the TMA results of BMI and its blends with PPO. However, a difference in the change of expansion coefficient in different temperature ranges is noticeable as shown in Table 4. In the high temperature range (300-350 °C), BMI gives smaller expansion coefficient as the result of its high crosslink density of the network. Higher expansion coefficients are observed for the blend samples due to the higher expansion coefficient of embedded PPO ($5.2 \times 10^{-5}/^{\circ}\text{C}$) [10] in the semi-IPN structure.

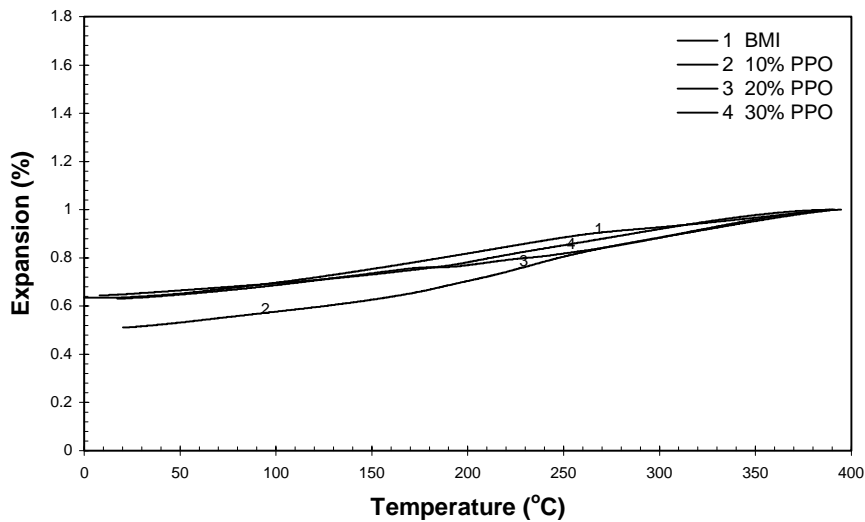


Fig. 10 Thermomechanical analysis of BMI and BMI/PPO blends

Table 4 Comparison of thermal Expansion coefficient (α) from TMA

α ($10^{-6}/^{\circ}\text{C}$)	BMI	10% PPO	20% PPO	30% PPO
50 ~ 100 $^{\circ}\text{C}$	10.8	18.8	9.3	8.6
300 ~ 350 $^{\circ}\text{C}$	10.1	29.1	19.7	18.3

CONCLUSION

BMI exhibits good miscibility in blending with PPO through solution method. Optical microscopy shows the dispersion of BMI phase with the increase in PPO content. The PPO phase affects the curing behaviour of BMI in the blends, increasing its curing temperature and reducing the reaction heat. On the other hand, BMI's melting behaviour is quite independent upon the presence of PPO. The improvement in PPO's thermostability has been confirmed in the blends through TGA and TMA analyses. The semi-IPN structure is also verified through TGA experiments.

ACKNOWLEDGMENT

The authors are grateful to the financial support by the Hong Kong Polytechnic University. Supports to the present project by the Department of Applied Physics and Department of Applied Biology & Chemical Technology are also acknowledged.

REFERENCES

1. Wilson, D., "Recent advances in polyimide composites", *High Performance Polymers*, No.5, 1993, pp. 77-95.
2. Stenzenberger, H.D. and Konig, P., "New functionalized poly(arylene-ether ketone)s and their use as modifiers for bismaleimide resin", *High Performance Polymers*, No.5, 1993, pp.123-137.
3. Stenzenberger, H.D., Romer, W., Hergenrother, P.M., Jensen, B. and Breitigam, W., "Functionalized poly(arylene ethers) as toughness modifiers for bismaleimides", *35th. International SAMPE Symposium*, Anaheim, California, USA, April 2-5, 1990, pp. 2175-2188.
4. Lan, L.W., Mu, Y.Z. and Jing, X.L., "Study of the toughening of bismaleimide resin", *Proceeding International Symposium of Polymer Alloys & Composites*, Hong Kong, December 9-11, 1992, Choy C.L. and Shin F.G., Eds, pp 314-316.
5. Wilkinson, S.P., Liptak, S.C., Wood, P.A., McGrath, J.E. and Ward, T.C., "Reactive blends of amorphous functionalized engineering thermoplastics and bismaleimide/diallyl bisphenol-A resins for high performance composite matrices", *36th. International SAMPE Symposium*, San Diego, California, USA, April 15-18, 1991, pp. 482-495
6. Rakutt, D., Fitzer, E. and Stenzenberger, H.D., "The fracture toughness and morphology spectrum of bismaleimide/polyetherimide moulding compounds", *High Performance Polymers*, Vol. 2, No. 2, 1990, pp. 133-147.
7. Wilkinson, S.P., Ward, T.C. and McGrath, J.E., "Effect of thermoplastic modifier variables on toughening a bismaleimide matrix resin for high-performance composite materials", *Polymer* Vol.34, No. 4, 1993, pp.870-884.
8. Glatz, F.P. and Mulhaupt, R., "Semi-interpenetrating networks of sulfur-containing bismaleimides" *High Performance Polymers*, No.5, 1993, pp. 297-305.
9. Taylor, S.M. and Fryer, P.J., "A numerical study of the use of the Kissinger analysis of DSC thermograms to obtain reaction kinetic parameters", *Thermochim. Acta*, Vol. 209, 1992, p113.
10. Brydson, J.A.; *Plastics Materials*; Butterworths Scientific, London, UK, 1989, p550.

A NEW CLASS OF THE THERMOTROPIC LIQUID CRYSTAL POLYMER: POLY(ARYL ETHER KETONE)S

Shanju Zhang¹, Yubin Zheng¹, Zhongwen Wu¹, Decai Yang², Ryutoku Yosomiya³

¹*Department of Chemistry, Jilin University, Changchun, 130023, P.R.China*

²*Polymer Physics Laboratory, Changchun Institute of Applied Chemistry,
Chinese Academy of Sciences, Changchun, 130022, P.R.China*

³*Department of Industrial Chemistry, Chiba Institute of Technology, 2-17-1,
Tsudanuma Narashino, Chiba, 275 Japan*

SUMMARY: The novel poly(aryl ether ketone)s containing chloro-side group were synthesized by nucleophilic substitution reactions of 4,4'-biphenol and chlorohydroquinone with either 4,4'-difluorobenzophenone (BP/CH/DF) or 1,4-bis(p-fluorobenzoyl)benzene (BP/CH/BF) and their thermotropic liquid crystalline properties were characterized by a variety of experimental techniques. The mesogen/hydroxy-quinone ratio is varied in the copolymers and the thermotropic liquid crystalline behavior was observed in the copolymers containing 50 and 70% biphenol. DSC results indicate that the copolymers had two melting transitions. The lower temperature transitions represent the crystal-to-liquid crystal transitions (T_m) while the higher temperature transitions refer to the liquid crystal-to-isotropic transitions (T_i). A banded texture was formed after shearing the sample in the liquid crystalline state. The novel poly(aryl ether ketone)s had relatively higher glass transition temperature (T_g) and lower melting temperature (T_m).

KEYWORDS: thermotropic liquid crystal polymer, poly(aryl ether ketone)s synthesis, liquid crystal behavior

INTRODUCTION

Poly(aryl ether ketone)s have been found very useful as advanced materials in applications because of their excellent thermal stability and good chemical resistance. However, poly(aryl ether ketone)s have several limitations in processing due to high melting temperature and high melt viscosities (1). Thermotropic liquid crystalline polymers (TLCP) are known to have melt viscosities significantly lower than structurally similar isotropic polymers. Furthermore, the TLCP materials exhibit anisotropy in extruded and molded articles as a result of preferential orientation of LCP domains or individual chains (2). Although 4,4'-biphenol-based homopoly(aryl ether ketone)s have been shown no liquid crystal properties, copolymers based on a crystal-disrupting monomer and a mesogenic biphenyl monomer may be an effective method to synthesize thermotropic poly(aryl ether ketone)s. Recently, Bennett and Farris (3) reported the synthesis and characterization of the novel thermotropic liquid crystalline poly(aryl ether ketone)s. These materials have potential applications as engineering thermoplastics or fibers. In addition, the materials may be useful as processing aids or reinforcing agents in blending with isotropic poly(aryl ether ketone)s. In this work, a series of thermotropic liquid crystalline poly(aryl ether ketone)s based on chlorohydroquinone and

biphenyl mesogen with either 4,4'-difluorobenzophenone or 1,4-bis(p-fluorobenzoyl)benzene were synthesized by the nucleophilic substitution reaction and characterized by several experimental techniques.

EXPERIMENTAL

Materials

The material 4,4'-biphenol was obtained from Honshu Kagaku Ltd. in the highest available purity. Chlorohydroquinone (Tokyo Kasei Co. Ltd.) was recrystallized from chloroform. Anhydrous potassium carbonate was ground and dried in an oven at 150°C. The xylene and tetramethylene sulfone (TMSO₂) were distilled under vacuum before use. 4,4'-difluorobenzophenone and 1,4-bis(p-fluorobenzoyl)benzene were prepared in our laboratory by the standard procedures.

Synthesis

The synthesis route of the copolymers is illustrated in a schematic (Fig.1). In a typical procedure, a three-necked flask was outfit with a platinum thermometer, nitrogen inlet, magnetic stirrer and a Dean-Stark trap. Appropriate mole ratio of the monomers were added into the reactor under nitrogen atmosphere. The temperature was slowly raised to 160°C over a period of 3h to allow phenolate formation and water / xylene azeotrope distillation which was collected in the trap. Subsequently the reaction temperature gradually raised to 200-220°C for polymerization over a period of 8h. The resulting polymer was separated by precipitation of the reaction mixture in methanol. The crude product was purified by hot methanol and water.

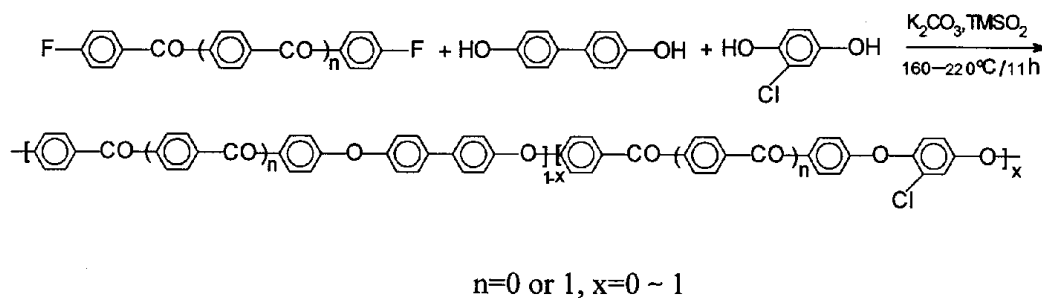


Fig.1: The synthesis route of poly(aryl ether ketone) copolymers

Characterization

The thermal analysis was carried out with a Perkin-Elmer DSC-7 instrument. The temperatures and heat flow scales were carefully calibrated by using standard materials indium and tin over a wide temperature range. Heating and cooling rates of 10/min were used under nitrogen atmosphere and the maximum of endotherm was taken as the transition temperature. A polarizing light microscope (PLM) of Opton R Pol was used for texture characterization of the copolymer samples. The wide angle x-ray diffraction (WAXD) was carried out in Japan D/max-γA X-ray instrument (Cu Kα radiation). The inherent viscosities of the copolymers were measured in a mixed solvent of p-chlorophenol/1,1,2,2-

tetrachloroethane at 45°C. Thermogravimetric analysis (TGA) was performed in a Perkin-Elmer TGA7 thermogravimetric analyser, using a heating rate of 20°C/min in nitrogen atmosphere.

RESULTS AND DISCUSSION

The data of the thermal properties are collected in Table 1. All of the copolymers had higher glass transition temperatures (T_g) between 160°C and 200°C as determined by DSC. The thermal stability (T_d) were also measured by TGA in the range of 430 ~ 520°C. The biphenol-based homopoly(aryl ether ketone)s, 100BP/100DF and 100BP/100BF, had one melting transitions (T_m). PLM results show that they have no birefringence above their T_m s. The side chains homopoly(aryl ether ketone)s, 100CH/100DF, and 100CH/100BF, had one glassy transition temperature (T_g). WAXD results show that they are amorphous polymers. Copolymers based on a crystal-disrupting diene-goup monomer and a mesogenic biphenyl monomer is an effective method to synthesize thermotropic liquid crystal poly(aryl ether ketone)s. The thermotropic liquid crystal behavior was observed in the copolymers containing 50 and 70% biphenol. As expected, each of the copolymers had relatively lower melting transition T_m (290 ~ 340°C) than the isotropic poly(aryl ether ketone) containing biphenyl because of the copolymerization effect of the side-group monomer. Both the crystalline-to-LC transitions (T_m) and the LC-to-isotropic transitions (T_i) were observed in the DSC thermograms of the copolymers, which were further confirmed by PLM observation. As the content of nonmesogenic comonomer units increased, the crystalline-to-LC transition (T_m) became broader and of lesser intensity. The later was indicated by the decrease in heat of fusion (ΔH_m) in Table 1.

For further characterization of the thermotropic liquid crystalline behavior, the copolymers were evaluated by visual observations on PLM. The thin samples were heated at 400°C for a few minutes, subsequently cooled slowly to liquid crystalline state and annealed at the temperature for 1h, and then quenched to room temperature.

Table 1: Thermal Properties of The Novel Copolymers

Sample	n	x	T_g (°C)	T_m (°C)	T_i (°C)	ΔH_m (kJ/g)	ΔH_i (kJ/g)	T_d (°C)
100BP/100DF	0	0	181	409	---	169	---	520
70BP/30CH/100DF	0	0.3	168	338	368	115	6	430
50BP/50CH/100DF	0	0.5	185	336	350	19	19	458
30BP/70CH/100DF	0	0.7	183	328	---	7	---	476
100CH/100DF	0	1	158	---	---	---	---	480
100BP/100BF	1	0	183	412	---	153	---	520
70BP/30CH/100BF	1	0.3	197	318	353	34	11	487
50BP/50CH/100BF	1	0.5	190	289	314	9	26	490
30BP/70CH/100BF	1	0.7	165	308	---	4	---	480
100CH/100BF	1	1	163	---	---	---	---	485

Fig.2a shows a photomicrograph of copolymer 70BP/30CH/100DF isothermally heat treated at 330°C for 1h. It displays a threaded texture, which is often found in the nematic phase. However, after the mechanical shearing and slight relaxation banded texture can be observed. The formation of banded textures after shearing is nearly ubiquitous for nematic polymers (7,8) (Fig.2b). This banded texture which is perpendicular to the shear direction has a width of

about $2\mu\text{m}$. For the copolymer 50BP/50CH/100DF, a second type of texture, fanlike texture, has been observed, which was recorded at room temperature after annealing the sample at 300°C for 1h and then air quenching (Fig.3). This fanlike texture shows that the copolymer 50BP/50CH/100DF has a ordered smectic phase.

Furthermore, the copolymer 70BP/30CH/100BF exhibited threaded texture, while the copolymer 50BP/50CH/100BF showed fanlike texture, too. The above results are well consistent to the results of DSC. Cooling the copolymer 70BP/30CH/100BF from 400°C at $5^\circ\text{C}/\text{min}$ resulted in the formation of threaded texture at 350°C (Fig.4a) and fanlike texture at 290°C (Fig.4b). Quenching the copolymer from 400°C resulted in another fanlike texture(Fig.4c). The reason is not known now. The copolymer 50BP/50CH/100BF formed the plate-like texture at 290°C (Fig.5). It is interesting to mention here that micrometer-size monodomains may also form in the copolymer 70BP/30CH/100BF in LC state under a strong mechanical, periodic shear force field (Fig.6). In general, one way to obtain monodomain in liquid crystalline polymers is to develop a homogenous orientation of the chain directors parallel to the substrate surface. Mechanical shearing may result in a homogeneous orientation in which the mesogenic moieties lie parallel to the substrate surface (9). Although molecular connectivity between the mesogenic moieties in liquid crystalline polymers may significantly affect this orientation process, the monodomain of nematic polymer has also been achieved by Cheng et al. under strong shearing (10).

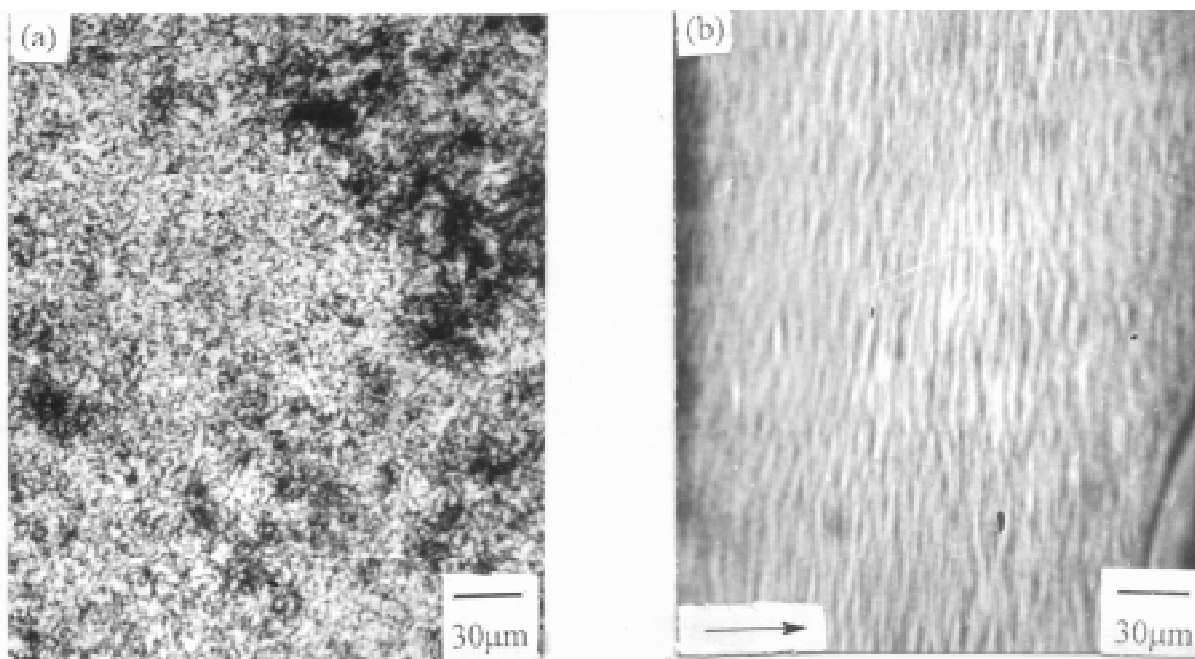


Fig.2: Optical micrographs of the copolymer 70BP/30CH/100DF after cooling from 400°C to 330°C and annealing for 1h and then quenching to room temperature, (a) without mechanical shearing and (b) with mechanical shearing. The arrow shows the shear direction.

CONCLUSION

The thermotropic liquid crystallinity can be achieved in the novel poly(aryl ether ketone)s. The copolymers containing 70% and 50% biphenol mesogen showed nematic and smectic texture, respectively. These copolymers may be of interest as potential engineering thermoplastics, fibers or films with unique anisotropic properties.

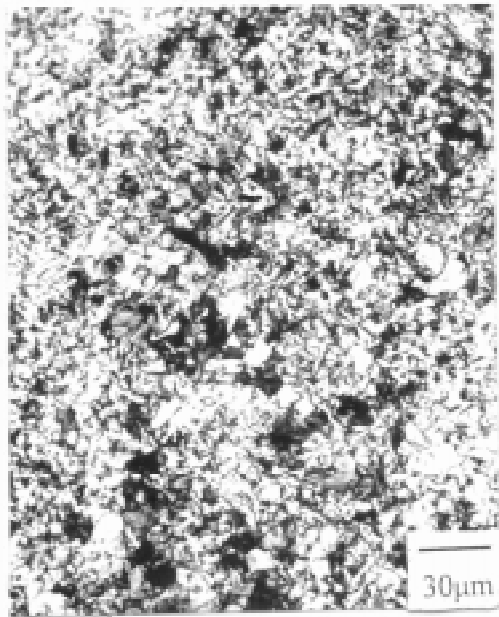


Fig 3: Optical micrograph of the sample 50BP/50CH/100DF after cooling from 400 °C to 300 °C and annealing for 1h and then quenching to room temperature.

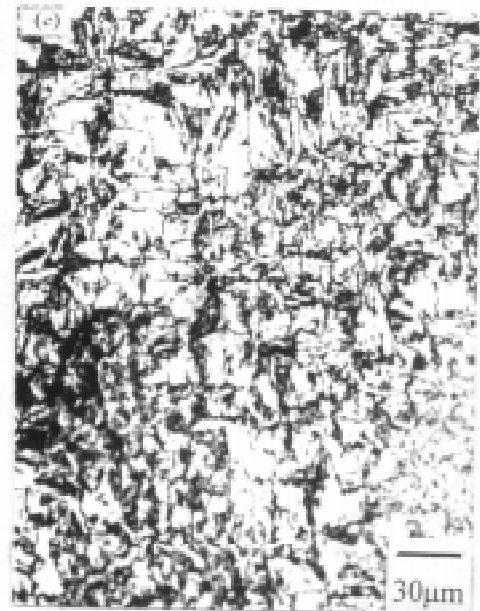
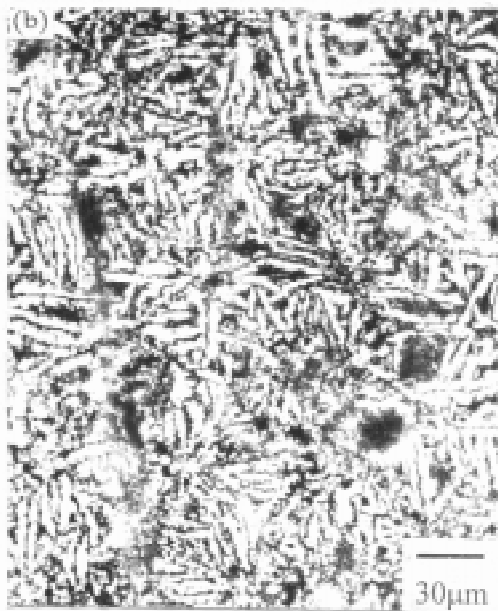
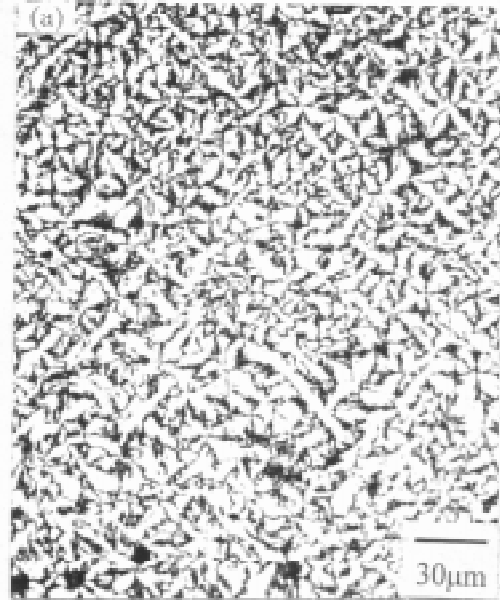


Fig 4: Optical micrograph of the sample 70BP/30CH/100BF after cooling from 400 °C to (a)350 °C (b)290 °C (c)room temperature.

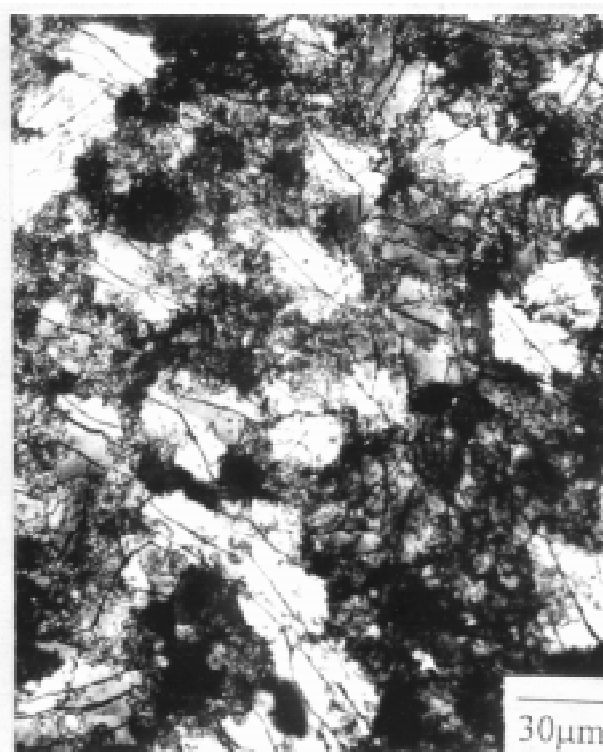


Fig.5: Optical micrograph of the sample 50BP/50CH/100BF after cooling from 400 to 290 and annealing for 1h and then quenching to room temperature.

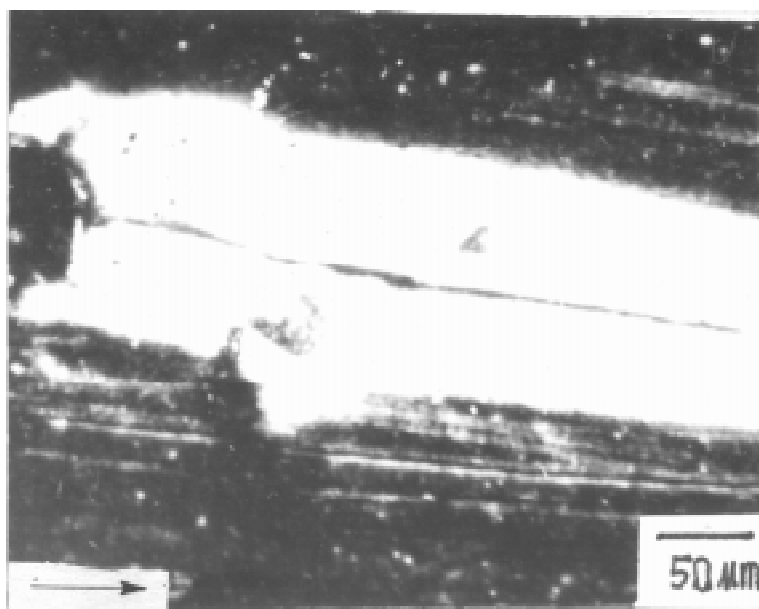


Fig.6: The monodomain of the copolymer 70BP/30CH/100BF after strong mechanical shearing at 350 and then air quenching. The arrow shows the shear direction.

ACKNOWLEDGMENT

The financial supports of Natural Science Foundation of China and the National Key Project of Fundamental Research, "Macromolecular Condensed State", the State Science and Technology Commission of China are gratefully acknowledged.

REFERENCES

1. Cao J.K., Su W.C., Wu Z.W. et al. (1994) *Polymer*, 35:3549
2. Wissbrum K.F.(1981) *J.Rheol*, 25:619
3. Bennett G.S. and Farris R.T. (1994) *Polym.Eng.Sci.* 34:781
4. Zhang S.J., Zheng Y.B. Wu Z.W. et al.(1996) *J.Jilin Univ.* 115:85
5. Bhowmik P.K., Atkins E.D.T., Lenz R.W. et al.(1996) *Macromolecules*, 29: 1910
6. Han H. ,Bhowmik P.K., Lenz R.W.(1994) *J.Polm.Sci. Part A:Polym.Chem.* 32:343
7. Xu G.Z., Wu W. ,Zhou Q.F. et al. (1993) *Polymer* 34:1818
8. Chen S.X., Song W.H., Jin Y.Z. et al.(1993) *Liq.Crystals* 15: 247
9. Uchida T.(1985) *Mol.Cryst.Liq.Cryst.* 123:15
10. Yoon Y., Zhang A.Q. ,Cheng S.Z.D. et al. (1996) *Macromolecules* 29:294

EFFECT OF SURFACE TREATMENT ON MODE I INTERLAMINAR FRACTURE BEHAVIOUR OF PLAIN GLASS WOVEN FABRIC COMPOSITES: REPORT OF A ROUND ROBIN TEST I

H. Saidpour & M. Sezen, *Bournemouth University, UK*
Y.J. Dong, H.S. Yang, Y.L. Bai & T.X. Mao, *Chinese Academy of Science, China*
C. Bathias, *CNAM/ITMA, France*
P. Krawczak, R. Bequignat & J. Pabiot, *Ecole des Mines de Douai, France*
S. Pinter & G. Banhegyi, *Furukawa Electric Institute of Technology, Hungary*
J.K. Kim & M.L. Sham, *Hong Kong University of Science & Technology, Hong Kong*
I. Verpoest, *Katholic University of Leuven, Belgium*
H. Hamada, Y. Hirai & K. Fujihara, *Kyoto Institute of Technology, Japan*
C.Y. Yue & K. Padmanabhan, *Nanyang Technological University, Singapore*
Y. Suzuki, *Nitto Boseki Co. Ltd, Japan*
K. Schulte, *Technical University of Hamburg-Harburg, Germany*
J.K. Karger-Kocsis, *University of Kaiserslautern, Germany*
W.J. Cantwell & R. Zulkifli, *University of Liverpool, UK*
L. Ye, *University of Sydney, Australia*
A. Lowe, *Australian National University, Australia*
S.V. Hoa, *Concordia University, Canada*
V.V. Smirnov, *Metal-Polymer Research Institute BAS, Belarus*
L.T. Drzal, *Michigan State University, USA*
W.R. Broughton, *National Physics Laboratory, UK*
J.J. Lesko, *Virginia Polytechnic Institute and State University, USA*
T. Tanimoto, *Shonan Institute of Technology, Japan*

SUMMARY: A round-robin test programme has been carried out to characterize the mode I interlaminar fracture behaviour of E-glass woven fabric reinforced vinyl ester matrix composites. Special emphasis has been placed on the effect of silane coupling agent on the stability of interlaminar crack propagation and the fracture toughness. Twenty laboratories were invited to participate in this programme. Each laboratory was supplied with composite laminates of thickness of its own choice which were fabricated by the Society for Interfacial Materials Science (SIMS), and conducted the tests to its own procedures. The results submitted by each laboratory are presented, and the observations and implications are discussed.

KEYWORDS: E-glass woven fabric reinforced vinyl ester composites; mode I interlaminar fracture toughness; silane coupling agents; interface; stability of crack propagation

INTRODUCTION

Composite laminates made from glass woven fabrics and vinyl ester resin have been developed for printed circuit board (PCB) applications, specifically aimed at low-end to mid-range systems. To improve the efficiency of stress transfer across the fibre-matrix interface glass fibres are commonly treated with silane coupling agents [1]. There are several factors which influence the chemical, physical and mechanical properties of the interface. They include the silane structure in treating solution and its organo-functionality, the drying conditions, and the morphology and chemical composition of the fibre surface. The concentration of coupling agent has been found to be a critical factor in determining the mechanical performance and fracture behaviour of the composite. An interface with strong adhesion is expected to give a composite with good shear, compressive and off-axis strengths, and the silane agents applied on glass make the composites more durable in hygrothermal environment [2].

The Society for Interfacial Materials Science (SIMS) has been established in 1993 with the aims to enhance our fundamental understanding of the science in composite interfaces of various nature by bridging the gap between material science, mechanics and manufacturing of composite materials, and to encourage the interactions between the research communities from academia and relevant industries for international collaborations in applied research and development. As one of the most important activities organized by the SIMS, the round robin test (RRT) program was developed to study the effect of fibre surface treatment on the mechanical properties of glass fibre reinforced vinyl ester matrix composites. In the first RRT program, tensile and bending strengths and moduli were measured of the composites containing woven fabrics treated with five different silane coupling agents: namely 0.01, 0.4 and 1.0 wt% methacryl silane (designated as M0.01, M0.4 and M1.0, respectively), methanol washed 0.4 wt% methacryl silane (MW0.4) and 0.4 wt% epoxy silane (E0.4).

Table 1 gives the average values of the results which were presented at the 10th International Conference on Composite Materials (ICCM-10) held in August 1995 [3]. The composites containing M0.01 had the lowest strength both in tension and bending. An increase in methacryl silane concentration resulted in improvement of these strengths. The tensile modulus was found to be relatively insensitive to the type and concentration of silane agents, whereas an increase in methacryl silane gave rise to marginal enhancement of bending modulus. Washing the treated fibres using methanol enhanced to a certain extent both the strength and modulus. Composites containing E0.4 displayed relatively lower strength than those containing fibres with methacryl silane treatment of the same concentration.

Following the success of the first RRT programme, twenty major laboratories were invited worldwide to participate in the second RRT, among which fifteen laboratories have completed the tests when this paper was written, see Table 2. The major aim of the present programme was to determine the effect of silane treatments on mode I interlaminar fracture behaviour. It is generally accepted that delamination represents the weakest failure mode, and is considered to be the most prevalent life-limiting failure modes in laminate composites. As such, ever-increasing attention has been directed toward proper characterization of the failure mode as well as to improve the durability against delamination.

Table 1 Strengths and moduli of glass woven fabric reinforced vinyl ester matrix composites measured in the weft direction¹². (Mean values \pm standard deviation)

Type and concentration of silane agent	Strength (MPa)		Modulus (GPa)	
	Tension	Bending	Tension	Bending
Methacryl silane 0.01wt%	270 \pm 21	372 \pm 20	19.5 \pm 5.2	18.1 \pm 1.5
0.4wt%	318 \pm 16	431 \pm 19	19.6 \pm 5.1	18.8 \pm 1.6
1.0wt%	329 \pm 31	444 \pm 40	20.2 \pm 5.2	19.7 \pm 1.9
Methanol washed Methacryl silane 0.4wt%	338 \pm 13	452 \pm 23	20.4 \pm 5.0	19.4 \pm 0.9
Epoxy silane 0.4wt%	321 \pm 32	380 \pm 27	20.3 \pm 5.0	19.3 \pm 1.1

Table 2 Participating laboratories.

Laboratory	Contact
Bournemouth University, UK	H. Saidpour
Chinese Academy of Science, China	T.X. Mao
CNAM / ITMA, France	C. Bathias
Ecole des Mines de Douai, France	P. Krawczak
Furukawa Electric Institute of Technology, Hungary	S. Pinter
Hong Kong University of Science & Technology, Hong Kong	J.K. Kim
Katholic University of Leuven, Belgium	I. Verpoest
Kyoto Institute of Technology, Japan	H. Hamada
Nanyang Technological University, Singapore	C.Y. Yue
Syonan Institute of Technology, Japan	T. Tanimoto
Technical University of Hamburg-Harburg, Germany	K. Schlute
University of Kaiserslautern, Germany	J.K. Karger-Kocsis
University of Liverpool, UK	W.J. Cantwell
University of Sydney, Australia	L. Ye

EXPERIMENTAL PROCEDURES

Materials and Test Specimen

Test materials were fabricated by the SIMS, and were supplied to the participating laboratories. Materials including fibres, matrix materials, silane coupling agents and fabrication procedures of the composite laminates employed in the present program were essentially the same as those used in the first RRT programme. The E-glass plain woven fabrics contained 44 (warp) x 34 (weft) strands per 2.5 cm x 2.5 cm square area (WE18W,

supplied by Nitto Boseki Co, Ltd., Japan). Each strand consisted of 400 filaments of 9 mm in diameter. The matrix material was made from an unsaturated vinyl ester resin (Ripoxy R806; Showa High Polymer, Japan) which was polymerised with 0.7 phr. methyl-ethyl-ketone (MEK) peroxide. The coupling agents used were g-methacryloxy-propyltrimethoxysilane (methacryl silane, A-174; Nippon Unicar Co., Japan) and g-glycidoxy-propyltrimethoxysilane (epoxy silane, A-187; Nippon Unicar Co., Japan). The aqueous solutions of silane coupling agents were acidified with acetic acid at pH 4.0. Five different combinations of silane coupling agents were used for fibre surface treatment: 0.01, 0.4 and 1.0 wt% methacryl silane (designated as M0.01, M0.4 and M1.0 respectively); methanol washed 0.4 wt% methacryl silane (MW0.4); and 0.4 wt% epoxy silane (E0.4). The glass fabrics were dipped into the aqueous solutions of the silane agents, which were subsequently squeezed between rollers and were dried for 10 min at 110°C.

The laminates were prepared by hand lay-up such that all warp strands were aligned in one direction, and were cured for 48 h at room temperature, followed by post cure for 3 h at 80°C and for 2 h at 150°C in an oven. A 40 mm thick polytetrafluoroethylene (PTFE) film was inserted at the mid-plane of the laminate as an initial crack during the lay-up. The average fibre volume fraction was found to be approximately 42.6% [3]. The instructions on the laminate thickness and the length of precracks were specified by each participating laboratory.

Each participating laboratory cut the laminates to its desired sizes and geometry. Typical double cantilever beam (DCB) specimen is illustrated in Figure 1. In most laboratories, specimen edges were painted with white correction liquid on which fine lines were scribed at certain intervals to assist locate the advancing crack tip. Either aluminium tabs or piano hinges were bonded to the specimens to allow gripping and loading the specimen in tension. Crack length was monitored with the corresponding load and displacement recorded simultaneously. Compliance values were taken in the interrupted unloading and reloading experiments. Each laboratory calculated the mode I interlaminar fracture toughness, G_{IC} , using its own data reduction schemes. Table 3 gives the details of the test specimen dimensions and test conditions used by each participating laboratory.

Data Reduction Schemes

There are basically four different linear elastic fracture mechanics methods to analyze the data obtained from the load-displacement records [4]: namely, (i) the area method; (ii) the compliance method; (iii) the load method; and (iv) the displacement method. Because the details of the relevant equations for G_{IC} values and the measurement techniques are given elsewhere [4], the same will not be repeated here. Due to the effects of various aspects of the practical DCB tests, such as end rotation and deflection of the crack tip, effective shortening of the beam and stiffening effect of the beam due to the presence of the end tabs, modified compliance methods have been proposed as standard methods.

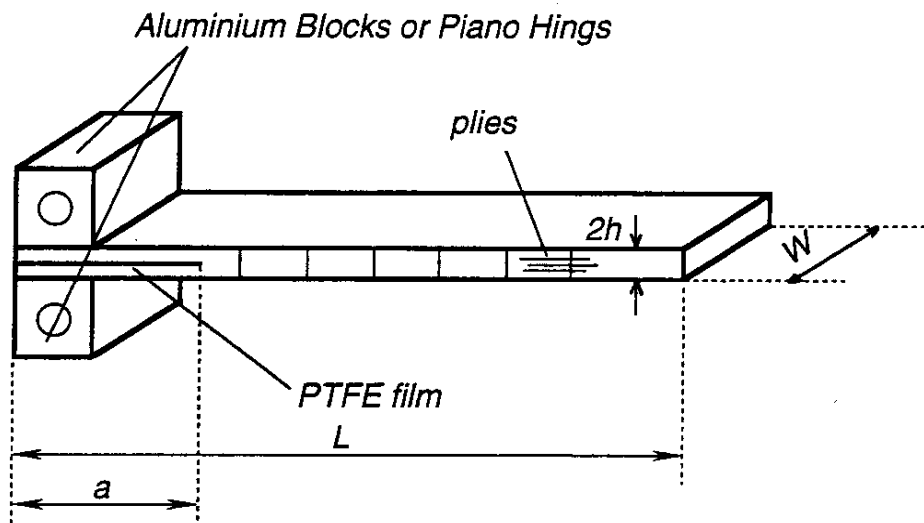


Figure1 Geometry of double cantilever beam specimen.

RESULTS AND OBSERVATIONS

Figure 2 shows typical load-displacement curves of the interlaminar fracture tests obtained for laminates containing fibres with different silane agent treatments. Based on the stability of crack propagation these curves can be classified into two groups: M0.01 and E0.4 for stable fracture; and M0.4, M1.0 and MW0.4 for unstable fracture. For the laminates in the first group, the load increased in a linear manner to a maximum, which was followed by a gradual decrease with further crack extension [5]. The crack propagated in a slow and stable manner. In sharp contrast, for the specimens M0.4, M1.0 and MW0.4, the load-displacement curves displayed "saw-teeth" type behaviour where the rising portion and the abrupt drop of the load corresponded to stable crack re-initiation and crack arrest after rapid, unstable crack propagation, respectively. The unstable fracture behaviour did not allow the measurement of the propagation G_{Ic} values.

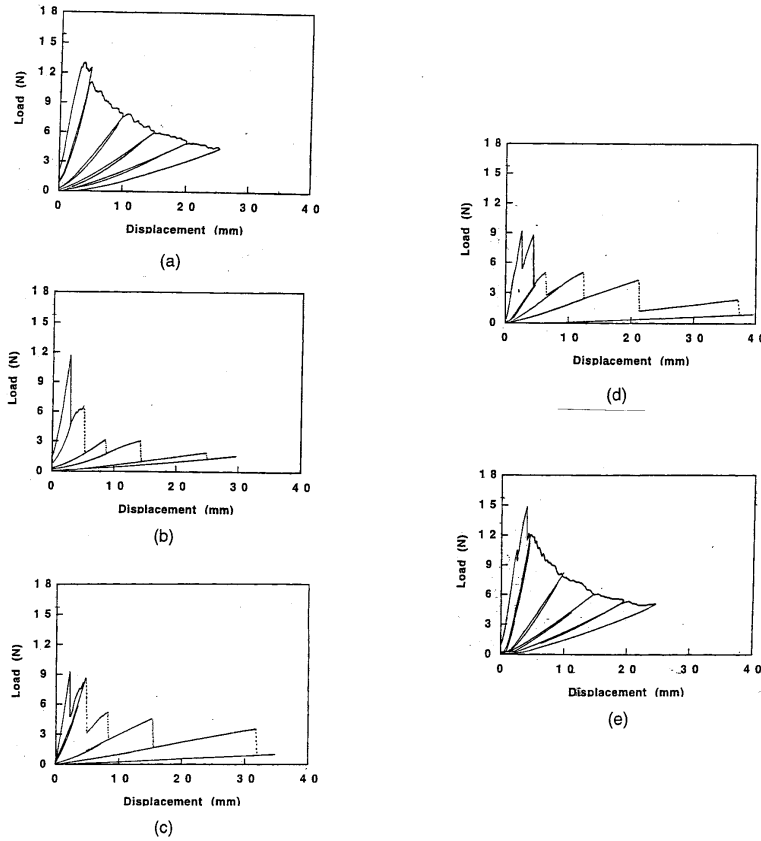


Figure 2 Typical load - displacement curves with five different surface treatments:
 (a) methacryl silane 0.01wt%; (b) methacryl silane 0.4wt%; (c) methacryl silane 1.0wt%;
 (d) methacryl silane 0.4wt% / methanol washed; (e) epoxy silane 0.4wt%.

Table 3 Specimen dimensions and data reduction schemes of each participating laboratory.

Laboratory	Width W	Thickness 2h	Length L	Crack length a	Cross-head speed (mm/min)	Data reduction scheme*
1	20	3	125	50	2.5	A
2	25	4	200	48	2.0	B
3	25	2	100	30	1.0	B
4	20	3	125-180	25-80	1.0	B
5	10	3	270	20	5.0	B and F
6	20	4	130	20	1.0	B
7						
8	25	4	100	20	1.0	C
9	12.5, 25	3	125	25	1.0	D
10	25	4	100	30	1.0	C
11	20	5	200	55	2.0	B
12	20	4	125	50	1.0	B
13	20	4	200	50	5.0	B
14	25	3.8	170	65	0.5	A and E

*A = modified compliance method (ASTM 5528 - 94a); B = corrected beam theory (ESIS Protocol); C = modified compliance method (JIS K7086); D = load method; E = displacement method; F = area method.

In the modified compliance calibration method specified by ASTM D5528-94a, the G_{Ic} value for crack propagation is given by:

$$G_{Ic} = \frac{3 P^2 C^{2/3}}{2 \alpha_1 b h} \quad (1)$$

where P is the applied load and a_1 is obtained directly from the slope of a/h versus $C^{1/3}$ plot. In the corrected beam theory recommended by the European Structural Integrity Society (ESIS) TC4 Group as a protocol in 1990, G_{Ic} is determined by:

$$G_{Ic} = \frac{n P \delta}{2 b a} \quad (2)$$

where n is the slope of the log-log plot of the compliance versus crack length (C vs Da) curve. The initiation value of G_{Ic} is taken at the force corresponding to the initial non-linearity of the load-displacement curve. The G_{Ic} value specified by JIS K7086 is calculated based on the equation:

$$G_{Ic} = \frac{3 P^2 (b C)^{2/3}}{4 h b^2 \alpha_2} \quad (3)$$

where a_2 is determined empirically.

Figure 3 gives the initiation and propagation G_{Ic} values from all participating laboratories. Due to the unstable crack propagation as discussed above, only the initiation G_{Ic} values are reported for specimens M0.4, M1.0 and MW0.4. It is found that the initiation G_{Ic} value decrease in general with increasing the methacryl silane concentration: in particular it is found that the G_{Ic} value is higher for M0.01 than for M1.0 (nearly 100%) except for a few isolated cases such as Laboratories 3, 4 and 13. Washing of the treated fibres with methanol did not change much the overall fracture behaviour (maximum of 40% and often below 10%), with largely varying initiation G_{Ic} values for different laboratories.

It is presumed that in composites containing M0.4 and M1.0 silane agents a thick and densely cross-linked, brittle interlayer is formed at the fibre-matrix interface region which was mainly responsible for the brittle, unstable crack propagation. In composites with M0.01 and E0.4, a more ductile, compliant interlayer is developed, giving rise to a stable, ductile crack growth. The concentration of the coupling agents has a drastic effect on interlaminar fracture behaviour of the laminates. An increase in methacrylate silane agent showed deteriorating effect on the stability of crack propagation and thus the fracture resistance of the laminate. Contrary to the expectation, removal of the loosely bound interlayer of the silane agent by washing with methanol did not improve greatly the overall fracture behaviour of the laminates. From the comparison between the specimens M0.4 and E0.4 which contain the same silane concentration, it is noted that the epoxy silane yielded significantly higher for a majority of laboratory and stable fracture resistance than methacryl silane. It is found that G_{Ic} values at initiation and propagation are higher for M0.01 specimens than for E0.4 specimens, except for two isolated cases (lab.5 and 6 at initiation).

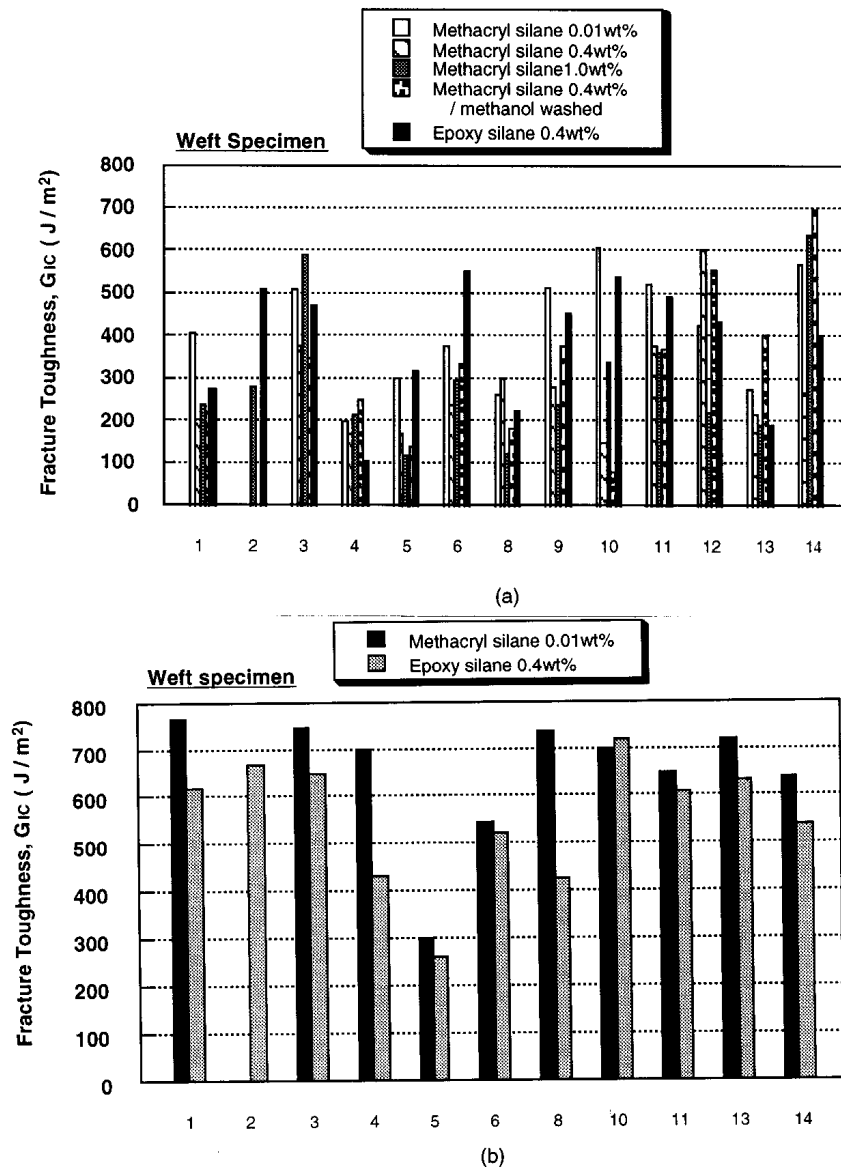


Figure 3 Mode I interlaminar fracture toughness of glass woven fabric / vinylester composites: (a) initial values; (b) propagation values.

Figure 4 shows typical crack growth resistance G_{IC} curves for specimens M0.01 and E0.4. G_{IC} values increased significantly with increasing crack length. This behaviour is ascribed to the presence of fibre bridging in the wake of the propagating crack in woven fabric laminates [6]. The fibre bridging contained the growth of the cracks, enhancing the stability of crack propagation. Certainly, the extent of the fibre bridging phenomenon is influenced by the fibre surface treatment, as it modifies the nature of interface bonding and the mechanical properties of the interface region.

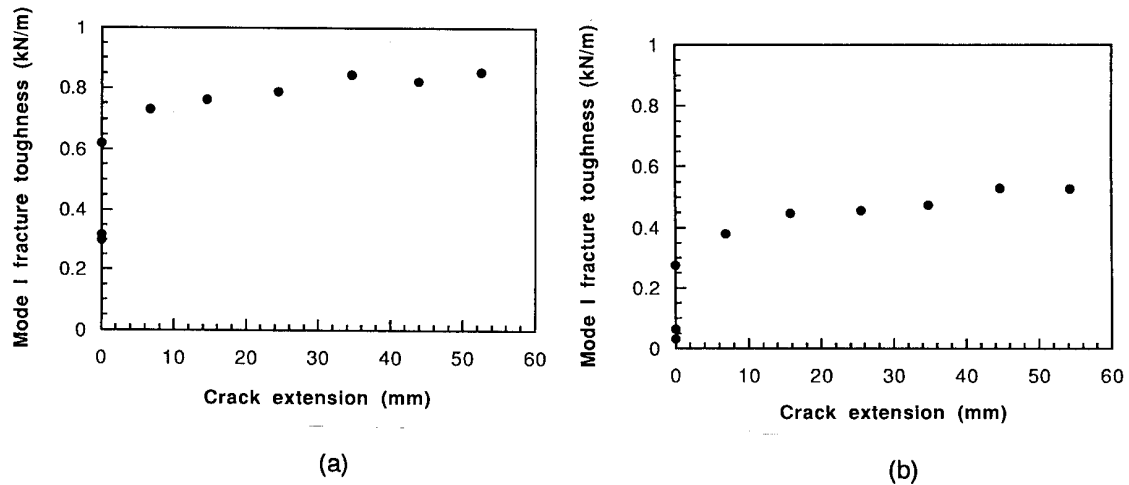


Figure 4 Typical crack growth resistance G_{Ic} curves for specimens: (a) M0.01 and (b) E0.4.

Examinations of the fracture surfaces using scanning electron microscopes suggested the followings:

- (i) For M0.01 and E0.4 specimens, the fibres were exposed on the fracture surface without resin adhering onto them.
- (ii) For M0.4 and M1.0 specimens, much of the fibre surface was covered by the matrix resin, in particular on the fracture surface corresponding to the unstable crack propagation.
- (iii) Much more fibres were covered with resin in specimens MW0.4 than M0.4.

The foregoing observations suggest that:

- (i) Crack propagation along the fibre-matrix interface region is relatively slower and more stable than crack propagation in the matrix material away from the interface.
- (ii) Change of the crack path occurred from the interface region to the matrix with increasing the methanol silane concentration. Wash of silane treated fibres with methanol further encouraged this behaviour, aggravating the instability of crack propagation.

CONCLUDING REMARKS

A round-robin test programme has been undertaken to characterize the mode I interlaminar fracture behaviour of glass woven fabric-vinyl ester matrix composites containing five different silane coupling agents on the fibres. All test materials were fabricated in a laboratory of the SIMS, and were supplied to the participating laboratories. The format of the programme was maintained loose in an effort of assess the current practice of the test method and the variability of test results affected by different specimen dimensions and data reduction procedures. For each test, the general procedures were pretty much similar, and major

differences were identified in the specimen dimensions and data reduction procedures used by some laboratories. The differences in the details of the tests and data reduction procedures resulted in a high degree of data scatter between the laboratories, albeit the general trend of interlaminar fracture toughness influenced by different silane agents were much consistent. To decrease the data scatter, the standards such as ASTM, JIS, ESIS etc. will be harmonized within the next 3 or 4 years under the cover of an ISO standard (ISO / CD.2 15024). It is considered that such movement will direct toward the helpful method which exchanges the concepts of many researchers and improve the durability against delamination in laminate composites.

M0.01 and E0.4 specimens displayed stable, slow crack propagation, whereas M0.4, M1.0 and MW0.4 specimens showed rapid, unstable crack propagation. As expected the G_{Ic} values increased with crack extension for both the specimens containing M0.01 and E0.04 which showed stable crack propagation. In this RRT programme, an over 100% variation was observed by all the laboratories on initiation values of mode I interlaminar fracture toughness with different silane treatments. These variations were higher than that of the results previously obtained for tensile and bending tests (below 25% on moduli and below 10% on strengths) and reported in the first RRT programme. Moreover the mode I method makes it possible to separate the cracks initiation and the cracks propagation phenomena on which the interface quality has a specific incidence. Hence, mode I interlaminar fracture toughness tests seem to be interesting method to investigate the fracture behavior of composite materials with interfaces of different qualities.

ACKNOWLEDGMENTS

The organizers of the 2nd round-robin test programme wish to thank all the participants who completed the tests as instructed and submitted the results in time. A special gratitude is also due to Y. Suzuki of Nitto Boseki Co. Ltd., Japan for the supply of glass woven fabrics.

REFERENCES

1. Koenig, J.L. & Emadipour, H., Mechanical characterization of the interfacial strength of glass reinforced composites, *Polym. Compos.* 6 (1985) 142-150.
2. Cheng, T.H., Jones, F.R. and Wang, D., Effect of fibre conditioning on the interfacial shear strength of glass fibre composites, *Compos. Sci. Technol.* 48 (1993) 89-96.
3. Bequignat, R., Krawczak, P., Cantwell, W., Schramuzzino, P., Desaegeer, M., Verpoest, I., Hamada, H., Hirai, Y., Kotaki, M., Hojo, M., Kim, J.K., Kocsis, J.K., Mackin, T.J., Mayer, J., Morii, T. & Tanimoto, T., Influence of different glass fibre sizings on the mechanical properties of glass fabric composites: Report on a round robin test, in *Proc. 10th Intern. Conf. on Composite Materials (ICCM-10)*, Whistler, Canada (1995) pp. 597-603.
4. Hashemi, S., Kinloch, A.J. and Williams, J.G. Corrections needed in double-cantilever beam tests for assessing the interlaminar failure of fibre-composites. *J. Mater. Sci. Lett.* 8 (1989) 125-129.
5. Suzuki, Y., Maekawa, Z., Hamada, H., Yokoyama, A., Sugihara, T. & Hojo, M., Influence of silane coupling agents on interlaminar fracture in glass fibre fabric reinforced unsaturated polyester laminates, *J. Mater. Sci.*, 28 (1993) 1725-1732.
6. Brisco, B.J. and Williams, D.R. Interlaminar fracture toughness of aramid/epoxy laminates. *Compos. Sci. Technol.* 46 (1993) 277-286.

THERMOPLASTIC COMPOSITE BEARINGS: TRIBOLOGICAL PROPERTIES AS A FUNCTION OF THE MATERIAL STRUCTURE

F. Hauptert, K. Friedrich, R. Reinicke

*Institute for Composite Materials, Ltd., University of Kaiserslautern,
PO Box 3049, D - 67653 Kaiserslautern, Germany*

SUMMARY: In the study presented here, thermoplastic filament winding of journal bearings with functional properties over their cross sections was performed by the use of different commingled yarns. The raw material of the sliding surface consisted of PTFE-, aramid-, and polyamide fibers, of which the latter were molten and then transferred into the final matrix of the composite tube element. For this special filament winding process, the processing parameters were optimized, in order to realize a bulk composite structure. The composition of the raw materials and the winding geometry were varied. Thus, the influence of these parameters on the tribological behaviour of the bearing could be determined.

KEYWORDS: Thermoplastic filament winding, thermoplastic composite materials, friction, wear, coefficient of friction, winding parameters, injection molding

INTRODUCTION

Polymeric composites are predestinated for low weight and high stiffness constructions. New developments have also focussed on the use of thermoplastic matrices, because of their advantageous mechanical properties, especially the higher toughness when compared to traditional thermosets. Another advantage of these thermoplastic matrices is that no final curing process in an oven or autoclave is necessary. Therefore, these materials are especially suitable for continuous manufacturing processes such as thermoplastic filament winding [1,2] or pultrusion [3]. Impregnation, consolidation and cooling are performed continuously during the manufacturing process. However, still a major problem in processing of thermoplastic composites is the high viscosity of the matrix material. As a result, processing parameters like temperature, pressure and winding speed have to be optimized properly in order to achieve both, a good fiber distribution and a strong bonding between fibers and matrix [4].

Composite journal bearings are presently manufactured by a thermoset filament winding technology. A better alternative, based on fundamental tribological studies, would be however, to use continuous fiber reinforced thermoplastic composites, because of their superior friction and wear properties. But one problem in using these materials for such purposes is, that special manufacturing processes are required.

THERMOPLASTIC FILAMENT WINDING EQUIPMENT

The possibility of welding continuous fiber reinforced thermoplastics enables the combination of two manufacturing steps, i.e. filament winding and consolidation, in one continuous production process. Filament winding of composite materials with thermoplastic matrices is more complicated than wet winding of thermosetting composites, due to the higher viscosity of thermoplastic polymers. During this process, the incoming yarn has to be melt impregnated and immediately consolidated onto the previously wound surface at the lay down point (nip point). The in situ filament winding device is shown in Figure 1. A two axis motion controller coordinated the mandrel's rotation and the movement of the support to which the tow guidance system was attached. Hence, a predetermined fiber path could be realized. Tow tension was measured and controlled. A defined compaction force was applied by employing a compaction roller, or a temperature controlled sliding shoe.

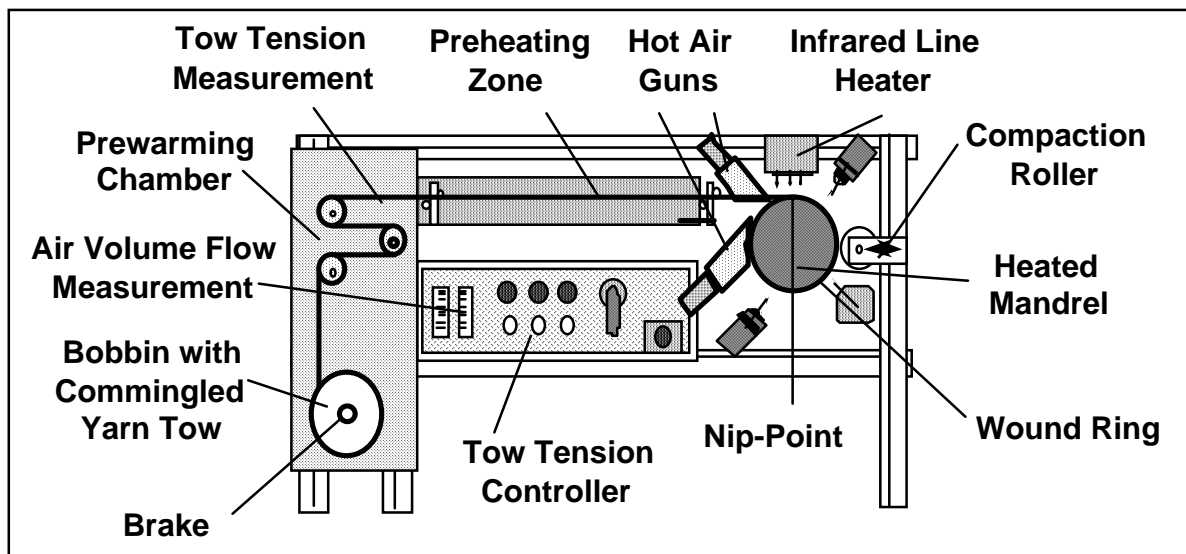


Figure 1: Thermoplastic filament winding device

The melting of the tow material was realized in the following way: The raw material bobbin was positioned in a prewarming chamber (Fig. 1), which raised the temperature of the tow in front of the preheating zone from room temperature up to about 200°C. In this way, the difference between the raw material temperature and the matrix material's melting temperature was significantly reduced. After leaving the prewarming chamber, the tow passed through a hot air preheating zone. The final heating arrangement occurred in the nip point area, which consisted of two hot air guns, the first one heating the incoming yarn, the second one the previously wound surface. An additional infrared line heater provided a fine tuning of the nip point temperature. The mandrel temperature was also measured and controlled. Measurements of the ring surface temperatures were carried out by two pyrometers. The first one was focused at the nip point, the second one at the incoming surface of the wound part before reaching the hot air zone. In this arrangement, the filament winding parameters were: winding speed (v_w), mandrel temperature (T_M), nip point temperature (T_{NP}), preheating temperature (T_{PH}), prewarming temperature (T_{PW}), consolidation force (F_C), and tow tension (F_T).

RAW MATERIALS FOR FILAMENT WINDING

The first type of yarn used in this study consisted of PTFE-, aramid-, and polyamide fibers, of which the latter were melted and therefore transferred into the final matrix of the composite tube element (Figure 2). The second material investigated was a polymer powder impregnated and with a thin polymer matrix sheath surrounded flexible reinforcing fiber bundle. The particular components consisted of glass fibers and a polyethyleneterephthalate matrix material (GF-PET-1200tex).

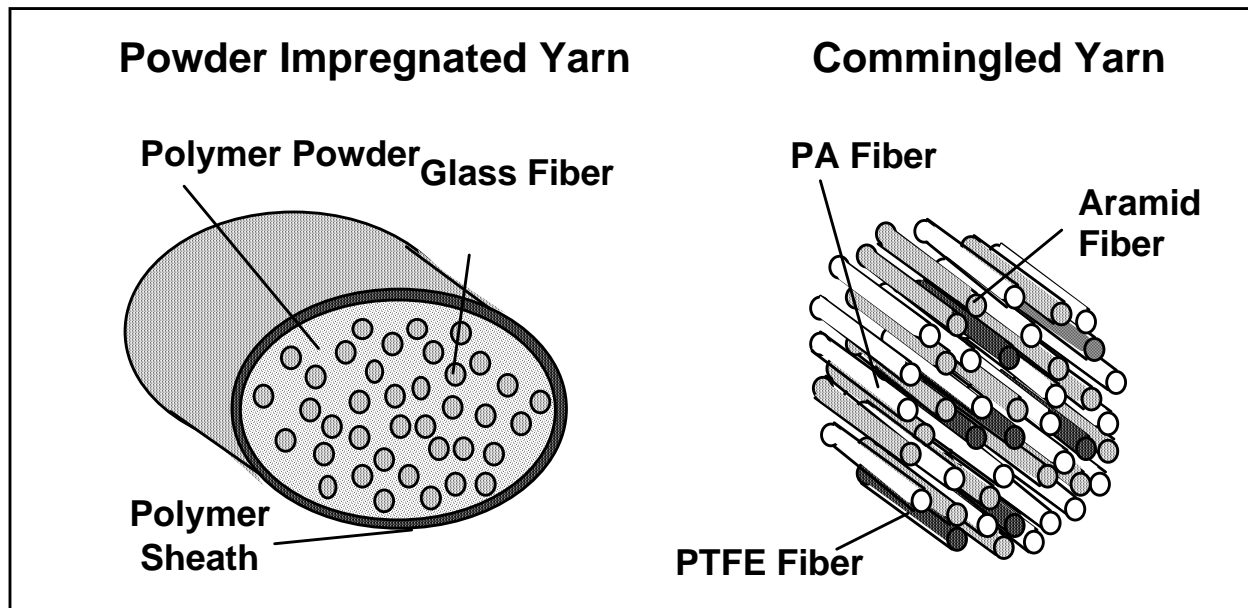


Figure 2: Raw materials for thermoplastic filament winding

INJECTION MOLDING EQUIPMENT AND PARAMETERS

In this study a commercially available fully hydraulic injection molding machine (ARBURG ALLROUNDER® 270 V) equipped with a SELOGICA® process control system was used. The most important processing parameters were the temperature of the molten thermoplastic, the mold temperature, the injection pressure, the injection time, the holding pressure and the holding time. Optimum processing parameters for a certain part were not only a function of the thermoplastic used but also a function of the mold geometry. For every commercially available, injection moldable thermoplastic polymer the processing properties are given in a certain range. Starting from this point, the injection parameters were systematically varied and optimized. At first, simple rings with an inner diameter of 40 mm, a width of 20 mm and a wall thickness of 4 mm were injection molded out of PA66, filled with 30 wt % short glass fibers. In the next step a filament wound ring with an inner diameter of 40 mm, a width of 20 mm and a thickness of about 2 mm was placed as an insert into the same mold and then preheated with a hot air gun (400°C) for one minute. Subsequently, it was embedded into a glass fiber reinforced thermoplastic PA66 matrix by injection molding. For this process, also the injection parameters such as mass temperature, tool temperature and injection pressure had to be optimized in order to achieve optimum material properties and strong bonding between insert and injected material.

COMBINATION OF FILAMENT WINDING AND INJECTION MOLDING

Alternatively to the complete manufacturing of the bearings by filament winding, a thinner filament wound bearing layer could be encapsulated by short glass fiber reinforced polyamide, injection molded around the wound insert [5]. Critical processing issues were (1) the control of the adhesion between the composite insert and the surrounding material, and (2) the different thermal expansion conditions of the two partners in contact. The correct design between the two is a basic requirement for dimensional stability of the final component.

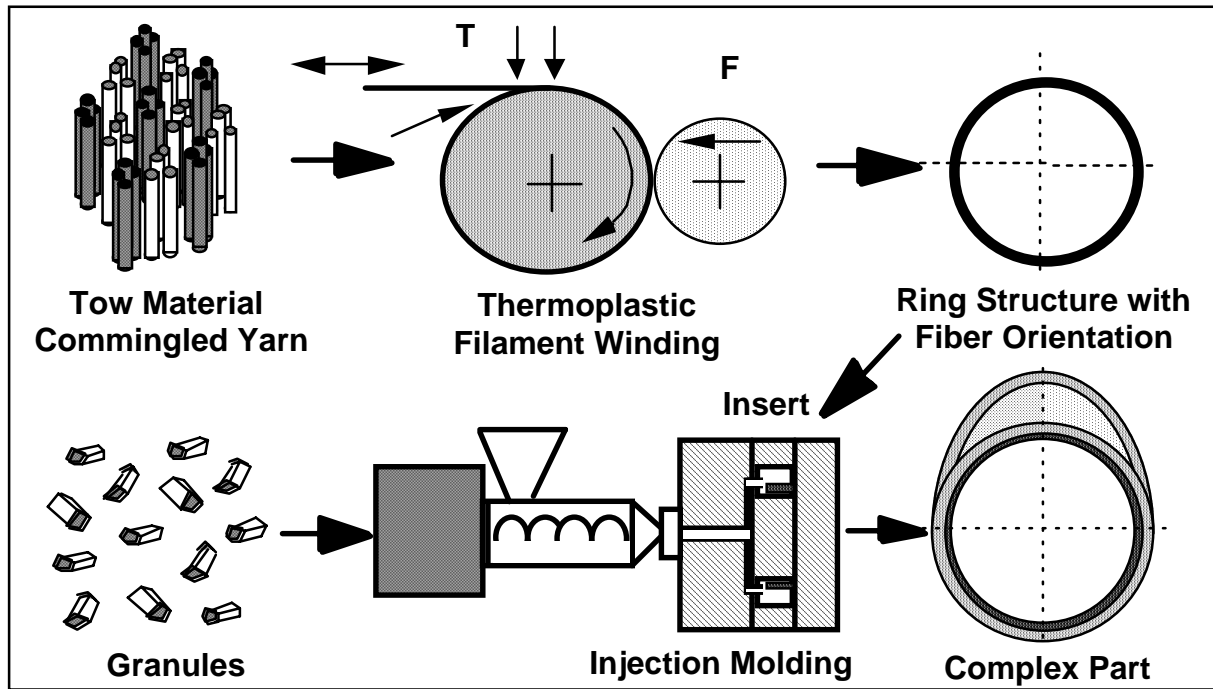


Figure 3: Combination of thermoplastic filament winding and injection molding

Injection molding technology allows the production of very complex geometries. The disadvantage is that only short fiber reinforced thermoplastics can be processed, and furthermore, that fiber orientation is highly dependent on the mold geometry and processing parameters. Thermoplastic filament winding, on the other hand, allows the production of continuous fiber reinforced, relatively simple structures such as rings with a defined fiber orientation and a high fiber volume content [1, 2]. The combination of these two technologies permits the fabrication of structural parts with complex geometries and functional properties. During this study, a thermoplastic filament wound ring was used as an insert embedded in a short fiber reinforced thermoplastic component of a different geometry, produced by injection molding (Figure 3).

TESTING OF THE COMPOSITE BEARINGS

Testing of this final component in a journal bearing tester indicated its good performance in terms of low coefficient of friction, low wear and high thermal stability under various pressure, temperature and velocity conditions. A cross section of the inner layer of such a bearing is presented in Figure 4.



Figure 4 : Cross section of the sliding surface of a thermoplastic composite bearing

Using optimized thermoplastic filament winding parameters, the winding angles and the composition of the sliding surface material were varied systematically. The influence of these parameters on the tribological properties of the bearings were investigated using a journal bearing tester. The components indicated a good performance in terms of low coefficient of friction, low wear and high thermal stability, in relation to competitive thermoset bearings under comparable pressure, temperature and velocity conditions. The correlation between winding angle and coefficient of friction is given in Figure 5. This lay down angle of the raw material on the mandrel was varied between 0° (hoop winding) and 30° . In the range between 0° and 7° , the coefficient of friction is nearly constant at a value of about 0,085. A further increase of the winding angle led to friction coefficients of 0,16.

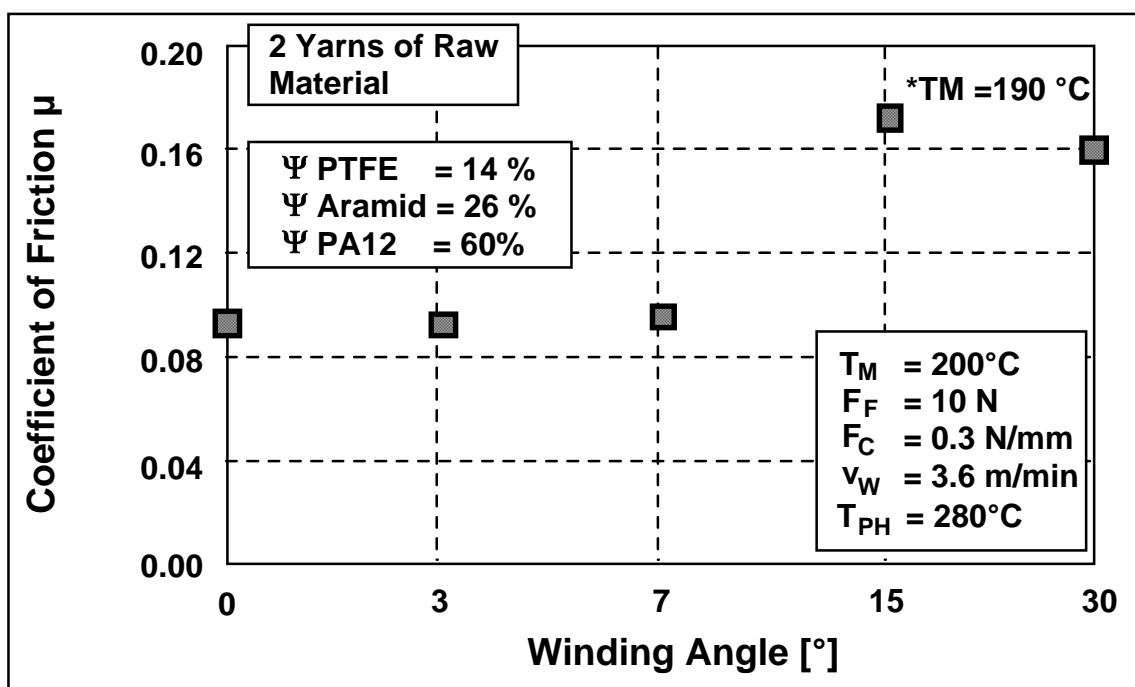


Figure 5: Coefficient of friction of filament wound thermoplastic composite bearings depending on the winding angle

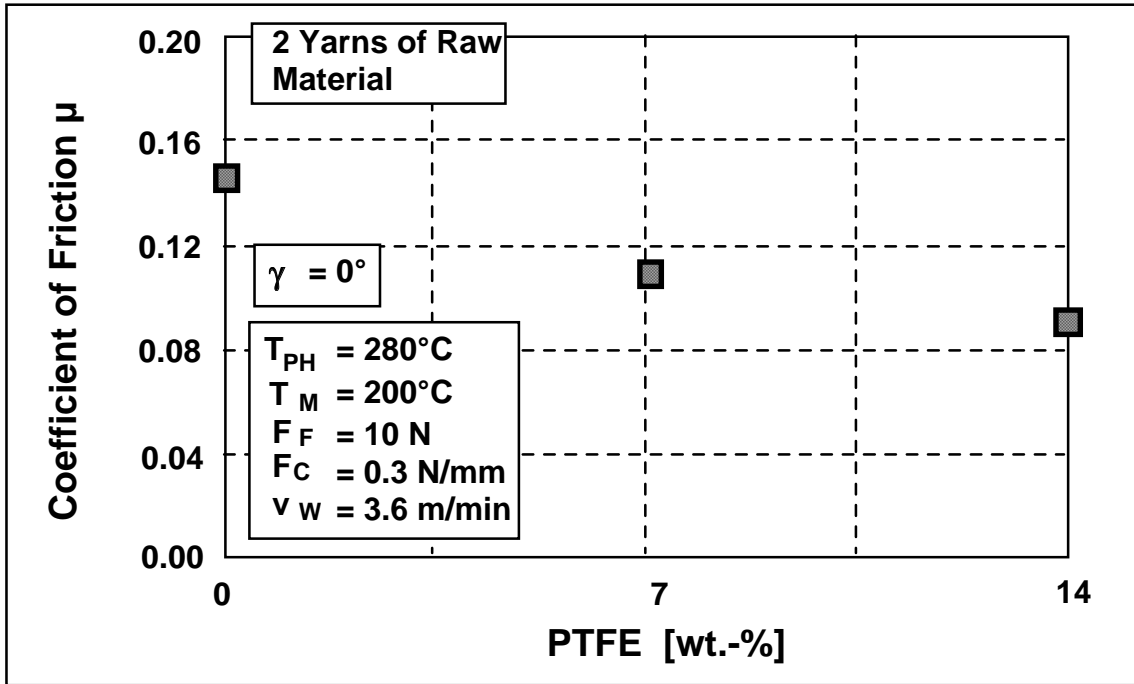


Figure 7: Coefficient of friction of filament wound thermoplastic composite bearings depending on the PTFE weight content

In further experiments, the composition of the composite material was varied. The weight content of PTFE was altered between 0 and 14%. The results can be seen in Figure 7. An increase of PTFE weight content resulted in lower coefficients of friction. In fact, the best coefficient of friction of 0.085 was measured with a PTFE content of 14% and a winding angle of 0°.

RESULTS OF INJECTION MOLDING EXPERIMENTS

The results of the injection molding experiments are given in Figure 8 and 9. In these experiments the filament wound sliding surface was used as an insert and the outer structure was injection molded around it. A preheating of the insert using hot air of 400°C was necessary to guarantee a strong bonding between insert and surrounding polymer. This bonding was determined using a special shear test [6]. The influence of the polymer's mass temperature during injection molding on the interlaminar shear strength between insert and polymer is shown in Figure 8. The mass temperature was varied between 260°C and 340°C. An increase of mass temperature up to 300°C resulted in shear strength values of 18 MPa. A further increase could not improve the bonding.

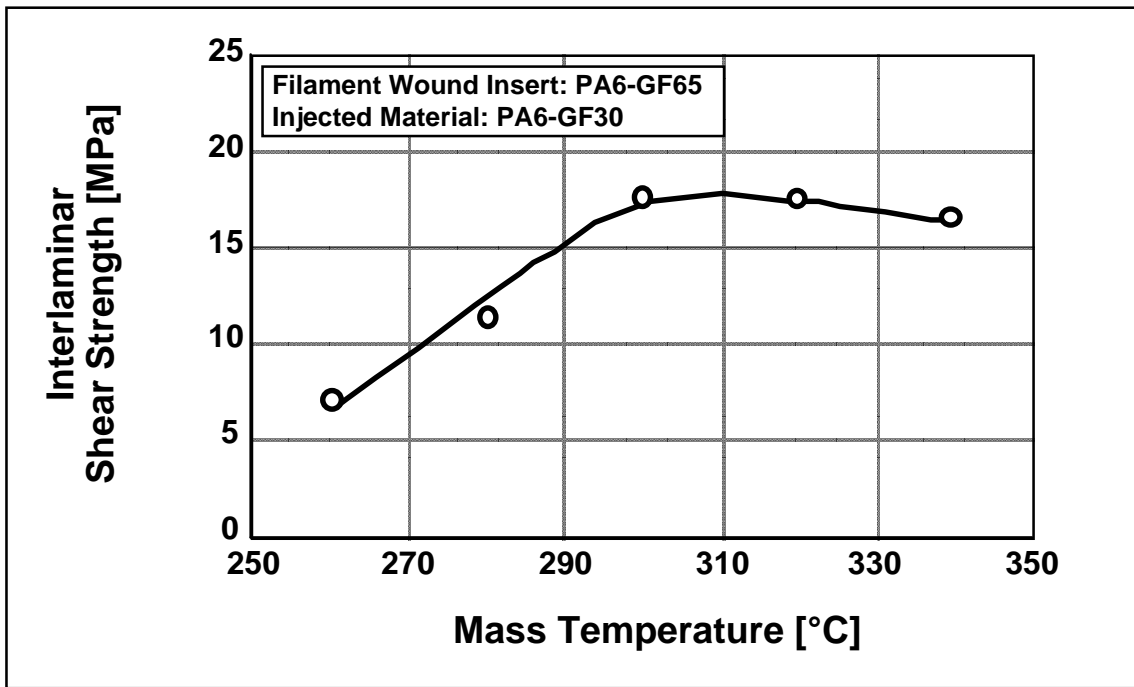


Figure 8: Interlaminar shear strength between insert and injected material as a function of mass temperature

The correlation between tool temperature and shear strength is given in Figure 9. During these experiments the tool temperature was varied between 20°C and 120°C. Here, an increase of temperature resulted in higher shear values. The highest tool temperature of 120°C let to shear values of about 20 MPa.

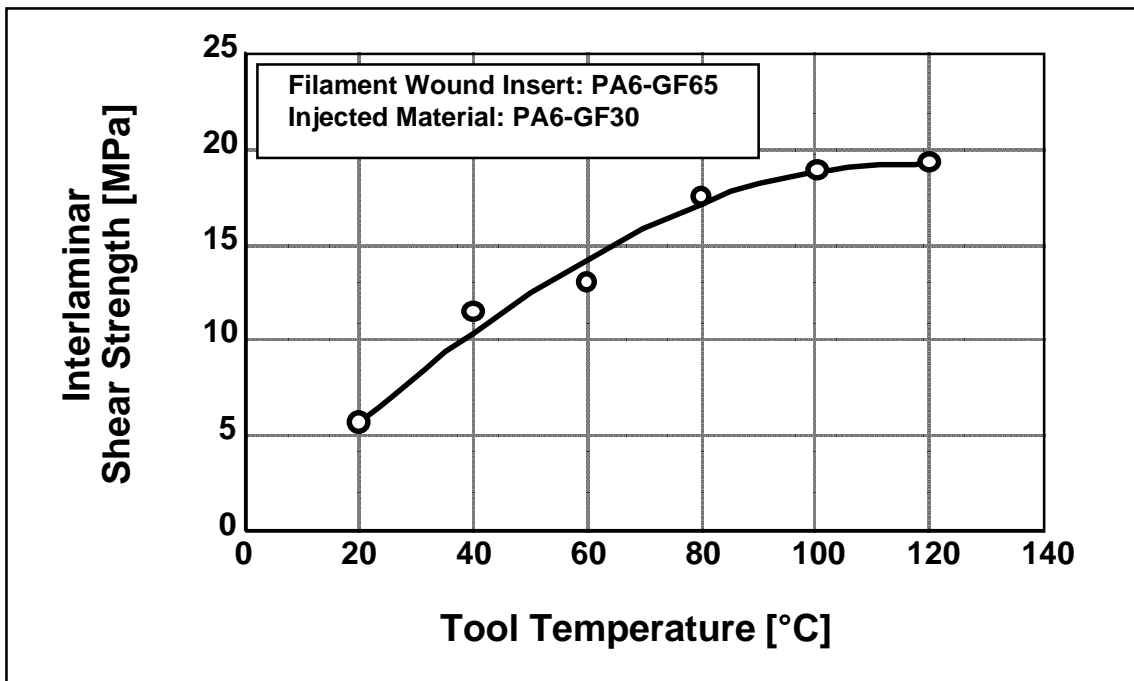


Figure 9 : Interlaminar shear strength between insert and injected material as a function of tool temperature

CONCLUSIONS

The manufacturing of a new type of bearing using thermoplastic matrix composites processed by filament winding, optionally in combination with injection molding, led to the following results: (a) Aramid fibers provided high strength and PTFE fibers, both embedded in a PA66 matrix, resulted in a low coefficient of friction of the bearings. The best results could be obtained with a PTFE weight content of 14 % and a winding angle of 0° (hoop winding). (b) During injection molding, preheating of insert rings resulted in much better adhesion to the injection molded outer part. For the materials investigated (PA66), a mass temperature of 300°C in combination with a tool temperature of 120 °C resulted in the best adhesion between insert and surrounding polymer. (c) Further work needs to be done in order to optimize the bearings by the use of a finer commingling quality of yarn, the adjustment of optimum fiber orientation angles in the sliding surface and other fiber matrix material combinations.

ACKNOWLEDGEMENTS

Prof. Friedrich gratefully acknowledges the help of the Fonds Der Chemischen Industrie, Frankfurt, for his personal research activities in 1997. The support of AGARD GX 3-96 for the Greek-German cooperation in the field of fiber placement is gratefully acknowledged. Further thanks are due to the Stiftung Industrieforschung for the Forschungspraktikum of R. Reinicke on this research topic.

REFERENCES

1. F. Hauptert, K. Friedrich: "On Processing and Properties of Rings Wound from Thermoplastic Powder Impregnated Continuous Fiber Composites", Proc. "Advancing with Composites '94", Milano, Italy, May 2-7, pp. 237-249, (1994)
2. F. Hauptert, K. Friedrich: "Processing Related Consolidation of High Speed Filament Wound Continuous Fiber / Thermoplastic Composite Rings", Proc. "Flow Processes in Composite Materials '94", Galway, Ireland, July 7-9, pp. 279-289, (1994)
3. V. Klinkmüller, K. Friedrich: "Pultrusion of Flexible, Continuous Glass Fibre / Thermoplastic Powder Impregnated Bundles", High Technology Composites in Modern Applications, Eds. S.A. Paipetis and A.G. Youtsos, University of Patras, Applied Mechanics Laboratory, pp. 214-221, (1995)
4. V. Klinkmüller, M.K. Um, M. Steffens, K. Friedrich, B.S. Kim: "A New Model for Impregnation Mechanisms in Different GF/PP Commingled Yarns", Applied Composite Materials **1**, pp. 351-371, (1995)
5. K. Friedrich, F. Hauptert, C. Chen, J. Flöck: New Manufacturing Techniques for Thermoplastic Composite Bearings, in Wang Tzuchiang, Tsu-Wei Chou (eds.): Progress in Advanced Materials and Mechanics, Peking University Press, Beijing, China, 1996, pp. 91-96
6. B. Lauke, K. Schneider, K. Friedrich: Interlaminar shear strength measurement of thin composite rings fabricated by filament winding, ECCM 5; Fifth European Conference on Composite Materials, Bordeaux, Frankreich, 7-10 April, 1992, pp. 313-318

TENSILE CREEP PROPERTY OF UNSYMMETRICAL AND MULTIDIRECTIONAL GFRP LAMINATES

Ken Kurashiki, Masaharu Iwamoto, Shigetoshi Araki and Toshihiko Maesaka

*Department of Mechanical and System Engineering, Kyoto Institute of Technology
Matsugasaki, Sakyo-ku, Kyoto 606, Japan*

ABSTRACT

The purpose of this study is to estimate the long-term creep behavior of the unsymmetrical and multidirectional GFRP laminates in short-term constant tensile loading tests. The creep equation is obtained using the tensile creep data of short-term tests, in consideration of stress, temperature and tensile angle to reinforced glass fiber. Long-term predictions of tensile creep strain could be made using the analytical result of power law equation and TTSP (Time Temperature Superposition Principle) method. A reasonable comparison between the prediction curve with the power law equation and the master curve with TTSP method is observed at time up to 10^8 second. The internal hydraulic pressure creep test on this GFRP pipe under end free conditions verified creep prediction curve.

KEYWORDS: tensile creep, internal pressure, FRP pipe, power law equation, creep constitutive equation, TTSP master curve

INTRODUCTION

In recent years, FRP materials and structures have been used as reinforcement, repair and preserve of construction and equipment which have been constructed. For example, constructed chimney or pier of bridge was reinforced by FRP materials to increase durability, earthquake-resistant and strength [1,2]. Renewal of an overage drain pipe or gas pipe is made by inserting pre-impregnated tube into overage pipe with air pressure, and then curing with ultraviolet rays. These application of FRP materials need long-term durability, and it becomes necessary to reveal the long-term mechanical behavior.

In this study, tensile creep tests were performed with the GFRP laminates, above-mentioned for renewal overage drain pipe or gas pipe, to obtain the fundamental property for predict the long-term creep behavior of the GFRP laminates under various conditions of stress, temperature and tensile angle. TTSP method was applied to FRP by many researchers [3-6], and it was also used to evaluate the long-term prediction with the results of the TTSP method by authors. Creep constitutive equation of the tensile creep is obtained based on short-term tensile creep tests, and the predicted curve was compared with the results of the TTSP method and the internal hydraulic pressure pipe test under end free conditions.

MATERIALS AND SPECIMENS

The test material is made up of the glass fiber mat, the woven roving cloth and ultraviolet polymerization unsaturated polyester resin. It was produced by INPIPE(AB, Sweden) and received in cylindrical form(pipe), which is called as uncured soft-sleeve. Fig. 1 represents the structure of pipe and the reinforcement configuration, inner layer of the fiber mat are called layer A, outer layer are called layer B.

Two types of creep test specimens were used. One was dumbbell type and another was pipe type. Dumbbell type specimens were cut from the uncured laminated pipe and then cured with ultraviolet rays. Cutting angle was determined in five kinds of directions, 0, $\pi/6$, $\pi/4$, $\pi/3$ and $\pi/2$ (rad) by considering the material anisotropy, in which 0(rad) is axial direction of pipe. Soft-sleeve, pipe specimen, was cured in the split mold with ultraviolet rays, consequently it have flash. Applied stress is given by following equation:

$$\sigma_{\theta} = P \cdot R / d$$

where σ_{θ} : circumferential stress, P: applied pressure, R: mean of internal radius, d: thickness. Specimen geometry is shown in Fig. 2 and Fig. 3.

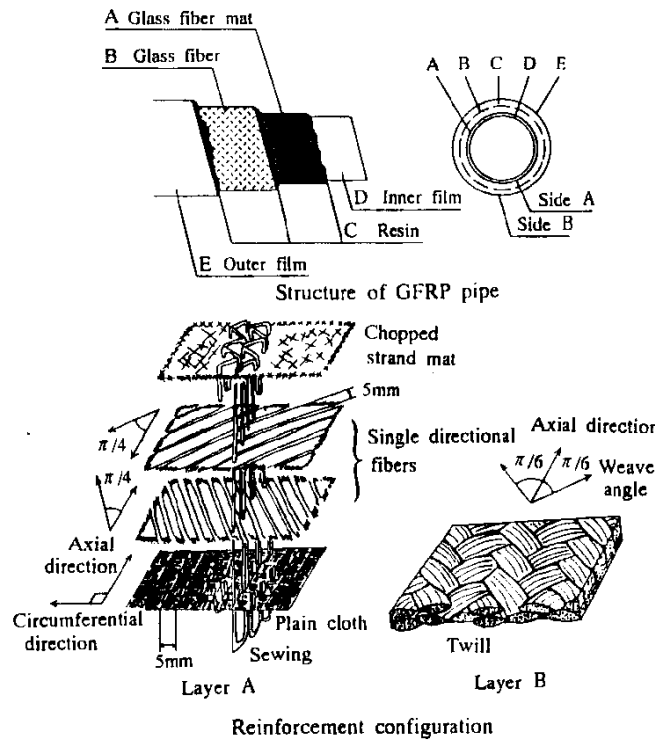


Fig.1 Structure and reinforcement configuration of GFRP pipe.

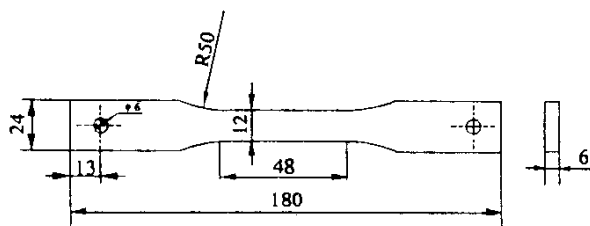


Fig.2 Geometry of dumbbell type specimen.

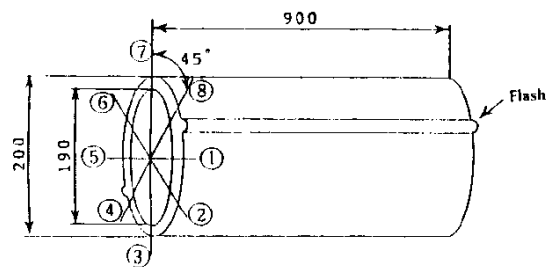


Fig.3 Geometry of pipe specimen.

EXPERIMENTAL DETAILS

TENSILE TESTS

Tensile tests were conducted with the dumbbell specimen using an autograph testing machine(Shimadzu) at a cross-head speed of 1 mm/min at a temperature 293K. Axial and transverse strains of the specimen are measured by strain gauge. Load and strain were measured and recorded with a strain meter and a digital recorder(TEAC,DR-F1).

TENSILE CREEP TESTS

In order to obtain the parameter of the creep constitutive equation, constant-loading tensile creep tests were conducted at various conditions by considering stress, temperature and tensile angle. The conditions are shown in Table 1.

The result of the test which carried out at various temperatures was applied to the TTSP method. The creep strain was measured by strain gauges(gauge length is 30mm) mounted on both surface of the specimen. Fig 4 shows creep testing machine equipped with temperature control devices, temperature controller capable of $\pm 0.2\text{K}$ resolution. Strain data were recorded on digital recorder for the first 2 minute at 5Hz, for 2~20 minute at 2Hz, for after 20 minute at 0.1Hz, and testing time was 10^5 second.

Internal hydraulic pressure creep tests

In order to apply internal hydraulic pressure to the pipe specimen, flanges are attached to both ends as shown in Fig.5. Four biaxial strain gauges($0,90^\circ$) were mounted on outer surface and center of the pipe at intervals of $\pi/2$. Tests were conducted with two specimens at a

Table 1 Tensile creep tests conditions.

Stress (MPa)	Temperature (K)	Tensile angle (rad)	Testing time (sec)
0~41.7	303	$\pi/2$	10^5
intervals of 2.45			
29.4	293~353	0	10^5
	intervals of 10	$\pi/2$	
29.4	293	$\pi/6$	10^5
		$\pi/4$	
		$\pi/3$	

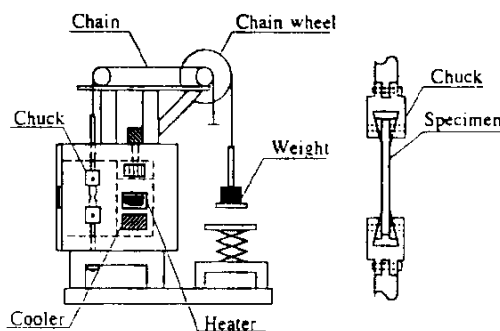


Fig.4 Creep testing machine.

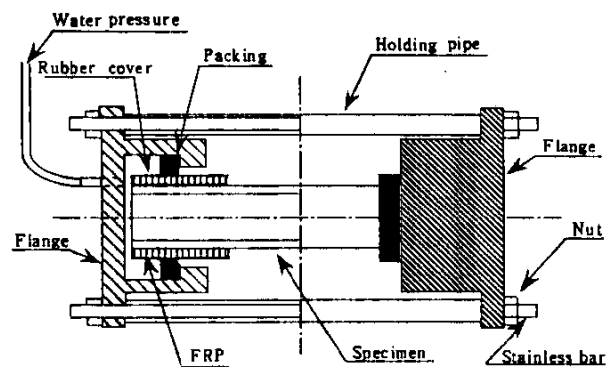


Fig.5 Pipe specimen attached flange.

circumferential stress 29.4MPa and at a temperature 293K in a water tank.

EQUATION OF CREEP STRAIN

One of the method to predict the long-term creep behavior is to use the equation based on short-term tests data. The Findley power law equation(eq. (1)) has been used to successfully characterize the viscoelastic behavior of a variety of amorphous, crystalline, and crosslinked polymers[7].

In this study, the creep response of the composite were modelled by applying the power law.

$$\epsilon(t) = (A + kt^n) \sigma_0 \tag{1}$$

where $\epsilon(t)$: strain, σ_0 : constant stress, A,n: material constants, t: time after creep loading, and k is material constants for linear viscoelastic, but it is function of stress for nonlinear viscoelastic.

So we have to classify the creep response as linear and nonlinear viscoelastic one. Materials which to behave with linear viscoelastic creep response were identified by isochronous stress-strain curves[8] previously. Therefore, k is considered a material constant. Prerequisite of the application of eq.(1) is the isotropic and homogeneous materials. In this study, we need to derive the equation taking account of anisotropic material, so that eq.(1) is used as an empirical equation. Parameters A,k,n are constant to the stress, but the variation for these parameters is possible with tensile angle(θ) and temperature(T). Then, eq.(1) may be expressed as follows.

$$\epsilon(t, \sigma, \theta, T) = \{ (A(\theta, T) + k(\theta, T)t^{n(\theta, T)}) \} \sigma \tag{2}$$

Now we need to determine the parameters $A(\theta, T), k(\theta, T), n(\theta, T)$ in eq.(2).

RESULTS AND DISSCUSSION

TENSILE TESTS

Table 2 shows mechanical properties of GFRP laminate for different tensile angle. Apparently, mechanical property varies much with the tensile angle.

Table 2 Mechanical properties.

Tensile angle θ (rad)	Tensile strength σ_B (MPa)	Modulus of elasticity E(Gpa)	Poisson's ratio ν
0	79.0	11.2	0.39
$\pi/6$	114.6	10.4	0.32
$\pi/4$	121.3	11.4	0.23
$\pi/3$	81.8	10.4	0.30
$\pi/2$	66.3	8.9	0.39

TENSILE CREEP TESTS

Fig.6 shows creep strains of both surfaces of the dumbbell specimen. In this figure, it is found that strains of side A and side B are very different. This is considered to be due to the

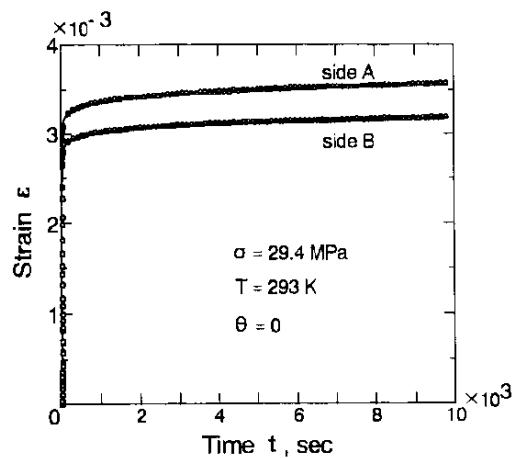


Fig.6 Creep strain curves.

difference of reinforcement in A and B layer. This difference is about 10^{-2} mm for the gauge length, so we assumed that strain distribution in the specimen is continuous in the direction of thickness. Then, the mean of both surface strains is regard as creep behavior of the specimen.

The $n(\theta, T)$ is determined as follows.

Fig.7 shows variation of n value to the data of each time by means of regressive calculation. In Fig.7, n value is stable after 10^3 second. So, 10^4 second is selected as the testing time. The power law exponent, n , is calculated based on the strain at 10^4 second for arbitrary stress(σ), temperature(T) and tensile angle(θ), shown in Fig.8. The n value is almost unchanged irrespective of σ , θ and T . Mean value of n , $n_{mean}=0.135$, which is obtained in various test conditions is determined as the typical value.

Moreover, A and k are calculated by means of regressive calculation by substituting $n=0.135$ into eq(2). Fig.9 shows A , k as a function of stress(σ) for test condition with $T=303$ K and $\theta = \pi/2$. Both A and k are constant, independent of σ . Fig. 10 shows $A(\theta, T)$ and $k(\theta, T)$ as the function of T under σ and $\theta (= \pi/2)$ are constant conditions. A and k against temperature(T) increase linearly with increasing temperature and can be written as eq.(3). Because the same tendency is observed for $\theta=0$, it is considered that A and k are affected by matrix resin.

$$A(T) = aT + b, \quad k(T) = \alpha T + \beta \quad (3)$$

Next, A and k against tensile angle(θ) are shown in Fig.11, solid and dotted line in the figure are approximation curves as follows, respectively.

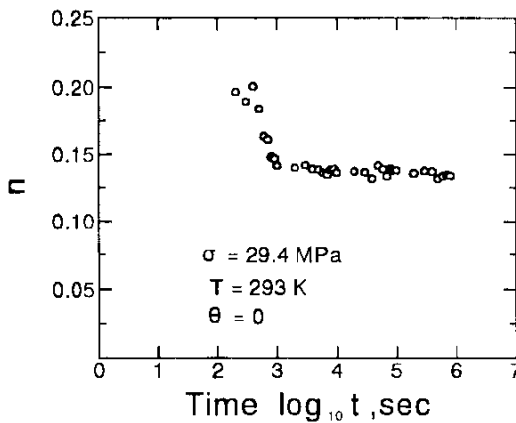
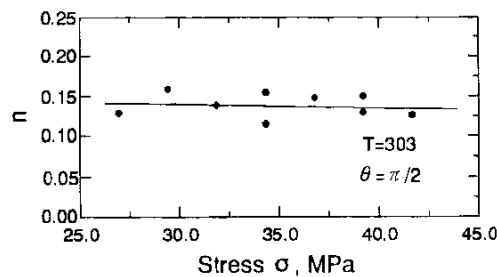
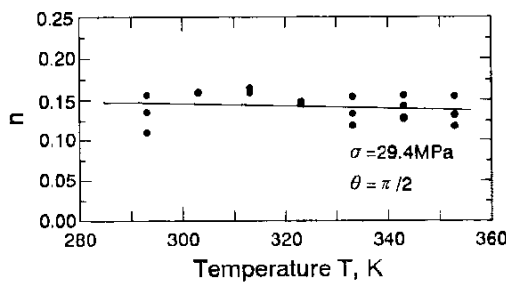


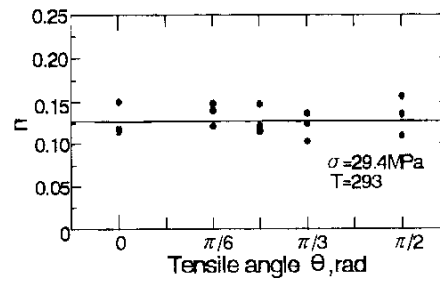
Fig.7 Variation of n value.



(a) $n - \sigma$.



(b) $n - T$.



(c) $n - \theta$.

Fig.8 Relation between n value and σ, T, θ .

$$A = p - q \sin^3 \theta, \quad k = P - Q \sin^3 \theta$$

In Fig.11 approximation curve fits the experimental data as a whole, where p and P are the center of amplitude and q and Q are the amplitude of the curves. Both A and k are minimized at $\pi/6$, i.e. weaving angle of roving cloth, hence it can be seen that the effect of roving cloth is expressed highly. Therefore, A and k for the tensile angle can be rewritten as follows.

$$A(\theta) = p - q \sin^3 \theta, \quad k(\theta) = P - Q \sin^3 \theta$$

Substituting above A, k in eq.(2), the following equation is obtained.

$$\varepsilon(t, \sigma, \theta, T) = \{p - q \sin^3 \theta + (P - Q \sin^3 \theta)t^n\} \sigma \tag{4}$$

where T is constant, and a,b, α , β , p,q,P,Q in eq.(3) or (4) imply $a(\theta)$, $b(\theta)$, $\alpha(\theta)$, $\beta(\theta)$, $p(T)$, $q(T)$, $P(T)$, $Q(T)$ parameters depend on T or θ , respectively.

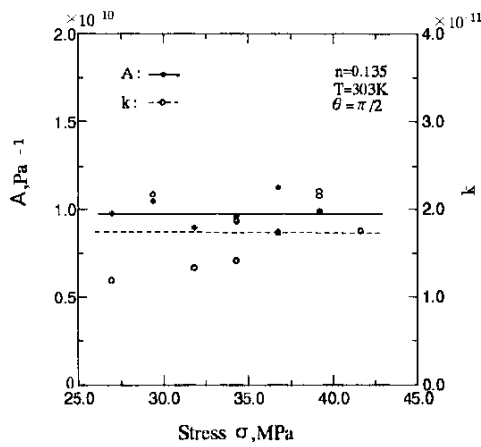


Fig.9 A, k as the function stress σ .

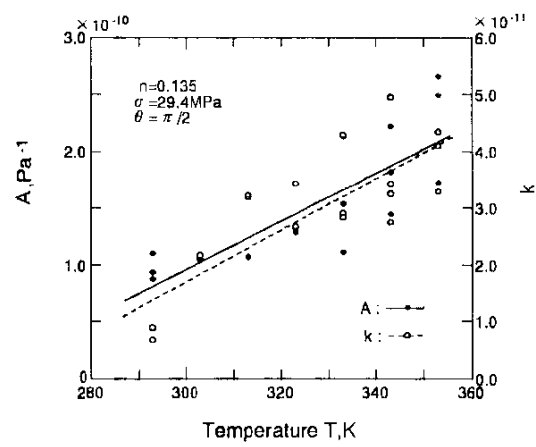


Fig.10 A, k as the function temperature T.

Because of the linearity of material, it can be assumed that amplitude of A and k curves against tensile angle, $q(T)$ and $Q(T)$, are variables independent of the temperature. Therefore eq.(4) can be rewritten as eq.(5).

$$\varepsilon(t, \sigma, \theta, T) = \{aT - q \sin^3 \theta + c + (\alpha T - Q \sin^3 \theta + C)t^n\} \sigma \tag{5}$$

Inclination of A and k curves against temperature, $a(\theta)$ and $\alpha(\theta)$, are constant regardless of tensile angle. All parameters in eq.(5) can be determine based on inclination, intercept, amplitude and center of the amplitude in Fig.10 or Fig.11. Values of these parameters are shown in Table 3. Thus, creep constitutive equation of the material is obtained. This equation is effective in the range of the temperature 293K~353K and the range of the stress 27.0MPa~41.7MPa that is the test condition.

PREDICTION OF THE LONG-TERM CREEP STRAIN

Fig.12 shows the prediction curve in which

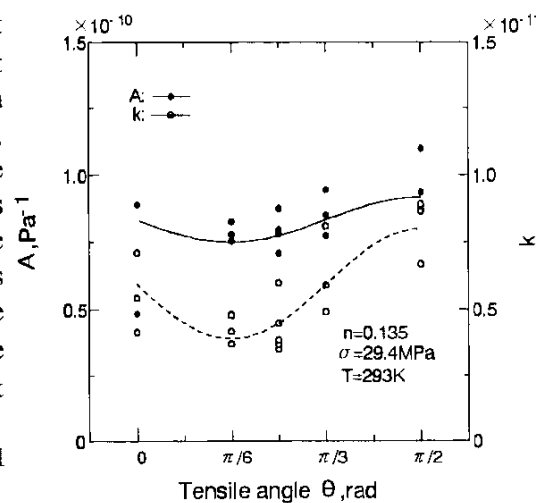


Fig.11 A, k as the function of tensile angle.

Table 3 Parameters of the creep constitutive equation.

A	1.98×10^{-12}	α	4.34×10^{-13}
q	1.67×10^{-11}	Q	4.18×10^{-12}
c	-5.02×10^{-10}	C	-1.20×10^{-12}

value of each parameter and σ, T, θ substituted in eq.(5) and experimental curves with the 10^6 second tests. Although experimental curves seems to scatter somewhat, prediction curve agreed well with that curves up to 10^6 second.

INTERNAL HYDRAULIC PRESSURE CREEP TESTS

Fig.13 shows creep strain of circumferential of the pipe under the conditions of internal hydraulic pressure tests and the predicted curve based on eq.(5). Strain of the test is obtained by the average value over 4 gauges. One of these results agreed with the prediction curve.

TTSP METHOD TESTS

In order to confirm the validity of the constitutive equation, constitutive equation curve is compared with the master curve according to the results of the TTSP method. Tests of the TTSP method were conducted with the specimen of 0(rad) and $\pi/2$ (rad) tensile angle. The result for $\pi/2$ (rad) tensile angle is shown in Fig.14. And the master curve by horizontal shifting of creep data where the reference temperature is 297K, is shown in Fig.15 with the prediction curve above-mentioned.

Relation between the time-temperature shift factor a_T and temperature is represented with a straight line as shown in Fig.16. Therefore the TTSP method can be applied in this test material. Reasonable comparison between the prediction curve and the master curve with the TTSP method is observed at time up to 10^8 second.

CONCLUSION

In this study, tensile creep behavior of the GFRP which have complex reinforcement

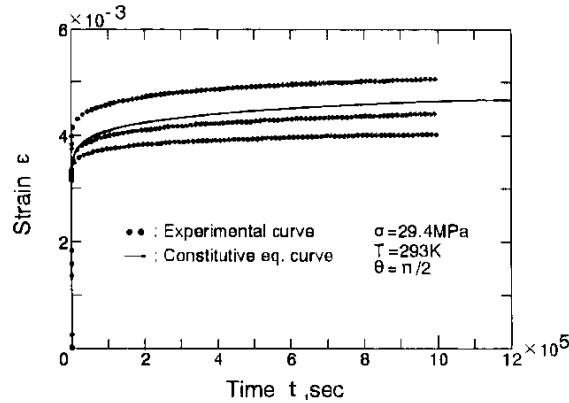


Fig. 12 Comparison of predicted and experimental tensile creep strain.

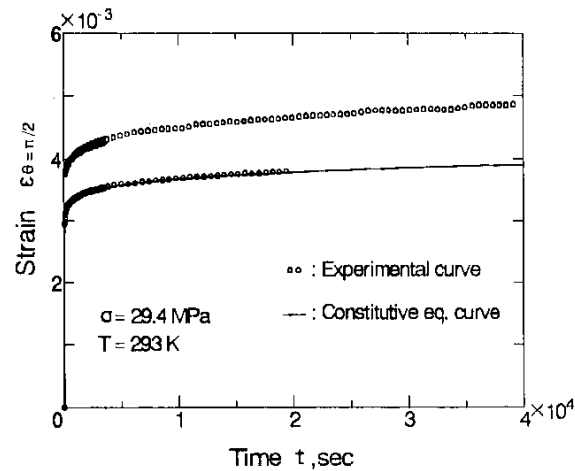


Fig. 13 Comparison between predicted and experimental internal hydraulic pressure strain.

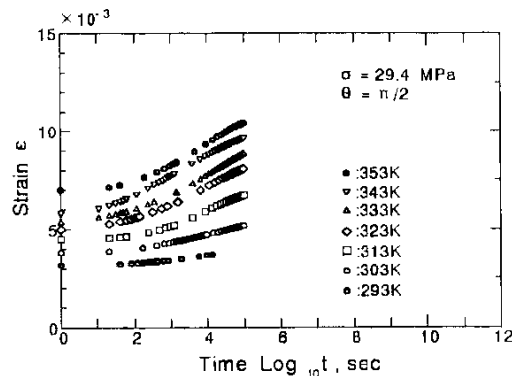


Fig. 14 Variations of creep strain at various temperature.

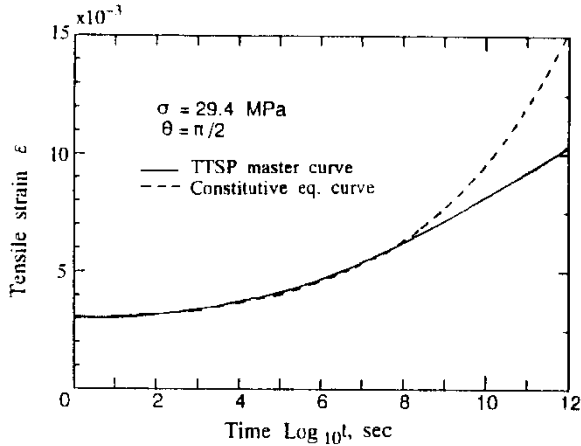


Fig.15 Comparison of the predicted creep strain curve and the master curve by the TTSP method.

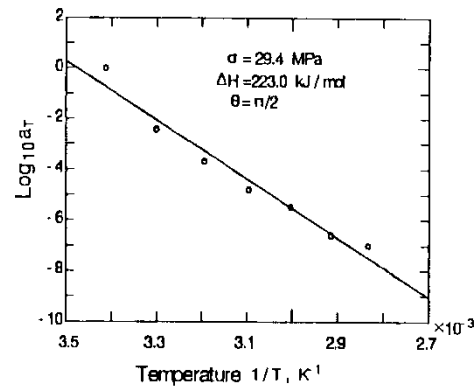


Fig.16 Arrhenius plot of shift factor a_T .

structure is observed under macroscopic consideration. And creep constitutive equation is obtained by considering stress, temperature and anisotropy of materials. The validity of this constitutive equation is confirmed by the experimental results of the tensile test, the internal hydraulic pressure test on the pipe under end free conditions and master curve with the TTSP method.

ACKNOWLEDGMENTS

The authors would like to express their thanks to Sekisui Chemical Co.,LTD. for preparation of the composite samples, and Mr. N. Matsuda, the technical official in K.I.T. for helping in the experiments.

REFERENCES

1. Nakatsuji, T., *Journal of the Japan Society for Composite Materials*, Vol.22, No.4, 1996, pp 129-135.
2. Miyazaki, M., "New Unidirectional Reinforcing Fiber Sheet for hand LAY-UP Molding and Its Application in Buiding and Civil Engineering", *Reinforced Plastics*, Vol.38, No.12, 1992, p.476.
3. Miyano, Y. and Suzuki, K., "Time-Temperature Dependence of GRP Plate under Flexural Loading", *Journal of the Society of Materials Science, JAPAN*, Vol.23, No.255, 1974, pp.515-519.
4. Takada, S., Tsukui, K., Yoshioka, S., and Hijikata, A., "Evaluation of Time-Dependent Deformation of High Modulus CFRP under a Constant Temperature Condition", *Journal of the Japan Society for Composite Materials*, Vol.18, No.5, 1992, pp 192-200.
5. Miyano, Y., Kasamori, M. and Hirazakura, Y., "Flexural Creep Behavior of Epoxy Resin and Transversal Direction of Fibers in CFRP", *Journal of the Japan Society for Composite Materials*, Vol.19, No.1, 1993, pp.20-25.
6. Furue, H., "The Master Curves on Creep Properties of CFRP, GFRP and CF/GF Sandwich Laminates", *Reinforced Plastics*, Vol.39, No.12, 1992, pp.515-519.
7. Tuttle, M.E. and Brison., H.F., "Accelerated Viscoelastic Characterization of T300/5208 Graphite-Epoxy Laminates", *NASA Contractor Report 3871*, 1985.
8. Tuttle, M.E. and Brison., H.F., "Prediction of the Long-Term Creep Compliance of General Composite Laminates", *Experimental Mechanics*, 1986, pp.89-102.

CREEP DEPENDENCE OF THE CONDUCTIVITY OF STEEL FIBER REINFORCED POLYPHENYLENE ETHER RESIN

Satoshi Somiya, Shigeki Katayama and Kazuo Igarashi

*Department of Mechanical Engineering, Keio University,
3-14-1 Hiyoshi, Kohoku-ku, Yokohama 223, Japan*

SUMMARY: The conductivity has been researched on PMC of metal fibers and modified PPE resin which was developed to evaluate the shielding effect against Electric-magnetic interference (EMI). The shielding efficiency against EMI is usually evaluated by the electric resistivity. And it is well known that it is sometimes affected by the surrounding conditions and mechanical deformation. In this study, the affect of deformation not only in glassy condition but also in viscoelastic condition at high temperature on the volume resistivity have been researched.

KEYWORDS: EMI,PMC, conductivity, viscoelastic deformation, PPE, steel fiber

INTRODUCTION

An electric-magnetic interference (EMI) become worldwide problem for health and in the industrial field[1] [2]. The effect of deformation and high temperature on the conductivity of PMC which was made with discontinuous stainless steel fibers and modified Poly-Phenylene Ether(PPE) has been researched. This is one kind of materials developed for EMI shielding[3][4] and it have not only the satisfactory electric resistance but also the good mechanical properties including creep resistance[5]. On the other hand, recently there were few reports on the affect of deformation and temperature on the conductivity . In this research, the effect of static bending deformation and viscoelastic deformation[6] at high temperature on the conductivity[7] has been studied.

MATERIAL AND TEST METHODS

Materials

A polymer blended thermoplastic; PPE has been used as a matrix resin. This modified PPE resin was consisted of polyphenylene ether (Weight percentage: 55%), Polystyrene (36%) and Plasticisers (a middle polymerization polymer; 9%). And stainless steel short fibers with 5%, 10% and 15% weight fractions were used as metal fiber in PMC. The metal fiber was about

7mm in length and about 8µm in diameter. After molding, fibers had the shape of spiral and they contacted on each other. In Table 1, the mechanical properties were shown.

Test method

The three point bending static test and creep test have been done in oven at room temperature about 23° C and at from 60° C to 110° C respectably. The applied stress condition was the 10 percent of bending strength according to ISO 75. The resistivity of material was measured by 4 point electric resistivity measurement method with the digital multimeter of Adventist Co. They were measured between two needles of copper which were inserted into and through the both end of specimen. The resistivity R_0 of PMCs of 5%, 10% and 15% were 1.6, 0.6 and 0.3 ($10^{-3} \Omega \cdot m$) respectively and the volume resistivity was inversely proportional to fiber volume fraction.

TEST RESULTS AND DISCUSSIONS

The deformation dependence of the conductivity

The conductivity of used material depended on the amount of deformation. Fig. 1(a), (b) and (c) shows the relationship between deflection and the change of the conductivity by the static bending loading. There were two step of the change of the conductivity. Here the lower deflection region I was defined from 1.3 to 1.8% strain level as shown at the point (A) in Fig. 1(c) and in this region the resistivity slightly increased. It was found that the amount of the change depended on the theory for strain dependence of the resistivity of metal material as follow:

$$R = R_0 (1 + \alpha \epsilon) \quad (1)$$

Where, R_0 is the volume resistivity of the materials before deformation and its dependency on the fiber volume fraction is shown in the previous section. The values of R_0 were over the minimum requirement for the conductivity of the electric instruments and decreased by the increasing of weight fraction. α is a constant of material and ϵ is static strain.

In the second stage II after the first stage I, the conductivity rapidly increased depending on the strain straightforwardly. The slope of this conductivity to strain i.e. the gradient of region II were measured and showed in Table 2. Increasing weight fraction, the slope decreased and it means that the effect of deformation on the conductivity decreased. It was found that the changing point of the conductivity is the same point that was the initiation of plastic deformation. It was assumed that the conductivity of these material must depended on the number of contacted fiber on each other. And these experimental results show that the numbers

were decreased according to increase in bending deformation, where plastic deformation was included. And also it means deflection decreased the shielding effect against EMI. If the resistivity depends on the number of the contacted fibers, it might be affected by thermal deformations.

Temperature dependence of the conductivity

Usually these materials are used in high temperature surrounding and at applied stress conditions. The temperature dependence of the resistivity have not been researched on this material. If the conductivity depended on the number of metal fibers as in the previous discussion, deformation by thermal expansion must affect the conductivity of the material. Because the amount and the direction of elongation of the contacted fibers on each other must be different, the contacted area begin to detach by the thermal deformation. In oven, the specimen which has two copper needles was put on the bending supports and the change of the resistivity between two needles were measured during heating.

Fig. 2 shows the changes of the resistivity during rising temperature on the constant rate ($2^{\circ}\text{C} / \text{min}$) for materials of $W_f=10\%$. Up to about 60°C , it kept almost constant value of the resistivity but over 60°C , the volume resistivity begun to rise and rapidly accelerated the speed of the increasing rate of resistivity as shown in the figure. The values of resistivity at 140°C reached about 3 times of the value at room temperature. This means the resistivity must depended on the contacting phenomena of metal fibers and at higher temperature, the relationship between the resistivity and the deformation was not the same to the relation of them at the room temperature. Because thermal expansion strain was calculated and the change of the resistivity was calculated using the equation (1). Thus the experimental result were very large to the calculated value. From this fact, the change of the resistivity of this material mainly depended on the contacting phenomena of composed fibers.

Creep behavior of metal fiber composed PPE

The creep behavior within the strain range up to 4% has been researched for the used materials. The creep compliance curves which were calculated from creep curves on some specified temperature were measured and the master curve was made from these compliance curves from the treatment of shifting the compliance curves to vertical direction that means along the time axis. Fig. 3 shows the three master curves for the materials of three kinds of fiber volume fractions. The horizontal axis shows the physical time axis. These shift factor curves which were used for making three master curves showed straight lines on an Arrhenius type graph. From these facts, it is recognized that the creep behaviors of used materials depended on the linear visco-elasticity as an Arrhenius type.

It was assumed that the viscoelasticity of composites must depend on only viscoelasticity of the matrix resin and the elasticity depended on the amount of the fiber too. Because these creep compliance master curves look like the same shape, even though the values of compliance and the position of the curves on the physical time are different. The total master curve for creep behavior was made with three fiber volume fraction's materials to discuss the reciprocity law of time-temperature- fiber volume fraction. The shifting of master curves have been made to the vertical and horizontal direction. The physical meanings of shifting directions are that the dependence on elastic modulus and the viscoelastic properties on the fiber volume fraction. Fig.4 shows that the total master curve of creep compliance was obtained by three kind of master curves for all of materials having three fiber volume fractions.

Viscoelastic deformation dependence of the conductivity

The temperature and time dependence of the resistivity have been researched for the material of $W_f=15\%$ with the test as same as the bending creep test. Fig. 5 shows the relationship between the volume resistivity and creep compliance to creep time for the case of 100°C . The creep behavior in this figure shows the stage I and the starting portion of stage II. The resistivity was increased according to increase the time on the two steps as same as the creep behavior. It was a little higher than the value at the same strain of the static bending test. Because the resistivity on creep test usually increased by the heating process from room temperature to the test temperature until the starting of creep test. It means, the resistivity did not depend only on the amount of strain of matrix resin but also on the temperature. And in addition, it was found that it was changed by the creep strain.

Fig. 6 shows the relationship between the resistivity and the creep strain of the material of $W_f=15\%$ at 100°C . In this figure, the horizontal axis shows the volume resistivity and the vertical axis shows the creep strain. The resistivity increased by the creep strain directly but they were two line corresponding to stage I and Stage II of creep behavior. It means the conductivity of this PMC depended on the creep deformation. The creep strain of stage I in this figure was smaller than the limit of the static elastic deformation as shown Fig. 1(c). But the change of the resistivity caused by creep strain was very large rather than the value calculated by the equation (1). It means that creep strain phenomena is not the same to the elastic deformation but is like to the plastic deformation as in the previous discussion.

CONCLUSIONS

The effect of Time-temperature and the deformation on the conductivity of metal fiber composed have been researched and the results were obtained as follows;

1. The conductivity of Metal fiber reinforced modified PPE resin PMC depend on the static deformation phenomena.

2. The volume resistivity were changed by deformation phenomena such as elastic deformation and plastic deformation. In the elastic deformation, it was calculated by the formula for the strain dependency of resistivity for metal material.
3. It was assumed the conductivity depend on the number of contacts point of fibers, which means contacting area of fibers on each other and the change of the resistivity according to increase the deformation, the contact point which were formed at molding left each other.
- 4 . The volume resistivity depended on the temperature. This phenomena was explained by the phenomena that was the contacted points of metal fibers decreased. This happens because of the difference of coefficient of thermal expansion.

ACKNOWLEDGMENT

The authors wish to acknowledge the assistance of Mr. K. Biswas for research and Hitachi Co. for the preparation of materials.

REFERENCES

1. A. S. Kaddour, F. A. R. Al-Salehi and S. T. S. Al-Hassani, "Electrical Resistance Measurement Technique for Detecting Failure in CFRP Materials at High Strain Rates" , *Composites Science and Technology*, Vol.151(1994), pp377-385.
2. Yoshinobu Isao and Toshihiro Nishikita, "Stress Relaxation and Change in Entanglement of Polyisobutylene in Large Shearing Deformations", *Polymer*, Vol.136, No.8(1995), pp1635-1638.
3. K. Jana, A. K. Mallick and S. K. De, "ElectroMagnetic Interference Shielding by Carbon Fiber-Filled Polychlorophrene Rubber Composites", *Composites*, Vol., No.(1991), pp451-455.
4. Jeng-Maw Chiou, Qijiun Zheng and D. D. L. Chung, "ElectroMagnetic Interference Shielding by Carbon Fiber Reinforced Cement", *Composites*, Vol.20, No.4(1989), pp379-381.
5. Nakamura, K. Nishizawa, N. Mother and H. Yanagida, "Strain Dependent Electrical Resistance of Carbon-Insulator Composite", *Journal of Material Science Letters*", Vol. 13, No.11(1994), pp829-831.
6. M. Howard and L. Hollaway, "The Characterization of the Non-linear Viscoelastic Properties of a Randomly Oriented Fiber/Matrix Composite", *Composite*, Vol.18, No.4(1987), pp317-323.
7. Schulte and Ch. Baron, "Load and Failure Analysis of CFRP Laminates by Means of Electrical Resistivity Measurements", *Composites Science and Technology*, Vol.36(1989), pp63-76.

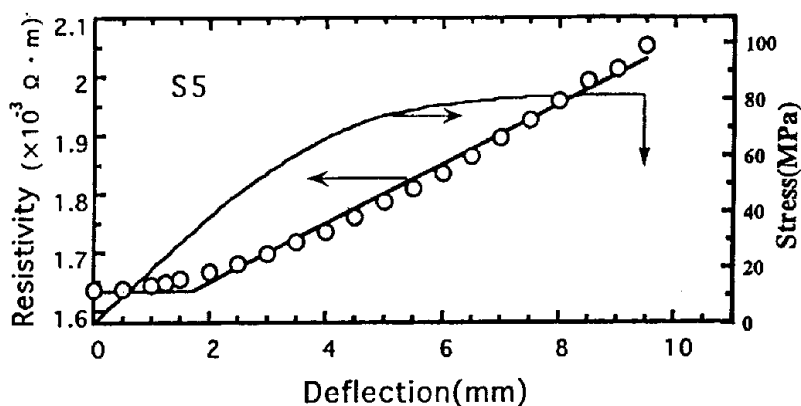


Fig. 1(a): Bending deformation dependence of volume resistivity on the material(S5) of weight fraction = 5% of steel fiber

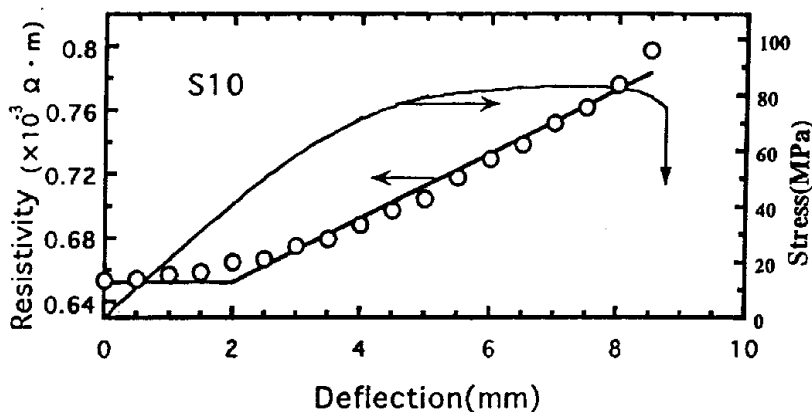


Fig. 1(b): Bending deformation dependence of volume resistivity on the material(S10) of weight fraction = 10% of steel fiber

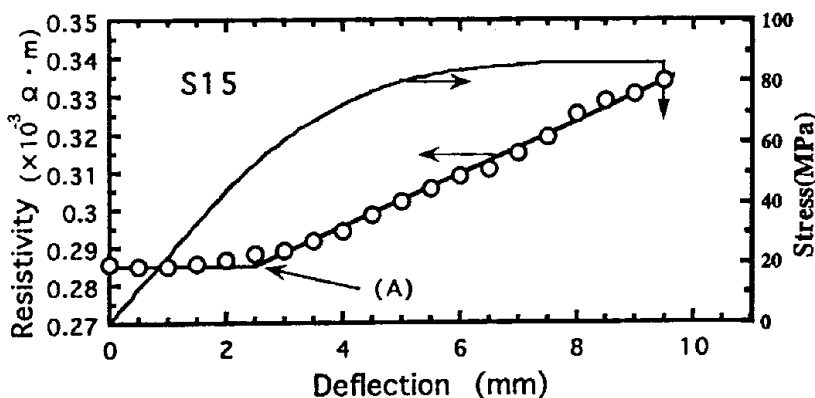


Fig. 1(c): Bending deformation dependence of volume resistivity on the material(S15) of weight fraction = 15% of steel fiber

Table 1: Mechanical properties of used materials

	Wf=5% (Vf=0.73%)	10 (1.52)	15 (2.39)
Bending modulus (GPa)	3.33	3.47	3.60
Bending strength (MPa)	90.8	91.7	91.4
Tensile modulus (GPa)	1.92	2.07	2.28
Tensile strength (MPa)	43.6	44.3	45.4

Table 2: Electric properties of Metal fiber composed PPE

Wf (%)	Vf (%)	Strain of region I (%)	Gradient of region II ($\times 10^{-3} \Omega \cdot m/m$)
5	0.73	1.31 <0.01>	56.21 <4.65>
10	1.52	1.52 <0.12>	21.10 <1.18>
15	2.39	1.76 <0.05>	8.20 <0.76>

< > : Standard deviation

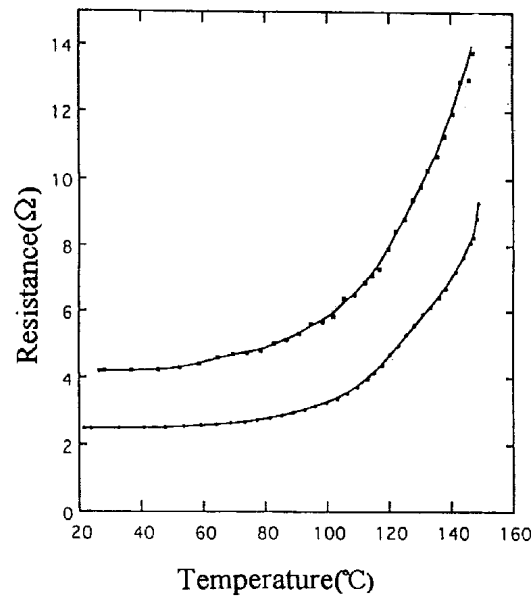


Fig. 2: Temperature dependence of resistance of S10

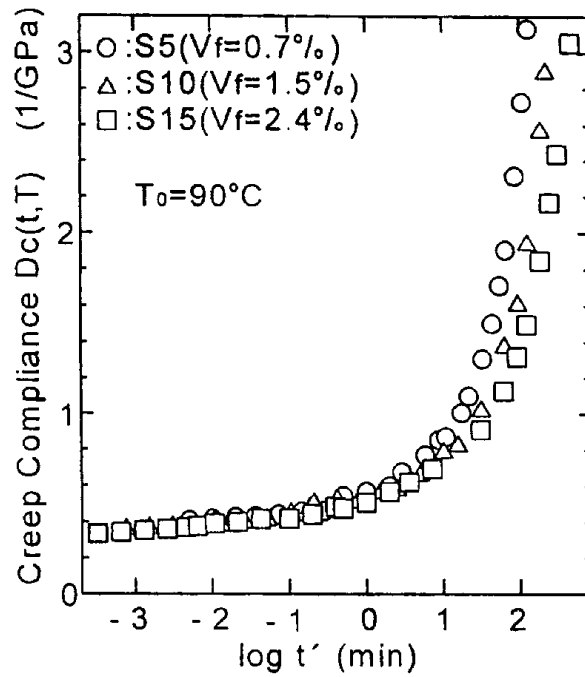


Fig. 3: Master curves of bending creep compliance of three materials; S5, S10 and S15 on physical times

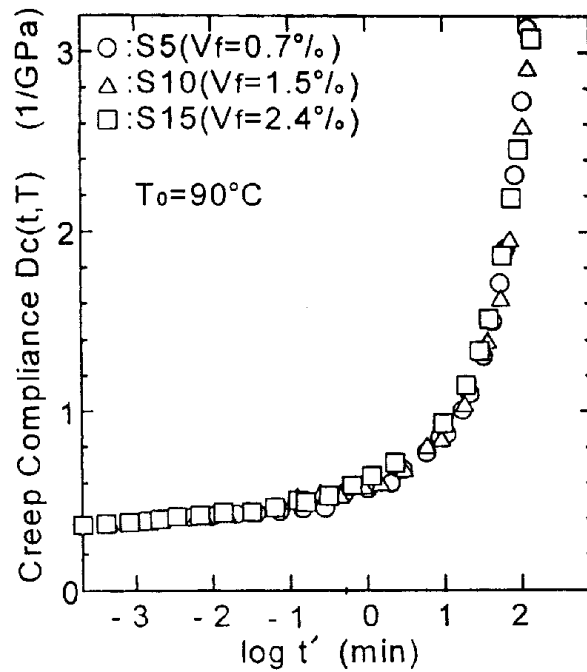


Fig. 4: The total master curve of bending creep compliance for S5, S10 and S15 shifting the curves on Fig. 3 on the physical time axis.

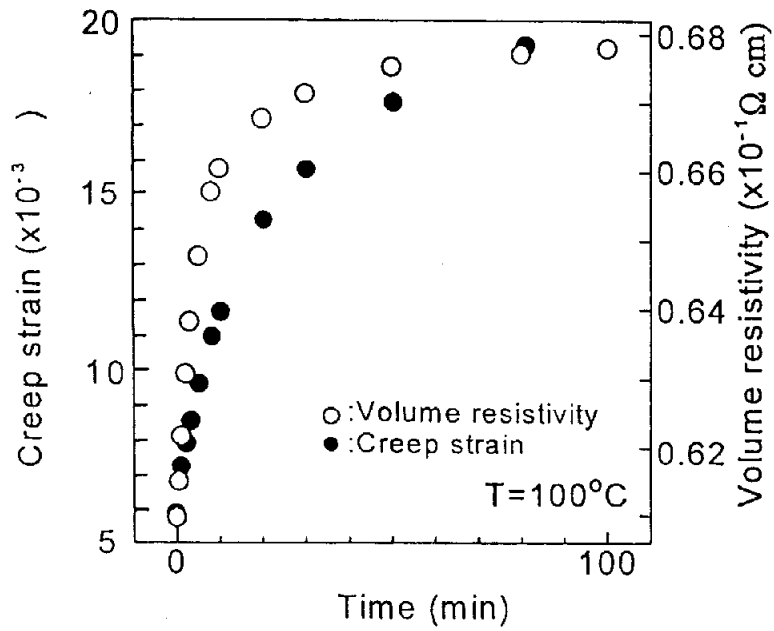


Fig. 5: Time dependence of volume resistivity and creep deflection of S15 material at 100 °C

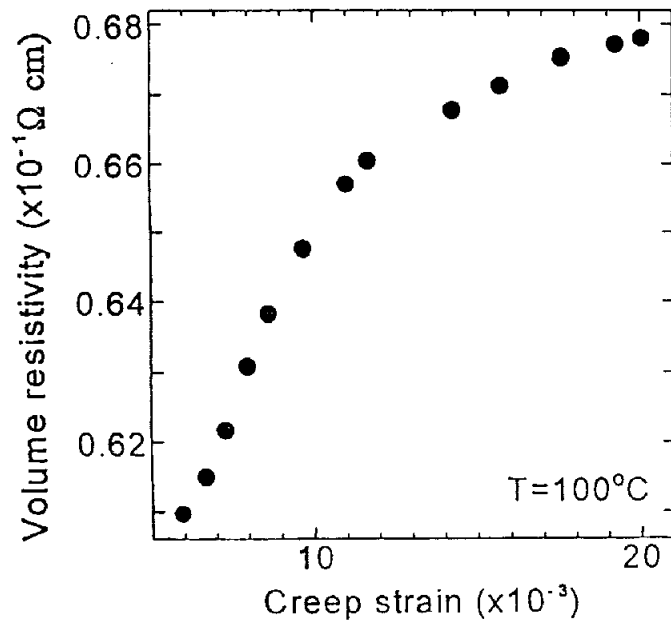


Fig. 6: Relationship between resistivity and creep deformation of Wf=15% at 100 °C

A FIBRE OPTIC ACOUSTIC EMISSION SENSOR WITH INHERENT DRIFT COMPENSATION

Anders Henriksson¹, Simon Sandgren² and Pierre-Yves Fonjallas³

¹ FFA, the Aeronautical Research Institute of Sweden, Box 110 21,
SE-161 11 Bromma, Sweden

² MYDATA automation, SE-161 70 Bromma, Sweden.

³ IOF, The Institute of Optical Research, SE-100 44 Stockholm, Sweden.

SUMMARY: The chirped Bragg grating technique have opened up new ways to measure transient strain events such as acoustic waves without encountering problems concerning the large dynamic range. Theoretical analysis shows that by using the "Chirped Grating Interferometer", CGI, concept with global strain and temperature compensation the sensor would mechanically maintain full sensitivity over global strain and temperature variations. A sensor that discriminates against global strain and temperature variations could be adapted to acoustic waves such as acoustic emission or other strain gradients. Properly adapted to the acoustic wavelength the two chirped gratings of the sensor will experience strain amplitudes of different sign and effectively enlarge the path imbalance of the sensor. Initial calculations for the acoustic application indicate that PZT-performance or even better is within reach.

KEY WORDS: fiber optic sensor, chirped gratings, gratings in fibers, acoustic emission, acoustic sensing, temperature compensation, strain compensation

INTRODUCTION

Background

In the field of "Aircraft Health Monitoring" one major objective is the continuous monitoring and characterisation of damage. Very few concepts of NDT are capable of an in service monitoring of damage evolution. However, the sensing of acoustic emission, AE, is a technique with such a potential and is therefore considered the primary candidate for a passive damage evolution monitoring scheme. The AE technique involves many complex and ambiguous interpretation procedures but does also have the benefit of a sensing range extending out from the sensor and also a limited location ability. Fiber optic sensing of AE is difficult due to several physical circumstances such as small displacements, short acoustic wavelengths and large bandwidth. Previous evaluation has been limited to various Fabry-Pérot interferometers (FPI) since quasi point wise interferometry offers a high degree of sensitivity at a specific location, see figure 1, Henriksson [1].

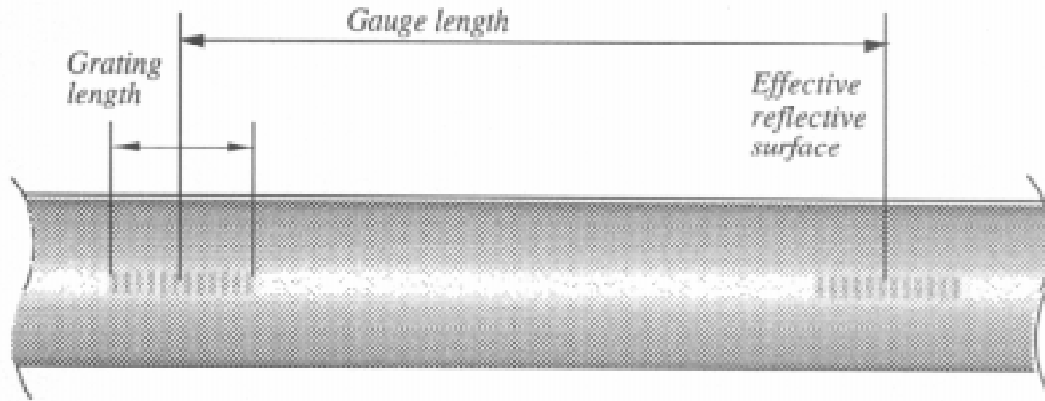


Figure 1. A Bragg grating Fabry-Pérot interferometer

The full Aircraft Structural Health Monitoring concept includes the monitoring of strain, temperature and damage evolution through a fiber optic sensor network embedded in an aircraft wing structure. In order to secure the sensor function but also to minimise the negative effects imposed by embedded sensors on the load carrying structure, the sensors should be solid and without inherent stress concentrations. Fiber optic sensors consisting of fiber Bragg grating elements seems to be the answer to most needs of smart structures; they have similar structural properties as those of an optical fiber, they do not cause higher stress concentrations than the optical fiber itself and reflectivity and bandwidth can be tailored to a large extent. A major problem with using FPI-sensors has been the need to keep the sensor at quadrature due to the "blind spots" in the sensing range. The quadrature refers to a phase difference of a quarter wavelength between the reflections that result in half fringe amplitude and maximum sensitivity. Much effort has so far been sunk into keeping the interferometer sensors at quadrature over global strain variations.

One of the drawbacks of most fibre optic sensors is the inability to discriminate between temperature and strain. Of the several methods to achieve this discrimination, most of them are based on using double sensors with different sensitivity factors to strain and temperature. A technically interesting alternative sensor concept to overcome the discrimination problem is the Chirped Grating Interferometer-, CGI-sensor, Henriksson [2], Henriksson et. al. [3]. According to this concept the sensor can be tailored to compensate for signals from global measurands such as temperature and global strain and hence effectively be insensitive to that input. Under some circumstances the compensation can even become selective and hence provide a discrimination concept. A sensor that compensates against global strain and temperature variations in the described manor would be very sensitive to strain gradients such as acoustic waves. For a sensor adapted to acoustic waves such as acoustic emission, with a length equal to half the acoustic wavelength, Henriksson [4], the minute displacements involved can very well be resolved.

Bragg Grating Sensors

A fibre optic Bragg grating is a periodic modulation of the refractive index in the core of an optical fibre. Such a modulation forms by itself a wavelength selective reflector, or rejection filter. In recent years this has rapidly become the dominant method to create reflectors inside optical fibres. The gratings are "written" in the optical fibre by exposure to a UV-light pattern. Like all gratings the Bragg grating is characterised by the physical length of the grating pitch,

i.e. the periodicity, Λ , and the effective refractive index n_{eff} for the wave guided mode. These quantities in turn defines the Bragg resonance wavelength $\lambda_B = 2n_{\text{eff}}\Lambda$. Furthermore the pitch of the grating, physically being a length, changes with strain and temperature. Hence the strain and temperature will affect the wavelength of the reflected light. The linearity and the fact that the sensor is a real strain sensor rather than a differential displacement sensor and the integrating length can be made small makes the method very attractive. The difficulty, however, is to separate strain and temperature induced signals.

Sometimes the gratings are "chirped", i.e. the grating pitch varies over the grating length, $\Lambda=\Lambda(x)$. This has two major effects: The spectrum of the reflected light is broadened and the penetration depth of a light pulse will vary with strain and temperature. The latter effect is explained by considering the in-grating position of the particular pitch that will reflect the incident light. The match will occur at different in-grating positions under affected compared to non-affected conditions. Commonly a chirped grating is a grating with a monotonic chirp, i. e. the grating pitch increases or decreases from one end of the grating to the other. The grating can of course be adapted to some arbitrary variation as well. This concept extends the tailoring potential of the gratings even more, not least for sensing applications. A rather new concept of using the tailoring potential of the grating has been described by Kersey and Davis [5], where a chirped Bragg grating is utilised to mechanically enlarge the optical path imbalance of a fibre optic Michelson interferometer, when used in conjunction with a pulsed light source. This is accomplished since the centre of reflection in the Bragg grating for the well specified wavelength actually is shifted along the grating as it is strained. This effect can naturally be used twice in a Bragg grating Fabry-Pérot sensor as illustrated in figure 2.

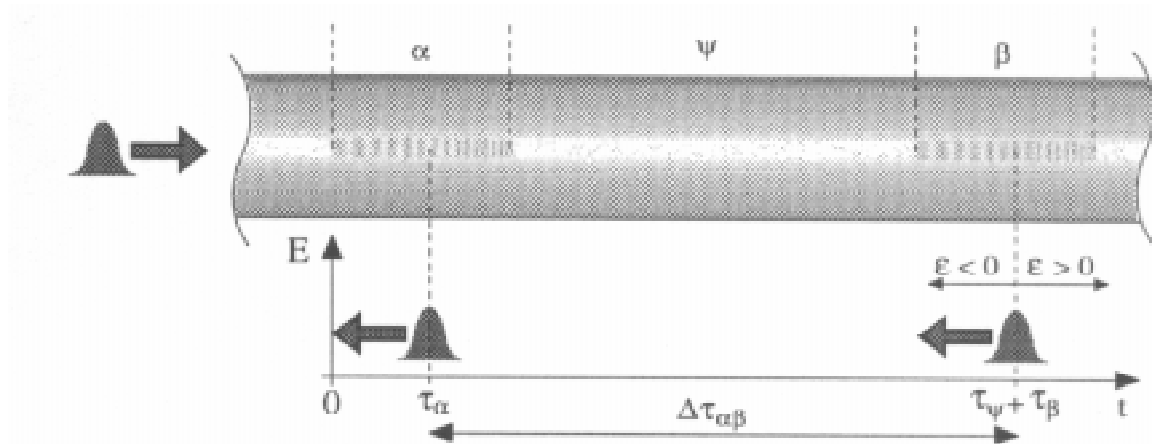


Figure 2. A Fabry-Pérot interferometer with chirped Bragg gratings as reflectors. The concept could be applied as well for signal enhancement as for signal compensation.

THE COMPENSATION

The CGI-Concept

The Chirped Grating Interferometer, CGI, concept is based on a fiber optic Fabry-Pérot interferometer with two chirped Bragg gratings as reflectors. This combination provides a powerful tool for the tailoring of fibre optic sensors. In the combined interferometer configuration of the CGI-sensor the optical path difference between the reflections is caused

by two effects. Primarily, the ordinary Fabry-Pérot interferometer type path difference; strain and temperature changes the physical distance between the reflectors but also the refractive index of the glass in between. Secondly, the penetration depth in either chirped grating changes with strain and temperature. Unless both gratings have exactly the same chirp function this will add or subtract an additional distance between the reflectors.

By utilizing the difference in penetration depth of the two chirped grating reflectors in an interferometer configuration the sensor response can be greatly altered or even cancelled. Differently put, the centre of the reflection in a chirped grating is effectively shifted along the grating as it is affected by the measurand and the amount of shift is controlled by the chirp function. Hence, it is possible to create a sensor with two different chirp functions and thereby controlling the path imbalance of the sensor. The sensor output can be tailored to range from negative signal response via cancellation to significantly enlarged. Figure 3 shows an attempt to graphically illustrate the sensor function.

The differential chirp function that will compensate for the input signal can hence be derived by equating the two contributions cavity and chirp induced change in optical path. This chirp function is referred to as differential since it concerns difference in shift of penetration depths. By subtracting half of this differential chirp function from a "basic" chirp function of the first grating and adding it to the "basic" chirp function of the second grating, the effective difference will be an exact match. The interested reader can find the full derivation in Henriksson et. al. [4]. The principle is illustrated in figure 3.

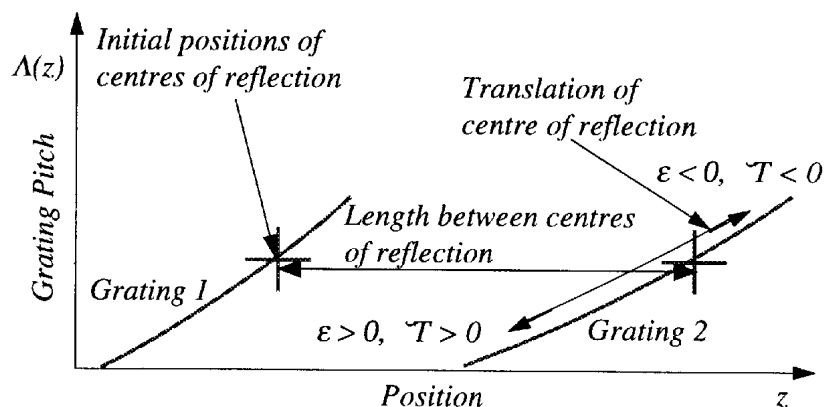


Figure 3. Diagram illustrating the compensation function of the CGI-sensor.

Variations in inherent optical fibre strain and temperature responsivity from plain fibre to grating would enable such a cancellation to be selective and provide a new discrimination approach for fibre optic Fabry-Pérot type sensors. Such variations could either be caused by the exposure to UV-light during the manufacturing process of fibre Bragg gratings or artificially created by using a different fibre in part of the sensor. If the chirp functions of the two gratings are properly matched to one another, the sensor geometry and its boundary conditions, the sensor can be designed to discriminate against either temperature or global strains. Some examples of applications are: strain-, temperature- and acoustic- sensors. The sensor has been given the acronym CGI-, sensor for Chirped Grating Interferometer- sensor. Eqs. (1) expresses the optical path in an optical fibre as a function of strain and temperature variation for plain fibre and fibre grating respectively. The correction factors of η_ϵ and η_T are introduced to handle possible changes in responsivity as a result of structural changes in

the grating. Factors n_i^0 and k_i^m are refractive index and the refractive index dependence to the measurand m for the different sections i of the sensor respectively.

$$\begin{cases} \Gamma_\psi(\varepsilon, \Delta T) \propto (n_\psi^0 + k_\psi^\varepsilon \varepsilon + k_\psi^T \Delta T)(1 + \varepsilon + k_\psi^\alpha \Delta T) \\ \Gamma_\gamma(\varepsilon, \Delta T) \propto (n_\gamma^0 + \eta_\varepsilon k_\psi^\varepsilon \varepsilon + \eta_T k_\psi^T \Delta T)(1 + \varepsilon + k_\gamma^\alpha \Delta T) \end{cases} \quad (1)$$

The discrimination condition is hence that eqs. (1) are linearly independent. If not, any compensation will cancel both global strain and temperature signals. The relevant discrimination is not however between the true strain and temperature but rather between load induced strains and temperature induced changes in the optical path length of the sensor.

Simulations of the Compensation Effects

Simulations were carried out according to a geometric grating model assuming continuous chirp and a strict geometrical reflection criterion. In these simulations the correction factors η_ε and η_T are assumed to be non-unity. These simulations illustrate the compensation effect for free sensors subjected to a matrix of load and temperature variation, figures 4 and 5.

ACOUSTIC SENSING ANALYSIS

Acoustic Sensing

This work is mainly focused on the acoustic respons of the chirped grating interferometer (CGI-sensor), Henriksson et al [6]. Even though the discrimination concept is a very interesting potential in itself a perhaps even more spectacular property of the sensor is the extreme sensitivity to acoustic waves and strain gradients. To optimize the sensor for acoustic waves the sensor length needs to match half the acoustic wave length so that the two gratings will experience strains of different signs. For e.g. acoustic emission the proper length can be rather short, only a few mm. In previous attempts to detect acoustic emission, AE, using EFPI- and FFPI-sensors one major problem has been to maintain the sensor at quadrature, Henriksson [1]. Choosing the compensated design as in this approach the sensor would mechanically maintain itself at quadrature over global strain and temperature variations. The sensor acoustic response, however, is mainly caused by the chirp induced change of the cavity length of the sensor. When the sensor length is adapted to the propagating acoustic wave mode of the AE such that the two reflectors of the sensor will experience strain amplitudes of different sign the chirp will effectively increase the response to the acoustic wave as compared to regular FPI-sensors, see figure 6.

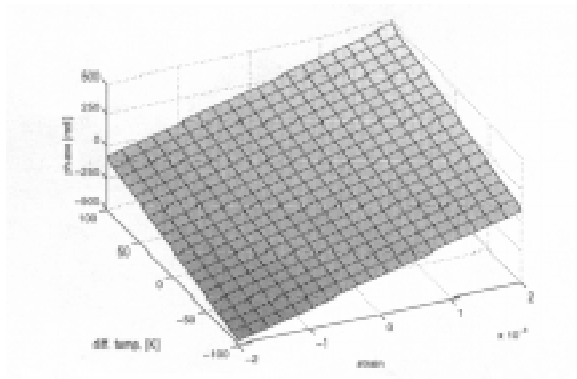


Figure 4. Simulated temperature and strain response for an ordinary FP-sensor with straight gratings as reflectors.

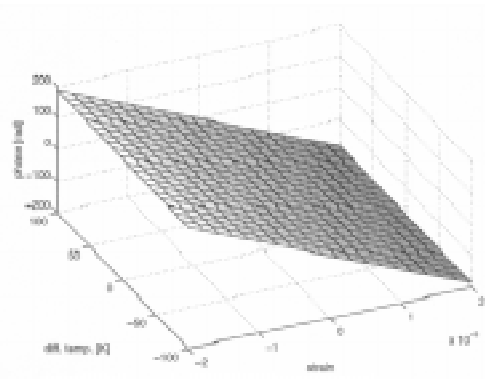


Figure 5. Simulated strain and temperature response for a temperature compensated FP-sensor with chirped grating reflectors.

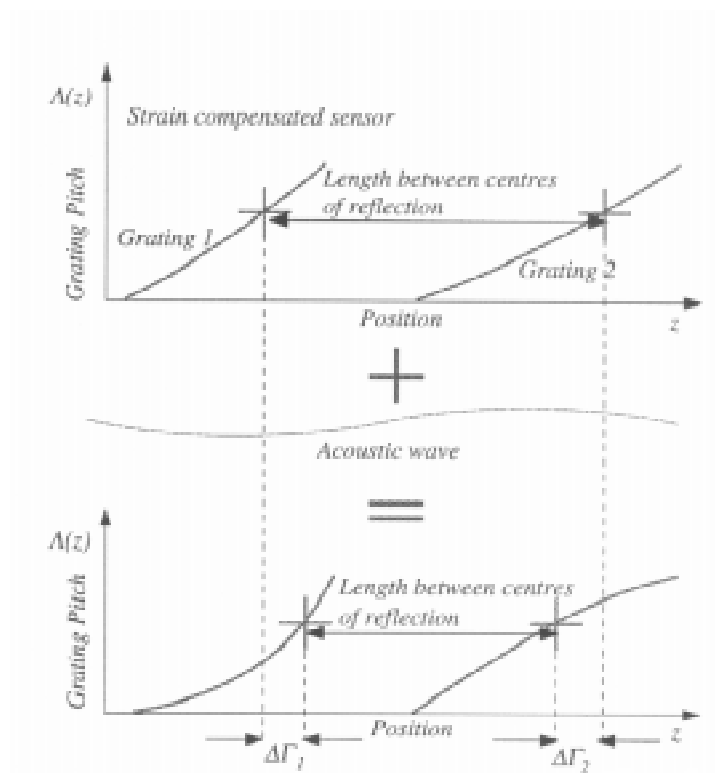


Figure 6. Diagram illustrating the large shift in penetration depth for a small amplitude acoustic wave.

The Chirp Limitations

Effectively the slope of the chirp function determines the dynamic range of the sensor. If the strain gradient of the acoustic wave is larger than the slope of the chirp function there can form double reflections within each grating that will disturb the interferometer output. Hence the limiting factor of the chirp function is that the slope should exceed the expected strain gradient of the largest acoustic wave. Apparently the resolution is opposed to the dynamic range but there is no definite theoretical limitation to the resolution.

Displacement Resolution Estimate

Approximating an AE with its dominating harmonic, e.g. a sinusoidal wave with the frequency 150 kHz, and applying a rather large AE-amplitude e.g. 1nm the dynamic range can be determined together with the minimum slope of the chirp function. The displacement of the wave is:

$$u = A \sin(\omega t + kz) \quad (1)$$

where A is the amplitude, ω is the circular frequency and k is the circular wave number. The first derivative of the displacement equals the strain wave:

$$\varepsilon = \frac{du}{dz} = kA \cos(\omega t + kz) \quad (2)$$

and the second is the strain gradient:

$$\frac{d\varepsilon}{dz} = -k^2 A \sin(\omega t + kz) \quad (3)$$

Hence the slope of the chirp function K should be:

$$K \geq \left| \frac{d\varepsilon}{dz} \right|_{max} = k^2 A \quad (4)$$

Strain effects on the refractive index are in this context less than the order 10^{-6} and can be neglected. Inserting values for the wave number and the amplitude, e.g. $k=\pi/3\text{mm}$, $A=1\text{nm}$, yields a chirp function slope of about $1.1 \cdot 10^{-3}$. A very moderate interferometer performance even for high a bandwidth is a fringe SNR of about 100. Used with an optical wavelength of 1550nm the resolution for length changes in the cavity is about 1.64nm. Splitting this number for the two gratings each grating apparently has to shift its penetration depth 0.82nm for detection when the sensor is at quadrature. With the penetration depth shifted 0.82nm and the strain field applied the Bragg resonance criteria should be fulfilled just as with Λ_0 :

$$\Lambda_0 = \Lambda_0 (1 + Kz)(1 + \varepsilon) \left(1 - \eta_\varepsilon \frac{n_0^2}{2} [P_{12} - \nu(P_{11} + P_{12})] \varepsilon \right) \quad (5)$$

Keeping just the first order terms in ε and Kz the equation is easily solved:

$$\varepsilon \approx - \frac{Kz}{\left(1 - \eta_\varepsilon \frac{n_0^2}{2} [P_{12} - \nu(P_{11} + P_{12})] \right)} \approx -1.32Kz = -1.19 \cdot 10^{-12} \quad (6)$$

The strain that would generate a shift of detectable magnitude is no larger than $1.2 \cdot 10^{-12}$. When the acoustic wave of that strain amplitude is integrated once the resulting displacement amplitude is as small as $1.1 \cdot 10^{-15}$! This level of sensitivity is for the proper acoustic wavelength match only. Obviously, the sensor will be sensing strain gradients in the material and not the displacements. In this respect much like the PZT-transducers commonly used to detect AE that sense accelerations. However, unlike the more or less resonant PZT-

transducers, the only bandwidth limiting factor is the sensor length. Hence the CGIA-sensor signal can be integrated twice into the true displacement amplitude. For other wavelengths the amplitude would naturally have to be larger to be detected.

Acoustic Sensor Conditions

For the acoustic sensing there are no discrimination requirements. The difference would merely be whether or not the sensor would detect temperature variations. Any such response would easily be filtered out, however, and the sensor function would be similar. The difficulties regarding the acoustic sensor are of a rather practical nature. If the target is AE the sensor would have to be rather short to span no more than half an acoustic wavelength. This imposes problems to the realization of the sensor since the applicability of the penetration depth function of Ouelette [7] for chirped gratings of such short lengths is questionable. Possibly somewhat longer gratings allowing for some overlap between the two gratings would be an option. Still, some response is expected even for short gratings and sensors.

Simulations of Acoustic Response

In the simulation the sensor models are subjected to a sinusoidal displacement wave with both time and position dependence. The simulated responses are illustrated in figures 7 and 8 for a sensor with straight and chirped gratings respectively. The slope of the chirp function in this case is 0.24 m^{-1} , i. e. much steeper than optimized, and the acoustic wavelength is 30 mm. Theoretically the increase in sensitivity for this particular combination is 661 times. The sensor would of course be sensing strain gradients in the material and not the actual displacement. It is an exact analogy with the acceleration detecting PZT-transducers commonly used to detect AE but with respect to position rather than time. This is actually what provides the sensitivity of these two methods; they will both detect second order derivatives of the displacement. For non-dispersive wave propagation these signals would, in principal, be identical.

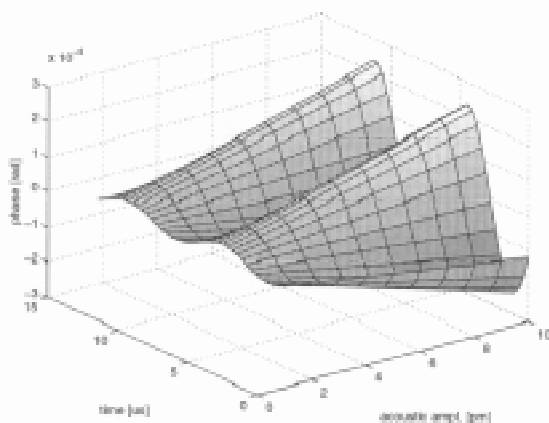


Figure 7. The phase response of a sensor with straight regular gratings to an acoustic wave.

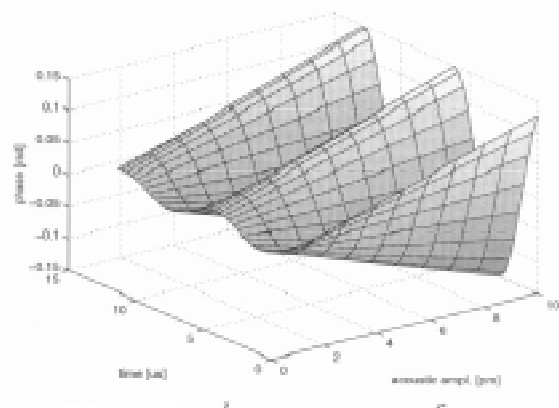


Figure 8. The phase response of a sensor with chirped gratings to an acoustic wave.

Experiments

Experimental determination of the dose dependent correction factors for strain and temperature dependence of the refractive index within the grating was carried out for boron co-doped fibre. Fibre optic gratings of different reflectivities were examined to determine the dose influence of the refractive index strain and temperature dependencies. Two different gratings of identical period and length but of significantly different UV-dose were subjected to temperature and load variations separately. The shift of the Bragg wavelength in response to the variations was taken as an indication of the dose dependencies.

The results showed no significant discrepancy. For boron co-doped hydrogen sensitised fibres no deviations could be detected. Hence, for such fibre, artificial variation of temperature dependence over the sensor is required to achieve discrimination. Though this is not a success for the discrimination concept it is indeed still interesting for the acoustic sensing concept. Effectively the compensated sensor would remain stable for both temperature and strain variations while very sensitive to acoustic waves. Evaluations are underway to see if fibre gratings formed with other physical mechanisms will perform differently.

The planned evaluation of the CGI-prototypes will involve composite DCB specimens with embedded fibre optic sensors. The fibre optic sensor response to the AE generated by the central mode I delamination will be registered parallel to the signals of conventional PZT-transducers. The relative waveforms and frequency contents from either sensor will be demonstrated together with the PZT-recordings for the same waves.

CONCLUSIONS

To accurately determine the correct chirp function of the sensor gratings each individual fibre would have to be evaluated with respect to photo elastic constants, thermal expansion coefficient and temperature dependence of the refractive index. Equally important is to consider the boundary conditions of the sensing environment. The compensation of an embedded sensor requires other chirps than compensation of a free sensor. The CGI-sensors acoustic sensitivity is not dependent on the discrimination between temperature and strain. In fact, the sensor would be even more stable if both the strain and temperature responses were removed. Then the sensor would inevitably be operational with a stable detectability by keeping the at quadrature.

A couple of comparisons are of interest:

Compared to the best results by previous fiber optic AE-systems obtained by Henriksson, [1], using the same detection scheme and circuitry the CGI-sensor concept offers a theoretical improvement in the order of 10^6 times regarding displacement resolution for AE. If these theoretical figures are experimentally verified they will indeed signify a breakthrough.

Even compared to the performance of conventional PZT AE-transducers the performance is good. So far the PZT-transducers have been outstanding in their very reliable and extremely sensitive operation. The PZT-transducer is actually an accelerometer for high bandwidths and as such it responds to force across the crystal or acceleration. The integrations to displacement resolution is of course bandwidth dependent and not exactly straight forward. Still, Pollack,

[8], claims an impressive PZT resolution of no more than $25 \cdot 10^{-12} \text{m}$. Even resolutions in the order of 10^{-14}m have been claimed, Brüel&Kjaer [9]. In comparison to these values the estimated $1.1 \cdot 10^{-15} \text{m}$ resolution of the CGI-sensor is very encouraging.

The CGI-sensor acoustic sensitivity is not dependant on the compensation. The sensor can indeed be operated with any chirp functions with varying sensitivity. The compensation does however enable a stable detectability by keeping the sensor at quadrature. It was shown in this study that optical fibers that would not discriminate between strain and temperature in the CGI-configuration are commonly available. Hence the compensation for global variations includes both of these measurands. If preferred the acoustic sensing could of course be combined with simultaneous temperature readings if the discrimination is enabled by an appropriate choice of fibre. Shifts due to temperature variations are easily dealt with. Mainly due to the difference in dynamic range.

For a complete aircraft health monitoring system, where strain, temperature and AE is acquired a combination of CGI-sensors appears to be very interesting. Generally in fiber optic sensing the discrimination between strain and temperature is the problem. With this approach however, the discrimination issue can be between AE and temperature variations. This task is considerably much easier since the dynamic range of the two measurands are so different, in the order of 1 Hz for temperature and 100 kHz for AE, and could easily be solved by simple filtering. A system including CGIS-sensors for strain detection and CGIT-sensors for temperature and AE detection holds a high potential to fulfil the needs of a health monitoring system .

The manufacturing of a chirped grating of the required accuracy is obviously very difficult. The compensating chirp functions are close to linear and if the manufacturing process would benefit from this it could of course be approximated as such. However, at IOF, the Institute of optical research in Stockholm, a technique to accomplish extremely accurate and repetitive chirped gratings of an arbitrary chirp function has been developed. Using this technique very long and superstructured gratings are composed by writing a set of consecutive sub gratings with interferometric control of the relative positions between sub gratings, R. Stubbe et. al. [10]. For chirped gratings, the chirp function is basically formed by imprinting the sub gratings with its own specific phase shift as compared to the former prints. In this manor very long gratings with a very accurate chirp function has successfully been manufactured. Attempts to realize the various CGI-sensors are currently underway.

ACKNOWLEDGEMENTS

Many thanks are expressed to Raoul Stubbe and Bengt Sahlgren at the Institute for Optical Research and Klas Levin at FFA for instructive discussions on Bragg grating performance. The reported work is a part of a joint project on Smart Composite Structures sponsored by FMV, the Defence Materiel Administration, Sweden. The participating organisations are FFA-The Aeronautical Research Institute of Sweden and IOF-The Institute for Optical Research, Sweden. The project is technically directed and co-ordinated by Klas Levin, FFA.

REFERENCES

1. A. Henriksson: "Evaluation and Development of Fiber Optic Sensors and Systems with respect to Acoustic Emission", FFA TN 1994-37, Stockholm, Sweden, 1994.
2. A. Henriksson: "A Temperature Invariant Fiber Optic Bragg Grating Fabry-Pérot Interferometer", FFA TN 1996-02, Stockholm, Sweden, 1996.
3. A. Henriksson, S. Sandgren and A. Asseh: "Temperature insensitivity of a fiber optic Bragg grating sensor", to appear in Proceedings "Fiber Optic and Laser Sensors XIV", SPIE Vol. 2803, Denver, 4-9 Aug. 1996.
4. A. Henriksson: "The Optimized Detection of Acoustic Emission Generated Lamb Waves using embedded Fiber Optic Fabry-Pérot Sensors", FFA TN 1996-32, Stockholm, Sweden, 1996.
5. A. D. Kersey and M. A. Davis: "Interferometric Fiber Sensor with a Chirped Bragg Grating Sensing Element", Proc. 10th Optical Fibre Sensors Conference, Glasgow, Scotland, UK, 11th - 13th October 1994.
6. A. Henriksson, S. Sandgren and A. Asseh: "Versatile Sensor Concept for Chirped Fibre Bragg Gratings", submitted to Smart Materials and Structures, Sept. 1996.
7. F. Ouellette: "Dispersion cancellation using linearly chirped Bragg grating filters in optical waveguides", Optics Letters, Vol. 12, No. 10, pp. 847-849, Oct. (1987).
8. A. A. Pollock (1989) "Acoustic Emission Inspection", Metals Handbook, 9th edition, Vol. 17, ASM International, 278-294.
9. Brüel&Kjaer, Manual for AE counter system, p 15, section 4.2.1 Units of sensitivity.
10. R. Stubbe, B. Sahlgren, S. Sandgren and A. Asseh: "Novel technique for writing long superstructured fiber Bragg gratings", "Photosensitivity and Quadratic Nonlinearity in Glass Waveguides, Fundamentals and Applications" Vol. 22, "Post Deadline" PD1-1, Sept. 9-11 (1995) Portland/Oregon, , USA.

CREEP STUDY OF FRP COMPOSITE REBARS FOR CONCRETE

Piyush K. Dutta¹ and David Hui²

¹*U.S. Army Cold Regions Research and Engineering Laboratory,
72 Lyme Road, Hanover, New Hampshire 03755-1290, USA*

²*Department of Mechanical Engineering, University of New Orleans,
New Orleans, Louisiana 70148, USA*

SUMMARY: Fiber-reinforced plastic (FRP) rebars, long rods produced by the “pultrusion” process and containing by volume about 55% E-glass fiber and about 45% thermoset resin, have been successfully applied as concrete reinforcement in many construction applications. However, creep, fatigue, and corrosion from alkaline environment of concrete are areas of concern for any large-scale application. In this investigation the creep study was limited to determine whether the commercially available FRP rebars would creep under a sustained tensile load over a wide range of temperatures: low temperature (−23°C, −10°F), room temperature (21°C, 70°F), and high temperature (49°C, 120°F). Because these rebars have fibers generally oriented in the longitudinal direction 12.70, 15.88 and 19.05 mm (1/2, 5/8, and 3/4 in.), the load would be carried primarily by the fibers. Six FRP rebars in nominal diameters with a spirally wrapped glass fiber strand were instrumented with strain gages to measure both the longitudinal and diametral strains under dead weight loads adjusted to tension each of these rebars to about 50 percent of its yield stress. In order to monitor temperatures, a thermocouple was attached to each rebar. For the room temperature tests, strain was measured for 1800 hours (75 days) and over this period the strain did not show any trend to continue to increase. The low temperature tests was continued for 3,552 hours and again no discernible trend of increasing strain was observed. The high temperature test was performed for 3,792 hours (158 days). From the creep data in which a very small trend of increasing strain could be observed, the values of creep parameters m and n were determined as $m = 9.45$, and $n = 0.297$. These values closely match with published values for commercially available pultruded FRP WF beams.

KEYWORDS: creep, composites, low temperature, FRP, polymer composites, sustained load, viscoelastic materials

INTRODUCTION

In recent times, FRP reinforcing bars are receiving increasing attention as the tension element in reinforced concrete [1]. This is primarily because corrosion of steel reinforcement in concrete by chloride ions has been determined to be the major cause of premature deterioration of concrete structures [2]. As available in market, these rebars, as long rods, are made of very fine continuous glass fiber strands which are bound together with a thermosetting polymer. Wu et al. [3] have reported that E-glass reinforced composite rods, from which these rebars are made, may have tensile strength in excess of 689 MPa (10^5 psi) and longitudinal elastic modulus about 51.7 GPa (7.5×10^6 psi). In tensile tests the bars fail without any significant yield (brittle failure).

Table 1. Comparison of mechanical properties of steel and FRP rebars [4].

Properties	Steel rebar	FRP rebar
Specific gravity	7.9	1.5– 2.0
Tensile strength MPa (psi × 10 ³)	483–690 (70–100)	517–1207 (75–175)
Yield strength MPa (psi × 10 ³)	276–414 (40–60)	—
Compressive strength MPa (psi × 10 ³)	276–414 (40–60)	310–482 (45–70)
Tensile modulus, GPa (psi × 10 ⁶)	200 (29)	41–55 (5.9–8.0)
Coeff. thermal expansion 10 ⁻⁶ /°C (°F)	11.7 (6.5)	9.9 (5.5)

The rods are produced by pultrusion process. Since glass is commonly used as the reinforcing fibers in these rebars, these rebars are also designated as GFRP (G stands for glass). Currently there are several FRP rebar companies actively marketing their products in the USA. Most FRP rebars contain by volume about 55 percent E-glass fiber and about 45 percent thermoset resin. The sizes (diameter) of the rebars follow the size designations of the steel rebars (e.g., #3, #4, or #7 rebars). Faza [4] has reported a number of successful applications of rebars in the USA, including applications in sea walls, hospital magnetic resonance imagers (MRIs), reactor pads, compass calibration pads, mill roofs, laser test facilities, highway barriers, residential foundations, and bridge decks. Table 1 gives a comparison of mechanical properties of the steel rebars and the FRP rebars.

The light weight, corrosion resistant and nonmagnetic properties make the FRP rebars an improved alternative to steel. One of the most critical problems to be overcome in large-scale applications of the FRP rebars is developing improved bond strength with concrete. Some available designs provide a helically convex surface made with a strand spirally wound and cured on the surface. Other designs suggest use of sand or grit coating on the rebars. A recent design includes a pultruded ribbed surface. A comparative survey of the bond quality of these surface modifications is still not available. Bond strength of composite rebars and the bending response for carrying concrete stresses had been investigated by many including GangaRao and Faza [5], Pleimann [6], Daniali [7], Larralde and Siva [8], Iyer and Anigol [9], Tao et al. [10], Challal and Benmokrane [11], Challal and Benmokrane [12], and Malavar [13].

There are several major barriers to FRP rebar applications. These include lack of sufficient data on durability or performance under extreme environments [14, 15). Creep, fatigue, and corrosion from the alkaline environment of concrete are the areas of concern for any large-scale application of FRP rebars. Unlike steel the FRP rebar is viewed as a viscoelastic material, and, as such, many of its properties are suspected to be time dependent. Creep refers to the slow deformation with time under a constant stress which is less than the yield stress. When a constant load is applied (except for a short initial duration when the strain may increase quite rapidly) to a viscoelastic material, the strain increases steadily. This increase of strain is the creep. If the creep increases beyond a certain limit, the effective stress owing to decrease in cross-section area increases. The increased stress results in further deformation, which in turn increases the stress even more. Thus, the deformation suddenly accelerates, leading to the failure of the material.

At the microstructural level the creep occurs due to the presence of mobile defects, such as dislocations that move (enlarge) primarily at increased stress and temperatures. Thus the general mathematical formulation of creep rate takes the form

$$d\epsilon/dt = F(\sigma, T) \tag{1}$$

where ϵ is the strain, t is time variable, and $F(\sigma, T)$ is the function of the stress σ , and temperature T .

In the case of composites, F is a function of the stresses produced in all the components, since the net creep resistance will depend on the creep resistance of all the components. If the two components of the composites have two different creep resistance, the creep of the low resistance component will be checked by the high resistance material owing to adhesion between them. Thus, with higher bond strength between the components a creep resistance even greater than that of its components should result.

Creep in polymeric composites has been the subject of investigation for a long time [16, 17]. Tunik and Tomashevskii [18] discussed creep and long time strength of glass FRP in interlaminar shear. Weidmann and Ogorkiewicz [19] studied tensile creep of a unidirectional glass fiber epoxy laminate. Creep strength of discontinuous fiber composite has also been studied by Bocker-Pedersen [20]. The power law approach to modeling the creep behavior of plastics and FRP is primarily due to the original work by Findley [21] which he again updated in 1987 [22]. Numerous other projects have also been reported in composites literature about creep behavior of FRP in general. These include the work by Holmes and Rahman [23] on creep in FRP beams. Brinson et al. [24], Hiel and Brinson [25], and Dillard and Brinson [26] used numerical methods of predicting creep and delayed failures. Transverse creep and tensile behavior of composite laminates were studied by Eggleston [27], whereas Huang and Gibson [28] performed both theoretical and experimental studies on sandwich beams with linear viscoelastic cores. Creep behavior of Kevlar/epoxy composites was studied by Beckwith [29], who concluded that the creep behavior in the laminate composites is primarily “fiber-dominated,” and independent of resin modulus. Krishnaswamy et al. [30] presented the results of a finite element model of ductile behavior of polymers. The creep effects in composite columns were studied by Chen and Lottman [31], Ueng [32], and Vinogradov [32]. Slattery [34] developed the procedure for predicting the accelerated failure rate by extrapolating short-term data and by taking into consideration the progression of fundamental damage mechanism. Recently, Mossalam and Bank [35], and Mossalam and Chambers [36] presented a simplified and efficient design procedure to predict deflection of pultruded composites under sustained load and a laboratory procedure for determining the creep coefficients. Thus, while a large volume of information is available on the creep characteristics of the FRP materials in general, the specific information on whether the FRP rebars would creep or not under sustained loading is very scant.

In this investigation the scope of the creep study was limited to determine whether the commercially available FRP rebars would creep under a sustained tensile load over a wide range of temperatures: low temperature (-23°C , -10°F), room temperature (21°C , 70°F), and high temperature (49°C , 120°F). Because these rebars have fibers generally oriented in the longitudinal direction, the load would be carried primarily by the fibers.

TEST DESCRIPTION

Commercially available fiberglass composite rebars (Fig. 1) made with 5- to 10-micron E-glass fibers in a polyester resin matrix were selected for this creep study. The mechanical characteristics of these bars as provided by the manufacturer is given in Table 2.

To conduct the creep tests, the deadweight creep test fixture shown in Fig. 2 was designed and fabricated. The gripping mechanism is shown in Fig. 3. The fixture provides a mechanical advantage of approximately 50 to 1. Six of these creep-test fixtures were mounted on a common base frame (Fig. 4).



Fig. 1: Examples of commercially available glass fiber reinforced composite rebars.

Initially six fiberglass composite rebars made by a vendor were selected for the tests. The rebars were obtained in 12.70, 15.88, and 19.05 mm (1/2, 5/8, and 3/4 in.) nominal diameters with a spirally wrapped glass fiber strand, wound approximately 19.05 mm (3/4 in.) in pitch. The entire rod was redipped in the resin and then cured to obtain an irregular wavy but drip surface to promote adhesion to the concrete. For fixing on the test jigs the 19.05-mm (3/4-in.) diameter rebar specimen proved to be the most difficult one to be gripped and was finally rejected from the test batch. Only 12.70-mm and 15.88-mm (1/2-in and 5/8-in.) diameter bars were finally tested.

Each composite rebar was instrumented with electrical foil strain gages to measure both the longitudinal and diametrical strains (Fig. 5). Only longitudinal strains were of interest in this creep study. The gages were centrally located along the length of each specimen and diametrically opposite to each other. Each longitudinal gage was axially aligned with the fiber direction and positioned so as not to interfere with the spiral wrapping of the rebar. They had an effective length of 1.58 mm (0.062 in.), 350-ohm resistance, and were temperature compensated for steel. The gages were bonded to the rebar surface according to the manufacturer's recommended procedure. To avoid modifying the rebar specimen resin, as per the gage manufacturer's instructions, the gages were cured overnight at room temperature. No elevated temperature curing was attempted. For measuring strain, each gage was put in full bridge configuration and initially balanced in a switching and balancing unit. All subsequent readings were referenced to this initial balance.

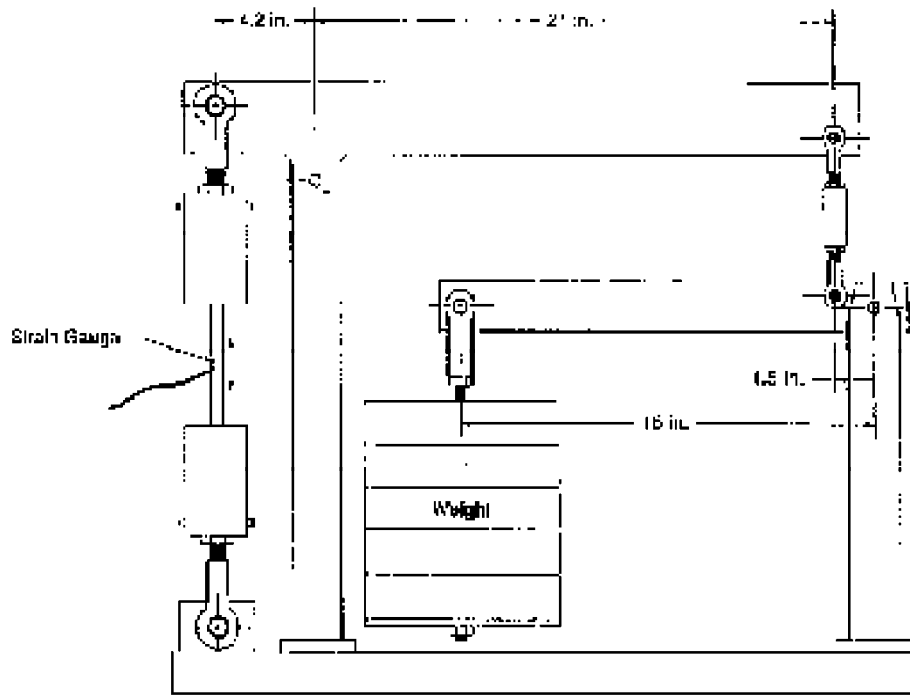


Fig. 2: Deadweight creep test fixture.

Table 2. Mechanical characteristics of composite rebars.

Density	1.85 g/cm ³ (0.067 lb/in. ³)
Ultimate tensile strength	117.9 MPa (17,098 psi)
Tensile modulus	54.206 GPa (7.86 × 10 ⁶ psi)
Coefficient of therm. exp.	9.9 × 10 ⁻⁶ mm/mm/°C (5.5 × 10 ⁻⁶ in./in./°F)
Matrix	Derakane 411-45 polyester resin
Fiber	E-glass
Spiral fiber pitch	0.75 in. (190.5 mm)

The deadweights were adjusted to tension of each of these rebars to about 50 percent of its ultimate strength, as specified by manufacturer of the rebars. In order to monitor temperatures, a thermocouple was attached to each rebar. Once the tension for the rebar was fixed, the apparatus was not disturbed. For the room temperature tests, temperature and strain readings were taken once a day for 1800 hours (75 days). The strain data are shown in Fig. 6a and b for the 12.70 mm (1/2 in.) and 15.88 mm (5/8 in.) bar, respectively. If any creep occurred, then the strain readings would be expected to continue to increase. However, the results show that over this period the strain did not indicate any trend to increase. The temperature variation of the room in which the test fixture was placed caused the daily variation of the strain as seen by the zigzag lines of the record, but the general trend did not reveal development of any creep under the test conditions.

If no creep could be detected at room temperature, then we should not expect any creep to occur at low temperature (-23°C, -10°F). However, creep might result if the low temperature induces any microcracking or degradation of the interface bond by the induced thermal

stresses from the thermal expansion coefficient mismatch between fibers and matrix. A relatively longer period of test was necessary to develop these effects. Accordingly the dead weight test fixture was placed in a refrigerated coldroom where the temperature was constantly maintained at approximately -10°C (-23°F). This test was continued for 3,552 hours (148 days). The strain records of the 12.70-mm (1/2-in.) and 15.88-mm (5/8-in.) rebars are shown in Fig. 7a and b. Again no discernible trend of increasing strain was observed.

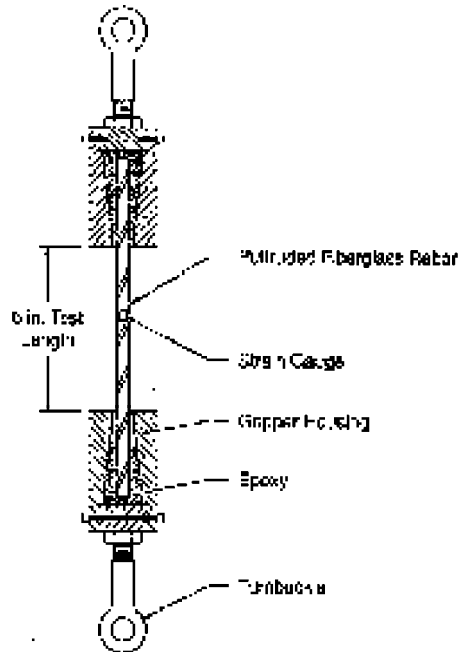


Fig. 3: Details of the gripping mechanism of the creep test fixture

For high temperature (120°F , 49°C) creep test a special environment chamber of $1.22 \times 1.22 \times 2.44$ m ($4 \times 4 \times 8$ ft) was built with a thermostatically controlled hot air blowing system that would control the temperature of the chamber between 50°C (122°F) and 47.2°C (117°F). At the end of the coldroom test, the strain gages on the 15.88 mm (5/8 in.) rebars were damaged and the bars were unsuitable for further testing. Accordingly only two 12.70 mm (1/2 in.) diameter rebars were tested in the high temperature chamber. Each of these specimens were instrumented with a thermocouple sensor, and a third thermocouple measured the air temperature of the chamber near the specimens. These specimens were subjected to again for a long period of test, from 25 April to 30 September, a total of 3,792 hours (158 days). The strain readings taken approximately once a week were remarkably steady over this period. The numerical data recorded for this test are shown in table 16. Fig. 8a and b gives the plotted data.

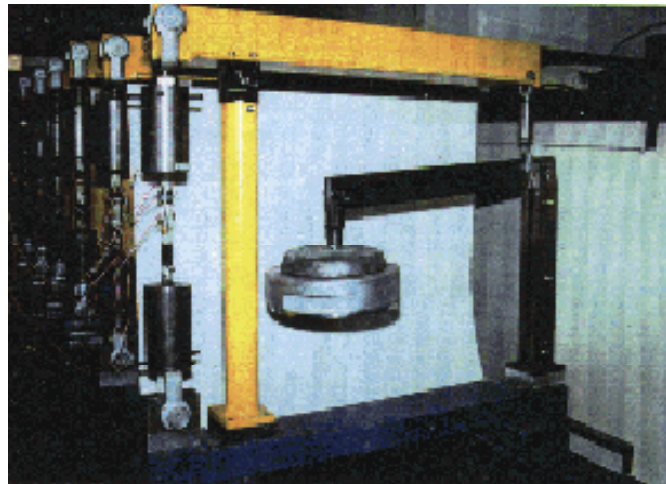


Fig. 4: Creep test platform with six creep test fixtures.



Fig. 5: Strain gage instrumentation on the test specimens. Test specimens shown removed from the test fixture after the test is over.

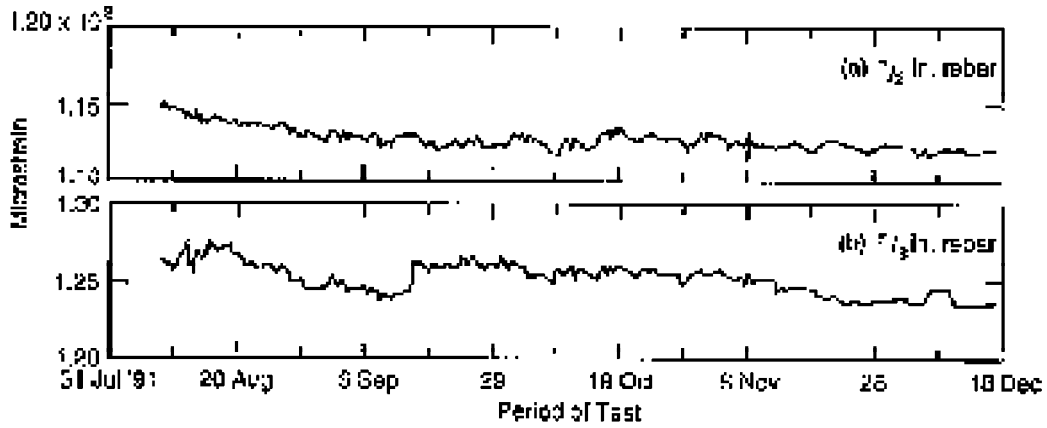


Fig. 6: Records of room temperature creep strain at (a) 12.70 mm (1/2 in.) diameter rebar, and (b) 15.88 mm (5/8 in.) diameter rebar.

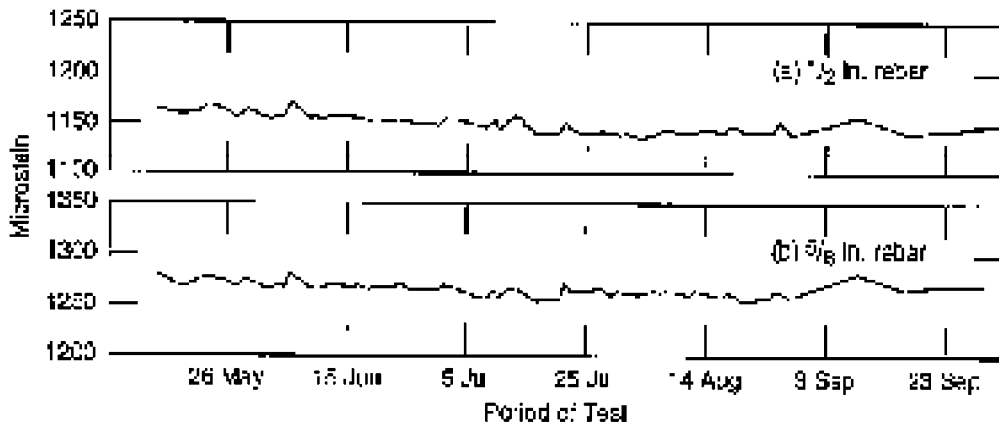


Fig. 7: Records of low temperature (-10 °F, -23 °C) creep strain at (a) 12.70 (1/2 in.) diameter rebar, and (b) 15.88 mm (5/8 in.) diameter rebar.

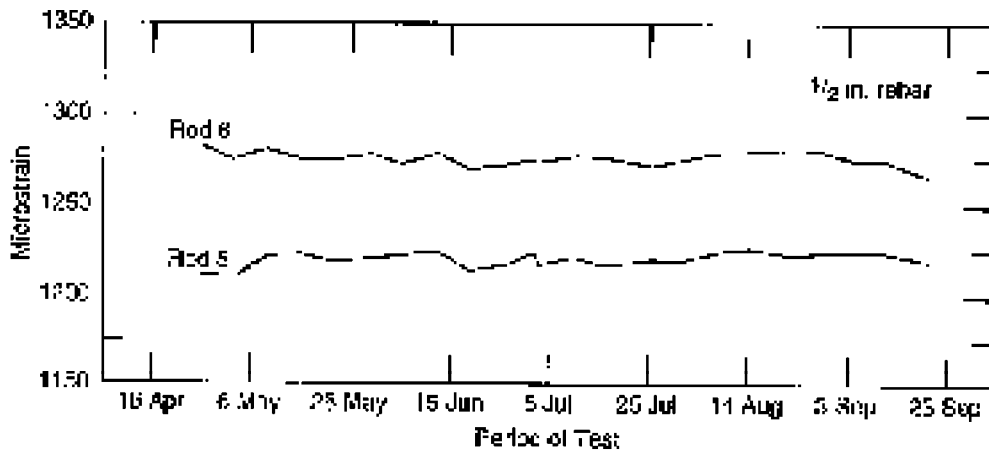


Fig. 8: Records of high temperature (49 °C, 120 °F) creep strain at (a) 12.70 mm (1/2 in.) diameter rebar, and (b) 15.88 mm (5/8 in.) diameter rebar.

ANALYSIS AND DISCUSSION

Findley's general theory [21] of creep behavior of viscoelastic polymer is represented by

$$\varepsilon = \varepsilon_0 + p (t/t_0)^q \quad (2)$$

where ε = the total strain

ε_0 = stress dependent strain

p = the coefficient of time dependent term, which is dependent on stress level

t = duration of loading (hours)

t_0 = unit time (hour)

q = a material constant, independent of stress.

Parameters p , and q are known as creep parameters. To obtain the particular values of p and q Eqn 2 can be rearranged and written in the form:

$$\log (\varepsilon - \varepsilon_0) = \log (p) + q \log (t/t_0) \quad (3)$$

Table 3. FRP rebar creep test data at 49°C (120°F).

Date	Chamber temp (°F)	Microstrain* in rebar no.5	Microstrain* in rebar no. 6
04/25/94	120	1209	1281
05/02/94	120	1209	1273
05/09/94	119	1220	1279
05/16/94	119	1221	1274
05/23/94	120	1216	1273
06/01/94	120	1218	1276
06/07/94	120	1220	1270
06/15/94	119	1222	1276
06/22/94	121	1211	1268
07/01/94	119	1215	1269
07/05/94	121	1220	1272
07/06/94	122	1220	1272
07/07/94	121	1215	1272
07/15/94	121	1218	1275
07/21/94	118	1213	1273
08/01/94	119	1217	1268
08/08/94	118	1216	1272
08/15/94	121	1221	1276
08/22/94	121	1223	1277
09/01/94	122	1219	1276
09/07/94	122	1221	1276
09/15/94	120	1221	1271
09/20/94	121	1221	1271
09/30/94	118	1216	1262

*microstrain = strain $\times 10^{-6}$

Equation 3 represents a straight line of slope n and intercept m at unit time if $\log(\epsilon - \epsilon_0)$ is plotted against $\log(t/t_0)$. Using the creep data of Table 3, in which a very small trend of increasing strain could be observed, the values of m and n were determined as $p = 9.45$, and $q = 0.297$. These values closely match Mosallam and Chamber's [36] published values for commercially available pultruded FRP WF beams: $p = 9.72$, and $q = 0.298$. Findley's equation, when plotted over the Table 3 data points as shown in Fig. 9, but the match is not very clear because of the scatter in the data. If the tests were continued over a longer time, a more discernible creep strain might have developed. The data at room temperature and low temperature had not shown any trend of increasing; therefore they were not analyzed with Findley's equation. It must be noted that Findley's theory applies very well to viscoelastic polymers, but in FRC composites rebars, when the stress is applied in the fiber direction, the behavior is not totally viscoelastic. In fact, with higher volume fraction of glass fibers oriented in loading direction creep in FRP composites is not expected to be a problem.

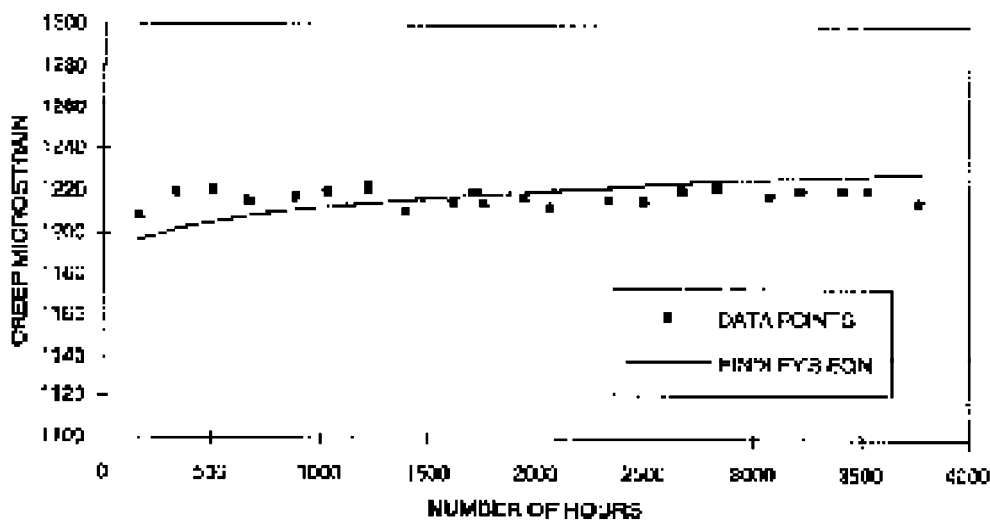


Fig. 9: Comparison of high temperature creep data with Findley's equation.

REFERENCES

1. Roll, R.D. (1991). Use of GFRP Rebar in Concrete Structures. *Advanced Composites Materials in Civil Engineering Structures*, S.L. Iyer, and R. Sen (Ed.), ASCE, pp. 93-98.
2. American Concrete Institute (ACI) Committee 208 (1958). Test Procedure to Determine Relative Bond Value of Reinforcing Bars, *ACI Journal*, Vol. 5, pp. 1-16.
3. Wu, W.P., GangaRao, H., and Prucz, J.C. (1990). Mechanical Properties of Fiber Reinforced Plastic Bars. Internal Report, Constructed Facilities Center, College of Engineering, West Virginia University
4. Faza, S.S. (1995). Properties of FRP Reinforcing Bars. *Fiber Reinforced Plastics Workshop*, Office of Technology Applications, FHWA, Washington DC.
5. GangaRao, H. and Faza, S.S. (1992). Bending and Bond Behavior and Design of Concrete Beams Reinforced with Fiber-Reinforced Plastic Rebars. Report on Phase I of West Virginia Department of Highways Project No. RP 83, 1992.

6. Pleimann, L.G. (1991). Strength, Modulus of Elasticity, and Bond of Deformed FRP Rods. Proc. of the Conference on Advanced Composite Materials in Civil Engineering Structures, ASCE, Las Vegas, NV, pp. 99–110.
7. Daniali, S. (1992). Development Length of Fiber Reinforced Plastic Bars. Advanced Composite Materials in Bridges and Structures, First International Conference, Sherbrooke, Quebec, Canada, pp. 179–188.
8. Larralde, J., and Siva, R. (1990). Bond Stress-Slip Relationships of FRP Rebars in Concrete, Serviceability and Durability in Construction Materials. Proc. of the First Materials Engineering Congress, Denver, CO, Aug. 1990, pp. 1134–1141.
9. Iyer, S. and Anigol, M. (1991). Testing and Evaluating Fiberglass, Graphite, and Steel Prestressing Cables for Pretensioned Beams. Proceedings of the Conference on Advanced Composite Materials in Civil Engineering Structures, ASCE, Las Vegas, NV, pp. 44–56.
10. Tao, S., Eshani, M.R., and Sadatmanesh, H. (1992). Bond Strength of Straight GFRP Rebars, Materials Performance and Prevention of Deficiencies and Failures. Proc. of the Materials Engineering Congress, ASCE, Atlanta, GA, pp. 598–605.
11. Challal, O., and Benmokrane, B. (1992). Glass-fiber Reinforcing Rod: Characterization and Application to Concrete Structures and Grouted Anchors, Materials Performance and Prevention of Deficiencies and Failures. Proc. of the Materials Engineering Congress, ASCE, Atlanta, GA, pp. 606–617.
12. Challal, O., and Benmokrane, B. (1993). Pullout and Bond of Glass-Fiber Rods Embedded in Concrete and Cement Grout. Materials and Structures, Vol. 26, pp. 167–175.
13. Malavar, L.J., (1994). Bond Stress-slip Characteristics of FRP Rebars. Technical Report TR-2013-SHR, Naval Facilities Engineering Service Center, Port Hueneme, CA.
14. Dutta, P.K. (1995). Durability of FRP Composites in Extreme Environment. Proc. of the Fifth International Offshore and Polar Engineering Conference, The Hague, The Netherlands, June 11–16, pp. 271–276.
15. GangaRao, H. (1995). McKinleyville Jointless Bridge with FRP Bars in Concrete Deck. Fiber Reinforced Plastics Workshop, Office of Technology Applications, FHWA, Washington DC.
16. Glaster, R.E., Moore, R.L., and Chiao, T.T. (1983). Life Estimation of an S Glass/Epoxy Composite under Sustained Tensile Loading. Composites Technology Review, Vol. 5, No. 21.
17. Glaster, R.E., Moore, R.L., and Chiao, T.T. (1984). Life Estimation of an S Glass/Epoxy Composite under Sustained Tensile Loading. Composites Technology Review, Vol. 6, No. 26.
18. Tunik, A.L. and Tomashevskii, V.T. (1974). Mekhanika Polimerov, Vol. 7, pp 893.
19. Weidmann, G.W. and Ogorkiewicz, R.M. (1974). Composites, Vol. 5, pp. 117.
20. Bocker-Pedersen, O. (1974). Journal of Materials Science, Vol. 9, pp. 948.
21. Findley, W.N. (1960). Mechanism and Mechanics of Creep in Plastics. SPE Journal, Vol., 16, No. 1, January 1960, pp. 57–65.

22. Findley, W.N. (1987). 26-Year Creep and Recovery of Polyvinyl Chloride and Polyethylene. *Polymeric Engineering and Science*, Vol. 27 No. 8, pp. 582–585.
23. Holmes, M. and Rahman, T.A. (1980). Creep Behavior of Plastic Box Beams. *Composites*, pp. 79–85.
24. Brinson, H.F., Griffith, W.I., and Morris, D.H. (1980). Creep Rupture of Polymer-Matrix Composites. Fourth SESA International Congress on Experimental Mechanics, Boston MA, pp. 329–335.
25. Hiel, C.C., and Brinson, H.F. (1983). The Nonlinear Viscoelastic Response of Resin Matrix Composites. *Composites Structure 2*, Proc. The Second International Conference on Composites Structures, Paisley, Scotland, pp. 271–281.
26. Dillard, D.A., and Brinson, H.F. (1983). A Numerical Procedure for Predicting Creep and Delayed Failures in Laminated Composites. ASTM STP 813, T.K.O'Brien (Ed.), ASTM, Philadelphia, pp. 23–37.
27. Eggleston, M.R. (1994). The Transverse Creep and Tensile Behavior of SCS-6/Ti-6AL-4V Metal-Matrix Composites at 482°C. *Journal of Mechanics of Composite Materials and Structures*, Vol. 1(1), pp. 53–73.
28. Huang, J.S. and Gibson, L.J. (1990). Creep of Sandwich Beams with Polymer Foam Composites, *ASCE Journal of Materials in Civil Engineering*, Vol. 2(3), pp. 171–182.
29. Beckwith, S.W. (1984). Creep Behavior of Kevlar/Epoxy Composites. Proc. 29th SAMPE Symposium, pp. 578–591.
30. Krisnaswamy, P., Tuttle, M.E., Emery, A.F., Ahmad, J. (1991). Finite Element Modeling of Time Dependent Behavior of Nonlinear Ductile Polymers. *Plastics and Plastic Composites*, MD-Vol. 29, ASME, NY, pp. 77–99.
31. Chen, S., and Lottman, R.P. (1991). Buckling Loads of Columns Made of Viscoelastic Materials. *Proceedings ASCE Mechanics, Computing in 1960's and Beyond*, H.Adeli, and R.L.Sierakowski (Eds.), pp. 691–695.
32. Ueng, C.S. (1991). The Elastic Stability of the Laminated Composite Columns. Proc. *Proceedings ASCE Mechanics, Computing in 1960's and Beyond*, H.Adeli, and R.L.Sierakowski (Eds.), pp. 971–974.
33. Vinogradov, A.M. (1989). Long-term Buckling of Composite Columns. Proc. *ASCE Structures Congress*, San Francisco, CA, pp. 536–545.
34. Slattery, K.T. (1994). Mechanistic Model of Creep-Rupture Process in Filamentary Composites. Proc. 3rd *Materials Engineering Conference*, ASCE, Infrastructure, New Materials and Methods of Repair, K.D.Basham (Ed.), San Diego, CA, pp. 215–222.
35. Mosallam, A.S., and Bank, L.C. (1991). Creep and Recovery of Pultruded FRP Frame. Proc. *ASCE Advanced Composite Materials in Civil Engineering Structures*, S.L.Iyer, and R. Sen (Ed.), Las Vegas, NV, pp 24–35.
36. Mosallam, A.S., and Chambers, R.E. (1995). Design Procedure for Predicting Creep and Recovery of Pultruded Composites. Proc. 50th Annual Conference, Composites Institute, The Society of Plastic Industry, pp. 6C/1–13.

STUDY OF SLIDING FRICTION AND WEAR PROPERTIES OF BISMALIMIDE AND ITS COMPOSITE AGAINST AL

Qu Jianjun¹, Luo Yunxia², Zhang Zhiqian¹, Qi Yulin¹ and Li Xiaoguang¹

1 Harbin Institute of Technology, Harbin, CHINA, 150001

2 Harbin University of Science And Technology, Harbin, CHINA, 150076

SUMMARY: Bismaleimide is a kind of thermosetting resin developed in 1970s, it has got the wide application in engineering field and aviation technology. However, its friction and wear properties, such as the influences of inorganic packings on its tribological characteristics, are not yet reported in current references. In order to develop a particular organic frictional material, a new bismaleimide was chosen. Under test, it was discovered that dry frictional coefficient of bismaleimide was higher but decreased with time and adhesive wear occurred between the bismaleimide and some metals. For the sake of improving its tribological characteristics, three kinds of inorganic fillers, namely CuO, Sillimanite and Wollastonite, were chosen as frictional modifier. The influences of the concentration of these fillers and the size of Sillimanite and wollastonite on sliding frictional properties of bismaleimide against hard AL (LY 12) were studied respectively with a ring-on-ring tribological machine and the modified mechanisms of these fillers were investigated primarily.

KEYWORDS: CuO, sillimanite, wollastonite, bismaleimide, friction material

INTRODUCTION

The friction and wear properties of polymer-based composite filled by inorganic packings have been studied frequently by scholars in tribology field. The fillers such as metal powder, oxide and other inorganic chemical compounds have been studied carefully, while the study on some natural mineral as filler is seldom done. The study on polymer has been mainly focused on thermoplastic polymers[1-5] such as HDPE, PTFE, PI, PA11 and PEEK, while the study on other kinds of polymers, especially thermosetting polymer is hardly done[6-7]. There are many opinions on the mechanism of friction and wear effects of fillers on polymers, but consistent conclusion has not been achieved until now[8].

Bismaleimide which is a new kind of thermosetting resin, has got wide applications in aviation and spaceflight industry field at first, and then, widely used in civil industry as engineering plastic with high temperature resistance in recent years. It has not only the superior properties, such as resistance to high temperature and humidity, high modulus of elasticity, moderate hardness, and high adhesive reliability to inorganic materials, but also it can be produced by the forming process similar to that of epoxy resin, which makes its production costs come down. In particular, it's supposed to be an adhesive to organic frictional materials[9], because its temperature resistance is superior to that of phenolic resin.

However, there is little research done in the field of friction and wear characteristics of BMI, especially the field of inorganic fillers; influence on its tribological characteristics.

In order to develop a special organic frictional material, a new kind of bismaleimide was selected as adhesive. The experiment on pure BMI polymer showed that its dry frictional coefficient was high, but the coefficient decreased with time. Furthermore, adhesive wear occurred between the bismaleimide and dual metals. Therefore, three kinds of inorganic fillers, namely CuO, sillimanite and wollastonite, were chosen as frictional modifier. Sillimanite and wollastonite which is abundant is two kinds of natural mineral fillers with low price. When BMI is filled by them, the composite's cost is lowered while properties improved. CuO is kind of inorganic chemical compound which has been studied carefully. It has been found out that when CuO is filled in thermoplastic polymer, the wear resistance is raised, so is their frictional coefficient[4-5]. But the influences when BMI is filled by CuO, are not yet reported in current references.

EXPERIMENT

Sample Preparation

Sample ingredient: three portions of sillimanite powder with the size of 100#, 200# and 300# respectively, main ingredient: AL₂O₃ and SiO₂, hardness: 6.5-7.0 Mohs; three portions of wollastonite powder with the size of 400#, 800# and 2000# respectively, main ingredient: SiO₂ and CaO, hardness: 4.5 Mohs; hardness of CuO: 3-3.5 Mohs; bismaleimide HF-9401 (BMI), hardness: HRM122

Sample making: These powder of wollastonite and sillimanite was rinsed with the mixture of alcohol and acetone, then was dried out. In proportion as weight, take 100 portions of BMI, 5, 10, 15, 20 portions of four concentrations of sillimanite respectively, 50, 100, 200 portions of three concentrations of wollastonite respectively, and mix them according to different size of powder, then using pressing method, produce biphase system circular BMI sample, the size of which is . Polish the top and bottom surface of the sample with 600# and 800# water sand paper respectively, rinse it with alcohol repeatedly, then finish making sample by drying it.

Experiment Procedure

The sliding test was accomplished with a ring-on-ring tribological machine MPX-200. The upper ring which rubbed against the composite sample was hard AL (LY12). Its size was with two edge sides polished with 800# water sand paper. It had been rinsed and dried before the experiment. The vertical pressure: 60N. The speed of main shaft: 370rpm. The duration of experimental time: 30min. Wear volume of the sample was measured by the weight difference before and after experiment, with precision of 0.0001g. The unit of wear rate is g/Nmm in this paper. The experiment was done in a state of dry friction under indoor temperature.

RESULTS AND DISCUSSIONS

Influence of CuO on the Friction and Wear Properties of Bismaleimide

As fig.1 shows, when BMI was filled by CuO, the frictional coefficient between the binary composite and AL ring tended to rise with the increasing of CuO weight fraction, while the

wear rate between them tended to decrease. But there was little influence on the wear rate when the concentration of CuO was over 25 parts. The cause of the phenomenon referred above is that CuO filled in BMI promotes the formation of the transfer film on the AL, as a result, the adhesive wear tendency liable to happen between pure BMI and AL ring declines. Under test, observing the surface appearance of AL ring which had rubbed against BMI which was filled by CuO, a layer of well-distributed black transfer matter which couldn't be cleaned up by absorbent cotton could be found. This shows transfer film has been formed and adhered tightly to AL ring. It's the protection of the transfer film on AL ring that make AL ring's wear rate drop. The wear resistance of the transfer film restrains the wear caused by the matter transfer on the composite's surface, and thus, decrease its wear rate. Friction and wear takes place between BMI's composite and the transfer film, the friction and wear model of which is shown in Fig.2, and there is strong molecular force between them. Furthermore, because CuO fraction is a substance with hardness, when it is filled in BMI, the mechanic meshing effect between the frictional pairs is strengthened. In conclusion, the increasing of both the mechanic effect and molecular force between the frictional pairs leads to the rise of friction coefficient between the composite and AL ring.

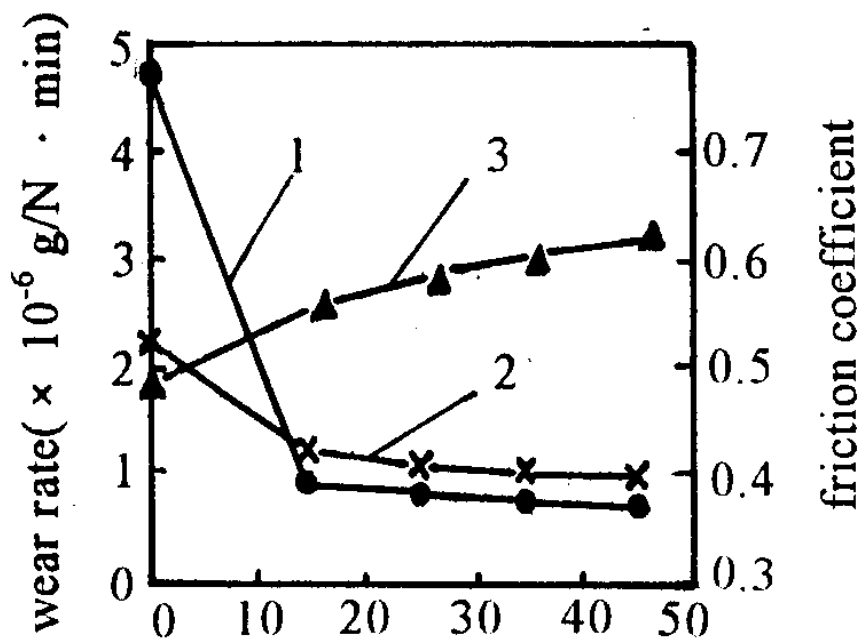


Fig. 1: Variation of wear rate and friction coefficient of BMI composite and AL ring with CuO weight fraction 1.BMI composite 2.AL ring 3.friction coefficient

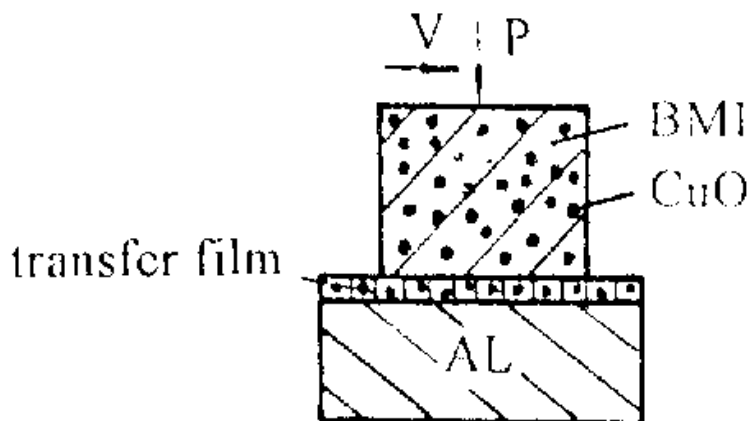


Fig.2 The sliding model of BMI composite filled by CuO against AL.

The effects of CuO have also been verified by Bahadure[4-5]. They found through experiment, the friction coefficient and wear resistance of thermoplastic polymer wear raised when CuO was filled in the polymer. The study in this paper shows the effects of CuO may be similar to different kinds of polymer.

Influence of Wollastonite on the Friction and Wear Properties of Bismaleimide

As Fig.3 shows, when BMI was filled by wollastonite powder, the frictional coefficient of BMI drops with the increase of wollastonite concentration. In addition, the antifriction effect of wollastonite on BMI was different according to the size of wollastonite powder. The size is larger, the decline of the friction coefficient is less.

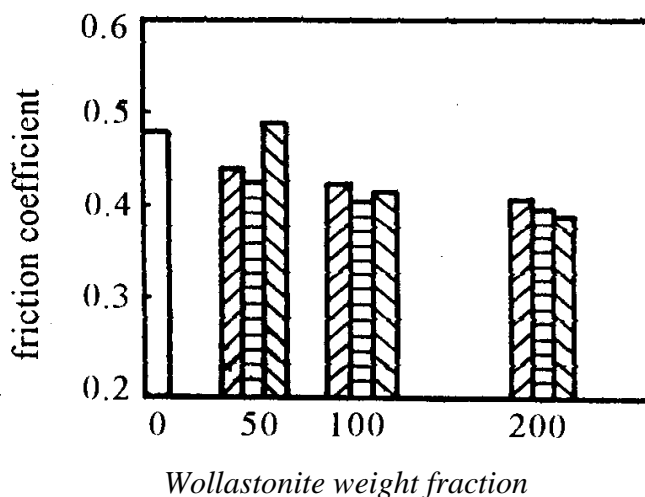


Fig.3 Variation of friction coefficient of BMI composite with wollastonite weight fraction.

□ pure BMI , ▨ 400[#]wollastonite
 ▩ 800[#], ▧ 2000[#]

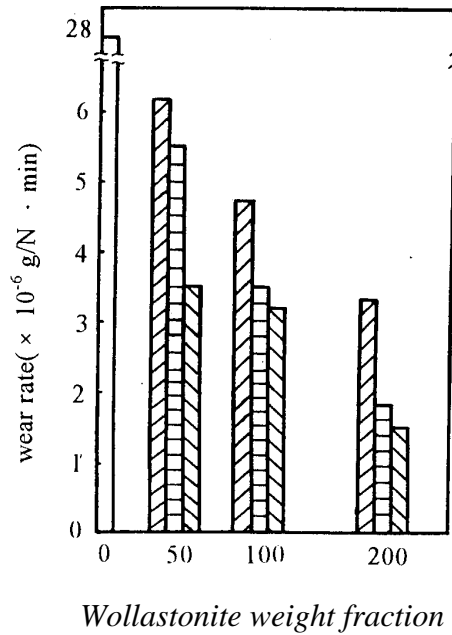


Figure 4: Variation of wear rate of BMI composite with wollastonite weight fraction

□ pure BMI , ▨ 400[#]wollastonite
 ▤ 800[#], ▩ 2000[#]

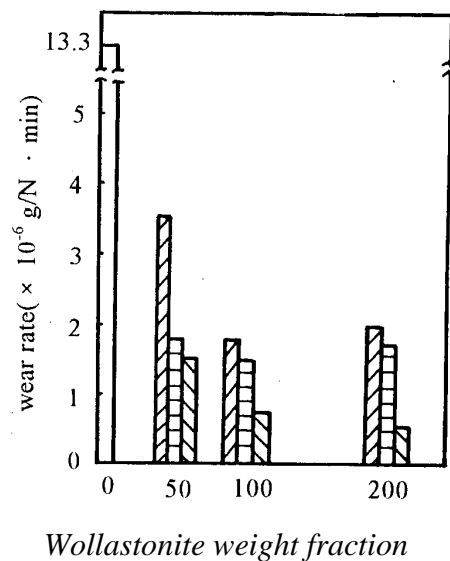


Figure 5: Variation of wear rate of AL ring with wollastonite weight fraction

□ pure BMI , ▨ 400[#]wollastonite
 ▤ 800[#], ▩ 2000[#]

As Fig.4 and Fig.5 show, when wollastonite powder was filled in BMI, the wear rate of BMI and the AL ring dropped obviously. Moreover, the antifriction effect was raised with the increasing concentration and decreasing size of wollastonite powder. But it's difficult for the wollastonite powder to be well distributed when it is ground mixedly, if the size of the

powder is too small. The wear resistance effect of wollastonite powder thanks to the inorganic filler's short-fiber structure with length and diameter in a ratio of 5:1-15:1. It's main ingredient is CaO and SiO₂. As referred above, the rub of pure BMI against AL ring is in the form of adhering transfer film which is not firm. When wollastonite powder is filled, in the break strength of the composite is raisen. In addition, the slender and hard particles of wollastonite cause polishing effect, which makes the oxidic film on the surface of AL ring peeled off and fresh surface exposed. CaO and SiO₂ which are composed of wollastonite can promote the formation of transfer film and the film's adherence of AL ring, which makes the film firm[8]. The wear of AL ring is allieviated because the sliding friction is between the surfaces of the transfer film and BMI's composite. Moreover, the wear resistance of the composite is raisen because the film which is firm and hard to wear away, prevent the further wear of the composite. Observed after experiment, the analysis above can be confirmed by the brown transfer film on the surface of AL ring and such smooth frictional surface appearance of BMI's composite as Fig.6 shows.

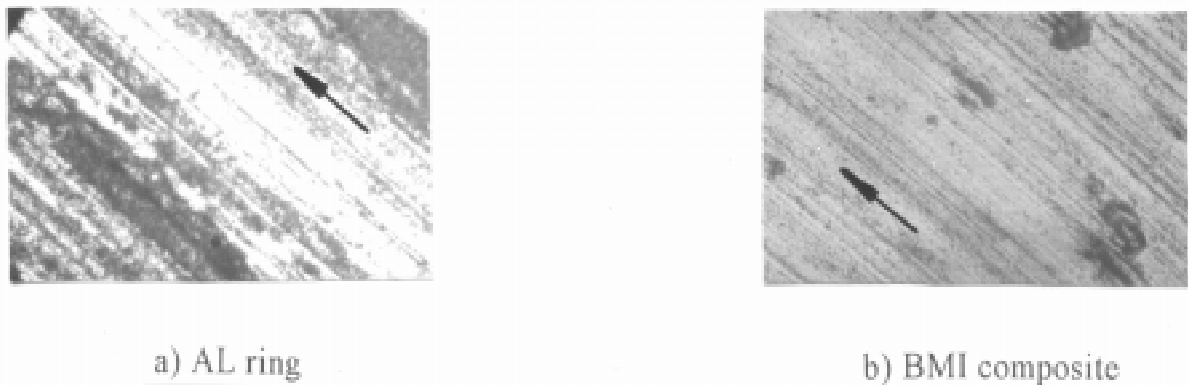


Fig. 6: Optical micrographs of wear of BMI composite and AL ring surface (arrow indicating sliding direction x500)

Influence of Sillimanite on the Friction and Wear Properties of Bismaleimide

As shown in Fig.7, the frictional coefficient of the compound system was raised with the increasing of concentration and size of the sillmanite powder filled in BMI. Fig.8 shows the variation of the frictional coefficient of BMI's compoite filled by 200# sillimanite with time, from which we learn the fact that the frictional coefficient of pure BMI increases first with time to a high value, then decline gradually and the variation is not stable. When sillimanite was filled, the frictional coefficient in a stable state was raised, the tribological characteristics were improved. The frictional coefficient increased with time and remained steady when it had risen to a high value. However it took longer to reach the stable state of friction if the concentration of sillimanite increased.

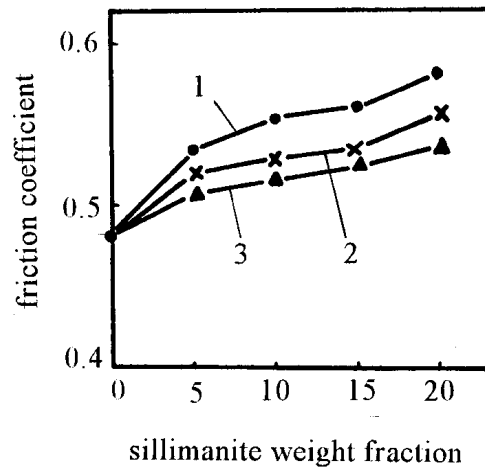


Fig. 7: Effect of sillimanite weight fraction on friction coefficient of BMI composite.
 1. 100[#] sillimanite 2. 200[#] sillimanite 3. 300[#] sillimanite

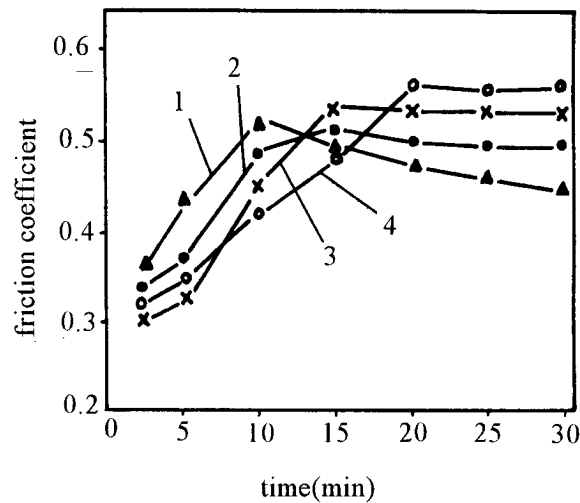


Fig. 8: Variation of friction coefficient of BMI composite filled by 200[#] size sillimanite with time. 1. Pure BMI 2. BMI + 5% sillimanite 3. BMI + 10% 4. BMI + 15%

The main reason of the phenomenon referred above is, if sillimanite which is rigid particle with high hardness filled in BMI, it is analogous to scatter relatively hard particles to soft basic body, therefore, sillimanite particles on sliding surface do great damage to the transfer film which influence the frictional stability. The sliding model is shown in fig.9. In addition, the uneven surface of the composite which is due to the different wear volume between the soft and hard materials strengthens mechanic meshing effect when rubbed against AL ring. Consequently, the frictional coefficient of BMI's composite raises, and then tends to be stable. The wear resistance of the composite is raised. Furthermore, as fig.10 shows, the wear rate is less, the rise of wear resistance is more remarkable, with the increasing of sillimanite concentration and its size. But it's not suitable if the concentration of sillimanite is too much, otherwise, it'll take longer for frictional coefficient to reach stability and the wear of dual AL ring will be grave. Under test, it's found if the content of sillimanite is over 15%, the wear of AL ring is serious, and the wear rate of AL ring against BMI filled by sillimanite is high than

that AL ring against pure BMI. Therefore, if the frictional material against AL ring is to be made, the content of sillimanite in the material is not suitable to be over 10%.

The main reason that sillimanite can improve BMI's composite's properties of wear resistance is analysed as the following. Sillimanite, the crystalline grain of which is needlelike has high ability to adhere to BMI resin and the adhesive strength is fairly high. The sillimanite particles on the sliding surface sustain the load in the process of friction, which decreases alleviates the wear of the basic body. In addition, it will cost much frictional work to remove the sillimanite particles from basic body. Therefore, the wear resistance of BMI's composite filled by sillimanite is raised and the effect is more notable with increasing of the concentration and size of sillimanite. In the process of friction, because sillimanite is harder than AL, its particles which have been filled in BMI on the sliding surface destroy the formation of the transfer film and its protective effect. Moreover, grave ploughing wear occurs on the relatively soft basic body of AL ring, which makes its wear rate increase.

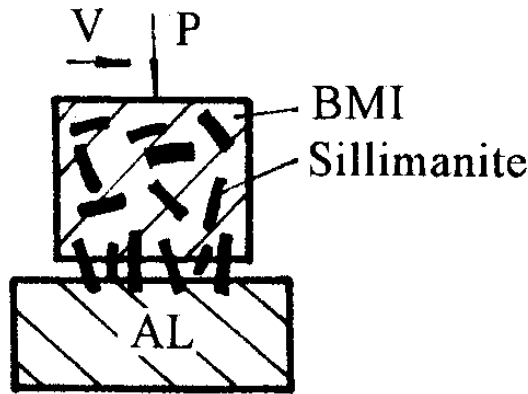


Figure. 9: The sliding model of BMI composite filled by sillimanite against AL.

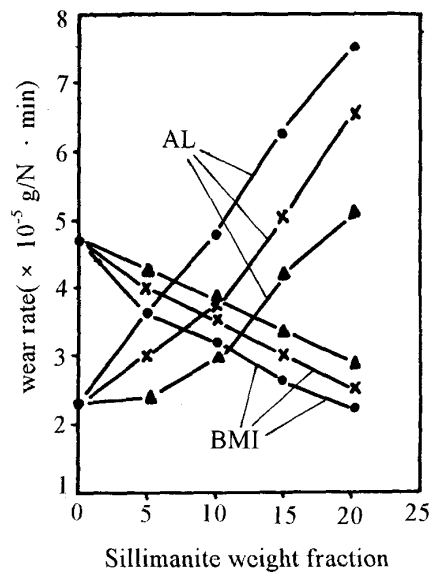


Fig. 10: Variation of wear rate of BMI composite and AL ring with sillimanite weight fraction. ● 100[#] sillimanite, × 200[#], ▲ 300[#]

CONCLUSION

1. Wollastonite, CuO and sillimanite, all of them can improve the wear resistance of BMI, and they are listed in an order from strong effect to weak one. CuO and sillimanite can raise the frictional coefficient of BMI, and sillimanite can also improve BMI's tribological characteristics.
2. The fact that wollastonite and CuO can improve the wear resistance of BMI and AL ring, mainly relates to the protective transfer film. Cao and SiO₂ in both CuO and wollastonite can promote the formation of the film, which makes its adhesive strength to basic body rise. Sillimanite can improve the wear resistance of BMI. Its mechanism is that the load is sustained by particles with high hardness, consequently, the wear of BMI is prevented. However, the wear of AL ring is raised because ploughing effect of hard particles destroys the formation of transfer film.
3. The frictional coefficient and wear resistance of BMI and AL ring is raised with the accumulation of CuO's concentration, while the rise slows down when the concentration is over 30 portions. As far as wollastonite is concerned, the wear resistance of BMI and AL ring is raised while the frictional coefficient between them declines with the increasing concentration and decreasing size of wollastonite. Moreover, the difference of the influence is little when the concentration is over 100 portions. The influence is almost identical when the size of wollastonite is 800# and 2000#. However, it's suitable to choose the size of 800# when well-distribute extent is taken into account. although sillimanite which is inorganic particles with high hardness can improve the wear resistance and frictional coefficient of BMI with the increasing of its concentration and size, the wear of the AL ring against BMI filled by sillimanite is aggravated. Therefore, its concentration should not exceed 10 portions and it's suitable to choose its size of 200#.

REFERENCES

1. B.J.Briscoe, A.K.Podosian and D.Tabor, The friction and wear of HDPE: the action of lead oxide and copper oxide fillers, wear, Vol.27, 1974, pp.19-34.
2. K.Tanaka and S.Kawakami, Effect of various fillers on the friction and wear of PTFE-based composites, wear, Vol.79, 1982, pp221-234.
3. K.Friedrich, Sliding wear performance of different polyimide formulations, Tribol. Int.,22(1989),pp.25-31.
4. S.Bahadur and D.Gong, The role of copper compounds as fillers in the transfer and wear behavior of PEEK, wear, 154(1992), pp.151-165.
5. S.Bahadur and D.Gong, The role of copper compounds as fillers in the transfer film formation and wear of nylon, wear, 154(1992), pp.207-223.
6. S.K.Rhee, Friction properties of a phenolic resin filled with iron and graphite-sensitivity to load, speed and temperature, wear, 28(1974), pp. 277-281.

7. Qu Jianjun, Zhang Yafeng, Zhang Zhi qian and Qi Yu Lin, Effect of two kinds of inorganic fillers on the friction and wear properties of sillmanite, *Mechanic Engeering, appending magazine* (1995), pp.11-12.
8. S.Bahadur and D.Gong, The action of fillers in the modification of the tribological behavior of polymers, *wear*, 158(1992), pp. 41-59.
9. Bai Yongping, Study of composite modified by sillimanite-based resin, [academic paper], Harbin: Harbin Institute of Technology.
10. S.Bahadur and D.Gong The role of copper compounds as filers in the transfer and wear behavior of polyetheretherketone. *wear* 154(1992), pp. 151-165.
11. Fiduothic. *Modern frictional materials*, translated by Xu Run, Bei Jing: Metallurgy industry press, 1983, pp. 150-200.

SUBJECT INDEX

2D-fibre architecture	1	compressibility of fibres	255
3D axisymmetrical problem	662	compression moulding	313
3-D woven preform	754	computer simulation	370
acoustic emission	833	concentrated fibre suspension	255
acoustic sensing	833	conductivity	824
adhesion mechanisms	691	consolidation	139, 237
aerospace structures	271	continuous fibre reinforced thermoplastic	352
amines-containing catalyst	615	controllability of fibre orientation	200
APC-2 towpreg	92	cooling rate	352
aqueous foam	246	co-reactants	181
aspect ratio	608	cowoven fabric	459
autoclave molding	217	creep	844
automated manufacture	474	creep constitutive equation	816
automation	85	creep of ceramics	633
azo group	537	crosslinking state unhomogeneity	771
benchtop	133	CSTF methodology	691
biaxial extensional flow	400	CuO	856
bisallyloxyimides	181	cure	324
bismaleimide	181, 856	cure cycle	171
bismaleimide (BMI)	779	cure process	217
blends	779	cure shrinkage	171
boric acid	643	cure simulation	422, 528
boron carbide	643	curing shrinkage	324
boron carbide fibers	643	curing, heat generation	190
bridged winding	288	cycle time	37
CAE system	190	damage	343
carbon	389	damage initiation and progression	431
carbon black	537	debonding	712
carbon fibre	237, 578, 615, 741, 754	debonding energy in shear	133
carbon/epoxy composite	731, 740	deep drawing	482
carbon/epoxy laminates	46	degree of crystallinity	92
carbon-carbon composites	747	degree-of-cure	123
carbothermic reduction	643	design for manufacture	103
casket molding techniques	75	design of experiments	92
cellulose	598	direct sizing	681
cellulose fibers	643	discontinuous aligned fiber composites	379
ceramic fibre	587	discontinuous fibres	255, 431
chemorheology	64	disperse planar fibre networks	255
chirped gratings	833	dispersibility	537, 546
classical laminate theory	559	distortion	302
CO ₂ laser	343	distribution model	608
coating	652	double belt press	210, 681
coefficient of friction	808	drape simulation	411
cold	623	drilling	343
co-mingled materials	313	DSC	64
commingle	459, 464	dual matrix composites	671
commingled fibres	139	dynamic mechanical analysis	681
composite fabrication and testing	75	dynamic testing	633
composite processing	452	E-glass woven fabric reinforced vinyl ester	
composites	379	composites	798
composites manufacture	302	elastic stress	255
composites processing	360	electron beam-cure	271
		EMI	824
		energy dissipation	681

epoxy	578	GRP	324
epoxy composites	271	GRP-phenolic	64
epoxy resin	771		
epoxy-modified thermoplast	263	heat sealing	547
evolution	731	heat transfer	123
experimental design techniques	313	Herschel-Bulkley-Model	379
		high temperature	587
fabric	441	Hi-Nicalon	587
fabric draping	411	hot drape forming	559
fabric reinforced polyamide 6.6	681	hybrid experimental-numerical approach	190
fabric shear	411	hybrid laminated materials	200
failure criteria	701	hygrothermal property	771
FEM	343, 662		
FEM modelling	701	image processing	519
fiber deformation	227	impregnation	210, 389
fiber optic sensor	833	initial deformation	190
fiber reinforced composite	246	initiation	731
fiber surface plasma treatment	754	injection	389
fibres density	55	injection moulding	519, 808
fibres hybrid	459	injection speed	519
fibres orientation	465, 473	injection temperature profiling	37
fibres orientation distribution	519	in-plane shear strength	263
fibres rearrangement	255	interface	578, 662, 798
fibres reinforced plastic composites	474	interfacial bond	623
fibres slippage	255	interfacial microdebonding	754
fibres suspensions	465	interfacial micro-mechanical properties	747
fibres/matrix interface	723	interfacial normal strength	652
fibres-bundle	113	interfacial shear strength	671, 712, 723, 754
fibres-matrix adhesion	263	interlaminar shear strength	11, 46, 92, 754
fibres	293, 598, 633	interlayer	731
fibrous composites	712	internal heating	161
fibrous particles	500	internal pressure	816
filament winding	113, 288, 360	internal strain	217
finish	681	interphase	652, 662, 741
finite difference method	528	intersection angle	411
finite element analysis	103, 547, 559	intra-ply shearing	559
finite element method	712	ion viscosity	217
finite element model	123		
finite element thermal analysis	150	Jeffrey-equation	379
finite elements	352		
flow simulation	441	Kelly-Tyson model	691
fracture mechanisms	11		
fragmentation test	671, 691	laminate tensile properties	37
friction	808	laser drilling	343
friction material	856	laser processing	701
FRP	844	liquid composite molding	441
FRP pipe	816	liquid crystal behavior	790
		liquid packaging bag	547
gel permeation chromatography	313	long fiber	389
GFRP	343	low temperature	623, 844
GFRP laminate	217	lubricated squeeze flow	400
glass	389		
glass mat	482	manufacture	293
glass mat thermoplastic	400	manufacturing	279
glass mat thermoplastics	313	manufacturing science	210
glass reinforced plastic	324	material modelling	333
GMT	400, 465	matrix crack	623
goodness-of-fit	608	matrix impregnation	246
gratings in fibers	833	matrix morphology	723
grid method	547	mechanical alloying	370

mechanical properties	279, 293, 301, 559, 587	polystyrylpyridine	1
mechanical property evaluation	75	porosity calculation	500
melt	113	post-cure	324
metal composites	293	powder coating	237
microcrack	731	powders	85, 389
microdroplet test	671	power law equation	816
micromechanical model	662	PPE	824
microperforation	701	PPS	723
microscopy	681	preform	411, 441
microstructure	587	preform permeability measurement	20
microwave heating	37	prepolymer	491
mixtures	500	prepreg	46, 237
mode I interlaminar fracture toughness	798	prepreg aging	422
modelling	510, 598	prepregging process	246
modified toughness	771	printed wiring board	343
mold filling simulation	27	process feasibility	491
molding	389	process simulation	333
Monte-Carlo simulation	712	process visualization	55
morpholgy	46	process-combination	113
mould fill rate	55	processing	161
moulding thickness	519	processing parameter	491
		production of boron carbide fibers	643
nodal control volume	150	progressive opening of multiple injection ports	27
nonlocal constitutive equations	465	properties	491
non-newtonian	465	property determination	133
numerical model	528	pultruder	133
nylon 6	237	pultrusion	113, 123, 139, 491
		push out test method	747
on-line (in-situ) consolidation	92	pyrolysis	615
on-line impregnation	113		
optical fiber strain sensor	217	radical polymerization	537
organic solvents	643	raman spectroscopy	598
		rayon	615
packing	500	reactive solvent	263
part/tool interaction	302	reinforcement deformation	103
peek	459	reinforcements	441
PEEK	723	residual strain	217
PEK-matrix	379	residual stresses	171, 360, 662
permeability	1, 227, 441	residual stresses from processing	431
phase separation	263	resin cure	150
phenolic resole resin	64	resin preheating	37
plasma polymerisation	691	resin transfer moulding	1, 11, 20, 27, 37, 46, 55
plastic film	547		75, 227
ply consolidation	474	resistance heating	161, 528
PMC	824	rheology	400, 465
poly(aryl ether ketone)s synthesis	790	ribbon	85
polycarbonate	399	robot	85
polycarbosilane	615	robotic end-effector	474
polycondensation	1	roll forming	200, 352
polyethylene fibre	279	RTM	64, 441
polyimides	85	rule of mixtures	559
polymer blends	263		
polymer composites	227, 844	sample size	608
polymer processing	20	sandwich materials	313
polymerization	171	segregation	255
polymer-solution infiltration	615	semi-IPN	779
polyphenylene oxide (PPO)	779	shaker ball mill	370
polyphenylene sulfide	452	shape fixability	352
polypropylene	400, 519	shear failure	701
polystyrene	491	shear strain	731

sheet forming	482	thermoplastic resin	246
sheet moulding compound	510	thermoplastics	465
short carbon fiber reinforced	452	thermoset	360
short fibre	519	thermotropic liquid crystal copolyester	741
silane coupling agents	798	thermotropic liquid crystal polymer	790
silicon carbide	587, 633	thick composites	422
sillimanite	856	thick laminates	161
single fibre fragmentation test	578	three dimensional woven structure	747
slippage flow	190	three-point bending	681
SMC	200	time dependency	731
SMC compression molding	190	titanium oxide	537
soaking method	643	towpreg	237
springforward	352	transcrystallinity	723
squeeze flow	465, 510	transparent tooling	55
SRIM	441	TTSP master curve	816, 823
stability of crack propagation	798	tube	293
steel fiber	824	tubes	324
strain	547	Tyranno Lox-E	587
strain compensation	833	Tyranno Lox-M	587
strain field measurements	661		
strength and reliability	712	ultimate tensile strength	379
stress	547	ultrafine silica	537
stress relaxation	360		
structural reaction injection molding	431	viscoelastic deformation	824
surface grafting of polymer	537	viscoelastic materials	844
suspension impregnation	452	viscoelasticity	360, 598, 633
sustained load	844	viscosity	1, 64
		visualized mold filling experiment	27
tackified textile fabrics	75	void content	92
tape	85	voidage	313
temperature compensation	833	voids	11, 46
tensile creep	816		
tensile strength	623, 701, 712	warpage	302
theory of elasticity	662	wavy fiber	623
thermal expansion	171	wear	808
thermal quench	37	Weibull distribution	712
thermal resistant material	779	Weibull fibre strength parameters	578
thermally stable polyimides	181	wetting	237
thermoforming	333, 379	whiskers	608
thermomechanical modeling	431	winding angle	288
thermoplastic	237, 389, 482	winding parameters	808
thermoplastic composite materials	808	winding rate ratio	288
thermoplastic composites	92, 139, 210, 701, 723	wollastonite	856
thermoplastic filament winding	808		
thermoplastic matrix	113	X-ray photoelectron spectroscopy.	691

AUTHOR INDEX

ANDREWS, Paul	411	GAO, Wen	754
AOYAMA, Eiichi	343	GASSAN, Jochen	762
ARAKI, Shigetoshi	816	GAUVIN, R.	441
AVVA, V. Sarma	75	GAVRILOV, Dmitri	370
BAI, Y.L.	798	GENIDY, Mohamed S.	171
BAKIS, Charles E.	161	GIBSON, A. Geoffrey	139, 400, 465
BANHEGYI, G.	798		510
BANTELL, Frank J.	161	GODA, Koichi	712
BATHIAS, C.	798	GOODWIN, A.A.	11, 46
BECK, A.	691	GRENOBLE, R.W.	85
BEEHAG, Andrew	723	GROENEWALD, W.H.	324
BEQUIGNAT, R.	798	HAHN, H. Thomas	422
BERGER, M.H.	587	HAKOTANI, Masahiro	200
BERSEE, H.E.N.	400	HAMAD, Wadood Y.	598
BHATTACHARYYA, D.	352	HAMADA, Hiroyuki	190, 798
BLAND, J.H.	400	HARMIA T.	113
BLEDZKI, Andrzej K.	762	HAUPERT, F.	808
BOHNE, Y.	643	HAYAKAWA, Yuuzou	200
BROOKS, R.	313, 519	HE, Yingchu	615
BROUGHTON, W.R.	798	HENRIKSSON, Anders	833
BROWN, James R.	64	HERSZBERG, Israel	474
BUNSELL, A.R.	587	HILL, D.J.	37
BUSHBY, R.S.	293	HIRAI, Y.	798
CAIN, T. A.	313	HIROGAKI, Toshiki	343
CAMPBELL, James R.	75	HOA, S.V.	798
CANTWELL, W.J.	798	HOCHET, N.	587
CHALLIS, Karen E.	64	HORRIGAN, D.P.W.	352
CHAN, Tze-chung	779	HOWE, C.A.	11, 46
CHAO, Shen	771	HSU, C.Y.	519
CHEN, A.S.	293	HU, Xiaobin	20
CHEN, Chin-Hsing	491	HUANG, Xiaozhong	615
CHEN, Xiangbao	459	HUANG, Yudong	747, 754
CLYNE, T.W.	701	HUH, Hoon	422
CRASTO, Allan S.	271	HUI, David	844
DAO, B.	181	IGARASHI, Kazuo	824
DENG, Shiqiang	578	INOUE, Hisahiro	343
DIALLO, M.L.	441	IWAMOTO, Masaharu	816
DOLLHOPF, Volkmar	1	JIANG, Bing	608
DONG, Y.J.	798	JIANG, Jianye	217
DRZAL, L.T.	798	JIANG, Jixiang	608
DUTTA, Piyush K.	623, 844	JIANG, Yong-Qui	662
DUVALL, Mark S.	389	JOHN, Sabu	474
DYKES, R.J.	352	JOHNSON, D.J.	741
EASON, T.	431	JOHNSON, M.S.	37
ENGEL, Renata S.	528	JOHNSTON, N.J.	85
FENG, Chunxiang	615	JONES, F.R.	691
FENG, Zhihai	754	JOSHI, S.C.	150
FONJALLAS, Pierre-Yves	833	KANG, Moon Koo	27
FRIEDRICH, K.	113, 808	KARGER-KOCSIS, J.K.	798
FU, Huo-Jun	662	KASHIRAMKA, Manoj	246
FUJIHARA, K.	798	KATAYAMA, Shigeki	824
FUKUDA, Takehito	217	KATAYAMA, Tsutao	200, 343
FUNCK, R.	113	KAWATSURA, Kazue	537
FUTAMATA, Keigo	190	KEMPNER, Evan A.	422
FUTASE, K.	547	KETTLE, A.	691

KIM, J.K.	798	OSAKA, Katsuhiko	217
KIM, Ran Y.	271	OUTWATER, John O.	133
KIM, Yeong K.	360	PABIOT, J.	798
KITADE, Shintaro	217	PADMANABHAN, K.	798
KITAHARA, Youji	343	PARK, Joung-Man	671
KONTANI, Yoshikazu	482	PARK, Soo-Jin	569
KOTSIKOS, G.	510	PARK, Won-Bae	569
KRAWCZAK, P.	798	PATON, Rowan	11, 46, 411
KRENKEL, Walter	1	PECK, Rodney A.	474
KUBOTA, Y.	547	PEIJS, T.	263, 652
KURASHIKI, Ken	816	PENG, Ping	615
KUROKAWA, Kazumasa	200	PINTER, S.	798
LACROIX, F.V.	279	POTTER, K.D.	103
LAI, Chyi-Lang	227	QU, Jianjun	856
LAM, Y.C.	150	RADFORD, D.W.	302
LEE, Jae-Rock	569	RAMANI, Karthik	389
LEE, Sang-H	671	RAMMOORTHY, M.	237
LEE, Woo Il	27	REINICKE, R.	808
LENG, Xingwu	288	RENNICK, T.S.	302
LESKO, J.J.	798	RICE, Brian P.	271
LI, Ma	474	RUDD, C. D.	37, 313
LI, Xiadong	615	RUSSELL, John D.	171
LI, Xiaoguang	856	SADLER, Robert L.	75
LIU, Hong-Yuan	578	SAALBRINK, A.	263
LIU, Xiao-Lin	150	SAIDPOUR, H.	798
LIU, Xiuying	615	SANDGREN, Simon	833
LONG, A.C.	313	SARMA AVVA, V.	75
LOOS, Alfred C.	92	SCHREURS, P.J.G.	652
LOPATTANANON, N.	691	SCHULTE, K.	798
LOU, Kuiyang	459	SCHUSTER, Jens	379
LOWE, A.	798	SCOTT, V.D.	293
LUDICK, J.	55	SERVAIS, Colin	255
LUTZ, A.	113	SEZEN, M.	798
MA, Yulu	20	SHAM, M.L.	798
MADHUKAR, Madhu S.	171, 623	SHAW, William J.D.	370
MAESAKA, Toshihiko	816	SHIH, Po-Jen	92
MAI, Yui-Wing	123, 578	SHIMAMOTO, A.	547
MAIER, Martin	333	SHIN, Dong-Woo	671
MÅNSON, Jan-Anders E.	255	SHIN, Franklin G.	779
MAO, T.X.	798	SHINOHARA, Masahiro	200
MARCHELLO, J.M.	85	SHIRAI, Yukio	537
MARTIN, H.-P.	643	SHIVAKUMAR, Kunigal N.	75
MATTHAMS, T.J.	701	SHULTE, K.	279
MAYER, Christoph	210, 681	SHYR, T.W.	741
MEURS, P.F.M.	652	SMIRNOV, V.V.	798
MILLER, A.	139	SOMIYA, Satoshi	824
MÖLLER, Frank	333	STANDLEY, D.	559
MORTON, T.C.	181	STERNSTEIN, S.S.	633
MOTOGI, Shinya	217	ST. JOHN, Nigel A.	64
MÜLLER, E.	643	SUN, Wenxum	747, 754
MUREAU, M.	263	SUN, Y.Q.	731
MUZZY, J.	237	SURATNO, Basuki R.	123
NAITO, Hajime	190	SUZUKI, Y.	798
NAKAMURA, Yasunori	482	TANIMOTO, T.	798
NEITZEL, Manfred	210, 681	TAYLOR, Mark W.	64
NOBE, Hiromichi	343	TIAN, J.	731
OCHOA, O.	431	TOLL, Staffan	255, 465
OGAWA, Keiji	343	TOMKA, J.G.	741
OOSTHUIZEN, J.F.	324	TOWELL, T.W.	85

TOWSE, A.	103	XIE, Bingyuan	452
TRIPATHI, D.	691	XU, D.L.	500
TROCHU, F.	441	XU, Jiarui	452
TSUBOKAWA, Norio	537	YANG, Decai	790
TSUKATANI, Hisashi	217	YANG, Guang	608
TZENG, Nana	389	YANG, H.S.	798
UMEZAKI, E.	547	YE, Lin	123, 578, 723
VERPOEST, I.	798		798
VINOGRADOV, Oleg	370	YOON, Dong-Jin	671
WAKEMAN, M.D.	313	YOSOMIYA, Ryutoku	790
WANG, Ge	615	YOUNG, Wen-Bin	227
WANG, John	411	YU, A.B.	500
WANG, Junshan	747	YUE, C. Y.	798
WANG, Wen-Si	491	YULIN, Qi	856
WANG, Xiaoming	210	YUNXIA, Luo	856
WANG, Youqi	246	ZENG, Hanmin	452
WARREN, R.C.	633	ZHANG, Shanju	790
WEAVER, C.D.	633	ZHANG, Zhiqian	747
WELLER, Steven A.	528	ZHAO, Xun	608
WERWER, M.	279	ZHENG, Yubin	790
WHITE, Scott R.	360	ZHIQIAN, Zhang	856
WISNOM, M.R.	103	ZHU, Bo	459
WO, Dingzhu	288	ZOU, R.P.	500
WU, Zhongwen	790	ZULKIFLI, R.	798
XIA, Zhi-yu	779		